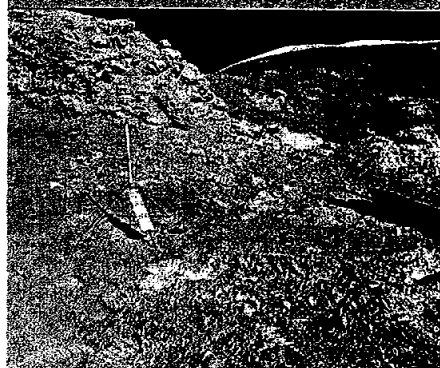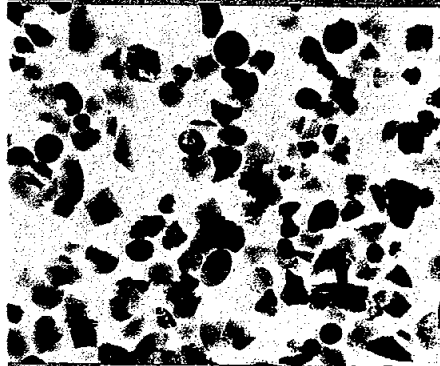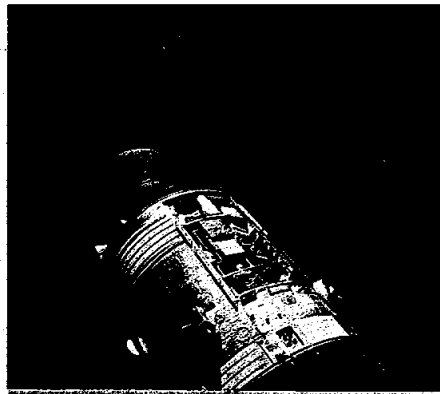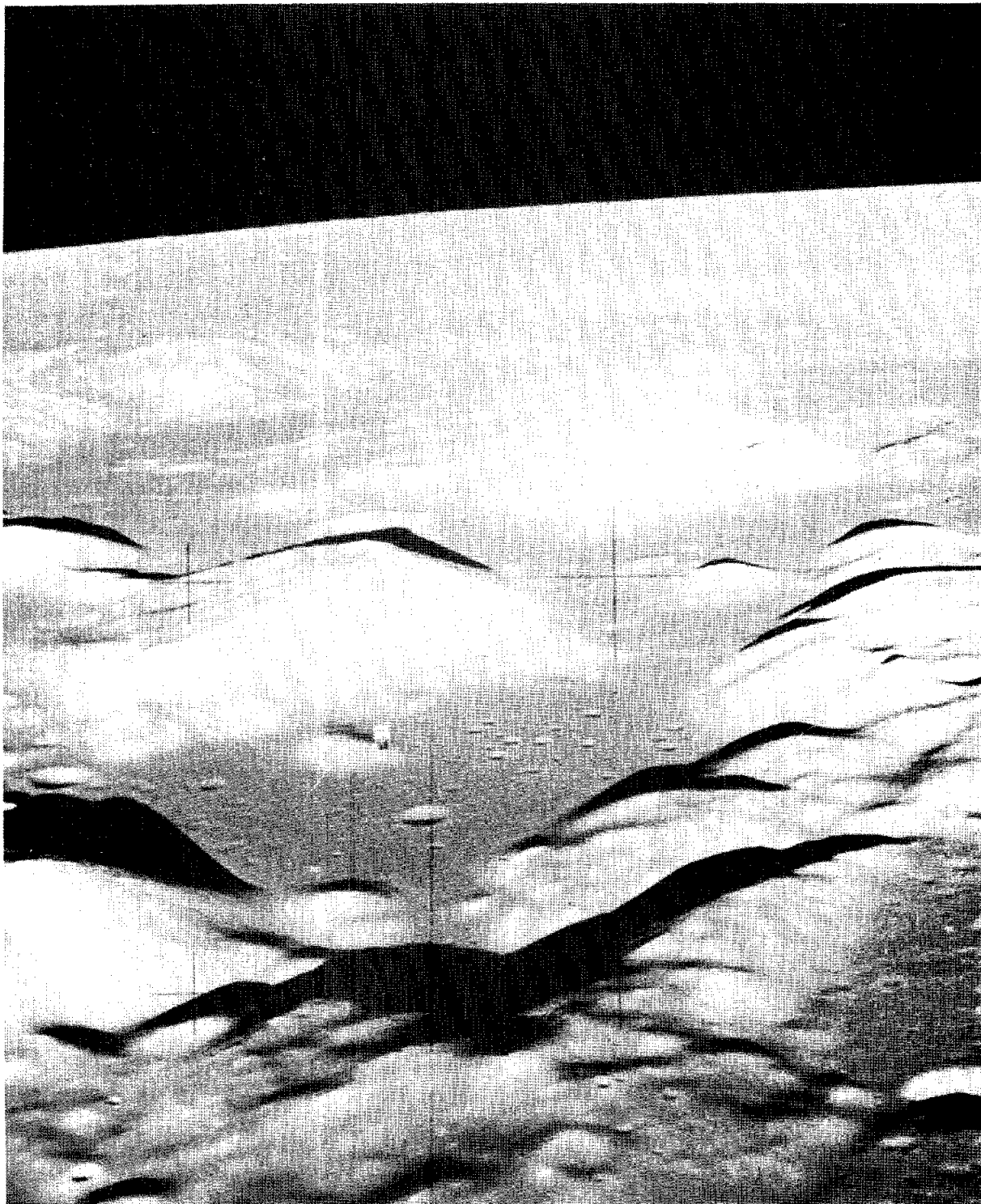# APOLLO 17

Preliminary Science Report

NATIONAL AERONAUTICS
AND SPACE ADMINISTRATION

APOLLO 17 PRELIMINARY SCIENCE REPORT

Apollo 17 command and service module over the Taurus-Littrow landing site.

APOLLO 17

Preliminary Science Report

PREPARED BY

LYNDON B. JOHNSON SPACE CENTER

EDITORIAL BOARD

Cover Photographs: Clockwise from upper right: (1) The command and service module scientific instrument module bay viewed from the lunar module. (2) Photomicrograph of a thin section of the orange soil sample collected at Shorty Crater. (3) Orange soil on the rim of Shorty Crater with the gnomon in the background. The soil consists of small orange glass spheres as shown in the photomicrograph above. (4) Large breccia boulder sampled near the base of the North Massif. The boulder appears to have rolled down the massif and broken into five pieces. The lunar roving vehicle is parked to the right of the boulder.

Foreword

The character of the Apollo 17 mission to Taurus-Littrow was such that it invited superlatives. By almost all measures, it was an immensely successful voyage of exploration: the greatest harvest of new scientific data, the most kilometers traveled on the surface of the Moon, the largest number of scientific experiments performed—both in real time, by a scientist on the surface, and by automatic instrumentation installed and left behind—the longest time spent on and around the Moon, and the greatest amount of lunar samples returned for study in laboratories all over the world. But numerical measures like these, pleasing though they may be to the thousands of us who had some connection with this mission, do not seem an adequate characterization of this sixth and last of the Apollo series of manned lunar landings.

We cannot now be sure how history will assess this extraordinary enterprise. It may be that, from the perspective of decades, the Apollo Program will stand out as the most singular achievement to date in the history of man's scientific and engineering endeavor. From this perspective, seen without hubris, it may be seen that all of us will be remembered for having lived at the time of Apollo. It may be that, in days to come, Apollo will be perceived as a threshold for mankind from the planet Earth.

Dr. James C. Fletcher
Administrator
National Aeronautics and Space Administration

Contents

CONTENTS ix

Introduction

*"There is nothing more difficult to take in hand,
or perilous to conduct, or more uncertain in its success,
than to take the lead in the introduction
of a new order of things."*

Niccolò Machiavelli

As the splashdown and recovery of the Apollo 17 crew marked the end of the Apollo flight program, this final volume marks the end of the Apollo Preliminary Science Reports. From every aspect, Apollo 17 was indeed a fitting capstone to the Apollo missions. Its awesome and magnificent midnight launch, its flawless operation, its 72-hr lunar stay time, its deployment of scientific instrumentation, its return of the richest collection of lunar materials from any lunar site, its orbital science coverage, and its glorious splashdown in the Pacific Ocean surely marked Apollo 17 as the mission most impressively exemplifying the Apollo Program.

The Taurus-Littrow landing site for Apollo 17 was picked as a location where rocks both older and younger than those previously returned from other Apollo missions and from the Luna 16 and 20 missions might be found. For this mission, it was hoped that the discovery of younger basaltic rocks, differing in crystallization age from the 3.2 to 3.7 billion years of previously returned mare basalts, would lead to an improved understanding both of volcanism and of the thermal history of the Moon. Similarly, it was hoped that the discovery of rocks formed earlier than 3.7 to 4.0 billion years ago would lead to further understanding both of the early lunar crust and of material present at the time of the formation of the Moon.

The identification and selection of the landing site resulted from Astronaut Worden's Apollo 15 orbital observations (he noticed dark patterns that looked like cinder cones in the Littrow region of the Moon) and from detailed analysis of the Apollo 15 imagery.

The rim of the Serenitatis basin in the Taurus-Littrow region seemed to have all the elements geologists would want to explore in this final Apollo mission. Cinder cones and steep-walled valleys with large boulders at their base presented the possibility of sampling, at the same location, both young volcanic rock from depth and older mountainous wall material. Thus, the setting for the conduct of the Apollo 17 landing was a unique place in which to carry out many investigations and to return lunar materials that could aid in answering many fundamental questions.

From the standpoint both of geologic features and of samples returned, the Taurus-Littrow region represents the most diverse landing site of the Apollo missions. Returned samples include a variety of mare basalts resembling those of the Apollo 11, 12, and 15 missions and Luna 16; a variety of breccias (including KREEP-like, anorthositic, and soil types) similar to those of the Apollo 14, 15, and 16 missions and Luna 20; two coarse-grained igneous rocks of a type not found on previous missions; dark mantle soils that appear to be erosional products of basalts; light mantle soils that appear to be dominantly the erosional products of highlands; a variety of exotic glasses; and, most characteristic of this mission, boulder samples that provide the best alternative to inaccessible outcrops of the lunar surface.

At Shorty Crater, orange and black glasses that were hopefully young volcanic material were observed and sampled. However, the old age of the glass and the astronaut observations and photographs suggest that this impact crater apparently excavated layers of very old pyroclastic material. Throughout

this landing site, 10 to 20 percent of each soil sample consists of these "exotic" glasses, apparently brought from subsurface layers and distributed by the gardening effect. The Apollo 17 mission provided the scientific world with the best lunar sample return in both potential quantity of information and variety of sample types. Except for the sampling of one possible outcrop on Apollo 15, the Apollo 17 boulder samples should allow the best possibility of placing returned lunar materials in their proper structural and stratigraphic context. One example of how sampling techniques have become more sophisticated since the Apollo 11 mission was the collection of samples from a large boulder at station 6. One part of the boulder was vesicular and green gray; the other part was practically nonvesicular and blue gray. Samples were taken from both parts of this boulder, as well as from various locations up to and through the contact. Further analysis suggests that the blue-gray material reacted to become more vesicular near the contact; this material also occurs as fragments within the green-gray material on the vesicular side of the contact. Sampling of this type provides insight into the evolution of the older crustal materials.

Knowledge of the Moon was also enhanced by the correlation of the traverse experiments, which provided better understanding of the site's subsurface relationships, obtained from the interpretation of seismic, electrical properties, and gravitational data. Seismic traverse experiments indicate that basaltic flows extend to a depth of approximately 1.2 km. The traverse gravimeter experiment has provided limits to the density of the underlying material, and the observed gravity anomaly allows development of a model for mass variations in the valley and in the massifs. This model may be of significance in interpreting the major mascons of the Moon. The electrical properties experiment has confirmed the gravity and seismic data by establishing that the basaltic thickness is between 1 and 1.5 km. These data also show that the regolith is relatively thick, perhaps 20 to 40 m, with some variation in thickness. The dielectric constant and loss tangent measurements are in good agreement with previously determined values obtained from lunar samples and ground observations.

The heat flow measurements at the Apollo 17 site have been shown to be roughly the same as those at the Apollo 15 site, indicating that, at least on the near side of the Moon, a reasonable value of heat flow may be 2 × 10^{-6} to 3 × 10^{-6} W/cm^2/sec.

Several other surface and orbital experiments were conducted on the Apollo 17 mission, which include the lunar atmospheric composition, the lunar ejecta and meteorites, the lunar tidal gravimeter, the ultraviolet spectrometer, the infrared scanning radiometer, and the lunar sounder. At the time of this writing, there are insufficient data to give an overview from these findings, which, in the future, are expected to give additional information about Taurus-Littrow and that region of the Moon covered by the command and service module groundtrack.

The sections that follow present the preliminary results obtained in the analysis of the Apollo 17 data to date. As will be seen, the Apollo 17 data fill some gaps in knowledge about the near-side surface of the Moon but, at the same time, raise many other questions. However, one cannot conclude a report on the Apollo 17 mission without again emphasizing that it was a fitting finale to the Apollo Program from the standpoint both of operations and of science. It is also important to review what has been learned in the brief 3.5 yr from the first lunar landing of Apollo 11 on July 20, 1969, to the final splashdown of Apollo 17 on December 17, 1972.

Before the Apollo Program, astronomical observations provided an early picture of the details of the lunar surface. In those days, intelligent speculation about the origin and history of the Moon was greatly inhibited because the scientific data required about the chemistry and about the internal condition of the planet could not be furnished even by the most powerful telescopes. Some of the most important scientific observations concerning the nature of the Moon and existing prior to the manned lunar landings are summarized below.

The discovery of the physiographic features of the Moon dates back to Galileo, who observed that the side of the Moon facing the Earth consisted of mountainous regions that he designated terra and smoother regions that he designated mare, similar to terrestrial continents and oceans. He also observed a marked difference in reflectivity between these two regions of the Moon: the mare was much darker than the terra. Further astronomical studies added much detail to Galileo's discovery, including rather fine features such as the rilles. However, before Apollo, the cause of these fundamental physiographic differences was not well understood. Later, some scientists hypothesized that the relatively smooth mare basins were very extensive lava flows. Others theorized that

they were extensive dust deposits, in fact, dust bowls. Still other scientists seriously suggested that the maria were filled by a type of sedimentary rock that was deposited at a very early stage in lunar history when the Moon had an atmosphere.

Before man landed on the lunar surface, two explanations for the origin of the circular depressions or craters, the most common physiographic feature on the lunar surface, were continuously debated: (1) that the features of the craters, similar to calderas on Earth, were of volcanic origin, and (2) that the craters were produced by projectiles impacting the lunar surface, in the same way that meteorites occasionally excavate craters on Earth. Now it is fully realized that the surface of the Moon could be sculpted both by impacts and by volcanic craters, but primarily by impacts.

Dialogue on the activity of the Moon and on the role of volcanism on the lunar surface developed into three schools of thought on the thermal history of the Moon. One school held that the Moon had been relatively inactive and had undergone some chemical differentiation only very early in lunar history. Another school propounded that the history of the Moon was similar to the Earth's long and continuous record of volcanism and chemical differentiation, and that lunar volcanoes were active in the recent past. Others thought the Moon had undergone no volcanic activity at all.

The chemical nature of the lunar surface, up to the time of Surveyor V, was totally unknown. However, there had been a number of suggestions. For example, it was suggested at one time that carbonaceous chondrites were typical of the dark mare regions; others suggested that meteorites known as eucrites were representative of the lunar surface; still others suggested that silica-rich glass found in mysterious objects called tektites must represent parts of the lunar surface. One could not even be sure that these hypotheses were mutually exclusive.

The pre-Apollo data obtained by unmanned satellites discovered (1) the mascons, which suggested a remarkedly rigid or strong lunar interior; (2) either a very weak lunar magnetic field or no field whatever; and (3) a physiographic difference between the lunar far side and the near side, in that the dark mare regions were essentially absent from the far side of the Moon.

As we now look back on the six Apollo landings, we are infinitely richer in facts concerning the Moon.

Some of these facts and observations have already been tentatively assembled in models that are leading to a much fuller understanding of lunar history. Although it is extremely difficult to account for the remaining facts with a consistent explanation, major areas of understanding can be briefly outlined.

A rather definite and reliable time scale for the sequence of events of lunar history has been developed. It has been established with some confidence that the filling of the mare basins largely took place between 3.2 and 3.8 billion years ago. This has been demonstrated from analysis of the mare basalts obtained from the Apollo 11, 12, 15, and 17 missions and Luna 16. Because these mare fillings represent a major physiographic feature on the lunar surface, it has been inferred that the time of formation of more than 90 percent of the cratering on the Moon was 4 billion years ago or earlier. In comparison, the ocean basins of the Earth are younger than 300 million years. (Terrestrial rocks older than 3 billion years are almost unknown.) The analysis of the highland material collected on the Apollo 14, 15, 16, and 17 missions and Luna 20 has shown the widespread occurrence of breccias with an apparent age of 3.8 to 4.1 billion years. There is strong circumstantial evidence that rocks dating back to 4.5 to 4.6 billion years ago must exist within the Moon, although very few of the Apollo rocks have crystallization dates lying between 4.0 and 4.6 billion years. It now appears that heat from the intense bombardment of the lunar surface by projectiles, ranging in size from microscopic to tens of kilometers in diameter, was effective in resetting most of the clocks used to determine the absolute age of the rocks.

The relative importance of volcanic and impact-produced features on the lunar surface appears to be well established with the conclusion of the Apollo missions. There seems to be almost unanimous agreement that the dark mare regions are underlain by extensive lava flows, shown both by rocks returned by the Apollo 11, 12, 15, and 17 missions and Luna 16 and by the high-resolution photographs that give convincing pictures of features comparable to terrestrial lava flows. Almost all craters appear to be caused by impacting projectiles, thus leaving the question of volcanic rocks in the terra regions unanswered. With the conclusion of Apollo 17, it has been suggested that volcanic activity in the highland region subsequent to approximately 3 billion years ago may be highly restricted or virtually nonexistent.

Apollo experiments investigating whether the Moon is "alive" or "dead" indicate that, compared to Earth, the Moon is seismically quiet. However, there are many very small quakes, possibly triggered by tides, at approximately 800 km below the lunar surface. Below 1000 km, the Moon is partially molten. A quiet Moon is consistent with the conclusion that volcanism and other types of tectonic activity have been rare or absent from the lunar surface for the last 2 to 3 billion years. Lunar seismology reveals that the Moon has a crust more than 60 km thick. Both the precise origin of this crust and the compositions causing the discontinuity in seismic velocity are still subjects of debate. From the Apollo Program, we can conclude that the Moon, at one time, was very much alive and now is very quiet.

The overall magnetic field of the Moon has been found to be negligible, as was thought before the Apollo missions. However, the magnetometers placed on the lunar surface reveal surprisingly strong local fields, variable both in direction and in intensity. Paleomagnetic studies have also determined that mare lava flows crystallized in a magnetic field that was much stronger than that of the present Moon. These discoveries raise the possibility that, during its early history, the Moon either was exposed to a relatively strong interplanetary magnetic field or had a magnetic field of its own that has since disappeared.

The interior structure of the Moon and its thermal characteristics have been investigated through a careful study of the fluctuations of the magnetic field induced by the solar wind, which reveals a relatively low lunar electrical conductivity. The conductivity of most silicates is, to the first order, a function both of temperature and of chemical composition (such as the abundance of ferrous and ferric iron). With preliminary measurements from the Apollo 12, 15, and 16 missions and with fluctuation measurements of the magnetic field, lunar conductivity can be derived. In conjunction with various chemical models of the Moon, this conductivity can be used to place constraints on the deep lunar interior temperatures, which are highly model dependent.

The thermal history of the Moon was investigated on the Apollo 15 and 17 missions through measurements of the heat escaping from the Moon. These measurements indicate that the energy flux escaping from the Moon is approximately half that of the Earth. This is surprisingly high, considering the relative size of the two planets. If these measurements

prove to be characteristic of the Moon, perhaps the explanation is that the Moon is richer than the Earth in the radioactive elements uranium and thorium and that these elements are strongly concentrated in the upper parts of the Moon.

Two current theories of lunar evolution have resulted from the consideration of information concerning (1) the concentration and location of radioactive materials, (2) the inferred volcanic history of the Moon, and (3) the inferred upper limits of internal temperature. The first hypothesis is that the planet was chemically layered during its formation. The low initial temperature of the lunar interior (below 500 km) gradually increased, perhaps reaching the melting point during the last billion years, while the initial hot temperature of the lunar exterior gradually decreased. Volcanism is entirely accounted for by early melting in the outer 400 km of the Moon. The alternate model of thermal evolution assumes that the Moon, chemically homogeneous during its formation, underwent extensive chemical differentiation that resulted in surface concentrations of radioactivity very shortly after its formation. In other words, much of the Moon was molten at its origin. Of course, both of these theories will undergo discussion and revision in the coming years.

The most extensive and diverse data obtained on the lunar surface are concerned with the chemistry and mineralogy of the surface materials. The study of samples from the six Apollo sites and the two Luna sites reveals a number of chemical characteristics. Although it is very early to generalize from these relatively few samples of the whole lunar surface, two orbital experiments provide excellent data regarding the regional distribution of various rock types: the X-ray fluorescence experiment and the gamma ray experiment.

The X-ray fluorescence experiment defined the prime difference between the chemistry of the mare and highland regions. The mare regions have aluminum concentrations 2 to 3 times lower than those of the terra or highland regions and magnesium concentrations 1.5 to 2 times greater than those of the terra regions. These differences in chemical concentrations throughout the equatorial region of the Moon are consistent with the chemical analysis of the returned samples. When orbital data and lunar sample data are combined, they provide an excellent explanation of the morphological and albedo differences. For example, all mare basalts have been found to be

unusually rich in iron and sometimes rich in titanium. The high iron concentrations in the mare, as opposed to the low concentrations in the highlands, is a basic explanation of the albedo differences, because both glass and mineral substances rich in iron and titanium are usually very dark.

The orbital gamma ray experiment results show that the region north and south of the crater Copernicus is remarkably rich in radioactive elements. A band going from north of the Fra Mauro site to west of the Apollo 15 site contains soil 20 times richer in uranium and thorium than either mare or terra in other parts of the Moon. The existence of a rock rich in these elements was also inferred from samples from the Apollo 12, 14, and 15 missions. The differences between lunar rocks and terrestrial rocks are so marked that the Moon must be chemically different from the Earth.

The Moon appears to be much richer in elements that form refractory compounds at temperatures of approximately 1600 to 1800 K. Many scientists are now coming to the conclusion that the chemistry of the lunar surface reveals that some separation of solid material and gas in the lunar dust cloud took place at temperatures in excess of 1600 K. The strong depletion of elements that are volatile at high temperatures in the outer portion of the Moon is consistent with the enrichment of refractory elements.

None of the three theories regarding the origin of the Moon—separation from the Earth, capture from a circumsolar orbit, or formation from a dust cloud surrounding the Earth—can be absolutely eliminated by the present data. However, the chemical differences between the Earth and the Moon, the depletion of volatile elements, and the enrichment of refractory elements in lunar samples make it unlikely that the Moon was torn out of the Earth.

In summary, the age of the Moon is well determined, and the Moon has a crust (the chemical composition of which is fairly well understood), a mantle, and a partially molten deep interior. The understanding of the mascons is well underway. Facts substantiating the early theories of the atmosphere have been obtained. Basic questions that were asked 5 yr ago, such as whether the Moon is hot or cold, alive or dead, or has craters formed by volcanism or impact, are no longer asked. Apollo data have changed the types of questions asked. Post-Apollo questions are more detailed, more specific, and more

sophisticated. Yet, despite the great strides taken in knowledge about the Moon, its origin and formation are still unknown.

A storehouse of resources has been returned from the Moon: almost 385 kg of lunar materials (obtained from six different landing sites on the near side of the Moon), 37 drive tubes, and 20 drill stems. To date, only 10 percent of this lunar material has been examined in detail. Approximately 33 000 lunar photographs and 20 000 reels of tapes of geophysical data have been collected. Thus, in 4 yr of lunar exploration, our knowledge of lunar characteristics has been substantially increased, and vast resources of scientific data have been collected that will lead to a decade of data analysis.

In the past decade, there have been two revolutions in planetary science studies. There has been a revolution in the new global tectonics describing the motions of continents and the generation and destruction of the sea floor. In its investigations of the origin, history, and formation of the Moon, the Apollo Program has led to a revolution in providing the first deep understanding of a planet other than the Earth through the development of new techniques of exploration, investigation, and analysis and through the integration of the scientific knowledge gained in interdisciplinary fields. The Apollo Program has provided Earth scientists with 4 yr of anxiety, excitement, and fulfillment. Apollo lessons may force a reconsideration of many of the techniques and models that are currently used in understanding the early history of the Earth. As we look to future generations, hopefully, we have developed a scientific program that carried out worthy and substantial preliminary investigations and that laid a very firm foundation for future scientific inquiry. In decades to come, the analysis of Apollo data may indeed lead to a polar orbital flight around the Moon or to a lunar base where men may explore the entire surface of the Moon. By studying the Moon, we can better understand processes of planetary accretion, evolution, and composition so that lunar studies have implications that extend beyond the Moon. Hopefully, our generation has performed a job that history will recognize as a commendable scientific endeavor, a contribution of valuable information—useful, meaningful, and inspirational.

Anthony J. Calio
NASA Lyndon B. Johnson Space Center

1. Apollo 17 Site Selection

N. W. Hinners[a]

Consideration of an Apollo 17 landing site began in earnest during debate over the Apollo 16 site, primarily because the Apollo Site Selection Board (ASSB) desired to consider Apollo 16 and 17, the last lunar missions, as a complementary pair. Therefore, in order to put the Apollo 17 site selection in context, it is necessary to discuss highlights of the Apollo 16 site selection as well. (For more details about the Apollo 16 site selection, see ref. 1-1.) Some of the content of this report is abstracted or paraphrased from the minutes of the ASSB meetings (written by the author) or from other unpublished documents (also written by the author) used as background material for or documentation of several meetings of an Ad Hoc Site Evaluation Committee. All that material is available on request.

PRE-APOLLO 16 SITE SELECTION STATUS

At the time of the Apollo 16 site evaluation, soon after the Apollo 14 flight, there was a clear consensus among the lunar science community that both the Apollo 16 and 17 missions should be targeted to highlands sites. The Apollo 15 mission had not been flown, but the mare region adjacent to Rima Hadley and Montes Apenninus had been selected as the Apollo 15 site. Only minor support existed for another mare mission, and it was mainly limited to the Marius Hills. That candidate site, however, became largely academic when a revised launch schedule resulted in the Marius Hills being operationally inaccessible, or only marginally accessible, for either the Apollo 16 or 17 time frame.

After imposition of the operational constraints, mainly accessibility and available photographic coverage, and after consideration of the scientific return,

Descartes and Alphonsus emerged as the prime highland contenders for the Apollo 16 site. It was assumed that one of these two candidates would be chosen for the Apollo 16 site and that the Apollo 17 site would be chosen from another candidate list. The Apollo 17 candidate sites under consideration at that time are discussed, in priority order, in the following paragraphs.

Tycho and Davy Crater Chain

No relative priority was established for Tycho and the Davy Crater chain. The objectives of a Tycho mission emphasized the southern highlands samples and impact phenomena.

A mission to the Davy Crater chain had the same general objectives as an Alphonsus mission, namely the sampling of highlands, upland basin fill (Cayley Formation), and rocks of "deep-seated" origin. The site differs, however, in that (1) the Cayley is not modified by rilles and other volcanic features peculiar to Alphonsus, (2) the putative deep-seated material would be sampled at a crater chain instead of at a dark-halo crater, and (3) the highlands region (presumably pre-Imbrian) was not considered as apt to be mantled by the Cayley "volcanic" material as that at Alphonsus. (At that time, there was no knowledge of the brecciated nature of the Cayley Formation as sampled at Descartes.) It was noted that adequate photographs of Davy did not exist and would have to be obtained on an Apollo 16 mission to Descartes.

Southwest of Mare Crisium and the "Central Highlands"

No relative priority was established for a site southwest of Mare Crisium and the "central highlands." The Apollo 15 mission was scheduled to overfly an extensive highlands region southwest of

[a]National Aeronautics and Space Administration, Washington, D.C.

Mare Crisium. It was believed that results from Apollo 15 X-ray and gamma ray spectrometers would enable determination of whether gross chemical differences exist between the Crisium and Hadley-Apenninus regions. An affirmative answer would increase the priority of the Crisium areas.

The central highlands between Descartes and Alphonsus were considered because they are expected to contain pre-Imbrian materials. As was true for Davy, a prerequisite to selection was acquisition of good photographs of the region on the Apollo 16 mission. It was recognized that a potential problem existed in using Apollo 16 photographs of either Davy or the central highlands for an Apollo 17 mission, but it was believed that the increased interval between flights, changed from 6 to 9 months, would make the turnaround possible.

Gassendi

A flight to Gassendi was viewed as a central-peaks mission with Copernicus-type objectives of sampling highlands materials (of impact-rebound origin) and of investigating impact phenomena. A mission to Gassendi had the additional objective of investigation of the crater floor, which exhibits features interpreted to result from isostatic rebound; also, the site is distant from Mare Imbrium.

Copernicus Central Peaks

The Copernicus central-peaks site, previously of high priority, was greatly reduced in priority for the Apollo 17 mission (as it had been for the Apollo 16 mission) because Copernicus ray material had probably been sampled on the Apollo 12 mission and because there were already three sites (Apollo 12, 14, and 15) in the circum-Imbrian region of the Moon.

A far-side site—most notably in Tsiolkovsky—was also briefly considered. Although it was shown to be possible, at first look, to support the mission by using a communications relay satellite beyond the Moon, it was believed that the time schedule for the mission preparation was too short and that the probability of a successful mission was less than that for a conventional near-side site.

APOLLO 16 SITE SELECTION MEETING

On June 3, 1971, the ASSB met to select the Apollo 16 site and to designate a prime candidate site for the Apollo 17 mission. At the meeting, the ASSB recognized both Descartes and Alphonsus as good sites. Descartes was selected as the Apollo 16 site, mainly for two reasons. First, more was known about the operational aspects of a Descartes mission because, in contrast to the only recently considered Alphonsus, Descartes had been a high-priority candidate site since before the Apollo 12 mission. Second, the Descartes prime objectives (sampling the Cayley and Descartes Formations) were independent of Apollo 14 and 15 results whereas an Alphonsus mission had a common objective with the Apollo 15 mission of "old highlands" sampling.

At the same meeting, the ASSB designated Alphonsus as the prime candidate site for the Apollo 17 mission. (Alternatively, Descartes would have been designated had it not been selected as the Apollo 16 site.) Alphonsus was designated partly because the scientific arguments that had made Alphonsus a prime candidate for the Apollo 16 site had convinced the ASSB of the validity of the Alphonsus objectives. More to the point, however, Alphonsus was known to be operationally acceptable whereas all other Apollo 17 candidate sites had actual or potential problems. First, Tycho was deleted from further consideration because of concern about the rough terrain surrounding the landing ellipse. Second, the central highlands and the Davy Crater chain were questionable because of the necessity to rely on Apollo 16 photographs (i.e., insufficient time to create operational maps, models, etc.). Third, Gassendi, although not fully analyzed, appeared to be dominated by rough terrain. Fourth, the Copernicus central peaks appeared to be losing scientific interest. Finally, one could not count on Apollo 15 successfully photographing a suitable site in the region southwest of Mare Crisium; that is, a site that was operationally acceptable and at least of equal scientific interest as Alphonsus. This, then, was the situation until after the flight of Apollo 15, on which were obtained both excellent photographs of the highlands between Mare Crisium and Mare Serenitatis and good X-ray and gamma ray data for extensive regions along the groundtrack. The next task was to determine if suitable sites could be found in this region.

POST-APOLLO 15 ACTIVITIES

The preliminary Apollo 15 gamma ray and X-ray spectrometer results indicated that the highlands region southwest of Mare Crisium is generally low in

radioactivity and has a high aluminum-to-silicon ratio, both thought to indicate an anorthositic highlands crust different from that of the Montes Apenninus region. Screening of the Apollo 15 photographs occurred during October 1971. Six highlands-containing candidate sites, spread between Mare Crisium and Mare Serenitatis, were selected. Four of those sites were subsequently eliminated for operational reasons (too far east to allow sufficient tracking time between acquisition of signal and powered descent initiation). The two remaining were a "pure" highland site, designated "southwest of Crisium," and a combination highland-volcanic site on the southeastern edge of Mare Serenitatis, designated Taurus-Littrow. (For a detailed discussion of the site characteristics, see sec. 6 of this report.)

When the two new sites were added to the still-viable high-priority candidates from the previous site selection discussion, a total of five Apollo 17 candidate sites emerged. In alphabetical order, they were Alphonsus, Copernicus central peaks, Gassendi central peaks, southwest of Crisium, and Taurus-Littrow. In December 1971, a Site Evaluation Document was sent to 32 lunar scientists, most of whom were either principal investigators for the Apollo 17 experiments or had been intimately involved in lunar studies and site selection discussions. The document included a presentation of the general scientific objectives for the Apollo 17 mission and a discussion of the particular attributes of the five previously mentioned sites. Recipients of the document were requested, first, to respond with their personal scientific priorities for the Apollo 17 mission and, second, to indicate how each candidate site might fulfill all the established objectives. They were cautioned against unrealistically adding new sites, were told that there could be no dependence on Apollo 16 photographs (the constraint which eliminated Davy Crater chain and the central highlands as candidates), and were further presented with the following strong caveats concerning two of the candidates.

1. The highland site southwest of Crisium is in the highland terrain unit accessible to a Russian unmanned sample return spacecraft. (Luna 20 subsequently landed in that region.) Additionally, the site is relatively homogeneous and thus would not make efficient use of the Apollo sampling system.

2. Most lunar scientists believe that samples from Copernicus were obtained in ray material acquired on the Apollo 12 mission.

The responses to the Site Evaluation Document were considered by an Ad Hoc Site Evaluation Committee in January 1972. A clear consensus among respondees and the Ad Hoc Site Evaluation Committee was apparent in terms of the following objectives for the Apollo 17 mission (in priority order). Each objective is discussed in more detail below.

1. Sampling pre-Imbrian highlands as far from the Imbrium Basin as possible
2. Sampling "young volcanics"
3. Orbital coverage
4. Traverse geophysics
5. Apollo lunar surface experiments package (ALSEP) (high priority for the heat flow experiment)

Pre-Imbrian Highlands

Samples acquired to date had been dominated by mare materials. Relatively much was known about mare composition and formation but, even considering the Fra Mauro and Hadley-Apenninus samples, relatively little was known about the highlands, which constitute approximately 85 percent of the Moon. Earth-based photogeologic mapping, Apollo 14 and 15 sample results, and Apollo 15 orbital data all indicated that the highlands are complex and heterogeneous. These factors led to the desire to sample highlands further, but as far away as possible from the Imbrium Basin (the source of Apollo 14 and 15 samples and possibly some Apollo 12 samples).

Young Volcanics

The limited lunar isotopic chronology developed to the time of committee discussion indicated that major lunar thermal and chemical evolution may have effectively ceased approximately 3 billion years ago. It was thought to be important to determine whether or not that theory is indeed true because the developing models of lunar origin and evolution were very sensitive to that assumption. The existence of lunar materials younger than 3 billion years was predicated on the evidence of superposition and relative crater densities. The putative "young" materials are generally dark and often associated with cone-type structures or dark-halo craters thought to be indicative of explosive volcanism. The explosive nature itself was judged significant for two reasons.

1. Explosive volcanism may indicate a relatively high content of volatiles in the erupting magmas; such volatiles were lacking in samples thus far seen.

2. On Earth, explosive volcanism sometimes brings deep-crustal or subcrustal rocks (xenoliths) to the surface in unaltered form.

Orbital Coverage

Orbital science coverage was discussed from two aspects. On the one hand, there was a desire to maximize the amount of new photography, which meant favoring sites the orbital groundtracks of which least duplicated those of Apollo 15 and 16. On the other hand, it was argued that some of the new orbital experiments on Apollo 17 (infrared radiometer and lunar sounder) would benefit most by groundtracks covering both the largest variety of features and the largest area (high-latitude sites). There was thought to be additional merit in flying the infrared radiometer and the lunar sounder over regions already covered by the Apollo 15 or 16 X-ray and gamma ray sensors and over a number of the circular mascon basins.

Traverse Geophysics

The Apollo 17 mission was scheduled to include three traverse geophysics experiments: lunar seismic profiling, surface electrical properties, and lunar traverse gravimeter. Because all these experiments were designed, basically, to detect layering, sites with a high probability of having layering were preferred by the respective principal investigators. The unanimous opinion of the Ad Hoc Site Evaluation Committee, however, was that the traverse geophysics should not be a determining factor in the site selection; rather, it was reasoned that after the site was selected for other factors, one should determine how best to use the traverse experiments.

Apollo Lunar Surface Experiments Package

A desire was expressed to emplace the heat flow experiment in a region significantly different from that of Apollo 15 (the only other heat flow location) or of the planned Apollo 16 site and to avoid local topography of a scale affecting the measurement. Opinion was also expressed that, given a choice, the mass spectrometer should be placed at a site that showed a history of transient events or "recent" volcanism. It should be noted that the decreased priority of ALSEP-related factors in the Apollo 17

site selection resulted mainly from the absence of the network-type experiments of previous missions (e.g., passive seismometer, magnetometer, and laser ranging retroreflector).

AD HOC SITE EVALUATION COMMITTEE DELIBERATIONS

The candidate sites Copernicus and southwest of Crisium generated no enthusiasm among respondees to the Site Evaluation Document or among committee members for the reasons noted previously. All three remaining sites (Alphonsus, Gassendi, and Taurus-Littrow) contain highlands material, but the Ad Hoc Site Evaluation Committee saw no obvious way to discriminate among the highlands of the sites regarding either age or composition. Gassendi fulfilled the objective of being farthest from the edge of the Imbrium Basin (approximately 1000 km), but the nearest, Taurus-Littrow, was approximately 800 km distant. The difference of approximately 200 km was not deemed significant. A question remained about whether the crater wall of Alphonsus, the expected source of highlands samples, is mantled by Cayley volcanics. Conversely, the highland blocks at Taurus-Littrow and the central peaks of Gassendi both appeared to contain "clean" exposures. Between Gassendi and Taurus-Littrow, an argument favoring Gassendi was made in that there had been no central-peak-type mission in the Apollo Program whereas Taurus-Littrow was a ring-basin near-side site similar to Hadley-Apenninus.

Young volcanics are not in evidence at Gassendi, and a strong argument could not be made regarding the relative value of the dark-halo craters at Alphonsus to the dark mantling blanket at Taurus-Littrow. Both regions were hypothesized to contain possible xenoliths or lavas (or both) from deep interior regions.

The orbital science coverage arguments were not compelling. It was recognized that a Gassendi mission would result in the least duplication of Apollo 15 and 16 photography and would have the positive attribute of flying over the Orientale Basin in sunlight. However, more weight was given to the argument that the infrared radiometer and the lunar sounder could benefit more by the Taurus-Littrow groundtracks because of the greater variety of overflown targets.

The Ad Hoc Site Evaluation Committee concluded that the Taurus-Littrow site was the best candidate,

followed by Gassendi, with Alphonsus a weak third. The overall result was based primarily on the fact that, in terms of sample acquisition, Taurus-Littrow was a two-objective site (highlands, young volcanics) whereas Gassendi was a single-objective site (central-peak highlands). The better orbital photography coverage for a Gassendi mission was not deemed equivalent to obtaining a second prime sampling objective. Alphonsus, also a dual-objective site, did not measure up to Taurus-Littrow primarily because of the uncertainty concerning Cayley mantling of the Alphonsus crater wall and the superior orbital science for Taurus-Littrow groundtracks. The ranking developed by the Ad Hoc Site Evaluation Committee, and presented to the ASSB, was consistent with that obtained by summarizing the 32 responses to the Site Evaluation Document.

APOLLO 17 SITE SELECTION MEETING

The ASSB met on February 11, 1972, to select the Apollo 17 site. The scientific arguments and recommendations discussed in the previous subsection were presented, followed by a presentation of the operational considerations, of which only selected highlights are discussed in this report.

Of the three candidate sites analyzed in detail, Gassendi presented the most problems. Although the terrain along the landing approach was acceptable, the landing area itself presented problems. Outside the nominal 3σ landing ellipse, which was acceptably smooth, the terrain is heavily cratered, rolling, or contains rilles. If the lunar module were to land down range of the nominal ellipse, it was likely that, even if the landing were successful, the crewmen would not be able to traverse to the prime objective (the central peaks), particularly if there were a failure of the lunar roving vehicle (LRV). These problems were deemed sufficient that the NASA Lyndon B. Johnson Space Center (JSC) considered Gassendi unacceptable as an Apollo 17 site.

At Alphonsus, both the approach terrain and the landing area were judged "highly acceptable," which was the status when Alphonsus was being considered for the Apollo 16 site. It was also determined that in the contingency situation of a walking mission (LRV failure), the crewmen could reach both the crater wall and the dark-halo crater material.

Although early analysis of the Taurus-Littrow site, performed just after the screening of the Apollo 15 photographs, had indicated that no serious problems were associated with the site, detailed plotting of the landing ellipse in the valley showed that with a 90° azimuth for the approach path and with a constraint to avoid the sudden rise in topography caused by the scarp, the fit of the ellipse in the valley became very tight. Because of the increased precision available from the Apollo 15 metric camera, however, it was shown that even without command module landmark tracking, the ellipse could be placed such that no landing problem would be caused by topography. (The westernmost part of the ellipse did include a small portion of the landslide, but it was well within the capability of the crew to redesignate out of that area should they be heading toward it.) In addition, as in the case of Alphonsus, it was determined that the prime objective at Taurus-Littrow was achievable on a walking mission (LRV failure), even if the landing were made outside the nominal ellipse.

The ASSB accepted the JSC evaluation that Gassendi was operationally unacceptable and then focused on Alphonsus and Taurus-Littrow. It was first noted that, although both Alphonsus and Taurus-Littrow were operationally acceptable, Alphonsus presented fewer risks. The risks were not related to safety but to mission success. The differences in probability of success were not quantifiable; that is, shades of gray rather than blacks and whites were involved. Because there were no strong operational discriminators, the discussion returned to the scientific attributes of the sites. A recapitulation showed that the scientific evaluation clearly favored Taurus-Littrow over Alphonsus; the decisive factors were the certainty of acquiring highlands material at Taurus-Littrow (remembering the possible mantling by Cayley materials of the highlands at Alphonsus), the superior orbital coverage, and the better use of LRV capabilities. The ASSB unanimously accepted that evaluation and recommended to the Associate Administrator for Manned Space Flight that Taurus-Littrow be the Apollo 17 landing site.

REFERENCE

1-1. Hinners, N. W.: Apollo 16 Site Selection. Sec. 1 of the Apollo 16 Preliminary Science Report. NASA SP-315, 1972.

2. Mission Description

Richard R. Baldwin[a]

The highly successful Apollo 17 manned lunar landing mission was the final in a series of three J-type missions planned for the Apollo Program. These J-type missions have been characterized by extended hardware capability, by a scientific payload larger than on the previous G- and H-series missions, and by the use of a battery-powered lunar roving vehicle (LRV). As a result of these additions, the Apollo 17 mission had a duration of 12.6 days, a time on the lunar surface of 75 hr with a total surface traverse distance of approximately 35 km, and a scientific instrument module (SIM) containing equipment for orbital experiments and photographic tasks. During their 22.1 hr of lunar surface extravehicular activity (EVA), crewmen collected approximately 110 kg of samples and took more than 2100 photographs. All Apollo landing missions are compared in figure 2-1 in terms of the science payload weight delivered to the lunar surface, the EVA duration, the surface distance traversed, and the weight of returned lunar samples.

The landing site for Apollo 17 is on the southeastern rim of Mare Serenitatis in a dark deposit between massif units of the southwestern Montes Taurus, as shown in figure 2-2. These massif units (which are believed to be breccias from large basin ejecta), the dark mantle material, and a possible debris flow 5 km southwest of the landing site are features of major geological interest in the Taurus-Littrow region.

Scientific objectives of the Apollo 17 mission included geological surveying and sampling of materials and surface features in a preselected area of the Taurus-Littrow region, deploying and activating surface experiments, and conducting inflight experiments and photographic tasks during lunar orbit and transearth coast (TEC). These objectives were satisfied on Apollo 17 by performance of scheduled science activities, which included 12 lunar surface experiments, five lunar orbital experiments, photographic and support tasks, and other experiments. The individual Apollo 17 experiments and photographic tasks were as follows.

1. Lunar surface
   a. Deployed experiments
      (1) Apollo lunar surface experiment package (ALSEP)
         (a) Heat flow
         (b) Lunar seismic profiling (LSP)
         (c) Lunar surface gravimeter (LSG)
         (d) Lunar atmospheric composition experiment (LACE)
         (e) Lunar ejecta and meteorites (LEAM)
      (2) Surface electrical properties (SEP)
      (3) Lunar neutron probe
      (4) Traverse gravimeter
      (5) Cosmic ray detector
   b. Sampling
      (1) Lunar geological investigation
      (2) Special samples
   (c) Soil mechanics
2. Lunar orbital
   a. Orbital experiments
      (1) Lunar sounder
      (2) Infrared (IR) scanning radiometer
      (3) Far ultraviolet (UV) spectrometer
      (4) S-band transponder
      (5) Sodium iodide (NaI) scintillation crystal
   b. Photographic and support tasks
      (1) Service module (SM) orbital photographic tasks
      (2) Command module (CM) photographic tasks
      (3) Visual observations from lunar orbit
3. Other
   a. Biomedical experiments
      (1) Biostack II
      (2) BIOCORE

[a]NASA Lyndon B. Johnson Space Center.

Apollo 11 (0.25)

Apollo 12 (2.0)

Apollo 14 (3.3)

Apollo 15 (27.9)

Apollo 16 (27.0)

Apollo 17 (35.0)

0   5   10   15   20   25   30   35
Distance, km

(a) Traverse distance.

Apollo 11 (102)

Apollo 12 (166)

Apollo 14 (209)

Apollo 15 (550)

Apollo 16 (563)

Apollo 17 (514)

0   100   200   300   400   500   600
Weight, kg
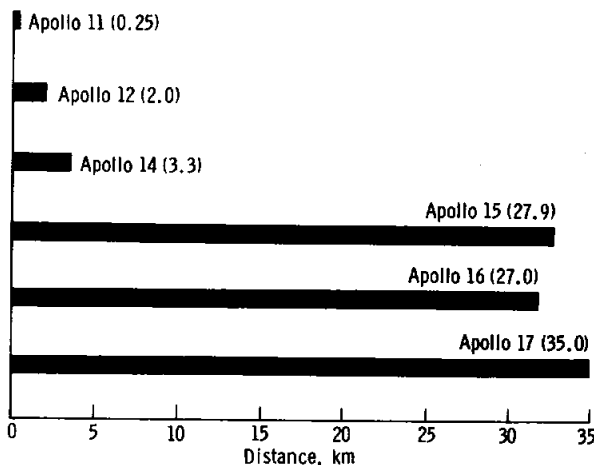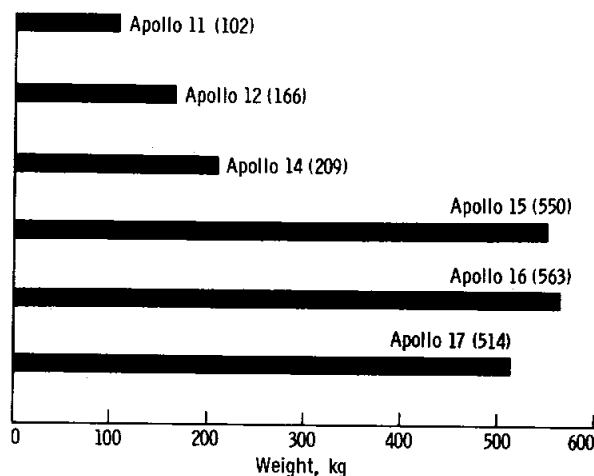
(c) Weight of experiment equipment landed on the lunar surface.

Apollo 11 (2:24)

Apollo 12 (7:29)

Apollo 14 (9:23)

Apollo 15 (18:33)

Apollo 16 (20:12)

Apollo 17 (22:05)

0   5   10   15   20   25
Time, hr

(b) Time outside the LM.

Apollo 11 (21)

Apollo 12 (34)

Apollo 14 (43)

Apollo 15 (77)

Apollo 16 94)

Apollo 17 (110)

0   20   40   60   80   100   120
Weight, kg
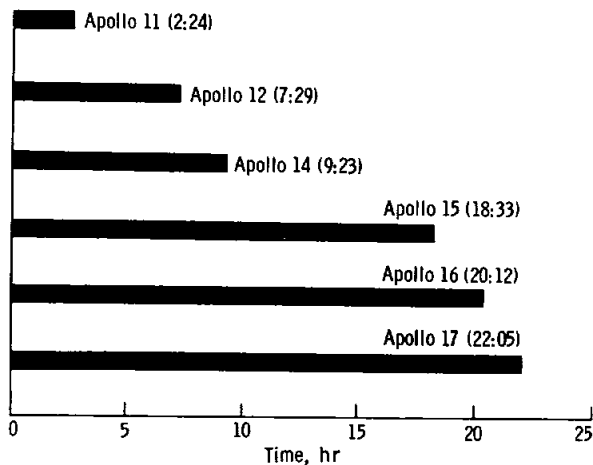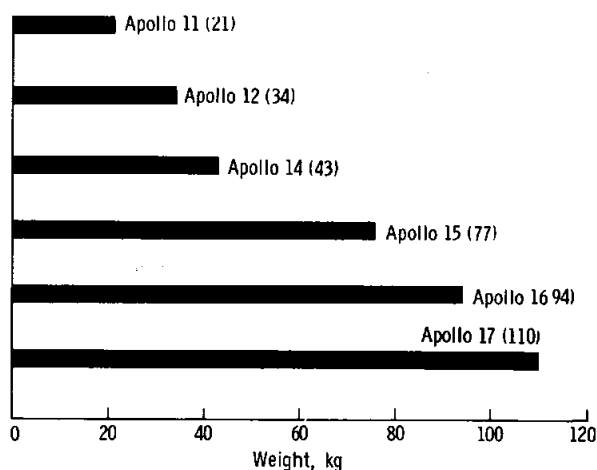
(d) Weight of lunar samples returned.

FIGURE 2-1.–Comparison of Apollo missions.

(3) Visual light flash phenomenon

b. Heat flow and convection demonstration

c. Apollo window meteoroid

Major operational events of the Apollo 17 mission are described in chronological order in the following subsections. Overviews of lunar surface activities, inflight experiments, and photographic tasks are presented.

The Apollo 17 space vehicle (manned by Eugene A. Cernan, commander (CDR); Harrison H. Schmitt, lunar module pilot (LMP); and Ronald E. Evans,

command module pilot (CMP)) was launched from the NASA John F. Kennedy Space Center at 11:33:00 p.m. c.s.t. on December 6, 1972 (05:33:00 G.m.t. on December 7, 1972). The command and service module (CSM), the lunar module (LM), and the SIVB booster stage were inserted 11 min 53 sec later into an Earth parking orbit of 91.2 by 92.5 n. mi. After two revolutions, at 08:45:37 G.m.t., the CSM, LM, and SIVB spent stage were inserted into translunar coast.

At 09:15:29 G.m.t. on December 7, the CSM was
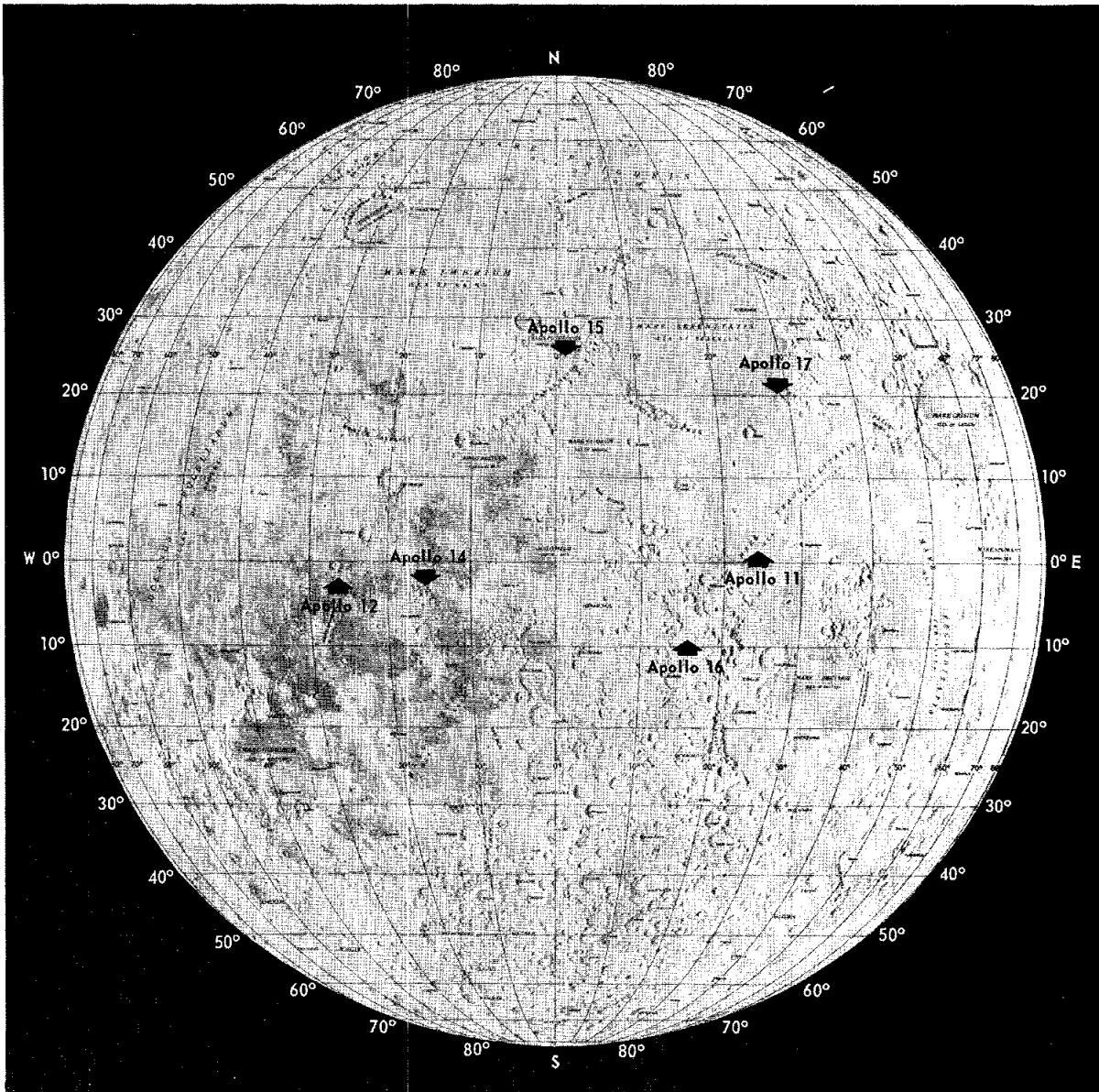
FIGURE 2-2.—Landing site of Apollo lunar landing missions. Apollo 11 landed in Mare Tranquillitatis on July 20, 1969; Apollo 12 in Oceanus Procellarum on November 19, 1969; Apollo 14 in the Fra Mauro highlands on January 31, 1971; Apollo 15 in the Hadley-Apennines region on July 30, 1971; Apollo 16 in the Descartes region on April 21, 1972; and Apollo 17 in a valley at Taurus-Littrow on December 11, 1972.

separated from the SIVB. Approximately 15 min later, the CSM docked with the LM. After CSM/LM extraction from the SIVB, the SIVB was targeted for lunar impact, which occurred on December 10 at 20:32:43 G.m.t. The impact location was approximately 84 n. mi. northwest of the planned target point, and the event was recorded by the passive seismic experiments deployed on the Apollo 12, 14, 15, and 16 missions.

Only one of the four planned midcourse corrections was required during translunar coast. A midcourse correction (MCC) made at 17:03:00 G.m.t. on December 8 was a 1.6-sec service propulsion system burn resulting in a 10.5-ft/sec velocity change. The

first of two 40-min heat flow and convection demonstrations was begun at 00:33:00 G.m.t. on December 9. The second demonstration was begun 2 hr 20 min later. The SIM bay door was jettisoned at 15:05:40 G.m.t. on December 10.

Lunar orbit insertion, executed at 19:47:23 G.m.t. on December 10, placed the spacecraft into a lunar orbit of 170.0 by 52.6 n. mi. Approximately 4 hr 20 min later, the orbit was reduced to 59 by 15 n. mi. The spacecraft remained in this low orbit for more than 18 hr, during which time the CSM/LM undocking and separation were performed. The CSM circularization maneuver, which was performed at 18:50:29 G.m.t. on December 11, placed the CSM into a 70.3- by 54.3-n. mi. orbit.

At 14:35:00 G.m.t. on December 11, the CDR and the LMP entered the LM to prepare for descent to the lunar surface. The LM was powered up and all systems were nominal. A maneuver at 18:55:42 G.m.t. on December 11 placed the LM in an orbit with a perilune altitude of 6.2 n. mi. Approximately 47 min later, the powered descent to the surface began.

LUNAR SURFACE ACTIVITIES

Following a nominal descent sequence, the spacecraft landed at 19:54:57 G.m.t. on December 11 in a valley at Taurus-Littrow, less than 200 m from the preferred landing point. The best estimate of the lunar surface landing position is latitude 20°10′ N and longitude 30°46′ E (ref. 2-1). The Apollo 17 landing site in relation to those of all previous lunar landing missions is shown in figure 2-2.

The first lunar surface EVA began at 23:54:49 G.m.t. on December 11, with the CDR egressing at 00:01:00 G.m.t. on December 12. Television coverage began after installation of the ground-commanded television camera and the high-gain antenna on the LRV. The first television pictures were received at 01:10:49 G.m.t. Before leaving the LM for the ALSEP site, the crew deployed the cosmic ray experiment. The site selected for the ALSEP was approximately 185 m west-northwest of the LM. Deployment of the heat flow experiment was nominal, with both probes inserted to a depth of 2.54 m. The LEAM experiment and the LSG were also deployed nominally. Preliminary operations with the gravimeter did not indicate the beam-nulling problem that was later encountered. The ALSEP group was

completed with deployment of the LACE and the LSP experiment (except for explosive charges). Total ALSEP deployment, with relative locations of the experiments, is shown in figure 2-3. The deep core sample was taken concurrently with ALSEP deployment. Although difficulty was experienced in extraction, all three core sections were obtained. The neutron flux probe was then deployed to full depth in the deep core hole. Both the receiver and transmitter of the SEP experiment were deployed as planned, with initial instrument operation scheduled during EVA-2.

During ALSEP deployment, extra time was required to level the central station and the antenna gimbal. The resulting time-line deficit was compensated for by relocating the first traverse station to an area near the rim of Steno Crater. At station 1A, the crew collected geological samples, including a rake sample, and took a traverse gravimeter reading. A total of six gravity measurements and one gravimeter bias measurement were taken during EVA-1. At station 1A, the crew also deployed a 1-lb explosive package for the LSP instrument. During their return to the LM, the crew deployed a ½-lb explosive package. The first ALSEP data were recorded at 02:54:00 G.m.t. on December 12. The first EVA, which was 7 hr 12 min long, was completed at 07:06:42 G.m.t. on December 12.
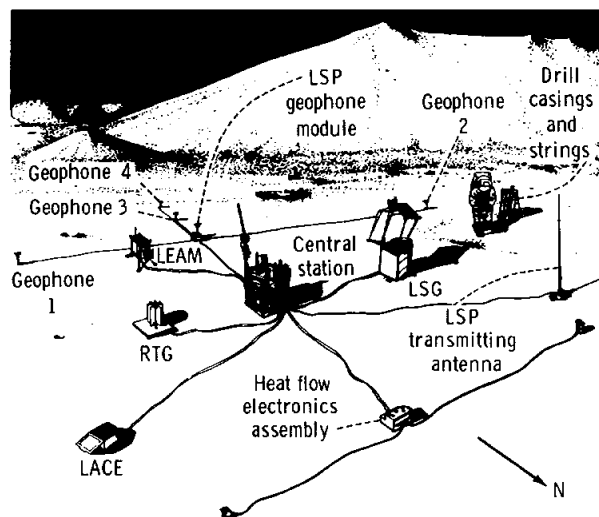
FIGURE 2-3.—Deployment of the Apollo 17 ALSEP, showing the relative locations of the central station, radioisotope thermoelectric generator (RTG), and the five experiments.

The second EVA was begun at 23:28:06 G.m.t. on December 12. The second major sampling stop of the mission was made early in EVA-2 at Nansen Crater, where the crew sampled primarily the rock debris at the base of the South Massif. After leaving Nansen Crater, the crew made an unscheduled stop (station 2A) to check the gravity gradient between the South Massif and the valley. The major geological objective of the third sampling site near Lara Crater was the scarp that runs north-south between the massif units. Activities at this stop included an exploratory trench and a core sample, which was stored in the core sample vacuum container. Traverse station 4 was at Shorty Crater, a 110-m dark-halo crater. Sampling at this location was focused on deposits and rocks at the crater rim. A trench dug in the crater rim exposed the much-discussed orange soil. A double core sample was also obtained at station 4. Blocks of subfloor basalt were found at Camelot Crater (station 5), and sampling included a search for dark mantle material. During the traverse on EVA-2, the SEP experiment was operated and the crew deployed 1/8-, 6-, and 1/4-lb explosive charges. Seven traverse gravimeter measurements were taken: one each at stations 2, 3, 4, and 5; one between stations 2 and 3; and two at the LM site. Finally, eight LRV sampling stops were made at points intermediate to the major stops to increase the areal density of geological sampling sites. During the second EVA, it was discovered that the sensor beam of the LSG could not be nulled, even though the LMP reverified that the instrument was level and the gimbal was free. The second EVA was 7 hr 37 min long and ended at 07:05:02 G.m.t. on December 13.

The third EVA began at 22:25:48 G.m.t. on December 13. The cosmic ray detector was recovered early in the EVA to avoid exposure to an excess of low-energy solar protons. The first two traverse stops (stations 6 and 7) of EVA-3 were made at the base of the North Massif. Geological activities in these areas emphasized boulders and boulder tracks and included the dark mantle material and the massif/valley interface. A rake sample and a single core sample were obtained at station 6, and several rock chips were collected from a 3-m boulder at station 7. At station 8 (Sculptured Hills), samples included the dark mantle plains material. The crew obtained a trench sample and a rake sample at this location as part of the sampling plan to look for differences between the Sculptured Hills and the Massifs. Sampling at station

9 (Van Serg Crater) was concentrated on the crest of the crater rim and the ejecta blanket southeastward of the rim, at both of which were found soft, dark-matrix breccias. A final trench sample and double core were obtained at this station. Station 10 was deleted to obtain additional closeout time for completion of ALSEP photography and for further attempts to resolve the gravimeter problem.

During EVA-3, four LRV sampling stops were made and traverse gravimeter measurements were taken at stations 6, 8, and 9 and at the LM. The remaining two explosive packages for the LSP experiment were also deployed. Late in EVA-3, the LMP made a last, unsuccessful attempt to null the sensor beam of the LSG. One of the final science activities in the EVA was retrieval of the neutron flux probe from the deep drill core hole. The third EVA ended at 05:40:56 G.m.t. on December 14.

The LM ascent stage lifted off the Moon at 22:54:37 G.m.t. on December 14. Lift-off and ascent were recorded by the ground-commanded television assembly on the LRV. After a vernier adjustment maneuver, the ascent stage was inserted into a 48.5- by 9.4-n. mi. orbit. The LM terminal phase initiation burn was made at 23:48:58 G.m.t. on December 14. This 3.2-sec maneuver raised the ascent stage orbit to 64.7 by 48.5 n. mi. The CSM and the LM docked at 01:10:15 G.m.t. When the LM ascent stage was jettisoned at 04:51:31 G.m.t. on December 15, the separation velocity was low, necessitating an evasive 2-ft/sec maneuver by the CSM. Deorbit firing of the ascent stage was initiated at 06:31:14 G.m.t. on December 15. Impact occurred 19 min 7 sec later approximately 0.7 n. mi. from the planned target at latitude 19°56' N and longitude 30°32' E. The ascent stage impact was recorded by the four Apollo 17 geophones and by each ALSEP at the Apollo 12, 14, 15, and 16 landing sites.

INFLIGHT EXPERIMENTS AND PHOTOGRAPHIC TASKS

Experiments and photographic tasks were performed in lunar orbit and during both the translunar and transearth coast phases of Apollo 17. Equipment needed for performance of CM photographic tasks, visual observations of the Moon, the visual light flash phenomenon, the NaI scintillation crystal experiment, and the heat flow and convection demonstration were stowed in the CM. Equipment for other
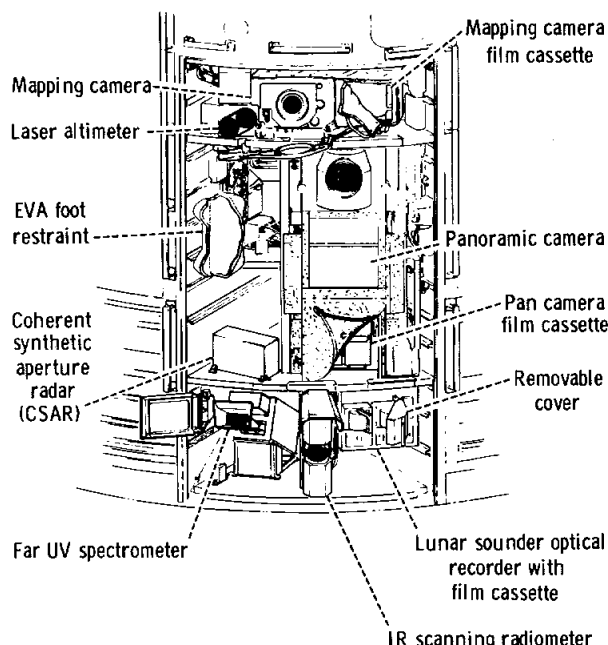
FIGURE 2-4.—Scientific equipment, including orbital experiment instruments and photographic equipment, located in the SIM bay of the service module.

scientific experiments and objectives was housed in the SIM bay. This equipment, illustrated in figure 2-4, includes the lunar sounder, IR scanning radiometer, far UV spectrometer, panoramic camera, mapping camera, and laser altimeter. The S-band transponder experiment used existing CSM S-band communication equipment. Operational periods for inflight experiments and photographic tasks are shown in figure 2-5. The envelope of suborbital tracks for the lunar orbital phase of the mission is shown in figure 2-6.

Inflight science activities on Apollo 17 were conducted over a period of approximately 220 hr, beginning with SIM bay door jettison at 15:05:40 G.m.t., December 10, and terminating approximately 3 hr before splashdown. During this interval, the following science activities were conducted; photography of most of the lunar surface area overflown in sunlight; active electromagnetic sounding of the lunar surface and subsurface over portions of the near side and the far side of the Moon; passive sounding for determination of electromagnetic interference and cosmic noise; thermal mapping of more than one-third of the lunar surface; investigation of lunar atmospheric
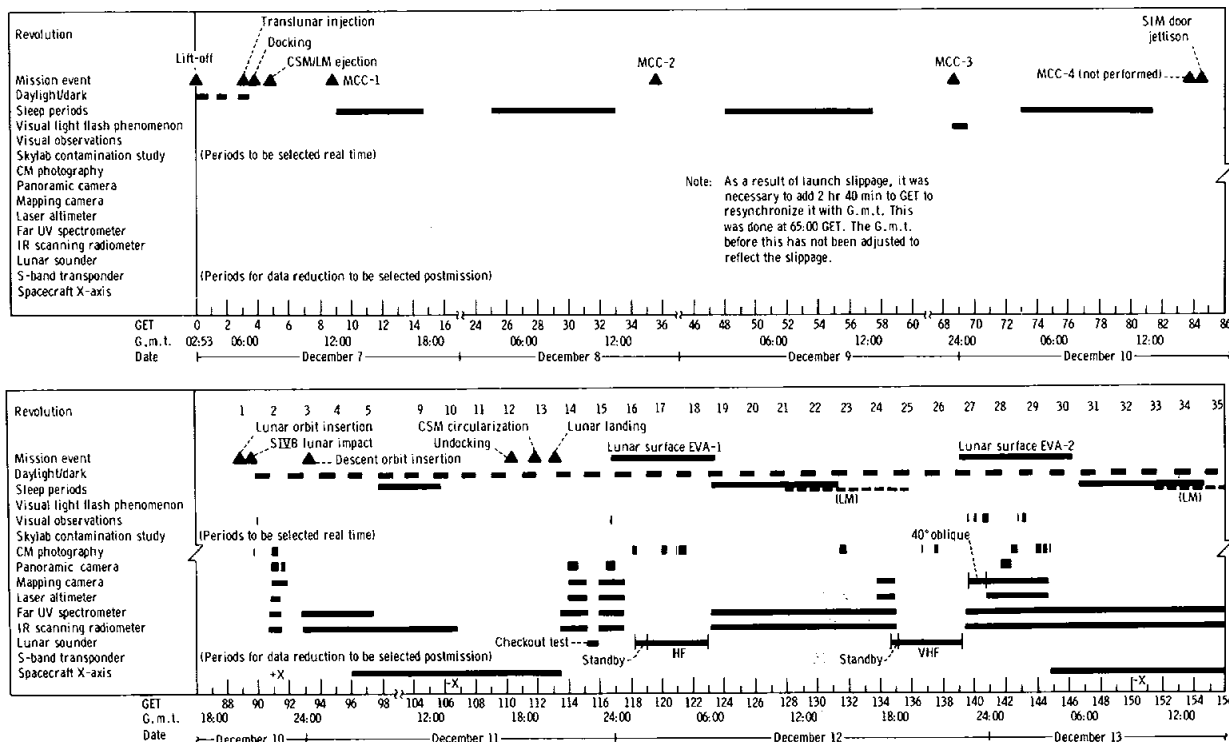
FIGURE 2-5.—Major mission events and data-collection periods correlated to G.m.t. and ground-elapsed time (GET).

composition by UV spectral measurements; determination of gross lunar topography along groundtracks; free-flight measurements of spacecraft velocity for determination of lunar gravity anomalies; visual geological surveys of selected lunar regions in sunlight; and observation of solar atmospheric, galactic, and extragalactic sources of far UV radiation.

Ten hr 31 sec of active lunar sounder data were recorded on film, including two consecutive revolutions each in the HF and VHF ranges, as well as specific targets in each of these ranges. The sounder was operated in the receive-only mode on both the lunar near side and far side. Near the landing site, receive-only data were obtained by the sounder, both with and without the SEP transmitter operating. The sounder was operated for 24 hr during transearth coast to help determine levels of terrestrial noise. Problems were encountered with the extension and retraction of the HF antennas. A faulty talkback indicator and low temperature of the extension/retraction mechanism were blamed for these operational delays, which caused no loss of data.

Infrared scanning radiometer data were obtained

for 100 hr in lunar orbit and 10.5 hr in transearth coast. A total of 10^8 radiometer measurements were made during orbital operation, covering one-third of the lunar surface.

Far UV spectral data were collected for a total of 80 hr in lunar orbit and approximately 60 hr during transearth coast. Experiment operation included a solar atmospheric observation added in real time.

High-quality S-band transponder data were obtained over Mare Serenitatis, Mare Crisium, and the Taurus-Littrow site. The data were taken in low-altitude orbits and will help confirm results obtained from the Apollo 15 mission.

The Apollo window meteoroid and the gamma ray crystal experiments were passive and required no crew activities. The CM window has been retrieved. Activation measurements on the gamma ray crystal were begun 1.5 hr after spacecraft entry, and early indications are that information return from the experiment is more than was expected.

Panoramic camera photography was obtained on portions of eight lunar orbit revolutions and after transearth injection. A five-frame sequence was ob-
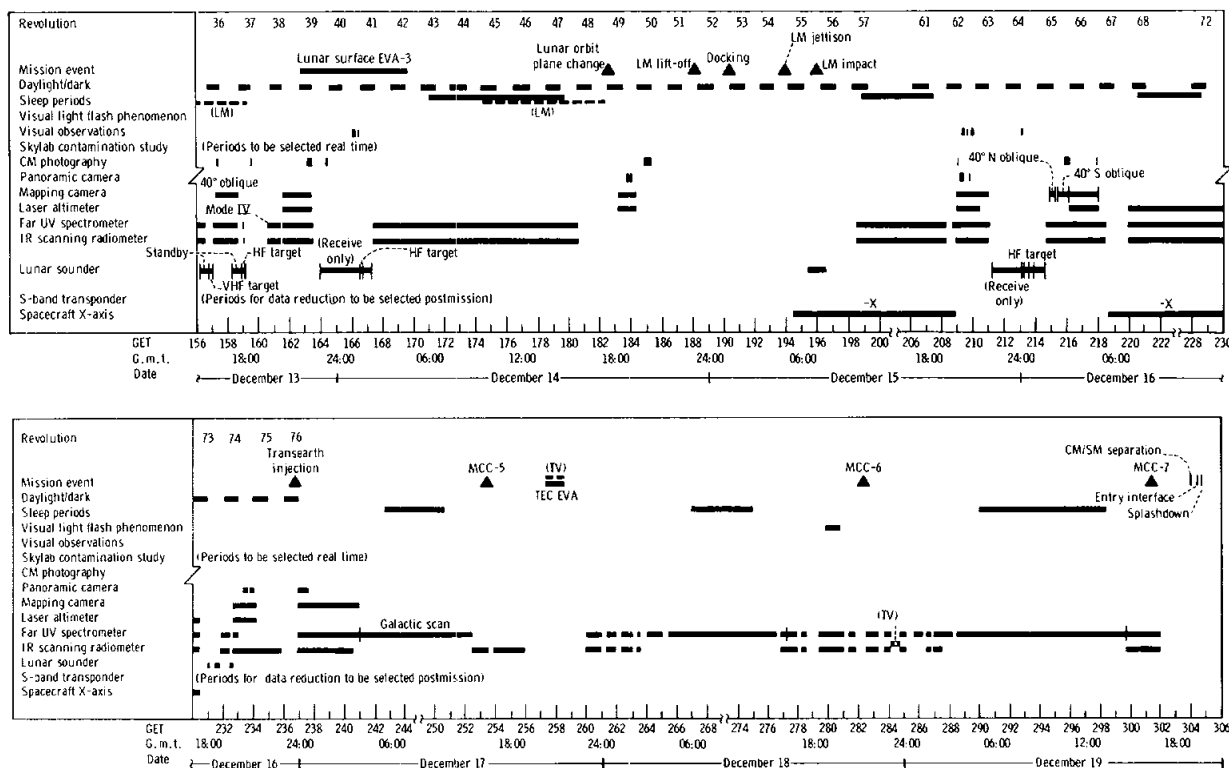
FIGURE 2-5–Concluded.
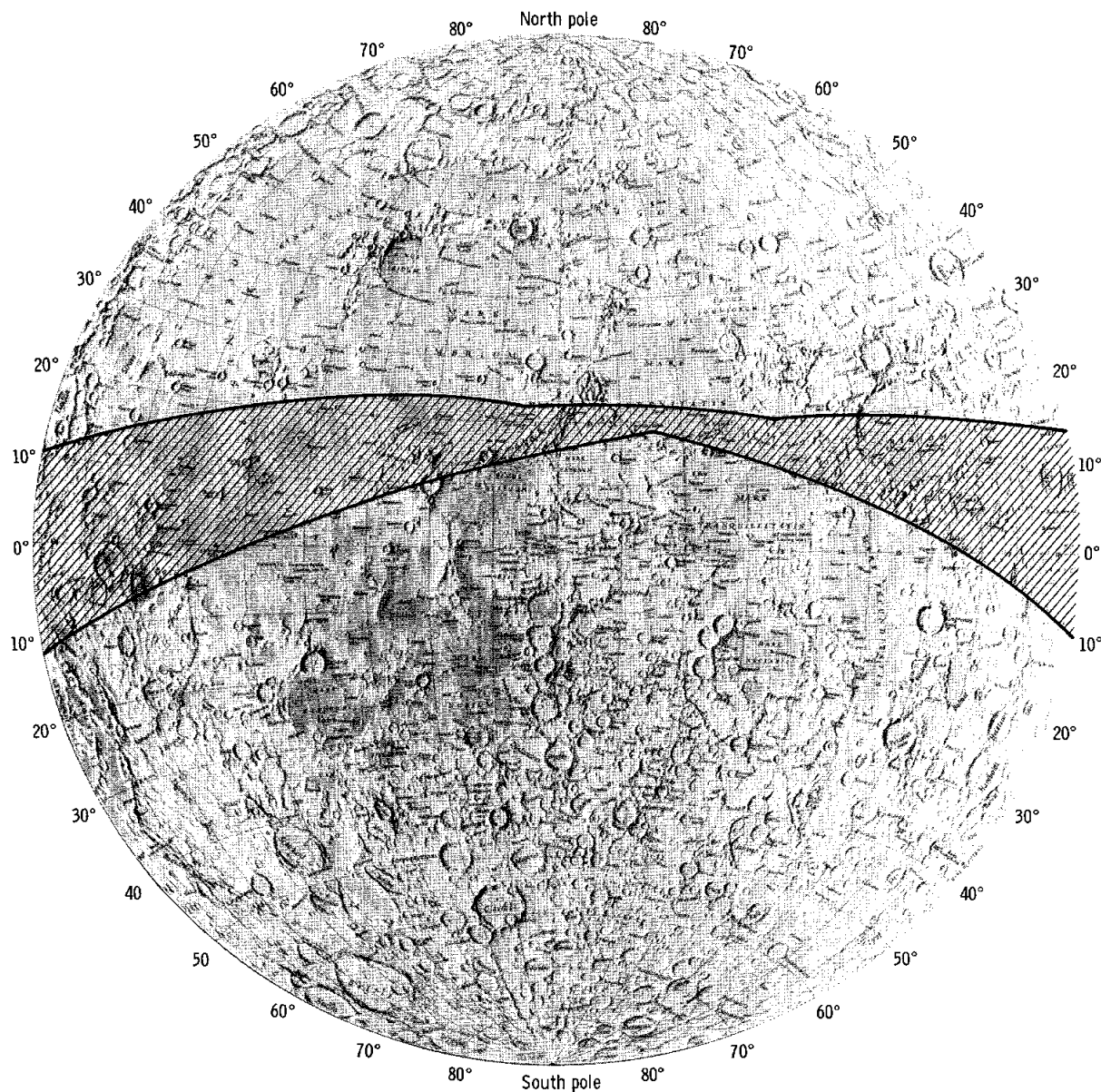
FIGURE 2-6.—Lunar surface groundtrack envelope of the Apollo 17 orbiting spacecraft for
revolutions 1 to 75. Areas of additional data coverage outside the envelope are determined by the
fields of view of experiment instruments and photographic cameras. (a) Near side.

tained on revolution 36 with the camera axis inclined
40° to the south of the groundtrack. On the third
sequence of photography during the 15th revolution,
an erratic velocity-to-height (V/h) signal was noted;
the remainder of panoramic photography was per-
formed with the camera V/h setting in the manual
override position. During the final lunar orbit opera-
tion of the camera, the stereographic drive motor

failed, causing the final 8 min of photography to be
obtained in the monographic rather than the planned
stereographic mode.

Vertical mapping camera photography was ob-
tained on 12 revolutions and after transearth injec-
tion. For the second mapping photography sequence,
the camera deployment time was longer than ex-
pected. To avoid possible failure of the deployment
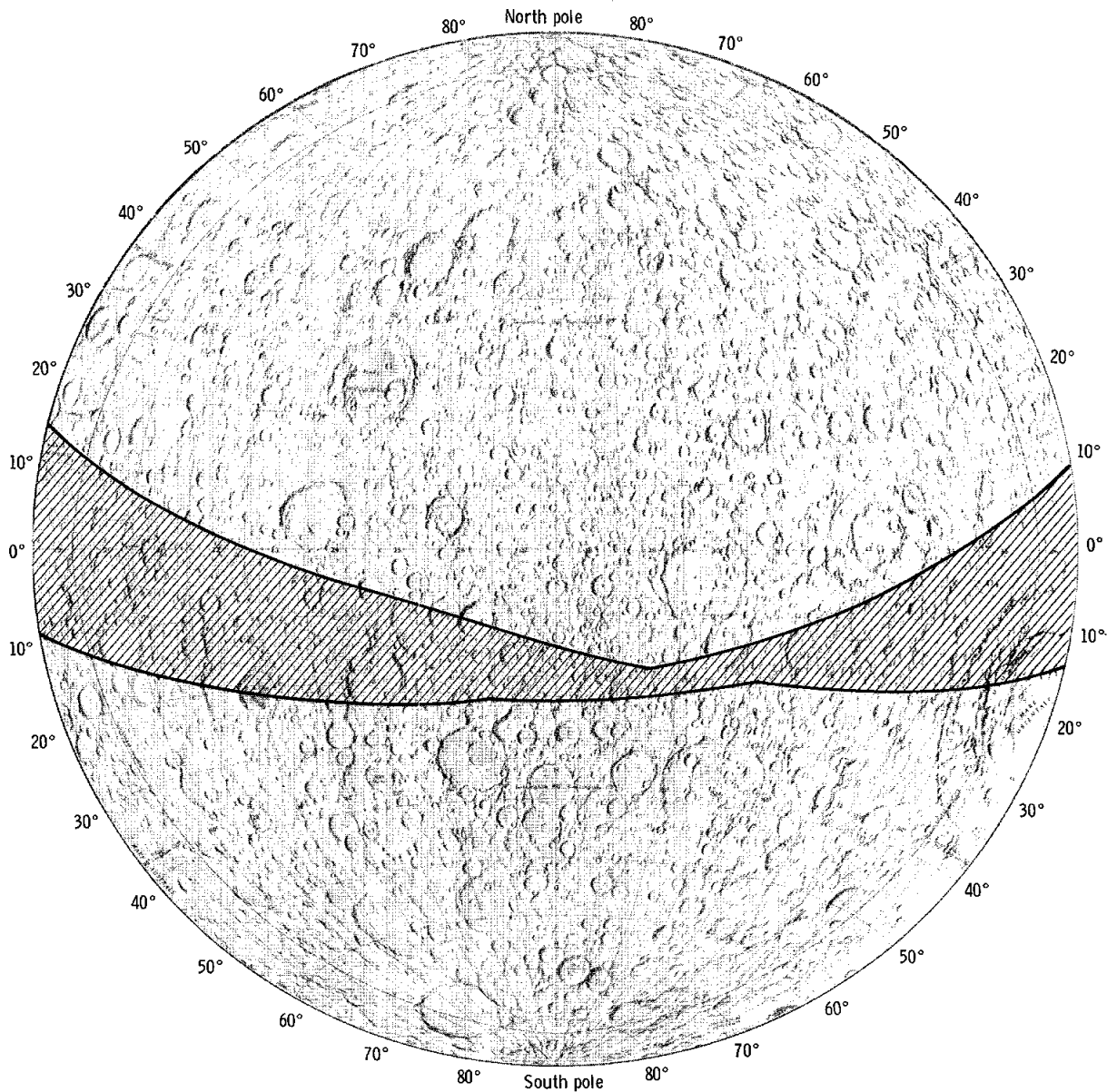
FIGURE 2-6.—(b) Far side.

mechanism, the camera was left deployed between several photographic passes. On revolution 49, the camera was operated from the retracted position, thus losing stellar camera coverage on this sequence.

The laser altimeter operated well throughout the mission, obtaining 3769 ranging measurements. A 30-min altimeter sequence scheduled for revolution 62 was deleted to allow a special attitude sequence for the far UV spectrometer. During the final sleep period in lunar orbit, the altimeter was operated to obtain 10 hr of continuous data, in addition to the planned coverage.

Photographic and visual observations from the CM were made as scheduled, with the exception of the second of two solar corona sequences, which was omitted because of time-line and attitude constraints. The zodiacal light was photographed three different times: once each in red light, blue light, and

plane-polarized white light. Photographs of the lunar surface from the CM included 10 color strips, eight black-and-white sequences near the terminator, and additional photographs to document visual observations. Formally scheduled visual observations of 10 lunar surface targets were made by the crew using 10-power binoculars. Accompanying comments by the crew were made and recorded for subsequent use.

The biostack II and BIOCORE experiments were passive and required no crew activities. The experiments were recovered after completion of the mission.

The CMP performed an inflight EVA at 20:27:40 G.m.t. on December 17 during transearth coast. The EVA lasted for approximately 1 hr 7 min, during which time the CMP retrieved the lunar sounder film and the panoramic and mapping camera film cassettes.

REFERENCE

2-1. Lunar Topographic Photomap of Taurus-Littrow. First ed., U.S. Army Topographic Command, Sept. 1972.

3. Summary of Scientific Results

Robert A. Parker[a]

The first phase of man's active exploration of the Moon came to an end with the Apollo 17 mission. Many questions about lunar science have been answered during the intensive activity of the last decade, but many more remain to be answered. Some of the unanswered questions will be answered in the future from data already returned but as yet not fully analyzed, and some will have to wait for data yet to be returned from instruments already in place on the lunar surface. Still other questions must await further exploration.

The basic objective of the Apollo 17 mission was to sample basin-rim highland material and adjacent mare material and investigate the geological evolutionary relationship between these two major units. In addition to achieving this general geological objective, it has also been possible to measure directly the thermal neutron flux in the regolith, to explore geophysically the subsurface structure of the valley floor, to determine the constituents of the lunar atmosphere and observe their variations during the lunar day and night, and to explore even more of the lunar surface remotely from orbit.

These initial results and others will someday be combined into a coherent picture of the evolution of the Moon that will reflect more light on both the abstract and specific problems of the evolution and current conditions of the Earth and other planets. That will be the true legacy of the Apollo Program— not just the sometimes apparently fragmented preliminary results seen here.

LUNAR FIELD GEOLOGY

Premission photogeology of the Taurus-Littrow valley and its environs led to the expectation of sampling five different major stratigraphic units: the light mantle, the dark mantle, the subfloor, the Sculptured Hills, and the massifs.

The light mantle unit was sampled at stations 2, 2A, and 3 and at two lunar roving vehicle (LRV) sampling stops. Preliminary indications from these samples are that the light mantle is primarily fine-grained debris that includes cataclasites and breccias similar to those attributed to the South Massif and different from the regolith elsewhere on the valley floor. These observations are in agreement with the hypothesis that the light mantle unit resulted from a slide down the northern face of the South Massif that occurred approximately 10^8 yr ago as indicated by crater counts. The slide perhaps was caused by the impact of some secondary ejecta at the top of the South Massif.

The dark mantle unit remains one of the enigmas of the Apollo 17 mission. Photogeological observations of the subdued appearance of the larger craters and the general paucity of craters on the valley floor had led to the expectation of a "mantling" unit which covered the valley floor sometime after most of the regolith formation had taken place and which was perhaps Copernican in age. Because of dark areas in depressions in the surrounding highlands, the mantling unit was expected to have also covered at least part of the highlands. No such unit has so far been detected in situ. Instead, everywhere on the valley floor except in the area of the light mantle, the soil appears to be regolith largely derived from the underlying subfloor basalt unit. A possible dark mantle component in the regolith is the dark glass sphere unit of unknown origin but possibly related to the orange glass of station 4. The age of the dark glass, however, is 3.7×10^9 yr, and it is apparently well mixed into the regolith, which seems to rule it out as the mantling unit.

The subfloor unit was well sampled at a number of stations (the Apollo lunar surface experiments package (ALSEP) site and stations 1A, 4, 5, and 9?) and

---

[a]NASA Lyndon B. Johnson Space Center.

was shown to be a 3.8×10^9-yr-old, massive, light-colored mare basalt unit containing 10 to 15 percent vesicles, 30 to 40 percent plagioclase, together with clinopyroxene and ilmenite as rock-forming plagioclase. Some local variations in texture, mineralogy, and chemistry exist. Geophysical experiments on the mission also indicate the existence of such a layer with a thickness of approximately 1 km. Samples of the subfloor basalt were primarily taken from boulder-size ejecta at large craters that penetrated the regolith to the underlying unit. Samples of the basalt were also obtained from the regolith that has been developed on top of it, notably in a widespread series of LRV samples as well as at the major geological stations. Samples from station 9 in particular may be from deep in the regolith (but not quite to the depth of the basalt unit).

The Sculptured Hills unit was investigated at station 8. Because of the lack of any identifiable material that has moved downslope, sampling of the Sculptured Hills unit consists of samples of the regolith from the lower part of the slope. Because the soil undoubtedly is composed of material from both the valley regolith and the Sculptured Hills regolith, identification of the Sculptured Hills rock types will have to be delayed until a comparison can be made between the valley regolith and the soil collected at station 8. At the moment, no more is known about the Sculptured Hills unit than that it is a highland unit morphologically different from the massifs and the reasons for this difference are unknown.

The massif unit was sampled at three locations at the bases of the South and North Massifs (station 2 and stations 6 and 7, respectively) and also in the light mantle. Five different boulders (one of which, at station 6, had broken into five boulder-size pieces) as well as soils were sampled at the three stations. The boulders undoubtedly represent units in place higher up the massif slopes (in the upper half of the South Massif and the lower third of the North Massif). All the boulders are breccias of a moderately complex nature, similar to those from the Apollo 15 and 16 sites, and are indicative of more than one brecciation event. There is indication of a correlation of breccia types between the North and South Massifs, but definitive conclusions on this must wait for additional geochemical analyses and detailed petrologic examination. In the meantime, it can be concluded that the massif unit, probably raised by the Serenitatis event,

is composed of breccias that probably were produced by one or more basin-forming events.

An event of great interest during the geological exploration of the valley of Taurus-Littrow was the discovery of deposits of orange glass on the rim of Shorty Crater. Present indications are that the orange glass is fairly old (3.7×10^9 yr); that shortly after its formation, it was well buried; and that only recently (20 to 30×10^6 yr ago), it was excavated by the Shorty Crater impact. Some traces of the orange glass spheres exist in the regolith elsewhere in the valley.

The general premission model of a graben valley that was formed as part of the Serenitatis event, perhaps reactivated since then, and later partly filled with a basalt flow (or flows) during the episode of mare filling is corroborated and more tightly defined by the data analyzed to date.

PRELIMINARY SAMPLE ANALYSIS

The suite of rock samples returned from the Apollo 17 mission is a quite varied one. Included in the samples are basalts, dark-matrix breccias and agglutinates, green-gray breccias, blue-gray breccias, light-gray breccias, brecciated gabbroic rocks, and others (including a dunite clast composed of more than 95 percent olivine).

The basalts are quite uniform in composition and are generally similar to the Apollo 11 basalts. They are generally vesicular, have variable grain sizes as large as 2 mm, and consist of approximately 25 to 30 percent plagioclase. The basalts are high in titanium like the Apollo 11 basalts but are much lower in nickel. In detail, chemical differences within the Apollo 17 basalt suite argue for at least two different basalt types.

The dark-matrix breccias and agglutinates are derived from the basalt regolith of the valley floor and contain clasts of basalt. The green-gray breccias are predominantly matrix with a small percentage of mostly mineral clasts. The matrix is coherent, is rich in poikilitic orthopyroxene, and has vesicles as large as several centimeters in diameter. The blue-gray breccias are matrix breccias with a more varied population of clasts than the green-gray breccias. The blue-gray matrix is slightly vesicular with some fine-scale banding and a recrystallized texture. The light-gray breccias are layered and foliated, have a higher percentage of clasts, and are less coherent than

the green-gray and blue-gray types. The clasts, both lithic and mineral, are generally feldspar rich and include first- and second-order breccias. The light-gray matrix texture is fragmental. The brecciated gabbroic rocks are similar to the crushed cataclastic anorthosites returned on the Apollo 15 and 16 missions.

The breccias can be divided chemically into two groups: the blue-gray, green-gray, and light-gray breccias with approximately 50 percent normative plagioclase and the brecciated gabbroic rocks with approximately 70 percent normative plagioclase. The blue-gray, green-gray, and light-gray breccias have strikingly more potassium, phosphorus, rubidium, yttrium, zirconium, and niobium than the brecciated gabbroic rocks. Based on analysis of one light-gray breccia, they appear to have slightly higher rubidium, yttrium, and zirconium contents and a slightly lower strontium and nickel content than the blue-gray and green-gray breccias. Both the major- and trace-element compositions of the blue-, green-, and light-gray breccias are very similar to those of the KREEP-like rocks (those that are rich in potassium, rare-earth elements, and phosphorus) from Descartes and are especially similar to those of the brown-glass-matrix breccia from Hadley-Apennine. The brecciated gabbroic rocks chemically resemble similar rocks from the Apollo 16 mission and especially closely resemble Apollo 15 sample 15418.

The Apollo 17 soils are generally divided into two types: soils on the valley floor derived as regolith from the underlying basalt and soils from the massifs and light mantle derived as regolith from the breccias. At the transition zones between the two units and at the foot of the Sculptured Hills, the soils are a mixture of the two types. Exotic glasses (orange and black glass spherules), first noticed at Shorty Crater, are present in soils throughout the valley. The orange soil is generally basaltic but has a higher percentage of magnesium and a very strikingly high abundance of zinc as well as other trace-element differences (e.g., high chromium oxide). The orange soil also contains more low-temperature volatiles than do other soil samples.

SURFACE ELECTRICAL PROPERTIES EXPERIMENT

The surface electrical properties (SEP) experiment was used to measure the dielectric constant of the lunar regolith in situ and also to provide information on the subsurface structure in the region covered by the geology traverses. Electromagnetic radiation at six frequencies between 1 and 32 MHz was transmitted from a fixed crossed-dipole antenna and received through an antenna attached to the LRV. Preliminary indications are that useful data were received only during the traverse from the SEP site to station 2. On the basis of early analysis of the signals recorded during that traverse, two different models can be developed. One model explains the observations in terms of a dielectric constant that increases as a function of depth, in particular with a marked discontinuity at a depth of approximately 50 m. The other model includes two layers having different dielectric constants the interface of which decreases in depth from approximately 20 m at the lunar module (LM) site to 15 m at station 2.

LUNAR TRAVERSE GRAVIMETER

By the comparison of measurements made on the Earth and at the Apollo 17 landing site with the same instrument, the lunar traverse gravimeter, the value of gravity at the LM site was found to be 162 695 ± 5 mgal. Relative gravity measurements were obtained for a network of 12 stations spread across the valley floor. At four stations near the LM (the LM, ALSEP, and SEP sites and station 1A), the 10 measurements agree within approximately ± 3 mgal. At four other stations on the valley floor located as far as 5 km from the LM (stations 3, 4, 5, and 9), the Bouguer anomaly is generally small and slightly negative (−5 to −10 mgal). At four other stations either at or very near the massifs (stations 2, 2A, 6, and 8), the Bouguer anomaly increases rapidly to between −20 and −25 mgal. Between stations 2A and 3, a distance of less than 1.5 km, the Bouguer anomaly changes from −20 to −5 mgal. The Bouguer anomaly curve has been interpreted in terms of a model with a 1-km-thick plate of basalt for the valley floor, assuming a density contrast of 0.8 g/cm^3 with respect to the material on either side.

LUNAR SEISMIC PROFILING EXPERIMENT

The lunar seismic profiling experiment is an extension of the active seismic experiment carried on the Apollo 14 and 16 missions. Eight explosive

charges (ranging in size from 57 to 2722 g) were deployed at distances between 100 and 2700 m from a triangular geophone array. These charges were later detonated on command from the Earth, and travel-time measurements were obtained that, together with the LM-impact signals, indicate a three-layer model for the valley floor at Taurus-Littrow. The first 248-m-thick surface layer has a seismic velocity of 250 m/sec. The second layer, extending to a depth of approximately 1200 m, has a seismic velocity of 1200 m/sec. Below 1200 m, the third layer, with a seismic velocity of approximately 400 m/sec, begins. A reasonable model, with basalt flows filling the valley of Taurus-Littrow to a depth of 1.2 km, can be derived from these observations. The 4000-m/sec velocity for the third layer is a valuable tie point between the shallow surface velocities measured earlier and the deeper velocities measured by the passive seismometers from distant events.

LUNAR SURFACE GRAVIMETER

The lunar surface gravimeter was designed to make very accurate (1 part in 10^{11}) measurements of the acceleration of lunar gravity and of its variation with time. These measurements should allow investigations of gravitational waves by using the Moon as an antenna and also investigations of tidal distortions of the shape of the Moon. Following deployment of the gravimeter, problems occurred in trying to balance the beam. These problems were probably caused by an incorrect mass of the beam and have at least partly been overcome by applying pressure on the beam with the mass-changing mechanism. Data in the form of seismic events at sunrise and sunset have been received, and it is hoped that the instrument can be used in its off-nominal mode to obtain the data for which it was designed.

LUNAR EJECTA AND METEORITES EXPERIMENT

The objectives of the lunar ejecta and meteorites experiment, which is part of the ALSEP, are to detect secondary particles that have been ejected by meteorite impacts on the lunar surface and to detect primary micrometeorites themselves. The particle detectors of the instrument are multilayered arrays that are capable of measuring the velocity and energy of incident particles. No meaningful results are yet available from this instrument.

LUNAR ATMOSPHERIC COMPOSITION EXPERIMENT

The lunar atmospheric composition experiment is designed to identify the various gases in the lunar atmosphere and to determine the concentration of each species. Previous measurements using the cold cathode ion gages have been limited to total gas concentrations. Preliminary results for the first three lunations indicate the presence of (1) three native species in the lunar atmosphere (helium, neon, and argon) and (2) a large number of other species, some of which are undoubtedly contaminants (e.g., atomic hydrogen, nitrogen, oxygen, chlorine, hydrochloric acid, and carbon dioxide). The measured concentrations of these contaminants has continued to decline with the passage of time.

The measured helium concentrations and their behavior as a function of phase in the lunation (increasing by a factor of 20 toward lunar midnight) are in agreement with predictions that helium does not freeze out on the surface at night and that its source is the solar wind. The concentration of neon, measured only at night, is a factor of 20 lower than predicted, and the results are not understood. The concentration of argon also decreases (in fact, becomes undetectable) during the night as expected for a gas that freezes out on the surface during the lunar night. Shortly before dawn, the argon concentration begins to rise, apparently indicative of the migration of argon across the approaching sunrise terminator (a predawn argon breeze); the behavior of the contaminants is markedly different in that they show a sharp rise just at local sunrise.

HEAT FLOW EXPERIMENT

The deployment of a second heat flow experiment on the lunar surface as a part of the Apollo 17 ALSEP allows comparison of lunar heat flow measured at two different stations, the Apollo 15 and 17 landing sites. Both Apollo 17 probes were successfully inserted to their full depth of 2.36 m.

Preliminary results indicate that the heat flow at the Apollo 17 site is 2.8×10^{-6} W/cm^2 for the first probe and 2.5×10^{-6} W/cm^2 for the second probe.

These values can be compared with a revised value for the Apollo 15 site of 3.1×10^{-6} W/cm². The uncertainty for all three values is ± 20 percent. The heat flow gradient for probe 1 is uniform in agreement with a similar observation made at the Apollo 15 site. For probe 2, however, the gradient is definitely not uniform and the difference is believed to be due to insertion of the probe very near a buried boulder.

Corrections for topography have not yet been applied to the heat flow values. Although the size of these corrections is not clear at this time, it would appear that they will result in a reduction of the present values by a factor of 15 to 25 percent for the Apollo 17 measurements and an uncertainty of ± 10 percent for the Apollo 15 measurements. The possible resulting difference between the heat flow values measured at the two different sites may be explainable in terms of higher thorium abundances, observed by the Apollo 15 gamma ray instrument, in southeastern Mare Imbrium as compared with southeastern Mare Serenitatis. In any case, values of the heat flow between 2.4×10^{-6} and 3.0×10^{-6} W/cm² are confirmed as characteristic of more than one site of the Moon. If applied generally to the entire Moon, those values argue for relatively large quantities of radioisotopes in the outer layers of the Moon.

LUNAR NEUTRON PROBE EXPERIMENT

Time-integrated fluxes of thermal neutrons ($\lesssim 1$ eV) as a function of depth in the regolith were measured using the lunar neutron probe. These measurements were accomplished with targets of boron-10 and uranium-235 placed at intervals along a 2-m rod that was inserted into the hole left by the deep drill core when it was extracted. Preliminary analysis of tracks in the mica detectors that were used in conjunction with the uranium-235 targets agrees with both the magnitude and shape of previous theoretical work on the neutron flux as a function of depth in the lunar regolith. Therefore, the problem concerning the fact that integrated neutron dosages for soil samples indicate more rapid and/or deeper regolith turnover than geological evidence indicates is not resolved. Hence, neither the mixing depth nor the time scale of the regolith model, both of which are needed to fully interpret the gadolinium ratios, has been defined.

PASSIVE SEISMIC EXPERIMENT

A passive seismometer station was not included in the Apollo 17 ALSEP. The impacts of the Apollo 17 LM and SIVB were observed by the four stations already in place at distances as great as 1750 km. These impacts and the occurrence of other natural events since the Apollo 16 mission (especially an impact on the far side near Mare Moscoviense) have helped to further define the lunar seismic model below the "crust" as being characterized by a thick, seismically inactive, relatively homogeneous lithosphere that encloses an asthenospheric zone of partial melting. Moonquake activity appears to be concentrated at the boundary between these two zones at a depth of approximately 1000 km. Evidence has also been found for the existence of two belts of seismic activity as plotted by epicenter locations. Seismic observations to date cannot be used to either confirm or deny the possible existence of a small iron-rich core.

COSMIC RAY EXPERIMENT

A new set of cosmic ray detectors was carried to the surface of the Moon on the Apollo 17 mission. Two sets of detectors (including mica, quartz, glass, plastic, and foil) were exposed, one set facing the Sun and one set in the shade facing away from the Sun. During the time that the detectors were exposed, no significant solar activity occurred. Although the absolute flux levels for the 0.02- to 1-MeV/amu energy range were considerably lower than those for the Apollo 16 mission, the shape of the spectrum is similar to that for the flare that occurred during the Apollo 16 mission and indicates that proportionate numbers of energetic particles are emitted by the Sun even during quiet periods. Heavy-element enrichment noted during flares is also present during the quiet periods. Tracks were also noted in the detectors facing away from the Sun. Because these particles also have a "solar energy" spectrum and presumably come from the Sun, the "antisolar" tracks indicate the existence of irregularities in the interplanetary magnetic field outside the orbit of the Earth that are capable of "reflecting" these solar cosmic rays.

SOIL MECHANICS EXPERIMENT

Although there is considerable local variability in the properties of the soil, large-scale averages have

been very similar for all Apollo landing sites with the exception of Descartes, where the relative density is notably lower than at the other sites. Although the soil density in the Apollo 17 double-core sample obtained from the orange soil is the highest yet found on an Apollo mission, the difficulty in driving the core tube was not exceptional, leading to the conclusion that it is not a low mean porosity but a high specific gravity of the individual grains that causes the observed high density. Because of the long-term stability of the deep drill hole, it is concluded that the soil strength is relatively high at depths on the order of 1 to 2 m.

APOLLO LUNAR SOUNDER EXPERIMENT

The Apollo lunar sounder experiment carried in the scientific instrument module (SIM) bay was a three-frequency (5, 15, and 150 MHz) chirped radar sounder. Depth of subsurface exploration, in terms of features defined by changes in the dielectric constant, decreased with increasing frequency.

The Apollo lunar sounder was designed for three primary modes of operation: sounding, profiling, and imaging. The sounding mode pertains to the detection and mapping of subsurface features such as a probable 100-m-deep interface detected in western Mare Serenitatis. The profiling and imaging modes, which are similar to conventional surface return radars, can provide quantitative metric and topographic data as well as albedo measurements.

Preliminary results obtained by processing some small selected portions of the data indicate that useful data were obtained.

ULTRAVIOLET SPECTROMETER

The ultraviolet spectrometer flown in the SIM bay of the Apollo 17 spacecraft was a single-channel scanner having a 12° by 20° field of view and covering a spectral range of 1180 to 1680 Å (118 to 168 nm). The entire spectral range was repetitively scanned every 12 sec. The primary objective of the instrument was to measure the lunar atmosphere using resonance line scattering. No lunar atmospheric constituents were detected except for a short-lived (2 to 4 hr) "cloud" just after the descent of the LM. Among new lower limits that were established is one of $\leqslant 10$ atoms/cm^3 for atomic hydrogen at the lunar

surface. This low value (at least 10 times lower than predicted for a transient lunar atmosphere resulting from the solar wind) implies that during diffusion at the lunar surface, hydrogen molecules are formed. The upper limits for hydrogen molecules from the current observations are not inconsistent with this idea. Xenon is also less abundant than predicted as a native constituent of the lunar atmosphere.

INFRARED SCANNING RADIOMETER

The infrared scanning radiometer, carried in the SIM bay, was used to map the lunar surface in 352-km-wide strips centered on the groundtracks with a resolution of better than 10 km. This mapping was accomplished by sweeping the 1° instantaneous field of view in contiguous strips perpendicular to the orbital groundtrack. The spectral bandpass extended from 1.2 to 70 μm.

In addition to a number of individual thermal anomalies, preliminary examination of the data shows, among other things, a great concentration of nighttime thermal hot spots in the Oceanus Procellarum region, particularly in contrast to the relative smoothness of nighttime scans of highland areas. The nighttime thermal picture of the far side of the Moon is relatively featureless compared to that of the near side.

S-BAND TRANSPONDER

The general similarities of the Apollo 15 and 17 groundtracks allowed good comparisons to be made between gravity data obtained on the two separate missions. Agreement in many areas (e.g., over Mare Crisium) was good. The model for the Serenitatis mascon, however, was shown to be inadequate; the Apollo 17 observations were 1.6 times larger than those predicted for the Apollo 17 groundtrack by the Apollo 15 model. Because the new Apollo 17 data increase the areal coverage of Mare Serenitatis, it is obvious that an improved model can be expected. Very good areal coverage was also obtained of Grimaldi Crater, and there is evidence that this mascon has the largest mass distribution yet observed for any mascon (approximately 1000 kg/cm^2).

An estimate derived from these observations for the value of lunar gravity at the landing site (162 722 mgal) compares very well with that obtained by the lunar traverse gravimeter (162 695 mgal).

BIOSTACK EXPERIMENT

The Apollo 17 biostack experiment (biostack II) was of very similar configuration to the Apollo 16 biostack experiment (biostack I). The total radiation dose received by biostack II was approximately 15 percent higher than that received by biostack I. The primary difference between the two experiments was the different set of species flown on the two missions. (Three of the four species flown on Apollo 16 were flown again on Apollo 17 as well as three other species.) Initial results, using organisms not hit by cosmic rays, show that, as on the Apollo 16 mission, viability is apparently not affected by other factors related to space flight. The Apollo 16 results showed markedly different sensitivity to radiation between different strains of the same species. These aspects will be further investigated as work is continued on biostacks I and II.

BIOCORE EXPERIMENT

Five pocket mice were flown in a self-contained unit in the Apollo 17 command module to study the effects of cosmic rays on living tissues, especially the brain. Four of the five mice survived the trip. Processing of the bodies of all five Apollo mice and of a number of control mice is underway. Sectioning of the brains has been delayed pending full analysis of the cosmic ray tracks in the subscalp monitors. An average of 16 tracks/monitor was found for the monitors on the mice that survived the trip. Portions of the scalp of one Apollo mouse have been examined and found to contain some lesions, but a direct relationship between these lesions and cosmic ray hits will have to await further analysis and comparison between locations in the scalp and in the monitors.

Other organs are also being examined, but no results are yet available.

VISUAL LIGHT PHENOMENON

Observations of the light flash phenomenon continued during the Apollo 17 mission. As on Apollo 16, the Apollo light flash moving emulsion detector was worn by one crewman for a 1-hr observing session during translunar coast. No results are yet available on the time history of tracks in these emulsions. When available, these data should define the particles responsible for the light flashes.

Some statistical data are available now on observations made during the last four Apollo missions. In particular, two items stand out. First, a relatively long period of time is required before the perception of the first event compared to the time between events thereafter. This fact would indicate that dark adaptation is involved and that the events occur in the eye. Second, the length of time before the observation of the first event was longer during transearth coast than during translunar coast; also, the rate of observed events, after the first one, was lower during transearth coast than during translunar coast. The cause of the greatly reduced ability to see the light flashes during transearth coast as opposed to translunar coast is not clear.

ORBITAL GEOLOGY

More than a score of individual investigations of surface and spatial features have been performed so far based on the Apollo 17 crew orbital observations and panoramic and metric camera photographs. The scope of these investigations ranges from studies of the structure of individual craters to studies of the sequences of mare stratigraphy and mare ridges to studies of the solar corona and zodiacal light.

4. Photographic Summary

M. C. McEwen[a] *and Uel S. Clanton*[a]

The photographic objectives of the Apollo 17 mission were to provide precisely oriented mapping camera photographs and high-resolution panoramic camera photographs of the lunar surface, to support a wide variety of scientific and operational experiments, and to document operational tasks on the lunar surface and in flight.

Lunar surface photographs are primarily of three types: (1) operational photographs, to document the condition, performance, orientation, or setting of equipment and the effectiveness of procedures; (2) scientific documentation photographs, to record samples in their undisturbed condition as well as their location, orientation, and detailed setting or to record features or materials that were not collected; and (3) panoramic views, to provide for the accurate location of traverse stations and to provide the capability to reconstruct the geologic setting of the landing site.

Orbital photographic tasks, other than mapping camera and panoramic camera operation, were for both operational and scientific purposes. Orbital science photography planned before the mission included (1) areas of geologic interest; (2) near-terminator areas, where details of relief are enhanced; (3) areas not covered by photography from other missions; (4) areas in earthshine; and (5) low-light-level astronomical phenomena, such as the solar corona and zodiacal light. In addition, film was allotted for crew-option photographs to be taken on the basis of real-time observations.

In tables 4-I to 4-III, the Apollo 17 cameras and film types are listed, and a general description of the tasks for which each was used is provided. The color film used in the command module (CM), SO 368, was intended primarily for well-lighted targets but was used with a high degree of success for target strips that extended almost to the terminator. Earthshine photographs, virtually for the first time on an Apollo mission, have provided usable imagery, including that of lunar surface areas where the crewmen reported seeing possible "flashes." Crew-option photographs include the "flash" areas, lunar surface color boundaries, areas with orange-colored strata, flows, and other features of geologic interest.

The lunar surface groundtrack envelope of the Apollo 17 spacecraft is illustrated in section 2 of this report (fig. 2-6). The orbital inclination was approximately $20°$ throughout the first 47 lunar revolutions and was increased to slightly more than $23°$ during revolution 48. The terminator advanced $75°$ across the lunar surface while the Apollo 17 spacecraft was in orbit. A portion of the lunar far side that had not been illuminated during the other J-series missions (Apollo 15 and 16) was in sunlight during the early revolutions of the Apollo 17 spacecraft. The panoramic and mapping cameras were used to photograph a part of this area centered along a line from approximately latitude $23°$ S, longitude $152°$ W, to latitude $17°$ S, longitude $180°$ W. Electric Hasselblad (EL) 70-mm photographs of the same area complement the scientific instrument module (SIM) camera photographs.

In the panoramic camera, 1623 images were exposed, of which approximately 1580 are high-resolution photographs from lunar orbit. The remainder are transearth coast (TEC) views of the lunar surface. The panoramic camera image is 11.4 by 114.8 cm and, at the 110-km altitude approximated in the near-circular orbit after revolution 12, covers a

[a]NASA Lyndon B. Johnson Space Center.

TABLE 4-I.—*Photographic Equipment Used in the Command Module*

Camera	Features	Film size and type	Remarks
Electric Hasselblad (EL)	Electric: interchangeable lenses of 80- and 250-mm focal length	70 mm SO 368 Ektachrome MS color-reversal film, ASA 64 2485 black-and-white film, ASA 6000	Used with 80-mm lens and color film to document operations and maneuvers involving more than one vehicle. Used with appropriate lens-film combinations to photograph preselected orbital science lunar targets, different types of terrain at the lunar terminator, crew-option lunar targets, astronomical phenomena, views of the Moon after trans-earth injection, and the Earth from various distances
Nikon	Mechanically operated; through-the-lens viewing and metering; 55-mm lens	35 mm 2485 black-and-white film, ASA 6000 SO 168 Ektachrome EF high-speed color-reversal film, ASA 160	Used for dim-light photographs of astronomical phenomena, photographs of lunar surface targets illuminated by earth-shine, and the Apollo light flash moving emulsion detector
Data acquisition camera (DAC)	Electric; interchangeable lenses of 10-, 18-, and 75-mm focal length; the DAC-sextant combination has an effective focal length of 229 mm; variable frame rates of 1, 6, 12, and 24 frames/sec	16 mm SO 368 Ektachrome MS color-reversal film, ASA 64 SO 168 Ektachrome EF high-speed color-reversal film, ASA 160 2485 black-and-white film, ASA 6000	Bracket mounted with mirror in command module (CM) rendezvous window to document maneuvers with the lunar module (LM) and CM entry; handheld for other photographs, including subjects inside and outside the CM; bracket mounted on sextant to document landmark tracking

21- by 330-km area of the lunar surface. Before revolution 12, the orbit was more highly elliptical, and the dimensions of the lunar surface area depicted vary significantly as a function of position along the groundtrack.

Of 3298 mapping camera frames, approximately 2350 contain imagery of the lunar surface. The remaining frames were used for calibration or camera cycling or were exposed over unlighted lunar surface either near terminators or when the camera was used in conjunction with the laser altimeter. The 11.4-cm² image of the mapping camera covers a lunar surface area approximately 150 km, or roughly 5°, on a side at the nominal 110-km altitude.

Throughout the lunar orbit phase of the mission, the nominal procedure was to operate the mapping camera over the entire sunlit portion of any pass in which it was used. Panoramic camera operation was more limited because of the much higher rate of film use and because of a 30-min continuous-operation constraint. The prime considerations in the pre-mission task of selecting revolutions on which the SIM cameras would be operated were that the groundtrack be sufficiently offset from other ground-tracks to permit coverage of new area and that camera operation be compatible with other mission activities.

Mapping and panoramic camera coverage of the lunar surface is indicated in figures 4-1 and 4-2, respectively. These maps were prepared during the Apollo 17 mission and are based on real-time trajectory data and telemetered camera-function data;

TABLE 4-II.—*Photographic Equipment in the Scientific Instrument Module*

Camera	Features	Film size and type	Remarks
Mapping	Electric; controls in command and service module (CSM); 7.6-cm-focal-length lens; 74° by 74° field of view; a square array of 121 Reseau crosses, 8 fiducial marks, and the camera serial number recorded on each frame with auxiliary data of time, altitude, shutter speed, and forward-motion control setting	467 m of 127-mm film type 3400, Panatomic-X aerial film, intermediate speed, extended red sensitivity	The 11.4-cm² frames with 78-percent forward overlap provide photographs of mapping quality. Data recorded on the film will permit reconstruction of lunar surface geometry with a high degree of accuracy.
Stellar	Part of mapping camera subsystem; 7.6-cm lens; viewing angle at 96° to mapping camera view; a square array of 25 Reseau crosses, 4 edge fiducial marks, and the lens serial number recorded on each frame with binary-coded time and altitude	157 m of 35-mm film type 3401, Plus-X aerial film, medium speed, high contrast, high acutance, extended red sensitivity	A 3.2-cm circular image with 2.4-cm flats records the star field at a fixed point in space relative to the mapping camera axis. Reduction of the stellar data permits accurate determination of camera orientation for each mapping camera frame.
Panoramic	Electric; controls in CSM, 61-cm lens; 10°46' by 108° field of view; fiducial marks printed along both edges; IRIG[a] B time code printed along forward edge; data block includes frame number, time, mission data, velocity/height, and camera-pointing altitude	1975 m of 127-mm film type 3414, slow speed, high contrast, extended red sensitivity	The 11.4- by 114.8-cm images are tilted alternately forward and backward 12.5° in stereoscopic mode. Consecutive frames of similar tilt have 10-percent overlap; stereopairs, 100-percent overlap. Panoramic photographs provide high-resolution stereoscopic coverage of a strip approximately 330 km wide, centered on the ground-track.

[a]Inter-range instrumentation group.

TABLE 4-III.—*Photographic Equipment Used in the LM and on the Lunar Surface*

Camera	Features	Film size and type	Remarks
Hasselblad data camera (DC), 2	Electric; 60-mm-focal-length lens; Reseau plate	70 mm SO 368 Ektachrome MS color-reversal film, ASA 64 3401 Plus-X black-and-white film, aerial exposure index (AEI) 64	Handheld within the LM; bracket mounted on the remote control unit for extravehicular activity (EVA) photographs; used for photography through the LM window and for documentation of surface activities, sample sites, and experiment installation
Hasselblad DC	Electric; 500-mm lens; Reseau plate	70 mm, 3401 Plus-X black-and-white film, AEI 64	Handheld; used to photograph distant objects from selected points during the three EVA periods
DAC	Electric; 10-mm lens	16 mm, SO 368 Ektachrome MS color-reversal film, ASA 64	Mounted in the LM right-hand window to record the LM pilot (LMP) view of the lunar scene during descent and ascent and to document maneuvers with the CSM
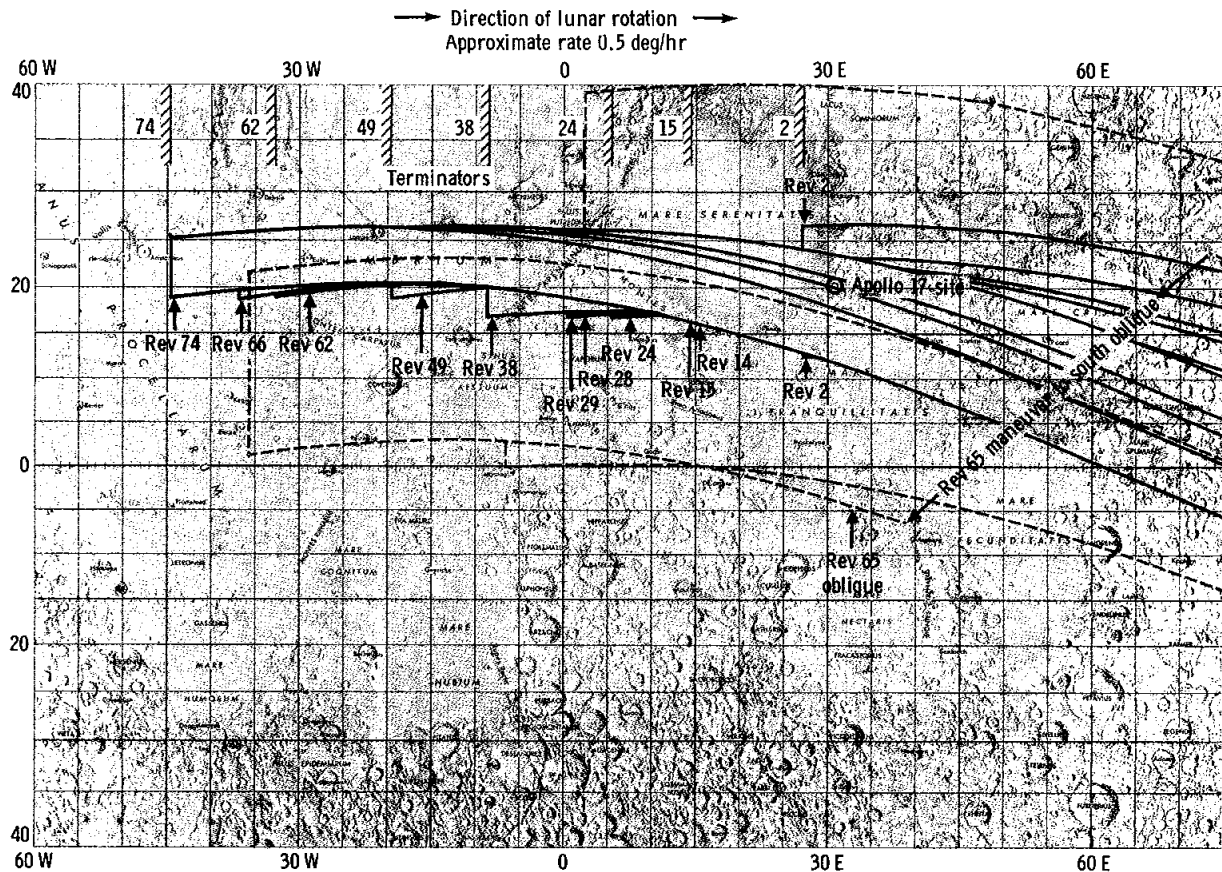
FIGURE 4-1.–Apollo 17 mapping camera coverage. The coverage is based on camera on/off times from telemetry, not

minor differences may become apparent between the indicated coverage and the actual coverage determined from examination of the photographs.

Hasselblad EL photographs exposed from the CM total 1170; Hasselblad data camera (DC) photographs exposed from the lunar module (LM) or on the lunar surface total 2422, most of which were taken on the lunar surface. The total number of 35-mm Nikon frames exposed is near 380. Of the 12 magazines of 16-mm film exposed on the Apollo 17 mission, four were used inside the LM and eight in the CM.

At the time of preparation of this report, the Apollo 17 photographs had been rapidly screened and the images had been identified and located. Index maps of orbital photographs and tabular indexes with supplemental information for all photographs, both from the spacecraft and the lunar surface, are in preparation.

EARTH ORBIT AND TRANSLUNAR COAST PHOTOGRAPHY

For the first time in an Apollo mission, the Antarctic continent was visible to and photographed by the orbiting astronauts. A spectacular group of 70-mm Hasselblad EL color photographs exposed in Earth orbit portray the sunlit portion of the Earth from the South Atlantic Ocean across Africa and the Indian Ocean to Australia. Cloud patterns are the subject of several of the photographs.

Lift-off is pictured in figure 4-3; figures 4-4 and 4-5 are Earth orbit views. Approximately 1 hr after the translunar injection (TLI) maneuver during the translunar coast (TLC) phase of the mission, the transposition, docking, and extraction (TD&E) maneuvers were executed. In sequence, the TD&E maneuvers included command and service module
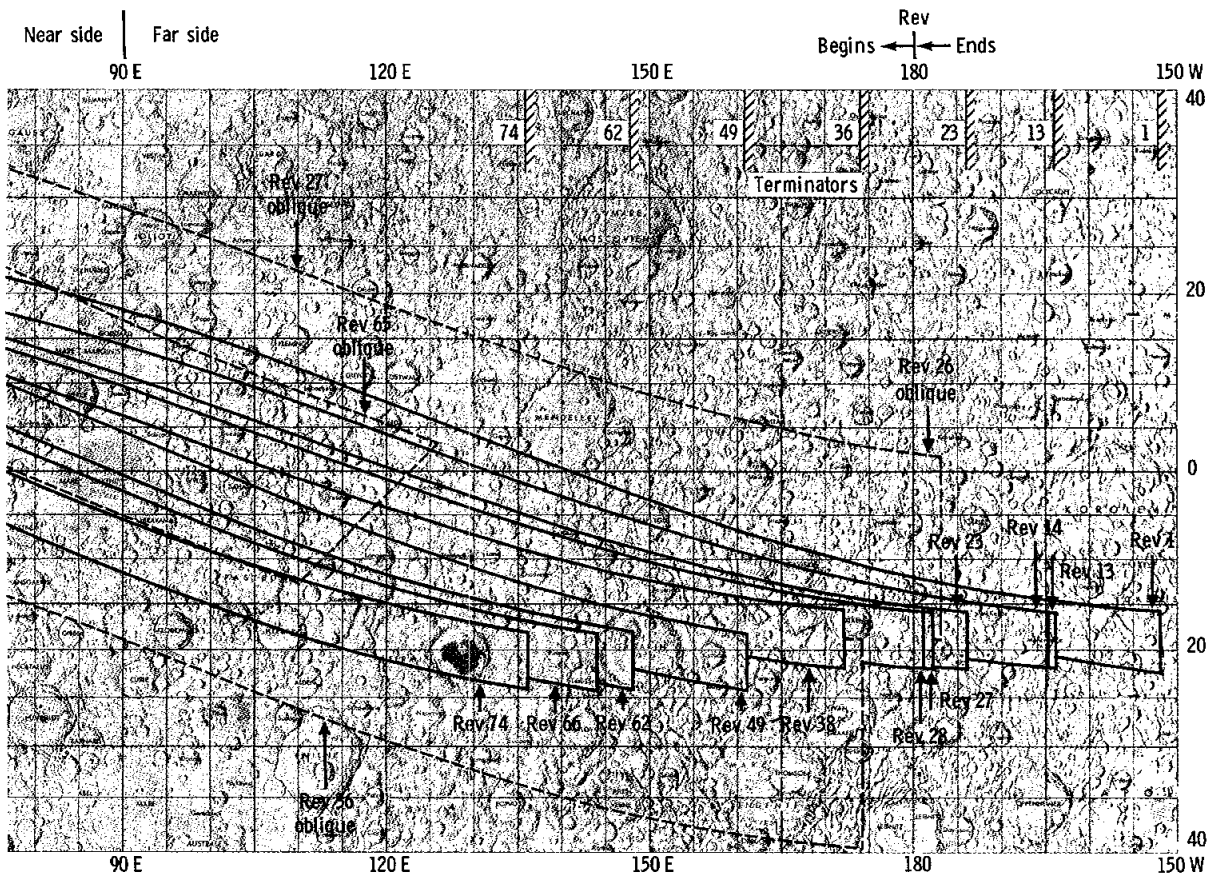
on analysis of photographs. Only sunlit coverage is indicated. The area photographed after transearth injection is not shown.

(CSM) separation from the SIVB, a 180° rotation of the CSM, docking of the CSM with the LM, and extraction of the LM from the SIVB. These maneuvers were documented from the CM with both the Hasselblad EL camera and the 16-mm data acquisition camera (DAC). The DAC was bracket mounted, and the views of the LM, SIVB, and Earth in this sequence are mirror images.

During TLC, the crew provided extensive descriptions of the Earth surface and of cloud patterns, and the view was repeatedly recorded with the DAC and the Hasselblad camera. Approximately 4.5 hr before lunar orbit insertion, the door that provided protective cover to the instruments in the SIM bay was jettisoned; its departure was photographed with the DAC. The hyperbolic trajectory of the SIM bay door eventually carried it beyond the lunar sphere of influence. Figures 4-6 to 4-9 are TLC photographs.

LUNAR ORBIT PHOTOGRAPHY PRECEDING LM TOUCHDOWN

During the first revolution of the spacecraft about the Moon, the lunar surface was in sunlight from approximately 151° W to 29° E longitude. As the spacecraft crossed the lunar sunrise terminator, the Hasselblad EL camera was used to photograph the Taurus-Littrow landing site (lat. 20.2° N, long. 30.8° E) at a very low Sun illumination angle.

When the spacecraft passed into sunlight again, near longitude 152° W, the panoramic and mapping cameras were switched on to photograph a lunar far-side area where high-quality photographic coverage had not been available previously. To complement the SIM camera photographs, the Hasselblad EL camera was used to document the area north of the groundtrack from the vicinity of the crater Galois
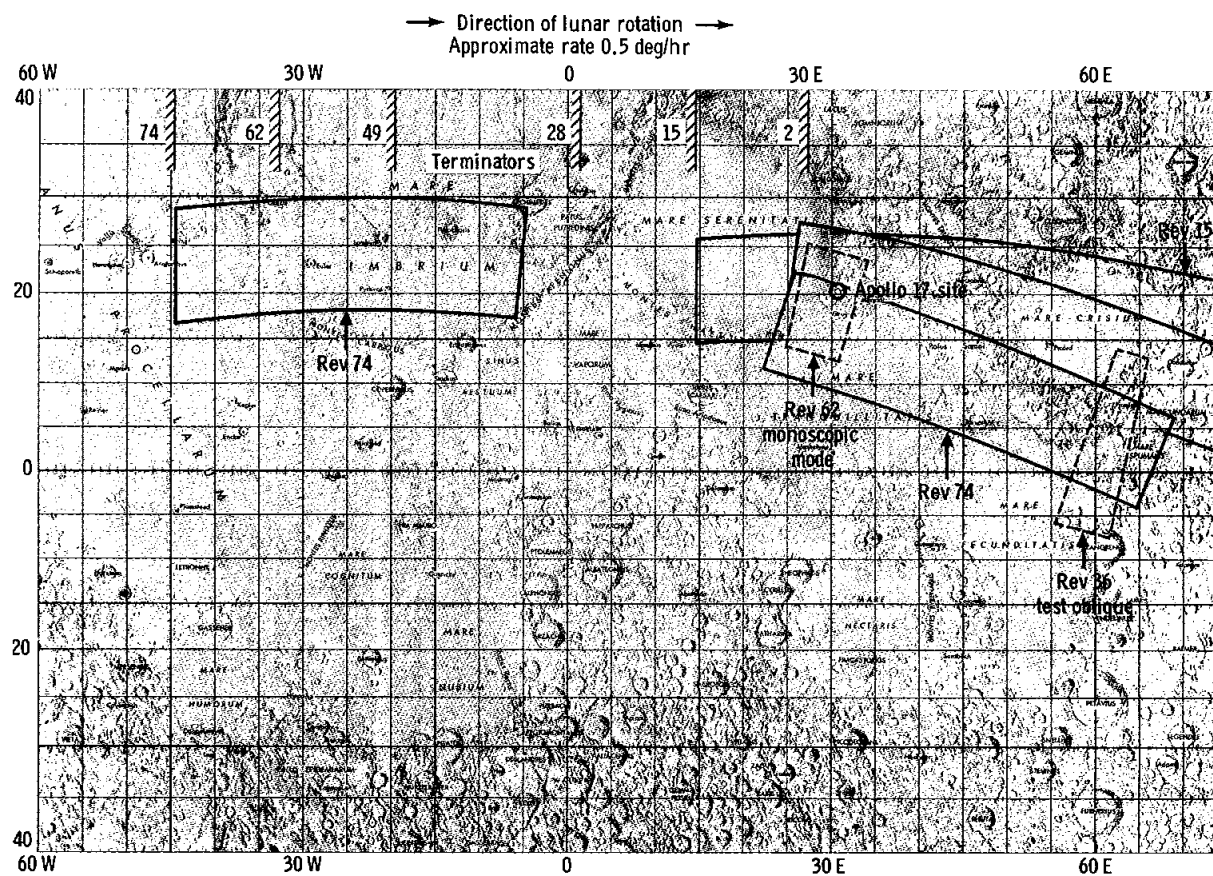
FIGURE 4-2.—Apollo 17 panoramic camera coverage. The coverage is based on camera on/off times from telemetry, not
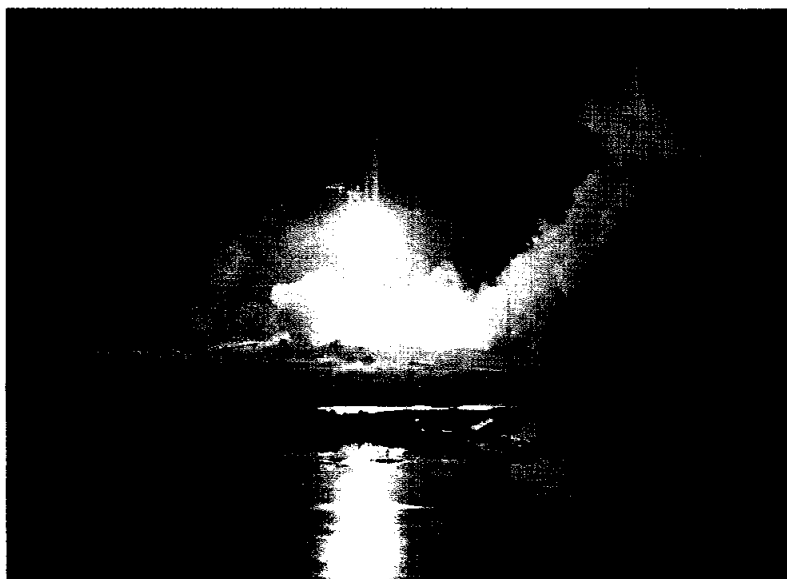
FIGURE 4-3.—Lift-off of the Apollo 17 vehicle from pad A, launch complex 39, NASA John F. Kennedy Space Center, Florida, December 7, 1972, 05:33:00 G.m.t., the only nighttime launch of the Apollo series (S-72-55070).
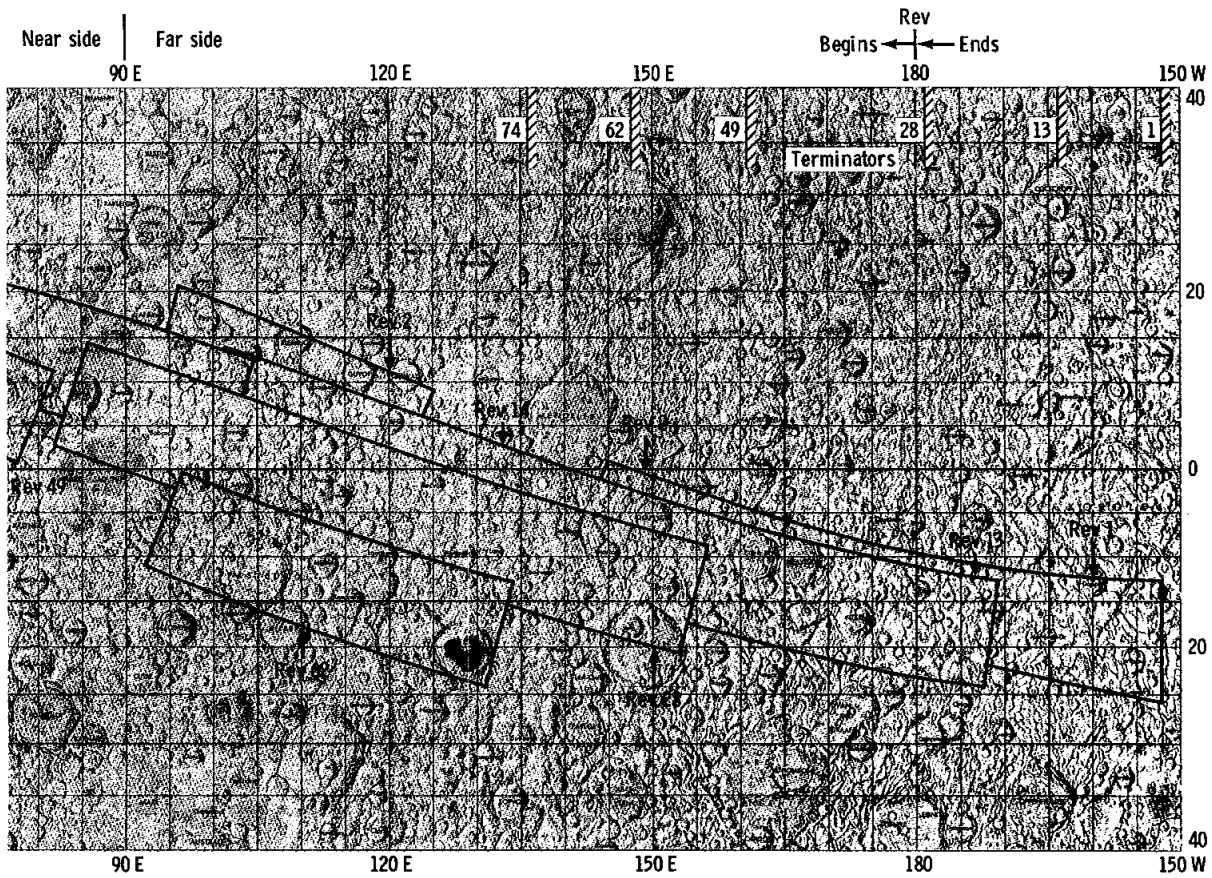
on analysis of photographs. Only sunlit coverage is indicated. The area photographed after transearth injection is not shown.

FIGURE 4-4.—Great Barrier Reef off the eastern shore of Cape York at the northern tip of Queensland, Australia, photographed during the first revolution of Earth orbit. In this near-vertical view, the shoreline forms an almost north-south line with the south end obscured by part of the spacecraft. The distance between the points at which the shoreline intersects the top and bottom of the photograph is 160 km (AS17-148-22609).

FIGURE 4-5.—In this oblique view of the west coast of Africa photographed on the second revolution of Earth orbit, the Cunene River at the right edge marks the border between Angola to the left and Southwest Africa to the right. Punta da Marca, now an island, extends 45 km into the Atlantic Ocean (AS17-148-22623).

FIGURE 4-6.—The LM viewed from the CM shortly after the TLI burn and shortly before the docking and extraction of the LM from the SIVB. Brightly reflective material flaked from the spacecraft fills the field of view around the LM. The circular LM upper hatch, used for transfer of crew and equipment from the LM to the CM, is centered in this view (AS17-148-22687).
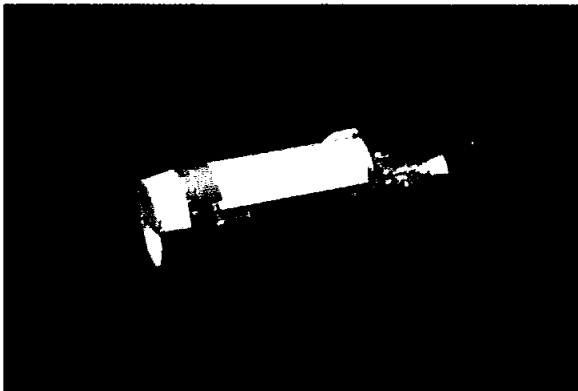
FIGURE 4-7.—The SIVB after extraction of the LM. The SIVB, 6.6 m in diameter, 18.1 m long, and 11 300 kg in mass (dry), provided the thrust for TLI and was subsequently impacted into the lunar surface to provide a data point for the Apollo 12, 14, 15, and 16 seismometers (AS17-148-22713).
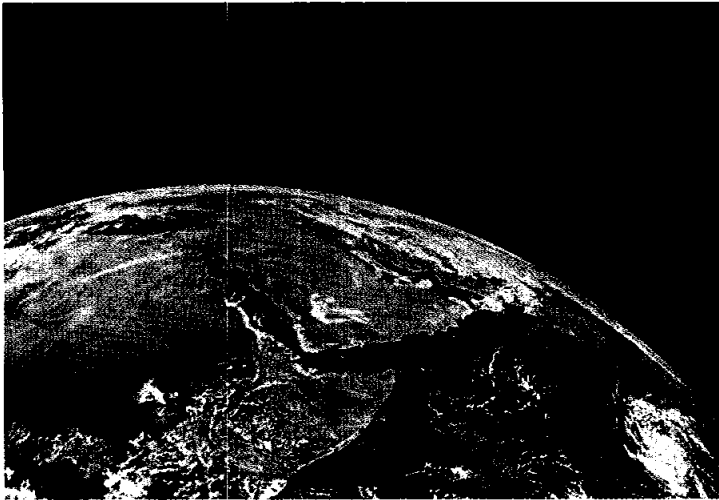
FIGURE 4-8.—Shortly after the LM was extracted from the SIVB, the crew viewed a portion of the Earth from the Mediterranean Sea to India. In Africa, the transition from desert (near the Mediterranean) through steppe and savannah to tropical rain forest (in the lower left corner) is apparent. The Nile River and Delta are clearly visible as are the Gulf of Kutch and the Gulf of Cambay in India (AS17-148-22718).
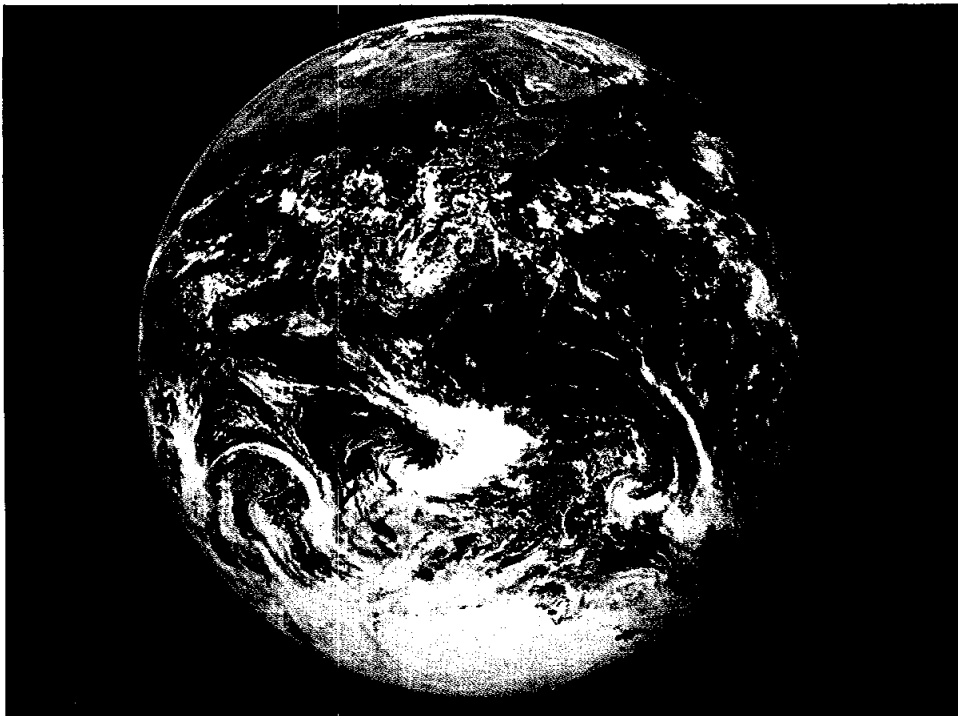
FIGURE 4-9.—For the first time on an Apollo mission, the Antarctic icecap was visible during the Apollo 17 TLC. This full-disk view encompasses much of the South Atlantic Ocean, virtually all the Indian Ocean, Antarctica, Africa, a part of Asia, and, on the horizon, Indonesia and the western edge of Australia (AS17-148-22727).

(lat. 15° S, long. 152° W) to near the crater Vil'ev (lat. 6° S, long. 144° E). The mapping camera was left in operation until the spacecraft passed above the near-side terminator, near longitude 28° E. The panoramic camera, constrained to not more than 30 min continuous operation, was turned off near longitude 144° E; it was operated again from longitude 122° to 95° E. The SIM cameras were not operated again until after the LM was on the lunar surface.

Although no additional orbital science photography was scheduled until after the LM landing on revolution 13, a number of crew-option photographs were exposed during the first several revolutions (figs. 4-10 and 4-11). Areas of special interest on the near side and the far side were photographed using the Hasselblad camera with color film or, in the case of near-terminator areas, with high-speed black-and-white film. Separation of the CSM and the LM on revolution 12 was documented with the Hasselblad camera and the DAC from each spacecraft. The CSM DAC photographed a mirror image.

FIGURE 4-11.—Earthrise. Shortly after the beginning of revolution 3, the gibbous Earth rising over the eastern limb of the Moon was photographed from the CM. Part of the LM ascent stage is visible in the right foreground. The orientation of the Earth is the same as that in figure 4-10; a comparison of the two photographs clearly shows the eastward rotation of the Earth under the sunset terminator (AS17-151-23188).

FIGURE 4-10.—Earthset. As the CSM and the LM rounded the western limb of the Moon on revolution 2, the crew photographed this unusual view of the gibbous Earth disappearing below the lunar horizon. The north pole of the Earth is toward the top of the photograph. On the left, the relief of the lunar surface near the western limb is sharply etched against the white clouds of the Earth; on the right is the sunset terminator of the Earth (AS17-151-23175).

FIGURE 4-12.—The LM after separation from the CSM on revolution 12. The LM descended to the lunar surface at the Taurus-Littrow landing site on revolution 13 (AS17-151-23201).
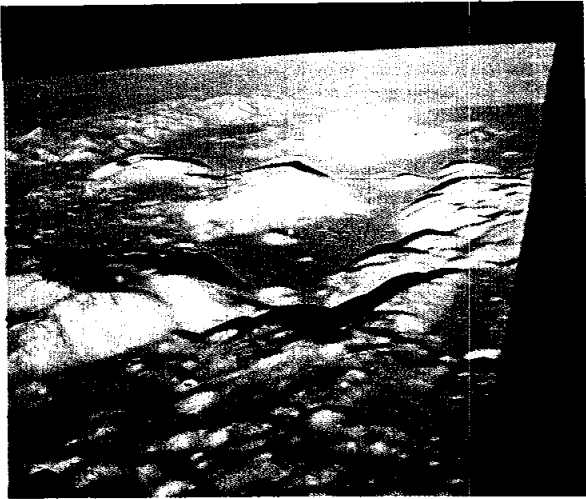
FIGURE 4-13.—The CSM, near the center of the photograph, is framed against the flat valley floor at the Taurus-Littrow landing site in this dramatic west-looking view from the LM shortly after separation on revolution 12. South Massif is the large mountain just beyond the CSM. The light-colored material that extends north (to the right) onto the valley floor from South Massif is the Rock Slide, and, opposite the Rock Slide, the mountain on the north side of the landing site is North Massif. The low hill nearly centered in the valley beyond the Rock Slide is Family Mountain. The crests of South Massif and North Massif are 2500 and 2100 m, respectively, above the landing site. To the west, color differences in the surface of southern Mare Serenitatis are evident even in this highly oblique photograph (AS17-147-22464).
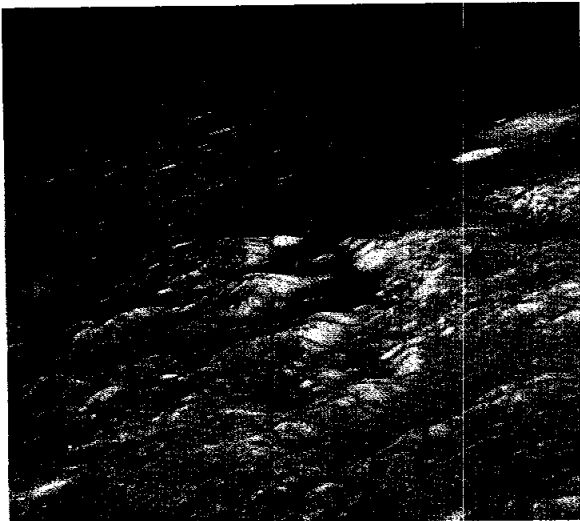
FIGURE 4-14.—The landing site from higher altitude on revolution 74. Topographic details are obscured and albedo differences are enhanced by the high Sun angle at the time this photograph was taken. The bright crater north and west of the landing site is Littrow B (AS17-148-22770).
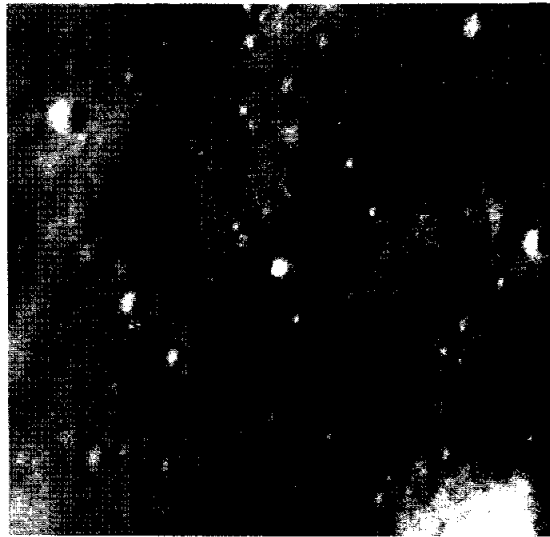
FIGURE 4-15.—The LM on the lunar surface at the Taurus-Littrow landing site. This photograph is a 49× enlargement of a portion of a panoramic camera frame that was exposed on revolution 15 when the Sun elevation at the site was 15°. The LM is the bright spot in the center; its shadow extends outward 5° north of west. The photograph represents a lunar surface area 300 m on a side (Apollo 17 panoramic camera frame AS17-2309).

The orbit of the CSM was circularized during revolution 12. On the 13th revolution, the CSM DAC was mounted on the sextant to document the tracking of two landmarks, the second of which was at the Taurus-Littrow landing site. Simultaneously, the powered descent of the LM, from time of pitchover to touchdown, was recorded by the LM DAC, mounted in the right side window.

The LM in orbit is pictured in figure 4-12. Figures 4-13 and 4-14 are orbital photographs of the landing site, and figure 4-15 is an enlargement showing the LM on the lunar surface.

LUNAR SURFACE PHOTOGRAPHY

During the stay on the lunar surface, the commander (CDR) and the LM pilot (LMP) exposed more than 2200 frames in their Hasselblad DC's. One magazine of DAC film was used to record the commander's initial activities on the lunar surface as viewed from the LM window; the LM DAC was not used again until lift-off.

The crew began photographic documentation of the landing site as they viewed it from the LM windows shortly after touchdown (fig. 4-16). Site-documentation photography was a continuing operation throughout the lunar surface stay. Figure 4-17 illustrates the intense activity of the three periods of extravehicular activity (EVA) at the site as it appeared from an LM window shortly before lift-off. Real-time observations of lunar surface activities were provided scientists and engineers on Earth by the television (TV) camera mounted on the lunar roving vehicle (LRV).

The lunar surface documentary photographs taken in the vicinity of the LM included the checkout drive of the LRV (fig. 4-18) and the traditional salute to the flag (fig. 4-19) taken during EVA-1. Before EVA-2, the LMP was photographed with the equipment required for the EVA (fig. 4-20). The CDR also documented their repair of the LRV fender that was broken during EVA-1 (fig. 4-21). A photograph of the Earth above the LM (fig. 4-22) was taken shortly before EVA-2 closeout.

The deployment of the lunar surface experiment equipment was documented with 70-mm Hasselblad photographs. Figures 4-23 to 4-27 show the Apollo lunar surface experiments package (ALSEP) site and several individual pieces of scientific equipment.

Sample documentation includes photographs of boulders from which samples were collected (figs. 4-28 and 4-29) and photographs that illustrate the use of sampling tools (figs. 4-30 and 4-31). Figure 4-32 is a typical presampling photograph. Perhaps the most
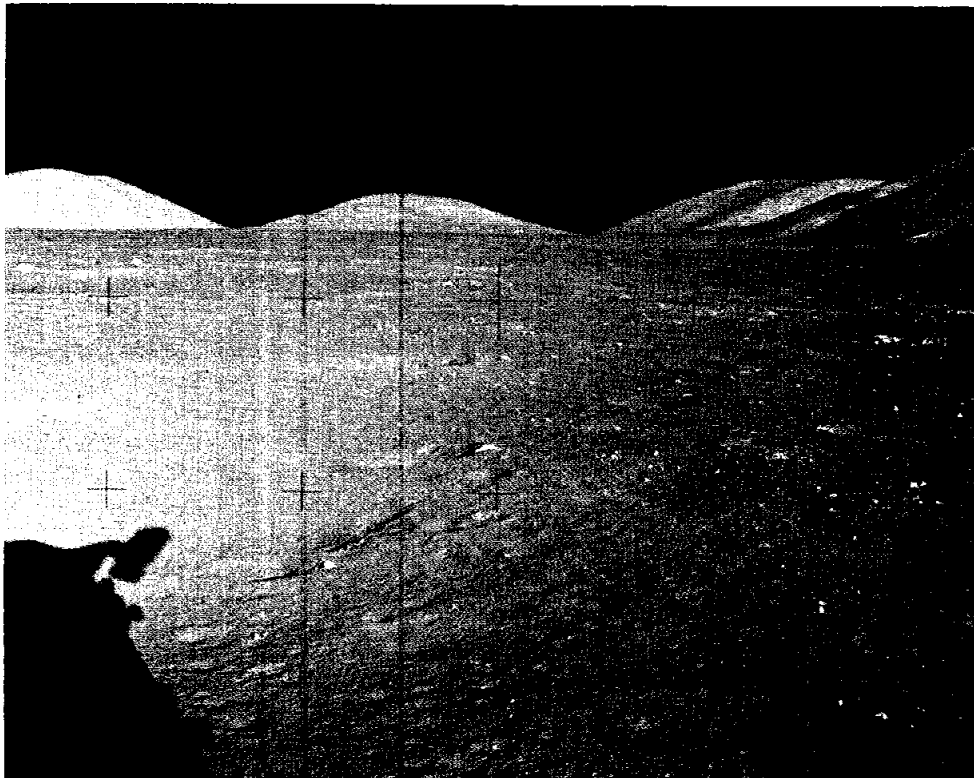
FIGURE 4-16.—A view of the Taurus-Littrow area from the LM window taken just after touchdown on the lunar surface. The shadow of the LM is along the lower left margin of the photograph. Family Mountain, on the horizon from the left margin to the center of the photograph, is almost 11 km distant; its crest is approximately 1000 m above the valley floor. The dark-gray basalt fragments on the lunar surface appear to be white in this down-Sun photograph (AS17-147-22470).
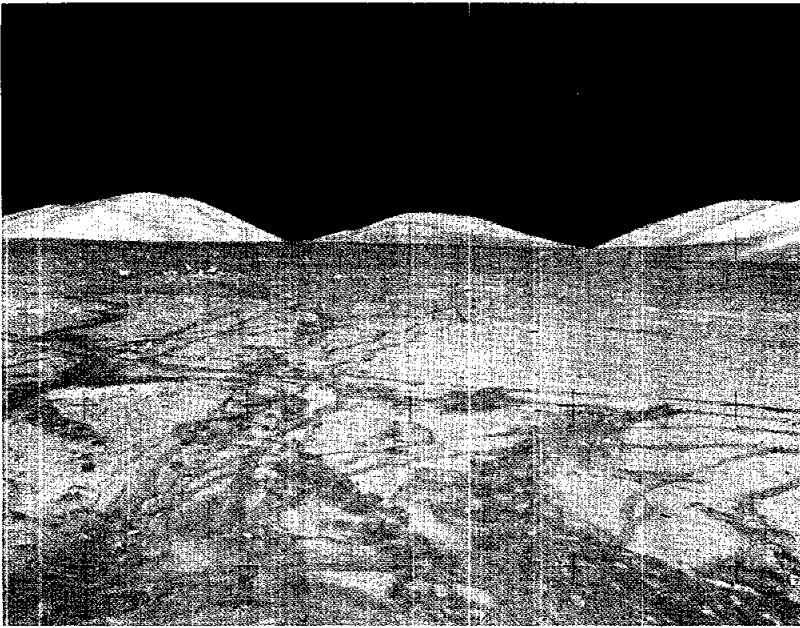
FIGURE 4-17.—A view of the landing site from the LM window taken just before lift-off. Compare this photograph with figure 4-16. The intense activity in the vicinity of the LM is indicated by the footprints and the LRV tracks. The Apollo lunar surface experiments package (ALSEP) components can be seen in the distance. The craters seen in the foreground of figure 4-16 are not visible in this photograph, which was taken at a higher Sun angle (AS17-145-22200).

FIGURE 4-18.—Shortly after deployment, the CDR drove the LRV through a series of maneuvers to check out the performance of the vehicle. The LRV was then loaded with tools, experiment hardware, a TV camera, and antennas. South Massif, the crest of which is 2500 m above the valley floor, forms the skyline 5 km behind the LM. The bands of dark gray are LRV tracks; bootprints in the lunar surface are visible near the right margin of the photograph (AS17-147-22527).
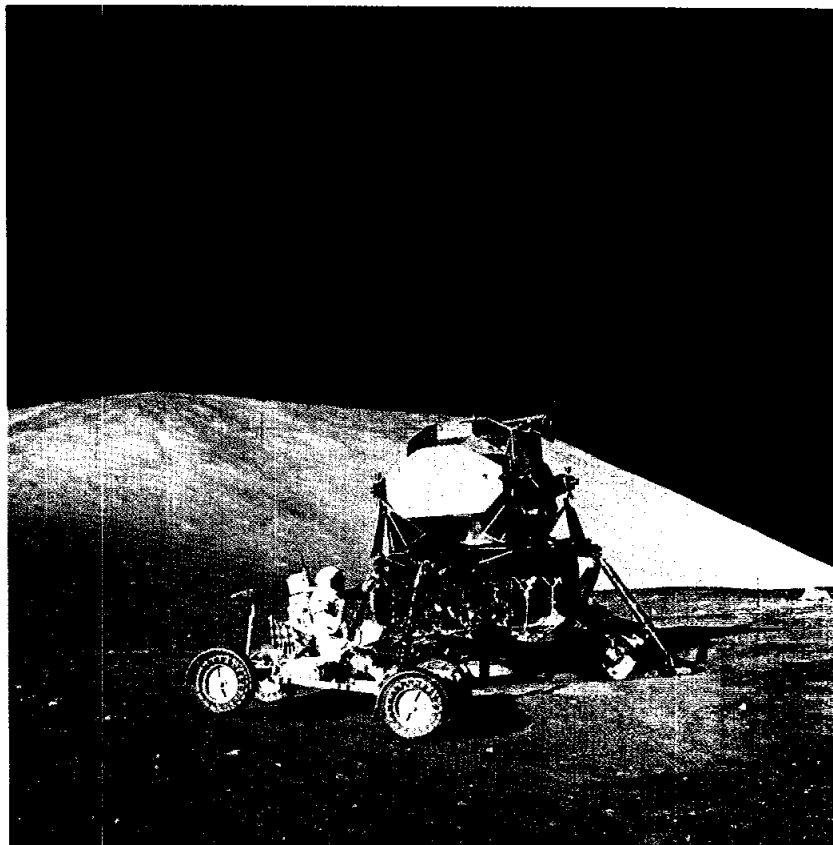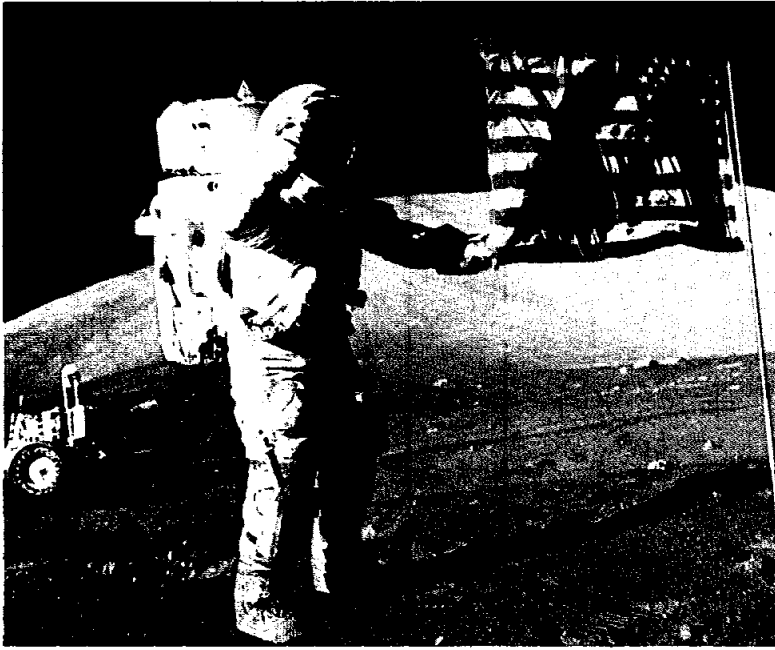
FIGURE 4-19.—The CDR salutes the flag of the United States implanted at the Apollo 17 landing site. Approximately 3 km in the distance, the 2100-m-high North Massif forms the skyline. The LRV is visible at the left margin of the photograph. The flag pictured was the backup flag for the Apollo 11 mission and was in the Mission Operations Control Room from July 1969 until just before the Apollo 17 mission (AS17-134-20386).
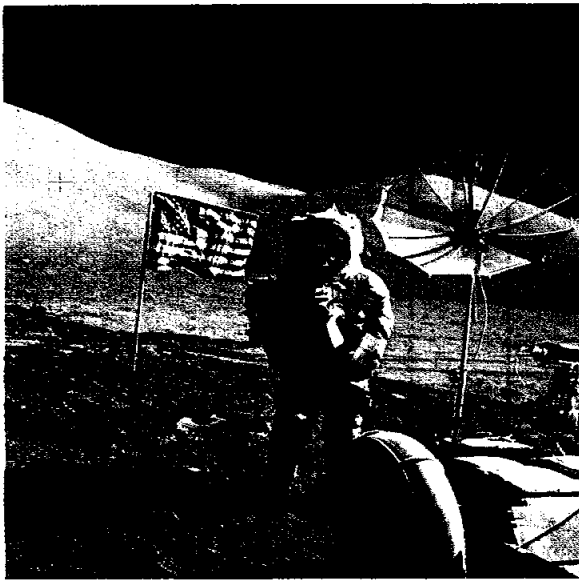
FIGURE 4-20.—The LMP stands in front of the LRV at the start of EVA-2. Sample bags are attached to the remote control unit on his chest. The sample collection bag is attached to the right side of the portable life-support system (PLSS). The cuff checklist, an outline of activities, is on his left wrist. The LRV sampler hangs in front of the astronaut. The gold-colored TV camera is at the right edge of the photograph. The reflection of the CDR can be seen in the LMP's visor (AS17-140-21386).
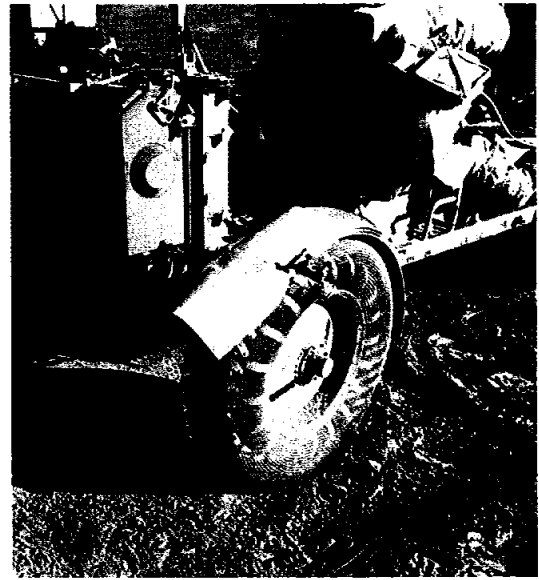
FIGURE 4-21.—The partial loss of the right rear fender during EVA-1 threatened to limit the use of the LRV. Without complete fenders, the wire mesh wheels threw a plume of lunar dust across the crew and the LRV. At the beginning of EVA-2, the crew replaced the missing section using maps, tape, and two clamps from the LM. The repairs proved to be satisfactory, and no further problems were experienced. The LMP sits in the LRV (AS17-137-20979).
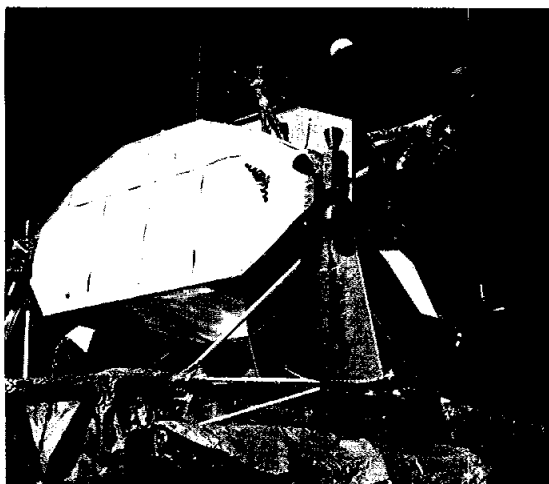
FIGURE 4-22.—A half Earth hangs over the LM on the lunar surface (AS17-134-20463).

FIGURE 4-23.—The gnomon with color chart sits next to one of the lunar seismic profiling geophones, indicated by the orange flag. The gold-colored, rectangular object near left center is the ALSEP central station; the white antenna extending above the central station telemeters data to Earth from each of the surrounding experiments. North Massif, 3 km in the distance, forms the skyline. On the slope of North Massif, to the right of the LRV, is a track made by a massive boulder as it rolled down the side of the mountain. The sharpness of the track suggests that the boulder may have been in its present position only a relatively short time (AS17-147-22549).

FIGURE 4-24.—A gold-colored Mylar transport bag covers the top of the lunar neutron probe (LNP) for temperature control during the 40-hr emplacement of the probe in the Moon. The LNP is designed to obtain data on neutron capture rates in the lunar regolith as a function of depth. The LNP was emplaced through the treadle assembly into the hole drilled for the core sample. The borestem and corestem rack is visible at the right margin of the photograph. The Apollo lunar surface drill power head lies on the lunar surface behind the rack. The ALSEP equipment is set up in the background. The Sculptured Hills and South Massif form the horizon (AS17-134-20505).

FIGURE 4-25.—The CDR inserts a heat flow probe into the borestem during the deployment of the ALSEP. The drill and rack with additional borestems and corestems are to the left of the astronaut. The heat flow experiment measures the heat flow from the interior of the Moon (AS17-136-20695).
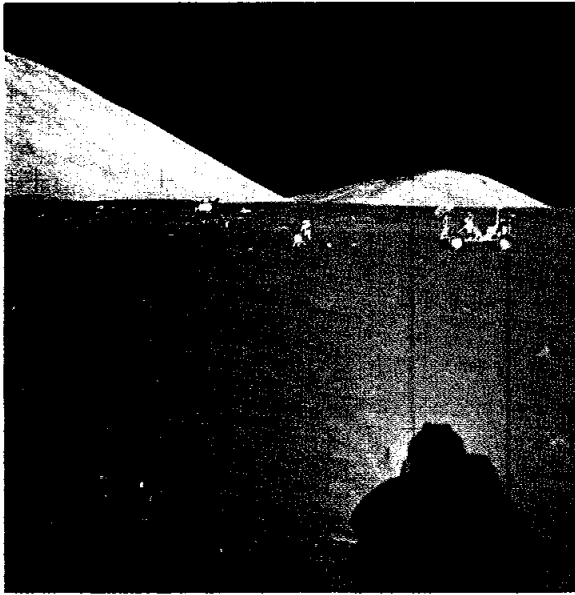
FIGURE 4-26.—The problem of distance perception on the Moon is well illustrated in this photograph. The distance to the LRV and the surface electrical properties (SEP) experiment is 35 m; the distance to the LMP is 70 m. The distance to the LM is 150 m; to the ALSEP, 350 m. Family Mountain is 11 km beyond the LRV, and South Massif is behind the LM. The wire in the foreground is part of the dipole antenna of the SEP experiment. Compare this photograph with figure 4-27 and note the relationship of size and distance (AS17-134-20435).
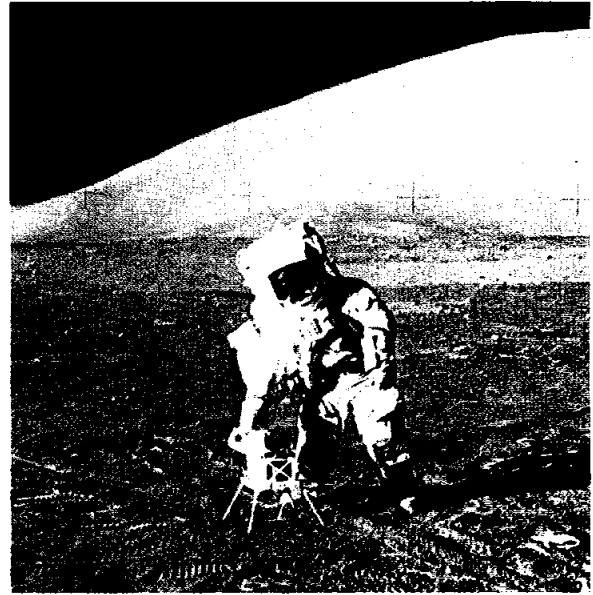
FIGURE 4-27.—The LMP emplaces the SEP experiment. The equipment shown, which supports the experiment, includes a transmitter to generate a signal and a dipole antenna that is laid out on the lunar surface by the crew. A receiver is carried on the LRV. The interference pattern of the transmitted waves provides information about the interior of the Moon. The restricted mobility caused by the pressure suit is illustrated by the body position required to make leveling corrections. The wires in the foreground are part of the SEP experiment antenna. South Massif forms the skyline (AS17-134-20440).
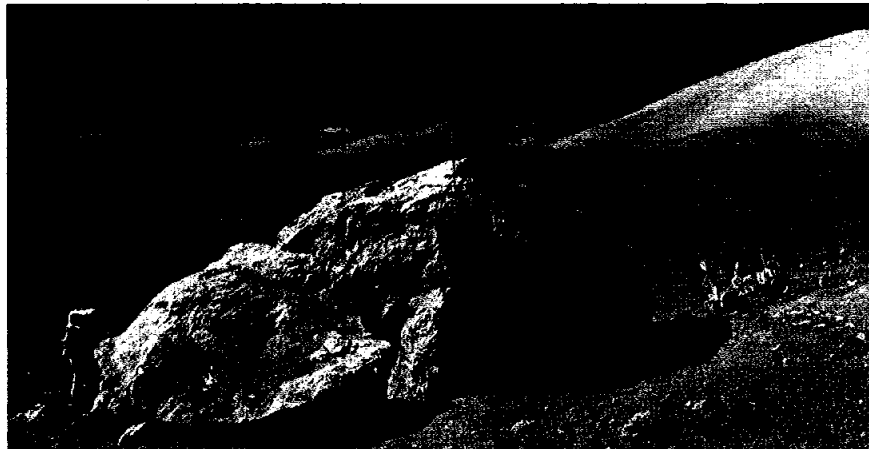
FIGURE 4-28.—The massive, broken boulder at station 6 is shown in this composite photograph. Scoop marks in the debris on the side of the boulder mark the location of a sample collected by the LMP. The boulder is a breccia, a rock composed of fragments of other rocks. The LRV, with the antenna pointed toward Earth, is parked to the right of the boulder. South Massif, 8 km distant, forms the right half of the skyline; East Massif forms the left half (AS17-140-21493 and 21497).

FIGURE 4-29.—Sampling at station 6 centered around the boulder behind the LMP. The dark bootprints in the foreground and near the base of the boulder indicate the areas of astronaut activity. The LRV is visible at the left side of the photograph (AS17-146-22294).
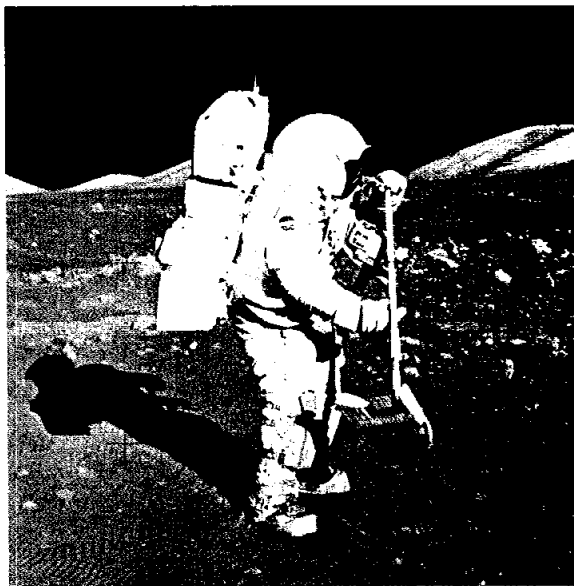
FIGURE 4-30.—The LMP uses the rake to collect a sample of rocks ranging from 1 to 4 cm in diameter. A soil sample was collected in the same area. The Hasselblad camera is attached to the remote control unit; the PLSS and the oxygen purge system comprise the backpack (AS17-134-20425).
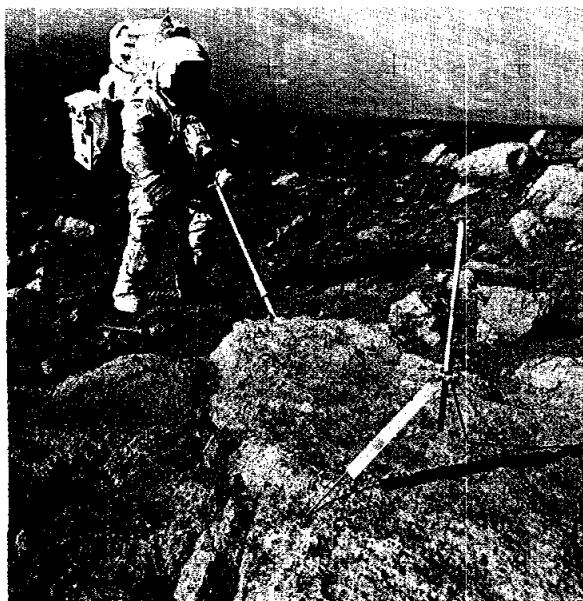
FIGURE 4-31.—The LMP uses the scoop to collect a sample at station 5. The high density of boulders along the rim of Camelot Crater is shown in this photograph (AS17-145-22157).

FIGURE 4-32.—The gnomon with color chart marks the location from which a sample will be collected. The white areas on the boulder to the left of the gnomon are clasts; the clasts are bound in a fine-grained gray matrix (AS17-137-20963).

widely known and highly publicized samples of the Apollo 17 mission were from the "orange soil" found at Shorty Crater during EVA-2 (figs. 4-33 and 4-34).

Features too large to record in single frames were documented in partial panoramas (fig. 4-35). The general setting of a station was routinely recorded in a complete 360° panorama. The 500-mm lens provided the capability to record distant features in single frames (fig. 4-36) or in partial panoramas.

After completion of the EVA-2 sampling activities, the LRV was parked east of the LM, and the Houston-controlled TV camera provided live coverage of the final closeout and of the ascent stage lift-off from the lunar surface.

LUNAR ORBIT PHOTOGRAPHY FROM LM TOUCHDOWN TO RENDEZVOUS AND DOCKING

All orbital photographic activities in the period between LM touchdown and rendezvous and docking (revolutions 13 to 52) were as planned. The mapping camera was operated from terminator to terminator on revolutions 13/14, 14/15, 23/24, 26/27 (north-looking oblique), 27/28, 28/29, 36 (south-looking oblique), 38, and 49. The designation "13/14" means that the camera was turned on near the end of revolution 13, which ends at 180°, and continued in operation during revolution 14 to the terminator. In several of these passes, the camera was also operated over unlighted lunar surface to obtain laser altimeter data. The north- and south-looking oblique photographs were exposed when the CSM was rolled 40°; the oblique photographs show the lunar surface to the horizon, approximately 20° from the spacecraft nadir. The panoramic camera was operated on revolutions 13/14, 15, 29, 36 (a cycle of five frames to prevent film set; south-looking oblique), and 49.

Hasselblad EL stereophotographic strips, exposed with either the 80- or the 250-mm lens and color film, are as follows: on revolution 16, a far-side strip at the spacecraft nadir from east of the crater Aitken to the crater Marconi; on revolution 17, a series south of the groundtrack from the crater Sniadecki to a point south of the crater Marconi; on revolution 25, the landing site and southwestern Mare Serenitatis; on revolution 28, a series south of the groundtrack from the crater Picard to Promontorium Archerusia on the
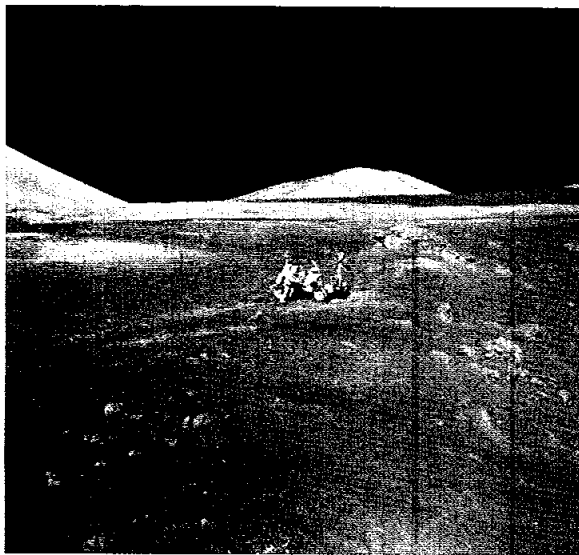
FIGURE 4-33.—The orange soil on the rim of Shorty Crater can be seen on both sides of the LRV. The rim of the crater extends from the left foreground to the middle right edge of the photograph. Samples were collected between the LRV and the large boulder. (See fig. 4-34.) The low mountain centered on the horizon is Family Mountain, 6 km in the distance (AS17-137-21011).

FIGURE 4-34.—A closeup of the trench dug in the orange band of soil. Behind the gnomon is the boulder pictured in figure 4-33 (AS17-137-20990).

FIGURE 4-35.—This panorama at station 9 shows the unique morphology of the 80-m-diameter crater Van Serg. The rough, blocky rim and floor indicate that the crater is relatively young. Locations such as this are excellent sampling sites. North Massif, 3 km in the distance, forms the skyline (AS17-142-21801, 21805, 21807, and 21811).

FIGURE 4-36.—One of a series of photographs taken by the CDR, while standing at the base of the North Massif, of the landing site and South Massif using the 500-mm photographic lens. This photograph of the valley floor shows the LM some 3 km in the distance. The large blocky craters to the right of the LM are Camelot, approximately 600 m in diameter, and Horatio, approximately 400 m in diameter. South Massif, 8 km in the distance, appears steeper in this photographic view (AS17-139-21205).

south margin of Mare Serenitatis; on revolution 29, a series north of the groundtrack from the crater Love to the crater Saenger and a second strip north of the groundtrack from eastern Mare Crisium to the crater Bessel; on revolution 36, a south-looking series from the crater Van de Graaff to the crater Serpiensky; and, on revolution 39, a strip from the crater Tacquet to an area north of the crater Eratosthenes.

Near-terminator areas photographed included Mare Serenitatis on revolution 17, Montes Haemus and northern Mare Vaporum on revolution 29, and the crater Aitken on revolution 37. The Hasselblad camera was also used repeatedly during revolutions 13 to 52 for crew-option documentation of other areas of interest.

Figures 4-37 to 4-42 are photographs of lunar far-side features; figures 4-43 to 4-49 include near-side features; figure 4-50 is a photograph of an earthshine-illuminated area; and figure 4-51 is a photograph of a near-terminator area.

The solar corona was photographed at spacecraft sunrise on revolution 25 using the bracket-mounted Hasselblad camera with 80-mm lens. The Nikon camera was used to photograph the zodiacal light; red, blue, and polarizing filters were used for these exposures.

Earthshine-illuminated areas photographed with the Nikon camera include the craters Eratosthenes, Copernicus, Grimaldi, and Riccioli, the Reiner γ prominence, and Mare Orientale. The Nikon camera was also used to document near-side and far-side near-terminator areas and other areas determined by the CM pilot (CMP) to be of interest. The sextant-mounted DAC was used to document the tracking of two landmarks on revolution 50.

As the CSM passed over the landing site during revolution 51, the LM ascent stage separated from the descent stage and lifted off from the lunar surface (fig. 4-52). The LM DAC, bracket mounted in the LM window, photographed lunar surface features, including the descent stage, the ALSEP instruments deployed at the landing site, and LRV tracks, as the LM passed above them (fig. 4-53). The rendezvous of the LM and CSM was documented with the DAC and Hasselblad from the CM but only with the Hasselblad
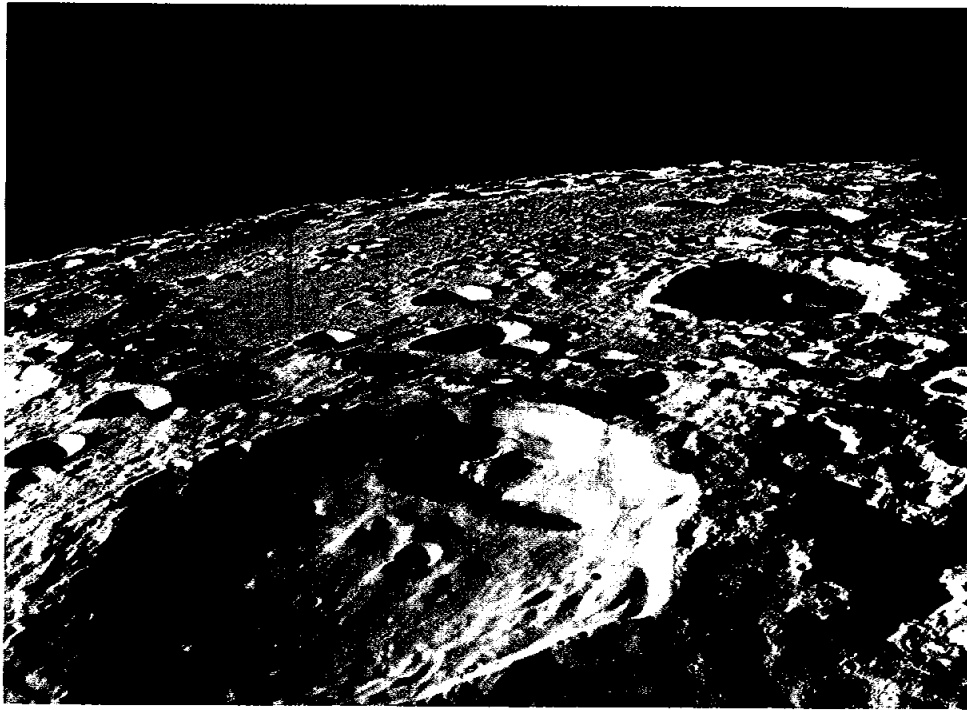
FIGURE 4-37.—North-looking, high-oblique view of the lunar far side near the lunar sunset terminator on the first revolution. The foreground crater containing several smaller craters is Doppler, centered at latitude 13° S, longitude 160° W, and approximately 100 km in diameter. The larger crater to the north which extends from the left side to the right side of the photograph is Korolev, approximately 450 km in diameter (AS17-151-23112).
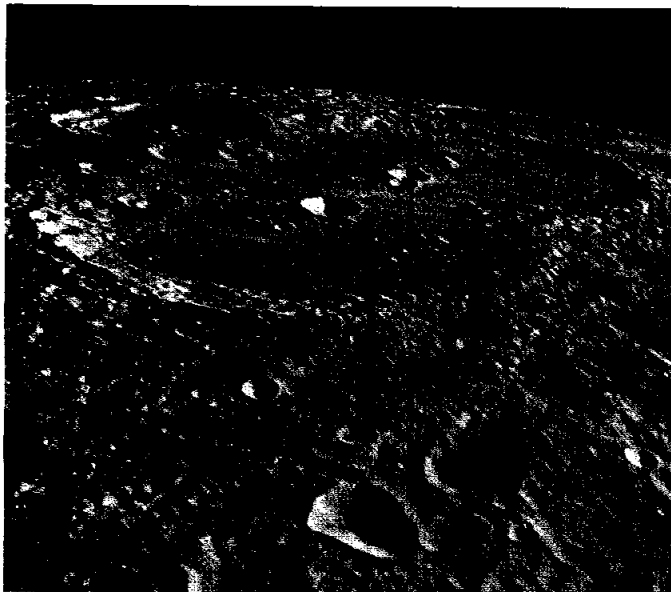
FIGURE 4-38.—The lunar far-side crater Van de Graaff, centered at latitude 28° S, longitude 173° E, is the large, flat-floored double crater in this south-looking, high-oblique view. Its long dimension is approximately 270 km. Adjoining Van de Graaff on the southeast is the crater Birkeland, which has terraced walls and a central peak. The circular, mare-filled crater on the right horizon is Thomson (AS17-150-22959).
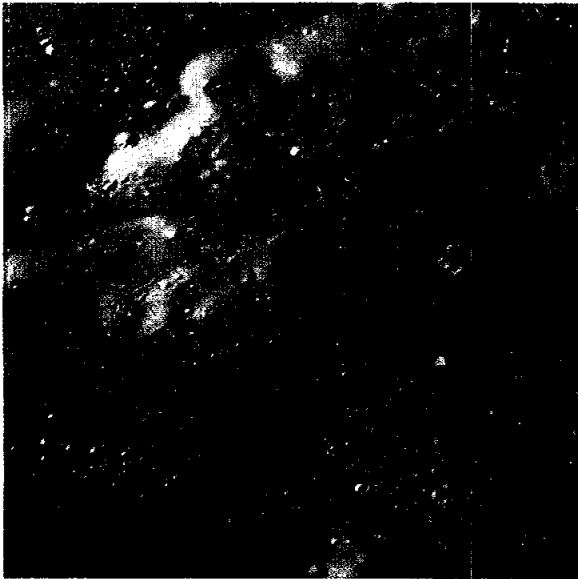
FIGURE 4-39.—This unnamed crater with a hummocky floor is in a far-side area that was very poorly documented before the Apollo 17 mission. The low-oblique view is to the southeast. The center of the 40-km-diameter crater is at latitude 21° S, longitude 169° W. Note the scarp that crosses the crater floor from the shadow at the right middle through the embayment in the crater wall at upper left and continues into the terrain outside the crater. In the upper right corner, the north rim of the crater Sniadecki is visible (AS17-151-23193).
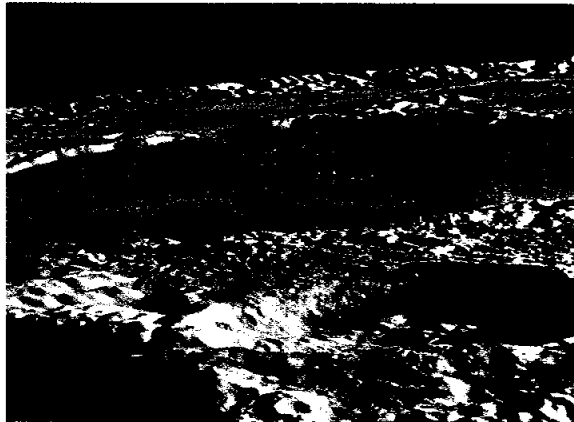
FIGURE 4-40.—The circular, flat-floored, mare-filled crater that extends beyond the left and right edges of this photograph is Thomson, a 150-km-diameter crater near latitude 32° S, longitude 166° E. Beyond Thomson to the south is the southeastern quarter of Mare Ingenii. The shadow in the lower left corner is in the southwest wall of Van de Graaff. The crater Zelinsky is in the right foreground (AS17-153-23543).

FIGURE 4-41.—Aitken, a far-side crater located at latitude 17° S, longitude 173° E, measures approximately 150 km from rim to rim. In this mapping camera photograph, exposed during revolution 15, north is at the top. Aitken is characterized by a flat, low-albedo, sparsely cratered floor, by a central peak, and by terraced walls. Ponded, marelike material is evident at various levels in the terraced walls as well as in smaller craters nearby. Details of a part of the eastern wall and floor are shown in figure 4-42 (Apollo 17 mapping camera frame AS17-0481).

FIGURE 4-42.—This photograph of a segment of the eastern wall and floor of Aitken (fig. 4-41) was exposed in the Hasselblad camera with a 250-mm lens. North is at the top of the photograph. The topographic features on the crater floor that resemble the wrinkle ridges common in lunar maria can be seen to continue into and across the hummocky, higher albedo material of the lower crater wall (AS17-149-22796).
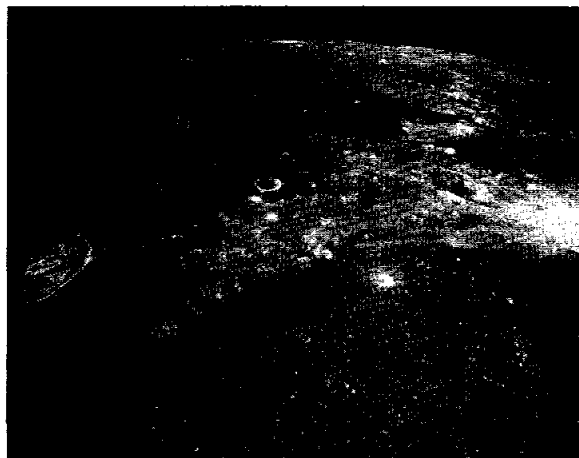
FIGURE 4-43.—Southern Mare Serenitatis (foreground), western Mare Tranquillitatis (left), and southeastern Montes Haemus (center). In this oblique mapping camera photograph, the view is almost due south. The 50-km-diameter crater Plinius is at the left edge; at the right edge, the bright crater with the excluded-ray zone is Menelaus, 25 km in diameter. Note that the Rimae Plinius and the Rimae Menelaus, roughly concentric to the southern edge of Mare Serenitatis, are confined to the area of low albedo (Apollo 17 mapping camera frame AS17-2415).

FIGURE 4-44.—Northwest-looking, low-oblique view of the crater le Monnier approximately 190 km north of the Apollo 17 landing site on the east margin of Mare Serenitatis. The Russian spacecraft Lunokhod 2, an Earth-controlled roving vehicle, landed in le Monnier January 15, 1973. The marelike flat floor of the 70-km-diameter crater has the low albedo characteristic of the surface material bordering Mare Serenitatis; some of the dark surface material bordering eastern Mare Serenitatis can be seen in the upper left corner of the photograph. The crater Littrow D is in the right foreground; between it and le Monnier, Rima Littrow II extends from the middle right to the lower left (AS17-153-23487).
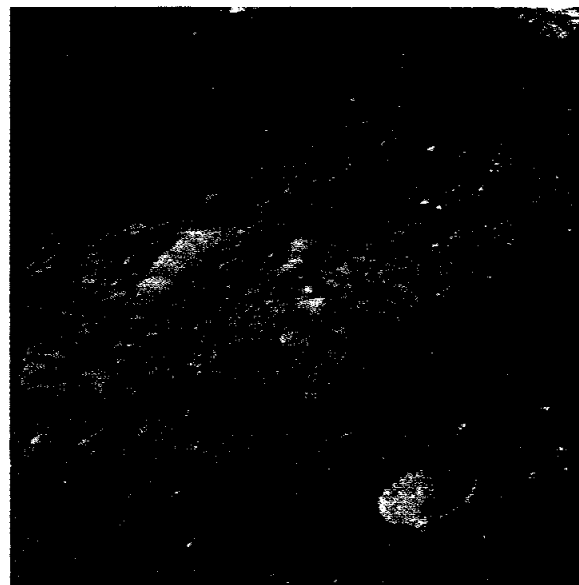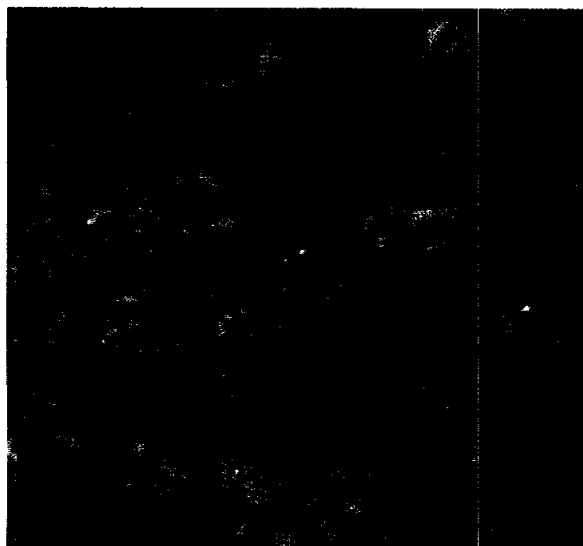
FIGURE 4-45.—An area of orange-hued material west of the crater Sulpicius Gallus. All three astronauts saw orange-hued material in and around craters in this area and could see orange talus on the slopes in the elongate crater just above right center. Many of the smaller craters, particularly in topographically low areas, are surrounded by the orange-hued ejecta. In this near-vertical 250-mm Hasselblad photograph, north is at the top. The elongate crater, situated at latitude 20° N, longitude 10.5° E, is 6 or 7 km long and is approximately 40 km west of Sulpicius Gallus. Rima Sulpicius Gallus I crosses the upper right corner. The Montes Haemus are in the lower left (AS17-149-22882).

FIGURE 4-46.—This southeastward oblique view shows the setting of the area pictured in figure 4-45. The Rimae Sulpicius Gallus converge on the crater Sulpicius Gallus in the upper middle. The Montes Haemus define the southwestern border of Mare Serenitatis along the right side of the photograph. The bright crater at the right edge is Sulpicius Gallus M. Note the unusual crater at left center with a dark rim and light ejecta (AS17-151-23258).
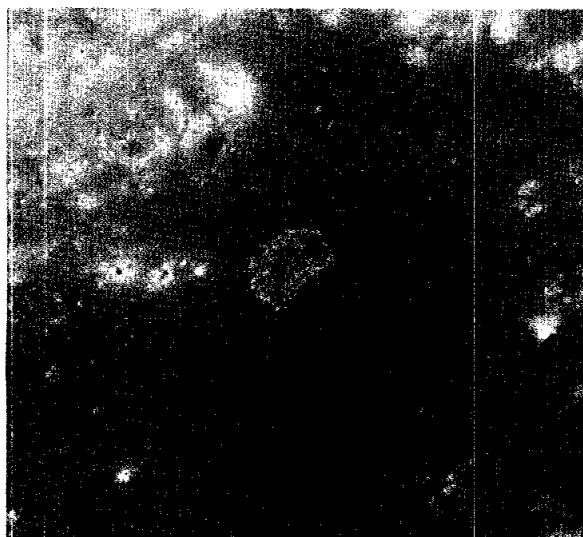
FIGURE 4-47.—The D-shaped feature in the center of this photograph was first seen in Apollo 15 panoramic camera photographs. Situated at latitude 18° N, longitude 5° E, the feature measures approximately 3 km along the straight edge and lies below the level of the surrounding dark, marelike material. The CMP has described the pale-blue color seen in this and other photographs of the feature as accurate (AS17-152-23287).

FIGURE 4-48.—Proclus, the most prominent excluded-ray-zone crater on the near side of the Moon, has
    been difficult to photograph successfully because of the brightness of its rays. In this near-vertical
    photograph, interior details are clear despite the relatively high Sun angle when exposed on
    revolution 28. North is at the top of the photograph. The object at the right is the CSM EVA
    floodlight (AS17-150-23046).
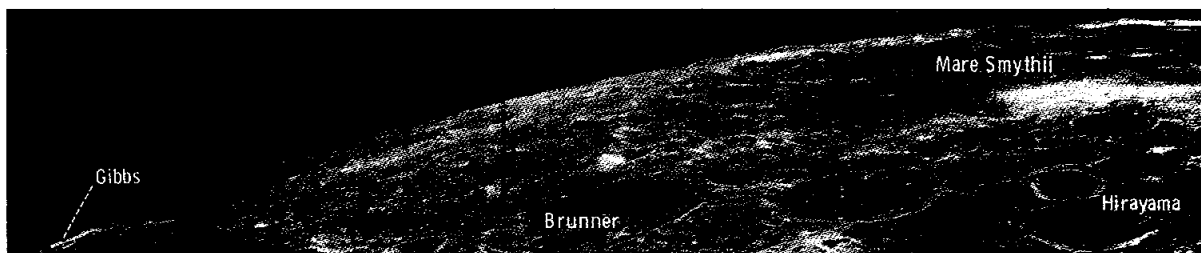
FIGURE 4-49.—This spectacular panoramic view of the eastern limb of the Moon was exposed when the CSM was in a
    pitched-up attitude during revolution 62. The panoramic camera was pointing along the groundtrack at an azimuth of
    290°. The entire area of Mare Smythii, more than 400 km from left to right, is visible. In the near field, the

from the LM; again, the CSM DAC had a mirror view of the LM and lunar background. On revolution 52, the CSM maneuvered to an attitude that would permit inspection of the SIM bay from the LM, and both spacecraft were photographed with the Hasselblad cameras (figs. 4-54 and 4-55). Much of the area south of the groundtrack from the eastern margin of Mare Crisium to the crater Copernicus was also documented with an LM Hasselblad (fig. 4-56). The CM TV provided Earth a view of the LM during docking maneuvers.

LUNAR ORBIT PHOTOGRAPHY AFTER RENDEZVOUS AND DOCKING

After docking on revolution 52 and transfer of the crew and equipment to the CSM from the LM, the LM ascent stage was jettisoned on revolution 54. The receding LM was photographed with CM DAC and the Hasselblad camera.

The mapping camera was operated from terminator to terminator on revolution 62. From the far-side terminator to near longitude 90° E, the CSM was pitched up, and the tilt of the resultant forward-looking oblique photographs varies somewhat with longitude. Normal vertical orientation of the SIM cameras was attained near longitude 90° E and was maintained throughout the remainder of the pass. On revolution 65, the CSM was in a 40° north-looking

oblique attitude when the mapping camera was switched on near longitude 107° E. With the camera in operation, the CSM began a maneuver to the 40° south-looking oblique attitude near longitude 65° E and continued in that attitude to the terminator. The last two periods of mapping camera operation in lunar orbit were terminator-to-terminator passes on revolutions 66 and 74.

The panoramic camera was operated on revolution 62 from near longitude 132° E to approximately 95° E, during which period the CSM was in a pitched-up attitude. As the CSM passed over the landing site on revolution 62, 11 frames were exposed with the camera in the monoscopic mode.

An area from Montes Apenninus across southern Mare Imbrium to the terminator was photographed with the Hasselblad camera and color film on revolution 65.

Scheduled near-terminator photography was accomplished on revolution 62 near the craters Gagarin and Lambert, on revolution 66 near the crater T. Mayer, and on revolution 74 west of the crater Brayley.

TRANSEARTH COAST AND EARTH ENTRY PHOTOGRAPHY

As the CSM receded rapidly from the Moon following the transearth injection (TEI) maneuver,
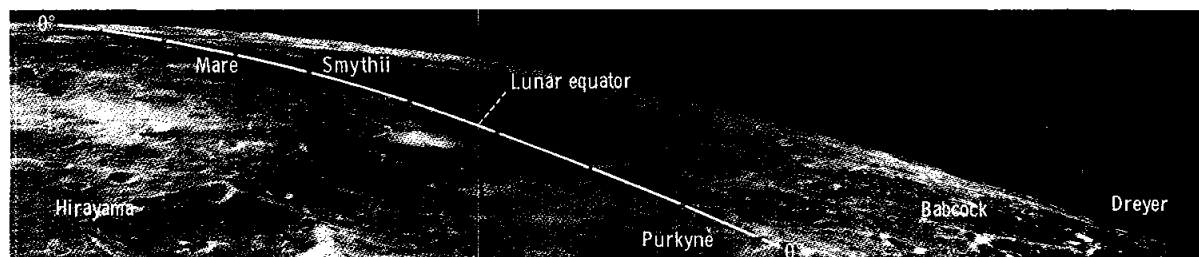
150-km-diameter crater Hirayama (centered at lat. 6° S, long. 93° E) extends across the middle one-third of the bottom of the photograph. The bright rays in the extreme left corner are from a crater near latitude 15.5° S, longitude 87.5° E. The crater Dreyer (lat. 10° N, long. 96° E) is just outside the extreme right corner (panoramic camera frame AS17-2871).
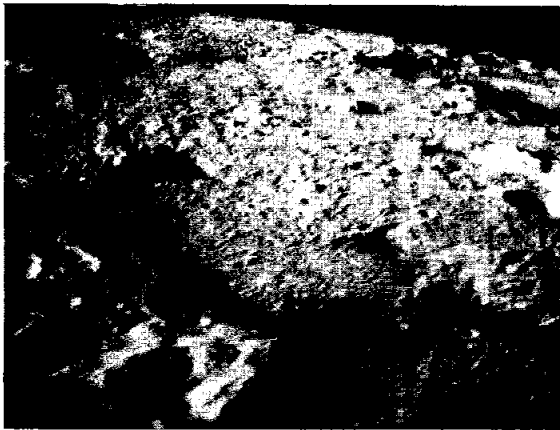
FIGURE 4-50.—Mare Orientale in earthshine. In this south-looking, high-oblique, 35-mm photograph, two of the rings of Mare Orientale are distinctly visible. The photograph includes the area in which the CMP reported seeing a possible light flash. The marelike area in the middle foreground is Lacus Autumni. Beyond it is Lacus Veris, at the south end of which is the crater Eichstadt K. The Montes Rook delineate the inner of the two rings pictured here. The outer ring, to the left, is marked by the Montes Cordillera (AS17-158-23902).
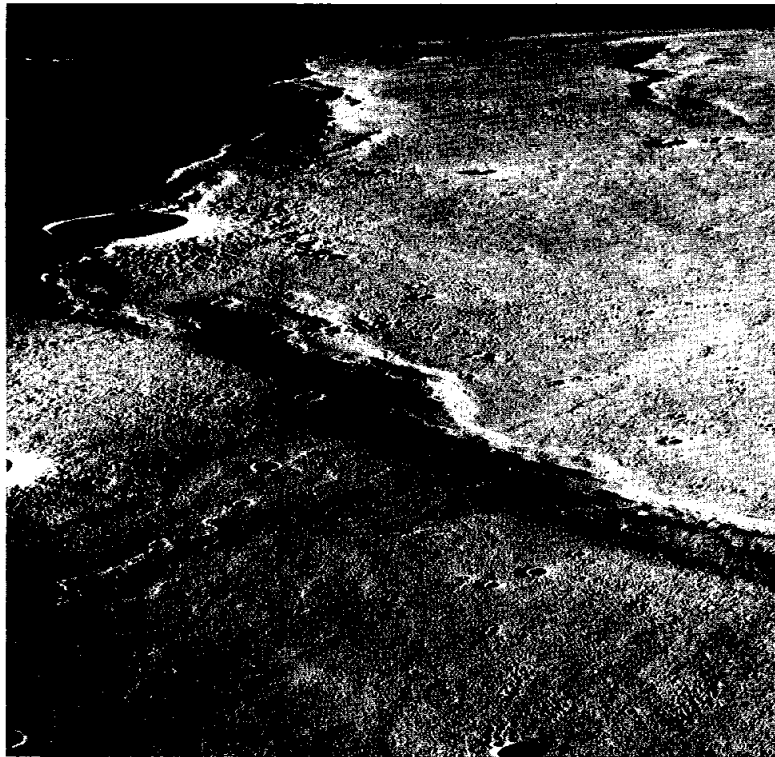
FIGURE 4-51.—Near-terminator photograph in Mare Imbrium. The very low angle of Sun illumination emphasizes topographic detail in this north-looking, high-oblique view of the crater C. Herschel and associated mare ridges. C. Herschel, approximately 15 km in diameter, is located at latitude 34.5° N, longitude 31° W (AS17-155-23712).
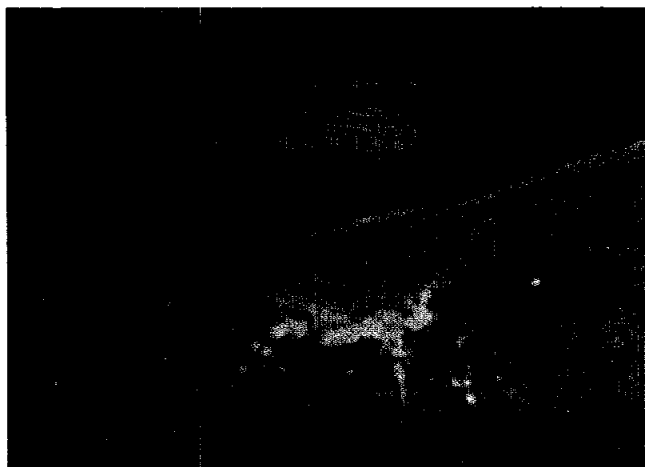
FIGURE 4-52.—Lift-off of the LM ascent stage. This photograph was made from the color TV picture transmitted from the Houston-controlled TV camera mounted on the LRV. The LM descent stage remains on the lunar surface (S-72-55421).
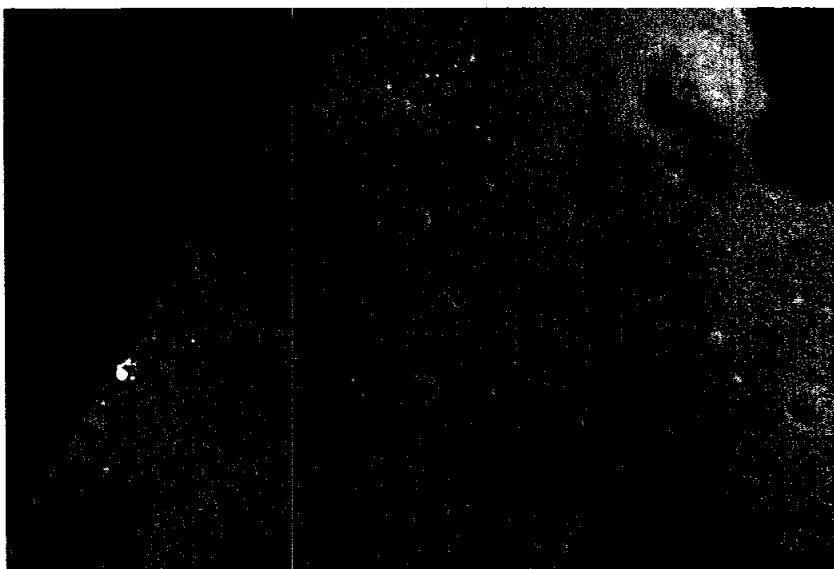
FIGURE 4-53.—This 16-mm frame was exposed in the LM DAC from the ascent-stage LMP window shortly after lift-off. The LM descent stage is at the lower left margin of the photograph, and the ALSEP instruments are visible near the upper left corner, approximately 190 m and slightly north of west from the LM. The irregular dark lines between the LM and the ALSEP instruments are LRV tracks. The largest crater in the field of view, at the upper right corner of the photograph, is Rudolph, approximately 50 m in diameter (Apollo 17 16-mm camera, magazine Q).

FIGURE 4-54.—The LM ascent stage pictured while stationkeeping with the CSM on revolution 52. The rendezvous radar antenna at the top of the LM is pointing at the CSM. The bell of the ascent propulsion engine is visible at the bottom of the spacecraft and, above it, the square hatch through which the crew egressed to the lunar surface. Above and to the viewer's right of the hatch, the commander's head is in sunlight in the triangular window. After docking and transfer of the crew and equipment to the CM, the LM ascent stage impacted into the lunar surface near the Apollo 17 ALSEP to provide a data point for the seismometer (AS17-149-22859).
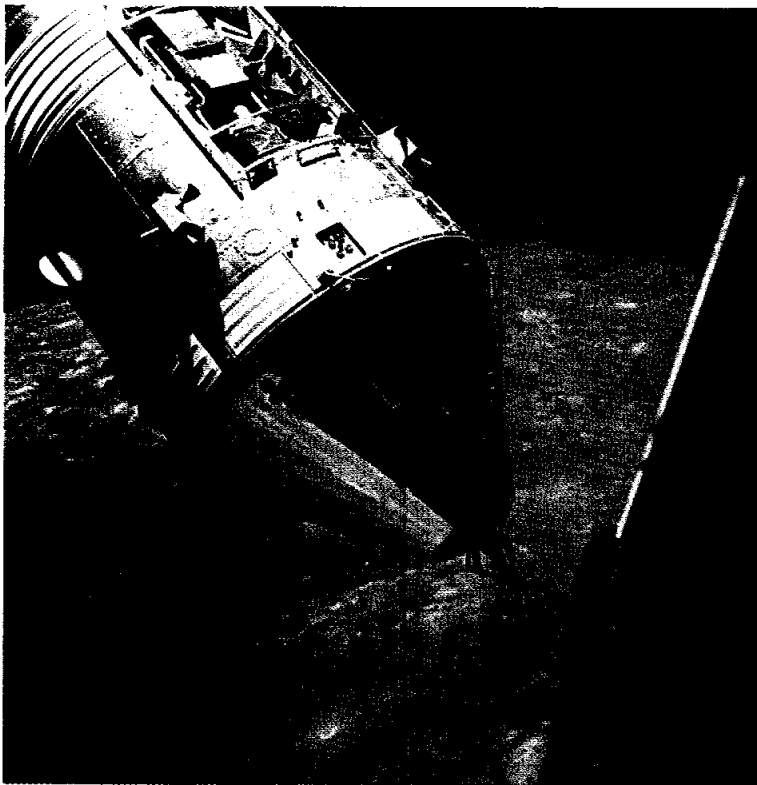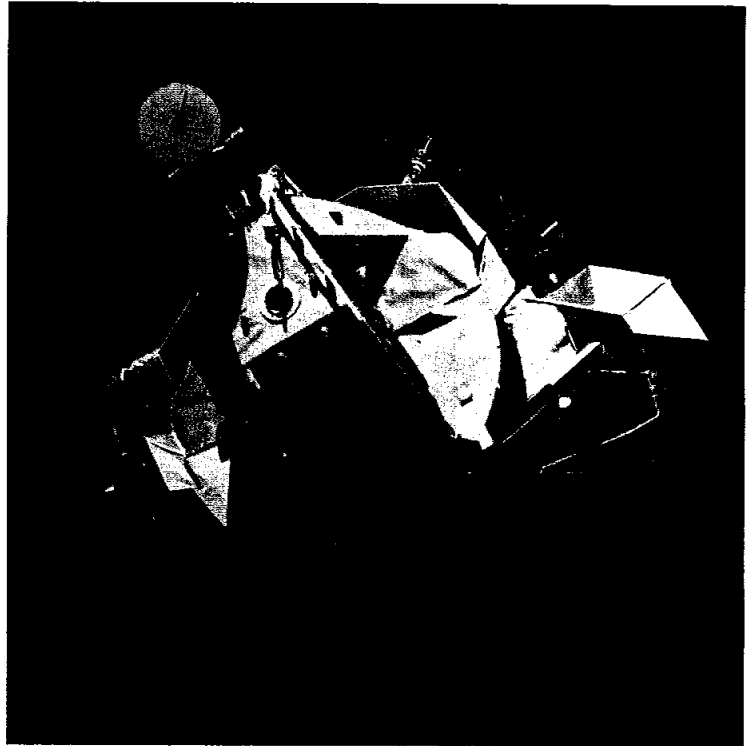
FIGURE 4-55.—The CSM viewed from the LM. While stationkeeping before docking with the LM on revolution 52, the CMP maneuvered the CSM to allow inspection of the SIM bay by the LM crew. The mapping camera film cassette, retrieved by the CMP during TEC, is under the dark cover in the near left corner of the SIM bay. The panoramic camera film cassette is under the square dark cover directly behind the mapping camera cassette. The docking probe is at the apex of the CM. The view is to the southeast; the number "23" at the bottom of the picture is centered in the crater Lick on the southern edge of Mare Crisium. The dark lunar surface area on the horizon at the upper right is Mare Fecunditatis (AS17-145-22257).
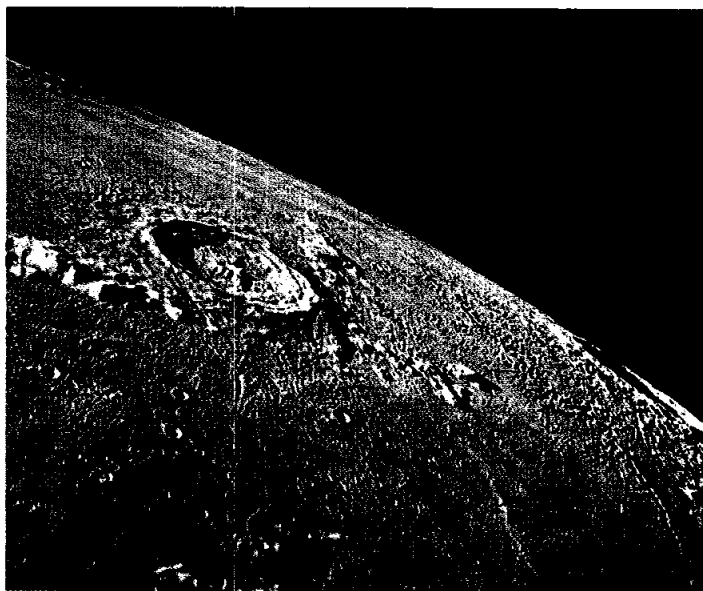
FIGURE 4-56.—This high-oblique view from the LM after lift-off from the
lunar surface includes the craters Eratosthenes, 60 km in diameter, at
left center, and Copernicus on the horizon at the right. The view is to
the southwest from southern Mare Imbrium. To the left of Eratosthe-
nes is the southern end of Montes Apenninus. Patterns of secondary
craters are emphasized in this low-Sun-angle photograph
(AS17-145-22285).

the crew photographed the lunar surface with the
DAC and with the Hasselblad camera, using the 80-
and the 250-mm lenses (figs. 4-57 to 4-59). The
crewmen also photographed the crescent Earth with
the Hasselblad camera and the DAC.

The mapping and panoramic cameras were
switched on as the CSM passed over the sunlit lunar
surface shortly after the TEI burn. Images of the
lunar surface were recorded on the 17 remaining
panoramic camera frames and on 107 mapping
camera frames before the lunar disk drifted from the
field of view. The TEC EVA, in which the CMP
retrieved the mapping camera and panoramic camera
film canisters from the SIM bay, was documented
with the DAC and the Hasselblad camera (fig. 4-60).

The fireball accompanying the CM entry into the
Earth atmosphere was photographed with the DAC,
as was the deployment of the drogue and main
parachutes. Approximately 13 min after Earth entry
interface, the CM splashed down in the South Pacific
Ocean near latitude 8° S, longitude 166° W (fig.
4-61).

FIGURE 4-57.—View of the northeastern quadrant of the
Moon taken during TEC. Mare Crisium is the circular
feature at the right; from bottom center up are Mare
Fecunditatis, Mare Tranquillitatis, and Mare Serenitatis.
The Apollo 17 landing site at the southeastern margin of
Mare Serenitatis is easily distinguished by the very dark
mantling material. The bright-rayed crater to the left of
Mare Crisium is Proclus (AS17-152-23339).
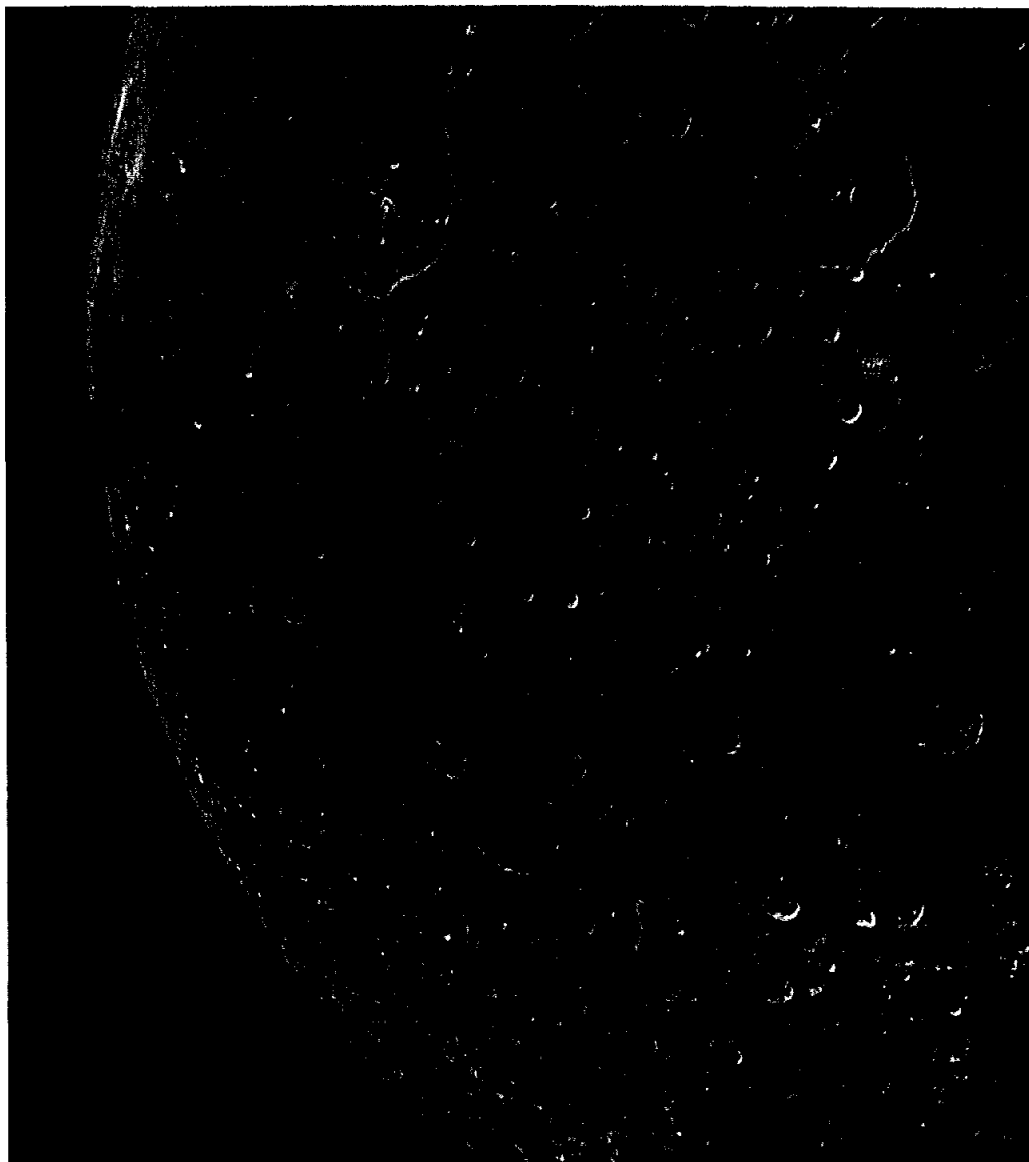
FIGURE 4-58.—A TEC view of Mare Australe. The center of this view is near latitude 35° S, longitude 90° E. In the upper middle, the large crater with dark material on its floor near both the left and right walls is Humboldt, centered at latitude 27° S, longitude 81° E (AS17-152-23288).
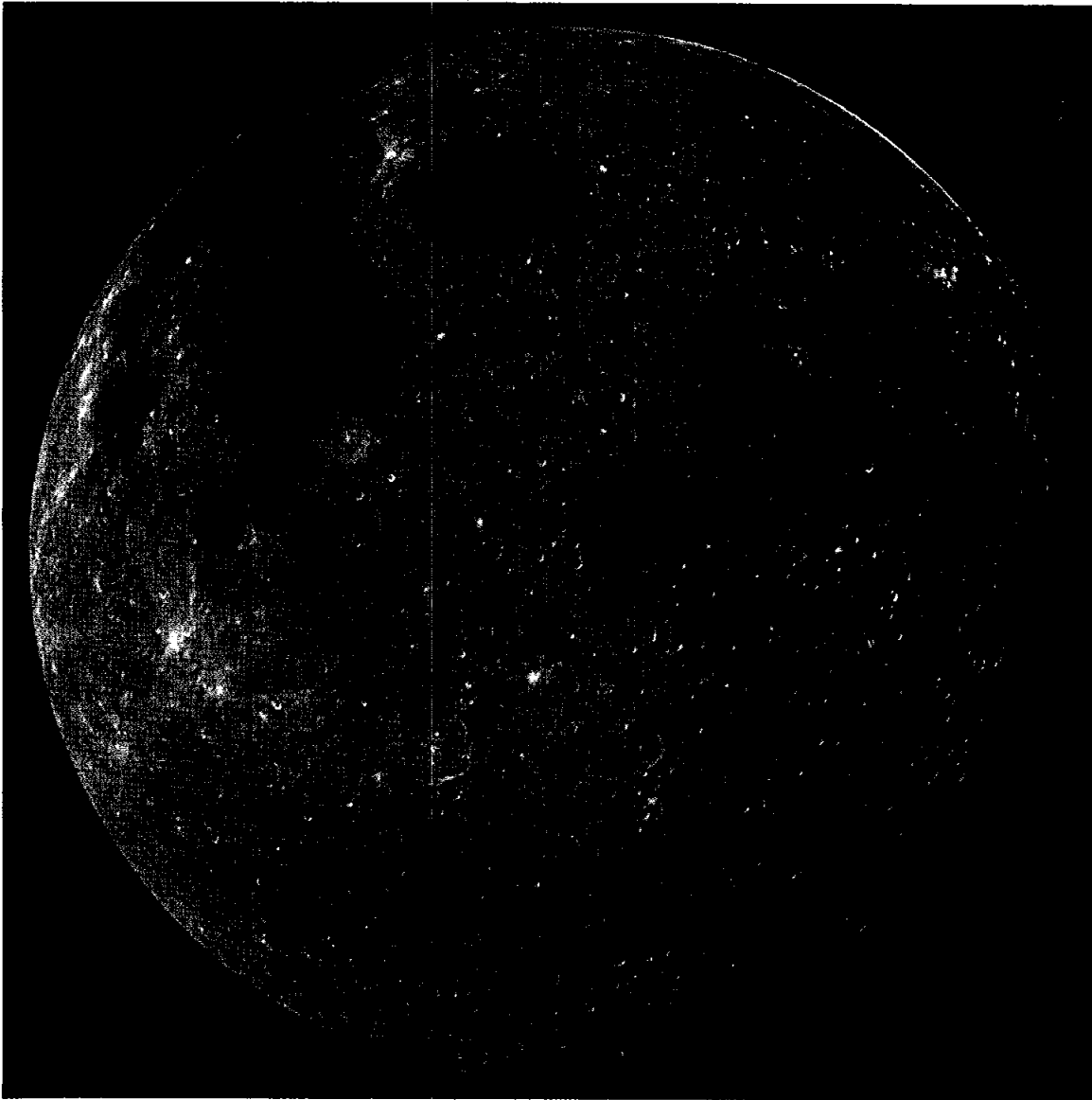
FIGURE 4-59.—A TEC view of the almost-full lunar disk. The dark-floored crater Tsiolkovsky is near the terminator at lower right. Humboldt Crater is to the left of and below center. Part of Mare Serenitatis is visible on the horizon at the top just to the left of center (AS17-152-23308).

FIGURE 4-60.—The CMP is pictured during his TEC EVA to retrieve film canisters from the mapping and panoramic cameras in the SIM bay of the service module (SM). The CMP is holding a handrail on the SM, and his body is extended over the open SIM bay. The mapping camera film canister is near his left elbow. At the rear of the SM, the lunar sounder experiment VHF antenna extends toward the top right corner of the photograph (AS17-152-23391).
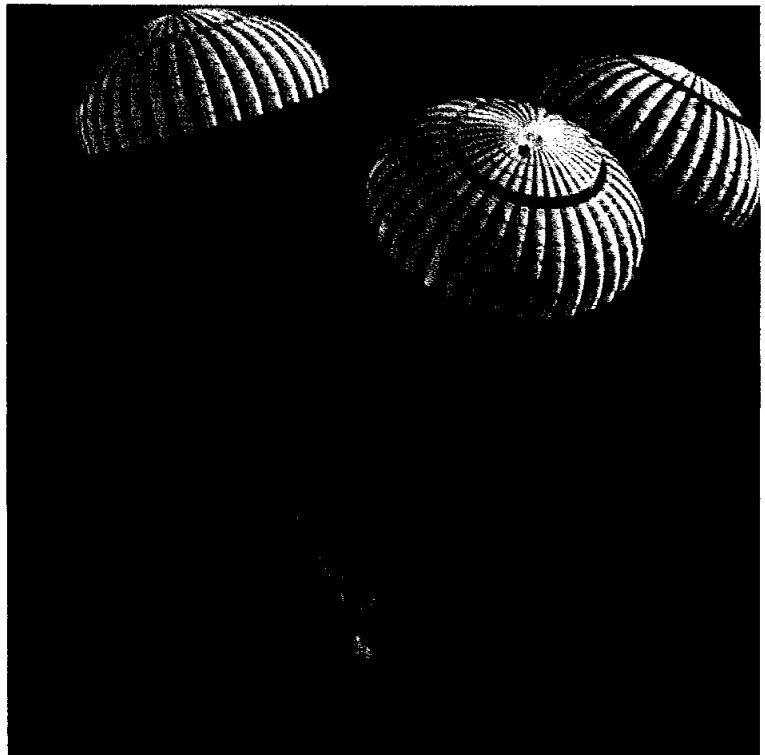
FIGURE 4-61.—The Apollo 17 CM nears splashdown in the South Pacific Ocean within approximately 1 km of the target point. Splashdown was at 07:24:59 G.m.t., December 19, 1972, 304 hr 32 min after lift-off from the NASA John F. Kennedy Space Center, Florida (S-72-55834).

Near-Terminator and Earthshine Photography

James W. Head[a] *and Douglas Lloyd*[b]

The purposes of this paper are to illustrate and describe two types of special photograph (near terminator and earthshine) taken during the Apollo 17 mission and to point out potential areas of its usefulness to encourage full utilization of the Apollo 17 photographs in scientific investigations. Where appropriate, some description and preliminary interpretation are given to demonstrate the potential of various photographs.

Lunar surface photographs taken in the vicinity of the sunshine terminator provide important information that is often unavailable on photographs taken at higher Sun-elevation angles (such as Lunar Orbiter and most Apollo orbital photographs). Features that are particularly enhanced include those of low relief (such as mare flow fronts), craters of different morphology (rimless depressions, secondaries, etc.), areas of contrasting crater densities, and small-scale structures occurring on other low-relief features (such as mare ridges). Technical details of Apollo near-terminator photography are given in references 4-1 to 4-4. During Apollo 17, two magazines of very-high-speed black-and-white (VHBW) film (2485) were exposed using the Electric Hasselblad (EL) camera on 70-mm film format.

Photographs were also obtained under earthshine conditions in areas near the crater Copernicus, in western Oceanus Procellarum, and around the Orientale basin. Technical details of these photographs are described in reference 4-2. During the Apollo 17 mission, VHBW 35-mm film was exposed with a Nikon camera.

---

[a]Brown University.
[b]Bell Telephone Laboratories.

NEAR-TERMINATOR PHOTOGRAPHY

Apollo 17 Landing Site

A near-terminator photograph of the Taurus-Littrow highlands and the Apollo 17 landing site (designated by the arrow) is shown in figure 4-62. The ejecta blanket of the crater Vitruvius (in the lower left, approximately 30 km in diameter) is embayed by smooth mare material, thus indicating a premare age for the crater. The differences between terrain types are enhanced in this low-Sun photograph. The flat, sparsely cratered mare regions around
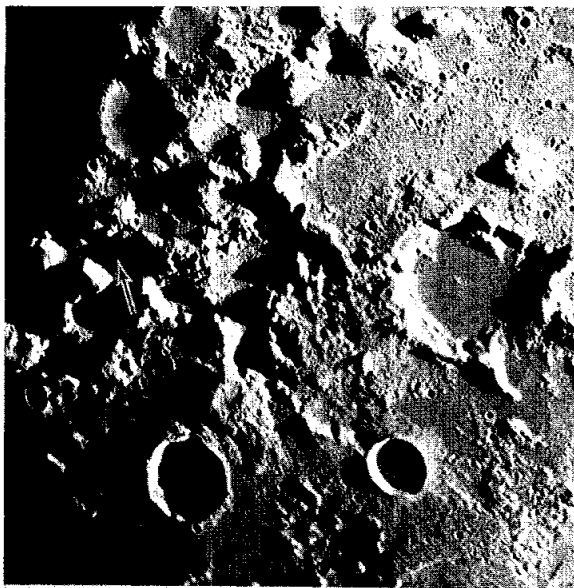
FIGURE 4-62.—Taurus-Littrow region; arrow indicates Apollo 17 landing site. Width of area shown is approximately 200 km (AS17-154-23602).

FIGURE 4-63.—Mosaic of photographs of a portion of Mare Imbrium just north of the crater Euler showing multiple flow lobes and flow fronts. Distance from lower left to upper right is approximately 110 km (AS17-155-23714 to 23716).

Vitruvius (in the lower right of the photograph) are in contrast with the pitted, more hummocky, cratered terrain of the upland plains. The 10- to 20-km-diameter, smooth-sided massive mountain blocks (massifs) around the landing site also stand in marked contrast to the finer-textured, domical, somewhat lineated Sculptured Hills, which make up the majority of the highlands in figure 4-62.

Flow Lobes and Flow Fronts

A series of overlapping flows and flow fronts is located in Mare Imbrium, north of the crater Euler (fig. 4-63). These trend to the north and contain a wide variety of leveed flow channels (lower left). The detailed sequence and history of these particular flows have been studied by Schaber (ref. 4-5). Although some of the major flow fronts have been visible on higher Sun photographs, the detailed structure and stratigraphy could not have been worked out without the low-Sun photographs.

Mare Ridges

A series of structures associated with mare ridges, which are typical of many mare structures, is shown in figure 4-64. Two broad mare arches (ref. 4-6) are visible. The lower, narrower arch is broad at the right,

narrows and sharpens to the left, and finally emerges as a zigzag scarp-like ridge. The much broader mare arch to the north shows a somewhat similar trend with the mare ridge being even more distinct as it crosses from one side of the arch to the arch axis. Several apparently flooded craters (arrows) also can be seen.

Potential Volcanic Source Areas

Several features of possible volcanic origin (fig. 4-65) are located in a group in southwestern Mare Imbrium. The area is characterized by a series of low hummocky hills; a large, central, irregular rimless depression; a series of crater chains; numerous meandering scarps; a long arcuate rille at the southeastern boundary; and a series of cone-like structures with central craters leading in a chain away from the northern end of the complex (base of fig. 4-65). The assemblage of volcanic structures located in this area suggests that it may have been a center of mare volcanic activity.

Mare Albedo and Structure Boundaries

Low-Sun photographs enhance the contrast between major mare units, such as the central fill of

FIGURE 4-64.—Mare arches and ridges (AS17-155-23767).

FIGURE 4-65.—Possible center of mare volcanic activity in southwestern Mare Imbrium. South is at the top; approximate width of center area is 45 km (AS17-155-23736).

Serenitatis and its surrounding dark annulus (fig. 4-66). The dark annulus, a low albedo unit, partially lines the inner edge of Mare Serenitatis and has been mapped as Eratosthenian in age, while the higher albedo central mare fill has been mapped as Imbrian in age (ref. 4-7). However, the dark annulus in southern Serenitatis (lower half of fig. 4-66) is laced with linear rilles that terminate at or are embayed by the central mare unit. Also, secondary craters from the crater Plinius (just off the photograph at the lower right) occur up to the boundary with the central mare but not on the other side. These relationships strongly suggest that the dark annulus predates the central mare of Serenitatis, at least in this area.

Domical Structures in Maria

Two general types of domical structures occurring in the maria are enhanced by low-Sun photographs. Low, broad circular domes with or without central pit craters form one type; examples from northern Mare Tranquillitatis are visible in figure 4-67(a) (arrows). A second example is visible west of the crater Copernicus near T. Mayer (fig. 4-67(b)); here a sinuous rille winds around the base of a low 15-km-diameter mare dome located near the base of a highland ridge. The dome has a central pit (tip of arrow). A second broad dome with an elongate central pit is just

to the left. These mare domes may represent the lunar equivalent of shield volcanoes and may be sources for some of the mare lavas.

A second type of domical mare structure is visible in southwestern Mare Imbrium near the crater Diophantus (figs. 4-68(a) and (b)). This structure (seen
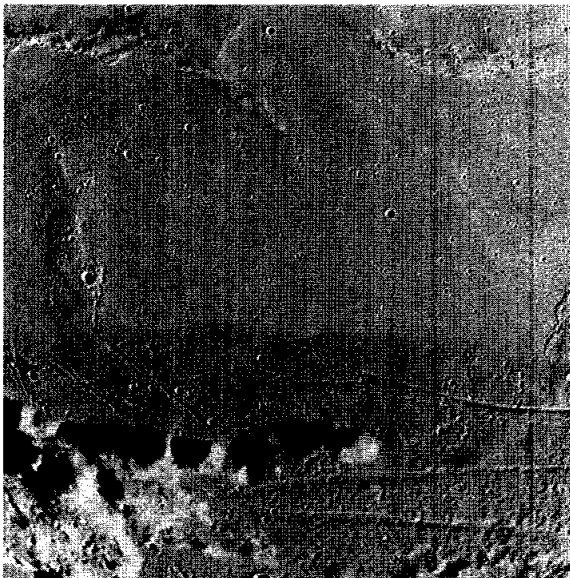
FIGURE 4-66.—Dark annulus in southern Mare Serenitatis. Frame width is approximately 95 km (AS17-154-23635).
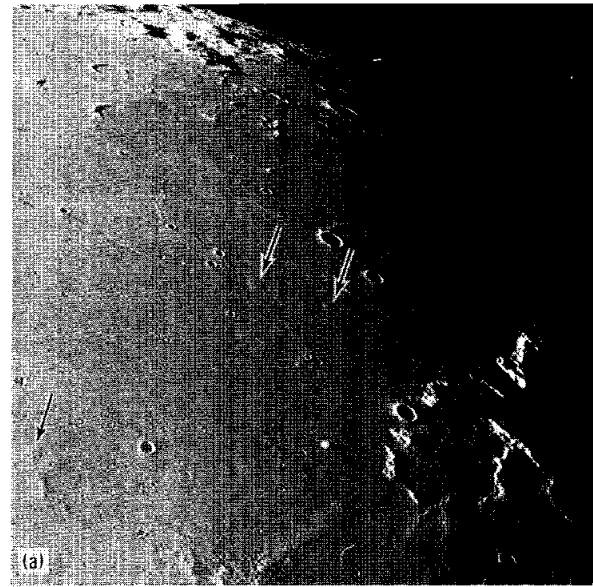
FIGURE 4-67.—Domical structures in lunar maria. (a) Domes in northern Mare Tranquillitatis (arrows). The domes average approximately 5 to 10 km in diameter (AS17-154-23604). (b) Domes near the crater T. Mayer. The dome designated by the arrow is approximately 15 km in diameter (AS17-155-23739).

under two different low-Sun conditions) is character-ized by an irregular scarp-like outline, central hill and groups of satellite hills, and various associated rilles. No obvious central pit can be identified. The sinuous rille visible here (fig. 4-68) terminates at the base of the domical structure, crosses over the crest adjacent to the central hills (just outside the figure), and terminates again at the northern end of the structure. The other rille apparently lies at the crest of the structure and may be structural in origin. A number of these features suggest that this mare dome may be the result of differential settling of mare lavas rather
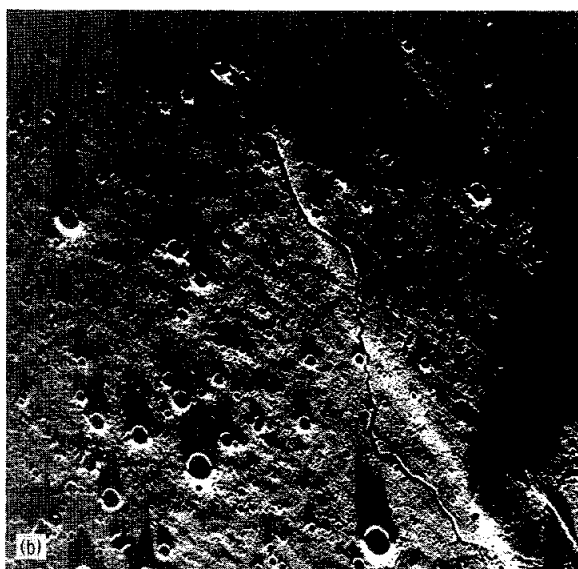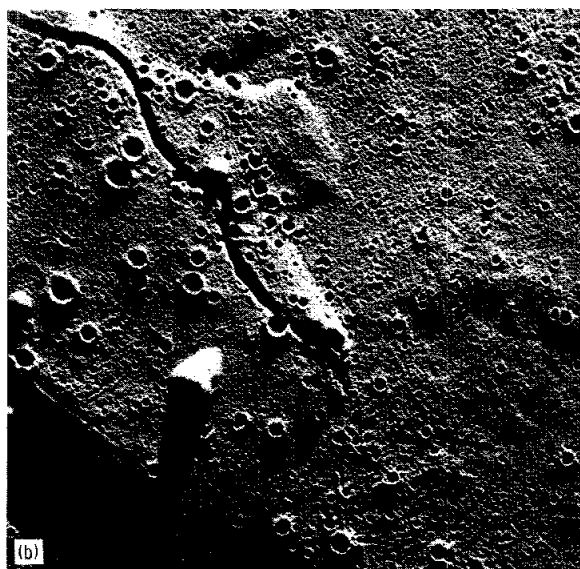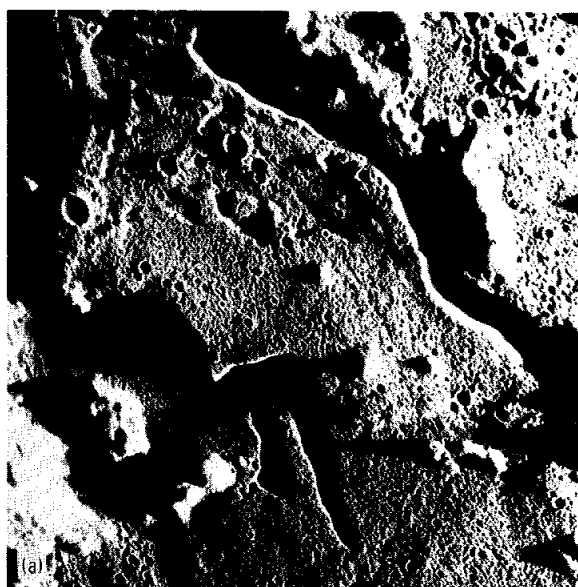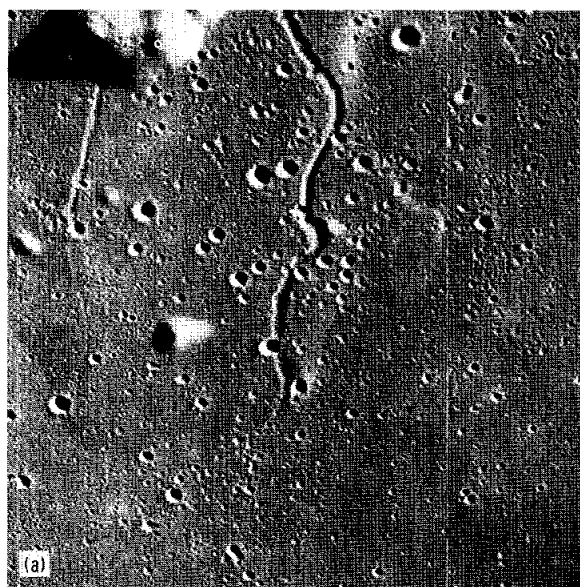
FIGURE 4-68.—Domical mare structure under different low-Sun conditions. (a) Domical mare structure in south-west Mare Imbrium near Diophantus. The sinuous rille is approximately 600 m wide (AS17-155-23755). (b) Same area as shown in part (a) but at a lower Sun angle (AS17-155-23749).

FIGURE 4-69.—Low-Sun photographs enhancing features associated with sinuous rilles. (a) Rilles and rimless depressions north of Mare Vaporum. The width of the area shown is approximately 25 km (AS17-154-23679). (b) Sinuous rille and mare ridge under near-terminator conditions (AS17-155-23723).

than extrusive volcanic buildup, as envisioned for the circular mare domes.

Sinuous Rilles

Figure 4-69 shows some of the features associated with sinuous rilles that are enhanced by low-Sun photographs. Figure 4-69(a) illustrates the complex of rimless depressions and partially collapsed structures just north of Mare Vaporum and associated with mare sinuous rilles. Figure 4-69(b) shows a sinuous rille crossing a mare arch several times, suggesting that the arch may have formed at a later stage than the rille.

EARTHSHINE PHOTOGRAPHY

Earthshine photography of three regions is illustrated in figure 4-70. Figure 4-70(a) shows the Reiner γ structure or surface marking seen under earthshine conditions in western Oceanus Procellarum. Figure 4-70(b) shows the crater Schlüter on the rim of the Orientale basin, and figure 4-70(c) shows the rim and interior of the Orientale basin with Lacus Autumni in the foreground and Lacus Veris in the background.

FIGURE 4-70.—Earthshine photographs. (a) The Reiner γ area (bright patch, approximately 80 km wide) in western Oceanus Procellarum (AS17-158-23897). (b) The crater Schlüter (approximately 90 km in diameter) on the rim of the Orientale basin (AS17-161-24013). (c) View looking southwestward into the Orientale basin with Lacus Autumni in the foreground and Lacus Veris in the background (AS17-158-23901).

REFERENCES

4-1. Head, J. W.; and Lloyd, D. D.: Near-Terminator Photography. Sec. 18, Part G, of the Apollo 14 Preliminary Science Report. NASA SP-272, 1971.

4-2. Lloyd, D. D.; and Head, J. W.: Lunar Surface Properties as Determined From Earthshine and Near-Terminator Photography. Proceedings of the Third Lunar Science Conference, vol. 3, MIT Press (Cambridge, Mass.), 1972, pp. 3127-3142.

4-3. Head, J. W.; and Lloyd, D. D.: Near-Terminator Photography. Sec. 25, Part R, of the Apollo 15 Preliminary Science Report. NASA SP-289, 1972.

4-4. Head, J. W.; and Lloyd, D. D.: Low-Relief Features in Terrain of the Descartes Region and Other Areas: Near-Terminator Photography. Sec. 29, Part U, of the Apollo 16 Preliminary Science Report. NASA SP-315, 1972.

4-5. Schaber, Gerald G.: Lava Flows in Mare Imbrium: Geologic Evaluation From Apollo Orbital Photography. Lunar Science IV (Abs. of papers presented at the Fourth Lunar Science Conference (Houston, Tex.), Mar. 5-8, 1973), pp. 653-655.

4-6. Strom, R. G.: Lunar Mare Ridges, Rings, and Volcanic Ring Complexes. Mod. Geol., vol. 2, 1971, pp. 133-157.

4-7. Wilhelms, D.; and McCauley, J. F.: Geologic Map of the Near Side of the Moon. U.S. Geol. Survey Misc. Geol. Inv. Map I-703, 1971.

5. A Geological Investigation of the Taurus-Littrow Valley

Harrison H. Schmitt[a] *and Eugene A. Cernan*[a]

The Apollo 17 mission visited the valley of Taurus-Littrow in the mountainous southeastern ring of the great plain of Mare Serenitatis. Between the 11th and 14th of December, 1972, we conducted 22 hr of surface exploration and experimentation in this valley. Six major geologically defined units within the valley and in the mountains surrounding it (figs. 5-1 and 5-2) were investigated. In the performance of this investigation, we visited 11 major sampling locations, traversed and observed 30 km of the valley floor, collected 97 major rock samples and 75 soil samples, and obtained 2200 documentation photographs. The nearly flawless characteristics of the mission plans and equipment (ref. 5-1), our experience and training in the geological sciences, and the close cooperation of the science team on Earth provided a much more extensive delineation of the geological context of our investigations than had ever before been possible on the Moon.

It now appears that, at Taurus-Littrow, we have looked at and sampled the ancient lunar record ranging backward from the extrusion of old mare basalts 3.7 billion years ago, through the formation of the Mare Serenitatis mountain ring, and thence backward into crystalline materials that may reflect the earliest history of the evolution of the lunar crust itself. Also, materials and processes that range forward from the formation of one of the earliest mare basalt surfaces through 3.7 billion years of modification of that surface have been found and can now be studied. The early portion of this modification included the addition of mantles of glassy spheres that may be the culmination of processes once active within the deep interior of the Moon.

EXPLORATION PLANS

The photogeology of the valley of Taurus-Littrow and exploration plans based on that geology are described in detail in references 5-2 and 5-3. Figure 5-3 is an Apollo 17 panoramic camera photograph that gives somewhat better detail of the area than was available from the Apollo 15 photographs used for the preflight planning.

The stratigraphy and historical sequence of events in the Taurus-Littrow area were largely understood before the Apollo 17 mission (refs. 5-2 and 5-3). This premission sequence, from older to younger events, is summarized as follows.

1. Pre-Serenitatis events included lunar crust development and pre-Serenitatis impact events.

2. The Serenitatis event included formation of the major mountain ring and initial formation of radial grabens such as the Taurus-Littrow valley. Uplift of the valley walls may have continued for an extended time after the Serenitatis event.

3. Ejecta blankets from the Nectaris and Crisium events probably extended across the Taurus-Littrow area.

4. The Imbrium event, in addition to contributing ejecta to the area, could have accented the formation of grabens like the Taurus-Littrow graben, which is radial to both the Imbrium and Serenitatis basins.

5. Post-Imbrium materials partially filled and leveled the valley floor after graben formation was complete or near completion.

6. The Camelot-age cratering events, which were apparently impact events, exposed subfloor material; crater materials are apparently partly mantled by dark material.

7. The Steno-age cratering events consisted of the formation of craters similar to but less subdued than the Camelot-age craters.

[a]NASA Lyndon B. Johnson Space Center.
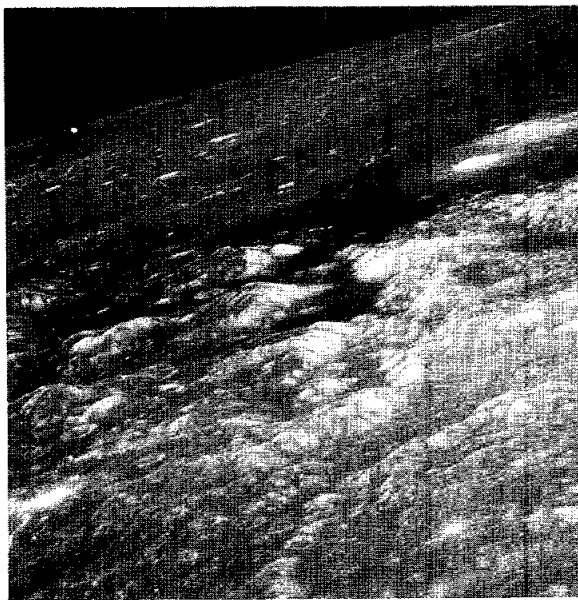
FIGURE 5-1.—The majestic valley of Taurus-Littrow, a dark, bay-like indentation in the broken mountain chain that defines the edge of Mare Serenitatis. Coordinates of the landing site are latitude 20°10' N, longitude 30°46' E. The view is northwestward, and the central width of the valley is approximately 7 km (AS17-148-22770).
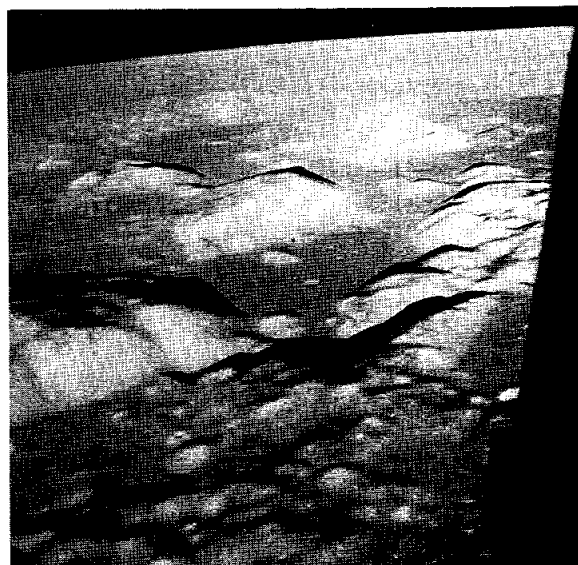
FIGURE 5-2.—The valley of Taurus-Littrow as seen from the lunar module Challenger on the orbit before powered descent. The command and service module America can be seen crossing the base of the 2300-m-high South Massif. At its narrowest point between the South and North Massifs, the valley is 7 km wide. Mare Serenitatis is on the horizon (AS17-147-22465).

8. The dark mantle deposition included mantling of older features on a regional scale; the deposits are interpreted as possibly pyroclastic.

9. Effects of the Lee-Lincoln Scarp formation are apparently superposed on North Massif talus; the age relation to the dark mantle material is uncertain.

10. The light mantle deposition was a probable avalanche deposit of massif materials transported over the dark mantle onto the valley floor.

11. The Shorty-age and Van Serg-age cratering events are indicated by small and relatively sharp craters superposed on the younger surfaces of the dark and light mantles.

12. For regolith and talus formation, it is assumed that impact-generated regolith formed on all exposed surfaces as a continuing process throughout lunar history. Talus has similarly accumulated at the base of all steep slopes.

The actual lunar surface traverses (fig. 6-2 of sec. 6) were very close to those planned for the Apollo 17 mission. It was intended to investigate the old, premare materials at the bases of both the South and North Massifs (station 2 and stations 6 and 7, respectively) and possibly at the base of the Sculp-

tured Hills (station 8). Wherever possible, large blocks were to be studied in preference to other features. Materials present beneath the valley floor and the nature of the major craters of the valley were to be studied specifically in the walls and on the rims of several large craters; that is, Emory Crater at station 1 (later moved to a location between the craters Steno and Powell), Camelot Crater at station 5, and Sherlock Crater at station 10 (later eliminated). These large-crater localities and the surface near the landing point were also intended to be prime areas for investigating the dark floor materials. A concentrated look at the light mantle that extends northeastward from the South Massif was planned for stations 2, 3, and 4. Little work on this problem was possible at station 4; however, a new station on the light mantle (station 2A) was added during the mission. Finally, a study of more recent cratering events, possibly volcanic in origin, was set for station 4 at Shorty Crater and for station 9 at Van Serg Crater.

The premission objectives also included extensive plans for sampling lunar soil on the various geologic units. This sampling included collection of samples from the lunar roving vehicle, core-tube samples,

FIGURE 5-3.—Apollo 17 panoramic camera photograph of the Taurus-Littrow valley with the informal names of various topographic features indicated. The central width of the valley from Nansen Crater to Henson Crater is approximately 7 km (Apollo 17 panoramic camera frame AS17-2309).

sample sequences from trenches, samples from special geometric situations, and a deep (3.2 m) core sample. All these objectives were met.

Several special observational and sampling projects as targets of opportunity were delineated on the basis of the implications of certain lines of interpretation for the origin and nature of various valley features. These special projects were as follows.

1. Coarsely crystalline rock suites associated with the massifs

2. Evidence of fumarolic alteration

3. Evidence of a source or vent of volcanic materials

4. Apparent xenoliths contained within igneous materials

5. Undisturbed glass masses that possibly cooled through the Curie point in situ

To greater or lesser degrees, each of these projects received special attention during the Apollo 17 lunar surface explorations.

OBSERVATIONAL CONSIDERATIONS

The raw data of our observations during the exploration of the Taurus-Littrow valley exist only in our verbal transcriptions, in videotapes, and in our minds. The synthesis of the data contained in transcripts and videotapes is relatively straightforward and constitutes the foundation of this report. The synthesis of the data contained in the mind is more difficult. Unlike normal field work on Earth, the pressures of time and total efficiency on the Moon prevent the conscious mental recording of visual images. Many images are recorded, to be sure, but some are not subject to direct recall. Not only may an

external stimulus, such as a photograph or a question, be required to release these data, but there is a continued problem, which worsens as time passes, of separating purely objective observational data from more subjective feelings acquired since the mission. In recognition of this problem, the transcripts and tapes have been used extensively for verification of observations. Possible interpretive explanations and alternatives are included in the last section of this paper.

The observational environment in the Taurus-Littrow valley is superb. Unfiltered sunlight is an excellent light for visual investigation. When this light is combined with generally clean rock surfaces, there is little difficulty in distinguishing mineralogical and textural differences. Albedo and textural differences in soil and rock surfaces also are readily apparent. For the most part, the sampling of rocks and soils was based on visually detectable differences or similarities. These characteristics were recognizable despite an overall brownish patina on most rock surfaces. Unfortunately, photographs cannot yet record much of the more subtle information available to the human eye.

NOMENCLATURE

In this report, consistency with our field (transcript) terminology has been maintained except in a few instances. The term "anorthositic gabbro" has been dropped in favor of "tan-gray matrix-rich breccia." The term "blue-gray breccia" has been subdivided into "blue-gray matrix-rich breccia" and "blue-gray fragment-rich breccia." Finally, the term "dark mantle" has been replaced by "dark floor material" because a mantling origin is subject to question at the time of preparation of this report. In most cases, breccias are distinguished as "matrix-rich" or "fragment-rich" depending on which textural component is visually dominant in a given boulder. For correlation of the field terms used in this section with those used in section 6 of this report, see table 6-III.

FIELD OBSERVATIONS

The general historical or stratigraphic sequence of major geologic units in the Taurus-Littrow region was well understood before our investigations on the surface. What remained to be done was the correlation of the detailed field stratigraphic sequences with this general regional sequence. The field observations are discussed in detail in the following paragraphs.

The North Massif

The North and South Massifs form the majestic walls of the Taurus-Littrow valley and rise to heights of 2000 and 2300 m, respectively, above the valley floor, with flanking slopes of approximately 25°. The massifs represent the major structural boundaries of the valley. Their faces contain intermittent exposures of thick sections of premare crustal rocks. Numerous fields, or "source-crops," of boulders are present on the upper one-half to two-thirds of the slopes of both massifs. Boulder tracks indicate that blocks have rolled into the valley from these sources. Several of these blocks were the prime field objectives of our traverses in the Taurus-Littrow valley.

The source-crops for the boulders on the slopes of the North Massif are linear but discontinuous. They are roughly horizontal in apparent orientation, and each is a few hundred meters in length. The large boulder investigated at station 6 (fig. 5-4) has a well-defined track above it and appears to have originated from the lowermost source-crop band approximately one-third of the way up the slope.

Based on what had been seen on previous lunar missions, the geologic complexity of the boulders at stations 6 and 7 was unexpected. Here, for the first time, it was possible to observe and sample across a major lithologic and structural contact. This contact was exposed sharply in boulders large enough that outcrop investigative techniques could be applied. As always, however, time was relentless and many
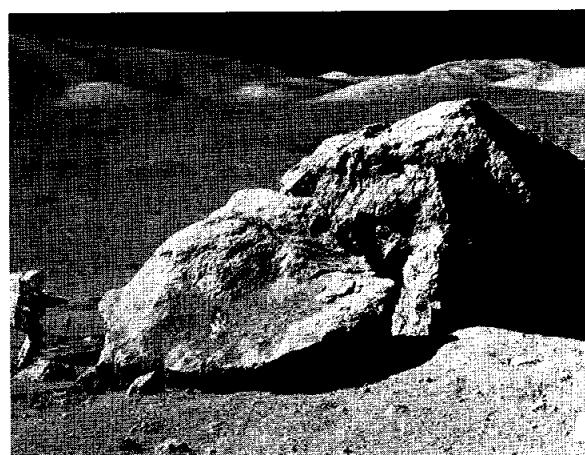
FIGURE 5-4.—View looking south from station 6 on the North Massif and including the large boulders of blue-gray breccia (left) and tan-gray breccia (right) sampled at this locality (AS17-140-21496).

questions were only partially answered. Still, much was learned.

Three major categories of stratigraphic materials were studied and sampled in the boulders at stations 6 and 7. A younger, finely crystalline, strikingly vesicular, tan-gray, *matrix-rich* breccia (fig. 5-5) is apparently in intrusive contact with an older, very finely crystalline, blue-gray, *fragment-rich* breccia (fig. 5-6). There are inclusions of blue-gray breccia in the tan-gray breccia at the contact in the station 6 boulder. A blue-gray *matrix-rich* breccia is the material in direct contact with the tan-gray breccia in both the contacts investigated. This blue-gray *matrix-rich* breccia forms a contact zone approximately 1 m wide, apparently produced from the blue-gray *fragment-rich* breccia in the boulder at station 6. The large vesicles in the tan-gray breccia are ellipsoidal in cross section and are generally alined parallel to the contact with the blue-gray breccia. There were some small vesicles in the blue-gray breccia near this contact in the boulder at station 6.

In addition to the common small blue-gray fragments that dominate the blue-gray *fragment-rich* breccia, there are distinctive clasts of light-gray breccias. Within the contact zone at station 7, one of these clasts is veined by blue-gray *matrix-rich* breccia

(fig. 5-7). The clasts also appear deformed and partially mixed with blue-gray material in the station 6 boulders. The distinctive clasts are apparently the oldest stratigraphic materials sampled at the Taurus-Littrow site.

Scattered, distinctive, light-colored clasts also are present in the tan-gray breccia; however, the stratigraphic relations of these clasts to either the blue-gray breccia or its included clasts were not apparent.

A marked brown patina is well developed on all weathered rock surfaces in the Taurus-Littrow valley. The patina is most prominent on the surfaces of the massif breccias, including the fractured surfaces of the blocks with well-preserved boulder tracks above them at station 6.

The light-gray walls of craters on the slopes of the North Massif and light-gray material we uncovered with our boots suggest that this type of fine debris, mixed with boulders, forms the bulk of the talus at the base of the massif. Fillets of this material are largely absent around boulders except on some uphill sides. Overlying the light-gray fine-grained talus is a medium-gray surface material that is generally a few centimeters thick. Unlike the filleted boulders of the
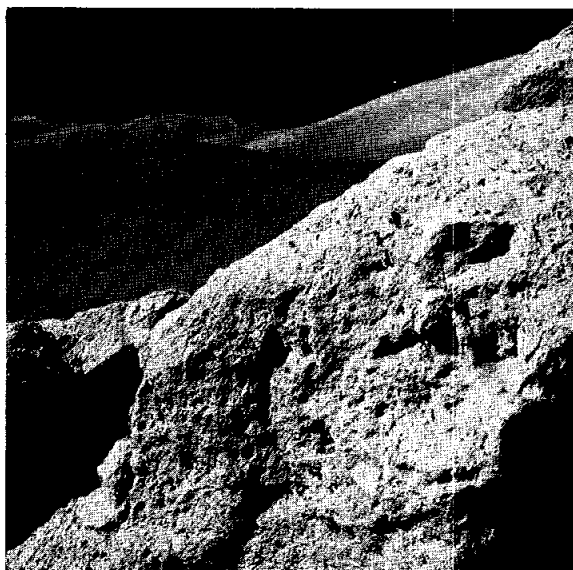
FIGURE 5-5.—Vesicular, tan-gray, *matrix-rich* breccia at station 6. Note the scattered distinctive light-colored clasts and the general alinement of vesicles trending from lower left to upper right. The horizontal width of the illuminated portion of the boulder is approximately 1.5 m (AS17-140-21423).
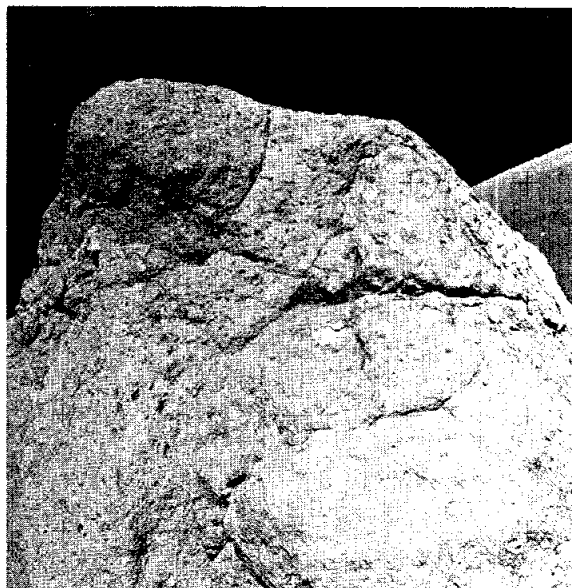
FIGURE 5-6.—The large boulder investigated at station 7 on the North Massif. The boulder is approximately 2 m wide and contains a sharp contact between vesicular tan-gray breccia on the left and blue-gray breccia on the right. A tabular distinctive clast is present on the extreme right, and a weathering patina is indicated by light areas where samples were taken (AS17-146-22336).
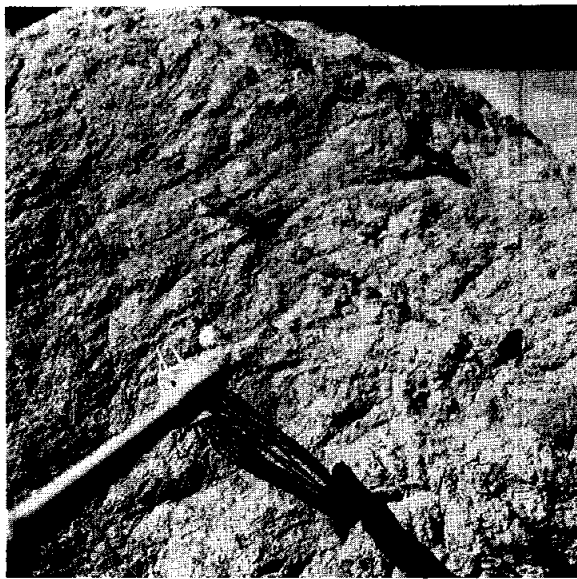
FIGURE 5-7.—Vein of blue-gray *matrix-rich* breccia cutting a distinctive clast of anorthositic matrix-rich breccia in the boulder at station 7. The vein is continuous with the major mass of blue-gray matrix-rich breccia that encloses the clast. The width of the angled end of the tongs is 6 cm (AS17-146-22327).

FIGURE 5-8.—Southwest-looking view of the 2300-m-high South Massif as seen from station 6 at the base of the North Massif. Station 2 is located near the center of the photograph and is approximately 10 km away. Southeast-to northwest-plunging albedo lineaments suggest the attitude of internal massif structure. North Massif talus debris is in the foreground (AS17-140-21491).

valley floor, the sides of boulders commonly overhang this surface material.

The South Massif

The rocks of the South Massif (fig. 5-8) constituted the prime geological objective on the mission to the Taurus-Littrow valley, although the long traverse to the South Massif clearly taxed the operational limits of our surface exploration capabilities. An hour-long trip to the edge of Nansen Crater at the base of the massif, for approximately 60 min of exploration time there, meant that the remainder of this excursion would be extremely limited in time available for exploration. The boulders that were our specific objectives held the promise of an unparalleled view into the history of the lunar crust. Although overshadowed by more spectacular later discoveries, we were not to be disappointed by "old station 2."

The most obvious sources for the boulders near station 2 are on the upper one-fourth of the South Massif slope. Visual inspection from a distance indicated that linear source-crops on this part of the massif and subtle linear color variations of blue-gray lying over tan-gray have an apparent dip of 10° to 15° to-

ward the west. Offsets of the color changes, downward to the east, suggest that normal faults dipping steeply eastward cut the massif structure.

The boulders investigated at station 2 (fig. 5-9) included crystalline, tan-gray matrix-rich breccia and blue-gray matrix-rich breccia, but no contact relations were observed. The tan-gray breccia is less vesicular and more heterogeneous in texture than its North Massif counterpart. The sampled blue-gray breccia is similar to that found in the contact zones of the North Massif boulders. From a distance, boulders of both these rock types have a tan-gray hue very similar to that of the materials below the blue-gray tones in the high portions of the South Massif.

The distinctive clasts of contrasting shades and hues in the tan-gray and blue-gray breccias of the South Massif generally appear similar to those in the North Massif breccias. However, one crystalline clast in the boulder of blue-gray matrix-rich breccia has proved to be composed largely of olivine (sec. 7). The preliminary examination of rocks from both the South and North Massifs also suggests that various crystalline mafic rocks and some ultramafic rocks make up a significant portion of the distinctive clast population.

The third boulder examined at station 2 was a strongly foliated and layered fragment-rich breccia

FIGURE 5-9.—View looking southwest and encompassing the boulders investigated at station 2. The boulders lie along the base of the South Massif talus slope. The surface of the light mantle is in the foreground. The lunar roving vehicle is 183 cm wide (AS17-138-21072).

FIGURE 5-10.—Foliated and layered breccia investigated at station 2. Four samples were obtained across the layering, which trends from the upper left to the lower right in the photograph. The visible portion of the gnomon rod is approximately 45 cm long (AS17-137-20903).

(fig. 5-10) that is much less coherent than either the tan-gray or blue-gray breccia types. This foliated and layered breccia contains large clasts of both dark- and light-colored older breccias in a generally light-colored matrix. There are also small clasts with distinctive dark coronas around them. From a distance, this boulder has a blue-gray hue very similar to that of the blue-gray materials observed near the top of the western portion of the South Massif.

Along the boundary between the South Massif and the valley floor, there is a trough. This trough is much broader and more continuous than had been apparent before the mission. The trough is a few hundred meters wide at station 2, is flat floored, and seems to include the crater Nansen as an integral, although much deeper, topographic unit.

The observed properties of the talus material at the base of the South Massif are very similar to those observed at the North Massif. In Nansen Crater, it is also clear that at least some of the South Massif talus forms a younger toe of debris over the valley floor, particularly over the light mantle deposits present in Nansen (fig. 5-11).
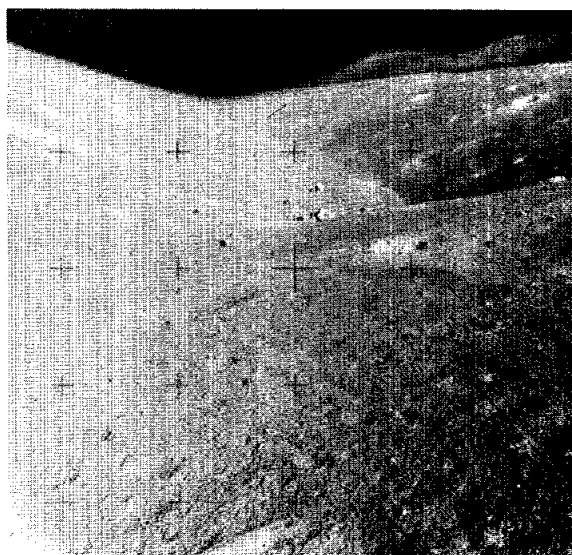
FIGURE 5-11.—View from near station 2, looking northwest into the crater Nansen and along the contact between the South Massif talus and the light mantle. Note the lobe of talus debris lying on the light mantle in Nansen. The boulders are on the order of 3 to 5 m in diameter (AS17-138-21058).

The Sculptured Hills

The interlocking domes of the Sculptured Hills form the northeastern wall of the Taurus-Littrow valley. The origin of this unusual physiographic unit remains unknown, although some relation to the processes associated with the Serenitatis impact event is indicated by morphologically similar units near other large lunar basins (ref. 5-2).

Our investigation at station 8 on the lower slopes of the Sculptured Hills gave no definitive evidence about the nature of bedrock units. Concentrations of boulders were observed only near the tops of the hills, and no boulder tracks were apparent above the few blocks visible on the lower slopes (fig. 5-12). The surface texture of the slope material on the Sculptured Hills is of much finer scale and is more wrinkled in appearance than that of comparably lighted slopes on the massifs.

Of the six blocks examined in the vicinity of station 8, five were composed of crystalline basalt similar to that in the Camelot-Steno area. The sixth block was a black, glass-coated, coarsely crystalline rock made up of approximately equal parts of a yellowish mafic mineral and white to bluish-gray plagioclase and maskelynite. This apparently exotic fragment was unfilleted and projected only a few centimeters into the underlying soil. Other exotic white fragments in small secondary craters appeared to be anorthositic matrix-rich breccias (fig. 5-13).

The soil on the slope material at station 8 has a uniform grain size and is medium to dark gray in color in a trench dug to a depth of 30 cm (fig. 5-14). In this regard, the slope materials of the Sculptured Hills resemble the soils on the dark floor material in the valley rather than those on the massifs or on the light mantle.

The Valley Floor

The dark floor of the Taurus-Littrow valley is underlain by a body of basalt between the bounding massifs. Since formation, this material has been subjected to a variety of cratering, depositional, structural, and possibly volcanic processes. In addition to the investigation of block fields in the valley, our goals included the study of the Camelot- and Steno-age cratering events, the depositional characteristics of the dark floor material, the structural history of the valley floor, and any volcanic features we might encounter.
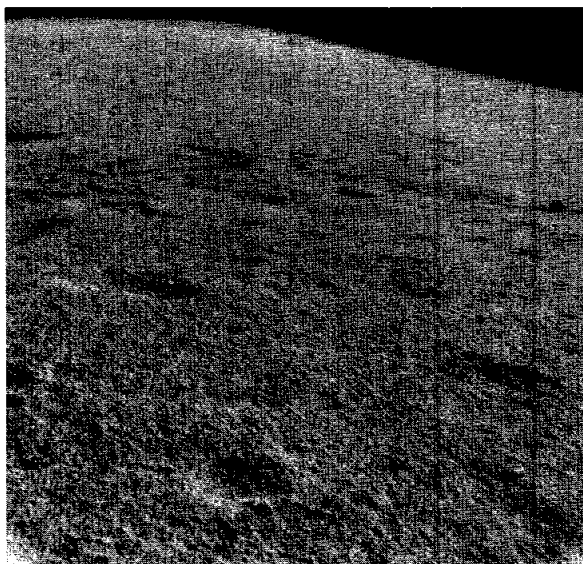
FIGURE 5-12.—View from station 8 looking northeast up the slope of the Sculptured Hills. Note the small number of boulders relative to the talus deposits around the massifs. The boulder in the distant center of the photograph is approximately 0.5 m in diameter (AS17-142-21734).

FIGURE 5-13.—Secondary crater approximately 1 m in diameter in the wall of a larger crater near station 8. The central portion of the secondary crater contains several fragments of white, anorthositic, matrix-rich breccia that appears to have been part of the crater-forming projectile (AS17-146-22399).

The block fields concentrated near and in the large craters in the Camelot-Steno area allowed a rather comprehensive investigation of the basalts. The blocks are largely massive, tan to pinkish-gray, coarse-grained, ilmenite basalts generally having a coarsely vesicular texture. Isolated examples of egg-sized vesicles were observed near the crater Bronte. Locally, there is a strong foliation formed by the occurrence of parallel parting planes or fractures (fig. 5-15). The blocks on the rim of Camelot Crater at station 5 showed parallel layers defined by differences in vesicle concentrations.

Only two fragments of aphanitic basalt were observed despite a search for this variety at each sampling site. Both fragments were finely porphyritic, and the one from the crater Shorty was very coarsely vesicular. Other fine-grained to aphanitic basalt fragments are present in the suites of small fragments collected in rake and soil samples (sec. 7).

In some blocks, finely textured blue-gray basalt forms isolated irregular lenses within the tan-gray coarse-grained basalt (fig. 5-16). Material of a similar blue-gray color was seen from a distance in the western wall of the crater Cochise, where it forms a unit several tens of meters thick over a tan-gray unit (fig. 5-17). The contact has an apparent dip of
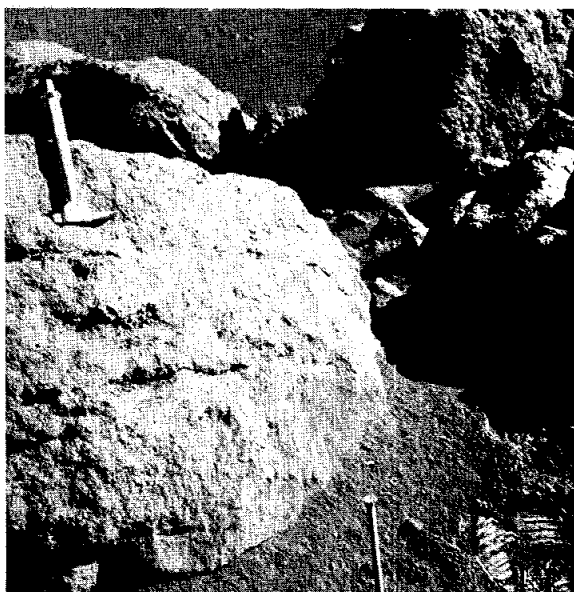
FIGURE 5-15.—Basalt block at station 5 on the southern rim of Camelot Crater showing foliation caused by the parallel orientation of vesicle concentrations. Hammer is 35.5 cm long (AS17-145-22153).
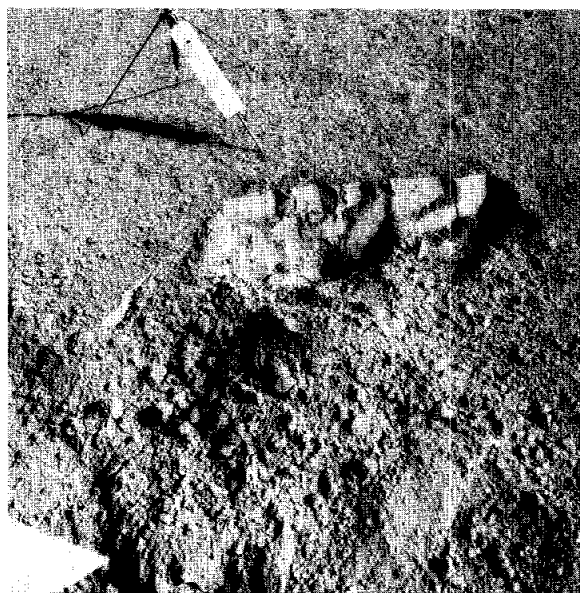
FIGURE 5-14.—The trench wall in soil at station 8 on the slope of the Sculptured Hills. Note the lack of apparent structure within the soil. The color scale on the gnomon leg is 15 cm long (AS17-142-21720).

FIGURE 5-16.—A large partly buried block of coarsely vesicular basalt ("geophone rock") investigated near the Apollo lunar surface experiments package (ALSEP) site. Note the irregular lenses of finely textured basalt and the absence of soil fillets. The visible portion of the boulder is approximately 4 m wide (AS17-147-22536).
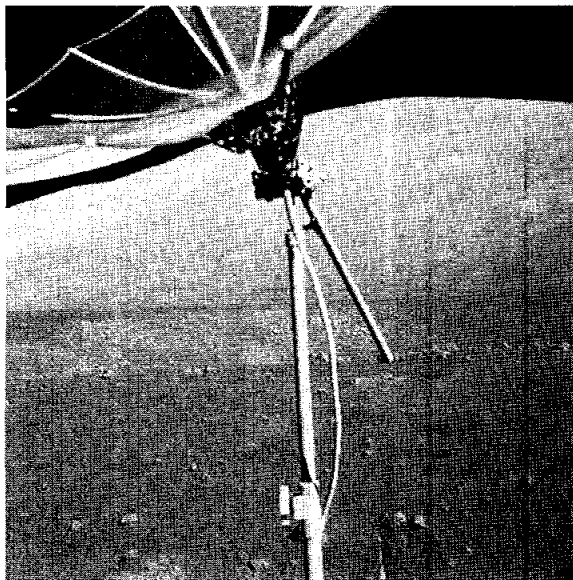
FIGURE 5-17.—View from the southern rim of the crater Cochise looking northwest. Note the medium-gray unit lying over the light-gray unit in the western wall of the crater. The apparent dip of the contact between the two units is to the north. The units are tentatively interpreted to be varieties of basalt based on visual similarities to other basalts investigated in detail (AS17-146-22411).

approximately 20° to the north. The units in Cochise Crater could be the two varieties of subfloor basalt. In general, however, the tan-gray coarsely vesicular variety of subfloor basalt is dominant (at least 95 percent) in the basaltic block fields along our traverses.

A general absence of obvious shock effects was noted in the blocks of basalt studied in the field. Other than the pervasively fractured basalt block at Shorty Crater and possibly the very-fine-grained mylonitic zones along isolated fractures in other blocks, the basalts seemed to have been only slightly metamorphosed by the formation of large craters in the valley. Despite the paucity of shock effects, the morphology of the large craters is consistent with their being impact craters of at least two general age groups that have been subsequently modified by the deposition of the dark floor material.

The floor of the valley is largely covered with this dark material. Below the dark floor surface, there are probably interlayered ejecta blankets from the various large craters. Boulders in these ejecta blankets project above the surface in the lunar module and Steno Crater areas.

The regolith on dark floor material consists of loose, fine, seriate debris with few fragments larger than approximately 1 cm (fig. 5-18). The regolith is a sparkling dark gray at the surface with even darker gray material just below the surface, at least in the optically lightened area near the lunar module (fig. 5-19).

Locally, the fragment populations on the dark floor material are quite variable. In the general vicinity of the Steno-class craters that form the cluster of craters south of the landing point, the fragment frequency is higher by a factor of 4 or 5 than it is near the Camelot-class craters or in areas along the traverse west of Camelot Crater and near the crater Shakespeare. Although coherent soil breccias were sought in this general area, none were recognized; however, a few examples were collected (sec. 7) inadvertently as a consequence of attempts to sample fine-grained basaltic materials.

The dark floor material has many field characteristics that suggest it is a mantling deposit, as do its characteristics as seen from orbit and in orbital photographs (ref. 5-4 and part B of sec. 29). The field characteristics are as follows.

1. The block fields associated with large craters
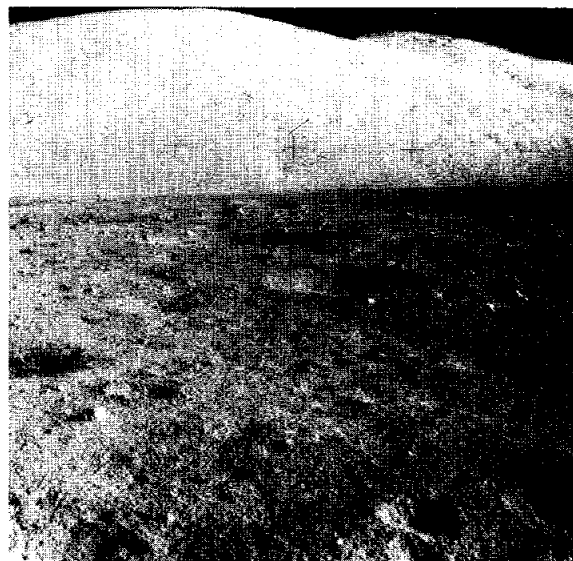
FIGURE 5-18.—View from the lunar module (LM) landing site looking north across dark floor material toward the North Massif. The surface in the foreground is typical of the dark floor material relative to the abundance of craters and basalt fragments. The small crater just right of center in the photograph is approximately 3 m in diameter (AS17-136-20693).
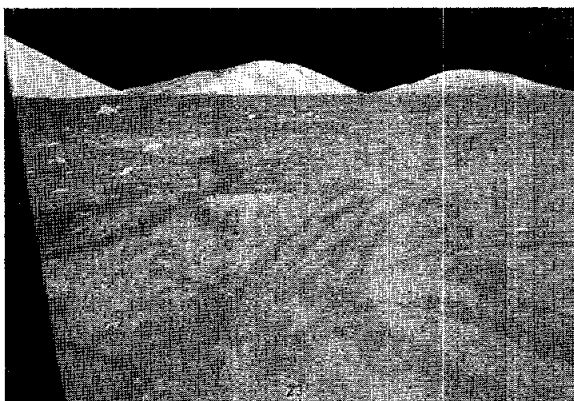
FIGURE 5-19.—View from LM window looking west toward Family Mountain. The ALSEP site is at the center of the photograph. Note that the local area around the LM has a higher albedo than that of more distant areas of the valley or of the disturbed dark floor material nearby. The mechanical effect of the descent engine effluents appears to have caused a change in the albedo of the immediate surface near the landing point (AS17-140-21355).

FIGURE 5-20.—View from station 5 looking north across the crater Camelot and toward the North Massif. Note both the concentration of blocks on the inner wall of the crater and the dark floor material that generally covers the crater rim. The crater is approximately 600 m in diameter, and the North Massif rises approximately 2200 m above the valley floor (AS17-145-22181).

are largely confined to the inner walls of the craters (fig. 5-20). The rims of these craters are generally covered by dark floor material for distances of 20 to 30 m down the crater wall from the rim. Locally, the block fields of the crater walls extend up to, but rarely over, the rim crest (fig. 5-21). In these few places, the edge of the block field terminates sharply against the dark floor material outside the crater. No differences were observed between dark floor material on or away from crater rims.

2. Dark floor material locally extends over crater walls in long downward-pointing fans that apparently bury the wall block fields. The crater floors are universally covered by the same material.

3. Dark floor material constitutes the interblock material in all block fields (fig. 5-22). If the large blocks of the block fields are assumed to be generally equidimensional in shape, then they are approximately half buried in the dark floor material that surrounds each individual block. However, no dark floor material distinctly mantles the top of any block.

4. All observed craters in dark floor material that are between approximately 5 and 80 m in diameter have dark floor material on their ejecta blankets, rims, walls, and floors. However, there is no indication of extensive filling of such craters. Van Serg was the only observed crater that had a clearly defined blocky rim. Fresh craters less than 5 m in diameter
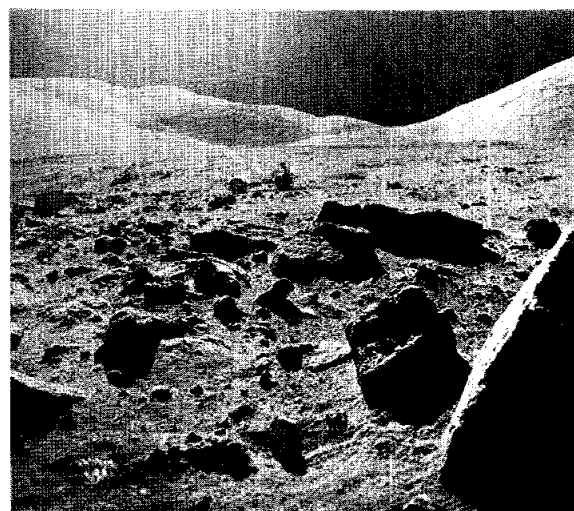
FIGURE 5-21.—View from station 5 looking east along the southern rim of the crater Camelot. Note the relatively sharp contrast between the basalt block fields and the dark floor material that covers the crater rim. The wheelbase of the lunar roving vehicle is 229 cm (AS17-145-22162).

have coverings of weakly coherent soil breccia fragments.

5. As will be detailed later, the orange and black
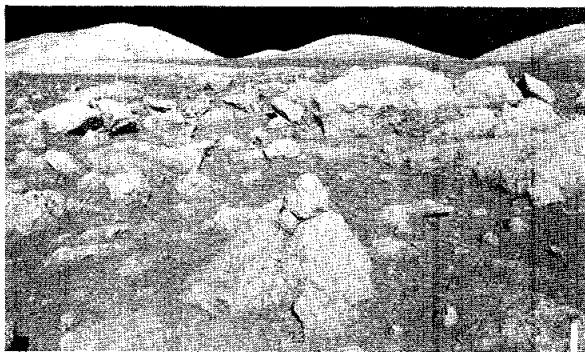
FIGURE 5-22.—View looking west from station 5 on the southern rim of Camelot Crater. The photograph shows the general slope and distribution of basalt blocks on the rim and inner walls of the crater. The large block just right of center is approximately 2 m high (AS17-145-22174).

glasses at Shorty Crater partially mantle that crater. These glasses have affinities with the fine-grained fractions of the dark floor material (sec. 7).

Boulder surfaces are generally free of dust except in depressions on horizontal rock surfaces where dust and relatively coarse rock and mineral debris have accumulated (fig. 5-23). Fillets tend to be low on boulders on the valley floor, although isolated exceptions to this rule were observed, particularly near the Apollo lunar surface experiments package (ALSEP) deployment site.

The visually apparent saturation crater size on the dark floor material is probably approximately 0.5 m, which suggests a 10-cm-deep gardened zone. Mechanical penetrability decreased markedly below approximately 10 to 15 cm, and hand penetration with a core tube was impossible below approximately 25 cm under the lunar module.

The Light Mantle Area

The plume- or ray-shaped light-albedo area that extends northward from the South Massif is known as the light mantle. Photogeologic interpretation suggested that this was a relatively young mantling material derived from the South Massif talus (ref. 5-3). The geometry of its contact and the dark material excavated by some of the larger craters on it strongly suggest that the light mantle deposition occurred after most of the dark floor material had been deposited. Whether this light mantle material was a ray of ejecta or mobilized South Massif talus or

FIGURE 5-23.—Regolithic debris partly filling cracks and depressions on a large basalt block at station 5. Note relative lack of debris on flat and more exposed surfaces of the block. The gray scale on the gnomon is 30 cm long (AS17-145-22155).

both and speculation on the possible mechanisms of deposition were questions posed in our premission planning.

The surface of the light mantle is composed of loose, medium-gray, finely seriate debris with an apparently large deficiency of fragments in size ranges greater than approximately 1 cm (fig. 5-24). Very few rock fragments or boulders larger than a few centimeters were observed; this characteristic contrasts sharply with the talus debris on the South Massif. The light mantle surface was very similar in general visual character, however, to the fine debris surface on the South Massif talus slope. Fragments of breccia similar to those at station 2 were found slightly concentrated on the rim of and inside the 30-m-diameter Ballet Crater in the light mantle at station 3 (fig. 5-25). In general, fragment concentrations were present on the rims and in the walls of craters having diameters greater than approximately 5 m.

A dilated and inverted section of the light mantle may be present in the fine-grained debris just outside the rim of Ballet Crater. A trench in this rim (fig. 5-26) showed the debris to be layered from the surface downward as follows.

1. Approximately 0.5 cm of medium-gray surface
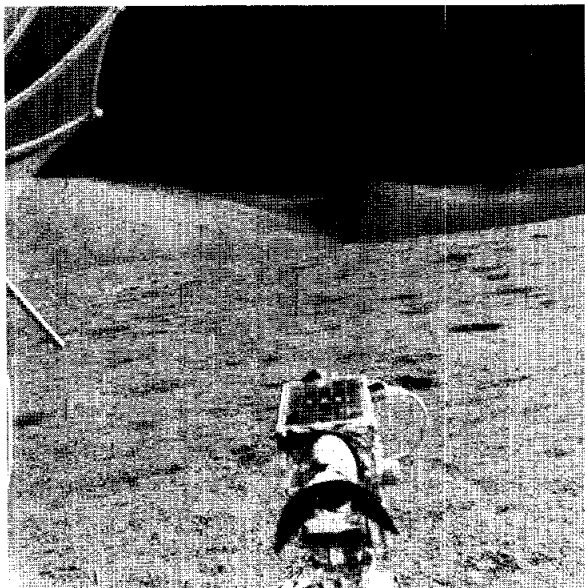
FIGURE 5-24.—View from the Roman Steppe looking northeast toward Wessex Cleft. Station 2A on the light mantle is in the general area of the center of the photograph. Note the low abundance of fragments on the surface of the light mantle (AS17-138-21095).

FIGURE 5-26.—The fine structure of the ejecta on the rim of Ballet Crater at station 3. This trench exposed the first such structure observed in situ on the Moon. The visible portion of the gnomon rod is approximately 40 cm long (AS17-138-21148).
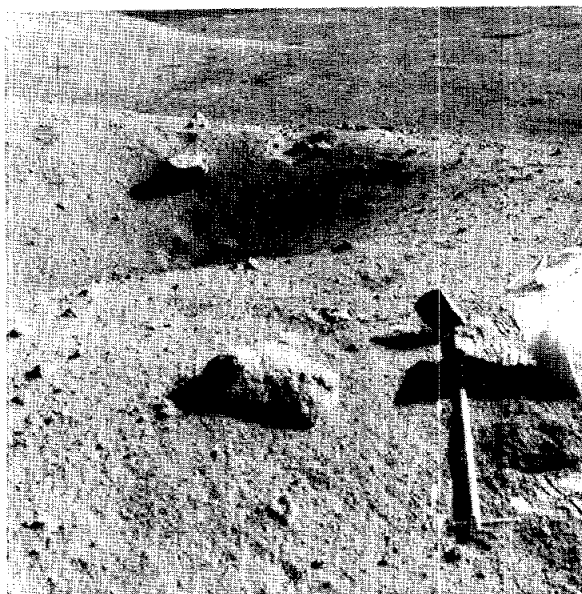
FIGURE 5-25.—Ballet Crater at station 3 looking north along the Lee-Lincoln Scarp. The crater is approximately 30 m in diameter and is typical of craters of this general size in the light mantle that expose fragments of buried breccia. The scoop handle is 76 cm long (AS17-138-21160).

material (possibly new regolith) similar to the surface layer on the light mantle

2. Approximately 3 cm of light-gray material similar to the subsurface material of the light mantle

3. At least 15 cm of medium- to dark-gray material into which light-gray material is marbled

The talus slopes of the massifs clearly have a higher rock fragment abundance than does the average surface of the dark floor material; however, the surface of the light mantle has a distinctly lower fragment abundance in the 2- to 10-cm size range. The same relations hold for fragments larger than 10 cm. Observations of crater characteristics infer that concentrations of rock fragments occur at depths of approximately 1 m below the surface of the light mantle.

Light-gray material is present 5 to 10 cm below the medium-gray surface material at all localities investigated in the light mantle area. Light-gray material is also present in the walls of all craters in this area having diameters greater than approximately 1 m. This soil profile is very similar to that developed on the massif talus slopes.

The contacts between the light mantle and both

the dark floor material of the valley and the dark material around Shorty Crater are gradational in albedo over a distance of approximately 10 m. A distinct difference in albedo of the two types of surfaces is visible when viewed at zero-phase angle. Also, there is an obvious change in the wall color of craters larger than 1 m in diameter. No topographic expression at these contacts was detected.

The light mantle surfaces above, on, or below the Lee-Lincoln Scarp show no discernible differences in crater population, fragment population, or surface texture.

Craters smaller than approximately 5 m in diameter were found to have a consistent morphology whether in light mantle, dark floor material, or massif talus (fig. 5-27). In summary, the freshest of these craters have the following characteristics.

1. The crater ejecta, rim, wall, and floor are covered with fragments of weakly coherent soil breccia as large as 10 to 15 cm in average diameter. The albedo of these soil breccias is much higher in the light mantle than on the dark floor material.

2. The soil breccia fragments inside the crater
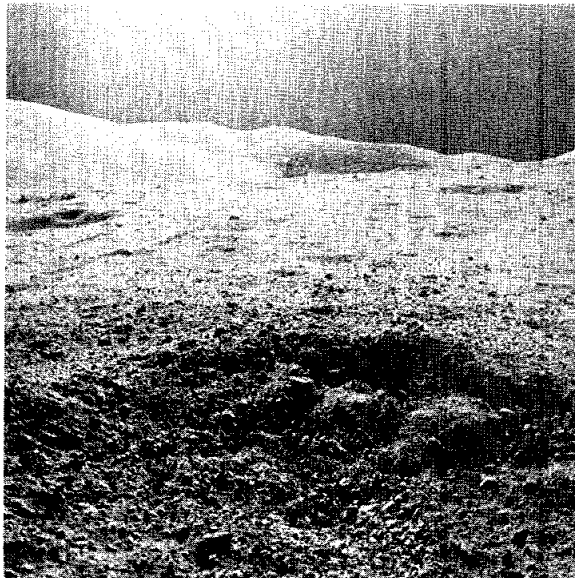
FIGURE 5-27.—View from between the LM and ALSEP sites looking east toward the LM. A portion of a fresh, 3-m-diameter crater is in the foreground. The glassy central pit of this crater is the slightly more reflective area in the center of the crater. Note the abundance of small fragments of soil breccia in and around the crater (AS17-145-22185).

tend to be oriented with their long axes radial to the center of the crater.

3. There is a central pit in an otherwise relatively flat floor. The diameter of the pit is approximately one-fourth to one-fifth the rim diameter of the crater. The pit is generally shallow, in most cases less than one-tenth the depth of the crater. However, this depth does vary; in one instance, the pit was nearly one-half the depth of the crater and roughly cylindrical in shape.

4. The central pit is glass lined with the glass forming a coating and partially cementing the soil breccia fragments.

5. The relative geometry of the pit with respect to the crater appears to be constant and independent of crater size or of geologic unit.

6. Overall, the albedo of the crater and its ejecta is slightly higher than that of its surroundings.

As the crater ages, the order of the disappearance of primary features is, first, the albedo contrast, then the glass in the central pit, then the soil breccias, and, finally, the central pit itself.

Shorty Crater

One of the premission alternatives around which our exploration was planned was the possibility that the 110-m-diameter crater Shorty was a volcanic vent. Although its general morphological appearance is that of a dark-rayed impact crater that had penetrated the light mantle, Shorty Crater held out the possibility of young volcanism. Other than Shorty, possible sources for the potential pyroclastic deposits of the dark floor material were difficult to delineate. The observations and sampling at Shorty Crater did not reveal directly what we had expected; however, the results of the investigation may yield equally important information from unexpected directions.

All the now classic difficulties in conducting geological operations on the surface of the Moon faced us at Shorty Crater. To begin with, we had made earlier decisions to spend extra time at previous localities without knowing what awaited us. Our oxygen supply limited the time we could spend at Shorty Crater to a clearly nonnegotiable 35 min. The normal "housekeeping" duties of dusting and reading the gravimeter demanded their usual but necessary due. Then, in addition to the usual complexities of lunar impact geology, an unexpected discovery appeared.

Shorty Crater has features consistent with an impact origin, although no one feature is conclusive in itself. Subfloor basalt appears to dominate the few blocks at the rim (fig. 5-28). One of these blocks is pervasively fractured and may be shocked. The crater wall is locally blocky and has several radial and transverse changes in texture and albedo. There is no continuous bench in the crater wall; however, several well-defined lobes of coarse and fine debris, similar to those in the walls, extend out onto the floor and may be the relics of such a bench (fig. 5-29). The blocky materials on the flat floor appeared to be highly fractured but otherwise uniform in texture. Parallel fracture organization is strong in some blocks.

The unexpected discovery at Shorty Crater was the presence of at least three deposits of very-fine-grained orange soil (fig. 5-30). There were also numerous indications of fine-grained black soil, which, together with the orange soil, was subsequently determined to be composed almost entirely of glass beads or devitrified glass beads of uniform composition (sec. 7). Two of the orange soil deposits are near the rim crest of the crater, whereas the other deposit is exposed on the western wall. In appearance, the deposits have many of the characteristics of fumarolic alteration halos; with this hope, we conducted our observation and sampling activities.

One deposit of orange soil was trenched across its trend along the crater rim. At this location, it was

FIGURE 5-29.—View of the northwestern wall of Shorty Crater. The diameter of the crater is approximately 110 m. Note the dark band on the far wall (AS17-137-20995).

FIGURE 5-28.—The southern rim of Shorty Crater looking west. The sampled orange soil deposit is at the left center of the photograph near the large boulder. Note the heterogeneity of boulder and albedo distribution patterns. The crater is approximately 110 m in diameter (AS17-137-21009).
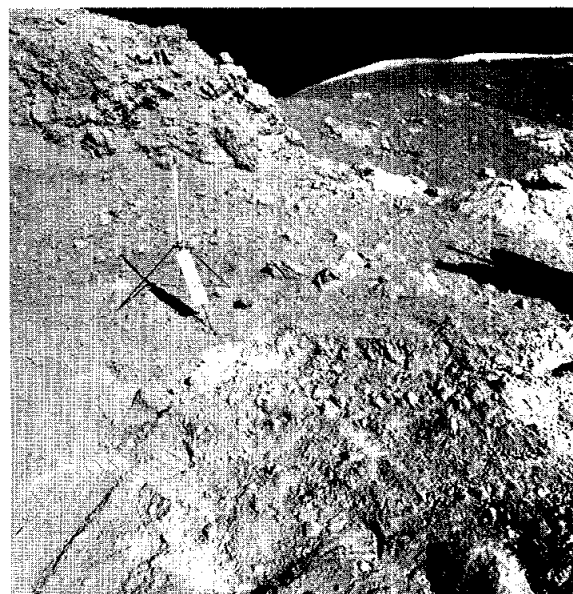
FIGURE 5-30.—Near-surface cross section of the startling deposit of orange soil on the southern rim of Shorty Crater. The pervasively fractured rock in the background is coarse-grained basalt. The gnomon rod is 46 cm long (AS17-137-20990).

sampled in detail and the following relationships were observed.

1. The deposit is approximately 1 by 4 m in size at the surface and is elongate parallel to the rim crest.

2. The deposit has no topographic relief relative to other rim surfaces. (This is also true for the other rim deposit.)

3. Dark-gray surface material forms an approximately 0.5-cm-thick surface layer over both the deposit and the surrounding light-gray materials. There is an orange tint to this surface material directly over the deposit.

4. The contact of the deposit with light-gray debris on either side is irregular in detail but essentially vertical to a depth of at least 20 cm.

5. From the vertical contacts inward, the deposit grades from a yellowish orange over a distance of approximately 10 or 15 cm to a reddish orange.

6. The reddish-orange inner portion of the deposit is moderately coherent and is crossed by at least two apparent joint sets.

7. During the postmission unpacking of a sample from the reddish-orange zone, a clod was observed that was sharply and concentrically zoned inward from orange brown-gray to bluish gray.

8. Examinations of the outer surface of the core tube drawn from the deposit showed that the orange glass changes sharply to a black material at a depth of approximately 25 cm. The black material extends to a depth of at least 70 cm.

One can conceive of many samples and observations left uncollected at this remarkable locality. However, few of our experiences in the Apollo Program better illustrate the inherent quality of scientific investigation that is possible from the integrated effort of so many in so short a time.

Van Serg Crater

Premission photogeologic studies suggested that the relatively fresh appearing 90-m-diameter crater Van Serg would provide an impact-generated sample of the section of units lying above the basalts of the valley. Located just south of the craters Cochise and Shakespeare, Van Serg Crater might also penetrate and sample ejecta from these much older craters. As at Shorty Crater, the unexpected again was encountered.

All features of Van Serg Crater were consistent with an impact origin (fig. 5-31). However, unex-

FIGURE 5-31.—View of the northwestern wall of Van Serg Crater. The diameter of the crater is approximately 90 m. The dark fans on the inner wall terminate at the top of a nearly continuous bench. The upper portion of the gnomon rod is approximately 30.5 cm long (AS17-146-22429).

pected, dark, matrix-rich, regolithic breccias were found to be the dominant rock type on the blocky rim and the equally blocky ejecta blanket. Such breccias had not been observed elsewhere in the valley.

A few of the Van Serg breccias are intensely fractured and very friable, and others are mixed or covered with black glass. No basalt was observed, although one fragment was obtained as a glass-coated grab sample. A dark surface cover a few centimeters thick exists over light-gray debris in some of the interblock areas and may cover all the ejecta blanket and rim. The dark cover may be the disintegration product of the dark breccias or, alternatively, it may be a separate mantle. Most blocks are partially embedded in this material.

The crater wall is very blocky and is interrupted by a nearly continuous bench approximately halfway down into the crater. Rocks below the bench are slightly darker in color than those above. Dark fans of dark-gray debris locally cross over the rim and down the upper wall but generally terminate at the bench. The crater floor is also very blocky with some intense

shattering of blocks, although, in contrast to Shorty Crater, the blocks are much larger. Some of the floor blocks are coarse, blue-gray, fragment-rich breccias with light-colored clasts as large as 1 m in diameter.

The general nature of the floor breccias of Van Serg Crater and the visual observation of a thick, northward-dipping, blue-gray unit above the subfloor basalt in the northern wall of Cochise Crater opens the possibility of a major new breccia unit in this portion of the valley. The possible origins and structural implications of such a unit are not yet clear.

SPECIAL FEATURES

A number of special features were examined and sampled during our general investigation of the Taurus-Littrow valley. These features are only peripherally related to the general stratigraphy of the area and are discussed separately in the following paragraphs.

Rock Fragment Weathering

In all instances except for Van Serg Crater and the small pit-bottomed craters, the rock fragments around and in craters on the dark floor surface are the very coherent subfloor basalts. The fragments associated with craters in the light mantle are the similarly coherent tan-gray and blue-gray breccias. In contrast, the Van Serg-type dark matrix-rich breccias and the soil breccias in the pit-bottomed craters appear to have limited durability in the valley environment.

The gross shape of coherent rock fragments is angular. Edges and corners are rounded except where recent impact fracturing has occurred. The gross shape of pervasively fractured and friable rock fragments also tends to be angular, but, in these cases, the edges and corners are also angular. The only generally rounded rock fragments observed were the unfractured dark matrix-rich breccias at Van Serg Crater.

The weathered surfaces of all subfloor basalts, except for the aphanitic group, are lighter colored than are the fresh surfaces. The lighter color appears to be due to the surficial shattering of feldspar in microcraters. This observation is generally true but to a lesser degree for the very finely crystalline breccias of the massifs. Glass linings in microcraters are more common on these breccia surfaces than they are on the basalt surfaces.

The coarse-grained subfloor basalts also have a

coarse mottled texture that shows a roughly horizontal lineation on near-vertical surfaces. The elongate light-colored areas that cause the mottling are approximately 1 by 2 cm in size. The origin of this mottling and its lineation was not apparent in the field but may be related to the impact geometry of secondary particles.

Boulder Tracks

Among the most striking and potentially most useful features of the massifs are the boulder tracks leading from source-crops high on the slopes to large boulders near their bases (fig. 5-32). It appears that once a boulder is jarred loose and begins to roll, only a decrease in slope or the disintegration of the boulder will stop it.

The tracks are made up of chains of small depressions. These chains are generally straight; however, gradual curves were noted in some instances. Not all tracks are exactly perpendicular to the contours, and, in some cases, the tracks curve noticeably.

Most boulders stopped rolling at least a few tens of meters before reaching the base of the massif slope. However, two large boulders in the crater Nansen moved across the base of the slope and up the other side of the crater for several tens of meters.
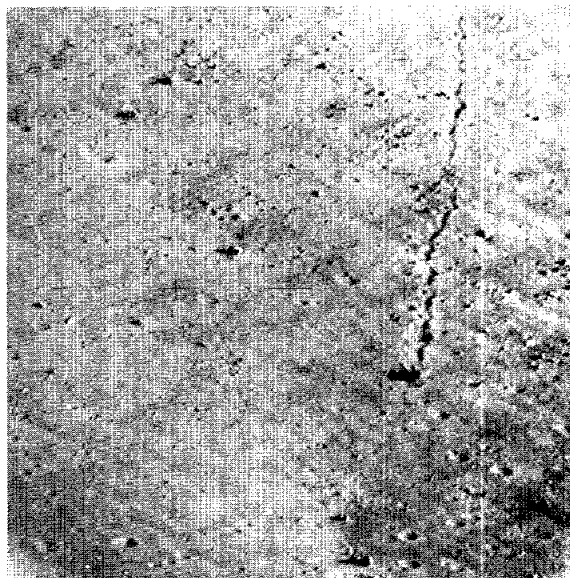
FIGURE 5-32.—A 500-mm-lens photograph of boulders and boulder tracks on the slopes of the North Massif. The largest boulders are on the order of 5 m in diameter (AS17-144-21991).

The Lee-Lincoln Scarp

Little new information was obtained on the Lee-Lincoln Scarp (fig. 5-33) through our surface observations. There is no surface expression of the scarp other than the topography, which was well known before the mission. The east-west trending lobes that characterize the scarp on the valley floor were particularly impressive. No indication of rocky bedrock was seen on any portion of the scarp, although large blocks are present on the northwestern wall of Lara Crater.

The most striking new observation was the change in surface texture across the Jefferson portion of the scarp on the North Massif. The lineations apparent on the North Massif are not present on the surface south and southwest of the scarp. Also, fewer craters are apparent on the southern and southwestern side. This less-textured surface appears to be continuous across the break in slope at the base of the North Massif.

Soil Sampling

The soils of the Moon are the prime historical record of the lunar surface environment and of the solar and cosmic environment of near-Earth space. The presence of the massifs, of boulder overhangs, of the Lee-Lincoln Scarp, and of a number of different stratigraphic surfaces made possible the collection of a wide variety of soil samples in the valley of Taurus-Littrow. In addition, at most documented-sample localities, a standardized 0.5- to 1-cm-thick skim sample of the local surface was obtained, followed by a sample of the underlying soil to a depth of approximately 5 cm. Also, most rock samples were bagged with a small amount of soil.

A new sampling device for sampling from the lunar roving vehicle permitted a substantial increase in statistical control of soil variations between stations. This device also made possible a broader sampling of the lunar module area in the course of other activities.

Soil samples for volatile migration studies, such as in east-west split boulder (or boulder-massif) situations, and from permanently shadowed overhangs were obtained at both the North and South Massif study sites. Samples in the center of and outside a boulder track were taken on the North Massif. Also, samples from underneath boulders were obtained at the South Massif and Sculptured Hills sites.
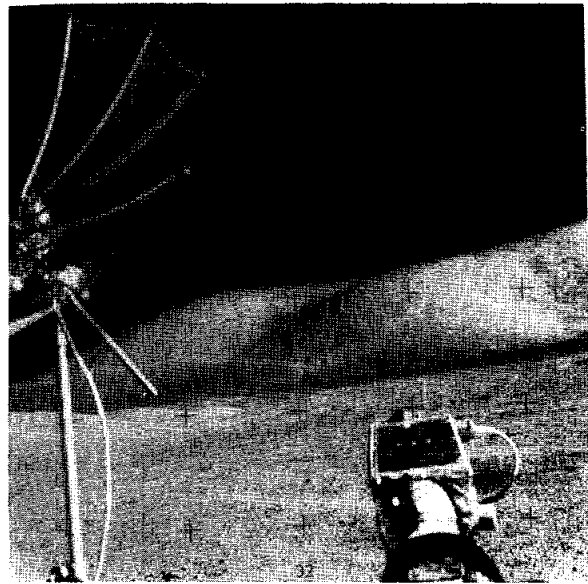
FIGURE 5-33.—View from near Hole-in-the-Wall looking north along the Lee-Lincoln Scarp and showing the Jefferson Scarp along the side of the North Massif. Station 3 is in the left foreground on the slope of the scarp. The scarp rises approximately 80 m above the surface of the valley, here covered by the light mantle (AS17-138-21118).

The possibility of increased volatile activity along the Lee-Lincoln Scarp was used to establish the site for a vacuum-sealed core-tube sample taken at a depth of 35 to 70 cm in soil on the scarp at station 3. Core-tube samples also were obtained in the soils of all major geologic units and in the orange/black glass deposit at Shorty Crater.

In addition to the vertical soil profiles sampled by the core tubes, trench profiles were sampled in the rim of Ballet Crater, in the slope material at the base of the Sculptured Hills, and in the ejecta blanket of Van Serg Crater.

Finally, to aid in examining the recent magnetic field of the valley, two agglutinated glass and soil breccia samples were obtained, one from the pit in a fresh crater west of the lunar module and the other from a glassy mass on the rim of Van Serg Crater. These glasses appeared to have been undisturbed since they cooled in situ.

The Regolith

It appears that regolith development on the massif talus materials and on the light mantle is indicated by

the average depth of medium-gray soil above the lighter gray material. The depth of this regolith is on the order of 5 to 10 cm.

The regolith on the dark floor material is more difficult to define visually. In the vicinity of the lunar module, the loose or very weakly coherent debris appears to be approximately 15 to 20 cm deep. This depth is roughly consistent with what appeared to be an approximately 0.5- to 1-m-diameter saturation crater size for the surface, which suggests that the age of the dark floor surface is only two or three times that of the light mantle surface or of the present talus surfaces.

Both the dark floor material and the light mantle have intercrater surfaces covered by the "raindrop" pattern of small craters. This pattern appears better defined and finer in scale on the light mantle than on the dark floor surface. No systematic linear structures were visible on either the light mantle surface or the dark floor surface. Such structure was apparent on the steep slopes of the massifs and the Sculptured Hills; however, these slopes are better analyzed photographically than visually.

STRATIGRAPHIC SUMMARY

It is yet very premature to come to any final conclusion on major portions of the stratigraphic sequence in the valley of Taurus-Littrow or on the nature of the processes by which this sequence came into being. The laboratory investigations have yet to be completed or to be integrated fully with the field observations. However, it is possible to summarize the probable stratigraphic sequences indicated by the field data and to list many of the interpretive alternatives for the petrogenesis of the major rocks and soils of the valley.

The Massifs

The oldest to youngest stratigraphic units that are present as bedrock in the North and South Massifs are as follows. (Interpretive statements are listed in parentheses.)

1. Light-gray breccia and crystalline rock as distinctive clasts in the blue-gray breccias. (These clasts may possibly be closely related to the differentiates of an early melted lunar crust.)

2. Crystalline, blue-gray, fragment-rich breccias and their metamorphic equivalents. (These breccias are possibly quenched and brecciated impact melts produced during the formation of the large lunar basins or even older events.)

3. Crystalline, tan-gray, matrix-rich breccia and any metamorphic effects associated with its intrusion into the blue-gray breccias. (These intrusions may be partially molten impact breccias, possibly of Serenitatis age, or polygenetic tuff-breccia eruptives of undetermined origin.)

4. Foliated and layered breccia of low metamorphic grade that is rich in a variety of breccia clasts and that appears to correlate with units near the crest of the South Massif. (These rocks may be representative of the youngest large-basin ejecta blankets in the region, possibly equivalent in mode of origin or even in age to the Fra Mauro Formation.)

Although certainly complex internally, the dominant fabric of the North Massif apparently is that of roughly horizontal structural units that may be depositional or intrusive layers. In the South Massif, these units appear to be tilted westward or southwestward. High-angle normal faulting and tan-gray breccia intrusions apparently break the continuity of the structural fabrics in both massifs. The tilting and faulting of massif units may relate to their uplift during the Serenitatis impact event or subsequent major basin events (or both).

A general similarity is evident in the visual and lithologic characteristics of the tan-gray and blue-gray breccias studied at the North and South Massifs. This similarity suggests that a general lithologic correlation can be made across the valley. The differences in rock characteristics may be explained by different ages of formation through similar processes or by different depths of burial (approximately 1.5 km in the North Massif and approximately 0.5 km in the South Massif).

The Valley Floor

The most complex stratigraphic and structural problems in the Taurus-Littrow valley are those of the valley floor and the materials beneath it. This complexity is introduced by two factors. First, there is the very great absolute age, approximately 3.7 billion years, of the orange/black glass deposit at Shorty Crater (ref. 5-5) and its relatively young exposure age, approximately 8 million years (ref. 5-6). Presumably, these ages apply to similar glasses in the dark floor materials. Second, there is the discovery of a thick (greater than 15 m) breccia unit of regolithic character at Van Serg Crater.

The purity, the geometric constraints, and the petrographic characteristics (sec. 7) of the orange/black glass deposit at Shorty Crater and the relative ages of the deposit require the following to hold true for its glasses.

1. The glasses were deposited at the lunar surface over a major unit of subfloor basalt or on an early regolith unit derived from the subfloor basalt.

2. The glasses were then almost immediately protected from regolithic mixing at the surface, possibly by an ejecta blanket or by a thin basaltic flow, for a period of approximately 3.7 billion years.

3. The glasses were then ejected onto or intruded into the rim of Shorty Crater less than 8 million years ago, producing a very restrictive geometric situation.

Glasses similar to the orange/black glasses have been reported mixed with basaltic debris in the dark floor materials (sec. 7). The apparently recent mantling over the valley craters by dark floor materials and the apparently thin regolith developed on these materials impose other general constraints on their stratigraphy and origin. The indications are very strong that since the formation of a widespread mantling deposit of orange/black glass approximately 3.7 billion years ago, some other process has acted more or less continuously to recycle this glass and produce the presently observed young mantling relationships.

In view of the presence of certain low-temperature volatile components in the orange/black glasses (sec. 7), it is possible that impact events in the general size range of Shorty Crater will trigger the release of such gas as a fluidizing medium for local remobilization and extrusion. The known field characteristics of the orange/black glass deposits and of the dark floor material are reconcilable with a process of this nature acting in and around impact craters of 25 to 100 m in diameter. Also, a similar process has been observed to occur at the 500-ton Dial Pack event (ref. 5-7) in Canada as a result of the explosive pressurization of water-saturated sand in a layer well below the floor of the crater produced by the explosion.

The other complicating factor in the interpretation of the valley floor is the great thickness of coherent regolithic breccias at Van Serg Crater relative to other portions of the valley. This thickness may be related to the position of Van Serg Crater on superposed ejecta blankets from Cochise and Shakespeare Craters. Also, the apparently rapid degradation of the Van Serg-type matrix-rich breccias in the valley

environment may account for their rarity around other, possibly older craters such as Shorty. The existence of orange and black glasses and of subfloor basalt fragments in these breccias (sec. 7) strongly suggests that they are the product of the general long-term regolith development in the valley.

Taking into account these considerations and the field evidence described previously, the following general subsurface sequence, from the surface downward, seems probable for the valley.

1. An average of 15 to 20 cm of new, very weakly coherent regolith on the present dark valley floor surface

2. An average of 1 to 2 m of mixed basaltic debris and orange/black glass having generally mantling relationships to most large craters and boulders

3. A zone of variable thickness, possibly from 10 to 20 m, containing interlayered dark floor material and the ejecta blankets from Steno- and Camelot-age impact events (Much of this material may be similar to the Van Serg breccia.)

4. A zone gradational with the zone above (item 3) consisting of regolithic debris derived from the subfloor basalts and possibly interlayered with orange/black glass zones

5. A few meters thick basalt flow or ejecta blanket, either of which probably is presently discontinuous in distribution but which protects portions of underlying deposits of orange/black glass

6. A deposit of orange/black glass of unknown thickness, also presently discontinuous

7. A few meters of regolith developed on underlying basalt

8. At least 100 m of coarse-grained subfloor basalt, the fine-grained portions of which have been largely incorporated into overlying regolith (The uniformity in the texture of ejected basaltic blocks throughout the valley strongly suggests that a single thick cooling unit of basalt may have filled the valley.)

The Light Mantle

All indications are that the light mantle was deposited as a single dynamic event on the dark floor materials that cover the valley. The materials of the light mantle appear to be identical to those of the South Massif talus, although vertical size sorting has probably occurred in the light mantle. Our observations tend to support the tentative conclusion of R.

Shreve[1] and the Apollo soil mechanics team (sec. 8) that the light mantle originated through an avalanche, or fluidized flow, of South Massif talus with fluidization provided by solar wind gases adsorbed within the original talus materials.

The probable internal structure of the light mantle from the surface downward appears to be as follows.

1. 5 to 10 cm of medium-gray soil (regolith?)

2. Approximately 1 m of light-gray debris containing few fragments larger than a few centimeters in diameter

3. Variable thicknesses of light-gray material containing numerous rock fragments larger than a few centimeters in diameter

4. A basal zone of mixing between light mantle and dark floor materials that may be marbled in texture

This is the last major report of crew observations obtained during the Apollo explorations of the Moon. We are confident that the future holds many other such reports as man continues his exploration of the frontier of the Earth and his use of the space environment. It is our belief that, as in past explorations, man's abilities and spirit will continue to be the foundation of his evolution into the universe. Full satisfaction from this evolution only comes with being there. The Apollo crewmen deeply appreciate their singular opportunity of having been there.

ACKNOWLEDGMENTS

REFERENCES

5-1. Anon.: Apollo 17 Mission Report. NASA JSC-07904, Mar. 1973.

5-2. Scott, David H.; Lucchitta, B. K.; and Carr, M. H.: Taurus-Littrow Region–Apollo 17. U.S. Geol. Survey Misc. Geol. Inv. Map I-800, 1972.

5-3. Wolfe, E. W.; Freeman, V. L.; Muehlberger, W. R.; Head, J. W.; Schmitt, H. H.; and Sevier, John: Apollo 17 Exploration at Taurus-Littrow. Geotimes, vol. 17, no. 11, Nov. 1972, pp. 14-18.

5-4. Lucchitta, B. K.: Taurus-Littrow Region–Apollo 17. U.S. Geol. Survey Misc. Geol. Inv. Map I-800, sheet 2 of 2, 1972.

5-5. Husain, L.; and Schaeffer, O. A.:^{40}Ar-^{39}Ar Crystallization Ages and ^{38}Ar-^{37}Ar Cosmic Ray Exposure Ages of Samples From the Vicinity of the Apollo 16 Landing Site. Lunar Science IV (Abs. of papers presented at the Fourth Lunar Science Conference (Houston, Tex.), Mar. 5-8, 1973), pp. 406-408.

5-6. Kirsten, T.; Horn, P.; Heymann, D.; Hubner, W.; and Storzer, D.: Apollo 17 Crystalline Rocks and Soils: Rare Gases, Ion Tracks, and Ages. EOS (Trans. Am. Geophys. Union), vol. 54, June 1973, pp. 595-598.

5-7. Roddy, D. J.: Event Dial Pack Symposium Report. Project LN303, U.S. Geological Survey Activities; Technical Cooperation Program, Panel N-2, vol. III, DNA 2722T, Nov. 1971.

---

[1] Written communication, November 1972.

6. Preliminary Geologic Investigation of the Apollo 17 Landing Site

W. R. Muehlberger,[a,b,†] R. M. Batson,[b] E. A. Cernan,[c] V. L. Freeman,[b] M. H. Hait,[b]
H. E. Holt,[b] K. A. Howard,[b] E. D. Jackson,[b] K. B. Larson,[b] V. S. Reed,[b] J. J. Rennilson,[d]
H. H. Schmitt,[c] D. H. Scott,[b] R. L. Sutton,[b] D. Stuart-Alexander,[b] G. A. Swann,[b] N. J. Trask,[b]
G. E. Ulrich,[b] H. G. Wilshire,[b] and E. W. Wolfe[b]

SUMMARY OF RESULTS

The Apollo 17 lunar module (LM) landed on the flat floor of a deep narrow valley that embays the mountainous highlands at the eastern rim of the Serenitatis basin. Serenitatis, the site of a pronounced mascon, is one of the major multi-ringed basins on the near side of the Moon. The Taurus-Littrow valley, which is radial to the Serenitatis basin, is interpreted as a deep graben formed by structural adjustment of lunar crustal material to the Serenitatis impact.

During their stay on the lunar surface, the Apollo 17 crew traversed a total of ≈30 km, collected nearly 120 kg of rocks and soil, and took more than 2200 photographs. Their traverses, sampling, direct observations, and photographs span the full width of the Taurus-Littrow valley.

The highlands surrounding the valley can be divided on the basis of morphology into (1) high smooth massifs; (2) smaller, closely spaced domical hills referred to as the Sculptured Hills; and (3) materials of low hills adjacent to the massifs and the Sculptured Hills. Boulders that had rolled down the slopes of the massifs north and south of the valley provided samples of that area. These boulders are composed of complex breccias that are generally similar to those returned from the Apollo 15 and 16 missions.

Materials of the valley fill were sampled at many stations. Ejecta around many craters on the valley

[a]The University of Texas at Austin.
[b]U.S. Geological Survey.
[c]NASA Lyndon B. Johnson Space Center.
[d]California Institute of Technology.
[†]Principal Investigator.

floor consists of basalt, showing that the graben was partly filled by lava flows. A relatively thick layer (≈15 m) of unconsolidated material overlies the subfloor basalt; this debris consists largely of finely comminuted material typical of the lunar regolith.

The surface material over much of the Taurus-Littrow region has a very low albedo and was believed to be a thin young mantle, possibly pyroclastic, that covered the valley floor and parts of the adjacent highlands. No clear evidence of the existence of such a mantle as a discrete layered unit has yet been found, but it may be mixed in with the more typical debris of the lunar regolith. An unusual bright deposit extends across the valley floor from the foot of the South Massif. This deposit consists of breccias similar to those of the massif and is interpreted as an avalanche generated on the massif slopes.

South Massif materials were collected from three breccia boulders that were probably derived from a blocky area near the top of the massif where a blue-gray unit overlying tan-gray material is exposed. Boulder 1, sampled at station 2, is a foliated and layered breccia, the only one of its type seen by the crew. The four samples collected from boulder 1 are breccias composed of dark-gray fine-grained lithic clasts in a light-gray friable matrix.

Boulder 2, sampled at the South Massif, is a fractured rock from which five samples of vuggy, annealed, greenish-gray breccia were collected. A breccia clast and its host were sampled from boulder 3 at the South Massif. The clast is light-greenish-gray breccia with abundant mineral clasts and sparse lithic clasts. The matrix of the clast consists largely of angular fragments of a mafic silicate embedded in a very-fine-grained groundmass. The host material is a blue-gray breccia with scattered vesicles.

Materials of the North Massif were sampled primarily from a 6- by 10- by 18-m fragmented boulder at station 6 and a 3-m boulder at station 7. The station 6 boulder, which broke into five pieces, is at the lower end of a boulder track the apparent beginning of which is in an area of light boulders approximately one-third of the way up the massif. Photographs using the 500-mm lens demonstrate that dark boulders are abundant higher on the mountain, and light boulders occur again in the upper part. Thus, there may be a layer or lenses of darker rock high on the mountain with lighter rocks both above and below. The source of the station 7 boulder on the North Massif is unknown, but the boulder contains rock types like those of the station 6 boulders.

Four of the five large pieces of the station 6 boulder were sampled. The boulder consists of two major breccia types, greenish-gray and blue-gray. They are in contact in a 0.5-m-wide zone that appears to be an area of mixing between the two rock types. The greenish-gray breccia is tough and annealed, with sparse lithic and mineral clasts set in a vuggy fine-grained matrix.

Samples of blue-gray breccia from the station 6 boulder contain a high proportion (40 to 60 percent) of blue-gray breccia fragments in a vuggy greenish-gray matrix. The matrix is a tough, finely crystalline material. Large friable inclusions ranging from 1 cm to 1 m across are in sharp irregular contact with the blue-gray breccia. Samples of one of these are very-light-gray cataclasites.

The station 6 boulder is intricately sheared. Comparison with the oriented returned samples shows that movement along some of the shear planes has deformed the clasts. Major events recorded in the station 6 boulder are the formation of the light cataclasite, its incorporation in the blue-gray breccia, and subsequent enclosure of the blue-gray breccia in the greenish-gray breccia.

The station 7 boulder is similar to the station 6 boulder in that the two major rock types, greenish-gray breccia and blue-gray breccia, are present. A large white clast (1.5 by 0.5 m), similar to those in the station 6 boulder, is penetrated by narrow blue-gray breccia dikes. The blue-gray breccia is in sharp irregular contact with the younger greenish-gray breccia. Like the station 6 boulder, the station 7 boulder is intricately fractured. At least two fracture sets are confined to the large white cataclasite inclusion and the blue-gray breccia.

Smaller chips collected at stations 6 and 7 include the major rock types of the two large boulders, as well as a few other breccia types, one coarse-grained gabbroic rock, and one light-colored fine-grained hornfels. A few basalt fragments that are probable ejecta from the valley floor were also collected.

The South Massif boulders most probably came from the highest part of the massif (boulder 1, station 2, from the blue-gray unit; boulder 2, station 2, from the underlying tan-gray unit), and the station 6 and 7 boulders probably came from within the lower third of the North Massif. Hence, two different stratigraphic intervals may have been sampled. Conversely, the lithologies of the South Massif boulders closely resemble those of the North Massif boulders in many respects. The similarity seen in early examination suggests the possibility that only one stratigraphic unit is represented. Whichever the case, the massifs are composed of intensely shocked breccias reasonably interpreted as ejecta from ancient large impact basins.

On the accessible part of the Sculptured Hills, hand-sized samples are essentially absent, and no boulders that clearly represent Sculptured Hills bedrock were found. Small fragments of basalt, probably ejected from the valley floor, and regolith breccia dominate the samples, which consist mainly of chips collected with soils or by raking. Samples of friable feldspathic breccia from the wall of a 15-m crater and of a glass-covered gabbroic boulder that is almost certainly exotic were also collected. The greater dissection, lower slopes, lack of large boulders, and limited sample suite suggest that the Sculptured Hills may be underlain by less coherent breccias than the massifs.

Subsequent to the formation of the Taurus-Littrow graben by the Serenitatis impact, the valley floor was inundated and leveled by basaltic lava flows. Geophysical evidence (secs. 10 and 13) suggests that the prism of basalt filling the valley is more than a kilometer thick. The uppermost 130 m was sampled in the ejecta of craters on the valley floor.

In general, the subfloor basalt blocks seen at the landing site were not visibly shocked or even intensely fractured. In some rocks, planar partings parallel bands expressed as differing concentrations of vesicles. Almost all returned samples of basalt can be divided into five classes: (1) vesicular, porphyritic, coarse-grained basalts; (2) vesicular coarse-grained basalts; (3) vesicular fine-grained basalts; (4) dense

aphanitic basalts; and (5) vesicular aphanitic basalts.

Before final accumulation of the Serenitatis mare fill, broad arching east of the Serenitatis basin tilted the subfloor lavas to the east, forming the present 1° eastward tilt of the valley floor. The subfloor basalt is overlain by fragmental debris ≈15 m thick. For the most part, this is impact-generated regolith similar to that developed on mare basalts elsewhere on the Moon. The central cluster ejecta, the light mantle, and the ejecta of Shorty and Van Serg Craters are discrete deposits recognized within the regolith.

The lower part of the regolith is thought to be represented in the abundant dark friable breccias in the ejecta of the 90-m-diameter Van Serg Crater. The breccias contain scattered, light-colored lithic clasts as well as abundant dark glass, mineral and lithic fragments derived from basalts, and variable percentages of orange glass spheres and fragments. They are interpreted to be regolith breccias indurated and excavated from the deeper, older part of the regolith by the Van Serg impact. Basalt bedrock is not known to have been excavated by Van Serg.

The central cluster ejecta is derived from the cluster of craters south and east of the LM. It is distinguished by the abundance of blocks in the unit, and the unit is too young for the blocks to have been reduced much in size by later impacts. All sampled blocks in the central cluster ejecta are subfloor basalt.

The young pyroclastic dark mantle anticipated before the mission was not recognized in the traverse area as a discrete surface layer. Strong photogeologic evidence for the existence of such a mantle on the valley floor and in parts of the highlands still exists. Albedo measurements show that abnormal surface darkening, consistent with the concept of the introduction of exotic dark material—the "dark mantle"—increases to the east and south in the Taurus-Littrow area. If the dark mantle is younger than the central cluster ejecta, it must be so thin in the landing site that it is thoroughly intermixed with the younger part of the regolith. Such mixed dark mantle may be represented by the dark glass spheres that abound in the soils of the valley floor. An alternative hypothesis is that the dark mantle may have accumulated shortly after the extrusion of the subfloor basalt. In this case, the deposit would be intimately mixed with subsequently formed regolith.

The light mantle is an unusual deposit of high-albedo material with finger-like projections that extend 6 km across dark plains from the South Massif. Rock fragments collected from the light mantle are similar in lithology to the breccias of the South Massif. This similarity supports the hypothesis that the light mantle is an avalanche deposit formed from loose materials on the face of the South Massif. A cluster of secondary craters on the top of the South Massif may record the impact event that initiated the avalanche. Size-frequency distribution and morphologies of craters on the light mantle suggest that its age is comparable to that of Tycho Crater, on the order of 100 million years.

Shorty is a 110-m-diameter impact crater penetrating the light mantle. Unusual orange soil was identified in two places on the rim of Shorty Crater and in the ejecta from a small crater on the inner wall. A trench on the crater rim exposed an 80-cm-wide zone of orange soil, now known to consist largely of orange glass spheres. A double drive tube sample showed that the orange soil overlies black fine-grained material (now known to consist of tiny, opaque, black spheres) at a depth of ≈ 25 cm. The old age for the orange glass material implies solidification shortly after the period of subfloor basalt volcanism. The black and orange glass material, whatever its origin, must have been present in the Shorty target area; it was excavated or mobilized by the Shorty impact.

Fine-grained soil, darker than the underlying unconsolidated debris, was recognized at the surface at Shorty Crater, at Van Serg Crater, on the light mantle, and on the massif talus. The soil is thin (e.g., 0.5 cm at Shorty, ≈ 7 cm on the flank of Van Serg) and probably represents the regolith that has formed on these young ejecta or talus surfaces. Relatively young structural deformation in the landing area is recorded by the Lee-Lincoln Scarp and by small fresh grabens that trend northwest across the light mantle. The sharp knickpoint at the base of the massifs may indicate that some fairly recent uplift of the massifs has kept the talus slopes active.

INTRODUCTION

Premission Geologic Studies

The Taurus-Littrow region lies on the southeastern rim of the Serenitatis basin (fig. 6-1) in an area of mountains, low hills, and plains. Serenitatis is one of the major multi-ringed basins on the near side of the Moon and is the site of a pronounced mascon. The landing site (lat. 20°10′ N, long. 30°46′ E) is located
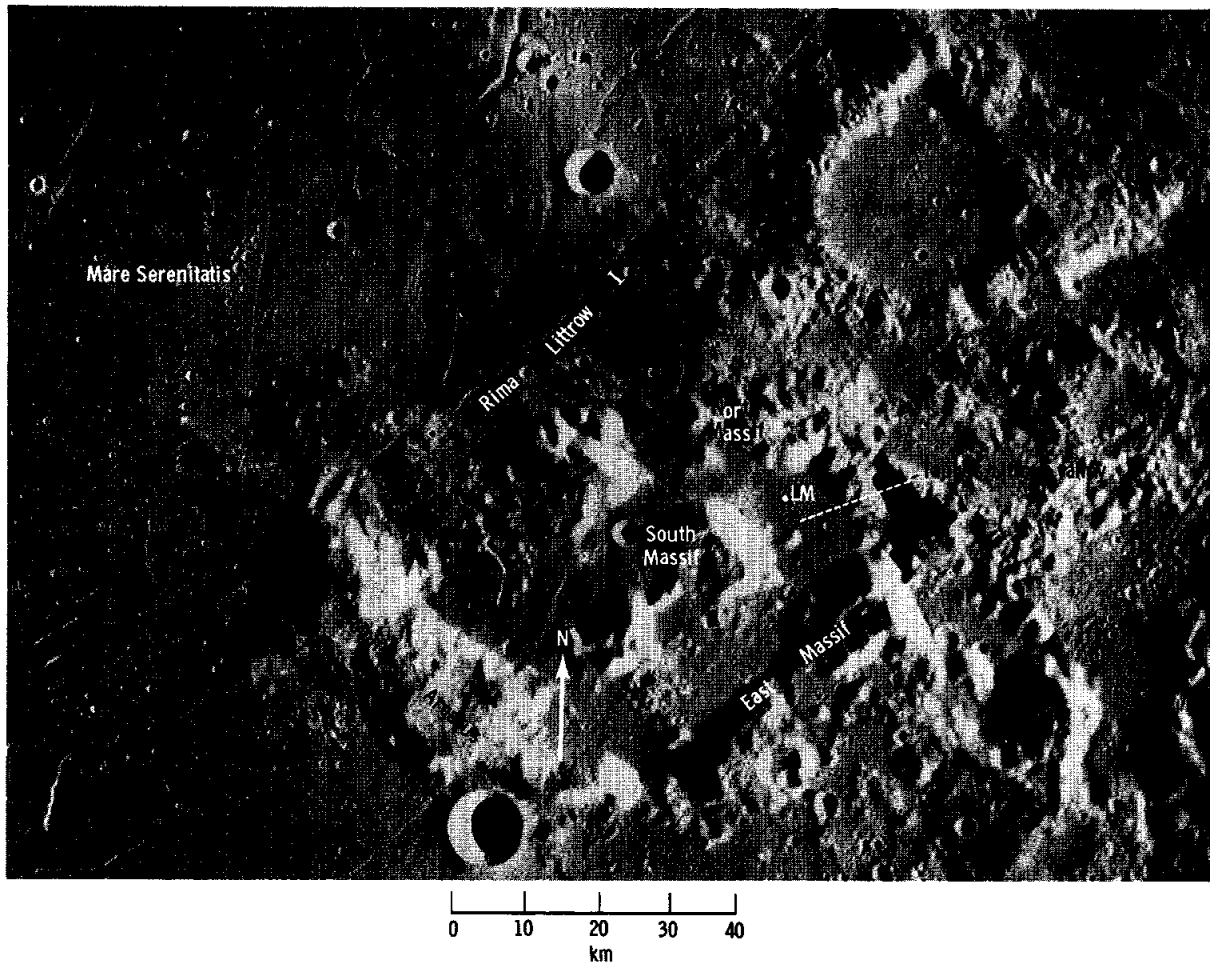
FIGURE 6-1.—Index map showing the Apollo 17 landing site and major geographic features of the
Taurus-Littrow region (Apollo 17 metric camera frame AS17-0447).

on the gently inclined floor of a narrow flat-floored
valley. The walls of the valley rise 2000 m above the
floor. The valley is interpreted as a deep graben
formed at the time of the Serenitatis impact.

The highlands surrounding the valley can be
divided on the basis of morphology into (1) high
smooth massifs, (2) smaller, closely spaced domical
hills referred to as the Sculptured Hills, and (3) low
hills adjacent to the massifs and the Sculptured Hills
(refs. 6-1 and 6-2). The highlands were interpreted in
premission studies as deposits of ejecta derived from
surrounding basins with major uplift occurring in the
Serenitatis event. A possible volcanic origin was also
considered but thought to be less likely (ref. 6-1).
The reason for the morphologic difference between
the massifs and the Sculptured Hills was not clear;

possibly, the difference reflects different responses to
the Serenitatis event and to later tectonic forces. The
low hills unit was considered to be downfaulted and
partly buried blocks of massif or Sculptured Hills
material.

The nearly level valley floor was apparently
formed by deep filling of the graben by fluid
plains-forming material (subfloor unit). The material
at the surface of much of the Taurus-Littrow region
has a very low albedo and was believed to be a thin
mantle, possibly pyroclastic, that covered the valley
floor and parts of the adjacent highlands. Overlap
relations with the typical mare material of Mare
Serenitatis and an apparent deficiency of small craters
indicated that the dark mantle might be very young
in the lunar geologic time scale (refs. 6-1 and 6-3).

Although quantitatively a minor deposit, its significance lay in its apparent young age and presumed volcanic origin. No volcanic rocks younger than 3.1 billion years had been returned before the Apollo 17 mission. Similar dark mantling deposits occur in relatively small tracts on the southwestern rim of the Serenitatis basin, at the outer edge of several other circular maria (ref. 6-4), and in other isolated patches on the lunar near side.

A contrasting unit of bright mantling material occurs in a limited area of the valley. This unusual deposit extends from the southern wall of the valley northeastward in finger-like extensions across the dark valley floor. The material was interpreted as an avalanche from the steep slope of the South Massif (ref. 6-3).

Geologic Objectives and General Results

The geologic objectives of the Apollo 17 mission may be divided into orbital and lunar surface data collection. The orbital objectives in the Taurus-Littrow area were to add to the knowledge of the regional geology of the site through direct visual observation and photographs and to assist in locating the LM on the surface. Additional aid in traverse location by panoramic camera photographs of the lunar roving vehicle (LRV) tracks and crew-disturbed areas was anticipated. The principal objectives of the ground crew were to deploy the Apollo lunar surface experiments package (ALSEP) and the surface electrical properties (SEP) experiment; to record gravity data on the traverse gravimeter; to describe the kinds and proportions of rocks in the various map units and to collect samples of them; to observe, describe, and collect samples of regolith and dark mantle that were thought to cover most of these units; to look for outcrop and, if found, to describe, photograph, and sample it; to describe structures, including lineaments, layers, and faults, in various units; and to observe and describe, where possible, the attitudes of and contacts between the major geologic units.

In detail, ground objectives were planned around groups of stations with the potential of yielding varied geologic information (fig. 6-2). The prime sampling areas of the massif and Sculptured Hills units were located in the station 2, 6 and 7, and 8 areas, as well as between stations 2 and 4, on the assumption that the light mantle unit was composed of materials derived from the South Massif. This broad station coverage was designed to yield maximum information about the lateral continuity of massif lithologies. The principal sampling areas for valley materials were planned at stations 1, 4, 5, 9, and 10B. This coverage was designed to allow detailed stratigraphic studies of both the dark mantle and the subfloor unit. Craters that were to be visited on the valley floor potentially offered samples of subfloor material from depths as great as 150 m. Regolith was, of course, expected throughout the traversed regions, but an unusually small thickness was anticipated because of the low crater density on the dark and light mantle units.

Boulders that had rolled down the slopes of the massifs north and south of the valley provided samples of that area. These boulders are composed of complex breccias; their general similarity to breccias returned from the Apollo 15 and 16 missions indicates that they are very ancient materials as anticipated. Their relation to the circular basins on the lunar near side is discussed subsequently. Crew observations and photographic evidence suggest that the materials of the massifs are layered and that at least two separate layers were sampled.

Materials of the valley fill were sampled at numerous stations around the LM and en route to and from the massifs. Ejecta around many craters on the valley floor consists of basalt, confirming that volcanic materials underlie the Taurus-Littrow valley floor. A relatively deep layer of unconsolidated material overlies the subfloor basalt; this debris consists of finely comminuted material typical of the lunar regolith. It may also contain the dark mantle mapped in premission studies. No clear evidence for the existence of a dark mantle as a discrete layered unit has yet been found, but it may well be mixed in with the more typical debris of the lunar regolith. The bright deposit extending across the valley floor from the foot of the South Massif consists of breccias similar to those of the massif; the interpreted origin of this deposit as a landslide thus appears to be confirmed.

Traverse Data

The Apollo 17 crew traversed ≈ 2 km during the first period of extravehicular activity (EVA), 18 km during EVA-2, and 10 km during EVA-3 for a total of ≈ 30 km. Nearly 120 kg of rocks and soil were collected and more than 2200 photographs were taken on the lunar surface. An index map of the
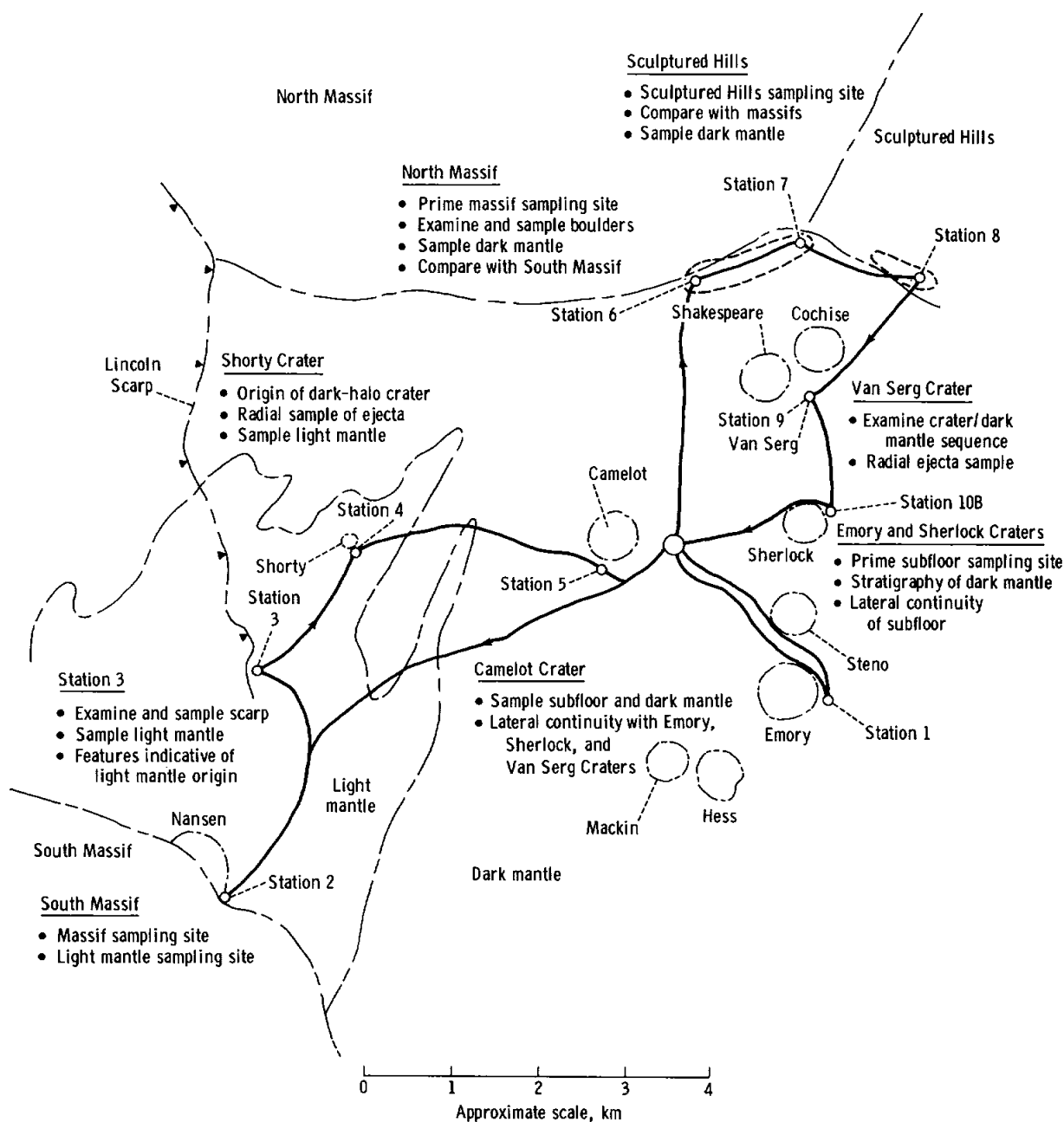
FIGURE 6-2.—Preplanned traverses and geologic objectives.

traverse area is shown in figure 6-3. Figure 6-4 shows the traverse path and stations in detail, and table 6-I lists map coordinates for traverse points. The lunar surface orientations of some of the Apollo 17 rock samples at the time of their collection are shown in appendix A (p. 6-60). Panoramic views and detailed planimetric maps of the traverse stations are shown in appendix B (p. 6-73).

STRATIGRAPHY AND PETROGRAPHY

The studied and sampled geologic units are described in approximate stratigraphic order. However, some parts of the sequence, such as the relative ages of the massifs and the Sculptured Hills units, are not well known. Similarly, regolith units and surficial deposits on the highlands and on the valley floor
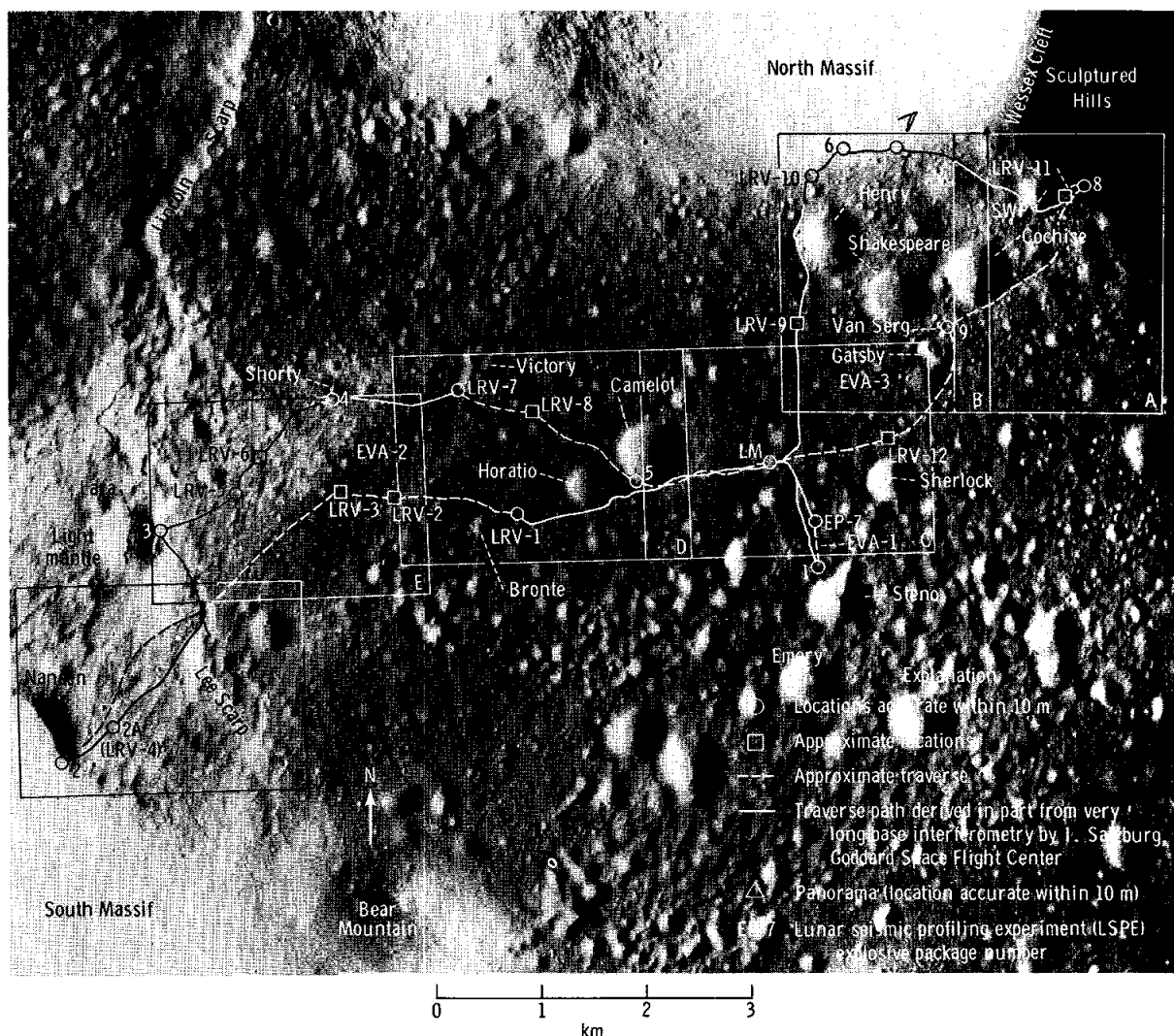
FIGURE 6-3.—Index of the traverse area. Lettered boxes (A through F) show boundaries of detailed traverse maps (figs. 6-4(a) to 6-4(f)) (Apollo 17 panoramic camera frame AS17-2309).

overlap in time. In neither case is rigorous chronology of development implied by the order of discussion.

Table 6-II summarizes the stratigraphy as seen in the field by the crew. Changes from lunar surface terminology are indicated at the appropriate place in the text. Table 6-III relates the field terminology to sampling areas, representative samples, and laboratory terminology.

South Massif

South Massif materials were collected from just above the break in slope at the base of the South Massif at station 2. The crew described the massif as composed of light-tan materials stratigraphically overlain by blue-gray materials (appendix B, fig. 6-109). A concentration of boulders occurs at and near the break in slope at the foot of the South Massif (fig. 6-5). Those boulders with visible tracks on the massif slopes (fig. 6-6) were emplaced after the avalanche that formed the light mantle, and probably emplacement of all the boulders postdates the light mantle. If they were a part of the avalanche itself, the boulders would be more uniformly distributed across the surface of the light mantle rather than concentrated near the base of the massif.

Most of the boulders probably rolled from blocky areas that may be outcrops high on the massif
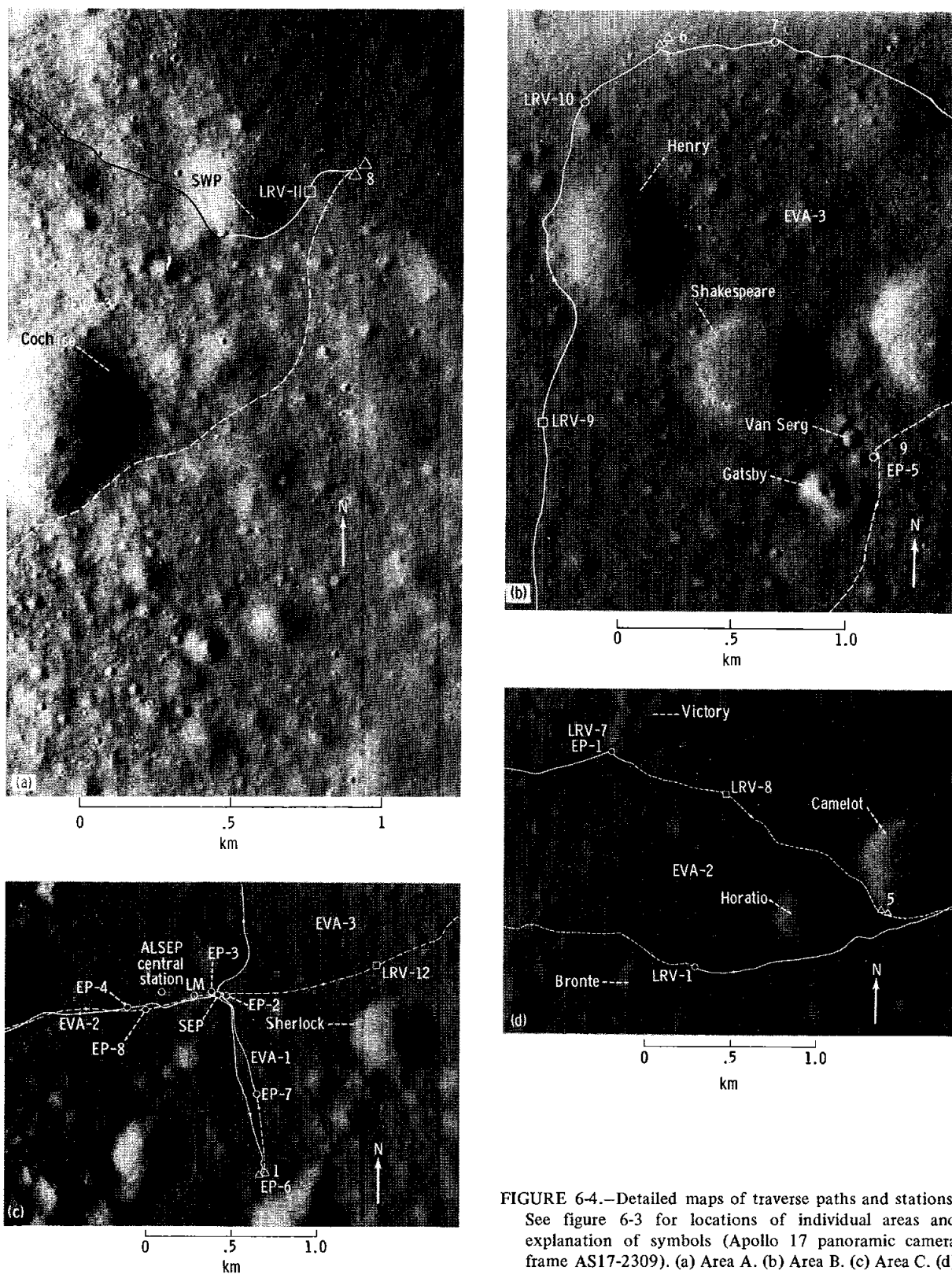
FIGURE 6-4.—Detailed maps of traverse paths and stations. See figure 6-3 for locations of individual areas and explanation of symbols (Apollo 17 panoramic camera frame AS17-2309). (a) Area A. (b) Area B. (c) Area C. (d) Area D. (e) Area E. (f) Area F.

(e)

0 .5 1.0
km

(f)

0 .5 1.0
km

TABLE 6-I.—*Map Coordinates of Traverse Points*[a]

Station (b)	X	Y
LM	83.4	DN.3
SEP	84.1	DN.4
ALSEP	82.5	DN.5
1	85.5	DH.1
EP-7	85.3	DK.5
LRV-1	71.3	DK.7
LRV-2	65.4	DM.1
LRV-3	62.7	DM.2
2	49.1	CY.4
2A (LRV-4)	51.7	DA.1
3	54.1	DK.8
LRV-5	57.7	DM.5
LRV-6	58.7	DP.1
4	62.5	DS.0
LRV-7	68.7	DS.2
LRV-8	72.1	DR.0
5	76.8	DM.5
LRV-9	84.9	DY.1
LRV-10	85.8	EC.1
6	87.4	ED.4
7	88.9	ED.6
LRV-11	97.8	EB.2
8	98.6	EB.6
9	92.1	DV.9
LRV-12	88.8	DP.3

[a]Coordinate system is that used in the premission data package.

[b]LRV-1, LRV-2 (etc.) refer to stations where samples were collected from the LRV with a long-handled sampling tool. Station 2A (LRV-4) was an unplanned station at which the crew dismounted from the LRV. EP-7 was the seventh explosive package used in the LSPE and the only explosive package that was not located at a sampling station.

fig. 6-7). These bouldery areas are mostly in the blue-gray unit. No apparent source for the boulders is visible on the lower two-thirds of the massif. The three boulders sampled at station 2 have no visible tracks on the massif slope. However, the boulders in the station 2 area are directly below a blocky area just above the contact between the blue-gray unit (above) and the tan-gray unit (below) (figs. 6-5 and 6-6). The three boulders are ≈ 50 m above the break in slope at the base of the South Massif in the field of boulders strewn near the base (fig. 6-5).

Station 2, Boulder 1

Boulder 1, the first boulder sampled at station 2, is a layered and foliated rock (fig. 6-8), the only one of this type seen by the crew. No other rocks of this type have been identified with certainty in the photographs. The boulder is ≈ 2 m across by 1 m high above the ground surface. It has a well-developed fillet ≈ 30 cm high on its uphill side and no fillet on its downhill side. The boulder appears to be highly eroded and has a hackly and knobby surface. The knobs range from < 1 to 15 cm across and were reported by the crew to be mostly fine-grained clasts eroded from a more friable fine-grained matrix. The crew also reported dark elongate clasts parallel to the bedding planes (S_a in fig. 6-8); these are not discernible in the photographs.

Based on the degree to which the bedding foliation is developed and on the erosion-produced characteristics, which are presumably related to the friability of

TABLE 6-II.—Field Stratigraphic Sequence in the Taurus-Littrow Area[a]

Lunar events	Taurus-Littrow events	North Massif	South Massif	Sculptured Hills	Camelot-Steno area	Light mantle area, station 2A	Light mantle area, station 3 Ballet Crater	Shorty area	Van Serg area
	Young regolith, boulder tracks, exotics	Medium-gray surface material	Medium-gray surface material	Slope material	Dark floor material[b]	Medium-gray material	Medium-gray surface material	Dark surface material	Dark surface material
		Light-gray talus material	Light-gray talus material						
	Station 3 crater						Light-gray material / Marbled material		
							(Medium-gray material)[c]		Dark matrix-rich breccia / Light-gray fragmental material[d]
	Van Serg Crater								
	?								(Dark floor material)
	Shorty Crater							Orange glass material / Black glass material / Light-gray fragmental material	
0.025 billion years Cone Crater								(Medium-gray material)	
	Light mantle					Light-gray material	(Light-gray material)	(Light-gray material)	
	Scarp					(Dark floor material)	(Dark floor material)	(Dark floor material)	
0.9 billion years Copernicus					(Central cluster ejecta)				
	Steno-age craters ?								
	Camelot-age craters				(Camelot ejecta)				
								Blocky floor material	Dark-matrix fragment-rich breccia
3.7 billion years Tranquillity Base mare								(Orange and black glass material)	
	Subfloor basalt				Aphanitic basalt / Fine-grained basalt / Coarse-grained basalt				
3.9 billion years Imbrium impact (Fra Mauro metamorphism)	Massif uplift	Foliated and layered breccia / Tan matrix-rich breccia (anorthositic gabbro) / Blue-gray matrix-rich breccia / Blue-gray fragment-rich breccia		(Sculptured Hills material) ?					
(?)[e] Serenitatis impact	Massifs	Distinctive clasts in blue-gray fragment-rich breccia							

[a]Table slightly modified from that presented by H. H. Schmitt at the Fourth Lunar Science Conference.
[b]Dark floor material includes all regolith units of the valley floor except the light mantle.
[c]Units shown in parentheses are extrapolated from beyond the immediate observation area.
[d]Internal stratigraphic sequence is not implied among bracketed units.
[e]Age not yet determined.

TABLE 6-III.—*Field and Laboratory Classification of Samples*

Geologic entity	Geologic unit	Collection site	Station	Sample number or type	Laboratory designation
Van Serg	Dark surface material	Van Serg ejecta	9	79220 and 79240	
	Light-gray fragmental material	Van Serg blanket trench	9	79260	
	Dark matrix-rich breccia	Van Serg ejecta	9	79035 and 79135	Dark-matrix breccia
	Dark-matrix fragment-rich breccia	Van Serg floor	9	Not sampled	
Shorty	Dark surface material	Shorty rim core	4	74002 (top 0.5 cm)	
	Orange glass material	Shorty rim trench	4	74220	
	Light-gray fragmental material	Shorty rim trench	4	74240 and 74260	
	Black glass material	Shorty rim core	4	74001	
	Floor material	Shorty floor	4		
Light mantle	Medium-gray material	Surface of light mantle	2A, 3	73220 and 73120	
	Light-gray material	Below medium-gray surface material of light mantle	2A, 3	73240 and 73140	
	Marbled material	Below medium- and light-gray	2A, 3		
	Light component	material of light mantle		73280	
	Dark component	on crater rim		73260	
Dark regolith	Dark floor material	Steno-Camelot area	0, 1, 5		
Subfloor	Aphanitic basalt	General area	0, 1, 5, 6, 8		Same terms as field classification
	Vesicular			74235	
	Nonvesicular			70215	
	Fine-grained basalt			71055	
	Coarse-grained basalt				
	Porphyritic			70035	
	Nonporphyritic			75055	
Massifs	Medium-gray surface material	South and North Massifs	2, 6	Rake samples	
	Light-gray talus material	South and North Massifs	2, 6	Rake samples	
	Foliated and layered breccia	South Massif	2	72255 and 72275	Light-gray breccia
	Tan matrix-rich breccia	South and North Massifs	2, 6, 7	76215 and 72395	Greenish-gray breccia
	Blue-gray matrix-rich breccia	South and North Massifs	2, 6, 7	72435 and 76315	Blue-gray breccia
	Blue-gray fragment-rich breccia	North Massif	6, 7	76275	Light-gray breccia and greenish-gray breccia
Sculptured Hills	Slope material	Sculptured Hills	8	78500 and 78530	
Source unknown	Gabbroic rocks	Exotics on Sculptured Hills and North Massif	6, 8	78235 and 76535	Gabbroic rocks
	Feldspathic breccia		6, 8	76335 and 78155	Cataclasite and hornfels

the matrix, the boulder is divided into five crudely layered zones (fig. 6-8). A fairly well-developed set of cleavage planes (S_b in fig. 6-8) that are roughly at right angles to the bedding planes is visible across the middle of the boulder, and a similar set with the same orientation occurs in sample 72255. These are probably shear planes. The eroded nature of the boulder and the well-developed fillet on its uphill side suggest that it has been in its present position for a considerable period of time.

Four samples (72215, 72235, 72255, and 72275)

FIGURE 6-5.—Part of the South Massif showing area sampled at station 2. Boulders are numbered in order of sampling and text discussion. Bright-rimmed crater (20-m diameter) above and to left of sample area is identified in figure 6-6. Probable source of boulder track shown in figure 6-6 is boulder field centered on the skyline in this view (AS17-138-21072).

were taken from boulder 1 (fig. 6-8). All samples are breccias with light-gray friable matrices (called tan breccia by the crew) containing dark-gray fine-grained lithic clasts. Sample 72215 is possibly a clast eroded from the friable matrix of the zone in which it occurred within the boulder. All the samples contain distinctive light-gray clasts with thin dark-gray selvages.

Station 2, Boulder 2

The second boulder, a greenish-gray breccia sampled at station 2, is ≈ 2 m across and 2 m high above the ground surface. It is rounded but smoother than boulder 1, which suggests that boulder 2 is more uniform than boulder 1. A poorly developed set of fractures (S_a) trends from upper left to lower right as seen in figure 6-9. This set dips gently at ≈ 5° into the surface of the rock and probably controls the

FIGURE 6-6.—Boulder tracks on the South Massif in the vicinity of station 2.
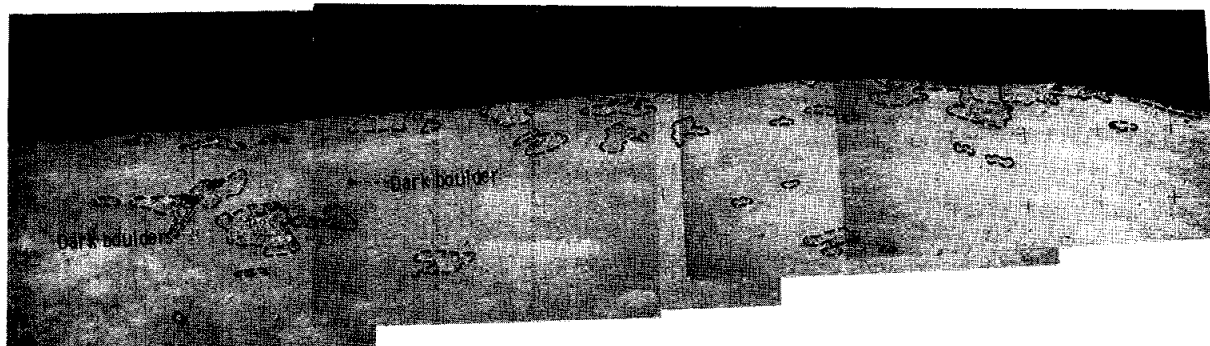
FIGURE 6-7.—Telephotographic mosaic of boulder concentrations near the top of the South Massif. Probable source area of station 2 boulders is shown in left frame (AS17-144-22051 to 22057).
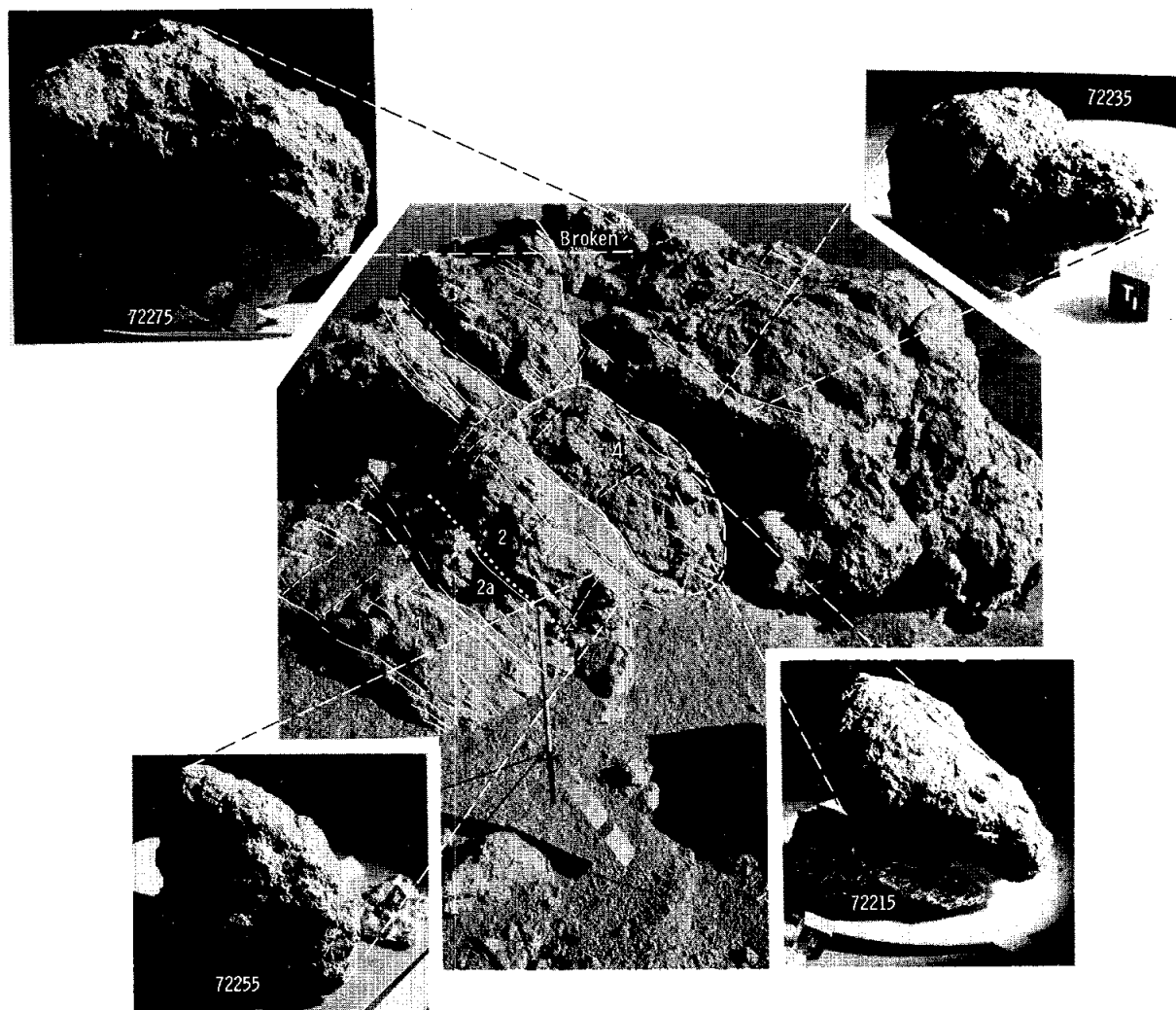
Explanation

- - - - Contact between layered zones

5 Hackly, moderately coherent, poorly developed foliation planes

4 Hackly, friable, poorly foliated; similar to zone 5

3 Moderately coherent, discontinuous, fairly well-developed foliation planes

2 Moderately coherent, well-developed, continuous foliation planes

2a Friable zone

1 Finely spaced discontinuous foliation planes

——— Trace of foliation along bedding planes (S_a)

- - - - Trace of cleavage planes (S_b)

·········· Approximate location of boundary between zones 2 and 2a

FIGURE 6-8.—Sketch map of boulder 1 at station 2 (AS17-137-20901). Inset photographs (clockwise from upper right: S-73-17963, 17987, 17989, and 17988) show lunar orientation of samples.

shape of the rock face on the right side of figure 6-9. A second set (S_b) dips from top center to lower left across the rock surface and appears to be nearly normal to the surface of the rock. A set of lineaments that appears to be traces of a third set (S_c) trends horizontally across the face of the boulder. The third set, or S_c, is visible in sample 72395 (fig. 6-10). Several irregular joints are present. No evidence of
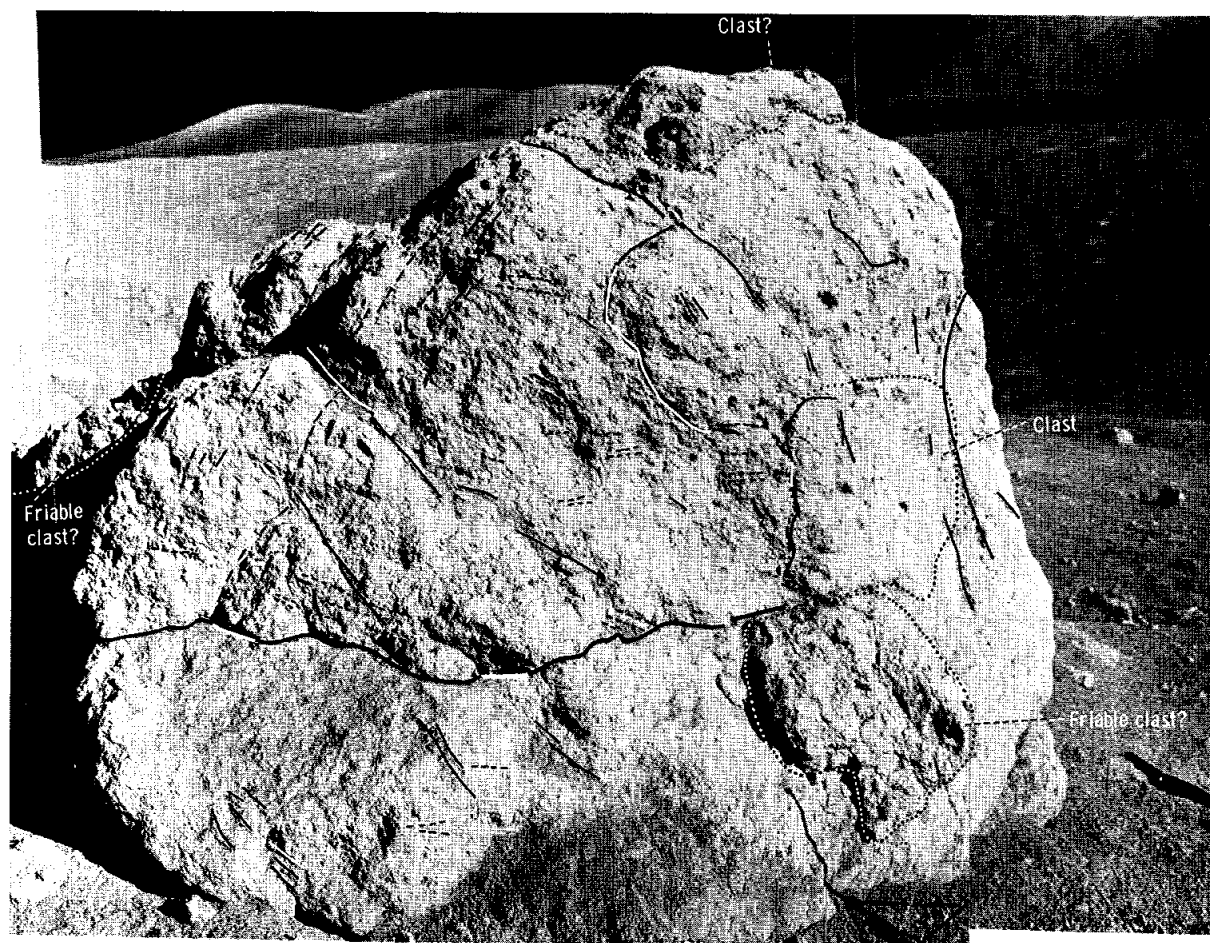
Explanation

Lines denoting planar structures:

——— S_a ━━━ Trace of joint

— — S_b ····· Outline of large clasts

----- S_c

FIGURE 6-9.—Sketch map of boulder 2 at station 2 (AS17-137-20912, 20913, 20914, 20919, and 20920).

bedding or of a fracture set parallel to bedding can be seen in the photographs. The boulder has a moderately well-developed fillet ≈ 0.25 m high on its uphill side but overhangs the ground surface on its downhill side.

Five samples (72315, 72335, 72355, 72375, and 72395) were taken from the second boulder at station 2 (fig. 6-10). Two of these samples (72315 and 72335) were taken from a 0.5-m clast at the lower edge of a spalled area, and the remaining three ·

samples were taken from the matrix of the boulder. Two relatively friable zones are visible in the photographs (fig. 6-9) and may also be clasts. These were not sampled. All five samples are vuggy greenish-gray breccias and, except for having smaller cavities, appear to be very similar to rocks called anorthositic gabbro by the crew at station 6. Lithic clasts, rarely more than 10 mm in diameter, are principally fine-grained hornfelses, but a few are cataclastically deformed plagioclase-rich rocks. Mineral clasts in-
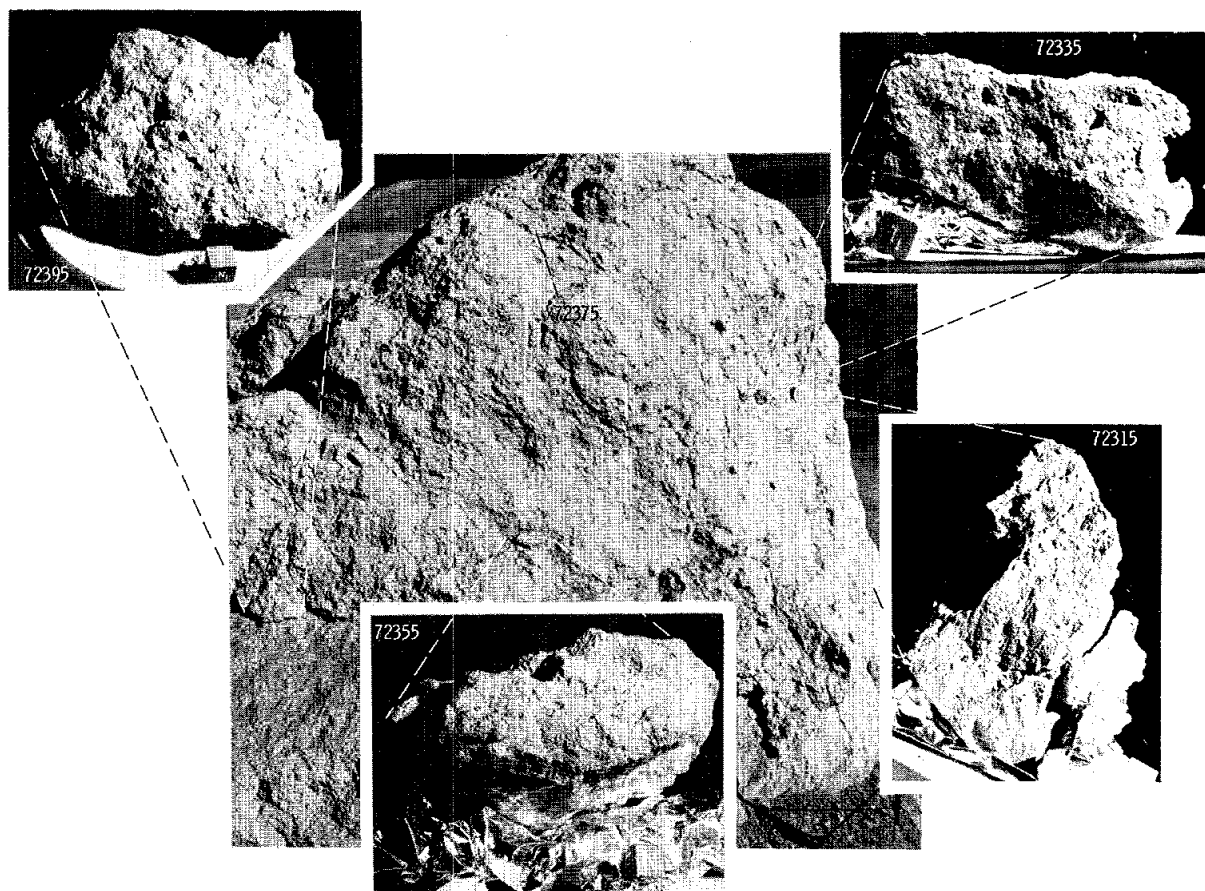
FIGURE 6-10.—Boulder 2 at station 2 (AS17-137-20913). Inset photographs (counterclockwise from upper right: S-73-21389, 18408, 17799, and 19586) show lunar orientation of samples (sample 72375 not oriented).

clude angular fragments of plagioclase and a mafic silicate mineral as large as 4 mm.

Station 2, Boulder 3

Boulder 3 is an equant, subangular breccia boulder ≈ 40 cm across. Its surface is rough on a scale of ≈ 1 to 2 cm. Several 2- to 4-cm clasts and one 10-cm light-gray clast in a gray matrix are visible in the photograph (fig. 6-11). No well-developed fracture or cleavage sets are visible, but two well-developed planar fractures at ≈ 90° to one another are visible. A third fracture, approximately parallel to the upper rock surface, is also visible.

The boulder has a poorly developed fillet, which, together with its subangular shape, suggests that it has been in its present position for a relatively short period of time. Two samples, 72415 and 72418 (a clast) and 72435 (matrix), were taken from the third boulder at station 2 (fig. 6-12). Sample 72435 is a blue-gray breccia that contains ≈ 10 percent lithic and mineral clasts in a tough, finely crystalline, deep-bluish-gray matrix. The rock has a local concentration of slit-like cavities in its matrix that are elongate parallel to a weak alinement of lithic clasts. The clast from this boulder represented by samples 72415 to 72418) is a light-greenish-gray breccia (with color but no stratigraphic implications) composed of abundant mafic silicate mineral clasts and sparse feldspathic lithic clasts set in a matrix, composed of the same constituents, that is moderately coherent, fine grained, and probably annealed.
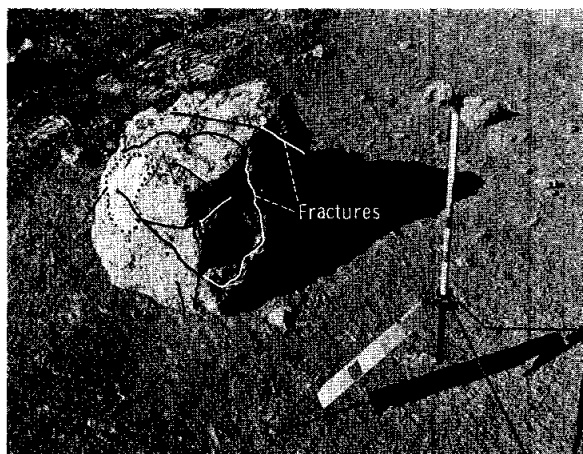
FIGURE 6-11.—Sketch map of boulder 3 at station 2 (AS17-137-20963).
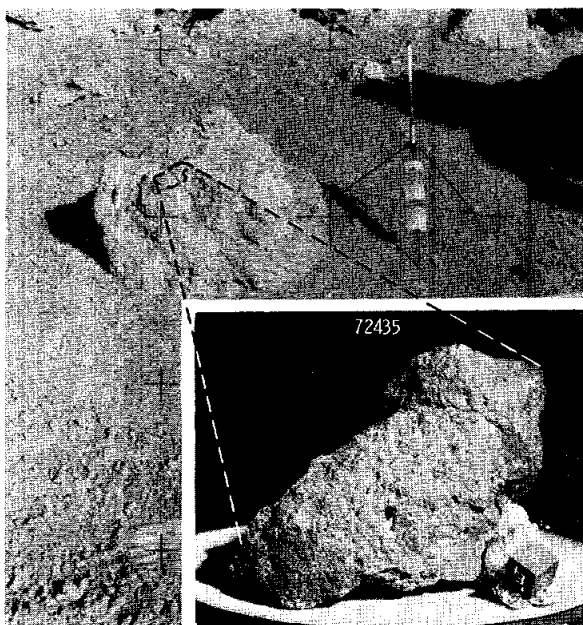
FIGURE 6-12.—Lunar orientation of sample 72435 from boulder 3 at station 2 (AS17-138-21049; inset photograph, S-73-19389).

North Massif

Stations 6 and 7 were designated as sampling sites for material that had been mass wasted from the North Massif. Station 6 lies on an 11° slope ≈ 20 m above the break in slope between the massif and the valley floor. Station 7 is ≈ 500 m east of station 6, on a 7° slope just above the break in slope (figs. 6-3 and 6-4). The surface in the area of the stations is covered by many large blocks and smaller fragments, most of which were derived from higher on the massif. There appears to be a bimodal distribution of fragments in the area. Fragments smaller than 2 to 3 cm and larger than 15 to 20 cm are abundant, whereas fragments between these two sizes are relatively sparse. Fragments smaller than 50 cm are scattered randomly over the surface; larger ones are generally located in clusters that may be fragments from a single larger rock that had rolled or been thrown into that area. Where the soil was disturbed by the crew, it is medium gray on the surface and lighter gray beneath (fig. 6-13).

Station 6 Boulder

Most of the samples collected at station 6 are from a large (6 by 10 by 18 m), fragmented boulder (fig. 6-14) lying at the end of a boulder track (fig. 6-15) that extends approximately one-third of the way (≈ 500 m) up the face of the massif. Two other boulder tracks appear to originate at approximately the same level (fig. 6-16). From this level to the top of the massif, boulder concentrations are common.
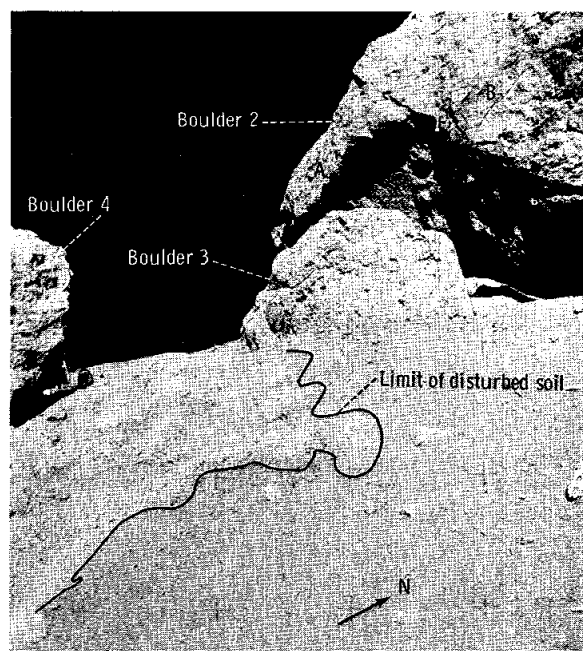
FIGURE 6-13.—Area of disturbed soil between boulders 3 and 4 at station 6. Soil is lighter beneath the thin gray surface layer. The letter designations indicate planar surfaces onto which boulder 4 may fit. Face A is the most likely fit. See text for discussion (AS17-140-21434).
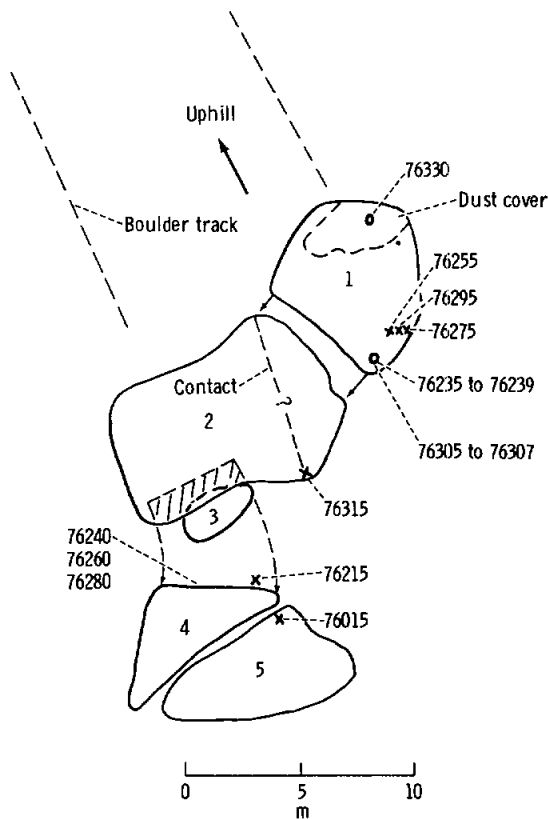
FIGURE 6-14.—Diagram of station 6 boulder showing relationships of large fragments and possible points of reassembly. Sample locations are designated on boulder fragments.

These boulder concentrations are probably derived from near-surface bedrock. At lower elevations, the bedrock in the massif is covered by a thick regolith and talus cover. At higher elevations, the massif is covered by a much thinner layer of fine material that allows the underlying bedrock to be easily excavated by the more abundant smaller cratering events. This is suggested by the change in slope from $25°$ in the upper two-thirds (upper 1000 m) of the massif to $21.5°$ in the lower one-third of the massif (≈ 500 m above the base). One boulder track visible in figure 6-16 extends nearly 1000 m up the slope. At the lower end of this track is a large boulder that is darker than most of the other boulders on the lower one-third of the massif (fig. 6-17) and that is also darker than the station 6 boulders. A concentration of dark boulders occurs near its apparent source, and similar concentrations are scattered at approximately the same level elsewhere on the mountain face. Thus,

a layer or lenses of darker rock may exist high on the mountain. Lighter boulders occur above and below. The lower light zone was sampled at the station 6 boulder.

The station 6 boulder broke into five pieces that are alined downslope. The largest is ≈ 8 m across. The original boulder can be pieced back together, generally with only a small amount of rotation of any of the blocks. Several large fragments that may have broken from the boulder as it rolled downhill can be seen in and around the boulder track (fig. 6-18). Boulders 4 and 5 can be reassembled by minor rotation until similar appearing faces fit together (fig. 6-19). When this is done, vesicle foliation is in a similar orientation in each boulder, and nonvesicular inclusions in both pieces also fit across the break. Boulders 1 and 2 also fit without substantial manipulation. It appears that boulder 1 can be raised and placed against boulder 2 (fig. 6-20). Boulders 2 and 3 are fitted together in much the same manner (fig. 6-21). The relationship of the structural split between boulders 1, 2, and 3 and boulders 4 and 5 is not as obvious, and the fit is still tentative. Figure 6-21 shows a nearly planar surface (A) on boulder 2, which dips approximately the same as the north face of boulder 4, as shown in figure 6-19. When boulder 4 is placed on this surface, the foliation, which appears to be planar concentrations of vesicles in boulder 2, is parallel with the foliation in boulders 4 and 5. Also, a series of widely spaced joints in boulder 4 is then alined with similar joints in boulder 2. A second, less-likely possibility is to place the north face of boulder 4 on planar surface (B) on boulder 2, adjacent to the one just described (fig. 6-13). However, structures seen in both boulders do not aline as well, and the shape of the fractured face of boulder 2 does not conform well with that of boulder 4.

Four of the five numbered boulder fragments were sampled. Two major breccia types can be distinguished: greenish-gray and blue-gray breccias. The third, fourth, and fifth boulders and part of the second are greenish-gray breccias, described by the crew as anorthositic gabbros. In boulder 2, there is an irregular contact between the greenish-gray breccia and a blue-gray breccia. This zone, ≈ 50 cm across, appears to be an area of mixing between the two rock types. Boulder 1 is also blue-gray breccia.

Two samples were collected from the greenish-gray breccia. Sample 76215 is part of a larger rock that spalled from boulder 4, and 76015 is from the top of

FIGURE 6-15.—Footprints of 500-mm mosaics of part of the North Massif that are shown in figures 6-16 and 6-18. Features identified by letters are visible in figures 6-16 and 6-18; primed letters denote objects visible in figure 6-18 only. The 500-m grid begins at the LM site (Apollo 17 panoramic camera frame AS17-2309).

boulder 5 (fig. 6-19). These rocks are tough annealed breccias with sparse lithic and mineral clasts set in a vuggy fine-grained matrix. The vugs, which range in size from 0.1 mm to ≈ 9 cm, are flattened and locally alined. Around the larger cavities, the sugary intergrowth of minerals that forms the matrices of these rocks gradually coarsens over a distance of ≈ 1 cm. At cavity walls, individual minerals of the matrix become distinguishable, and the rock has a poikiloblastic texture. Lithic clasts, all < 1 cm across,

include granoblastic intergrowths of plagioclase and a yellow-green mineral.

Two unsampled rock types are present within the greenish-gray breccia. Several baseball-sized light-gray clasts are scattered randomly throughout the rock. The clasts appear nonvesicular and are in sharp irregular contact with the greenish-gray breccia. On boulder 5 (fig. 6-22), a large (0.5 by 1 m), gray nonvuggy area is evident within the greenish-gray breccia. Photographs suggest that the nonvuggy rock

FIGURE 6-16.—Mosaic of 500-mm photographs taken from LM area showing boulder tracks on the North Massif. Dashed lines indicate boulder concentrations. The grid perspective is the same as that in figure 6-15. Elevations of grid corners (in parentheses) were taken from the NASA Lunar Topographic Photomap, Taurus-Littrow, 1:25 000, first ed., Sept. 1972, by the Defense Mapping Agency. According to this map, the elevation of the landing point is 4510 m, and the summit of the North Massif is 6178 m. (AS17-144-21991, 22119 to 22122, and 22127 to 22130).

may differ only in texture, not composition, from the host breccia. The dense area is sharply bounded by vuggy breccia on two sides and grades into it on a third side. This area may be an inclusion that was incorporated in the greenish-gray breccia, which vesiculated along the margins, or a locally nonvesiculated interior of the boulder. The former is preferred because of the sharpness of the contact on two sides. A set of planar structures occurs within the dense material parallel to the fracture face between boulders 4 and 5. It is not clear what these structures are, but they do not appear to be compositional layers. They do not continue into the vuggy part of the boulder, which further suggests that the nonvesicular rock is an inclusion rather than a central nonvesiculated core of the boulder.

Two samples from the blue-gray part of boulder 1

FIGURE 6-17.—View of the North Massif showing principal elevation data on prominent boulder tracks. Samples were collected adjacent to Turning Point Rock (station LRV-10). The light color of Turning Point Rock and station 6 boulders in contrast to the dark color of the large rock that rolled from high on the North Massif is clearly evident (AS17-141-21550).
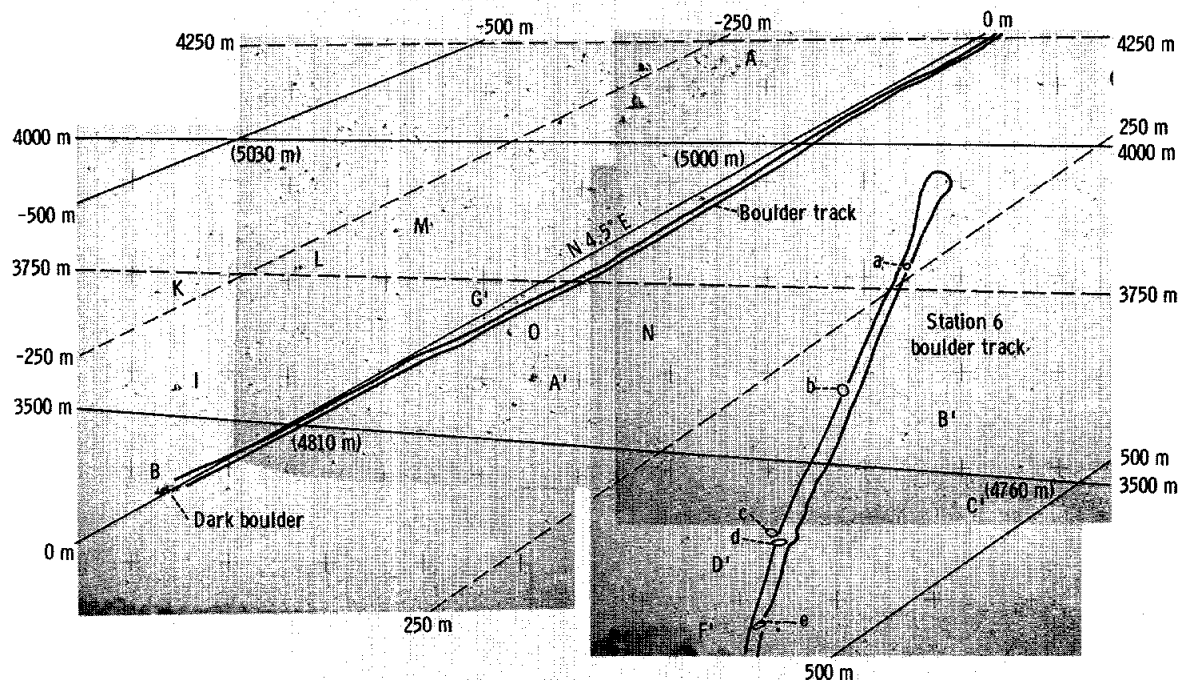
FIGURE 6-18.—Telephotographic view of prominent boulder tracks on the lower North Massif showing probable source area of station 6 boulder. Lowercased letters indicate fragments that may have broken from station 6 boulder. The large boulder in the lower left, at the end of the prominent track that heads at an elevation of 5550 m, is distinctly darker than any others in this area; its darkness is characteristic of some boulder concentrations high on the mountain as seen in figure 6-16 (AS17-139-21252, 21254, 21262, and 21263).
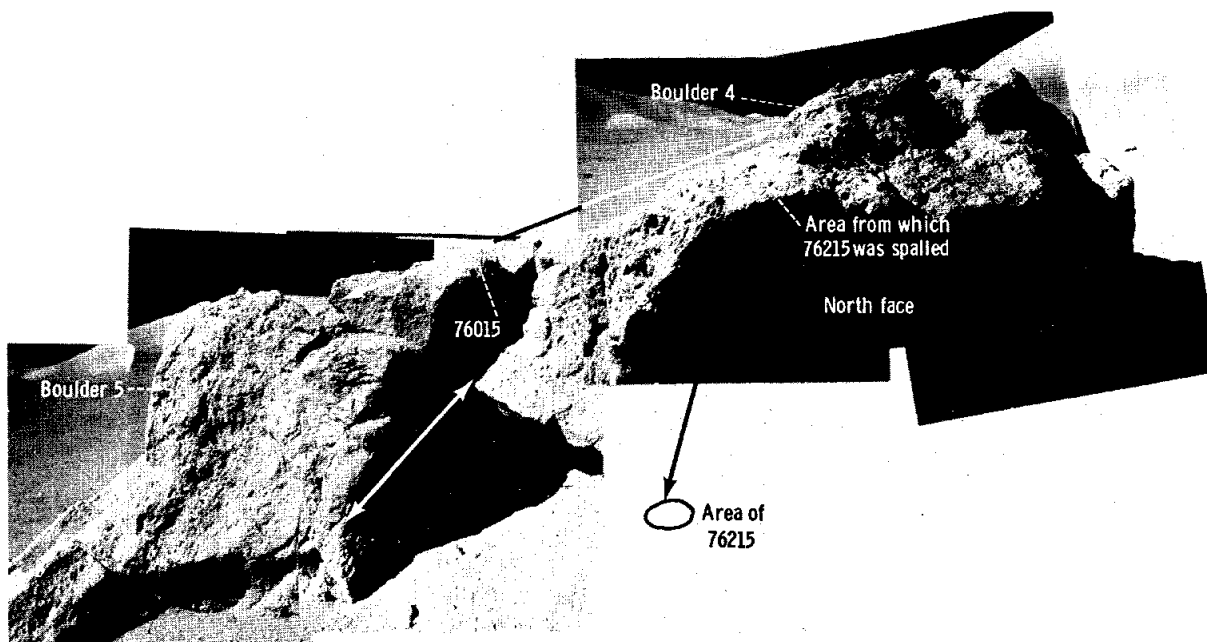
FIGURE 6-19.—Boulders 4 and 5 at station 6. Arrows indicate probable matchpoints between the two boulders (AS17-140-21414, 21416, 21418, 21429, 21432, and 21433).
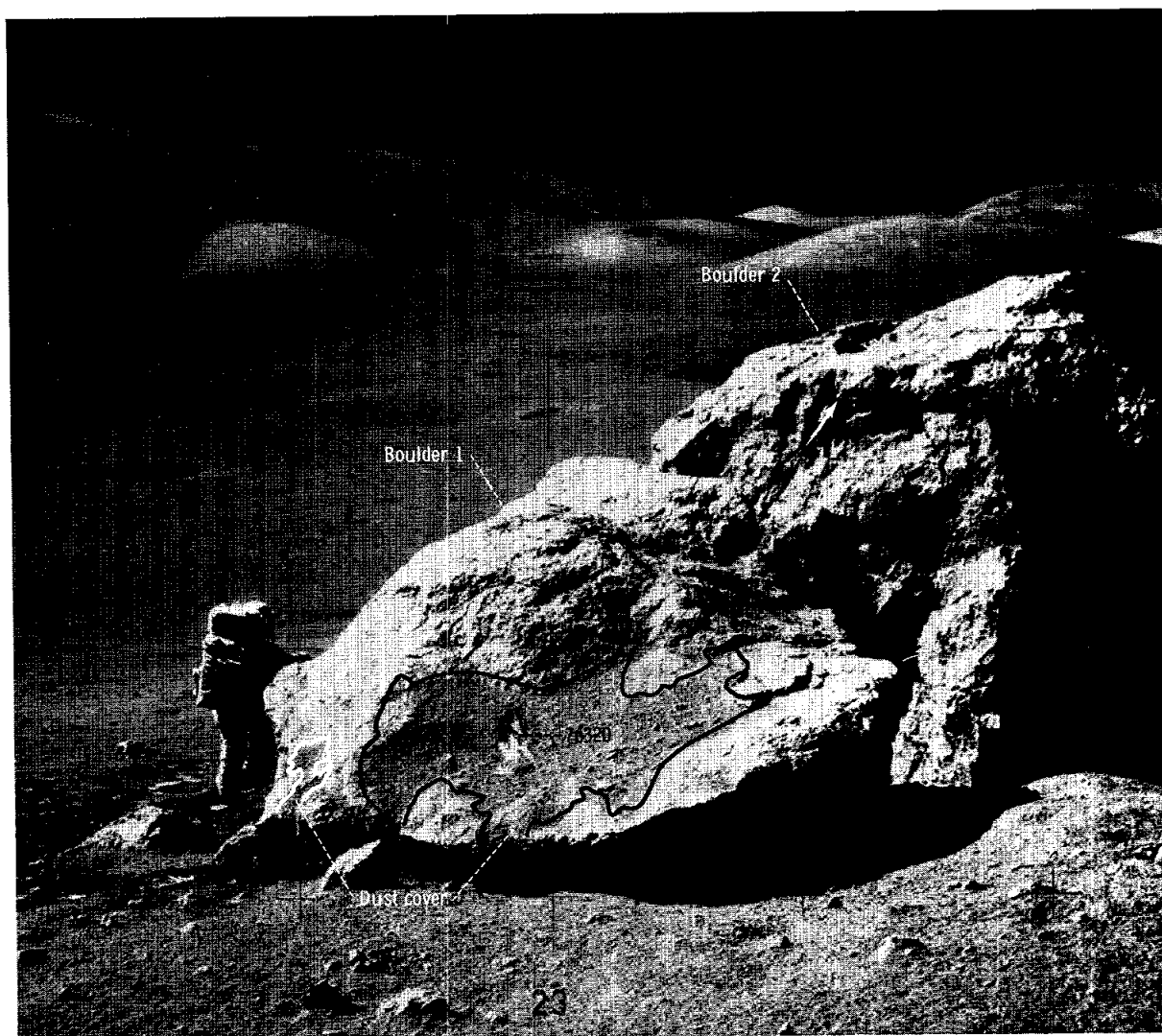
FIGURE 6-20.—Boulders 1 and 2 at station 6. Arrows indicate probable matchpoints between boulders (AS17-140-21497).

(fig. 6-23) (samples 76275 and 76295) are composed largely of blue-gray breccia clasts in vuggy greenish-gray matrices. The proportion of clasts in these two samples is high (40 to 60 percent), and the matrix is somewhat browner and darker than the typical vuggy greenish-gray rocks. Vugs, which are ≈ 2 to 5 mm across, are in most cases lined by rich-brown pyroxene and plagioclase with or without ilmenite plates. The matrices of these samples are tough, finely crystalline material composed principally of angular mineral debris (plagioclase, yellow-green mineral, brown pyroxene) and small lithic fragments of blue-gray breccia. The clasts are dominantly fine crystal-

line blue-gray breccias that contain sparse finely recrystallized light-gray clasts.

In the blue-gray breccia of boulder 1, there are light-gray friable inclusions ranging in size from 1 to 2 cm to 1 m across that are in sharp irregular contact with the blue-gray breccia. Eight small samples (76235 to 76239 and 76305 to 76307) are chips that represent one of these inclusions (fig. 6-24). These samples are very light-gray cataclasites composed of angular mineral debris that includes yellow-green and pale-grass-green mafic silicates and plagioclase.

Two other types of inclusions in the blue-gray breccia were not sampled. There are a few inclusions
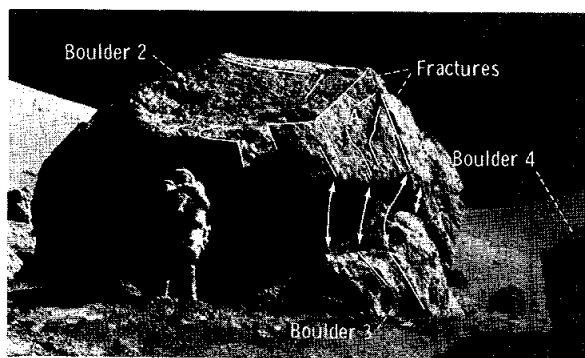
FIGURE 6-21.—Boulders 2 and 3 at station 6. Arrows indicate fractures that are alined when boulders are fitted together. Letter designations, particularly A, indicate planar surfaces onto which boulder 4 may fit. See text for discussion (AS17-146-22293).
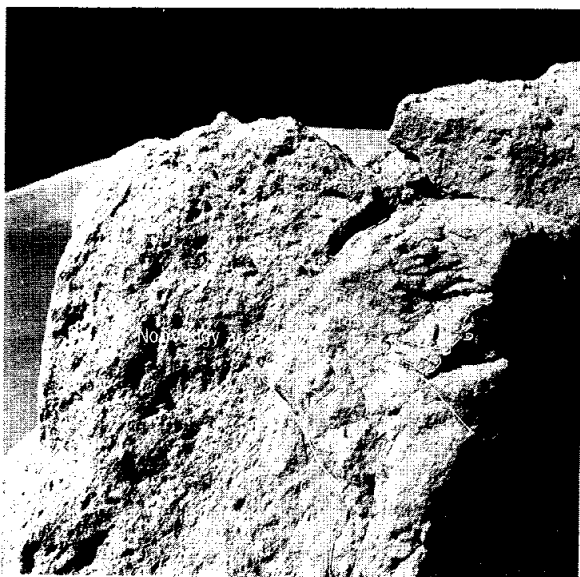
FIGURE 6-22.—Boulder 5 at station 6 showing nonvuggy area in vuggy greenish-gray breccia. Dashed lines show planar structures in the nonvuggy portion. Solid lines are joints (AS17-140-21432).

(fig. 6-23, lower left) that are not as friable in appearance and are a darker gray than the light-gray inclusions sampled. A second type, which is rare, is medium gray and vesicular with sharp irregular boundaries (fig. 6-23, upper left).

One sample (76255, collected from boulder 1) is a breccia that contains clasts of blue-gray set in a friable light-gray to brownish-gray matrix. The sample

is prominently foliated, with alternating layers of abundant or sparse blue-gray breccia clasts. The blue-gray breccia clasts contain sparse, sugary, white hornfels clasts and moderately abundant mafic silicate fragments. The largest blue-gray clast in the rock has a string of vuggy patches 3 to 12 mm across of plagioclase and rich-brown pyroxene along one edge.

Sample 76315, collected from boulder 2 near the contact, appears to be transitional between blue-gray breccia and the type represented by sample 76255. The rock is mainly blue-gray breccia with a few white clasts; a large (3 by 8 cm) white clast at one end of the specimen is veined by blue-gray material. Both components were subsequently weakly brecciated so that pieces of blue-gray rock are now encased in a white matrix.

In boulder 1, several throughgoing planes (S_a through S_g) can be recognized in stereoscopic study of the photographs (figs. 6-23 and 6-25). The lettering sequence does not imply a sequence of development in the rocks. When comparing these planes with the oriented returned samples, it can be seen that they represent shear planes along some of which movement has occurred. Two types are evident. Along the S_a plane, shearing has deformed the clasts to create discontinuous compositional banding. The zoning in sample 76255 is parallel to the S_a shears. This type shear is closely spaced (a few centimenters or less), but it is not a plane that had any substantial control over the shape of the boulder because the fracture surfaces are discontinuous and the rock is coherent across these surfaces. Planes S_b and S_f are also this type. Planes S_c and S_d are typical of the second type; they appear to be somewhat more widely spaced planes that form fracture faces on the surface of the boulder. Sample 76295 parted along S_d when sampled. Planes S_e and S_g are also this type. Most of the shears appear to penetrate the boulder. Planes S_a and S_b, for example, can be seen in two places on the boulder over a meter apart.

Throughout the boulder, movement along the shears does not appear to have been uniform. In the area where sample 76255 was collected, one of the large light-gray clasts has been intensively sheared. The large clast from which samples 76235 to 76239 and 76305 to 76307 were collected has not been substantially deformed. The direction of shearing is the same in two areas, but the amount of movement is different. Two fracture sets (A and B in fig. 6-23), which have not been identified in the samples, are
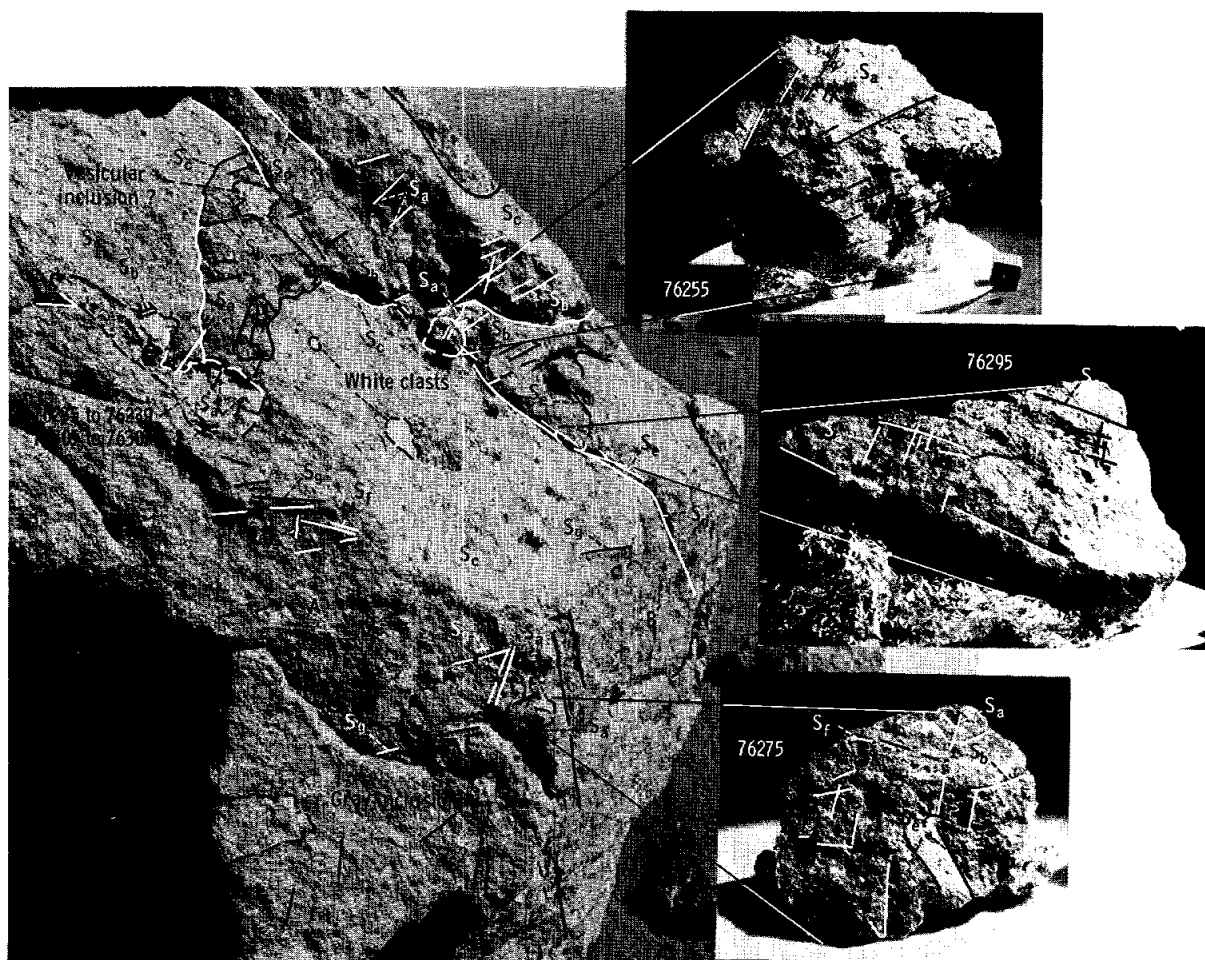
FIGURE 6-23.—Locations of samples removed from boulder 1 at station 6. Known orientations are shown in insets. Heavy solid lines indicate traces of shear planes, S_a through S_g. Dashed lines outline inclusions and samples. A and B denote fracture surfaces bounding boulder (AS17-140-21443) (inset photographs, S-73-19375, 19387, and 19385, respectively).

major mutually perpendicular fractures that shape the south and east faces of the boulder.

At least one and possibly two of these sets of shears can be seen in boulder 2. Sample 76315, collected near the contact in boulder 2, shows some evidence of shearing. In figure 6-26, the face shown on boulder 2 is parallel with the S_c structures of boulder 1. Figure 6-27 shows this face, together with what is probably an expression of the S_d planes. The other structures are probably in this boulder also; but, because of the lower resolution and the direction from which this photograph was taken, they are not visible. It does not appear that the S_c planes penetrate boulder 2 completely. They appear to die

out as the contact between the two breccia types is approached. Assuming that the boulders have been reassembled correctly, it is not evident that these shears are present in the greenish-gray breccia. Some planar structures can be seen on boulders 4 and 5, but they neither coincide with nor look the same as the shear planes seen in boulders 1 and 2. They are generally spaced several centimeters apart and appear to be fractures rather than the shear planes. No evidence of shearing is seen in samples 76015 and 76215 collected from these boulders.

One of the first events represented in the station 6 boulder was the formation of the light-gray to white cataclasite. This breccia was enclosed by the blue-gray
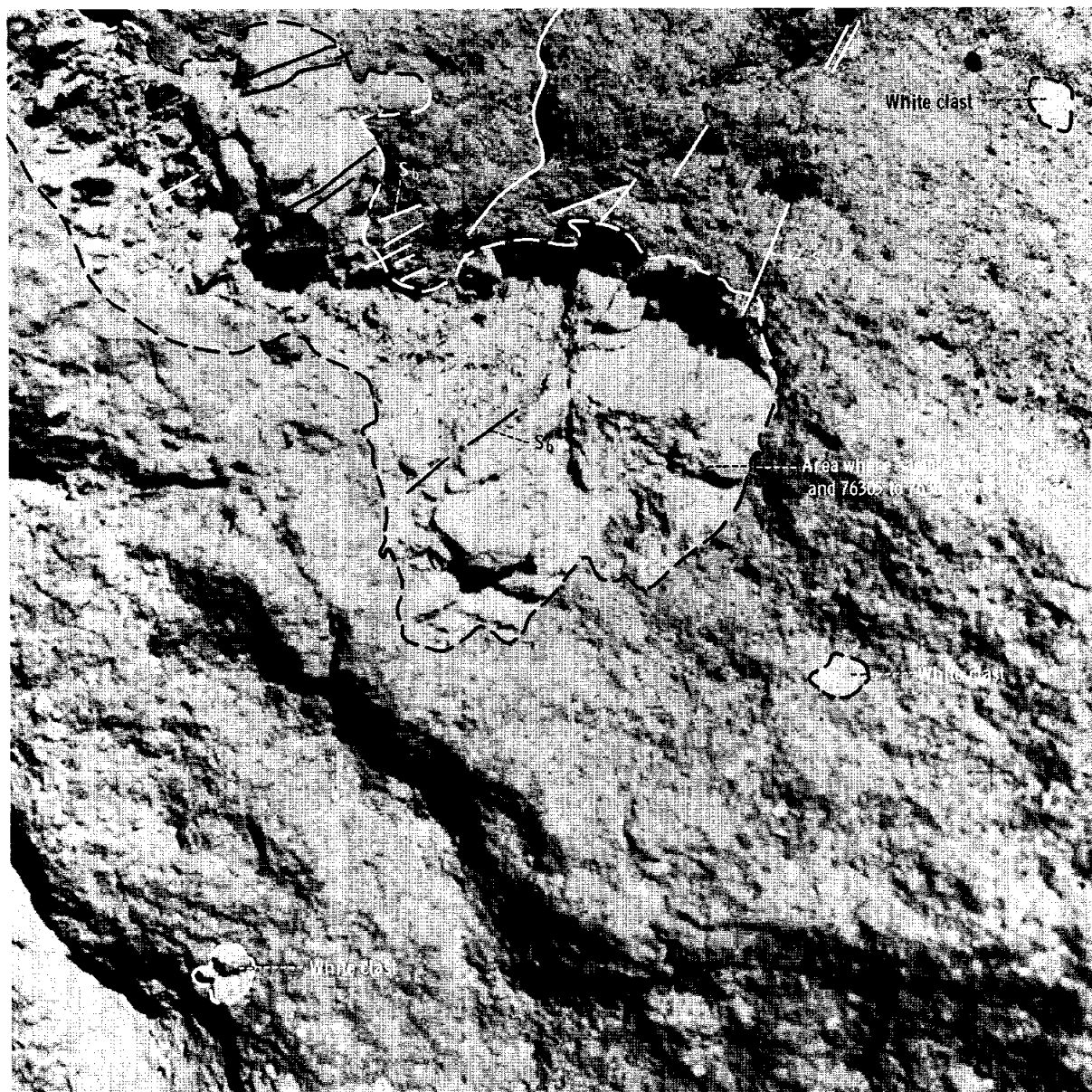
FIGURE 6-24.—Large light-gray clast in blue-gray breccia of boulder 1 at station 6. Solid lines show traces of shear plane sets S_a and S_b (AS17-140-21445).

breccia, either during the same event or a later one. The two unsampled clast types in the blue-gray breccia probably have similar histories. The blue-gray breccia was heated enough to allow minor vesiculation. The blue-gray breccia was then incorporated by the greenish-gray breccia, which must have been heated enough to allow intensive vesiculation. The vesicles define a foliation parallel to the contact with the blue-gray breccia. The shearing seen in the blue-gray breccia portion of the boulder, which caused the banding seen in sample 76255, apparently occurred before and/or during its incorporation into the greenish-gray breccia, because no extension of these shears is evident in the greenish-gray breccia.
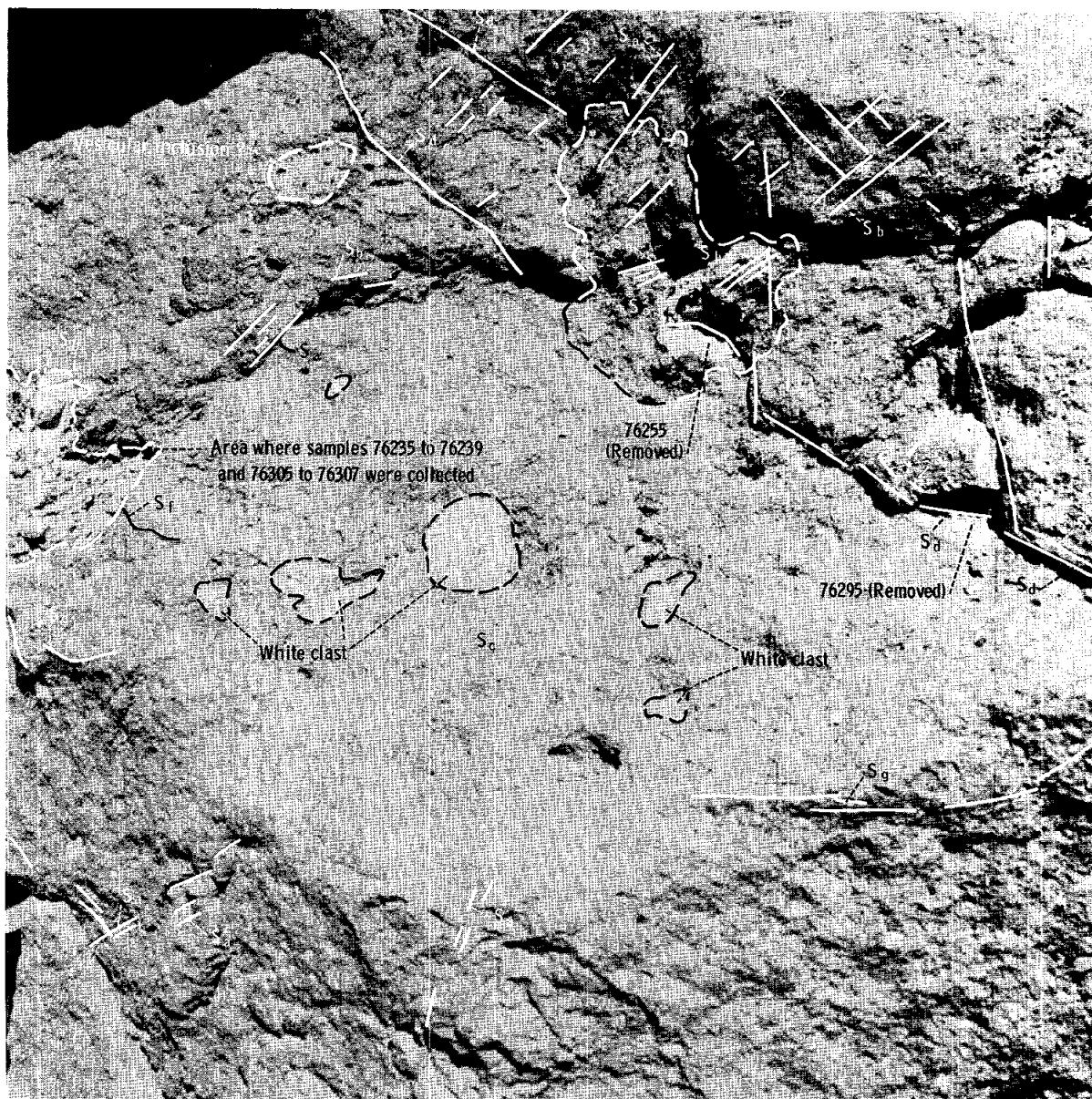
FIGURE 6-25.—View of boulder 1 at station 6 after removal of samples; shows shear sets, S_a through S_g. Dashed area denotes a crushed zone with mixing between light-gray and blue-gray breccia. Note the large fracture face of blue-gray breccia with light-gray clasts (AS17-140-21456).

The blue-gray breccia may, however, be more susceptible to shearing than the greenish-gray breccia.

It is not clear whether the vesicular patch seen in boulder 1 is of the same generation as the greenish-gray breccia because its relation to the contact cannot be seen in three dimensions. The color and vesicularity of it suggest that it is the same; however, it is not known if the vesicular patch was injected into the blue-gray zone during this time.

Station 7 Boulder

Sampling in the station 7 area consisted of collecting four samples from a 3-m boulder (fig. 6-28)
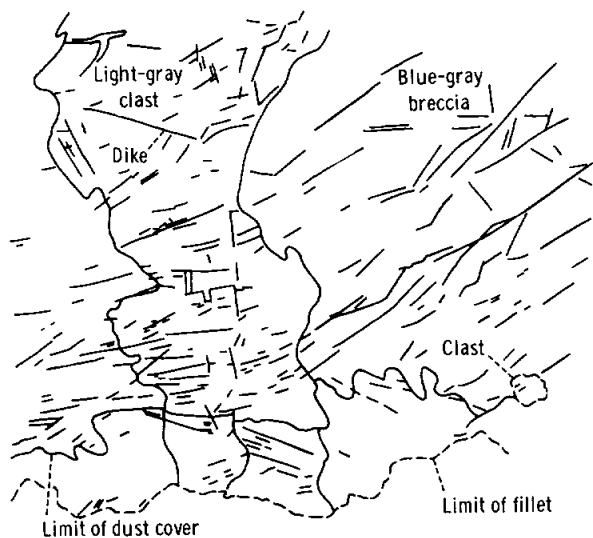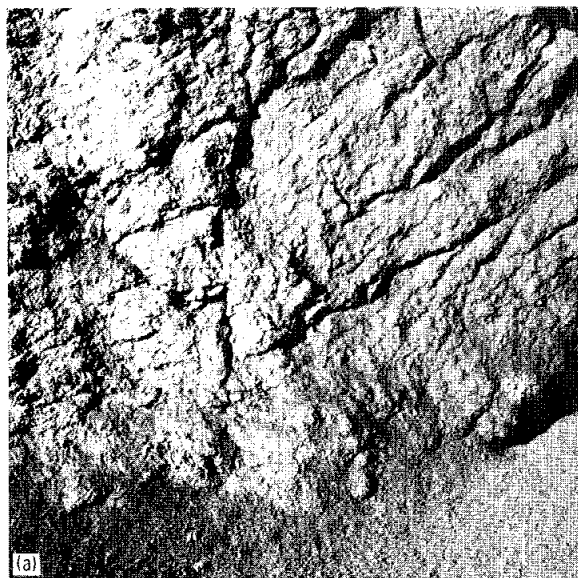
FIGURE 6-31.—Fractures in blue-gray breccia and light-gray inclusion in station 7 boulder. Note differences in spacing of fractures. (a) Photograph AS17-146-22310. (b) Sketch map.

FIGURE 6-32.—Station 7 boulder showing closely spaced fractures in a light-gray clast. (a) Photograph AS17-146-22306. (b) Sketch map. Unlabeled lines show fracture traces.

sample, and 76280 is a 6-cm-deep scoop of soil Another soil sample, 76320 (fig. 6-20), was collected from the north face of boulder 1. This soil was probably picked up by the boulder as it fell into its present position. Sample 76220 is soil collected from the center of the boulder track ≈ 10 m northwest of

boulder 1. Approximately 5 m south of the LRV, a single drive tube, 76001, was collected. All these samples probably represent a mixture of breccia fragments from the massif and subfloor material, with the major contribution derived from the massif.

Rock samples from stations 6 and 7, other than
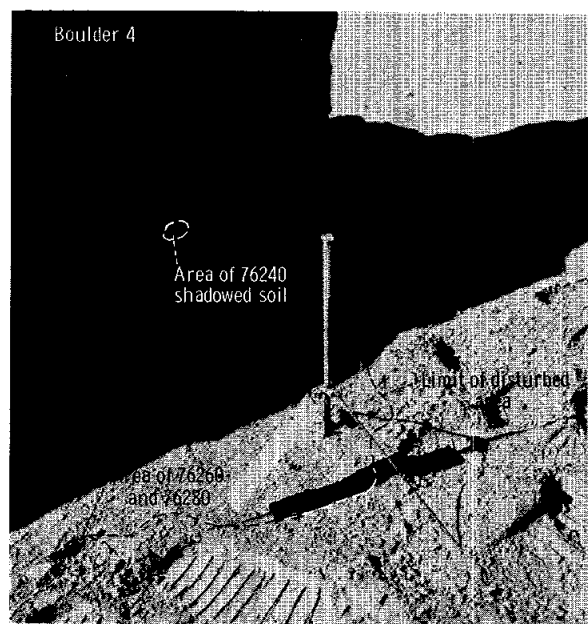
|FIGURE 6-33.—North face of boulder 4 showing permanently shadowed soil and references to other soil samples (AS17-140-21406).

those collected from boulders and other than basalts, include five white cataclasites (76355, 76536, 76558, 76559, and 77017); 14 greenish-gray breccias (76055, 76556, 76557, 76577, 77035, 77515, 77517, 77518, 77519, 77525, 77526, 77637, 77539, and 77545); five blue-gray breccias (76036, 76035, 76555, 76569, and 76575); two light-gray breccias (76505 and 77538) with small blue-gray clasts in a moderately coherent matrix; six dark-matrix breccias with small white clasts (76506, 76545, 76546, 76547, 76548, 76549, 76565, 76566, and 76568); one coarse-grained gabbroic rock with ≈ 35 percent pyroxene (76535); one light-gray regolith breccia (76567); and one light-colored fine-grained hornfels (76576). The cataclasites are chalky white rocks, but 77017 is laced by dark glass veins and one side is covered by a thick coating of dark glass with many inclusions of cataclasite. The greenish-gray breccias include two large rocks (76055 and 77035) with irregularly distributed small slit-like cavities that are locally alined. A smaller sample grouped with the greenish-gray breccias (77517) and two small pieces (77525 and 77526) that may have been broken from it have abundant medium light-gray to light-blue-gray aphanitic clasts in a vug-free, annealed, light-gray matrix. Sample 76035 is an unusual blue-gray breccia that contains a shattered clast of light-gray hornfels.

Blue-gray matrix completely envelops pieces of the broken clast around its periphery, but the interior of the clast is incompletely penetrated by blue-gray matrix so that the fragments form a porous aggregate. The blue-gray matrix appears to be holocrystalline and fine grained and has a small proportion of smooth-walled vesicles and irregular vugs. Other clasts in the blue-gray matrix include a distinctive fragment that consists of 2-mm euhedral plagioclase crystals, interstitial light-brown pyroxene, annealed plagioclase-rich fragments, and mineral debris.

Several basalts were collected in the rake and grab samples at these two stations: four vesicular, porphyritic, coarse-grained basalts (76037, 76538, 77535, and 77536); two vesicular fine-grained basalts (76136 and 77516); and two dense aphanitic basalts (76537 and 76539). The presence of the basalts indicates there is some mixing of subfloor materials in the talus of the massif material. This area is also down range from the central crater cluster that dominates the landing area and that probably threw debris onto the slopes of the North Massif and adjacent Sculptured Hills.

Sculptured Hills

The single location on the Sculptured Hills from which samples were collected (station 8) lies ≈ 20 m above the valley floor on a southwest-facing slope just southeast of Wessex Cleft and 4 km northeast of the landing point. The station is within the zone mapped as dark mantle (refs. 6-1 and 6-5). This unit locally mantles the lower slopes and linear valleys of the Sculptured Hills (fig. 6-34) and is likely to have been mixed with the underlying regolith. The terrain is undulating on a general slope of 10° to 30°, being steepest above the station 8 area (figs. 6-35 and 6-36).

From a distance on earlier traverses, the crew described these hills as being pockmarked (by small craters), darker gray, more hummocky and lineated, and as having lower slopes than the massifs. During late mission orbits under highest Sun elevations (58°), the hills were characterized as incorporating "the albedo both of the North Massif and the (dark) mantle area . . . to give . . . an in-between gray albedo, but the sculpturing is produced by the darker albedo that looks like the mantle and the lighter albedo that looks like the massif." These observations are borne out by both the high Sun orbital and the surface photographs.

While approaching the hills, the crew noted that
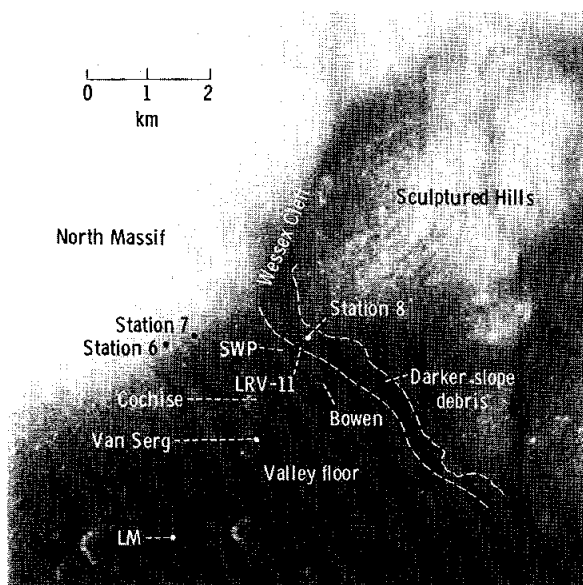
FIGURE 6-34.—Panoramic camera view of station 8 area showing distribution of dark mantle on the Sculptured Hills, Wessex Cleft, and valley floor (Apollo 15 panoramic camera frame AS15-9557).

FIGURE 6-35.—Station 8 area at Sculptured Hills as viewed from the LM, 4 km away. Note the contrast between the hills on the right and the massif material directly above Wessex Cleft, although both slopes have similar orientations (AS17-137-20876).

rocks larger than 20 cm are very rare on the Sculptured Hills slopes compared with their relative abundance at the foot of the North and South Massifs. Most of the fragments are small clods and create a downslope pattern of small lineaments indicating youthful mass wasting on currently active slopes (appendix B, fig. 6-121). However, the three boulders investigated on this slope showed no evidence of having moved downslope, and the only other large rocks on the hill are described as farther upslope. These latter blocks are the fragments visible within the patches of dark mantle in figure 6-36.

The few fragments seen on the local surface are subrounded to subangular; some are partly buried, but the two sampled boulders and most of the soil clods are perched on the surface. The lack of blocks around fresh craters as large as 50 m in diameter (fig. 6-36) indicates that bedrock is more than 10 m below the surface slope material. The soil in this area, at least to the 20- to 25-cm depth of the trench samples, consists of fine-grained cohesive clods and particles. The soil has a moderately dark appearance characteristic of the mantle throughout the valley floor.

No large craters are present in the immediate area; those as large as several meters in diameter are common, however, and have a continuum of morphologies from fresh-appearing, topographically sharp

features to highly subdued depressions. The craters have neither prominently raised nor blocky rims, although one secondary crater lower on the slope (fig. 6-37) forms a cloddy rim similar to that sampled from the LRV on the rim of SWP Crater (LRV-11, fig. 6-34).

The sample suite collected at the foot of the Sculptured Hills is represented mainly by basalts that are most likely ejecta deposited on the Sculptured Hills slopes by valley floor craters and subsequently concentrated by mass wasting toward the base of the hills. The samples are all from the subtle dark-gray apron interpreted on premission maps as dark mantle (fig. 6-34).

One large basalt fragment (sample 78135, fig. 6-38) was taken from near a half-meter-wide boulder, probably also basalt, that was too hard to be sampled directly. Other basalt fragments were collected in the rake and soil samples. The basalts are not obviously shocked or glass veined, and the crew indicated the basalts resembled others sampled at different localities on the valley floor.

Perhaps the more important samples for interpreting the lithologic nature of the Sculptured Hills are represented by the smaller rocks and soils. Unfortunately, their relationship to the underlying hills is not known. The friable feldspathic breccia (sample 78155) collected from the wall of a 15-m crater is a particularly good candidate for Sculptured Hills material. Its friability and color are compatible with the more rounded topography of the Sculptured
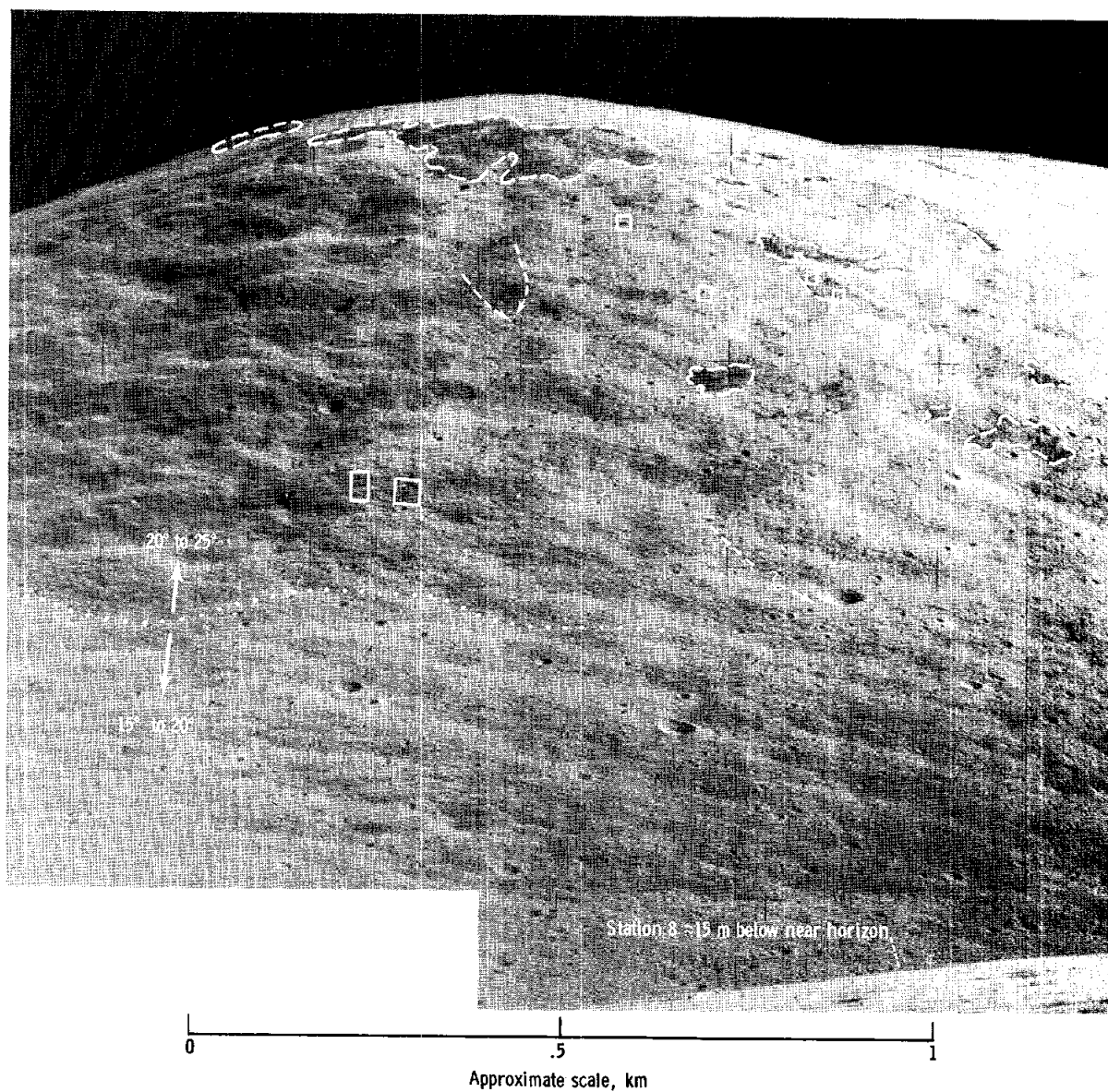
FIGURE 6-36.—Telephotographic mosaic of Sculptured Hills slope above station 8 as viewed from station 2A. Sun elevation is 28° (AS17-144-22034 and 22035).
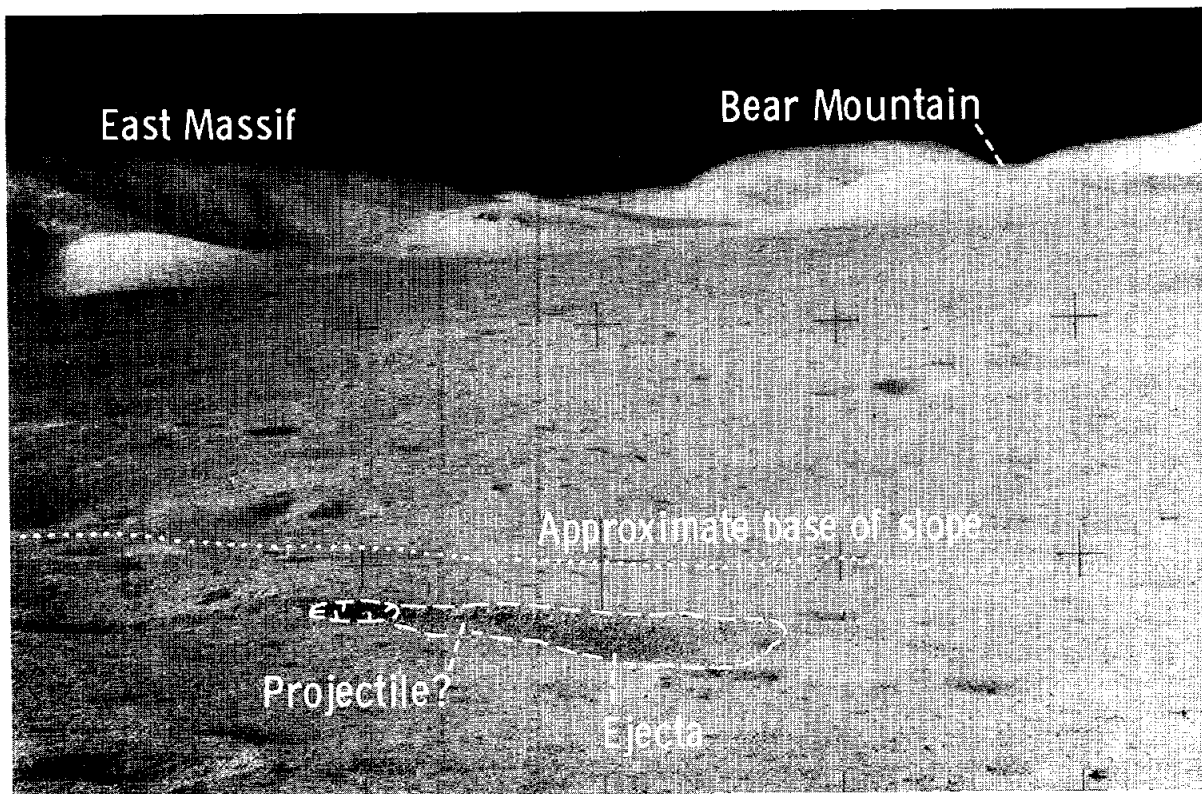
FIGURE 6-37.—Cloddy secondary crater on slope below station 8. Break in slope is ≈200 m from camera (AS17-142-21741).

Hills, the general absence of boulders, and the light-colored, generally fine-grained ejecta seen in the largest craters of this area. Samples larger than 1 cm taken from soil bags and the rake samples include 22 dark-matrix breccias, most of which have small, white, lithic fragments and clasts of mare basalt (78508, 78516, 78518, 78535 to 78539, 78545 to 78549, 78555 to 78559, and 78565 to 78568), one rock composed of regolith clods loosely cemented by glass (78525), one dunite(?) (78526), one nonvesicular metaclastic rock (78527), and one white feldspathic breccia (78517).

The gabbroic rocks (samples 78235 to 78238, 78255, and 78256) are from the top and bottom of another half-meter-size boulder. The rock is coarse grained, composed of ≈50 percent each of plagioclase and pyroxene, intensely shocked, and heavily glass coated and glass veined (figs. 6-39 and 6-40). No fillet existed on the boulder in its original position. These properties and its strongly fluted, glassy surface suggest that it originated from outside the sample area and was emplaced relatively recently at station 8.

The lack of blocky craters or related boulder tracks upslope argues against a local source.

The well-documented trench samples (78420 to 78480) have not been described yet, but they should typify the soils of the lower slopes of the Sculptured Hills. They are probably a mixture of valley floor debris and Sculptured Hills soils. The soil sample collected from a dark cloddy crater on the rim of SWP Crater (78120) at LRV-11 was just at the base of the slope and may represent either deeper material from SWP Crater or mass-wasted material from upslope (fig. 6-34). Perhaps the original composition of the hills can best be determined by subtracting from these soils the average composition of the typical valley floor.

Relationships Between the Massifs and the Sculptured Hills

The upper slopes of the North, South, and East Massifs are alike in morphology and outcrop occurrence. The samples from the North and South Massifs
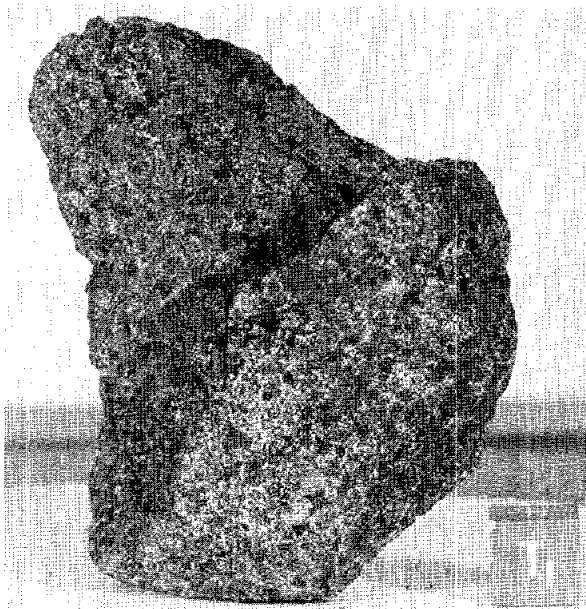
FIGURE 6-38.—Basalt fragment (sample 78135) collected from beside a hard boulder at station 8. The cube is 1 cm on the edge (S-73-15003).

FIGURE 6-39.—Glass-coated coarse-grained gabbroic rock (sample 78236) from shock-fluted, rolled boulder at station 8. The cube is 1 cm on the edge (S-73-15394).

are strikingly similar breccias. The Sculptured Hills, in this region at least, are notably different in their greater dissection, lower slopes, and lack of large boulders. These features in combination with the limited sample suite suggest that the Sculptured Hills are underlain by less coherent breccias than the massifs. They do seem to have more slope debris deposited at their base and a greater possibility of contamination from the thinly mantling dark material above and below the sample area. If the Sculptured Hills reflect a different structural history than the massifs, no evidence was developed during the mission to demonstrate it.

Outcrops on the North Massif occur on the upper two-thirds (1000 m) of the slope. On the South Massif, only the upper one-third (700 m) of the slope has exposed blocks. Sampled boulders are thought to represent the uppermost part of the South Massif and the lower one-third of the North Massif. Hence, two distinct stratigraphic levels may have been sampled.

However, rocks collected from the North and South Massifs closely resemble each other in many respects.

1. Vuggy greenish-gray breccias from both massifs are similar except that cavities in rock samples from station 2 are smaller than those from station 6.

2. Greenish-gray breccias that lack cavities occur on both massifs.

3. Blue-gray breccias are identical, at least insofar as can be determined with the binocular microscope. In both places, these rocks have small proportions of white clasts and have fine-grained to aphanitic matrices.

4. Light-gray breccias from both massifs are also similar; although, as a class, these rocks are variable.

The characteristics of friable matrices, dominance of dark- over light-colored clasts, and local occurrences of foliation are shared by samples from both massifs. Subordinate features of the breccias are also similar in the samples from the North and South Massifs: (1) brown pyroxene-lined vugs occur in rocks from both areas, although they are much better developed in the North Massif samples; (2) rare blue-gray breccias with vesicles were returned from stations 2 and 6; and (3) rare breccias with abundant honey-brown mineral and distinctive dark-gray mineral clasts were found at stations 3 and 7.

Significant differences include the virtual lack of large light-colored clasts and prominent vesicles from the boulders studied at the South Massif. Both these features are found in the North Massif boulder samples; in addition, the station 7 boulder has dikes of blue-gray material injecting a large clast. Minor differences between the North and South Massif
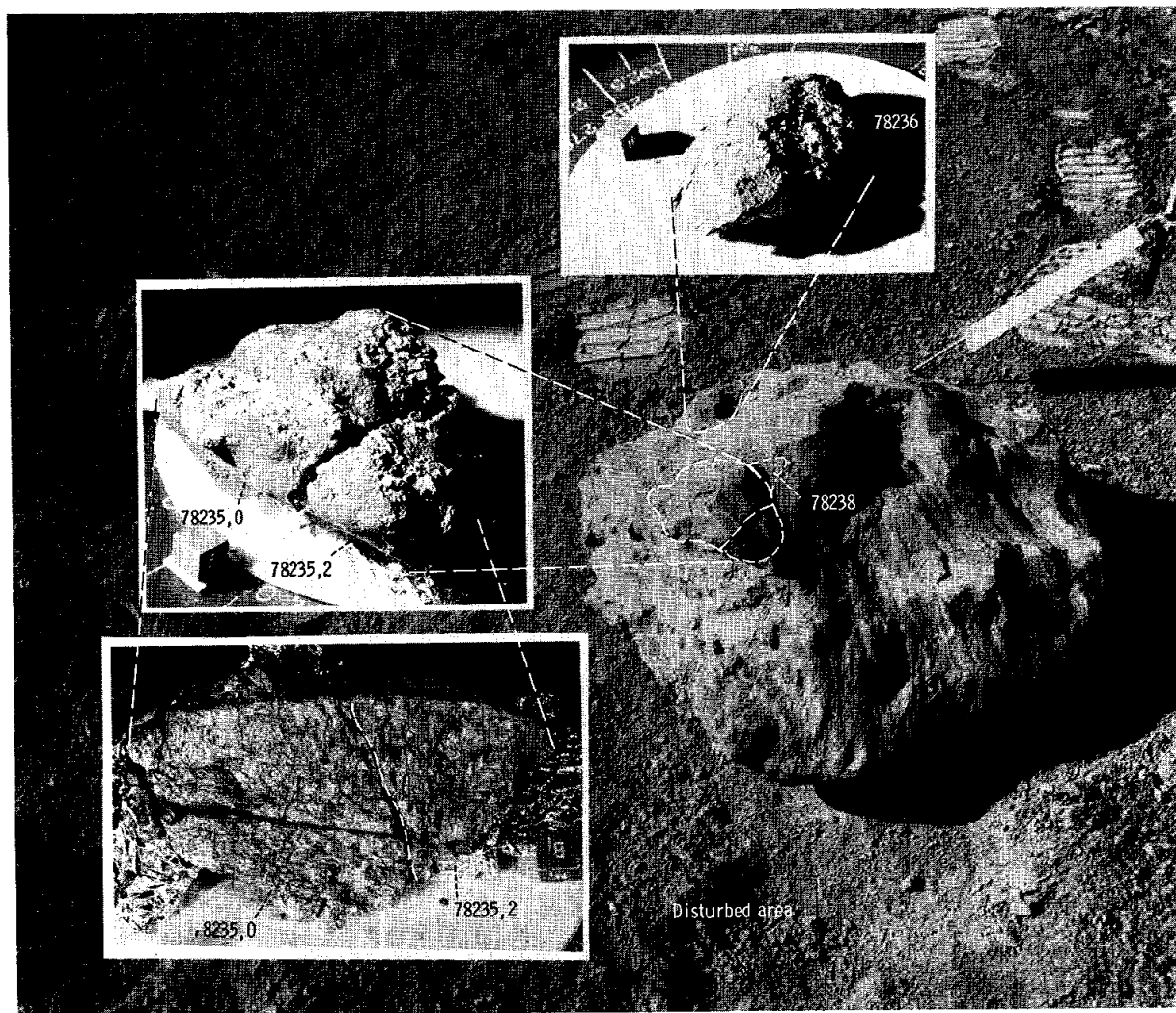
FIGURE 6-40.—Locations and orientations of gabbroic rocks (samples 78235 and 78236) from top of rolled boulder. Fluted surface is glass coated and glass veined (AS17-146-22370) (inset photographs, S-73-17817, 17962, and 17814, respectively).

breccias include: (1) vuggy metaclastic clasts occur only in station 2 breccias; (2) light-gray breccia at station 2 occurs as a large boulder, whereas light-gray breccias from the North Massif are known only as subordinate inclusions in station 6 boulders; and (3) many friable cataclasites were returned from the North Massif.

The similarity of the rock types between the North and South Massifs suggests that the samples may represent only one stratigraphic unit. The greenish-gray breccia, light-gray breccia, and blue-gray breccia, seen as discrete boulders at station 2, are all components of the same boulder at station 6. This evidence indicates that they may come from a single unit in the South Massif. There apparently is an unsampled type of dark rock that occurs high on the North Massif. It may represent a layer or lenses in the upper part of the massif. The foliated and layered breccia (station 2, boulder 1) is different and probably represents the capping blue-gray unit of the South Massif that was recognized in the field by the crew. Boulder 2 at station 2 appeared to the crew to resemble the tan-gray unit that underlies the blue-gray unit of the South Massif.

Subfloor Basalts

Field Occurrence

Subfloor basalts occur in the dark portions of the valley floor both as scattered blocks and fragments and as concentrations of blocks on the walls and rims of the larger craters. The areas in which the basalts were most thoroughly sampled were on the rims of Shorty and Camelot Craters, in the LM/ALSEP/SEP area, and at station 1.

Several varieties of basalt were described on the lunar surface. The predominant types were coarse-grained, vesicular, relatively light-colored basalts composed of clinopyroxene, ilmenite, and 30 to 40 percent plagioclase. Vesicles as large as ≈ 1 cm in diameter typically comprised 10 to 15 percent of these rocks. In some rocks, planar partings paralleled bands expressed as differing concentrations of vesicles. Finer-grained and less vesicular varieties of basalt were recognized locally.

Shorty Crater.—Subfloor basalts were sampled on the rim crest of Shorty Crater in the vicinity of a 5-m boulder (fig. 6-41). Debris that may have been shed from the boulder lies on the nearby surface, and blocks are abundant on this part of the inner crater wall. All the rocks examined were basalts that are commonly intensely fractured; some show irregular knobby surfaces that resemble the surfaces of terrestrial flow breccias.

Shorty Crater is 110 m in diameter and is most probably a young impact crater. Its blocky floor is ≈ 10 to 15 m below the general surface level near the crater, and its walls are largely composed of relatively fine fragmental material. The impacting projectile should have encountered hard rock at a depth of no less than 10 to 15 m, and ejecta was therefore excavated from depths no greater than ≈ 20 m (approximately one-fifth crater diameter). It is possible that basalt fragments on the crater rim may be ejecta derived from within the upper 5 to 10 m of bedrock of the subfloor basalt unit at the Shorty site. An alternative interpretation is that coherent bedrock was not excavated by Shorty and that the basalt fragments on its rim are blocks ejected from pre-Shorty regolith.

Camelot Crater.—Subfloor basalts were collected from the rim of the large (650 m) crater Camelot. The blocks, which are partly buried by soil, are exposed near and along the low, rounded rim crest of the crater and extend downward into the crater walls (fig. 6-42) where, as in other craters, blocks are abundant. Outward from the rim crest, the block population decreases rapidly within a few meters.

Within the block field, individual rocks, varying from cobble to boulder size, are subrounded to
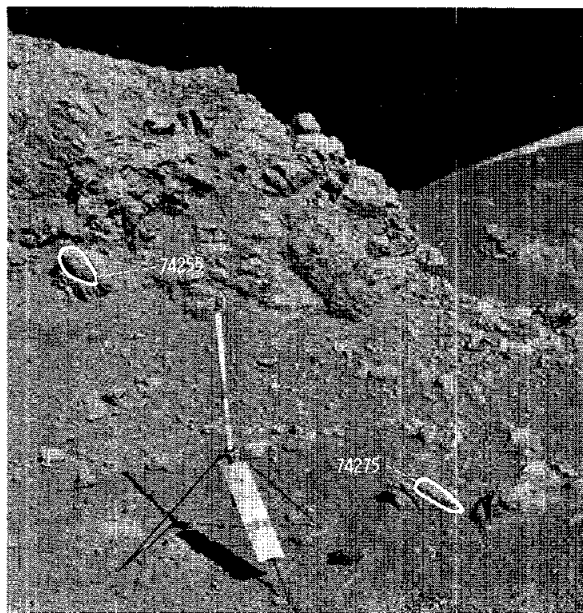
FIGURE 6-41.—Northwest-looking photograph showing intensely fractured basalt boulder on rim of Shorty Crater and locations of samples 74255 and 74275 (AS17-137-20990).
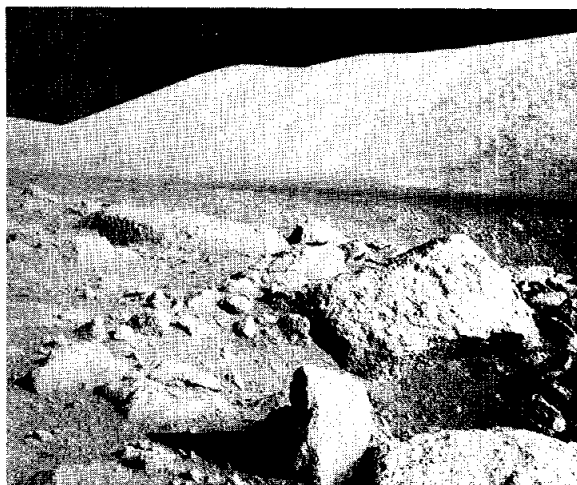
FIGURE 6-42.—North-looking photograph of part of station 5 area showing tabular basalt boulders on southwest rim and inner wall of Camelot Crater. Prominent banding is visible in large block in right near field (AS17-145-22178).

subangular, are moderately to deeply buried, and cover ≈ 30 percent of the surface. The rocks tend to be tabular in shape (fig. 6-42) and no doubt preferentially broke along the well-developed set of partings (fig. 6-43). The partings parallel bands formed by variations in vesicle concentration. Descriptions by the crew indicated that the rocks were predominantly coarse-grained, subophitic, pyroxene-bearing basalts with shiny ilmenite platelets in the vugs and vesicles. The rocks appear to be notably uniform except for gray zones that may represent finer-grained or non-vesicular areas.

The large basalt blocks on the Camelot rim undoubtedly represent ejecta from the crater. Impact theory suggests that the stratigraphically lowest target materials will most probably be located in the ejecta nearest the crater rim and that the maximum depth from which material is likely to be excavated is approximately one-fifth crater diameter—130 m deep in the case of Camelot. However, the crater is old, and the rim has been eroded. The rocks sampled may not, therefore, represent the uppermost part of the original ejecta, and 130 m should be regarded as the maximum possible depth of their origin.

LM/ALSEP/SEP area.—Large boulders of subfloor basalt were observed and sampled in the LM/ALSEP/

SEP area. The crew described the rocks as uniform, coarse, vesicular, porphyritic, clinopyroxene-bearing basalts with ≈ 30 to 40 percent plagioclase and with ilmenite platelets in the vugs and vesicles. Vesicles commonly make up 10 to 15 percent of rock surfaces. A foliated effect is created by partings that parallel bands of differing vesicle concentration. The rocks are commonly fractured. A single set of parallel fractures is visible in one boulder (fig. 6-44), whereas so-called "Geophone Rock" is intricately fractured (fig. 6-45).

Blocks in the LM/ALSEP/SEP area belong to a population of boulders that project through the dark floor material throughout the area east of Camelot Crater. Scarcity of such boulders west of Camelot suggests that the boulders near the LM are probably not Camelot ejecta but rather ejecta from the craters east of the LM in the central cluster.

Station 1.—Station 1 is located on the northwestern flank of Steno Crater ≈ 150 m from the Steno rim crest. Subfloor basalt was collected as small fragments from the soil and as chips from two vesicular 0.5-m boulders on the rim of a 10-m crater (fig. 6-46). As at Camelot Crater, the large boulders are bounded in part by tabular faces and contain parallel parting planes. A distinct planar boundary between coarsely vesicular basalt and finely vesicular basalt is oblique to a set of parallel fractures in one of the boulders.

FIGURE 6-43.—Northwest-looking photograph of vesicles and prominent parallel partings in basalt boulder on southwest rim of Camelot Crater. Bootprint treads (lower right) are ≈ 2 cm wide (AS17-133-20333).
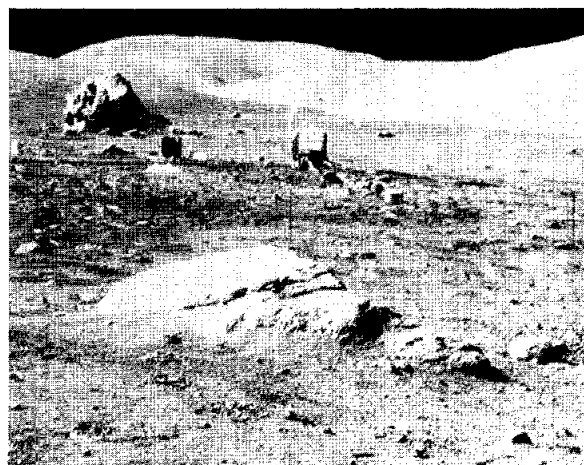
FIGURE 6-44.—South-looking photograph showing parallel fractures in 0.5-m-high boulder south of deep drill site. Geophone Rock is at upper left (AS17-134-20505).
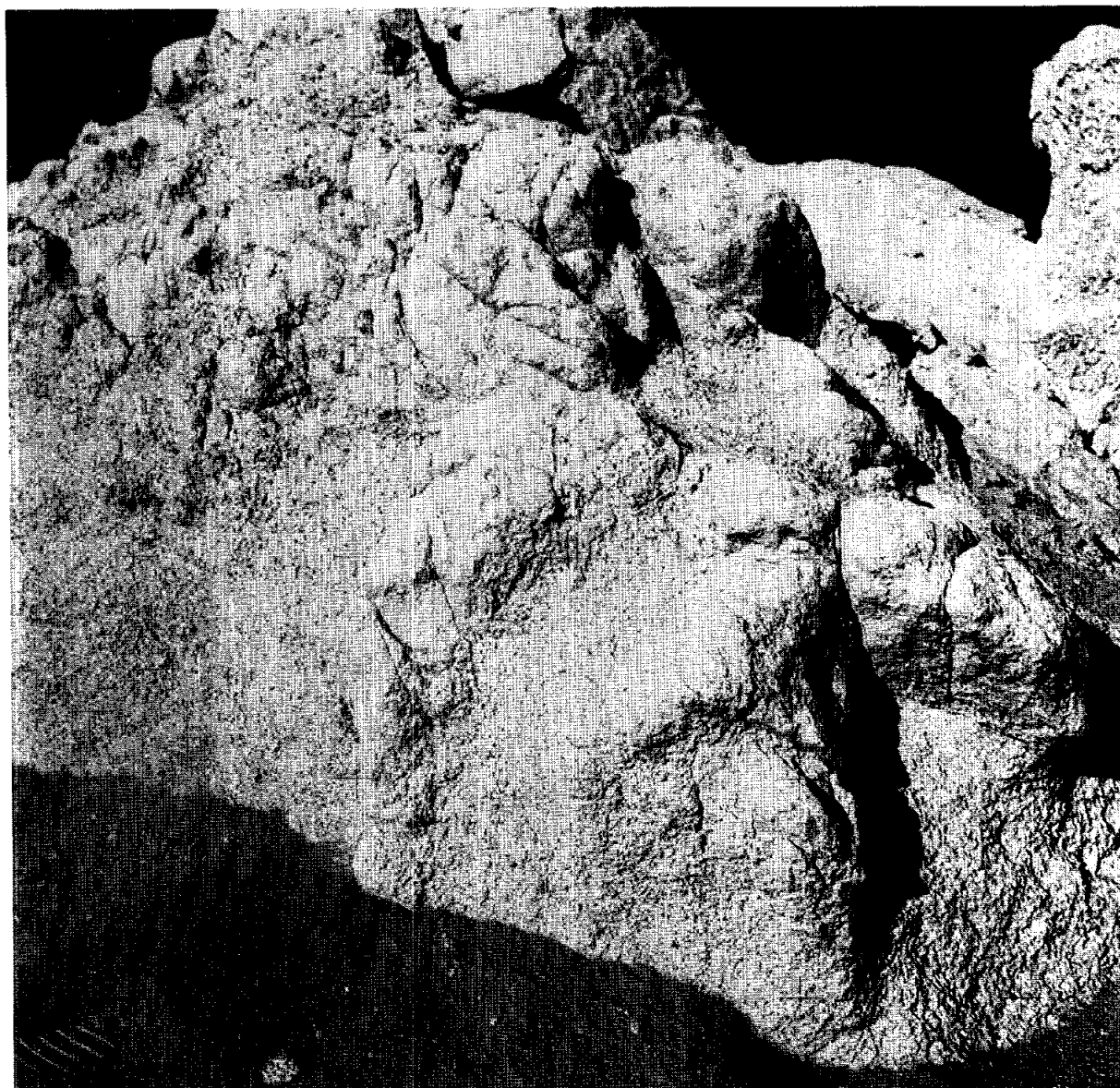
FIGURE 6-45.—Southwest-looking photograph of Geophone Rock, an intricately-fractured, vesicular, 3-m-high basalt boulder (AS17-147-22535).

The 10-m crater presumably reexcavated basalt blocks from within the upper 2 m of the ejecta blanket of Steno Crater. Steno Crater is 600 m in diameter; the maximum depth from which rocks might have been excavated in the Steno impact is ≈ 120 m. The sampled blocks occur approximately one-fourth crater diameter from the Steno rim, however, and probably were derived from some intermediate depth in the Steno target.

Petrography

Returned basalt samples may be divided into five classes of hand specimens:

1. Vesicular, porphyritic, coarse-grained basalts
2. Vesicular coarse-grained basalts
3. Vesicular fine-grained basalts
4. Dense aphanitic basalts
5. Vesicular aphanitic basalts

FIGURE 6-46.—Northwest-looking photograph showing 10-m crater at station 1 with sampled 0.5-m boulders on its rim. Boulder in foreground contains distinct planar boundary (solid line) between zone of coarse vesicles (left) and zone of fine vesicles (right). Dashed lines indicate traces of planar fracture set dipping to right (AS17-136-20741).

Individual samples of types (1) and (2) were generally termed "vesicular gabbro" by the Apollo 17 crew. Examples of (3), (4), and (5) were described as "fine-grained basalt," "basalt," and "obsidian," respectively.

Rocks called vesicular, porphyritic, coarse-grained basalts are characterized by 3- to 4-mm, blocky, pyroxene-ilmenite intergrowths that are present in amounts ranging from 5 to 15 percent in the basalts of this class. Olivine is present in trace amounts in some of these rocks; where present, it commonly occurs as partially reacted cores in the pyroxene phenocrysts. The ilmenite content, while high for mare basalts as a whole, is relatively low compared to other Apollo 17 basalts and averages between 15 and 20 percent. The plagioclase content averages 25 to 35 percent. Some layering occurs in larger hand samples: in one case, grain-size variations are noted; in others, feldspar and ilmenite laths are alternately foliated and randomly oriented. Vugs are more common than vesicles, although both may be present in the same rock. Cavity content is variable but averages 10 to 15 percent; vugs are alined in planes, are clearly elongate, and are layered by abundance. Sample 70035 is a typical example of this class of basalts.

Vesicular coarse-grained basalts are very similar to those of the above class except that they lack the pyroxene-ilmenite phenocrysts, and their average grain size tends to be somewhat finer (≈ 1.0 mm). This class of basalts is typified by sample 75055.

Vesicular fine-grained basalts are characterized by a high proportion of vugs and vesicles with ilmenite-rich linings and by a groundmass grain size ranging from 0.3 to 0.6 mm. Olivine is commonly present in rocks of this class as microphenocrysts in amounts of 1 to 2 percent. These rocks are characterized by vug and vesicle abundances of more than 30 percent; some are frothy. Sample 71055 is a typical example of this class of basalts.

Dense aphanitic basalts are characterized by their very low abundance of cavities and their extremely fine grain size. Olivine microphenocrysts are widely represented but not abundant. The average grain size of these rocks is ≈ 0.1 to 0.2 mm. Sample 70215 is typical of this class of basalts.

Vesicular aphanitic basalts are characterized by abundant and exceptionally large cavities and very fine grain size. Small amounts of olivine are present in some samples. Vugs are commonly as large as a centimeter and reach 3 to 4 cm. Sample 74235 typifies this group.

It is possible that the two coarse-grained basalt types are gradationally related by decrease of porphyritic pyroxene-ilmenite aggregates, but our best judgment at present is that they represent separate flow units. It seems more likely that the vesicular fine-grained basalts are gradationally related to the vesicular aphanitic basalts through decrease in grain size and increase in vesicle size. The dense aphanitic basalts seem clearly to be fragments of a separate flow unit.

A few samples cannot at present be fitted into these five categories. Samples 71549, 71557, and 71568 are coarse-grained basalts, but we cannot at present say whether or not they are porphyritic. Sample 71597 contains 20 to 25 percent olivine—more than any other basalt in the Apollo 17 collection.

Stratigraphy

A classification of basalts by type and Lunar Receiving Laboratory (LRL) number is summarized in table 6-IV. Station numbers are implicit in LRL numbers. (LRV samples are given the station number to which the LRV was proceeding when the sample was taken.) As evidenced by table 6-IV, the five basalt types have a fairly wide distribution over the traverse area. It is also apparent that the distribution is asymmetric in detail: for example, only one coarse-grained basalt was collected at station 4, and no fine-grained types were collected at station 5.

TABLE 6-IV.—*Hand Specimen Classification*[a] *of Apollo 17 Basalts*

Vesicular, porphyritic, coarse-grained basalts	Vesicular coarse-grained basalts	Vesicular fine-grained basalts	Dense aphanitic basalts	Vesicular aphanitic basalts
[b]70017	[b]70185	[c]71035 and 71036	[d]70075	[d]71075
[c]70035	[d]71049	[c]71055	[b]70215	[d,e]71525 to 71528
[c]70135 to 70139	[d]71067 and 71068	[d]71087	[b]70255	[d,e]71546 and 71547
[c]70145 to 70149	[d]71086	[c]71135 and 71136	[d]71048	[d,e]71555
[c]70155 to 70157	[d]71503	[c]71155 to 71157	[d]71065 and 71066	[b,e]71577 and 71578
[d]70165(?)	[c]75015	[b]71175	[d]71089	[d,e]71585
[b]70275	[c]75035	[d]71507	[d]71096 and 71097	[d,e]71587
[b]70315	[c]75055	[d,e]71535	[d]71505 and 71506	[d,e]71596
[d]71045 to 71047	[d]78505	[d,e]71548	[d,e]71529	[b]74235
[d]71069	[d,e]78575(?)	[d,e]71556	[d]71537 to 71539	[d]74245
[d]71085		[d,e]71558	[d,e]71545	[d]74247
[d]71088		[b]71565 to 71567	[d,e]71569	[d]74249(?)
[d]71095		[b]72155	[d,e]71575 and 71576	[d]74285(?)
[d]71509		[b]72155	[d,e]71579	[d]74286
[d,e]71536		[d]76136	[d,e]71586	[d,e]78585
[d,e]71559		[b]77516	[d,e]71588 and 71589	[d,e]79516(?)
[c]74255(?)		[d]78507(?)	[d,e]71595	
[b]75075		[d]78509(?)	[d]73219	
[d]76037		[d,e]78577	[d]74246	
[d,e]76538		[d,e]78578	[d]74248	
[b]77535		[d,e]78579	[d]74248	
[b]77536		[d,e]78588	[d]74287(?)	
[b]78135(?)		[b,e]78597	[c]74275	
[d]78506		[d,e]79515(?)	[d,e]76537	
[d]78576			[d,e]76539	
[b]79155(?)			[d,e]78569	
			[d,e]78586	
			[d,e]78587	
			[d,e]78589	
			[d,e]78595	
			[d,e]78596	
			[b,e]78598	
			[b,e]78599	

[a]Rake samples 71549, 71557, 71568, and 71597 not classified at this time. (?) indicates questionable classification.
[b]Loose rock > 5 cm.
[c]Chip from large boulder.
[d]Small fragment 1 to 5 cm.
[e]Rake sample.

Because large blocks are less likely to have been reworked than small ones, the general relation of basalt fragments to their source craters is probably better established from the larger blocks. The basalts listed in table 6-IV are therefore subdivided on the basis of whether they were collected from sizable blocks, whether they were loose rocks on the surface, or whether they were collected as small fragments in soil or rake samples. Sample distribution by size and by classification type for all basalts examined to date is plotted on a traverse map (fig. 6-47).

As shown in figure 6-47, large blocks were sampled only on the rims of Shorty and Camelot Craters, in the LM/ALSEP/SEP area, and at station 1. Large blocks can be confidently related to specific source craters only at Camelot and station 1, where some limits on depth of origin can be inferred. In general, the small fragments appear widely mixed, and their distribution seems to have little stratigraphic significance.

The large blocks on the rim of Camelot Crater are, so far as we know, all composed of vesicular
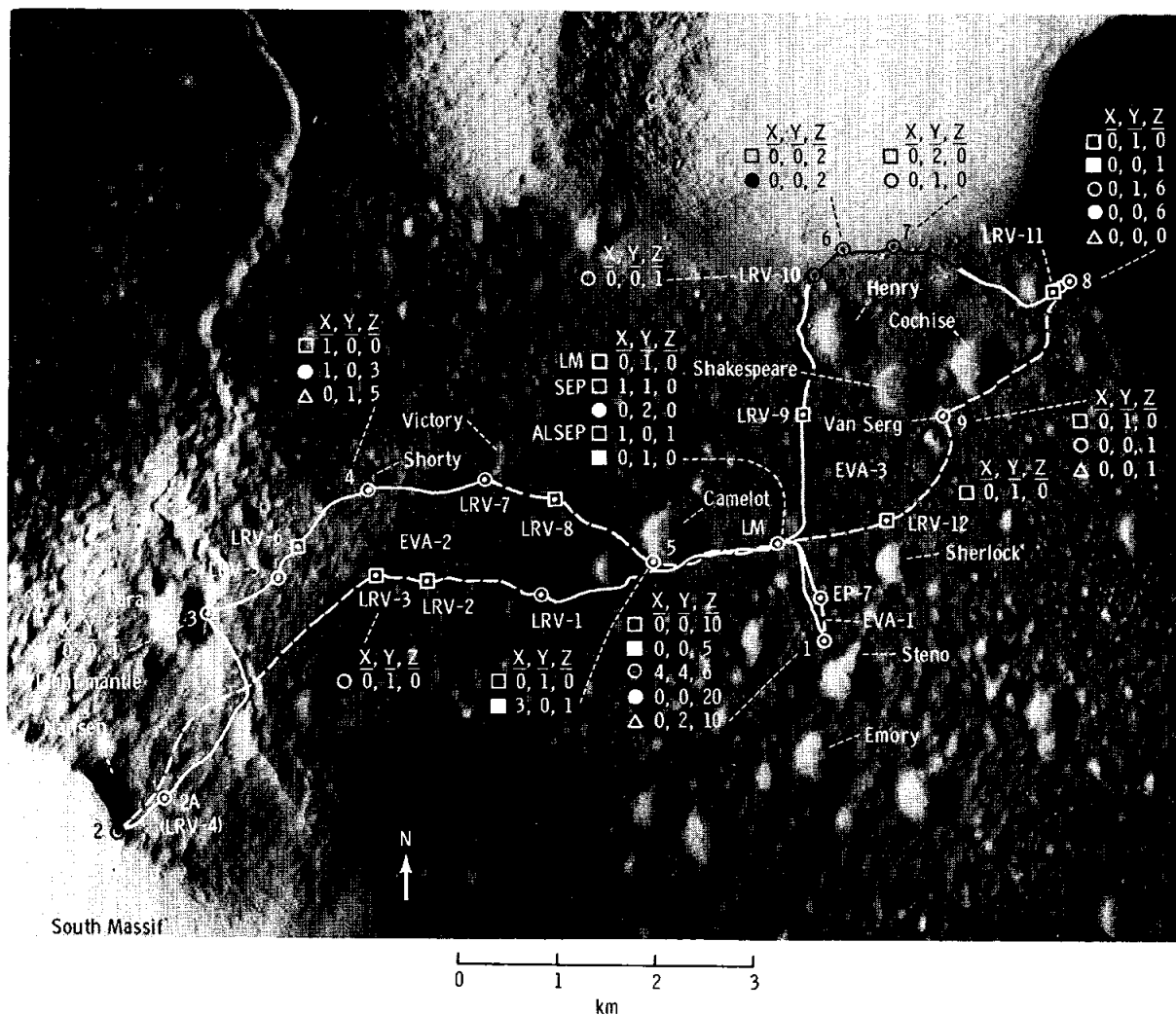
FIGURE 6-47.—Map showing distribution of subfloor basalt samples by size and type (Apollo 17 panoramic camera frame AS17-2309).

coarse-grained basalt. The maximum depth from which the basalt boulders on its rim were excavated is ≈ 130 m. Vesicular coarse-grained basalt, represented by Camelot rim ejecta, may be the deepest subfloor material sampled on the mission, and the contact between vesicular coarse-grained material and the

next shallower unit may be at some depth < 130 m.

At station 1, which lies approximately one-fourth crater diameter out on the flank of Steno Crater, the larger blocks and most of the loose rocks larger than 5 cm in diameter are of vesicular fine-grained basalt. The station is within the mappable continuous ejecta

of Steno. If these are original Steno ejecta, material from intermediate depths (< 120 m) could be expected in that part of the ejecta blanket.

In the LM/ALSEP/SEP area, the large blocks are vesicular, porphyritic, coarse-grained basalts. They belong to the population of large blocks that characterized the central cluster ejecta (see section entitled "Regolith and Mantle Units of the Valley Floor"). Those in the LM area are difficult to relate to the continuous ejecta of any single crater and may, in fact, represent rays or ballistic ejecta from one or more central cluster craters. If so, they could have been derived from any depth within the sequence penetrated by the central cluster craters. The largest craters are ≈ 600 m in diameter; hence, maximum sampling depth is ≈ 120 m (one-fifth crater diameter). If this rock type intergrades with the vesicular coarse-grained basalt sampled at Camelot, it probably comes from a slightly higher stratigraphic level.

Except for the intensely fractured 5-m boulder at Shorty, which is vesicular, porphyritic, coarse-grained basalt, all fragments collected there are of dense aphanitic or vesicular aphanitic basalt. If the interpretation that the coarse basalts are related is correct, the large 5-m boulder may have been reexcavated by Shorty Crater from the ejecta of some older large crater. The absence of this basalt among the other fragments that were collected at Shorty also suggests that it does not represent the upper part of the local bedrock, whereas the exclusive concentration of aphanitic basalt fragments suggests that these may indeed represent shallow bedrock.

Sampled subfloor basalts were most probably derived from depths between ≈ 20 and 130 m. The stratigraphically lowest basalt unit is interpreted to be the vesicular coarse-grained basalt sampled at the Camelot rim. This unit may grade upward into the coarse-grained porphyritic type sampled in the LM/ALSEP/SEP area. The next stratigraphic unit, proceeding upward, is the vesicular fine-grained basalt represented in the Steno ejecta, and the aphanitic basalts of the Shorty ejecta may be the shallowest recognizable types. It should be stressed that this stratigraphic succession is speculative.

Origin

The landing site valley is interpreted to be a deep graben formed at the time of the Serenitatis impact event. Geophysical data collected during the mission suggest that the graben floor is overlain by 1 km or more of high-density material (secs. 10 and 13). The sampled part of the subfloor basalt is interpreted to represent the upper part of the high-density graben-filling material, which may consist entirely of basalt. Radiometric age determinations (ref. 6-6) suggest that filling of the valley by lava flows may have been completed by approximately 3.8 billion years ago. Before the final accumulation of the Serenitatis mare fill, broad arching east of the Serenitatis basin tilted the subfloor lavas to the east as shown in the present 1° eastward tilt of the valley floor.

Highlands Regolith and Surficial Deposits

The formation of a regolith of impact-generated debris has been a continuous process in the highlands of the Taurus-Littrow area as elsewhere on the Moon. The amount of regolith formed on any surface is porportional to the length of time that the surface has been exposed to bombardment by impacting bodies, whereas the thickness of regolith now present is also a function of the rate of removal of the loosened debris. Theoretically, there is no net loss of debris on flat surfaces because the debris ejected from a point of impact is balanced by the influx of debris from nearby and distant impacts. On slopes, there is a net loss of regolith as impacts at lower levels fail to throw balancing amounts of debris to the higher levels. Such a net loss of debris, sufficient to expose bedrock, occurs at the lip of Rima Hadley, the Apollo 15 landing site (ref. 6-7).

The rolling tops of the massifs and the Sculptured Hills are considered very old surfaces with thick accumulations of regolith. On the generally flat surface above the Sculptured Hills, in particular, very thick regolith is implied by the close spacing of the many large craters. The regolith there is probably several tens of meters thick.

The upper slopes of the massifs are nearly free of regolith as shown by exposures of bouldery zones that may represent near-surface bedrock. Such zones occur on the upper one-third of the South Massif, high on the East Massif, and on the upper two-thirds of the North Massif. These zones seem to have been the sources of most of the large boulders now resting lower on the slopes as indicated by boulder tracks. The slope of the Sculptured Hills just above station 8 is either mostly covered with thick regolith or is

composed of material so friable that boulders or bedrock ledges are rapidly disintegrated by impact.

In addition to the net downslope movement of ejecta, loose material tends to roll, slide, or bounce down steep slopes in response to gravity. Such movements may be initiated by jarring due to impacts or seismic events or by oversteepening of slopes by cratering or faulting. Deposits formed by these processes are distinguished herein as surficial deposits.

Volumetrically, the most important surficial deposit is talus, a poorly sorted deposit composed of debris that has arrived essentially piece by piece at its place of deposition on the lower slopes. The boulders resting near the bases of slopes and at the ends of trails leading down the slopes are clearly visible parts of the talus. Impact fragments thrown onto the lower slopes also comprise part of the talus. At the bases of large slopes, the talus forms a continuous apron. Separate talus streaks rather than aprons are clearly visible on the inner slopes of some of the large fresh craters in the region.

Other surficial deposits, denoted herein as mass movement deposits, occur as masses of debris that lie beyond the bases of the slopes. These deposits result when masses of loose debris, mostly regolith, move downslope as tumbling or sliding units driven by gravity and gather sufficient momentum to move beyond the steep slopes. These materials are commonly set in motion by some jarring event or when they become unstable on oversteepened slopes.

Surficial deposits are undoubtedly present on the lower parts and at the bases of all the large steep slopes of the highlands. Gentle intermediate slopes near the base may reflect the occurrence of a high-lava mark of subfloor basalt. The slopes are more probably talus deposits that may have been partly redistributed valleyward by impacts. At stations 2, 6, and LRV-10, located on the gentle slopes immediately above the valley floor, fillets occur preferentially on the upslope sides of boulders, which indicates that debris is currently moving downslope.

Along much of the base of the South Massif, the talus intersects the valley floor at a sharp angle, which suggests that downslope movements have been renewed so recently, perhaps as a consequence of recent massif uplift, that impact processes have not had time to round the knickpoint. Part of this talus deposit has filled approximately three-fourths of Nansen Crater. The Nansen impact undoubtedly caused oversteepening at the base of the talus slope.

Probably the oversteepened, already fragmented rock debris started moving immediately to fill enough of the crater to reestablish equilibrium at the angle of repose.

Except for a few boulders with enough energy to climb slightly up the opposing slope of the north wall of Nansen, the debris merely slid into the crater but did not cross it. The present appearance of the massif slope into Nansen is that of an active talus apron that is slowly continuing to fill the crater.

The best documented mass movement deposit is the light mantle at the base of the South Massif, which is presumed to be a mass of debris that obtained enough kinetic energy to spread out across the valley floor for a distance of ≈ 6 km. In several places, there is evidence for mass movement deposits older than the talus aprons. Subdued lobes extend from the highland slopes onto the valley floor along the base of the North Massif and along the base of the South Massif between Nansen Crater and Bear Mountain. It is possible that some of these lobes are mass movement deposits overlying the subfloor basalt.

Mass movements and formation of talus deposits should date back to the earliest uplift of the massifs. If the bounding faults were, as we suppose, steeper than the angle of repose for loose fragments, there must have been a large transfer of material down the newly formed slopes until the angle of repose was reached. Thus, mass movement deposits and thick talus aprons buried by subfloor basalt are inferred to overlie the still older rocks that formed the initial floor and walls of the Taurus-Littrow valley.

Regolith and Mantle Units of the Valley Floor

The subfloor basalt is overlain by fragmental debris that is as much as 15 m thick where it is cut by Shorty and Van Serg Craters. A complete understanding of this material must await detailed descriptions of the numerous soil and core-tube samples. Part of the material is undoubtedly impact-generated regolith similar to that developed on mare basalts elsewhere on the Moon. Premission geologic maps of the Apollo 17 site (ref. 6-1) indicated, in addition to normal regolith, light and dark mantle units. The light mantle unit was identified and sampled at stations 2, 2A, and 3 and at LRV sample stops 2, 5, and 6. The dark mantle was not recognized on the lunar surface as a distinct stratigraphic unit; a unique darkening com-

ponent, if present, is apparently intimately mixed with the impact-generated regolith.

In this report, the fragmental material overlying the subfloor basalt is divided into an older regolith, information on which comes mainly from the Van Serg Crater ejecta, and a younger regolith that occurs at or close to the surface. In addition, major crater ejecta blankets around the central crater cluster and Shorty and Van Serg Craters are mapped and described as separate portions of the surficial debris layer. Inferred stratigraphic relationships among these units are shown in figure 6-48.

Petrography of Regolith Breccias

A total of 14 samples of breccia (70018, 70019, 70175, 71515, 72135, 79035, 79115, 79135, 79175, 79195, 79225, 79226, 79227, and 79228) was collected from the valley floor at stations 1, 9, LM/ALSEP/SEP, and LRV-1. Most of the samples are probably soil breccias ejected from the older regolith. Some, however, such as 70019, are soil breccias formed by impacts in the younger regolith. These breccias are all dark to very dark gray, are friable to moderately coherent with numerous penetrative fractures, and typically have low clast populations.

Samples 79115 and 79135 are layered, with alternating layers on the order of several centimeters thick that are distinguished by differing clast abundances. Similar layering is also visible in lunar surface photographs of breccia boulders at Van Serg Crater (fig. 6-49). Surfaces of penetrative fractures are commonly weakly slickensided, as was typical of regolith breccias returned from earlier Apollo missions. Slickensides are especially well developed in sample 79135. Clasts larger than 1 mm make up from 1 to ≈ 15 percent of the breccias; most clasts are smaller than 1 cm, although the crew reported clasts as large as 0.5 m in breccias of this type at Van Serg

Crater. Samples 70019 and 79175 are breccias composed of friable dark clods loosely cemented by dark glass; these also closely resemble rocks returned by earlier Apollo missions.

Regolith breccias were also found at two areas marginal to the valley floor. Five small breccia fragments (78508 and 78515 to 78518) were found in a soil sample from station 8. Samples taken from SWP Crater (e.g., 78120), did not survive in pieces larger than 1 cm but appear to be similar to the other regolith breccias.

Older Regolith

The ejecta of the 90-m-diameter Van Serg Crater includes a large proportion of soft, dark, matrix-rich breccias (figs. 6-49 and 6-50) the petrography of which is described in the preceding section. On the crater rim, the breccias contain scattered light-gray lithic clasts that are as large as ≈ 2 cm in diameter. Light clasts as large as 0.5 m in diameter were seen in the dark-matrix fragment-rich breccia on the crater floor.

The Van Serg breccias can be interpreted as regolith materials indurated by the impact that formed Van Serg Crater. So far as we know, subfloor basalt was not excavated by the impact, although traverse gravity data (sec. 13) imply its presence in the subsurface. At least 15 m of regolith material is

FIGURE 6-49.—South-looking photograph of layered dark matrix-rich breccia in the ejecta of Van Serg Crater (AS17-142-21821).

FIGURE 6-48.—Schematic diagram of stratigraphic nomenclature of valley floor deposits.

FIGURE 6-50.—West-looking photograph showing dark matrix-rich breccia boulders on rim of Van Serg Crater. Note small white clasts in the foreground boulder and sheared aspect of boulder to the right of the gnomon (AS17-142-21791).

interpreted to have overlain the subfloor basalt in the Van Serg area when the crater was formed. The deepest part, represented by the Van Serg rim and floor rocks, is presumed older than the central cluster ejecta and hence represents older regolith material.

Central Cluster Ejecta

The regolith is subdivided locally by recognizing as unique a portion that is considered to be the complex ejecta blanket of a cluster of large craters that lie mostly to the south and east of the LM (fig. 6-51). This unit, distinguished by an abundance of blocks visible at the surface, is termed the central cluster ejecta. Younger deposits are apparently too thin to bury the blocks in the unit, and the unit is too young for the blocks to have been reduced much in size by later impacts. The general distribution of blocks considered as central cluster ejecta is shown in figure 6-51. It is assumed that beyond a crater diameter from the nearest crater of the cluster, the fine-grained ejecta will be present in significant amounts only discontinuously. The unit probably does not extend as far as the LRV station at Tortilla Flat but may coat station 5.

The shape of the central cluster ejecta unit must be that of a very complex lens as it is composed of the ejecta, rim, and continuous blanket deposits of each of the craters within the cluster. At station 1, a 2-m-deep crater does not appear to have penetrated the total thickness of the unit, which is expectable because station 1 is only approximately one-fourth crater diameter out from the rim of Steno, a member of the cluster. At the deep core site, ≈ 40 m north of the ALSEP central station, the central cluster ejecta is assumed to be thin because the site is more than a crater diameter away from any large member of the cluster. The deep core probably penetrated the entire unit; the change of soil appearance, seen in corestem joints, at a depth of ≈ 1 m probably indicates the base of the central cluster ejecta.

All blocks from the central cluster ejecta that were sampled are considered to be subfloor basalts. Smaller sampled fragments are more difficult to relate to a source, but the preponderance of surface rock fragments from the LM/ALSEP/SEP and station 1 sites must have come from the subfloor basalt either directly or after reexcavation. Soil samples in the area must be considered as originating from the overlying younger regolith unit. The ejecta of the central cluster unit is inferred from crater depths and estimated regolith thickness to contain roughly three times as much subfloor basalt as older regolith. The older regolith contains a large percentage of fine basalt fragments, so the expected amount of basalt in the central cluster ejecta, or later reexcavated deposits, is at least 80 percent. A net effect of the central cluster ejecta was to create an immature regolith surface layer overlying what must have been, in general, a very mature regolith. The immaturity is most easily seen in the common occurrence of blocks and rock fragments. It is also reflected in the lithologic composition by the high percentage of fragments newly derived from the subfloor basalt and a little admixture of exotic components such as ejecta from impacts in the highlands.

Samples collected from the central cluster ejecta, either directly from boulders protruding through the younger regolith or from reexcavated parts of the unit adjacent to some recent crater, would be expected to consist mostly of subfloor basalts that originally came from the uppermost 120 m of that unit.

Younger Regolith

Premission mapping of the Taurus-Littrow valley
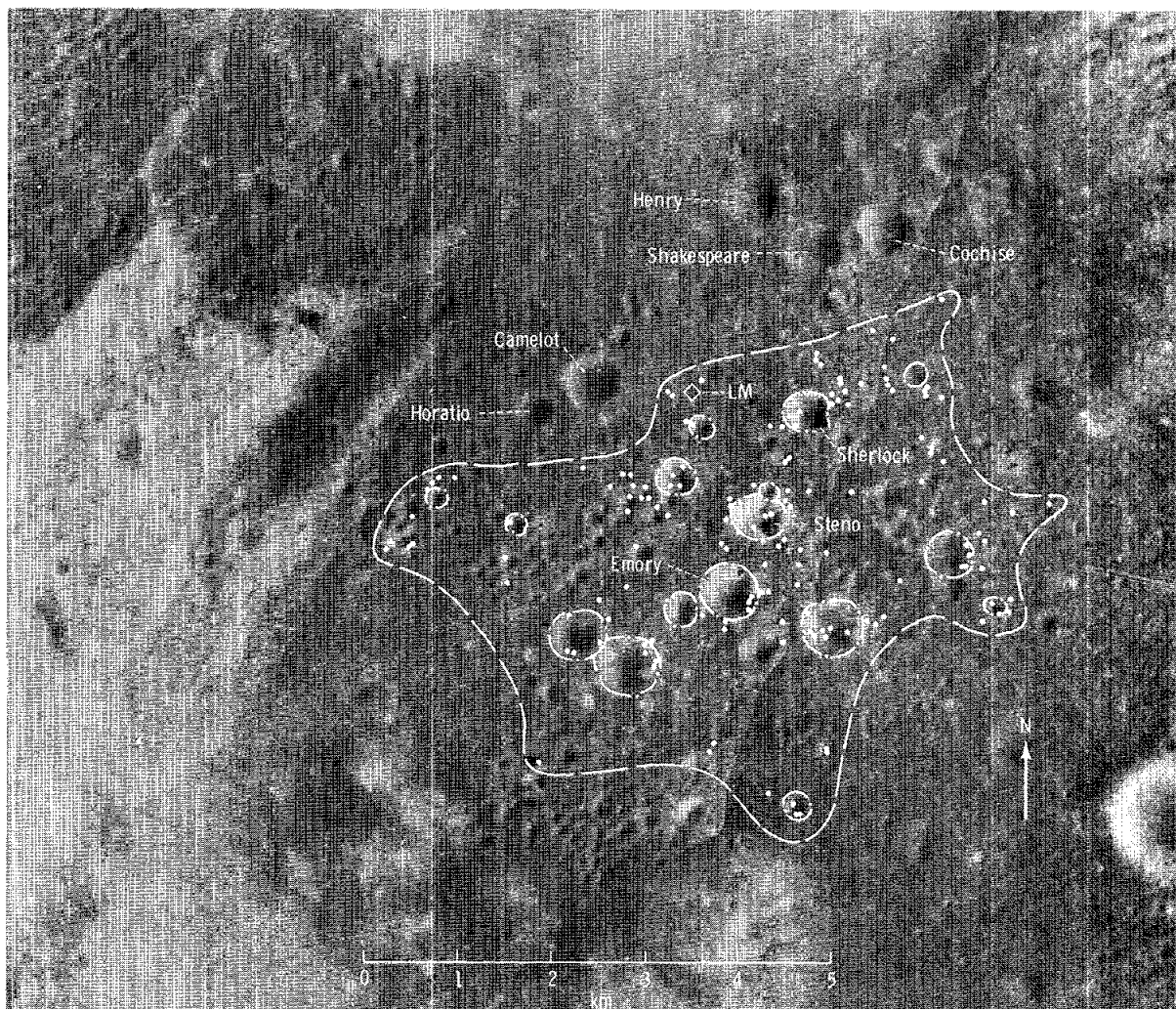
FIGURE 6-51.—Map showing the craters of the central cluster, related boulders, and the outline of the central cluster ejecta.

showed the valley floor to be covered with a dark mantle unit considered younger than the subfloor basalts and older than the light mantle. With the recognition of the central cluster ejecta unit, the definition of the dark mantle must be modified. The surface layer of material that overlies the central cluster ejecta where it is present is herein considered as a unit, composed of both regolith and whatever dark mantle may be present, and is termed the younger regolith. The surface of this unit was traversed, so all shallow soil samples should be part of it. The light mantle is considered as a local unit that is equivalent to some central part of the younger regolith. Regolith younger than the central cluster ejecta is certainly present at the landing site, but a

unique component that can be called dark mantle has not been identified. The reasons for having postulated a dark mantle unit during premission mapping remain valid and will be briefly stated. The findings of the Apollo 17 crew will then be summarized.

An area of very low albedo is present along the southeastern edge of the Serenitatis basin as shown on full-Moon photographs (fig. 6-52). The boundaries of this area have been mapped somewhat differently by various mappers and the interpretations of the very low albedo have differed, but the presence of an anomalous area has been recognized by previous workers (refs. 6-1 and 6-2 and part B of sec. 29). Photographs taken during the Apollo 15 mission indicated that dark areas existed along the edge of
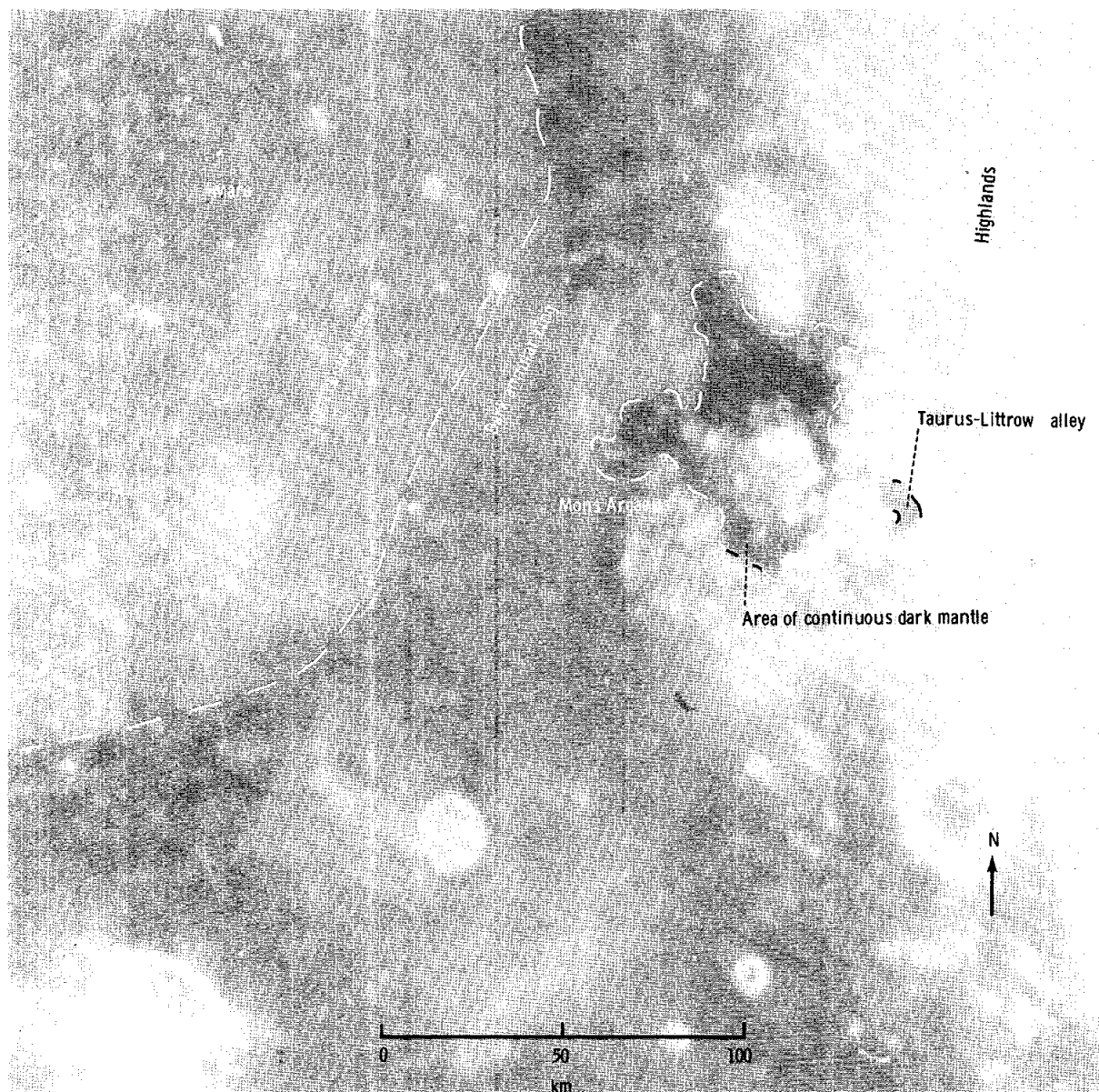
FIGURE 6-52.—Earth-based telescopic view of southeastern part of Mare Serenitatis showing light central mare, dark annular ring, and dark mantle (U.S. Navy photograph 5819).

Mare Serenitatis, in the valleys to the southeast, and as spots and discontinuous coatings in the highlands. This distribution seemed to require an interpretation of a thin mantling unit that conformed to underlying topography. Several experiments seemed to confirm the presence of a dark mantle unit, especially the spectral results that indicated a compositional difference from other mare volcanic types (ref. 6-8).

Because it is widespread, the dark mantle was interpreted as most likely to be a volcanic pyroclastic deposit with many source vents located both in the highlands and in the valleys. The thickness was considered to range from as much as 20 m to as little as a few centimeters within the traverse area planned for the Apollo 17 crew. The reasons for the existence of a dark mantling unit are discussed in detail in part B of section 29.

The photographs taken from orbit during the

Apollo 17 mission permit a reevaluation of the very-low-albedo area seen on the full-Moon photographs. The low Sun angles of the Apollo 17 photographs permit individual mare units to be separated. A comparison of the Apollo 17 photographs with the full-Moon photograph shows that, in the Mons Argaeus area, the dark mantle edge cuts across mare unit contacts and is thus independent of the mare units. In the Mons Argaeus area, the dark mantle apparently overlies the high-albedo, main mare unit of Mare Serenitatis. As shown in figure 6-52, the very low albedo of the dark mantle unit extends from the Mons Argaeus area eastward to include the landing site. Hills west of the landing site, in addition to having a very low albedo, have a more rounded and subdued appearance than adjacent brighter hills as though covered by a thin mantle.

In summary, the weight of evidence favors the formation of a dark mantle sometime after the deposition of the subfloor basalt in the Taurus-Littrow region. Evidence that the mantle is substantially younger than the subfloor is present in one area to the west of the landing site. The dark material apparently has been mixed with underlying material into a regolith unit.

The thickness of dark mantle that was suggested in premission studies ranged from several centimeters to 20 m. The 20-m thickness was based on the hypothesis that Shorty Crater had ejected only dark mantle from beneath light mantle. Most of the thickness at Shorty between the light mantle and subfloor basalt is now considered older regolith, and no distinct dark mantle layer was seen. If only several centimeters of dark mantle were present, it could be mixed with the regolith portion of the valley fill unit. Although no unique dark mantle component has been identified at the Apollo 17 site, the evidence for such a component at the edge of Mare Serenitatis seems inescapable. The low albedo may be caused by the presence of many tiny opaque black spheres found in the soils (sec. 7).

New photographs from orbit reinforce other evidence for the existence of a mantling component in the Family Mountain region just a few kilometers west of the traverse route. The evidence is the presence of surface areas that appear distinctly different. On Lunar Orbiter V and Apollo 15 photographs, a triangular area, which appeared slightly out of focus or fuzzy, had been noticed between Family Mountain and the South Massif. This area includes the cone considered as a cinder cone (ref. 6-9). On the Apollo 17 photographs taken at a low Sun angle, the area has many sharply defined small craters, but larger features are definitely more rounded in appearance than they are in adjacent areas. The best explanation seems to be that the area is a unit of mantling material of local extent. Its area might include the western edge of the light mantle. Two other small areas of smooth surfaces nearby are adjacent to steep slopes; the smoothing unit, however, could be debris derived from the nearby slopes.

In general, the areas of smooth surface are considered to be evidence for dark mantle, and their nearness to the traverse area suggests that at least a few centimeters of dark mantle might exist in the traverse area. Such a thin unit with the degree of cratering seen in the smooth areas would be gardened by impacts to a depth greater than its thickness; that is, it would not exist as a pure layer but would be mixed with underlying material into a regolith layer.

Light Mantle

The light mantle is a deposit of high-albedo material with finger-like projections that extend 6 km across dark plains from the South Massif. The light mantle was interpreted from premission photographs as a probable landslide or avalanche from the steep northern slope of the South Massif (refs. 6-1 and 6-10). The samples collected at stations 2, 2A, and 3 on the light mantle are similar to those that comprise the South Massif, which supports this hypothesis (sec. 7). A cluster of apparent secondary craters that is visible on top of the South Massif in the low-Sun-angle panoramic camera photographs from Apollo 17 may record the impacts that initiated the avalanche.

Thirteen rock samples were collected from stations on the light mantle. Three of these samples (73155, 73217, and 73235) are blue-gray breccias with light-gray clasts and appear to be very similar to those collected at station 2. Sample 73217 is unusual in that it has a blue-gray portion of the breccia with a veneer on one edge that is composed of blue-gray and white sugary clasts in a friable light-gray matrix. The main body of this rock may be a clast from light-gray breccia. Two samples (73215 and 73255) are light-gray breccias composed of gray clasts in a light-gray friable matrix and appear to be very similar to those sampled from boulder 1 at station 2. Sample 73215 has a crude foliation resulting from alternating bands

of gray and white material. Three samples (73216, 73218, and 73275) are greenish-gray breccias and appear to be similar to those collected from boulder 2 at station 2. Five samples collected at LRV-6 (74115 to 74119) are very friable, medium light-gray regolith breccias that contain a few white clasts.

The materials of the light mantle have an albedo of ≈ 20 percent at the surface, which is slightly lower than the 25 percent of the massif slopes (see section entitled "Albedo Measurements"). This albedo difference is probably due to the formation of a regolith and consequent darkening of the surface of the light mantle; continued downslope movement of materials of the South Massif brings newly exposed materials to the surface of the massif, hence the darkening process is not so effective on the steep slopes. At a distance, the crew recognized that the bright aspect of the light mantle is primarily manifested by numerous small craters the walls and rims of which are brighter than any in the dark plains. These craters probably expose fresh material.

The light mantle consists mainly of unconsolidated fines. Comments by the crew and photographs taken at stations 2A and 3 and while driving indicate that rocks > 25 cm across are sparse on the surface of the unit. Smaller rocks are fairly common but not abundant. A single large (3 to 4 m) boulder was encountered on the traverse. The scarcity of rocks suggests that the avalanche mainly consisted of regolith from the surface of the massif and did not involve the sliding of underlying bedrock.

The light mantle feathers out at its margins away from the South Massif. Near the extremities of the mantle, Shorty Crater and a smaller nearby crater appear to penetrate through the slide into underlying valley regolith. Craters of this size nearer the South Massif do not penetrate to darker underlying material.

A greater thickness near the base of the massif is also suggested by the occurrence of numerous low ridges that become less distinct farther from the massif (fig. 6-53). The ridges are alined in the apparent direction of movement of the avalanche away from the massif and are spaced 25 to 100 m apart. In some orbital photographs, lineaments appear to form V's that open away from the massif. Similar lineament patterns are visible in areas of similar relief just northwest of the light mantle. This similarity suggests that the V lineaments are not necessarily associated with the emplacement of the avalanche.
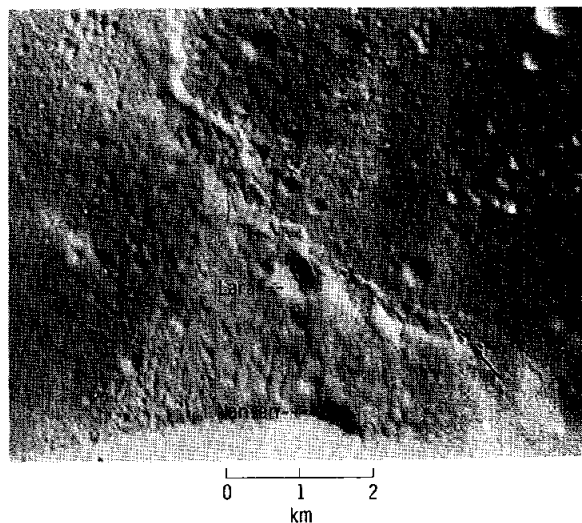
FIGURE 6-53.—Panoramic camera photograph showing details of the light mantle and Lee-Lincoln Scarp (Apollo 17 panoramic camera frame AS17-2309).

The lineaments may be enhanced or created by the lighting condition, an effect that is not fully understood (refs. 6-11 and 6-12). On the other hand, the lineament patterns resemble interference patterns seen in the lee of obstacles in a moving fluid.

Descriptions by the crew at station 2A indicate that the upper portion of the light mantle is composed of 5 to 15 cm of medium-gray material underlain by light-gray material. The medium-gray material may be regolith, darkened by the formation of impact glass, that has been formed from small contributions of dark soil from impacts occurring on the dark portions of the valley floor.

The trench (fig. 6-54) at station 3 was dug into the rim of a 10-m crater. The bottom of the trench exposed a marbled zone of light- and medium-gray materials. The texture of the marbled material is similar to the textures and ejecta from terrestrial impacts such as Meteor Crater (fig. 6-55), and this material may be ejecta from the 10-m crater in which undiluted light mantle was mixed with precrater regolith. Overlying the marbled material is a 3-cm-thick layer of light material, which may represent unmixed light mantle ejected from well below the precrater regolith. Where the trench was dug, on the rim of the 10-m crater, the upper part of the stratigraphic sequence had probably been eroded by impact of small meteorites (refs. 6-7 and 6-13). Thus, the 3-cm layer of light material was probably signifi-
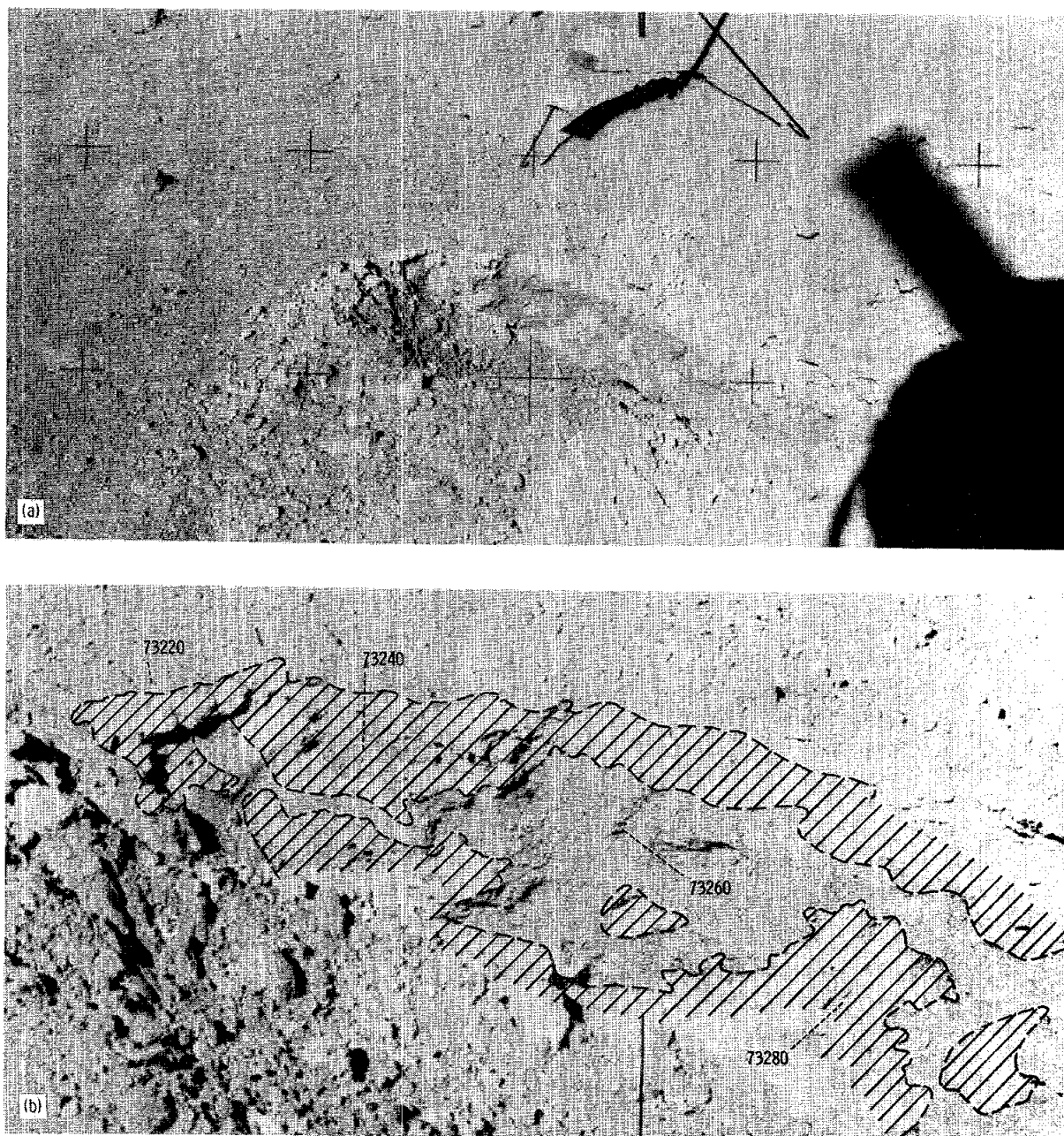
FIGURE 6-54.—Presampling view of trench wall at station 3. (a) Southwest-looking view (AS17-138-21148). (b) Enlargement of part of figure 6-54(a). Hachured area is light-gray material; remainder is medium gray. The 0.5 cm of medium light-gray regolith that caps the mapped units is not separately mapped (AS17-138-21148).

cantly thicker at its time of deposition as crater ejecta. The uppermost layer in the trench is 0.5 cm of medium-gray material that is slightly lighter than the medium-gray component of the marbled zone. This layer is interpreted to be the regolith that has formed on the ejecta of the 10-m crater (fig. 6-56).

The size-frequency distribution and morphologies of craters on the light mantle suggest that its age is

FIGURE 6-55.—Marbled texture in ejecta at Meteor Crater, Arizona. Compare with figure 6-54 (U.S. Geological Survey, Center of Astrogeology photograph 76824).

Bottom of trench at station 2A

Bottom of trench at station 3

10-m crater at station 3

Explanation

☐ Medium-gray (lighter than medium-gray component of marbled mantle) regolith formed on crater ejecta

▨ Marbled mantle (the old medium-gray regolith and light-gray mantle) over-turned and mixed

▨ Precrater medium-gray regolith

☐ Light-gray mantle

FIGURE 6-56.—Interpretation of stratigraphy as seen in trenches on the light mantle at stations 2A and 3.

comparable to that of the crater Tycho, or on the order of 100 million years. Crater counts show that the saturation crater size is 2 to 4 m. The saturation crater size at Tycho is 2.8 m (ref. 6-14).

Another way to estimate age uses the crater degradation model of Soderblom and Lebofsky (ref. 6-13). The diameter of the largest unshadowed crater (Dx) on Apollo 17 panoramic camera frame 2308 (Sun angle $SA = 16.3°$) is 30 ± 10 m. By using this calculation, the age expressed as the diameter of a crater (D_L) which would be eroded to $1°$ slopes was calculated as 13 ± 5 m. This age compares with that of Tycho Crater, where $D_L = < 20$ m (ref. 6-13). A minimum age for the light mantle is the exposure age (20 to 30 million years) for the orange soil deposited on the rim of Shorty Crater (ref. 6-15).

The light mantle is larger than most other lunar avalanches and, unlike many, has no conspicuous source ledge on the slope above. New evidence suggests that the avalanche was triggered by secondary impacts from a distant crater. This evidence is based on the recognition on Apollo 17 low-Sun-angle orbital photographs of a cluster of 100-m craters on the top of the South Massif and a similar cluster on the plains adjacent to the northwest side of the light mantle. The elongation of the cluster craters suggests that they are secondaries from a distant crater to the southwest, possibly of Tycho. If impacts from the same cluster of secondaries impacted the north-western slope of the South Massif, they could have initiated the avalanche. Elsewhere on the Moon are

other avalanches that clearly were similarly initiated by the impact of crater ejecta on slopes facing away from the primary crater (ref. 6-10).

Shorty Crater

Shorty is a fresh 110-m crater located near the north edge of the light mantle. It resembles other craters that have been interpreted as young impact craters. The floor is hummocky, with a low central mound and with marginal hummocks that resemble slumps forming discontinuous benches along the lower parts of the crater wall. The rim is distinctly raised and is sharp in orbital views. The dark ejecta blanket is easily distinguished from the high-albedo surface of the surrounding light mantle, which it overlies. However, the low albedo of the ejecta is similar to that of the dark younger regolith elsewhere on the plains surface.

Samples were collected in a low place on the rim crest of Shorty Crater just south of a 5-m boulder of fractured basalt (fig. 6-57). Debris that may have been shed from the boulder lies on the nearby surface, and blocks are abundant on this part of the inner crater wall. All the rocks examined are basalt. Most are intensely fractured and some show irregular knobby surfaces that resemble the surfaces of terrestrial flow breccias. Rocks range from angular to subrounded; some are partially buried; some are filleted, including the upslope sides of a few of the larger boulders on the inner crater wall.
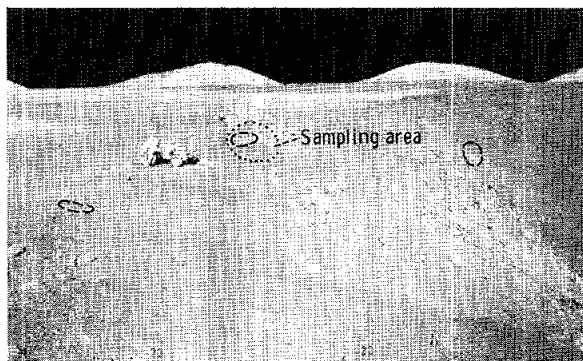
FIGURE 6-57.—Northwest-looking view of southwest rim of Shorty Crater showing sampling area and areas of orange soil as indicated by dashed lines. Large sampled boulder on rim is 5 m wide (AS17-137-21009 and 21011).

FIGURE 6-58.—North view across 110-m-diameter Shorty Crater. Far crater wall, blocky benches encircling floor, and jagged rocks of central mound are visible (AS17-137-21001).

FIGURE 6-59.—Schematic cross section through Shorty Crater with vertical scale exaggerated.

The floor material, exposed in the central mound (fig. 6-58), is blocky and extremely jagged. It may differ in lithology from the basalts of the rim. The hummocks or benches that encircle the floor as well as portions of the walls are also blocky. However, the wall, the rim, and the outer flank of Shorty Crater consist largely of dark material that is much finer grained than the floor. On the crater rim, fragments as large as ≈ 15 cm in diameter typically cover < 3 percent of the surface. Scattered coarser fragments, ranging up to at least 5 m in diameter, are present. The crater rim and flanks are pitted by scattered, small (to several meters) craters the rims of which range from sharp to subdued. Typically, their ejecta are no blockier, except for clods, than the adjacent surfaces.

Although a volcanic origin has been considered for Shorty Crater, no compelling data to support the volcanic hypothesis have been recognized. The type of pure accumulation of basaltic spatter or cinders that forms steep-sided terrestrial volcanic cones has not been recognized; nor does the steeply raised sharp rim of Shorty resemble the low rounded rims of terrestrial maar craters. Most probably, Shorty is an impact crater. Its blocky floor may represent either impact-indurated soil breccia or the top of the subfloor basalt, which is buried by 10 to 15 m of poorly consolidated regolith, including light mantle (fig. 6-59). The predominantly fine-grained wall, rim, and flank materials are probably ejecta derived largely from materials above the subfloor, and the basalt blocks may be ejecta derived from the subfloor. Regardless of its origin, the crater is clearly younger than the light mantle.

Unusual orange soil is known to occur in two places on the Shorty Crater rim crest as well as in the ejecta of a small fresh crater high on the northwest interior wall of Shorty (fig. 6-57). A trench exposed an 80-cm-wide orange zone that trends parallel to the crater rim crest for several meters. The orange soil is markedly coherent as shown by the systematic fractures in the trench wall (fig. 6-60). It is also zoned; a wide central reddish zone, now known to consist largely of small red and orange glass spheres and fragments, grades laterally to marginal yellowish zones ≈ 10 cm wide (fig. 6-61). The yellowish zones in turn are in sharp steep contact with light-gray fragmental material that is probably typical of the Shorty Crater rim. A double drive tube placed in the axial portion of the colored zone bottomed in black fine-grained material now known to consist of tiny, opaque, black spheres (sec. 7). The contact between orange and black glass occurs within the upper drive

FIGURE 6-60.—North-looking photograph showing orange glass material and light-gray fragmental material exposed in trench on rim crest of Shorty Crater. Short lines indicate more prominent fractures in the orange glass material (AS17-137-20986).

tube at a depth estimated from the debris smeared on the exterior of the tube to be ≈ 25 cm.

The origin of the red and black glass materials is uncertain. The radiometric age determination for the orange glass material implies solidification during or shortly after the period of subfloor basalt volcanism. Shorty Crater, of course, is much younger. Such glass, whether ejected from an impact crater or a volcanic
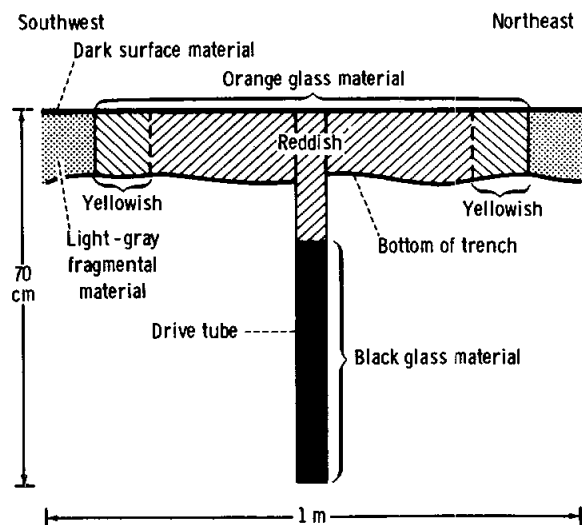
FIGURE 6-61.—Schematic cross section showing materials in trench and double drive tube on Shorty Crater rim crest.

vent, may have lain as a layer (or layers) either within the upper part of the subfloor basalt sequence or deep within the regolith overlying the subfloor basalt in the target area. If so, the orange and black glassy materials may represent clods of ejecta excavated by the Shorty impact. However, the symmetrical color zonation of the orange soil, internal color zoning of at least one clod, and apparent parallelism of the steep boundaries of the zone with both the internal color banding and the axis of the rim crest are improbable features for a clod of ejecta unless the clod has undergone alteration subsequent to its emplacement, a process heretofore unknown on the Moon. The color zoning and steep contacts might be more readily explained if the glass material, derived from a layer of similar material in the target, were mobilized by the impact and driven dike-like into concentric fractures. However, the occurrence of black glass material below the orange glass material in the double drive tube (fig. 6-61) and the absence of the black glass at the surface suggests the existence of horizontal or gently dipping layering, a geometric arrangement that would be reasonable in a clod of ejecta but is difficult to reconcile with injection of old glass material into a concentric fracture.

A 0.5-cm-thick layer of dark fine-grained soil overlies both the orange soil zone and the adjacent light-gray fragmental material. This dark surface material may represent the regolith that has formed since the formation of Shorty Crater.

Van Serg Crater

Van Serg is a fresh 90-m-diameter impact crater. It has a blocky central mound $\approx$ 30 m across, discontinuous benches on the inner walls, and a raised blocky rim with a distinct crest from which the blocky ejecta blanket slopes outward. The bench is particularly well developed on the north wall, where the crew reported that materials in the crater wall above the bench were darker than those below. Its ejecta blanket is distinct in lunar surface views because of its blockiness, which is greater than that of the adjacent plains. The ejecta blanket can be recognized, at least in part, in orbital photographs as a distinct topographic feature, but it is inseparable from the adjacent plains on the basis of albedo.

Rocks in the Van Serg ejecta range to $\approx$ 30 cm, with a few boulders as large as 1 to 2 m in diameter. At the rim crest, fragments larger than 2 cm cover $\approx$ 10 percent of the surface, but they cover no more than 3 percent of the surface on the outer flank of the crater. The predominant rock type at station 9 is soft or friable dark matrix-rich breccia. White clasts ranging to $\approx$ 2 cm in diameter are visible in some rocks on the crater rim, and light-colored clasts possibly as large as 0.5 m in diameter were seen in rocks of the central mound. Some rocks are slabby. Closely spaced, platy fractures occur in some, and a few show distinct alternating light and dark bands. Some frothy glass agglutinate was also sampled. Despite their apparent softness, the rocks are typically angular. Many are partially buried, but there is little or no development of fillets even on the steep inner walls of Van Serg Crater.

Soil at the surface is uniformly fine and gray with no visible linear patterns. The uppermost 1 or 2 cm is loose and soft. A trench on the outer flank of the crater exposed $\approx$ 10 cm of light-gray fragmental material below a 7-cm layer of dark surface material (fig. 6-62).

Craters younger than Van Serg are extremely rare in the station 9 area. A few small ($\approx$ 1 m) craters are present. A large subdued depression immediately south of Van Serg may be an old crater now mantled by Van Serg ejecta. The frequency and angularity of blocks, the paucity of craters, the general absence of fillets, and the uneroded nature of the crater rim and
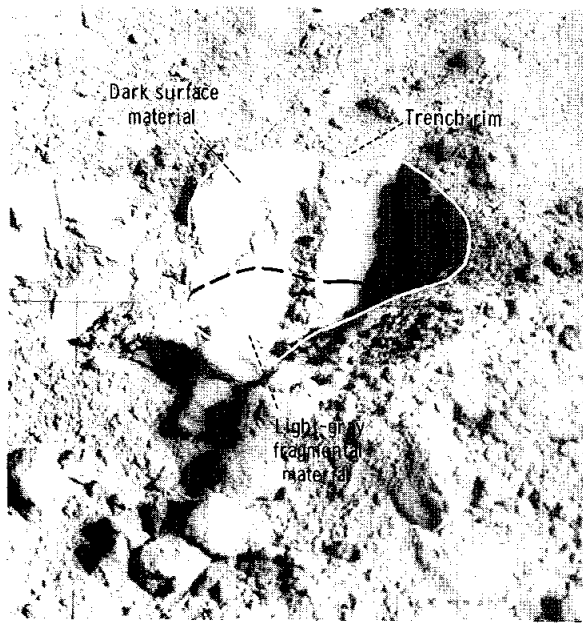
FIGURE 6-62.—North-looking photograph showing trench on outer flank of Van Serg Crater ≈ 70 m from rim crest. Dark surface material overlies light-gray fragmental material (AS17-142-21827).

the central mound attest to the extreme youth of Van Serg Crater. Evidence for its being younger than Shorty is equivocal. Its rim seems to be slightly sharper than the rim of Shorty in orbital photographs, and small craters may be slightly more abundant on the Shorty rim.

There is no evidence that the Van Serg impact excavated subfloor basalt. The fragment-rich breccias and dark matrix-rich breccias of its floor, rim, and outer flank may be regolith breccias indurated in the Van Serg impact. If this reasoning is correct, then at least 15 m of regolith is inferred to overlie the subfloor basalt in the Van Serg area. However, these breccias may be of a volcanic type not previously recognized and may be associated with the orange and black glass formations.

Near coincidence of the albedos of the blocky Van Serg ejecta blanket and the nearby smooth regolith surface is puzzling. Possible explanations are that the elusive dark mantle material is represented in the ejected older regolith as well as at the present regolith surface or that the dark surface material recognized on the crater rim and flank has masked any distinction between the Van Serg ejecta and the nearby undisturbed regolith surface.

STRUCTURAL GEOLOGY

Geologic Structure of the Landing Site

The valley in which Apollo 17 landed is bounded by high steep-sided mountain blocks that form part of the mountainous eastern rim of the Serenitatis basin. The blocks are thought to be bounded by high-angle faults that are largely radial and concentric to the Serenitatis basin. Hence, the valley itself is interpreted as a graben formed at the time of the Serenitatis impact. Some of the prominent faults are not concentric or radial to Serenitatis, although major displacements probably occurred along them when Serenitatis was formed. The faults may have been preexisting zones of weakness related to older basins such as Tranquillitatis or to the so-called lunar grid.

Massifs and Sculptured Hills

Each massif block probably is a structural entity uplifted during the Serenitatis event. Rejuvenation of these older structural elements may have occurred during the Imbrian event as suggested by the elongation of the Taurus-Littrow valley, which is radial to both Imbrium and Serenitatis. Segmentation of the massifs may be an inheritance from the even earlier Tranquillitatis event.

The massifs adjacent to the landing site appear similar in slope, albedo, and degree of cratering. They contrast with the closely spaced domical hills of the Sculptured Hills, which also form fault block mountains. No unequivocal Sculptured Hills material has been recognized among the samples; hence, the reason for the differing appearances of the massifs and the Sculptured Hills is not clearly understood. The massifs may consist of distinctly different materials with more friable material occurring in the Sculptured Hills. For example, the massifs may consist largely of pre-Serenitatis ejecta uplifted in the Serenitatis event, whereas the Sculptured Hills may consist mainly of Serenitatis ejecta. Alternatively, each might consist mainly of a different facies of Serenitatis ejecta, with more thorough recrystallization increasing the coherence of the massif materials. On the other hand, the initial materials of the two units may be similar, but subsequent deformational history may have caused their different aspects. For example, relatively recent uplift selectively affecting the massif blocks may have rejuvenated slope proces-

ses to create the relatively uninterrupted steep slopes that distinguish the massifs from the Sculptured Hills.

Single, major bounding faults are inferred along the face of each mountain block. Such faults can be recognized at younger, less modified basin margins (e.g., Orientale, Imbrium). These faults are probably very steep—more than 60° and probably close to 90° for the radial faults. They are buried under the talus aprons and lie valleyward from the lowest outcrops visible on the massif faces. Sharp knickpoints at the massif bases suggest that additional later uplift may have reinitiated downslope movement of talus.

Valley

The Taurus-Littrow valley appears to be a long narrow graben radial to the Serenitatis basin. The graben probably is composed of several structural blocks and did not move as an entity. Its floor, now buried, is thus visualized as having steps between blocks the separate tops of which are at different elevations. These buried tops probably resemble in roughness the present tops of the massifs and the Sculptured Hills.

The present uniformity of the valley floor is due to the continuity of the valley fill surface. The fill probably consists of rubble created at the time of block faulting overlain by basalt (subfloor) and regolith materials that are younger than any large differential movements of the structural blocks. The surface continuity must be due mainly to infilling by subfloor basalts that are interpreted from geophysical measurements (secs. 10 and 13) to be 1 km or more thick.

The valley floor slopes $\approx 1°$ toward its eastern end. This small dip is interpreted as structural rather than depositional because it is coincident with other regional surface slopes. The NASA Lunar Topographic Orthophoto Map (1972) shows an east-tilted belt that includes the Taurus-Littrow valley and the floor of the crater Littrow (fig. 6-1). The tilt is interpreted to record development of a broad arch formed by uplift along the mountainous Serenitatis rim after the subfloor basalt fill had accumulated in the Taurus-Littrow graben. Long shallow grabens largely concentric to the Serenitatis basin were created during this deformation. They were truncated by younger mare-filling deposits that subsequently accumulated in the Serenitatis basin.

Younger deformational features on the valley floor include the Lee-Lincoln Scarp, which is discussed subsequently and several small sharp grooves that are visible on the surface of the light mantle in the low-Sun-angle photographs taken with the Apollo 17 panoramic camera. These grooves appear to be small grabens similar to the small graben rilles that are common on mare surfaces. They were probably formed by minor tectonic movements that occurred after the emplacement of the light mantle.

Lee-Lincoln Scarp

The origin and nature of the Lee-Lincoln Scarp are still puzzling. Its steep face nearly everywhere faces east, commonly in a pair of steps the total relief of which reaches 80 m in the center of the valley. A few prominent smaller west-facing scarps are present, best seen from Lara Crater northward where the shadowed highlighting is enhanced by the whiteness of the light mantle (fig. 6-53). Individual segments disappear along strike as another picks up the displacement; in places, it appears almost braided. The trends of individual segments of the scarp appear to alternate between north and northwest as if controlled by an underlying prismatic fracture system. This same set of trends is identifiable in segments of the scarp along the western base of the North Massif. Here, however, the scarp is single and always faces east—toward the massif—in the form of a reverse or thrust fault. Forty kilometers to the north, the scarp passes out onto the dark plains surface where it cuts Rima Littrow I (fig. 6-1).

The overall length, trend, asymmetry, and morphologic character of the scarp resemble that of the larger wrinkle ridges of the adjacent Serenitatis mare (part A of sec. 29). This similarity suggests a common origin—possibly folding and thrusting of a thin plate (décollement sheet) eastward. The relative youth of this deformation is indicated by the transection of fresh Copernican craters by wrinkle ridges in the mare, by the fresh, possibly rejuvenated scarplets that may be younger than the light mantle, and by the good preservation of the scarp in the unconsolidated materials of the North Massif face. An alternative possibility is that the Lee-Lincoln Scarp is the surface trace of a complex high-angle fault that changes strike where it follows the old North Massif boundary fault immediately north of the valley.

ALBEDO MEASUREMENTS

Lunar surface and orbital photographs were used to map albedo in the Taurus-Littrow area. Down-Sun 60-mm photographs at each traverse station in combination with high-resolution 500-mm photographs of the mountain slopes provided the control for photometric measurements made from orbital photographs.

Relative film densities of Apollo 15 panoramic camera frames 9557 and 9559 were measured on a Joyce-Loebl microdensitometer. The scanning aperture was 50 μm square, equivalent to an integrated 9 m^2 of lunar surface. Film densities, after calibration to normal albedo as determined in down-Sun lunar surface photographs in areas of fine-grained regolith and after adjustment to remove the effects of topographic slopes, are proportional to albedos of lunar surface materials. Topographic corrections were derived from the NASA preliminary topographic map of part of the Littrow region of the Moon.

The resulting map (fig. 6-63) was smoothed to remove scanning noise and high-frequency albedo variations. Important qualifications are that the usual lunar photometric function was applied for the Apollo 17 areas and that the albedo adjustments for topography are approximate because of inaccuracies of slope orientations. Comparisons of albedo values are most reliable between areas with similarly oriented slopes.

The albedo map (fig. 6-63) can be compared with an orbital photograph of the area at a similar scale (fig. 6-64). The east-west trending valley floor is the most continuous physiographic unit. Except for the light mantle, in which albedo ranges from 14 to 23 percent, the albedo of the valley floor is low. It ranges from 14 percent in the western part to 9 percent over the eastern portion. The albedo of the floor generally increases gradually (3 to 4 percent) along a 300- to 600-m-wide outer zone (generally depicted by unit 6) adjacent to the base of the surrounding mountains. This zone is considered to represent mixing of lighter highlands regolith with the much darker floor regolith and is remarkably narrower than the 1- to 2-km width of a similar zone at the Apollo 15 site (ref. 6-16). The lighter valley floor area between the South Massif and Family Mountain may represent a more extensive mixing zone, perhaps related to the proximity of uplands material at the surface or to its presence at very shallow depths in the subsurface. Even so, the mixing zone at the foot of the South Massif (depicted by unit 5) seems to be as narrow as along the northern side of the valley floor.

The massifs and hills surrounding the valley generally have albedos ranging from 15 to 34 percent, as is normal for lunar highlands. However, local small depressions contain dark material with albedo as low as 10 percent. The lightest regolith material occurs on the steepest slopes and on top of some rounded domes. The slopes of the South Massif are lightest from one-fourth to three-fourths of the way down the slope front and darker near the top and bottom of the slopes. The small undulating plains area on top of the South Massif (unit 5) is as dark as the valley floor between the massif and Family Mountain (14 percent) with tongues of the material draping over the edge of the upper massif slopes and extending down the steeper slopes. The North Massif has lighter regolith on the tops of rounded domes and down the upper two-thirds of the slopes. Small closed depressions on top of the massif that are too small to be shown in figure 6-63 show slight darkening in the western part and increasing darkening toward the eastern part. The Sculptured Hills show a general darkening toward the east with the regolith in similar small depressions ranging in albedo from 17 to 14 percent. The large upland basin to the northeast has extensive regolith with 12-percent albedo. The East Massif is similar to the North Massif, but the small closed depressions darken toward the southeast. Albedos as low as 10 percent occur immediately south of the map area.

The surfaces of the small intramassif and intrahill depressions are from 1200 to 2000 m higher than the floor of the Taurus-Littrow valley. These dark areas are considered to contain bedrock material similar to the surrounding massif or hill bedrock. There is no observed geologic evidence to suggest that any mare-like basalt could have flooded these small depressions. Yet the darker albedos of many depressions are similar to the albedos of the mare areas and of the Taurus-Littrow valley floor.

The lunar regolith is generally considered to be developed primarily by repetitive crushing of local bedrock by impact processes (ref. 6-17). The product is a fine-grained layer that is darker than the original bedrock. Mare basalt fragments with albedos ranging from 13 to 21 percent occur with fine-grained regolith of 9- to 13-percent albedos (ref. 6-7). The ratio of the albedo of the fine-grained regolith to the

Explanation

☐ Unit 1, > 25 percent   ☐ Unit 3, 19 to 21 percent   ▦ Unit 5, 15 to 17 percent   ▦ Unit 7, 11 to 13 percent
▦ Unit 2, 21 to 25 percent   ▦ Unit 4, 17 to 19 percent   ▦ Unit 6, 13 to 15 percent   ■ Unit 8, 9 to 11 percent
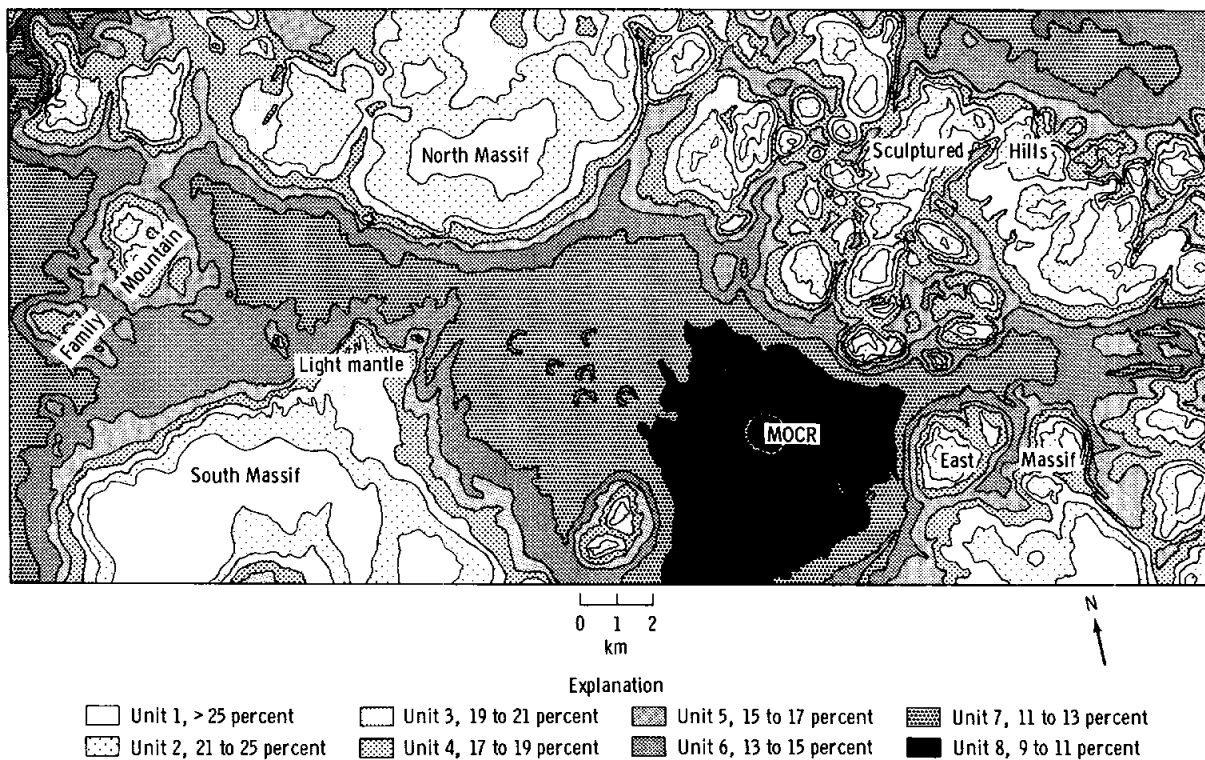
FIGURE 6-63.—Albedo map of Apollo 17 landing site. Albedo information obtained by digitization of panoramic photographs AS15-9557 and 9559. Albedo values were adjusted for local slope effects.
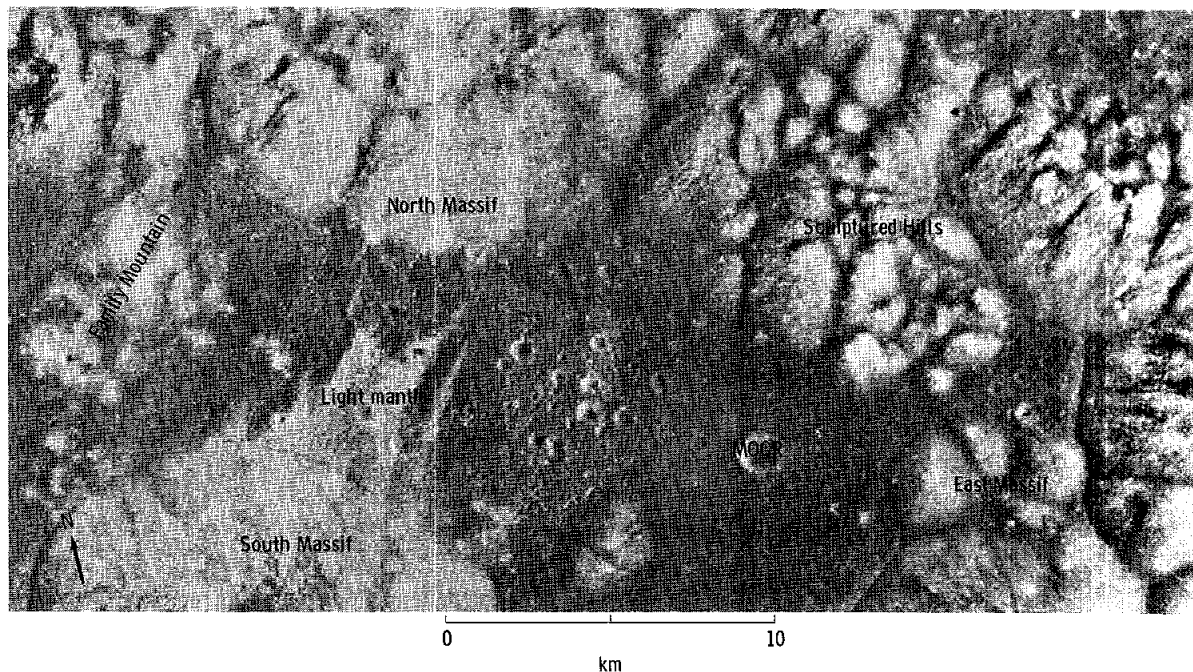
FIGURE 6-64.—Orbital photomap of area shown in figure 6-63. Sun angle is 55°. Base map prepared for NASA by U.S. Army Topographic Command under the direction of the Department of Defense, 1972.

contained rock fragments for mare surfaces ranges from 0.62 to 0.68 and for highland surfaces from 0.55 to 0.68. Thus, the percentage of regolith darkening with maturity is only slightly greater for the highlands (32 to 45 percent) than for the mare (32 to 38 percent).

On the floor of the Taurus-Littrow valley within the landing area, average normal albedos of the floor and the subfloor basalt blocks are 12 and 18 percent, respectively, yielding a ratio of 0.66, which is average for mare regolith darkening. In the vicinity of MOCR Crater at the eastern end of the valley, albedos of the dark floor material and the crater wall are 9 and 18 percent, respectively, giving a ratio of 0.50, which is the greatest degree of mare regolith darkening ever measured on the Moon. It is probable that some darker material (black glass?) has been deposited over and mixed with an original bedrock-derived regolith. The surface in this area, which coincides with the darkest albedo unit (fig. 6-63, unit 8), also appears somewhat smooth and subdued, in contrast to the landing area.

The North and South Massifs show average albedos of ≈ 26 percent for fine-grained regolith and 34 percent for rocks, producing a ratio of 0.76 for regolith darkening, slightly less darkening than at Hadley Delta (Apollo 15 site). The Sculptured Hills and the East Massif show local maximum albedos that are similar to the maximums for the North and South Massifs. This similarity suggests that bedrock with similar albedo occurs in all four mountain masses. The average albedo of the Sculptured Hills and the East Massif is ≈ 18 percent, which gives an average regolith darkening ratio of 0.53. This is considerably darker than the 0.74 on Hadley Delta and the 0.76 on the North and South Massifs.

Careful study of the Sculptured Hills and the East Massif revealed 11 small closed depressions with areas of smooth floors. The normal albedo of the regolith on the depression floors should show the maximum darkening effects because mass-wasting processes tend to expose fresher brighter material on slopes. The albedos of the depression floors decrease eastward in the northern part of the Sculptured Hills, ranging from 17 to 12 percent. The albedos of depression floors in the East Massif decrease southward beyond the mapped area from 14 to 10 percent. The regolith darkening ratio decreases from 0.50 to 0.29, which is much lower than any other measured area on the Moon. A darkening ratio of 0.50 or less strongly

implies addition of material darker than local regolith, but a ratio of 0.29 is strong evidence for the addition of dark material from another source.

The increased darkening, to the south and east, of regolith developed on different geologic materials (i.e., the eastern valley floor, the Sculptured Hills, and the East Massif) is best interpreted as the effect of addition of material darker than 9-percent normal albedo from sources to the east or southeast of the Taurus-Littrow valley. The absence of any apparent ballistic shadowing by the mountains indicates that the material was transported along high-angle trajectories. The only lunar material known to have such low albedo is dark to black glass or glassy material. A pyroclastic-like mantle of dark glassy material fits the observed geological relationships and albedo data.

GEOLOGIC HISTORY

Before the Serenitatis basin was formed, older major basin impacts should have covered the Taurus-Littrow area with sheets of ejecta derived from still older ejecta deposits and ultimately from igneous lunar crustal material. Because of their proximity, Tranquillitatis and Fecunditatis should have contributed large amounts of ejecta that may be exposed in the massifs. The older major basin impacts should also have developed radial and concentric fracture zones comparable to those around the younger, better preserved basins. Some of these fractures were presumably reactivated in the Serenitatis event.

The major physiographic units (e.g., the Massifs, the Sculptured Hills, and the Taurus-Littrow valley) of this region were produced by the impact that formed the Serenitatis basin. Major radial faults bound the Taurus-Littrow valley and Mons Argaeus; major concentric faults bound the South Massif and the East Massif.

Deposits of Serenitatis ejecta must have been thick and widespread. By analogy with deposits around younger multi-ringed basins such as Imbrium and Orientale, they are interpreted to comprise most of the Sculptured Hills terrain. Whether Serenitatis ejecta comprises a major portion of the massifs as well or occurs only as a veneer overlying older ejecta deposits is unknown. Deposits from the younger multi-ringed basins are probably also present but have not been specifically identified. Such deposits, which may be present on the highlands and beneath or intercalated with the lower part of the subfloor

basalts, could have been derived from the Nectaris, Humorum, Crisium, Imbrium, and Orientale basins, listed from oldest to youngest (ref. 6-18).

Uplift of the massifs following the Serenitatis impact was probably rapid and occurred along high-angle faults. Thus, the graben walls are thought to have stood at angles steeper than the angle of repose. Rapid reduction of slope angles by accumulation of thick talus wedges on the lower slopes and of mass movement deposits on the graben floor must have occurred.

With the major physiographic features now formed, the next major event was flooding of the valley by lavas that filled it with ≈ 1200 m of basalt (sec. 10). Samples collected from the upper 130 m of the subfloor basalt show it to be similar to Apollo 11 mare basalt but slightly older with an age of ≈ 3.8 billion years.

Either as a late stage of the subfloor basalt volcanism or as totally separate slightly younger events, spherical orange and black glass particles were deposited in the area of Shorty Crater and probably over much of the Taurus-Littrow region. Whether of volcanic or impact origin, the glass spheres, which solidified ≈ 3.7 billion years ago, were rapidly buried so as to be preserved for eventual excavation at Shorty Crater.

After subfloor basalt extrusion was completed, warping around the Serenitatis margin produced a broad anticlinal arch with the Taurus-Littrow valley and Littrow Crater on its eastern limb. Long narrow grabens such as Rima Littrow I formed along the Serenitatis basin side of the crest of the arch, which was eventually overlapped by younger mare basalts of the Serenitatis basin.

A long period of regolith formation and accumulation of surficial deposits ensued. Some of the earlier formed regolith may be represented by the floor materials of Van Serg, in which light-colored lithic clasts presumably derived from the uplands are common. Relatively late events recorded in the regolith sequence are the formation of older, large craters (Camelot, Henry, Shakespeare, and Cochise), formation of the younger central cluster (Steno, Emory, Sherlock, Powell, etc.), and emplacement of the light mantle as an avalanche of debris that may have been triggered when ejecta struck the South Massif.

Photogeologic evidence in the general Taurus-Littrow area indicates that an unusually dark man-

tling deposit was deposited on both the plains and upland surfaces during this long period of regolith formation. The unusual concentration of glass spheres in dark soils from the valley (sec. 7) may represent the dark mantle thoroughly intermixed with more normal impact-generated regolith.

Relatively young deformational events that took place during the long period of regolith formation include a slight eastward tilting of the Serenitatis basin (ref. 6-19) and the development of wrinkle ridges in Mare Serenitatis and the Lee-Lincoln Scarp in the landing area. Very recent deformation is suggested by the occurrence of small grabens on the surface of the light mantle and by the apparent youth of parts of the Lee-Lincoln Scarp.

The youngest large events of special significance to the mission were the impacts that formed Shorty and Van Serg Craters in that order. Both craters are younger than the light mantle, and both penetrate deeply into the regolith.

REFERENCES

6-1. Scott, D. H.; Lucchitta, B. K.; and Carr, M. H.: Geologic Map of the Taurus-Littrow Region of the Moon. U.S. Geol. Survey Misc. Geol. Inv. Map I-800, 1972.

6-2. Wolfe, E. W.; Freeman, V. L.; Muehlberger, W. R.; Head, J. W.; Schmitt, H. H.; and Sevier, J. R.: Apollo 17 Exploration at Taurus-Littrow. Geotimes, vol. 17, no. 11, Nov. 1972, pp. 14-18.

6-3. Scott, D. H.; and Pohn, H. A.: Geologic Map of the Macrobius Quadrangle of the Moon. U.S. Geol. Survey Misc. Geol. Inv. Map I-799, 1972.

6-4. Wilhelms, D. E.; and McCauley, J. F.: Geologic Map of the Near Side of the Moon. U.S. Geol. Survey Misc. Geol. Inv. Map I-703, 1971.

6-5. Wolfe, E. W.; and Freeman, V. L.: Detailed Geologic Map—Apollo 17 (Taurus-Littrow) Landing Area. U.S. Geol. Survey Open-File Rept., 1972. (Available from Center of Astrogeology, Flagstaff, Ariz.)

6-6. Schaeffer, O. A.; and Husain, L.: Isotopic Ages of Apollo 17 Lunar Material. EOS (Trans. Am. Geophys. Union), vol. 54, June 1973, p. 614.

6-7. Swann, G. A.; Bailey, N. G.; Batson, R. M.; Freeman, V. L.; et al.: Preliminary Geologic Investigation of the Apollo 15 Landing Site. Sec. 5 of the Apollo 15 Preliminary Science Report. NASA SP-289, 1972.

6-8. Pieters, C.; McCord, T. B.; Zisk, S.; and Adams, J. B.: Lunar Black Spots and Nature of the Apollo 17 Landing Area. J. Geophys. Res., vol. 78, no. 26, Sept. 10, 1973.

6-9. El-Baz, Farouk: The Cinder Field of the Taurus Mountains. Sec. 25, Part I, of the Apollo 15 Preliminary Science Report. NASA SP-289, 1972.

6-10. Howard, K. A.: Lunar Rock Avalanches and Apollo 17. Science, vol. 180, June 8, 1973, pp. 1052-1055.

6-11. Wolfe, E. W.; and Bailey, N. G.: Lineaments of the Apennine Front—Apollo 15 Landing Site. Proceedings of the Third Lunar Science Conference, vol. 1, MIT Press (Cambridge, Mass.), 1972, pp. 15-25.

6-12. Howard, K. A.; and Larsen, B. R.: Lineaments That Are Artifacts of Lighting. Sec. 25, Part G, of the Apollo 15 Preliminary Science Report. NASA SP-289, 1972.

6-13. Soderblom, L. A.; and Lebofsky, L. A.: Technique For Rapid Determination of Relative Ages of Lunar Areas from Orbital Photography. J. Geophys. Res., vol. 77, no. 2, Jan. 10, 1972, pp. 279-296.

6-14. Morris, E. C.; and Shoemaker, E. M.: Television Observations From Surveyor. Science Results. Part II of Surveyor Project Final Report, JPL Tech. Rept. 32-1265, 1968, pp. 65-69.

6-15. Kirsten, T.; Horn, P.; Heymann, D.; Hübner, W.; and Storzer, D.: Apollo 17 Crystalline Rocks and Soils: Rare Gases, Ion Tracks, and Ages. EOS (Trans. Am. Geophys. Union), vol. 54, June 1973, pp. 595-598.

6-16. Swann, G. A.; Bailey, N. G.; Batson, R. M.; Freeman, V. L.; et al.: Geologic Setting of the Apollo 15 Samples. Science, vol. 175, no. 4020, Jan. 28, 1972, pp. 407-415.

6-17. Shoemaker, E. M.; Hait, M. H.; Swann, G. A.; Schleicher, D. L.; et al.: Lunar Regolith at Tranquillity Base. Science, vol. 167, no. 3918, Jan. 30, 1970, pp. 452-455.

6-18. Stuart-Alexander, Desiree E.; and Howard, Keith A.: Lunar Maria and Circular Basins—A Review. Icarus, vol. 12, no. 3, May 1970, pp. 440-456.

6-19. Sjogren, W. L.; and Wollenhaupt, W. R.: Lunar Shape via the Apollo Laser Altimeter. Science, vol. 179, no. 4070, Jan. 19, 1973, pp. 275-278.

APPENDIX A

LUNAR SURFACE ORIENTATIONS OF APOLLO 17 ROCK SAMPLES

R. L. Sutton[a]

The lunar surface orientations of some of the Apollo 17 rock samples at the time of their collection (table 6-V) are shown in this appendix (figs. 6-65 to 6-87). These orientations were determined by correlating lunar photographs of samples before collection with shapes and shadow characteristics of the same samples in the LRL under oblique illumination with nearly collimated light. The light source in the laboratory simulates the Sun. It is important to emphasize that the orientations shown are those at the time of collection and do not necessarily apply to the entire history of the exposure of a rock on the lunar surface. Tumbling and turning of some rock fragments on the lunar surface has already been well documented.

The small lettered cube included in each laboratory orientation photograph is not meant to indicate the lunar attitude of samples but is designed to tie the lunar perspective orientations to documentary views of the same samples in orthogonal and stereoscopic photographs (mug shots) taken in the LRL using the same orientation cube.

Not all the photographs showing sample orientations are in this appendix; some have been included with the discussions of the South Massif, the North Massif, and the Sculptured Hills. Table 6-V identifies the appropriate illustrations for these samples.

During the sample orientation studies, it became apparent that the special lighting used for orienting rock samples was also useful for enhancing structural and textural alinements that, for some samples, could be correlated with mappable lineations in boulders from which the samples were broken. This is especially true for the breccias. Most of the lineations in breccia samples appear to be closely spaced, thin shears. Some of these have deformed preexisting minerals and clasts or controlled recrystallization so

---

[a]U.S. Geological Survey.

as to form alternating light- and dark-colored streaks that offer variable resistance to lunar weathering on exposed surfaces. Other alinements are apparently covered by changes in composition, possibly representing initial layering in the breccias. Figures 6-88 to 6-96 are views of some samples that portray enhanced linear features.

TABLE 6-V.—*Lunar Orientation of Apollo 17 Rock Samples*

(a) Samples for which the orientation at the time of sampling has been established by correlation with lunar surface photographs

Sample no.	Lunar top (a)	Lunar north (a)	Figure no.
70185	T	E/N	6-65
70255	N	E/B	6-66
70275	T	E	6-67
71035	N/T	E/B	6-68
71055	S	E/T	6-69
71175	N/T	S/W	6-70 and 6-71
72155	T	N/E?	6-72
72215	B	S	6-8
72235	N	B/W	6-8
72255	S/B	W	6-8
72275	B	S	6-8
72315	W/T	N/B	6-10
72335	T/N	N/B	6-10
72355	N/T	S/W	6-10
72395	T	S/W	6-10
72435	B	N/W	6-12
73155	B/N	N/E	6-73
73235	T	S/E	6-74
73255	B	N	6-75
73275	T	W	6-76
74255	B	N/E	6-77
74275	T	S/E	6-78
75035	S/W	B/W	6-79
75055,1	T/N/E	S/E	6-80
75075	B	S/W	6-81 and 6-82
76015	W	B/S	6-83
76255	N	B	6-23
76275	T	W/S	6-23
76295	B	N/E	6-23
77135	S	T/W	6-84
78135	T	W	6-85
78235,0,2	T	S/E	6-40
78236	T	E/N	6-40
79175	W	N	6-86
79215	N	E/B	6-87

ªDirections are those of the identification cube used in orthogonal and stereoscopic photography (LRL mug shots): north, south, east, west, top, and bottom.

TABLE 6-V.—*Lunar Orientation of Apollo 17 Rock Samples*—Concluded

(b) Samples deleted from orientation attempt

Sample no.	Reason
70017	Insufficient lunar surface photographs
70018	Insufficient lunar surface photographs
70019	Breakage in transit
70035	Insufficient lunar surface photographs
70135	Insufficient lunar surface photographs
70175	Insufficient lunar surface photographs
70215	Insufficient lunar surface photographs
70295	Insufficient lunar surface photographs
70315	LRV sample; insufficient lunar surface photographs
71036	Inaccessible because of special storage
72135	LRV sample; insufficient lunar surface photographs
72415	Small size; not identifiable in lunar surface photographs
73215	Insufficient lunar surface photographs
73216	Insufficient lunar surface photographs
73217	Insufficient lunar surface photographs
73218	Insufficient lunar surface photographs
74235	Insufficient lunar surface photographs
75015	Breakage in transit; unsuccessful attempt
76035	Insufficient lunar surface photographs
76055	Insufficient lunar surface photographs
76135	LRV sample; insufficient lunar surface photographs
76215	Insufficient lunar surface photographs; unsuccessful attempt
76235	Breakage in transit
76315	Small size; not identifiable in lunar surface photographs
76335	Insufficient lunar surface photographs
77017	Insufficient lunar surface photographs
77035	Insufficient lunar surface photographs
77075	Breakage in transit
77115	Small size; not identifiable in lunar surface photographs
77215	Small size; not identifiable in lunar surface photographs
78238	Small size; not identifiable in lunar surface photographs
78255	Small size; not identifiable in lunar surface photographs
79035	Insufficient lunar surface photographs
79115	Small size; not identifiable in lunar surface photographs; unsuccessful attempt
79135	Small size; not identifiable in lunar surface photographs; unsuccessful attempt
79155	Insufficient lunar surface photographs
79195	Breakage in transit
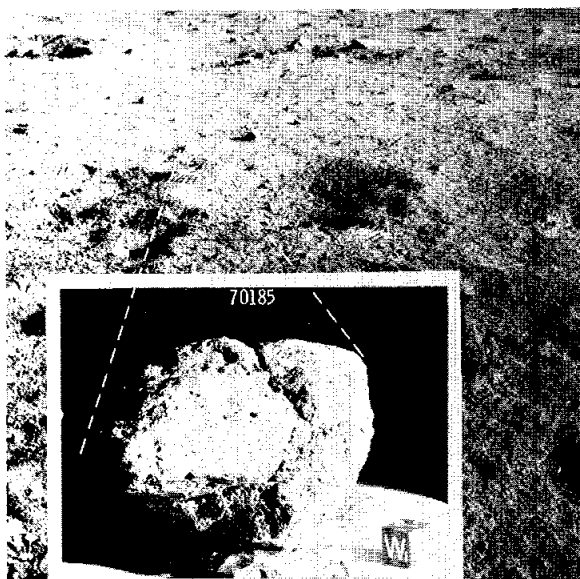
FIGURE 6-65.—Sample 70185 showing approximate lunar orientation reconstructed in the LRL compared to a portion of photograph AS17-136-20721, looking north (inset photograph, S-73-17797).

FIGURE 6-67.—Sample 70275 showing approximate lunar orientation reconstructed in the LRL compared to a portion of photograph AS17-135-20539, looking north (inset photograph, S-73-21388).

FIGURE 6-66.—Sample 70255 showing approximate lunar orientation reconstructed in the LRL compared to a portion of photograph AS17-135-20537, looking southwest (inset photograph, S-73-21974).
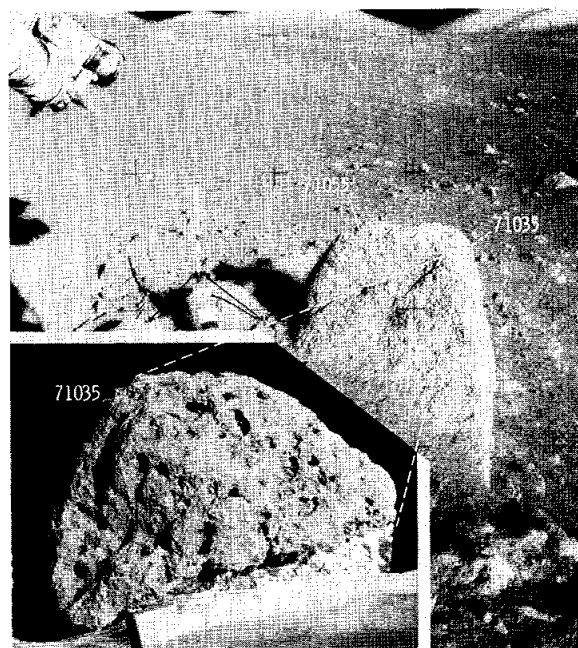
FIGURE 6-68.—Sample 71035, chipped from the same boulder as sample 71055, showing approximate lunar orientation reconstructed in the LRL compared to a portion of photograph AS17-136-20739 taken down-Sun, looking northwest (inset photograph, S-73-17804).
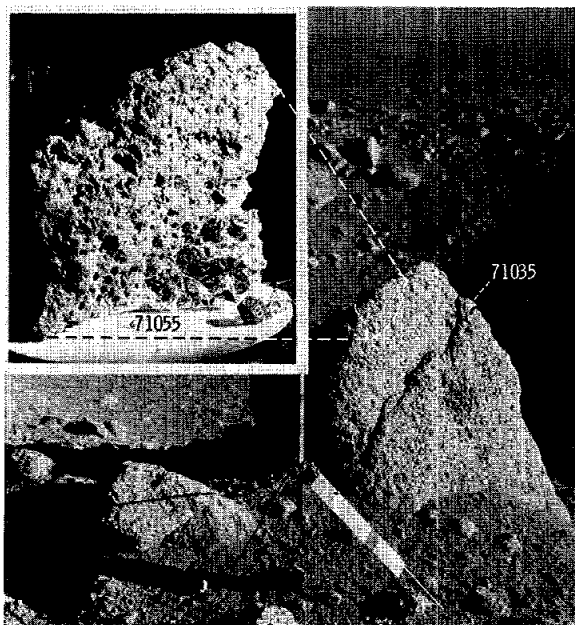
FIGURE 6-69.—Sample 71055, chipped from the same boulder as sample 71035, showing approximate lunar orientation reconstructed in the LRL compared to a portion of AS17-134-20394, looking north (inset photograph, S-73-17798).
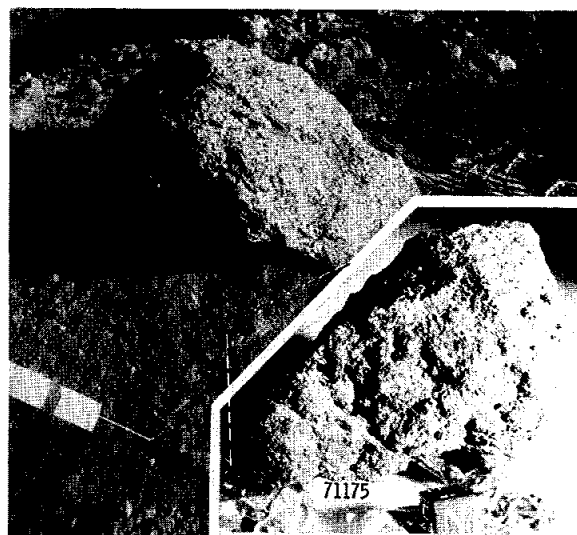
FIGURE 6-71.—Sample 71175 showing approximate lunar orientation reconstructed in the LRL compared to a portion of photograph AS17-134-20399, looking north (inset photograph, S-73-17802).
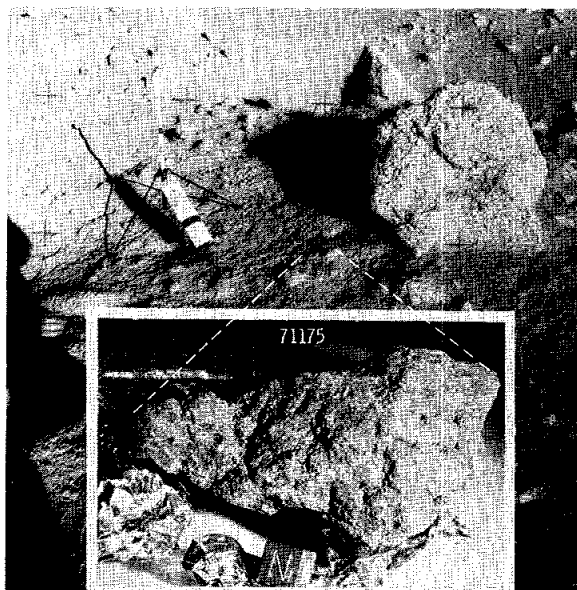
FIGURE 6-70.—Sample 71175 showing approximate lunar orientation reconstructed in the LRL compared to a portion of photograph AS17-136-20741 taken down-Sun, looking northwest (inset photograph, S-73-17803).
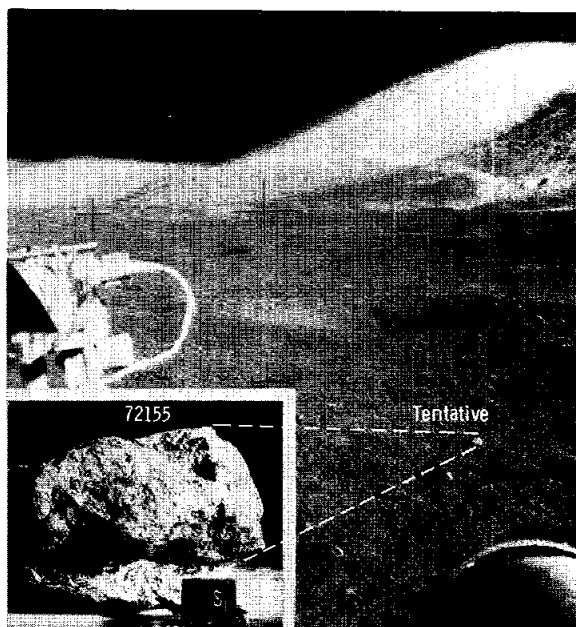
FIGURE 6-72.—Sample 72155 showing approximate lunar orientation reconstructed in the LRL tentatively compared to a portion of LRV driving photograph AS17-135-20649, looking north. No photograph was taken after collecting the sample (inset photograph, S-73-18406).

FIGURE 6-73.—Sample 73155 showing approximate lunar orientation reconstructed in the LRL compared to a portion of photograph AS17-138-21098, looking northwest (inset photograph, S-73-19595).

FIGURE 6-75.—Sample 73255 showing approximate lunar orientation reconstructed in the LRL compared to a portion of photograph AS17-138-21148 taken down-Sun, looking southwest (inset photograph, S-73-19592).

FIGURE 6-74.—Sample 73235 showing approximate lunar orientation reconstructed in the LRL compared to a portion of photograph AS17-138-21143, looking south (inset photograph, S-73-16968).
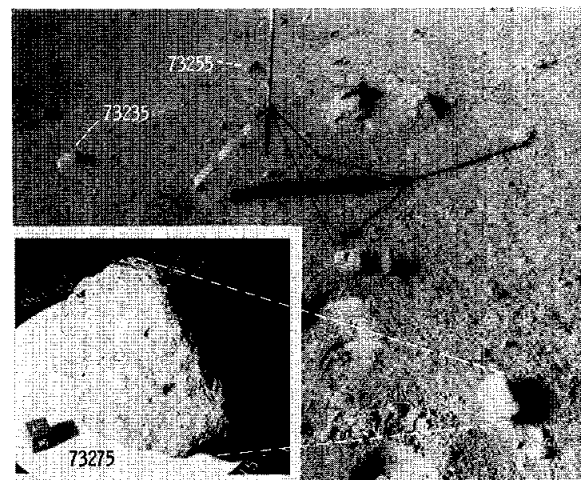
FIGURE 6-76.—Sample 73275 showing approximate lunar orientation reconstructed in the LRL compared to a portion of photograph AS17-138-21144, looking south (inset photograph S-73-16969).
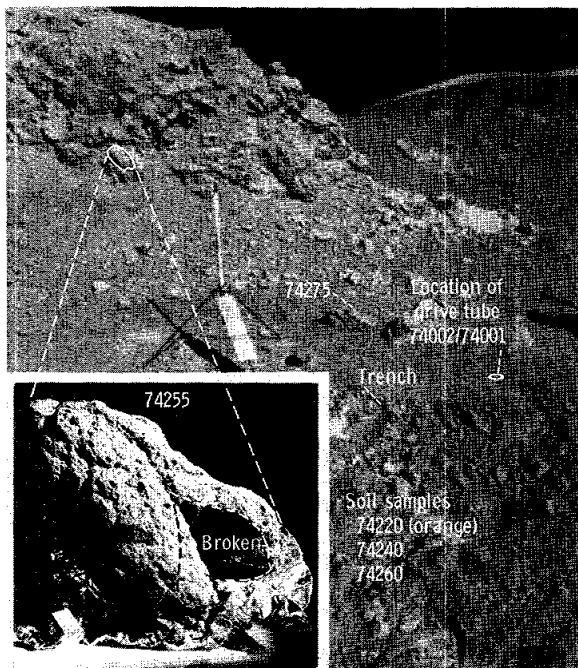
FIGURE 6-77.—Sample 74255 showing approximate lunar orientation reconstructed in the LRL compared to a portion of photograph AS17-137-20990 taken down-Sun, looking southwest. The sample broke from the boulder along existing fractures (inset photograph, S-73-18404).
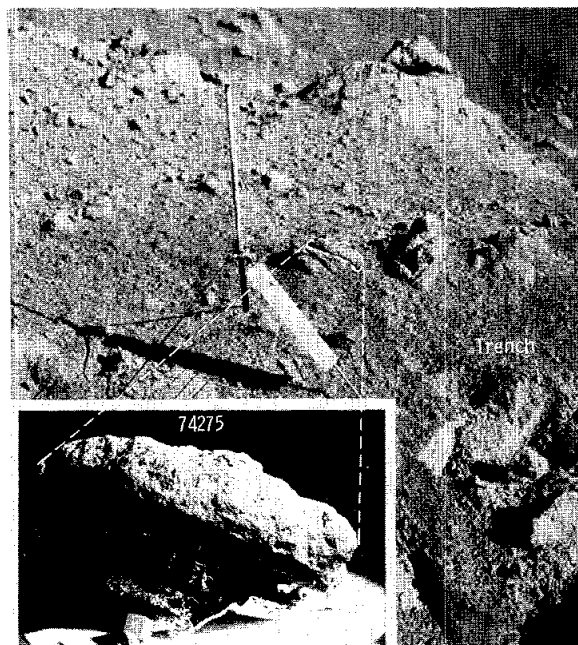
FIGURE 6-78.—Sample 74275 showing approximate lunar orientation reconstructed in the LRL compared to part of photograph AS17-137-20982, looking north. The sample was broken from the larger rock along a planar fracture (inset photograph, S-73-18405).
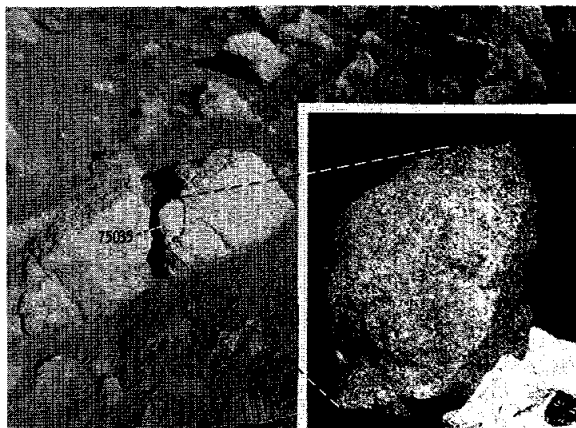
FIGURE 6-79.—Sample 75035, chipped from a boulder, showing approximate lunar orientation reconstructed in the LRL compared to part of photograph AS17-145-22138, looking northwest (inset photograph, S-73-19593).
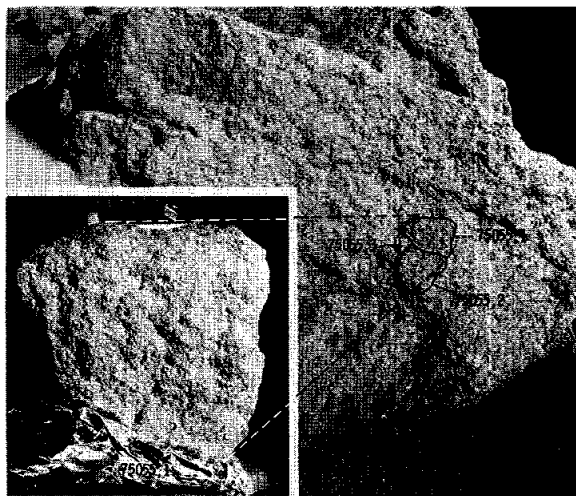
FIGURE 6-80.—Sample 75055, chipped from a boulder, showing approximate lunar orientation reconstructed in the LRL compared to part of photograph AS17-145-22148, looking north (inset photograph, S-73-17796).
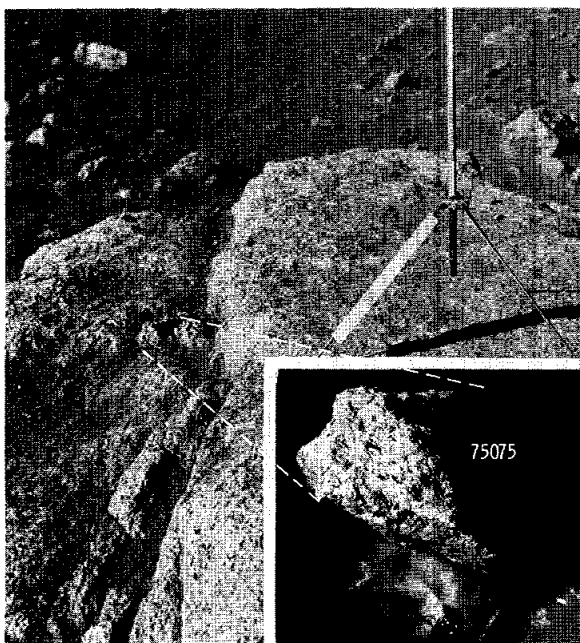
FIGURE 6-81.—Sample 75075, picked from the top of a large boulder, showing approximate lunar orientation reconstructed in the LRL compared to part of photograph AS17-145-22154, looking south (inset photograph, S-73-17800).
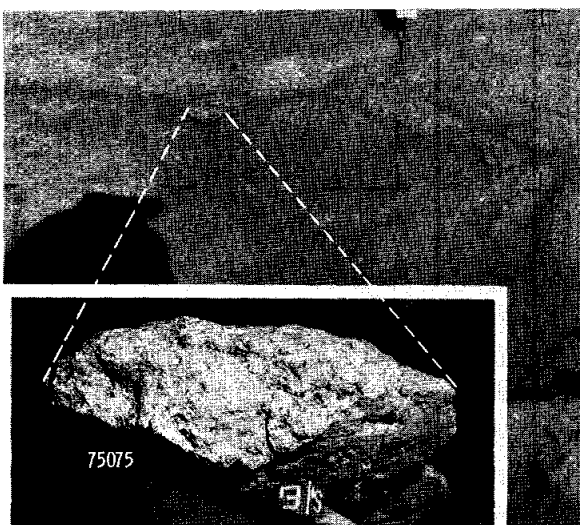
FIGURE 6-82.—Sample 75075 showing approximate lunar orientation reconstructed in the LRL compared to part of photograph AS17-133-20337 taken down-Sun, looking west (inset photograph, S-73-17801).
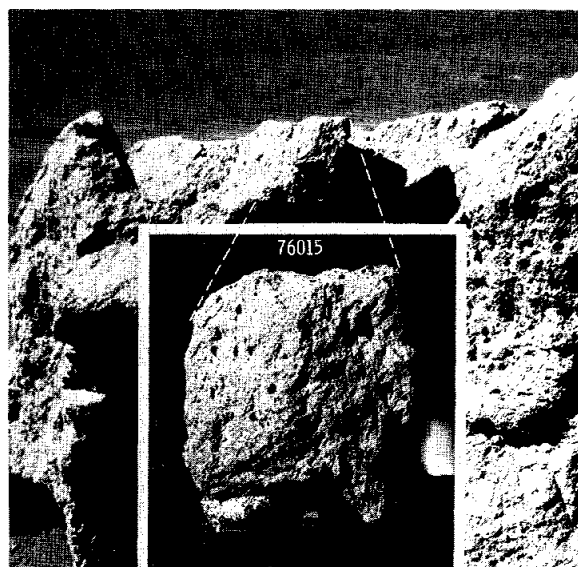
FIGURE 6-83.—Sample 76015 showing approximate lunar orientation reconstructed in the LRL compared to part of photograph AS17-140-21411 (inset photograph, S-73-19376).
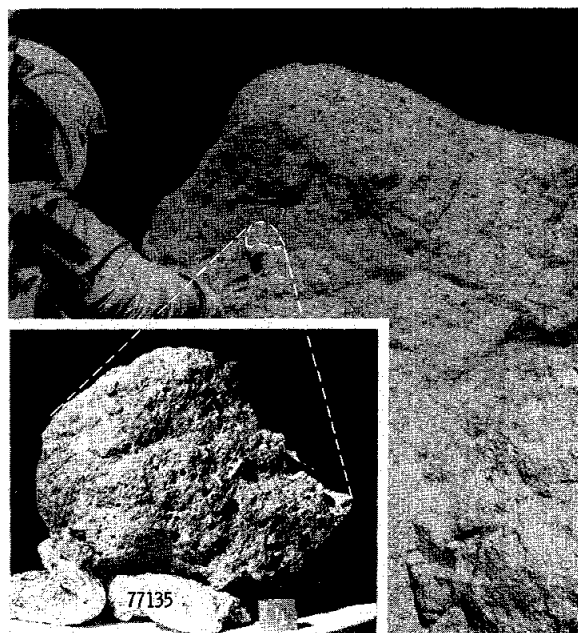
FIGURE 6-84.—Sample 77135, chipped from a large boulder, showing approximate lunar orientation reconstructed in the LRL compared to part of photograph AS17-146-22388 taken down-Sun, looking northwest (inset photograph, S-73-19386).
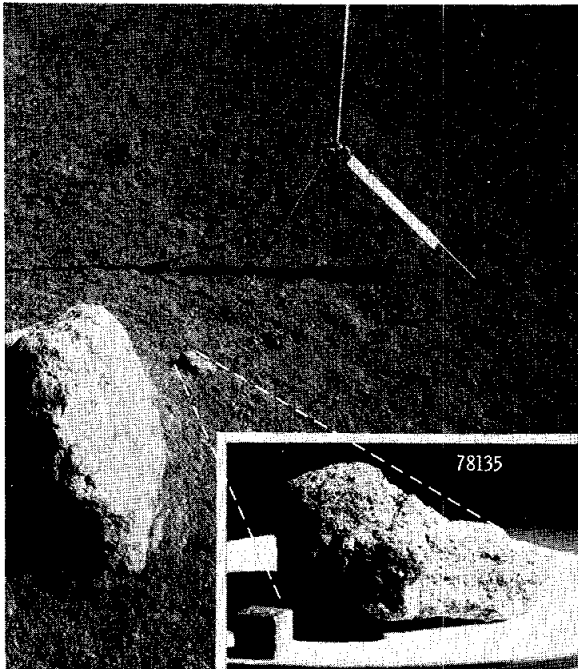
FIGURE 6-85.—Sample 78135 showing approximate lunar orientation reconstructed in the LRL compared to part of photograph AS17-146-22365, looking north (inset photograph, S-73-21073).

FIGURE 6-87.—Sample 79215 showing approximate lunar orientation reconstructed in the LRL compared to part of photograph AS17-143-21837, looking north (inset photograph, S-73-19590).
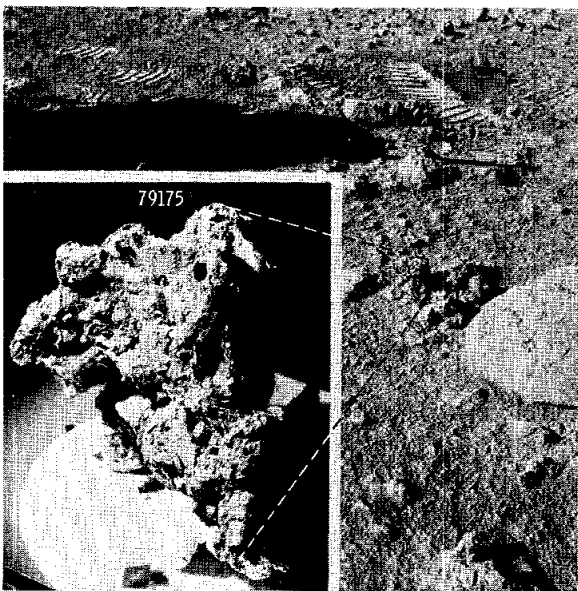
FIGURE 6-86.—Sample 79175 showing approximate lunar orientation reconstructed in the LRL compared to part of photograph AS17-146-22421, looking south (inset photograph, S-73-19594).
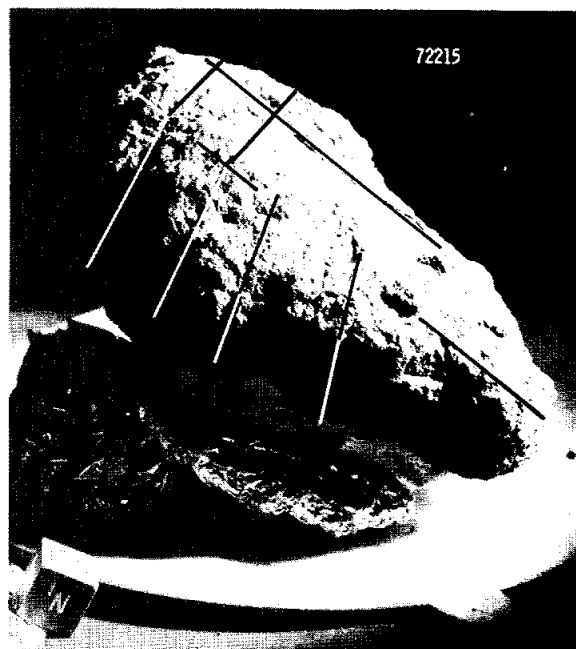
FIGURE 6-88.—Sample 72215 with enhancement of surface lineations by oblique lighting (S-73-17987). (See fig. 6-8 for reconstructed lunar orientation.)

FIGURE 6-90.—Sample 72275 collected from the top of a foliated, stratified breccia boulder as shown in figure 6-8 at station 2. Compositional layering seen in the sample is apparently parallel to a set of lineaments in the boulder (S-73-17988).
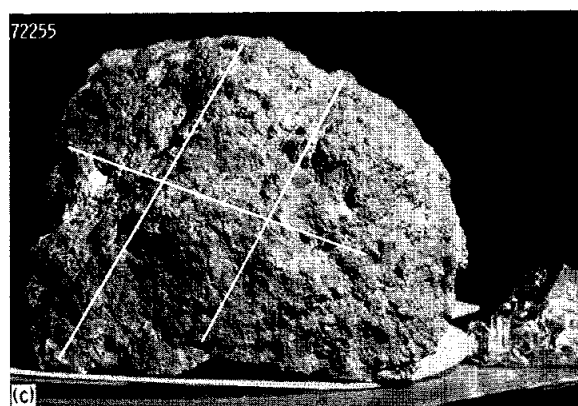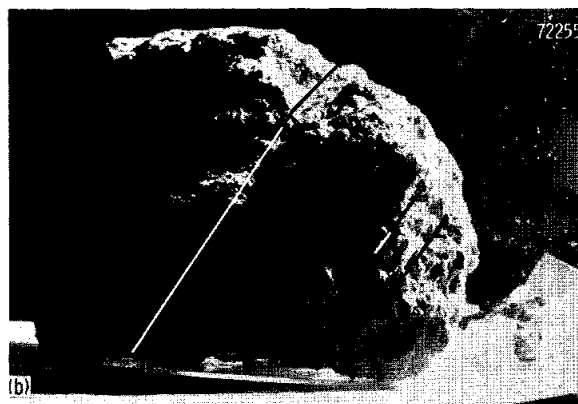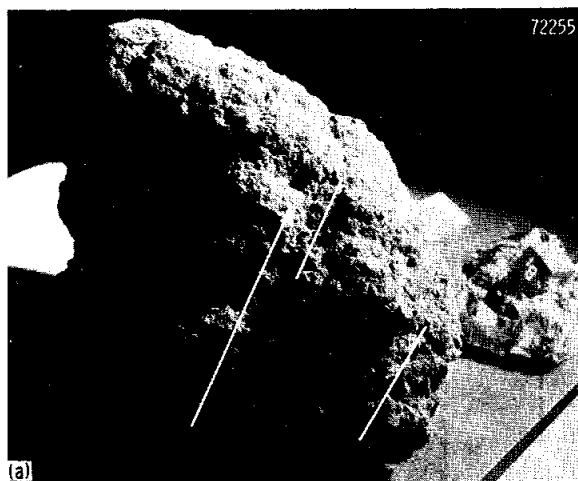
FIGURE 6-89.—Sample 72255 in reconstructed lunar orientation (S-73-17989). (a) Cross-Sun view. (b) Surface lineations that may be the traces of shear planes reconstructed with camera lower than in view (a). (c) Same view as shown in figure 6-89(b) with oblique lighting adjusted to enhance closely spaced shear traces on weathered surface.
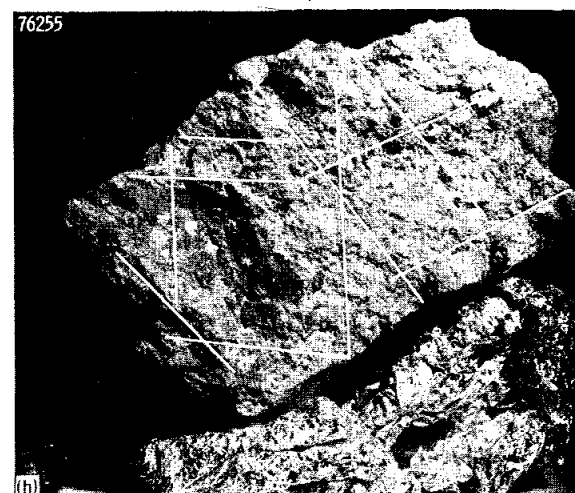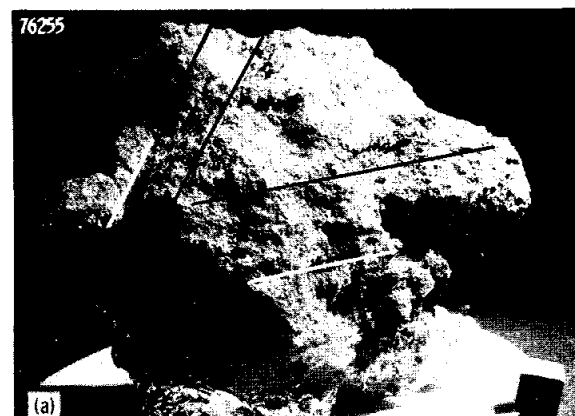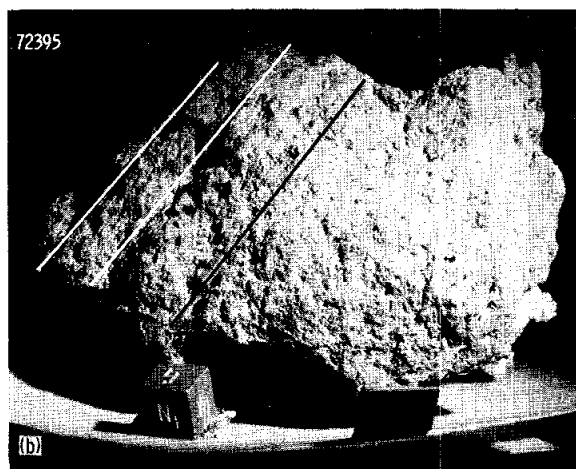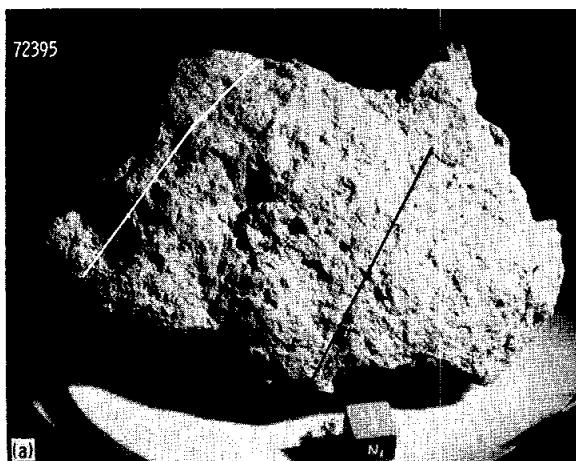
Figure 6-91.—Sample 72395 in reconstructed lunar orientation (S-73-19586). (a) Lines indicate shear traces on weathered surface. (b) Same view as shown in figure 6-91(a) with oblique lighting adjusted to accentuate surface streaks that may be traces of thin shears.
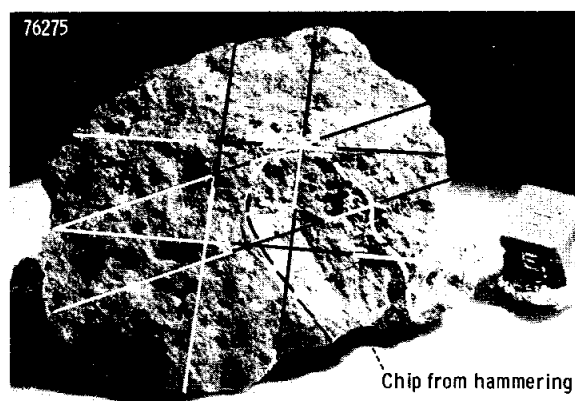
FIGURE 6-93.—Sample 76275 with oblique lighting adjusted to accentuate traces of shears on weathered surface. (See fig. 6-23 for reconstructed lunar orientation.)

FIGURE 6-92.—Sample 76255 in reconstructed lunar orientation. (a) Lines indicate shear traces on weathered surface (S-73-19375). (b) Lighting adjusted to accentuate traces of thin shear zones on freshly broken surface (S-73-19374).
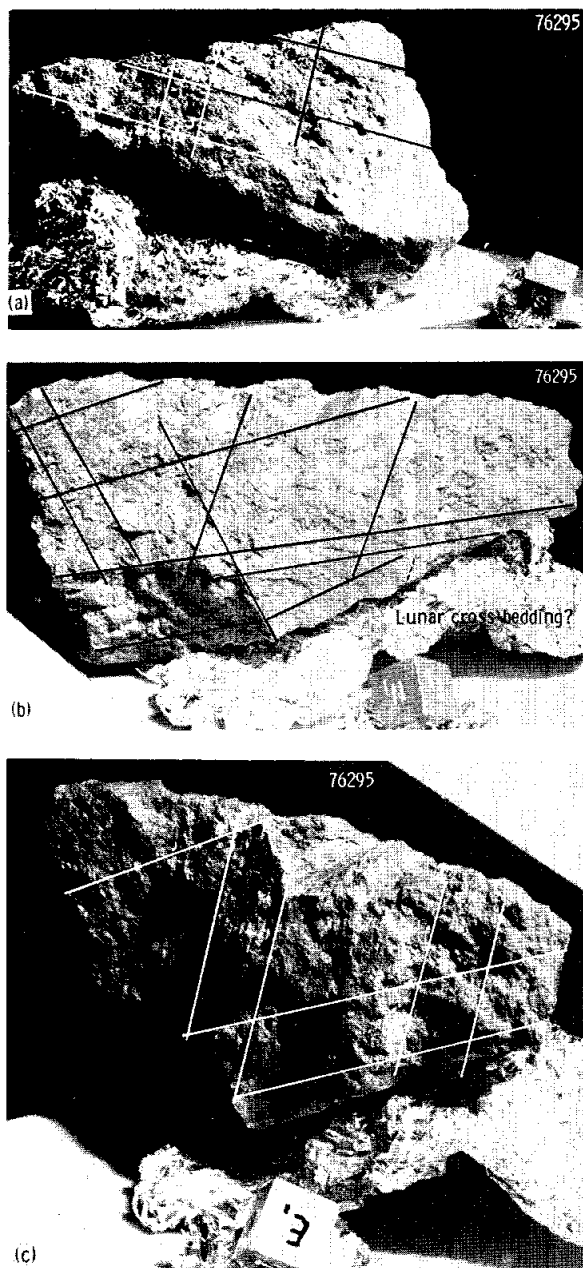
FIGURE 6-94.—Sample 76295 in reconstructed lunar orientation. (a) Lines indicate shear traces on weathered surface (S-73-19387). (b) Freshly broken surface obliquely lighted to enhance linear shear traces. (c) Alternate view.
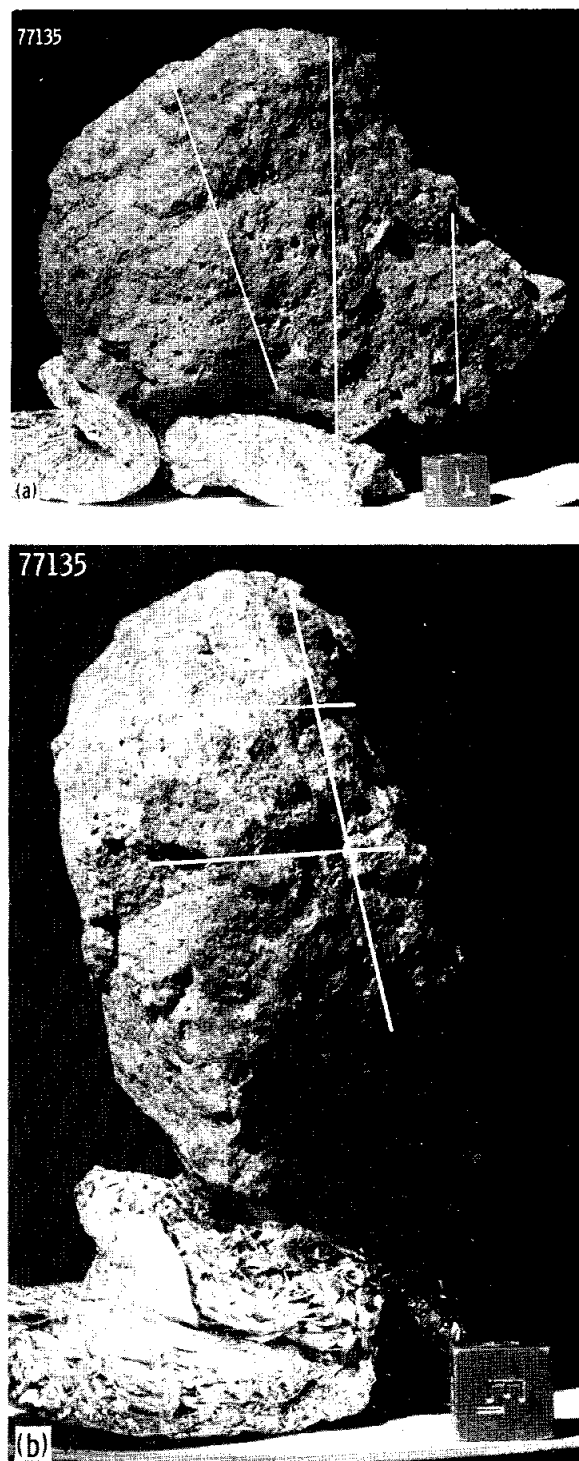
FIGURE 6-95.—Sample 77135 in reconstructed lunar orientation. (a) Lines indicate shears on weathered surface (S-73-19386). (b) In oblique lighting, lines indicate traces of shears in weathered surface. (c) Freshly broken surface lighted obliquely to accentuate shear traces.
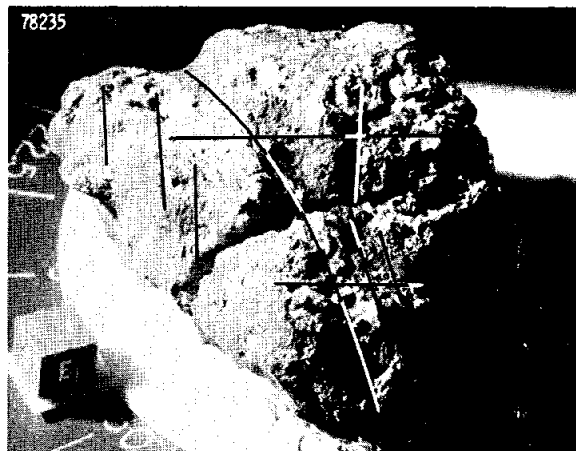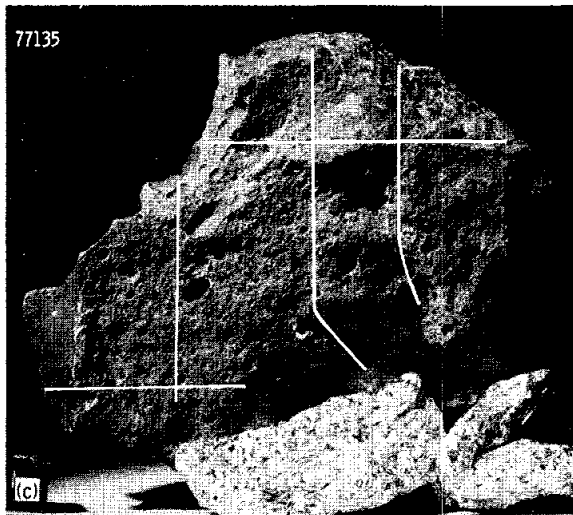
FIGURE 6-96.—Sample 78235 in reconstructed lunar orientation with oblique lighting to enhance traces of shears on weathered surface (S-73-17962).

APPENDIX B

PANORAMIC VIEWS AND DETAILED PLANIMETRIC MAPS
OF THE TRAVERSE STATIONS

Explanation of terms and symbols used in panoramic views and
planimetric maps (figs. 6-97 to 6-123)

70275	Sample number assigned by Lunar Receiving Laboratory
x	Sample location
70018?	Sample location uncertain
▫	Rake and soil sample location
DT 73002/73001	Drive tube, upper/lower tube number
C/S	ALSEP central station
G/M	Geophone module
EP-6	Explosive package number 6
Geo-2	Geophone number 2
HFE	Heat flow experiment
LEAM	Lunar ejecta and meteorites experiment
LM	Lunar module
LACE	Lunar atmospheric composition experiment
LSG	Lunar surface gravimeter experiment
LSP	Lunar seismic profiling experiment
Pan △	60-mm Hasselblad panorama
P pan △	Partial panorama
RTG	Radioisotope thermoelectric generator
SCB	Sample collection bag
SEP	Surface electrical properties experiment transmitter
LRV ▭	Lunar roving vehicle; dot shows front of vehicle
●	Boulder (letters refer to large blocks on maps and panoramas)
⊘	Crater

AS17-137-20886 20867   20868 20869   20870 20871   20873   20875

FIGURE 6-97.—Panoramic view taken south of the LM.

FIGURE 6-98.—Planimetric map of the LM-ALSEP-SEP area.
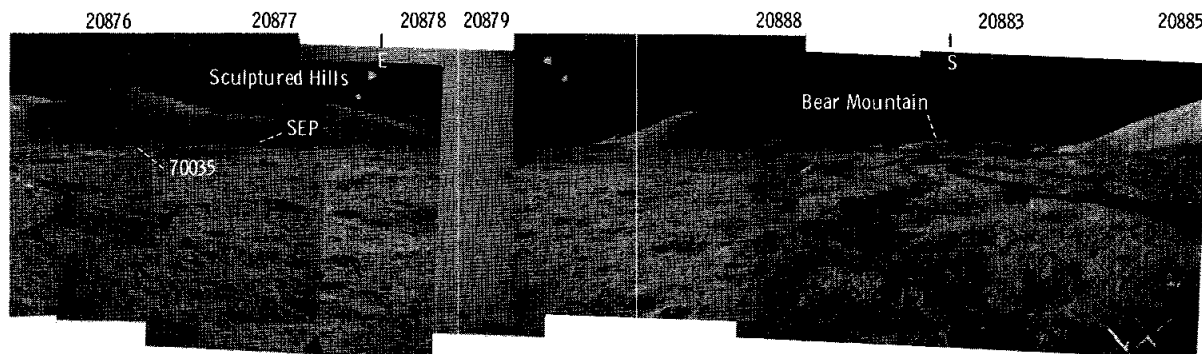
FIGURE 6-97.—Concluded.
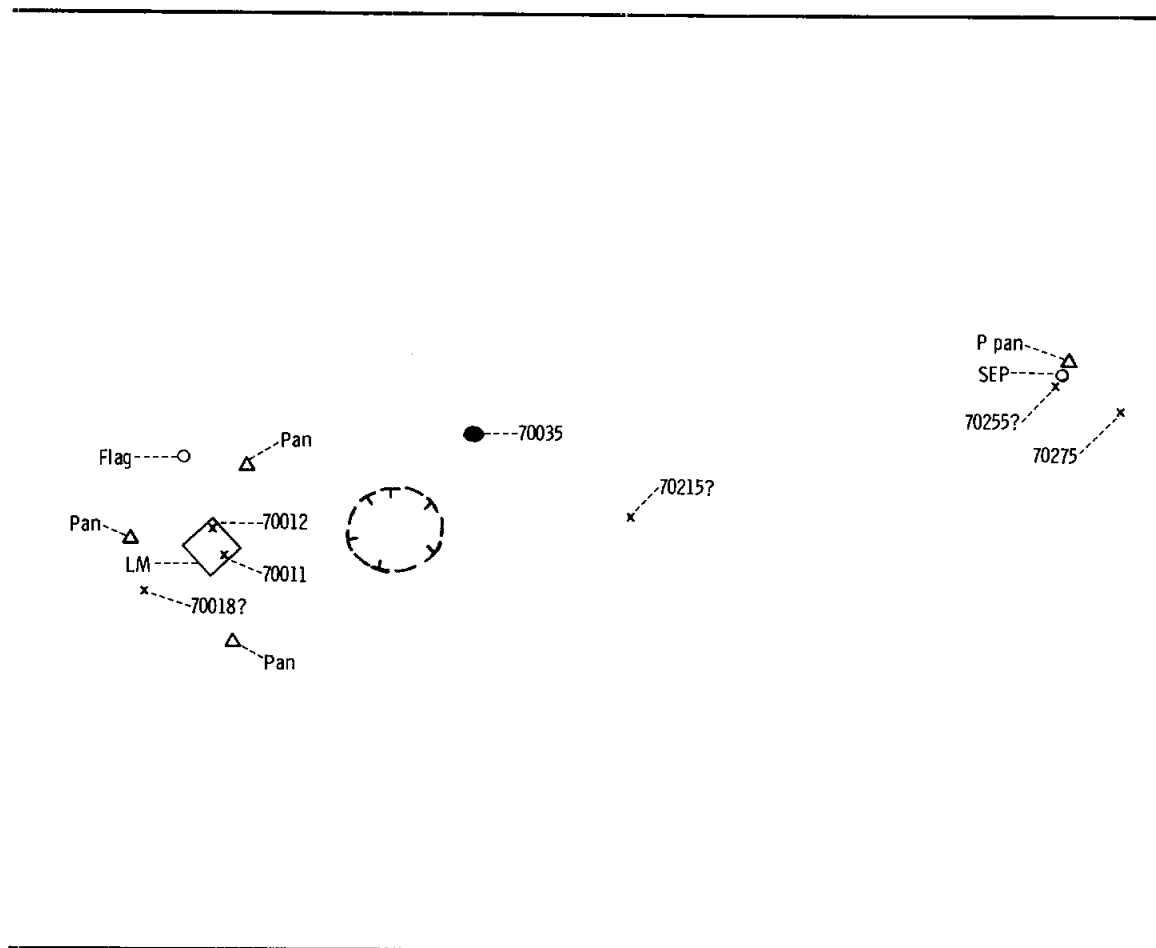
FIGURE 6-98.—Concluded.
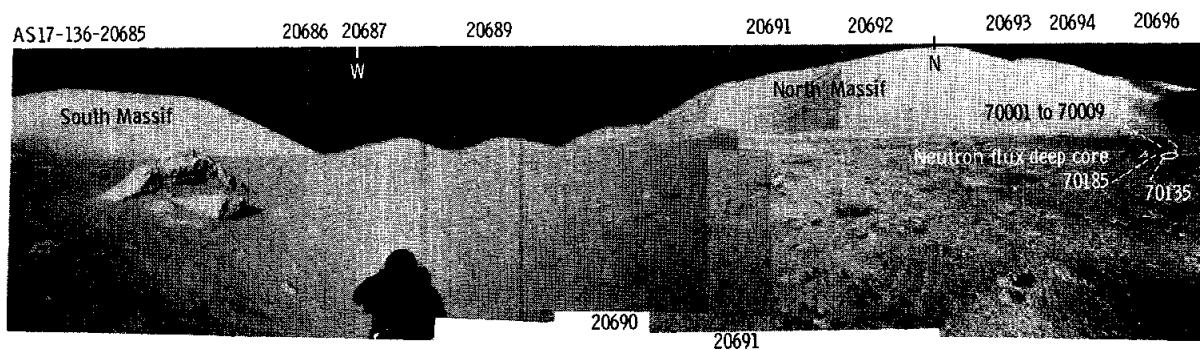
FIGURE 6-99.—Panoramic view taken northwest of the ALSEP central station.
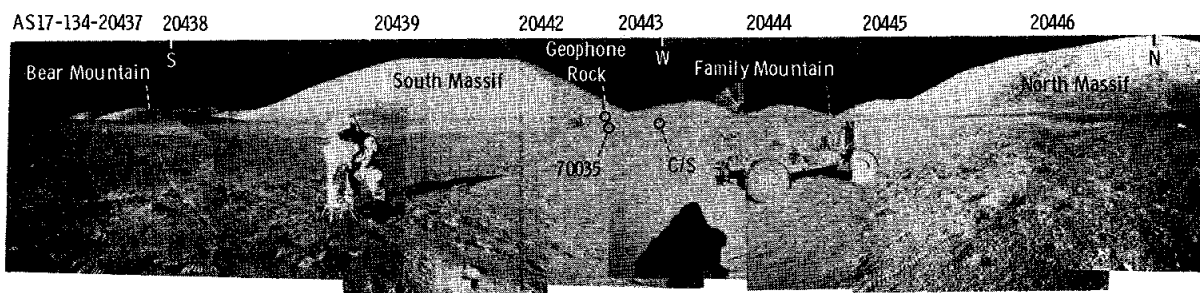
FIGURE 6-100.—Partial panorama of SEP site.
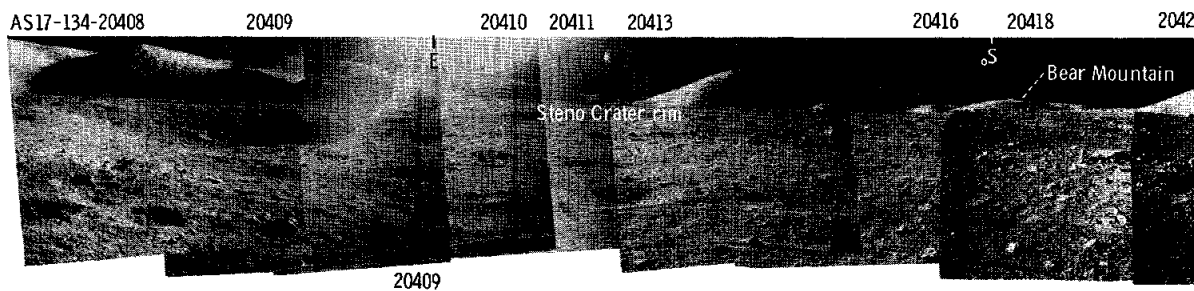
FIGURE 6-101.—Panoramic view taken east of station 1.
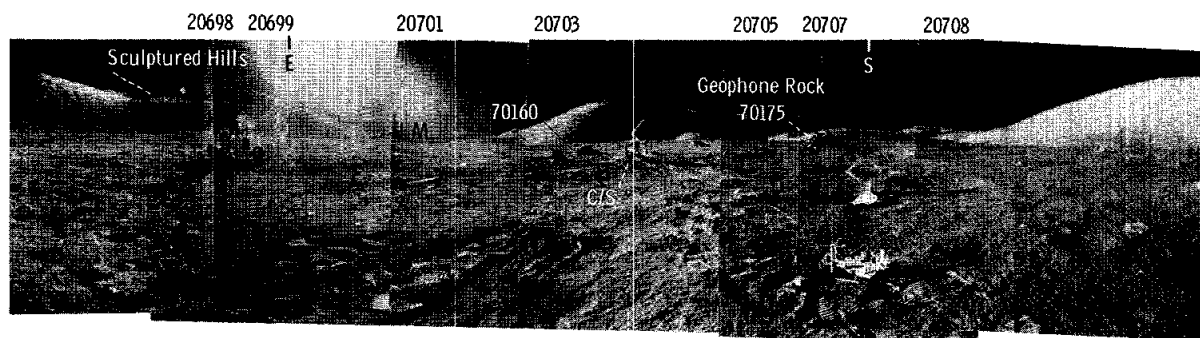
FIGURE 6-99.—Concluded.
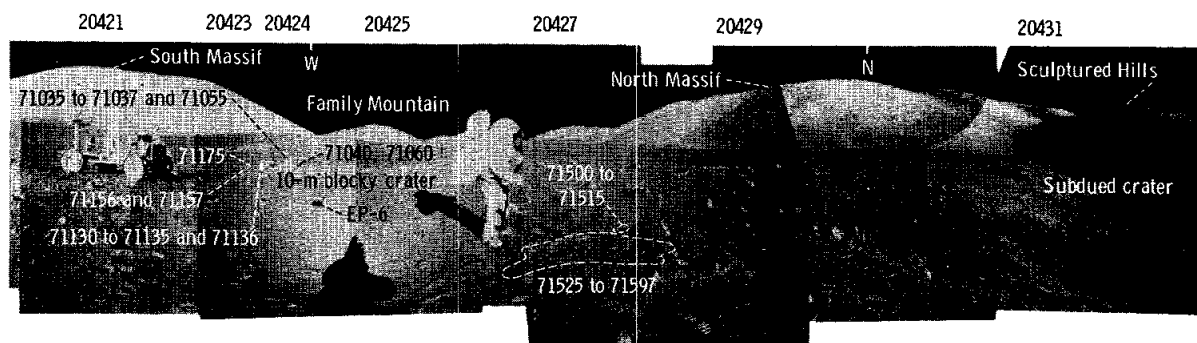
FIGURE 6-101.—Concluded.
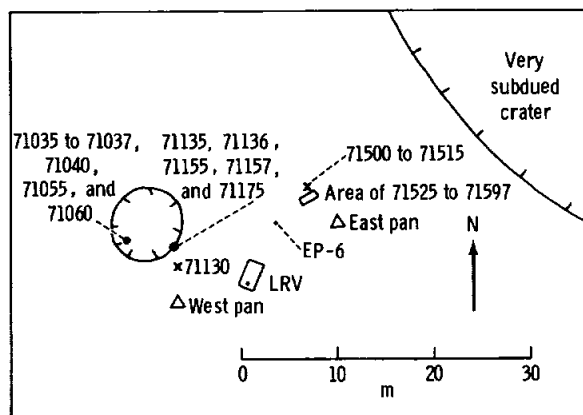
FIGURE 6-102.—Planimetric map of station 1.
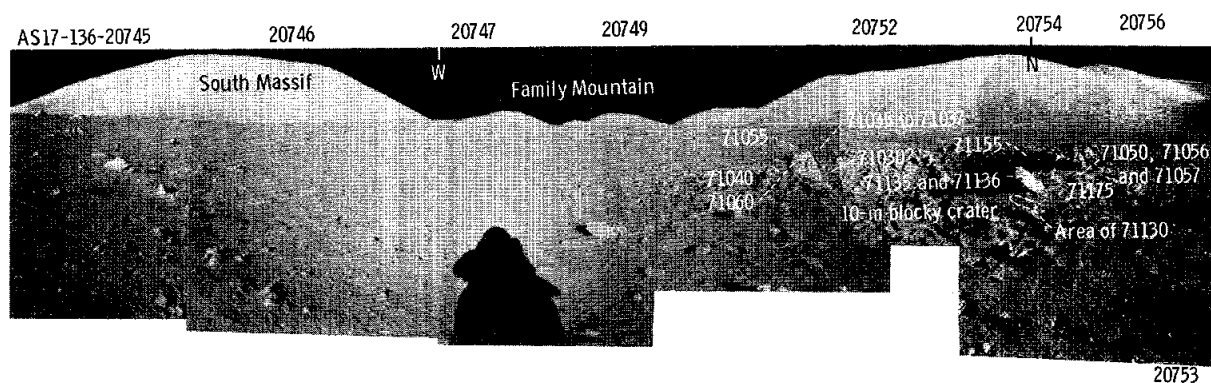
FIGURE 6-103.—Panoramic view taken west of station 1.
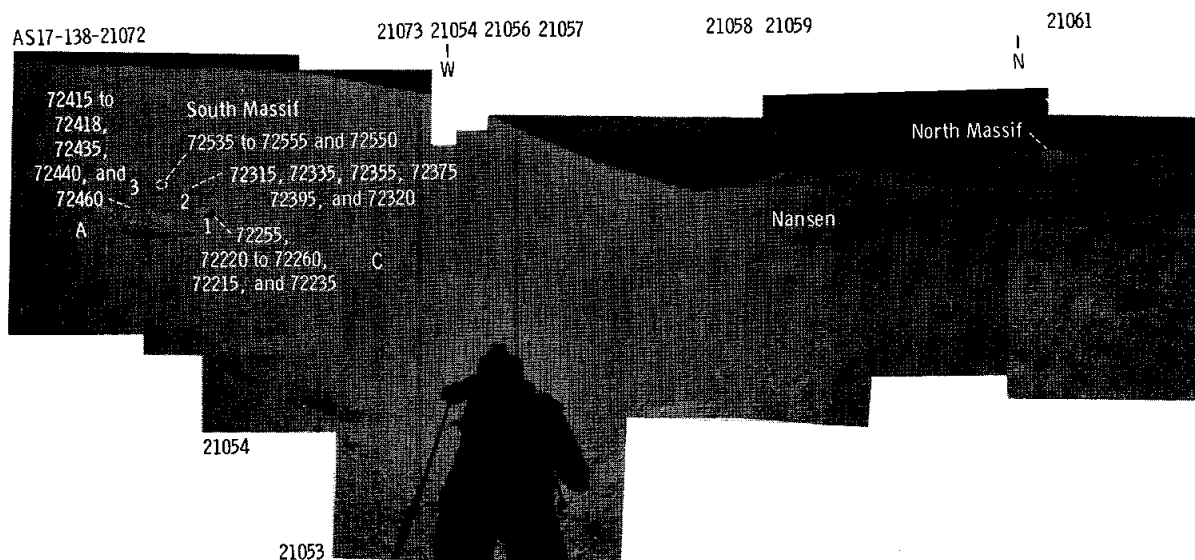
FIGURE 6-104.—Panoramic view taken northeast of station 2.
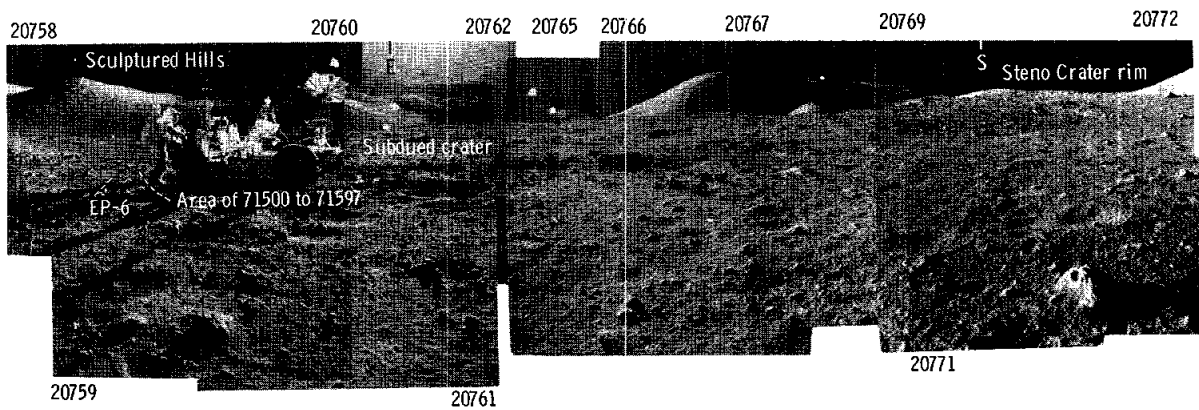
FIGURE 6-103.—Concluded.
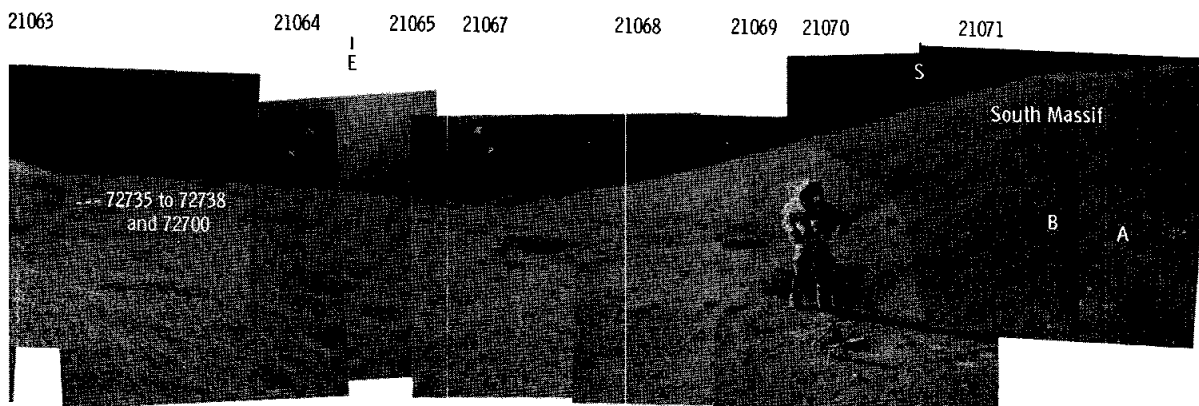
FIGURE 6-104.—Concluded.
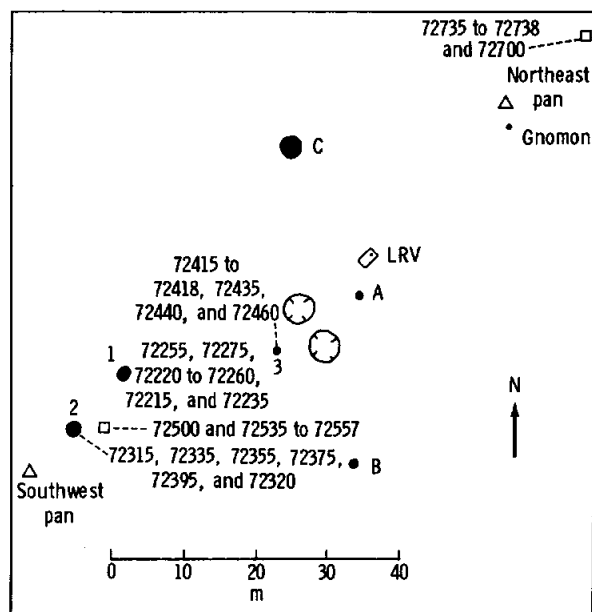
FIGURE 6-105.—Planimetric map of station 2.
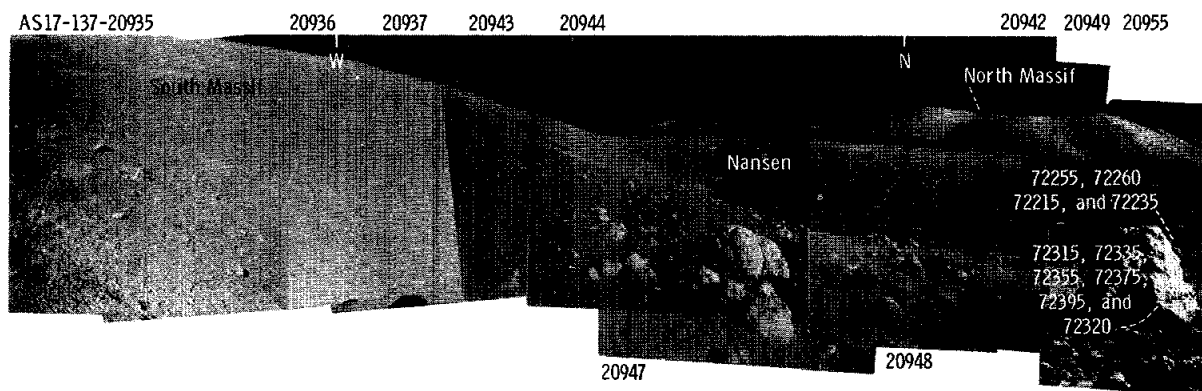
FIGURE 6-106.—Panoramic view taken southwest of station 2.
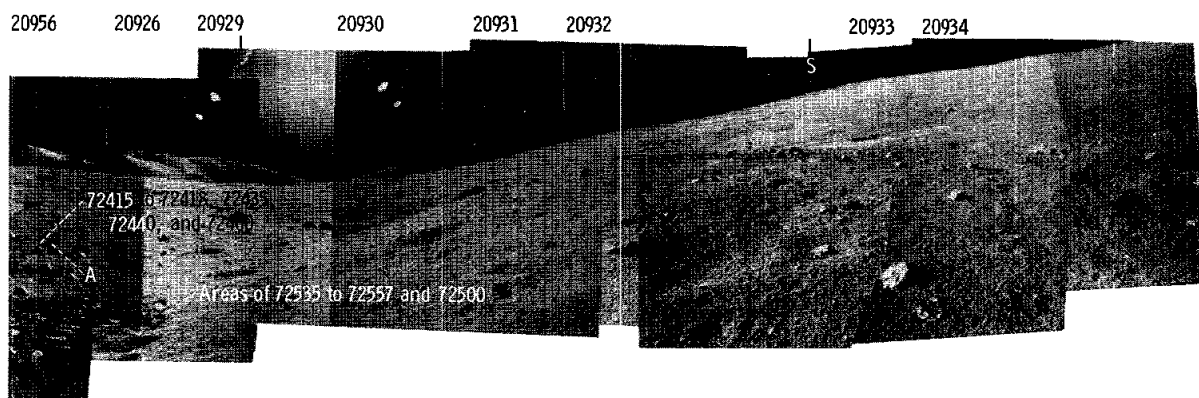
FIGURE 6-106.—Concluded.
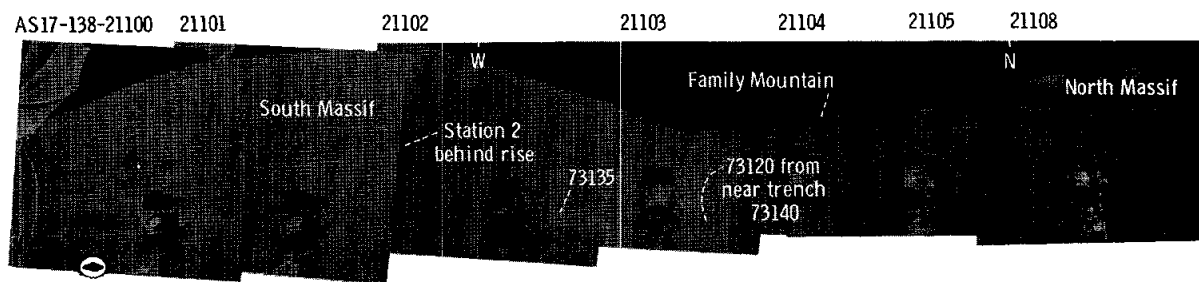
FIGURE 6-107.—Panoramic television view of station 2A taken at the LRV.
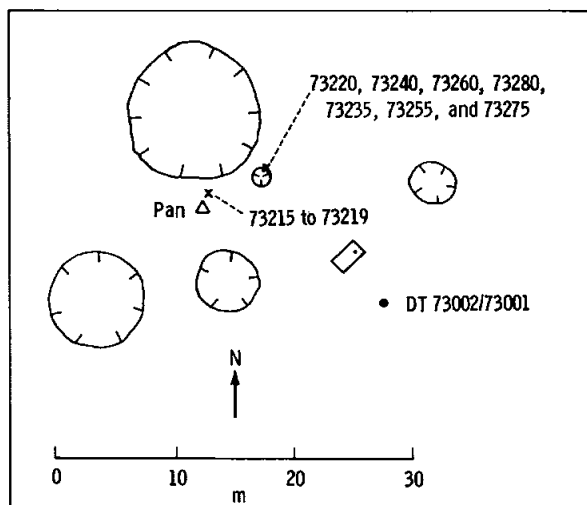
FIGURE 6-108.—Planimetric map of station 3.
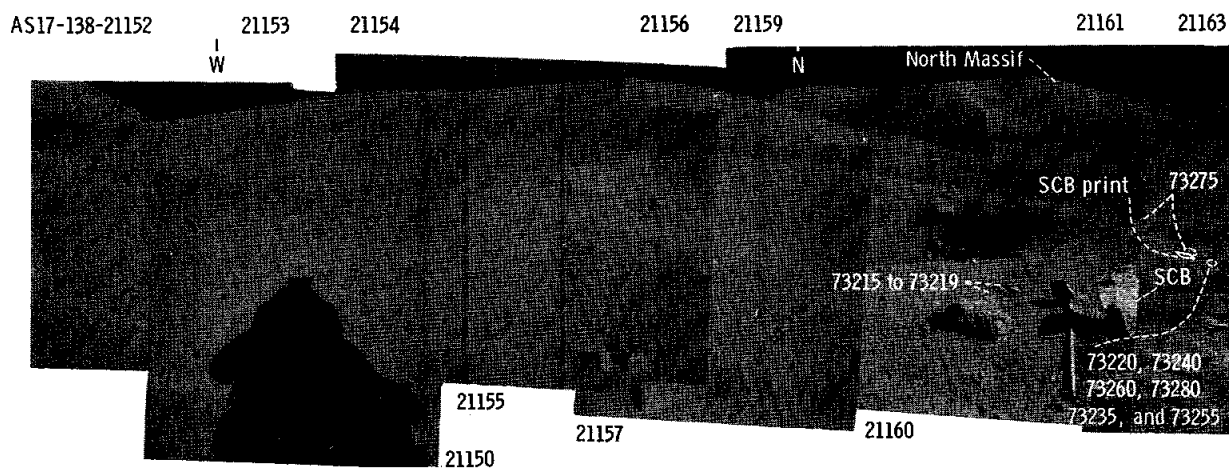
FIGURE 6-109.—Panoramic view of station 3.
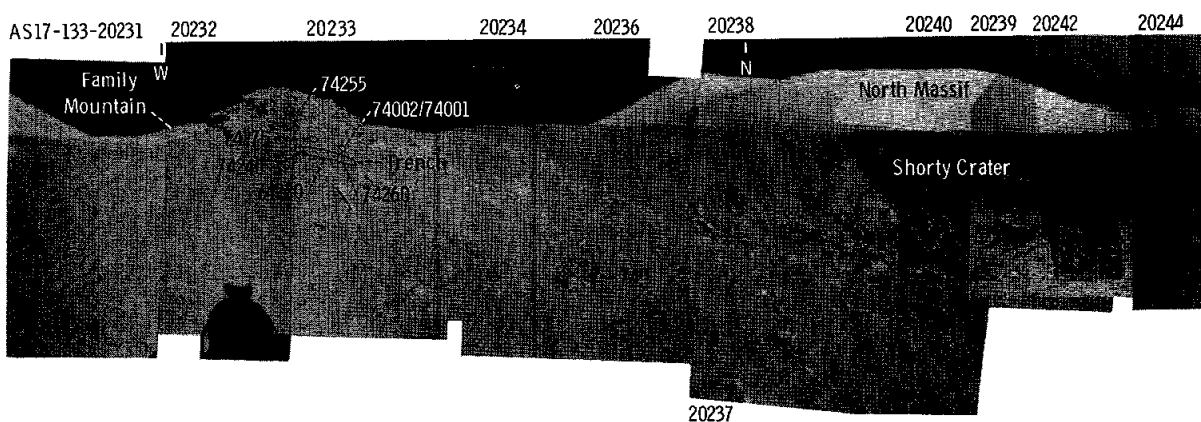
FIGURE 6-110.—Panoramic view taken west of station 4.
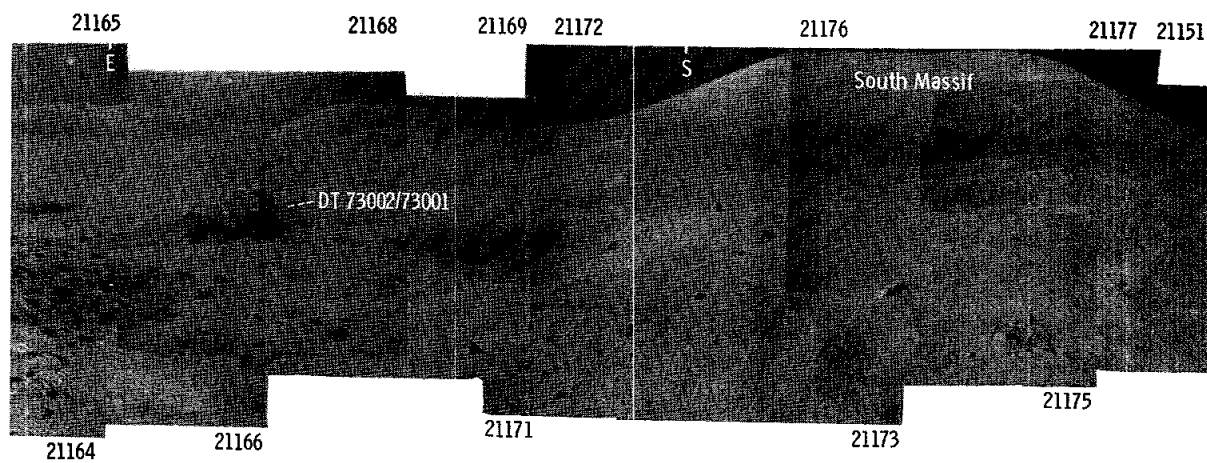
FIGURE 6-109.--Concluded.
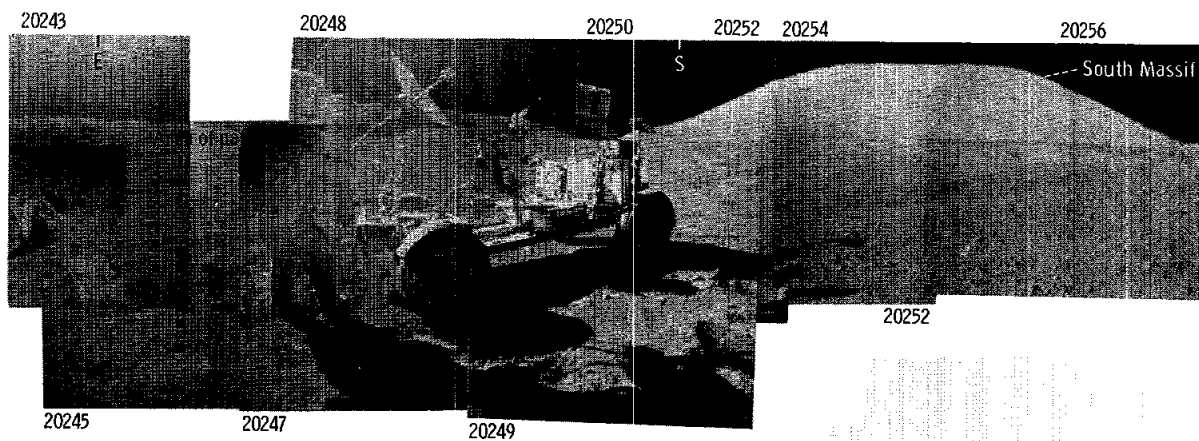
FIGURE 6-110.--Concluded.
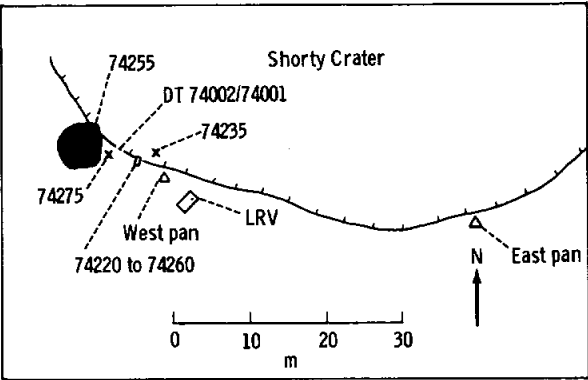
FIGURE 6-111.—Planimetric map of station 4.
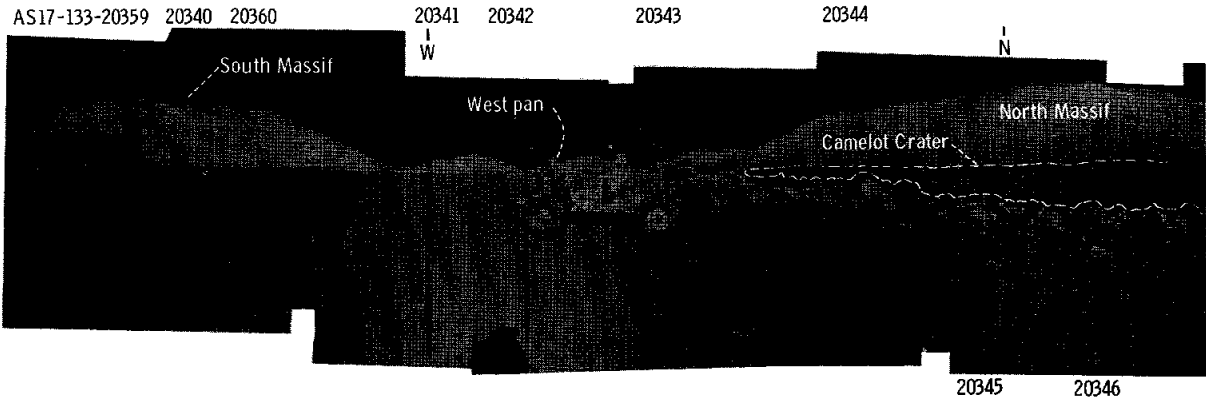
FIGURE 6-112.—Panoramic view taken east of station 5.
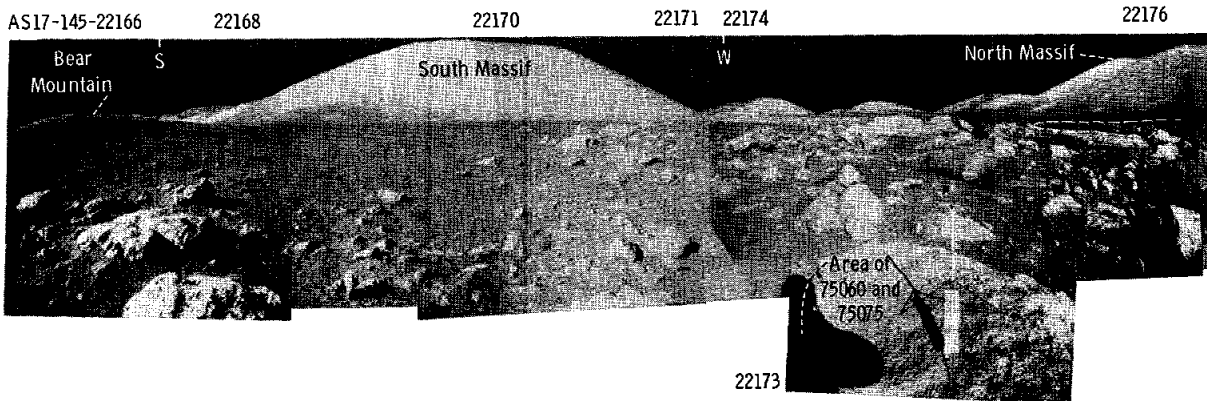
FIGURE 6-114.—Panoramic view taken west of station 5.

FIGURE 6-113.—Planimetric map of station 5.

FIGURE 6-112.--Concluded.

FIGURE 6-114.—Concluded.
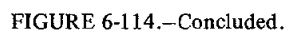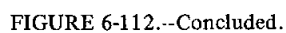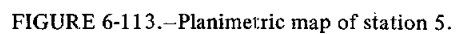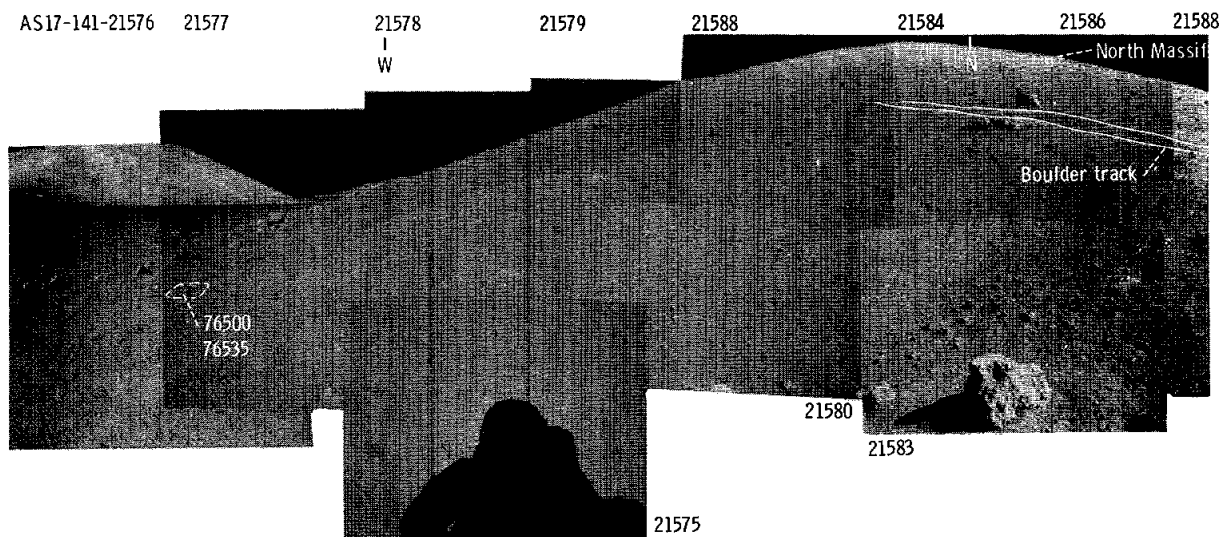
FIGURE 6-115.—Panoramic view taken south of station 6.
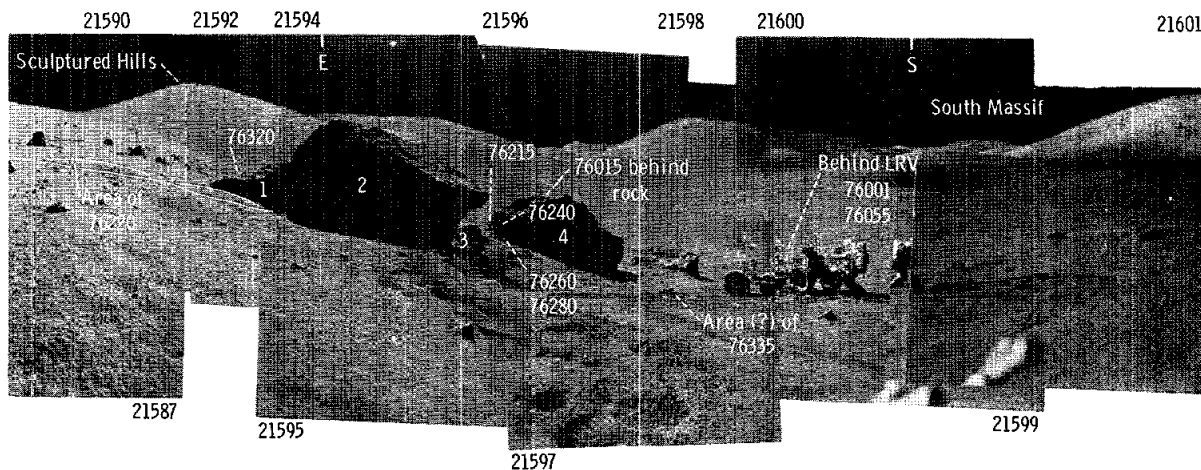
FIGURE 6-115.—Concluded.
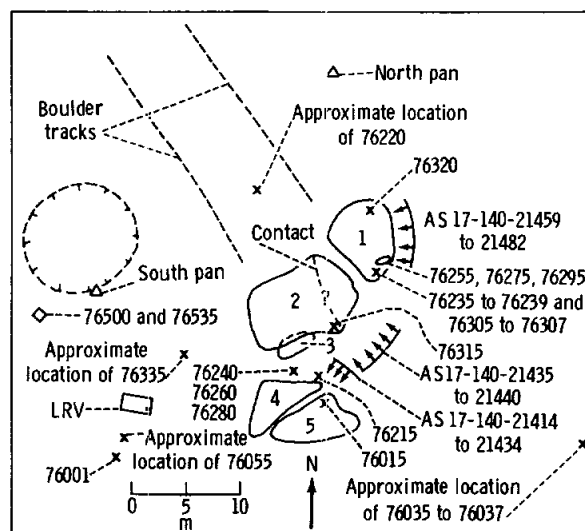
FIGURE 6-116.—Planimetric map of station 6.

AS17-140-21502   21508   21507   21505   21503   21501   21499

N

Sculptured Hills
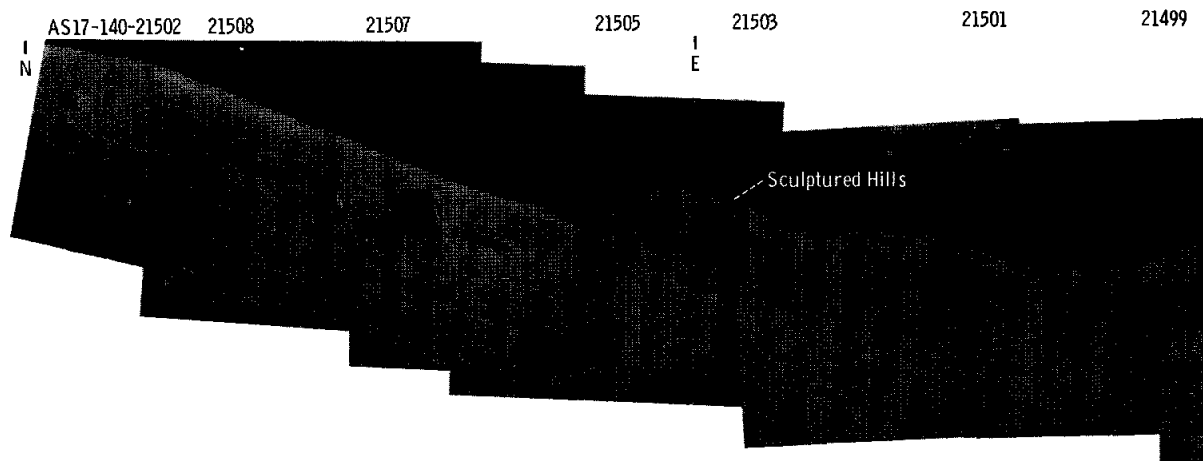
FIGURE 6-117.—Panoramic view taken north of station 6.

AS17-146-22341   22342   22344   22346   22348   22350   22352

E   S

Sculptured Hills   South Massif

77215 and
77075 to 77077

77135

Area of 77035   77115

Area of 77515 and 77017
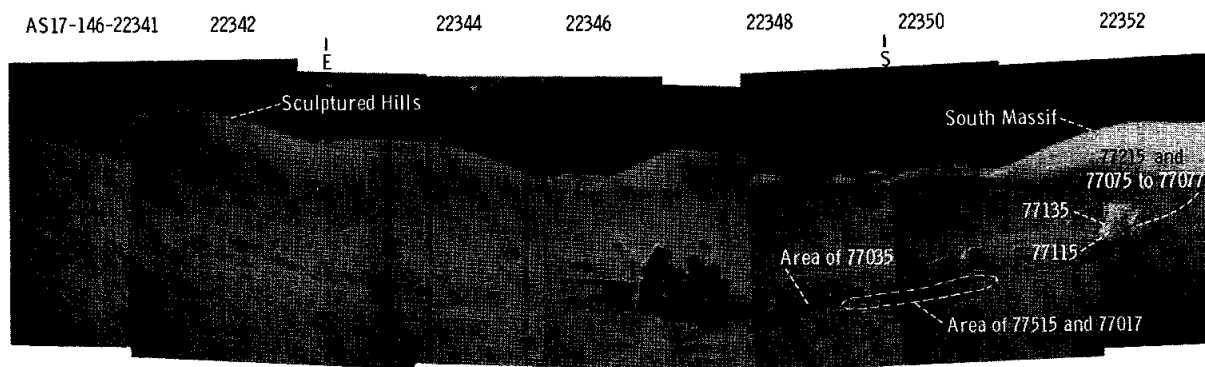
FIGURE 6-118.—Panoramic view taken north of station 7.

FIGURE 6-119.—Planimetric map of station 7.

FIGURE 6-117.—Concluded.

FIGURE 6-118.—Concluded.
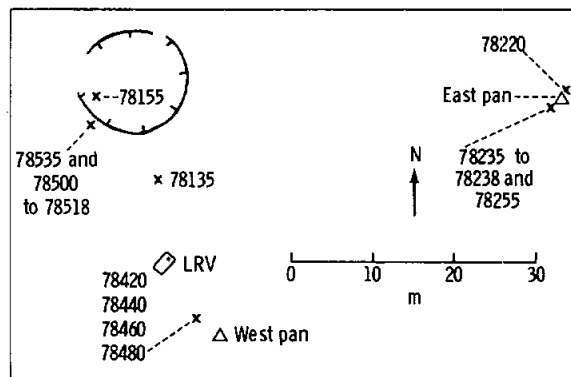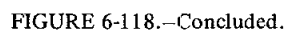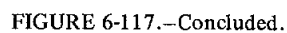
FIGURE 6-120.—Planimetric map of station 8.
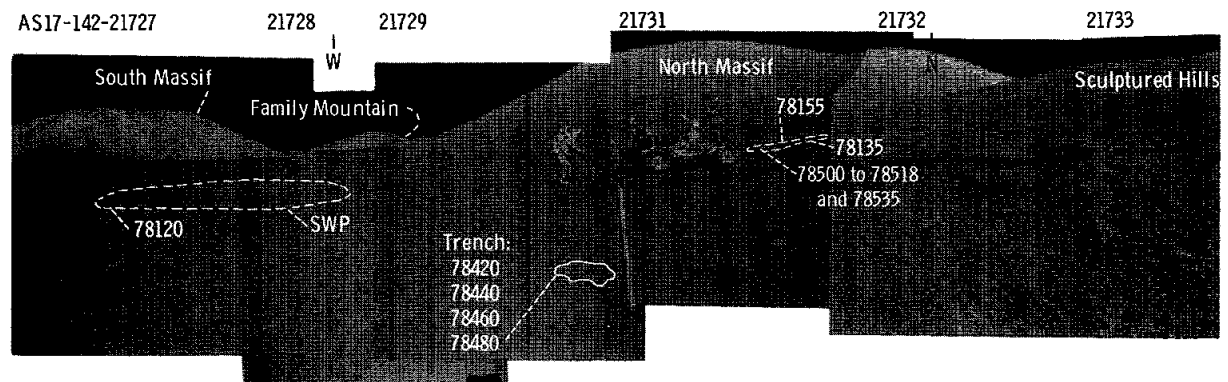
FIGURE 6-121.—Panoramic view taken west of station 8.
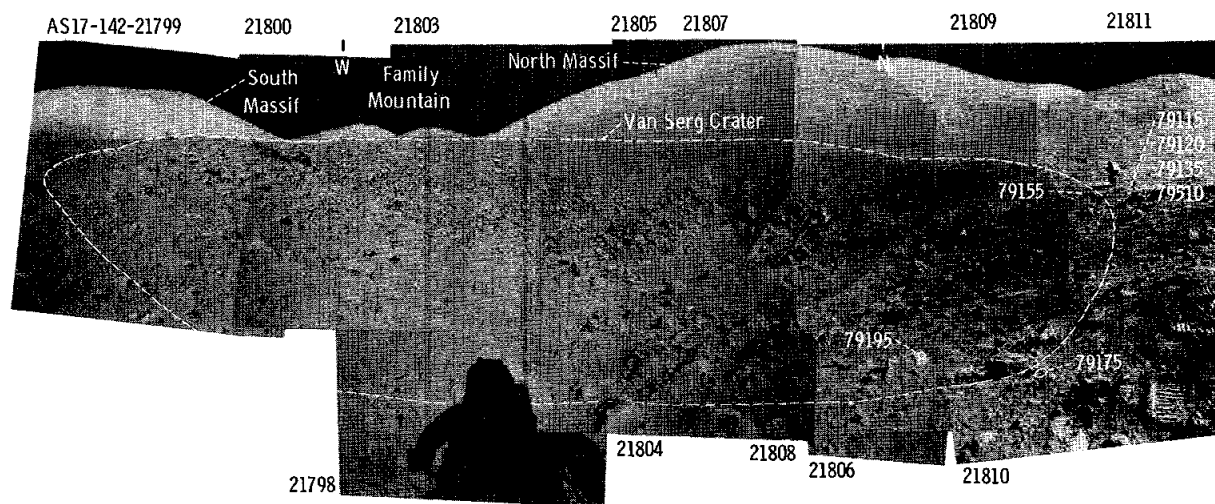
FIGURE 6-122.—Panoramic view taken west of station 9.

FIGURE 6-121.—Concluded.

FIGURE 6-122.—Concluded.

FIGURE 6-123.—Planimetric map of station 9.
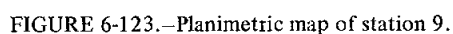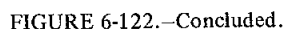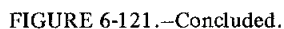
7. Preliminary Examination of Lunar Samples

The Lunar Sample Preliminary Examination Team[a]

The returned samples from the five previous Apollo and the two previous Luna missions include basaltic rocks and soils from four mare basins, glassy to crystalline breccias and soils from the Fra Mauro Formation and the Apennine Front, and highly aluminous, crystalline breccias and soils from two lunar highland sites. Isotopic dating of mare basalts (refs. 7-1 and 7-2) indicates that mare volcanism covered a timespan of 600 million years, beginning approximately 3.7 billion years ago. Similar studies of breccias (refs. 7-3 and 7-4) indicate an intense period of crystallization and an inferred formation of less than 200 million years, beginning approximately 4.0 billion years ago. Some anorthositic breccias from the 2- to 4-mm fragments of Apollo 16 soils have somewhat older crystallization ages of approximately 4.1 to 4.2 billion years (ref. 7-5) and may be remnants of earlier periods of formation. The breccias have undergone many generations of crushing, partial melting, and recrystallization, which has changed the initial textures of rocks from the early lunar crust.

These data raise important questions concerning both lunar and solar-system history. Do the measured basalt ages represent a restricted period of lunar volcanism, or is there evidence of younger or older volcanism in the unsampled areas? Answers to such questions are crucial to understanding the lunar thermal history and the origin of lunar magmas. Do the ages of breccia formation represent a restricted period of the major impacts that shaped the lunar surface, or have only the breccias associated with the last few major impacts been sampled? Answers to these questions are of profound importance to studies of the particle flux and the accretionary history of the early solar system. Are the breccias too highly modified to identify initial textures of the early

crustal rocks from which they were formed? To determine whether the early crust consisted of volcanic material, layered gabbroic complexes, or other possible rock types, the textural relationships among remnants of these materials must be studied.

For the final Apollo mission, it was imperative that a site be chosen to potentially provide answers to as many of these (and other) questions as possible. From orbit on the Apollo 15 mission, the command module pilot reported seeing dark patches that resembled young cinder cones southeast of the Serenitatis basin in the Taurus-Littrow region (ref. 7-6). Steep-walled valleys with over 2000 m of relief were also evident in this area. The possibility of relatively young volcanic activity and mountains consisting of a sequence of old, large-scale ejecta blankets made this an attractive site for further exploration.

Analysis of high-resolution photographs obtained during the Apollo 15 mission showed that a 6- to 10-km-wide valley between the second and third rings of the Serenitatis basin allowed access to two steep-sided mountains and a dark-mantled valley floor that might produce evidence of young volcanism (refs. 7-7 and 7-8). Detailed mapping provided five major photogeologic units for sampling: dark mantling material, a valley-filling rock unit below the mantle, a light-gray mantle apparently deposited by a slide or avalanche that spread across part of the valley floor, a group of domical, closely spaced hills ranging from 1 to 5 km in diameter (Sculptured Hills), and two steep mountains (North and South Massifs) with slopes showing several boulder tracks that were traceable from possible outcrops to the base of the slopes where some of the boulders lay within sampling range. These boulder tracks originated at various elevations on the massifs and may represent rock types from several different units in what might be a sequence of ejecta blankets from several major impacts.

The lunar module (LM) landed within 200 m of the targeted landing point (lat. 20°09'55" N, long. 30°45'57" E), and three traverses were completed (sec. 6). Three hundred thirty-five rocks (fragments greater than 1 cm across), 73 soils, eight drive tubes, and the deep drill string were collected. A complete list of Apollo 17 rocks and their designated types is presented in table 7-I. Several samples from large boulders were collected at stations 2, 6, and 7. From studies of samples, it is clear that the valley fill and the "dark mantle" are mare-type basalts or soils derived from them and the two massifs and the light mantle are various types of breccias and their derivatives, respectively. At present, it is not clear whether a specific set of rocks can be associated with the Sculptured Hills. In this paper, the chemical and petrographic characteristics of a representative suite of the Apollo 17 rock and soil specimens are summarized.

PETROGRAPHIC CHARACTERISTICS

Rocks

Visual and microscopic examinations of rocks from the Apollo 17 site indicate that they are the most variable collection returned by any mission. Some rocks show the cataclastic, highly crushed textures that were common in those returned during the Apollo 16 mission. Many are crystalline breccias with petrographic characteristics that indicate varying degrees of recrystallization or partial melting. Others are friable and dark gray like the many regolith breccias of previous missions. Others display features typical of the lavas returned from the Apollo 11, 12, and 15 mare sites, whereas few have the coarse-grained igneous textures typically developed during slow crystallization from basaltic melts. Such variety is a striking contrast to the rather restricted set of complex breccias returned from the Apollo 16 highland site.

In the preliminary examination, all rock samples were cleaned with a jet of nitrogen gas to remove dust coatings from their surfaces. The surfaces were then examined and described with a low-power binocular microscope. In addition, thin sections from 35 rocks were prepared and studied by conventional petrographic methods. From these examinations, the rocks may be placed in seven broad groups and two miscellaneous types.

1. Basalts

2. Dark matrix breccias

3. Glass-bonded agglutinates

4. Vesicular green-gray breccias (called anorthositic gabbros by the Apollo 17 crew during the lunar traverses)

5. Blue-gray breccias

6. Layered, foliated, light-gray breccias

7. Brecciated gabbroic rocks

8. Miscellaneous: crushed dunite and black fine-grained material from a dike.

Basalts

The basalts are generally vesicular to vuggy (fig. 7-1) and similar in both composition and texture to the Apollo 11 type B basalts (ref. 7-9), except for some of the detailed relationships between opaque minerals and pyroxene zonation. Modal estimates indicate 45 to 55 percent clinopyroxene (both pigeonite and augite), 25 to 30 percent plagioclase, 15 to 25 percent opaque minerals, and small amounts of olivine. In some instances, the olivine occurs as cores of pyroxene; but it usually occurs as phenocrysts, which generally comprise only a few percent of a rock but occasionally as much as 20 percent. Grain sizes range from coarse (1 to 2 mm) through fine to vitrophyric. In some coarse-grained rocks, the clinopyroxene may occur both as coarse, sectorially zoned phenocrysts and as finer grains in poikilitic plagioclase (fig. 7-2). There also may be fine fibrous or plumose intergrowths of plagioclase and clinopyroxene. Traces of cristobalite, tridymite, a needle-shaped phase, and very fine (perhaps partly glassy) material occur interstitially to the larger grains. The vitrophyres (now largely divitrified) contain skeletal crystals of olivine (fig. 7-3) that, in some instances, display overgrowths of clinopyroxene, skeletal ilmenite and armalcolite, and a few patches of plumose intergrowths of plagioclase and pyroxene. For a given sampling area, the entire range of textures may be present.

Opaque minerals in the subfloor basalts are present in abundances of as much as approximately 25 percent (by volume); most rocks average approximately 20 percent. Ilmenite, armalcolite, chrome-spinel, ulvöspinel, rutile, metallic iron-nickel (Fe-Ni), and troilite have been identified optically; all of these minerals occur in most of the rocks. Ilmenite is by far the most abundant oxide mineral (approximately 15 to 20 volume percent); reflection pleochroism and

TABLE 7-I.--*Complete List of Apollo 17 Rocks*[a]

Sample number (b)	Weight, g (c)	Rock type	Sample number (b)	Weight, g (c)	Rock type
70017	2957	Coarse basalt	71175	207.8	Medium basalt
70018	51.38	Dark matrix breccia	71505 RS	29.45	Fine basalt
70019	159.9	Agglutinate	71506 RS	12.11	Fine basalt
70035 B_1	5765	Coarse basalt	71507 RS	3.962	Medium basalt
70075	5.64	Fine basalt	71508 RS	3.423	Coarse basalt
70135 B_2	446.3	Medium to coarse basalt	71509 RS	1.690	Coarse basalt
70136 B_2	10.65	Medium to coarse basalt	71515 RS	1.635	Agglutinate
70137 B_2	6.16	Medium to coarse basalt	71525 R	3.900	Fine basalt
70138 B_2	3.66	Medium to coarse basalt	71526 R	12.91	Fine basalt
70139 B_2	3.16	Medium to coarse basalt	71527 R	2.186	Fine basalt
70145 B_2	3.07	Medium to coarse basalt	71528 R	11.25	Fine basalt
70146 B_2	1.71	Medium to coarse basalt	71529 R	6.025	Medium basalt
70147 B_2	1.35	Medium to coarse basalt	71535 R	17.71	Coarse basalt
70148 B_2	.92	Medium to coarse basalt	71536 R	5.322	Coarse basalt
70149 B_2	.95	Medium to coarse basalt	71537 R	12.25	Fine basalt
70155 B_2	.77	Medium to coarse basalt	71538 R	8.038	Fine basalt
70156 B_2	.63	Medium to coarse basalt	71539 R	10.90	Fine basalt
70157 B_2	.57	Medium to coarse basalt	71545 R	17.26	Fine basalt
70165 S	2.143	Coarse basalt	71546 R	150.7	Fine basalt
70175	339.6	Dark matrix breccia	71547 R	12.54	Medium basalt
70185 S	466.6	Coarse basalt	71548 R	25.46	Medium basalt
70215	8110	Fine basalt	71549 R	7.903	Medium basalt
70255	277.2	Fine basalt	71555 R	4.547	Medium basalt
70275 S	171.4	Medium basalt	71556 R	29.14	Coarse basalt
70295	361.2	Dark matrix breccia	71557 R	40.35	Coarse basalt
70315 S	148.6	Coarse basalt	71558 R	15.81	Coarse basalt
71035 B_1	144.8	Medium basalt	71559 R	82.16	Coarse basalt
71036 B_1	118.4	Medium basalt	71565 R	24.09	Coarse basalt
71037 B_1	14.39	Medium basalt	71566 R	415.4	Coarse basalt
71045 S	11.92	Medium basalt	71567 R	146.0	Coarse basalt
71046 S	3.037	Medium basalt	71568 R	10.02	Coarse basalt
71047 S	2.780	Coarse basalt	71569 R	289.6	Fine basalt
71048 S	2.457	Fine basalt	71575 R	2.113	Fine basalt
71049 S	1.860	Fine basalt	71576 R	23.54	Fine basalt
71055 B_1	669.6	Medium basalt	71577 R	234.7	Fine basalt
71065 S	28.83	Fine basalt	71578 R	353.9	Medium basalt
71066 S	19.96	Fine basalt	71579 R	7.937	Medium basalt
71067 S	4.245	Medium basalt	71585 R	13.86	Medium basalt
71068 S	4.208	Medium basalt	71586 R	26.92	Medium basalt
71069 S	4.058	Fine basalt	71587 R	41.27	Medium basalt
71075 S	1.563	Medium basalt	71588 R	48.98	Medium basalt
71085 S	3.402	Medium basalt	71589 R	6.860	Medium basalt
71086 S	3.329	Fine basalt	71595 R	25.21	Medium basalt
71087 S	2.200	Fine basalt	71596 R	61.05	Medium basalt
71088 S	2.064	Fine basalt	71597 R	12.35	Coarse basalt
71089 S	1.733	Medium basalt	72135 S	336.9	Dark breccia of basalt fragments
71095 S	1.483	Medium basalt	72145 S	1.25	Dark matrix breccia
71096 S	1.368	Medium basalt	72155	238.5	Medium basalt
71097 S	1.355	Medium basalt	72215 B_1	379.2	Layered light-gray breccia
71135 S, B_2	36.58	Fine basalt	72235 B_1	61.91	Layered light-gray breccia
71136 S, B_2	25.39	Fine basalt	72255 B_1	461.2	Layered light-gray breccia
71155 S, B_2	26.15	Fine basalt	72275 B_1	3640	Layered light-gray breccia
71156 S, B_2	5.420	Fine basalt	72315 B_2	131.4	Vesicular poikilitic clast
71157 S, B_2	1.466	Fine basalt	72335 B_2	108.9	Vesicular poikilitic clast

TABLE 7-I.—*Complete List of Apollo 17 Rocks*[a]—Continued

Sample number (b)	Weight, g (c)	Rock type	Sample number (b)	Weight, g (c)	Rock type
72355 B$_2$	367.4	Green-gray breccia	74249 S	4.183	Fine basalt
72375 B$_2$	18.16	Green-gray breccia	74255 B	737.3	Coarse basalt
72395 B$_2$	536.4	Green-gray breccia	74275	1493	Fine basalt
72415 B$_3$	32.34	Brecciated dunite clast	74285 S	2.212	Medium basalt
72416 B$_3$	11.53	Brecciated dunite clast	74286 S	2.102	Medium basalt
72417 B$_3$	11.32	Brecciated dunite clast	74287 S	1.568	Fine basalt
72418 B$_3$	3.55	Brecciated dunite clast	75015 B$_1$	1006	Coarse basalt
72435 B$_3$, S	160.6	Blue-gray breccia	75035 B$_2$	1235	Medium basalt
72505 RS	3.09	Green-gray breccia	75055 B$_3$	949.4	Coarse basalt
72535 R	221.4	Blue-gray breccia	75065 S	1.263	Medium basalt
72536 R	52.30	Blue-gray breccia	75066 S	.980	Dark-gray basalt
72537 R	5.192	Blue-gray breccia	75075 B$_4$	1008	Medium basalt
72538 R	11.09	Blue-gray breccia	75085 S	4.298	Medium basalt
72539 R	11.22	Blue-gray breccia	75086 S	2.323	Medium basalt
72545 R	4.055	Blue-gray breccia	75087 S	2.321	Medium basalt
72546 R	4.856	Blue-gray breccia	75088 S	1.992	Fine basalt
72547 R	5.045	Blue-gray breccia	75089 S	1.718	Fine basalt
72548 R	29.29	Blue-gray breccia	75115 S	2.600	Fine basalt
72549 R	21.00	Green-gray breccia	76015 B	2819	Green-gray breccia
72555 R	10.48	Green-gray breccia	76035 S	376.2	Blue-gray breccia
72556 R	3.861	Green-gray breccia	76036 S	3.95	Blue-gray breccia
72557 R	4.559	Green-gray breccia	76037 S	2.52	Medium basalt
72558 R	5.713	Green-gray breccia	76055	6412	Green-gray breccia
72559 R	27.84	Feldspathic breccia	76135 S	133.5	Green-gray breccia
72705 RS	2.39	Anorthositic breccia and glass	76136 S	86.6	Medium basalt
72735 R	51.11	Green-gray breccia	76137 S	2.46	Fine-grained crystalline
72736 R	28.73	Tan breccia	76215 B	643.9	Green-gray breccia
72737 R	3.33	Tan breccia	76235 B	26.56	Brecciated olivine norite
72738 R	23.75	Blue-gray breccia	76236 B	19.18	Brecciated olivine norite
73145 S	5.60	Dark matrix breccia	76237 B	10.31	Brecciated olivine norite
73146 S	3.01	Brecciated anorthosite	76238 B	8.21	Brecciated olivine norite
73155 S	79.3	Blue-gray breccia	76239 B	6.23	Brecciated olivine norite
73156 S	3.15	Fine crystalline	76245 S	8.24	Green-gray breccia
73215 S	1062	Light-gray breccia	76246 S	6.50	Green-gray breccia
73216 S	162.2	Green-gray breccia	76255 B	406.6	Banded tan and blue-gray breccia
73217 S	138.8	Blue-gray breccia	76265 S	1.75	Greenish-gray breccia
73218 S	39.67	Blue-gray breccia	76275 B	55.93	Blue-gray fragment breccia
73219 S	2.88	Fine basalt	76285 S	2.208	Not described
73225 S	3.66	Crystalline (green-gray breccia?)	76286 S	1.704	Not described
73237	878.3	Blue-gray breccia	76295 B	260.7	Banded tan and blue-gray breccia
73245 S	1.60	Brecciated anorthosite clast	76305 B	4.01	Brecciated olivine norite
73255	394.1	Light-gray or blue-gray breccia	76306 B	4.25	Brecciated olivine norite
73275	429.6	Green-gray breccia	76307 B	2.49	Brecciated olivine norite
73285 S	2.58	Glass-coated, gray, friable breccia	76315 B	671.1	Blue-gray breccia
74115 S	15.36	Friable clod	76335	352.9	Friable anorthositic breccia
74116 S	12.68	Friable clod	76505 RS	4.69	Greenish-gray breccia
74117 S	3.69	Friable clod	76506 RS	2.81	Friable dark matrix breccia
74118 S	3.59	Friable clod	76535 R	155.5	Coarse norite
74119 S	1.79	Friable clod	76536 R	10.26	Brecciated norite
74235	59.04	Basalt vitrophyre	76537 R	26.48	Fine basalt
74245 S	64.34	Fine or devitrified basalt	76538 R	5.870	Medium basalt
74246 S	28.81	Dark matrix breccia	76539 R	14.80	Vitrophyric basalt
74247 S	7.761	Fine or devitrified basalt	76545 R	7.676	Dark vitreous matrix breccia
74248 S	5.682	Fine or devitrified basalt	76546 R	23.31	Dark vitreous matrix breccia

TABLE 7-I.—*Complete List of Apollo 17 Rocks*[a]—Continued

Sample number (b)	Weight, g (c)	Rock type	Sample number (b)	Weight, g (c)	Rock type
76547 R	10.05	Dark vitreous matrix breccia	78526 R	8.77	Breccia with green glass veins
76548 R	2.527	Dark vitreous matrix breccia	78527 R	5.16	Brecciated gabbroic rock
76549 R	9.175	Dark vitreous matrix breccia	78528 R	7.00	Fine basalt
76555 R	8.435	Crystalline matrix-rich breccia	78535 R	103.4	Coherent dark matrix breccia
76556 R	7.396	Crystalline matrix-rich breccia	78536 R	8.67	Coherent dark matrix breccia
76557 R	5.592	Crystalline matrix-rich breccia	78537 R	11.76	Coherent dark matrix breccia
76558 R	.683	Crystalline matrix-rich breccia	78538 R	5.82	Coherent dark matrix breccia
76559 R	.747	Crystalline matrix-rich breccia	78539 R	3.73	Coherent dark matrix breccia
76565 R	11.60	Friable dark matrix breccia	78545 R	8.60	Coherent dark matrix breccia
76566 R	2.639	Friable dark matrix breccia	78546 R	42.66	Coherent dark matrix breccia
76567 R	5.490	Friable dark matrix breccia	78547 R	29.91	Friable dark matrix breccia
76568 R	9.477	Basalt-rich breccia	78548 R	15.95	Friable dark matrix breccia
76569 R	4.207	Crystalline breccia (blue-gray?)	78549 R	16.09	Friable dark matrix breccia
76575 R	16.25	Crystalline clast-rich breccia	78555 R	6.64	Friable dark matrix breccia
76576 R	5.327	Crystalline light-gray breccia	78556 R	9.50	Friable dark matrix breccia
76577 R	13.54	Crystalline light-gray breccia	78557 R	7.19	Friable dark matrix breccia
77017	1730	Brecciated olivine gabbro	78558 R	3.78	Friable dark matrix breccia
77035	5727	Green-gray breccia	78559 R	3.05	Friable dark matrix breccia
77075 B	172.4	Dark-gray dike	78565 R	3.50	Friable dark matrix breccia
77076 B	13.97	Dark-gray dike	78566 R	.77	Friable dark matrix breccia
77077 B	5.45	Dark-gray dike	78567 R	18.88	Friable dark matrix breccia
77115 B	115.9	Blue-gray breccia	78568 R	3.57	Friable dark matrix breccia
77135 B	337.4	Green-gray breccia	78569 R	14.53	Friable dark matrix breccia
77215 B	846.4	Brecciated norite	78575 R	140.0	Coarse basalt
77515 R*	337.6	Green-gray breccia	78576 R	11.64	Coarse basalt
77516 R*	103.7	Medium basalt	78577 R	8.84	Coarse basalt
77517 R*	45.6	Feldspathic breccia	78578 R	17.13	Coarse basalt
77518 R*	42.5	Green-gray breccia	78579 R	6.07	Medium basalt
77519 R*	27.4	Green-gray breccia	78585 R	44.60	Fine basalt
77525 R*	1.19	Feldspathic breccia	78586 R	10.73	Fine basalt
77526 R*	1.07	Feldspathic breccia	78587 R	11.48	Fine basalt
77535 R*	577.8	Coarse basalt	78588 R	3.77	Fine basalt
77536 R*	355.3	Coarse basalt	78589 R	4.10	Fine basalt
77537 R*	71.7	Green-gray breccia	78595 R	4.19	Fine basalt
77538 R*	47.2	Light-gray breccia	78596 R	7.55	Fine basalt
77539 R*	39.6	Tan-gray breccia	78597 R	319.1	Fine basalt
77545 R*	29.5	Green-gray breccia	78598 R	224.1	Fine basalt
78135	133.9	Medium basalt	78599 R	198.6	Fine basalt
78155	401.1	Gabbroic breccia	79035	2806	Dark matrix breccia
78235 S, B	199.0	Coarse norite	79115 B₁	346.3	Dark matrix breccia
78236 S, B	93.06	Coarse norite	79125 S	1.91	Dark matrix breccia
78238 S, B	57.58	Coarse norite	79135 B₁	2283	Dark matrix breccia
78255 B	48.31	Coarse norite	79155	318.8	Coarse basalt
78465 S	1.039	Not described	79175	677.7	Agglutinate
78505 RS	506.3	Coarse basalt	79195 B₂	368.5	Dark matrix breccia
78506 RS	55.97	Coarse basalt	79215	553.8	Brecciated troctolite
78507 RS	23.35	Coarse basalt	79225 S	7.42	Friable dark matrix breccia
78508 RS	10.67	Friable dark matrix breccia	79226 S	6.73	Friable dark matrix breccia
78509 RS	8.68	Basalt	79227 S	5.57	Friable clod
78515 RS	4.76	Coherent dark matrix breccia	79228 S	2.50	Friable clod
78516 RS	3.18	Friable dark matrix breccia	79245 S	10.11	Crystalline
78517 RS	1.82	Friable white breccia	79265 S	2.60	Fine basalt
78518 RS	.88	Friable dark matrix breccia	79515 S	33.00	Medium basalt
78525 R	5.11	Agglutinate	79516 S	23.92	Fine basalt

TABLE 7-I.—*Complete List of Apollo 17 Rocks*[a] —Concluded

Sample number (b)	Weight, g (c)	Rock type	Sample number (b)	Weight, g (c)	Rock type
79517 S	10.23	Dark matrix breccia	79528 S	2.38	Dark matrix breccia
79518 S	5.20	Dark matrix breccia	79529 S	1.84	Dark matrix breccia
79519 S	3.65	Dark matrix breccia	79535 S	1.69	Dark matrix breccia
79525 S	3.03	Dark matrix breccia	79536 S	1.66	Dark matrix breccia
79526 S	2.93	Dark matrix breccia	79537 S	1.05	Dark matrix breccia
79527 S	2.65	Dark matrix breccia			

[a]This inventory includes a total of 335 samples, including 132 rake samples.

[b]B = rock chipped from boulder. Where more than one boulder was sampled at an individual station, each boulder is identified by subscripts. S = rock in bag with soil. Most of the smaller fragments in this category resulted from sieving. RS = rock from soil collected at rake-sample area. R = rock from rake sample. R* = rock collected with scoop but treated as a rake sample.

[c]Fifteen rocks weighed more than 1 kg; 111 rocks, between 25 g and 1 kg; 52 rocks, between 10 g and 25 g; and 157 rocks, less than 10 g.
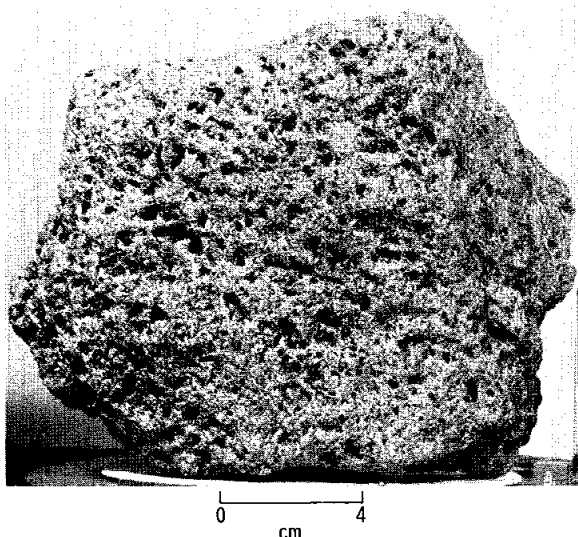
FIGURE 7-1.—Typical example of vesicular to vuggy basalts (sample 70017) from the valley floor. Note the coarse diabasic to subophitic texture (AS17-73-15720).

color indicate that much of it is rich in magnesium (Mg). Ilmenite crystals in the coarser grained rocks may be blocky or may display rectangular cross sections in addition to the usual lath-shaped morphology, suggesting that ilmenite may be a pseudomorph of an earlier phase. Ilmenite, especially in the coarser grained rocks, contains abundant lamellae and irregular masses of rutile on rhombohedral planes, and lamellae of a chromium-rich spinel phase parallel to the basal plane. Some metallic Fe is associated with these phases as blebs and narrow fracture fillings. In

rocks of intermediate grain size, blocky grains of ilmenite occur in a matrix that is rich in feathery ilmenite laths (e.g., sample 72135). Vitrophyric and fine-grained basalts are rich in prisms and lozenge-shaped grains of armalcolite rimmed by a selvage of ilmenite. Trace amounts of chrome-spinel and chromium-ulvöspinel occur in almost all basalts; ulvöspinel commonly shows evidence of subsolidus reduction to ilmenite and metallic Fe. Metallic Fe occurs as blebs in troilite and as discrete grains that are similar to the Fe seen in other mare basalts.

The similarity of basalt composition and textural variation throughout the Apollo 17 landing site suggests a similar source for all of these rocks. On the basis of the petrographic data, it is difficult to determine whether the samples represent several separate flows or different parts of a single relatively thick flow that may be at the top of a thick sequence of flows filling the valley.

Dark Matrix Breccias and Agglutinates

The dark matrix breccias range from friable "soil" types to a more coherent type crossed by closely spaced fracture sets that form a delicate set of irregularly shaped plates (fig. 7-4). Clasts in the breccias are primarily basalt; but, at station 9 (Van Serg Crater), the breccias contain a variety of clasts, including basalts, several types of glasses, some breccia fragments with accretionary coats, and a variety of recrystallized feldspathic rocks presumed

0   .5
mm

FIGURE 7-3.—Needles and plates of armalcolite and ilmenite (black) and skeletal olivine crystals (white) in a devitrified matrix of dendritic intergrowths of pyroxene and plagioclase (sample 74235,11, plane light view) (AS17-73-19967).

0   .5
mm
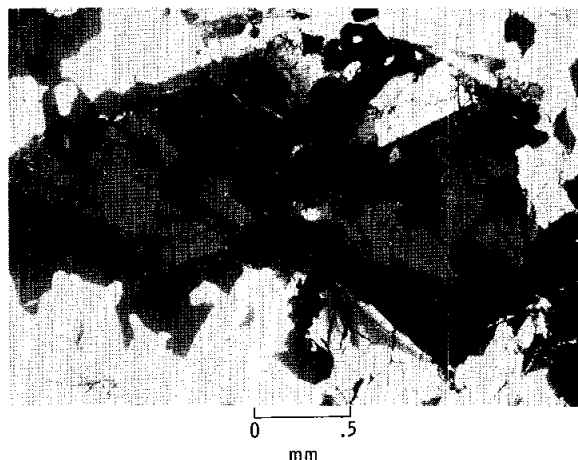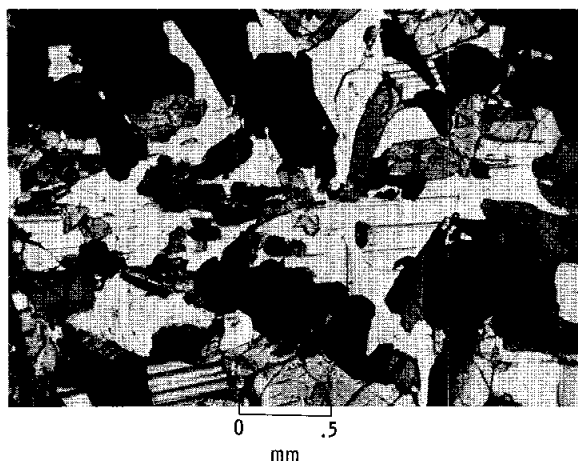
FIGURE 7-2.—Thin sections of basalts. (a) Late development of twinned, poikilitic plagioclase (light gray) enclosing earlier formed pyroxenes (dark gray) and opaque minerals (sample 70035,14, crossed polars view) (AS17-73-19846). (b) Large clinopyroxene with sectoral zonation enclosed in matrix of other pyroxenes and plagioclase. Note the opaque inclusions in the large clinopyroxene (sample 70035,14, crossed polars view) (AS17-73-19850).

to be derived from the surrounding highlands. Orange glass similar to that found at station 4 occurs in limited quantities in most breccias throughout the landing site. Matrix material is largely dark-brown glass, which imparts the dark color to these rocks.

A few large samples of glass-bonded agglutinates (fig. 7-5) occur throughout the Taurus-Littrow valley. Fragments are predominantly dark matrix breccias and some basalts cemented by dark-gray glass. The crew noted that these rock types occur in glass-lined bottoms of small (as much as 3 m in diameter)

0   4
cm

FIGURE 7-4.—Dark matrix breccia from Van Serg cratering ejecta (sample 79135). Although this material is coherent enough to maintain fractures that produce small plates and wedges, the fragments are quite friable and break from the specimen during handling. Note the various light-gray clasts, some of which are feldspathic breccias (AS17-73-15443).

craters. Although most breccias and agglutinates appear to have formed by induration of the present regolith, the breccias at Van Serg Crater are more complex and appear to reflect multibrecciation events rather than a simple induration of present day regolith.
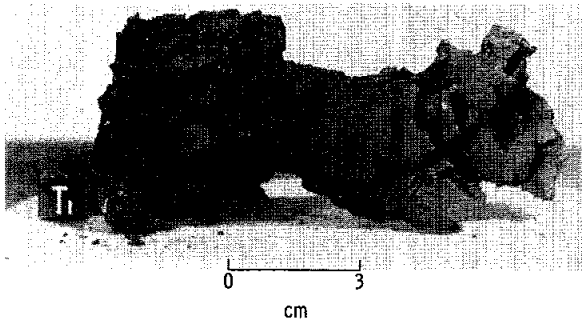
FIGURE 7-5.—One of the large glass-bonded agglutinates of dark matrix breccias (sample 70019) collected from the bottom of a 3-m-diameter crater (AS17-73-15333).

Green-Gray Breccias

The green-gray breccias are very coherent and consist almost entirely of a vesicular to vuggy matrix that is rich in poikilitic orthopyroxene (fig. 7-6). The degree of both vesicularity and development of poikilitic texture varies significantly from sample to sample, and, in some cases, the vesicles or vugs are several centimeters across. Mineral clasts of olivine and plagioclase and a few lithic clasts comprise a small percentage (5 to 20 percent) of each rock. One of these breccias (sample 76055) contains two distinct textures: a poikilitic and almost nonvesicular set of fragments in a nonpoikilitic and vesicular matrix in which the vesicles are planar and well foliated, curving around the more dense fragments as in a flow structure.

The matrix of the green-gray breccias generally consists of at least 50 percent poikilitic orthopyroxene (some may be pigeonite) with numerous small laths of plagioclase both inside and outside the oikocrysts (fig. 7-7). Small olivine grains occur in the oikocrysts, but they are generally concentrated along with opaque minerals outside the oikocrysts. A few rounded to angular larger clasts, scattered throughout the rock, consist primarily of plagioclase and olivine. The oikocrysts range from well developed (as much as 2 mm long and enclosing 70 percent of the matrix) to poorly developed (as much as 0.1 mm long and enclosing 5 percent of the matrix). Lithic clasts are quite rare and are chiefly feathery to equigranular, fine grained, and plagioclase-rich.

Green-gray breccia occurs as a major rock type collected from boulders and smaller rocks sampled at stations 2, 6, and 7 and as smaller fragments in the light mantle at station 3; it must be considered as a
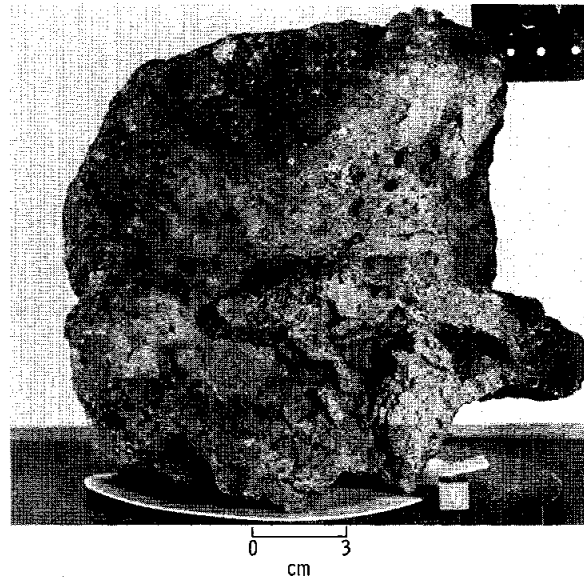
FIGURE 7-6.—Green-gray breccia (sample 76015). Although some cavities are smooth walled, many have drusy linings, especially the larger ones. The dark-gray coating (patina) with numerous zap pits is typical of the exposed surfaces of this rock type. Note the scarcity of macroscopic clasts (AS17-73-15013).

major stratigraphic unit of the North and South Massifs. These rocks are similar in texture, mineralogy, and chemistry to the poikilitic rocks collected at the Apollo 16 site (ref. 7-10). The green-gray breccias are also chemically similar to the brown-glass matrix breccias collected at the Apennine Front (ref. 7-11).

Blue-Gray Breccias

The blue-gray breccias form the most complex group of rocks. This group consists predominantly of a very coherent, slightly vesicular, blue-gray matrix containing angular to subrounded white clasts (fig. 7-8). There are some cases where the blue-gray breccias seem to exist as fragments in a tan matrix, or there may be a banded relationship between blue-gray and tan matrix breccias (fig. 7-9). These rocks have no poikilitic matrix but may contain poikilitic clasts as well as mineral clasts of plagioclase, pyroxene, and subordinate olivine. Many of these mineral grains have been shocked. A few mineral clasts have fine-grained rinds that may have been partially glassy at some stage of development. The matrix also contains traces of glass (sample 73235) or divitrified glass and displays some thin bands and oriented clasts

(a)

FIGURE 7-8.—One of the more vesicular varieties of blue-gray breccia (sample 72435). A variety of subangular to rounded feldspathic clasts are apparent. Cavities are generally smooth walled (AS17-73-16187).
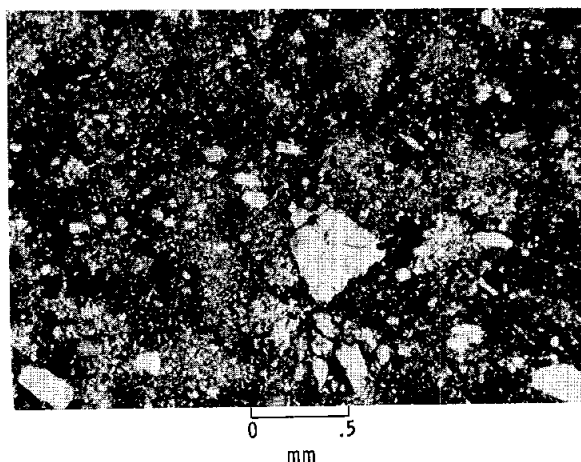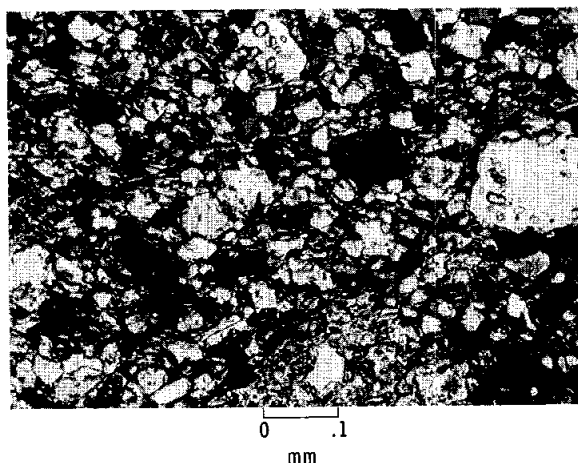
(b)

FIGURE 7-7.—Thin sections of green-gray breccias. (a) Lighter gray areas are poikilitic orthopyroxenes that compose over 50 percent of matrix and contain numerous chadacrysts of plagioclase and some olivine. Subrounded to subangular clasts are principally olivine and plagioclase (sample 77135,7, crossed polars view) (AS17-73-19912). (b) Alinement of small plagioclase laths (white) is common in some areas of green-gray breccia matrices, generally in areas between oikocrysts. Several larger blocky grains of plagioclase occur as clasts (white and black). Olivine grains also occur as larger clasts (medium gray) and as smaller grains the origin of which is less certain. Note that the small laths "wrap around" the clasts (sample 76055,11, crossed polars view) (AS17-73-19877).

(fig. 7-10(a)); some bands of crushed minerals contain pink spinel that also occurs in clasts (fig. 7-10(b)). The tan material is considerably coarser than the blue-gray material and contains numerous brown mineral fragments, which, in a thin section of sample

FIGURE 7-9.—Banded blue-gray and tan breccia (sample 76255). The lighter areas (tan) seem to intrude on the darker (blue) areas. The coarser grained nature of the lighter areas can be seen clearly as can the foliated nature of the light material (AS17-72-56415).

76255, appear to be inverted pigeonites with relatively coarse exsolution lamellae.

The blue-gray matrix ranges from a very fine-grained to a coarse-grained texture. The fine-grained matrix consists of intergrowths of pyroxene and plagioclase only a few micrometers in size in some examples, whereas the coarse-grained matrix consists of subophitic pyroxene and plagioclase where some plagioclase laths may reach 50 to 100 μm in length. In contrast to the green-gray breccias, a large proportion of the mineral clasts are pyroxenes of various types. Lithic clasts include very-fine-grained, prob-

0   .5
mm

0   .1
mm
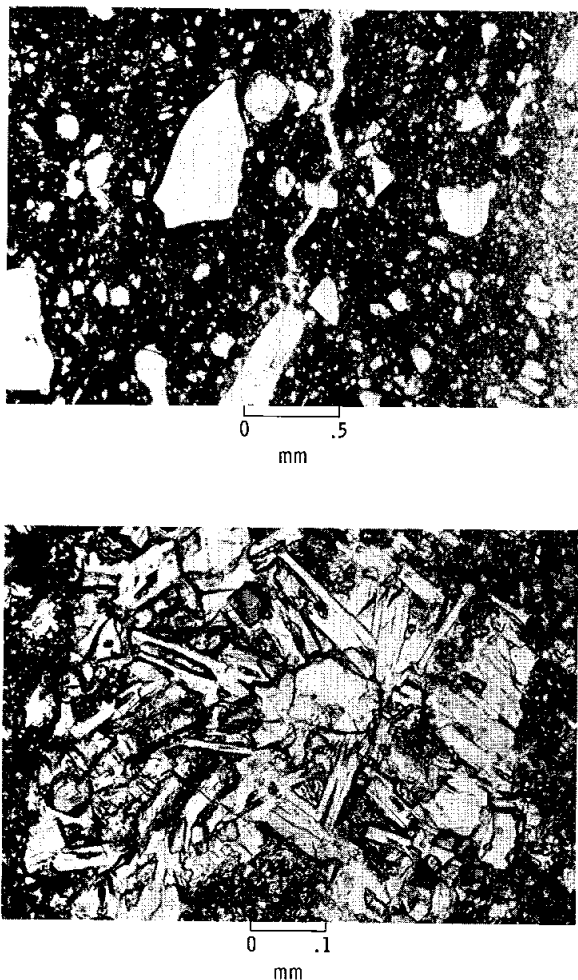
FIGURE 7-10.—Thin sections of blue-gray breccias. (a) Clasts and very-fine-grained dark matrix of blue-gray breccia (sample 76315,11). Note the alinement of elongate clasts and foliation of light and dark streaks in matrix. Several pink spinels (medium gray) occur in the light band along the edge of the photograph (plane light view) (AS17-73-19998). (b) Clast in blue-gray breccia (sample 76315,11). Several equant, pink spinels (medium gray) occur in this plagioclase and olivine clast, suggesting a source for the crushed material in the spinel-bearing light band of figure 7-10(a) (plane light view) (AS17-73-20000).

ably devitrified material, poikilitic rocks, relatively coarse-grained anorthositic types, feathery feldspar intergrowths, and basalts.

The blue-gray breccias occur as a major part of the boulders, as smaller rocks at stations 2, 6, and 7, and as fragments in the light mantle at station 3; they must be considered a major stratigraphic unit on both massifs. The blue-gray breccia was reported by the crew as being a major part of the large boulder at station 6, where it was in contact with green-gray breccia. The latter contained several inclusions of blue-gray breccias near the contact, suggesting that the green-gray breccias were largely fluid at the time of incorporation.

Layered, Foliated, Light-Gray Breccias

The layered, foliated, light-gray breccias contain approximately 60 percent matrix and are less coherent than the green-gray and blue-gray breccias. There is some variability in the coherence of the light-gray breccias, apparently as a result of the degree of annealing of an originally glassy matrix, some of which remains as glass. On a macroscopic scale, these breccias are nonvesicular to very slightly vesicular. A large proportion of clasts in these breccias have white, feldspar-rich cores rimmed by a dark-gray glass-rich material. In the less coherent breccias, clasts stand out in relief on eroded surfaces. On both macroscopic and microscopic scales, there occur white veins, layers, and lenses that, in some cases, appear to intrude the light-gray matrix (fig. 7-11).

The light-gray matrix consists of numerous small fragments of lithic debris, plagioclase, olivine, pyroxene, and opaque minerals set in a brown, glassy to very fine devitrified mesostasis. The white veins and lenses contain no brown interstitial material but consist of a few lithic fragments of the gray matrix breccias and mineral debris that is largely feldspathic. Mineral fragments are mostly plagioclase but also include olivine, pyroxene, and spinel. Lithic fragments are primarily breccias but also include anorthositic types, basalts, and poikilitic rocks. Some clasts show accretionary structures consisting of brown, glassy matrix mantles surrounding lithic cores (fig. 7-12). Breccia clasts within breccia clasts indicate a complex history for the formation of the light-gray breccias.

This rock type is found as a boulder at station 2 and among the smaller fragments in the light mantle at station 3; therefore, it appears to be associated with the South Massif.

Brecciated Gabbroic Rocks

Several samples consist of brecciated or crushed anorthositic to gabbroic rocks. Some samples show evidence of crushing with little or no mixing, thus
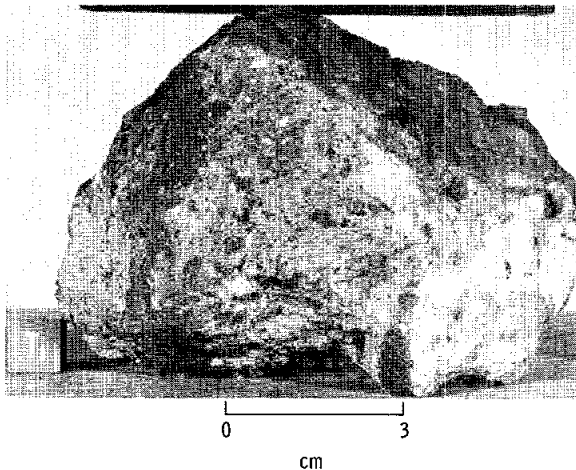
FIGURE 7-11.—Layered, foliated, light-gray breccia from a boulder at station 2 (sample 72215). The darker areas that appear in some instances to be clasts are very fine grained, probably devitrified. The lighter areas that appear to be veins are essentially crushed crystalline material (AS17-73-16661).

(a)

(b)

FIGURE 7-12.—Thin sections of light-gray breccias. (a) Glassy to devitrified rounded clasts (black) in a matrix of more crystalline debris. However, the matrix at top of photograph is more glass-rich and similar to clasts (sample 72275,11, plane light view) (AS17-73-20085). (b) Crystal clasts in a brown-glass matrix (black) that itself forms a clast in a matrix of glass and crystalline debris (sample 72255,7). In some cases, these brown-glass matrix clasts contain breccia clasts in addition to mineral fragments (plane light view) (AS17-73-20082).

allowing possible reconstruction of original textures. For example, a coarse norite (sample 78235) shows a good cumulate texture on a macroscopic scale (fig. 7-13), but it has undergone some crushing on a microscopic scale (fig. 7-14). Conversely, a gabbro (sample 78155) has been highly crushed and may be mixed as well (fig. 7-15). One rock (sample 76535) is a coarse-grained norite and shows no signs of having been sheared (fig. 7-16); although there are no thin sections of this rock, it may well have maintained its original texture. In another example (sample 77017), the degree of crushing appears to vary from a margin injected with glass veins to a less disturbed inner region of cumulate plagioclase and olivine in clino-pyroxene oikocrysts (fig. 7-17). Two crushed and recrystallized anorthositic rocks were sampled from large clasts in the blue-gray breccia portions of the boulders at stations 6 and 7 and may present some clues to the source region of this breccia. Some of the less crushed and mixed samples of these originally coarse-grained rocks may present the best opportunities from all of the Apollo missions for reconstructing the textures and mineral compositions of rocks from the early lunar crust.

Miscellaneous Rocks

The miscellaneous rocks include a dunite sample from a large clast in one of the boulders at station 2 and a fine-grained black dike with a very-fine-grained igneous-looking matrix from the large boulder at station 7. The dunite contains over 95 percent olivine as millimeter-sized fragments in a crushed matrix of the same material (fig. 7-18). Chemical analysis of this rock indicates an olivine in the Fo_{85-90} range. The black dike appears to originate within the blue-gray breccia part of the station 7 boulder and
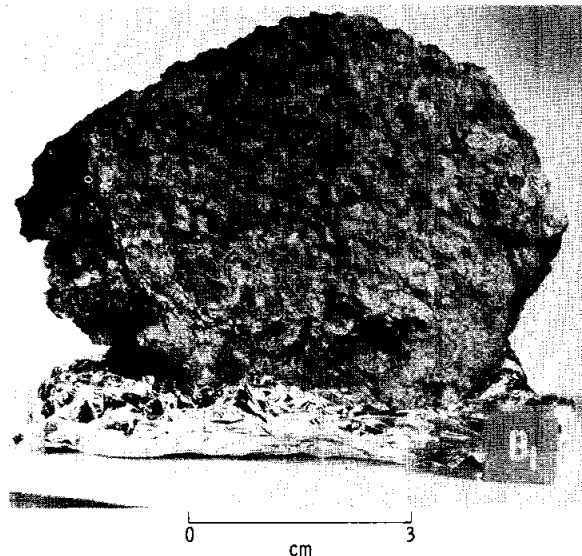
FIGURE 7-13.—Coarse-grained norite (sample 78236) with glassy-appearing plagioclase and crushed pyroxene. Note the dark glassy coating on the lower right side of rock. This glass occurs also as veins in the rock (AS17-73-15393).
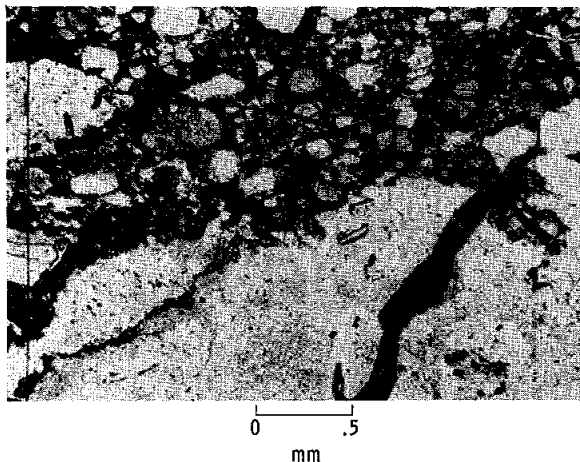
FIGURE 7-14.—Thin section of coarse-grained norite (sample 78236), showing area of crushed plagioclase and pyroxene (top half of figure), large plagioclase crystals that are largely isotropic (white), and a brown-glass vein (lower right) (plane light view) (AS17-73-19929).

crosscuts an anorthositic norite clast. Although the dike contains approximately 15 percent mineral clasts, the remainder of the dike consists of 5- by 10-μm plagioclase laths in 30- by 50-μm pyroxene oikocrysts. Within 0.5 mm of the contact, the vein material decreases in grain size, and the plagioclase becomes more skeletal in form.
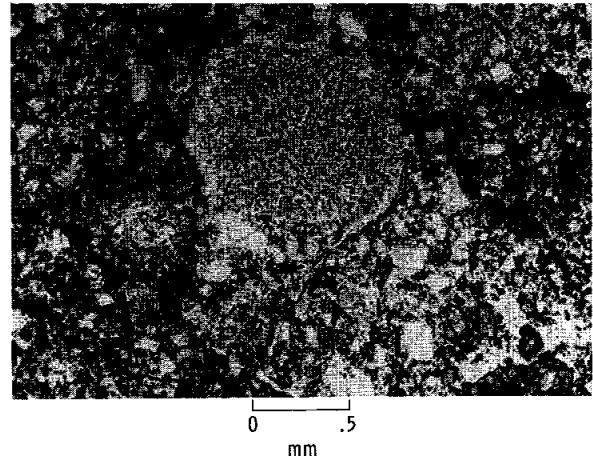
FIGURE 7-15.—Thin section of crushed and stirred anorthositic rock (sample 78155,8). Texture ranges from a very-fine-grained clastic mixture of plagioclase (white) and pyroxene (gray) to lathy diabasic patches (plane light view) (AS17-73-19921).

SOILS

Soils were collected by the Apollo 17 crew to aid in characterizing four major photogeologic units determined by preflight studies: (1) the "dark mantle" that covers the plains surface and was interpreted as a possible pyroclastic deposit overlying basalt flows, (2) the South Massif and the light mantle that was interpreted as an avalanche deposit from that massif, (3) the North Massif that was interpreted as highland breccias or possibly volcanic domes, and (4) the Sculptured Hills that were interpreted as highlands terrain composed of breccias.

Five core tubes, one 2.92-m-long drill core, and 73 soils, including both surface samples and samples from several trenches, were collected. All soils were described surficially in the Lunar Receiving Laboratory; 64 were sieved into five size fractions, and 18 were studied further in thin section and by additional sieving.

Grain-Size Analyses

The methods of grain-size analysis are outlined in McKay et al. (ref. 7-12). The mean grain size of soils from the black-mantled terrain ranges from near the mean grain size for lunar soils ($\approx 70~\mu$m) to 125 μm (table 7-II). The soils from the North and South Massifs are fine grained (coarse silt size), with mean grain sizes of 45 to 64 μm. As in most lunar soils, nearly all these soils are very poorly sorted. Soils
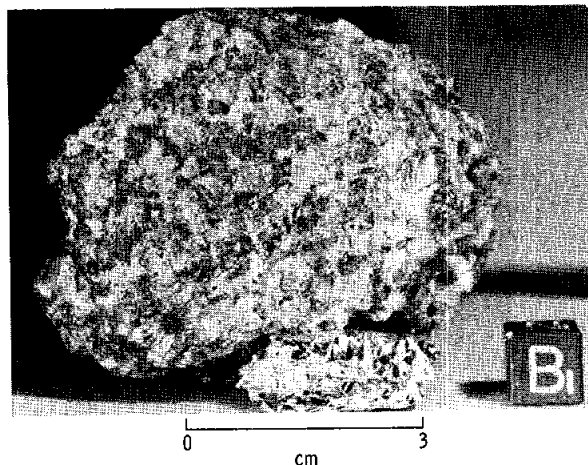
FIGURE 7-16.—Coarse-grained norite (sample 76535) with fresh-appearing plagioclase (white to light gray) that has typical striations of albite twinning. Although pyroxenes (medium gray) are fractured along cleavage planes, they do not appear badly crushed (AS17-73-19458).

FIGURE 7-17.—In an anorthositic rock having a generally crushed texture, this area shows several blocky to lath-shaped plagioclase grains (white) in optically continuous augite (gray) that extends over most of the photograph, except the upper left corner. A few very thin glass veins (black lines) occur (sample 77017,11, plane light view) (AS17-73-20008).

from station 4 composed predominantly of glass spheres have median grain sizes of 40 to 43 μm and are poorly sorted.

Soils from the "Dark Mantle"

Soils from stations 1 and 5 and the LM area are mostly the comminuted products of basalt. The bulk of these soils is composed of basalt fragments, agglutinates, and grains of clinopyroxene, plagioclase, and ilmenite (table 7-III). The basalt fragments have a range of texture and composition, although two types are most common.

1. Equigranular to subophitic, medium to coarse crystalline basalt containing 50 percent clinopyroxene (augite and pigeonite), 25 percent feldspar, and 25 percent ilmenite. Olivine, cristobalite, and opaque phases are present in lesser amounts.

2. Finely crystalline, variolitic basalt with titanium augite, ilmenite, and plagioclase.

Agglutinates, a ubiquitous component of lunar soils (refs. 7-12 and 7-13), consist of mineral and lithic detritus bonded by grape-like clusters of nearly opaque, brown glass. In soils from the plains floor, the agglutinates have a dull, nearly metallic luster in contrast to agglutinates in soils from the massifs. Coarse-grained agglutinates (250 to 500 μm) are very vesicular and contain irregular, coalescing cavities 5 to 150 μm long.

FIGURE 7-18.—Thin section of dunite with large olivine crystals set in a crushed matrix of the same material comprise this entire clast (sample 72415,12, plane light view) (AS17-73-19947).

In the < 1-mm fraction, there is a considerable difference between the surface and the trench-bottom (−17 cm) samples at station 9. The surface sample contains twice as much agglutinate as the trench-bottom sample and very different breccia components (table 7-III). The finer fractions may be mostly comminution products of the dark-gray vitric brec-

cias that are the most common rock types at station 9.

Station 4 is on the rim of Shorty Crater, which appears to be a crater that penetrated the thin white mantle and ejected mostly dark plains material. At station 4, three of the most unique soils from the Apollo 17 site were collected: orange, gray, and black. The orange soil forms a band with sharp boundaries between the two gray soils. A core driven through the band penetrated a black soil. Thus, the three soil types are present within a few square meters.

The orange soil (sample 74220) consists of cohesive clods that withstood transport back to Earth. At least one of these clods has color zoning, having a pale orange-brown center and a moderate orange-

TABLE 7-II.—*Grain-Size Parameters of Some Apollo 17 Soils*

Sample number	Median grain size		Inclusive graphic mean		Inclusive standard graphic deviation	Inclusive skewness	Kurtosis
	ϕ	μm	ϕ	μm			
70161	3.95	64.0	3.88	68.0	2.08	− 0.12	1.08
70181	4.10	58.3	3.98	63.3	2.02	− .17	1.01
71061	3.20	108.2	2.62	163.0	3.30	− .24	.79
74240	3.22	108.0	2.64	160.0	3.32	− .26	.86
75061	3.16	112.0	3.17	112.0	2.62	− .25	1.19
75081	3.65	79.9	3.48	89.0	2.42	− .17	1.07
76501	4.22	53.4	3.92	66.0	2.58	− .28	1.09
78421	4.61	40.0	4.47	44.8	2.02	− .18	1.02
78501	4.70	37.5	3.97	64.0	2.94	− .33	1.15
79261	3.60	82.0	3.0	125.0	2.94	− .29	.84
[a]74001	4.60	40.0	4.52	43.0	1.70	− .06	.99
[a]74220	4.61	40.0	4.60	40.0	1.59	—	—
[a]74260	4.36	48.0	4.14	56.4	2.03	—	—

[a]Without > 1-mm data.

TABLE 7-III.—*Petrographic Grain-Type Analyses for Apollo 17 Soils*

Components	70161, fillet near ALSEP		70181, reference for core		71061, at − 5 to 6 cm in depth		71501, rake soil		73221, skim sample at trench		73261, medium gray in trench		73281, white in trench		74001, bottom of core	
	90 to 150 μm	250 to 500 μm	90 to 150 μm	250 to 500 μm	90 to 150 μm	250 to 500 μm	90 to 150 μm	250 to 500 μm	90 to 150 μm	250 to 500 μm	90 to 150 μm	250 to 500 μm	90 to 150 μm	250 to 500 μm	90 to 150 μm	250 to 500 μm
Agglutinates	34.0	36.5	56.0	45.8	9.3	10.0	35.0	23.8	26.3	9.7	34.3	34.1	24.6	11.1	−	−
Basalt	15.0	22.4	14.0	29.4	19.6	51.5	24.6	69.0	3.0	2.2	2.0	10.4	3.7	7.8	−	−
Breccia																
Low grade (brown)	5.0	4.7	4.6	7.1	3.6	6.9	2.3	−	18.3	28.0	18.7	17.7	23.7	35.6	−	−
Low grade (colorless)	−	Tr	.3	−	.6	1.5	.6	−	10.3	17.2	4.7	6.3	2.3	8.9	−	−
Medium grade	2.0	2.4	2.6	3.5	1.6	−	2.3	−	18.0	16.1	15.7	17.7	20.6	23.3	−	−
High grade	−	−	−	−	−	−	−	−	−	2.2	−	−	−	−	−	−
Anorthosite	−	−	−	−	.3	−	−	−	.3	1.1	.3	−	.3	−	−	−
Cataclastic anorthosite	−	−	.3	1.2	−	−	−	−	.3	2.2	1.6	2.1	1.6	−	−	−
Plagioclase	9.0	5.9	4.3	4.7	17.3	8.5	5.0	−	11.3	12.9	9.7	4.2	9.3	5.6	1.6	2.0
Clinopyroxene	21.6	15.3	10.3	3.5	21.0	10.7	17.3	−	8.0	2.2	7.0	1.0	7.3	2.2	.3	−
Orthopyroxene	−	−	.3	−	−	−	.6	−	Tr	−	−	−	Tr	1.2	−	1.0
Olivine	.3	−	−	−	−	−	−	−	1.3	−	−	−	.3	−	−	−
Opaques (mostly ilmenite)	5.0	2.4	2.3	4.7	4.6	2.3	9.0	2.4	−	2.2	.6	−	1.3	−	−	−
Glass																
Orange	2.0	1.2	3.0	−	6.3	.8	1.6	2.4	Tr	−	1.7	−	1.3	2.2	8.0	7.0
Colorless	.3	1.2	.3	−	1.3	1.5	.6	−	.3	2.2	.6	2.1	.6	−	−	−
Brown	.6	5.9	.6	−	4.6	−	.3	−	.6	2.2	1.3	2.1	2.0	1.1	−	2.0
Ropy	−	−	−	−	−	−	−	−	−	−	1.0	−	−	−	16.6	−
Tachylyte	2.6	1.2	.6	−	5.6	2.3	.3	−	−	−	−	−	−	−	−	−
Gray	−	−	−	−	−	−	−	2.4	−	−	−	1.0	.3	1.1	−	−
Green	−	−	−	−	−	−	−	−	−	−	−	−	−	−	−	−
Metal spheres	2.6	−	Tr	−	4.0	3.8	1.0	−	−	−	−	−	−	−	−	−
Barred spheres	−	−	−	−	−	−	−	−	2.6	−	.6	1.0	.3	−	73.3	88.0
Norite	−	1.2	−	−	−	−	−	−	−	−	−	−	−	−	−	−
Number of grains	300	85	300	85	300	130	300	42	300	93	300	96	300	90	300	100

brown rim. Contacts between the zones are sharp. Surficially, the soil is composed of ruby-red to black glass spheres and broken spheres that, in thin section, are homogeneous, pale orange, and nonvesicular. There is no evidence of included detritus in the orange glass, but there is a trace of olivine phenocrysts. Nearly half the orange glass spheres are partly or completely crystallized to small sheaf-like bundles of very fine crystals to parallel bars of ilmenite and olivine.

Black soil from the bottom of the core at station 4 (sample 74001) consists mostly of barred or broken spheres. These spheres may be completely crystallized equivalents of the orange glass droplets, consisting of olivine and orthopyroxene (?) phenocrysts in a very small amount of brown to orange glass. These spheres are crossed by ragged, thin ilmenite plates that impart the black color to this soil. Traces of spinel and metal are present. The core soil also contains 10 to 20 percent completely devitrified brown-glass spheres that are purple in thin section.

The gray soils (samples 74240 and 74260) that flank the band of orange soil contain a variety of components (table 7-III), including a significant amount of "ropy" glass that occurs as light-gray spindle-shaped droplets with abundant, fine-grained,

angular detritus welded to the grain surfaces. The various orange and black soil components are present in nearly all of the "dark mantle" soils in portions of 5 to 20 percent of the total mass of the sample (average is 10 percent). These components are also present in low-grade breccias from the plains. A surface sample at the LM area (sample 70180) contains approximately 8.1 percent (by weight) of these "exotic" components (table 7-IV). As illustrated in table 7-IV, most of the exotic components are in the < 100-μm fraction and are not adequately represented in table 7-III. The wide distribution of these glasses beyond the limits of Shorty Crater is a possible indication that layers of this material are present to depths of tens of meters below the present valley floor and are penetrated by the deeper impact craters. The uniformity of composition and morphology of the "exotic" components supports a theory that these components are droplets formed during lava fountaining, which would form lenses or layers within the strata underlying the Apollo 17 landing site. It is possible that the components were subsequently buried by lava flows; they have no agglutinates and appear to have had no history of exposure at the lunar surface before their exhuming as ejecta at Shorty Crater.

TABLE 7-III.—*Petrographic Grain-Type Analyses for Apollo 17 Soils*—Concluded

number, type, and grain-size fraction

74220, orange soil		74240, gray soil		74260, gray soil		75061, skim from top of flat boulder		75081, interboulder		76501, rake soil		78421, bottom of 25-cm trench		78501, rake soil		79221, top 2 cm of trench		79261, lowest layer in 17-cm trench	
90 to 150 μm	250 to 500 μm	90 to 150 μm	250 to 500 μm	90 to 150 μm	250 to 500 μm	90 to 150 μm	250 to 500 μm	90 to 150 μm	250 to 500 μm	90 to 150 μm	250 to 500 μm	90 to 150 μm	250 to 500 μm	90 to 150 μm	250 to 500 μm	90 to 150 μm	250 to 500 μm	90 to 150 μm	250 to 500 μm
1.3	4.0	8.0	8.2	7.7	17.4	24.0	35.3	31.0	31.6	47.2	26.3	62.6	47.1	35.3	23.0	44.4	53.0	22.3	18.0
1.6	4.0	30.0	34.2	23.7	26.1	26.6	41.2	12.0	30.2	1.7	3.9	5.7	8.8	11.0	46.2	14.4	13.6	13.3	23.6
.3	–	1.6	16.4	7.4	–	2.6	11.8	6.3	6.6	3.8	10.5	7.0	3.9	2.3	–	8.5	14.8	1.3	15.7
–	–	13.3	5.5	5.4	26.1	2.0	–	–	–	--	3.9	1.3	13.7	.3	–	1.0	1.2	.3	4.5
–	–	2.0	2.7	3.3	–	.3	–	2.6	3.9	8.3	19.7	2.6	8.8	8.0	–	1.0	2.5	8.0	9.0
–	4.0	–	–	–	–	--	--	–	–	--	–	–	–	–	–	–	–	.3	2.2
--	--	–	–	–	--	–	–	–	–	--	–	.3	–	Tr	–	–	–	.6	3.4
–	–	.6	–	–	–	–	–	–	1.3	1.4	2.6	.6	2.0	2.0	–	.3	–	.6	2.2
–	–	4.6	1.4	2.7	4.3	4.6	5.9	11.0	6.6	7.2	28.9	7.3	6.9	13.3	–	6.9	3.7	12.7	4.5
.3	–	11.3	8.2	13.7	8.6	29.6	5.9	26.3	18.4	7.6	–	9.0	2.9	6.0	–	6.5	3.7	16.6	4.5
--	–	–	--	--	--	–	–	–	–	7.9	–	–	–	7.3	–	–	–	1.6	2.2
–	–	–	--	.3	–	.3	–	–	–	.7	–	.6	–	--	–	–	–	–	–
–	–	1.3	--	2.3	–	5.3	–	7.6	1.3	1.7	–	–	–	3.7	–	1.3	–	7.0	1.1
95.6	88.0	4.0	1.4	7.7	–	1.0	–	.6	–	.7	–	.6	1.0	2.0	–	4.2	–	4.0	2.2
.3	--	4.6	2.7	3.7	–	1.6	–	.6	–	1.4	–	1.3	2.9	1.0	–	2.3	1.2	3.2	–
–	--	3.6	–	1.7	–	1.6	–	1.6	–	--	4.3	.6	1.0	2.3	–	2.3	–	3.6	3.3
–	--	14.3	17.8	18.1	--	–	–	–	–	--	–	–	–	.3	--	3.6	2.5	–	–
–	–	–	1.4	1.7	13.0	--	--	–	–	.3	2.6	–	–	–	–	–	–	.6	4.5
–	–	–	–	–	–	--	--	–	–	--	–	–	–	–	7.7	–	2.5	1.3	–
–	–	–	–	.3	4.3	–	–	–	–	--	–	–	–	2.0	23.0	–	–	–	–
--	–	–	–	.3	--	--	--	–	–	--	–	.3	1.0	3.0	–	Tr	--	2.0	–
–	–	–	--	–	–	–	–	–	–	--	–	--	–	–	–	3.3	1.2	–	–
–	–	–	--	–	--	--	--	–	–	--	–	--	–	Tr	–	–	–	.3	–
300	25	300	73	300	23	300	17	300	76	300	76	300	103	300	13	300	81	300	89

TABLE 7-IV.—*Determination of the Approximate Weight of Orange and Black Soil (exotic) Components in Soil Sample 70181*[a]

Grain-size fraction, μm	Mass, percent of total soil	Exotic glasses in each size fraction, percent	Weight percent of exotic glass fraction (b)
20 to 45	19.6	10.0	1.96
45 to 75	16.8	20.0	3.3
75 to 90	12.8	15.0	1.92
90 to 150	4.5	9.0	.4
150 to 250	12.6	3.6	.45
250 to 500	9.0	0	0
> 500	9.0	0	0

[a]Station 10.
[b]Total percent = 8.13.

South Massif and Light Mantle

The South Massif and the light mantle or avalanche deposits were sampled at stations 2, 2A, and 3; these appear to be the comminution products of a variety of breccias with a trace of mare basalt (table 7-III). Viewed superficially, the coarser fractions consist of mostly medium-gray fine-grained breccia. Dark-gray breccias with white clasts < 1 mm in diameter were evident in lesser amounts.

Vitric breccias of low metamorphic grade, 1 to 3 of Warner (ref. 7-14), contain 1- to 200-μm-long clasts of mineral and lithic detritus in matrices of brown, colorless, and banded glass. Most of the clasts consist of angular feldspar grains with lesser amounts of clinopyroxene or orthopyroxene; however, some grains contain a myriad of clast types.

Breccias of medium metamorphic grade, 4 to 6 of Warner (ref. 7-14), have fine-grained to coarse-grained equigranular textures; they are composed of mostly feldspar and orthopyroxene, with traces of ilmenite and olivine.

White and gray marbled units from the trench at station 3 have nearly the same mineralogic composition, but the gray layer has a higher agglutinate content. Similar white and gray units exist in a mottled texture at station 2A. Assuming that the gray, agglutinate-rich units represent surface layers, it is possible that a layered regolith sequence was mixed as it avalanched down the slopes of the South Massif. Soils from the South Massif and the light mantle contain the lowest content of mare basalt and the largest variety of breccias of any Apollo 17 soil; this observation agrees well with the interpretation of the light mantle as an avalanche deposit from the South Massif.

North Massif

The coarse fraction of soils from stations 6 and 7 consists of mostly patchy, medium-gray to dark-gray breccias, with lesser amounts of white breccias and agglutinates. The < 1-mm fraction is characterized by abundant plagioclase and pyroxene grains, low-grade brown-glass breccias, and medium-grade breccias (table 7-III). Some of the medium-grade breccias have a poorly defined poikilitic texture.

North Massif soils have more breccias of medium metamorphic grade and a higher plagioclase content than South Massif soils. However, they are not greatly different from South Massif soils.

Sculptured Hills

At station 8, a surface soil and a soil from the bottom of a 25-cm-deep trench differ mainly in their relative maturity; the trench soil contains twice the amount of agglutinates. Breccia types in soils from the Sculptured Hills are nearly the same as those in soils from the South Massif (table 7-III); but there is a greater amount of basalt in both the Sculptured Hills soil samples as compared to those from the South Massif.

At station 9, located between the Sculptured Hills and the LM, the soil composition in the "dark mantle" appears to be transitional between the two stratigraphic units. The coarse-grained fraction of station 9 soils consists of dark-gray, fine-grained, vitric breccia fragments and aphanitic basalt.

CHEMICAL CHARACTERISTICS

Rocks

Nearly all chemical characteristics of the Apollo 17 rocks can also be found in rocks from previous missions. Mare basalts with high iron oxide (FeO) and titania (TiO_2) contents, noritic breccias with a major element composition broadly similar to KREEP (potassium, rare-Earth elements, and phosphorus; here called KREEP-like rocks) but with roughly one-half the minor and trace element content, and brecciated anorthositic gabbros with relatively high lime (CaO) and alumina (Al_2O_3) contents have all

been observed previously. However, unusually high zinc (Zn) concentrations in the orange soil and the exceptionally low Ni content of the basalts suggest different source materials than those for previously returned igneous rocks. The trace element contents of the anorthositic rocks are significantly different from nearly all those previously returned, again suggesting variations in the source regions.

Basalts

Basalts exhibiting wide textural variation have been extensively sampled in the vicinity of Steno and Camelot Craters (stations 1 and 5), the LM and Apollo lunar surface experiments package (ALSEP) site, and also from Shorty Crater (station 4). Analyses of three of these samples are given in table 7-V. The basalts are characterized by high FeO contents and by correspondingly high FeO/MgO (magnesia) ratios (fig. 7-19); hence, they are similar to other mare basalts sampled at the Apollo 11, 12, and 15 and the Luna 16 landing sites. These characteristics and low soda (Na_2O) concentrations distinguish mare basalts from all terrestrial basalts.

In detail, these basalts have high TiO_2 and correspondingly low silica (SiO_2) concentrations and are broadly comparable with basalts from Mare Tranquillitatis (figs. 7-20, 7-21, and 7-22). The sulfur (S) content of these rocks, about twice that found in the Apollo 12 and 15 basalts, also compares closely with the Apollo 11 basalts. The Ni content (approximately 2 ppm), exceptionally low even for lunar rocks, is much lower than in previously sampled mare basalts.

One sample (75055) is slightly quartz normative and compares closely in both major and trace element chemistry with typical low potassium (K) Apollo 11 basalts. The other two analyzed basalts (samples 70035 and 70215) differ from sample 75055 in that they are olivine normative and higher in TiO_2 (fig. 7-20) and MgO than low-K Apollo 11 basalts, and are correspondingly lower in SiO_2, Al_2O_3, CaO, and the trace elements rubidium (Rb), zirconium (Zr), yttrium (Y), and strontium (Sr). Although chemically comparable, these two basalts differ in texture. Sample 70215 is very fine grained (probably a devitrified vitrophyre), whereas sample 70035 is a coarse-grained (1 to 2 mm) vesicular basalt. The aphyric texture of sample 70215 indicates that high-titanium magmas have been erupted onto the

lunar surface and that rocks of this composition are not necessarily of cumulate origin. The compositional differences observed between sample 75055 and the other two samples are too large to have been produced by near-surface crystal fractionation, indicating that at least two basalt types have been sampled at the Apollo 17 site.

Massif Rocks

Rocks from the South and North Massifs have been sampled at stations 2, 3, 6, 7, and 8. Analyses of representative samples are given in table 7-V. In contrast to the wide textural and petrographic variations observed in these rocks, two distinct, chemically defined rock types can be recognized: noritic breccias, corresponding to the petrographically defined suites of green-gray, blue-gray, and light-gray breccias; and anorthositic gabbros, corresponding to the petrographically defined suite of brecciated gabbroic rocks. The latter group was found as clasts in the noritic breccias and as isolated samples at stations 6, 7, and 8. Figures 7-21 and 7-22 show that both rock types plot close to the plagioclase-control trend that is typical of highland rocks, particularly those from the Apollo 16 site.

The Apollo 17 noritic breccias are characterized by approximately 50 percent normative plagioclase and are broadly comparable in bulk chemistry with KREEP-like rocks sampled on previous missions (e.g., samples 15265, 62235, and 60315). The noritic breccias have slightly higher Al_2O_3 concentrations and MgO/FeO ratios than typical Apollo 14 breccias (fig. 7-21); in this respect, they are more closely comparable with the Apollo 16 KREEP-like rocks (figs. 7-21 and 7-22). Although closely comparable in major element chemistry, the noritic breccias are lower in Na_2O, potash (K_2O), and phosphorus pentoxide (P_2O_5) than the Apollo 14 breccias, but they resemble the broadly defined composition of low- to moderate-K Fra Mauro basalt composition proposed by Reid et al. (ref. 7-15) on the basis of glass compositions in the Apollo 15 soils. Elements that are abundant in KREEP, such as Rb, Y, Zr, and niobium (Nb), are also lower in these rocks than in the Apollo 14 breccias. Figure 7-23 shows that, in comparison with their abundances in Apollo 14 breccias, these elements are depleted in rocks with the major element composition of KREEP from the Apollo 17, 16, and 15 sites. In all cases, K and Rb are

TABLE 7-V.—*X-Ray Fluorescence Analyses of Apollo 17 Rocks*[a]

Component or element	Rock type and sample number												
	Basalts			Noritic breccias					Anorthositic rocks			Dunite clast	Soil breccia
	75055,6	*70035,1*	*70215,2*	*72435,1*	*72275,2*	*76315,2*	*77135,2*	*76055,5*	*78155,2*	*77017,2*	*76230,4*	*72415,2*	*79135,1*
Abundance, percent													
SiO_2	41.27	37.84	37.19	45.76	47.54	45.82	46.13	44.65	45.57	44.09	44.52	39.93	42.29
TiO_2	10.17	12.97	13.14	1.54	.91	1.47	1.54	1.24	.27	.41	.20	.03	5.15
Al_2O_3	9.75	8.85	8.67	19.23	17.01	18.01	18.01	16.47	25.94	26.59	27.01	1.53	15.08
FeO	18.24	18.46	19.62	8.70	11.58	8.94	9.11	9.11	5.82	6.19	5.14	11.34	14.01
MnO[b]	.29	.28	.28	.11	.18	.11	.13	.11	.10	.08	.06	.13	.19
MgO	6.84	9.89	8.52	11.63	9.35	12.41	12.63	16.33	6.33	6.06	7.63	43.61	10.42
CaO	12.30	10.07	10.43	11.72	11.71	11.06	11.03	9.93	15.18	15.43	15.17	1.14	11.44
Na_2O	.44	.35	.32	.52	.38	.57	.53	.48	.33	.30	.35	< .02	.40
K_2O	.09	.06	.04	.23	.28	.27	.30	.20	.08	.06	.06	.00	.10
P_2O_5	.07	.05	.09	.27	.35	.29	.28	.19	.04	.03	.05	.04	.07
S	.19	.15	.18	.08	.08	.08	.08	.07	.04	.15	.03	.01	.10
Cr_2O_3[c]	.27	.61	.42	.20	.36	.19	.20	.19	.14	.13	.11	.34	.39
Total	99.92	99.58	98.90	99.99	99.73	99.22	99.97	98.97	99.84	99.52	100.33	98.12	99.64
Quartz	1.97	—	—	—	—	—	—	—	—	—	—	—	—
Orthoclase	.53	.35	.24	1.36	1.65	1.60	1.77	1.18	.47	.35	.35	.00	.59
Albite	3.72	2.96	2.71	4.40	3.22	4.82	4.48	4.06	2.79	2.54	2.96	.00	3.38
Anorthite	24.36	22.40	22.10	49.46	43.88	45.79	45.88	42.20	69.07	71.03	71.95	4.17	39.06
Diopside	30.00	22.11	23.81	5.74	10.01	5.96	5.81	4.78	4.91	4.37	2.44	.99	14.12
Hypersthene	19.41	24.53	23.97	23.23	36.91	24.66	25.49	19.21	16.52	10.09	8.74	1.53	19.76
Olivine	—	1.72	.33	12.01	1.13	12.70	17.72	24.52	5.31	10.01	13.25	90.91	12.30
Ilmenite	19.32	24.63	24.96	2.92	1.73	2.79	2.92	2.36	.51	.78	.38	.06	9.78
Apatite	.15	.11	.20	.59	.76	.63	.61	.42	.09	.07	.11	.09	.15
Total	99.46	98.81	98.32	99.71	99.29	98.95	99.68	98.73	99.67	99.24	100.18	97.75	99.14
Abundance, ppm													
Sr	209	176	121	165	121	175	172	155	145	141	145	11	166
Rb	.7	.7	< .2	3.8	8.7	5.8	7.3	5.1	2.3	1.2	.3	< .2	2.1
Y	112	75	75	107	129	111	107	76	16	14	12	1.1	55
Zr	272	205	183	450	613	510	494	341	59	50	42	2.6	185
Nb	25	20	20	30	32	33	33	23	4.8	4.1	3.2	.3	14
Ni	2	2	2	112	67	149	110	155	53	95	166	173	218
Zn	7	4	5	2	3	4	4	1	4	4	2	4	72

[a]Analysis performed by J. M. Rhodes, K. V. Rodgers, and B. M. Bansal.
[b]Manganese oxide.
[c]Chromium oxide.
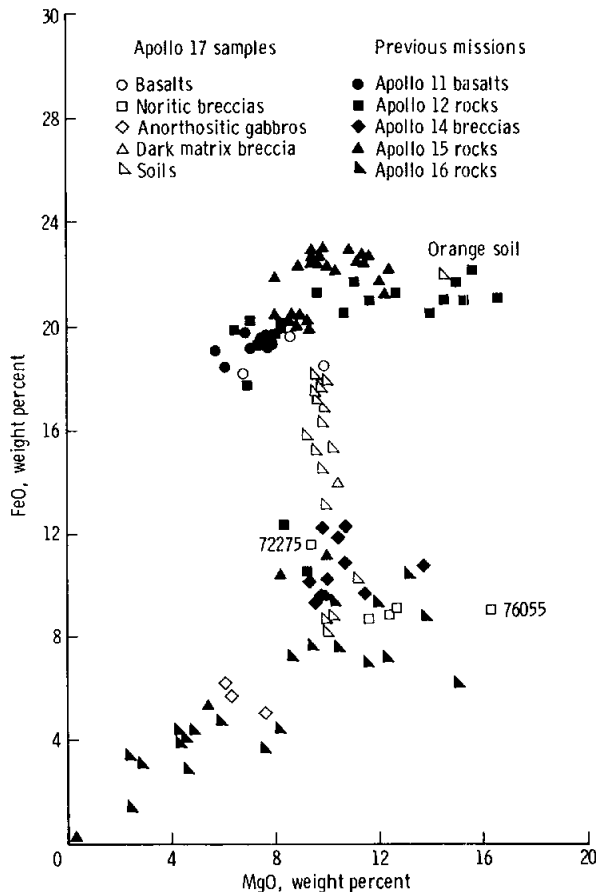
FIGURE 7-19.—The MgO and FeO content of Apollo 17 lunar rocks and soils compared with data for rocks from previous missions.

FIGURE 7-20.—The SiO_2 and TiO_2 variation in Apollo 17 basalts and in other mare basalts from previous missions.
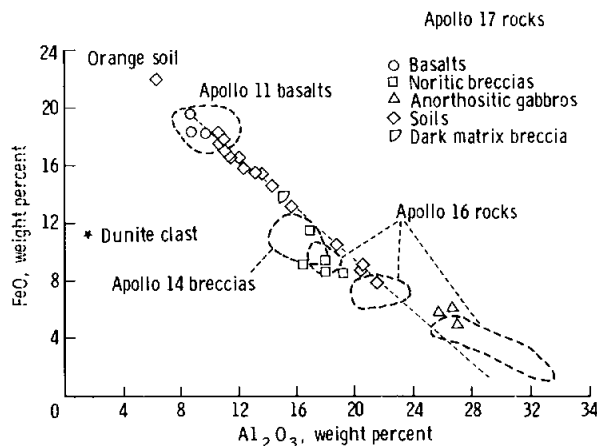
FIGURE 7-21.—The FeO and Al_2O_3 variation in Apollo 17 rocks and soils compared with data from previous missions.

more depleted than sodium (Na), phosphorus (P), Y, Zr, and Nb, but Sr is only slightly depleted. The Apollo 17 noritic breccias and the brown matrix breccias from the Apollo 15 site are more depleted in these elements than the KREEP-like rocks from the Apollo 16 site.

Some internal variation within the Apollo 17 noritic breccias is illustrated in figure 7-23. Sample 72275, classified petrographically as a foliated, light-gray breccia, is characterized by lower Sr and Na and higher P, Y, and Zr concentrations than the other breccias. These differences in minor and trace element abundances accompany small but important differences in major element chemistry. These differences include higher FeO and CaO in sample 72275 for a given Al_2O_3 content and distinctly lower MgO/FeO ratios, reflected in a higher normative

orthopyroxene content relative to plagioclase and olivine. These differences indicate that the foliated, light-gray breccias are derived from a different lithological unit than the other gray matrix breccias. This distinction is emphasized by the much lower Ni content of this rock compared with the other noritic breccias (table 7-V). If the Ni content is largely of meteoritic origin, then the possibility exists that the foliated, light-gray breccias form a stratigraphic unit the materials of which have undergone a much
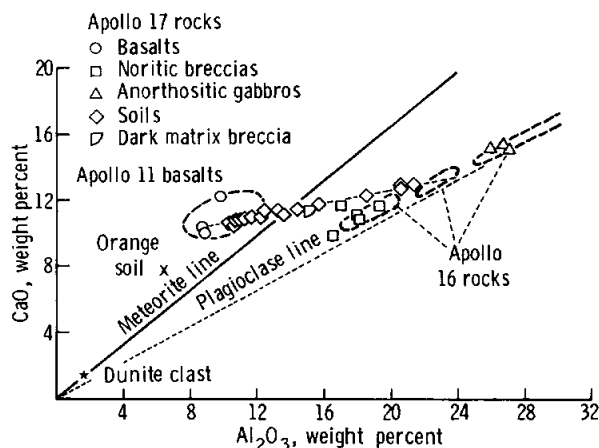
FIGURE 7-22.—The CaO and Al_2O_3 variation in Apollo 17 rocks and soils compared with Apollo 16 and 11 rocks.

FIGURE 7-24.—The Al_2O_3 and Zr variation in Apollo 17 rocks and soils. Data for previous missions were taken from references 7-9 and 7-10.

FIGURE 7-23.—Concentrations of Sr, Na, K, Rb, P, Y, Zr, and Nb in Apollo 17 noritic breccias, Apollo 16 KREEP-like rocks (ref. 7-9), and Apollo 15 brown-glass matrix breccia (ref. 7-10) relative to Apollo 14 breccias (ref. 7-17).

shorter period of surface exposure than other analyzed materials from the South and North Massifs.

In addition to the clasts of anorthositic gabbro, clasts of dunite and olivine are also present in the noritic breccias. An analysis of a large dunite clast (72415) sampled at station 2 is given in table 7-V. Abundant inclusions of olivine and dunite in sample 76055 are reflected in the high MgO content of this sample and in the low trace element abundances compared with the other breccias (fig. 7-23). Sample 76055 is slightly displaced in composition toward the dunite clast (sample 72415) from the other noritic breccias (figs. 7-21, 7-22, and 7-24).

Three samples of anorthositic gabbro have been analyzed (table 7-V). The samples are of restricted composition, all containing just over 70 percent normative plagioclase. They compare broadly in major element chemistry with such samples as 15418 and 68415 and with the highland basalt composition (ref. 7-16). Figure 7-21 shows that they are slightly more mafic than comparable rocks from the Apollo 16 site. The trace element contents of these rocks, particularly Zr, Y, and Sr, tend to be lower than those in the Apollo 16 rocks, being slightly over half their content in sample 68415 (ref. 7-9). In this respect, the samples are more closely comparable with sample 15418 (ref. 7-10 and fig. 7-24), providing evidence for a spectrum of trace element concentrations in rocks with the bulk composition of anorthositic gabbro.

Soils

The compositional range of soils from the Apollo 17 landing site is greater than that found at any previous landing site. There is a complete range of soils—from those approaching the basalt in composition to the highly aluminous, light mantle soils derived from the South Massif. Analyses of 17 soils from most of the major sampling stations and an analysis of Apollo 11 sample 10084 are given in table 7-VI. The latter sample is included for comparative purposes and as an indication of the accuracy of the results.

The major element chemistry of these soils appears relatively straightforward, suggesting a simple two-

component mixing trend involving basalt and an aluminous end-member intermediate in composition between the noritic breccias and the anorthositic gabbros (figs. 7-19, 7-21, and 7-22). In detail, however, the mixing is more complex because three compositional groups can be recognized, largely on the basis of trace and minor elements (fig. 7-24). In addition to compositional distinctions, selenographic distinctions can be made among these three groups.

"Dark Mantle" Material.—Soil samples taken at stations 1 and 5 are considered to be the best candidates for "dark mantle" material, particularly sample 75061, a soil sampled from the top of a boulder. The samples are of uniform chemistry and are compositionally very close to the subfloor basalts (figs. 7-19, 7-21, 7-22, and 7-24), which, together with orange-glass fragments, constitute approximately 80 percent of these soils. The remainder is accounted for by aluminous material from the adjacent massifs. Soils from station 4 and the LM-ALSEP site are slightly more aluminous and less mafic than the station 1 and 5 soils, containing slightly more of the massif component.

The Ni content of these soils is fairly constant, averaging approximately 120 ppm in the station 1 and 5 soils, but it increases with the increasing aluminous component in the other soils. Because the basalts, which account for the bulk of these soils, are very low in Ni (table 7-V), most of the Ni in the soil is probably of meteoritic derivation, corresponding roughly with a 1-percent chondrite component.

Light Mantle Material.—Light mantle, derived from the South Massif, has been sampled at stations 2, 2A, and 3. These soils are the most aluminous sampled at this landing site, and, apart from a small (5 percent) basaltic component, they are intermediate in both major and trace element chemistry between the noritic breccias and anorthositic gabbros (figs. 7-19, 7-21, 7-22, and 7-24). If the light mantle is representative of the South Massif, it implies that the massif is composed predominantly of noritic breccias and anorthositic gabbros in roughly equal proportions. The average Ni content of these soils is approximately 220 ppm. If one allows for the high Ni in the source rocks (approximately 100 to 120 ppm), which may also be of meteoritic origin (during an earlier phase of lunar history), then the meteoritic component inferred for these soils is approximately 1 percent, similar to that previously inferred for "dark mantle" soils.

North Massif and Sculptured Hills Material.—Soils collected near the North Massif and the Sculptured Hills from stations 6, 8, and 9 are more aluminous and less mafic than the "dark mantle" and related soils from the valley floor, and they are intermediate in major element chemistry between the basalts and the light mantle soils (figs. 7-19, 7-21, and 7-22). However, these soils are depleted in K, Zr, and Y with respect to a simple mixture of these two end components. This fact is illustrated in the case of Zr in figure 7-24. Thus, in these soils, anorthositic gabbro is more abundant relative to noritic breccias than it is in the light mantle soils, suggesting that anorthositic gabbro may be more abundant in the North Massif or the Sculptured Hills (or both) than it is in the South Massif.

Orange Soil

The orange soil (sample 74220) sampled at Shorty Crater is composed almost entirely of glass and devitrified glass spherules. It differs markedly in composition from all other soils, including adjacent soils from station 4 (table 7-VI), and is broadly comparable with the basalts, having high FeO and TiO_2 concentrations. In contrast to these rocks, the orange soil contains 14.4 percent MgO and could be derived from the basalt composition by the addition of approximately 24 percent olivine (Fo_{66}). However, both the Sr and Rb abundances (table 7-VI) are too high in the orange soil with respect to the basalts, thus precluding a direct relationship between the two. The Zn content of 292 ppm is exceptionally high for lunar materials (table 7-VI); the only other material approaching this composition is the Apollo 15 green glass (60 to 100 ppm) (ref. 7-18). The high volatile element content of the orange soil (in addition to Zn and abundant chlorine (Cl), found semiquantitatively during preliminary examination and confirmed by G. W. Reed (personal communication)) implies a source different from that of the basalts, irrespective of whether the glass in the soil is of volcanic or impact origin. Furthermore, the high Zn content cannot be attributed to any reasonable level of meteoritic contamination during impact.

Because Zn concentrations in both the basaltic and massif rocks are low, approximately 2 to 5 ppm, the higher concentrations observed in the soils (table 7-VI) must reflect the orange-glass (or its devitrified derivatives) content of these soils. On this basis, the orange-glass content is highest in the other soils from

TABLE 7-VI.—X-Ray Fluorescence Analyses of Apollo 17 Soils[a]

Component or element	74220,3 (b)	75061,4	71041,3	71501,3	75081,3	71061,3	70161,3	Sample 74240,3
								Abundance,
SiO_2	38.57	39.32	39.74	39.82	40.27	40.09	40.34	40.78
TiO_2	8.81	10.31	9.57	9.52	9.41	9.32	8.99	8.61
Al_2O_3	6.32	10.42	10.80	11.13	11.31	10.70	11.60	12.54
FeO	22.04	18.19	17.73	17.41	17.20	17.85	17.01	15.84
MnO	.30	.25	.24	.25	.25	.24	.23	.24
MgO	14.44	9.53	9.72	9.51	9.59	9.92	9.79	9.15
CaO	7.68	10.72	10.72	10.85	10.97	10.59	10.98	11.36
Na_2O	.36	.33	.35	.32	.33	.36	.32	.38
K_2O	.09	.08	.08	.07	.08	.08	.08	.12
P_2O_5	.04	.06	.07	.06	.07	.07	.08	.09
S	.07	.13	.13	.12	.12	.13	.12	.14
Cr_2O_3	.75	.48	.47	.46	.46	.49	.46	.41
Total	99.47	99.82	99.62	99.52	100.06	99.84	100.00	99.66
Quartz	—	—	—	—	—	—	—	—
Orthoclase	.53	.47	.47	.41	.47	.47	.47	.71
Albite	3.05	2.79	2.96	2.71	2.79	3.05	2.71	3.22
Anorthite	15.36	26.72	27.66	28.73	29.14	27.35	29.98	32.16
Diopside	18.43	21.37	20.54	20.25	20.33	20.29	19.64	19.33
Hypersthene	20.13	22.84	22.83	23.63	24.05	23.76	23.38	23.09
Olivine	24.32	5.31	6.22	5.01	4.67	6.46	5.99	4.06
Ilmenite	16.73	19.58	18.18	18.08	17.87	17.70	17.07	16.35
Apatite	.09	.13	.15	.13	.15	.15	.17	.20
Total	98.65	99.21	99.01	98.95	99.47	99.23	99.41	99.12
								Abundance,
Sr	205	166	165	157	165	174	168	163
Rb	1.2	1.6	1.1	1.2	1.1	1.1	1.4	2.3
Y	49	83	73	74	77	75	77	80
Zr	182	237	217	214	229	215	218	235
Nb	15	21	19	19	20	19	19	19
Ni	83	115	117	131	140	100	161	80
Zn	292	25	51	33	35	88	41	83

[a]Analysis performed by J. M. Rhodes, K. V. Rodgers, and B. M. Bansal.
[b]Orange soil.
[c]Control soil (Apollo 11).

Shorty Crater, ranging from 27 to 36 percent, and lowest in the light mantle soils, averaging approximately 5 percent. The Zn content of "dark mantle" soils indicates variable amounts of orange glass, ranging from 7 to 29 percent (averaging approximately 14 percent). The soils from stations 9, 8, and 6 contain progressively less Zn away from the valley floor. The correlation between modal orange-glass content (this does not include devitrified glass) and glass content calculated from the Zn concentrations is positive for the cases where comparison is possible.

Total Carbon Analysis

The total carbon (C) contents for the Apollo 17 soils range from 4 to 170 ppm C and are similar to

TABLE 7-VI.—*X-Ray Fluorescence Analyses of Apollo 17 Soils*[a]—Concluded

number

70181,3	74260,2	79221,2	79261,2	78501,2	76501,2	72501,2	72701,2	73141,1	10084,42 (c)
percent									
40.87	41.22	41.67	42.26	42.67	43.41	45.12	44.87	45.06	41.78
8.11	7.68	6.52	6.09	5.47	3.15	1.56	1.52	1.29	7.41
12.30	13.25	13.57	14.43	15.73	18.63	20.64	20.60	21.52	13.47
16.37	15.31	15.37	14.60	13.15	10.32	8.77	8.65	8.10	15.65
.24	.23	.21	.20	.18	.14	.11	.12	.11	.22
9.82	9.47	10.22	9.82	9.91	11.08	10.08	9.97	10.04	8.07
11.05	11.37	11.18	11.48	11.77	12.28	12.86	12.80	13.04	12.13
.35	.38	.34	.35	.35	.35	.40	.40	.38	.37
.08	.12	.09	.11	.09	.10	.16	.16	.15	.15
.06	.09	.06	.07	.05	.08	.13	.15	.12	.12
.11	.12	.12	.12	.10	.07	.09	.07	.06	.14
.44	.41	.42	.40	.37	.26	.23	.23	.21	–
99.80	99.65	99.77	99.93	99.84	99.87	100.15	99.54	100.08	99.51
–	–	–	–	–	–	–	–	–	–
.47	.71	.53	.65	.53	.59	.95	.95	.89	.89
2.96	3.22	2.88	2.96	2.96	2.96	3.38	3.38	3.22	3.13
31.76	34.10	35.24	37.48	41.09	48.97	54.05	53.94	56.57	34.65
18.57	17.75	16.26	15.59	13.87	9.30	7.29	7.04	6.01	20.42
23.12	22.60	22.27	23.06	22.55	16.98	19.29	19.32	18.22	23.18
6.83	5.96	9.54	7.95	7.88	14.58	11.62	11.39	12.20	2.76
15.40	14.59	12.38	11.57	10.39	5.98	2.96	2.89	2.45	14.07
.13	.20	.13	.15	.11	.17	.28	.33	.26	.26
99.24	99.13	99.23	99.41	99.38	99.53	99.82	99.24	99.82	99.36
ppm									
169	167	156	153	155	147	153	155	148	–
1.9	2.0	1.7	1.9	2.1	2.5	4.2	3.9	3.5	–
70	75	61	59	58	46	64	54	54	–
216	239	193	183	189	158	271	275	236	–
18	19	16	16	15	13	18	18	15	–
190	99	236	177	194	206	241	227	195	–
47	109	51	48	40	29	21	22	18	–

those found during earlier missions. The majority of the samples depicted in figure 7-25 have values ranging from 110 to 170 ppm C, which is typical of mature dark-colored soils. Exceptions include the orange soil (sample 74220), its adjacent soils (samples 74240 and 74260), and samples 71041, 71501, and 71061 from station 1. The analyzed split of sample 71061 has a noticeably larger grain size than normal fines.

Because C abundance has been shown to be correlated with surface exposure and the proportion of finer material, it is not unexpected that the coarser fines would be lower in C. The results verify previous proposals that the major portion of C found in lunar fines is from solar wind. Although the value recorded for the orange soil (sample 74220) is 4 ppm C, an earlier split was analyzed and had 100 ppm C. The 4 ppm C from a carefully selected and handled sample
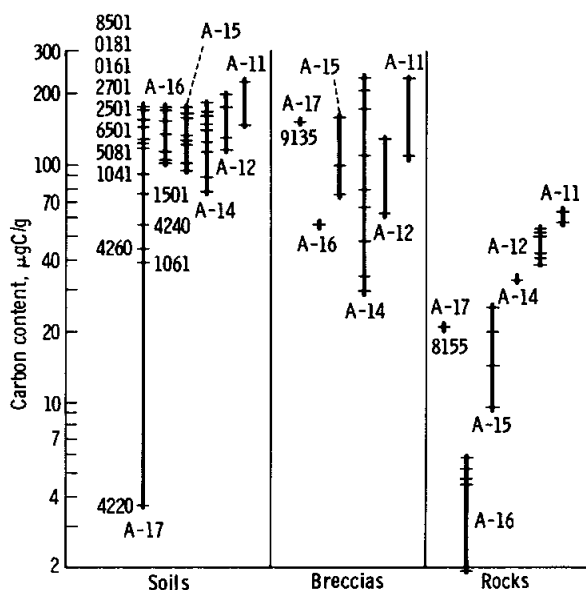
FIGURE 7-25.—A comparison of the total carbon abundances for the Apollo 17 samples with those of samples from previous missions. The latter data are from reference 7-9. Apollo 17 samples are shown by the last four digits of the inventory number.

is considered valid for sample 74220; the earlier high value is attributed to contamination in some form, although real variations in the sample cannot be completely ruled out. The soil breccia (sample 79135) has a normal total C content of 150 ppm, and the anorthositic gabbro (sample 78155) has a value of 21 ppm C, which is similar to anorthositic rocks from Apollo 15 and 16.

The gas-release profile (fig. 7-26) for the orange soil (sample 74220,5) is distinct for any lunar sample. The sample shows evidence of water (H_2O), carbon dioxide (CO_2), and sulfur dioxide (SO_2) loss below 350° to 400° C. The abundances, temperature release ranges, and sequence of release are different from lunar soils that have been derived through normal lunar regolith processes. The release profile for H_2O is similar to the release of absorbed water (released below 150° C) and a more tightly bound H_2O component, which might be associated with the large abundance of glass in the sample. The low-temperature release of CO_2 (from 10 to 15 ppm CO_2) and of SO_2 (from 10 to 15 ppm SO_2) is especially unusual. Mature lunar soils do not evolve SO_2 until temperatures approach 800° to 900° C. The high-temperature SO_2 results from the reaction of sulfides, such as

troilite, with the silicates in the matrix (ref. 7-19). The SO_2 resulting from the reaction products is seen in figure 7-26 in the temperature interval from 1000° to 1200° C. Mature lunar soils evolve trace amounts (less than 8 ppm) of CO_2 (ref. 7-20) over a wide temperature interval from 200° to 500° C, and it has been proposed by Hayes (ref. 7-21) to represent CO_2 that has been reimplanted from the lunar atmosphere. The low abundance of solar wind hydrogen (released from 200° to 700° C) for sample 74220,5 lends support to the observation of an almost total lack of agglutinates and a low exposure age (ref. 7-22) for the sample. Additional gases released above 700° C are reaction products of components found in the soil.

Cosmic-Ray-Induced Radionuclides

The amounts of radioisotopes produced on rock surfaces and on the top few millimeters of soils from the Apollo 17 site (table 7-VII) are much larger than amounts observed in samples from previous Apollo missions. These high activities resulted from a series of solar flares that occurred from August 2 to 12, 1972, the largest solar cosmic ray event that has ever been observed on Earth (ref. 7-23).

Sodium-22 (^{22}Na) activities doubled when compared to the values seen for Apollo 11, whereas cobalt-56 (^{56}Co) and manganese-54 (^{54}Mn) activities increased an order of magnitude in some cases. The isotopes beryllium-7 (^{7}Be), chromium-51 (^{51}Cr), and ^{58}Co were observed for the first time in lunar samples, and more definitive numbers for ^{57}Co content were obtained. The measurements of these additional isotopes and the increased activity of the other isotopes should serve as a better baseline for processes involving interaction of solar protons with the target elements involved.

Several rock samples appear to be unsaturated in aluminum-26 (^{26}Al) (samples 70255, 78135, and 78235), but, because these samples are chips from large rocks, chemical analysis will be necessary for confirmation.

DRIVE TUBES AND DRILL CORE

Three double drive tubes, two single drive tubes, and a deep drill core were collected to sample the stratigraphy of stations 3, 4, 6, and 9, and the ALSEP and LM sites. On return, these samples were assigned an inventory number, unpacked, externally cleaned,
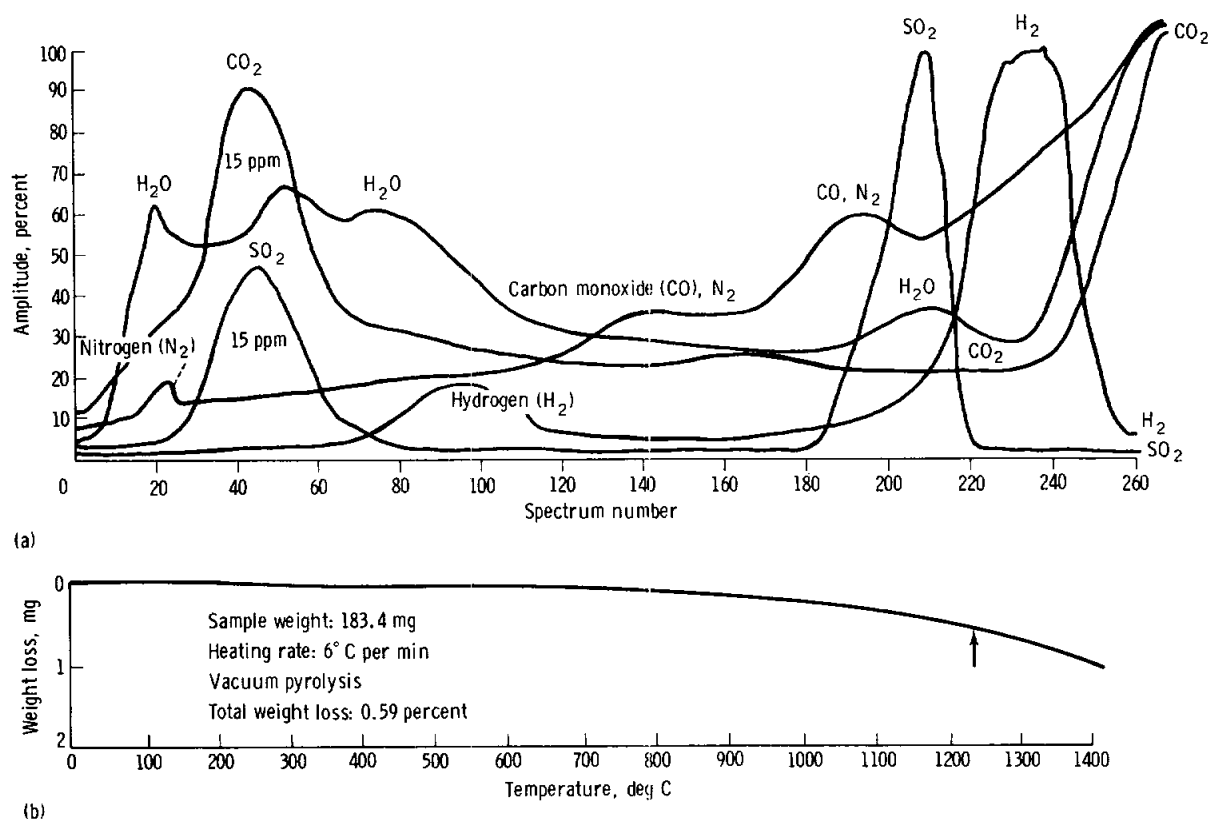
FIGURE 7-26.—Gas-release profile of soil sample 74220,5 (orange soil). Note the low-temperature release of CO_2 and SO_2. The gas-release patterns as compared to temperature have been plotted so that each of the gases have been normalized to 100-percent amplitude in their region of greatest abundance. The arrow on the weight-loss curve represents the initial melting of the sample. (a) Gas-release profile. (b) Weight-loss curve.

weighed, and then transferred to the Core Studies Laboratory.

The drill stems and drive tubes were X-rayed with Fe radiation for 5 sec at 90 kV and 50 mA. Descriptions and illustrations in the following section are derived from the study of X-radiographs and the examination of samples taken from the upper ends of some deep drill sections. The samples were described under the binocular microscope and split into coarse and fine fractions. The fine fractions were allocated to Principal Investigators; the coarse fractions were photographed and stored. The drill bit (70001) and the second section from the top of the deep drill string (70008) were dissected, and the material was described under the binocular microscope. Samples were also removed from two drive tubes: from 70012 because of a spillage problem and from 74001 for scientific purposes.

The stereopair X-radiographs provide a preliminary guide to stratification and dissection as well as a permanent, three-dimensional record of the location and attitude of many rock fragments. Changes in size, shape, sorting, packing, and composition affect the opacity of X-radiographs; also, primary depositional structures and sampling artifacts are readily visible. Because particles with a low X-ray absorption, such as feldspars, tend to be invisible, data on grain size, sorting, and density may be ambiguous. The exact location of components may be uncertain because of parallax distortion.

Deep Drill Core

The deep drill core was taken at the ALSEP site, approximately one crater diameter east of the 400-m-diameter Camelot Crater. Following extraction, the drill string was broken down into three segments for return: 70001 to 70004, 70005 and

TABLE 7-VII.—*Gamma Ray Analyses of Apollo 17 Lunar Samples*

Sample no.	Weight, g	Laboratory (a)	Th,[b] ppm	U,[c] ppm	K, percent	^{26}Al, dpm/kg	^{22}Na, dpm/kg	^{54}Mn, dpm/kg
71041,4	111.1	BNW	0.86 ± 0.03	0.22 ± 0.01	0.063 ± 0.004	126 ± 4	126 ± 4	198 ± 10
71041,4	111.1	JSC	.90 ± .02	.20 ± .06	.06 ± .02	115 ± 20	135 ± 20	220 ± 30
71061,5	100.0	JSC	1.15 ± .15	.30 ± .03	.07 ± .02	45 ± 10	65 ± 10	114 ± 10
73131,1	100.18	ORNL	2.24 ± .11	.63 ± .03	.116 ± .006	54 ± 3	126 ± 5	75 ± 10
73221,0	46.0	ORNL	2.13 ± .11	.63 ± .03	.118 ± .006	197 ± 10	310 ± 15	230 ± 30
73241,1	100.06	ORNL	2.25 ± .11	.64 ± .03	.122 ± .006	93 ± 5	110 ± 5	80 ± 8
73261,4	100.52	ORNL	2.40 ± .12	.67 ± .04	.109 ± .006	57 ± 4	42 ± 4	52 ± 12
74220,92	100.0	RCL	.65 ± .09	.164 ± .010	.068 ± .002	45 ± 4	51 ± 3	50 ± 3
74220,92	100.0	JSC	.65 ± .07	.16 ± .02	.065 ± .015	43 ± 7	58 ± 8	86 ± 15
75061,5	100.0	BNW	.87 ± .03	.22 ± .01	.060 ± .003	174 ± 6	171 ± 6	286 ± 12
75061,5	100.0	RCL	.91 ± .13	.248 ± .015	.066 ± .002	180 ± 16	187 ± 10	200 ± 10
76240,2	104.98	RCL	2.5 ± .3	.61 ± .03	.119 ± .004	154 ± 14	42 ± 3	29 ± 6
76240,2	104.98	BNW	2.30 ± .06	.60 ± .02	.110 ± .005	151 ± 6	42 ± 2	31 ± 8
76261,1	100.7	RCL	2.1 ± .3	.49 ± .02	.102 ± .003	182 ± 17	148 ± 8	93 ± 7
76261,1	100.7	BNW	1.92 ± .04	.51 ± .02	.097 ± .004	171 ± 5	142 ± 4	106 ± 8
76501,4	97.89	ORNL	1.39 ± .14	.38 ± .04	.090 ± .005	90 ± 9	90 ± 9	60 ± 10
78421,1	94.51	BNW	1.58 ± .07	.41 ± .02	.084 ± .003	55 ± 2	39 ± 2	12 ± 8
78481,1	101.27	BNW	1.49 ± .05	.39 ± .02	.095 ± .003	257 ± 12	244 ± 12	264 ± 10
78481,4	101.27	JSC	1.4 ± .2	.4 ± .1	.07 ± .02	230 ± 30	290 ± 40	310 ± 40
78501,4	113.24	ORNL	1.11 ± .11	.28 ± .03	.077 ± .004	90 ± 9	105 ± 10	96 ± 10
79221,4	100.2	ORNL	1.12 ± .06	.36 ± .03	.070 ± .004	130 ± 7	165 ± 10	215 ± 20
79261,4	100.2	ORNL	1.08 ± .05	.31 ± .02	.070 ± .004	45 ± 4	43 ± 4	44 ± 6
70135,0	446	ORNL	.32 ± .06	.11 ± .02	.046 ± .010	37 ± 8	45 ± 9	42 ± 10
70175,0	338.8	RCL	.40 ± .04	.105 ± .007	.055 ± .002	42 ± 5	76 ± 18	156 ± 9
70185,0	449	ORNL	.30 ± .03	.10 ± .02	.042 ± .004	70 ± 4	50 ± 4	95 ± 10
70255,0	224.9	RCL	.31 ± .03	.107 ± .008	.048 ± .008	49 ± 6	72 ± 7	137 ± 15
70275,0	171.4	RCL	.42 ± .04	.107 ± .008	.0421 ± .0018	92 ± 9	90 ± 16	190 ± 50
71035,0	144.1	BNW	.44 ± .03	.11 ± .01	.027 ± .003	90 ± 8	97 ± 8	157 ± 15
71155,0	25.8	BNW	.29 ± .05	.13 ± .02	< .030	105 ± 4	112 ± 4	227 ± 40
71155,0	25.8	RCL	.31 ± .08	.109 ± .018	.039 ± .003	93 ± 17	112 ± 24	160 ± 80
72255,0	402.57	RCL	4.4 ± .4	1.20 ± .15	.184 ± .008	78 ± 6	61 ± 5	41 ± 6
72355,0	367.4	RCL	5.3 ± .3	1.39 ± .04	.253 ± .005	84 ± 6	87 ± 6	66 ± 7
72415,0	29.47	RCL	< .15	< .06	.012 ± .007	77 ± 6	290 ± 30	77 ± 16
75055,2	405.9	BNW	.40 ± .02	.10 ± .01	.065 ± .005	69 ± 7	85 ± 5	139 ± 15
76015,0	2819.0	JSC	8 ± 3	2 ± .3	.30 ± .06	Detected	Detected	Detected
76215,0	642.8	RCL	4.6 ± .2	1.27 ± .06	.215 ± .014	56 ± 3	60 ± 4	22 ± 17
76255,0	393.2	BNW	2.33 ± .05	.58 ± .02	.291 ± .006	79 ± 4	71 ± 4	38 ± 9
76275,0	55.93	BNW	5.4 ± .4	1.39 ± .10	.222 ± .009	111 ± 9	95 ± 6	103 ± 20
76295,0	260.7	ORNL	5.30 ± .27	1.50 ± .08	.227 ± .011	67 ± 5	54 ± 4	38 ± 15
76295,0	260.7	BNW	5.76 ± .17	1.55 ± .05	.230 ± .009	71 ± 4	64 ± 3	70 ± 30
77135,0	316.7	BNW	5.5 ± .5	1.42 ± .14	.185 ± .018	110 ± 11	100 ± 10	21 ± 15
78135,0	133.9	RCL	.26 ± .05	.107 ± .012	.0525 ± .0018	42 ± 4	74 ± 5	180 ± 20
78235,0	128.8	RCL	.59 ± .08	.196 ± .016	.0490 ± .0015	77 ± 7	111 ± 8	55 ± 8
79155,0	316	ORNL	.31 ± .06	.12 ± .03	.041 ± .004	70 ± 10	77 ± 10	110 ± 20

[a]BNW = Battelle Pacific Northwest Laboratory (L. A. Rancitelli, R. W. Perkins, W. D. Felix, and N. A. Wogman); JSC = NASA Lyndon B. Johnson Space Center (Ernest Schonfeld); ORNL = Oak Ridge National Laboratory (G. D. O'Kelley, J. S. Eldridge, and K. J. Northcutt); and RCL = Radiation Counting Laboratory at JSC (J. E. Keith and R. S. Clark (JSC) and W. R. Portenier and M. K. Robbins (Northrop Services, Inc.)).

TABLE 7-VII.—*Gamma Ray Analyses of Apollo 17 Lunar Samples*—Concluded

^{56}Co, dpm/kg	^{46}Sc,[d] dpm/kg	^{48}V,[e] dpm/kg	^{60}Co, dpm/kg	^{7}Be, dpm/kg	^{51}Cr, dpm/kg	^{57}Co, dpm/kg	^{58}Co, dpm/kg	Th/U	K/U
364 ± 10	72 ± 3	27 ± 15	< 2.2	—	—	—	—	3.9 ± 0.2	2900 ±200
480 ± 50	85 ± 30	—	—	—	—	14 ± 5	—	4.5 ± 1.4	3000 ± 1300
130 ± 30	34 ± 15	—	—	106 ± 120	—	—	—	3.8 ± .6	2300 ± 700
119 ± 12	15 ± 3	—	—	—	—	—	—	3.6 ± .2	840 ± 130
810 ± 40	33 ± 6	—	—	450 ± 350	—	—	—	3.4 ± .2	1870 ± 130
95 ± 10	10 ± 3	—	—	—	—	—	—	3.5 ± .2	1900 ± 130
5 ± 10	8 ± 5	—	—	—	—	—	—	3.6 ± .3	1630 ± 130
31 ± 6	19.1 ± 1.6	13 ± 14	< 5	—	—	—	—	4.0 ± .6	4100 ± 280
48 ± 16	40 ± 15	—	—	< 110	—	3 ± 2	—	4.0 ± .7	4100 ± 1100
548 ± 30	112 ± 7	27 ± 15	< 2.8	350 ± 120	—	18 ± 7	21 ± 4	4.0 ± .2	2700 ± 180
490 ± 30	86 ± 5	47 ± 12	5.7 ± 1.3	—	—	—	—	3.7 ± .6	2700 ± 180
25 ± 4	7.5 ± .9	7.0 ± 1.4	4.0 ± 1.6	—	—	—	—	4.1 ± .5	2000 ± 120
27 ± 3	8 ± 4	2.6 ± 1.4	.8 ± .4	—	—	—	—	3.8 ± .2	1800 ± 100
240 ± 20	23 ± 2	18 ± 12	12 ± 5	—	—	—	—	4.3 ± .6	2100 ± 100
245 ± 8	27 ± 3	19 ± 10	< 1.5	—	—	—	—	3.8 ± .2	1900 ± 110
120 ± 12	18 ± 4	15 ± 10	—	—	—	—	—	3.7 ± .5	2400 ± 300
< 20	9.2 ± 2.5	—	1.6 ± .8	—	—	—	—	3.9 ± .3	2000 ± 120
606 ± 30	59 ± 3	34 ± 15	1.6 ± .8	370 ± 90	< 340	18 ± 8	18 ± 12	3.8 ± .2	2400 ± 150
700 ± 50	100 ± 20	—	—	250 ± 80	100 ± 60	14 ± 4	33 ± 16	3.5 ± 1.0	1800 ± 660
150 ± 10	30 ± 6	10 ± 8	—	—	—	—	—	4.0 ± .6	2800 ± 300
470 ± 25	65 ± 7	30 ± 20	—	—	—	—	—	3.1 ± .3	1900 ± 200
26 ± 10	15 ± 4	—	—	—	—	—	—	3.5 ± .3	2260 ± 190
59 ± 20	30 ± 10	—	—	—	—	—	—	2.9 ± .8	4200 ± 1200
300 ± 70	39 ± 5	17 ± 5	.29 ± .08	—	—	—	—	3.8 ± .5	5200 ± 400
105 ± 10	47 ± 5	—	—	—	—	—	—	3.0 ± .7	4200 ± 900
211 ± 19	63 ± 6	< 30	< .25	—	—	—	—	2.9 ± .4	4500 ± 800
200 ± 20	35 ± 4	32 ± 15	.17 ± .08	—	—	—	—	3.9 ± .5	3900 ± 300
328 ± 30	84 ± 6	—	—	—	—	—	—	4.0 ± .5	2500 ± 400
310 ± 20	80 ± 4	—	< 4	—	—	—	—	2.2 ± .5	—
280 ± 70	81 ± 7	—	—	—	—	—	—	2.8 ± .9	3600 ± 700
35 ± 15	6 ± 6	—	—	—	—	—	—	3.7 ± .6	1500 ± 200
58 ± 13	12 ± 3	< 9	< .4	—	—	—	—	3.8 ± .2	1820 ± 60
150 ± 30	8 ± 3	—	—	—	—	—	—	—	—
210 ± 15	62 ± 7	< 22	4 ± 2	140 ± 25	75 ± 40	7.4 ± 1.7	7.0 ± 3.5	4.0 ± .4	6500 ± 800
Detected	Detected	—	—	Detected	Detected	—	Detected	.4 ± 1.6	1500 ± 400
45 ± 6	5 ± 3	< 24	< .4	—	—	—	—	3.6 ± .2	1690 ± 140
37 ± 4	3.9 ± 1.3	5.7 ± 2.6	—	—	—	—	—	4.0 ± .2	5000 ± 200
64 ± 6	7 ± 2	—	< 1.1	—	—	—	—	3.9 ± .4	1600 ± 130
41 ± 7	5 ± 2	—	—	—	—	—	—	3.5 ± .3	1510 ± 110
35 ± 5	6.4 ± 2.6	—	< 1.2	—	—	—	—	3.7 ± .2	1500 ± 80
66 ± 7	7.2 ± 2.2	3 ± 3	4 ± 3	—	—	—	—	3.9 ± .5	1300 ± 200
240 ± 20	76 ± 5	18 ± 5	< 3.5	—	—	—	—	2.4 ± .5	4900 ± 600
52 ± 9	1.4 ± .9	< 12	3.4 ± 1.2	—	—	—	—	3.0 ± .5	2500 ± 200
155 ± 30	62 ± 10	—	—	—	—	—	—	2.6 ± .8	3400 ± 900

[b]Thorium.
[c]Uranium.
[d]Scandium.
[e]Vanadium.

70006, and 70007 to 70009. Each section has a potential collecting length of 39.9 cm, except for the basal section (70002), which is 37.0 cm long attached to the 6.5-cm-long bit (70001). From X-radiographs, the estimated length of returned sample was 294.5 cm (9.66 ft) out of a potential return of 322.5 cm (10.6 ft). Because drilling became difficult and was stopped with 30 ± 2 cm of the drill stem still above the lunar surface, a void of similar length at the top of the core was expected. Actual empty space occupied approximately 27 cm, but it was distributed unevenly. There was a 15-cm void at the top of 70009, a 2-cm void at the top of 70008, and an estimated 10-cm void in the top half of 70007 (the top 2 cm of 70007 were empty, and the next 16 cm were approximately half full of loose material, sloping from empty to completely full). Hence, recovery of actual material sampled is close to 100 percent. Stratal separation took place at the top of 70007; apparently, the soil of the upper two sections moved as a plug, possibly aided by air of pressurization entering through the connection between 70007 and 70008.

In gross aspect, the deep drill core contains three major stratigraphic intervals: an upper, massive, coarse-grained interval dominated by basaltic and crystalline rock fragments; a middle, very-fine-grained interval dominated by anorthositic fragments; and a lower distinctly stratified interval containing a variety of breccias and crystalline fragments (fig. 7-27).

The upper interval, which includes units 52 through 64, is 107 cm thick (from the lunar surface), characteristically massive and coarse grained, and more poorly stratified than the rest of the drill string. Principal layering occurs near the top and bottom of this interval. The uppermost 17.5 cm contain five layers (units 60 through 64), including a basal, fine-grained, thin bed that is overlain by 14.5 cm of fining-upward sequence. Conversely, unit 59, the major massive bed, is 61.5 cm thick and occupies the lower 7.5 cm of 70009, all of 70008, and the upper 16 cm of 70007. This massive unit is packed with poorly sorted rock fragments; in 70008, which has been dissected, these fragments show an upward succession from soil breccias, through massive to flaky, black, devitrified glass, to fresh-appearing vesicular basalts and gabbroic anorthosites. Very little glass was found in this part of the core. Units 52 through 58 are fairly distinct and extend the coarse-grained interval to a depth of 107 cm. Basaltic and crystalline rocks are dominant at the top of 70006.

The fine-grained middle interval, which is 56 cm thick, includes units 36 through 51 and contains a few widely scattered coarse rock fragments. The sample removed from the top of 70005 contains small, anorthositic rock fragments and a few breccias; X-ray characteristics indicate similar texture and composition throughout the interval.

The 131.5-cm-thick basal interval, which is heterogeneous and well stratified, includes units 1 through 35. Although there are some units over 10 cm thick and others less than 0.5 cm thick, most range from 2 to 5 cm. Similarly, although sorting ranges from very poor to good and grain size ranges from medium coarse to very fine, most soils of this interval are well sorted and fine grained. Samples removed from the top of sections 70004, 70003, and 70002, and from the dissected bit, 70001, tend to be fine grained and moderately well sorted, with a small percentage of coarse fraction dominated by soil and glassy matrix breccias. Although vesicular basalts and gabbros are present, they are subordinate to glasses and breccias.

Field and stratigraphic data suggest the following tentative subfloor regolith stratigraphy and history. The lower interval, with its many thin layers, relatively fine grain size, good sorting, and abundance of breccia and glass, was deposited either slowly by accretion over a long period of time or rapidly with extensive reworking over a long period of time. The middle interval, which is fine grained, relatively well sorted, and rich in powdery anorthosite, could signify either the culmination of the working and slow accretion of beds of the lower interval or the distal end of a landslide from one of the massifs.

The upper interval appears to be associated with events that produced nearby craters. The lower strata (fig. 7-28) may be ejecta from subdued older craters, such as Poppy and San Luis Rey. In 70008, the reverse stratigraphic sequence of soil breccia through glassy breccia to crystalline rocks, the abundance of fresh-appearing plagioclase, and the scarcity of breccia and spatter glass are taken as evidence to indicate that the main unit accumulated by rapid deposition, probably from the Camelot cratering event. The thin, fine-grained bed above unit 59 may represent an eroded and pulverized horizon. The uppermost, fining-upward, thin-bedded sequence (units 61 through 64) is tentatively interpreted to be base surge ejecta from nearby Rudolph Crater, which does not contain coarse, blocky, subfloor ejecta. This sequence was not found in drive tube 70012, where a hard layer probably represents the packed fragmental unit.

Depth,
cm

Unit

300

70001 | 70002

— UNIT 9   Depth: TDS, 286.5 to 289 cm; lunar surface, 259.5 to 262 cm   Thickness: 2.5 cm
    Thin interval with scattered mottles.
9 Matrix: 95 percent; moderately transparent, indistinctly granular, with a trace of pinpoint opaques.
    Coarse fraction: 5 percent; semiopaque, indistinct outline, 2- to 5-mm crenulate mottles scattered randomly throughout
—   the interval.

8
— UNIT 8   Depth: TDS, 289 to 290 cm; lunar surface, 262 to 263 cm   Thickness: 1 cm
7 Thin bed with small, sorted rock fragments.
— Matrix: 80 percent; high transparency with pinpoint opaques, as in unit 7.

   Coarse fraction: 20 percent; semiopaque with moderately distinct outline, 1 to 3 mm in diameter, well sorted, chip-shaped
6   fragments with relatively straight margins and angular corners. A few fragments show an indistinct outline on one
—   side.

   UNIT 7   Depth: TDS, 290 to 291 cm; lunar surface, 263 to 264 cm   Thickness: 1 cm
   Fine-grained thin bed with transparent matrix.
   Matrix: 100 percent; as in unit 4, uniformly finely granular, high transparency, and a trace of pinpoint opaques.

   UNIT 6   Depth: TDS, 291 to 293 cm; lunar surface, 264 to 266 cm   Thickness: 2 cm
5 Thin bed with large rock fragments.
   Matrix: 60 percent; high transparency, as in unit 5, but with no pinpoint opaques.
   Framework: 40 percent; 30 percent is semiopaque rock fragments with distinct outline, bimodal sorting, and large frag-
     ments, 0.8 to 1.2 cm, are equant and lumpy as in unit 2, and 2- to 4-mm chip-like fragments as in unit 5; 10 percent
     is semiopaque mottles, 1 to 3 mm in diameter, with indistinct but smooth, not crenulate, outlines.

   UNIT 5   Depth: TDS, 293 to 301 cm; lunar surface, 266 to 274 cm   Thickness: 8 cm
— Thick interval with transparent matrix and small, sorted rock fragments.
   Matrix: 90 percent; high transparency with traces of pinpoint opaques as in unit 4.
4 Coarse fraction: 10 percent; semiopaque rock fragments with distinct outline, slightly elongate to chip shaped, 2 to 4 mm
     in diameter, sorted, with straight edges and angular corners.

   UNIT 4   Depth: TDS, 301 to 305 cm; lunar surface, 274 to 278 cm   Thickness: 4 cm
— Fine-grained unit with transparent matrix.
   Matrix: 100 percent; distinctly less dense and opaque than underlying unit, featureless except for a trace of pinpoint
     spherical opaques.

3 UNIT 3   Depth: TDS, 305 to 310 cm; lunar surface, 278 to 283 cm   Thickness: 5 cm
   Medium-thin bed with dense matrix and indistinct mottles.
   Matrix: 85 percent; relatively high opacity, somewhat granular in appearance, with a distinct fairly planar upper bound-
     ary and a tendency to an indistinctly mottled appearance, but with no opaque particles.
— Coarse fraction: 15 percent; traces of opaque, 1-mm fragment, subrounded blocky fragment; 15 percent is semiopaque,
     indistinct outline with highly crenulate widely sized mottles scattered throughout the entire length of the interval,
     no distinct layering.

   UNIT 2   Depth: TDS, 310 to 316 cm; lunar surface, 283 to 289 cm   Thickness: 6 cm
2 Medium-thick interval with poorly sorted rock fragments.
   Matrix: 70 percent intermediate transparency with trace of shard-like opaques.
   Framework: 30 percent; traces of 1-mm-diameter, equant, globular opaques; 20 percent is semiopaque rock fragments
     with distinct outline, 2 to 9 mm in diameter, average ≈3 mm, poorly sorted, equant to slightly elongate, mostly with
     irregular lumpy appearance, subordinate number with smooth straight outline; 10 percent is semiopaque, indistinct
—   outlined equant mottles with vaguely crenulate outlines as much as 8 mm in diameter, but averaging 2 to 3 mm.

   UNIT 1   Depth: TDS, 316 to 322.5 cm; lunar surface, 289 to 294.5 cm   Thickness: 5.5 cm
1 Fine-grained unit with sparse rock fragments. Comprises all of 70001, the drill bit. Because of the thick walls, it is not
     possible to distinguish many soil characteristics.
   Matrix: ≈90 percent; reveals no texture except that it appears fine grained.
   Coarse fraction: ≈10 percent; appears to contain scattered, 1- to 3-mm, well-sorted rock fragments (equant, semiopaque
     to X-rays, but with distinct subrounded outline).
—

X-radiograph symbols

Granular matrix   Opaque particles   Indistinct fragments

Light matrix   Distinct rock fragments   Void space

FIGURE 7-27.—Interpretation of X-radiographs of Apollo 17 deep drill string. The top of the drill
    string is represented by the abbreviation TDS. Depth values are direct from X-radiographs and
    therefore are somewhat expanded.

Depth,
cm

Unit

UNIT 38   Depth: TDS, 174.5 to 178.5 cm; lunar surface, 147.5 to 151.5 cm   Thickness: 4 cm
Medium-thin interval with abundant, small, well-sorted rock fragments.
Matrix: 70 percent; moderate to high transparency, with less than 10 percent fine mottles and only a trace of pinpoint
opaques, near limit of resolution.
Framework: 30 percent; 20 percent is semiopaque rock fragments with distinct outline, 2 to 4 mm in diameter, well
sorted, blocky to wedge shaped with nearly straight sides and angular to subangular corners; 10 percent is semiopaque
density concentrations with indistinct outline, 2 to 4 mm diameter, fading out over relatively straight and even edge,
suggesting breccia fragments.

UNIT 37   Depth: TDS, 178.5 to 183 cm; lunar surface, 151.5 to 156 cm   Thickness: 4.5 cm
Densely granular interval with sparse rock fragments.
Matrix: 95 percent; more opaque than unit 36, densely and finely granular with traces of minute spherical opaques.
Coarse fraction: 5 percent; semiopaque with indistinct outline, appearing as equant density concentrations 1 to 3 mm
in diameter, with regular and even fadeout, sorting and type of semitransparency suggest breccia fragments rather
than clods.

UNIT 36   Depth: TDS, 183 to 190 cm; lunar surface, 156 to 163 cm   Thickness: 7 cm
Massive interval with sparse rock fragments and abundant opaque fragments.
Matrix: 90 percent; uniformly fine grained and noticeably transparent with ≈1 percent spherical opaques, 0.5 mm to limit
of resolution.
Coarse fraction: 10 percent (decreasing upward); 5 percent is semiopaque rock fragments having distinct outline, moder-
ately well sorted, 2 to 3 mm in diameter, best sorting at top of bed, continuous gradation upward; 4 percent is semiopaque
mottles, 1 to 4 mm in diameter with crenulate fadeout; 1 percent is opaque fragments, averaging 1 mm in diameter, blocky
equant to comma shaped.

UNIT 35   Depth: TDS, 190 to 194.5 cm; lunar surface, 163 to 167.5 cm   Thickness: 4.5 cm
Rock fragmental zone with relatively transparent matrix.
Matrix: 60 percent; decidedly less dense in appearance than underlying unit with ≈1 percent spherical opaques, 0.5 mm
in diameter to limit of resolution; matrix becomes progressively more transparent upward.
Framework: 40 percent; rock fragments, similar in appearance to unit 34, ≈30 percent is semiopaque rock fragments with
distinct outline; 10 percent is crenulate mottles with indistinct outline.

UNIT 34   Depth: TDS, 194.5 to 200 cm; lunar surface, 167.5 to 173 cm   Thickness: 5.5 cm
Rock fragmental zone with relatively opaque matrix.
Matrix: 65 percent; relatively opaque to X-rays, compared to unit 35, but appears to be uniformly dense throughout with
no distinct mottles or opaque fragments.
Framework: 35 percent; 25 percent is semiopaque rock fragments with distinct outline, 2 to 11 mm in diameter, poorly
sorted, equant to slightly elongate, polygonal, relatively straight sided, subangular corners; 10 percent is semiopaque
with indistinct outline, appears as indistinct mottles, 1 to 4 mm in diameter with finely crenulate fadeout.

UNIT 33   Depth: TDS, 200 to 202.5 cm; lunar surface, 173 to 175.5 cm   Thickness: 2.5 cm
Moderately thin bed with abundant rock fragments.
Matrix: 80 percent; intermediate transparency with some granules as unit 32.
Coarse fraction: 20 percent; 10 percent is semiopaque rock fragments with distinct outline, 2 to 5 mm in diameter,
moderately well sorted, elongate-equant polygonal with straight edges, subangular corners; 10 percent is semiopaque
with indistinct outline, 2- to 5-mm-diameter clods or mottles, fading out irregularly, but not on a crenulated margin.

UNIT 32   Depth: TDS, 202.5 to 205 cm; lunar surface, 175.5 to 177 cm   Thickness: 1.5 cm
Thin bed with scattered rock fragments.
Matrix: 90 percent; intermediate transparency with ≈5 percent granules, 0.5 mm to limit of resolution.
Coarse fraction; 10 percent; semiopaque rock fragments with distinct outline, 2 to 3 mm, well sorted, ovoid and sub-
rounded.

UNIT 31   Depth: TDS, 204 to 207 cm; lunar surface, 177 to 180 cm   Thickness: 3 cm
Transparent matrix interval with scattered rock fragments.
Matrix: 95 percent; nearly uniformly transparent with only a trace of granularity or pinpoint opaques.
Coarse fraction: 5 percent; semiopaque, indistinct outline, 0.5- to 2-mm elongate mottles, resembling shard-like
rock fragments, but indistinct.

UNIT 30   Depth: TDS, 207 to 209.5 cm; lunar surface, 180 to 182.5 cm   Thickness: 2.5 cm
Finely mottled zone with sorted rock fragments.
Matrix: 70 percent; similar to unit 29 in being moderately opaque and finely mottled throughout.
Coarse fraction: 30 percent; 10 percent is semiopaque rock fragments, well sorted, 2.5 to 5 mm in diameter, elliptical,
subangular to subrounded with even surfaces; 20 percent is semiopaque, indistinct to partially distinct outline,
1 to 6 mm in diameter, fading out over irregular but not highly crenulate edges.

FIGURE 7-27.—Continued.

Depth,
cm

Unit

UNIT 48   Depth: TDS, 146.5 to 148 cm; lunar surface, 119.5 to 121 cm   Thickness: 1.5 cm
Fine-grained thin bed with transparent matrix.
Matrix: 100 percent; uniformly fine grained with a trace of widely scattered and evenly distributed pinpoint mottles, near
51   limit of resolution, no opaques.

UNIT 47   Depth: TDS, 148 to 151 cm; lunar surface, 121 to 124 cm   Thickness: 3 cm
Medium-thin bed with moderately opaque matrix and scattered rock fragments.
Matrix: 85 percent; intermediate transparency because of 10 percent granularity and pinpoint density concentrations,
50   but with a noticeable absence of opaques in contrast to unit 46.
Coarse fraction: 15 percent; semiopaque rock fragments with distinct to semidistinct outline, well sorted, 2 to 4 mm in
diameter, equant to polygonal with relatively straight edges and subangular corners, slightly lumpy and irregular
(not crenulate) fadeout on semidistinct edges.

UNIT 46   Depth: TDS, 151 to 154 cm; lunar surface, 124 to 127 cm   Thickness: 3 cm
Transparent matrix and fine-grained interval with abundant opaque fragments.
49   Matrix: 100 percent; noticeably more transparent than in unit 45 with less than 5 percent pinpoint semiopaque density
concentrations (in contrast to 20 percent of unit 45), 2 percent opaque particles, equant, subrounded polygons with
a suggestion of straight edges or spheroids, less than 1 mm in diameter to limit of resolution.

UNIT 45   Depth: TDS, 154 to 156 cm; lunar surface, 127 to 129 cm   Thickness: 2 cm
Moderately opaque interval, as in unit 44, but with no rock fragments.
48   Matrix: 100 percent; moderately opaque with ≈20 percent indistinct pinpoint mottles, near limit of resolution to 0.5 mm,
but with no opaque spherules; contact with overlying bed appears very distinctly as an irregularly planar surface, with
striking decrease in density in overlying unit 46.

47   UNIT 44   Depth: TDS, 156 to 160 cm; lunar surface, 129 to 133 cm   Thickness: 4 cm
Moderately opaque interval with small, scattered, sorted rock fragments.
Matrix: 85 percent; moderately opaque with ≈20 percent indistinct equant mottles, near limit of resolution to 0.5 mm, 1
percent opaque spherules less than 0.5 mm in diameter.
46   Coarse fraction: 15 percent; semiopaque with partially distinct outline (probably partially concealed by density of matrix),
3 to 5 mm, well sorted, equant to ovoid, subrounded particles, long axes tend to be alined horizontally.

UNIT 43   Depth: TDS, 160 to 164 cm; lunar surface, 133 to 137 cm   Thickness: 4 cm
45   Rock fragmental unit fractured at top of core.
Matrix: 70 percent; appears similar to that of unit 42, but is strongly permeated by cracks and fractures, contains
≈20 percent finely granular mottles, traces of opaque spherules, near limit of resolution.
Coarse fraction: 30 percent; clumps or rock fragments with distinct outline, 2 to 11 mm in diameter, subovoid to
polygonal with irregular angularly wavy edges most commonly defined by cracks in matrix.

44   UNIT 42   Depth: TDS, 164 to 166 cm; lunar surface, 137 to 139 cm   Thickness: 2 cm
Thin bed with moderately opaque matrix and small sorted rock fragments.
Matrix: 80 percent; intermediate opacity, finely mottled with 20 percent pinpoint mottles, less than 1 mm in diameter,
but no opaques.
Coarse fraction: 20 percent; semiopaque rock fragments with moderately distinct outline, 1 to 4 mm in diameter,
average 2.5 mm with few fragments being much smaller or larger, fragments with one or two relatively straight
43   margins, but fading out along crenulate margins on other side of fragment.

UNIT 41   Depth: TDS, 166 to 170 cm; lunar surface, 139 to 143 cm   Thickness: 4 cm
Fine-grained interval with scattered fine mottles and sparse rock fragments.
42   Matrix: 95 percent of intermediate to low opacity, with 5 to 15 percent mottles under 1 mm in diameter and ≈1 percent
spherical opaques, limit of resolution to 0.8 mm.
Coarse fraction: 5 percent; semiopaque rock fragments with distinct outline, blocky slightly elongate with relatively
straight edges and angular corners.

UNIT 40   Depth: TDS, 170 to 170.5 cm; lunar surface, 143 to 143.5 cm   Thickness: 0.5 cm
41   Thin rock layer.
Matrix: 60 percent; moderately transparent and uniformly fine grained.
Framework: 40 percent; semiopaque rock fragments with distinct outline, 1 to 4 mm in diameter, moderately well sorted,
40   equant to slightly elongate, with smoothly faceted to blocky outline, subangular to angular corners.

UNIT 39   Depth: TDS, 170.5 to 174.5 cm; lunar surface, 143.5 to 147.5 cm   Thickness: 4 cm
Fine-grained interval with indistinct granules.
39   Matrix: 95 percent; moderately high transparency, but with 2 percent opaques, ranging from spheroids at limit of
resolution to shards 1 mm long; elongate opaques tend to have long axes alined horizontally.
Coarse fraction: 5 percent; semiopaque density concentrations with indistinct outline, 1 to 3 mm in diameter with
regular and even fadeout as in unit 37.

FIGURE 7-27.—Continued.

Depth,
cm

Unit

UNIT 57   Depth: TDS, 110.5 to 115 cm; lunar surface, 83.5 to 88 cm   Thickness: 4.5 cm
Medium-thin bed with sparse small rock fragments and abundant opaques.
Matrix: 90 percent; intermediate to high transparency and with 10 to 15 percent semiopaque granules, 1 mm in diameter
   to limit of resolution, ≈1 percent blocky to spherical opaque fragments as much as 1 mm in diameter.
Coarse fraction: 10 percent; 5 percent is semiopaque rock fragments with distinct outline, well sorted, 1 to 2 mm in
   diameter, equant and blocky with angular corners; 5 percent is semiopaque mottles, 2 to 3 mm in diameter with
   crenulate fadeout as in unit 56.

UNIT 56   Depth: TDS, 115 to 119 cm; lunar surface, 88 to 92 cm   Thickness: 4 cm
Medium-thin bed with small well-sorted rock fragments.
Matrix: 80 percent; intermediate to high transparency with less than 10 percent fine granularity, only trace amounts
   of spherical opaques, near limit of resolution.
Coarse fraction: 20 percent; 15 percent is semiopaque rock fragments with distinct outline, well sorted, mostly 2 to 4 mm
   in diameter, blocky and equant to bladed and elongate with relatively straight sides and angular corners; 5 percent is
   semiopaque density concentrations with indistinct crenulate fadeout. These fragments range from 1 to 5 mm in
   diameter and are randomly distributed throughout the unit.

UNIT 55   Depth: TDS, 119 to 122.5 cm; lunar surface, 92 to 95.5 cm   Thickness: 3.5 cm
Thin bed packed with basalt fragments. (2.5 cm of this unit are in core 70007, and 1 cm is in the base of core 70007.)
Matrix: 30 percent; relatively transparent, very finely granular with no opaques.
Framework: 70 percent (examined during end sampling for early allocation); packed with semiopaque rock fragments with
   distinct outline, equant, poorly sorted, blocky fragments with nearly straight edges; on examination of actual speci-
   mens, they turned out to be coarsely crystalline basalt fragments with 15 to 20 percent vesicles as much as 5 mm in
   diameter. No other rock types were present.

UNIT 54   Depth: TDS 122.5 to 127 cm; lunar surface, 95.5 to 100 cm   Thickness: 4.5 cm
Massive unit with mixed rock fragments and relatively transparent matrix. In X-radiograph, this unit appears to be
   very similar in composition to unit 52.

UNIT 53   Depth: TDS, 127 to 129 cm; lunar surface, 100 to 102 cm   Thickness: 2 cm
Thin bed, packed with rock fragments.
Matrix: 50 percent; relatively transparent, sparingly mottled, apparently as in unit 52, but mostly concealed by abundant
   rock fragments.
Framework: 50 percent; 45 percent is semiopaque rock fragments with distinct outline, moderately well sorted, 2 to 9 mm
   in diameter, but mostly 5 ±1 mm, blocky, smooth-edged and subangular fragments, similar to those of unit 52, but
   much more abundant; 5 percent is semiopaque mottles, averaging 2 to 3 mm in diameter with irregular lumpy to
   indistinct outline.

UNIT 52   Depth: TDS, 129 to 134 cm; lunar surface, 102 to 107 cm   Thickness: 5 cm
Massive unit with mixed rock fragments and transparent matrix.
Matrix: 70 percent; relatively transparent with ≈5 percent fine semiopaque mottles less than 1 mm in diameter, a trace
   of spherical opaques, near limit of resolution.
Coarse fraction: 30 percent; 20 percent is semiopaque rock fragments with distinct outline, poorly sorted, ranging from
   1 to 8 mm in diameter, tending to be blocky to wedge-shaped equant fragments; 10 percent is semiopaque density con-
   centrations with indistinct outline, 2 to 5 mm in diameter, fading out over an irregular to lumpy outline as in unit 51.

UNIT 51   Depth: TDS, 134 to 138.5 cm; lunar surface, 107 to 111.5 cm   Thickness: 4.5 cm
Massive interval with granular matrix and abundant clods and rock fragments.
Matrix: 70 percent; moderately opaque with ≈20 percent pinpoint to 0.5-mm semiopaque granules scattered throughout,
   traces of opaque spherules less than 0.5 mm in diameter.
Coarse fraction: 30 percent; 5 percent is semiopaque rock fragments with distinct outline, 2 to 5 mm in diameter,
   moderately poorly sorted, blocky outline with straight to nearly straight edges; 25 percent is semiopaque mottles
   or clods with indistinct outline, ranging up to 8 mm in diameter, but very poorly sorted. Fragments, possibly
   breccias, tend to have a lumpily irregular appearance and are not crenulate. Entire interval appears to be reverse
   graded and is roughly coarser at the top.

UNIT 50   Depth: TDS, 138.5 to 140 cm; lunar surface, 111.5 to 113 cm   Thickness: 1.5 cm
Fine-grained thin bed with high transparency matrix.
Matrix: 100 percent; as in unit 48, uniform with trace of pinpoint mottles and opaques.

UNIT 49   Depth: TDS, 140 to 146.5 cm; lunar surface, 113 to 119.5 cm   Thickness: 6.5 cm
Medium-thin bed with moderately opaque matrix and scattered rock fragments.
Matrix: 85 percent; intermediate transparency with 10 percent granularity, but with noticeable absence of opaque frag-
   ments or density concentrations.
Coarse fraction: 15 percent; semiopaque rock fragments with distinct to semidistinct outline, moderately well sorted,
   2 to 5 mm in diameter, equant to polygonal with generally straight edges and subangular corners, even fadeout areas
   where edges are indistinct.

FIGURE 7-27.—Continued.

Depth,
cm   Unit

UNIT 64   Depth: TDS, 15 to 18 cm; lunar surface, 0 to 3 cm   Thickness: 3 cm
Fine-grained unit with transparent matrix and scattered opaque spheroids.
Matrix: 100 percent; high transparency with ≈ 10 percent density concentrations and semiopaque granules less than 1 mm
    in diameter; 1 percent opaque shards and spheroids ranging from 1 mm in diameter to limit of resolution. On the
    X-radiograph, the unit appears to fade out over a 2-cm distance along the upper margin because of slumping.

60

UNIT 63   Depth: TDS, 18 to 23 cm; lunar surface, 3 to 8 cm   Thickness: 5 cm
Massive fine-grained unit with coarse but indistinct mottles.
Matrix: 100 percent; intermediate to high background transparency, but with 50 to 60 percent indistinct mottles as much
    as 2 mm in diameter, granular density concentrations generally less than 1 mm in diameter.

UNIT 62   Depth: TDS, 23 to 26 cm; lunar surface, 8 to 11 cm   Thickness: 3 cm
Fine-grained interval with sorted small rock fragments and clod-like particles.
Matrix: 75 percent; relatively opaque because of granularity, represented by 30 percent semiopaque density concentra-
    tions less than 1 mm in diameter, but with no opaques.
Coarse fraction: 25 percent; 15 percent is semiopaque rock fragments with distinct outline. Rock fragments are well
    sorted, 1.5 to 4 mm in diameter, equant to subequant with irregular lumpy outlines; 10 percent is semiopaque cren-
    ulate mottles less than 5 mm in diameter.

UNIT 61   Depth: TDS, 26 to 29.5 cm; lunar surface, 11 to 14.5 cm   Thickness: 3.5 cm
Medium-thin bed with abundant, mixed rock fragments.
Matrix: 55 percent; moderately opaque (but noticeably less opaque than unit 60) with 20 percent semiopaque granular
    density concentrations, less than 0.5 mm in diameter, no opaques.
Framework: 45 percent; 35 percent is semiopaque rock fragments with distinct outline. (Of the semiopaque rock frag-
    ments, 25 percent is represented in equant rock fragments with irregular, lumpy, subangular to subrounded outline.
    These fragments are poorly sorted, ranging from 1 to 9 mm in diameter. The other 10 percent of distinct-outlined
    rock fragments is elongate chips, splinters, and blocky rock fragments with straight edges and angular to subangular
    corners, but these fragments are as poorly sorted as the equant fragments). Remaining 10 percent of framework
    consists of semiopaque crenulate mottles 2 to 6 mm in diameter.

59 UNIT 60   Depth: TDS, 29.5 to 32.5 cm; lunar surface, 14.5 to 17.5 cm   Thickness: 3 cm
Fine-grained interval with clod-like coarse fraction.
Matrix: 80 percent relatively opaque, distinctly granular with 30 percent semiopaque granular density concentrations,
    less than 1 mm in diameter, a trace of pinpoint spherical opaques.
Coarse fraction: 20 percent; semiopaque crenulate mottles and density concentrations, 2 to 5 mm in diameter, with
    fairly even size distribution, indicating good sorting if these particles represent rock fragments and not soil clods.

70008

80

70007

UNIT 59   Depth: TDS, 32.5 to 106 cm; lunar surface, 17.5 to 79 cm   Thickness: 61.5 cm
Note: Soil in unit 59 consists of 38 cm in 70008, 16 cm in 70007, and 7.5 cm in 70009. The 16 cm of soil in 70007 com-
    prised 6 cm of drill stem packed with sample and 20 cm of drill stem averaging 50 percent full; thus, a total of 16 cm.
Massive unit packed with poorly sorted, large rock fragments.
Matrix: 50 percent; moderate to low transparency with 30 to 50 percent fine semiopaque granules less than 1 mm in
    diameter, a trace of opaque spherules, 0.5 mm in diameter to limit of resolution.
Framework: 50 percent; 45 percent is semiopaque rock fragments with distinct outline, 1 mm to 2.5 cm in diameter.
    Fragments are very poorly sorted, mostly equant to ovoid-elongate with blocky or irregular polygonal outline, angular
    to subangular corners; 5 percent is semiopaque density concentrations with indistinct outline, but fading out smoothly
    to slight unevenly, not fading out over crenulate margins.
In 70008, there are especially large rock fragments at approximately 16 and 30 cm from the top; otherwise, character-
    istics of the unit seem to apply throughout.

UNIT 58   Depth: TDS, 106 to 110.5 cm; lunar surface, 79 to 83.5 cm   Thickness: 4.5 cm
Medium-thin bed with abundant, small, well-sorted rock fragments.
Matrix: 70 percent; moderate transparency with approximately 25 percent finely granular texture, granules semiopaque,
    less than 1 mm in diameter, a trace of spherical opaques, near limit of resolution.
Coarse fraction: 30 percent; 25 percent is semiopaque rock fragments with distinct outline, well sorted, all fragments
    being 2.5 ±1 mm in diameter; most fragments are slightly elongate rectangular polygons to chips with sharply curved
    edges and angular corners. The other 5 percent is semiopaque crenulate mottles 1 to 3 mm in diameter, possibly
    breccia fragments.
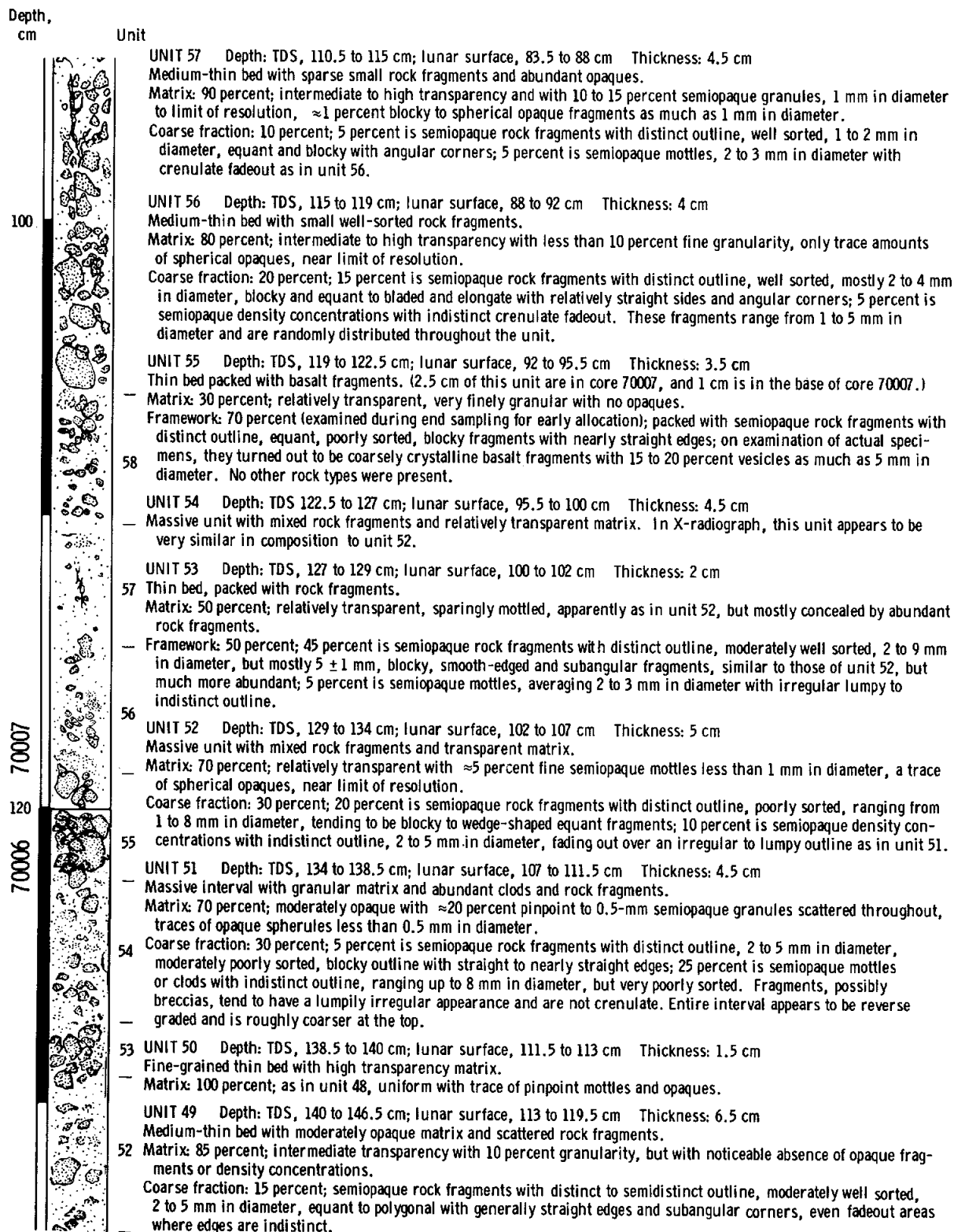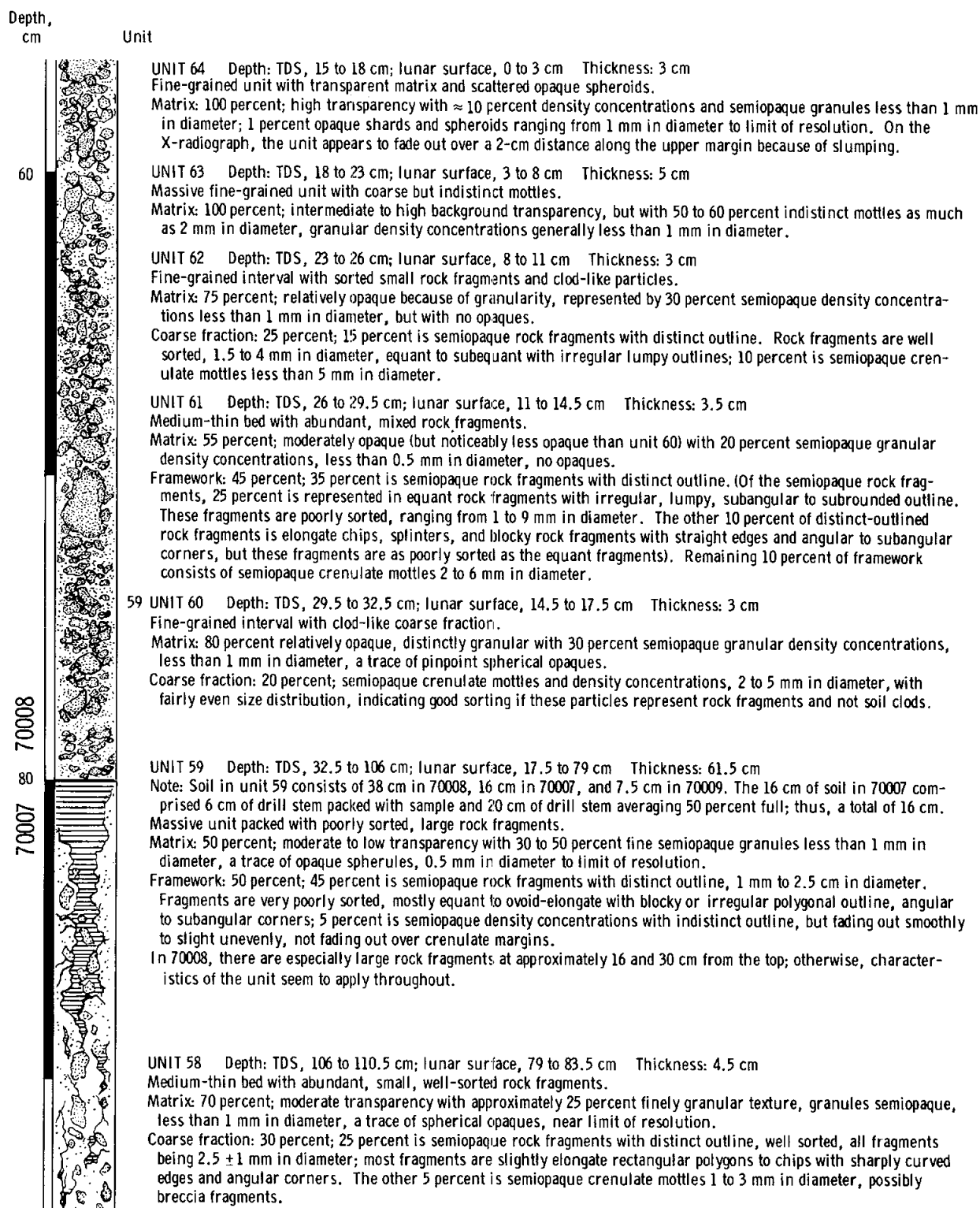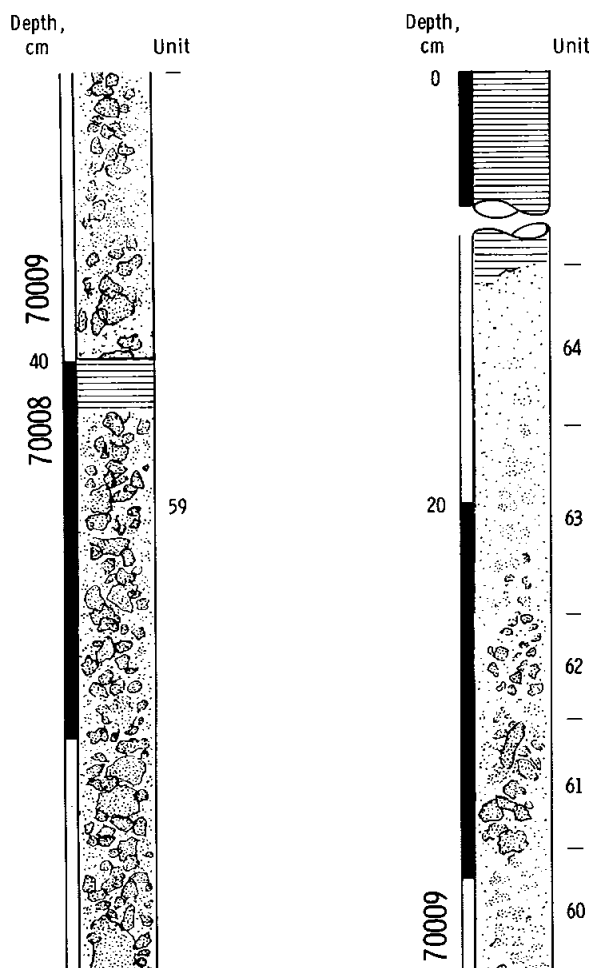
FIGURE 7-27.—Continued.

FIGURE 7-27.—Concluded.

Drive Tube 70012 (L52)

This core was hand driven to a hard layer at 28 cm depth 0.5 m inside the plus-Y footpad of the LM. The site lies on regolith developed on basaltic subfloor, near the center of the valley, approximately 750 m equidistant between the large (300 to 400 m) craters Camelot and Sherlock. The sample was collected in a relatively flat area with common, but subdued, 10- to 30-cm-diameter craters (ref. 7-42). Most of the surface appeared fine grained with particles near the limit of resolution of the surface photographs, but 1 to 2 percent of the surface was covered with particles as much as 3 or 4 cm in diameter. Similar material is in the core. Although this core was not disturbed by footprints (AS17-147-22517), the top 1 or 2 cm were probably depleted in fine soil by the LM descent propulsion engine. When the buddy secondary life-

Explanation

▓ Rudolph ejecta

■ Surficial fines (includes mapping unit termed "dark mantle")

▒ Camelot ejecta

▨ Ejecta from craters north of diagram

☰ San Luis Rey ejecta

▤ Poppy ejecta

☐ Anorthositic fines of middle interval

▨ Mixed basalt and breccia fragmental layers and fine layers of lower drill-stem interval

▨ Fractured and glassy subfloor

▨ Subfloor basalt flows
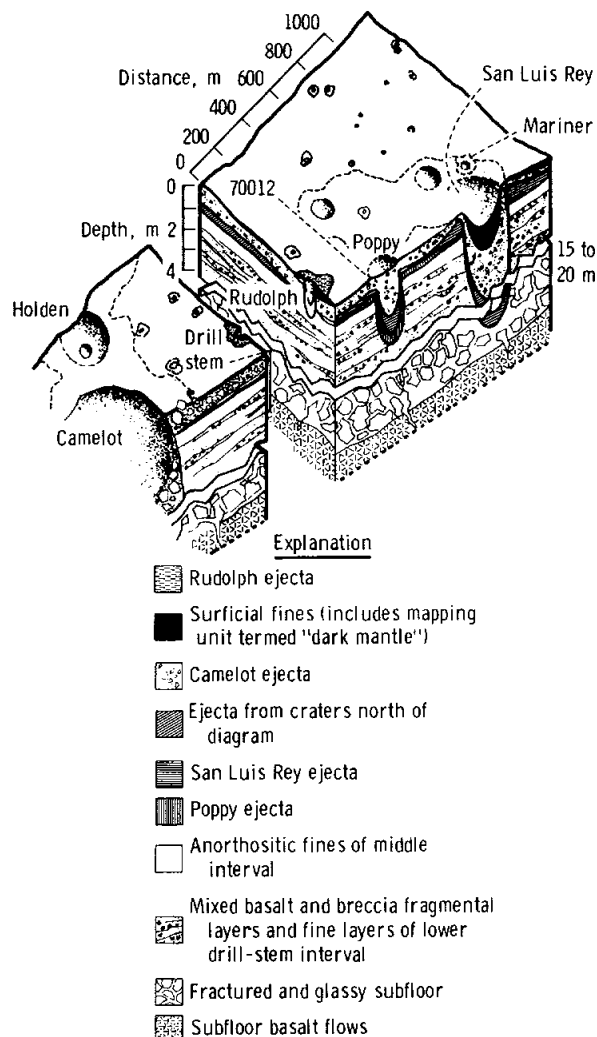
FIGURE 7-28.—Block diagram depicting the reconstruction of regolith history in the vicinity of deep drill string (LM area). The front face is a radial section through Camelot Crater, the drill-stem site, and the LM site; the other faces parallel the standard lunar surface grid. (Vertical exaggeration is 200×.)

support system (BSLSS) bag was opened in the Lunar Receiving Laboratory, the bottom cap of the core was off and lying nearby, and soil was spilling from the bottom. Forty-seven grams of slumped material were excavated from the base of the core to provide a fresh vertical face, which was then supported by a plug of aluminum foil. The upper follower was in place, and the X-radiograph indicated no serious cracking or slumping in the remainder of the core (fig. 7-29).

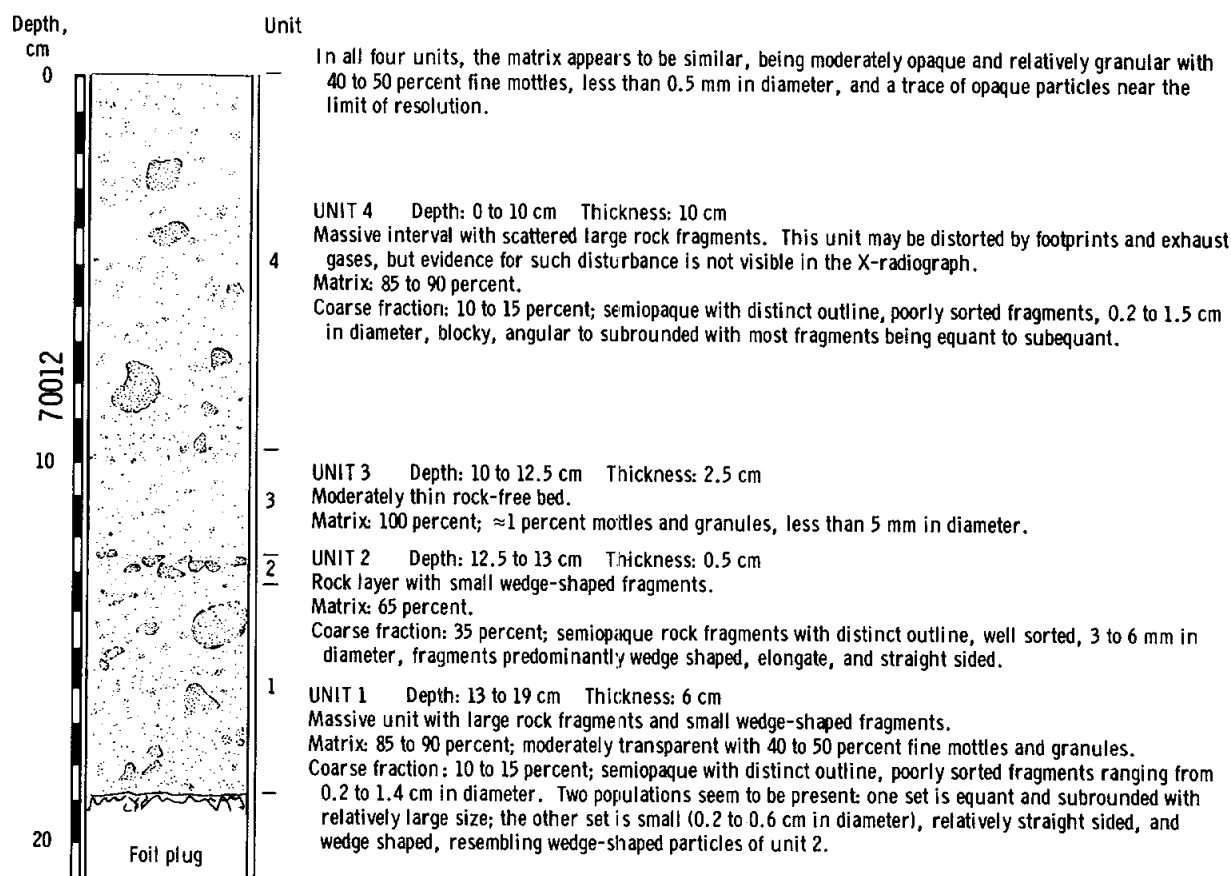The excavated material was mostly fines, with 5 to

Depth,
cm

Unit

In all four units, the matrix appears to be similar, being moderately opaque and relatively granular with 40 to 50 percent fine mottles, less than 0.5 mm in diameter, and a trace of opaque particles near the limit of resolution.

UNIT 4   Depth: 0 to 10 cm   Thickness: 10 cm
Massive interval with scattered large rock fragments. This unit may be distorted by footprints and exhaust gases, but evidence for such disturbance is not visible in the X-radiograph.
Matrix: 85 to 90 percent.
Coarse fraction: 10 to 15 percent; semiopaque with distinct outline, poorly sorted fragments, 0.2 to 1.5 cm in diameter, blocky, angular to subrounded with most fragments being equant to subequant.

UNIT 3   Depth: 10 to 12.5 cm   Thickness: 2.5 cm
Moderately thin rock-free bed.
Matrix: 100 percent; ≈1 percent mottles and granules, less than 5 mm in diameter.

UNIT 2   Depth: 12.5 to 13 cm   Thickness: 0.5 cm
Rock layer with small wedge-shaped fragments.
Matrix: 65 percent.
Coarse fraction: 35 percent; semiopaque rock fragments with distinct outline, well sorted, 3 to 6 mm in diameter, fragments predominantly wedge shaped, elongate, and straight sided.

UNIT 1   Depth: 13 to 19 cm   Thickness: 6 cm
Massive unit with large rock fragments and small wedge-shaped fragments.
Matrix: 85 to 90 percent; moderately transparent with 40 to 50 percent fine mottles and granules.
Coarse fraction: 10 to 15 percent; semiopaque with distinct outline, poorly sorted fragments ranging from 0.2 to 1.4 cm in diameter. Two populations seem to be present: one set is equant and subrounded with relatively large size; the other set is small (0.2 to 0.6 cm in diameter), relatively straight sided, and wedge shaped, resembling wedge-shaped particles of unit 2.

70012

Foil plug
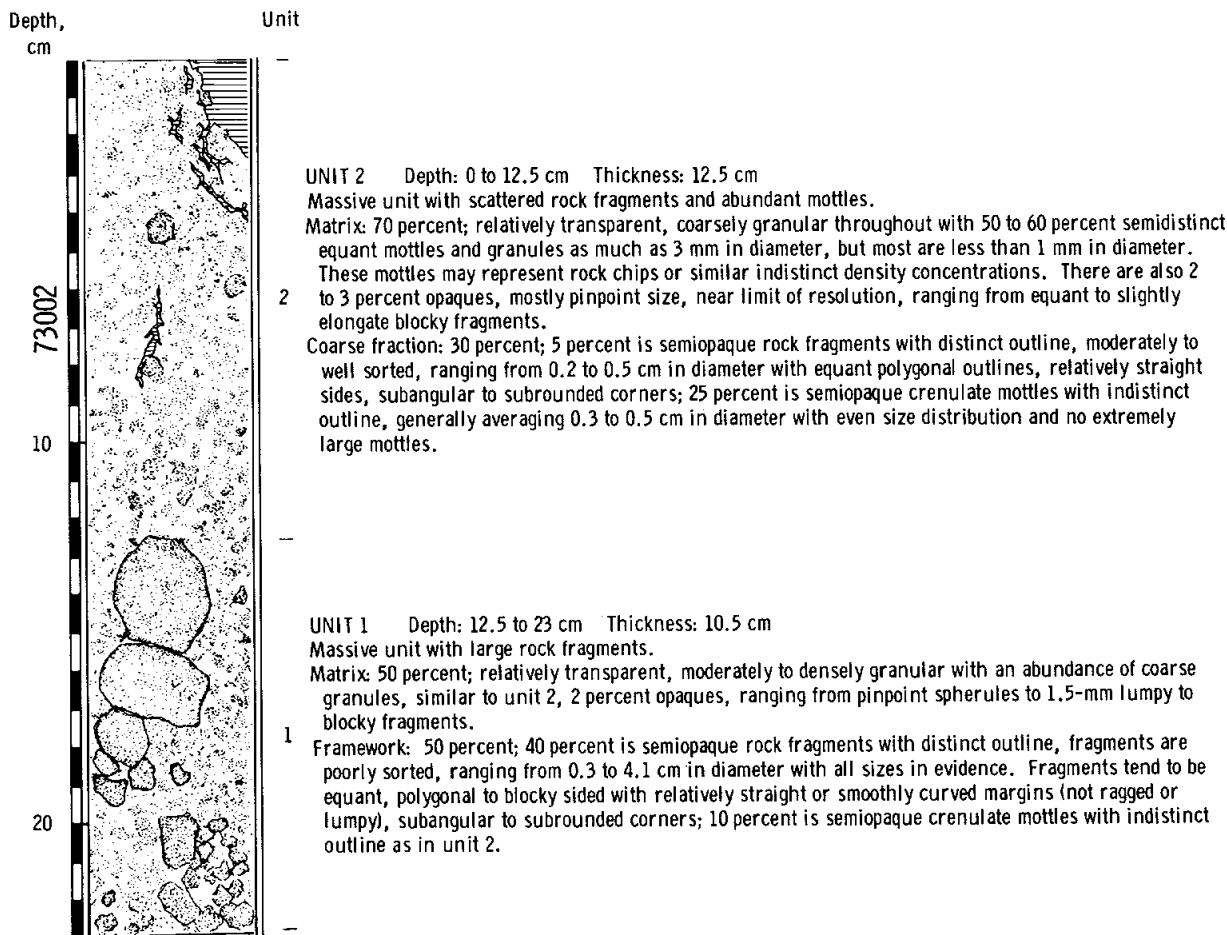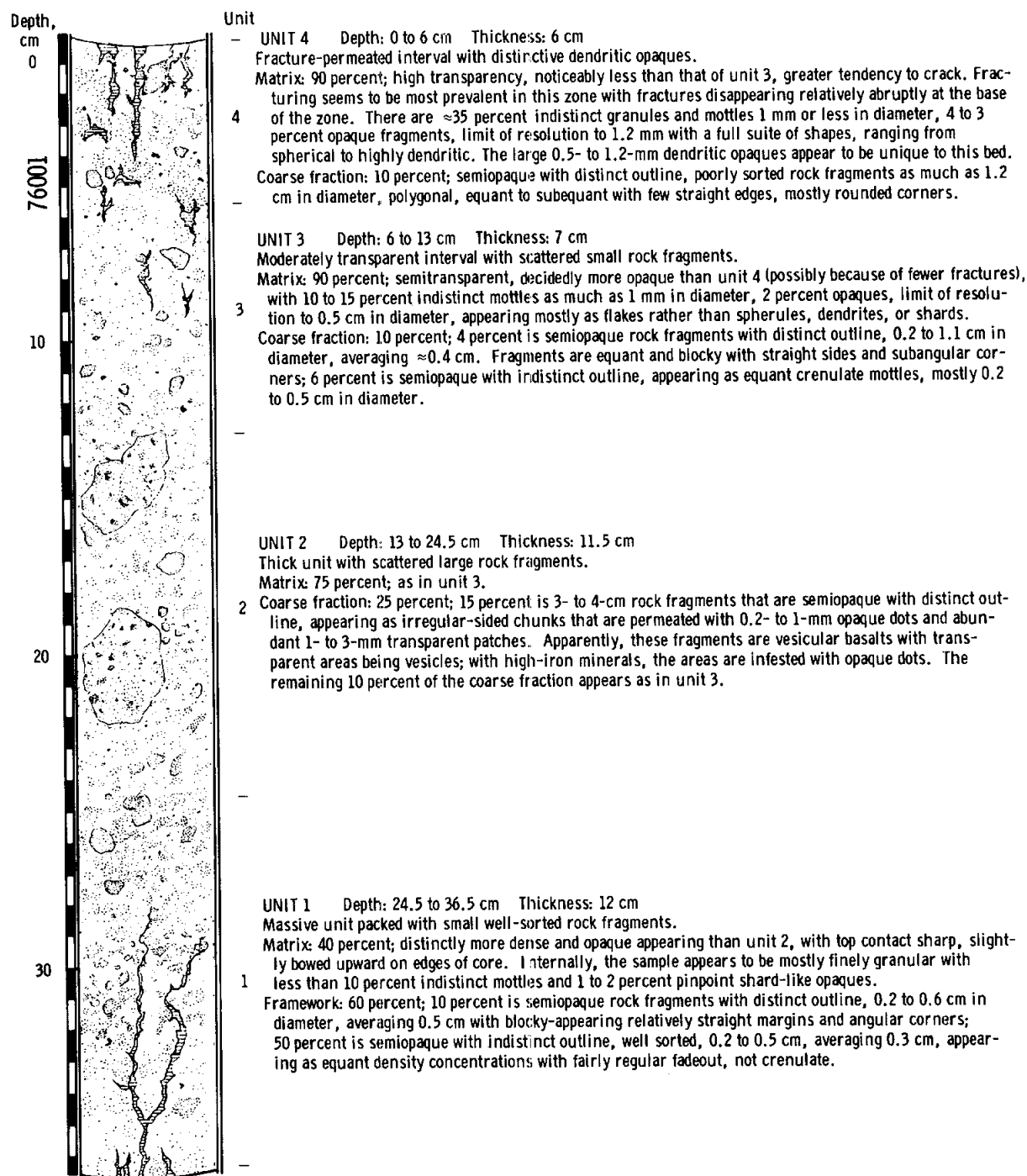
FIGURE 7-29.—Interpretation of X-radiograph of 70012 drive tube. The X-radiograph symbols are the same as in figure 7-27.

10 percent being fragments of medium- to coarse-grained vesicular basalt as much as 11 mm in diameter. Although this sample is petrographically similar to the upper beds of 70008, it is finer grained. None of the breccia fragments or coarse-grained framework-textured soil of the deep drill string appear in this core; however, the hard layer, which prevented further penetration, could be the coarse-grained deposit. If so, there is a deeper layer of fines on top of the coarse ejecta at this location. Nevertheless, the basaltic coarse fraction of 70012 parallels that of 70008, indicating a subfloor source for the upper soil layers.

Drive Tubes 73002 and 73001 (U31 and L45)

A double drive tube was taken at station 3 to collect an undisturbed sample of the regolith developed on the light mantle. Although the lower drive tube was sealed in the core sample vacuum container, the 23-cm-long upper drive tube should provide significant data.

The sampling site lies near the base of a major scarp that crosses the Taurus-Littrow valley. This site is approximately 50 m east of the 700-m Lara Crater and is surrounded by small, local craters. The largest of these craters, a moderately fresh 10-m-diameter pit, lies approximately 18 m northwest of the coring site, and several other craters over 5 m in diameter lie within 20 m. Small (as much as 1 m in diameter) craters are abundant, and the soil surface is fairly rough, with approximately 20-percent cover by 1- to 2-cm fragments (AS17-137-20981). A trench 20 cm deep near the 10-m-diameter crater revealed a medium-gray 0.5-cm surface layer over a light-gray 3-cm layer, which in turn overlies a medium-gray marbled or mottled zone that seems to be representative of subsurface soils in the light mantle.

Much of 73002 is permeated by cracks (fig. 7-30), possibly caused by the wedging of large fragments into the drive tube or the spillage of 4 cm of soil onto the lunar surface. Whether or not these cracks have disrupted the stratigraphy is uncertain; at least two major stratigraphic intervals seem to be present on the X-radiograph, but there is no indication of the soil profile seen in the nearby trench. The material is coarse grained and massive with distinct rock fragments (probably subfloor basalt), reflecting expected surface conditions near local craters and within the Lara Crater ejecta blanket.

Drive Tube 76001 (L48)

This single drive tube from station 6 is the only certain stratigraphic sample of massif regolith and is the only core that can be oriented with certainty. It was driven into firm soil on an 11° slope to the south. The surface shows a 20-percent cover of moderately well sorted and rounded fragments as much as 4 cm in diameter (ref. 7-25) on fine-grained soils that are cohesive enough to retain the hole after the drive tube was extracted (AS17-146-22295). Subdued craters as much as 30 cm across are rare; one such crater, located approximately 1 m north of the sampling site, has abundant 3- to 4-cm blocks on the rim.

Core 76001 is subdivided into four units on the basis of matrix content and the size and type of included rock fragments (fig. 7-31). Most rock fragments are indistinct, only slightly more opaque than the matrix, and probably represent anorthosites or breccias of massif origin; however, two large fragments in unit 2 are noticeably different. These

Depth, cm   Unit

73002

10

20

UNIT 2   Depth: 0 to 12.5 cm   Thickness: 12.5 cm
Massive unit with scattered rock fragments and abundant mottles.
Matrix: 70 percent; relatively transparent, coarsely granular throughout with 50 to 60 percent semidistinct equant mottles and granules as much as 3 mm in diameter, but most are less than 1 mm in diameter. These mottles may represent rock chips or similar indistinct density concentrations. There are also 2 to 3 percent opaques, mostly pinpoint size, near limit of resolution, ranging from equant to slightly elongate blocky fragments.
Coarse fraction: 30 percent; 5 percent is semiopaque rock fragments with distinct outline, moderately to well sorted, ranging from 0.2 to 0.5 cm in diameter with equant polygonal outlines, relatively straight sides, subangular to subrounded corners; 25 percent is semiopaque crenulate mottles with indistinct outline, generally averaging 0.3 to 0.5 cm in diameter with even size distribution and no extremely large mottles.

2

UNIT 1   Depth: 12.5 to 23 cm   Thickness: 10.5 cm
Massive unit with large rock fragments.
Matrix: 50 percent; relatively transparent, moderately to densely granular with an abundance of coarse granules, similar to unit 2, 2 percent opaques, ranging from pinpoint spherules to 1.5-mm lumpy to blocky fragments.
Framework: 50 percent; 40 percent is semiopaque rock fragments with distinct outline, fragments are poorly sorted, ranging from 0.3 to 4.1 cm in diameter with all sizes in evidence. Fragments tend to be equant, polygonal to blocky sided with relatively straight or smoothly curved margins (not ragged or lumpy), subangular to subrounded corners; 10 percent is semiopaque crenulate mottles with indistinct outline as in unit 2.

1
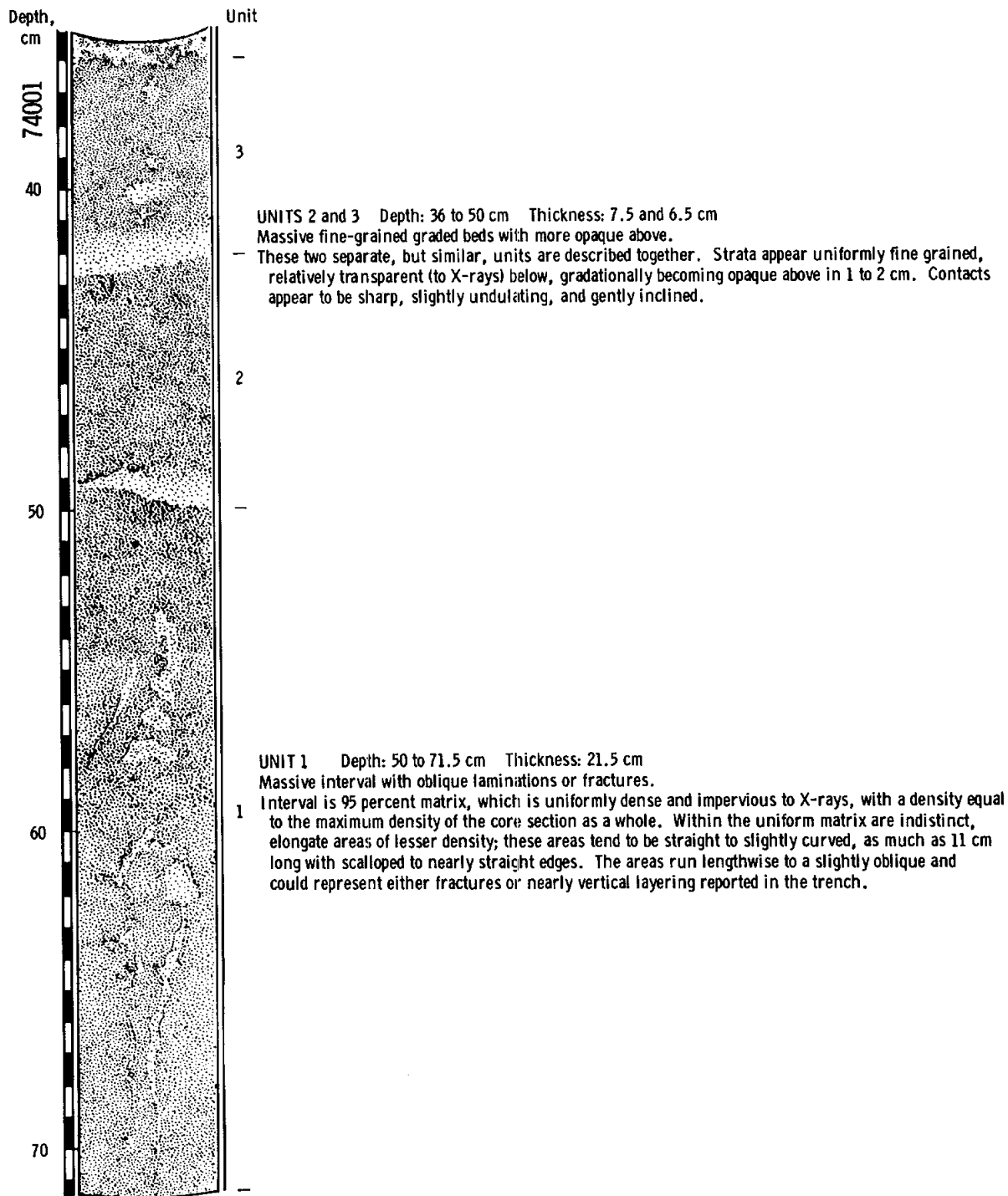
FIGURE 7-30.—Interpretation of X-radiograph of 73002 drive tube. The X-radiograph symbols are the same as in figure 7-27.

Depth, cm

Unit

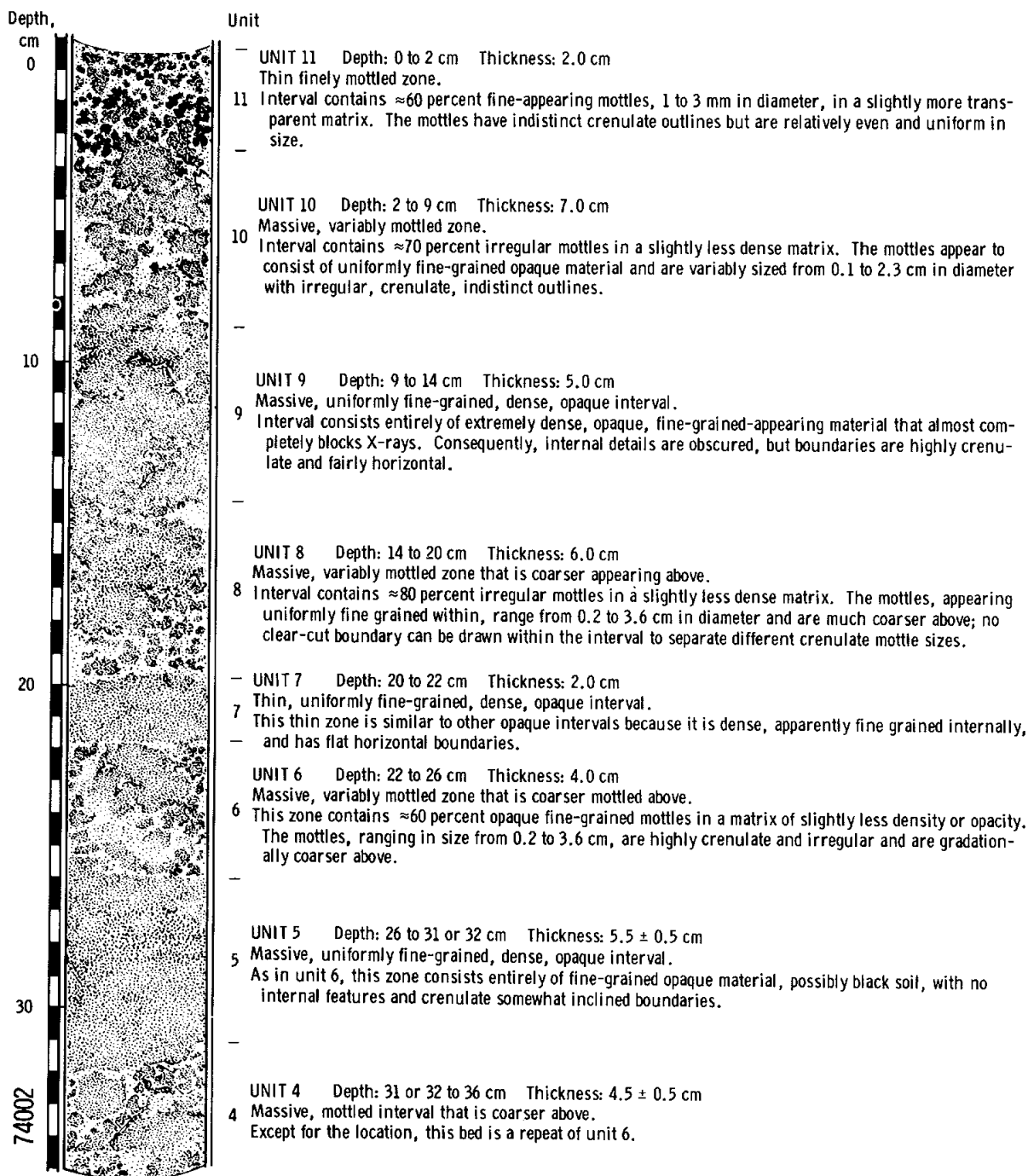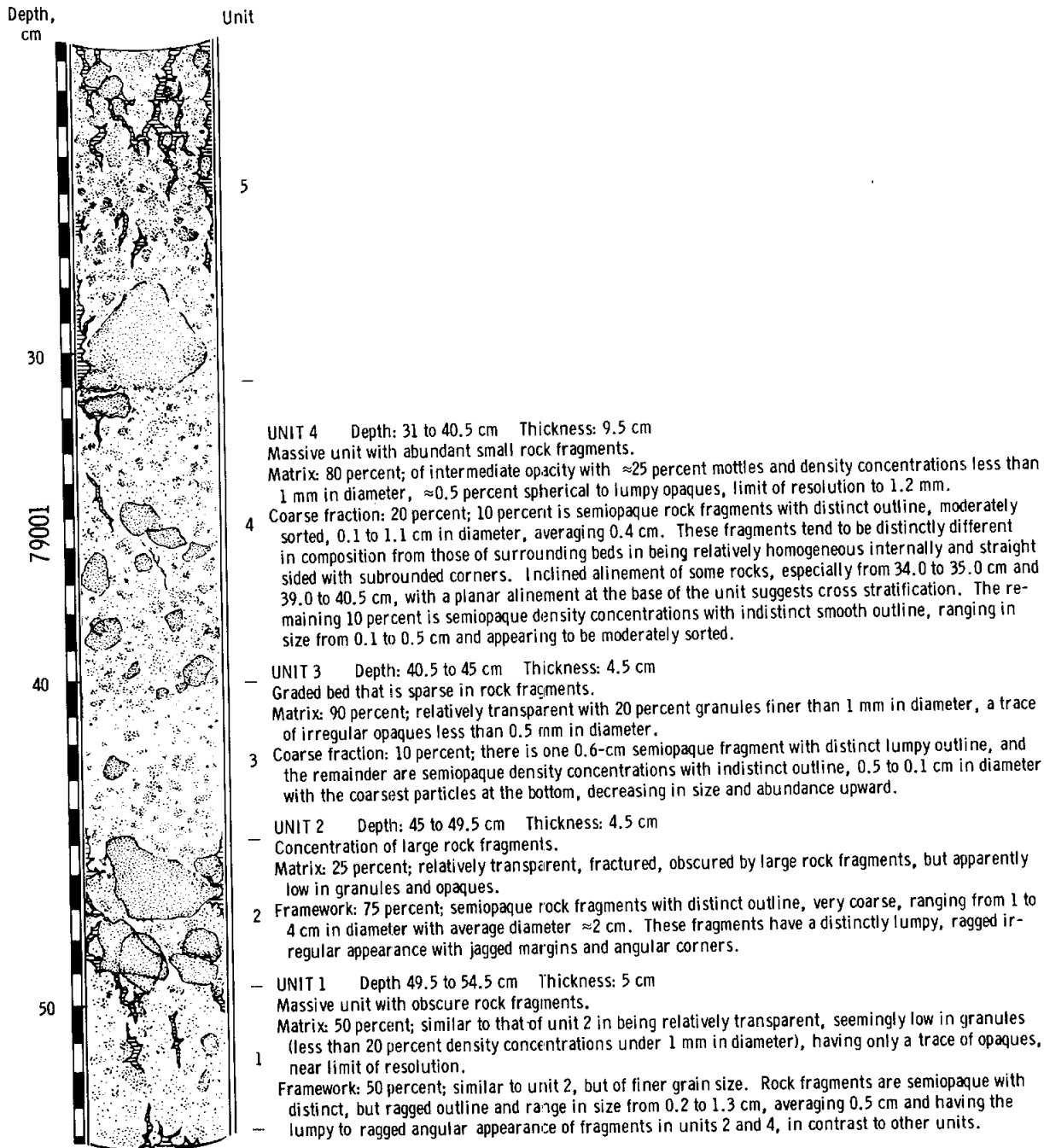UNIT 4   Depth: 0 to 6 cm   Thickness: 6 cm
Fracture-permeated interval with distinctive dendritic opaques.
Matrix: 90 percent; high transparency, noticeably less than that of unit 3, greater tendency to crack. Fracturing seems to be most prevalent in this zone with fractures disappearing relatively abruptly at the base of the zone. There are ≈35 percent indistinct granules and mottles 1 mm or less in diameter, 4 to 3 percent opaque fragments, limit of resolution to 1.2 mm with a full suite of shapes, ranging from spherical to highly dendritic. The large 0.5- to 1.2-mm dendritic opaques appear to be unique to this bed.
Coarse fraction: 10 percent; semiopaque with distinct outline, poorly sorted rock fragments as much as 1.2 cm in diameter, polygonal, equant to subequant with few straight edges, mostly rounded corners.

UNIT 3   Depth: 6 to 13 cm   Thickness: 7 cm
Moderately transparent interval with scattered small rock fragments.
Matrix: 90 percent; semitransparent, decidedly more opaque than unit 4 (possibly because of fewer fractures), with 10 to 15 percent indistinct mottles as much as 1 mm in diameter, 2 percent opaques, limit of resolution to 0.5 cm in diameter, appearing mostly as flakes rather than spherules, dendrites, or shards.
Coarse fraction: 10 percent; 4 percent is semiopaque rock fragments with distinct outline, 0.2 to 1.1 cm in diameter, averaging ≈0.4 cm. Fragments are equant and blocky with straight sides and subangular corners; 6 percent is semiopaque with indistinct outline, appearing as equant crenulate mottles, mostly 0.2 to 0.5 cm in diameter.

UNIT 2   Depth: 13 to 24.5 cm   Thickness: 11.5 cm
Thick unit with scattered large rock fragments.
Matrix: 75 percent; as in unit 3.
Coarse fraction: 25 percent; 15 percent is 3- to 4-cm rock fragments that are semiopaque with distinct outline, appearing as irregular-sided chunks that are permeated with 0.2- to 1-mm opaque dots and abundant 1- to 3-mm transparent patches. Apparently, these fragments are vesicular basalts with transparent areas being vesicles; with high-iron minerals, the areas are infested with opaque dots. The remaining 10 percent of the coarse fraction appears as in unit 3.

UNIT 1   Depth: 24.5 to 36.5 cm   Thickness: 12 cm
Massive unit packed with small well-sorted rock fragments.
Matrix: 40 percent; distinctly more dense and opaque appearing than unit 2, with top contact sharp, slightly bowed upward on edges of core. Internally, the sample appears to be mostly finely granular with less than 10 percent indistinct mottles and 1 to 2 percent pinpoint shard-like opaques.
Framework: 60 percent; 10 percent is semiopaque rock fragments with distinct outline, 0.2 to 0.6 cm in diameter, averaging 0.5 cm with blocky-appearing relatively straight margins and angular corners; 50 percent is semiopaque with indistinct outline, well sorted, 0.2 to 0.5 cm, averaging 0.3 cm, appearing as equant density concentrations with fairly regular fadeout, not crenulate.

FIGURE 7-31.—Interpretation of X-radiograph of 76001 drive tube. The X-radiograph symbols are the same as in figure 7-27.

fragments are distinct in outline, are relatively opaque, contain abundant minute opaque particles less than 1 mm in diameter, and have 5- to 10-percent transparent circular areas as much as 2 mm in diameter; these features are typical of vesicular subfloor basalts.

Except for the large vesicular rock fragments, this core is fairly fine grained and moderately well sorted. The relatively small surface craters at station 6 have contributed little to the massive, indistinctly stratified upper 25 cm of the core. Rock types in the core, plus field evidence, indicate subfloor as well as massif contributions to this site, with massif source predominating. Possibly, the large, vesicular, presumably basaltic rock fragments in unit 2 were associated with a major cratering event large enough to propel basalt fragments from the valley to this point on the massif.

The X-radiograph of this massif-derived soil is similar to those of the Apollo 16 drive tubes, probably because the anorthositic terrain of the massifs and the Descartes highlands produce similar soil-forming components. Both soils are (1) relatively transparent to X-rays, with a very sparsely granular matrix, (2) relatively low in distinct rock fragments, possibly because of the abundance of semitransparent anorthosites, and (3) extremely high in tiny opaque fragments of diverse shapes ranging from dendritic to spheroidal.

Drive Tubes 74002 and 74001 (U35 and L44)

The double drive tube that sampled the contact between the orange and black soil on the southern rim of Shorty Crater was completely filled with unusually dense soil (74001 was 2.35 g/cm^3 and 74002 was 2.00 g/cm^3) and was nearly impervious to X-rays. Consequently, rather mediocre X-radiographs were obtained even after near-maximum-intensity radiation. The clod-like layering encountered is shown in figure 7-32.

It is hoped that these cores will preserve the spatial distribution of soils in the adjacent trench, where a surficial 0.5 cm of gray soil overlies an interval of orange soil, which, in turn, overlies black ilmenite-bearing glass droplets seen in the top and bottom ends of the lower tube (ref. 7-26).

Stratification in the upper tube consists of alternating layers of massive soil, impenetrable to X-rays, and very distinctly mottled soil that appears as poorly defined clods 0.3 to 3.5 cm in diameter. Presumably, the cloddy intervals contain orange soil, and the

obscured intervals contain black soil. Cloddy intervals occur in 74002 from 0 to 8, 14 to 20, 22 to 25.5, and 32 to 37 cm, including the upper 2 cm of 74001. The next 14 cm contain massive, nearly opaque (to X-rays) beds with slightly lower opacity at the base. The lowest 22 cm are massive, with subparallel lengthwise lineations of lower opacity, which may be fractures or steeply inclined bedding as observed in the trench.

Approximately 2 g of material were excavated from the bottom of 74001 and examined under the binocular microscope. The material is unusually cohesive and consists of very dark to black opaque spheres and conchoidally fractured fragments.

Drive Tubes 79002 and 79001 (U37 and L50)

A double core was taken at station 9, which is approximately 70 m southeast and downslope from the rim of Van Serg Crater. Two fresh, sharp 1-m craters lie within 10 m of the coring site, and a subdued 60-m crater occupies the area 15 m west of the sampling area. Although lunar surface photographs indicate massive boulders on or near the rim of Van Serg Crater, the largest surficial fragments in the core area range from 20 to 2 cm (ref. 7-27), are poorly sorted, angular, and unfilleted, and cover less than 3 percent of the surface. A 12-cm trench approximately 1 m southwest of the coring site has medium-gray soil in the upper 7 cm but has light-gray to whitish soil in the lower part. The upper portion might represent "dark mantle" over the ejecta blanket from Van Serg Crater. However, this color change is not reflected in the X-radiograph of the drive tube, possibly because the core is permeated by fractures, which are undoubtedly a result of rocks being jammed into the coring device during sampling (fig. 7-33).

DISCUSSION AND CONCLUSIONS

The unit that partly filled and leveled the Taurus-Littrow valley is mare basalt similar to that returned from Mare Tranquillitatis. Early studies of the ages of both the basalts and the orange glass (ref. 7-5) indicate that they are similar but slightly older than the Mare Tranquillitatis samples. Whether these samples represent one or several flows is not clear (chemical data suggest at least two); but it is evident that widespread volcanism involving very-titanium-rich melts occurred over much of the eastern limb of

Depth, cm

Unit

74001

40

50

60

70

3

2

1

UNITS 2 and 3   Depth: 36 to 50 cm   Thickness: 7.5 and 6.5 cm
Massive fine-grained graded beds with more opaque above.
These two separate, but similar, units are described together. Strata appear uniformly fine grained, relatively transparent (to X-rays) below, gradationally becoming opaque above in 1 to 2 cm. Contacts appear to be sharp, slightly undulating, and gently inclined.

UNIT 1   Depth: 50 to 71.5 cm   Thickness: 21.5 cm
Massive interval with oblique laminations or fractures.
Interval is 95 percent matrix, which is uniformly dense and impervious to X-rays, with a density equal to the maximum density of the core section as a whole. Within the uniform matrix are indistinct, elongate areas of lesser density; these areas tend to be straight to slightly curved, as much as 11 cm long with scalloped to nearly straight edges. The areas run lengthwise to a slightly oblique and could represent either fractures or nearly vertical layering reported in the trench.

FIGURE 7-32.—Interpretation of X-radiographs of 74002 and 74001 drive tubes. The X-radiograph symbols are the same as in figure 7-27.

Depth, cm   Unit

UNIT 11   Depth: 0 to 2 cm   Thickness: 2.0 cm
Thin finely mottled zone.
11 Interval contains ≈60 percent fine-appearing mottles, 1 to 3 mm in diameter, in a slightly more transparent matrix. The mottles have indistinct crenulate outlines but are relatively even and uniform in size.

UNIT 10   Depth: 2 to 9 cm   Thickness: 7.0 cm
Massive, variably mottled zone.
10 Interval contains ≈70 percent irregular mottles in a slightly less dense matrix. The mottles appear to consist of uniformly fine-grained opaque material and are variably sized from 0.1 to 2.3 cm in diameter with irregular, crenulate, indistinct outlines.

UNIT 9   Depth: 9 to 14 cm   Thickness: 5.0 cm
Massive, uniformly fine-grained, dense, opaque interval.
9 Interval consists entirely of extremely dense, opaque, fine-grained-appearing material that almost completely blocks X-rays. Consequently, internal details are obscured, but boundaries are highly crenulate and fairly horizontal.

UNIT 8   Depth: 14 to 20 cm   Thickness: 6.0 cm
Massive, variably mottled zone that is coarser appearing above.
8 Interval contains ≈80 percent irregular mottles in a slightly less dense matrix. The mottles, appearing uniformly fine grained within, range from 0.2 to 3.6 cm in diameter and are much coarser above; no clear-cut boundary can be drawn within the interval to separate different crenulate mottle sizes.

UNIT 7   Depth: 20 to 22 cm   Thickness: 2.0 cm
Thin, uniformly fine-grained, dense, opaque interval.
7 This thin zone is similar to other opaque intervals because it is dense, apparently fine grained internally, and has flat horizontal boundaries.

UNIT 6   Depth: 22 to 26 cm   Thickness: 4.0 cm
Massive, variably mottled zone that is coarser mottled above.
6 This zone contains ≈60 percent opaque fine-grained mottles in a matrix of slightly less density or opacity. The mottles, ranging in size from 0.2 to 3.6 cm, are highly crenulate and irregular and are gradationally coarser above.

UNIT 5   Depth: 26 to 31 or 32 cm   Thickness: 5.5 ± 0.5 cm
5 Massive, uniformly fine-grained, dense, opaque interval.
As in unit 6, this zone consists entirely of fine-grained opaque material, possibly black soil, with no internal features and crenulate somewhat inclined boundaries.

UNIT 4   Depth: 31 or 32 to 36 cm   Thickness: 4.5 ± 0.5 cm
4 Massive, mottled interval that is coarser above.
Except for the location, this bed is a repeat of unit 6.

FIGURE 7-32.—Concluded.

the Moon approximately 3.7 X 10⁹ yr ago. Thus, the known timespan of mare volcanism, approximately 600 million years, remains essentially the same as before the Apollo 17 mission.

Breccias in various stages of crystallization appear to have been derived from several stratigraphic units present in the massifs. To date, the one reported breccia age from Apollo 17 of approximately 4.0 X

Depth,
cm

Unit

5

30

79001

40

50

UNIT 4   Depth: 31 to 40.5 cm   Thickness: 9.5 cm
Massive unit with abundant small rock fragments.
Matrix: 80 percent; of intermediate opacity with ≈25 percent mottles and density concentrations less than
1 mm in diameter, ≈0.5 percent spherical to lumpy opaques, limit of resolution to 1.2 mm.
Coarse fraction: 20 percent; 10 percent is semiopaque rock fragments with distinct outline, moderately
sorted, 0.1 to 1.1 cm in diameter, averaging 0.4 cm. These fragments tend to be distinctly different
in composition from those of surrounding beds in being relatively homogeneous internally and straight
sided with subrounded corners. Inclined alinement of some rocks, especially from 34.0 to 35.0 cm and
39.0 to 40.5 cm, with a planar alinement at the base of the unit suggests cross stratification. The re-
maining 10 percent is semiopaque density concentrations with indistinct smooth outline, ranging in
size from 0.1 to 0.5 cm and appearing to be moderately sorted.

UNIT 3   Depth: 40.5 to 45 cm   Thickness: 4.5 cm
Graded bed that is sparse in rock fragments.
Matrix: 90 percent; relatively transparent with 20 percent granules finer than 1 mm in diameter, a trace
of irregular opaques less than 0.5 mm in diameter.
Coarse fraction: 10 percent; there is one 0.6-cm semiopaque fragment with distinct lumpy outline, and
the remainder are semiopaque density concentrations with indistinct outline, 0.5 to 0.1 cm in diameter
with the coarsest particles at the bottom, decreasing in size and abundance upward.

UNIT 2   Depth: 45 to 49.5 cm   Thickness: 4.5 cm
Concentration of large rock fragments.
Matrix: 25 percent; relatively transparent, fractured, obscured by large rock fragments, but apparently
low in granules and opaques.
Framework: 75 percent; semiopaque rock fragments with distinct outline, very coarse, ranging from 1 to
4 cm in diameter with average diameter ≈2 cm. These fragments have a distinctly lumpy, ragged ir-
regular appearance with jagged margins and angular corners.

UNIT 1   Depth 49.5 to 54.5 cm   Thickness: 5 cm
Massive unit with obscure rock fragments.
Matrix: 50 percent; similar to that of unit 2 in being relatively transparent, seemingly low in granules
(less than 20 percent density concentrations under 1 mm in diameter), having only a trace of opaques,
near limit of resolution.
Framework: 50 percent; similar to unit 2, but of finer grain size. Rock fragments are semiopaque with
distinct, but ragged outline and range in size from 0.2 to 1.3 cm, averaging 0.5 cm and having the
lumpy to ragged angular appearance of fragments in units 2 and 4, in contrast to other units.

FIGURE 7-33.—Interpretation of X-radiographs of 79002 and 79001 drive tubes. The X-radiograph
symbols are the same as in figure 7-27.

10^9 yr (ref. 7-28) does not extend the rather restricted limits mentioned previously. Breccias range from those containing a high percentage of mineral and lithic debris with a small amount of interstitial glass to those containing a small percentage of mineral and lithic debris in well-crystallized poikilitic textures. Problems still exist as to the extent of partial melting and the origin of the oikocrysts in the

Depth, cm

Unit

79002

6 UNIT 6   Depth: 0 to 3.5 cm   Thickness: 3.5 cm
Extensively fractured relatively fine-grained interval.
Matrix: 80 percent; at least 50 percent is permeated by fractures, relatively transparent with 30 percent
1-mm density concentrations and fine mottles, ≈1 percent spherical to ovoid opaques, less than 1 mm
in diameter.
Coarse fraction: 20 percent; 5 percent is semiopaque rock fragments with distinct outline. These fragments
range from 0.2 to 0.7 cm in diameter, are moderately well sorted, rectangular to equant, blocky outlined,
and relatively straight sided with subangular to angular corners; 15 percent is semiopaque density con-
centrations and indistinct but relatively smooth-edged mottles, 0.2 to 0.9 cm in diameter, but mostly
less than 0.5 cm and subequant.

UNIT 5   Depth: 3.5 to 31 cm   Thickness: 27.5 cm
Massive unit with very large rock fragments.
Matrix: 79 percent; somewhat fractured, of intermediate transparency with 30 to 40 percent granularity,
granules less than 1 mm in diameter, a trace of spherical to ovoid opaques, limit of resolution to 1.3 mm
in diameter.
5 Coarse fraction: 30 percent; 15 percent is semiopaque rock fragments with distinct outline, 0.1 to 3.5 cm
in diameter, poorly sorted with all sizes being present. Most fragments tend to be equant to slightly
elongate, relatively straight sided; 15 percent has a ragged indistinct outline with subangular to well-
rounded corners and a distinctive ragged appearance.

FIGURE 7-33.—Concluded.

latter breccias (refs. 7-29, 7-30, and 7-31). Detailed studies of the boulders that contain vesicles and vugs several centiments across, inclusions of one breccia in another, contact relationships between two breccia units, and the black dike that displays evidence of a chilled margin may help to answer these problems. The variety of breccia textures resulted from different extends of melting and different rates of heating and cooling associated with large masses of ejecta from major cratering events.

The similarity of both major and trace component concentrations of the brown-glass matrix breccias from the Apennine Front, the recrystallized breccias from Apollo 16, and the various crystalline breccias from Apollo 17 suggests that a genetic relationship may exist between these widespread breccias and KREEP-like chemistry. The occurrence in these breccias of clasts of plagioclase, olivine, and pyroxene similar to those of coarse-grained anorthositic and gabbroic rocks suggests that the latter formed the

source of the breccias and provides the interesting possibility that partial melting similar to that postulated for the production of KREEP-like melts (refs. 7-17 and 7-32) may be associated with large impacting events that can produce large volumes of melt (ref. 7-33). Grieve and Plant (ref. 7-34) have reported an example of a breccia having gabbroic composition and containing interstitial melt and glass veins of KREEP-like composition.

As was the case in past missions, the anorthositic rocks are generally crushed and recrystallized, thus obscuring the original textures. However, two coarse-grained norites and at least one gabbroic rock with some areas of original texture should offer some insight into the chemistry and perhaps ages of the early crustal rocks.

The occurrence of a large dunite clast in a boulder at station 2 suggests that the source material of the breccias must include coarse-grained segregations of magnesian olivine, thus providing further evidence for

an early crust composed of a coarse-grained igneous complex of anorthositic, gabbroic, and ultramafic rocks.

The "dark mantle" consists largely of the products produced by micrometeorite erosion of basalts, 5 to 20 percent of the orange and black glass found at station 4, and some lithic fragments derived from the massifs. The rather pure orange and black soils at station 4 suggest that there may be layers of these materials in the upper few tens of meters below the surface. If such layers are widespread throughout the valley, cratering events would be expected to excavate this material along with the basalts, producing the 5 to 20 percent of orange and black glasses found in the "dark mantle" soils. Anomalously high values of Zn and Cl for lunar soils and the relatively high Sr and Rb contents indicate that the orange glass is not directly related to the mare basalt melts, unless by some undefined complex fractionation scheme.

Although the soils from the North Massif, the South Massif, and the light mantle are similar petrographically and appear in binary plots of major elements to be simple mixtures of basalts and anorthositic rocks, the trace elements indicate a more complex pattern. The South Massif and light mantle materials are considerably enriched in Zr and other trace elements relative to the North Massif or to any mixture of basalts and anorthositic rocks. Thus, a KREEP component must be utilized to explain mixing models for the soils and the metamorphosed and partially melted breccias.

ACKNOWLEDGMENTS

REFERENCES

7-1. Wasserburg, G. J.; and Papanastassiou, D. A.: Age of an Apollo 15 Mare Basalt: Lunar Crust and Mantle Evolution. Earth Planet. Sci. Letters, vol. 13, no. 1, Dec. 1971, pp. 97-104.

7-2. Papanastassiou, D. A.; and Wasserburg, G. J.: Rb-Sr Age of a Luna 16 Basalt and the Model Age of Lunar Soils. Earth Planet. Sci. Letters, vol. 13, no. 2, Jan. 1972, pp. 368-374.

7-3. Tera, F.; Papanastassiou, D. A.; and Wasserburg, G. J.: A Lunar Cataclysm at ~ 3.95 AE and the Structure of the Lunar Crust. Lunar Science IV (Abs. of papers presented at the Fourth Lunar Science Conference (Houston, Tex.), Mar. 5-8, 1973), pp. 723-725.

7-4. Papanastassiou, D. A.; and Wasserburg, G. J.: The Rb-Sr Age of a Crystalline Rock from Apollo 16. Earth Planet. Sci. Letters, vol. 16, no. 2, Oct. 1972, pp. 289-298.

7-5. Husain, L.; and Schaeffer, O. A.: ^{40}Ar-^{39}Ar Crystallization Ages and ^{38}Ar-^{37}Ar Cosmic Ray Exposure Ages of Samples from the Vicinity of the Apollo 16 Landing Site. Lunar Science IV (Abs. of papers presented at the Fourth Lunar Science Conference (Houston, Tex.), Mar. 5-8, 1973), pp. 406-408.

7-6. El-Baz, F.; Worden, A. M.; and Brand, V. D.: Astronaut Observations from Lunar Orbit and Their Geologic Significance. Proceedings of the Third Lunar Science Conference, vol. 1, MIT Press (Cambridge, Mass.), 1972, pp. 85-104.

7-7. El-Baz, F.: New Geological Findings in Apollo 15 Lunar Orbital Photography. Proceedings of the Third Lunar Science Conference, vol. 1, MIT Press (Cambridge, Mass.), 1972, pp. 39-61.

7-8. Wolfe, E. W.; Freeman, V. L.; Muehlberger, W. R.; Head, J. W.; Schmitt, H. H.; and Sevier, J. W.: Apollo 17 Exploration at Taurus-Littrow. Geotimes, vol. 17, no. 11, Nov. 1972, pp. 14-18.

7-9. The Lunar Sample Preliminary Examination Team: Preliminary Examination of Lunar Samples from Apollo 11. Science, vol. 165, no. 3899, Sept. 19, 1969, pp. 1211-1227.

7-10. Apollo 16 Preliminary Examination Team: The Apollo 16 Lunar Samples: Petrographic and Chemical Description. Science, vol. 179, no. 4068, Jan. 5, 1973, pp. 23-34.

7-11. Apollo 15 Preliminary Examination Team: The Apollo 15 Lunar Samples: A Preliminary Description. Science, vol. 175, no. 4020, Jan. 28, 1972, pp. 363-374.

7-12. McKay, D. S.; Heiken, G. H.; Taylor, R. M.; Clanton, U. S.; et al.: Apollo 14 Soils: Size Distribution and Particle Types. Proceedings of the Third Lunar Science

Conference, vol. 1, MIT Press (Cambridge, Mass.), 1972, pp. 983-994.

7-13. McKay, D. S.; Morrison, D. A.; Clanton, U. S.; Ladle, G. H.; and Lindsay, J. F.: Apollo 12 Soil and Breccia. Proceedings of the Second Lunar Science Conference, vol. 1, MIT Press (Cambridge, Mass.), 1971, pp. 755-774.

7-14. Warner, J. L.: Metamorphism of Apollo 14 Breccias. Proceedings of the Third Lunar Science Conference, vol. 1, MIT Press (Cambridge, Mass.), 1972, pp. 623-643.

7-15. Reid, A. M.; Warner, J. L.; Ridley, W. I.; and Brown, R. W.: Major Element Composition of Glasses in Three Apollo 15 Soils. Meteoritics, vol. 7, Sept. 30, 1972, pp. 395-415.

7-16. Reid, A. M.; Ridley, W. I.; Harmon, R. S.; Warner, J. L.; et al.: Highly Aluminous Glasses in Lunar Soils and the Nature of the Lunar Highlands. Geochim. Cosmochim. Acta, vol. 36, no. 8, Aug. 1972, pp. 903-912.

7-17. Hubbard, N. J.; Gast, P. W.; Rhodes, J. M.; Bansal, B. M.; et al.: Nonmare Basalts: Part II. Proceedings of the Third Lunar Science Conference, vol. 2, MIT Press (Cambridge, Mass.), 1972, pp. 1161-1179.

7-18. Cavarretta, G.; Funiciello, R.; Giles, H.; Nicholls, G. D.; et al.: Geochemistry of Green Glass Spheres from Apollo 15 Samples. The Apollo 15 Lunar Samples, Lunar Science Institute (Houston, Tex.), 1972, pp. 202-205.

7-19. Gibson, E. K., Jr.; and Johnson, S. M.: Thermal Analysis—Inorganic Gas Release Studies of Lunar Samples. Proceedings of the Second Lunar Science Conference, vol. 2, MIT Press (Cambridge, Mass.), 1971, pp. 1351-1366.

7-20. Chang, S.; Kvenvolden, K. A.; and Gibson, E. K.: Simulated Solar Wind Implantation of Carbon and Nitrogen Containing Ions Into an Analogue of Lunar Fines. Lunar Science IV (Abs. of papers presented at the Fourth Lunar Science Conference (Houston, Tex.), Mar. 5-8, 1973), pp. 124-126.

7-21. Hayes, J.: Extralunar Sources for Carbon on the Moon. Space Life Sci., vol. 3, Oct. 1972, pp. 474-483.

7-22. Hintenberger, H.; and Weber, H. W.: Trapped Rare Gases in Lunar Fines and Breccias. Lunar Science IV(Abs. of papers presented at the Fourth Lunar Science Conference (Houston, Tex.), Mar. 5-8, 1973), pp. 365-367.

7-23. Kohl, J. W.; and Bostrom, C. O.: Observations of the August '72 Solar Events by the Solar Proton Monitor on Explorer 41. Trans. Am. Geophys. Union, vol. 53, Dec. 1972, p. 1055.

7-24. Apollo Lunar Geology Investigation Team: Documen-

tation and Environment of the Apollo 17 Samples: A Preliminary Report. U. S. Geol. Survey Interagency Rept.: Astrogeology 71, Jan. 21, 1973, p. 39.

7-25. Apollo Lunar Geology Investigation Team: Documentation and Environment of the Apollo 17 Samples: A Preliminary Report. U. S. Geol. Survey Interagency Rept.: Astrogeology 71, Jan. 21, 1973, pp. 137-138.

7-26. Apollo Lunar Geology Investigation Team: Documentation and Environment of the Apollo 17 Samples: A Preliminary Report. U.S. Geol. Survey Interagency Rept.: Astrogeology 71, Jan. 21, 1973, p. 117.

7-27. Apollo Lunar Geology Investigation Team: Documentation and Environment of the Apollo 17 Samples: A Preliminary Report. U.S. Geol. Survey Interagency Rept.: Astrogeology 71, Jan. 21, 1973, p. 188.

7-28. Kirsten, T.; Hann, P.; Heymann, D.; Hubner, W.; and Storzer, D.: Apollo 17 Crystalline Rock and Soils, Rare Gases, Ion Tracks and Ages. Trans. Am. Geophys. Union, vol. 54, no. 6, June 1973, p. 595.

7-29. Simonds, C. H.; Warner, J. L.; Phinney, W. C.; and Gooley, R.: Mineralogy and Mode of Formation of Poikilitic Rocks from Apollo 16. Lunar Science IV (Abs. of papers presented at the Fourth Lunar Science Conference (Houston, Tex.), Mar. 5-8, 1973), pp. 676-678.

7-30. Bence, A. E.; Papike, J. J.; Sueno, S.; and Delano, J. W.: Pyroxene Poikilitic Rocks from Apollo 16. Lunar Science IV(Abs. of papers presented at the Fourth Lunar Science Conference (Houston, Tex.), Mar. 5-8, 1973), pp. 60-62.

7-31. Albee, A. L.; Gancarz, A. J.; and Chodos, A. A.: Sanidinite Facies Metamorphism of Apollo 16 Sample 65015. Lunar Science IV(Abs. of papers presented at the Fourth Lunar Science Conference (Houston, Tex.), Mar. 5-8, 1973), pp. 24-26.

7-32. Hubbard, N. J.; and Gast, P. W.: Chemical Composition and Origin of Nonmare Lunar Basalts. Proceedings of the Second Lunar Science Conference, vol. 2, MIT Press (Cambridge, Mass.), 1971, pp. 999-1020.

7-33. Howard, K. A.; and Wilshire, H. G.: Flows of Impact Melt at Lunar Craters. Lunar Science IV (Abs. of papers presented at the Fourth Lunar Science Conference (Houston, Tex.), Mar. 5-8, 1973), pp. 389-390.

7-34. Grieve, R. A. F.; and Plant, A. G.: 64455, An Ellipsoidal Glass Coated Highland Basalt Projectile. Lunar Science IV (Abs. of papers presented at the Fourth Lunar Science Conference (Houston, Tex.), Mar. 5-8, 1973), pp. 317-319.

8. Soil Mechanics

James K. Mitchell,[a†] W. David Carrier, III,[b] Nicholas C. Costes,[c]
William N. Houston,[a] Ronald F. Scott,[d] and H. John Hovland[e]

The objectives of the soil mechanics experiment were to determine the physical characteristics and mechanical properties of the lunar soil at the surface and subsurface and the variations in lateral directions and to relate this knowledge to the interpretation of lunar history and processes. Data obtained on the lunar surface in conjunction with observations of returned samples of lunar soil are used to determine in-place density and porosity profiles and to determine strength characteristics on local and regional scales.

The soil mechanics experiment on the Apollo 17 mission to the Taurus-Littrow area of the Moon was passive and involved no apparatus or crew time unique to the experiment. The preliminary analyses and interpretations presented in this report have been deduced from studies of extravehicular activity (EVA) transcripts and kinescopes, mission photographs, data on the lunar roving vehicle (LRV) performance, debriefings, and limited examination of returned lunar samples by the Lunar Sample Preliminary Examination Team (LSPET).

SUMMARY OF PREVIOUS RESULTS

The mechanical properties of lunar soil as deduced through the Apollo 15 mission were summarized by Mitchell et al. (ref. 8-1). The Apollo 16 results agreed generally with those of earlier missions and also provided more specific quantitative information on density and strength and their variability than was available previously. Even though lunar and terrestrial soils differ greatly in mineralogical composition, lunar soil behavior is similar to that of terrestrial soils of comparable gradation (silty fine sand). Particle-size distribution, particle shape, and relative density (ref. 8-2) control behavior.

Soil porosity, density, and strength vary locally and with depth. Absolute densities may range from approximately 1.0 to 2.0 g/cm^3, and values > 1.5 g/cm^3 are probable at depths > 10 to 20 cm. The relative density of the soil near the surface is extremely variable but is generally quite high (> 80 percent) below a depth of 10 to 20 cm. Although local (meter scale) variations in density and porosity exist, Houston et al. (ref. 8-3) and Mitchell et al. (ref. 8-4) have shown that the mean porosity at each of the Apollo sites from footprint analysis is approximately the same for the upper few centimeters of soil. Analysis by Costes (ref. 8-5) of vehicle tracks at the same Apollo sites and at the Mare Imbrium site of the Soviet Luna 17 yields higher average porosity values at crater rims and other soft spots than for firm soil located in intercrater areas. The soil on crater rims and on slopes appears to be more variable and, on the average, less dense and weaker than does soil in intercrater plains areas.

Relative density (or porosity) is probably the most important single variable controlling strength, with most probable values of cohesion in the range of 0.1 to 1.0 kN/m^2 and friction angle in the range of 30° to 50°. The higher values are associated with higher relative densities.

DATA SOURCES

Soil mechanics data were derived from crew commentary and debriefings, television, lunar surface photographs, performance data and observations of interactions between soil and the LRV, drive-tube and deep drill samples, and sample characteristics as determined by the LSPET.

[a]University of California at Berkeley.
[b]NASA Lyndon B. Johnson Space Center.
[c]NASA Marshall Space Flight Center.
[d]California Institute of Technology.
[e]Pacific Gas and Electric Company.
[†]Principal Investigator.

Information from these data sources has been used in a manner similar to that from previous Apollo missions to deduce qualitative and semiquantitative information about soil properties. A statistical study of footprint and LRV track depths has been used as a basis for quantitative analysis of near-surface soil porosity. Premission orbital photographs and surface photographs have indicated a number of boulder tracks on the steep slopes of the North Massif and South Massif. These tracks have been analyzed by using the method of Hovland and Mitchell (ref. 8-6). Additional quantitative estimates have been based on LRV track depths and other specific observations as noted later in this section.

RESULTS AND INTERPRETATIONS

General Soil Characteristics at the Taurus-Littrow Site

Soil cover is present at all points visited in the Taurus-Littrow landing area. The surface is a similar color (gray and gray-brown) to that at the other Apollo sites, although lighter soil layers were encountered at shallow depths in some areas and orange-colored soil was exposed in a limited zone on the rim of Shorty Crater (station 4). Surface textures range from smooth areas almost free of rock fragments through patterned ground to areas heavily concentrated with larger rocks and fragments. Variability in soil properties is evident locally. Qualitative indications of this variability on a meter scale are provided in figures 8-1 to 8-3.

Soil behavior during landing, walking, driving, and sampling was comparable to that observed during previous missions. Dust was readily kicked up under foot and by the LRV, tended to adhere to any surface with which it came in contact, and inhibited normal operations on several occasions.

As readily apparent from the study of lunar surface photographs and from crew commentary, disturbed areas on the lunar surface appear darker than undisturbed areas, as has been the case at the previous landing sites. Subsequent crew observations of the landing sites from lunar orbit indicated that the disturbed areas were lighter than the undisturbed areas. This difference in appearance could indicate that the apparent changes in surface color caused by disturbance result from texture-related changes in albedo that influence the appearance when viewed
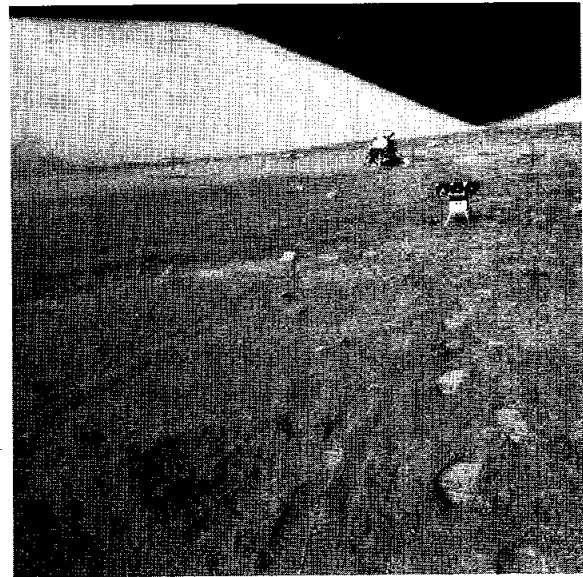
FIGURE 8-1.—Variable soil conditions in the vicinity of the surface electrical properties (SEP) experiment as evidenced by variable depths of LRV tracks and footprints (AS17-141-21517).

FIGURE 8-2.—Variable soil conditions in the light mantle at station 3 as evidenced by color differences (AS17-138-21148).

from different positions and at different Sun angles rather than from real color changes as a result of the exposure of new material. Alternatively, the different appearance might result from differences in scale between viewing from the surface and from orbit.
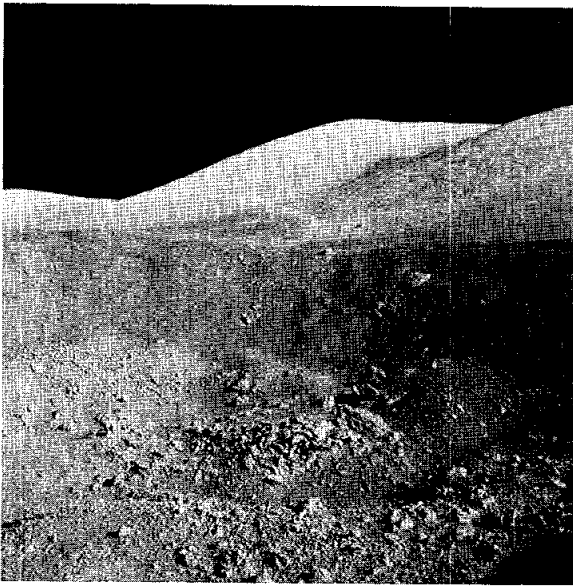
FIGURE 8-3.—Variable soil conditions inside Shorty Crater (station 4) as evidenced by different surface textures and slopes (AS17-137-21001).

FIGURE 8-4.—Descent trajectories for the Apollo 14, 15, and 17 missions.

Soil Observations During Lunar Module Descent and Landing

Both the postmission descent trajectory data and the crew comments indicate that the Apollo 17 descent was fairly rapid with vertical velocities of approximately 1 to 1.5 m/sec at altitudes of 60 to 70 m above the lunar surface, slowing to somewhat less than 1 m/sec at an altitude of approximately 15 to 20 m. The descent was accompanied by a fairly constant forward velocity of approximately 0.7 m/sec in the final 20 m of descent. Thus, the lunar module (LM) came in on an oblique trajectory similar to that of Apollo 14 (fig. 8-4). Previous analyses and mission results have shown that this kind of trajectory causes least disturbance of the lunar surface material during landing. In contrast, vertical descents, such as that of the Apollo 15 LM, generate substantial amounts of erosion. Blowing dust was first observed at a height of approximately 20 m above the lunar surface but caused no visibility difficulties during the final descent; in fact, the surface remained clearly visible all the way to contact.

The descent engine was shut down approximately 1 sec after contact was indicated, and the LM dropped to the lunar surface while maintaining some forward velocity. The crew noted that the rear (-Z) footpad probably hit the lunar surface first and that the primary shock absorber may have stroked slightly. Photographs (e.g., AS17-134-20388) show some crumpling of the Mylar insulation on the lower portion of the leg, indicating a possible stroking of 1 or 2 cm. This crumpling did not happen on any of the previous missions. From the photographs, no crushing of or damage to the footpad can be observed.

As in the other landings, the descent engine exhaust swept the lunar surface in the vicinity of the landing site. Compared to adjacent areas, there were relatively fewer small rock fragments and soil clumps beneath the LM, although rocks 10 cm in diameter and larger remained. The crew observed that there were clear indications of the interaction of the descent propulsion system exhaust gas with the lunar surface to a distance of approximately 50 m from the LM.

From the crew's comments during sampling, the lack of blowing dust during the final stages of the descent does not appear to be caused by soil properties different from those experienced in prior landings. As noted in the subsequent sections, the grain-size distribution, cohesion, and density of the soil around the LM are similar to those previously established for lunar soil. This similarity tends to confirm previous conclusions that the amount of blowing dust during a landing is directly related to the descent trajectory and descent rate.

Grain-Size Distribution and Soil Composition

At the time this report was prepared, the LSPET had determined the complete grain-size distribution of 15 samples and the distribution of a small aliquot of the black soil taken from the bottom of the double core-tube sample taken at station 4. The results are shown in figure 8-5. These gradations are generally similar to those observed at previous landing sites. The band of 11 samples in figure 8-5 is slightly coarser in the coarse fractions than the composite distribution band for Apollo 11, 12, 14, and 15 (ref. 8-7), primarily because of the excess particles in the fraction that is > 10 mm. This observation was also noted for some of the Apollo 16 soils (ref. 8-4) and was attributed to the recent addition of coarse fragments that had not yet been worked into the soil matrix from the South Ray Crater event. Sample 71060 was taken at station 1 from beneath a slight overhang of a rock, and the crew observed that there were chips in the soil. The distribution for sample 74240, the gray soil found next to the orange soil, was changed considerably when the total sample was included.

Despite the similarity of the grain-size distributions of the samples from various stations, the LSPET has found that the composition of the soil is highly variable in terms of proportions of basalt, breccia, mineral fragments, glass, and agglutinates. The soils from the massif stations appear to be derived from breccias, whereas much of the dark mantle on the plains was probably derived from basalts. The orange soil at station 4 is unique and is composed almost entirely of orange glass.

A knowledge of particle composition is important for the interpretation of data from many lunar experiments because, at the same relative density, soils consisting of coherent particles are stronger and conduct heat and seismic signals better than soils composed of friable particles.

Core Samples

Drive Tubes.—Data on the drive-tube samples are summarized in table 8-I, and the sampling at station 6 is shown in figure 8-6. The bulk densities of the samples in the drive tubes as a function of depth in the lunar surface are presented in figure 8-7. In all instances, the density of the soil in the lower tube is greater than that in the upper tube; that is, density
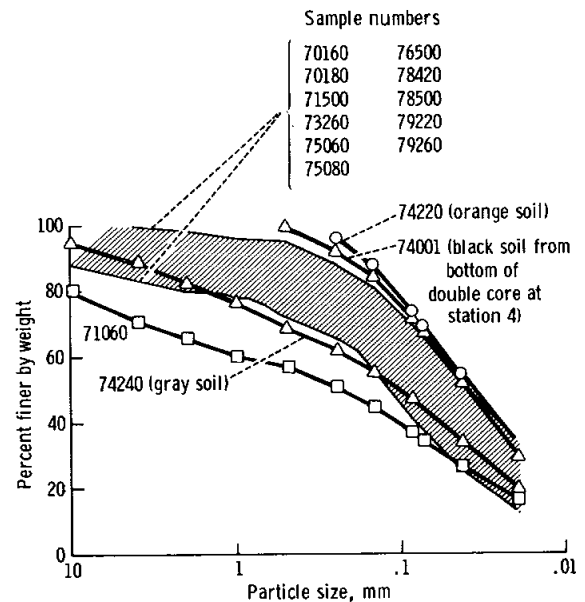
FIGURE 8-5.—Grain-size distribution curves for several Apollo 17 samples.

increases with depth, an observation consistent with findings at the Apollo 15 and 16 sites (fig. 8-7). However, the Apollo 17 core-tube densities (with the exception of the double core at station 4) are much more uniform with depth than were the Apollo 15 and 16 core-tube samples. The Apollo 17 core-tube densities tend to be higher near the surface and slightly lower below a depth of 20 to 30 cm than do the average densities for the Apollo 15 and 16 drive-tube samples.

The high core recovery percentages at stations 4 and 6 and at the LM are comparable to those of the Apollo 15 and 16 samples for which the same type of core tube was used. The lower core recovery percentages at stations 3 and 9 indicate that the returned bulk densities will have to be corrected for sample compression.

Densities in the double core from the rim of Shorty Crater at station 4 (2.03 to 2.29 g/cm^3) are distinctly higher than heretofore observed for any lunar samples. The upper tube contains orange-red soil with fine-grained black soil in the lower part. Black soil is exposed at the top and bottom ends of the lower tube. The orange soil, which is composed almost entirely of glass particles, is unusually compact and exhibits a high cohesion. A trench excavated into the material illustrates the high cohesion in the

TABLE 8-I.—*Preliminary Data on Apollo 17 Drive-Tube Samples*

Station	Serial no.	Sample no.	Sample weight, g	Sample length,[a] cm	Bulk density, g/cm^3	Tube depth (pushed), cm	Total depth (pushed and driven), cm	No. of hammer blows	Core recovery, percent
3	2031	73002	[b]429	21.8	[c]1.60 ± 0.10	?	70.6 ± 5	≥ 9	82 ± 2
	[d]2046	73001	[b]809	[e]34.9	1.73				
4	2035	74002	[b]910	33.3	2.04	?[f]	[f,g]71 ± 2	≥ 28	96 ± 3
	2044	74001	1071.4	34.9	2.29				
6	2048	76001	711.6	34.5	[c]1.57	16.2 ± 0.5	37.1 ± 0.5	[h]5 or 6	93 ± 2
9	2037	79002	409.4	19.4	[c]1.67	?	[g]71 ± 2	< 19	76 ± 2
	2050	79001	743.3	[i]31.9	[i]1.74				
LM	2052	70012	[j]434.8	[j]18.4	1.77	[h]28 ± 3	[h]28 ± 3	0	97 ± 10

[a]Determined from X-radiographs, except as noted.

[b]Sample weights are ± 4 g; better accuracy will be possible when tubes are removed from stretch cans.

[c]Corrected for voids.

[d]Core sample vacuum container.

[e]Assumed length.

[f]Camera failure; photographs were blank.

[g]Estimated from kinescopes.

[h]Crew estimate.

[i]Either 41 cm^3 of sample fell out of the top of the tube or the keeper compressed the top of the sample. The former is considered the more likely explanation; thus, density has been calculated accordingly.

[j]Approximately 114 cm^3 fell out of the bottom of the tube after it was placed in the sample collection bag because of a loose cap.

form of a tendency of the material to break into chunks (fig. 8-8).

The number of hammer blows (table 8-I), as indicated by the kinescopes, required to drive the core tube at station 4 was not exceptionally high compared to the driving resistance encountered on earlier missions, indicating that the porosity was not significantly less (or the relative density higher) at this location than had been previously encountered. Thus, the much higher bulk density is most likely caused by a higher specific gravity of the individual particles. Whereas the maximum reported value of specific gravity is 3.2 for an Apollo 15 sample (ref. 8-2), the soil in the lower half of the double core may have a value as high as 4. The black soil in the double core is composed primarily of crystalline droplets, olivine phenocrysts, a trace of glass, and 25-percent ilmenite that has a specific gravity of 4.7. The LSPET has found that the black material is the first lunar soil studied thus far that contains no agglutinates.

Drill Stems.—The deep core was drilled to a depth of 3.05 ± 0.01 m at a point approximately 40 m north of the Apollo lunar surface experiment package (ALSEP) central station. Core recovery was 95 to 97 percent, and preliminary data on the eight drill-stem sections are given in table 8-II.

Unfortunately, the top of the soil column in the top three drill-stem sections, which were returned as a unit, moved approximately 15 cm, causing some loosening and disturbance. However, because the initial sample length is known, it is possible to estimate the initial average density for the top three drill-stem sections to be 1.99 ± 0.05 g/cm^3, as shown in table 8-II.

The bulk density as a function of depth in the lunar surface for the drill-stem samples is shown in figure 8-9. Values for the Apollo 15 and 16 deep drill-stem samples are shown for comparison. Because the core recovery was nearly 100 percent, the measured bulk densities should be quite close to the in situ values.

All the bulk densities are high; that of the second drill stem (2.11 g/cm^3) is remarkably so. The X-radiographs indicated this section to be quite gravelly, and dissection by the LSPET has confirmed this. This zone may be related to the hard layer encountered in the LM area at the end of EVA-3 where a single core-tube sample was obtained. The fourth through the seventh drill stems all have essentially the same density; the X-radiographs show uniformity as well.

The absolute densities at the Apollo 17 drill site
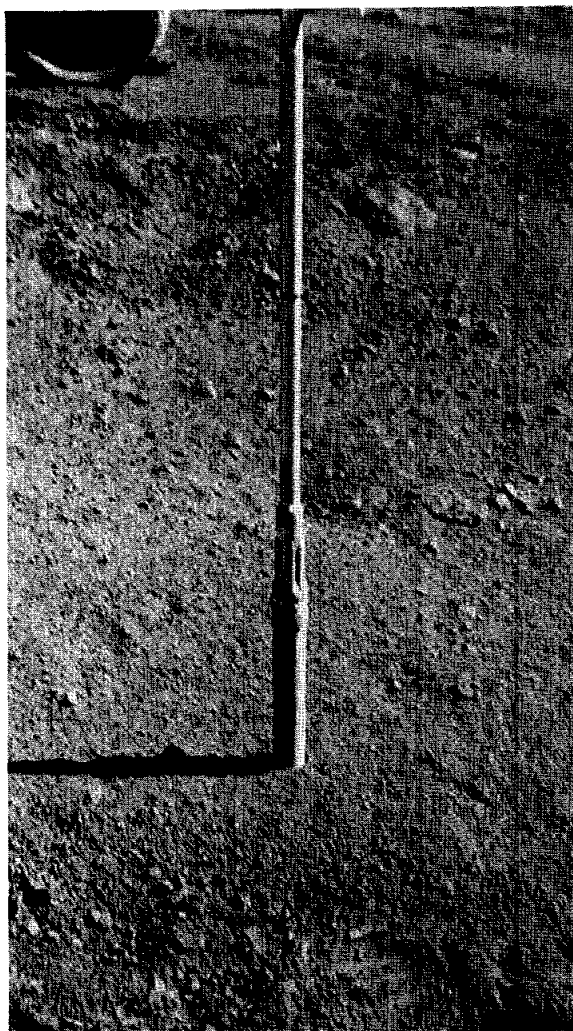
FIGURE 8-6.—Single drive tube at station 6. The drive tube has just been pushed to a depth of approximately 16 cm. A special orientation mark is visible above and to the right of the numeral 8 on the tube. This is the only drive tube from Apollo 17 that has been positively oriented in the lunar surface. After this photograph was taken, the drive tube was hammered to a final depth of 37 cm (AS17-146-22291).
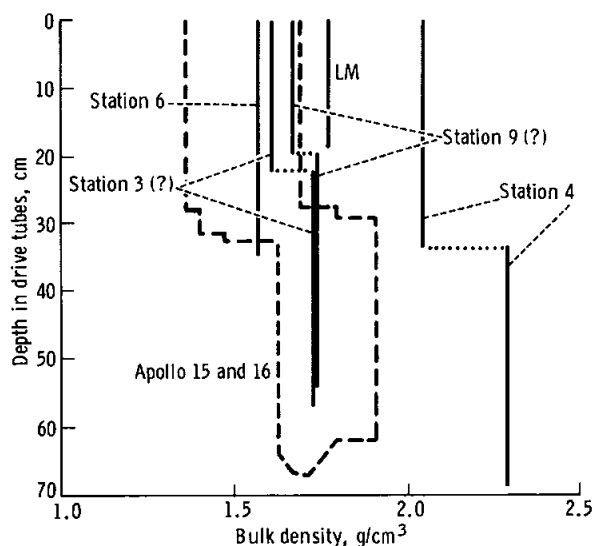
FIGURE 8-7.—Bulk density as a function of depth in the lunar surface for drive-tube samples.

FIGURE 8-8.—Trench excavated into orange soil on rim of Shorty Crater at station 4. The chunky texture reflects the high cohesion of this soil (AS17-137-20989).

are generally higher than those measured at the Apollo 15 and 16 drill sites, and the distribution of densities as a function of depth suggests a depositional history entirely different from either of the previous two sites. The average drill rate of the first Apollo 17 heat flow borestem was approximately 70 cm/min, indicating that the relative density at the the Apollo 17 site is considerably higher than that at Apollo 16 site. If the later borestem design of Apollo

16 and 17 had been available, the predicted drill rate at the Apollo 15 site would have been the same or slightly less than that measured at the Apollo 17 site, indicating that although the absolute densities in the Apollo 15 drill stem were less than those of Apollo 17, the relative densities were generally the same or higher. This indication implies a significantly different soil composition. Even though the relative densities at the Apollo 17 drill sites were indicated to

TABLE 8-II.—*Preliminary Data on Apollo 17 Drill-Stem Sections*

Drill-stem serial no.	Sample no.	Returned sample weight,[a] g	Returned sample length,[b] cm	Returned bulk density,[c] g/cm³	Original sample length,[d] cm	Original bulk density,[c] g/cm³	Drill-stem depth, cm	Core recovery, percent
061	70009	143.3	25 ± 2	1.76 ± 0.14	[e]10 ± 2	} 1.99 ± 0.05		
067	70008	260.9	[f]38	2.11	39.9			
063	70007	179.4	[g]34 ± 2	1.62 ± 0.10	39.9			
065	70006	234.2	39.9	1.80	39.9	1.80	} 305 ± 1	95 to 97
069	70005	240.6	39.9	1.85	39.9	1.85		
066	70004	238.8	39.9	1.84	39.9	1.84		
062	70003	237.8	39.9	1.83	39.9	1.83		
070	70002	207.7	} [h]42.0	1.74	42.5	1.74		
179 (bit)	70001	29.8						

[a]Total weight is 1772.5.

[b]Determined by X-radiography.

[c]Based on a sample diameter of 2.04 cm.

[d]Total length is 292 ± 2.

[e]Core-tube rammer-jammer was inserted to a depth of 30 ± 2 cm before drill stem was withdrawn from soil.

[f]Approximately 2-cm void at top of stem.

[g]Approximately 6-cm void at top of stem.

[h]Nominal length is 42.5 cm; 0.5 cm fell out of bottom of drill stem on lunar surface.
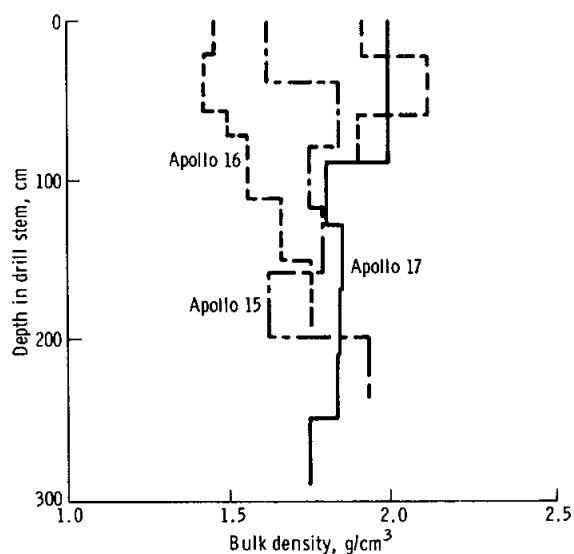
FIGURE 8-9.—Bulk density as a function of depth in the lunar surface for drill-stem samples.

be generally quite high, the observed drill rates were quite variable and reflected hard and soft layers at depth.

After the easy drilling experiences of Apollo 16, it was assumed that the hard drilling encountered at Apollo 15 was exceptional. On the basis of three data points, it must now be concluded that hard drilling is not uncommon for the lunar surface and that the soil at the Apollo 16 site may have been anomalously soft. Softer soil conditions near the surface are also indicated for the Apollo 16 site by the porosity as determined by analysis of footprint depths and LRV tracks (ref. 8-1).

After extraction of the drill stem, the neutron flux probe was inserted to a depth of 2.1 m (length of probe) in the vacated hole. Before insertion of the probe, it was noted that the hole was intact and flared at the top. No resistance to insertion of the probe was encountered, except at approximately one-third the depth where a slight obstruction was noted. This resistance may have coincided with the location of the gravel layer. There was no noticeable resistance to withdrawal of the neutron flux probe at the end of EVA-3, at which time it had been in the ground for 49 hr. This suggests that there was no caving or squeezing of the soil under the increased shear stresses caused by the presence of the hole, in agreement with premission predictions.

A stability analysis of the open drill hole provides lower bound estimates of the soil strength parameters as shown by Mitchell et al. (ref. 8-8). In that report, the horizontal scale in figure 7-24 is in error. A corrected plot of the relationship between soil cohesion and friction angle and the depth to the bottom of the elastic zone in an open borehole is given in

figure 8-10. Below the depth corresponding to any given combination of friction angle and cohesion, a plastic zone should develop, and there should be soil yielding that would lead to closure of the hole by inward squeezing of the soil.

If no yielding of the soil developed to a depth corresponding to the length of the neutron flux probe (and little could have occurred because the probe diameter is only slightly less than the hole diameter), then the required strength parameters are as indicated by the vertical line in figure 8-10 at a depth of 2.1 m. Even for high friction angles ($> 50°$), a soil cohesion exceeding 1.0 kN/m² is required. Strength parameters of this magnitude are likely only for conditions of high relative density and would be consistent with the hard drilling discussed previously. High strength is not required for the full depth of the hole. Stability can be maintained for conditions of strength increasing with depth to satisfy figure 8-10 at any depth.
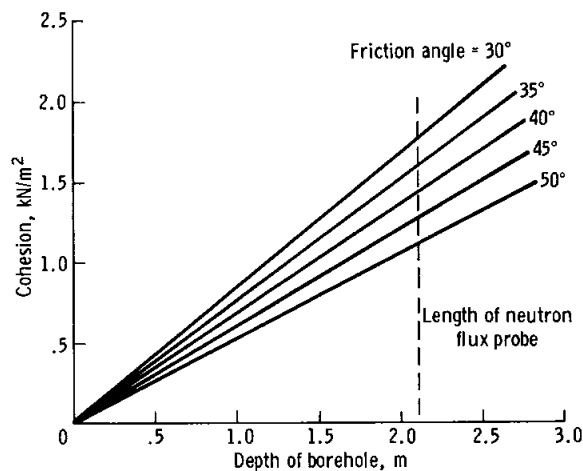
FIGURE 8-10.—Depth to bottom of the elastic zone in an open borehole as a function of soil strength parameters.

Although the open holes remaining after extraction of the drill stem suggest quite high strengths for depths of approximately 2 m at both the Apollo 16 and 17 sites, strengths of this magnitude are not commonly encountered at shallow depths as indicated by the values determined by penetrometer testing at the Apollo 16 site (ref. 8-1).

Boulder Tracks

More than 300 tracks made by boulders rolling, bouncing, and skidding down lunar slopes were identified by Grolier et al. (ref. 8-9) in the Lunar Orbiter photographs. The Apollo 17 mission provided the first opportunity for a close study of these interesting features because many tracks can be seen on the Taurus-Littrow hills. Unfortunately, prints of the 500-mm lunar surface photographs, which permit the most detailed study of the tracks, were not available to the soil mechanics team during the preparation of this report. Hence, the analyses, based mainly on 60-mm and premission orbital photographs, are tentative, and the results are subject to subsequent refinement. In a qualitative sense, boulder tracks serve as exploratory trenches and can provide information about regolith thickness and history, and the relative sharpness of track features provides some indication of soil movement after track formation.

Quantitative analysis of boulder tracks, from which information can be derived relating to soil strength and density, is possible. Studies of this type have been reported by Filice (ref. 8-10), Eggleston et al. (ref. 8-11), Moore (ref. 8-12), Moore et al. (ref. 8-13), and Hovland and Mitchell (ref. 8-6) for boulder tracks found in Lunar Orbiter photographs. The method in reference 8-6 is used here. An oblique closeup view of a larger boulder and its associated track visited at station 6 on the south slope of the
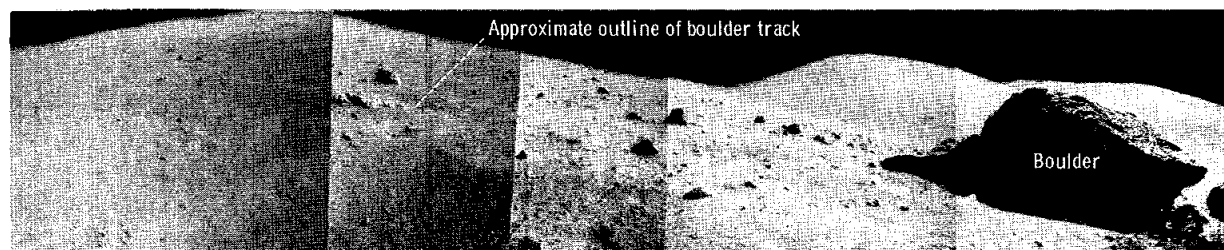
FIGURE 8-11.—Partial panorama at station 6 showing a large boulder and the track down which it rolled (AS17-141-21582, 21584, 21586, 21590, and 21594).

North Massif during EVA-3 is shown in figure 8-11.

Several tracks were located on the premission orbital photographs of the East Massif and the Sculptured Hills; their locations are indicated in figure 8-12. Several tracks on the South Massif are identified in figure 8-13. Additional tracks on the

≅ 530 m   — — — — — Boulder tracks

FIGURE 8-12.—Locations of boulder tracks on the East Massif and on the Sculptured Hills. For tracks identified by a letter, a definite causative boulder could be located; for tracks identified by a number, only the most probable causative boulder could be located.
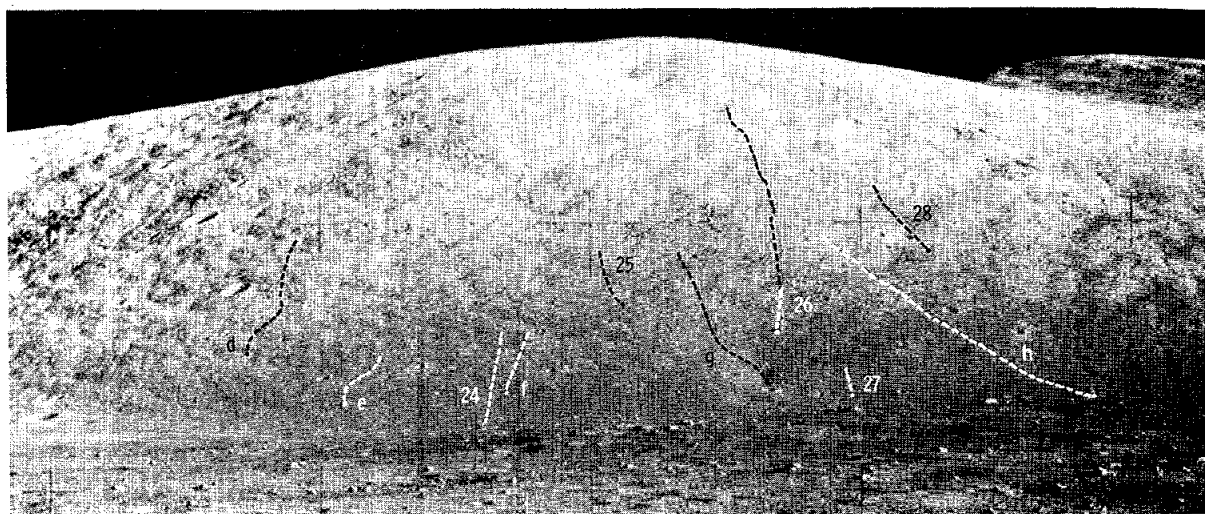
------ Boulder tracks

FIGURE 8-15.—Boulder tracks on the North Massif as seen from the LM (track identifications are the
same as for fig. 8-12) (AS17-147-22502).

and is used with a bearing capacity equation adapted
to the case of a rolling sphere. The resulting relation-
ships between soil friction angle, slope angle, and
track-width-to-boulder-diameter ratio are shown in
figure 8-16. A soil density of 1.6 g/cm^3 and a
cohesion of 1 kN/m^2 were assumed. This value of
cohesion is near the upper end of the range of
cohesion values determined for the lunar soil thus far
(refs. 8-1 and 8-4). The effect of an overestimation in
cohesion by as much as a factor of 10 will lead to an
underestimation of friction angle of only 1° to 2°,
however. An estimate of the variations in friction
angle that are likely to result from errors in a
measurement of track depth and width and in
boulder size has been made (ref. 8-6). The analysis
indicated that friction could differ by as much as ± 2°
because of measurement errors.

The frequency distribution of the soil friction
angles derived from the boulder track data is shown
in figure 8-17 and is generally compatible with the
soil gradations, densities, and porosities found at
other locations on the Moon. Although the range is
similar to that determined by other means (refs. 8-1
and 8-4), the most frequent values are somewhat less
than would be expected because tracks of the size
analyzed must involve considerably greater soil
depths than for the other determinations. This
difference may reflect limitations in the analysis.

Thus, the variability indicated by figure 8-17 is
considered more reliable than the absolute values of
friction angle.

Surface Soil Porosity Deduced from Footprint Analysis

Previously developed methods (refs. 8-3 and 8-4)
have been used to extend the statistical analysis of
lunar soil porosity as deduced from footprint depths
to include the Apollo 17 site. The curve correlating
footprint depth with average porosity and relative
density of the upper few centimeters of the lunar
surface, based on results of model test and theoretical
analyses (ref. 8-14), is shown in figure 8-18.

A total of 144 different footprints from the
Apollo 17 photographs were analyzed, and the results
are summarized in table 8-IV. A histogram showing
all data for Apollo 17 is presented in figure 8-19. Also
summarized in table 8-IV are results for previous
Apollo missions. For the Apollo 17 site, only three
footprints on crater rims were analyzed. This sample
size is too small to characterize crater rims statis-
tically; thus, the values shown in table 8-IV are
essentially applicable only to intercrater areas.

The data in table 8-IV show that neither the
intercrater average porosity (43.4 percent) nor the
standard deviation (2.4) differ significantly from the

TABLE 8-III.—*Apollo 17 Boulder Tracks*

Location	Reference	Track no.*	Slope angle, deg	Track length, km	Track width, w, m	Boulder diameter, D, m	w/D	Track depth, m	Friction angle, deg
East Massif	Fig. 8-12	1	23	1.3	13	17	0.76	3.0	40
		2	26	.6	10	10	1.00	5.0	30
		3	26	.6	8	15	.53	1.1	49
		4	26	.5	5	6	.83	1.3	35
		5	26	.9	12	12	1.00	6.0	30
		6	26	.7	10	16	.62	1.7	46
		a	26	1.3	9	11	.82	2.4	37
		b	26	1.7	8	10	.80	2.0	37
Sculptured Hills	Fig. 8-12	7?	25	1.3	26?	–	–	–	–
		8?	25	1.4	26?	–	–	–	–
South Massif	Fig. 8-13	9	27	0.9	10	13	0.77	2.4	39
		10	27	.9	11	16	.69	2.2	43
		11	27	2.5	10	13	.77	2.2	39
		12	27	.5	8	11	.73	1.8	41
		13	25	.4	11	15	.73	2.4	42
		14	25	.6	14	14	1.00	7.0	30
		15	25	1.4	12	12	1.00	6.0	30
		c	25	.8	16	20	.80	4.0	39
	Fig. 8-14	16	25	≈ .1	1.5	–	–	–	–
		17	25	≈ .2	3.0?	3.0	1.00	1.5	–
		18	25	≈ .05	1.8	2.1	.86	0.5	27
		19	25	≈ .3	5.0	–	–	–	–
		20	25	≈ .1	3.0?	3.0	1.00	1.5	–
		21	25	≈ .3	4.5	–	–	–	–
		22	25	≈ .3	6.0	–	–	–	–
		23	25	≈ .2	3.0	2.0?	–	–	–
North Massif	Fig. 8-15	24	26	≈ .5	7	–	–	–	–
		25	26	≈ .5	8	8	1.00	4.0	29
		26	26	≈ 1.8	10	18?	–	–	–
		27	24	≈ .1	3.6	4.5	.80	0.9	35
		28	24	≈ .7	6	8	.75	1.4	39
		d	24	≈ .9	8	10	.80	2.0	38
		e	24	≈ .4	7	9	.78	1.7	38
		f	26	≈ .4	6	6	1.00	3.0	28
		g	24	≈ 1.0	7	8	.88	2.1	33
		h	23	≈ 2.0	8.5	12	.71	1.7	41

*For tracks identified by a letter, a definite causative boulder could be located; for tracks identified by a number, only the most probable causative boulder could be located.

average values for previous Apollo sites. The Apollo 16 average (45.0 percent) is slightly higher. The statistical parameters for Apollo 17 also compare closely with both the weighted average values for all Apollo sites (44.0 percent and 2.75) and the unweighted values (43.5 percent and 2.55). The unweighted values were obtained by computing a simple arithmetic average of the averages for each site without regard to the number of observations at any one site. Conversely, the weighted average porosity (44.0 percent) is weighted heavily in favor of Apollo 16 where an unusually large number of footprint observations was possible. Thus, the unweighted values (43.5 percent and 2.55) probably represent a better estimate for a randomly selected location on the lunar surface.

No distinguishable difference in porosity was found between the Apollo 17 traverse stations and
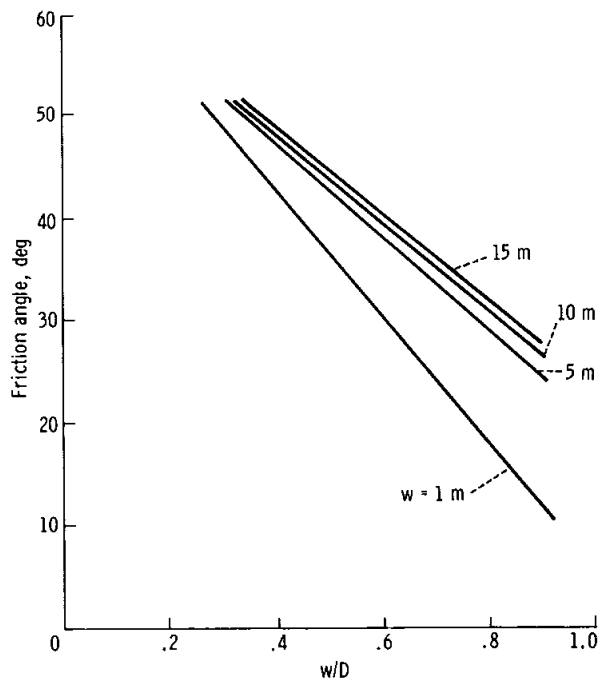
(a) Slope angle = $0°$.
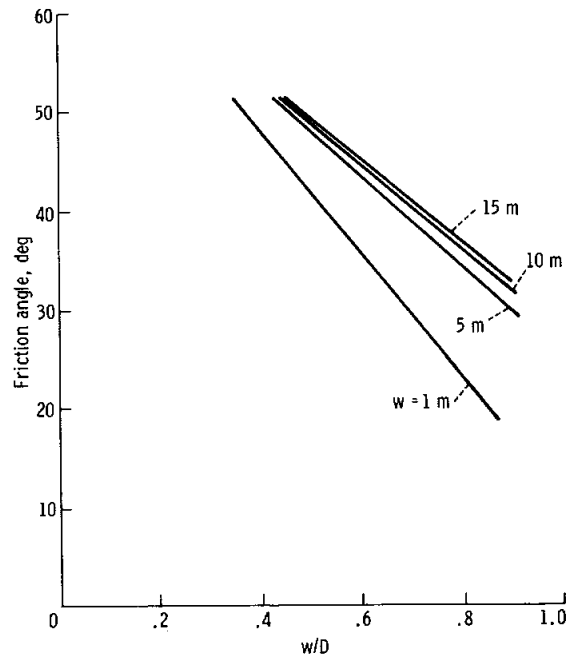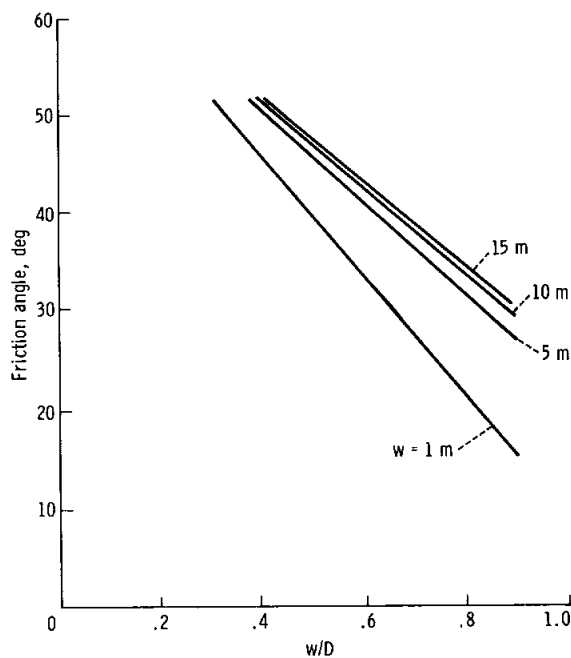
(b) Slope angle = $10°$.
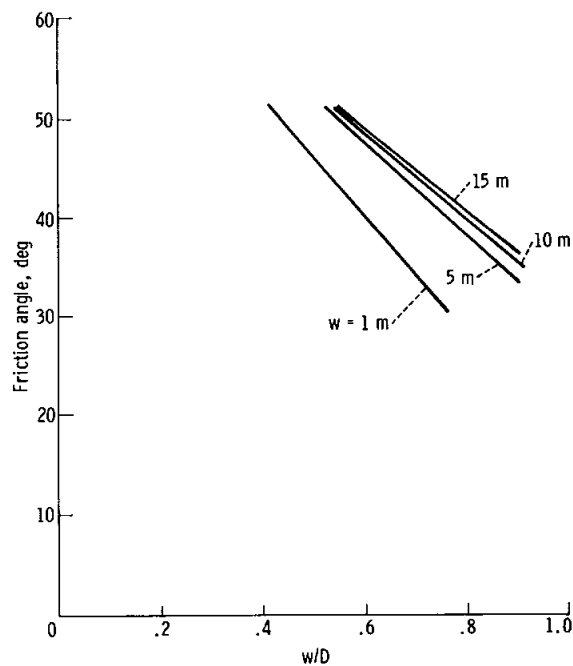
(c) Slope angle = $20°$.

(d) Slope angle = $30°$.

FIGURE 8-16.—The relationship between friction angle ϕ and track width to boulder diameter ratio w/D for lunar soil, where soil density ρ_s is 1.6 g/cm^3; cohesion c is 1 kN/m^2; and rock density/soil density ρ_r/ρ_s is 2.
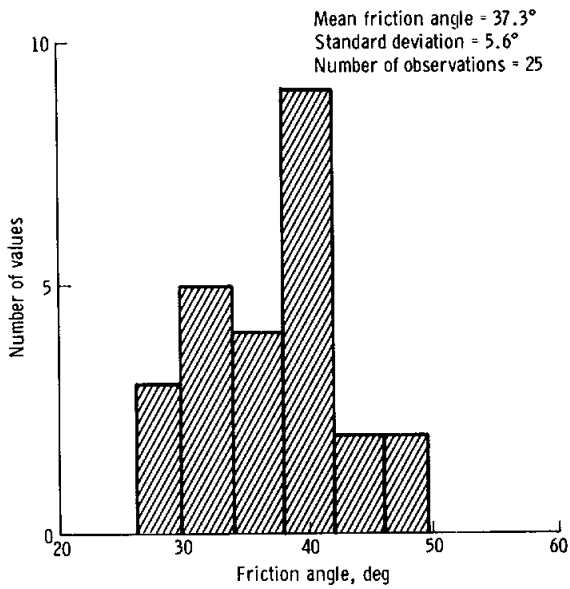
FIGURE 8-17.—Frequency distribution of friction angle values deduced from boulder tracks in the Taurus-Littrow area.
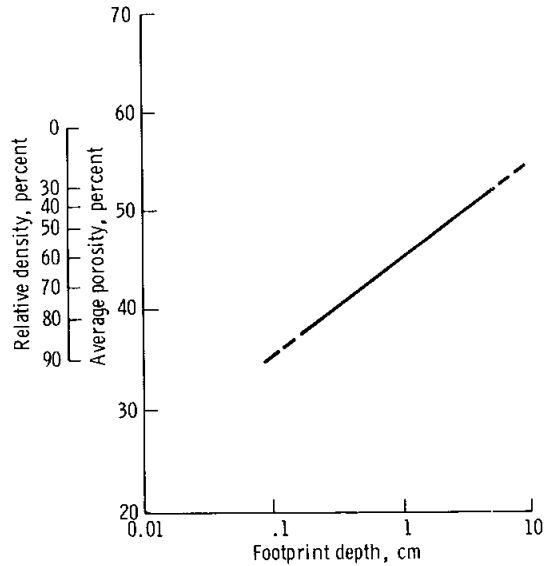
FIGURE 8-18.—Predicted variation of footprint depth with average porosity and relative density in the top 10 cm of the lunar surface. Average porosity is based on a 58.3-percent maximum and a 31-percent minimum. Footprint depth assumes a contact stress of 7 kN/m^2.

TABLE 8-IV.—*Results of Statistical Analysis of Porosities Deduced from Footprint Depths*

Location	No. of observations	Mean porosity,[a] percent	Standard deviation	Mean relative density, percent
Apollo 17 site				
All data	144	43.4	2.4	67
LM and ALSEP area	80	43.2	2.65	67
All traverse stations	64	43.65	1.95	66
Intercrater areas				
Apollo 11	30	43.3	1.8	67
Apollo 12	88	42.8	3.1	68
Apollo 14	38	43.3	2.2	67
Apollo 15	117	43.4	2.9	67
Apollo 16	273	45.0	2.8	61.5
Apollo 17	141	43.4	2.4	67
Apollo 11, 12, 14, and 15	273	[b]43.2	[b]2.8	67
All Apollo sites				
Crater rims	89	[b]46.5	[b]4.3	55.5
Intercrater areas	687	[b]44.0	[b]2.75	65
Intercrater areas	687	[c]43.5	[c]2.55	66

[a]Based on assumption that n_{max} = 58.3 percent and n_{min} = 31 percent.
[b]Weighted average.
[c]Each Apollo site given equal weight regardless of number of observations.

LRV A-hr integrator read-outs: Soil model B
△   Battery 1 ϕ = 35°
○   Battery 2   c = 0.17 kN/m²
—— Predicted from soil k_ϕ = 0.81 N/cm³
      model B k_c = 0.35 N/cm
                                 n = 1.0
                                 K = 1.0 cm
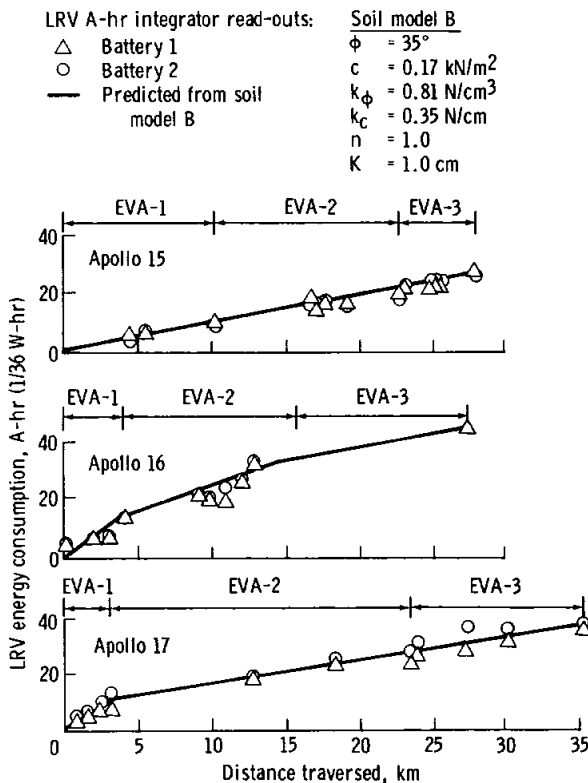
FIGURE 8-21.—Measured energy consumption of the LRV in relation to the predicted values based on the soil properties indicated.

core-tube samples. As shown in figure 8-21, the same soil model, which had been based on Surveyor data for soil near the surface (ref. 8-20), yields results that closely agree with the measured LRV energy consumption at both the Apollo 16 and 17 sites.

In figure 8-21, the symbols ϕ and c designate, respectively, the soil friction angle and cohesion; K is a normalizing constant conditioning the amount of shear strength and the thrust mobilized by the soil at a given wheel slip; and k_ϕ, k_c, and n describe the pressure-sinkage characteristics of the soil under wheel loads (ref. 8-21).

$$p = \frac{k_c}{b} + k_\phi z^n \qquad (8\text{-}2)$$

in which p is the wheel contact pressure in N/cm², b is the wheel footprint width in centimeters, and z is wheel sinkage in centimeters. If for a given wheel the pressure-sinkage relationship is linear ($n = 1$), the coefficients k_c and k_ϕ are analogous to the penetration resistance gradient of the soil G.

From these parameters, pull as a function of slip and torque as a function of slip relationships were calculated using analytical expressions developed by Bekker (ref. 8-21). These expressions were then used as computer input data, together with other information relating to the mission, terrain, and vehicle characteristics, to calculate the LRV energy consumption at each site (ref. 8-19).

Because of the small amount of wheel sinkage, the LRV wheel/soil interaction with the lunar surface involved predominantly surface shear. Accordingly, a value of ϕ = 35° is consistent with average friction angle values deduced from the analysis of LRV tracks (table 8-V) on the basis of in-place plate shear tests performed on a lunar soil simulant (refs. 8-15 and 8-16). The values of coefficients k_c and k_ϕ are consistent with the average G values deduced from LRV tracks (table 8-V). Finally, based on other lunar soil mechanics observations and measurements (e.g., soil erosion during LM descent), an average cohesion value of 0.17 kN/m² for the top surficial material was adopted.

In general, the soil/LRV interaction data support the conclusion that the surficial lunar soil is less compact, more deformable and compressible, and has lower strength than does the subsurface material.

Downslope Movements Caused by Meteoroid Impacts

Houston et al. (ref. 8-22) have assessed the relative importance of vibrations induced by meteoroid impact as a mechanism for mass movement of lunar soil downslope. The seismic energy generated by impacts of various-size meteoroids was estimated, and the associated incremental movement was computed for each impact. Movements were summed over the range in meteoroid sizes producing significant movement, both with respect to distance from point of impact and with respect to time, using meteor flux rates derived by Gault (ref. 8-23) with an adjustment based on more recent estimates of the age of the Moon.

The results indicated that the flattest slope on which significant cumulative downslope soil movement of approximately 1 m is likely to have occurred because of impact-produced ground accelerations is approximately 25°. The flattest slope on which cumulative downslope movement of several hundred to a few thousand meters is likely to have occurred is approximately 48°. Because of the great length of

most of the highland lunar slopes, it is estimated that downslope movements of a few thousand meters would be required to cause flattening of the slopes by as much as 1° or 2°. Thus, it appears that only on very steep lunar slopes could there have been significant downslope soil movements caused by shaking from meteoroid impacts alone, and that large-scale slope degradation must have developed primarily by other mechanisms. However, this conclusion does not mean that soil movement, once triggered by meteoroid impact, could not continue as a result of changes in strength properties of the soil mass or fluidization.

Origin of the Light Mantle

It has been hypothesized (ref. 8-24) that the light mantle that extends outward over the plains area north of the base of the South Massif (fig. 8-22) originated as an avalanche from the slopes of the

South Massif. A study of stereographic photographs obtained from orbit during the Apollo 17 mission using the panoramic camera gives some indication of a scarp on the South Massif that could define the boundary of a slide mass. Furthermore, according to the LSPET, the light mantle material on the plains appears to be compositionally similar to that from the South Massif. Thus, reasonable evidence exists that a slide or avalanche did occur. If a slide did occur, then an important question to be resolved is the mechanism by which the material spread out onto the valley floor and came to rest with a nearly level surface.

As the slope of the South Massif is only approximately 25° to 30°, meteoroid impact is unlikely to have been able to do much more than just initiate movement. Incremental movements accumulating from impacts alone could not account for the magnitude of movements indicated. However, once a
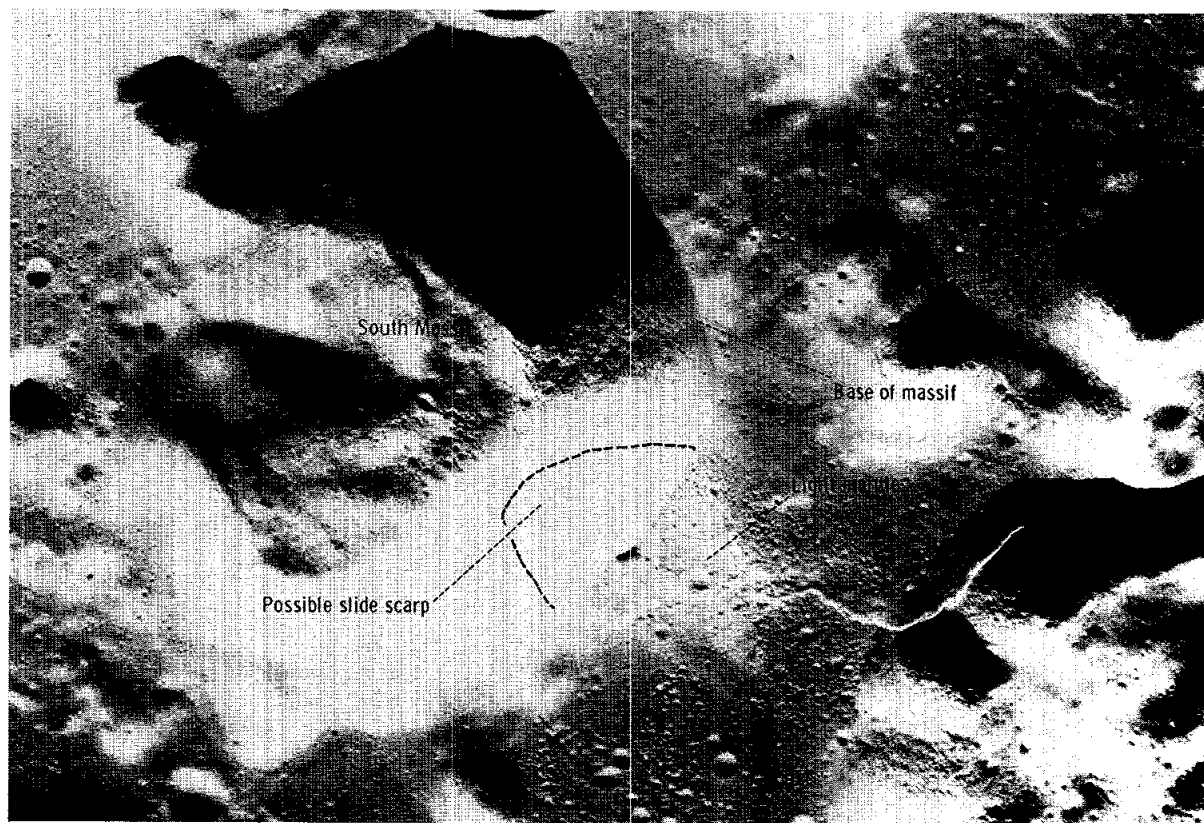
FIGURE 8-22.—Orbital view of the Apollo 17 landing area. The light mantle to the north of the South Massif may have been an avalanche produced by the mechanisms proposed in text. A possible slide scarp can be seen located as indicated on high-resolution panoramic camera photographs (Apollo 17 panoramic camera frame AS17-2314).

slide was triggered, if the soil strength were to decrease significantly or if the mass became fluidized because of the generation or liberation of significant quantities of gas, then continued movement might be possible.

In the analysis of downslope movements referred to previously, no change in soil strength was assumed once failure occurred. The nature of lunar soil particles, particularly the agglutinates and breccias, is such that particle breakdown during shear is likely. The results of strength and compression tests on lunar soil samples by Carrier et al. (ref. 8-25) suggest that particle breakdown does indeed occur. Mitchell and Houston (ref. 8-26) found that decreasing the particle size of a basalt lunar soil simulant resulted in a significant decrease in the angle of internal friction. It is not likely, however, that particle comminution could lead to a decrease in friction angle to a value less than 25°, which would be required to result in any slope flattening on the South Massif. A loss in strength caused by a friction-angle decrease sufficient to allow spreading of the material over the level plains does not seem possible.

The plausibility of fluidization as a mechanism hinges on the generation or liberation of sufficient gas during the initial stages of movement to provide a sufficient uplift pressure on the overlying soil to reduce or eliminate frictional resistance to downslope movement. Gas of solar wind origin was liberated in the compression and strength tests described in reference 8-24; however, the amount was too small by orders of magnitude to cause fluidization. Conversely, other investigators have generated gas by a combination of grinding and heating.

Clanton et al. (ref. 8-27) and Bogard et al. (ref. 8-28) have confirmed that agglutinates are enriched in solar wind and thus could serve as a source of gas when broken down. The Apollo 17 soil composition analyses indicate that the samples from the massifs contain greater proportions of breccias, approximately the same proportion of agglutinates, and less basalt than does the dark mantle material on the plains. Thus, a fluidization mechanism may be tenable to account for the origin of the light mantle, whereas fluidization would be very unlikely if the massifs were composed only of ground-up basalt.

CONCLUSIONS

The physical and mechanical properties of the soil at the Apollo 17 landing site are generally similar to those of the soils at the previous Apollo sites. Although no crew tasks or lunar surface measurements were done specifically for the purpose of obtaining quantitative soil mechanics data, a number of preliminary analyses and interpretations have been made using EVA transcripts and kinescopes, photographs, data on soil/LRV interactions, debriefings, and limited examination of returned lunar samples. The following specific conclusions have been developed.

1. Soil cover is present at all points visited in the Taurus-Littrow landing area. Surface textures and colors are similar to those at the other Apollo sites.

2. There is considerable local (meter scale) variability in soil properties.

3. Particle-size distributions of samples from different traverse stations are generally similar to each other and to those observed at previous landing sites, even though soil compositions are highly variable among the stations in terms of proportions of basalt, breccia, mineral fragments, glass, and agglutinates.

4. The drive-tube samples indicate some increase in density with depth but more uniformity with depth than the Apollo 15 and 16 samples. Soil density in the double drive tube taken on the rim of Shorty Crater (station 4) is higher than heretofore observed for any lunar sample. The presence of high specific gravity particles, such as ilmenite, is a more probable cause than is very low porosity.

5. Absolute densities at the Apollo 17 drill site are generally higher than those measured at the Apollo 15 and 16 drill sites, and the distribution of densities with depth suggests a different depositional history from that at the previous two sites.

6. Stability analysis of the open drill-stem hole, into which the neutron flux probe was placed and removed without soil resistance, indicates that there was little or no squeezing or caving of the soil during a 49-hr period and that soil strength at a depth of 2 m must have been considerably greater than the average strength near the surface.

7. Tracks caused by the rolling and bouncing of boulders are common on the slopes of the massifs and the Sculptured Hills. A frequency distribution of soil friction angles was deduced from rolling boulder track data that is consistent with the soil gradations, densities, and porosities found at other locations on the Moon, although the absolute values of friction angle were computed to be somewhat lower than was anticipated.

8. Near-surface soil porosities deduced from foot-

print depths indicate that neither the intercrater average porosity nor the standard deviation differ significantly from the average values for previous Apollo sites. The average relative density for all Apollo landing sites, as deduced from 687 observations of footprint depth, is approximately 66 percent. Large local (meter scale) variations exist in porosity and relative density.

9. The LRV performance, including slope-climbing capability and power consumption, was within the predicted limits. Analysis of track depth, shape, and texture indicated no discernible variations in the average consistency of the surface soil throughout the Taurus-Littrow region or relative to the Apollo 14 through 17 and Luna 17 landing sites, although variations about the average existed on a small scale at all sites.

10. Only on very steep lunar slopes ($> 25°$) could there have been significant downslope soil movements caused by shaking from meteoroid impacts alone, and large-scale slope degradation must have developed primarily by other mechanisms.

11. There is evidence to support an avalanche as the origin of the light mantle covering the plains north of the South Massif. Fluidization of the soil mass by gas pressures generated during the initial phases of soil movement would be required to account for the large-scale movements observed.

Finally, soil mechanics data from all the Apollo missions support the general conclusion that processes affecting the entire lunar surface, such as meteoroid impact and the solar wind, control the average properties such as grain-size distribution and relative density, which are nearly the same at all sites. On the average, the soil on slopes is less dense than the soil on level areas because of the effects of downslope movement. Local geology and topography on a small scale and specific cratering events appear to control the variations about the average to the extent that the standard deviation can be relatively large.

REFERENCES

8-1. Mitchell, J. K.; Houston, W. N.; Scott, R. F.; Costes, N. C.; et al.: Mechanical Properties of Lunar Soil: Density, Porosity, Cohesion, and Angle of Internal Friction. Proceedings of the Third Lunar Science Conference, vol. 3, MIT Press (Cambridge, Mass.), 1972, pp. 3235-3253.

8-2. Carrier, W. D., III; Mitchell, J. K.; and Mahmood, Arshud: The Relative Density of Lunar Soil. Lunar Science IV (Abs. of papers presented at the Fourth Lunar Science Conference (Houston, Tex.), Mar. 5-8, 1973), pp. 118-120.

8-3. Houston, W. N.; Hovland, H. J.; and Mitchell, J. K.: Lunar Soil Porosity and Its Variation as Estimated from Footprints and Boulder Tracks. Proceedings of the Third Lunar Science Conference, vol. 3, MIT Press (Cambridge, Mass.), 1972, pp. 3255-3263.

8-4. Mitchell, J. K.; Carrier, W. D., III; Houston, W. N.; Scott, R. F.; et al.: Soil Mechanics. Sec. 8 of the Apollo 16 Preliminary Science Report. NASA SP-315, 1972.

8-5. Costes, N. C.: Regional Variations in Physical and Mechanical Properties of Lunar Surface Regolith. Lunar Science IV (Abs. of papers presented at the Fourth Lunar Science Conference (Houston, Tex.), Mar. 5-8, 1973), pp. 159-161.

8-6. Hovland, H. J.; and Mitchell, J. K.: Mechanics of Rolling Sphere-Soil Slope Interaction. Final Rept. (NASA Contract NAS 8-21432), Vol. II, Space Sci. Lab., Univ. of California at Berkeley, July 1971.

8-7. Carrier, W. D., III: Lunar Soil Grain Size Distribution. The Moon, vol. 8, 1973.

8-8. Mitchell, J. K.; Bromwell, L. G.; Carrier, W. D., III; Costes, N. C.; et al.: Soil-Mechanics Experiment. Sec. 7 of the Apollo 15 Preliminary Science Report. NASA SP-289, 1972.

8-9. Grolier, M. J.; Moore, H. J.; and Martin, G. L.: Lunar Block Tracks. A Preliminary Geologic Evaluation of Areas Photographed by Lunar-Orbiter V Including an Apollo Landing Analysis of One of the Areas. NASA Langley Research Center, Rept. LWP-506, 1968, pp. 143-154.

8-10. Filice, A. L.: Lunar Surface Strength Estimate from Orbiter II Photographs. Science, vol. 156, no. 3781, June 16, 1967, pp. 1486-1487.

8-11. Eggleston, J. M.; Patterson, A. W.; Throop, J. E.; Arant, W. H.; and Spooner, D. L.: Lunar Rolling Stones. Photogrammetric Eng., vol. 34, no. 3, Mar. 1968, pp. 246-255.

8-12. Moore, H. J.: Estimates of the Mechanical Properties of Lunar Surface Using Tracks and Secondary Impact Craters Produced by Blocks and Boulders. U.S. Geol. Survey Interagency Rept.: Astrogeology 22, July 1970.

8-13. Moore, H. J.; Vischer, W. A.; and Martin, G. L.: Boulder Tracks on the Moon and Earth. U.S. Geol. Survey Prof. Paper 800-B, 1972, pp. B165-B174.

8-14. Houston, W. N.; and Namiq, L. I.: Penetration Resistance of Lunar Soils. J. Terramechanics, vol. 8, no. 1, 1971, pp. 59-69.

8-15. Green, A. J.; and Melzer, K. J.: Performance of the Boeing LRV Wheels in a Lunar Soil Simulant: Effect of Wheel Design and Soil. Tech. Rept. M-71-10, Rept. 1, USAE WES, Vicksburg, Miss., 1971.

8-16. Melzer, K. J.: Performance of the Boeing LRV Wheels in a Lunar Soil Simulant: Effect of Speed, Wheel Load, and Soil. Tech. Rept. M-71-10, Rept. 2, USAE WES, Vicksburg, Miss., 1971.

8-17. Vinogradov, A. P., ed.: Lunokhod-1, Mobile Lunar Laboratory. Nanka Publishers (Moscow), 1971. (Available from National Technical Information Service, Springfield, Virginia.)

8-18. Mitchell, J. K.; Bromwell, L. G.; Carrier, W. D., III; Costes, N. C.; and Scott, R. F.: Soil Mechanical Properties

at the Apollo 14 Site. J. Geophys. Res., vol. 77, no. 29, Oct. 10, 1972, pp. 5641-5664.

8-19. Costes, N. C.; Farmer, J. E.; and George, E. B.: Mobility Performance of the Lunar Roving Vehicle. Terrestrial Studies: Apollo 15 Results. NASA TR R-401, 1972.

8-20. Scott, R. F.; and Roberson, F. I.: Soil Mechanics Surface Sampler. Part II: Surveyor Project Final Report, Calif. Inst. Tech. JPL-TR-32-1265, 1968, pp. 195-207.

8-21. Bekker, M. G.: Introduction to Terrain-Vehicle Systems. The University of Michigan Press (Ann Arbor, Mich.), 1969.

8-22. Houston, W. N.; Moriwaki, Y.; and Chang, C. S.: Downslope Movement of Lunar Soil and Rock Caused by Meteor Impact. Lunar Science IV (Abs. of papers presented at the Fourth Lunar Science Conference (Houston, Tex.), Mar. 5-8, 1973), pp. 384-385.

8-23. Gault, D. E.: Saturation and Equilibrium Conditions for Impact Cratering on the Lunar Surface: Criteria and Implications. Radio Sci., vol. 5, no. 2, Feb. 1970, pp. 273-291.

8-24. Howard, K. A.: Lunar Avalanches. Lunar Science IV (Abs. of papers presented at the Fourth Lunar Science Conference (Houston, Tex.), Mar. 5-8, 1973), pp. 386-388.

8-25. Carrier, W. D., III; Bromwell, L. G.; and Martin, R. T.: Behavior of Returned Lunar Soil in Vacuum. J. Soil Mechanics Foundations Div., ASCE, Nov. 1973.

8-26. Mitchell, J. K.; and Houston, W. N.: Lunar Surface Engineering Properties Experiment Definition. Final Rept., Vol. 1 (NASA CR-102963), Space Sci. Lab., Univ. of California at Berkeley, 1970.

8-27. Clanton, U. S.; McKay, D. S.; Taylor, R. M.; and Heiken, G. H.: Relationship of Exposure Age to Size Distribution and Particle Types in the Apollo 15 Drill Core. The Apollo 15 Lunar Samples, Lunar Science Institute (Houston, Tex.), 1972, pp. 54-56.

8-28. Bogard, D. D.; Nyquist, L. E.; Hirsch, W. C.; and Moore, D. R.: Trapped Noble Gas Abundances in Surface and Sub-Surface Fines From Apollo 15 and 16. Lunar Science IV (Abs. of papers presented at the Fourth Lunar Science Conference (Houston, Tex.), Mar. 5-8, 1973), pp. 79-81.

9. Heat Flow Experiment

Marcus G. Langseth, Jr.,[a][†] *Stephen J. Keihm,*[a] *John L. Chute, Jr.*[b]

The objectives of the heat flow experiment (HFE) were to make a direct measurement of the vertical component of heat flow from the lunar interior through the surface and to determine the thermal properties of the upper 3 m of the lunar regolith.

The age of the Moon is placed at 4.6×10^9 yr. For a planetary body as small as the Moon, much of the initial heat energy has been lost to space since formation. Even if the Moon were initially at molten temperatures, the present flux at the surface would be small. The major contribution to the surface heat flow comes from heat generated by the disintegration of long-lived radioisotopes of uranium (^{235}U and ^{238}U), potassium (^{40}K), and thorium (^{232}Th). Thus, the present surface heat flux reflects the abundance of these isotopes to a depth of approximately 300 km, or 43 percent of the volume of the Moon. It is now certain that extensive differentiation occurred during the early history of the Moon that would concentrate these isotopes in the outer shells. In this case, the present surface heat flow would very nearly indicate the total abundance of these isotopes.

More than 5000 heat flow determinations made on Earth show the average global flux to be 6.3×10^{-6} W/cm^2 (ref. 9-1). (Throughout this report, W-sec will be used as the unit of heat energy. Other commonly used units are the calorie, which equals 4.18 W-sec, and the erg, which equals 10^{-7} W-sec. The average Earth heat flow is 1.5×10^{-6} cal/cm^2-sec and 63 ergs/cm^2-sec.) Urey (ref. 9-2) pointed out that the total rate of heat flow from the Earth is essentially equal to the total rate of heat production in the Earth if it were constituted of materials with chondritic abundances of uranium, potassium, and thorium. However, Gast (ref. 9-3) showed that Earth rocks were strongly depleted in potassium relative to solar and chondritic abundances, which led Wasserburg et al. (ref. 9-4) to propose that, to explain the heat flow from Earth, a higher abundance of uranium (nearly 3 times that of chondrites) is needed. They estimated a uranium abundance of approximately 30 ppb for the Earth.

The large variations of heat flow observed over the surface of the Earth are principally related to the present tectonism of the Earth lithosphere (ref. 9-5). The largest variations are observed at extensional and compressional boundaries of vast lithospheric plates that are moving relative to each other. Seismic observations (ref. 9-6) and the preservation of ancient surface features on the Moon demonstrate that no comparable tectonic movements have occurred on the Moon for the past 3×10^9 yr. The Moon is tectonically dead compared to the Earth; therefore, any variations in surface heat flow over the surface should reflect either deep-seated changes in abundances of radioisotopes or in convective patterns in the Moon. Because of the static nature of the outer crust of the Moon, heat flow determinations at a single location might be quite representative of a very large region of the Moon if local surficial effects such as refraction by conductive inhomogeneities and topography are properly accounted for.

Numerous attempts have been made to determine the surface heat flow from the Moon by detecting thermal radiation from the Moon in the microwave band. Because of the partial transparency of lunar surface material, energy with wavelengths greater than 1 mm received at Earth-based antennas originates in the subsurface and contains information on subsurface temperatures. By making estimates of thermal and electrical properties, the heat flow can be determined from the change of brightness temperature with wavelength. The earliest heat flow determination was that of Baldwin (ref. 9-7), who estimated an upper limit of 1×10^{-6} W/cm^2. Russian investigators estimated the heat flow to be very

[a]Lamont-Doherty Geological Observatory.
[b]H. H. Lehman College, City University of New York.
[†]Principal Investigator.

nearly equal to that of the Earth, based on a very careful set of radio-telescope observations in the wavelength band 3 to 50 cm (ref. 9-8). These same measurements were later revised by using different thermal properties and a layered model to give heat flows in the range 3×10^{-6} to 4×10^{-6} W/cm^2 (ref. 9-9).

During the Apollo 15 mission, the first direct measurement of heat flow through the lunar surface was made at Rima Hadley (lat. 26°06' N and long. 3°39' E). A second measurement was made during the Apollo 17 mission at the Taurus-Littrow site (lat. 20°10' N and long. 30°46' E). At Taurus-Littrow, two probes to determine heat flow were emplanted approximately 11 m apart. Analysis of data taken during the first 45 days after emplacement indicates that the heat flow is 2.8×10^{-6} W/cm^2 (0.67 μcal/cm^2-sec) at one probe location and 2.5×10^{-6} W/cm^2 (0.60 μcal/cm^2-sec) at the second probe location. For comparison, the value measured at Rima Hadley is 3.1×10^{-6} W/cm^2 (0.74 μcal/cm^2-sec). The Rima Hadley measurement and Taurus-Littrow probe 1 measurement have an estimated error of ± 20 percent. The probe 2 measurement at Taurus-Littrow has a slightly larger uncertainty because the heat flow appears to be locally disturbed. These measurements have not been corrected for local topography.

EXPERIMENT DESCRIPTION

Experiment Concept and Design

The concept on which the HFE is based is the direct measurement of the vertical flow of heat through the regolith. The measurement should be made far enough below the surface so that the time-varying heat flow resulting from the very large diurnal variations of surface temperature is small compared with the flow from the interior. At Taurus-Littrow, this depth is approximately 100 cm. Below this depth, the increase in temperature with depth results principally from the hotter lunar interior. The outward flow of heat is directly proportional to the rate of temperature increase with depth. These quantities are related by the equation

$$F_z = -k_m (\mathrm{d}T/\mathrm{d}z) \qquad (9\text{-}1)$$

where F_z is the vertical component of the heat flow,

T is the temperature, z is the depth, and the constant k_m is the thermal conductivity. The negative sign indicates that the heat flows in a direction opposite to the increase of temperature.

The experiment is designed to measure accurately the vertical temperature gradient in the lunar soil to a depth of 2.3 m. Surface temperature measurements are also made that can be used to deduce the thermal properties of the upper 10 to 15 cm of regolith. In situ measurements of thermal conductivity of the regolith at depths where the gradient is measured are also performed. Two measurements of heat flow at locations separated by approximately 10 m are made to detect possible lateral variations.

The essential parts of the heat flow instrument are two identical temperature-sensing probes. Each probe consists of two 50-cm-long sections (fig. 9-1(a)). In each probe section are two platinum resistance bridges; each bridge consists of four 500-ohm filamentary platinum elements interconnected by Evanohm wire (fig. 9-1(b)). Opposing arms of a bridge are wound together in a single sensor housing; two sensor housings, comprising a complete bridge, are mounted at opposite ends of a probe section.

Voltage measurements on a bridge can be interpreted by accurate calibrations in terms of average bridge temperature T_a and temperature difference ΔT between sensors. The temperature at each sensor is simply determined from $T_a \pm 1/2 \Delta T$. The accuracies of the HFE temperature measurements are given in table 9-I.

The cable thermocouples consist of a string of four Chromel/constantan junctions embedded in each probe cable. The lowermost junction is positioned inside the gradient sensor housing at the top of the probe. The reference junction for each cable is inside the electronics housing and is mounted in an isothermal block with a platinum resistance thermometer (the reference thermometer). The thermocouple (TC) circuit is shown in figure 9-1(c).

The accuracy of the thermocouple measurements has special significance for interpreting the subsurface temperature profiles at the Apollo 17 site. Therefore, certain features of the thermocouple measurement, which affect the accuracy, should be described. First, only the Chromel/constantan junction (TC1) inside the topmost gradient is coupled with the reference junction during a measurement sequence. Junctions TC2, TC3, and TC4 are coupled with TC1 so that, in effect, TC1 becomes the reference junction and the

(a) Heat flow probe.

FIGURE 9-1.—Heat flow probe and circuits.

(b) Typical platinum resistance bridge circuit.

(c) Thermocouple circuit.
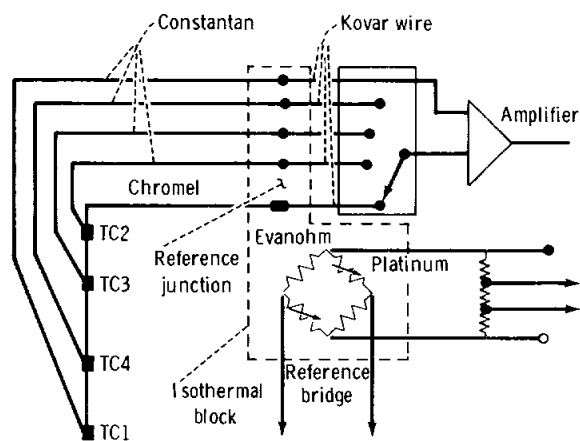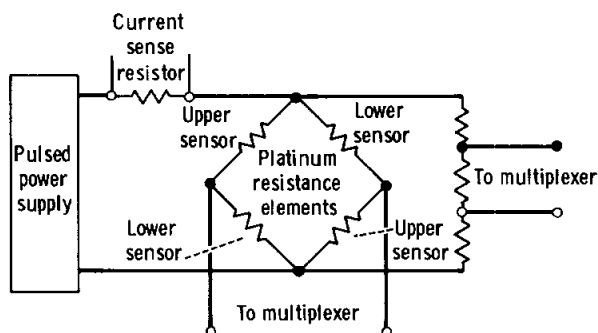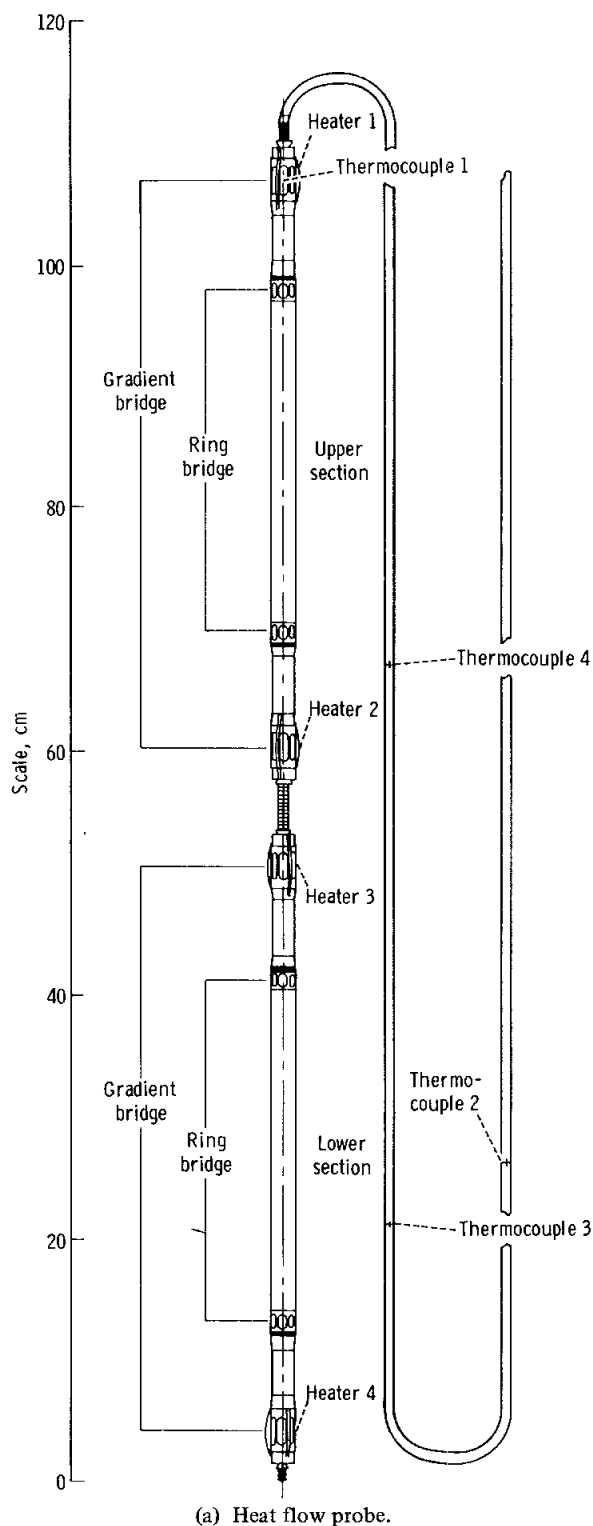
top gradient sensor becomes the reference thermometer. Because the temperatures of TC3 and TC4 are much closer to that of TC1 than to that of the thermometer in the electronics box, the calibration errors are reduced by this technique. Second, the placement of junction TC1 inside the gradient sensor permits a direct comparison between the two sensors on the Moon. Thus, an in situ calibration of the thermocouple circuit against the much more accurate gradient sensor is performed.

Conductivity experiments are made using 1000-ohm heaters that surround each of the gradient sensor housings. The experiments can be operated in either of two modes by energizing the heaters at 0.002 or 0.5 W, depending on the conductivity of the surrounding regolith. Because of the low conductivity of lunar material at Taurus-Littrow, only the lower power was used for the Apollo 17 conductivity experiment. After initiation, power is left on for 36

> 20 hr, the temperature rise $\Delta T(t)$ is well defined by the simple relationship

$$\Delta T(t) = c_1 \ln(t) + c_2 \qquad (9\text{-}5)$$

where c_1 and c_2 are constants. The form of equation (9-5) is the same as that for a heated infinite cylinder in an infinite homogeneous medium at long times (i.e., > 20 hr for a cylindrical source with a radius and heat capacity per unit length of the HFE probe/borestem system) (ref. 9-13).

For an infinite cylindrical source

$$c_1 = Q/4\pi k_m \qquad (9\text{-}6)$$

where Q is the power per unit length in W/cm. Thus, c_1 depends solely on the heater power per unit length and on conductivity. The constant c_1 can be determined easily because it is the slope of the temperature rise curve when plotted versus ln t; therefore, cylindrical sources are often used as a practical technique for measuring conductivity.

Conductivity is determined from lunar experiments by comparing observed slopes on a logarithmic time scale with values of c_1 calculated with the finite difference models. Parametric studies, in which certain thermal properties are varied singly in the numerical model, show that for times > 20 hr, c_1 is very nearly insensitive to changes in pc of the surrounding medium, changes in borestem conductance, and changes in the thermal links between the probe and borestem and the borestem and lunar medium. However, c_1 is sensitive to changes in conductance in the probe body, which can alter the flow of heat from the heater axially along the probe. Assumptions of thermal properties in the numerical models that influence axial heat transfer along the probe are probably the largest source of error in the conductivity determinations.

The similarity in performance of the lunar conductivity experiment and of an infinite cylindrical source is principally due to the relatively efficient flow of heat axially along the borestem. Even though the probe heater is very short (1.9 cm), it heats a section of borestem that is long compared to the borestem diameter. For times > 20 hr, the isotherms in the surrounding medium are roughly cylindrical in the vicinity of the heater as shown in figure 9-2. The numerical computations also show that the experiment is most sensitive to lunar material within approximately 5 cm of the borestem wall.
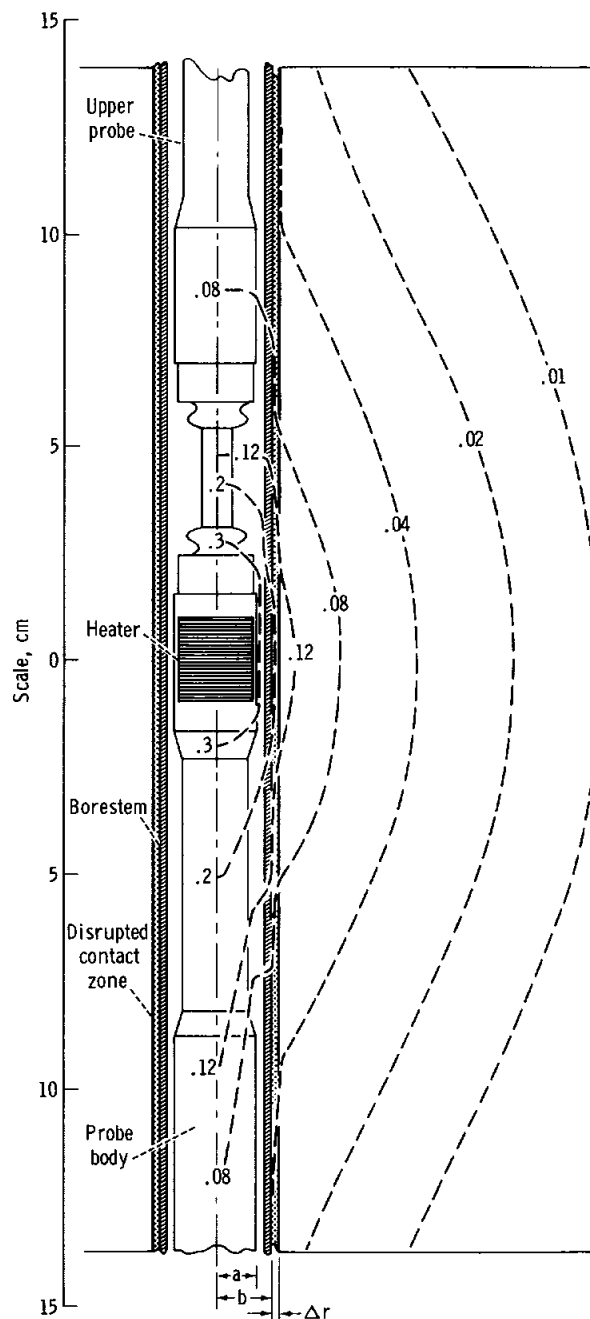
FIGURE 9-2.—The geometry of the probe, borestem, contact zone, and lunar regolith in the vicinity of a conductivity experiment. The dashed lines show surfaces of equal temperature rise in kelvins after the heater has been on for 36 hr. The model parameters are k_m = 2.4 × 10⁻⁴ W/cm-K and H_2 = 1.5 × 10⁻⁴ W/cm²-K.

The effective conductance of the contact zone has a pronounced effect on the magnitude of the sensor temperature rise at any given time. Because k_m can

be determined independently, the conductance of the contact zone is the principal remaining unknown parameter and can be determined by matching observed and theoretical temperature curves for times > 0.5 hr.

Variations in Surface Temperature and Its Effect at Depth

Lunar surface temperatures vary nearly 300 K from just before lunar dawn to lunar noon. This variation induces subsurface variations that propagate downward as thermal waves. For a homogeneous medium of diffusivity α with a sinusoidal variation $A_O \cos \omega t$ at the surface, the temperature at a given depth z is given by

$$T(t,z) = A_O e^{-\delta z} \cos(\omega t - \delta z) \qquad (9\text{-}7)$$

where A_O is the amplitude of the surface variation in degrees, ω is the angular frequency in rad/sec (2.5 $\times$ 10^{-6} for the diurnal variation and 2 $\times$ 10^{-7} for the annual variation), and

$$\delta = \sqrt{\frac{\omega}{2\alpha}} , \ cm^{-1} \qquad (9\text{-}8)$$

Equation (9-7) indicates that the variation decreases in amplitude by a factor e^{-1} and is delayed in phase 1 rad for every δ^{-1} centimeters of depth.

The propagation of surface temperature variations into the lunar regolith is more complex for a number of reasons. First, the surface variation is not a simple sinusoid but contains significant higher harmonics. Second, thermal properties vary significantly with depth; and third, radiative transfer, which depends on T^3, plays an important role in the upper few centimeters of the lunar soil. It is necessary to resort to numerical calculations that include these complications to determine the expected temperature variations in the subsurface. In figure 9-3, the peak-to-peak attenuation and phase lag of the diurnal variation are shown as a function of depth for the conductivity profile at the Apollo 17 heat flow site. The upper part of the conductivity profile is derived from surface temperature measurements that are described in the section entitled "Surface Temperatures Deduced From Thermocouple Measurements." For depths greater than a few centimeters, the amplitude decreases in a simple exponential fashion, as evidenced by the nearly straight line on a semilogarithmic scale. Similarly, the phase lag shows a
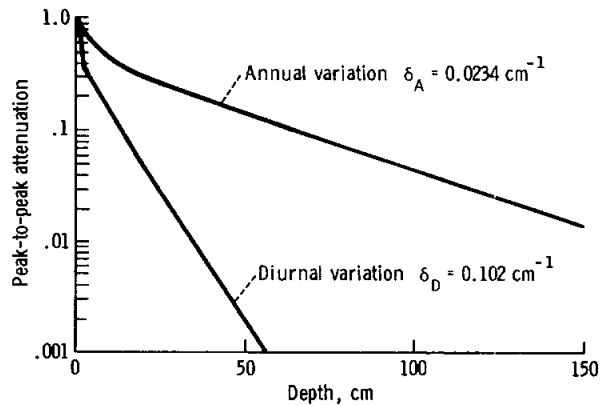
(a) The attenuation of the peak-to-peak amplitude of the diurnal and annual temperature with depth in the regolith. The δ in each equation is the effective decay constant deeper than 20 cm.
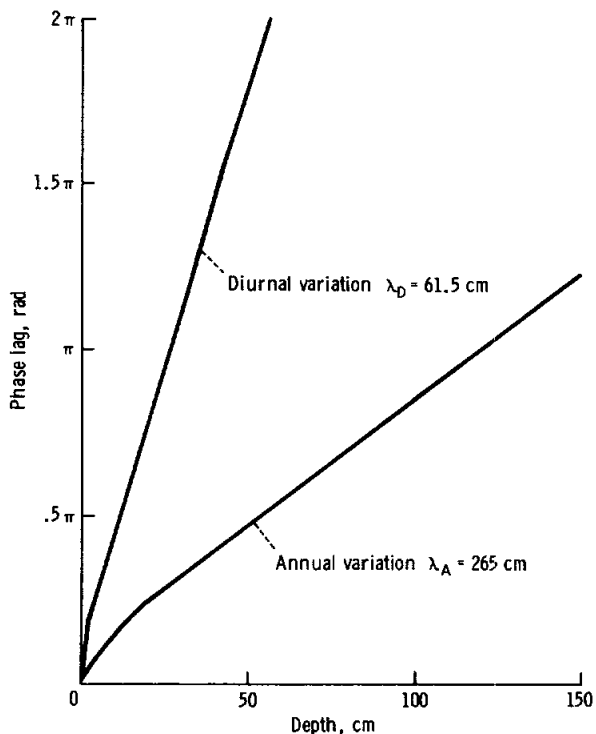
(b) Phase lag with depth. The values of λ are the wavelengths of the thermal wave below 20 cm. The model used for the diurnal variation is from Apollo 17 data. (See the section entitled "Surface Temperatures Deduced From Thermocouple Measurements.") The annual curves are calculated from a Rima Hadley thermal properties model (ref. 9-14).

FIGURE 9-3.—Peak-to-peak attenuation and phase lag as a function of depth.

nearly linear increase with depth below a few centimeters. Thus, the simple relationship of equation (9-7) would apply to a close approximation below these depths.

The temperature at lunar noon varies throughout the year because of the varying distance of the Earth-Moon system from the Sun. The noon temperature increases approximately 6 K from aphelion to perihelion. The mean temperature (i.e., surface temperature averaged over a lunation) varies approximately 3 K throughout a year. Although the amplitude of the annual cycle is one-hundredth of the diurnal variation, the decay constant δ is $\sqrt{12}$ times smaller; consequently, annual variations penetrate deeper and induce significant heat flows to depths of a few meters and must be considered in the interpretation of the experimental results. The attenuation of amplitude and the increase in phase lag for the annual wave are shown in figure 9-3 as a function of depth. Annual wave effects shown in figure 9-3 are based on the conductivity profile at Rima Hadley.

As shown in figure 9-3, temperature fluctuations attributable to the diurnal cycle become virtually undetectable at depths > 100 cm and would have had little effect on heat flow below this depth before the probe and borestem were emplaced. Once the borestem is emplanted in the regolith, the higher conductivity of the borestem and the radiative transfer inside the borestem will enhance the downward propagation of thermal waves. However, thermometers at 130 cm below the surface do not detect any temperature variation during a lunation cycle.

Corrections for the Shunting Effects of the Borestem and Probe

The axial conductance of the epoxy borestem is considerably higher than that of a vertical column of lunar soil of equal cross section. This fact, combined with the finite length of the borestem, results in some shunting of the steady-state heat flow through the borestem to the surface. Certain short sections of the borestem, such as the bit and joints, are made of titanium or steel, and sizable disturbances occur near these parts. A second related effect results from the fact that the probes are radiatively coupled to the borestem walls and have a small axial conductance. Consequently, the probe bridges register slightly smaller temperature differences than those registered at points on the borestem next to sensors.

These effects can be estimated by simplified analytical models and by laboratory experiments; both methods were used in the earlier analysis of the Apollo 15 results. However, for the Apollo 17 analysis and the refined Apollo 15 results presented in this report, a numerical model of the probe in a medium in which heat is flowing parallel to the probe axis has been used. The numerical model is more detailed and allows examination of certain combined effects that are difficult to estimate with analytical models.

The numerical model computations show that the borestem and probe disturbances to the steady-state heat flow are small. In the extreme case, the temperature difference across a probe section is 7 percent lower than the temperature difference across the same vertical distance interval far from the borestem. The numerical model has been used to apply corrections to all probe observations.

RESULTS

Apollo 17 Subsurface Temperatures

The HFE was turned on while probe 2 was being inserted into the borestem, and temperatures were recorded only minutes after drilling was completed. These temperatures ranged from 295 to 301 K. The early cooling histories of probe 1 indicate similar initial temperatures. After emplacement, the probes cool toward the undisturbed regolith temperatures. The temperature histories of all sensors deeper than 65 cm for the first 45 days are shown in figure 9-4. After 45 days, some sensors are continuing to cool; however, the expected future temperature decrease is probably less than the error of absolute temperature measurement.

The equilibrium temperature differences and the absolute temperatures of each sensor are listed in table 9-II. The correction for the steady-state disturbance of the heat flow by the borestem and probe system is applied to temperature data listed under the headings entitled "Corrected temperature difference" and "Corrected temperature." The appropriate corrections of the temperature difference attributable to the annual thermal wave during January 1973 (listed in the far right column) have not been applied because they are based on the conductivity profile at Rima Hadley. Note that the largest correction is approximately −4 percent.
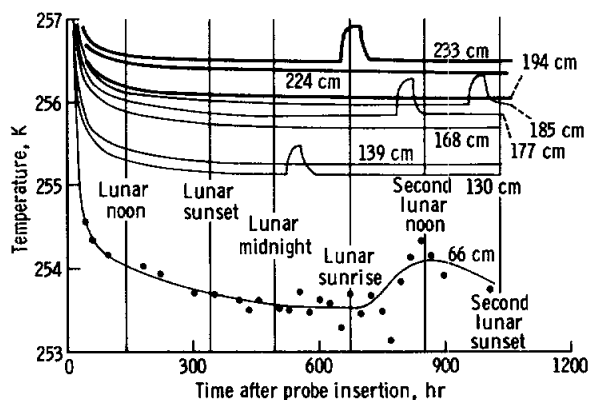
(a) Probe 1 (TC14).
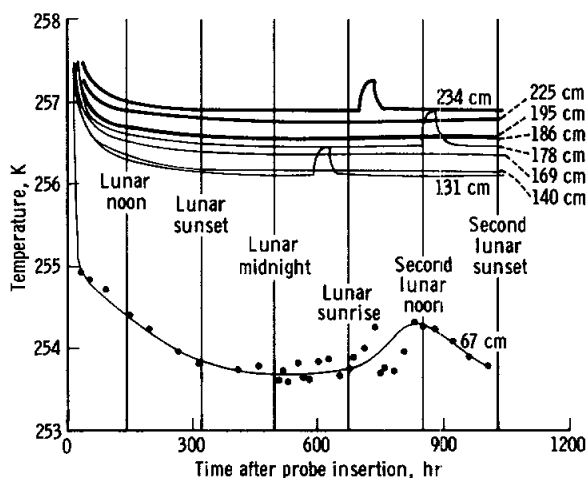
(b) Probe 2 (TC24).

FIGURE 9-4.—Apollo 17 temperature histories of all sensors 65 cm or deeper. The short pulses appearing on some of the sensor traces result from heater initiation for conductivity experiments. The numbers on each curve refer to the depths below the surface. The lowermost curves on each plot are TC4 thermocouple measurements. Some representative data points from the thermocouples are shown to indicate the scatter of these measurements. Temperatures shown are calculated by subtracting TC1 values from those of TC4 and adding them to the top gradient sensor temperature. The corrections given in table 9-III have not been added.

Temperature measurements of thermocouples TC14 and TC24 are also shown in figure 9-4. Some randomly sampled representative points are shown, and the solid curve is fitted visually to show the trend. The standard deviation of the points around

the smoothed curve is approximately 0.3 K during the day and about half that value during the night. The values shown are calculated by subtracting the temperature at TC1 from that at TC4 and adding the result to the temperature at the top gradient sensor.

Comparison of the temperatures measured by TC11 and TC21 with those at the top gradient sensors shows relatively large errors in absolute temperature measurement (table 9-III). The source of these errors has been traced to the copper/Kovar (Cu/Ko) junctions, in each thermocouple electronics circuit, that are mounted on circuit boards in the electronics housing. The errors are proportional to temperature differences between the Cu/Ko junctions. Thus, the errors in TC11 and TC21 are direct measures of this temperature difference and can be used to estimate errors at all junctions. The larger errors during the night result from larger temperature gradients across the Cu/Ko junctions at night, and the larger errors at probe 2 junctions are caused by the greater distance between the Cu/Ko junctions in the probe 2 circuit. A preliminary analysis of electromotive forces produced by Cu/Ko junctions was used to calculate the corrections that should be applied to the data in figure 9-4. These corrections virtually erase the apparent variation between night and day measurements. The corrections have been applied to the data compiled in table 9-II. The uncertainty of determining these corrections is estimated as ± 0.4 K. Studies of the accuracies of the thermocouple measurements are continuing.

The thermocouple temperatures given in table 9-II represent the averages of the values obtained during the time from lunar sunset of the first day to lunar sunset of the second day. The amplitude of the diurnal variation at 66 cm cannot be determined with the present accuracy of the data (± 0.5 K).

In figure 9-5, the equilibrium temperatures are plotted as a function of depth. Temperatures along the body of probe 1 show a steady decrease in gradient with depth. The gradient decreases from 0.016 K/cm in the depth range 130 to 177 cm to 0.012 K/cm in the range 185 to 233 cm. This decrease is principally due to a general increase in conductivity of the regolith over the interval of measurement. The thermocouple temperature indicates a gradient of 0.013 K/cm from 66 to 130 cm; however, the accuracy of this measurement is poor.

At probe 2, the probe thermometers at a depth range of 131 to 234 cm indicate a rather uniform

TABLE 9-II.—*Apollo 17 HFE Subsurface Temperature Data*

(a) Temperature difference measurements

Bridge	Interval, cm	Equilibrium temperature difference, K^a	Corrected temperature difference, K^b	Annual wave correction, K
Probe 1				
DTG11	130 to 177	0.707	0.755	− 0.027
DTR11	139 to 168	.435	.467	− .018
DTG12	185 to 233	.533	.559	− .001
DTR12	194 to 224	.322	.326	< .001
Probe 2				
DTG21	131 to 178	.370	.390	− .027
DTR21	140 to 169	.218	.223	− .018
DTG22	186 to 234	.336	.359	− .001
DTR22	195 to 225	.206	.212	< .001

[a]The error associated with extrapolating to equilibrium temperature differences is ± 0.003 K.
[b]The uncertainty introduced by these corrections is estimated to be ± 2 percent.

(b) Absolute temperature measurements

Sensor type	Depth, cm	Equilibrium temperature, K^a	Corrected temperature, K^b
Probe 1			
Thermocouple TC4	66	254.20	254.20
Platinum resistance	130	255.06	255.02
Platinum resistance	139	255.19	255.17
Platinum resistance	168	255.62	255.64
Platinum resistance	177	255.76	255.78
Platinum resistance	185	255.91	255.91
Platinum resistance	194	256.03	256.04
Platinum resistance	224	256.36	256.37
Platinum resistance	233	256.44	256.47
Probe 2			
Thermocouple TC4	67	254.70	254.70
Platinum resistance	131	256.07	256.05
Platinum resistance	140	256.09	256.09
Platinum resistance	169	256.31	256.31
Platinum resistance	178	256.44	256.44
Platinum resistance	186	256.48	256.48
Platinum resistance	195	256.52	256.51
Platinum resistance	225	256.73	256.73
Platinum resistance	234	256.82	256.84

[a]The accuracy of extrapolated absolute temperatures is ± 0.05 K for the platinum resistances.
[b]The correction for the annual wave to be applied to the thermocouple is 0.04 K.

gradient of 0.0078 K/cm, whereas the gradient between 67 and 131 cm is 0.021 K/cm, a change by a factor of approximately 3. This large variation of gradient can be accounted for only partially by the variation of conductivity of the regolith immediately surrounding the borestem.

Apollo 15 Subsurface Temperatures

Subsurface temperatures measured at Rima Hadley below the depth disturbed by diurnal variations were reported in reference 9-11 without correction for the annual wave. In addition, corrections for the bore-

TABLE 9-III.—*Errors and Corrections in Absolute Temperature Measurements*

Sensor	Lunar day	Lunar night
Error (compared with top gradient sensor TC1), K		
TC11	1.1	1.9
TC21	1.4	2.5
Estimated corrections,[a] K		
TC14	0.4	0.7
TC24	.6	1.2

[a]The uncertainty in determining these corrections is estimated as ± 0.4 K.

stem and probe disturbance were derived from much simpler models than those discussed herein. Temperatures measured at longer times after probe insertion are now available, and a more accurate determination of equilibrium temperatures is possible. The temperatures and temperature differences at four sensors on probe 1 at Rima Hadley are presented in table 9-IV. More accurate corrections for the borestem disturbance and a correction for the annual wave effect have been applied. These measurements will be the basis for a slightly revised heat flow value.

Conductivity Estimates from Cooldown Analysis

Because of the uncertainties in the total heat energy associated with drilling, two cases assuming different initial conditions have been examined. These cases have been described in the preceding section on theory. Results derived assuming initial borestem and contact zone temperatures to be equal to the initial probe sensor temperature are listed in table 9-V under the heading entitled "Conductivity with drill heating effects." Conductivity estimates derived assuming that only the borestem and probe were initially at elevated temperatures are listed under the heading entitled "Conductivity without drill heating effects." The two cases are considered to be bracketing assumptions of the actual initial conditions. Cooldown conductivity estimates were made for each of the eight sensors along each probe. Additionally, cooldown analyses were performed assuming drill heating effects for the thermocouples located 65 cm above each probe.
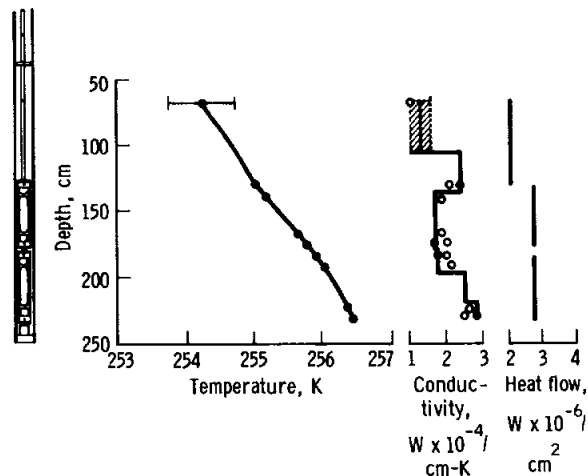
(a) Probe 1.
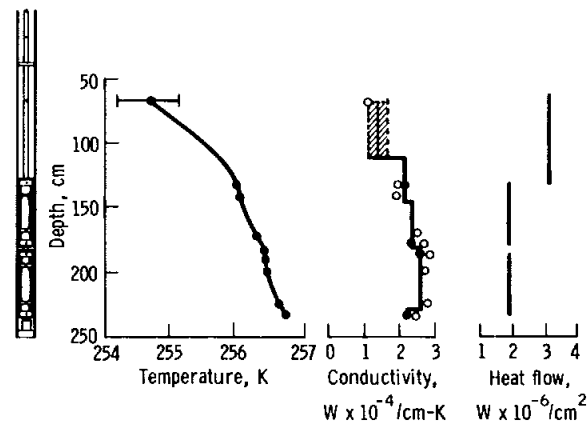
(b) Probe 2.

FIGURE 9-5.—Equilibrium temperatures, conductivities, and heat flows measured by the Apollo 17 probes. The open circles on the conductivity plot are calculated from cooldown curves assuming maximum drilling energy, and the solid circles are heater-activated experiment results. The solid line represents a layered model used for calculating heat flow. In the heat flow figure, the solid lines give heat flow over the three largest intervals. The geometry of the probe in the subsurface is shown at the far left.

The large noise on the thermocouple data limits the accuracy of conductivities deduced from the cooling history. Deductions of the conductivity at depths from 3 to 15 cm below the surface, which will be discussed later in this section, give values of approximately 1.2×10^{-4} W/cm-K. Based on these results at shallow depths, we estimate the conductivity lies in the range 1.0×10^{-4} to 1.6×10^{-4}

TABLE 9-IV.—*Apollo 15 HFE Subsurface Temperature Data*

(a) Temperature difference measurements

Bridge	Interval, cm	Equilibrium temperature difference, K	Corrected temperature difference, K[a]	Annual wave correction, K
Probe 1				
DTG12	91 to 138	0.803	0.833	− 0.37
DTR12	100 to 129	.484	.479	− .28

(b) Absolute temperature measurements

Sensor type	Depth, cm	Equilibrium temperature, K	Corrected temperature, K
Probe 1			
Platinum resistance	91	252.20	252.16
Platinum resistance	100	252.33	252.33
Platinum resistance	129	252.81	252.81
Platinum resistance	138	253.00	253.01

[a]The effect of the annual wave on Sept. 29, 1971, has been removed.

TABLE 9-V.—*Conductivities from Cooldown Histories*

Sensor depth	Heater location	Conductivity with drill heating effects, $W \times 10^{-4}/cm\text{-}K$	Conductivity without drill heating effects, $W \times 10^{-4}/cm\text{-}K$
Probe 1			
66		1.0	—
130	H11	2.3	1.3
139		1.9	1.1
168		1.9	1.1
177	H12	2.0	1.0
185	H13	1.9	1.1
194		2.1	1.1
224		2.8	1.4
233	H14	2.7	1.6
Probe 2			
67		1.0	—
131	H21	2.0	1.2
140		2.0	1.1
169		2.4	1.3
178	H22	2.7	1.7
186	H23	2.9	1.7
195		2.7	1.5
225		2.8	1.5
234	H24	2.5	1.5

W/cm-K at 66 cm. This range is indicated in figure 9-5.

By comparison with the more accurate heater-activated conductivity determinations discussed in the next section, it is evident that drill heating effects cannot be neglected if reliable conductivity information is to be extracted from the cooldown data. When substantial drill heating effects are included in the cooldown analyses, conductivity determinations and variations with depth agree well with the heater-activated conductivity experiment results. The cooldown conductivity estimates are particularly valuable in interpolating between the more accurate heater-activated conductivity determinations.

Heater-Activated Conductivity Experiments

Conductivity experiments at each of the eight heater locations have been performed. Figure 9-6 shows the sensor temperature rise history and theoretical curves for one such experiment. The conductivities k_m and contact conductances H_2 are given in table 9-VI. These results and the cooldown estimates with drill heating effects are shown in figure 9-5. It is clear that the conductivity does not vary in any simple way with depth.
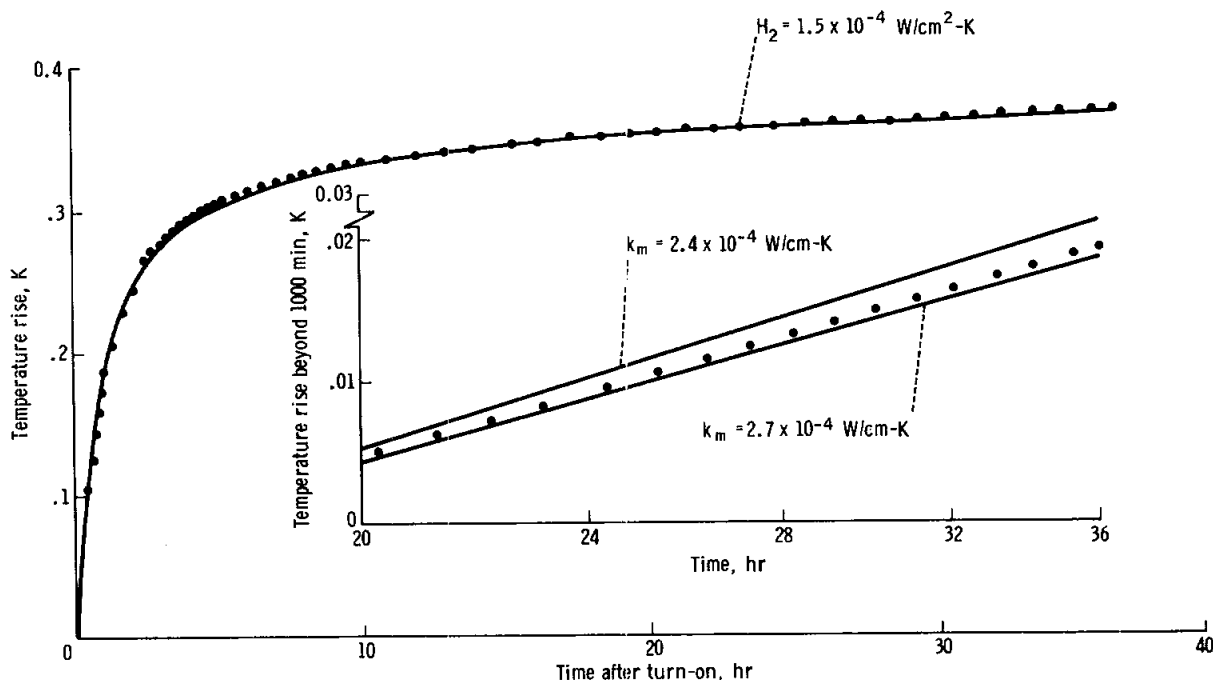
FIGURE 9-6.—Temperature rise during a conductivity experiment (dots) is compared with a theoretical curve derived from a model with $k_m = 2.7 \times 10^{-4}$ W/cm-K and $H_2 = 1.5 \times 10^{-4}$ W/cm²-K. In the inset, the temperature rise for times > 1000 min is shown on an expanded scale plotted against the logarithm of time. The observed data are compared with two bracketing theoretical curves. The reduced conductivity is 2.64 W/cm-K.

A rough correlation exists between the drill penetration rate during borestem drilling and the measured conductivity. The more resistant layers where the drill penetrated slowly correspond to depths where higher conductivity is observed. The more resistant layers likely correspond to more compacted regolith materials or possibly to a higher concentration of centimeter-size rock fragments. Either of these phenomena can increase the bulk conductivity. The relatively high conductivity measured at 130 cm on probe 1 lies within a zone from 80 to 130 cm where penetration was slow. Directly below this layer, drilling rates were relatively high and the conductivity values are correspondingly lower. These correlations are used to interpolate values between discrete measures. In figure 9-5, the solid line that passes through the heater-activated conductivity values represents a layered model of conductivity in the regolith based partly on penetration rates and partly on cooldown estimates. At probe 2, some of the drilling operation was not visually monitored so that correlations with conductivity cannot be made during the unmonitored period, which includes

approximately half the depth range where probe 2 is emplaced.

One interesting feature of these conductivity results is a rather large difference between the conductivity profiles at probe 1 and probe 2. It is possible that layers, as defined by conductivity, have some dip relative to the surface. For example, the high conductivity layer at 100 cm at probe 1 could correspond to the high conductivity layer between 170 and 230 cm at probe 2.

The contact conductance H_2 arises from low conductivity material lying in a disturbed zone just outside the borestem. We estimate this zone to be 2.2 mm thick. The conductivity k_c of material in the contact zone is given by

$$k_c = H_2\left(b + \frac{\Delta r}{2}\right)\ln\left(\frac{b + \Delta r}{b}\right) \qquad (9\text{-}9)$$

(See fig. 9-2 for definition of parameters in this equation.) As an example, for $H_2 = 1.4 \times 10^{-4}$ W/cm²-K, $k_c = 3.0 \times 10^{-5}$ W/cm-K. This value of conductivity is approximately a factor of 6 less than that of the surrounding regolith.

TABLE 9-VI.—*Results of the Conductivity Experiments*

Heater location	Depth, cm	Conductivity,[a] $W \times 10^{-4}$ /cm-K	Contact conductance,[b] $W \times 10^{-4}$ /cm²-K
Apollo 17 probe 1			
H11	130	2.50	1.4
H12	177	1.72	1.6
H13	185	1.79	1.4
H14	233	2.95	1.2
Apollo 17 probe 2			
H21	131	2.06	1.6
H22	178	2.36	1.1
H23	186	2.64	1.5
H24	234	2.24	2.3
Apollo 15 probe 1			
H11	35	1.41	0.8
H12	83	2.11	.8
H13	91	1.60	.9
H14	138	2.50	1.0
Apollo 15 probe 2			
H23	49	1.46	0.5
[c]H24	96	2.43	.6

[a]The estimated error of conductivity measurement is ± 15 percent.

[b]Estimated error is ± 20 percent. In the theoretical model the thickness of the contact zone is 2 mm.

[c]It is probable that a section of broken borestem lies just outside this location so that the uncertainty of this measurement is very large.

Apollo 15 Results

Six conductivity experiments using a heater power of 0.002 W were performed on the Apollo 15 probes. The analyses of three of these measurements were not described in reference 9-11 because it was very difficult to separate changes attributable to heater turn-on from large diurnal variations in temperature. Subsequently, two of the measurements have been repeated at times in the lunation when the rate of temperature change at the heater location was minimal. In addition, the diurnal temperature variation from preceding and succeeding lunations is available to help interpolate trends during the time that the heater is on. Lastly, some refinements have been made in the finite difference models of the conduc-

tivity experiments. The newer models indicate small adjustments in the previously published values. The revised Apollo 15 conductivity values at each heater location are given in table 9-VI.

Heat Flow

The magnitude of the vertical component of heat flow in the regolith can be calculated from the temperature and conductivity profiles in figure 9-5. Over each depth interval z_1 to z_2

$$F_z = k_{ave} \frac{\Delta T_{z_1 - z_2}}{z_2 - z_1} \qquad (9\text{-}10)$$

where $\Delta T_{z_1 - z_2}$ is the corrected temperature difference listed in tables 9-II and 9-IV and k_{ave} is the average conductivity in the depth interval $z_1 - z_2$ calculated from the layered models in figure 9-5.

Gradients, average conductivities, and heat flows calculated from the Apollo 15 and Apollo 17 results are presented in table 9-VII. The heat flow data over the entire depth range of temperature measurement

TABLE 9-VII.—*Heat Flow Data*

Depth interval, cm	Temperature gradient, K/cm	Average conductivity, $W \times 10^{-4}$ /cm-K	Heat flow, $W \times 10^{-6}$ /cm²
Apollo 17 probe 1			
66 to 130	0.0130	1.60	2.10
130 to 177	.0158	1.79	2.83
139 to 168	.0163	1.72	2.80
185 to 233	.0118	2.39	2.81
194 to 224	.0113	2.48	2.81
66 to 233	.0140	1.80	2.50
Apollo 17 probe 2			
67 to 131	0.0210	1.50	3.10
131 to 178	.0082	2.26	1.86
140 to 169	.0078	2.30	1.79
186 to 234	.0076	2.50	1.89
195 to 225	.0074	2.53	1.87
67 to 234	.0130	2.00	2.50
Apollo 15 probe 1			
91 to 138	0.0175	1.78	3.11
100 to 129	.0166	1.68	2.82

are presented on the bottom lines of table 9-VII for
Apollo 17 probes 1 and 2. At probe 1, the most
representative value of heat flow (2.8 × 10^{-6}
W/cm^2) is thought to be that determined by the
probe data over the interval 130 to 233 cm. At probe
2, the measurement is possibly disturbed, as will be
discussed in the next section, and the most represen-
tative value (2.5 × 10^{-6} W/cm^2) is that calculated
using data between 67 and 234 cm. The heat flow
calculated over the interval 91 to 138 cm is believed
to be the best value from the Apollo 15 measure-
ments.

At the Apollo 17 probe 1 site, the heat flow is
quite uniform over the entire depth range. The
variation falls well within the estimated error of
measurement. Probe 2 results show a uniform heat
flow along the length of the probe, but heat flow
between 67 and 131 cm is 70 percent greater. The
large change in gradient is partly compensated for by
an increase in conductivity with depth. The overall
heat flow of 2.5 × 10^{-6} W/cm^2 is in fair agreement
with the probe 1 value of 2.8 × 10^{-6} W/cm^2.

DISCUSSION OF HEAT FLOW RESULTS

The Probe 2 Measurements

The change in heat flow at probe 2 by a factor
slightly less than 2 over the depth range of 67 to 234
cm is most reasonably explained by refraction of heat
flow in the vicinity of a large buried boulder. A
relatively large number of rocks are strewn over the
ALSEP area. Lunar basalts have conductivities of
approximately 1.2 × 10^{-2} to 1.8 × 10^{-2} W/cm-K at
250 K (ref. 9-15). These values are 60 to 90 times the
conductivity of the fine-grained regolith material.
Thus, large blocks of solid rock in the subsurface can
result in significant shunting of heat flow.

To illustrate the shunting effect, the distortion of
heat flow lines and isotherms around and through a
square of material having 60 times the conductivity
of a surrounding infinite medium is shown in figure
9-7. The model is two-dimensional and symmetric at
the left margin of the figure. One significant feature
of the model is that very little effect is evidenced at
distances greater than one-half of the width of the
rock. Thus, heat flow measurements would have to be
made quite close to a rock (less than one-fourth of
the width) to detect a disturbance as large as that at
probe 2. However, probe 2 must be more than 5 cm
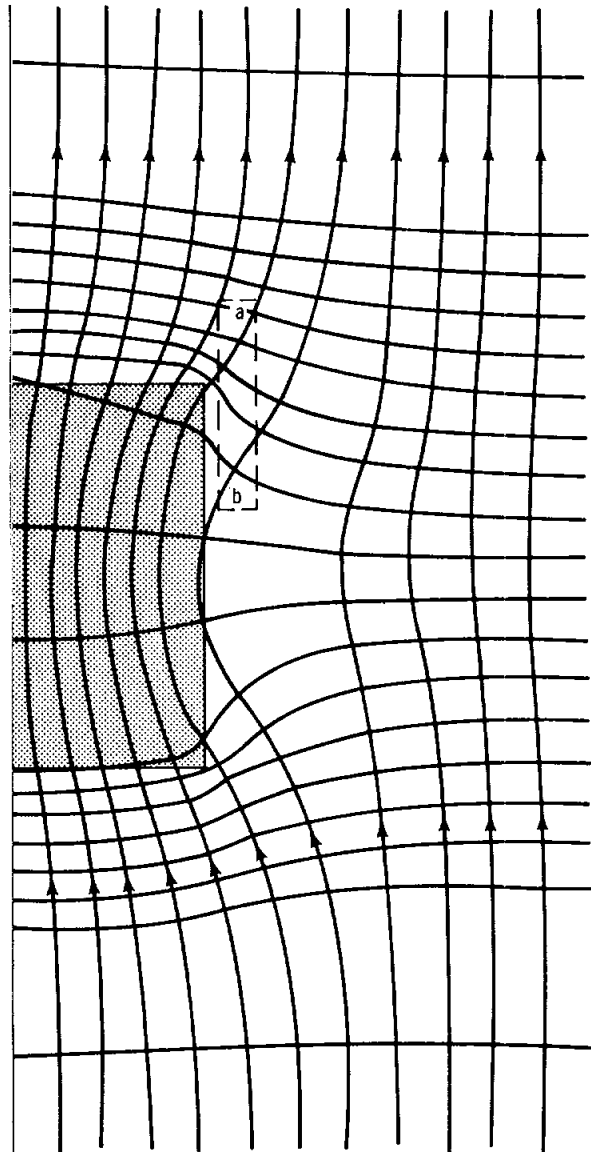
FIGURE 9-7.—The effect of a square of material on vertical
heat flow (shaded area) which has a conductivity 60 times
that of the surrounding material, shown by the distortion
of isotherms and flow lines. These results are based on a
finite difference model computation.

from a rock in order for the rock not to have a
detectable effect on the heater-activated conductivity
experiments.

If probe 2 were located relative to a large
subsurface boulder in a zone defined by the dashed
rectangle in figure 9-7, a temperature profile similar
to that observed would result. Other features such as

tion coefficient for the lunar-surface/space interface.

For the very low electrical conductivities found in the lunar regolith, the electromagnetic penetration depth $\ell_e(\lambda)$ may be written for the centimeter wave spectral region as

$$\ell_e(\lambda) = \lambda/(2\pi\sqrt{\epsilon}\ \tan\ \Delta) \qquad (9\text{-}12)$$

where ϵ is the dielectric constant and $\tan\ \Delta$ is the loss tangent at centimeter wavelengths.

The average temperature gradient of 0.017 K/m measured in situ at the Apollo 15 and 17 sites would produce the observed spectral gradient if $\sqrt{\epsilon}\ \tan\ \Delta \cong$ 0.003, assuming $R = 0.05$. The feasibility of such a value for $\sqrt{\epsilon}\ \tan\ \Delta$ is supported by direct surface observations in the 0.4- to 3-cm wavelength range (ref. 9-19). Direct measurements of returned Apollo samples over a wide range of frequencies indicate a dielectric constant for the regolith material in the range 2.2 to 3.2 that is nearly frequency independent.

However, loss tangent measurements yield values in the range 0.0004 to 0.01 and are frequency dependent (refs. 9-20 and 9-22). Additional electrical property measurements and refined analysis of the existing data on regolith samples must be made before the thermal gradient measured in situ can be supported on a moonwide basis by the spectral gradient observations.

The Representativeness of the Two Heat Flow Measurements

The regional geological settings of Rima Hadley and Taurus-Littrow are quite similar. Both are located on lava-flooded embayments at the edge of mascon basins. If the heat flow is influenced by structural or compositional anomalies unique to this type of region, the anomalies would affect both measurements. To that extent, they would not be representative of global flux from the Moon. However, the

FIG. 9-8.—Photograph of probe 2 borestem protruding from the lunar surface. The heat flow experiment housing is in the background. The thermocouple is in the black portion of cable approximately 10 cm from the top of the stem (AS17-134-20492).

possible compatibility of the results with the microwave emission spectral gradient between 5- and 20-cm wavelengths lends support to the possibility that local anomalies at the two sites are not large.

Despite the reservations in the previous paragraphs, the existing data concerning heat flow from the lunar interior indicate that a significant area of the Moon is characterized by a flux of between 2.5 and 3.0 μW/cm^2. Numerous thermal history calculations have shown that the contribution of initial heat (e.g., that gained during accretion) to the present surface flux is relatively small (refs. 9-11 and 9-23) even if the Moon were molten throughout initially. Some scientists have suggested that, at the present time, the Moon is thermally at steady state (e.g., ref. 9-24). In either case, it follows that a predominant part of the surface flux (2.0 to 3.0 μW/cm^2) must result from radioactive isotopes in the Moon. The geochemical data are convincing that most of these isotopes are concentrated in the outer layers of the Moon. In addition, the abundances indicated by the heat flow values would require the heat sources to be located near the surface to prevent melting in the outer several hundred kilometers.

The radiogenic heat production per cubic centimeter of rock can be expressed in terms of the abundance of uranium, because the ratios of the other important long-lived, heat-generating isotopes (^{40}K and ^{232}Th) to uranium are well established and quite uniform in the lunar samples. The heat production per unit volume at the present time in W/cm^3 is approximately 0.71 times the uranium abundance in parts per million (e.g., refs. 9-23 and 9-25). If most of the uranium is concentrated within 300 km of the surface so that it contributed to the present flux, then the total lunar uranium abundance required to contribute 2.0 to 3.0 μW/cm^2 to the heat flow is approximately 0.05 to 0.075 ppm. These abundances are much greater than chondrites and significantly higher than estimates of the Earth abundance of approximately 0.03 ppm (ref. 9-4).

SURFACE TEMPERATURES DEDUCED FROM THERMOCOUPLE MEASUREMENTS

At each of the two heat flow holes, one of the thermocouples is embedded in a section of the cable that is approximately 15 cm from the top of the borestem and suspended above the lunar surface as shown in figure 9-8. These thermocouples, in radiative balance with the lunar surface, with the solar flux, and with space, thus provide a measurement of the surface brightness temperature throughout the lunation. The flux balance equation governing the thermocouple temperature is

$$2\pi a_c dl \epsilon_c \sigma T_c^4 = 2\pi a_c dl F_{c-m} \epsilon_m \alpha_{cir} \sigma T_m^4$$
$$+ 2a_c dlS\alpha_{cs} \sqrt{1 - p^2}$$
$$+ 2\pi a_c dlSA\alpha_{cs} F_{c-m} \cos \lambda \sin \phi$$

$$(9-13)$$

where T_c = thermocouple temperature

T_m = lunar surface brightness temperature

a_c = radius of thermocouple cable

dl = elemental length of cable

ϵ_c = infrared emissivity of cable

α_{cir} = infrared absorptivity of cable

α_{cs} = absorptivity of cable to solar flux

F_{c-m} = view factor of cable to the lunar surface, including the surrounding mountains

p = cosine of the angle between the Sun line and the cable axis, a function of cable orientation and lunar phase angle

λ = selenographic latitude at Taurus-Littrow

ϕ = lunar phase angle measured from local sunrise

ϵ_m = infrared emissivity of the lunar surface ($\cong 1.0$)

S = the mean solar constant of 0.1352 W/cm^2

A = lunar albedo of 0.08

σ = the Stefan-Boltzmann constant

The first term on the right side of equation (9-13) represents flux into the cable element from the lunar surface; the second term represents direct flux from the Sun; the third term represents solar energy reflected diffusely from the lunar surface and impinging on the cable.

The radiative properties of the cable ϵ_c, α_{cir}, and α_{cs} were determined by laboratory measurement before the Apollo 17 mission. The cable orientations for both probe locations were determined from ALSEP photographs.

Solving equation (9-13) for the surface brightness temperature yields

core penetration rates and surface disturbance caused by crew activity reported by J. Mitchell (personal communication, 1972) of the Apollo 15 soil mechanics team. The density profile for the Apollo 17 site was determined from preliminary examination of returned core tube samples (D. Carrier, personal communication, 1973). In both the Apollo 15 and 17 models, the heat capacity as a function of temperature was taken from Robie et al. data (ref. 9-29) on returned Apollo 11 samples. In both models, a low conductivity layer approximately 2 cm thick is required to fit the steep drop in surface temperature immediately after sunset. The Apollo 15 model then requires a steep, but not discontinuous, rise in conductivity with depth down to 5 cm to produce the increased flattening of the cooldown curve through the lunar night. The Apollo 17 model, however, requires a very sharp rise in conductivity at a depth of approximately 2 cm to produce the abrupt flattening of the cooldown curve at a phase angle of approximately 190°. The subsequent increase in conductivity with depth is slight enough so that the Apollo 17 model may be considered essentially a two-layer model. The large jump in conductivity at 2 cm is also supported by the preliminary density profile, which indicates a fairly high density quite close to the surface. The Apollo 15 density profile, however, supports the possibility that a substantial conductivity gradient exists over the upper 30 cm of the regolith.

The most critical surface temperature data required for the purpose of determining thermal regolith profiles are those obtained during the 10 to 30 hr immediately after sunset. Surface temperature data during this period have been the most difficult to obtain from remote infrared brightness scans. The level and steepness of the cooldown data immediately after sunset are controlled almost entirely by the thermal properties of the upper 2 cm. If the very early nighttime data are not sufficiently accurate to constrain the thermal properties of the upper 2 to 3 cm of the dust layer within ± 30 percent, then subsequent attempts to determine deeper conductivity values unambiguously from the flattened part of the cooldown curve will not be possible. For example, the broken-line curve of figure 9-10 fits the nighttime data after 192° phase angle well within the error bands of the data. However, discrepancies in the early postsunset fit produced by different conductivities within the upper 2 cm lead to discrepancies as

much as a factor of 2 in conductivity determinations for depths below 2 cm (curve 17a, fig. 9-10 inset).

CONCLUSIONS

During the Apollo missions, two heat flow measurements were successfully made on the lunar surface. Both measurement sites are in similar regional settings in the northeast quadrant of the Moon. The Taurus-Littrow and Rima Hadley sites are located in embayments in the mountainous rims of the Imbrium and Serenitatis mascon basins that have been flooded by mare-type basalts.

Surface brightness temperatures were calculated from the temperature of thermocouples suspended several centimeters above the lunar surface. The mean surface temperature at Rima Hadley throughout a lunation cycle is 207 K. The mean temperature increases with depth very rapidly in the upper few centimeters and is approximately 252 K at a depth of 90 cm. The main reason for this increase of 45 K is the predominant role of radiative heat transfer in the loosely packed upper layer. During the lunar night, the surface temperature at Rima Hadley falls to 93 K. From the cooldown history after sunset, we have deduced that the upper 2 cm of the regolith is characterized by a conductivity of 1.5×10^{-5} W/cm-K. Below this depth, the conductivity increases rapidly and probably in a continuous manner until it reaches values of approximately 1.5×10^{-4} W/cm-K at depths where the probes are emplaced.

At Taurus-Littrow, the mean surface temperature is 216 K and, as in the case of Rima Hadley, increases a few tens of degrees in the upper 2 cm so that, at a depth of 67 cm, a mean temperature of 254 K is measured. The minimum temperature just before lunar dawn is 103 K, 10 K higher than that at Rima Hadley. This higher temperature is primarily attributable to the existence of a relatively high conductivity layer at a depth 2 cm below the surface. From the point of view of thermal properties, the regolith at Taurus-Littrow can be described as two layers: an upper 2-cm, loosely packed layer of very low conductivity (1.5×10^{-5} W/cm-K) in which heat transfer by radiation predominates and a lower layer with much higher conductivity ($> 1.2 \times 10^{-4}$ W/cm-K) and higher density (1.8 to 2.0 g/cm³).

Subsurface temperature and conductivity measurements at depths below 90 cm, where the large diurnal variations are negligibly small, indicate a steady-state

heat flow through the surface at Rima Hadley of 3.1 X 10^{-6} W/cm^2 and at Taurus-Littrow of 2.8 X 10^{-6} W/cm^2 with an estimated error of ± 20 percent. These fluxes are deduced from average temperature gradients in the regolith between 1.3 and 1.7 K/m and an average conductivity in the range of 1.7 X 10^{-4} to 2.0 X 10^{-4} W/cm-K. Conductivity generally increases with depth in the regolith although some layering, with high conductivity materials overlying lower conductivity materials, is found at both sites (table 9-VI). A conductivity value of almost 3 X 10^{-4} W/cm-K was measured at the bottom of probe 1 at the Apollo 17 site. Thermal gradients decrease with depth, in some cases, in response to the increase in conductivity. At Taurus-Littrow probe site 2, a large decrease in gradient with depth is possibly attributable to a large subsurface boulder in close proximity to the probe.

The heat flows at both sites are affected to some extent by local topography. Preliminary estimates indicate that a correction of −15 to −25 percent may be applicable to the Taurus-Littrow values because of the adjacent massifs. However, a more refined analysis is required.

The heat flow measured at the two sites is approximately one-half the average heat flow of the Earth (6.3 X 10^{-6} W/cm^2). If these two values are representative of heat flow from the Moon as a whole, then a heat flow of one-half that of the Earth requires a heat production per unit mass for the lunar interior of more than twice that of the Earth. This statement assumes both planetary bodies are near steady state so that total surface heat loss is nearly equal to the present interior heat production.

Because the long-lived radioisotopes of ^{40}K, ^{235}U, ^{238}U, and ^{232}Th are the principal source of heat in the Earth and Moon, the heat flow results imply a twofold to threefold enrichment of uranium in the Moon relative to that in the Earth. Lunar samples show that the abundance of potassium relative to uranium is one-third to one-fourth that of the Earth so that, in the Moon, uranium is the main contributor to internal heating. At present, these isotopes must be concentrated in the outer 100 to 200 km of the Moon to avoid extensive melting at shallow depth.

Reinterpretation of Earth-based measurements of microwave brightness temperatures using the new data on regolith thermal and electrical properties will be important in determining the representativeness of the in situ lunar heat flow measurements. Additional,

more refined microwave observations of the Moon, especially narrower beamed measurements over discrete portions of the lunar disk, would be valuable in determining possible variations of heat flow over the lunar surface.

ACKNOWLEDGMENTS

REFERENCES

9-1. Lee, W. H. K.; and Uyeda, S.: Review of Heat Flow Data. Terrestrial Heat Flow, American Geophysical Union (Washington, D.C.), 1965, pp. 68-190.

9-2. Urey, H. C.: Proc. Natl. Acad. Sci. U.S., vol. 42, 1956, p. 889.

9-3. Gast, P. W.: Limitations on the Composition of the Upper Mantle. J. Geophys. Res., vol. 65, no. 4, Apr. 1960, pp. 1287-1297.

9-4. Wasserburg, G. J.; MacDonald, G. J. F.; Hoyle, F.; and Fowler, W. A.: Relative Contributions of Uranium, Thorium, and Potassium to Heat Production in the Earth. Science, vol. 143, no. 3605, Jan. 31, 1964, pp. 465-467.

9-5. Langseth, M. G., Jr.; and Von Herzen, R. P.: Heat Flow Through the Floor of the World Oceans. The Sea, vol. 4, part I, 1971, pp. 299-352.

9-6. Latham, G. V.; Ewing, M.; Press, R.; Sutton, G.; et al.: Passive Seismic Experiment. Sec. 9 of the Apollo 16 Preliminary Science Report. NASA SP-315, 1972.

9-7. Baldwin, J. E.: Thermal Radiation from the Moon and the Heat Flow Through the Lunar Surface. Monthly Notices, Roy. Astron. Soc., vol. 122, 1961, pp. 513-522.

9-8. Krotikov, V. D.; and Troitskii, V. S.: Detecting Heat Flow from the Interior of the Moon. Soviet Astron., vol. 7, no. 6, May/June 1964, pp. 822-826.

9-9. Tikhonova, T. V.; and Troitskii, V. S.: Effect of Heat from Within the Moon on Its Radio Emission for the Case of Lunar Properties Which Vary with Depth. Soviet Astron., vol. 13, no. 1, July/Aug. 1969, pp. 120-128.

9-10. Smith, B. D.: The Lunar Heat Flow Experiment. Bendix Tech. J., vol. 4, no. 2, 1971, pp. 64-79.

9-11. Langseth, M. G., Jr.; Clark, S. P., Jr.; Chute, J. L., Jr.; Keihm, S. J.; and Wechsler, A. E.: Heat-Flow Experiment. Sec. 11 of the Apollo 15 Preliminary Science Report. NASA SP-289, 1972.

9-12. Langseth, M. G., Jr.; Drake, E. M.; Nathanson, D.; and Fountain, J. A.: Development of an In Situ Thermal Conductivity Measurement for the Lunar Heat Flow Experiment. Thermal Characteristics of the Moon. AIAA Progress in Astronautics and Aeronautics Series, vol. 28, MIT Press (Cambridge, Mass.), 1972, pp. 169-204.

9-13. Jaeger, J. C.: Conduction of Heat in an Infinite Region Bounded Internally by a Circular Cylinder of a Perfect Conductor. Australian J. Phys., vol. 9, no. 2, June 1956, pp. 167-179.

9-14. Keihm, S. J.; Chute, J. L.; Peters, K.; and Langseth, M. G., Jr.: Apollo 15 Measurement of Lunar Surface Brightness Temperatures: Thermal Conductivity of the Upper 1-1/2 Meters of Regolith. Earth Planet. Sci. Letters, vol. 19, no. 3, July 1973.

9-15. Horai, K.; Simmons, G.; Kanamori, H.; and Wones, D.: Thermal Diffusivity and Conductivity of Lunar Material. Science, vol. 167, no. 3918, Jan. 30, 1970, pp. 730-731.

9-16. Buhl, D.; Welch, W. J.; and Rea, D. G.: Anomalous Cooling of a Cratered Lunar Surface. J. Geophys. Res., vol. 73, no. 24, Dec. 15, 1968, pp. 7593-7608.

9-17. Lachenbruch, A. H.: Rapid Estimation of the Topographic Disturbance to Superficial Thermal Gradients. Rev. Geophys., vol. 6, no. 3, Aug. 1968, pp. 365-400.

9-18. Metzger, A. E.; Trombka, J. I.; Peterson, L. E.; Reedy, R. C.; and Arnold, J. R.: Lunar Surface Radioactivity: Preliminary Results of the Apollo 15 and Apollo 16 Gamma-Ray Spectrometer Experiments. Science, vol. 179, no. 4075, Feb. 23, 1973, pp. 800-803.

9-19. Weaver, H.: The Interpretation of Thermal Emissivity from the Moon. Solar System Radio Astronomy, Plenum Press, (New York) 1965, pp. 295-354.

9-20. Gold, T.; O'Leary, B. T.; and Campbell, M.: Some Physical Properties of Apollo 12 Lunar Samples. Proceedings of the Second Lunar Science Conference, vol. 3, MIT Press (Cambridge, Mass.), 1971, pp. 2173-2184.

9-21. Katsube, T. J.; and Collett, L. S.: Electrical Properties of Apollo 11 and Apollo 12 Lunar Samples. Proceedings of the Second Lunar Science Conference, vol. 3, MIT Press (Cambridge, Mass.), 1971, pp. 2367-2379.

9-22. Strangway, D. W.; Chapman, W. B.; Olhoeft, G. R.; and Carnes, J.: Electrical Properties of Lunar Soil Dependence on Frequency, Temperature, and Moisture. Earth Planet. Sci. Letters, vol. 16, no. 2, Oct. 1972, pp. 275-281.

9-23. Hanks, T. C.; and Anderson, D. L.: Origin, Evolution, and Present Thermal State of the Moon. Phys. Earth Planet. Interiors, vol. 5, no. 5, Oct. 1972, pp. 409-425.

9-24. Turcotte, D. L.; Hsui, A. T.; Torrance, K. E.; and Oxburgh, E. R.: Thermal Structure of the Moon. J. Geophys. Res., vol. 77, no. 35, Dec. 10, 1972, pp. 6931-6939.

9-25. Hays, J. F.: Radioactive Heat Sources in the Lunar Interior. Phys. Earth Planet. Interiors, vol. 5, no. 1, Jan. 1972, pp. 77-84.

9-26. Watson, K. I.: Thermal Conductivity Measurements of Selected Silicate Powders in Vacuum from 150-350 K, II. An Interpretation of the Moon's Eclipse and Lunation Cooling Curve as Observed Through the Earth's Atmosphere from 8-14 Microns. Ph.D. Dissertation, California Institute of Technology, 1964.

9-27. Cremers, C. J.; and Birkebak, R. C.: Thermal Conductivity of Fines from Apollo 12. Proceedings of the Second Lunar Science Conference, vol. 3, MIT Press (Cambridge, Mass.), 1971, pp. 2311-2315.

9-28. Linsky, J. L.: Models of the Lunar Surface Including Temperature-Dependent Thermal Properties. Icarus, vol. 5, no. 6, Nov. 1966, pp. 606-634.

9-29. Robie, R. A.; Hemingway, B. S.; and Wilson, W. H.: Specific Heats of Lunar Surface Materials from 90 to 350 Degrees Kelvin. Science, vol. 167, no. 3918, Jan. 30, 1970, pp. 749-750.

10. Lunar Seismic Profiling Experiment

Robert L. Kovach,[a][†] *Joel S. Watkins,*[b]
and Pradeep Talwani[a]

The successful installation of a geophysical station at the Taurus-Littrow landing site of the Apollo 17 mission marked the culmination of an exciting period of manned lunar exploration and vastly improved current knowledge of the lunar interior. Before the Apollo 17 mission, there was a gap in our knowledge concerning the upper 10 km of the lunar crust because of the large hiatus in pertinent traveltime data between the coverage provided by the previous active seismic experiments on Apollo 14 and 16 and that of the earlier lunar module (LM) and SIVB impacts. In particular, it was not possible to resolve whether the seismic velocity increased smoothly or stepwise in the upper 5 km of the Moon.

The purpose of the Apollo 17 lunar seismic profiling experiment (LSPE) was to record the vibrations of the lunar surface as induced by explosive charges, by the thrust of the LM ascent engine, and by the crash of the LM ascent stage. Analyses of these seismic data were planned to determine the internal characteristics of the lunar crust to a depth of several kilometers. The traveltimes of seismic waves are inverted to determine the seismic velocity structure with depth and to provide the direct means of probing the lunar interior. A secondary objective of the LSPE was to monitor lunar seismic activity during periodic listening intervals.

Strong seismic signals were recorded from the detonation of eight explosive charges that were armed and placed on the lunar surface by the crewmen at various points along the traverses. Recording of these seismic signals generated traveltime data to a distance of 2.7 km.

One of the more significant events of the Apollo 17 mission was the recording of the seismic signals from the LM ascent stage, which struck the lunar

surface 8.7 km southwest of the landing site. The characteristic reverberation from this impact spread outward and was first detected at the Apollo 17 station approximately 6 sec after impact. The seismic signals received from this impact provided a valuable traveltime datum for determining the variation of seismic velocity with depth in approximately the upper 5 km of the Moon.

The most significant discovery resulting from the analysis of the data recorded by the LSPE is that the seismic velocity increases in a marked stepwise manner beneath the Apollo 17 landing site (fig. 10-1). A surface layer with a seismic velocity of 250 m/sec and a thickness of 248 m overlies a layer with a seismic velocity of 1200 m/sec and a thickness of 927 m, with a sharp increase to approximately 4000 m/sec at the base of the lower layer. The seismic velocities for the upper layers are compatible with those for basaltic lava flows, indicating a total thickness of approximately 1200 m for the infilling mare basalts at Taurus-Littrow. Major episodes of deposition or evolution are implied by the observed abrupt changes in seismic velocity.

INSTRUMENT DESCRIPTION AND PERFORMANCE

The LSPE consists of a geophone array, eight explosive packages, and electronics within the Apollo lunar surface experiments package (ALSEP) central station. Four identical geophones are used in a triangular array; the geophones are miniature seismometers of the moving coil-magnet type. The coil is the inertial mass suspended by springs in the magnetic field. Above the natural resonant frequency of the geophones (7.5 Hz), the output is proportional to ground velocity. The LSPE geophone array was deployed without difficulty in the nominal configuration at the Apollo 17 site approximately 148 m

---

[a]Stanford University.
[b]The University of Texas at Galveston.
[†]Principal Investigator.
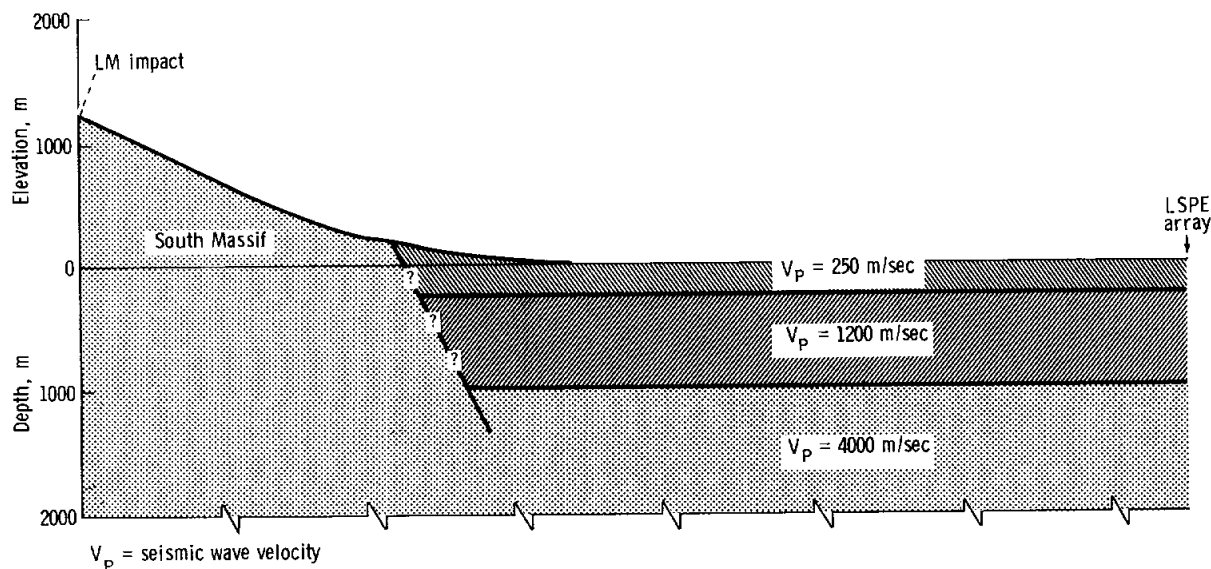
FIGURE 10-1.—Seismic cross section at the Taurus-Littrow landing site (no vertical exaggeration).

west-northwest of the LM (fig. 10-2). Figure 10-3 is a photographic panorama from geophone 2 to the LM as viewed from geophone 3.

A four-channel amplifier and a logarithmic compressor condition the geophone signals before conversion into a digital format for telemetering to Earth. Because the LSPE signal levels are distributed throughout the dynamic range of the system, logarithmic compression is used. This compression gives signal resolution as some constant fraction of signal amplitude. The logarithmic compressor used in the LSPE has the transfer function

$$V_{out} = \pm M \ln \left| V_{in} \right| + b' \qquad (10\text{-}1)$$

where V is voltage, the constant M determines the slope of the transfer function, and b' is specified by the dc offset of the compressor output and the system noise level. The values of M and b' are determined by calibration of the system to provide at least 6-percent accuracy of the data referenced to the level of the input signal. The properties of the LSPE system are listed in tables 10-I and 10-II, and the nominal frequency response is shown in figure 10-4. The output of the logarithmic compressor is referenced to 2.5 V dc.

The analog output of the logarithmic compressor is converted to a 7-bit binary element in the LSPE control electronics by an analog-to-digital converter
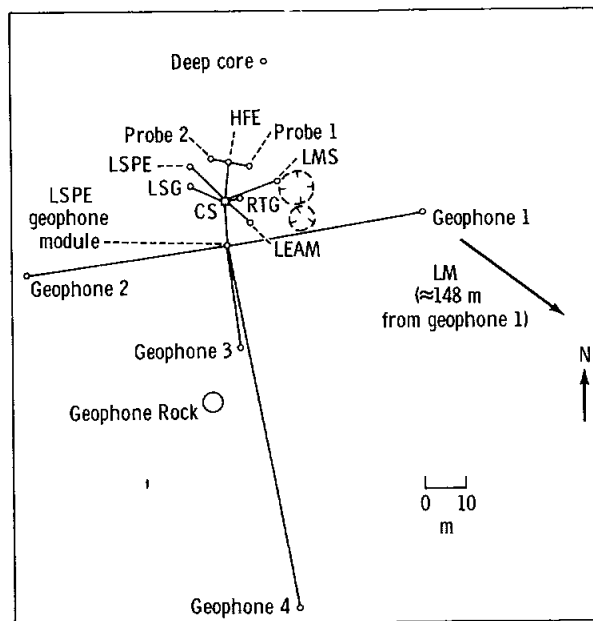
Key: CS = central station
HFE = heat flow experiment
LEAM = lunar ejecta and meteorites experiment
LMS = lunar mass spectrometer
LSG = lunar surface gravimeter
RTG = radioisotope thermoelectric generator

FIGURE 10-2.—The LSPE nominal deployment.

FIGURE 10-3.—Panorama from geophone 2 to the LM as viewed from behind geophone 3 (AS17-147-22546, 22548, 22550, 22552, 22554).

TABLE 10-I.—*Apollo 17 LSPE Characteristics*

Component characteristics	Channel no.			
	1	*2*	*3*	*4*
Amplifiers:				
Noise level, mV rms at input	0.75	0.75	0.83	0.83
Dynamic range, rms signal to rms noise				
in dB at 10 Hz	73.4	76.2	75.6	75.8
Geophones:				
Resistance, ohm	5970	5953	6080	6153
Generator constant, V/m/sec at 40 Hz . .	235.6	239.2	237.1	235.3
Natural frequency, Hz	7.38	7.31	7.40	7.35
System:				
Signal-to-noise ratio (rms signal to rms noise in dB for a 6-nm rms signal at 10 Hz)	24.4	26.9	26.8	26.8
Amplitude sensitivity (measured at input to log compressor), V/μm of peak-to-peak ground displacement at 10 Hz . .	7.33	7.02	7.12	7.13

TABLE 10-II.—*LSPE System Sensitivity*

Frequency, Hz	Sensitivity, V/μm			
	Channel 1	*Channel 2*	*Channel 3*	*Channel 4*
1	0.1	0.1	0.1	0.1
2	.7	.8	.8	.8
3	1.7	1.7	1.7	1.7
4	2.4	2.5	2.5	2.5
6	4.3	4.2	4.3	4.3
8	6.0	5.8	5.9	5.8
10	7.3	7.0	7.1	7.1
15	10.9	10.5	10.6	10.6
20	13.2	12.8	12.8	13.0

and transmitted to Earth through the ALSEP communications network. The 7-bit binary encoding provides for an amplitude resolution of 1.277 dB ($\approx$16 percent). Each geophone channel is sampled 118 times/sec to provide a minimum of 5 samples/sec at a frequency of 20 Hz.

Digital Portions of the LSPE

The data format used is shown in figure 10-5. A data frame consists of three subframes, each consisting of twenty 30-bit words. The first word of each subframe consists of one 10-bit synchronous word
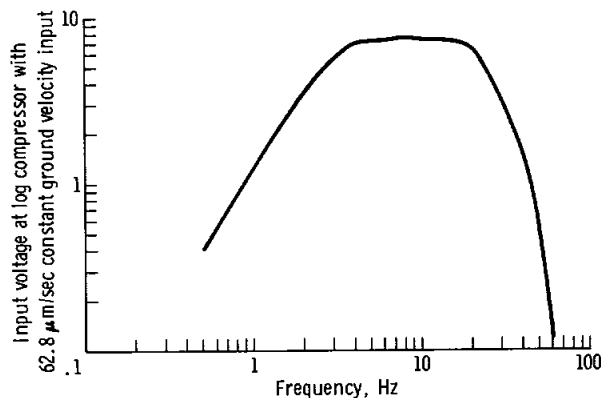
FIGURE 10-4.—Nominal frequency response of the LSPE.
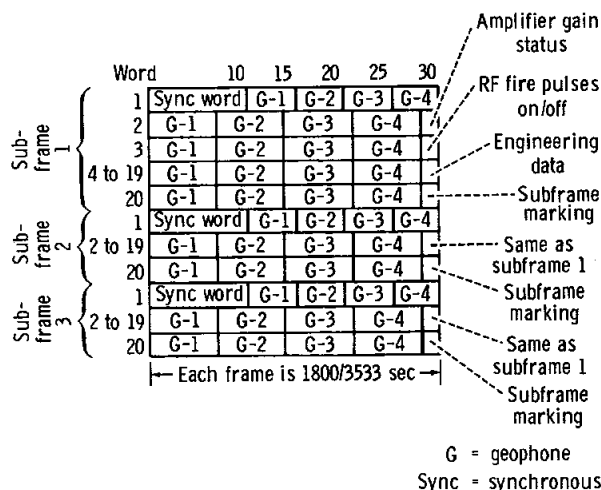
FIGURE 10-5.—The LSPE data format. Each data frame consists of three subframes of twenty 30-bit words each. Geophone data words are normally 7 bits long except for those in word 1, which are 5-bit samples.

Notes: (1) Pull ring 1 – pulls one pin to start SAFE/ARM slide timer

(2) Pull ring 2 – swing up ring; rotate 90° counterclockwise; pull pin to release SAFE/ARM plate

(3) Pull ring 3 – pulls two pins to free firing pin and start thermal battery timer

FIGURE 10-6.—Arming sequence for an LSPE explosive package.

and one 5-bit seismic data sample from each of the four seismic data channels. Words 2 to 20 of each subframe are 7-bit samples from each of the four seismic data channels. Engineering data are interleaved and subcommutated, using the remaining 2 bits to form 30-bit words.

In words 2 to 19, geophone samples are sampled on the bit preceding the word on which they are read out; the most significant bit is read out first. In the first word of each subframe, the timing of the data sampling is the same as that in words 2 to 19 except that the samples are stored and read out in the last 20 bits with one 5-bit word/channel.

The time of the RF fire pulses must be accurately known. When the LSPE is commanded to the fire

pulses "on" mode, a fire pulse set is transmitted once every 29.55 sec and is flagged in word 3 of subframe 1. This occurs once every 58 frames.

A command system provides for 11 commands associated with the LSPE. Two commands turn the LSPE on and off; two commands control the bit rate; and two commands control down-link formatting. In addition, commands are used to control amplifier gain status, transmission of fire pulses, and calibration of the geophones.

Explosive Package Description and Performance

An LSPE explosive package is shown in figure 10-6. The eight explosive packages are identical

except for the amount of high explosive and the preset runout time of the mechanical timers. An explosive package is activated by removing three pull pins (fig. 10-6). Removal of the first pull pin activates the SAFE/ARM slide timer, which is preset at 89.75, 90.75, 91.75, or 92.75 hr. Removal of the second pull pin releases the SAFE/ARM slide from its constrained SAFE position. Removal of the third pull pin removes a constraint on the firing pin and activates the thermal battery timer.

The LSPE transmitter, which is located within the ALSEP central station, transmits a repetitive pulsed carrier signal. A series of three pulses properly spaced in time is required to elicit a FIRE signal from the signal processor within the explosive package and to detonate the explosives train. The thermal battery, activated by the timer, has a minimum life of 2 min. This 2 min provides a time window long enough to ensure that at least one fire pulse set is received while

the explosive package is energized electrically. Because the seismic data subsequently collected must be accurately referenced to the instant of detonation, it is necessary to establish which specific set of pulses is effective. This is done by comparing known times of pulse-set transmission with the time of arrival at the geophones of the initial seismic data. Pulse sets are spaced at 29.55-sec intervals to make such identification possible without ambiguity.

No difficulty was experienced in the deployment of the explosive packages during the periods of extravehicular activity (EVA) (fig. 10-7). The 454-g explosive package (EP-6) was deployed at station 1, and the 227-g explosive package (EP-7) was positioned on the return to the LM from station 1. Explosive packages 4, 1, and 8 were armed and placed on the lunar surface during the second EVA. During the third EVA, explosive packages 3, 5, and 2 were deployed. It was necessary to place the 1361-g
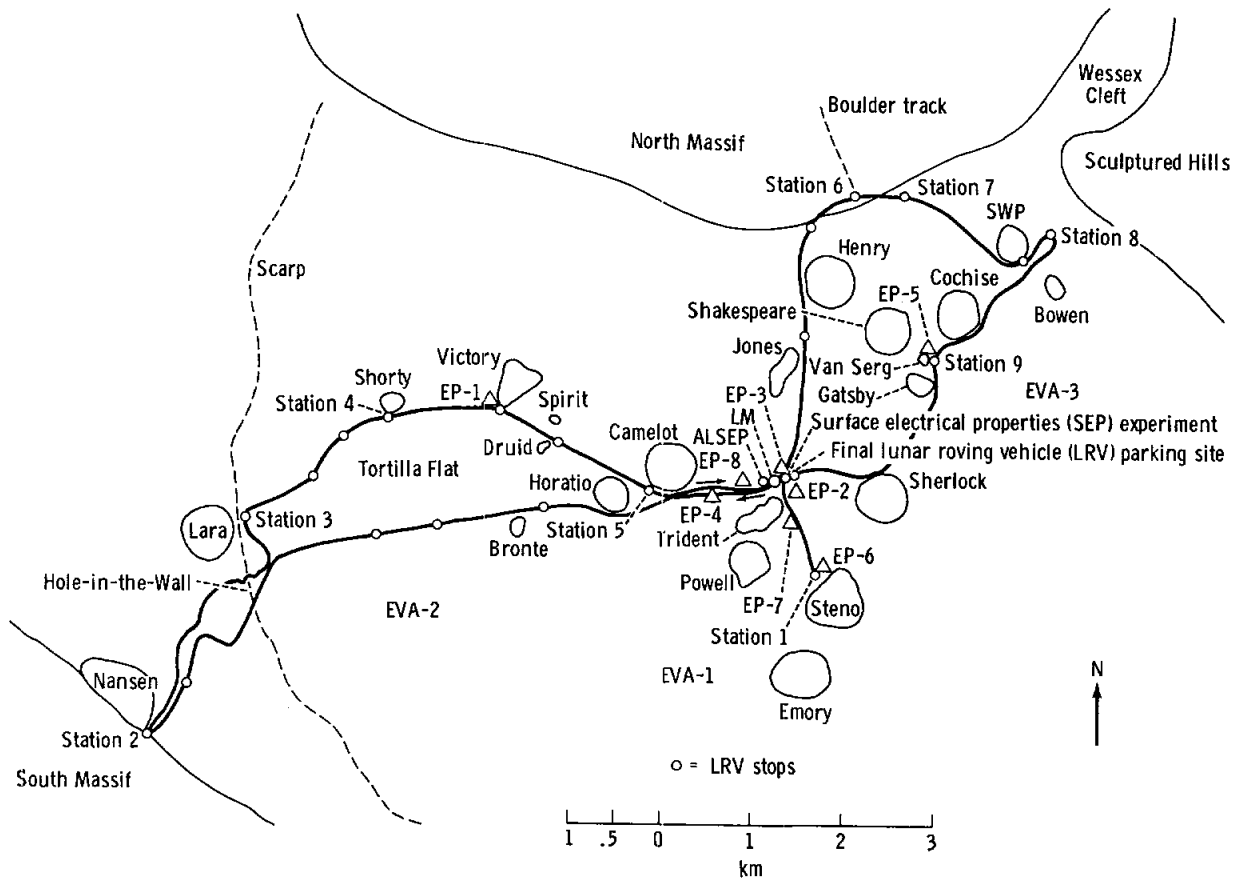
FIGURE 10-7.—Extravehicular activity traverses showing positions of deployed explosive packages at the Apollo 17 landing site.

explosive package (EP-5) at station 9 when it became apparent that insufficient time remained for a visit to the crater Sherlock. All the explosive packages were successfully detonated (table 10-III), and the detonation of EP-7 was visible from the television camera on the lunar roving vehicle (LRV). Figure 10-8 is a photograph showing EP-8 on the lunar surface approximately 296 m west of the LM.

DESCRIPTION OF RECORDED SEISMIC SIGNALS

The Apollo 17 LSPE was planned to contribute to the understanding of the shallow lunar structure in two major ways: (1) by providing traveltimes of the seismic signals from explosive packages, which were to be detonated on the lunar surface at distances ranging from 100 to 2700 m, to the LSPE geophone array and (2) by impacting the Apollo 17 LM at a nominal distance of 10 km to provide traveltime data for deciphering the variation of seismic velocity with depth in the upper 5 km of the Moon. In addition, monitoring of the seismic signals generated by the LM ascent engine at lunar lift-off provided useful data.

Lunar Module Ascent

The LSPE was commanded on at 22:24:00 G.m.t. on December 14, 1972, to record the impulse produced by the thrust of the LM ascent engine. The effective zero time for the seismic impulse from the LM ascent-engine ignition was determined from NASA postflight analyses, which gave engine buildup pressure data at 5-msec intervals for the LM lift-off. The assigned ignition time of 22:54:38.424 G.m.t.
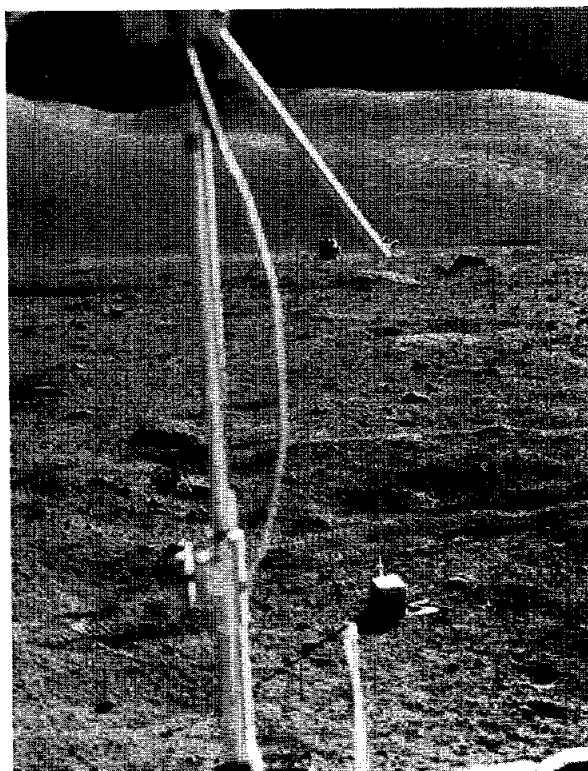
FIGURE 10-8.—Photograph of EP-8 on the lunar surface 296 m west of the LM (AS17-145-22184).

TABLE 10-III.—*Detonation Times of Explosive Packages*

Charge no.	Explosive weight, g (lb)	Date, 1972	Time, G.m.t.
EP-6	454 (1)	Dec. 15	23:48:14.56
EP-7	227 (1/2)	Dec. 16	02:17:57.11
EP-4	57 (1/8)	Dec. 16	19:08:34.67
EP-1	2722 (6)	Dec. 17	00:42:36.79
EP-8	113 (1/4)	Dec. 17	03:45:46.08
EP-5	1361 (3)	Dec. 17	23:16:41.06
EP-2	113 (1/4)	Dec. 18	00:44:56.82
EP-3	57 (1/8)	Dec. 18	03:07:22.28

corresponds to the time when the LM ascent engine achieved 20 percent of its maximum propulsion pressure. Clear seismic signals were recorded by the LSPE geophone array at distances of 148, 244, 190, and 187 m (fig. 10-9). Interpretation of the traveltime data is presented in the subsection entitled "Shallow Lunar Structure."

Lunar Module Impact

The LSPE was commanded on at 06:36:00 G.m.t. on December 15 to record the LM ascent-stage impact. The impact occurred at latitude 19.91° N, longitude 30.51° E, 8.7 km southwest of the Apollo 17 landing site. Other pertinent parameters for the LM impact are given in table 10-IV.

A portion of the seismic signal from the Apollo 17 LM impact is shown in figure 10-10 in a compressed time scale. The impact signal is similar in character to previous impact signals; that is, these signals have an emergent beginning and a long duration. The initial portion of the impact signal on an expanded time

FIGURE 10-9.—Seismic signals recorded by the LSPE geophones from the lift-off of the Apollo 17 LM ascent stage (Dec. 14). Arrows point to onset of the first seismic arrival.

TABLE 10-IV.—*Parameters of Apollo 17 LM Impact*

Parameter	Value
Day, G.m.t.	Dec. 15, 1972
Range time,[a] G.m.t., hr:min:sec	06:50:20.84
Real time, G.m.t., hr:min:sec	06:50:19.60
Velocity, km/sec	1.67
Mass, kg	2260
Kinetic energy, J	3.15×10^9
Heading, deg	283

[a]Range time is the time the signal of the event was observed on Earth.

scale is shown in figure 10-11. The arrival time of the first compressional wave (P-wave) is marked at 06:50:25.35 G.m.t., giving a traveltime of 5.75 sec.

The amplitude of the impact signal is of interest when compared with the P-wave amplitudes for previous LM and SIVB impact signals. Comparison of previous LM impact and SIVB impact signal amplitudes demonstrated that the LM impact data had to be adjusted upward by a factor of 17.4 to allow for the lower kinetic energy and a shallower angle of impact. Extrapolating the earlier LM impact data to a distance of 8.7 km leads to a predicted peak-to-peak amplitude of 26 nm. The Apollo 17 LM impact signal is centered at 4 Hz and has a measured peak-to-peak amplitude of 400 nm. This amplitude was caused by
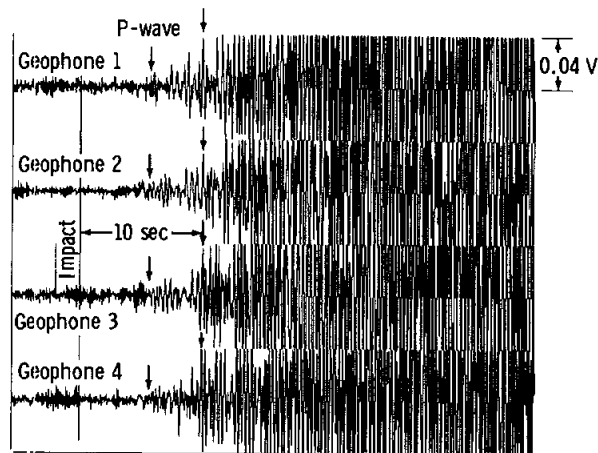
FIGURE 10-10.—Compressed time-scale record of the seismic signal received from the Apollo 17 LM impact (Dec. 15). Arrows point to measured first and second seismic arrivals.

the Apollo 17 LM ascent stage striking the side of the mountainous South Massif rather than grazing the lunar surface. In other words, if the predicted amplitude of 26 nm is multiplied by the factor 17.4, the resulting figure is 452 nm, which agrees well with the observed amplitude of 400 nm. The LM impact traveltime data are discussed in the subsection entitled "Shallow Lunar Structure."

P-wave 06:50:25.35 G.m.t.
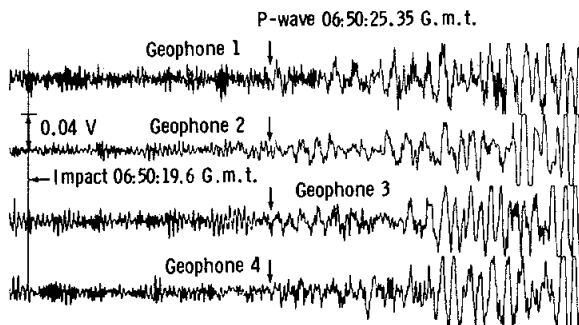
FIGURE 10-11.—Expanded time-scale record of the seismic signal from the Apollo 17 LM impact.

Begins at 23:16:23.027 G.m.t.

FIGURE 10-12.—Seismic signals produced by detonation of EP-5 on the lunar surface (Dec. 17). Arrows point to onset of seismic arrival.

Analyses of previous lunar seismic impact signals (ref. 10-1) have demonstrated that many of their characteristics (signal rise time, duration of signal, and lack of coherence between horizontal and vertical components of motion) can be explained by wave scattering. Seismic energy is considered to spread with a diffusivity ξ proportional to the product of the average seismic velocity and the mean distance between scattering centers; that is, the larger the value of diffusivity, the smaller the amount of scattering. For a surface impact, the theory predicts (ref. 10-1) that the signal rise time (the time from signal onset to its maximum value) is given by R^2/ξ where R is the range.

The Apollo 17 LM impact seismic signal rise time of 56 sec leads to a diffusivity of 1.35 km^2/sec, which is significantly larger than the value of 0.033 km^2/sec inferred at the Apollo 16 site (ref. 10-2) from analysis of the seismic signals generated by the LRV at distances of approximately 4 km. The implication is that the Apollo 17 landing area is more homogeneous, for the dimensions of the seismic waves considered (approximately 25 m), than either the Apollo 15 or 16 landing areas. Such a difference in near-surface properties of these landing sites may be attributable to differing ages of the different areas and to the effects of differing amounts of comminution and gardening by meteoroid impacts.

Explosive Packages

All eight of the explosive packages placed on the lunar surface were successfully detonated. The seismic data recorded for EP-5, which was detonated at station 9, are shown in figure 10-12. The arrows point to the measured onset of the first seismic arrival.

Transmissions of the fire pulses at 29.55-sec intervals from the LSPE antenna (fig. 10-2) were observable as crosstalk on the individual geophone data channels and produced convenient, accurate references for selecting the detonation time of the individual explosive packages.

The locations of the explosive packages with respect to the LSPE geophone array were taken from preliminary postmission analyses (refs. 10-3 and 10-4). Adjustments in the absolute distances of the explosive packages will undoubtedly be necessary when subsequent analyses of the appropriate Apollo 17 lunar surface photographs are completed. However, it is not anticipated that any revisions in the distances will have a major effect on the traveltime data discussed in the following subsection.

SHALLOW LUNAR STRUCTURE

The traveltime/distance data obtained from the detonation of the eight explosive packages are shown in figure 10-13. Two sets of seismic wave first arrivals were observed traveling at velocities of 250 and 1200 m/sec. The shortest explosive-charge-to-geophone distance was approximately 100 m. If a seismic velocity of 100 m/sec is assumed for the regolith at the Apollo 17 site, a regolith as thick as 25 m would not have been detected. The depth of penetration of seismic waves is nominally one-fourth the explosive-charge-
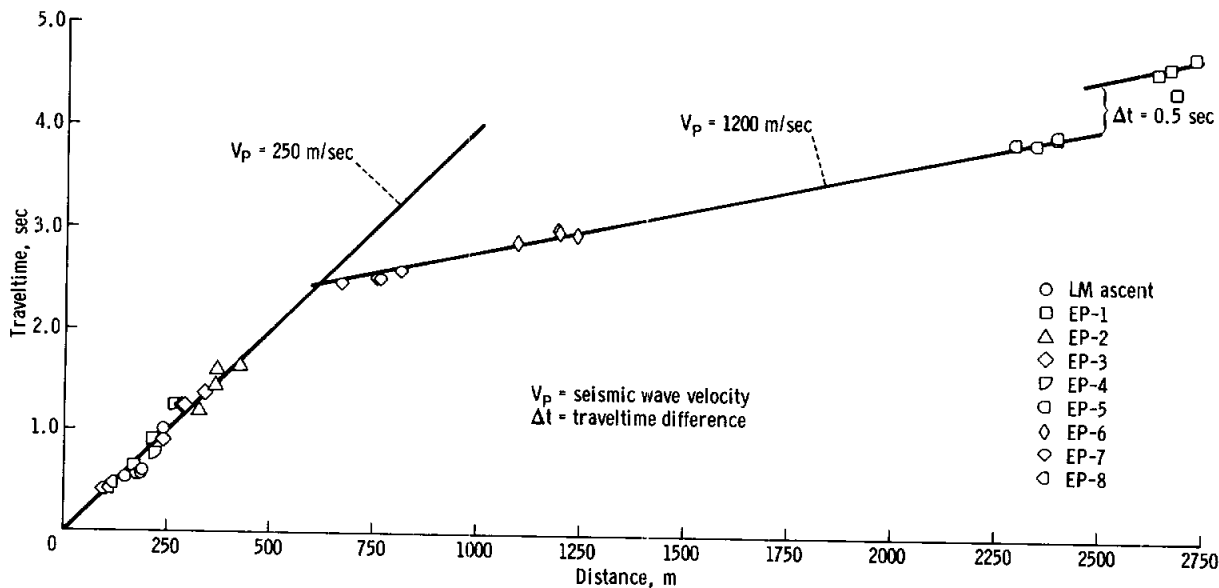
FIGURE 10-13.—Seismic arrivals from the detonation of the explosive charges plotted on a traveltime/distance graph.

to-receiver distance. However, it is probable that the regolith is significantly thinner than 25 m, inasmuch as the 250-m/sec velocity curve extrapolates to a zero intercept time.

The faster seismic arrival with a velocity of 1200 m/sec was observed beginning at a distance of 612 m, indicating that the thickness of the 250-m/sec material was 248 m. Considering uncertainties in the charge distances and in the inferred seismic velocities, the depth estimates are considered accurate to 10 percent. The 1200-m/sec velocity was observed to a distance of approximately 2.5 km. At this distance, the observed traveltimes for EP-1 were offset by approximately 0.5 sec with respect to the 1200-m/sec line.

Examination of the path between EP-1 and the LSPE geophone array revealed that the seismic path was affected by the presence of the 600-m-diameter crater Camelot. The observed time delay on the seismic path can be explained by postulating that low-velocity material extends to a greater depth beneath the crater Camelot than along the remainder of the traveltime path. A simple model approximation for Camelot Crater that explains the observed traveltime delay is shown in figure 10-14.

The traveltime data from the LSPE explosive charges can be combined with the observed traveltime for the LM impact to provide information about the
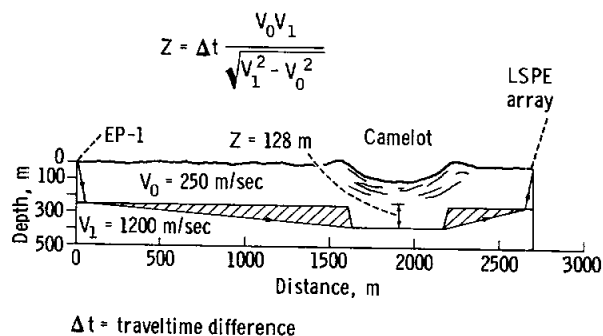
FIGURE 10-14.—Model approximation for seismic ray path from EP-1 to LSPE array that crosses Camelot Crater. Observed time delay is produced by presence of low-velocity material (of thickness Z) beneath crater.

seismic velocity to a depth of several kilometers. Traveltime data from the seismic signals produced by the LM impact and the explosive charges are shown in figure 10-15. A line with an apparent velocity of 4 km/sec can be fitted through the LM impact data point to intersect close to the corrected traveltime data point for EP-1. Because of obvious uncertainties in allowing for the time delay through the crater Camelot, there is no a priori reason to force a specific apparent-velocity line through the EP-1 data point. The first-order conclusion is that high-velocity material ($\approx$4 km/sec) must lie beneath the 1200-m/sec material.
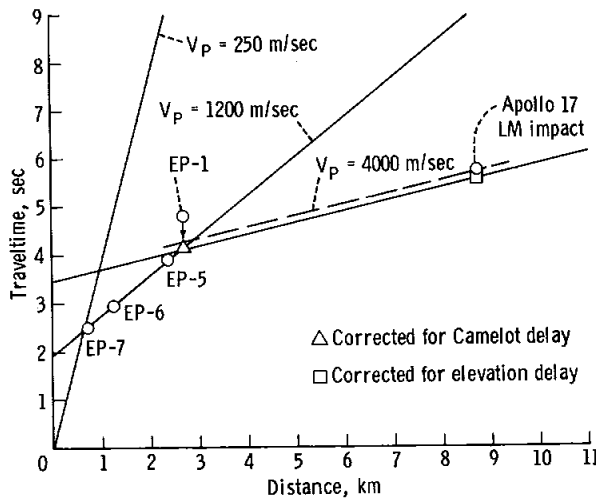
FIGURE 10-15.—Seismic traveltimes from LM impact and LSPE explosive charges. Traveltime for EP-1 has been corrected for Camelot Crater delay, and LM impact traveltime has been corrected for 1.2-km elevation difference between the impact point and the LSPE array. These corrections shift the position of the 4-km/sec apparent velocity slightly downward as shown.

Inasmuch as the LM impacted at an elevation of 1.2 km (fig. 10-1) above the valley floor at the Apollo 17 landing site, the LM impact traveltime can be adjusted to the same reference elevation as the LSPE geophone array. The 1.2-km difference in elevation contributes an additional delay time equal to the ratio of the elevation difference to the seismic velocity of the material traversed multiplied by the cosine of the angle of incidence at which the particular seismic arrival under consideration departed the source (impact point). Inserting the appropriate values in this case leads to a time correction of 0.18 sec. This correction will shift the position of the 4-km/sec apparent-velocity line downward as shown in figure 10-15 such that its zero distance time intercept is decreased. The end result is a decrease in the derived thickness of the 1200-m/sec material from 1020 to 927 m.

It is possible that a dipping interface exists beneath the 1200-m/sec material that might result in a high apparent velocity, or that the particular seismic ray passed through a high-velocity heterogeneity somewhere along its path. Some of the uncertainty may be resolved by subsequent digital velocity filtering (beam steering) of the LM impact signal on the LSPE array.
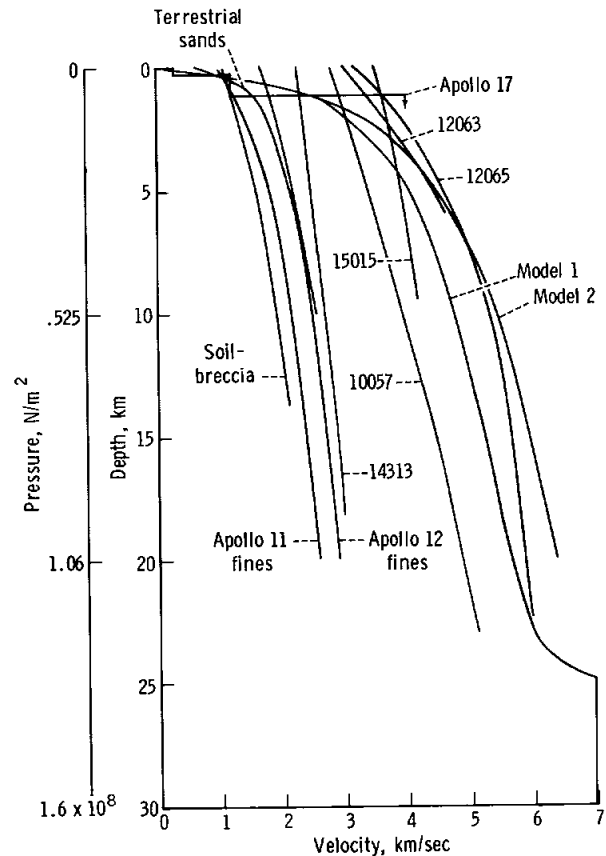
FIGURE 10-16.—Inferred compressional-wave velocity profiles for the Moon and velocities of lunar and terrestrial rocks measured in the laboratory as a function of pressure. Lunar rocks are identified by sample number. Lunar models 1 and 2 are based on results available through Apollo 16. Apollo 17 results reveal a marked stepwise increase in seismic velocity in the upper 2 km of the Moon.

Before the Apollo 17 mission, the best estimates of the seismic velocity variation in the upper 20 km of the Moon were as depicted by lunar model 1 or 2 in figure 10-16. The seismic velocity was known to increase very rapidly from values of 100 to 300 m/sec in approximately the upper 100 m to a value of ≈4 km/sec at a depth of 5 km. Even though the seismic velocity variation was depicted as a smooth increase with depth, it was surmised (ref. 10-5) that such a rapid increase of velocity (≈2 km/sec/km) could not be explained solely by the pressure effect on dry rocks with macrocracks and microcracks nor by the self-compression of any rock powder.

Laboratory velocity measurements on returned lunar soils (refs. 10-6 to 10-10) and recent measure-

ments under hydrostatic pressure conditions on terrestrial sands and basaltic ash have indicated velocity-depth gradients of 0.4 to 0.8 km/sec/km, but such gradients occur only to pressures of $\approx 50 \times 10^5$ N/m^2 (a lunar depth of ≈ 1 km). The measurements on unconsolidated sands and rock powders also have demonstrated that no unique relation exists between seismic velocity and porosity in granular material. An examination of these experimental data led to the inference that compositional or textural changes must be important in the upper 5 km of the Moon (ref. 10-5).

The LSPE results have shown that, at least beneath the Taurus-Littrow site, the seismic velocity increases in a stepwise manner in the upper several kilometers. It is of interest to examine the in situ velocity information with reference to the surface geological investigations at the Apollo 17 site, the laboratory velocity measurements from returned lunar samples, and the seismic velocity measurements on terrestrial lunar analogs.

Premission analyses indicated that much of the Apollo 17 landing site area is covered by a dark mantling material, possibly volcanic ash (ref. 10-11). Crew observations of the lunar surface revealed that there was no readily discernible boundary between the overlying thin regolith and the dark mantling material. The thickness of the dark mantling material was estimated to be between 5 and 10 m (ref. 10-3). As pointed out earlier, whether the dark mantling material/subfloor interface represents a sharp seismic discontinuity or is gradational cannot be determined because the shortest explosive-charge-to-receiver distance was approximately 100 m.

The dominant rock type observed underlying the dark mantling material is a medium-grained vesicular basalt believed to be primarily mare-type basalt. Crew observations of the crater walls revealed textural variations that suggest the involvement of individual flow units. Seismic observations have indicated 248 m of 250-m/sec material overlying 927 m of 1200-m/sec material.

The abrupt change in seismic velocity from 250 to 1200 m/sec and, by inference, in other physical properties suggests a major change in the nature of the evolution or deposition of the Apollo 17 subfloor basalts. However, a similar range of seismic velocities has been observed with refraction surveys on terrestrial lava flows. Some insight can be gained by considering specific lava flows that have been examined in some detail as possible lunar analogs: the Southern Coulee, the SP flow, and the Kana-a flow (refs. 10-12 and 10-13).

The Southern Coulee is a recent lava flow near the Mono Craters in eastern California. Seismic velocities range from 160 m/sec at the surface to 2000 m/sec at depth. The higher velocities are found in more competent, denser lava that underlies higher porosity, lower density surface material. The SP flow is a blocky basalt flow located in the northern part of the San Francisco volcanic field near Flagstaff, Arizona. Vesicularity ranges from 5 to 50 percent, and in situ seismic velocities range from 700 to 1100 m/sec. The Kana-a flow, also located near Flagstaff, is an olivine basalt flow intermingled with ash; seismic velocities range from 700 to 1200 m/sec.

Observed velocities on terrestrial lava flows bracket the velocities measured at the Apollo 17 site and therefore support the presence of lava flows in the Taurus-Littrow valley. Whether the 250-m/sec velocity is representative of a separate flow or is merely the manifestation of shattered near-surface basalts mixed with pyroclastic materials cannot be resolved from the seismic data. Nevertheless, a surface layer of fractured, loose, blocky material merging into more welded flows is a common occurrence on Earth. Photographs of the walls of Hadley Rille (ref. 10-14) also attest to the blocky nature of the near-surface mare basalts. Because of the similarity in structure and the analogous seismic velocities on the Earth and the Moon, the sum of the 248 m of 250-m/sec material and 927 m of 1200-m/sec material, 1175 m, is designated as representing the full thickness of the subfloor basalts at the Apollo 17 site.

The material underlying the basalts with a seismic velocity of ≈ 4 km/sec is difficult to classify by rock type. Based on the geological evidence, it seems likely that the highland massif material that rings the narrow, grabenlike valley at the Apollo 17 site underlies the basalt flow or flows. Several rock types were recognized in the North and South Massifs, but the dominant rock type is apparently a coherent breccia believed to be similar to the breccias sampled at the Apennine Front (Apollo 15) and at Descartes (Apollo 16).

Laboratory velocity measurements have been reported for two Apollo 15 breccias, 15418 and 15015 (ref. 10-15). Sample 15418 is described as a dark-gray breccia of chemical composition similar to that of anorthite-rich gabbro. Sample 15015 is a more friable

breccia of unknown composition. The in situ value of $\approx$4 km/sec is close to the seismic velocities measured in the laboratory for sample 15015 and shown in figure 10-16.

CONCLUSIONS

Before the Apollo 17 mission, the question of how the P-wave velocity increased from 100 to 300 m/sec near the surface (refs. 10-16 to 10-19) to $\approx$6 km/sec at a depth of 15 to 20 km (ref. 10-2) was unexplained. The main reason for the uncertainty was the gap in traveltime data between the range of a few hundred meters (previous active seismic experiments) and 67 km (Apollo 14 LM impact as recorded by the Apollo 14 passive seismic experiment). The Apollo 17 lunar seismic profiling results have demonstrated that the seismic velocity increases in a sharp stepwise manner in the upper 2.5 km. A surface layer with a seismic velocity of 250 m/sec overlies a layer with a velocity of 1200 m/sec. Beneath the 1200-m/sec layer, the seismic velocity increases sharply to 4000 m/sec. The velocities of 250 and 1200 m/sec agree with those observed for basaltic lava flows, indicating a total thickness of approximately 1200 m for the infilling mare basalts at Taurus-Littrow. When the Apollo 17 results are combined with earlier traveltime data for direct and surface-reflected seismic arrivals from LM and SIVB impacts (ref. 10-2), it will be possible to construct a velocity model for the upper lunar crust believed to be representative for a mare basin. Such work is now underway.

REFERENCES

10-1. Latham, Gary V.; Ewing, Maurice; Press, Frank; Sutton, George; et al.: Passive Seismic Experiment. Sec. 6 of Apollo 14 Preliminary Science Report. NASA SP-272, 1971.

10-2. Latham, Gary V.; Ewing, Maurice; Press, Frank; Sutton, George; et al.: Passive Seismic Experiment. Sec. 9 of Apollo 16 Preliminary Science Report. NASA SP-315, 1972.

10-3. Apollo Lunar Geology Investigation Team: Preliminary Report on the Geology and Field Petrology of the Apollo 17 Landing Site. U.S. Geol. Survey, Interagency Rept.: Astrogeology 69, Dec. 17, 1972.

10-4. Apollo Lunar Geology Investigation Team: Documentation and Environment of the Apollo 17 Samples: A Preliminary Report. U.S. Geol. Survey, Interagency Rept.: Astrogeology 71, Jan. 21, 1973.

10-5. Kovach, R. L.; and Watkins, J. S.: The Velocity Structure of the Lunar Crust. The Moon, vol. 7, Apr. 1973, pp. 63-75.

10-6. Kanamori, Hiroo; Nur, Amos; Chung, D.; Wones, D.; and Simmons, G.: Elastic Wave Velocities of Lunar Samples at High Pressures and Their Geophysical Implications. Science, vol. 167, no. 3918, Jan. 30, 1970, pp. 726-728.

10-7. Kanamori, H.; Mizutani, H.; and Hamano, Y.: Elastic Wave Velocities of Apollo 12 Rocks at High Pressures. Proceedings of the Second Lunar Science Conference, vol. 3, MIT Press (Cambridge, Mass.), 1971, pp. 2323-2326.

10-8. Anderson, Orson L.; Scholz, Christopher; Soga, Naohiro; Warren, Nicholas; et al.: Elastic Properties of a Micro-Breccia, Igneous Rock and Lunar Fines from Apollo 11 Mission. Proceedings of the Apollo 11 Lunar Science Conference, vol. 3, Pergamon Press (New York), 1970, pp. 1959-1973.

10-9. Mizutani, H.; Fujii, N.; Hamano, Y.; Osako, M.; et al.: Elastic Wave Velocities and Thermal Diffusivities of Apollo 14 Rocks. Lunar Science–III (Rev. abs. of the Third Lunar Science Conference (Houston, Tex.), Jan. 10-13, 1972), Feb. 18, 1972, pp. 547-549.

10-10. Warren, N.; Schreiber, E.; Scholz, C.; Morrison, J. A.; et al.: Elastic and Thermal Properties of Apollo 11 and Apollo 12 Rocks. Proceedings of the Second Lunar Science Conference, vol. 3, MIT Press (Cambridge, Mass.), 1971, pp. 2345-2360.

10-11. McGetchin, T. R.; and Head, J. W.: Lunar Cinder Cones. Science, vol. 180, no. 4081, Apr. 6, 1973, pp. 68-71.

10-12. Watkins, J. S.: Annual Report, Investigation of In Situ Physical Properties of Surface and Subsurface Site Materials by Engineering Geophysical Techniques. NASA Contract T-25091(G), July 1966.

10-13. Watkins, Joel S.; Walters, Lawrence A.; and Godson, Richard H.: Dependence of In Situ Compressional-Wave Velocity on Porosity in Unsaturated Rocks. Geophysics, vol. 37, no. 1, Feb. 1972, pp. 29-35.

10-14. Howard, Keith A.; Head, James W.; and Swann, Gordon A.: Geology of Hadley Rille. Proceedings of the Third Lunar Science Conference, vol. 1, MIT Press (Cambridge, Mass.), 1972, pp. 1-14.

10-15. Todd, Terrence; Wang, Herbert; Baldridge, W. Scott; and Simmons, Gene: Elastic Properties of Apollo 14 and 15 Rocks. Proceedings of the Third Lunar Science Conference, vol. 3, MIT Press (Cambridge, Mass.), 1972, pp. 2577-2586.

10-16. Kovach, Robert L.; Watkins, Joel S.; and Landers, Tom: Active Seismic Experiment. Sec. 7 of Apollo 14 Preliminary Science Report. NASA SP-272, 1971.

10-17. Kovach, R. L.; and Watkins, J. S.: The Near-Surface Velocity Structure of the Moon. Lunar Science–III (Rev. abs. of the Third Lunar Science Conference (Houston, Tex.), Jan. 10-13, 1972), Feb. 18, 1972, pp. 461-462.

10-18. Watkins, Joel S.; and Kovach, Robert L.: Apollo 14 Active Seismic Experiment. Science, vol. 175, no. 4027, Mar. 17, 1972, pp. 1244-1245.

10-19. Kovach, Robert L.; Watkins, Joel S.; and Talwani, Pradeep: Active Seismic Experiment. Sec. 10 of Apollo 16 Preliminary Science Report. NASA SP-315, 1972.

11. Passive Seismic Experiment

Gary V. Latham,[a][†] Maurice Ewing,[a] Frank Press,[b]
James Dorman,[a] Yosio Nakamura,[a] Nafi Toksoz,[b]
Davis Lammlein,[a] Fred Duennebier,[a] and Anton Dainty[b]

The impacts of the SIVB and the lunar module (LM) ascent stage of the Apollo 17 mission concluded a series of nine such impacts from which seismic signals have been recorded by the Apollo seismic network. The network includes stations installed at the landing sites of the Apollo 12, 14, 15, and 16 missions and spans the near side of the Moon in an approximately equilateral triangle with 1100-km spacing between stations. (The Apollo 12 and 14 stations are 181 km apart at one corner of the triangle.) The oldest of these stations, Apollo 12, has now operated for more than 3 yr, and the entire network has been in operation for 1 yr as of April 1973. Four seismometers are included at each station: three low-frequency components forming a triaxial set (one sensitive to vertical motion and two sensitive to horizontal motion) with sensitivity to ground motion sharply peaked at 0.45 Hz, and a fourth seismometer sensitive to vertical motion with peak sensitivity at 8 Hz (high-frequency component). These instruments can detect vibrations of the lunar surface as small as 0.05 nm at maximum sensitivity. Of the 16 separate seismometers, all but two are presently operating properly. The high-frequency component at the Apollo 12 station has failed to operate since initial activation, and one of the low-frequency seismometers at the Apollo 14 station (vertical component) became unstable after 1 yr of operation.

Moonquakes have been detected by the low-frequency seismometers of each station at average rates of between 600 and 3000 per year, depending on the station; all the moonquakes are quite small by terrestrial standards (Richter magnitude 2 or less). Thousands of even smaller moonquakes are detected by the high-frequency seismometers. Meteoroid impacts are detected by the low-frequency seismometers at average rates of between 70 and 150 per year. Although less numerous than moonquakes, meteoroid impacts generate the largest signals detected.

Several criteria have been useful in distinguishing moonquake signals from meteoroid impact signals. The most useful are the character of shear waves and the time interval from the beginning of a signal to its maximum amplitude (the signal rise time). Moonquake signals have impulsive shear wave arrivals and short rise times relative to those of impact signals. In addition, many of the moonquake signals can be grouped into sets of matching events; signals of each set have nearly identical waveforms. Signals from meteoroid impacts cannot be matched with one another.

Analysis of the seismic signals from the manmade impacts and from natural sources has led to a model for the Moon that is quite different from that of the Earth. Refinements in the present lunar model can be expected as data accumulate from natural events. In this report, the major findings to date from the passive seismic experiment are summarized.

STRUCTURE AND STATE OF THE LUNAR INTERIOR

The surface of the Moon is covered by a highly heterogeneous zone in which, because of the nearly complete absence of volatiles, seismic waves propagate with very little damping. Scattering in this zone accounts for the prolongation of lunar seismic signals and for the complexity of the recorded ground motion relative to typical terrestrial signals (refs. 11-1 and 11-2). Most of the scattering occurs in the outer several hundred meters, but significant scattering may occur to depths as great as 10 to 20 km. The

---

[a]The University of Texas at Galveston.
[b]Massachusetts Institute of Technology.
[†]Principal Investigator.

"granularity" within the scattering zone ranges from micron-size fragments to heterogeneity on a scale of at least several kilometers. The roughness of the lunar surface undoubtedly contributes to the scattering of seismic waves.

Some find the combination of intensive scattering and low damping of seismic waves to be confusing because, on Earth, scattering is normally associated with a high degree of damping. However, these can be regarded as independent phenomena. On Earth, the presence of water is the dominant factor in dissipation of seismic energy at shallow depth; scattering results if heterogeneity is present on a scale comparable to the signal wavelengths. In the outer shell of the Moon, heterogeneity results in scattering, but it is the nearly complete absence of water (or any other fluid), and the consequent high transmission efficiency (low damping), that leads to the extreme prolongation of lunar seismic signals.

Knowledge of the lunar structure below the scattering zone is derived mainly from analysis of seismic signals from impacts of Apollo space vehicles of two types: the LM ascent stage and the SIVB stage of the Saturn booster. Each LM was guided to impact following the return of the surface crewmen to the command and service module in lunar orbit. Following separation from the Apollo spacecraft, the SIVB stages were directed to planned impact points by

remote control from Earth. Nine impacts were accomplished successfully. Seismic signals from these impacts were recorded at ranges from 67 to 1750 km. Impact coordinates and the distances and azimuths from the receiving stations are listed in table 11-I. The Apollo 17 LM impact was also recorded by the geophones of the active seismic experiment, located at the Apollo 17 landing site, at a range of 9 km. These data, combined with data from high-pressure laboratory measurements on returned lunar samples, provide information on lunar structure to a depth of approximately 150 km. Information on lunar structure below this depth is derived principally from analysis of signals from deep moonquake and distant meteoroid impacts. Analysis of the manmade impact data has revealed a major discontinuity at a depth between 55 and 65 km in the eastern part of Oceanus Procellarum (refs. 11-3 and 11-4). By analogy with the Earth, the zone above the discontinuity is called the crust and the zone below, the mantle. Whether the crust is regional or is a global feature cannot be determined from the present seismic network. However, the early formation of a crust by igneous processes on a global scale would appear to explain such observations as the unexpectedly high heat flow (ref. 11-5) and the presence of large-scale petrological provinces inferred from orbital X-ray fluorescence data (ref. 11-6) and from lunar sample analysis. The

TABLE 11-I.—*Coordinates, Distances, and Azimuths of Stations and Impacts*

Station or impact	Coordinates[a]	Distance and azimuth from Apollo seismic station—			
		12	14	15	16
Apollo 12 station	3.04° S, 23.42° W	–	181 km, 276°	1188 km, 226°	1187 km, 276°
Apollo 14 station	3.65° S, 17.48° W	181 km, 96°	–	1095 km, 218°	1007 km, 277°
Apollo 15 station	26.08° N, 3.66° E	1188 km, 40°	1095 km, 33°	–	1119 km, 342°
Apollo 16 station	8.97° S, 15.51° E	1187 km, 100°	1007 km, 101°	1119 km, 160°	–
Apollo 12 LM impact point	3.94° S, 21.20° W	73 km, 112°	–	–	–
Apollo 13 SIVB impact point	2.75° S, 27.86° W	135 km, 274°	–	–	–
Apollo 14 SIVB impact point	8.09° S, 26.02° W	172 km, 207°	–	–	–
Apollo 14 LM impact point	3.42° S, 19.67° W	114 km, 96°	67 km, 276°	–	–
Apollo 15 SIVB impact point	1.51° S, 11.81° W	355 km, 83°	184 km, 69°	–	–
Apollo 15 LM impact point	26.36° N, 0.25° N	1130 km, 36°	1048 km, 29°	93 km, 276°	–
Apollo 16 SIVB impact point	[b] 1.3 ± 0.7° N, 23.8 ± 0.2° W	132 km, 355°	243 km, 308°	1099 km, 231°	–
Apollo 17 SIVB impact point	4.21° S, 12.31° W	338 km, 96°	157 km, 96°	1032 km, 209°	850 km, 278°
Apollo 17 LM impact point	19.96° N, 30.50° E	1750 km, 64°	1598 km, 61°	770 km, 98°	985 km, 27°

[a]Listed coordinates are derived from the Manned Space Flight Network Apollo tracking data. Locations based on these data are referenced to a mean spherical surface and may differ by several kilometers from coordinates referenced to surface features.

[b]Premature loss of tracking data reduced the accuracy of the estimate. The listed coordinates for this impact are estimated from seismic data.

velocity of compressional waves in the lower half of the crust is between 6.3 and 7.0 km/sec, a velocity range appropriate for the aluminous basalts and gabbroic anorthosites that predominate in the lunar highlands sampled thus far. Thus, the most plausible hypothesis is that a widespread crust, formed early in the history of the Moon, outcrops in the present lunar highlands. The thickness of the crust is likely to vary greatly. There is some evidence for a discontinuity within the crust at a depth of 25 km that may define the base of the mare basalts in Oceanus Procellarum (ref. 11-3).

Below the crust, a relatively homogeneous zone extending to a depth of approximately 1000 km is suggested by the nearly constant velocity of seismic waves. The average velocity of compressional waves in the homogeneous zone is approximately 8 km/sec. A slight decrease in velocity with depth probably occurs in the lower half of this zone. Very low attenuation of both compressional and shear waves in this zone precludes the presence of any appreciable melting. Poisson's ratio is approximately 0.25 at the top of the mantle.

A striking contrast has been found between signals that originate on the near side of the Moon and those from far-side sources. Direct shear waves, normally prominent in signals from near-side moonquakes and weakly defined in near-side meteoroid impact signals, cannot be found in the seismograms recorded at several of the seismic stations from far-side events. For example, as shown in figure 11-1, shear waves from a large meteoroid that struck the far side near the crater Moscoviense arrive at the Apollo 15 station at the expected time, but they are missing at the Apollo 14 and 16 stations when expected. Much later phases arrive at these stations at times predicted for surface-reflected shear waves (SS) that travel through the upper mantle of the Moon. Similarly, shear waves from far-side moonquakes that can be identified at the Apollo 15 and 16 stations are missing at the Apollo 14 station (fig. 11-2).

Although available data are not sufficient to derive a detailed seismic velocity model for the deep interior, these observations can be explained by introducing a "core" with a radius between 600 and 800 km in which shear waves either do not propagate or are highly attenuated (dissipation factor Q of approximately 100 or less) (ref. 11-7). The compressional wave velocity within this zone may be slightly lower than that in the mantle. The maximum

allowable velocity decrease for compressional waves is approximately 0.3 km/sec. The term "core" as applied in this discussion is not meant to imply a major compositional or structural discontinuity as it does for the Earth. In the lunar case, it is simply a central zone in which the characteristics of seismic wave transmission differ from those in the surrounding material. However, the presence of a small "inner" core in the terrestrial sense is not precluded by present data.

Seismic wave attenuation is strongly temperature dependent, showing rapid increase with increasing temperatures and increasing sharply with the onset of melting (ref. 11-8). Thus, temperatures approaching the solidus (melting point) in the lunar interior may account for the lack of shear wave transmission indicated by the seismic data. Assuming an interior of mafic silicate composition, this state would require temperatures of between 1700 and 1900 K at a depth of approximately 1000 km. This model is in substantial agreement with several thermal models recently proposed by Toksoz et al. (ref. 11-9). Partial melting of silicate material is considered to be a possible cause of the low Q, low-velocity zone of the upper mantle of the Earth (refs. 11-8 and 11-10). A completely molten core of the size indicated, however, is not likely because a decrease of the compressional wave velocity exceeding the value of 0.3 km/sec obtained by the preliminary analysis would be expected. Other possibilities, such as increased volatiles in the deep interior of the Moon, cannot be eliminated at present.

The possibility of a high-density, molten metallic core similar to that of the Earth is eliminated by both moment-of-inertia and seismic-wave-velocity considerations. The radius of approximately 700 km is too large for such a core.

By analogy with the Earth, the lithosphere—the relatively rigid outer shell of the Moon—can be considered to be approximately 1000 km thick. The core of the Moon is equivalent to the asthenosphere (low-velocity zone) of the Earth.

MOONQUAKES AND LUNAR TECTONISM

Thermal Moonquakes

Thousands of small seismic signals have been detected by the high-frequency seismometers at the Apollo 14, 15, and 16 stations. (The high-frequency
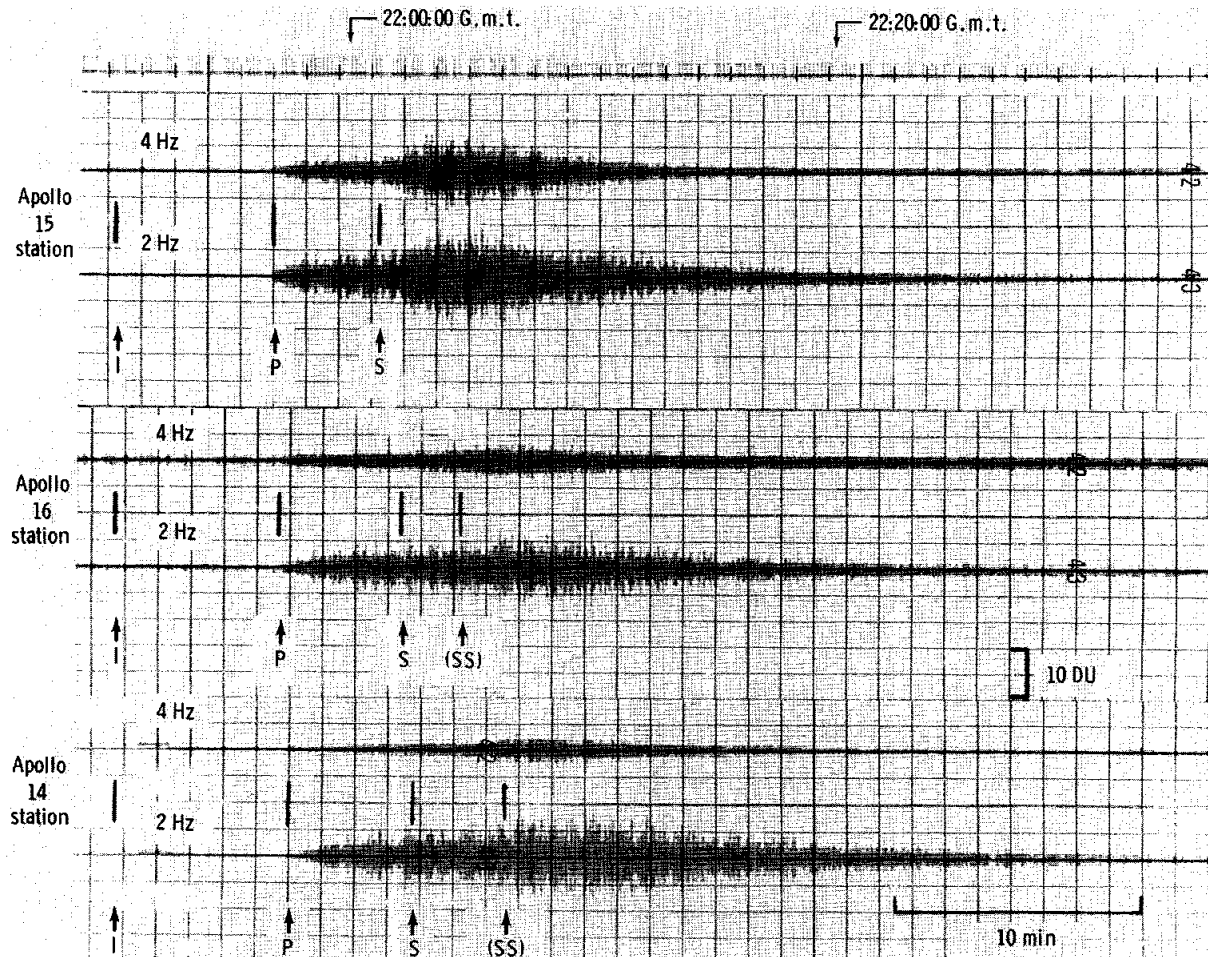
FIGURE 11-1.—Filtered short-period seismograms of seismic events detected on July 17, 1972. The signal is believed to be from a meteoroid impact on the far side of the Moon. Traces for two different filter settings are shown for each station. The frequencies given, 4 and 2 Hz, are the center frequencies of the narrow band-pass filters used in the data playback. The I indicates the estimated time of impact; P, the observed arrival time of the direct compressional wave; and S, the expected arrival time of the direct shear wave. Note that the characteristic shear wave bulge, clearly visible at the Apollo 15 station, is missing at the Apollo 16 and 14 stations when expected. A digital unit (DU) is the signal variation that corresponds to a change in the least significant bit of the 10-bit data word.

seismometer at the Apollo 12 station failed to operate.) These signals are not recorded by the low-frequency seismometers because of the restricted bandwidth of these instruments. The high-frequency signals are generated (1) by thermoelastic stresses within the LM descent stage and other equipment left on the lunar surface at each site, (2) by small meteoroid impacts at near ranges (a few tens of kilometers and less), and (3) by small moonquakes (micromoonquakes) that originate within a few kilometers of each station. Micromoonquake activity

begins abruptly approximately 2 days after lunar sunrise and decreases rapidly after sunset (ref. 11-2). These events are recognized by the repetition of nearly identical signals, implying a highly localized source for each set. Forty-eight sets of matching micromoonquake signals have been identified at the Apollo 14 station, and 245 sets at the Apollo 15 station. Micromoonquake activity at the Apollo 16 station is very low in comparison with that at the Apollo 14 and 15 stations. Signals of each set occur at monthly intervals, usually one event per month per
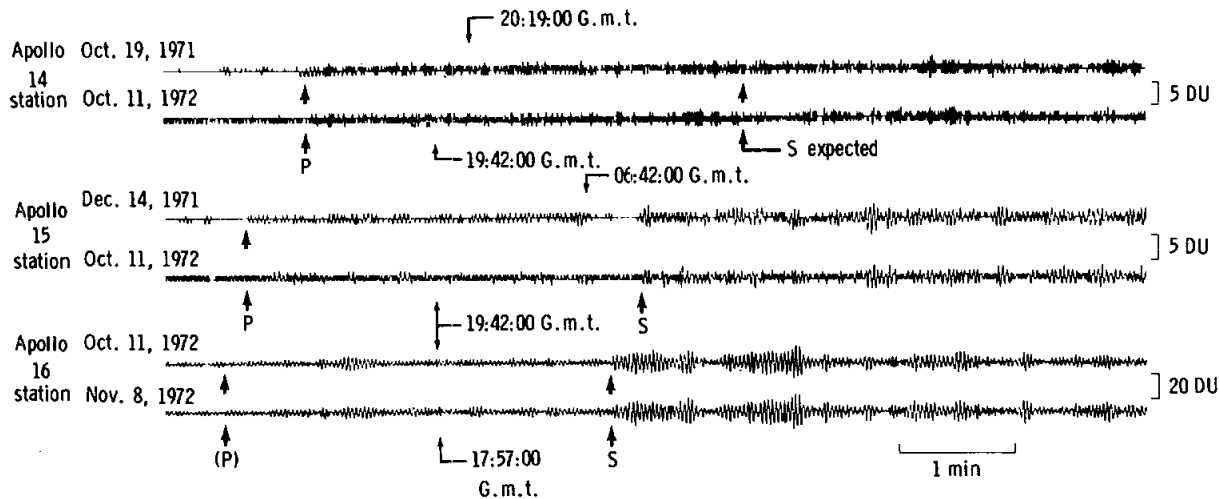
FIGURE 11-2.–A comparison of signals from selected moonquakes detected at the Apollo 14, 15, and
16 stations. One of the four moonquakes (Oct. 11, 1972) is common to all three stations. The
signals were too weak to be detected at the Apollo 12 station. Only the horizontal-component
seismogram is shown for each event at each station. These moonquakes originated at the same
point within the far half of the Moon. Note that the shear wave is not observable at the Apollo 14
station when expected (marked "S expected"). The P-wave at the Apollo 16 station is too weak to
be identified with confidence.

set, and at the same time relative to sunrise to within
a few hours. The strong correlation with sunrise and
sunset indicates that micromoonquakes are of ther-
mal origin.

Two possible source mechanisms for thermal
moonquakes are suggested: (1) cracking or move-
ment of rocks along zones of weakness and (2)
slumping of soil on lunar slopes triggered by thermal
stresses. The characteristics of the signals imply that
motion is always in the same direction and that some
thermal moonquake sources change position slightly
from one lunar day to the next, but the source
mechanism is not yet understood.

Distant Moonquakes

Moonquakes detected by the low-frequency
seismometers of each station were soon recognized as
being distant from all stations. The characteristics of
the low-frequency moonquake signals are also quite
different from those of the locally generated moon-
quakes described previously. With a few possible
exceptions, all low-frequency moonquake signals that
are large enough to examine in detail can be grouped
into sets of matching events. Events of each set occur
at monthly intervals, usually once per month, with
longer term variations in the moonquake magnitudes.

Forty-one categories of matching events have been
recognized thus far. As in the case of thermal
moonquakes, the repetition of seismic signals of
identical waveforms indicates that the point of origin
remains fixed probably to within a few kilometers.
Thus, there are at least 41 active zones within the
Moon at which moonquakes originate. Seismic signals
from these focuses represent only 10 percent of the
total number of signals believed to be of moonquake
origin based on their signal character. Thus, the
existence of many more focuses from which the
signals are too small for detailed waveform compari-
son is likely. Peaks in moonquake activity occur at
biweekly intervals corresponding to the apogee/
perigee cycle, as shown in figure 11-3 for the Apollo
14 station. A 7-month variation in activity, corre-
sponding to the solar perturbation of the lunar orbit,
is also apparent in such plots. If the activity is
examined at a given moonquake focus, as shown in
figure 11-4 for the active zone designated A_1, not
only the monthly and 7-month cycles but also a
longer term variation can be recognized. The longer
term variation may correspond to the 6-yr term in the
variation of lunar gravity. These correlations strongly
suggest that tides are the dominant source of energy
released as moonquakes. It is possible, in fact, likely,
that a small secular component of stress, introduced
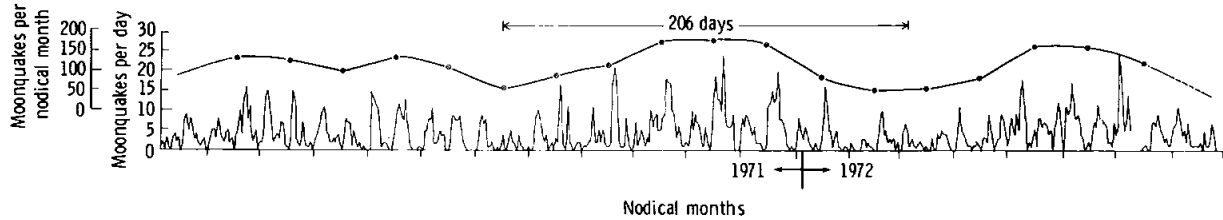
FIGURE 11-3.—Moonquake activity recorded at the Apollo 14 station between February 7, 1971, and July 27, 1972, showing the number of moonquakes detected per day. Peaks in activity occur at 2-week intervals corresponding to the apogee/perigee cycle. A longer term variation in moonquake activity, with a period of 206 days, is also seen in the smoothed activity plot shown above the daily count. This 206-day period corresponds to the period of the tidal variation introduced by solar perturbation of the lunar orbit.
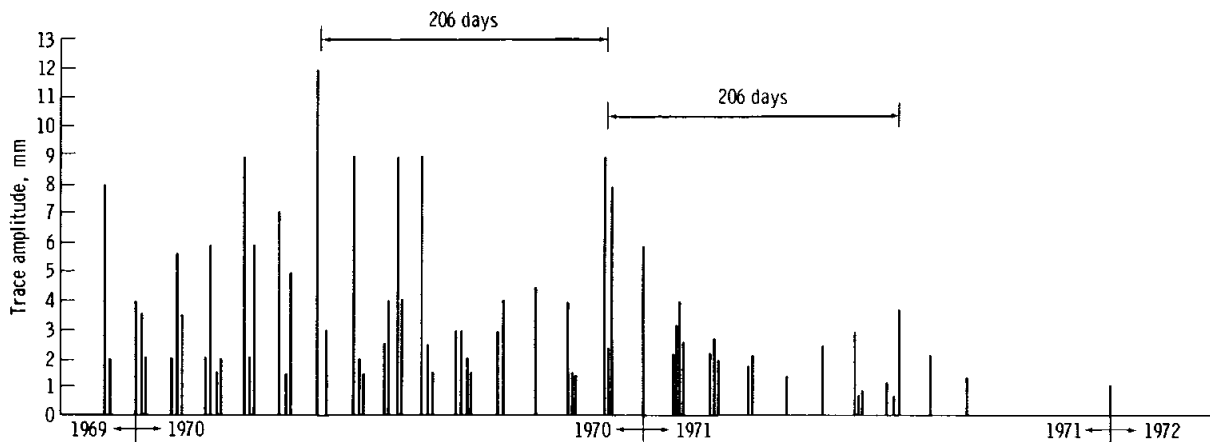
FIGURE 11-4.—History of occurrence of category A_1 moonquakes as recorded at the Apollo 12 station between November 1969 and January 1972. The length of each bar is proportional to the maximum amplitude of the recorded signal. Monthly and 206-day cycles are evident in this plot together with a longer term variation that may correspond to the 6-yr variation in tidal stress.

possibly by the recession of the Moon from the Earth or by heating or cooling of the lunar interior, is also present.

The distribution of moonquake epicenters located thus far is shown in figure 11-5. In this distribution, two narrow belts of activity lying approximately along arcs of great circles are recognized. The western belt runs approximately north-south over a length of at least 2500 km. The eastern belt trends northeast-southwest over a length of at least 2000 km. The focuses of these events are concentrated at depths of 800 to 1000 km, as shown in figure 11-6. Earlier suggestions of possible correlations between moonquakes and mare rims are no longer supported by the increased data now available.

According to our present model, moonquakes occur at the base of a thick, rigid shell (the lithosphere) immediately above a relatively weak central zone (the asthenosphere). If this model is correct, then the depth of the moonquake zone may simply be a consequence of the differing yield strengths of the material within these two zones. Slow changes in the shape of the Moon, in response to time-varying tidal stresses, will produce stress concentrations at the lithosphere/asthenosphere boundary. When the stress exceeds the shear strength of the material, rupture will occur. The availability of fluids migrating upward from a partially molten zone would also facilitate dislocation in the lunar lithosphere.

The alinement of moonquake focuses in long, narrow belts is more difficult to understand. These belts may be a consequence of large-scale variations in the mechanical properties of the material of the

FIGURE 11-5.—Map showing the locations of the Apollo seismic network stations and of 26 moonquake epicenters. The epicenters are the points on the surface immediately above the active zones (focuses) in which moonquakes originate. Solid circles indicate focuses for which the depth of the focus can be determined. Open circles correspond to cases in which data are not sufficient for determination of depth. A depth of 800 km has been assumed in these cases. The number at each epicenter is an arbitrary identification code used by the experiment team. Note that in two cases (epicenters 1 and 6 and epicenters 18 and 32) the epicenters are so closely spaced that their separation cannot be distinguished at the scale plotted.

lithosphere or of the asthenosphere. They may, for example, be zones of increased temperature or they may reflect compositional heterogeneity. Alternatively, the moonquake belts may be manifestations of weak, large-scale convective motions or they may be residual stress dating from the time of formation of the Moon. The belts do not appear to lie along large, continuous fractures, because the orientation of tidal

FIGURE 11-6.—The depth distribution of moonquakes for which present data are sufficient for determination of focal depths (18 cases). Question marks in the zone labeled "asthenosphere" indicate that present data are not sufficient to define the inward extent of this zone. The asthenosphere, in which partial melting is believed to occur, may extend to the center of the Moon or it may be restricted to a thin shell at a depth of approximately 1000 km.

stresses leading to moonquakes varies greatly among the focuses of a given belt. Thus, varying orientations of the dislocation planes are implied. Further speculation on the possible origin of the zones of moonquake activity is postponed until the zones can be delineated with greater certainty.

Surface features that appear to be tensional have been taken as evidence of slight past expansion as the lunar interior grew warmer. However, lack of moonquakes at shallow and intermediate depths suggests that, presently, the Moon is neither expanding nor contracting at an appreciable rate. Hence, the Moon must be close to thermal equilibrium at the present time; that is, the rate of heat flow out of the Moon must be approximately equal to the rate of internal heat production.

METEOROID FLUX

Seismic signals detected by the Apollo seismic network from meteoroid impacts appear to be generated by objects in the mass range from 100 g to 1000 kg. Results obtained to date have been derived by a method using only the statistical distribution of maximum amplitudes of seismic signals recorded from meteoroid impacts (ref. 11-2). The average flux estimated from data of more than 1 yr is log $N = -1.62 - 1.16$ log m where N is the cumulative number of meteoroids of mass m (in grams) and greater that strike the Moon per year per square kilometer. This flux estimate is 1 to 3 orders of magnitude lower than that derived from earlier Earth-based measurements. Our estimate is lower than the average flux estimated from the distribution of crater sizes on the youngest lunar maria. This flux is consistent with a hypothesis that the population of small fragments in the solar system decreases with time as the fragments are gathered up by collisions with the planets. The seismic data predict that a meteoroid of 7 to 10 kg mass can be detected by the least sensitive station (Apollo 12) from any point on the Moon. Approximately 50 percent of the impacts detected by a station occur more than 1000 km from the station. The total data appear to contain at least two distinct meteoroid populations: the normal fragment distribution that varies little throughout the year and a population of relatively large objects that intersect the lunar orbit from April through July each year. Because the latter are detectable seismically from anywhere on the Moon, the Apollo seismic network affords greater exposure to these rare events than any other method of measurement.

SUMMARY AND CONCLUSIONS

Seismic activity within the Moon is extremely low compared to that within the Earth. The Moon is characterized by a rigid, dynamically inactive outer shell, approximately 1000 km thick, surrounding a core that has markedly different elastic properties. Current moonquake activity is concentrated near the boundary between these two zones. It is likely that temperatures within the lunar core are at, or near, the temperature of the beginning of melting (solidus

point) and that the core is much weaker than the outer shell. If so, the outer shell may be regarded as the lunar lithosphere and the weak central zone as the asthenosphere. The transition between these zones appears to be quite gradual. Thus, the term "core" is not meant to imply a major structural or compositional discontinuity as it does for the Earth. However, the presence of a true core, in the terrestrial sense, somewhere below the lithosphere/asthenosphere boundary is not precluded by present data. The great thickness of the lunar lithosphere relative to that of the Earth probably accounts for the widely differing tectonism of these two planets.

Lack of shallow seismic activity indicates that the Moon is neither expanding nor contracting appreciably at the present time. Thus, the rate of heat flow out of the Moon must be approximately equal to the rate of internal heat production. The presence of a thick lunar crust suggests early, intense heating of the outer shell of the Moon.

REFERENCES

11-1. Latham, G. V.; Ewing, M.; Press, F.; Sutton, G.; et al.: Apollo 11 Passive Seismic Experiment. Proceedings of the Apollo 11 Lunar Science Conference, vol. 3, Pergamon Press (New York), 1970, pp. 2309-2320.

11-2. Latham, Gary V.; Ewing, Maurice; Press, Frank; Sutton, George; et al.: Passive Seismic Experiment. Sec. 9 of the Apollo 16 Preliminary Science Report. NASA SP-315, 1972.

11-3. Toksoz, M. N.; Press, Frank; Anderson, Ken; Dainty, A.; et al.: Velocity Structure and Properties of the Lunar Crust. The Moon, vol. 4, no. 3/4, June/July 1972, pp. 490-504.

11-4. Latham, Gary; Ewing, Maurice; Press, Frank; Sutton, George; et al.: Lunar Structure and Dynamics—Results from the Apollo Passive Seismic Experiment. The Moon, vol. 5, 1973, pp. 272-296.

11-5. Langseth, Marcus G., Jr.; Clark, Sydney P., Jr.; Chute, John L., Jr.; Keihm, Stephen J.; and Wechsler, Alfred E.: Heat-Flow Experiment. Sec. 11 of the Apollo 15 Preliminary Science Report. NASA SP-289, 1972.

11-6. Adler, I.; Trombka, J.; Lowman, P.; Schmadebeck, R.; et al.: Results of the Apollo 15 and 16 X-Ray Fluorescence Experiment. Lunar Science IV (Abs. of papers presented at the Fourth Lunar Science Conference (Houston, Tex.), Mar. 5-8, 1973), pp. 9-10.

11-7. Nakamura, Y.; Lammlein, D.; Latham, G.; Ewing, M.; Dorman, J.; et al.: New Seismic Data on the State of the Lunar Interior. Science, vol. 181, no. 4094, July 6, 1973.

11-8. Jackson, D.; and Anderson, D.: Physical Mechanisms of Seismic Wave Attenuation. Rev. Geophys., vol. 8, no. 1, 1970, pp. 1-64.

11-9. Toksoz, M. Nafi; Solomon, Sean C.; Minear, John W.; and Johnston, David H.: Thermal Evolution of the Moon. The Moon, vol. 4, no. 1/2, Apr. 1972, pp. 190-213.

11-10. Solomon, Sean C.: Seismic-Wave Attenuation and Partial Melting in the Upper Mantle of North America. J. Geophys. Res., vol. 77, no. 8, 1972, pp. 1483-1502.

12. Lunar Surface Gravimeter Experiment

John J. Giganti,[a] J. V. Larson,[a] J. P. Richard,[a] and J. Weber[a]†

The primary objective of the lunar surface gravimeter (LSG) is to use the Moon as an instrumented antenna (refs. 12-1 to 12-8) to detect gravitational waves predicted by Einstein's general relativity theory. A secondary objective is to measure tidal deformation of the Moon. Einstein's theory describes gravitation as propagating with the speed of light. Gravitational waves carry energy, momentum, and information concerning changes in the configuration of their source. In these respects, such waves are similar to electromagnetic waves; however, electromagnetic waves only interact with electric charges and electric currents. Gravitational waves are predicted to interact with all forms of energy.

The visible light, radio, and X-ray emissions, together with the cosmic rays, are the sources of all our present information about the universe. Gravitational radiation is a totally new channel that would be capable of giving information about the structure and evolution of the universe.

BASIC THEORY

It is possible to study many forms of energy-carrying waves by generating and detecting them in the laboratory. At present, this type of study is not feasible for gravitational radiation. The ratio of mass to electric charge for elementary particles is so small that only 1 graviton is emitted for every 10^{43} photons in ordinary laboratory experiments. Only objects the size of stars or galaxies can generate enough gravitational radiation to be detected by present apparatus.

Detailed mathematical analysis using Einstein's equations has shown that an elastic solid would serve as a gravitational radiation antenna. Dynamic forces associated with the gravitational waves set up internal vibrations in the antenna. These forces are somewhat similar to the gravitational forces that cause the tides. Observation of internal vibrations is limited by noise.

If gravitational waves of sufficiently high intensity covering certain bands of frequencies are incident on the Moon, internal vibrations of the Moon will be excited. These vibrations may cause oscillatory surface accelerations. Theory predicts that only the lowest allowed frequency and certain overtones can be excited in this way. The kinds of vibrations that are excited by gravitational waves are believed to have symmetry. Thus, the "breathing" mode of the Moon, in which all points of the lunar surface move outward together, and half a cycle later, all points move inward together, is not expected to be driven by gravitational radiation. However, the "football" mode is expected to be excited by gravitational radiation. In the "football" mode, all points on the lunar equator move outward at the same time that points on the lunar poles are moving inward. Half a cycle later, all points on the equator are moving inward while the polar regions are moving outward.

Very little is known about possible sources of gravitational radiation. An object may emit considerable gravitational radiation and have very little emission of light and vice versa. At present, the search for this radiation must be made by developing the best possible instruments and operating them at the limits of sensitivity. Approximate estimates suggest that present procedures have a fair chance of observing real effects by using the Moon because of the relative quiet of the lunar environment.

The Earth is also an instrumented antenna, but it has a high level of noise because of the atmosphere, the oceans, and seismic activity. Quiet periods exist when it may be possible to observe the coincident response of the Earth and Moon to gravitational waves. The surface acceleration of the Earth is measured with a somewhat similar gravimeter and recorded as a function of time. Comparisons between

---

[a]University of Maryland.
†Principal Investigator.

the lunar and terrestrial records should allow searches for simultaneous sudden surface accelerations. By delaying one recording relative to the other one, the rate of chance coincidences may be measured. A significant excess of zero-delayed as compared to time-delayed (chance) coincidences can establish the existence of correlations.

Experiments have been conducted in the kilohertz region using aluminum cylinder masses of several thousand kilograms that are isolated from terrestrial effects. The existence of such coincidences has been established using antennas at the University of Maryland and at the Argonne National Laboratory near Chicago, Illinois. The high frequency (seismic output) of the LSG will be compared with the records of the aluminum cylinder experiments in an effort to find numbers of coincident amplitude increases over and above the chance rate.

The LSG was also designed to measure the tidal effects on the Moon and to serve as a one-axis seismometer. The lunar orbit is slightly elliptical, and the Moon undergoes librations. For these reasons, the gravitational fields of the Earth and Sun sensed by a given part of the lunar surface will vary with time. This variation results in time-dependent tidal forces on the Moon. The figure of the Moon will be distorted in consequence of the tidal forces, and the amount of this distortion gives information about the internal composition of the Moon.

EQUIPMENT

The LSG (fig. 12-1) was emplaced on the Moon by the Apollo 17 crew. This instrument is a sensitive balance with a mass, spring, and lever system and with electronics for observation of accelerations in the frequency range from 0 to 16 Hz. The LSG has a nominal sensitivity of approximately one part in 10^{11} of lunar gravity.

A schematic diagram of the spring-mass suspension system is shown in figure 12-2. In the instrument, the major fraction of the force supporting the sensor mass (beam) against the local gravitational field is provided by the zero-length spring. A zero-length spring is one in which the restoring force is directly proportional to the spring length; such a spring is very useful in obtaining a long-period sensor (ref. 12-9). Small changes in force tend to displace the beam up or down. This imbalance is adjusted to the null position by repositioning the spring pivot points by
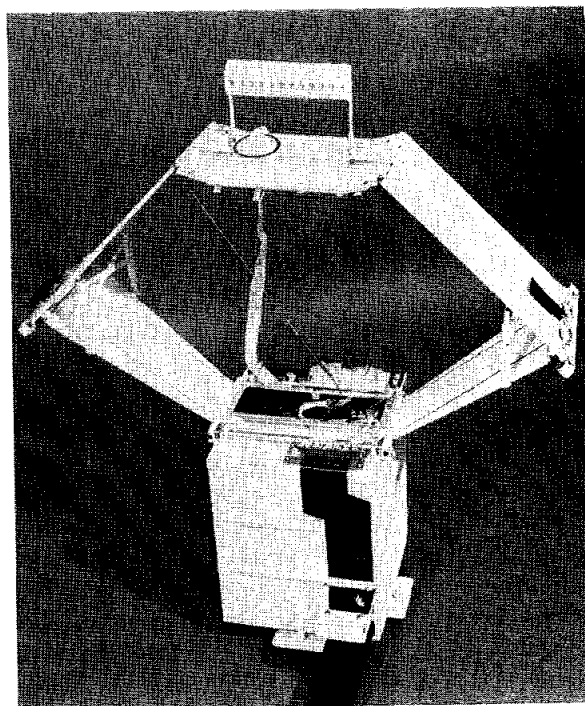
FIGURE 12-1.—Lunar surface gravimeter.
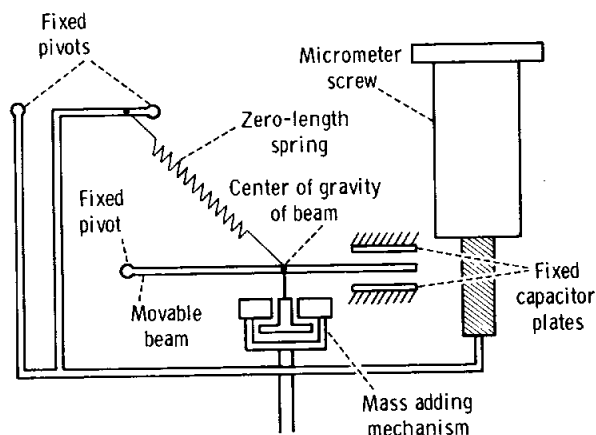
FIGURE 12-2.—Schematic diagram of the lunar gravity sensor.

use of micrometer screws. The sensor mass is modified by the addition or removal of small weights, permitting the range of the sensor to be extended from Earth testing to lunar operation. The electronic sensing portion of the instrument consists of a set of capacitor plates. Two plates, which are part of a radio-frequency bridge circuit, are fixed to the frame of the sensor and are geometrically concentric with a

third plate of similar size, which is attached to the movable beam of the sensor. The plates are so arranged that the center plate is located exactly between the two outer plates when the beam is exactly horizontal. If the force on the mass changes, it tends to move the beam, and the resulting bridge unbalance creates an ac error voltage. This voltage is amplified and rectified with the size of the output voltage determined by the direction of the displacement. A fixed dc bias voltage is applied to the capacitor plates balanced with respect to ground, and these plates are also connected to the rectified error voltage.

If the error voltage is zero, the balanced bias plate voltage produces equal and opposite electrostatic forces on the mass. If a positive error voltage is present, the voltage applied to one plate is increased and the voltage applied to the other plate is decreased. The resulting force tends to restore the mass to its originally centered position. This rectified voltage is a measure of the changes in surface acceleration. The mass does not follow fast changes. However, the fast-changing servomechanism error voltage is a measure of the rapidly changing components of the surface acceleration.

The LSG can also be operated with the voltage output not fed back to restore the beam to equilibrium. As indicated in figure 12-3, the different configurations have different responses to surface accelerations.

The data cover the frequency range from 0 to 16 Hz in three bands. The rectified integrated error voltage over the range dc to 1 cycle per 20 min gives information on the lunar tides. A filter with amplification covers the range from 1 cycle per 20 min to 3 cpm. Another filter amplifies the fast components in the range from 3 cpm to 16 Hz. The latter range is of interest for seismology and for search for high-frequency gravitational radiation from sources such as the pulsars. The complete response function of the sensor and electronics for several different configurations is given in figures 12-3 and 12-4.

THERMAL CONTROL

The gravimeter uses a metal spring with a force constant that is, in general, temperature dependent. There are two temperatures at which thermal effects are minimal; for the LSG, one of these occurs near 323 K. To obtain the required performance, it is necessary to control the temperature of the spring to within better than 1 mdeg near the optimum temperature throughout the lunar day/night cycle. Thermal control is accomplished by use of thermal insulation, which limits heat exchange with the lunar surface. A hole in the top of the LSG radiates heat to the cold sky so that an internal heater is required to maintain the 323 K temperature sensed by thermistors. A sunshade prevents the solar heat from directly entering the LSG. The sunshade is tilted at an angle corresponding to the latitude of the emplaced instruments. The thermal control system has controlled the temperature of the spring to within 1 mdeg.
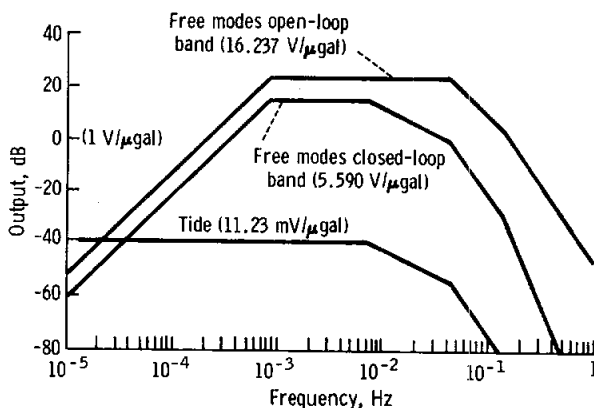
FIGURE 12-3.—Tide and free mode science channel frequency response.
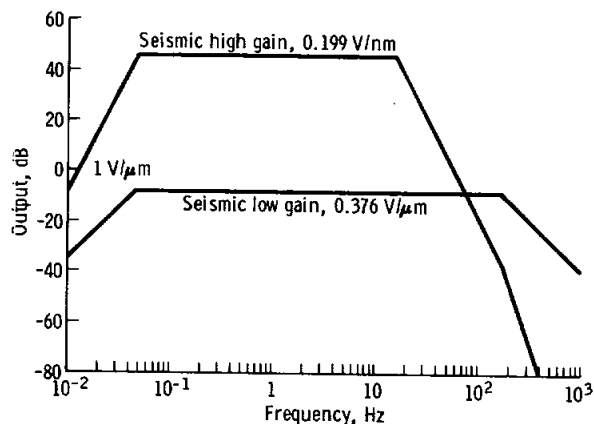
FIGURE 12-4.—Seismic science channel frequency response.
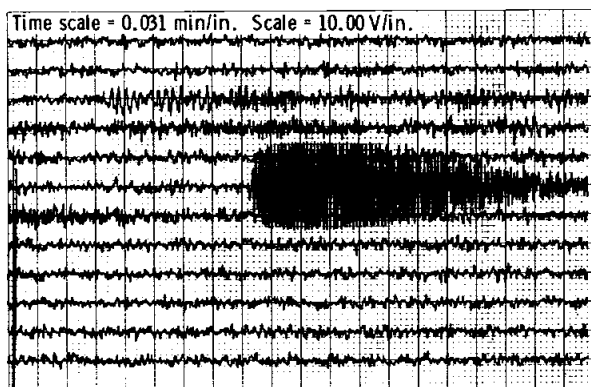
FIGURE 12-5.—Lunar surface activity near sunrise (April 1973).

FIGURE 12-7.—Power spectrum analysis of quiet period.

FIGURE 12-6.—Power spectrum analysis of lunar sunrise data.

When the LSG was emplaced, it was impossible to balance the beam by sending commands to add or subtract mass. The motion of the beam suggested that an additional force corresponding to lunar gravity acting on approximately a gram of mass would balance the beam. Such a force can be exerted by operating the mass-changing mechanism beyond the point of addition of all masses so that it contacts the beam, moving it to midposition. In this configuration, the instrument is apparently behaving like a gravimeter with resonances at 1.5 Hz and possibly at a much lower frequency. The seismic output appears to be that corresponding to the sensitivity indicated in figure 12-4, and noise output in the free modes open-loop band (fig. 12-3) suggests that surface accelerations are being sensed in these bands of frequencies. The seismic channel output during a several minute period associated with lunar sunrise is

shown in figure 12-5. A power spectrum analysis of these data is depicted in figure 12-6. For comparison, the power spectrum of a period preceding sunrise is illustrated in figure 12-7. Thus, it appears that the LSG may carry out the search for gravitational waves.

ACKNOWLEDGMENTS

REFERENCES

12-1. Weber, Joseph: The Detection of Gravitational Waves. Sci. Am., vol. 224, no. 5, May 1971, pp. 22-29.

12-2. Weber, Joseph: Pulses of Gravity. Science Year: The World Book Science Annual. Field Enterprises, Inc. (San Francisco), 1972.

12-3. Weber, Joseph: Detection and Generation of Gravitational Waves. Phys. Rev., vol. 117, no. 1, Jan. 1960, pp. 306-313.

12-4. Weber, Joseph: General Relativity and Gravitational Waves. Interscience Pub., Inc. (New York), 1961.

12-5. Weber, Joseph: Evidence for Discovery of Gravitational Radiation. Phys. Rev. Letters, vol. 22, no. 24, June 1962, pp. 1320-1324.

12-6. Weber, Joseph: Gravitational Radiation Experiments. Phys. Rev. Letters, vol. 24, no. 6, Feb. 1970, pp. 276-279.

12-7. Weber, Joseph: Anisotropy and Polarization in the Gravitational-Radiation Experiments. Phys. Rev. Letters, vol. 25, no. 3, July 1970, pp. 180-184.

12-8. Weber, Joseph: Computer Analyses of Gravitational Radiation Detector Coincidences. Nature, vol. 240, no. 5375, Nov. 1972, pp. 28-30.

12.9. Flügge, Siegfried, ed.: Geophysik II. Vol. XLVIII of Handbuch der Physik, Springer-Verlag (Berlin), 1957, p. 803.

13. Traverse Gravimeter Experiment

Manik Talwani,[a†] *George Thompson,*[b] *Brian Dent,*[b] *Hans-Gert Kahle,*[a] *and Sheldon Buck*[c]

The primary goal of the traverse gravimeter experiment (TGE) was to make relative gravity measurements at a number of sites in the Apollo 17 landing area and to use these measurements to obtain information about the geological substructure. A secondary goal was to obtain the value of the gravity at the landing site relative to an accurately known value on Earth. Both these goals were successfully achieved by the experiment. A gravity tie has been obtained between the Taurus-Littrow landing site and the Earth with an estimated accuracy of approximately 5 mgal. Relative gravity measurements that can be used to infer the substructure of the area have been obtained at stations visited during each period of extravehicular activity (EVA).

BASIC THEORY

Free-Air and Bouguer Anomalies

The basic theory for the interpretation of the traverse gravity measurements can be described with the help of the sketch in figure 13-1. As a simplifying approximation, two-dimensionality is assumed; the sketch is a hypothetical geological cross section. The gravity measurements are made at the lunar module (LM) landing site and at certain stations (stations 1, 2, 3, 4, 5, etc.). The gravity value at the LM site is subtracted from the values at the other stations, and, for this report, only the relative values at the stations will be considered.

The first step in the interpretation of the relative gravity values is to make the free-air correction for elevation; that is, to allow for the differences in the

distances of these stations from the center of the Moon. If g_m denotes the gravity at the surface of the Moon, M the mass of the Moon, r the radius of the Moon, and k the universal constant of gravitation, then

$$g_m = \frac{kM}{r^2} \qquad (13\text{-}1)$$

The free-air gradient then is

$$\frac{\partial g_m}{\partial r} = \frac{-2kM}{r^3} = \frac{-2g_m}{r} \qquad (13\text{-}2)$$

and the free-air correction is $2g_m/r$, which yields a value of 0.19 mgal/m. The elevation in meters is measured from an arbitrary elevation datum (fig. 13-1). The free-air correction is added to the relative gravity values to obtain the free-air anomalies.

The next step in the interpretation of the free-air anomalies involves the Bouguer correction. The Bouguer correction allows for the gravity effect (i.e., the vertical component of the gravitational attraction) of the material above the elevation datum

---
[a]Lamont-Doherty Geological Observatory.

[b]Stanford University.

[c]Charles Draper Laboratory, Massachusetts Institute of Technology.

[†]Principal Investigator.
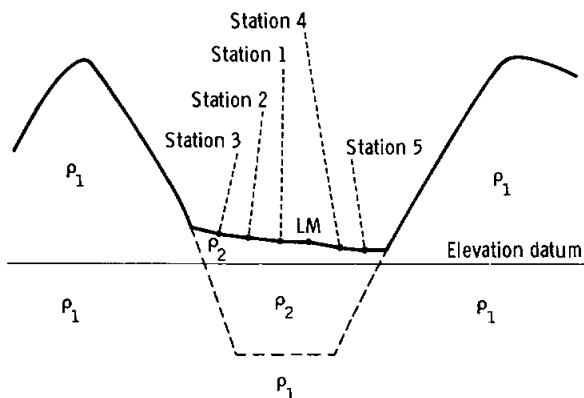
FIGURE 13-1.—Schematic diagram showing assumed density configurations for a hypothetical geological cross section.

computed at the gravity stations. This correction involves a knowledge of the density of the material above the elevation datum. In the sketch in figure 13-1, densities of ρ_1 for the material comprising the massifs and ρ_2 for the material of the valley floor have been assumed. The fact that the actual situation can be much more complicated must be considered in the interpretation of the Bouguer anomalies.

In gravity interpretation, the Bouguer correction is usually applied in two steps. The first, the flat-plate Bouguer, assumes that the elevation is the same at all points as at the station where the correction is being applied. The second, the terrain correction, allows for the departure of the actual terrain from a plane at the height of the station. For the Taurus-Littrow landing site, the terrain corrections are large, and no particular advantage is gained by computing the flat-plate Bouguer corrections and the terrain corrections separately. By computing the gravity effect of all the material above the elevation datum with a single computation, the combined Bouguer correction is applied, and, by adding it to the free-air anomaly, the Bouguer anomaly is obtained. In these calculations of the Bouguer corrections, a flat Moon rather than a spherical Moon is used. The relative error at the different stations is negligible for the present calculations.

The final step is the interpretation of the Bouguer anomalies. The Bouguer anomalies have allowed for the elevation differences between the different stations and for the gravitational effect of the material above the elevation datum. Therefore, the Bouguer anomalies are interpreted in terms of, and provide information about, the density contrasts of rocks lying below the elevation datum. In the simplified model shown in figure 13-1, for instance, the density contrast $\rho_1 - \rho_2$ between the material comprising the massifs and the material lying below the valley floor gives rise to the Bouguer anomalies at the stations. The actual structural situations as well as the density variations are probably much more complicated than those shown in the sketch. The interpretation approach will be to work with simple models consistent with available geological information and to see how these models explain the gravity data. The final structural solution will be constrained by the gravity results, by considerations of geological plausibility, and by the results from the other geological and geophysical data.

Two-Dimensional Calculations

As a first approximation, two-dimensionality is assumed. The gravity effect of a body is obtained by approximating its cross section by an irregular polygon. The gravity effect of a body with a polygonal cross section has been given by Talwani et al. (ref. 13-1).

Three-Dimensional Calculations

For more careful analysis of the gravity data, it is essential both to compute the Bouguer anomalies and to interpret them without the assumption of two-dimensionality. The basic formula used in this calculation is the gravity effect of a vertical prism, which is given by Jung (ref. 13-2). For distant areas, prisms of large area can be chosen and an average elevation assumed for them. For closer areas, prisms of smaller area must be chosen. By actual trial and error, prisms of optimum area are chosen at various distances from the landing site for use in the calculations. Such a determination has been made. The three-dimensional calculations are not complete at the present time, and only the results of two-dimensional calculations will be discussed in this report.

EQUIPMENT

Sensor

The gravity sensor used in the TGE is a Bosch Arma D4E vibrating string accelerometer (VSA). The accelerometer is schematically shown in figure 13-2. Each of the two strings, when energized, generates continuous vibrations with its own frequency, the value of which depends on the value of g. The difference between the two frequencies can be obtained. The difference frequency between the two strings Δf_n when the sensor is in its normal vertical position can be written as

$$\Delta f_n = k_0 + k_1 g + k_2 g^2 + k_3 g^3 + \ldots \quad (13\text{-}3)$$

Terms of order higher than 3 can be neglected. Nominal values for k_0, k_1, et cetera, for the flight vibrating string accelerometers are $k_0 = 7$ Hz, $k_1 = 129$ Hz/g, $k_2 = -0.00034$ Hz/g^2, and $k_3 = 0.003$ Hz/g^3. A principal reason for the use of a double-stringed rather than a single-stringed instrument is the
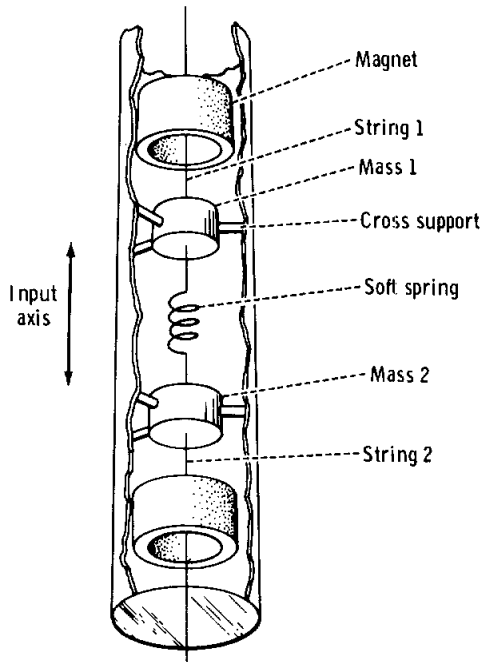
FIGURE 13-2.--Schematic view of double-stringed VSA.

reduction in the values of the higher order terms. Even-order terms of the type $k_2 g^2$ give rise to nonlinear rectification of inertial accelerations caused by vibrations; therefore, it is very important to keep the terms small.

The constants k_0, k_1, k_2, and k_3 are determined for the sensor before the mission. However, experience with sensors of this type had shown that k_0 is subject to drift as well as tares (sudden dc shifts). Any shift of k_0 would degrade the Earth-Moon gravity tie. (Shifts in k_1, k_2, etc., are much less important.) Also, if, at a station during a traverse, a large difference of gravity from the value at the LM site was indicated, it would be necessary to inquire whether this was a real variation in gravity or whether the value of k_0 had shifted. For this reason, provision was made to make independent determinations of k_0 when necessary. Such a determination is called a bias determination and is made by inverting the instrument. In the inverted case

$$\Delta f_i = -k_0 + k_1 g - k_2 g^2 + k_3 g^3 \qquad (13\text{-}4)$$

By assuming the values of k_1, k_2, and k_3, the values of k_0 and g can be determined from the values of Δf_n and Δf_i by combining equations (13-3) and (13-4).

Filtering and Phase Lock Loop

The electrically conducting VSA strings are placed in a permanent magnetic field (fig. 13-2). When a voltage is applied across the string, the resulting current causes motion of the string and induces a voltage across the string. The voltage is regenerated through a stable, high-gain amplifier and fed back to the string.

The output of each VSA string is a sine wave of a frequency between 9.25 and 9.75 kHz. The signal is fed to a phase lock loop module. The purposes of the phase lock loop module are to determine the difference frequency between the outputs of the two strings and to filter the effect of undesirable vibrations from the resultant signal.

Should any vibrations cause the input frequency from the VSA to exceed a previously specified limit, a phase lock loop alarm is generated. This alarm is indicated by the TGE display.

Measurement

Because the lunar value of g is approximately 163 000 mgal and a measurement to the precision of 0.1 mgal is desired, the difference frequency of the VSA must be measured to an accuracy of approximately 1×10^{-6}. Because the nominal values of the difference frequencies in the normal and inverted positions are approximately 28 and 14 Hz, respectively, a simple counting of the cycles obviously will take an impossibly long time. Instead, a gate is generated that is inversely proportional to the difference frequency. For the normal case, the gate consists of 1536 cycles of the difference frequency Δf_n (approximately 55 sec at this frequency); for the inverted case, the gate consists of 384 cycles of the difference frequency Δf_i (approximately 27 sec). The width of the gate is measured by counting the pulses from a precision 125-kHz clock by a counter. If D_n and D_i are the counts in the normal and inverted case

$$\Delta f_n = \frac{1536 \times 125 \times 10^3}{D_n} = \frac{1.92 \times 10^8}{D_n} \qquad (13\text{-}5)$$

$$\Delta f_i = \frac{384 \times 125 \times 10^3}{D_i} = \frac{4.8 \times 10^7}{D_i} \qquad (13\text{-}6)$$

If k_0, k_1, k_2, and k_3 are all known, equation (13-3) can be used to determine the value of g from Δf_n. If

k_0 is not assumed to be known, equations (13-3) and (13-4) together can be used to determine the value of g as well as k_0 from Δf_n and Δf_i.

Leveling

If the VSA axis is not vertical but is inclined at an angle θ to the vertical, $g \cos \theta$ is measured instead of θ. For a small θ, the error is $0.5g\theta^2$. The TGE is designed to keep θ less than $00°03'$ of arc and, consequently, the error caused by leveling less than 0.06 mgal.

To provide the leveling, the sensor is mounted on a gimbaled frame. Two vertical pendulums mounted on the gimbal frame sense departures from the vertical through comparator circuits. These comparator circuits provide information to stepping motors that drive the gimbals until the pendulums are level. The leveling is accomplished in two modes. When a pendulum is more than $00°32'$ of arc from level, the corresponding stepper motor slews faster; at less than $00°32'$, the motor slews at a slower rate to avoid overshoot. When the pendulums are within $00°03'$ of arc of being level, the slew commands are disabled.

When the instrument has to be inverted in the bias mode, a set of bias pendulums is used that gives signals unless the gimbal frame is similarly leveled in an inverted position.

The TGE can be leveled only if it is initially placed in a position less than $15°$ from level. In the normal mode, time for leveling is between 0 and 20 sec; in the bias mode, the time is between 90 and 130 sec.

Temperature Control and Monitoring

Because the VSA sensor is extremely sensitive to temperature, it is necessary to control its temperature to within 0.01 K. The VSA and its oscillator-amplifiers are encased in a precision oven that is maintained at a temperature near 322 K to within 0.01 K by the temperature control and monitor circuit. The precision oven, in turn, is encased in an outer oven that protects the inner oven from the external thermal disturbance.

The precision oven temperature circuit has proportional and rate control and uses an electrical heater and a resistance thermometer element for a sensor. The complete temperature sensor is an ac excited bridge, two arms of which are thermistors. The bridge output is demodulated and used to control drivers for

the precision heaters. A tap from the demodulator output is converted to digital form and forms a digit of the TGE display. The displayed digit marks the deviations of the precision oven temperature from a preset value. The outer oven thermostat and heater circuit merely react to temperature changes to control the power supplied to a heater.

A thermal blanket provides good thermal insulation for the TGE. A radiator at the top of the instrument provides the primary means of heat expulsion.

The mode of operation of the instrument was such that the radiator was left closed during each EVA. The instrument electronics produced heat, but this heat merely reduced the heating to be done by the ovens. Between EVA periods, the instrument was placed in the shade with the radiator open, and heat was then expelled into space. The temperature monitors are the eighth and ninth digits of the TGE display. The eighth digit gives the thermal condition of the outer oven and the sign for the ninth digit. The ninth digit of the numerical display is a number from 0 to 7 that represents a deviation of the precision oven temperature from a set point of 0.005 K times the digit displayed. Polarity of the deviation is obtained from the value displayed in the eighth digit.

Physical Description of the TGE

The TGE consists of the instrument package, a battery pack assembly, a thermal blanket, and an isoframe assembly. A cutaway view of the TGE is shown in figure 13-3.

Outer Structure.—The outer structure of the TGE is cylindrical with a flat rear surface. A folding handle at the top of the instrument is used for hand carrying and for latching the instrument to the isoframe assembly. Three feet at the base of the instrument enable lunar surface operations. A radiator at the top of the instrument provides the primary means of heat expulsion. The radiator and the display panel are protected from the environment by hinged insulating covers over each.

Inner Structure.—The inner structure of the TGE consists of a two-axis gimbal system, which contains a VSA housed in a thermally protected and evacuated two-stage oven assembly. The oven assembly is enclosed in an electronic frame (E-frame) assembly of similar structural design. The E-frame assembly is pivoted about its axis and supported by a middle
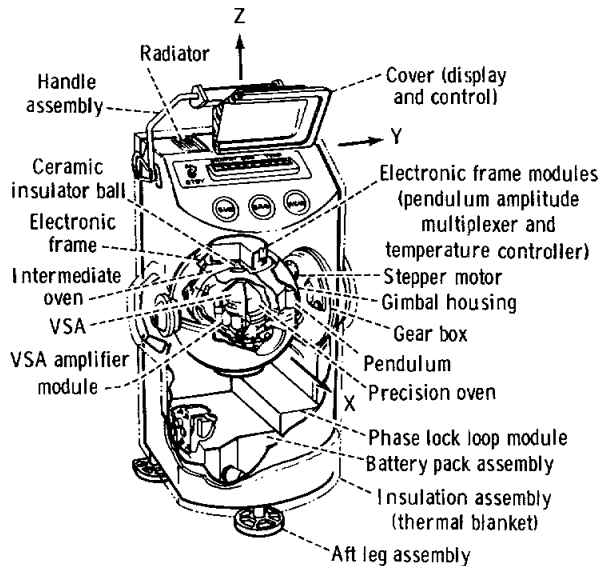
FIGURE 13-3.—Cutaway view of the TGE.

gimbal assembly. The middle gimbal controls the vertical positioning of the inner gimbal over a 30° range. The middle gimbal assembly is attached through bearings to the base housing and can rotate 210°. Stepper motors and a gear train provide the drive and positioning of the gimbal assemblies. The stepper motors react to signals from pendulums that act as level sensors.

Deployment and Operation of Instrument

Gravimeter measurements were made both with the TGE mounted on the lunar roving vehicle (LRV) and with the TGE placed on the surface. During a measurement, the TGE must be placed on a surface such that the vertical axis of the TGE is within 15° of vertical. The TGE must not be disturbed for approximately 3 min after a measurement has been initiated.

A normal measurement (one with the sensor in the normal, vertical position) is initiated by depressing the "GRAV" pushbutton on the TGE (fig. 13-3). The measurement cycle starts with leveling of the instrument. During the leveling cycle, the indicator light flashes off and on. When the instrument comes to a rest within 00°03' of arc of the vertical, the light stops flashing and remains illuminated until the difference frequency of the strings has been measured. The number of counts of a precision clock (from which the frequency can be obtained) forms the first seven digits of the TGE display. The eighth

and ninth digits of the display are thermal monitors, as explained in the section entitled "Temperature Control and Monitoring."

The display stays on for 20 sec. The display can, however, be turned on at any subsequent time by depressing the "READ" pushbutton, and it stays on for 20 sec.

A measurement with the sensor in the inverted position is made by depressing the "BIAS" pushbutton. The bias pendulums are used for leveling, and the indicator light flashes on and off until the sensor is leveled in an inverted position. The counting and display then proceed as for the normal measurement.

To conserve power, a toggle switch is provided to select the "STANDBY" or "ON" mode of operation. In the "STANDBY" mode, power is supplied only to the oven temperature controls and to the VSA oscillator-amplifiers. Cycling the switch from "ON" to "STANDBY" to "ON" will erase any stored data. Depressing the "READ" pushbutton after such a switching provides valid readings only for the eighth digit, which is the temperature monitor for the outer oven and for the battery.

RESULTS

Number of Readings

Of the 26 readings obtained (table 13-I), three (readings 1, 10, and 18) were obtained to learn the thermal state of the instrument before the EVA periods. No gravity values were obtained with these readings.

Reading 8 at the LM site showed that the TGE had been moved during the measurement as indicated by the phase lock loop alarm, which gives zeros in the first three digits of the display in such instances. This reading, therefore, was valueless, and another reading was obtained at the same site.

At the LM site, nine readings were made. Six of these were readings in the normal TGE position (upright) on the lunar surface (readings 3, 9, 11, 17, 19, and 25); one reading was made at the start of each EVA and one at the end of each EVA. Two readings (4 and 26) were made in the inverted position to determine the value of the bias term k_0 at the beginning and end of the measurements. One reading (2) was made on the LRV to compare "on LRV" and "off LRV" measurements.

Besides the readings at the LM site, 11 other

TABLE 13-I.—*Traverse Gravimeter Readings*

Reading	Location	Elapsed time at which measurement initiated, hr:min:sec	Display	$D_n - D_{n\ base}$[a]	$\Delta g = (D_n - D_{n\ base}) \times (-0.03245),$ mgal	Δg after application of empirical correction,[b] mgal	Elevation, m	Comments
					EVA-1			
1	LM site	–	XXX XXXX OX	–	–	–	–	Thermal monitor reading
2	LM site	01:17:32	670 0031 01	− 141	4.6	− 1.4	4510	On LRV
3	LM site	01:40:32	670 0172 01	0	0	0	4510	Off LRV; adopted as base reading D_n base
4	LM site	01:44:29	337 4540 01	–	–	–	–	Off LRV; inverted position
5	ALSEP[c] site	02:15:16	670 0026 01	− 146	4.7	− 1.3	4510	On LRV
6	Station 1	05:08:03	670 0129 01	− 43	1.4	− 4.6	4510	On LRV
7	SEP[d] site	05:56:03	670 0101 01	− 71	2.3	− 3.7	4510	On LRV
8	LM site	06:39:44	000 1332 01	–	–	–	–	Off LRV; measurement disturbed and disregarded
9	LM site	06:55:42	670 0215 01	43	− 1.4	− 1.4	4510	Off LRV
					EVA-2			
10	LM site	–	XXX XXXX OX	–	–	–	–	Thermal monitor reading
11	LM site	00:17:46	670 0177 01	5	− 0.2	− 0.2	4510	Off LRV
12	Station 2	02:18:05	670 1552 01	1380	− 44.8	− 50.8	4625	On LRV
13	Station 2A	03:21:09	670 1235 01	1063	− 34.5	− 40.5	4605	On LRV
14	Station 3	04:02:40	670 0497 01	325	− 10.5	− 16.5	4565	On LRV
15	Station 4	04:56:12	670 0125 01	− 47	1.5	− 4.5	4543	On LRV
16	Station 5	06:00:11	670 0314 01	142	− 4.6	− 10.6	4525	On LRV
17	LM site	–	670 0235 01	63	− 2.0	− 2.0	4510	Off LRV
					EVA-3			
18	LM site	–	XXX XXXX OX	–	–	–	–	Thermal monitor reading
19	LM site	00:17:20	670 0270 01	98	− 3.2	− 3.2	4510	Off LRV
20	Station 6	01:29:00	670 1098 01	926	− 30.0	− 36.0	4575	On LRV
21	Station 8	03:20:XX	670 0960 01	788	− 25.6	− 31.6	4575	On LRV
22	Station 8	03:45:39	670 1173 01	1001	− 32.5	− 32.5	4575	Off LRV
23	Station 9	04:30:46	670 0378 01	206	− 6.7	− 12.7	4515	On LRV
24	Station 9	–	670 0571 01	399	− 12.9	− 12.9	4515	Off LRV
25	LM site	05:55:58	670 0107 01	− 65	2.1	2.1	4510	Off LRV
26	LM site	06:03:00	337 4171 01	–	–	–	–	Off LRV; inverted position

[a]Difference between the display (first seven digits) at a station D_n and the display at the LM site $D_{n\ base}$ (reading 3).

[b]Empirical correction of − 6.0 mgal applied to all on-LRV values; off-LRV values are unchanged.

[c]Apollo lunar surface experiments package.

[d]Surface electrical properties experiment.

discrete measurements were made at different sites (readings 5, 6, 7, 12, 13, 14, 15, 16, 20, 21, and 23). Two extra measurements (readings 22 and 24) were made at stations 8 and 9 on the lunar surface to compare on-LRV and off-LRV measurements at these sites.

In the preliminary evaluation of gravity in table 13-I, the constants k_2 and k_3 of equation (13-3) are ignored and a value of k_1 = 0.0001318 Hz/mgal is assumed. For obtaining the value of gravity Δg at the stations relative to the value at the LM site, it can be shown that, when k_2 and k_3 are ignored, an approximate value is given by

$$\Delta g = \left(D_n - D_{n \text{ base}}\right) \times (-0.03245) \quad (13\text{-}7)$$

where D_n is the display (first seven digits) at that station and $D_{n \text{ base}}$ is the display at the LM site. The first off-LRV reading at the LM site (3) was chosen as the $D_{n \text{ base}}$. The values of Δg thus obtained are given in table 13-I.

Gravimeter Drift

For the flight instrument, it was determined before the mission that the drift during the EVA period ($\approx$ 7 hr) was essentially zero. Therefore, it was decided to adopt a zero drift rate unless the off-LRV values at the LM site showed a consistent drift pattern. The off-LRV values at the LM site are given in table 13-II. Relative to the first reading, the gravity values range from 2.1 to − 3.2 mgal. The only positive value, 2.1 mgal, was reading 25. Before reading 25, during the traverse from station 9 to the LM site, the pallet on which the traverse gravimeter was mounted swung open, and, as noted later in the

TABLE 13-II.—*Off-LRV*
Δg Values at LM Site
Relative to First Value
Obtained
[rms deviation = 1.8 mgal]

Reading	Δg, mgal
3	0.0
9	− 1.4
11	− .2
17	− 2.0
19	− 3.2
25	2.1

report, the resultant banging of the pallet may have caused instrument problems resulting in an erroneous reading 25. All the remaining values were negative. Nevertheless, a consistent drift pattern was not detected; hence, a zero drift was adopted. The variation in values is attributed to instrument noise, which has an rms value of 1.8 mgal.

Comparison of On-LRV and Off-LRV Values

Readings 2 and 3 were both obtained at the LM site. Reading 2 was taken with the gravimeter on the LRV, and reading 3 was taken with the gravimeter on the lunar surface. The difference between the two readings was 4.6 mgal. In an effort to determine whether this difference was random or systematic, on-LRV and off-LRV readings also were taken at stations 8 and 9. As shown in table 13-III, the lunar surface readings are, in all three cases, lower than the LRV values (the free-air difference is negligible) by amounts ranging from 4.6 to 6.9 mgal. There is no explanation for this difference; however, on the basis of three readings, an empirical correction of − 6.0 mgal has been made to all on-LRV measurements (table 13-I). Some support for this correction comes also from postmission tests with the engineering and spare flight models. When the handle of the gravimeter was jarred, temporary shifts in the gravimeter measurements occurred that were always in the same direction (although these shifts were < 6 mgal). By applying the − 6.0-mgal correction to the value at the Apollo lunar surface experiments package (ALSEP) site, this measurement is brought into agreement with the measurement at the LM site. The gravity values at the two sites are expected to be close. However, agreement between the value at the LM site and that at the nearby surface electrical properties (SEP) experiment site deteriorates slightly as a result of this correction.

Earth-Moon Gravity Tie

On the basis of normal reading 3 and inverted reading 4 (table 13-IV), a value of g = 162 694.6 mgal was measured at the LM site at Taurus-Littrow. The constants k_1, k_2, and k_3 used in this determination were obtained during preflight tests. The value of k_0 obtained as a result of readings 3 and 4 was 7.21591 Hz. A predicted value of k_0 based on laboratory test data was 7.2144 Hz. The total shift during the

TABLE 13-III.—*Comparison of Off-LRV and On-LRV Values at LM Site, Station 8, and Station 9*

[rms on-LRV/off-LRV difference without empirical correction, 6.0 mgal; with empirical correction, 1.0 mgal]

| Location | On LRV | | Off LRV | | Difference, mgal | Difference after application of empirical correction,[a] mgal |
	Reading	Δg, mgal	Reading	Δg, mgal		
LM site	2	4.6	3	0.0	4.6	− 1.4
Station 8	21	− 25.6	22	− 32.5	6.9	.9
Station 9	23	− 6.7	24	− 12.9	6.2	.2

[a]Empirical correction of − 6.0 mgal applied to on-LRV values.

TABLE 13-IV.—*Determination of* k_0 *and* g *at LM Site from Readings in Normal and Inverted Positions*

Reading	Position	Display	$\Delta f_n = \dfrac{192 \times 10^8}{D_n}$, Hz	$\Delta f_i = \dfrac{4.8 \times 10^7}{D_i}$, Hz	k_0, Hz	g, mgal
			EVA-1			
3	Normal	$D_n = 670\ 0172$	28.655981	—	} 7.215910	162 694.6
4	Inverted	$D_i = 337\ 4540$	—	14.224161		
			EVA-3			
25	Normal	$D_n = 670\ 0107$	28.65626	—	} 7.215272	162 701.5
26	Inverted	$D_i = 337\ 4171$	—	14.225716		

translunar phase was 0.0015 Hz. This corresponds to a bias shift of approximately 11 mgal, which is considered reasonable when compared to typical bias shifts experienced during acceptance and vibration testing.

On the basis of normal reading 25 and inverted reading 26, a second value of g = 162 701.5 mgal was determined after EVA-3. The value for the bias constant k_0 differed by approximately 0.00064 Hz from the initial value, which implies a shift of approximately 5 mgal in the bias value. However, the normal measurement of gravity obtained for reading 25, if the initial value of k_0 is used, differs by only 2 mgal from the initial value. During the traverse from station 9 to the LM site, the pallet on which the traverse gravimeter was mounted apparently swung loose and banged against the LRV. This was the only time during the entire mission that the gravimeter was shocked in this manner. Because deterioration in the performance might have resulted from this shock, less emphasis has been placed on readings 25 and 26 and

the initial determination of 162 694.6 mgal has been adopted. An uncertainty of ± 5 mgal is ascribed to this measurement.

DISCUSSION

Computation of Bouguer Anomalies

For a preliminary interpretation of the gravity measurement, two-dimensionality is assumed. The problem then essentially is reduced to the determination of the substructure of the linear Taurus-Littrow valley with linear massifs on either side. The stations at which the gravity measurements were made are shown in figure 13-4; the values at these stations were projected to a roughly southwest-to-northeast cross section. The value at station 6 could not be appropriately projected to this cross section and has been ignored in the present discussion. The great structural relief of the area makes three-dimensional calculations necessary. Such calculations will be described in
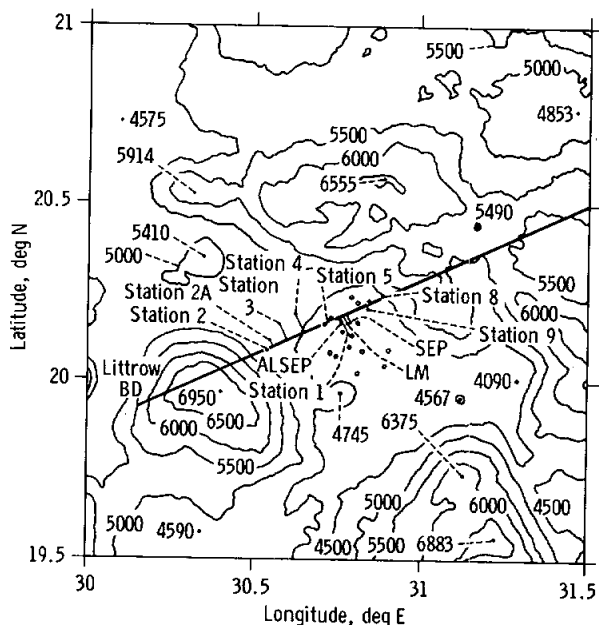
FIGURE 13-4.—Contour map of Taurus-Littrow landing site, showing the stations at which gravity measurements were made. The straight line starting near Littrow BD Crater (lower left) and trending northeast through the landing site is the cutting plane for the cross section to which the gravity measurements were projected. (Based on operational topographic map prepared by U.S. Army Topographic Command, October 1972. Contour interval, 500 m.)

FIGURE 13-5.—Topographic profile showing locations of projected stations. Station 1 and the ALSEP and SEP sites have been omitted because their elevations are the same as that of the LM site. The elevation datum (abscissa) is the elevation of the LM site.
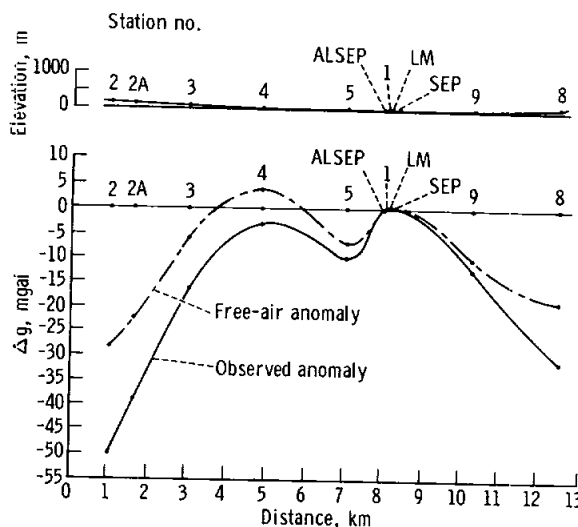
FIGURE 13-6.—Observed anomaly and free-air anomaly profiles across the Taurus-Littrow valley.

a later report. The topographic profile with the locations of the projected stations is shown in figure 13-5.

The observed anomaly Δg, as obtained in table 13-I, is plotted as a function of distance in figure 13-6. The observed anomaly is approximately 50 mgal lower at station 2, closest to the South Massif, and approximately 30 mgal lower at station 8, closest to the North Massif, relative to the value of gravity at the LM site. The observed anomaly curve therefore shows a pronounced dip toward the massifs on either side.

The free-air correction is applied by using the correction previously given, $2g_m/r$. The free-air anomaly thus obtained (also plotted in fig. 13-6) dips to approximately $- 30$ mgal near the South Massif and to $- 20$ mgal near the North Massif relative to the value at the LM site.

The Bouguer correction is applied next. In making the free-air correction, as well as the Bouguer correction, an elevation datum must be chosen (fig.

13-1). The elevation datum chosen was the elevation of the LM site (fig. 13-5), which was the lowest elevation on the profile.

The Bouguer correction is, in effect, made in three parts to show the effect of (1) the valley floor (i.e., material lying between the elevation of the stations and the elevation datum; shown with a density of ρ_2 in fig. 13-1), (2) the North Massif, and (3) the South Massif. The three Bouguer correction curves and the total Bouguer correction are shown in figure 13-7. Note that the effect of the valley floor tends to cancel the effect of the massifs; hence, the total Bouguer effect is quite small (< 5 mgal). The Bouguer correction was calculated using a density of 2.0 g/cm^3 ($\rho_1 = \rho_2 = 2.0$ g/cm^3). This value is lower than the values for breccia densities shown in figure 13-8(a). However, if an average density of 2.5 g/cm^3 were used instead of 2.0 g/cm^3, the difference in the
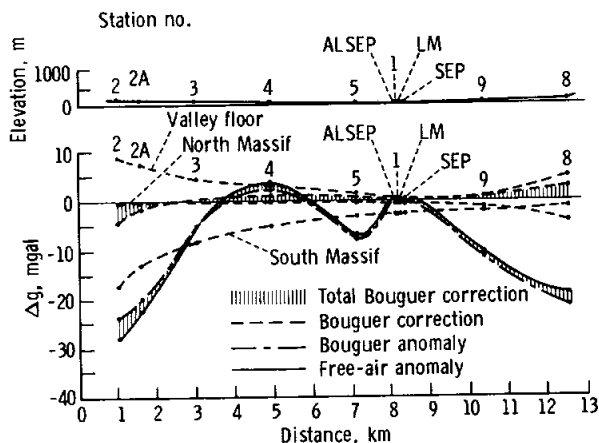
FIGURE 13-7.—Application of the Bouguer correction to determine the Bouguer anomaly profile across the Taurus-Littrow valley, showing the effect of the valley floor, of the North Massif, and of the South Massif and the total Bouguer correction. The free-air anomaly curve (fig. 13-6) is included for comparison with the Bouguer anomaly curve.

computed total correction would, in all cases, be less than 1 mgal. That difference can be ignored for the present discussion.

The resultant Bouguer anomaly curve, included in figure 13-9, shows minimums of near − 25 mgal at the stations closest to the massifs. The variation in the central part of the valley floor is within 10 mgal of the value at the LM site. This curve has to be interpreted in terms of the substructure of the valley. To do so, what is known about the densities of the lunar rocks must be considered first.

Densities of Lunar Rocks

No particular effort has yet been made to measure the bulk densities of the returned lunar rock samples. However, a few measured density values have been reported in the literature (refs. 13-3 to 13-21).[1] Most of these values were obtained in the course of measuring other physical properties of the lunar rocks (e.g., seismic velocity, heat conductivity, etc.). These published values are plotted in the histograms in figures 13-8(a) (lunar breccias) and 13-8(b) (lunar basalts).

The method used to obtain the density values was

---

[1] Also N. Warren, private communication, 1972, and G. D. O'Kelley, personal communication, 1973.

not always indicated in the sources but, when given, was one of the following.

1. The volumes of aluminum foil models of the whole rocks were measured, and the bulk densities were computed using the weights of the rocks. Because the aluminum foil models were not made to great accuracy, these density values can have 10 percent or even greater errors.

2. The volumes of small, precisely shaped samples of the rocks were computed by measuring their linear dimensions. The small samples are generally parallelepipeds, 1 by 1 by 2 cm. The densities were then computed using the measured weights of the small samples.

3. The densities of some small samples were measured directly using Archimedes' principle.

The density values tended to group on the basis of the method used to compute the density: the first method giving low values, the third method giving high values, and the second method giving values in the middle. This result is reasonable because the samples were generally vuggy, vesicular, porous, or highly fractured. Thus, the first method includes the effects of the largest vugs and vesicles and the third method includes only the effect of the unconnected pores and cracks; the second method will generally eliminate the effect of large vesicles and vugs but not that of small cracks and pores that cannot be avoided in cutting the small samples. Thus, an intrinsic density of approximately 3.4 g/cm^3 for the lunar basalts is indicated in figure 13-8(b).

Porosities have been measured for a few samples by point counts on thin sections or cut surfaces. A plot of density as a function of porosity and the intrinsic densities calculated from the porosities is given in figure 13-10. The intrinsic densities range from 3.25 to 3.49 g/cm^3 for the three basalts and from 2.99 to 3.14 g/cm^3 for the five breccias.

Figures 13-8(b) and 13-10 indicate that the bulk densities of mare basalt samples are determined by their porosity and that the samples have an intrinsic density of approximately 3.4 g/cm^3. Thus, a thick, mare lava flow with a thin, vesicular top would have a bulk density somewhat less than 3.4 g/cm^3. The data on the breccias are not as conclusive, but there is no evidence that the highly fractured rocks and breccias forming the highlands are more dense, on the average, than the average of the breccia samples thus far reported. Therefore, the density contrast between a

(a)

Number

*G. D. O'Kelley, personal communication, 1973
**N. Warren, private communication, 1972

14321
B13-5

---NASA lunar sample identification number

Reference number or data source

Type of density measurement:
A = aluminum foil models
B = shaped samples
C = hydrostatic weighing
D = method not reported

Chart (a) boxes:

62295 A*
15015 B13-20
14321 B13-21
14318 D13-18
14313 C13-17
14305 B**
14301 D13-16
10046 B13-6
10065 B13-7
10046 D13-5

67055 A*
61135 A*
12034 A*
10019 A13-4
10018 A13-4

66075 A*
15285 A13-3
14321 A*
10048 D13-5
14271 A*

61155 A*
66035 A*
14272 A*

65095 A*
61195 A*
15498 A*
12013 A*

15418 B13-20
14311 C13-17

61016 A*
12073 A*

Density, g/cm^3

2.0   2.5   3.0   3.5

(b)

Number

* G. D. O'Kelley, personal communication, 1973

Chart (b) boxes:

15557 A*
15545 A*
15065 A*
12002 B13-15
60315 A*

61156 A*
15476 A*
15058 A*
14310 B13-20
10057 B13-7
10072 A13-4

15499 A*
15076 A*
15016 A*
12031 A*

10057 A13-4
10003 A13-4

15495 A*
15475 A*
10069 B13-19

10049 B13-19
10020 B13-7
10017 B13-6

15597 A*
12063 B13-13
10017 B13-9

14310 D13-16
12022 C13-12
12002 C13-12
12065 B13-11
12052 B13-11
12022 B13-10
12018 B13-13
12050 D13-5

10049 D13-5
10047 D13-5
10044 D13-5
10022 D13-5
12002 A*

Density, g/cm^3

2.0   2.5   3.0   3.5

FIGURE 13-8.—Measured density values for lunar samples. (a) Breccia. (b) Basalt.
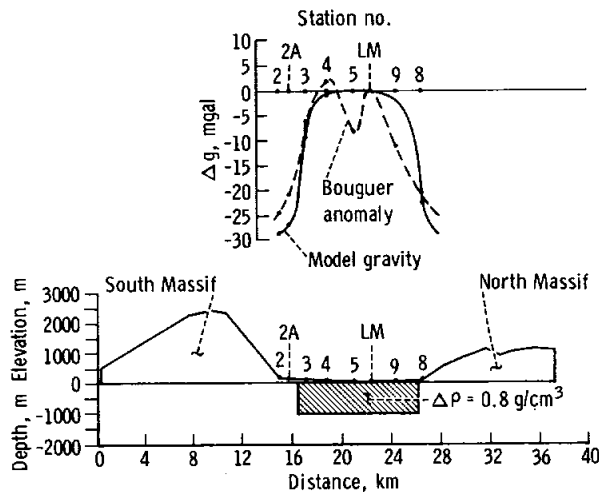
FIGURE 13-9.—Assumed model for subvalley densities to explain gravity anomalies, including the Bouguer anomaly curve. On the ordinate for the topographic profile, the elevation and depth are referenced to the elevation datum (0 m), which is the elevation of the LM site. The shaded rectangle represents a postulated block of basaltic material underlying the valley floor, where $\Delta\rho$ is the positive density contrast with respect to brecciated highland material on either side.

thick, mare basalt formation and highland breccia material should be at least $3.2 - 2.8 = 0.4$ g/cm^3 and may be as much as $3.3 - 2.3 = 1.0$ g/cm^3.

Structural Model

From the results of the last section, a very simple model has been used to explain the gravity results. Assuming that the subvalley floor material consists of basalt flows that have a positive density contrast of 0.8 g/cm^3 with respect to brecciated highland material on either side, a thickness of 1 km is obtained for the block of basaltic material (fig. 13-9). The large Bouguer gradients at the valley edges indicate steep sides for the postulated block of basaltic material. The sides are not at the edges of the valley but lie approximately 1 km inside the edges of the valley.

These are very preliminary conclusions based on the work performed to date. More elaborate models have not been presented because we expect that the three-dimensional terrain and Bouguer corrections will change the final Bouguer anomalies by 30 to 40 percent. These three-dimensional calculations will be based on the newer topographic maps currently being compiled. Changes are expected in the total Bouguer
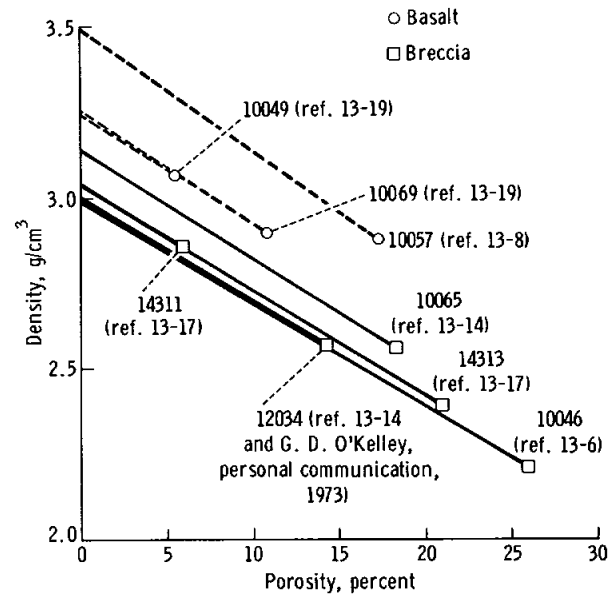
FIGURE 13-10.—Dependence of density on porosity for breccia and basalt lunar samples.

anomaly amplitude (from edge of valley to center of valley) as well as in the slope of the Bouguer anomaly curve near the edges. In this connection, the values obtained at stations 2A and 6 will be especially useful in refining the nature and position of the margin of the inferred high-density body underlying the valley floor.

SUMMARY AND CONCLUSIONS

The successful performance of the TGE indicated that the value of gravity at the Taurus-Littrow landing site is 162 694.6 ± 5 mgal. The Bouguer anomaly, analyzed with a two-dimensional approximation, shows values approximately 25 mgal lower at the edges of the valley than at the LM site. The Bouguer anomaly curve is interpreted in terms of a 1-km-thick block of basaltic material lying below the valley floor with a positive density contrast of 0.8 g/cm^3 with respect to the material on either side.

REFERENCES

13-1. Talwani, Manik; Worzel, J. Lamar; and Landisman, Mark: Rapid Gravity Computations for Two-Dimensional Bodies with Application to the Mendocino Submarine Fracture Zone. J. Geophys. Res., vol. 64, no. 1, Jan. 1959, pp. 49-59.

13-2. Jung, K.: Schwerkraftverfahren in der Angewandten Geophysik. Akademische Verlags Gesellschaft, Geest and Portig K. (–G.), Leipzig, Germany, 1961.

13-3. O'Kelley, G. Davis; Eldridge, James S.; Schonfeld, E.; and Northcutt, K. J.: Concentrations of Primordial Radioelements and Cosmogenic Radionuclides in Apollo 15 Samples by Nondestructive Gamma-Ray Spectrometry. Lunar Science-III (Rev. abs. of the Third Lunar Science Conference (Houston, Tex.), Jan. 10-13, 1972), pp. 587-589.

13-4. O'Kelley, G. D.; Eldridge, J. S.; Schonfeld, E.; and Bell, P. R.: Primordial Radionuclide Abundances, Solar Proton and Cosmic Ray Effects and Ages of Apollo 11 Lunar Samples by Nondestructive Gamma-Ray Spectrometry. Proceedings of the Apollo 11 Lunar Science Conference, vol. 2, Pergamon Press (New York), 1970, pp. 1407-1423.

13-5. Schmitt, H. H.; Lofgren, G.; Swann, G. A.; and Simmons, G.: The Apollo 11 Samples: Introduction. Proceedings of the Apollo 11 Lunar Science Conference, vol. 1, Pergamon Press (New York), 1970, pp. 1-54.

13-6. Anderson, O. L.; Scholz, C.; Soga, N.; Warren, N.; and Schreiber, E.: Elastic Properties of a Micro-Breccia, Igneous Rock and Lunar Fines from Apollo 11 Mission. Proceedings of the Apollo 11 Lunar Science Conference, vol. 3, Pergamon Press (New York), 1970, pp. 1959-1973.

13-7. Horai, K.; Simmons, G.; Kanamori, H.; and Wones, D.: Thermal Diffusivity, Conductivity and Thermal Inertia of Apollo 11 Lunar Material. Proceedings of the Apollo 11 Lunar Science Conference, vol. 3, Pergamon Press (New York), 1970, pp. 2243-2249.

13-8. Kanamori, H.; Nur, A.; Chung, D. H.; and Simmons, G.: Elastic Wave Velocities of Lunar Samples at High Pressures and Their Geophysical Implications. Proceedings of the Apollo 11 Lunar Science Conference, vol. 3, Pergamon Press (New York), 1970, pp. 2289-2293.

13-9. Stephens, D. R.; and Lilley, E. M.: Loading-Unloading Pressure-Volume Curves to 40 kbar for Lunar-Crystalline Rock, Micro-Breccia and Fines. Proceedings of the Apollo 11 Lunar Science Conference, vol. 3, Pergamon Press (New York), 1970, pp. 2427-2434.

13-10. Stephens, D. R.; and Lilley, E. M.: Pressure-Volume Properties of Two Apollo 12 Basalts. Proceedings of the Second Lunar Science Conference, vol. 3, MIT Press (Cambridge, Mass.), 1971, pp. 2165-2172.

13-11. Kanamori, H.; Mizutani, H.; and Hamano, Y.: Elastic Wave Velocities of Apollo 12 Rocks at High Pressures. Proceedings of the Second Lunar Science Conference, vol. 3, MIT Press (Cambridge, Mass.), 1971, pp. 2323-2326.

13-12. Wang. H.; Todd, T.; Weidner, D.; and Simmons, G.: Elastic Properties of Apollo 12 Rocks. Proceedings of the Second Lunar Science Conference, vol. 3, MIT Press (Cambridge, Mass.), 1971, pp. 2327-2336.

13-13. Warren, N.; Schreiber, E.; Scholz, C.; Morrison, J. A.; et al.: Elastic and Thermal Properties of Apollo 11 and Apollo 12 Rocks. Proceedings of the Second Lunar Science Conference, vol. 3, MIT Press (Cambridge, Mass.), 1971, pp. 2345-2360.

13-14. Chao, E. C. T.; Boreman, J. A.; and Desborough, G. A.: The Petrology of Unshocked and Shocked Apollo 11 and Apollo 12 Micro-Breccias. Proceedings of the Second Lunar Science Conference, vol. 1, MIT Press (Cambridge, Mass.), 1971, pp. 797-816.

13-15. Katsube, T. J.; and Collett, L. S.: Electrical Properties of Apollo 11 and Apollo 12 Lunar Samples. Proceedings of the Second Lunar Science Conference, vol. 3, MIT Press (Cambridge, Mass.), 1971, pp. 2367-2379.

13-16. Chung, D. H.; and Westphal, W. B.: Dielectric Properties of Apollo 14 Lunar Samples. Lunar Science—III (Rev. abs. of the Third Lunar Science Conference (Houston, Tex.), Jan. 10-13, 1972), pp. 139-140.

13-17. Mizutani, H.; Fujii, N.; Hamano, Y.; Osako, M.; and Kanamori, H.: Elastic Wave Velocities and Thermal Diffusivities of Apollo 14 Rocks. Lunar Science—III (Rev. abs. of the Third Lunar Science Conference (Houston, Tex.), Jan. 10-13, 1972), pp. 547-549.

13-18. Chung, Dae H.: Laboratory Studies on Seismic and Electrical Properties of the Moon. The Moon, vol. 4, nos. 3/4, June/July 1972, pp. 356-372.

13-19. Horai, Ki-iti; and Fujii, Naoyuki: Thermophysical Properties of Lunar Material Returned by Apollo Missions. The Moon, vol. 4, nos. 3/4, June/July 1972, pp. 447-475.

13-20. Todd, Terrence; Wang, Herbert; Baldridge, W. Scott; and Simmons, Gene: Elastic Properties of Apollo 14 and 15 Rocks. Proceedings of the Third Lunar Science Conference, vol. 3, MIT Press (Cambridge, Mass.), 1972, pp. 2577-2586.

13-21. Chung, D. H.; Westphal, W. B.; and Olhoeft, G. R.: Dielectric Properties of Apollo 14 Lunar Samples. Proceedings of the Third Lunar Science Conference, vol. 3, MIT Press (Cambridge, Mass.), 1972, pp. 3161-3172.

14. S-Band Transponder Experiment

W. L. Sjogren,[a†] W. R. Wollenhaupt,[b] and R. N. Wimberly[a]

The purpose of this experiment was to measure the variations in the lunar gravitational field near the trajectory of orbiting space vehicles (i.e., the command and service module (CSM) and the small particles and fields subsatellites ejected from the Apollo 15 and 16 spacecraft). New information has been obtained from all Apollo orbiting spacecraft; however, this report shall be limited to the results from the Apollo 17 CSM and the Apollo 16 subsatellite. The data acquisition technique and data reduction methods have been presented in previous reports (refs. 14-1 and 14-2) and will not be discussed in this report. The data acquired are precise speed measurements of the orbiting spacecraft from which accelerations or gravity profiles may be inferred. Feature resolution is controlled by the spacecraft altitude and is almost a direct relationship (i.e., data taken from a 50-km altitude will resolve approximately a 50-km feature). Therefore, revolutions 3 to 12, when the CSM was in the low-altitude orbits, provided the clearest information.

The characteristics of the Apollo 17 CSM and the Apollo 15 CSM orbits were very similar. Consequently, some of the larger lunar features were traversed by both vehicles, permitting a broadening of the detailed investigation of the Serenitatis, Imbrium, and Crisium mascons. At present, one gravity profile has been reduced. The surface track of that profile and an Apollo 15 track are shown in figure 14-1. The corresponding gravity profile is shown in figure 14-2. These are line-of-sight accelerations (i.e., accelerations projected along the Earth-Moon line) and have no corrections applied for altitude or viewing geometry. The pronounced features are again Mare Serenitatis and Mare Crisium; however, additional features are identifiable.

PRELIMINARY RESULTS

A large negative gravity region[1] between the Serenitatis and Crisium mascons is located very near the Apollo 17 landing site (long. 30° E, fig. 14-2). Using this anomaly with a 43-percent increase attributable to least-squares filtering (ref. 14-3) and with the best estimate of the landing site lunar radius (1734.5 km), an absolute gravity estimate of 162 722 mgal is obtained. This estimate compares favorably with the traverse gravimeter result of 162 694 mgal (sec. 13) and instills additional confidence in the remote-sensing results. The difference of 28 mgal could be accounted for by the altitude difference, because our result was obtained at spacecraft altitude (15 km) rather than at the surface, or by small local anomalies of this order as measured by the traverse gravimeter (sec. 13).

Farther west on the figure 14-2 profile, the Mare Vaporum region (long. 3° E) is a negative anomaly. A stronger negative anomaly at longitude 4.5° W is over part of Montes Apenninus and between two ridge formations. At longitude 10° W, the edge of the Sinus Aestuum mascon was sampled. The small negative anomaly at longitude 20° W is produced by the crater Copernicus. The other anomalies across Oceanus Procellarum do not seem to correlate well with any visible surface features; however, they do correlate perfectly with previous work (refs. 14-4 and 14-5). The 50-mgal high at longitude 66° W is produced by Grimaldi (peak displaced because of geometric effect). When data from all 10 revolutions (3 to 12) are reduced, there will be 10 east-west Grimaldi profiles evenly spaced from the northern to the southern edge.

Some of the most obvious points concerning the

---

[1] A negative gravity region, often referred to as a negative anomaly, is defined as a region having a mass deficiency with respect to a homogeneous spherical body. A corresponding definition applies to a positive gravity region (or positive anomaly), sometimes called a gravity high.

[a]Jet Propulsion Laboratory.
[b]NASA Lyndon B. Johnson Space Center.
[†]Principal Investigator.
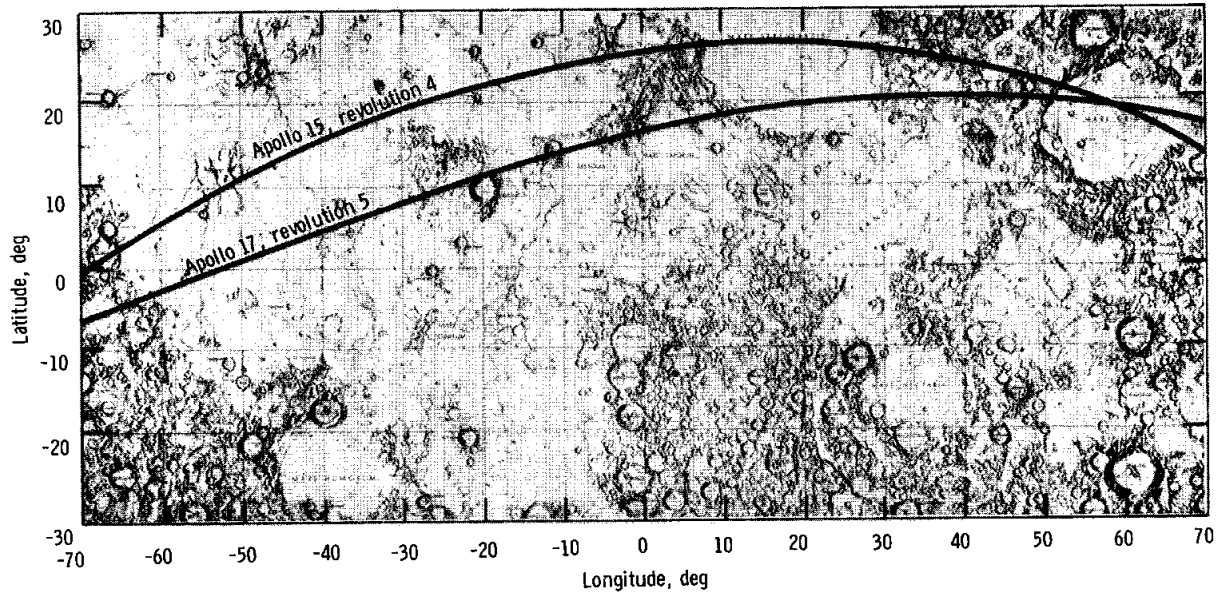
FIGURE 14-1.—Surface tracks of the Apollo 15 CSM during revolution 4 and of the Apollo 17 CSM during revolution 5.
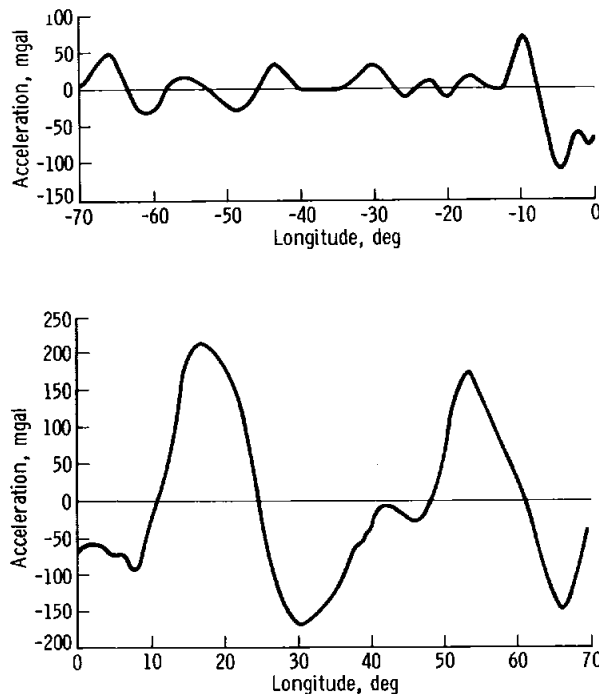
FIGURE 14-2.—Line-of-sight gravity profile derived from Apollo 17 revolution 5.

mascon profiles are that (1) the Serenitatis profile from the Apollo 17 data has almost the same maximum acceleration as the Apollo 15 profile (fig. 14-3) even though it is more than 200 km off center, (2) the western shoulder seen in the Apollo 15 profile of Serenitatis is not seen in the Apollo 17 profile, and (3) the Crisium profiles from the Apollo 15 and 17 data are very similar and cover approximately the same region (figs. 14-1 and 14-4). A theoretical gravity profile for Apollo 17 revolution 5 was generated using the best model of Serenitatis developed from Lunar Orbiter V and Apollo 15 data. The comparison of the actual and theoretical curves is shown in figure 14-3. There is approximately a 40-percent error from the actual observations, showing that new information can be extracted from these data. The same comparison is shown in figure 14-4 for the Crisium mascon, but the differences are relatively small.

The Grimaldi anomaly was analyzed using a surface disk model in which the mass, the radius of the disk, and the longitude of the disk center were estimated simultaneously. Doppler data were generated with this model and reduced in precisely the same manner as the actual observations. Several
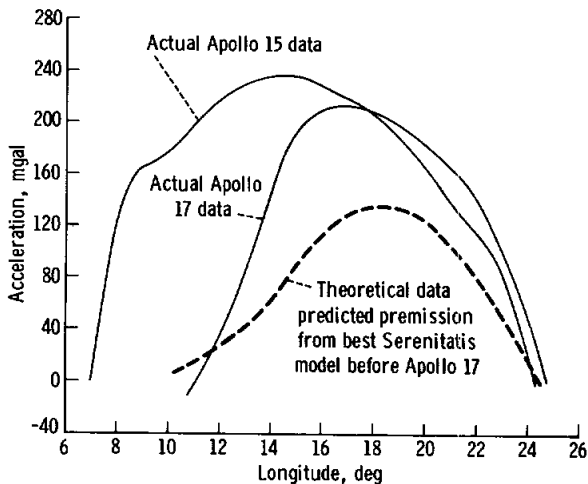
FIGURE 14-3.—Mare Serenitatis gravity profiles.
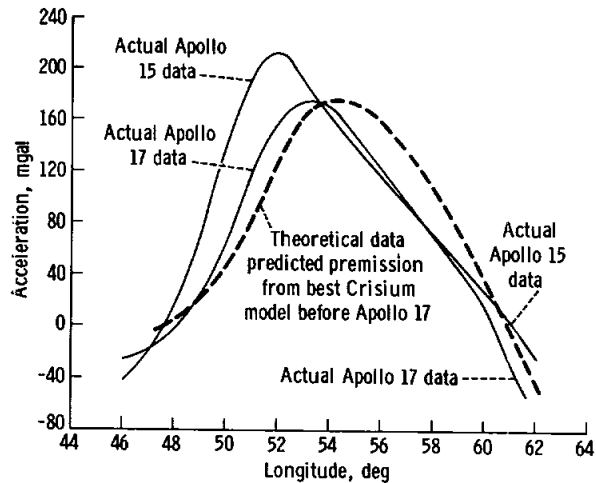
FIGURE 14-4.—Mare Crisium gravity profiles.
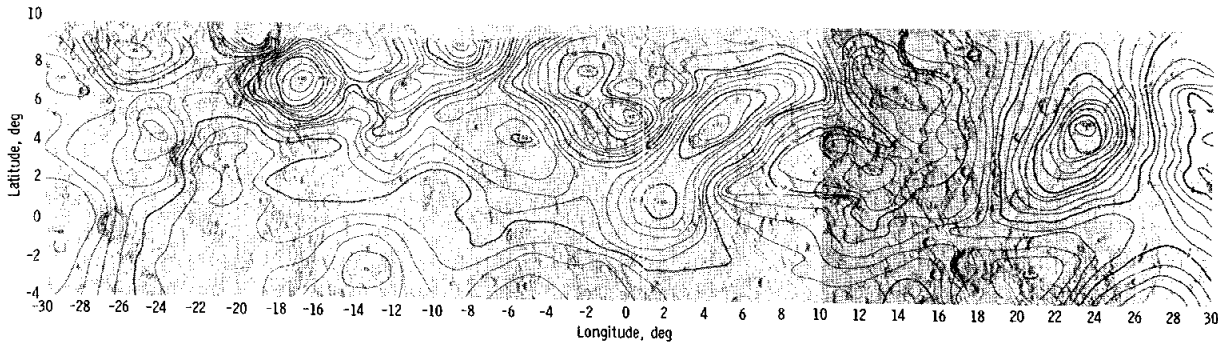
FIGURE 14-5.—Contour map of gravity from longitude 30° to −30° based on line-of-sight acceleration data from the Apollo 16 subsatellite. (Contour units are in milligals.)

iterations using a least-squares criterion on the acceleration profile yielded a mass of 1.03×10^{20} g and a radius of 70 km at −68° longitude. (Latitude was held at −5.50°.) The mass distribution from this result yields 1000 kg/cm², which is 25 percent higher than that determined for the other mascons. These very preliminary results may change when all profiles are analyzed together.

The Apollo 16 subsatellite at an orbital inclination of 9.5° provided new high-resolution observations over a region from latitude 9.5° N to 4° S and from longitude 70° E to 70° W. The altitude was approximately 20 km at latitude 6° N, 40 km at latitude 3° N, and 60 km at latitude 4° S. The data were acquired during 68 revolutions, which provided highly redundant coverage. The acceleration profiles from these revolutions have been contoured and superimposed on lunar charts. Only the central

section from longitude 30° W to 30° E is shown in figure 14-5 because that section contains most of the new features. A more detailed presentation is given in reference 14-5. The outstanding features are as follows.

1. The negative anomaly centered in Copernicus, which is another example of an unfilled crater having a negative anomaly

2. The positive anomaly just southeast of Copernicus that does not coincide with a visible surface feature but may be correlated with a large, ancient ring structure south of Imbrium (as shown in ref. 14-6)

3. The Aestuum positive anomaly that was detected in the original mascon mapping (ref. 14-7)

4. The gravity high at longitude −6°, latitude 4°

5. The Sinus Medii gravity high

6. The Triesnecker positive anomaly centered over the dense rille formation just north of the main crater

7. The Lamont positive anomaly in Mare Tranquillitatis centered over the flooded crater and wrinkle-ridge structure

The last two positive anomalies seem to be associated with rille and wrinkle-ridge features that are often referred to as volcanic examples. They are also the first strong positive anomalies over maria terrain that are not correlated with ringed basins.

CONCLUSIONS

The Apollo 17 data will provide a more detailed determination of the Serenitatis mascon, because it is clearly evident that the present model is inadequate. Grimaldi has a mass distribution larger than other mascon distributions, but this very preliminary result may change and show better agreement. The Apollo 16 subsatellite data reveal high gravity regions over mare areas not associated with ringed basins but over formations of probable volcanic origin (refs. 14-8 to 14-10). A positive anomaly southeast of Copernicus does not correlate with any visible feature and may be part of an ancient ringed structure that is almost obliterated.

ACKNOWLEDGMENTS

REFERENCES

14-1. Sjogren, W. L.; Gottlieb, P.; Muller, P. M.; and Wollenhaupt, W. R.: S-Band Transponder Experiment. Sec. 16 of the Apollo 14 Preliminary Science Report. NASA SP-272, 1971.

14-2. Sjogren, W. L.; Gottlieb, P.; Muller, P. M.; and Wollenhaupt, W. R.: S-Band Transponder Experiment. Sec. 20 of the Apollo 15 Preliminary Science Report. NASA SP-289, 1972.

14-3. Gottlieb, Peter: Estimation of Local Lunar Gravity Features. Radio Science, vol. 5, no. 2, Feb. 1970, pp. 301-312.

14-4. Sjogren, W. L.; Gottlieb, P.; Muller, P. M.; and Wollenhaupt, W.: Lunar Gravity via Apollo 14 Doppler Radio Tracking. Science, vol. 175, 1972, pp. 165-168.

14-5. Sjogren, W. L.; Wollenhaupt, W. R.; and Wimberly, R. N.: Lunar Gravity via the Apollo 15 and 16 Subsatellites. The Moon, vol. 8, 1973.

14-6. Wilhelms, D. E.; and McCauley, J. F.: Geologic Map of the Near Side of the Moon. U.S. Geol. Survey Misc. Geol. Inv. Map I-703, 1971.

14-7. Muller, P. M.; and Sjogren, W. L.: Mascons: Lunar Mass Concentrations. Science, vol. 161, no. 3843, Aug. 16, 1968, pp. 680-684.

14-8. Morris, E. C.; and Wilhelms, D. E.: Geologic Map of the Julius Caesar Quadrangle of the Moon. U.S. Geol. Survey Misc. Geol. Inv. Map I-510, 1967.

14-9. Schmitt, H. H.; Trask, N. J.; and Shoemaker, E. M.: Geologic Map of the Copernicus Quadrangle of the Moon. U.S. Geol. Survey Misc. Geol. Inv. Map I-515, 1967.

14-10. Wilhelms, D. E.: Geologic Map of the Mare Vaporum Quadrangle of the Moon. U.S. Geol. Survey Misc. Geol. Inv. Map I-548, 1968.

15. Surface Electrical Properties Experiment

Gene Simmons,[a][†] David Strangway,[b][‡] Peter Annan,[c] Richard Baker,[a]
Lawrence Bannister,[a] Raymon Brown,[a] William Cooper,[a] Dean Cubley,[b]
Joseph deBettencourt,[d] Anthony W. England,[e][‡] John Groener,[a] Jin-Au Kong,[a]
Gerald LaTorraca,[a] James Meyer,[a] Ved Nanda,[a] David Redman,[c]
James Rossiter,[c] Leung Tsang,[a] Joseph Urner,[d] and Raymond Watts[c]

The surface electrical properties (SEP) experiment was used to explore the subsurface material of the Apollo 17 landing site by means of electromagnetic radiation. The experiment was designed to detect electrical layering, discrete scattering bodies, and the possible presence of water. From the analysis of the data, it was expected that values of the electrical properties (dielectric constant and loss tangent) of lunar material in situ would be obtained.

The SEP experiment is important for several reasons. First, the values of the electrical properties of the outer few kilometers of rock and soil of the Moon, measured in situ for the first time, may help others interpret many observations already made with both Earth-based and lunar orbital bistatic radar. Second, the SEP experiment will provide data that are needed to interpret the observations made with the lunar sounder, an Apollo 17 orbital experiment. In the Apollo lunar sounder experiment, the time intervals required for electromagnetic waves to penetrate the Moon, be reflected, and return to the surface of the Moon were measured. Of more interest than times, however, are depths, which can be obtained from the lunar sounder delay times and the dielectric constant that is measured in the SEP experiment. Third, the results of the SEP experiment are expected to help define the stratigraphy of the Apollo 17 landing site. Visual observations made by the crewmen and recorded with cameras are restricted

to the surface of the Moon. The SEP experiment will extend to depth those visual observations made at the surface and perhaps reveal features at depth that do not reach the surface.

DESCRIPTION OF THE EXPERIMENT

The basic principle of the SEP experiment is interferometry. This principle involves only the interference of two or more waves to produce an interference pattern. The inversion of the interference pattern in terms of the spatial distribution of the electrical properties is the basic aim of the experiment (fig. 15-1). The experiment is most easily understood in terms of a single dipole antenna for radiating electromagnetic energy and a loop receiver for measuring the magnitudes of the fields. In the
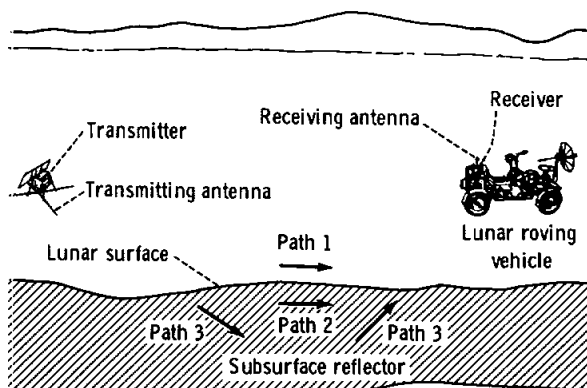
FIGURE 15-1.—Simplified schematic diagram of the SEP experiment. Electromagnetic radiation from the transmitting dipole antenna travels along path 1 (above the surface), along path 2 (below the surface), and, if reflectors are present, along path 3.

[a]Massachusetts Institute of Technology.
[b]NASA Lyndon B. Johnson Space Center.
[c]University of Toronto.
[d]Raytheon Company.
[e]U.S. Geological Survey.
[†]Principal Investigator.
[‡]Coinvestigator.

early developmental stages of this experiment, exactly this configuration was used (ref. 15-1).

The electromagnetic energy radiated from the transmitting antenna travels along various paths. In the "half-space" case, one wave travels above the interface through "free" space and another travels below the interface through subsurface material. Because the velocity of electromagnetic waves in a solid medium is different from that in free space, the two waves interfere and produce a distinctive interference pattern. This case has been studied extensively from both experimental and theoretical viewpoints since 1909 (ref. 15-2). The correct mathematical solutions, although somewhat complicated, are now well known (ref. 15-3). An example of a theoretical interference pattern for the half-space case is shown in figure 15-2. The spacing between successive maximums or successive minimums is related to the frequency of the wave and to the dielectric constant

of the medium, and the rate at which the field strength decreases with distance is related to the loss tangent of the medium. This type of pattern is present in some of the lunar data.

If a reflecting horizon occurs at depth, such as the case shown schematically in figure 15-1, then a reflected wave will interfere at the surface of the medium with the other waves. Figure 15-3 is a theoretical curve showing the distinct interference pattern produced by a reflected wave. The presence of additional reflecting horizons in the subsurface would produce still more complicated interference patterns.

In the Apollo 17 SEP experiment, two crossed dipole antennas that radiated sequentially were used. In addition, several frequencies—1, 2.1, 4, 8.1, 16, and 32.1 MHz—were used. Because each transmitting antenna radiates at each frequency for a sufficiently long time, the experiment results can be analyzed in terms of continuous waves. The shortest sampling time at the lowest frequency includes approximately 33 000 cycles.

THEORETICAL BASIS

The SEP experiment is the first geophysical field technique to use the dielectric properties of rocks rather than the conductive properties. In that sense, the experiment is entirely new. Consequently, all the

FIGURE 15-2.—Theoretical interference pattern for a half-space case, in which medium 1 is solid and medium 2 is free space; where depth $d = 0$, medium 1 loss tangent $p_1 = 0.0300$, medium 2 loss tangent $p_2 = \infty$, medium 2 dielectric constant $\epsilon_{r_2} = \infty$, and frequency $f = 299.8$ MHz. The symbol H_z represents the vertical component of the magnetic field. The points on the ordinate indicate the maximum (max) values of each wave pattern.

FIGURE 15-3.—Theoretical curve for the case of a single layer over a reflector. The layer is four free-space wavelengths $(4\lambda_0)$ thick (ref. 15-8).

experimental techniques and most of the theoretical basis have been developed specifically for the lunar experiment. Descriptions of the early versions (circa 1968) of the technique are given in references 15-1, 15-4, and 15-5. In this report, the physical and mathematical basis of the experiment is outlined and the discussions in references 15-6 to 15-8 are followed. Theoretical work has been limited to the electric and magnetic fields that result from dipole antennas on plane, horizontal, layered media. For mathematical details, the reader is referred to the original sources.

In the theoretical development, consideration is given first to electromagnetic propagation in an unbounded, homogeneous, isotropic dissipative medium and next to propagation near the plane interface of two semi-infinite homogeneous media (specialized to a lossy dielectric below an empty (or free) space region, popularly called the half-space case). Then, the effects of inhomogeneous horizontal stratification are considered, specialized initially to a lossy dielectric region of two layers, the first of depth d and the second of infinite depth and having electrical properties differing from the adjacent layer and the semi-infinite space above.

UNBOUNDED, HOMOGENEOUS, LOSSY DIELECTRIC MEDIA

Electromagnetic propagation in unbounded dissipative media is treated adequately in references 15-3 and 15-9 to 15-13. Variation of electric and magnetic fields with time t is usually expressed as $\exp(j\omega t)$ where the rotative operator $j = \sqrt{-1}$ and the radian frequency $\omega = 2\pi f$ (where the frequency f is expressed in hertz); this exponential is hereafter suppressed. Meter-kilogram-second units are used where, in vacuo, the dielectric constant or permittivity $\epsilon_0 = 1 \times 10^{-9}/36\pi$ F/m and the permeability $\mu_0 = 4\pi \times 10^{-7}$ H/m. The phase velocity in vacuo is $c = 1/\sqrt{\mu_0\epsilon_0} = 3 \times 10^8$ m/sec. Mathematically, the field expressions are solutions to Maxwell's equations.

The dissipative medium is characterized by its electrical constants, real relative dielectric constant ϵ_r and conductivity σ (mho/m). (For a vacuum, $\epsilon_r = 1$.) The media are customarily considered to be nonmagnetic with permeability $\mu = \mu_0$. The finite value of σ gives rise to a complex relative dielectric constant ϵ_r', a complex refractive index N, and a complex phase constant $k = \beta - j\alpha$ where β is the phase constant and

α is the attenuation constant. A typical component of electric field E at a large distance R from the radiating source varies with R according to

$$E = E_0 e^{-jkR} = E_0 e^{-\alpha R} e^{-j\beta R} \qquad (15-1)$$

where E_0 is a reference value of E (independent of R).

The complex relative dielectric constant is

$$\epsilon_r' = \epsilon_r(1 - jp) = \epsilon_r - jx \qquad (15-2)$$

where p is the loss tangent

$$p = \frac{\sigma}{\omega\epsilon_0\epsilon_r} = 60\sigma\frac{\lambda_0}{\epsilon_r} \qquad (15-3)$$

with λ_0 the free-space wavelength in meters.

The refractive index relative to vacuum is

$$N = \sqrt{\epsilon_r'} = \sqrt{\epsilon_r}(1 - jp)^{1/2} \qquad (15-4)$$

The evaluation of the complex radical may be accomplished by the 50-yr-old method of G. W. Pierce (ref. 15-14), recently revived by King (ref. 15-9), as follows.

$$\sqrt{1 - jp} = f(p) - jg(p) \qquad (15-5)$$

where

$$f(p) = \cosh\left(\frac{1}{2}\sinh^{-1}p\right) = \left[\frac{1}{2}\left(\sqrt{1 + p^2} + 1\right)\right]^{1/2}$$

$$g(p) = \sinh\left(\frac{1}{2}\sinh^{-1}p\right) = \left[\frac{1}{2}\left(\sqrt{1 + p^2} - 1\right)\right]^{1/2}$$

Thus, the complex phase constant k may be written as

$$k = \beta - j\alpha = \beta_0\sqrt{\epsilon_r'} = \beta_0 N = \beta_0\sqrt{\epsilon_r}[f(p) - jg(p)] \qquad (15-6)$$

where the phase constant (real) in vacuo $\beta_0 = 2\pi/\lambda_0 = \omega\sqrt{\mu_0\epsilon_0}$. Hence

$$\left.\begin{aligned} \beta &= \beta_0\sqrt{\epsilon_r}f(p), \text{ rad/m} \\[6pt] \lambda &= \frac{3 \times 10^8}{f}, \text{ m} \\[6pt] \alpha &= \beta_0\sqrt{\epsilon_r}\,g(p), \text{ Np/m} \end{aligned}\right\} \qquad (15-7)$$

When the loss tangent p is small, say $p < 0.5$, then $f(p) = 1$ and $g(p) = p/2$; this is the case encountered in the lunar SEP experiment, so that

$$
\left.\begin{aligned}
\beta &= \beta_0\sqrt{\epsilon_r} = \frac{2\pi}{\lambda}, \text{ rad/m} \\[6pt]
\lambda &= \frac{\lambda_0}{\sqrt{\epsilon_r}}, \text{ m} \\[6pt]
\alpha &= \frac{60\pi\sigma}{\sqrt{\epsilon_r}}, \text{ Np/m} \\[6pt]
&= 1.64 \frac{\sigma}{\sqrt{\epsilon_r}}, \text{ dB/km}
\end{aligned}\right\} \tag{15-8}
$$

and α is independent of frequency. If σ and ϵ_r are constant with frequency, then p is proportional to f; if p is constant with f, then σ/ϵ_r is proportional to f.

Propagation in Layered Media

For propagation in semi-infinite space near and above a semi-infinite, homogeneous (nonlayered) lossy dielectric, see references 15-3, 15-9, 15-10, and 15-15 to 15-17. References 15-16 and 15-17 are especially useful for layered media. Earlier application was to ground-wave propagation along the surface of the Earth, generally where the loss tangent of the Earth is large. The mathematical solutions are involved; they were solved initially by Sommerfeld in 1909 (ref. 15-2) with later (1926) correction of the famous $\sqrt{-1}$ sign error (ref. 15-18). A complete history, with proof of the existence of Sommerfeld's controversial surface wave, is given by Baños (ref. 15-3). The resulting field equations (for electric field E and magnetic field H) depend on the nature of the source. In theory, there are four source dipoles: the horizontal electric dipole (HED) and vertical electric dipole (wires), the horizontal magnetic dipole, and the vertical magnetic dipole (VMD). In the SEP experiment, a tuned series of wire antenna radiators (thus extensions of the elemental HED) is used, and the cylindrical coordinate values of magnetic field H_ρ, H_ϕ, and H_z are measured.

The major difference in typical ground-wave propagation from that on the Moon (or in earthbound glaciers and deserts) is in the low values of ϵ_r and p for the latter. For the case of a semi-infinite Moon below semi-infinite space, the solution is that for the so-called half-space case; the integral method of solution (ref. 15-3) involves general integrals of the type

$$
I(a,b,r) = \int_{-\infty}^{\infty} F(\lambda) e^{-\gamma_1 a - \gamma_2 b} H_0^1(\lambda r)\lambda \; d\lambda \tag{15-9}
$$

where the function $F(\lambda)$ is devoid of exponential behavior, H_0^1 is the zero-order Hankel function of the first kind, and $\gamma_i = (\lambda^2 - k_i^2)^{1/2}$ may be called a complex propagation factor ($i = 1$ denoting the lunar soil and $i = 2$ the space above). The variable λ used in equations (15-9) and (15-10) is a complex separation (or eigen) variable of integration and should not be confused with the wavelength.

In a cylindrical coordinate system with the source dipole at a height h above the origin of the coordinates (ρ, ϕ, z), two essential integrals $U(a,b,r)$ and $V(a,b,r)$ are required to determine the vector potential Π from which the fields E and H are derived. The relationship of E and H is derived from Maxwell's equations and continuity relations at the space-dielectric plane boundary ($z = 0$). The U and V integrals differ in the value of $F(\lambda)$ used; thus, for the V integral

$$
F(\lambda) = \frac{k_1^2\gamma_2 - k_2^2\gamma_1}{\left(k_1^4 - k_2^4\right)\left(\lambda^2 - k_0^2\right)} \tag{15-10}
$$

where

$$
\left.\begin{aligned}
k_0^2 &= \frac{k_1^2}{N^2 + 1} \\[6pt]
N &= \frac{k_1}{k_2} = \frac{k_1}{\beta_0} = \sqrt{\epsilon_{r1}'}
\end{aligned}\right\} \tag{15-11}
$$

In equation (15-11), the refractive index N (eq. (15-4)) is the reciprocal of n used by Baños (ref. 15-3) and others.

For evaluating a component of the magnetic field (e.g., H_z) in the SEP experiment, the U integral is required (actually the partial derivative of U). Here, $a = 0$, $b = h + z$, and the exponential involving a in equation (15-9) is unity; thus, U is written as $U(0,b,r)$. If $h = 0$, then U becomes $U(0,z,r)$.

The integral solution involves, generally, saddle-

point or double-saddle-point approximation methods (ref. 15-3). However, if $h = z = 0$, the solution for $U(0,0,r)$ is exact, as found by Van der Pol. Thus, the expressions for H_z waves broadside to the horizontal wire (HED) are exact as are those for the tangential component of electric field E_ϕ (VMD) (first noted by Wait (ref. 15-16)). If h or z (or both) are nonzero values, approximate methods must be used; these methods are very laborious because complex contour integration must be used with consequent studies of poles and branch cuts in the integrals $I(a,b,r)$.

The resulting field expression for the half-space case consists of two components, one a wave traveling above the surface with the phase velocity of space and the second a lateral wave; these two waves interfere. An example is shown in figure 15-2 for H_z lateral waves broadside to an HED for several values of ϵ_{r_1} and $p_1 = 0.03$. The lateral wave is that component of energy traveling in the dielectric but refracting across the boundary to reach the receiver at height $h = z$.

For typical terrestrial soils, the loss tangent p of the ground is so high that the lateral wave is relatively too small to be observed. However, in glaciers, polar regions, and deserts, such interference patterns as those shown in figure 15-3 may be observed.

Horizontal Stratification

Two Layers.—Wave propagation in stratified regions has been treated generally by Brekhovskikh (ref. 15-17) and Wait (ref. 15-16); the properties of antennas in such regions have been discussed by Galejs (ref. 15-15). As specified for the SEP experiment, the previously mentioned treatments in references 15-6 and 15-8 find useful application. The geometry is that of figure 15-4. The solutions are
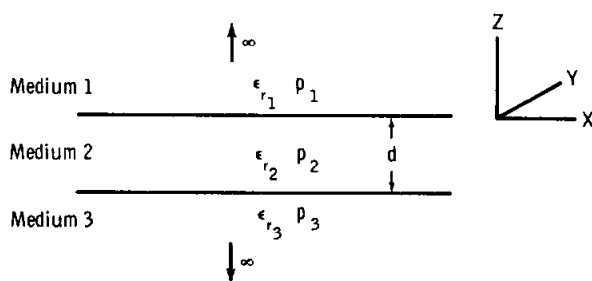
FIGURE 15-4.—Geometry for the case of a single layer over a half space. Medium 1, $a \geq 0$ (free space); medium 2, $-h \leq z \leq 0$; medium 3, $a < -h$.

integrals, similar to equation (15-9). The theoretical problem is reduced to that of solving the integrals. Three techniques have been used: (1) numerical integration on a digital computer, (2) asymptotic expansions that lead to geometrical optics approximations, and (3) contour integration to yield a normal mode solution (mode). In the geometrical optics approximation (GOA) method, the resulting field at the receiver consists of the space and lateral wave components (the half-space case) plus those attributable to reflections from the boundary between the upper layer of thickness d and the lower semi-infinite layer. (Lateral waves at this boundary and their effects have been generally neglected.) The formulation of reflections is approximate, but the GOA solution is considered satisfactory if the depth d is greater than the wavelength λ in the upper layer. An example is shown in figure 15-3, where $d = 4\lambda_0$, for lateral waves broadside to an HED. In the mode approach, the contributions to the integrals are identified in terms of the normal modes of wave propagation.

Multiple Layers.—Solutions to the various integrals (eq. (15-9)) for multiple layers can also be obtained by numerical integration and by using normal mode theory. The numerical integration method (refs. 15-8 and 15-19) provides quite exact solutions but requires much computer time; however, the method provides a check on other techniques and can be extended readily to large numbers of layers. In the GOA method, the problem is treated in terms or rays (thus, distances must be large compared with various wavelengths); therefore, solutions that are readily interpretable against a background of physical optics are provided. Unfortunately, the GOA is invalid for "thin" layers, the case for both glaciers and the Moon for at least some of the SEP experiment frequencies. The formulation and solutions for certain parameters are given in references 15-6 and 15-8. The theoretical curve for one set of parameters is shown in figure 15-5. The lack of agreement between the GOA and the numerical integration at distances less than 7λ is caused by the approximations in the GOA and indicates clearly that the proper solution must be chosen for a particular experimental situation. The normal mode solution, valid for thin layers such as appear to be present at the Apollo 17 site, was formulated by Tsang, Kong, and Simmons (ref. 15-8).

We are rather sure that our various formulations of the solution are correct. These formulations have
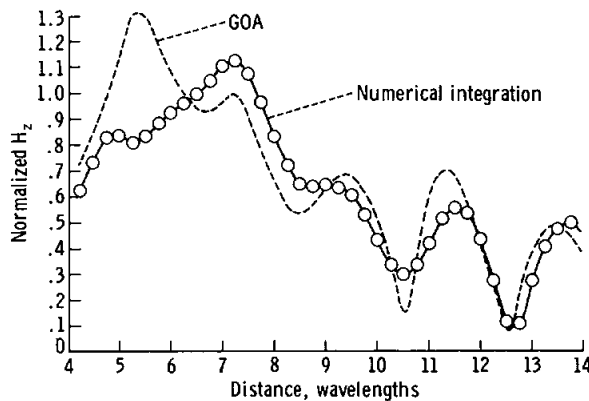
FIGURE 15-5.—Comparison of the geometrical optics approximation (dashed curve) with the Tsang exact solution (solid curve), obtained by numerical integration, for a single-layer case (ref. 15-8). Note the excellent agreement for all peaks except the first.

been tested against field data collected on glaciers for which the geometry was known from previous investigations using such other techniques as seismic, gravity, and drilling (refs. 15-1, 15-8, and 15-20). They have also been tested against laboratory data obtained with analog scale models.

The antenna radiation patterns of both the receiving loops and the transmitting dipoles are important in the analysis of the lunar data. The theoretical patterns for the transmitting antenna have been calculated (ref. 15-21), and the results are shown in figure 15-6. It has not been possible to calculate, with equal confidence, the patterns for the receiving antennas because of the effects of the lunar roving vehicle (LRV). From the data obtained on the Moon, however, it is deduced that the influence on the H_z component is minimal; thus, our preliminary data analysis is based on that component. In order to interpret the H_ρ and H_ϕ components, the effect of the radiation pattern of the receiving antenna must be removed.

THE EQUIPMENT

On the Moon, the crewmen deployed a small, low-power transmitter (fig. 15-7) and laid on the surface two crossed dipole antennas that were 70 m long tip to tip. The receiver and receiving antennas, shown in figure 15-8, were mounted on the LRV. Inside the receiver, there was a tape recorder which recorded the data on magnetic tape. The entire tape recorder, the data storage electronics assembly (DSEA), was returned to Earth. In addition to the
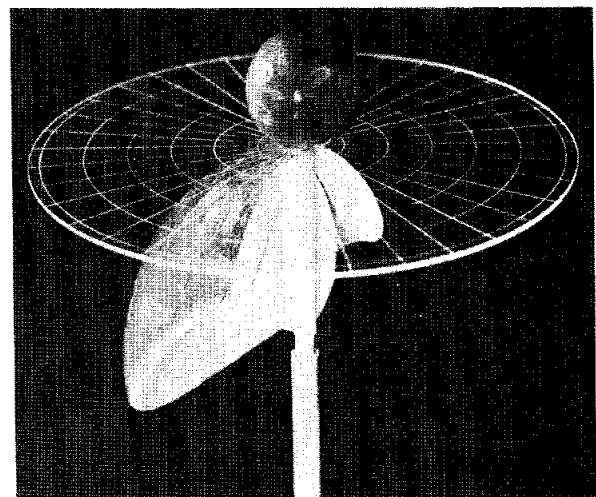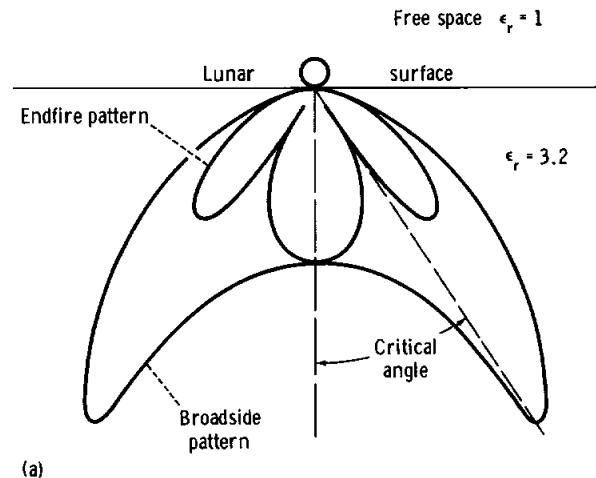
FIGURE 15-6.—Model of the theoretical radiation pattern for the SEP experiment transmitting antenna on the Moon (ref. 15-22). (a) Diagram. (b) Photograph.

SEP experiment data, information on the location of the LRV, obtained from the LRV navigation system, was also recorded on the tape.

Description

The electromagnetic radiation at the six SEP experiment frequencies is transmitted and received according to the scheme shown in figure 15-9. One data frame, which is 38.4 sec in duration, consists of six 6.4-sec subframes that are identical except for the receiver calibration and synchronization process. In subframe 1, for example, the receiver is calibrated at 32.1 and 16 MHz and the synchronization signal is
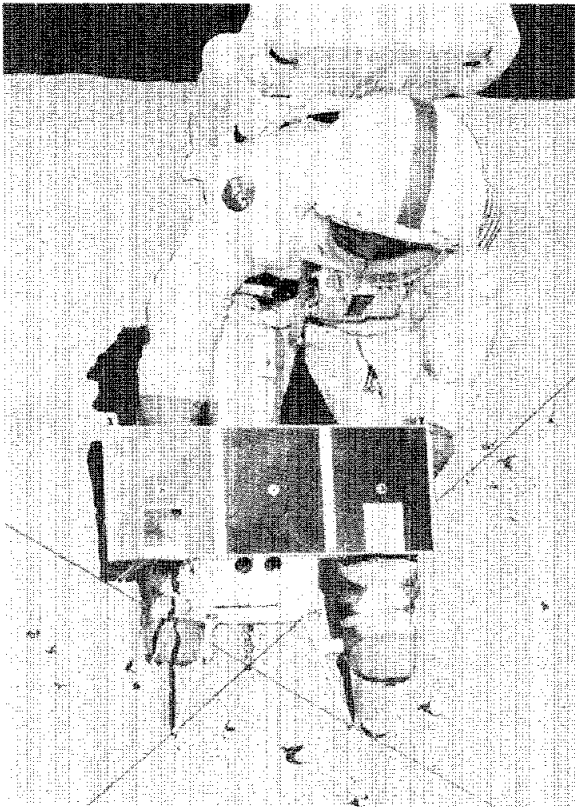
FIGURE 15-7.—The SEP experiment transmitter shown with the solar panel power source and dipole antennas deployed. The transmitter electronics package is covered on the bottom five sides with a thermal blanket. Because the top of the unit is shaded by the solar panel, the uncovered surface needs only a coat of thermal paint to provide adequate cooling for the enclosed electronics. The balance between heat lost to cold space by radiation and that generated inside the unit by the electronics equipment is very delicate and requires careful thermal design.

transmitted on the north-south (N-S) dipole antenna and received on the X antenna. In subframe 2, the receiver is calibrated at 8.1 and 4 MHz and the synchronization signal is transmitted on the east-west (E-W) antenna and received on the Y antenna. Each experiment frequency sequence is repeated exactly as shown in all six subframes. Each experiment frequency is transmitted first on the N-S antenna for 100 msec and then on the E-W antenna for 100 msec. During each 100-msec transmission interval, the receiver "looks" at the transmitted signal for a period of 33 msec with each of the three orthogonal (X,Y,Z) receiving loops. In addition to the preceding operations, once each subframe, the receiver observes environmental noise and records its amplitude.
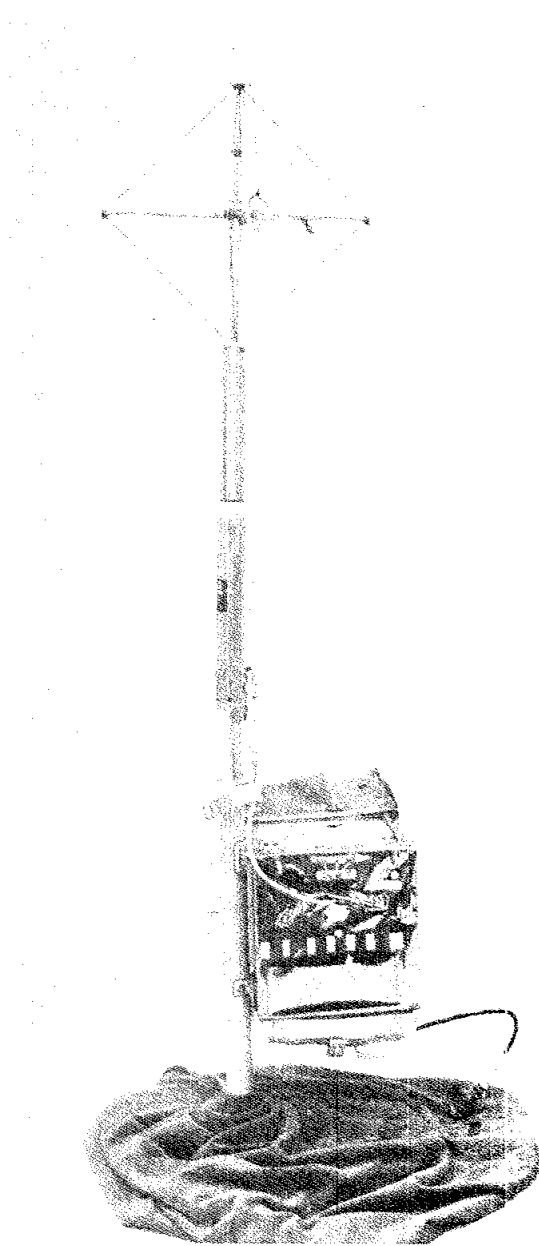
FIGURE 15-8.—The SEP experiment receiver and antennas. The receiver electronics, including tape recorder and battery, are contained in the box (23 cm^3), which usually is completely enclosed in a thermal blanket. The thermal blanket has been opened to show optical surface reflectors. The three-loop antenna assembly, folded during the journey to the Moon, is shown unfolded as it was used on the Moon.

The receiver acquires the transmitter signal sequence automatically as long as the signal exceeds a given threshold. Synchronization of the receiver is
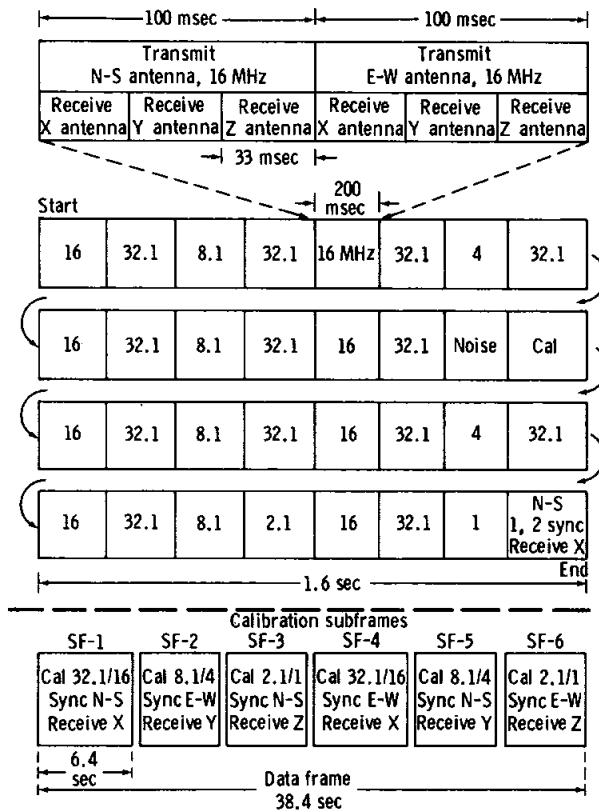
FIGURE 15-9.—The SEP experiment data format. The basic cycle, shown in the center of the diagram, starts with the 16-MHz signal and ends with the synchronization (sync) frame in the lower right corner. The cycle is 6.4 sec long. (Values are frequencies in megahertz.) The upper part of the figure shows a typical "data" frame. However, the single calibration (cal) frame changes successively through the subframe (SF) sequence shown at the bottom of the diagram.

accomplished when both (or either of) the 1- and 2.1-MHz signals exceed a given threshold. A block diagram of the SEP experiment receiver is shown in figure 15-10.

The loop antennas are connected sequentially to a low-noise amplifier section, which amplifies, converts (in frequency), and logarithmically compresses the amplitude of the received signal. A constant amplitude, variable frequency signal (in the band 300 to 3000 Hz) corresponding to the logarithm of the received signal amplitude was recorded on magnetic tape in the DSEA. The DSEA can record nearly 10 hr of data. Upon completion of the experiment, the DSEA was removed from the receiver for return to Earth.

Such functions as signal synchronization, frequency mixing, and antenna switching are controlled by the timing section, which is, in turn, crystal controlled for stability. The entire receiver assembly is battery powered using primary cells and is enclosed, except for the antenna assembly, in a thermal blanket. The thermal blanket has two flaps that may be opened to expose optical surface reflectors, which form a thermal radiator for internally produced heat while reflecting heat from the Sun, to control the internal temperature of the receiver.

The SEP experiment transmitter (figs. 15-7 and 15-11) is powered by solar cell panels that are designed to provide a minimum output of 10.0 W at 15 V and 1.10 W at 5 V. Like the receiver, the transmitter timing sequence is crystal controlled for stability. Also, separate stable crystal oscillators generate the signals that are radiated by the dipole antennas placed on the lunar surface. Because the antennas are required to radiate energy at six different frequencies, they are constructed in sections (fig. 15-12), and each section is electrically separated by electrical filters (signal traps). Each section of the antenna is of the proper electrical length for optimum performance. The dipole antennas, each 70 m long (tip to tip), are made of insulated wire between signal traps and were stored on reels until deployed.

Performance on the Lunar Surface

The crewmen deployed the SEP experiment equipment during the first period of extravehicular activity (EVA-1). Photographs of the receiver and of the transmitter and the transmitting antenna are shown in figures 15-13 and 15-14, respectively. Stereographic photographs will be used to obtain the location of the starting point of the SEP experiment profiles to within 1 m. The LRV, with its navigation system, was used to mark straight, orthogonal lines to be used as guides for deploying the antenna. Especially important for the analysis of the data was the fact that the arms of the transmitting antenna were laid out straight and at right angles to each other. The SEP experiment operations were nominal during EVA-1. During the rest period between EVA-1 and EVA-2, however, the temperature of the SEP experiment receiver increased; subsequent overheating hampered the SEP experiment operation until the DSEA recorder was removed in the middle of EVA-3 to prevent loss of data that had been recorded already
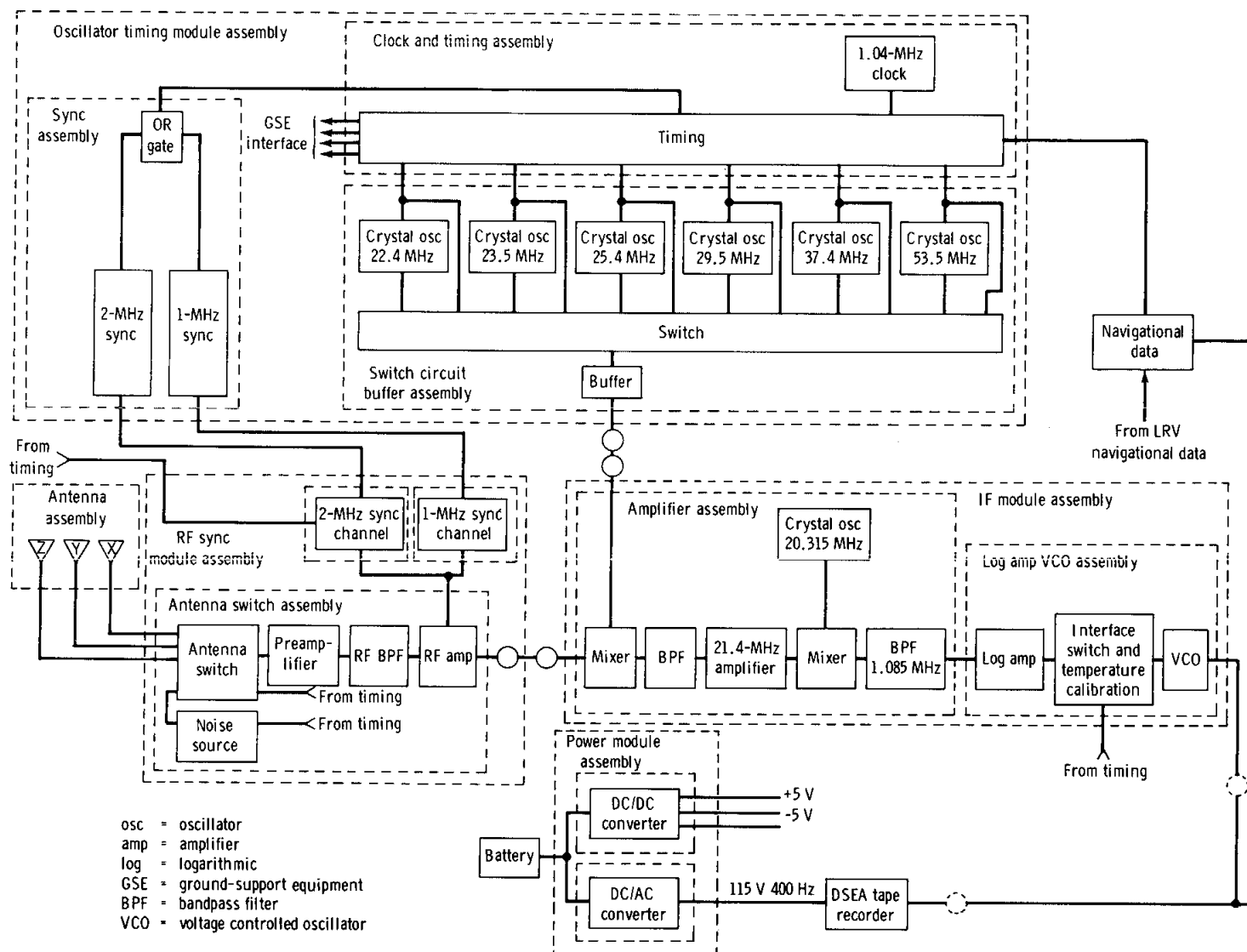
FIGURE 15-10.—Block diagram of the SEP experiment receiver.

osc = oscillator
amp = amplifier
log = logarithmic
GSE = ground-support equipment
BPF = bandpass filter
VCO = voltage controlled oscillator
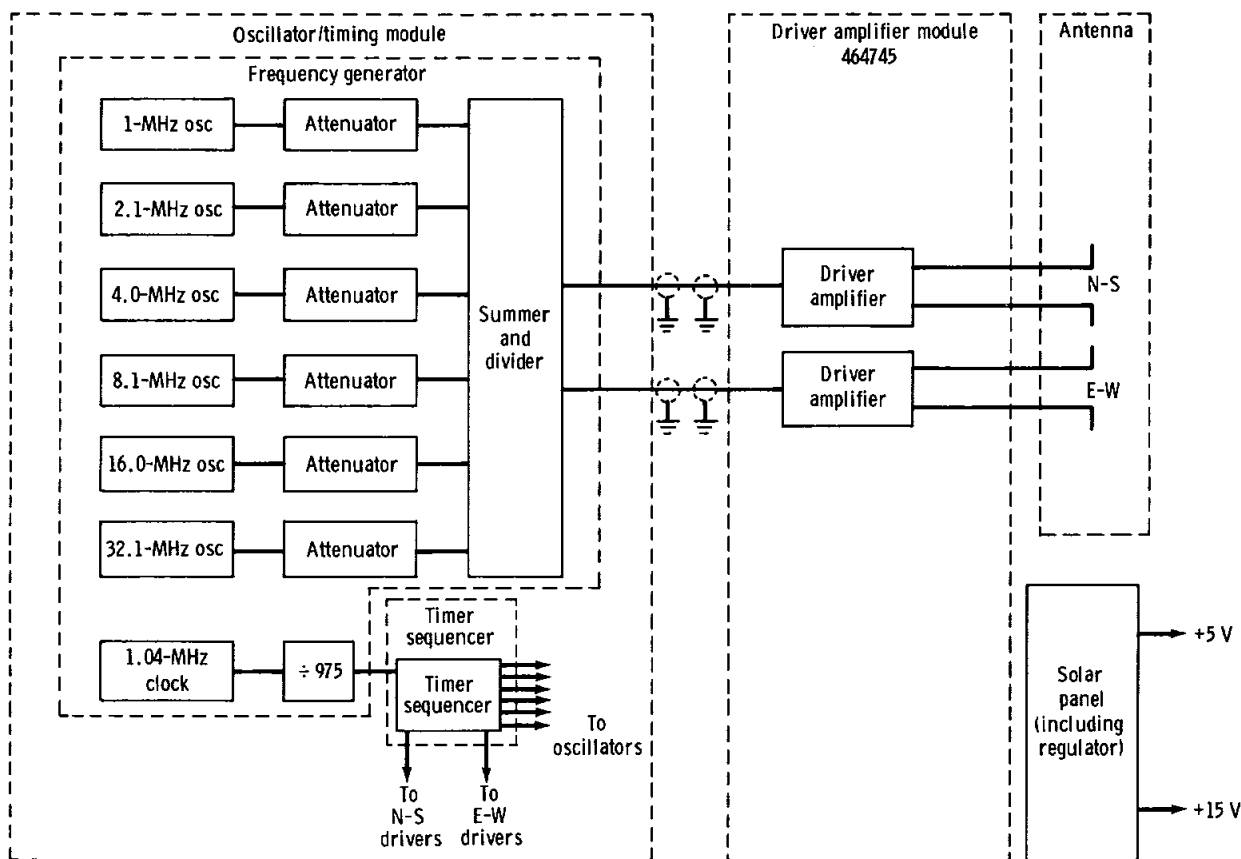
FIGURE 15-11.—Block diagram of the SEP experiment transmitter.

on the magnetic tape. The receiver contained a thermometer that was monitored by the crewmen. Despite the efforts of the crewmen to control the temperature, the receiver became too hot and was turned off by a thermally operated switch.

Data were obtained during EVA-2 on the traverses from the SEP experiment site toward station 2 and from station 4 toward the SEP experiment site. Data were not obtained during the early part of EVA-3 because the receiver switch was in the "standby" position rather than "operate." Apparently, the transmitter operated nominally throughout the mission.

THE DATA

Three kinds of data were recorded in the SEP experiment: navigational data, electromagnetic field strengths, and the internal temperature of the receiver. The navigational data, obtained from the LRV navigation system, included odometer pulses at 0.5-m increments from two wheels, the computed range to

the SEP experiment transmitter in 100-m increments, and the computed bearing to the SEP experiment transmitter in 1° increments. The navigational data are approximate because of wheel slippage on the lunar surface and will be improved greatly by including additional data on the LRV location obtained from photographs, crew comments, and long-baseline interferometry.

The second kind of data, the primary SEP experiment data, consists of the three orthogonal magnetic components H_z, H_ρ, and H_ϕ, recorded as a function of frequency and of transmitting antenna (N-S or E-W). An example of the field strength data is shown in figure 15-15.

The third kind of data, temperature of the SEP experiment receiver, was obtained for use in the postflight analysis of the experiment. Because of the sensitivity of all magnetic tape to temperature, the potential loss of data from excessive temperature in the SEP experiment receiver had been anticipated. Although protection against overheating had been
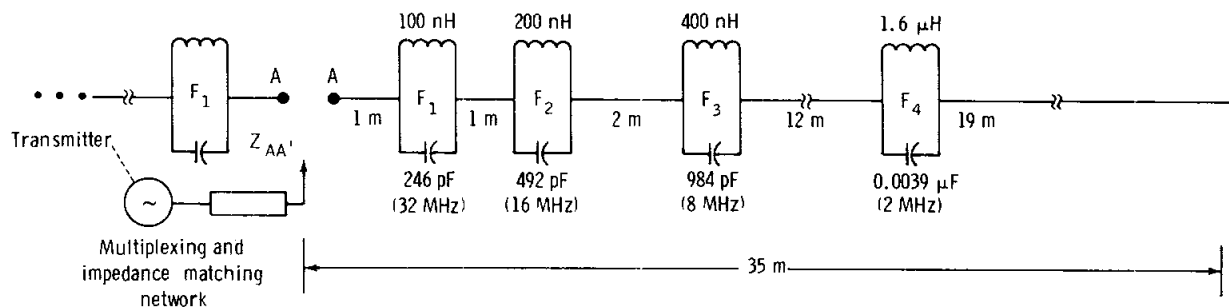
FIGURE 15-12.—Electrical schematic diagram of the SEP experiment transmitting antenna. Only one-half is shown because the antenna is symmetric about the midpoint (A', A). Total physical length (tip to tip) of each section of the antenna used for each SEP experiment frequency is 2, 4, 8, 32, and 70 m. The symbol Z represents impedance, and the components labeled F_1 to F_4 are filters.

FIGURE 15-13.—The SEP experiment receiver mounted on the LRV (AS17-141-21512).

FIGURE 15-15.—Comparison of lunar data for H_z, 16-MHz, N-S transmitting antenna with the theoretical curve calculated from mode theory. Parameters are given in table 15-I.

FIGURE 15-14.—The SEP experiment transmitter and antenna deployed at the Apollo 17 site (AS17-141-21517).

built in, it was desired to have data on the actual temperature. A portion of the temperature curve is shown in figure 15-16.

PRELIMINARY ANALYSIS

The analysis of each individual component at each frequency for each of the transmitting antenna orientations is quite straightforward. However, a single model that fits all the data has not been found, perhaps because of the limitations of our present
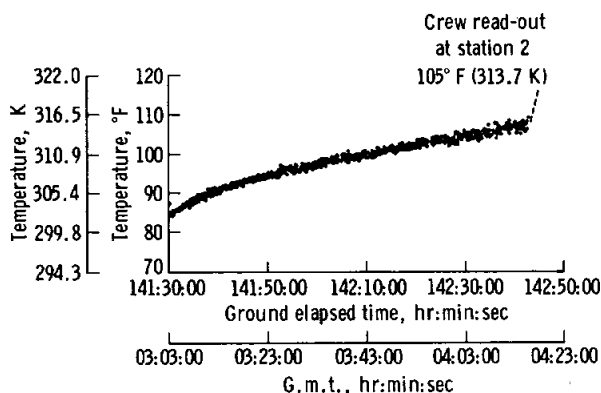
FIGURE 15-16.—Internal temperature profile of the SEP experiment receiver during the traverse from the SEP experiment site to station 2 on December 13, 1972.

TABLE 15-I.—Preliminary Results for H_z, N-S Transmitting Antenna

$[p = 0.003]$

Transmitter frequency, MHz	ϵ_{r_1} (a)	ϵ_{r_2} (b)	Layer depth, m
32.1	2.7	3.0	5.7
16	3.7	3.9	10
8.1	4.1	4.2	18
4	4.2	4.8	37
2.1	6.3	6.4	57
1	6.1	6.3	122

[a]Dielectric constant of layer.
[b]Dielectric constant of semi-infinite half space beneath layer.

theoretical development. For rigorous solutions, we are limited to models with homogeneous layers bounded by plane, horizontal surfaces. However, even within the limitations of our present theory, values of the properties of the lunar material in situ have been estimated, and some interesting conclusions about the electrical structure of the Taurus-Littrow site have been obtained.

The discussion in this report is based mainly on the analysis of H_z, the vertical component of the magnetic field, for two reasons. First, although the radiation patterns of the receiving antennas have not been measured, it is expected that the H_z data are less distorted than those of the other two components. Second, the appearance of the H_z data resembles more closely the glacier data, which comprise our background data.

Two quite different structural models of the Apollo 17 site have been developed to account for the observations. Although neither is based on rigorous theory, we believe that each is correct in the essential features. The first model, preferred by most members of the SEP experiment team, is one in which the dielectric constant increases with depth. Each of the lunar profiles can be matched quite well with the theoretical curves based on a single layer. The parameters for each of these six single-layer models are shown in table 15-I, and a typical example of the match between the theoretical and observed curves is shown in figure 15-15. The composite of these several models is shown in figure 15-17. We believe that the H_z data indicate that the dielectric constant increases with depth from a value of 2.5 to 3

near the surface to approximately 5 at a depth of 50 to 60 m. A discontinuity is present at 50 to 60 m, where ϵ_r increases to a value of 6 to 6.5. Because no reflection appears to be present in the 1-MHz data, we expect that ϵ_r does not increase between 60 m and at least 2.5 km. Compared to terrestrial values, the loss tangent is quite low (approximately 0.003) at all SEP experiment frequencies. On the basis of this low value of the loss tangent, we infer that water is probably not present at the Apollo 17 site.

In the alternate structural model, the cause of the apparent change of dielectric constant with depth is assigned to a sloping interface between a thin upper layer with $\epsilon_r = 3$ to $\epsilon_r = 4$ and $p < 0.04$ and a thick lower layer with $\epsilon_r = 6.5$ and $p = 0.04$. Rigorous theoretical expressions have not yet been obtained for this case either. However, we have confidence in the general effects attributed to a sloping interface because of the following limiting cases of horizontal interfaces.

1. For a very thin layer (thickness $< 0.1\lambda$), the interference pattern is equivalent to that of a half space in which ϵ_r and p have the values of the lower layer (fig. 15-18, upper curve).

2. For a layer with thickness between 0.1λ and 0.3λ, the individual "wiggles" of the interference pattern disappear (fig. 15-18, intermediate curves).

3. For a layer with thickness greater than approximately 0.3λ, the usual "reflected" wave appears in the pattern.

The sensitivity of the interference pattern of a thin
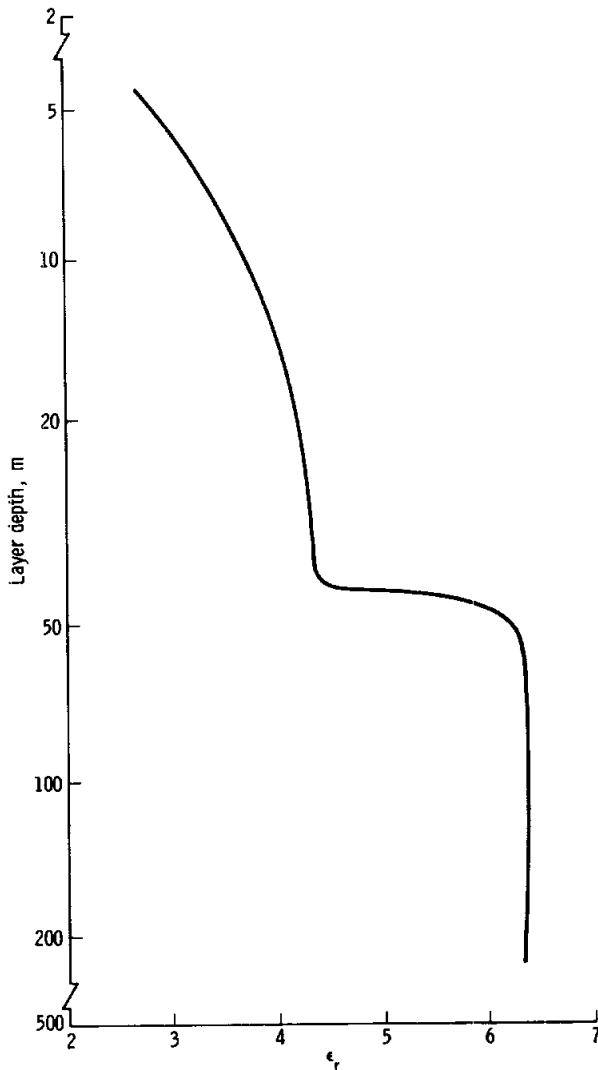
FIGURE 15-17.—Model for Apollo 17 site in which the dielectric constant varies with depth. The values of ϵ_r for each frequency are shown in table 15-I. In this figure, the approximate continuous function of ϵ_r is shown. Note that this interpretation is preliminary and, although the theoretical solution for each frequency is rigorous, the "solution" for the continuous variation of ϵ_r with depth is somewhat intuitive at present.

FIGURE 15-18.—Theoretical curves for thin layers, where $p_1 = 0.0300$, $\epsilon_{r_1} = 3.000$, $p_2 = 0.0400$, and $\epsilon_{r_2} = 6.000$. The points on the ordinate indicate the maximum values of each wave pattern. These plots are based on correct theory for horizontal layers, and they are used to "guess" a solution for an inclined interface.
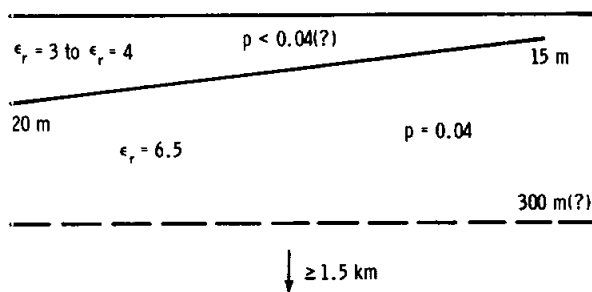
FIGURE 15-19.—The alternate model of the electrical structure at the Apollo 17 site. A layer of thickness between 0.2λ and 0.3λ is present at the SEP experiment site (left) and thins toward station 2 (right). The broken line at 300 m indicates a possible discontinuity in ϵ_r at that depth.

layer to the exact thickness is shown clearly in figure 15-18. The basis for this type of model is best seen in the 2.1-MHz profile, which resembles the intermediate theoretical curve of figure 15-18 near the SEP experiment site and resembles the upper theoretical curve of figure 15-18 farther away. The structure that best fits this analysis is shown in figure 15-19. The

layer is perhaps 20 m thick beneath the SEP experiment site and thins to 15 m at station 2. In addition, there is a hint of a discontinuity in ϵ_r at a depth of approximately 300 m.

CONCLUSIONS

1. The relative dielectric constant of the lunar material at Taurus-Littrow, at frequencies of 1 to 32 MHz, is approximately 3 to 4 near the surface and increases to 6 to 7 at a depth of approximately 50 m. The loss tangent is less than 0.04 and possibly as low as 0.003.

2. The electrical structure at Taurus-Littrow is not simple horizontal layering.

3. No liquid water is present in the outer 1 to 2 km.

4. Scattering of electromagnetic waves at frequencies of 1 to 32 MHz is insignificant.

5. Continuing postflight analysis of navigational data, photographs, and other data will provide location of the LRV on the EVA-2 traverse to an accuracy of a few meters.

6. Additional theoretical and scale model work is being done to solve the problem of continuous variation with depth of the dielectric properties and the problem of dipping interface.

ACKNOWLEDGMENTS

REFERENCES

15-1. Rossiter, J. R.; LaTorraca, G. A.; Annan, A. P.; Strangway, D. W.; and Simmons, G.: Radio Interferometry Depth Sounding: Part II—Experimental Results. Geophysics, vol. 38, no. 3, June 1973, p. 581.

15-2. Sommerfeld, A.: Über die Ausbreitung der Wellen in der drahtlosen Telegraphie. Ann. Physik, vol. 28, 1909, pp. 665-737.

15-3. Baños, Alfredo, Jr.: Dipole Radiation in the Presence of a Conducting Half-Space. Vol. 9 of International Series of Monographs on Electromagnetic Waves, Pergamon Press, Inc. (New York), 1966.

15-4. Annan, A. P.: Radio Interferometry Depth Sounding. M.S. Thesis, Univ. of Toronto, 1970.

15-5. Simmons, G.; Strangway, D. W.; Bannister, L.; Baker, R.; et al.: The Surface Electrical Properties Experiment. Lunar Geophysics: Proceedings of a Conference at the Lunar Science Institute, Houston, Tex., Oct. 18-21, 1971,

D. Reidel Pub. Co. (Dordrecht, Holland), 1973, pp. 258-271.

15-6. Annan, A. P.: Radio Interferometry Depth Sounding: Part I—Theoretical Discussion. Geophysics, vol. 38, no. 3, June 1973, p. 557.

15-7. Kong, J. A.: Electromagnetic Fields Due to Dipole Antennas Over Stratified Anisotropic Media. Geophysics, vol. 37, no. 6, Dec. 1972, pp. 985-996.

15-8. Tsang, L.; Kong, J. A.; and Simmons, G.: Interference Patterns of a Horizontal Electric Dipole Over Layered Dielectric Media. J. Geophys. Res., vol. 78, no. 17, June 19, 1973, pp. 3287-3300.

15-9. King, Ronold W. P.: Electromagnetic Engineering, Vol. I—Fundamentals. McGraw-Hill Book Co., Inc. (New York), 1945.

15-10. Jordan, Edward C.; and Balmain, Keith G.: Electromagnetic Waves and Radiating Systems. Second ed., Prentice-Hall, Inc. (Englewood Cliffs, N.J.), 1968.

15-11. Stratton, Julius Adams: Electromagnetic Theory. McGraw-Hill Book Co., Inc. (New York), 1941.

15-12. Smythe, W. R.: Static and Dynamic Electricity. McGraw-Hill Book Co., Inc. (New York), 1950.

15-13. Lorrain, Paul; and Corson, Dale R.: Electromagnetic Fields and Waves. W. H. Freeman (San Francisco), 1970.

15-14. Pierce, G. W.: A Table and Method of Computation of Electric Wave Propagation, Transmission Line Phenomena, Optical Refraction, and Inverse Hyperbolic Functions of a Complex Variable. Proc. Am. Acad. Arts Sciences, vol. 57, 1922, p. 175.

15-15. Galejs, Janis: Antennas in Inhomogeneous Media. Vol. 15 of International Series of Monographs on Electromagnetic Waves, Pergamon Press, Inc. (New York), 1969.

15-16. Wait, James R.: Electromagnetic Waves in Stratified Media. Vol. 3 of International Series of Monographs on Electromagnetic Waves, Pergamon Press, Inc. (New York), 1962.

15-17. Brekhovskikh, Leonid M. (David Lieberman, trans.): Waves in Layered Media. Vol. 6 of Applied Mathematics and Mechanics, Academic Press (New York), 1960.

15-18. Sommerfeld, A.: Über die Ausbreitung der Wellen in der drahtlosen Telegraphie. Ann. Physik, vol. 81, 1926, pp. 1135-1153.

15-19. Tsang, Leung: Electromagnetic Near Fields of Horizontal Dipole on Stratified Lunar Surface. B.S. Thesis, Mass. Inst. of Tech., 1971.

15-20. Strangway, D. W.; Simmons, G.; Watts, R.; LaTorraca, G.; et al.: Radio Frequency Interferometry—A New Technique for Studying Glaciers. J. Glaciology, vol. 12, 1973.

15-21. LaTorraca, Gerald A.: Half Wavelength Dipole Antennas Over Stratified Media. NASA CR-115561, 1972.

15-22. Simmons, Gene; Meyer, James W.; Baker, Richard H.; and Strangway, David W.: Brief Introduction to the Surface Electrical Properties Experiment. MIT Press (Cambridge, Mass.), Aug. 1972.

16. Lunar Ejecta and Meteorites Experiment

O. E. Berg,[a][t] *F. F. Richardson,*[a] *and H. Burton*[a]

For the past 20 yr, astronomical interest in the cosmic dust particle has been partially dominated by a concern for the mechanical devastation imparted by meteoroid impacts or the so-called meteoroid hazard. Today, the meteoroid hazard has been accurately evaluated and found to be essentially nonexistent (ref. 16-1). Now we are witnessing an interesting period of transition for cosmic dust studies from simply determining the number and size of particles impinging on a certain area in a certain time to an astronomical interest in the nature and the source of the material. The cosmic dust particle is emerging as a much more interesting object than its larger cousin, the meteoroid, which is often seen blazing a path across the atmosphere of the Earth. Both are affected by gravity, solar wind erosion, and planetary atmospheres, but, because of its small size and consequently its high surface-to-mass ratio, the micrometeoroid is also significantly affected by solar radiation pressure, magnetic fields, electric fields, and probably the shadow or umbra of the Earth. The extraterrestrial microparticles encountered by the lunar ejecta and meteorites (LEAM) experiment may be divided into three distinct and interesting classes: lunar ejecta, interstellar grains, and cometary debris.

OBJECTIVES

The lunar ejecta particle depicted in figure 16-1 is the offspring of a meteoroid encounter with the lunar surface. The Moon, like the Earth, is continually bombarded by meteoroids traveling at hypervelocities (speeds in excess of the speed of sound in a material (ref. 16-2)). The lunar surface, unprotected by an atmosphere, receives the impact at full velocity from 2.4 to 72 km/sec. Because of the high velocity, the projectile and the immediate area of the impact

become molten and behave similarly to liquid masses. Secondary particles (or lunar ejecta) are ejected radially and at high velocities from the impact site. The volume of lunar ejecta material relative to primary particle volume and the range of velocities for lunar ejecta are currently conjecture based on laboratory studies using hypervelocity projectiles. Lunar ejecta mass is probably comparable, in most cases, to the mass of the impacting meteoroid. Laboratory studies have shown that ejecta velocities may exceed the primary particle velocity, but, in general, it is assumed that a relatively small percentage of the ejecta particles have velocities in excess of the lunar escape velocity of 2.4 km/sec; thus, the bulk of material returns to the lunar surface (ref. 16-3). The LEAM experiment intercepts ejecta particles and records information useful in establishing the history of the Moon.

The manner in which interstellar particles or grains invade our solar system is depicted in figure 16-2. Our
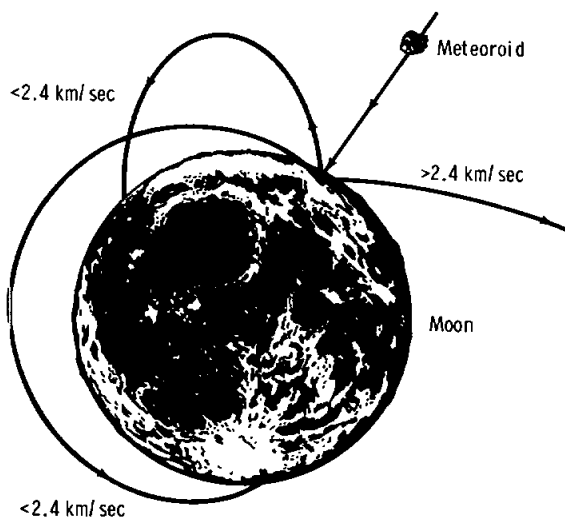
FIGURE 16-1.–Lunar ejecta.
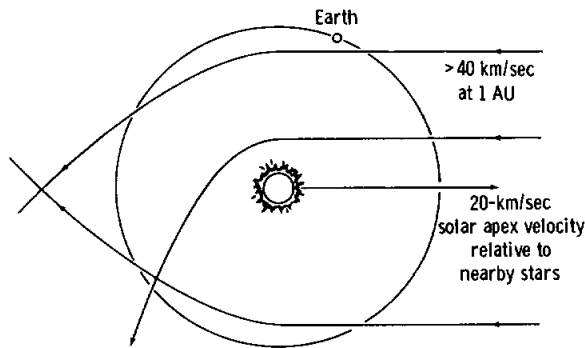
FIGURE 16-2.—Interstellar grains. Interstellar grains <40 km/sec are trapped by the solar system; those >40 km/sec pass on through.

FIGURE 16-3.—Cometary debris.

Sun and its planets are moving through the Milky Way Galaxy at approximately 20 km/sec relative to nearby stars. In so doing, our solar system passes through "clouds" of interstellar dust (ref. 16-4) with relative encounter velocities approaching and possibly exceeding 100 km/sec. Although the particles are extremely small (probably 10^{-15} g), their detection probability by the LEAM experiment is high because the experiment responds to the cube of the particle velocity; thus, it is extremely sensitive to high-speed particles. Two forerunners of the LEAM experiment, in the heliocentric satellites Pioneer 8 and 9, have detected two (and possibly more) interstellar grains that are believed to be the first impact registrations of this type of particle (ref. 16-5). Because the LEAM experiment measures particle speed, radiant (or source) direction, and particle kinetic energy, the encounters by interstellar grains may be readily distinguished from encounters by other types of cosmic dust.

Cometary debris is considered the most abundant component of cosmic dust within our solar system. It is generally accepted that comets are gigantic "dirty snowballs" with nuclei diameters on the order of 10 km and are principally composed of frozen mixtures of gases and liquids (ref. 16-6). Embedded in this "snowball" are solids ranging in diameters from tenths of micrometers to large boulders. As the comet approaches its perihelion, as shown in figure 16-3, it undergoes partial disintegration because of the effects of radiation pressure and spews out a tail of gases, vapors, and solid particulates. For larger comets, the tail is often visible to the eye as diffuse illumination pointing away from the Sun. Large particulate matter may separate from the parent comet and attain a
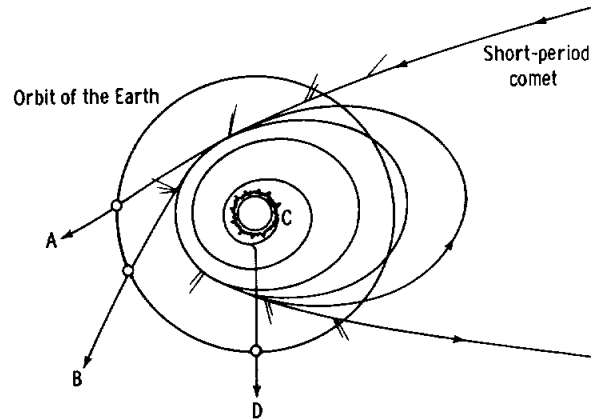
heliocentric orbit similar to its parent; the large particulates will remain in this orbit until they are perturbed by other planets or bodies or collide with the Moon, the Earth, or other planets. These large particulates are the blazing meteoroids mentioned previously. After separation from the parent comet, the smaller particulates, micrometeoroids, behave much less predictably because they are affected by two forces: the force of gravity, which is a function of the particle mass and therefore the cube of the particle radius $(4/3\pi r^3)$ and the force of solar radiation pressure, which is a function of the cross-sectional area of the particle and therefore the square of the radius (πr^2). If the force of radiation pressure exceeds the force of gravity at the moment of separation from the parent comet, the particle will assume a hyperbolic trajectory, as shown for A and B in figure 16-3, and the particle will leave our solar system. If the force of gravity exceeds the force of radiation pressure at the moment of separation from the parent comet, the particle will spiral in toward the Sun very slowly under the Poynting-Robertson effect. Here again, as postulated, a second separation of particles occurs (ref. 16-7). Because of their heat capacity, the larger dust particles continue into the Sun and are absorbed, as shown by C. As the smaller dust particles approach to within a few solar radii of the Sun, they partially evaporate, and, because the relative mass or gravity (r^3) reduction is faster than the relative cross-sectional area (r^2) reduction, the force of radiation pressure soon exceeds the force of gravity for the particle, and it is ejected quasi-radially from the Sun, as depicted by D.

Essentially all the particles intercepted by the Pioneer 8 and 9 instruments were outgoing particles,

suggesting ejected cometary fragments rather than particles in elliptical orbits (ref. 16-8). Accordingly, the LEAM experiment is shielded by the Moon from primary particle impacts during lunar night. However, the formation and presence of lunar ejecta from large meteoroid impacts are quite independent of lunar day/night conditions—a set of conditions that helps to distinguish between impacts by primary particle events and impacts by lunar ejecta. During each lunar cycle, each of three sensor systems incorporated into the LEAM experiment is alternately exposed to and shielded from impacts by these particles.

The position of the LEAM experiment on the lunar surface and the associated alternated exposure and shielding feature of the sensor systems offer an opportunity for the experiment to verify Earth focusing effects (fig. 16-4). Microparticles that are ejected, one way or another, into our solar system will tend to be ejected radially away from the Sun. For simplicity, microparticles are shown as having parallel trajectories in figure 16-4. As they are blown past the Earth, they are perturbed toward the Earth and tend to focus into a concentration extending outward from the shaded side of the Earth. Thus, as shown in figure 16-4, the LEAM experiment will, once per lunar cycle, be ideally exposed to this postulated concentration and/or perturbation effects.

THE LEAM INSTRUMENT

The major objectives of placing a cosmic dust experiment on the Moon can readily be met by the LEAM instrument (fig. 16-5). This instrument measures the particle speed, particle direction, total particle energy (kinetic), and particle momentum for particles having parameters as shown. The LEAM
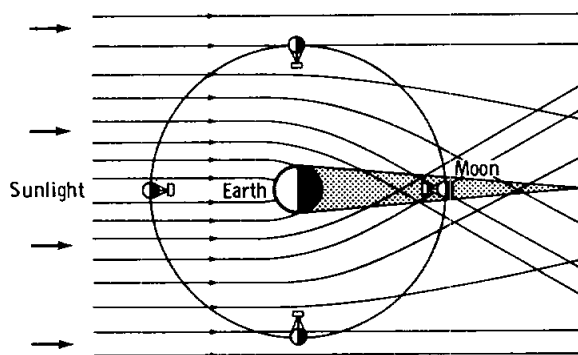
FIGURE 16-4.—Earth focusing effect.
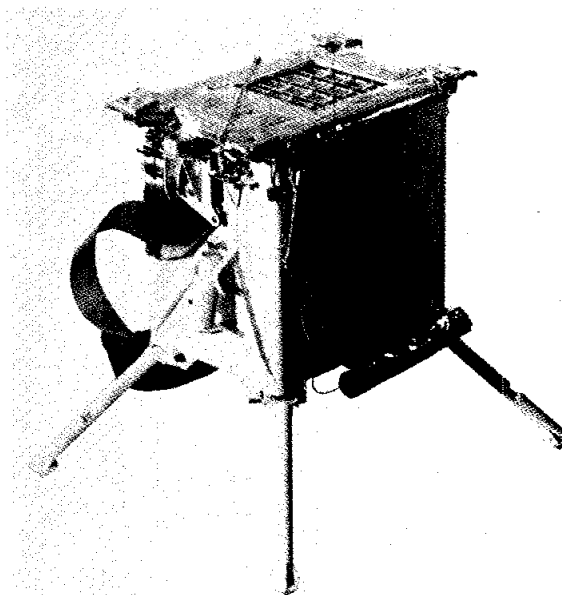
FIGURE 16-5.—The LEAM experiment, which responds to impacts of microparticles having a mass as low as 10^{-14} g, a diameter as small as 2×10^{-5} cm, and a speed as high as 75 km/sec.

experiment consists of three sensor systems: the east sensor, the west sensor, and the up sensor. Only the up and west sensors are visible in figure 16-5.

The basic sensor for each array is shown schematically in figure 16-6. The basic sensor consists of a front (A) film-grid sensor array and a rear (B) film-grid sensor array spaced 5 cm apart (film plane to film plane) and an acoustical impact plate upon which the rear film is mounted. The performance of the sensors depends upon two basic measurable phenomena that occur when a hypervelocity particle impacts upon a surface: the formation of a plasma and a transfer of momentum.

In conjunction with the following explanation of the operation of the LEAM experiment, refer to figure 16-6 and consider three probable types of cosmic dust particles: a high-energy hypervelocity particle (>1.0 erg); a low-energy hypervelocity particle (<1.0 erg); and a relatively large high-velocity particle ($>10^{-10}$ g). The third type includes the majority of lunar ejecta particles. As a high-energy hypervelocity particle enters the front film sensor, it yields some of its kinetic energy toward the generation of ionized plasma at the front film. Electrons from the plasma are collected on the positively biased grid (+24 V), producing a negative-going pulse that is
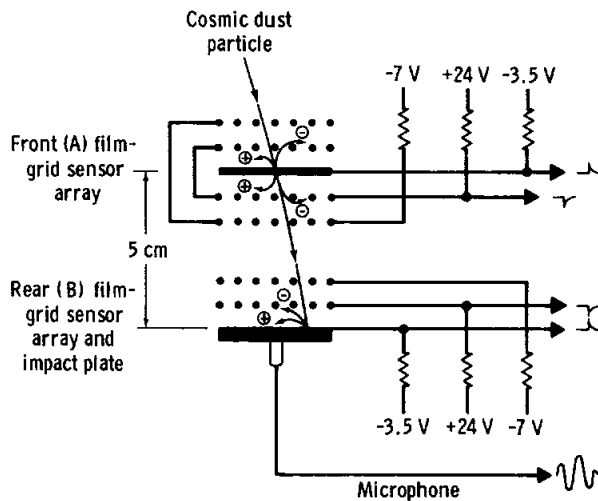
FIGURE 16-6.—The basic sensor.

amplified as shown (fig. 16-6). The ions from the plasma are collected on the negatively biased film (−3.5 V), producing a positive-going pulse that is amplified as shown (fig. 16-6) and pulse-height-analyzed as a measure of the kinetic energy of the particle. As the particle continues on its path, it yields its remaining energy at the rear sensor film (and plate), generating a second set of plasma pulses and an acoustical pulse (if the momentum of the particle is sufficient). A pulse-height analysis is performed on the positive-going plasma pulse, and a peak-pulse-height analysis is performed on the acoustical sensor output as a measure of the remaining momentum of the particle.

As a low-energy hypervelocity particle enters the front sensor, it yields all its kinetic energy at the front film. A pulse-height analysis is performed on the positive output signal as a measure of the kinetic energy of the particle.

As a relatively large high-velocity particle enters the LEAM experiment, it may pass through the front and rear film sensor arrays without generating a detectable ionized plasma but still impart a measurable impulse to the acoustical sensor. In this event, a peak-pulse-height analysis is performed on the acoustical sensor output pulse.

An electronic clock registers the time of flight of the particle as the time lapse between positive pulses (front film and rear film output signals), which is used to derive the speed of the particle. The time-of-flight sensor represents one of 256 similar

sensor systems that comprise the east and up sensor arrays. The west sensor array was designed specifically to record low-speed ejecta impacts on the microphone plate without retardation by a front film; consequently, this array has no capability to measure particle speed. Figure 16-7, an exploded schematic of the overall LEAM experiment, shows that four vertical film strips are crossed by four horizontal grid strips to affect 16 front and 16 rear film sensor arrays, creating 256 possible combinations. Each grid strip and each film strip connects to a separate output amplifier. The output signals from these amplifiers are used to determine the segment in which an impact occurred. Thus, knowing what front film segment was penetrated and what rear film segment was affected by an impact, the direction of the incoming particle can be determined with respect to the sensor axis and, eventually, to the Sun.

SENSOR CONTROLS

An ideal sensor control is one that is exposed to the same environment as the active or main sensor. Environment encompasses electrical and magnetic radiation, thermal radiation, thermal gradients, and so forth. Controls installed somewhere in the experiment and sheltered from the total environment are ineffective. The controls used in this experiment are designed to perform, as much as possible, under the same conditions as the main sensor. An upper portion of the rear film array and a lower portion of the front film array of the east sensor system are used as controls for the plasma sensors. An epoxy resin coating covers the control grids and films, isolating them from the products of ionization caused by impacts on their area (e.g., electrons and ions generated by hypervelocity impacts on the epoxy cannot be collected on the grids or films). However, the resin coat does not constitute a shield from electrical or magnetic radiation. (Thermal noise is not an important factor in ionization sensors.) A microphone control is unique in that it is a "live microphone" attached to a separate impact plate having one-third the effective area of the main microphone plate. Thus, the control is truly exposed to the same environment as the main microphone sensor, including impacts by cosmic dust; an approximate ratio of 1:3 would be expected between impacts on the control and impacts on the main microphone sensor.
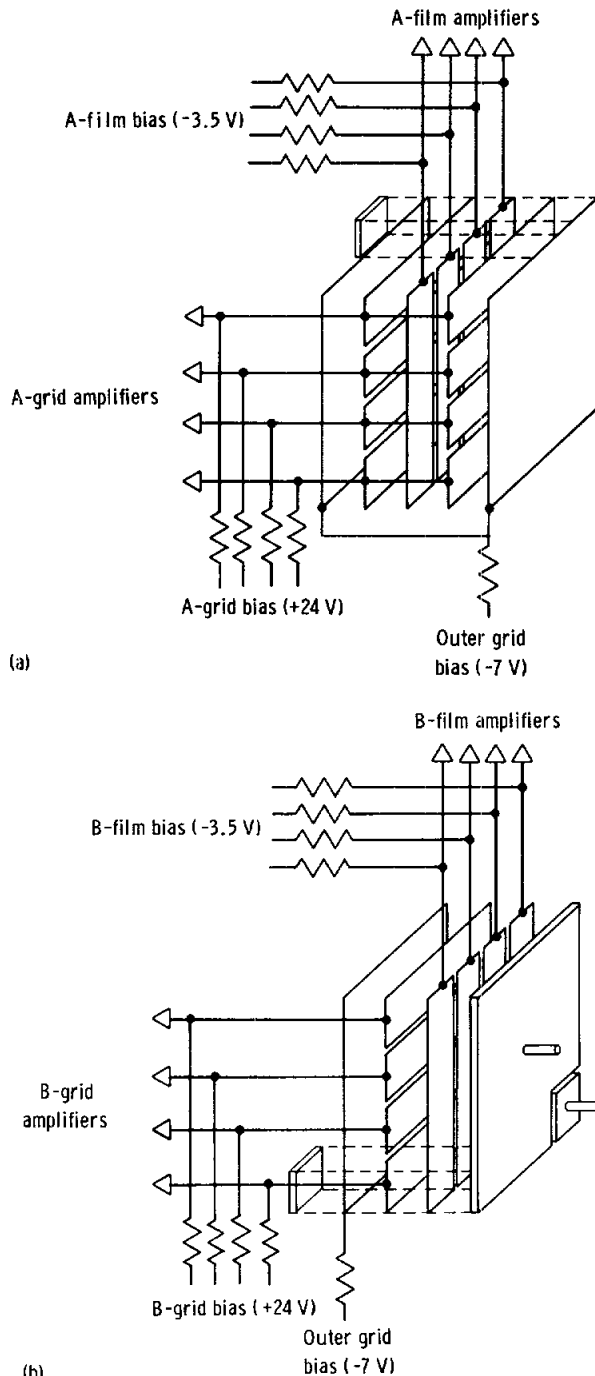
FIGURE 16-7.—Schematic of time-of-flight sensor. (a) Front
sensor array. (b) Rear sensor array.

CALIBRATIONS

Extensive calibrations have been performed on the
sensors using a 2-MV electrostatic accelerator. Unfort-
unately, the particles used for calibration have been
limited to high-density hard spheres of iron
(10^{-13} g < mass < 10^{-9} g) and to velocities corre-
sponding to the low end of the meteoroid velocity
spectrum (1 to 25 km/sec). Accordingly, when
considering the sensitivities of the sensors as derived
from these calibrations, the possible latent discrepan-
cies must be considered that may become manifest in
subsequent measurements in space when the sensors
are exposed to projectiles of diverse density, struc-
ture, composition, and higher velocities. The plasma
sensors respond nearly linearly to the product $mv^{2.6}$
(m = mass, v = velocity) over the limited particle
parameter range specified previously for the labora-
tory simulator. The acoustical sensors respond to the
momentum of the particle for that same particle
range. The threshold sensitivity of the front film
sensor array to laboratory particles is 0.6 erg. Time of
flight is registered for laboratory particles having
kinetic energies of 1.0 erg or greater. The electronics
of the time-of-flight sensor are design limited to
particles having velocities ranging from 2 to 72
km/sec. The threshold sensitivity of the acoustical
sensor is 2×10^{-5} dyn-sec (including deceleration by
the front film).

Hypervelocity particles passing through the front
film of the sensors are decelerated in inverse propor-
tion to their kinetic energy (for a velocity range of 1
to 20 km/sec). For particles having the minimum
energy required to exhibit time of flight (1.0 erg), the
deceleration is 40 percent. Deceleration drops to 5
percent for particles having 10 ergs. In situ calibration
is provided and can be initiated either automatically
or by ground command. Two different formats of
simulated data pulses are alternately presented by the
experiment to the input of each of the amplifier
systems to check the condition of the electronics and
the plasma sensors. Two formats alternately provide a
high and a low amplitude pulse to monitor the lower
and the upper sensitivities of the amplifiers. Front
film sensor pulses and rear film sensor pulses are
appropriately spaced and in proper sequence to
monitor the time-of-flight electronics. All accumula-
tors advance with inflight calibration.

EXPERIMENT ELECTRONICS

A simple block diagram of the electronics in one
of the dual (east, up) sensor arrays is shown in figure
16-8. A preamplifier receives the positive-going pulse
from each A-film strip. After a gain of 3, the pulse
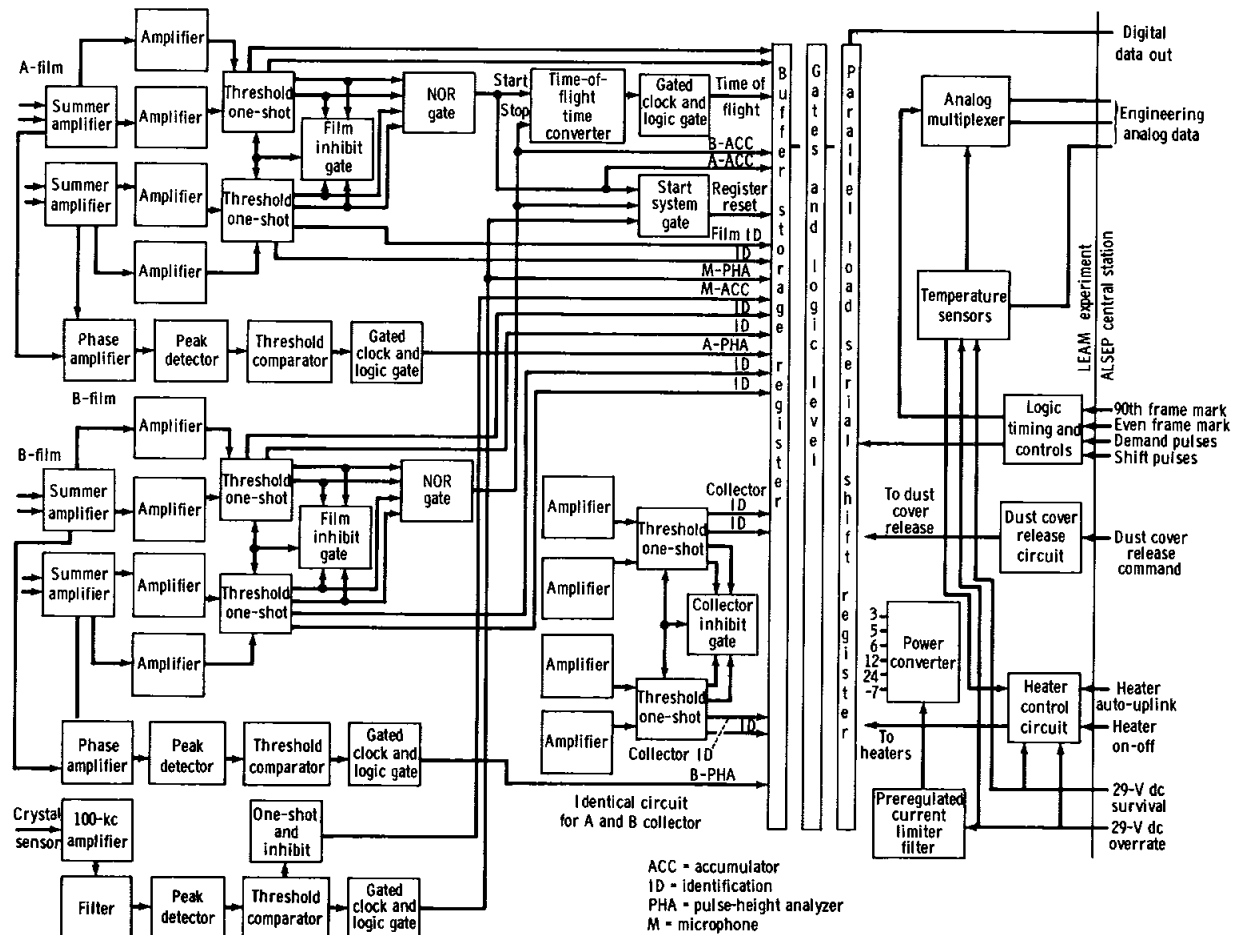
FIGURE 16-8.—Diagram of LEAM central electronics.

divides into two separate paths. In one path, it is amplified (voltage gain V_g equals 3.2 for each input), its pulse height is analyzed, and its amplitude is recorded in the storage register. In the other path, it is amplified (V_g = 5) and fed into a threshold one-shot. The output pulse performs three functions: its origin identification is impressed directly on the storage register; it passes through the logical NOR gate and initiates the time-of-flight measurement; and it is gated back to the threshold one-shot to inhibit any other A-film pulse until the measurement has been completed.

An inhibit signal to the other three films is necessary to avoid capacitative crosstalk for high-energy impact signals. The A-film pulse is pulse-height analyzed, and the results are stored in the register to await read-out.

Positive-going pulses from the B-film pass through

a similar but separate electronic path, except that the B-film pulse is used to stop the time-of-flight clock. If no B-film pulse follows an A-film pulse, the time-of-flight register goes to the full (63 count) state and remains full until another event occurs.

Negative-going pulses from each of the grids (A and B) are amplified through separate units and identity (ID) registered as shown. For simplicity, only one set of collector amplifiers is shown in the lower center area of figure 16-8. Each film strip and each grid strip in both the front and the rear sensor arrays connects to its own separate amplifier system.

The output signal from the crystal sensor (microphone), as it responds to impacts, is a ringing sinusoidal wave that increases to a maxium and then decays. After amplification in a tuned amplifier, the peak signal amplitude is used to advance the microphone accumulate, to start the register reset

(read-out of register data), and to record the amplitude of the impulse imparted to the microphone sensor plate. The one-shot and the inhibit block shown in the microphone circuit inhibit further processing of subsequential microphone pulses until after the final pulse is placed in the storage register.

Pulses from the control microphone (not shown in the block diagram) follow a similar but separate electronic course, except that no pulse-height analysis is performed and the pulses do not trigger the register reset.

The sensors have been subjected to solar radiation simulators, including 3 MeV proton radiation and ultraviolet radiation. They showed no response or effects from radiation values as high as 100 solar constants.

DEPLOYMENT

The LEAM experiment was emplaced in the Taurus-Littrow area; its location is 43° east of north from the ALSEP central station at a distance of 7.5 m. As requested, the east sensor axis of the LEAM was directed 25° north of east to accommodate interstellar grains. The LEAM instrument was commanded "on" to operate for a period of 2 hr after deployment to verify proper performance. During this 2-hr period, two calibration commands were transmitted. The LEAM experiment responded with normal read-outs. It was commanded to the "off" mode until after lunar module (LM) ascent and detonation of the surface charges. The LEAM experiment was protected by two dust covers that were removed by ground command. One cover, designed to protect the thermal mirrors from dust contamination during LM ascent or from surface-charge detonations, was removed at a Sun angle of 130° (90° = lunar noon). A second cover, designed to protect the three sensor systems, was commanded "off" at 60 hr after lunar sunset of the first lunation. Because of the low data event rates anticipated (one event per day) for the LEAM experiment, it was essential to obtain a good measurement of the background noise or the extraneous pulse rate. Accordingly, the LEAM experiment output was recorded for periods of 60 hr of lunar day and 60 hr of lunar night with the sensor covers on. The covers were removed by a redundant squib system that was fired by command. A monitor signal indicated successful firing of both sets of squibs. In the case of the mirror-cover removal, a

sudden decrease in the LEAM experiment temperatures verified successful removal.

However, in the case of the sensor covers, there was no noticeable change of temperature conditions inside the experiment following cover deployment. That fact and several subsequent observations of temperature excursions in the experiment have prompted an extensive study into the LEAM experiment temperature anomalies.

THE LEAM EXPERIMENT TEMPERATURES

Predicted temperatures for the LEAM experiment included a maximum of 146° F (336 K) at lunar noon and a minimum of −24° F (242 K) during lunar night. An automatic heater in the LEAM experiment turns on at 0° F (255 K) and off at 9° (261 K). The heater is designed to remain on continuously during lunar night and to keep the LEAM experiment temperatures above −24° F (242 K). In all cases, predicted temperatures were based on laboratory simulation studies. Actual temperatures for the LEAM experiment frame plotted against Sun angle (90° = lunar noon) during the first three lunations are shown in figure 16-9. The plot shows that the LEAM experiment is command "off" as its temperature approaches 167° (348 K), an arbitrarily acceptable operating temperature based on the highest operating temperature tested in the laboratory. This acceptable temperature will be increased to probably 212° F (378 K), pending the results of a total investigation of the temperature anomalies.

It is interesting to follow the temperature history of the LEAM experiment from the time of lunar emplacement. At a Sun angle of 130° during the first lunation, the mirror covers were removed, and the temperature decreased markedly. At a Sun angle of 162°, the LEAM experiment was commanded "on," in which mode it remained throughout the first lunar night. The thermostatically controlled heater cycled on and off approximately once per 6 hr. Temperature cycling was not unexpected while the sensor covers remained on. At a Sun angle of approximately 220° on the first lunar night, the sensor covers were commanded "off." No noticeable changes occurred in temperature cycling, although predictions indicated a temperature decrease and continuous heater operation.

At dawn of the second lunar day, the temperature
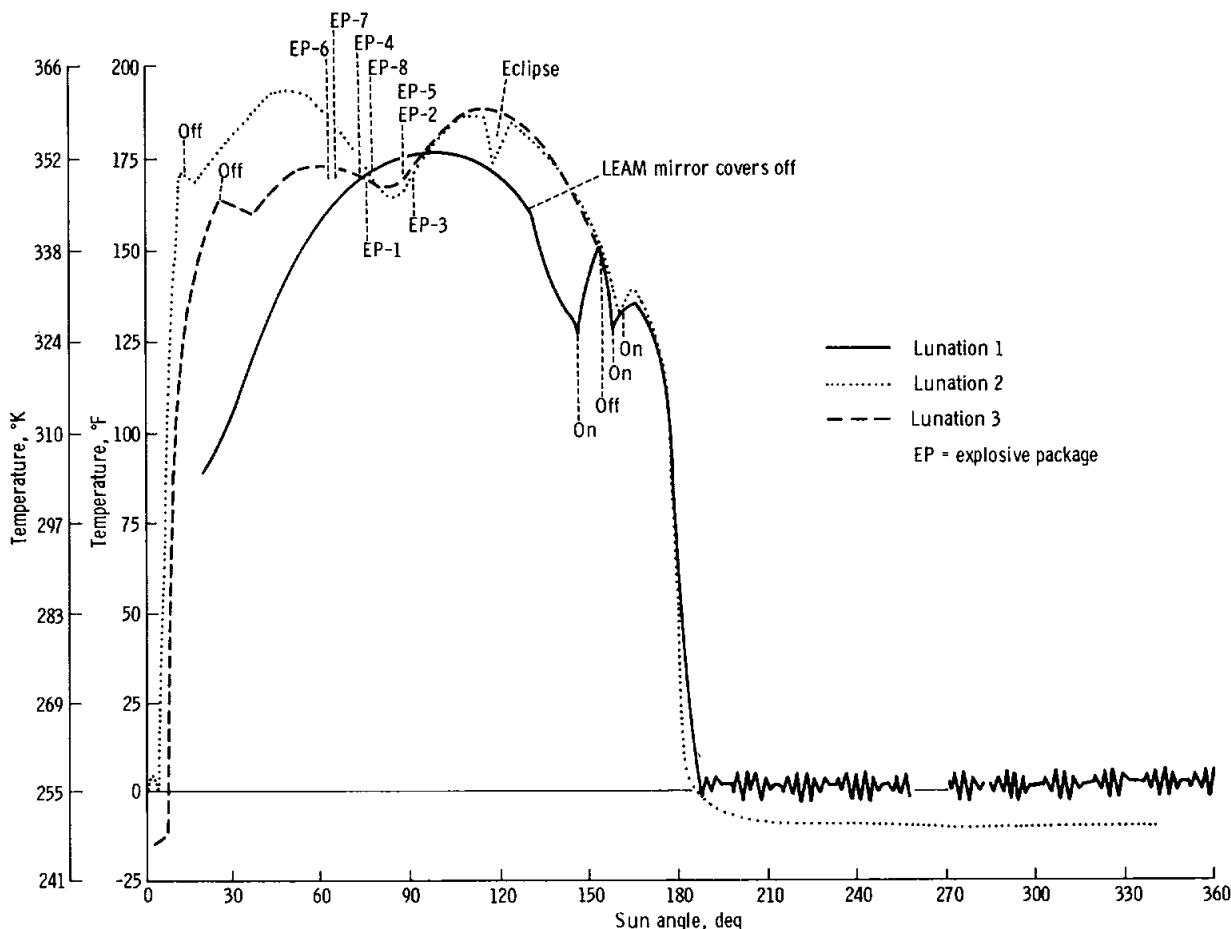
FIGURE 16-9.—The LEAM temperature history for three lunar days and two lunar nights.

rose rapidly to approximately 170° F (350 K) at a Sun angle of 15°, and the LEAM experiment was commanded "off" and remained in the "off" mode until a Sun angle of 160° when it was commanded "on." The LEAM experiment remained in this mode until dawn of the third lunar day. During the second lunar night, the registered temperatures were normal (as predicted), and the heater stayed on continuously. The strange behavior of the thermal sensor during the first lunar night compared to its normal behavior during the second lunar night indicated that the sensor covers had failed to deploy fully because of the extremely low temperatures. The temperature of the dust cover may have approached lunar surface temperatures. The sensor covers had presumably deployed sometime during dawn of the second lunation. The rapidly rising temperature at dawn of the second lunation is more difficult to explain.

A plausible explanation for the thermal anomalies is an accumulation of lunar dust on the sensor films. There is some evidence for electrostatic levitation of dust at the lunar sunset line (refs. 16-9 and 16-10). Positively charged dust particles would be attracted to and deposited on the negatively biased films; they would change the absorption/emission characteristics of a relatively large area of the LEAM experiment and cause heating. To preclude electrostatic dust accumulation at sunrise of the third lunation, the LEAM experiment was commanded "off" for a period of 75 min so that the experiment (and films) would maintain a similar potential to the lunar surface at the LEAM experiment site. Conceivably, the dust already deposited might be removed by electrostatic repulsion at sunrise. Interestingly, the third lunation temperatures were as much as 35° F (19.5 K) lower than the second lunation temperatures under identi-

cal conditions (Sun angle of 15°). A few degrees after lunar noon, the temperatures for the second and the third lunations were essentially identical.

It is interesting to consider further whether or not the LEAM experiment has, at least partially, verified electrostatic levitation of lunar dust. The LEAM experiment may eventually be manipulated to accommodate such studies; however, immediate plans are to operate it only at temperatures below 348 K to preserve it for the partial eclipse in June 1973. After the eclipse, the LEAM experiment will be operated continuously. Prelaunch thermal degradation analyses of the LEAM instrument show that it will operate at temperatures as high as 373 K with negligible degradation. (All electronic components for the LEAM experiment were qualified (tested) to a temperature of 257° F (398 K).) Meanwhile (preeclipse), the LEAM experiment will be operating during lunar nights, when conditions are ideal for the study of lunar ejecta, a major objective of the experiment.

RESULTS

No significant results are reported at the time of this report for the following reasons.

1. The anticipated event rate from the LEAM experiment is approximately one event per day (periods of and effects from meteoroid shower activity excepted).

2. It is now assumed that the sensor covers were not removed before dawn of the second lunation and probably were removed only hours before the experiment was commanded "off" during the lunar day. Accordingly, no significant real-time data were obtained during the 45-day support period.

3. All data tapes received to date contain only 150 hr of lunar day data and 620 hr of lunar night data with the LEAM experiment in the full operating mode (the experiment in the "on" mode and the sensor covers removed).

Meaningful results from the LEAM experiment can only be derived from a long-term statistical and correlative study between primary particle events and ejecta events. In view of the relatively short-term measurement of primary particles, it seems premature to extend results beyond making a statement that, with the exception of the high temperatures, the LEAM experiment is performing normally.

REFERENCES

16-1. Berg, O. E.; and Gerloff, U.: More Than Two Years of Micrometeorite Data From Two Pioneer Satellites. Space Research XI. Akademie-Verlag (Berlin), 1971, pp. 225-235.

16-2. Charters, A. C.: High-Speed Impact. Sci. Am., vol. 203, no. 4, Oct. 1960, pp. 128-140.

16-3. Shoemaker, Eugene; Moore, Henry; and Gault, Donald: Spray Ejected From the Lunar Surface by Meteoroid Impact. NASA TN D-1767, 1963.

16-4. Greenberg, J. M.: A Possible Inter-Relation Between Interstellar and Interplanetary Cosmic Dust. Space Research IX. North-Holland Publishing Co. (Amsterdam), 1969, pp. 111-115.

16-5. Gerloff, Uli; and Berg, Otto E.: The Orbits of 14 Elliptic and 6 Hyperbolic Micrometeoroids Derived From Pioneer-8 and -9 Measurements. Paper presented at the XVth COSPAR Meeting (Madrid, Spain), May 1972.

16-6. Rahe, J.; Donn, B.; and Wurm, K.: Atlas of Cometary Forms: Structures Near the Nucleus. NASA SP-198, 1969.

16-7. Kaiser, C. B.: The Thermal Emission of F Corona. Astrophys. J., vol. 159, Jan. 1970, pp. 77-92.

16-8. Berg, Otto E.; and Grun, Eberhard: Evidence of Hyperbolic Cosmic Dust Particles. Space Research XIII. Akademie-Verlag (Berlin), 1973.

16-9. O'Keefe, J. A.; Adams, J. B.; Gault, D. B.; Green, J.; et al.: Theory and Processes Relating to the Lunar Maria From the Surveyor Instruments. Surveyor 6 Mission Report. Part II: Science Results. Calif. Inst. Tech. Rept. JPL-TR-32-1262, Jan. 10, 1968, pp. 171-176.

16-10. Criswell, David R.: Lunar Dust Motion. Proceedings of the Third Lunar Science Conference, vol. 3, MIT Press (Cambridge, Mass.), Oct. 1972, pp. 2671-2680.

17. Lunar Atmospheric Composition Experiment

J. H. Hoffman,[a†] R. R. Hodges, Jr.,[a] F. S. Johnson,[a] and D. E. Evans[b]

On the Apollo 17 mission, a miniature mass spectrometer, called the lunar atmospheric composition experiment (LACE), was carried to the Moon as part of the Apollo lunar surface experiments package (ALSEP) to study the composition of and variation in the lunar atmosphere. The instrument was successfully deployed in the Taurus-Littrow valley with its entrance aperture oriented upward to intercept and measure the downward flux of gases at the lunar surface (fig. 17-1).

Initial activation of the LACE instrument occurred on December 27, 1972, approximately 50 hr after sunset, and operation continued throughout the first lunar night. Sunrise brought a high background gas level and necessitated discontinuing operation during lunar daytime except for a brief check near noon. Near sunset, operation was resumed and continued throughout the night. This sequence was repeated for the second and third lunations.

The atmosphere of the Moon is very tenuous. Gas molecules do not collide with each other but, instead, travel in ballistic trajectories between collisions with the lunar surface, forming a nearly classical exosphere.

Possible sources of the lunar atmosphere are the solar wind, lunar volcanism, and meteoroid impact (ref. 17-1). Of these sources, the only one amenable to prediction of the composition of the lunar atmosphere is the solar wind. Thermal escape is the most rapid loss mechanism for light gases (hydrogen and helium). For heavier gases, photoionization followed by acceleration by the solar wind electric field accounts for most of the loss. More detailed descriptions of the formation and loss mechanisms of the lunar atmosphere are given in references 17-1 to 17-4.

The Apollo 14 and 15 cold cathode gage experi-

ments have determined an upper bound on the gas concentrations at the lunar surface of approximately 1×10^7 molecules/cm^3 in the daytime and 2×10^5 molecules/cm^3 at night (ref. 17-2). This large daytime increase suggests that most of the lunar gases are readily adsorbed on the cold nighttime surface. Hodges and Johnson (ref. 17-5) have shown that gases that are not likely to be adsorbed at night, such as neon and nitrogen, should be distributed in concentration as a function of temperature $(T^{-5/2})$ and thus have nighttime maximums. Contaminant gases originating from the lunar module (LM) or from other ALSEP experiments, or being adsorbed on surfaces in the site area could be influencing the daytime cold cathode gage readings, although such outgassing would have to exhibit very stable long-term rates because of the repeatability of the data from day to day. If the daytime maximum is a natural feature of the atmosphere, then it is probably a result of condensable gases, some of which may be of volcanic origin, while the nighttime level represents the noncondensable gases. The LACE was designed to identify the various gases in the lunar atmosphere and to determine the concentration of each species. A brief description of the instrument and a discussion of the results obtained during the first three lunations after deployment of the instrument are given in this section.

INSTRUMENTATION

Identification of gas molecules in the lunar atmosphere by species and determination of concentrations are accomplished by a miniature magnetic-deflection mass spectrometer. Gas molecules entering the instrument aperture are ionized by an electron bombardment ion source, collimated into a beam, and sent through a magnetic analyzer to the detector system.

The ion source contains two tungsten (with 1 percent rhenium) filaments, selectable by command,

---

[a]The University of Texas at Dallas.

[b]NASA Lyndon B. Johnson Space Center.

[†]Principal Investigator.
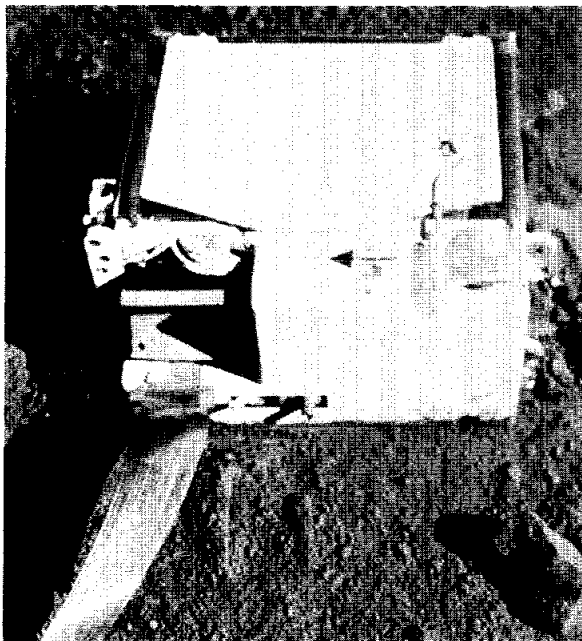
FIGURE 17-1.—The LACE deployed on the Moon. The entrance aperture covered by a nylon dust screen is at the lower right corner of the instrument. The mass analyzer is mounted behind the front cover with the electronics in a box to the rear. The white dust cover on top protects the mirrored surface during mission activities and LSPE explosive package detonations. The instrument package measures 34 by 32 by 17 cm and weighs 9.1 kg. The cable connecting the spectrometer to the central station is at the bottom of the photograph (AS17-134-20498).

as electron emitters. In the normal mode of operation, the fixed mode, the electron bombardment energy is fixed at 70 eV with the electron emission current regulated at 250 μA. This produces a sensitivity to nitrogen of 5×10^{-5} A/torr, sufficient to measure concentrations of gas species in the 1×10^{-15}-torr range. An alternate mode, the cyclic mode, provides four different electron energies (70, 27, 20, and 18 eV) that are cycled by successive sweeps of the mass spectrum. Identification of gases in a complex mass spectrum is greatly aided when the spectra are taken at several different electron ionization energies because the cracking patterns of complex molecules are strongly dependent on the bombardment electron energy. Also, at low energy, many gas species are eliminated from the spectrum, thus greatly simplifying the task of identifying parent molecules.

Two small heaters, consisting of ceramic blocks

with embedded resistors, are mounted in the ion source, enabling its temperature to be raised to 520 K for in situ outgassing. The gas entrance is pointed upward and has a dust trap around the source region that precludes the possibility of dust falling into the source itself.

Voltage scan of the mass spectrum is accomplished by a high-voltage stepping power supply. The ion-accelerating voltage (sweep voltage) is varied in a stepwise manner through 1330 steps from 320 to 1420 V with a dwell time of 0.6 sec/step. Each step is synchronized to a main frame of the telemetry format. Ten steps of background counts (zero sweep voltage) and 10 steps of an internal calibration frequency are inserted between sweeps, making a total of 1350 steps/spectrum. The sweep time is 13.5 min.

In an alternate mode, the sweep voltage may be commanded to lock on to any of the 1350 steps, enabling the instrument to monitor continuously any given mass number peak in the spectrum with a time resolution of 0.6 sec/sample. A one-step advance command is also available. The lock mode permits high time resolution monitoring of mass peaks that may be suspected to be of volcanic origin.

The sweep step number, being a function of the ion-accelerating voltage, is directly related to ion mass number. Each sweep step number, in turn, is uniquely related to a main frame telemetry word. Therefore, word position in the telemetry format serves as the identifier of atomic mass number in the spectrum.

Ions accelerated from the source region by the sweep voltage are collimated into a beam and directed through a magnetic field of 0.43 T. Three allowed trajectories (of radii 1.21, 4.20, and 6.35 cm) through the magnetic field region define the locations of three collector slits. Figure 17-2 is a schematic drawing of the analyzer showing the major parts and the three ion beam trajectories. Thus, three mass ranges are scanned simultaneously, namely 1 to 4, 12 to 48, and 27.4 to 110 amu, termed low-, mid-, and high-mass ranges, respectively. The advantage of a triple-channel analyzer is that a wide mass range may be scanned by a relatively narrow voltage excursion. Also, the mid- and high-mass ranges are so related that mass 28 and 64 peaks are detected simultaneously. Therefore, in the lock mode, carbon monoxide (CO) and sulfur dioxide (SO_2), which may be candidates for volcanic gases, can be monitored simultaneously.

Resolution of the analyzer is set at approximately
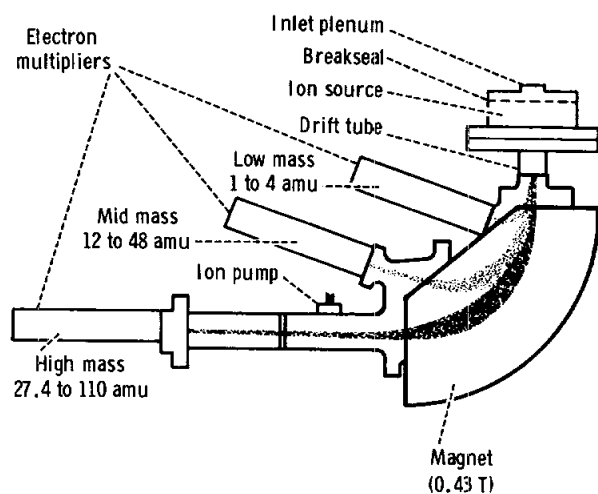
FIGURE 17-2.—Schematic diagram of mass analyzer. An ion beam is formed in the ion source from gas molecules entering the inlet plenum aperture. Three ion trajectories are shown through the magnet. Electron multipliers serve as charge amplifiers. An ion pump is used to check the internal analyzer pressure before application of high voltage to the ion source or the electron multiplier electrodes.

100 for the high-mass channel at mass 82. This is defined as less than a 1-percent valley between peaks of equal amplitude at mass 82 and 83. Krypton is used to verify the resolution.

Standard ion-counting techniques employing electron multipliers, pulse amplifiers, discriminators, and counters are used, one system for each mass range. The number of counts accumulated per voltage step (0.6 sec) for each channel is stored in 21-bit accumulators until sampled by the telemetry system. Just before interrogation, the 21-bit word is converted to a floating point number in base 2, reducing the data to a 10-bit word, consisting of a 6-bit number and a 4-bit multiplier. This scheme maintains 7-bit accuracy (1 percent) throughout the 21-bit (2×10^6) range of data counts.

Electron multiplier gains may be adjusted by command to a high or low value, differing by an order of magnitude. Likewise, the discriminator threshold level may be set at high or low (6-dB change) by command. The high level is used most of the time because it tends to minimize a spurious background noise that occurs toward the high-voltage end of the mass ranges. The internal calibration frequency read between each spectral scan verifies the operation of the counter system, the discrimination level, and the data compression circuits.

Housekeeping circuits monitor 15 functions within the instrument (supply voltages, filament current, emission current, sweep voltage, and several temperatures). One temperature sensor monitors the ion source temperature; this value is used in data reduction. Housekeeping words are subcommutated, one each 90 main frames, thus requiring a full spectral scan time to read each monitor once.

The mass spectrometer analyzer, magnet, ion source, and detectors are mounted on a baseplate that bisects the instrument package and are covered by a housing as shown in figure 17-1. The entrance aperture, which was sealed by a ceramic cap until it was opened by the crewman, points upward, enabling the downward flux of gas molecules to be measured. Behind the baseplate is a thermally controlled box containing the electronics. The top of the box has a mirrored surface covered by a dust cover that was commanded open after the last lunar seismic profiling experiment (LSPE) explosive package was detonated, 6 days after deployment. An arrow and bubble level on top of the package aided in proper deployment of the instrument.

Calibration of the instrument was performed at the NASA Langley Research Center (LRC) in a manner similar to that of the lunar orbital mass spectrometers flown on the Apollo 15 and 16 missions (ref. 17-6). A molecular beam apparatus produces a beam of known flux in a liquid helium cryochamber. The instrument entrance aperture intercepts the beam at one end of the chamber. With known beam flux and ion source temperature, instrument calibration coefficients are determined. Variation of gas pressure in the molecular beam source chamber behind a porous silicate glass plug varies the beam flux and provides a test of the linearity of the instrument response. Good linearity was achieved to as high as 5×10^5 counts/sec, where the onset of counter saturation occurs.

Calibrations were done with a number of gases that may be candidates for ambient lunar gases; for example, argon, carbon dioxide (CO_2), CO, krypton, neon, nitrogen, and hydrogen. Because helium is not cryopumped at the wall temperature, no helium beam can be formed in the chamber; therefore, helium calibrations are not possible with this system. Sensitivity to helium was determined in the ultrahigh vacuum chamber at the University of Texas at Dallas using the LRC absolute argon calibration of the instrument as a standard for calibrating an ionization

pressure gage. The gage calibration for helium was subsequently inferred from the ratio of ionization cross sections for helium and argon (ref. 17-7). The resulting helium sensitivity is the ratio of the calibrated gage pressure to the helium counting rate.

RESULTS

Operation of the instrument commenced approximately 50 hr after the first sunset after deployment (16 days). Performance was very good in general. All housekeeping monitors were nominal, and data were recorded on all three mass channels. Figure 17-3 is an example of a typical "quick look" nighttime spectrum recorded on a strip chart recorder in real time near the antisolar point during the third lunar night. Time, which is equivalent to voltage step number and related to atomic mass number, is plotted against the counting rate. Principal peaks are identified by mass number. The large-amplitude square pulse at the beginning and end of the spectrum in each channel is the internal calibration pulse; it is preceded by a zero

each channel. All the data presented in this section have been obtained from quick-look charts such as figure 17-3 and are considered preliminary at this time.

Each of the major peaks in the spectrum in figure 17-3 will be discussed in turn and will be given a tentative identification, which is essential in trying to determine its origin (native or artifact). Although many of the mass peaks observed undoubtedly arise from outgassing of the instrument or other materials at the landing site, three gases have been identified that are believed native to the Moon—helium, neon, and argon.

Peaks at mass 1, 2, and 4 are identifiable in the low-mass channel. Mass 1, atomic hydrogen, is almost certainly due to dissociation of artifact hydrocarbon molecules and other hydrogen compounds, including molecular hydrogen, in the ion source. Mass 2, molecular hydrogen, results largely from outgassing of the ion source, as it is steadily decreasing with time. Eventually, a stable hydrogen peak may appear that will then probably be truly lunar hydrogen.

vapor. Even in the daytime, the mass 18 peak is not large relative to other peaks. An upper limit of 2 X 10^7 water molecules/cm^3 has been established for the second lunar day, which indicates that little water vapor is present at the site.

Mass 19 being a dominant peak is a puzzle. The H_3O^+ ion is precluded because of the small H_2O peak. Fluorine is the only other possibility. This implies that much of the mass 20 peak may be hydrogen fluoride (HF) instead of neon. The mass 20 peak is smaller than the mass 19 peak by a factor of 3 at night and larger by the same factor in the daytime. The origin of the fluorine is unknown, but possibilities are the outgassing of solvents used in cleaning the instrument before flight, the outgassing of other warm areas of the site (e.g., instruments, the central station, or the radioisotope thermoelectric generator), or the natural degassing of the lunar materials. To study the neon question further, the temperature of the ion source was reduced from 270 K several times during the lunar night by turning off the filament for periods of approximately 30 min. Reactivation of the filament just before scanning the mass 20 to 22 range revealed stable, net mass 20 and 22 peaks with an amplitude ratio of approximately 13, in close agreement with the solar wind isotopic ratio of neon determined by Geiss et al. (ref. 17-9). The mass 44 peak was not large enough at the time to contribute significantly to the mass 22 peak as a doubly ionized species. A neon concentration of 7 X 10^4 molecules/cm^3 results, which is a factor of 20 less than that predicted by Johnson et al. (ref. 17-2).

The mass 28 peak is probably nitrogen or possibly CO, and mass 32 corresponds to oxygen. These will be discussed subsequently. Peaks at mass 35, 36, 37, and 38 fall into the same category as mass 19 and 20, most likely being chlorine and hydrogen chloride (HCl). The mass 35 to 37 ratio corresponds to the terrestrial chlorine isotopic ratio. As with fluorine, the origin of the chlorine is undetermined but is likely the same as that of fluorine. The ion source temperature reduction test was conducted for the mass 36 and 40 range also. The mass 36 and 38 peaks decreased to essentially zero; the mass 40 peak also was essentially zero, indicating a late night upper limit for any of the argon isotopes less than 200 molecules/cm^3. These tests indicate that the formation of HF and HCl is strongly temperature dependent and may arise from a reaction with hydrogen in the ion source $H_2 + F_2 = 2HF$ or $H_2 + Cl_2 = 2HCl$.

Hydrocarbon peaks at this time are all near zero amplitude. Native argon-40 (^{40}Ar) has been identified at other times and its diurnal behavior will be discussed later. Mass 44 is CO_2, thought to originate primarily from outgassing of the instrument. The remaining mid-mass peaks are mainly hydrocarbons principally from outgassing of the ion source.

The high-mass range spectrum duplicates the mid range below mass 44. Additional peaks of significant amplitude are the group near mass 61 and peaks at mass 78 and 85 that, as yet, are unidentified. The latter two are continuing to decrease in amplitude with time and are not considered significant. The unresolved set of peaks from 91 to 93.5 amu is probably doubly charged species in the mass 182 to 187 range that are the isotopes of tungsten and rhenium, originating from vaporization of the filament. The group near mass 61 may be triply charged tungsten and rhenium. At this measured vaporization rate (concentration of 1 X 10^3 molecules/cm^3), the useful filament lifetime is estimated at 10 yr. The remaining peaks are again thought to be artifact hydrocarbons.

Figure 17-4 is a reduced spectrum derived from raw data by subtracting from each peak amplitude the counts in the adjacent valleys due to background noise and scattered ions. Small-angle scattering of ions from neutrals in the mass spectrometer is a strong function of pressure but does occur to some
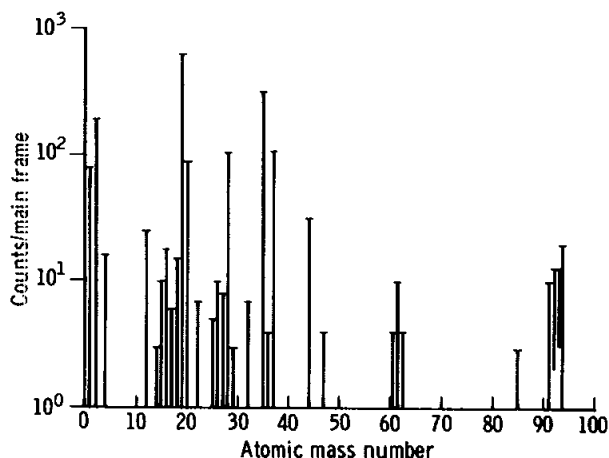
FIGURE 17-4.—Reduced spectrum taken 100 hr before sunrise of the third lunar night after deployment (16:30:00 G.m.t., Mar. 5, 1973). The solar zenith angle is 140°. Corrections have been applied for background counting rates.

extent in daytime data where the peak amplitudes are very large, that is, more than 1×10^5 counts/main frame in some cases. However, the corrections from scattering are typically less than 5 percent and frequently less than 1 percent. The accuracy of peak amplitudes at this stage of data analysis is estimated to be ±30 percent with some of the very small peaks having an uncertainty of a factor of 2. Most of the error comes from using the quick-look-type charts as the data source. The data are shown as counts/main frame as a function of atomic mass number. Differences between the mid- and high-mass overlapping ranges are removed by averaging. Counting rates ($\sec^{-1}$) can be obtained by multiplying each peak amplitude by 1.65. The example given in figure 17-4 is data from the third lunar night, a few calendar days later than the spectrum of figure 17-3. At this time, the ion source temperature had been reduced from its normal operating level of 270 K to near 200 K by turning the ion source off for approximately 30 min before the measurement.

The minimum nighttime total gas concentration observed to date is 4.6×10^5 molecules/cm^3, of which nearly 20 percent is hydrogen and 25 percent is mass 19, both of which are believed to be artifact. In addition, neon and helium, both believed to be native, exist at the 15-percent level. The total gas concentration at noon of the second lunation is 4×10^8 molecules/cm^3, of which 25 percent is hydrogen and 7 percent is mass 36 (HCl), with the remaining peaks all lower in abundance. Water vapor is 5 percent of the total. All the large peaks are believed to be dominated by outgassing of the instrument, the LM, the landing site, and so forth, in the heat of the day.

Diurnal variation of helium-4 (^{4}He) is shown in figure 17-5, starting with first activation of the instrument on December 27 at a solar zenith angle of −155°. Time progresses to the right through the lunar night and into the day. The first lunation continues to sunset (−90°). The complete second lunation is also shown ending at sunset (Feb. 22, 1973). The dashed curve indicates regions where the instrument was not operating. No significance is attached to the lack of tracking of the two curves because the differences are within the errors associated with reading quick-look data. Helium concentration, plotted along the ordinate, is shown to vary from approximately 2×10^3 molecules/cm^3 at lunar noon to 4×10^4 molecules/cm^3 near midnight. Because of
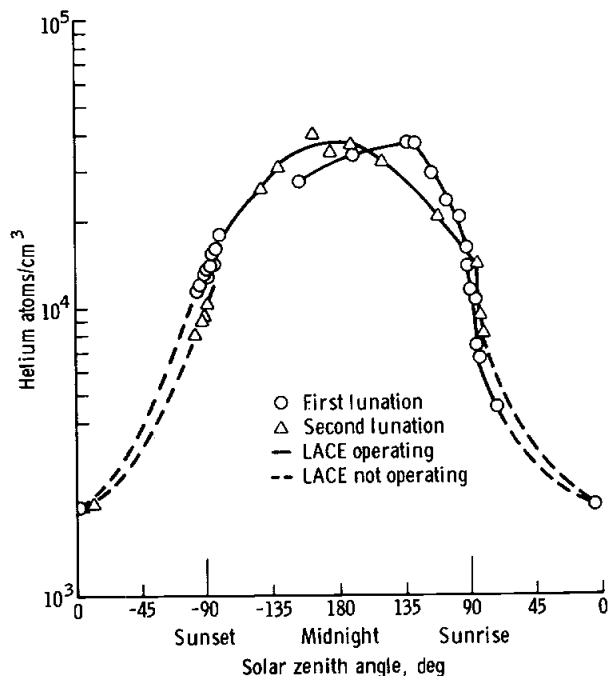
FIGURE 17-5.—Diurnal variation of ^{4}He. Concentration is plotted as a function of solar zenith angle with nighttime in the center of the figure. The distribution is typical for a noncondensable gas.

the very low level of the daytime helium (only three data counts after a correction for residual helium within the instrument is made based on preflight measurements of the helium and hydrogen ratio of laboratory spectra), the night-to-day ratio of helium can only be roughly estimated to be in the range of 15 to 30. This distribution is generally what would be expected of a noncondensable gas; that is, one that does not freeze out at the lunar nighttime temperature of 85 to 90 K (ref. 17-5).

The present measurement agrees with the daytime helium concentration of 3×10^3 molecules/cm^3 predicted by Johnson et al. (ref. 17-2). Hodges et al. (ref. 17-8) have done a Monte Carlo calculation of the distribution of solar wind helium around the Moon and found an equatorial night-to-day concentration ratio of 24, which should be slightly greater than at the 20° latitude of the instrument location. This distribution leads to a theoretical nighttime concentration of 4.1×10^4 molecules/cm^3 and a daytime value of 1.7×10^3 molecules/cm^3 for the same solar wind flux used by Johnson et al. (ref. 17-2); that is, 1.3×10^7 molecules/cm^2/sec. These values are in good agreement with the measurements, considering

the large variability of the solar wind flux (ref. 17-10).

The helium nighttime maximum occurring significantly before dawn (the coldest surface temperature occurs just before dawn) indicates that, because of the large-scale size of the helium trajectory (115 km at night), significant helium is lost from predawn and postsunset to the day side, from which thermal escape is a rapid loss mechanism.

The ^{40}Ar diurnal distribution is shown in figure 17-6. The coordinates are similar to those of figure 17-5. The difference between the nighttime minimums of the three lunations is believed to be due to a continual decrease in outgassing of the instrument with time. A significant feature is the large predawn increase in concentration. The very low, late night concentration of less than 200 molecules/cm^3 (which must be considered to be an upper limit of ^{40}Ar because the peak amplitude is essentially zero) indicates that it is a condensable gas and freezes out as the surface temperature falls below its freezing point. As the dawn terminator approaches the site but before any local heating occurs, the ^{40}Ar peak increase is due to argon being released from the warming surface and traveling several scale heights into the night side before being adsorbed by the lunar surface. The only other peak that exhibits this marked behavior is mass 36, probably ^{36}Ar. When the terminator passes the site and rapid local heating occurs, outgassing of hydrocarbon peaks dominates the argon contribution to mass 40. The trough just after 90° may be due to local depletion of argon from the surface all along the terminator. The trough is visible because of the delay in local sunrise after terminator crossing due to topographical conditions. It may be expected that the argon concentration would decrease slowly during the day until the onset of the rapid decrease after sunset. This would reflect the typical behavior of a condensable gas. However, argon may not condense on the surface until late night when the temperature reaches its freezing point.

The mass 36 peak exhibits a predawn enhancement but of a magnitude less than 10 percent of that of the ^{40}Ar, further supporting the evidence that the major contribution to the mass 36 peak is HCl when the ion source temperature is at its normal nighttime equilibrium value of 270 K. An upper limit for ^{36}Ar at night is 200 molecules/cm^3. As a comparison, the diurnal concentration of CO_2 (44 amu), which is a condensable gas at the night lunar surface tempera-
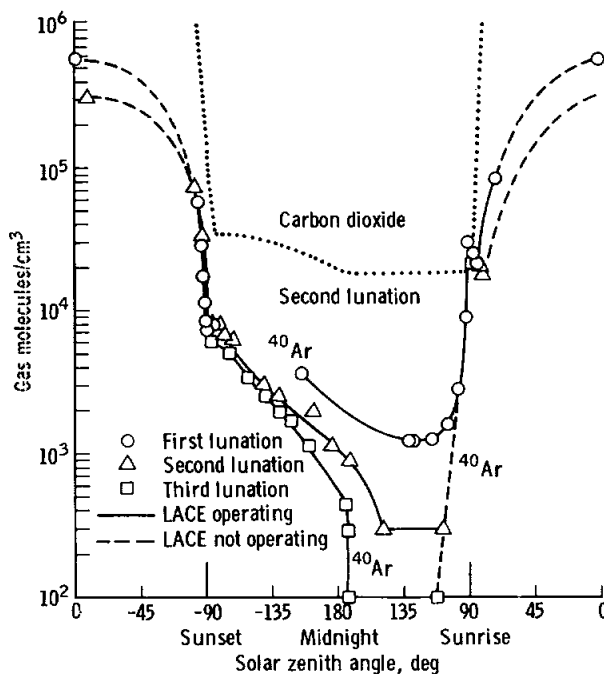
FIGURE 17-6.—Diurnal variation of ^{40}Ar. Coordinates are similar to those of figure 17-5. Predawn enhancement suggests boiloff of condensed gas from the warm approaching terminator region. Daytime increases are due to outgassing of hydrocarbon gases from the instrument, the LM, and the landing site. Carbon dioxide is shown as an example of a gas not showing predawn enhancement.

ture, is also given in figure 17-6. This peak shows no predawn enhancement but does show a very sharp increase at local sunrise and a similarly sharp decrease at sunset. Because the instrument is located in the Taurus-Littrow valley, local sunrise occurs nearly 8 hr after terminator crossing of the site longitude; local sunset occurs approximately 6 hr early. The lag in the CO_2 decrease beyond sunset very likely results from a thermal lag in the instrument and from other equipment degassing at the site.

The concentrations of two other gases, nitrogen and CO at mass 28 and oxygen (at mass 32), are plotted in figure 17-7. Again, the coordinates are similar to those of the two previous figures. The behavior closely tracks that of CO_2, with no predawn enhancement. Oxygen would be expected to freeze out at night more readily than argon because its freezing point is several degrees higher than that of argon, and the ion source temperature reduction tests indeed showed a zero amplitude peak for mass 32. The conclusion is that essentially all the oxygen is

artifact, and an upper limit on the lunar oxygen is in the low 10^2 molecules/cm^3 range.

Conversely, mass 28, whether it is nitrogen or CO (no distinction is made at this time), would not condense at night temperatures and should have its

FIGURE 17-7.—Mass 28 (nitrogen and carbon monoxide) and mass 32 (oxygen) concentrations as a function of solar zenith angle during the second lunation.

maximum concentration at night. However, it is believed that the concentration of 3×10^4 molecules/cm^3 is still at least partially artifact because of the large decrease (a factor of 4) from the first lunation to the second. This appears to be merely an outgassing rate decrease. Perhaps several lunations hence, the value may stabilize and mass 28 will become a candidate for a native gas.

CONCLUSIONS

From the data obtained during the first three lunations after deployment of the LACE instrument, three gases—helium, neon, and argon—have been identified as being native to the lunar atmosphere. A summary of the measured concentrations of these gases compared with several predictions is presented in table 17-I. The helium concentrations and the diurnal ratio are in excellent agreement with predictions based on the solar wind as a source, indicating that the basic tenets of the theory of a noncondensable gas are correct. However, the neon measured concentration is a factor of 20 below predictions, indicating possibly some adsorption or retention on the night side of the Moon. If true, this phenomenon is unexpected because of the very low freezing temperature (27 K) of neon. The Apollo 16 lunar orbital mass spectrometer experiment (ref. 17-11) did detect neon on the night side near the sunset terminator at a concentration approximately 1×10^5 molecules/cm^3. This is approximately a factor of less

TABLE 17-I.—*Concentrations of Gases Determined from Current Lunar Mass Spectrometer Data, Cold Cathode Gage Data, and Predictions*

Gas	Mass spectrometer data, molecules/cm³		Cold cathode gage data, molecules/cm³		Predicted data, molecules/cm³	
	Day	*Night*	*Day*	*Night*	*Day*	*Night*
Hydrogen (H₂)	1×10^8	1×10^5			[a]3.6×10^3	[a]2.3×10^4
Helium	2×10^3	4×10^4			([b]3×10^3 \ [a]1.7×10^3	[a]4.1×10^4
Neon		[c]7×10^4			[b]5×10^4	[b]1.3×10^6
³⁶Ar		[c]2×10^3			[b]3×10^2	[b] 8×10^3
⁴⁰Ar		[c]2×10^3				
[d]Total	4×10^8	4.6×10^5	1×10^7	2×10^5		

[a]Predicted by R. R. Hodges, Jr., in unpublished data.

[b]Reference 17-2.

[c]Upper limit; argon freezes out at night.

[d]Total gas concentrations from mass spectrometer during second lunar day and third lunar night after deployment; from cold cathode gage after 10 lunations.

than 2 higher than the present value and is within the experimental errors of the measurements. This discrepancy between theory and measurement for neon is a serious problem and is one of the major tasks to be considered in the future.

Argon appears to be adsorbed on the late night (coldest) part of the lunar surface as none of its isotopes are detected at this time. A significant predawn enhancement of ^{40}Ar indicates a release of the gas from the warm approaching terminator region. The ^{36}Ar and ^{38}Ar are masked by HCl peaks at this time. Future presunrise tests with a cooled ion source should reveal the actual amounts of ^{36}Ar and ^{38}Ar. Clearly, argon does not behave as a noncondensable gas and, therefore, cannot be compared to predictions. Furthermore, ^{40}Ar probably results mainly from potassium-40 decay and subsequent "weathering" of lunar surface materials, so its presence is evidence of a truly native lunar gas.

The remaining peaks of the spectra are all considered to be dominated by artifact gases at this time. The total nighttime gas density of 4.6×10^5 molecules/cm^3 is a factor of 2 higher than the measured values from the Apollo 14 and 15 cold cathode gage experiments. This is not surprising (notwithstanding errors in calibration of both instruments) because the mass spectrometer ion source is warmer than the cold discharge source of the gage and therefore would have a higher outgassing rate. However, the residual being measured by both instruments is clearly not entirely neon but a multitude of gases, including helium.

As the instrument, the LM, and the landing site continue to be cleansed in the high daytime temperatures, the passage of several more lunations should produce much cleaner spectra and yield more definitive data on concentrations of true lunar gases or, at a minimum, reduce the upper limits now determined.

ACKNOWLEDGMENTS

REFERENCES

17-1. Johnson, F. S.: Lunar Atmosphere. Rev. Geophys. Space Phys., vol. 9, no. 3, Aug. 1971, pp. 813-823.

17-2. Johnson, Francis S.; Carroll, James J.; and Evans, Dallas E.: Lunar Atmosphere Measurements. Proceedings of the Third Lunar Science Conference, vol. 3, MIT Press (Cambridge, Mass.), 1972, pp. 2231-2242.

17-3. Hoffman, J. H.; Hodges, R. R., Jr.; and Evans, D. E.: Lunar Orbital Mass Spectrometer Experiment. Proceedings of the Third Lunar Science Conference, vol. 3, MIT Press (Cambridge, Mass.), 1972, pp. 2205-2216.

17-4. Siscoe, G. L.; and Mukherjee, N. R.: Upper Limits on the Lunar Atmosphere Determined From Solar Wind Measurements. J. Geophys. Res., vol. 77, no. 31, Nov. 1, 1972, pp. 6042-6051.

17-5. Hodges, R. R., Jr.; and Johnson, F. S.: Lateral Transport in Planetary Exospheres. J. Geophys. Res., vol. 73, no. 23, Dec. 1, 1968, pp. 7307-7317.

17-6. Hoffman, J. H.; Hodges, R. R.; and Evans, D. E.: Lunar Orbital Mass Spectrometer Experiment. Sec. 19 of Apollo 15 Preliminary Science Report. NASA SP-289, 1972.

17-7. Von Ardenne, Manfred: Tabellen der Elektronenphysik Ionenphysik und Ubermikroskopie. Vol. 1, Deutscher Verlag der Wissenschaften (Berlin), 1956, p. 488.

17-8. Hodges, R. R., Jr.; Hoffman, J. H.; Johnson, F. S.; and Evans, D. E.: Composition and Dynamics of Lunar Atmosphere. Lunar Science IV (Abs. of papers presented at the Fourth Lunar Science Conference (Houston, Tex.), Mar. 5-8, 1973), pp. 374-375.

17-9. Geiss, J.; Buehler, F.; Cerutti, H.; Eberhardt, P.; and Filleux, Ch.: Solar Wind Composition Experiment. Sec. 14 of Apollo 16 Preliminary Science Report. NASA SP-315, 1972.

17-10. Hundhausen, A. J.; Bame, S. J.; Asbridge, J. R.; and Sydoriak, S. J.: Solar Wind Proton Properties: Vela 3 Observations from July 1965 to June 1967. J. Geophys. Res., vol 75, no. 25, Sept. 1, 1970, pp. 4643-4657.

17-11. Hodges, R. R.; Hoffman, J. H.; and Evans, D. E.: Lunar Orbital Mass Spectrometer Experiment. Sec. 21 of Apollo 16 Preliminary Science Report. NASA SP-315, 1972.

18. Lunar Neutron Probe Experiment

Dorothy S. Woolum,[a] *D. S. Burnett,*[a†] *and C. A. Bauman*[a]

Primary cosmic ray protons incident on the lunar surface interact with lunar material by means of nuclear reactions, which produce neutrons as secondary products. The initial investigations of the Apollo 11 samples (ref. 18-1) showed that gadolinium in lunar materials contained isotopic variations that could be unambiguously ascribed to neutron capture. Such a record of neutron bombardment had not been observed previously in natural samples, either terrestrial or meteoritic, because, unlike meteorites, lunar samples are materials from a large body that is capable of developing an appreciable secondary flux of low-energy (< 1 eV) neutrons, and because, unlike the Earth, the Moon has no thick overlaying atmosphere to protect the surface materials from neutron exposure. Since the Apollo 11 mission, neutron capture on samarium-149 (^{149}Sm) (ref. 18-2), europium-151 (ref. 18-3), bromine-79 (^{79}Br) and bromine 81 (ref. 18-4, (barium-130 (^{130}Ba) (refs. 18-5 to 18-9), tungsten-186 (ref. 18-10), cobalt-59 (ref. 18-11), and calcium-40 (ref. 18-12) also has been observed with fluences (time-integrated fluxes) that range from $< 1 \times 10^{15}$ to 1×10^{17} neutrons/cm^2. These data have been used to determine regolith mixing rates and depths, depths of irradiation for lunar rocks, and accumulation rates and deposition times for core samples (refs. 18-1 to 18-7, 18-13, and 18-14). However, all these conclusions depend on knowing the equilibrium neutron energy spectrum, the neutron flux as a function of depth in the regolith, and the absolute rate of neutron production. Until recently, only the theoretical calculations of Lingenfelter et al. (ref. 18-15) and Armstrong and Alsmiller (ref. 18-16) have provided estimates for these quantities. These calculations were of sufficient complexity that it was not possible to be fully confident of the interpretation of the lunar sample

data, and, for this reason, the lunar neutron probe experiment (LNPE) was performed. The LNPE was designed to obtain a direct in situ experimental measurement of neutron capture rates as a function of depth in the regolith, as well as to retrieve some information about the energy distribution of the equilibrium neutron flux.

This section contains a complete description of the lunar neutron probe and a preliminary account of the data obtained to date. Preliminary results also have appeared in the abstracts for the Fourth Lunar Science Conference (ref. 18-17). All data processing for the LNPE occurs after the return of the instrument to Earth, and complete processing of the data will require several more months. The account contained in this section should be viewed as a progress report on the first stages of data processing.

EXPERIMENT DESCRIPTION

Principle of Neutron Detection

The LNPE is in the form of a rod that is inserted into the lunar regolith to permit the measurement of neutron capture rates to a depth of 2 m. The LNPE contained two passive particle-track-detector systems: (1) cellulose triacetate plastic (Triafol TN) detectors were used in conjunction with boron-10 (^{10}B) targets to record the alpha particles emitted by neutron capture on ^{10}B; and (2) muscovite mica detectors were used to detect the fission fragments resulting from neutron-induced fission in uranium-235 (^{235}U) targets. In addition, 0.46-mm-thick cadmium absorbers were included at two locations in order to obtain information about the neutron energy spectrum. The cadmium strongly absorbs neutrons that have energies below 0.35 eV; consequently, only the fraction of the neutron population above this energy will be measured at these locations. Further spectral information will be available from analyses of

---

[a]California Institute of Technology.
†Principal Investigator.

krypton-80 and krypton-82 produced by bromine neutron capture in potassium bromide (KBr) contained in three evacuated capsules inserted in the probe. The bromine neutron capture occurs at energies (10 to 100 eV) that are significantly higher than those for ^{235}U and ^{10}B. Krypton analyses will be performed by Marti and Osborne of the University of California (San Diego), and results will appear separately.

Instrument Description

The LNPE was taken to the Moon in a deactivated mode, activated and deployed during the first period of extravehicular activity (EVA-1), then deactivated at the end of EVA-3 and returned to Earth for processing of the track detector materials. Figure 18-1 is a schematic, cross-sectional view of the lunar neutron probe showing the layout of the target-detector systems and illustrating the mechanism of activation and deactivation. The ^{10}B targets are mounted on one-half of the outer circumference of a

Activated   Deactivated

▐▐▐▐▐ Mica   ▨▨▨▨ Central rod
▨▨▨▨ Boron   ▨▨▨▨ Rib cage
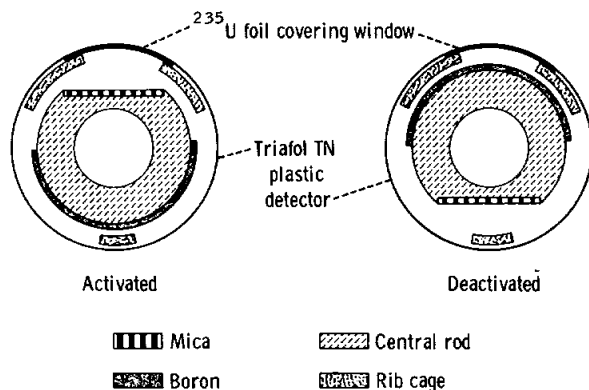
FIGURE 18-1.—A schematic, cross-sectional view of the lunar neutron probe, illustrating the disposition of the targets and detectors in the activated (on) and deactivated (off) modes. The boron targets and mica detectors are mounted on the central rod; the plastic detectors and uranium targets are mounted on the rib cage. When activated, the targets face their respective detectors; when deactivated, the target and detector systems are 180° out of alinement.

FIGURE 18-2.—A portion of the central rod, showing the boron target half cylinders mounted on it. The dark, circular area contains one of the uranium-238 (^{238}U) metal disks masked to a diameter of approximately 1 mm. The ^{238}U was used to provide fiducial marks in the plastic detectors for verifying activation and deactivation. The boron targets are 7.5 cm long.
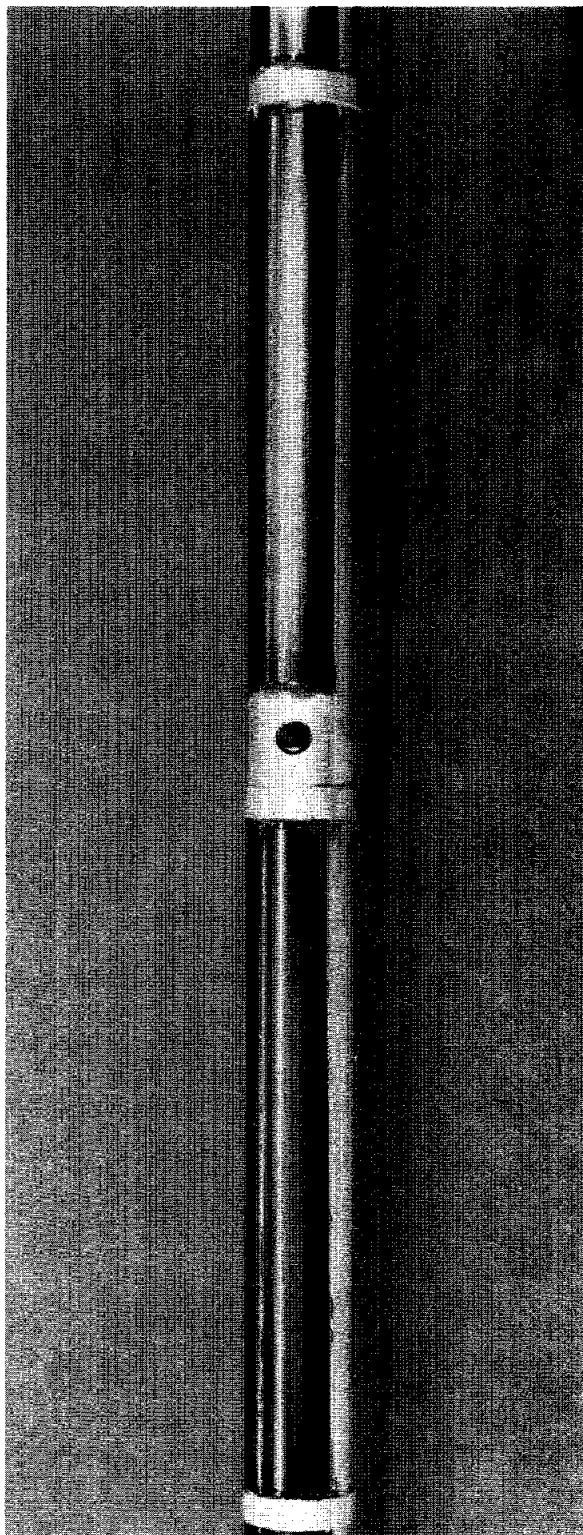
central rod (fig. 18-2). The mica detectors are fixed on flats milled on the opposite side of the central rod (fig. 18-3). Concentric with and surrounding the central rod is an open, cylindrical frame structure (rib cage) around which sheets of the plastic detector are wrapped. The ^{235}U targets are mounted in discrete positions over windows in the rib cage (fig. 18-4). A continuous, black-anodized tube (not shown in fig. 18-1) is used as a casing to enclose and protect the target-detector systems.

The probe is activated and deactivated by a 180° rotation of the central rod with respect to the rib cage (fig. 18-1). In the activated configuration, the uranium-mica and the boron-plastic target-detector pairs are brought into alinement. In the deactivated configuration, the uranium and boron targets are adjacent and the mica and plastic detectors likewise. In the latter configuration, particles emitted from the target surfaces cannot enter the respective detectors; thus, the probe is deactivated. The activation and deactivation mechanism was necessary to prevent the accumulation of background events from neutrons produced by cosmic ray interactions in the spacecraft and by the plutonium-238 power source for the Apollo lunar surface experiments package (ALSEP), the radioisotope thermoelectric generator (RTG), which is a strong neutron source ($\approx 7 \times 10^7$ neutrons/sec).

Figure 18-5 is a schematic, cutaway view of the LNPE showing the manner in which the various detectors were deployed along the length of the probe. For reference, the theoretically predicted depth (in units of grams per square centimeter) profile of the neutron capture rate is plotted. To permit accurate definition of the flux profile, the length of the probe was chosen to be 2 m, a depth which is well below the theoretically predicted peak of the profile (≈ 150 g/cm^2). The boron-plastic detection system was essentially continuous along the full length of the probe. As shown in figure 18-5, 16 uranium targets and mica detectors were mounted at eight discrete locations along the probe. The
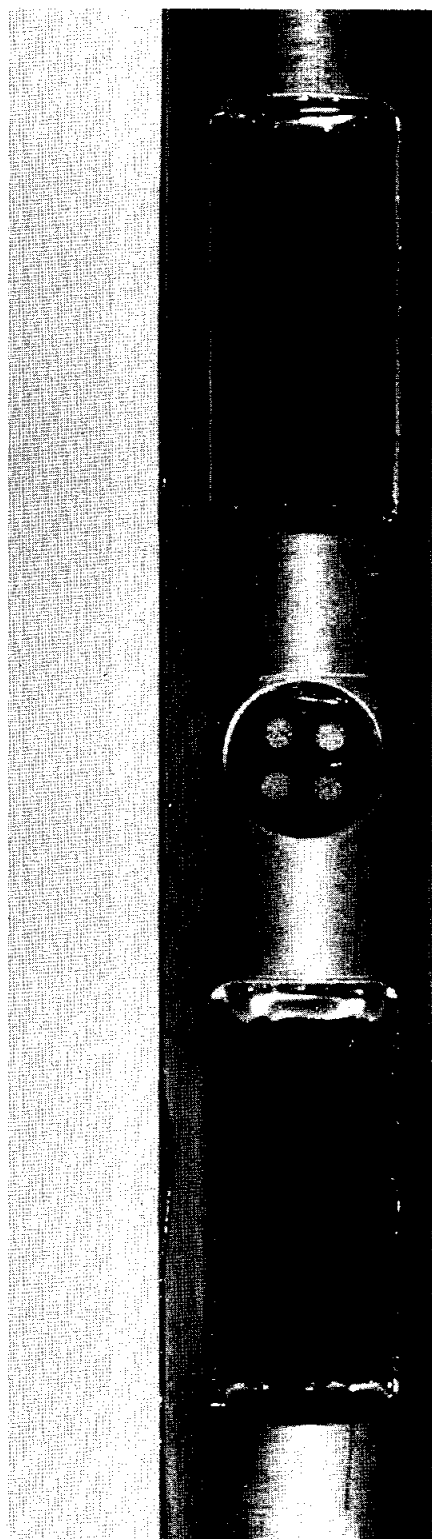
FIGURE 18-3.—A photograph of two rectangular mica detectors mounted on flats in the central rod. The mica detectors are 1.8 cm long. Also included at this location is one of the circular temperature sensors. None of the four circular indicators had turned black, indicating that the temperature never exceeded 333 K. The photograph was taken during the photodocumentation of the LNPE after the Apollo 17 mission.
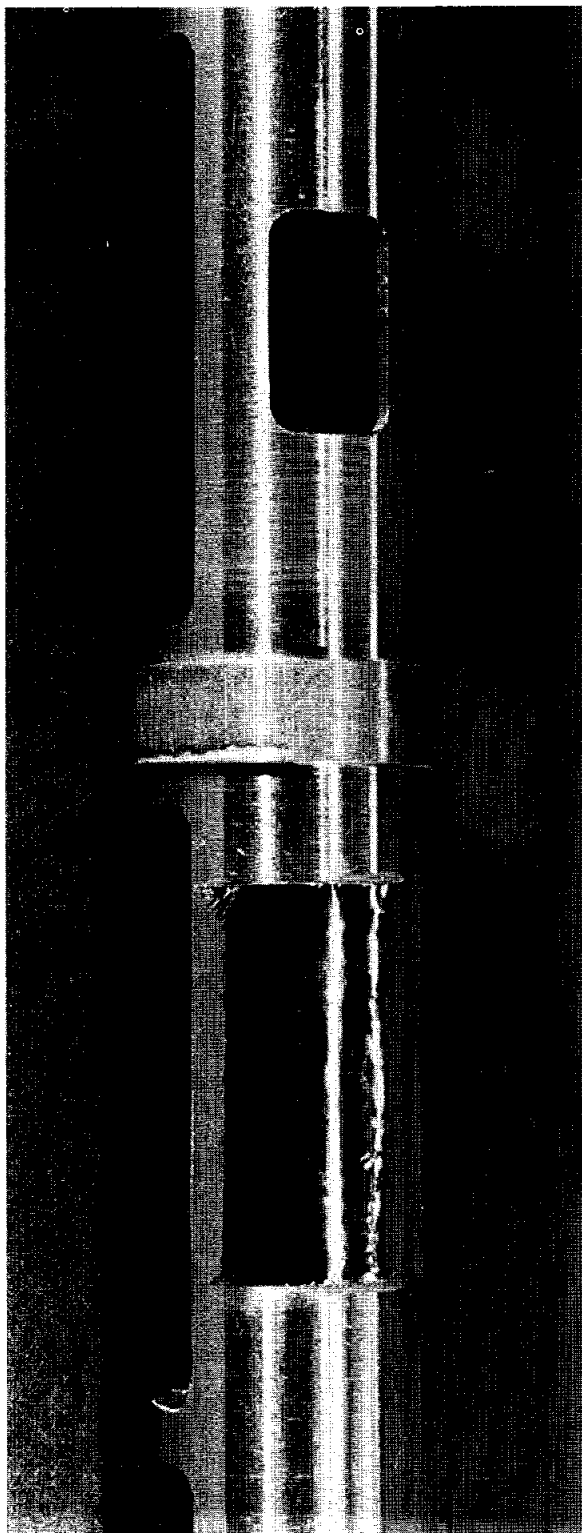
FIGURE 18-4.—A portion of the rib cage during the early stages of the assembly of the probe, before the mounting of the plastic detectors. Visible are one of the open windows and a window covered with a ^{235}U metal target that has, in turn, been completely covered with aluminum foil to prevent the registration of alpha particles in the plastic detectors when they are wrapped onto the rib cage. The windows are 1.2 cm long.

uranium-mica target-detector pairs were mounted with uniform separations in the lower half of the probe but were closely spaced and concentrated toward the top in the upper half of the probe. This arrangement was chosen for two reasons. First, the temperature of the probe was expected to be highest near the surface, and the investigators were concerned about thermal annealing of the tracks in the plastic detectors. Fission tracks in mica are not annealed even at peak lunar surface temperatures; thus, if data were lost in the plastic at the top of the probe, the mica data would still provide the near-surface record. Second, from theoretical predictions, the lowest track densities were expected near the surface, and results from the Apollo 16 cosmic ray experiment (ref. 18-18) suggested that these densities might be quite
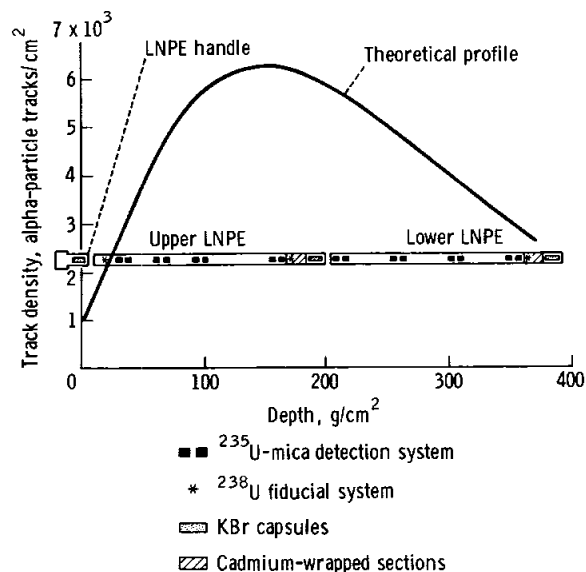
FIGURE 18-5.—A schematic view of the lunar neutron probe showing how the various targets and detectors are distributed with depth and including the theoretically predicted track density versus depth curve. The ^{10}B targets and plastic detectors (not shown) are essentially continuous along the entire length of the probe.

low. At such densities, mica detectors give more reliable results than plastic detectors.

Also displayed in figure 18-5 are the locations of the two cadmium absorbers near the bottom and middle of the probe. A 0.46-mm-thick cadmium sheet was wrapped around the rib cage over the plastic detector at each site (fig. 18-6). The evacuated KBr capsules were inserted at the top, middle, and bottom of the probe, as shown. In addition, three point sources of uranium-238 (^{238}U) were mounted near the bottom, middle, and top of the probe in flats milled on the side of the central rod on which the ^{10}B targets were mounted (fig. 18-2). The reason for including the point sources was twofold. The alpha particles emitted by these point (1 to 2 mm) sources registered in the plastic detectors only while the probe was activated and thus provided fiducial marks from which the proper activation of the probe can be verified. Also, from the track densities and the appearance (length, width, etc.) of the ^{238}U alpha-particle tracks, it will be possible to determine whether the tracks in the plastic detectors have been thermally annealed during and after the activation and the lunar surface exposure.

In wrapping the plastic sheets on the rib cage, an overlapping second layer was placed over the window areas, primarily to secure the plastic to the rib cage better. Because the second layer is never exposed to any of the targets, however, four small portions of plastic in this outer layer were preirradiated with a known dose of ^{238}U alpha particles to provide an additional check on thermal annealing in the plastic. Further, the areas of the plastic detectors in this second layer that are not preirradiated provide a continuous record of background events resulting from cosmic rays and tracks produced by nuclear interactions (recoils) of the RTG fast neutrons with the plastic. Based on analyses of small pieces of the Triafol TN plastic carried on the Apollo 15 spacecraft, the background from cosmic ray alpha particles and heavy ions was expected to be negligible. The Apollo 16 cosmic ray experiment results had suggested that the plastic would register tracks from fast-neutron interactions (ref. 18-18). Separate experiments using both californium-252 and
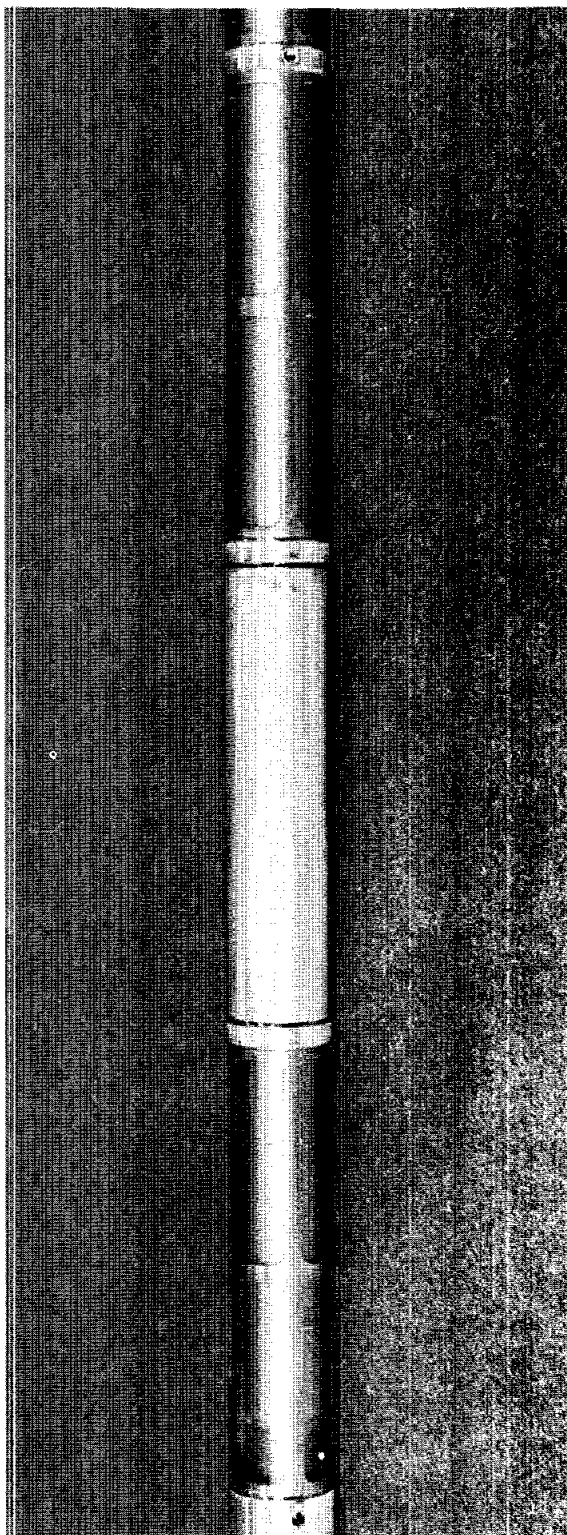
FIGURE 18-6.—A portion of one of the fully assembled rib cages. Two plastic detectors and one of the cadmium-wrapped areas are shown. The cadmium cylinder is 7.5 cm long.

plutonium-beryllium (Pu-Be) neutron sources have shown that fast (MeV) neutrons produce tracks with an efficiency of $\approx 2 \times 10^{-6}$. For this efficiency, an RTG fast-neutron background track density of ≈ 150 tracks/cm^2 is expected in the plastic during the flight to the lunar surface. This value is not large compared to predicted ^{10}B alpha-particle track densities (> 1000 tracks/cm^2).

To provide an actual measurement of the maximum temperature exposure of the LNPE, temperature indicators were fastened to flats in the central rod at four positions along the probe (fig. 18-3). Each temperature indicator contained four separate temperature-sensitive compounds that irreversibly turn black at 140°, 160°, 180°, and 200° F (333, 344, 355, and 366 K), respectively.

The completely assembled flight unit is shown in figure 18-7. For convenient stowage on the spacecraft, the LNPE was fabricated in two 1-m-long sections that could be activated separately. The upper section (on the right in fig. 18-7) was activated by depressing a bar on the large handle at the upper end and rotating the handle 180°. The lower section was activated by removing the dust cap at its upper end and using it as a tool to rotate the central rod. The center rod was spring loaded to snap into one of two stable configurations differing by a 180° rotation. After activation, the two sections could be coupled for deployment by simply screwing the two sections together.

Targets and Detectors

The boron targets were prepared with a process especially developed for this experiment. The ^{10}B is vacuum deposited as metallic boron by the thermal cracking of diborane onto 0.05-mm-thick tantalum half cylinders. The deposition temperature was approximately 1073 K. The ^{10}B targets were made "infinitely thick"; that is, they were deposited to an average thickness of 1.4 ± 0.2 mg/cm^2, which is greater than the range of the 1.6-MeV alpha particles emitted with neutron capture on ^{10}B. Each target was
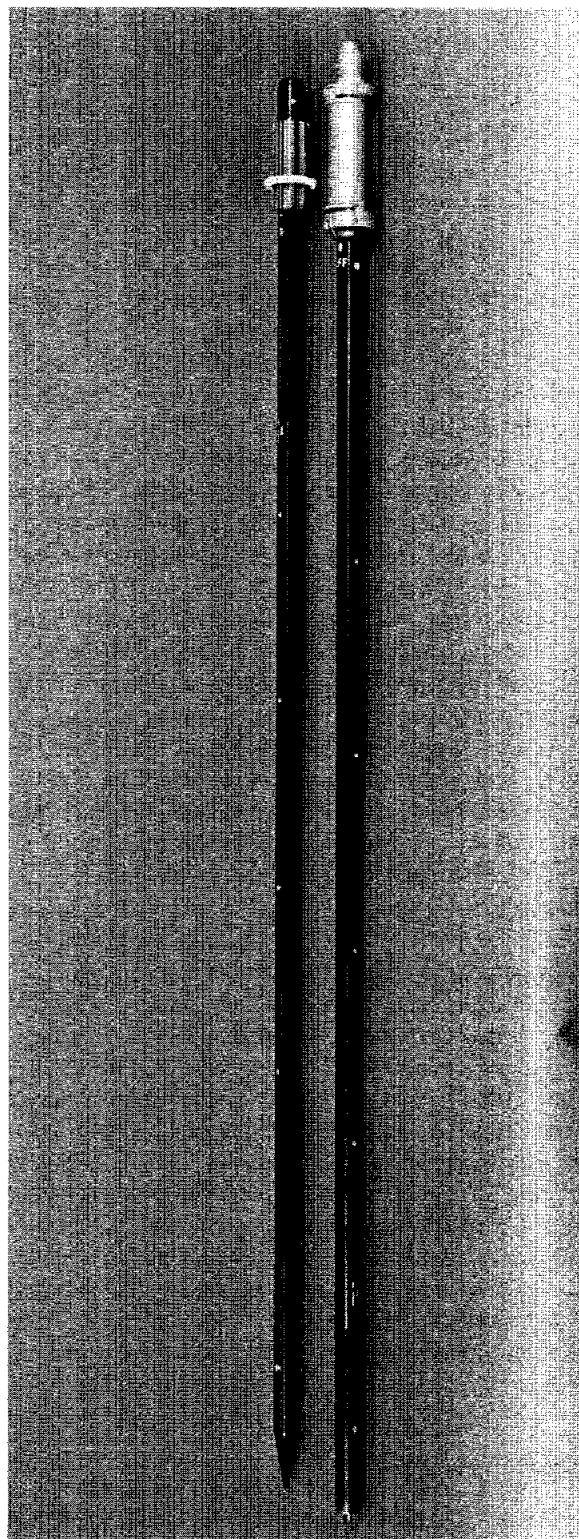
FIGURE 18-7.—The assembled flight unit of the lunar neutron probe. The upper section, with the probe handle at the top, is on the right. The lower section with its removable dust cap is on the left. Coupling of the two sections is accomplished by screwing the lower and upper units together after removing the dust cap. Each section is approximately 1 m long.

tested individually using a Pu-Be neutron source. The thickness and uniformity of several targets also were checked by alpha backscattering techniques using the California Institute of Technology tandem Van de Graaff accelerator.

The ^{235}U targets were cut from 0.025-mm-thick foil sheets of 99-percent enriched ^{235}U, cleaned in nitric acid (HNO_3), and then coated with a 30-nm-thick layer of silver to prevent oxidation and corrosion of the uranium. A film of this thickness produces negligible attenuation of the emitted fission fragments. Alpha-particle counts were determined for each target to verify the relative quality and uniformity of the targets used.

Experimentation with Triafol TN has shown that this plastic is somewhat nonuniform in its track registration properties. Exposure to monoenergetic accelerated alpha particles indicates an energy registration interval from ≈ 0.25 to 2.5 MeV, which probably applies to most samples. However, some batches of plastic show considerably reduced sensitivity, which is critically dependent on whether the irradiations are performed in air or in vacuum. One batch in particular will not register alpha particles in vacuum but does in air. These phenomena presumably reflect the critical role played by oxygen in track formation in plastic. This oxygen influence has been studied previously by Monnin (ref. 18-19) and by Crawford et al. (ref. 18-20). Because of the lack of uniformity, the registration properties of representative samples of the plastic used for the flight unit were determined by using vacuum neutron irradiations of the plastic samples exposed to a ^{10}B target. The registration of the plastic was uniform to better than ± 10 percent over an area of $\approx 0.3 \ m^2$. Comparison of air and vacuum registration shows a small vacuum effect, with the vacuum registration efficiency being less by approximately 12 ± 3 percent.

Before incorporation into the probe, the plastic and mica detectors were preannealed to remove any possible background tracks. Preannealing of the mica was particularly important because muscovite, like most natural micas, has a nonnegligible density of fossil fission tracks from the spontaneous fission decay of trace uranium impurities. The mica was annealed at 903 K for 3.5 hr; the plastic, at 389 K for 9 days. In addition to being preannealed, the mica was pre-etched 4 hr in 48 percent hydrofluoric acid (HF) at room temperature and then silver coated (≈ 30 nm thick). Because normal etching time for fission tracks in muscovite mica usually is 20 min to 1 hr, any small, shallow pits left after the preannealing appear as huge, shallow troughs and cannot be confused with the smaller diameter lunar-neutron-induced fission tracks. The silver coating was applied to monitor any possible flaking of the prime detecting surface of the mica. The coating does not affect the registration properties of the mica.

The techniques used for preparing the detectors for data analysis are standard. The mica detectors are first desilvered in a 35-percent solution of HNO_3 and then etched in 48 percent HF for 25 min or 1 hr. Data reported in this section are from samples etched 25 min and scanned in an optical microscope at 630 X magnification. Samples etched 1 hr have larger tracks and are scanned at a lower (500 X) magnification. When a sample was etched for 25 min and counted, then etched further to 1 hr and recounted, the results agreed within one standard deviation. The plastic detectors are etched in a bath consisting of five parts 12 percent sodium hypochlorite and seven parts 6.25N sodium hydroxide at 313 K. The alpha-particle tracks in Triafol TN range only to approximately 4 μm in length and, consequently, are scanned at a magnification of 1000X.

The LNPE Deployment

The deployment of the LNPE was nominal. The LNPE was retrieved from the modularized equipment stowage assembly (MESA) where it was stowed and was loaded on the lunar roving vehicle at the beginning of EVA-1. To prevent overheating, the two sections were kept in a thermal bag during the EVA activities before actual deployment. Following the ALSEP deployment, the deep drill corestem sample was acquired at a site approximately 40 m north (ref. 18-21) of the ALSEP central station and the RTG power source. After the recovery of the deep core, the two LNPE sections were removed from the thermal bags, activated, coupled, and emplaced in the deep drill corestem hole. The insertion was made after first passing the probe through the hole in the treadle used for recovering the deep core. The treadle was used because, in retrieving the deep core, the top of the hole had been widened; thus, the possibility existed that the probe would drop too far into the hole to be retrieved. Full emplacement of the LNPE was achieved manually. The deployment site was in a shallow depression and behind a meter-sized rock,

which should have provided additional shielding from the RTG neutrons. To prevent overheating, the top of the probe protruding above the surface was covered with the thermal bag during exposure. The LNPE was recovered, decoupled, deactivated, and returned to the lunar module at the very end of EVA-3, after accruing 49 hr of exposure.

The LNPE has been returned to the investigators and has been disassembled. The targets and detectors are in excellent condition; no flaking was observed in the mica detectors or on the boron targets. Furthermore, the temperature indicators showed that the probe temperature did not reach 333 K.

RESULTS

Depth Profile of the ^{235}U Fission Rate

To date, only the mica detectors have been examined. The processing of the plastic detectors has been delayed in order to explore a suggestion[1] for processing the plastic that may produce better developed tracks, which would be easier to recognize and count.

Figure 18-8 is a plot of the experimental data (shown as points in the figure) from nine of the 16 mica detectors; at least one mica from each of the eight distinct pairs located along the probe was sampled. The error bars are one standard deviation based solely on counting statistics. The depths in grams per square centimeter were calculated from the measured bulk densities of the samples in the deep drill core sections.[2] The solid curve in figure 18-8 is the theoretical profile of the neutron flux (ref. 18-15), which has been normalized to the measured track density at 150 g/cm^2. No adjustment of the depth scale has been made. Because the neutron energy spectrum below approximately 1 eV is expected to be independent of depth except for the first few centimeters, the theoretical profile defines the depth dependence of the neutron capture rate for all elements that capture neutrons in this energy region.

The depth profile assumes a uniform chemical composition corresponding to Apollo 11 sample 10084; however, from the work of Lingenfelter et al.

---
[1] Michel Monnin, private communication, 1973.

[2] D. Carrier, G. Heiken, and S. Nagel, private communication, 1973.
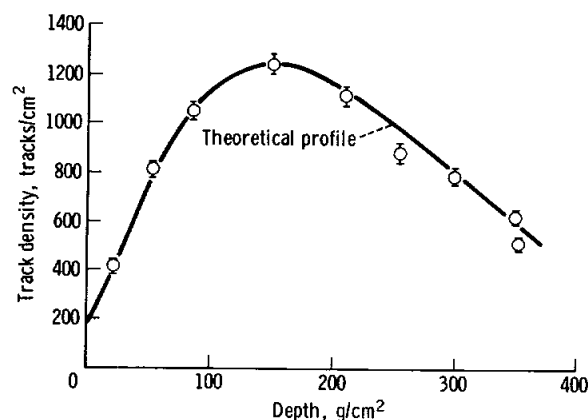
FIGURE 18-8.—Comparison of the raw fission track data from the mica detectors and the neutron flux theoretical profile (ref. 18-15), which has been normalized to the measured track density at 150 g/cm^2. The error bars on the data points are one standard deviation, based solely on counting statistics. The depth scale has not been adjusted.

(ref. 18-15), it can be argued that the profile would not change significantly if a chemical composition corresponding to samples from any other site had been chosen instead because the depth profile for the flux is determined only by the depth distribution of the neutron production rate and the neutron moderating properties of the soil. Only the latter depends on the chemistry, being governed by the most abundant elements, silicon and oxygen, the abundances of which do not vary appreciably from site to site on the Moon. If the chemical composition in the deep drill corestem sample is not homogeneous and if the concentrations of either the major-element neutron absorbers (primarily titanium and iron) or the trace-element absorbers (for instance, the rare-earth elements) vary significantly, the variations will have to be considered in the final comparison between the theoretical and experimental profiles. The deep core materials, once analyzed, will provide the information necessary to construct the appropriate theoretical curve for comparison. Also, after the postflight calibration data analyses have been completed, corrections for possible minor differences in the uranium-target efficiencies can be applied. These corrections have not been made in the data presented in figure 18-8. An additional small correction to the experimental profile may be necessary for the distortion caused by the finite size of the drill-stem hole in which the probe was inserted.

Based on the results of a field simulation experiment, significant corrections for background from the RTG neutrons probably will not be required; however, quantitative estimates for this correction are not currently available. The rapid decrease of the observed track densities near the surface also suggests that the RTG background is small because the track density profile produced by RTG neutrons is expected to peak much closer to the surface; this would cause the curve of the observed track densities to flatten out as it approached the surface.

Despite these qualifications, if the current data are accepted at face value, the trend of the data points is in very good agreement with the theoretical profile.

Absolute Value of the ^{235}U Fission Rate

The relationship between the measured track density ρ (tracks/cm^2) in the mica detectors and the neutron fission rate n (fissions/g(^{235}U)-sec) in the uranium targets is given by

$$f\rho = n \frac{R}{2} GT \qquad (18\text{-}1)$$

where T is the exposure time of the probe, R is the mean range in grams per square centimeter of a single fission fragment in metallic uranium, and G is a dimensionless constant defining the geometrical efficiency of the mica detectors compared to 2π geometry ($G < 1$). The quantity of $R/2$ is the average depth from which fission fragments produced in the uranium will register in a mica detector placed on the surface of the uranium (2π geometry). In the actual experimental configuration, because of the necessity for the on-off mechanism, the targets and detectors were not in contact; G is the factor that accounts for the decrease in detector efficiency caused by the required separation. A correction for self-absorption f must be applied because the target materials in the neutron probe are strong neutron absorbers; consequently, the neutron flux and hence the measured track densities in the presence of the probe are somewhat depressed compared to their values in the absence of the probe materials. As defined in equation (18-1), f is a dimensionless constant and must have a value $\geqslant 1$. The values for f, R, and G are obtained from laboratory calibration experiments. Equation (18-1) is also applicable to the boron-plastic system if the factor $R/2$ is replaced by $R/4$. This

substitution is necessary because two fragments are emitted in the fission of ^{235}U but only one alpha particle is produced with neutron capture on ^{10}B. Data are not yet available for plastic track detectors; the following discussion applies only to the uranium-mica system.

The factors in equation (18-1) can be evaluated in several ways, but only one method, in which f, R, and G are evaluated independently, has been used so far. The value of R is expected to be close to the radiochemically determined fission-fragment range in metallic uranium (10×10^{-3} g/cm^2, ref. 18-22). However, as indicated by the studies of Reimer et al. (ref. 18-23), the range value appropriate for equation (18-1) may be slightly less than measured radiochemically. Based on natural-uranium/mica detectors irradiated in 2π geometry in a well-thermalized neutron flux, monitored by goldfoil activation, an effective range of 8.4×10^{-3} g/cm^2 is obtained for the standard etching and scanning conditions. The following two methods have been used to determine G.

1. The neutron probe was assembled with some mica samples mounted in direct contact with the standard configuration on the center rod flats. After neutron irradiation, G was calculated from the ratio of the fission track densities in the mica samples on the center rod to the mica samples irradiated in 2π geometry.

2. The probe was assembled with pieces of the plastic detector mounted on the center rod flats and also in contact with the uranium targets. The value for G was calculated from the ratio of the uranium alpha-particle track densities in the center rod plastics to those in contact with uranium, as in (1).

Good agreement was found between the G values obtained (0.60 ± 0.02) by using these two methods. To eliminate self-absorption effects, natural uranium was used for all determinations of R and G values.

At present, the principal uncertainty in the absolute fission rate lies in the value of f. The determination of f is more complicated than the determination of the other factors in equation (18-1) because the value of f varies with neutron energy. However, it is possible to estimate f using only the general features of the lunar neutron energy distribution without depending on the accuracy of the theoretical energy spectrum. The calibration proce-

dures used to date have been designed to determine f using neutron energy spectra that are harder and softer than the lunar spectrum and thus bracket the lunar self-absorption factor.

Lunar material is a good absorber of low-energy neutrons; thus, the neutron energy spectrum in the region below 1 eV will be significantly shifted to higher energies compared to the Maxwell-Boltzmann distribution that would be expected if the low-energy neutrons were able to come into thermal equilibrium. This shift is shown, for example, by the measured ratio of samarium to gadolinium neutron capture in lunar samples, which is much higher than the ratio expected for a thermalized neutron energy distribution (ref. 18-2).

Because neutron self-absorption is greatest at those energies at which the fission cross sections are large and because the ^{235}U fission cross section is highest at low neutron energies, the self-absorption factor obtained in an irradiation with a thermal spectrum will be an upper limit for the value of f that is appropriate for the lunar data.

A calibration irradiation was performed in a well-thermalized neutron flux, and f was determined by comparing track densities from the actual ^{235}U targets with those from much more dilute ^{235}U targets, consisting of either natural uranium (0.72 percent ^{235}U) or depleted uranium (0.409 percent ^{235}U), in which the self-absorption was negligible. The ^{235}U targets were mounted at one end of the probe in the actual experimental configuration, including ^{10}B targets on the center rod. At the other end of the probe, isolated from any ^{10}B targets, the natural- and depleted-uranium targets were similarly mounted. The measured value of f thus includes the effect of the ^{10}B targets on the ^{235}U fission rate as well as the effect of the ^{235}U foils themselves. A self-absorption factor of 1.37 ± 0.04 was obtained. Thus, the value for f has been bracketed: $f \leqslant 1.4$ and $f \geqslant 1$ (by definition). Consequently, $f = 1.2 \pm 0.2$ has been adopted as the self-absorption factor appropriate for the lunar ^{235}U fission rate. Additional calibration using a harder flux will yield a somewhat more precise value for f by providing an experimental lower limit.

Using the values of R, G, and f given previously, a ^{235}U fission rate of 3.5 ± 0.6 fissions/g(^{235}U)-sec is obtained at a depth of 150 g/cm^2, which approximately corresponds to the peak of the neutron flux profile.

For comparison, the theoretical ^{235}U capture rate can be calculated by

$$n = S \int_0^\infty N\sigma_F(E)\phi(E)\,dE \qquad (18\text{-}2)$$

where N is the number of ^{235}U atoms per gram, σ_F is the fission cross section for ^{235}U, E is neutron energy, $\phi(E)$ is the energy distribution of the neutron flux as calculated by Lingenfelter et al. (ref. 18-15), and S is the ratio of the cosmic ray neutron production rate for the 2 days when the neutron probe was deployed on the lunar surface to the average rate over the 11-yr solar cycle. Although S can be estimated from terrestrial atmospheric neutron monitor data, this estimation has not yet been made. For the present, $S = 1$ should be a reasonable estimate because the Apollo 17 landing occurred at a time roughly between solar maximum and minimum and because neutron monitor counting rates do not show long-term time variations larger than approximately 20 percent. The value of $\phi(E)$ calculated for the composition of Apollo 11 soil sample 10084 at a temperature of 200 K has been used. This value is a reasonable approximation to the Apollo 17 conditions, but the actual Apollo 17 chemistry and temperature will be used in the final comparison. The theoretical value obtained for 150 g/cm^2 is 3.2 fissions/g(^{235}U)-sec; thus, within the present experimental uncertainties, agreement is obtained between the experimental and theoretical capture rates. However, it should be emphasized that this agreement may be somewhat fortuitous. In particular, no reliable estimate of the error in the assumption of $S = 1$ is available currently.

CONCLUSIONS

Although the analysis is still at a preliminary stage, it appears that good agreement exists between the experimental results and the theoretical calculations of Lingenfelter et al. (ref. 18-15). If the subsequent refinement of the experimental data and of the theoretical predictions confirms this agreement, the conclusions drawn previously from lunar sample data and the theoretical calculations can be accepted with some confidence. The following discussion is based on this assumption.

Some justification is required for the assumption that agreement between the theoretical and experi-

mental capture rates for ^{235}U (or ^{10}B) implies agreement for other elements. This assumption probably is good for gadolinium-157 (^{157}Gd) and ^{149}Sm because these nuclei capture neutrons in an energy range similar to that of ^{235}U or ^{10}B; however, the assumption is less valid for such nuclei as ^{130}Ba or ^{79}Br, which capture neutrons at higher energies. This argument is illustrated in figure 18-9, in which the fraction of neutron captures that occur at different neutron energies for these nuclei is shown. These curves were calculated using the neutron energy spectrum of Lingenfelter et al. (ref. 18-15). The curves for ^{157}Gd, ^{10}B, and ^{235}U are qualitatively similar and peak at much lower energies than the curve for ^{130}Ba or ^{79}Br, although ^{235}U has a distinct contribution (≈ 20 percent) from neutron capture at energies higher than 10 eV. In all cases, a neutron energy spectrum must be assumed in order to calculate the relative capture rates of ^{235}U or ^{10}B to other nuclei. Figure 18-9 shows that the uncertainties in the neutron energy spectrum are less important for ^{157}Gd than for ^{130}Ba or ^{79}Br. The ^{79}Br capture rate will be measured directly from the KBr capsules contained in the LNPE.

The gadolinium and samarium isotopic variations measured in the Apollo 15 deep core sample showed a distinct peak at ≈ 200 g/cm^2, which is approxi-

mately 50 g/cm^2 higher than the theoretically predicted maximum (ref. 18-15). The peaked distribution unambiguously indicates that this area of the lunar surface has remained uncratered for a relatively long period ($\approx 500 \times 10^6$ yr). The LNPE data show that the difference between the observed and the theoretical peak depths cannot be ascribed to the uncertainties in the theoretical flux profile but, instead, must reflect a recent ($\leq 50 \times 10^6$ yr) deposition of ≈ 50 g/cm^2 of material at this site. The deposition may have resulted from a single event or from a large number of events.

Even after allowing for the relatively large uncertainties that currently exist, the LNPE data place strong constraints on the interpretation of the measured neutron fluences in lunar soil samples. As discussed extensively in previous papers (refs. 18-1, 18-3, and 18-13), the observed fluences in soil samples from all Apollo missions are much lower than expected for material that has resided in the upper few meters of the lunar surface for times corresponding to the age of the site. One interpretation is that the low fluences reflect deep mixing of the lunar regolith on a 1×10^9-yr time scale by which the observed fluences for surface soil samples are diluted. However, the required mixing depths calculated from this model using the theoretical ^{157}Gd capture rate are high; for example, approximately 15 m for Apollo 11, a depth which is roughly 3 times greater than regolith depths estimated from photogeology (ref. 18-24). The LNPE data indicate that this factor-of-3 difference cannot be ascribed to inaccuracies in the theoretical capture rates used previously. Thus, if a regolith depth of 5 m is accepted as correct for the Apollo 11 site, it must be concluded that the previously mentioned uniform mixing model is not valid and that the lunar regolith has not been well mixed to a depth of 5 m over a time scale of approximately 1×10^9 yr. Instead, it would appear that the upper portions of the regolith contain the least irradiated material and that the deeper portions of the regolith must contain the more heavily irradiated material.
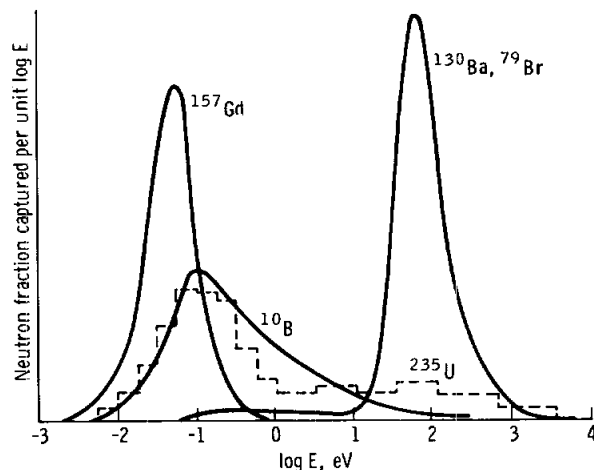
FIGURE 18-9.—A comparison of the calculated fractional neutron capture rate (linear scale) and the neutron energy for several important neutron absorbers in lunar samples. The differences in the energy response of the nuclei are graphically demonstrated. The relative peak capture rates are dependent on the equilibrium neutron energy spectrum assumed; the Lingenfelter et al. (ref. 18-15) energy spectrum was used for these calculations.

ACKNOWLEDGMENTS

not have been possible without the active cooperation of a very large number of personnel from NASA and its contractors. We are also grateful for the encouragement and advice given to us by many of our colleagues, in particular G. P. Russ III, M. Monnin, R. M. Walker, and G. J. Wasserburg. The support of the Kellogg Radiation Laboratory at the California Institute of Technology, particularly from T. Tombrello and R. Kavanaugh, was vital.

REFERENCES

18-1. Eugster, O.; Tera, F.; Burnett, D. S.; and Wasserburg, G. J.: The Isotopic Composition of Gd and the Neutron Capture Effects in Samples from Apollo 11. Earth Planet. Sci. Lett., vol. 8, 1970, pp. 20-30.

18-2. Russ, G. P. III; Burnett, D. S.; Lingenfelter, R. E.; and Wasserburg, G. J.: Neutron Capture on ^{149}Sm in Lunar Samples. Earth Planet. Sci. Lett., vol. 13, no. 1, Dec. 11, 1971, pp. 53-60.

18-3. Russ, G. Price III: Apollo 16 Neutron Stratigraphy. Earth Planet. Sci. Lett., vol. 19, 1973.

18-4. Lugmair, G. W.; and Marti, Kurt: Exposure Ages and Neutron Capture Record in Lunar Samples from Fra Mauro. Proceedings of the Third Lunar Science Conference, vol. 2, MIT Press (Cambridge, Mass.), 1972, pp. 1891-1897.

18-5. Eberhardt, P.; Geiss, J.; Graf, H.; Grogler, N.; et al.: Correlation Between Rock Type and Irradiation History of Apollo 11 Igneous Rocks. Earth Planet. Sci. Lett., vol. 10, 1970, pp. 67-72.

18-6. Marti, K.; and Lugmair, G. W.: Kr^{81}-Kr and K-Ar^{40} Ages, Cosmic-Ray Spallation Products, and Neutron Capture Effects in Lunar Samples from Oceanus Procellarum. Proceedings of the Second Lunar Science Conference, vol. 2, MIT Press (Cambridge, Mass.), 1971, pp. 1591-1605.

18-7. Huneke, J. C.; Podosek, F. A.; Burnett, D. S.; and Wasserburg, G. J.: Rare Gas Studies of the Galactic Cosmic Ray Irradiation History of Lunar Rocks. Geochim. Cosmochim. Acta, vol. 36, Mar. 1972, pp. 269-302.

18-8. Kaiser, W. A.; and Berman, B. L.: The Average ^{130}Ba (n,γ) Cross Section and the Origin of ^{131}Xe on the Moon. Earth Planet. Sci. Lett., vol. 15, no. 3, July 1972, pp. 320-324.

18-9. Berman, B. L.; and Browne, J. C.: Microscopic ^{130}Ba (n,γ) Cross Section and the Origin of ^{131}Xe on the Moon. Phys. Rev. C., vol. 17, no. 6, 1973.

18-10. Michel, R.; Herpers, U.; Kulus, H.; and Herr, W.: Isotopic Anomalies in Lunar Rhenium. Proceedings of the Third Lunar Science Conference, vol. 2, MIT Press (Cambridge, Mass.), 1972, pp. 1917-1925.

18-11. Finkel, R. C.; Wahlen, M.; Arnold, J. R.; Kohl, C. P.; and Imamura, M.: The Gradient of Cosmogenic Radionuclides to a Depth of 400 g/cm² in the Moon. Lunar Science IV (Abs. of papers presented at the Fourth Lunar

Science Conference (Houston, Tex.), Mar. 5-8, 1973), pp. 242-244.

18-12. Kornblum, J. J.; Levine, M.; Aronson, A.; and Fireman, E. L.: Neutrons in the Moon. Lunar Science IV (Abs. of papers presented at the Fourth Lunar Science Conference (Houston, Tex.), Mar. 5-8, 1973), pp. 441-443.

18-13. Burnett, D. S.; Huneke, J. C.; Podosek, F. A.; Russ, G. Price III; and Wasserburg, G. J.: The Irradiation History of Lunar Samples. Proceedings of the Second Lunar Science Conference, vol. 2, MIT Press (Cambridge, Mass.), 1971, pp. 1671-1679.

18-14. Russ, G. Price III; Burnett, D. S.; and Wasserburg, G. J.: Lunar Neutron Stratigraphy. Earth Planet. Sci. Lett., vol. 15, 1972, p. 172.

18-15. Lingenfelter, R. E.; Canfield, E. H.; and Hampel, V. E.: The Lunar Neutron Flux Revisited. Earth Planet. Sci. Lett., vol. 16, no. 3, Nov. 1972, pp. 355-369.

18-16. Armstrong, T. W.; and Alsmiller, R. G., Jr.: Calculation of Cosmogenic Radionuclides in the Moon and Comparison with Apollo Measurements. Proceedings of the Second Lunar Science Conference, vol. 2, MIT Press (Cambridge, Mass.), 1971, pp. 1729-1745.

18-17. Woolum, Dorothy S.; Burnett, D. S.; and Bauman, C. A.: The Apollo 17 Lunar Neutron Probe Experiment. Lunar Science IV (Abs. of papers presented at the Fourth Lunar Science Conference (Houston, Tex.), Mar. 5-8, 1973), pp. 793-795.

18-18. Burnett, D.; Hohenberg, C.; Maurette, M.; Monnin, M.; et al.: Solar Cosmic Ray, Solar Wind, Solar Flare, and Neutron Albedo Measurements. Sec. 15, Part C, of the Apollo 16 Preliminary Science Report. NASA SP-315, 1972.

18-19. Monnin, Michel: Interaction des Ions Lourds avec des Dielectriques Organiques Macromoleculaires: Contribution a l'Étude des Detecteurs Solides de Traces. Thesis, Université de Clermont, France, 1969.

18-20. Crawford, W. T.; Desorbo, W.; and Humphrey, J. S., Jr.: Enhancement of Track Etching Rates in Charged Particle-Irradiated Plastics by a Photo-Oxidation Effect. Nature, vol. 220, Dec. 28, 1968, pp. 1313-1314.

18-21. Apollo Lunar Geology Investigation Team: Documentation and Environment of the Apollo 17 Samples: A Preliminary Report. U.S. Geol. Survey, Interagency Rept.: Astrogeology 71, Jan. 21, 1973, p. 323.

18-22. Alexander, John M.; Gazdik, M. F.; Trips, A. R.; and Wasif, Saad: Kinetic Energy Release in 23 MeV Deuteron Fission of U^{238}. Phys. Rev., vol. 129, no. 6, Mar. 15, 1963, pp. 2659-2663.

18-23. Reimer, G. M.; Storzer, D.; and Wagoner, G. A.: Geometry Factor in Fission Track Counting. Earth Planet. Sci. Lett., vol. 9, 1970, pp. 401-404.

18-24. Shoemaker, E. M.; Bailey, N. G.; Batson, R. M.; Dahlem, D. H.; et al.: Geologic Setting of the Lunar Samples Returned by the Apollo 11 Mission. Sec. 3 of the Apollo 11 Preliminary Science Report. NASA SP-214, 1969.

19. Cosmic Ray Experiment

INTRODUCTION

The scientific objectives of the lunar surface cosmic ray experiment (LSCRE) were (1) to measure the flux of solar wind particles with atomic number $Z > 26$ using mica detectors, (2) simultaneously to determine the flux of light, rare-gas solar wind ions using metal foils, (3) to measure the flux of low-energy particles in space, both solar and galactic, during quiet Sun conditions using plastic, glass, and mica detectors, and (4) to determine the radon concentration in the lunar atmosphere using mica detectors.

Several different groups, each of which provided different detector materials, collaborated in the experiment. The overall design, construction, and coordination of the experiment were provided by R. M. Walker and E. Zinner of Washington University. The mica detectors are currently being studied by R. M. Walker, E. Zinner, and M. Maurette of the University of Paris. The glass detectors are being studied by the General Electric Company (GE) group of R. L. Fleischer, H. R. Hart, and R. T. Woods. The Lexan plastic is being examined by the University of California group, headed by P. B. Price. The aluminum and platinum foils are being used by P. Eberhardt and J. Geiss of the University of Bern to measure the flux of light solar wind ions in a greatly scaled down version of their solar wind composition experiments.

A much larger particle-detector experiment, with similar objectives and mostly the same investigators, was flown on the Apollo 16 mission. A solar flare that occurred during the Apollo 16 mission made it possible to obtain unique and important information concerning solar flares, particularly at low energies (refs. 19-1 to 19-5). However, the great abundance of solar flare particles created a background that made it impossible to realize many of the original objectives of the experiment.

In mid-1972, a group of investigators proposed the LSCRE particle detector described in this report for the Apollo 17 mission. Because of the short time available before the mission, the proposed experiment was designed to have minimal weight and to require minimal astronaut time on the lunar surface. In part A of this section, a general description of the experiment and its deployment on the lunar surface is given. A status report on the scientific results being obtained with the mica detectors is also presented. In parts B and C, the results obtained with the glass and Lexan detectors, respectively, are described. At the time of preparation of this report, no data were available on the solar-wind-implanted metal foils.

PART A

MEASUREMENTS OF HEAVY SOLAR WIND AND HIGHER ENERGY SOLAR PARTICLES DURING THE APOLLO 17 MISSION

R. M. Walker,[a] E. Zinner,[a] and M. Maurette[b]

DESCRIPTION OF THE EXPERIMENT

In the Apollo 17 lunar surface cosmic ray experiment (LSCRE), one set of particle detectors was mounted inside a shallow, rectangular aluminum box; a separate set was mounted inside a sliding cover (fig. 19-1). The box was deployed in sunlight and the sliding cover in shade. The detectors mounted in each part are listed in table 19-I; the detector numbers are keyed to figure 19-1(c). Both the Sun half and the shade half had temperature labels on the sides opposite those on which the detectors were mounted.

In each half, the mica detectors (numbers 1 and 13 in fig. 19-1(c)) consisted of a single slab of cleaved muscovite that had been previously annealed for 100 hr at 853 K in an argon atmosphere to remove fossil tracks. The mica detector also had 18 spots, each 0.24 cm in diameter, of evaporated silver deposited on the external surface to aid in distinguishing solar wind particles from more energetic, penetrating particles. One-third of these spots had a metal thickness of ≈55 nm; the remaining two-thirds were equally divided between thicknesses of ≈100 and ≈150 nm. The mica plates were held in position with two metal straps and were also lightly tacked down with spots of Dow Corning 6-1104 silicone glue.

Two mica detectors (number 6 in fig. 19-1(c)) were also mounted in rectangular recesses milled in the edge of the Sun half. The purpose of these auxiliary mica detectors was to determine the precise orientation of the Sun during exposure from the shadowing of solar wind tracks by the edges of the recess. Because the mica was intended primarily to detect solar wind particles, careful microphotographs of all mica pieces were taken using oblique lighting, both before and after the mission, to assess the degree of dust covering.

The 5-μm-thick platinum and aluminum foils

(numbers 2, 3, and 12 in fig. 19-1(c)) were glued to 1.5-mm-thick aluminum with 3M 467 adhesive film. The plates were in turn glued into the box and cover. In addition, two platinum foils 5 by 0.8 and 9.5 by 0.8 cm were glued into recesses on the sides of the box (numbers 7 and 8 in fig. 19-1(c)). The different orientations of foils as well as the use of different metals (platinum and aluminum) were to provide redundant information on the direction of the light solar wind and also to look for a flux of low-energy ions at large angles to the solar wind direction.

The glass detectors (numbers 4, 5, 9, and 10 in fig. 19-1(c)) are described in more detail in part B of this section. For a description of the Lexan detector (number 11 in fig. 19-1(c)), see part C.

The LSCRE was transported to the Moon in the closed position, in which both sets of detectors were inside the box. In this position, the end rings, one attached to the box and one attached to the cover, were on opposite sides of the box. The cover was held in place by spring loading and also by a Velcro strap, attached at one end to the end ring on the box, looped around the entire assembly. To avoid contamination, the LSCRE was transported to the Moon in a plastic bag inside the lunar module (LM) cabin. The total weight of the assembled package was 163 g, and the overall dimensions were 22.5 by 6.3 by 1.1 cm.

DEPLOYMENT AND RECOVERY ON THE LUNAR SURFACE

The LSCRE was deployed by first pulling the slide cover off while in the shade of the LM and hanging the cover in place on a hook attached to the side of the LM. The cover remained in the shade, with the detectors pointed toward space, for 45.5 hr. After deployment of the cover, the box portion of the LSCRE was carried into sunlight and hung on the strut of the LM using the Velcro strap attached to the end ring. Deployment was nominal and was completed early in the first period of extravehicular

[a]Washington University, St. Louis, Missouri.
[b]Laboratoire René Bernas, Orsay, France.

TABLE 19-I.—*Detectors in the LSCRE*

Number	Detector	Component measured	Exposed area, cm^2
		Sun-half detectors	
1	Mica	Heavy solar wind and low-energy cosmic rays	12.2
2	Aluminum foil	Light solar wind	5.1
3	Platinum foil	Light solar wind	11.2
4	Fused quartz (Suprasil 2)	Low-energy cosmic rays	5.4
5	Lead phosphate glass (Lal)	Low-energy cosmic rays	1.85
6	Mica	Heavy solar wind (Sun direction)	1.2
7	Platinum foil	Light solar wind	3.8
8	Platinum foil	Light solar wind	8.0
		Shade-half detectors	
9	Lead phosphate glass (Lal)	Low-energy cosmic rays	1.76
10	Phosphate glass (GE-1457)	Low-energy cosmic rays	1.62
11	Lexan	Low-energy cosmic rays	14.0
12	Platinum foil	Control piece for foils in Sun	6.8
13	Mica	Low-energy cosmic rays and radon atmosphere	9.1

FIGURE 19-1.—The LSCRE. (a) View of interior. (b) View of exterior. (c) Schematic diagram. For information on numbered detectors, see table 19-I.

activty (EVA) at 01:23 G.m.t., December 12, 1972 (118:30 GET).

The location of the two sets of detectors is shown schematically in figure 19-2. The Sun-half detector set is shown deployed on the lunar surface in figure

19-3. The exact orientation of the Sun half with respect to the Sun has not yet been precisely determined. However, the lack of shadowing in the photograph (fig. 19-3), taken at the time the experiment was terminated, shows that the Sun-half detector must have been close to being perpendicular to the Sun line as stated by the LMP at the time of initial deployment. The Sun elevation angle changed from 13° to 34° during the time the experiment was deployed; the corresponding total change in azimuth angle was 10°.

Because of the possibility of a substantial enhancement in the flux of interplanetary particles, the experiment was terminated at the beginning of EVA-3 instead of at the end, as originally planned. The experiment was terminated by the LMP, who first removed the Sun-half detector and then walked into the shade and mated it with the shade-half detector. The latter was thus never exposed to the Sun. The LSCRE was then placed in a plastic bag for transport back to Earth. The total exposure time was 45.5 hr.
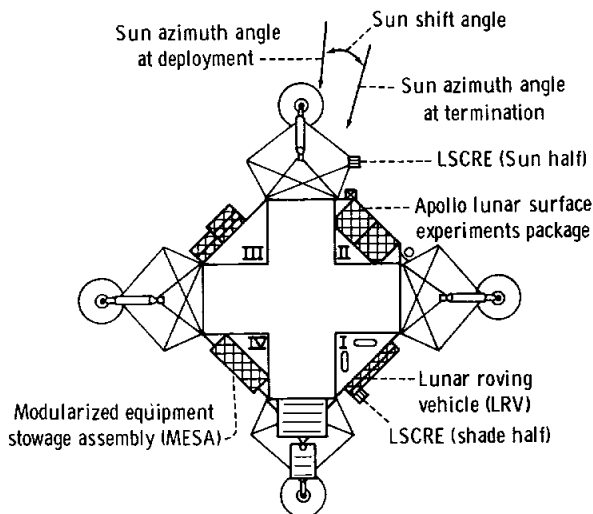
FIGURE 19-2.—Schematic top view of the LM showing the locations of the Sun half and the shade half of the deployed LSCRE as well as the azimuthal Sun angle at the time of deployment and at the time of termination of the experiment.

Examination of the detector package after its reception in the investigators' laboratory showed that the detector surfaces were in an essentially pristine condition. Less than 5 percent dust cover was observed on the mica and the metallic foils, and it is clear that the detectors had not been touched by the astronaut in the deployment and termination sequences. The temperature labels indicated that temperatures of the Sun-half detectors had reached 393 K but stayed below 403 K; the shade-half detectors were always cooler than 316 K. The temperature of the Sun-half detector was somewhat higher than anticipated but well below the design limit of 423 K.

SOLAR ACTIVITY IMMEDIATELY BEFORE AND DURING THE APOLLO 17 MISSION

During the period December 11 to 13, 1972, there were two major active regions on the Sun. Region 496, which reached an apparent optical maximum on December 12, produced only a few subflares. Region 500, which emerged on December 10 and 11, also produced only minor subflares during the period December 11 to 13. At 14:55 G.m.t. on December 13, an eruptive prominence was observed on the eastern limb. Figure 19-4 is an optical photograph showing the active solar regions.
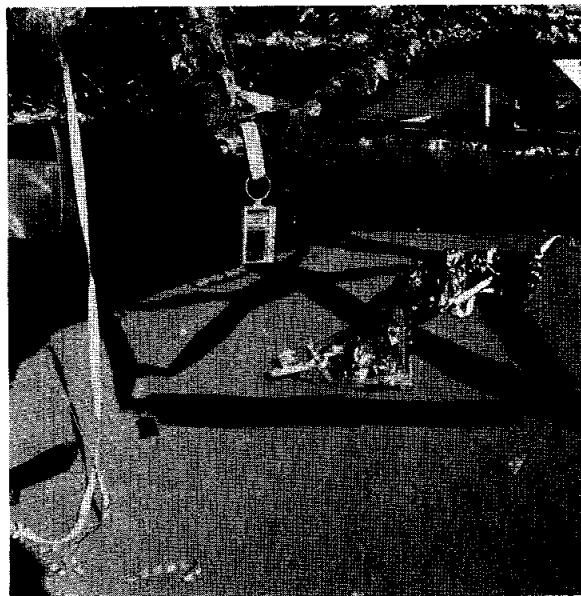
FIGURE 19-3.—The Sun half as deployed on the Moon. This photograph is one of a pair of stereoscopic pictures taken by the lunar module pilot (LMP) from a distance of 2.13 m (7 ft) immediately before termination of the experiment (AS17-140-21381 and 21382). Another pair of stereoscopic photographs was taken of the shaded portion (AS17-140-21383 and 21384).

The following satellite proton monitor channels showed no significant increase above background during the entire Apollo 17 mission.

Satellite	Channel energy range, MeV
[a]IMP-G	> 10, > 30, > 60
IMP-H	> 8, > 25, > 95
IMP-I	> 10, > 30, > 60
Pioneer 9	> 13.9, > 40
Vela	0.88 to 3.2, 3.2 to 5, 7.7 to 12

[a]IMP = Interplanetary Monitoring Platform.

In contrast, monitors on board the first Applied Technology Satellite (ATS-1) and the lower energy channels on Vela showed significant increases throughout most of December 13, 1972. In particular, the ATS-1 3- to 21-MeV channel showed a slow increase starting at 08:52 G.m.t. on December 13 and a more pronounced increase at 15:00 G.m.t. on December 13. During the quiescent period before 08:52 G.m.t. on December 13, the counting rate was 0.38 proton/ cm^2/sec. During the period from 08:52 to 15:00 G.m.t. on December 13, the average rate
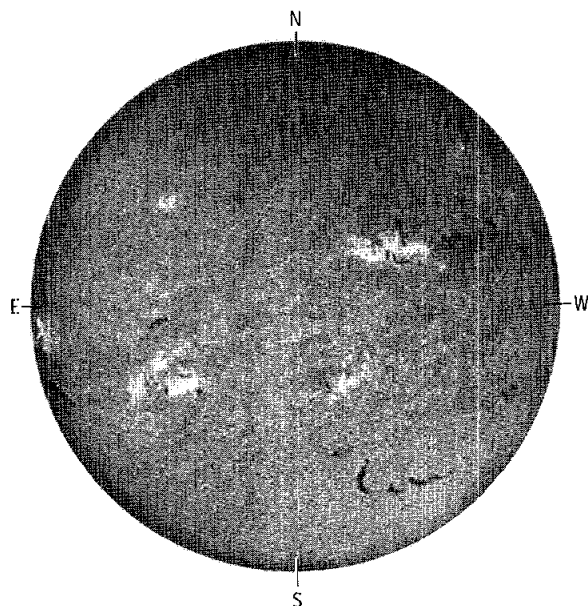
FIGURE 19-4.–The Sun as observed in hydrogen alpha: The photograph was taken at 09:35 G.m.t., December 13, 1972, through the optical telescope on Canary Island, one of the Solar Particle Alert Network sites.

increased to 2.0 protons/cm²/sec. From 15:00 G.m.t. on December 13 to the time the experiment was terminated (22:53 G.m.t.), the average counting rate was 5.3 protons/cm²/sec. No significant increase above background was observed in the 21- to 70-MeV channel.

Possibly more significant for this experiment are the results from the low-energy proton channels on the Vela satellite. Starting at approximately 04:00 G.m.t. on December 13, the 0.20- to 0.47-MeV channel showed an increase to a new level of ≈45 protons/cm²-sec-sr-MeV from the previous background of ≈7 protons/cm²-sec-sr-MeV. A similar increase from 1.3 to ≈6.5 protons/cm²-sec-sr-MeV was observed in the 0.47- to 0.88-MeV channel. These higher levels were maintained for the rest of the time the experiment was exposed on the Moon and contributed to the decision to terminate it earlier than planned.

In the period immediately before the mission, one energetic solar event occurred early on November 28; thereafter, solar activity was very low. The November 28 event was a class M1 event from active region 483. No proton enhancement was observed near the Earth, but the Pioneer 6 and 7 spacecraft observed enhanced 0.6- to 13-MeV proton fluxes on November 29.

10 μm
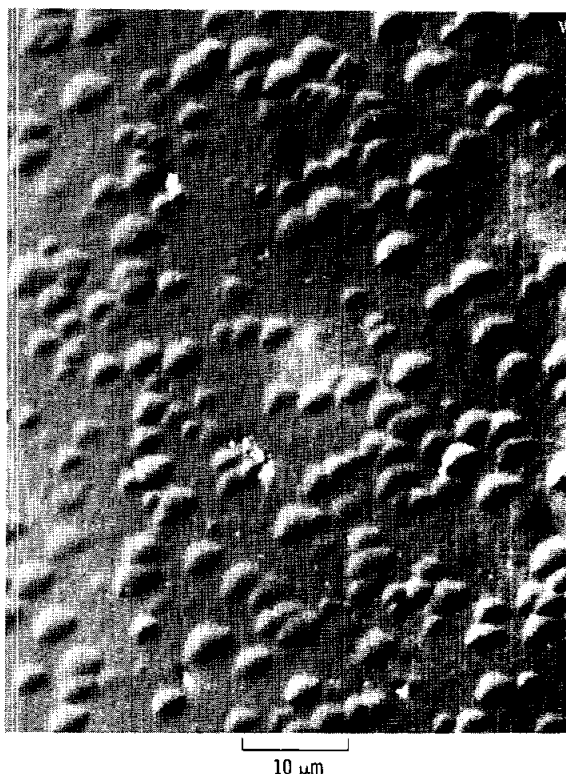
FIGURE 19-5.–Surface of mica showing pits of 1-keV/ nucleon xenon ions. After the surface was bombarded with the ions, the mica was etched for 2 hr in 40 percent HF at 303 K. The photograph was taken on Kodak high-contrast copy film through a Leitz microscope using the Smith interference contrast method in reflected light.

In summary, the period immediately before and during the mission was one of relatively low, but not completely negligible, solar activity.

OBSERVATION OF HEAVY SOLAR WIND PARTICLES

When mica is irradiated with heavy ions having energies of ≈1 keV/nucleon, subsequent etching produces shallow etch pits (fig. 19-5). Although the physical reasons are not well understood, it is found empirically that the diameters of the etch pits depend on the charge of the bombarding particles. For example, after 2 hr of etching at 303 K in a 40-percent solution of hydrofluoric acid (HF)—the standard etch treatment for all results reported herein—we find that manganese ions produce very small pits (<1 μm), whereas heavier ions produce

larger pits as follows: krypton, ≈2.1 μm; xenon, ≈3.0 μm; and lead, ≈4.9 μm.

This dependence of etch-pit size on the charge of the bombarding particles is the basis for the attempt to determine directly the abundance of extremely heavy ions in the solar wind. Although the average pit size is a monotonically increasing function of charge, any given ion results in a range of pit sizes that is quite large. For this reason, the experiment does not permit a precise determination of the charge of individual ions; rather, it gives a statistical sampling of broad groups of ions.

We have found empirically that the average pit size is not strongly dependent on the orientation of the beam with respect to the mica. At shallow incident angles to the surface, however, the distribution of pit sizes becomes somewhat narrower. The range of the angles of incidence of the solar wind is such that no effect on the registration properties of heavy ions is expected.

Because the registration of very-low-energy ions is not well understood either theoretically or experimentally, the possibility exists that subtle differences in the physical state of different mica samples may affect the track registration properties. For this reason, a complete set of recalibration experiments has been undertaken on the micas that were actually sent to the Moon. These calibrations are not yet complete; for this reason, the results reported here are mostly qualitative.

The results are also preliminary because only the crudest and quickest method of observation has been used. In practice, three methods can be used: interference contrast optical microscopy, transmission electron microscopy, and scanning electron microscopy. After a 2-hr etch, producing wide pits (as much as 6 μm in diameter), the pits are easily observed by interference contrast optical microscopy. In this technique, the surface is first silvered and then observed either in a Zeiss microscope using the Nomarski interference system or in a Leitz microscope using the Smith interference system. In our experience, the two systems seem to be roughly equivalent, with the former giving somewhat higher resolution and the latter somewhat better contrast. These differences, however, may have resulted from imperfect alinement of either or both of the systems.

The optical microscope is capable of giving relatively quick results, but the large pit sizes involved have two consequences. When the density of tracks is large (as is the case here), the pits overlap and the occasional large pits tend to be obscured. In principle, observation of surface replicas of briefly etched samples using a transmission electron microscope should give more detailed measurements than those reported herein. Scanning electron microscopy of lightly etched surfaces is possible in principle, but we have not been able to get enough contrast in the images to make this technique practicable.

In figures 19-6 to 19-9, it is shown that heavy solar wind ions are registering in the mica as expected. Figure 19-6 shows a sample of mica exposed on the Sun half that has been etched for 2 hr in a 40-percent HF bath at 303 K. The photograph was obtained using the Smith interference system. The surface is clearly covered with a background of small, shallow pits, present in such abundance as to be unresolvable. The estimated concentration of solar wind ion atoms was 1.2×10^9 atoms/cm^2; laboratory irradiations with 1×10^9 atoms/cm^2 manganese ions of 1 keV/nucleon produce a similar background at the same etch time. A region of the Sun-exposed mica

10 μm
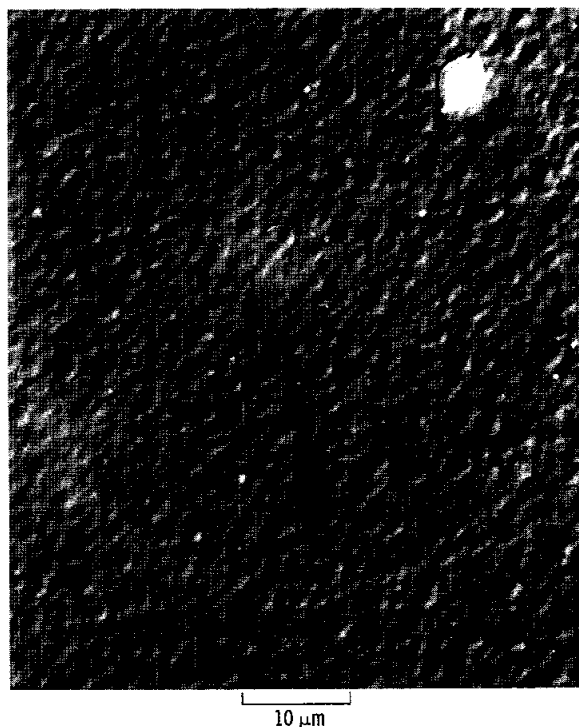
FIGURE 19-6.—Mica surface of LSCRE exposed to sunlight during 45.5 hr on the Moon. Etching and microphotography conditions were the same as those for figure 19-5.

that was covered with a 0.5-mm-thick stainless steel strap is shown in figure 19-7. Clearly, the bulk of the particles causing the shallow background have been stopped by the strap. In figure 19-8, a region of the Sun-half mica that was covered with ≈150 nm of silver is shown. Again, a striking difference is observed in the background of very shallow pits. Finally, in figure 19-9, an etched sample of the shaded mica is shown. The extensive background of shallow pits is again missing.

Although the extensive shallow pit background is missing in those areas of mica not exposed directly to the Sun, all areas of both the shade-half and Sun-half micas contain a considerable density of deep pits corresponding to higher energy particles. Figure 19-10 is a scanning electron microscope photograph of one such deep pit. Because of the relatively quiescent behavior of the Sun during the Apollo 17 mission, these higher energy particles were not expected. They are discussed separately in the section entitled "Energetic Solar Particles."

The photographs (figs. 19-5 to 19-9) illustrate

another effect that complicates the analysis of the solar wind composition. In addition to the bright (deep) pits, the covered and shaded portions of the mica contain a low background of shallow, broad pits. These pits were probably produced by high-energy ions similar to those producing the bright pits, but of lower mass. Particles such as 100-keV/nucleon oxygen are capable of producing pits (ref. 19-6) caused by occasional, damage-producing, close nuclear encounters with the near-surface atoms of the mica detectors. These pits thus constitute a background that must be subtracted to obtain information about extremely heavy solar wind ions.

Close examination of figures 19-7 to 19-9 further shows that the mica that was covered with 150 nm of silver has a higher background of very small, shallow pits than either the mica that was exposed in the shade or the Sun-half mica that was covered with the metal strap. Contrary to expectations, some solar

10 μm
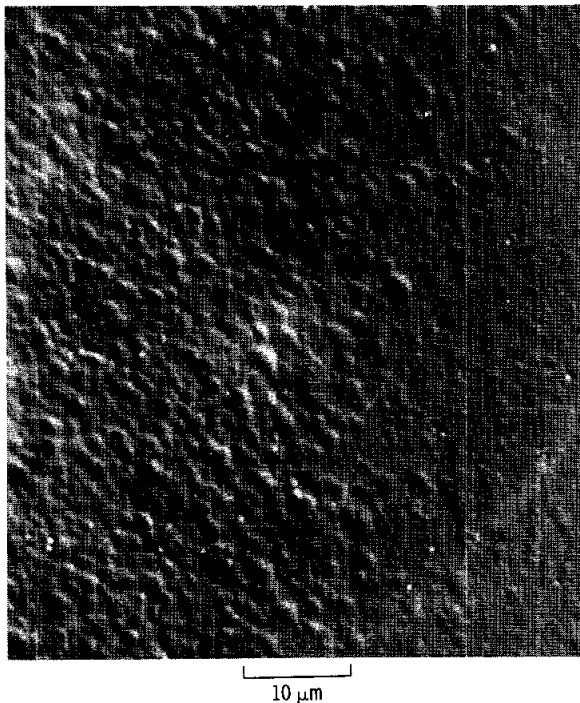
FIGURE 19-7.–Mica surface from the sunlit portion of the LSCRE. The right half of the picture shows an area under a 0.5-mm-thick steel strap. Etching and microphotography conditions were the same as those for figure 19-5.

10 μm

FIGURE 19-8.–Mica surface from the sunlit portion that was covered with 150 nm of silver during exposure. Etching and microphotography conditions were the same as those for figure 19-5.

10 μm

FIGURE 19-9.—Mica surface from the shaded portion of the LSCRE. Etching and microphotography conditions were the same as those for figure 19-5.

10 μm

FIGURE 19-10.—One of the deep pits produced by energetic heavy particles as seen on the Sun-half mica. The photograph was taken in a scanning electron microscope. Similar tracks from energetic particles are seen in the mica exposed in shade (fig. 19-9).

wind ions are apparently capable of penetrating the 150 nm of silver. Additional measurements on the mica regions covered with 50 to 100 nm of silver should clarify this point.

For this preliminary analysis, the periodic table above charge $Z = 30$ has been divided into three broad groupings of elements. The first, consisting of charges from 30 to 40 (group I), is much more abundant than the others, which include $Z = 40$ to $Z = 60$ (group II) and the group of charges from 60 to 92 (group III). (Most of group III is made up of elements of $Z = 78$ and $Z = 82$.) The expected pit densities in various size ranges from these three groups are summarized in table 19-II. The contribution of the group I elements to the expected density of pits may be overestimated by as much as a factor of 3 because an efficiency of pit registration of unity in this range has been assumed; in reality, the efficiency may be as low as 0.3. The registration efficiency of the group II elements is at least 50

percent; of the group III elements, it is essentially 100 percent.

Also shown in table 19-II are the experimental results obtained to date for pits >2 μm in diameter. The results are not in good agreement with the calculated values. In particular, the experimental values for large pits are much lower than expected. To fit the predicted values, eight pits >4 μm in diameter and four pits >5 μm in diameter should have been seen in the area scanned; none, in fact, were observed.

Taken at face value, this deficiency would imply a depletion of both group II and group III elements in the solar wind. In view of existing measurements of xenon abundances in both lunar samples and meteorites, a depletion of group II elements seems most unlikely. A more likely explanation is that the larger shallow pits have been obscured by the large background of small, iron-group pits developed by the long etching times used in this first-scan look. More detailed measurements using shorter etching times are in progress. If the apparent depletion is still found in these experiments, then the effects of other factors,

TABLE 19-II.—*Pit Density Distribution*

Pit size, μm	Track density, tracks/cm^2				
	Calculated contribution[a] of group—			Total	Measured
	$^b I$	$^c II$	$^d III$		
1 to 2	2.1×10^5	9×10^3	0	2.2×10^5	—
2 to 3	2.25×10^5	0.15×10^5	0	2.4×10^5	7.5×10^5
3 to 4	5.6×10^4	1.2×10^4	0.2×10^4	7×10^4	3.0×10^4
4 to 5	5.8×10^3	5.9×10^3	5.0×10^3	1.7×10^4	—
5 to 6	0	1.6×10^3	5.1×10^3	6.7×10^3	—
6 to 7	0	0	1.0×10^3	1.0×10^3	—

[a]Based on solar abundances.
[b]Atomic numbers 30 to 40.
[c]Atomic numbers 40 to 60.
[d]Atomic numbers 60 to 92.

principally the potential fading of tracks by solar ultraviolet irradiation, will have to be pursued before any final conclusions can be reached.

ENERGETIC SOLAR PARTICLES

As previously noted, both the shade-half and Sun-half mica detectors had numerous bright pits corresponding to longer tracks. Scanning by normal transmission optical microscopy, where the shallow pits are not observable, gave consistent track densities of $6.4 \pm 0.6 \times 10^3$ tracks/cm^2 for a shade-half sample and $5.8 \pm 0.6 \times 10^3$ tracks/cm^2 for a Sun-half sample. The high-energy particles therefore are distributed isotropically in space and appear to have no relationship to the solar wind. From comparison with scanning electron microscope data, it is estimated that the track densities obtained by optical microscopy correspond to pits $\gtrsim 0.5$ μm in depth.

Although much higher in energy than the solar wind, the particles being detected have rather modest energies in comparison with many solar flare particles or galactic cosmic rays. Only four tracks corresponding to iron ions of $\gtrsim 1$ MeV/nucleon were found in a scan of a 0.5-cm^2 area.

The distribution of track densities compared to energy, assuming registration of iron ions only, is shown in figure 19-11. Two curves are shown: in one, the measured track length has been taken as a measure of the total range of the iron ions; in the other, it is assumed that iron ions do not register in the last 1.7 μm of their range. This estimate of the "range deficit" is taken from the work of Blok et al. (ref. 19-7), in which the etching time used was only 20 min instead of 2 hr as used in this study and the

etching temperature was only 293 K as opposed to 303 K. Whereas our previous work has shown that, in other mica samples etched with our conditions, 30-keV/nucleon nickel ions produce pits with depths of 0.75 μm as compared to calculated ranges of 1.0 μm, recent preliminary calibration data show that iron ions of the same energy result in only very shallow pits (<0.1 μm deep) in the mica used in this experiment. These results indicate that the registration of low-energy ions in mica varies with the particular sample and might depend strongly on its annealing history. The long etching times (chosen for examination of shallow pits) made it difficult to measure lengths below ≈ 5 μm with precision, and the lower energy points are probably somewhat underestimated. Additional measurements are in progress using a transmission electron microscope on replicas from the mica. Until these measurements have been made and final calibration data on the range deficit are obtained, the curves in figure 19-11 should be considered as lower limits on the fluxes of particles in this energy range.

The assumption that only iron ions are responsible for the tracks is not strictly correct because ions as light as neon can produce tracks toward the end of their range. As previously noted, even low-energy oxygen ions can give observable, shallow pits. As shown in the report on the Apollo 16 cosmic ray experiment (ref. 19-3), inclusion of lighter ions would have the net effect of flattening somewhat the apparent energy spectrum shown in figure 19-11. In view of the uncertainties in the range-deficit problem and the fact that calibration data for the particular mica in question will soon be available, the light ion correction has not been included in figure 19-11.
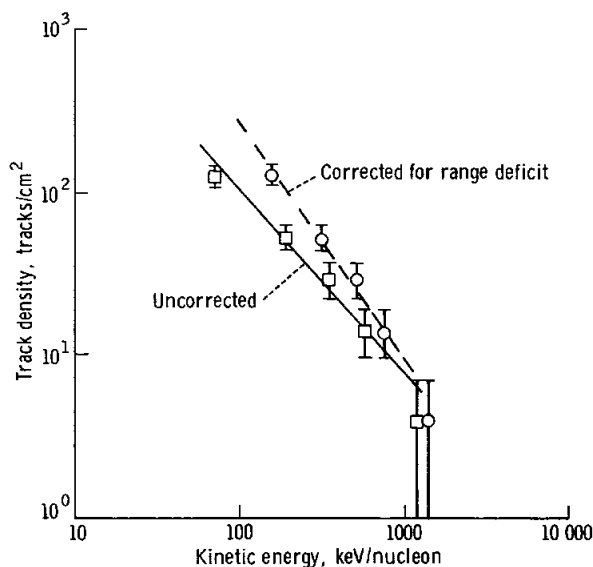
FIGURE 19-11.—Integral energy spectrum of the energetic iron particles observed in the sunlit and shaded micas. One set of points (squares) is obtained by assuming the tracks are etched for their total range. The circled points are plotted assuming a range deficit of 1.7 μm as given by Blok et al. (ref. 19-7).

The integral energy spectrum shown in figure 19-11 can be fitted between 80 keV/nucleon and 1 MeV/nucleon by a power law of the form $N(>E) = KE^{-\gamma}$ with spectral index $\gamma = 1.1$, where N is the track density, E is the kinetic energy, and K is a constant. Adding the maximum range deficit to the data only changes the exponent γ slightly to 1.3. The Apollo 16 flare data showed a similar power law dependence, but with a larger value of γ of ≈ 2. Long-term values of solar flare very-heavy particle ($20 \leqslant Z \leqslant 28$) energy spectra derived from studies of lunar rocks are intermediate between the values measured here and in the Apollo 16 experiment. Although it cannot be proved that the high-energy particles observed in this experiment are solar in origin, the general similarity of the energy spectrum to that observed in solar flares strongly suggests that they originate in the Sun.

Although probably solar in nature, the precise source of the particles is unclear. As outlined in the section entitled "Solar Activity Immediately Before and During the Apollo 17 Mission," although the Sun was generally quiescent, some activity was observed. Particle counting rates also rose considerably above background at low energies early on the morning of December 13, 1972. Possibly, the particles observed

were directly associated with this rather modest solar activity. They could also represent particles stored in the interplanetary regions from earlier solar emissions. Here again, however, the solar activity was rather modest immediately before the mission. The possibility that the Sun emits a more or less continuous flux of such low-energy particles, independent of any visible solar activity, cannot be ruled out. Testing this point will require additional measurements of extremely low energy particles outside the magnetosphere.

Lunar sample investigators have normally attributed fossil track observations of low-energy particles to the influence of solar flares. The present result confirms this interpretation. The quiet-time fluxes measured in this experiment, although higher than expected, are simply too low to account for the lunar observations. In this connection, it should be noted that the rather modest flare observed during the Apollo 16 mission contributed 200 times as many track-producing particles as were observed in this experiment.

LIMITS ON THE RADON ATMOSPHERE AT THE APOLLO 17 SITE

Recoiling atoms from alpha-particle decay processes have kinetic energies similar to those in the solar wind. It was, in fact, the observation of fossil alpha-particle recoil tracks in terrestrial micas (ref. 19-8) that originally led to the suggestion that mica could be used as a heavy solar wind monitor. Two important sources of alpha-particle recoil tracks are radon-222 (^{222}Rn) atoms in the lunar atmosphere and corresponding polonium-210 (^{210}Po) atoms that should be deposited on the surface from prior ^{222}Rn decay.

Assuming that recoils of polonium atoms from the surface register with unity efficiency, the total number of alpha-particle recoil tracks per square centimeter per second should be approximately the same as the number of alpha particles per square centimeter per second from ^{222}Rn decay measured in a detector the surface of which is normal to the lunar surface. In a preliminary scan of the shaded mica, only one pit >5 μm in diameter was found in an area of 2.8×10^{-4} cm^2. Because half of all alpha-particle recoil tracks should have diameters greater than this value, we conclude that the density of alpha-particle recoil tracks is $\lesssim 1 \times 10^4$ tracks/cm^2. This density

gives an equivalent upper limit on the alpha-particle recoil production rate of ≈ 3.6 disintegrations/min/cm^2. This value is considerably higher than the most recent orbital measurement of the lunar average of ≈ 0.06 disintegration/sec/cm^2 by Gorenstein and Bjorkholm (ref. 19-9), but is comparable to earlier measurements of ≈ 1.2 disintegrations/min/cm^2 for each alpha-active ^{222}Rn daughter measured on the Surveyor V, VI, and VII spacecraft (ref. 19-10). The present statistics are clearly too poor to comment further on this problem.

SUMMARY

The LSCRE, consisting of sets of mica, glass, plastic, and metal foil detectors, was successfully deployed on the Apollo 17 mission. One set of detectors was exposed directly to sunlight and another set was placed in shade.

Preliminary scanning of the mica detectors shows the expected registration of heavy solar wind ions in the sample exposed directly to the Sun. The initial results indicate a depletion of very-heavy solar wind ions. The effect is probably not real but is caused by scanning inefficiencies.

Despite the lack of any pronounced solar activity, energetic heavy particles with energies extending to >1 MeV/nucleon were observed. Equal track densities of $\approx 6 \times 10^3$ tracks/cm^2 of tracks $\gtrsim 0.5$ μm in length were measured in mica samples exposed in both sunlight and shade. The energy spectrum of these particles can be represented as a power law of the form $N(>E) = KE^{-\gamma}$ between 60 keV/nucleon and 1 MeV/nucleon. The value of γ of 1.1 is somewhat lower than the long-term average of ≈ 1.5 measured in studies of low-energy particles in lunar samples, but the general agreement in the nature of the energy dependence suggests that the particles are solar in origin.

The fluxes of these quiet-time energetic particles are too low to account for very many of the fossil tracks seen in lunar samples. As has commonly been assumed, the fossil tracks appear to have been produced predominantly in solar flares.

A preliminary upper limit of ≈ 3.6 disintegrations/min/cm^2 was obtained for the flux of recoiling nuclei from alpha-particle decay processes such as ^{222}Rn decay in a local lunar atmosphere.

ACKNOWLEDGMENTS

PART B

QUIET TIME ENERGY SPECTRA OF HEAVY NUCLEI FROM 20 TO 400 keV/amu

R. T. Woods,[ab] *H. R. Hart, Jr.,*[a] *and R. L. Fleischer*[a]

The main objective of the General Electric (GE) portion of the Apollo 17 cosmic ray experiment was to measure the abundance and energy spectra and, hopefully, to infer the origin of heavy low-energy nuclei at solar quiet time. The experiment consisted of three varieties of glass solid-state track detectors, which were exposed on the surface of the Moon for

[a]General Electric Research and Development Center.
[b]State University of New York at Albany.

45.5 hr from December 11 to 13, 1972. The detectors were arrayed in two groups, one of which was exposed facing the Sun and the other in the shade facing away from the Sun.

In December 1972, solar activity was approaching the minimum predicted to occur in 1975, and the activity in December 1972 should have been lower than at any time since 1966. As a result, the diminution by the solar magnetic field irregularities of the flux of galactic cosmic rays entering the solar

system (so-called "solar modulation") should also have been approaching its minimum. Characteristically, the fluxes of these galactic particles have been observed to decrease with decreasing energy in the range from a few hundred MeV/amu to the lowest energies previously measured (≈ 40 MeV/amu for heavy nuclei) (ref. 19-2). In contrast, solar flare particles are found, generally, to decrease in abundance with increasing energy (ref. 19-11) and, specifically, for heavy nuclei in the same energy range as that considered in this part (refs. 19-2 to 19-5). The primary key for deciding whether the low-energy nuclei are solar or galactic in origin appears, therefore, to be the slope of the energy spectrum—a positive slope being the signature of the galactic particles and a negative slope being characteristic of solar nuclei.

As a secondary objective, compositional abundances and energy dependence of specific ions will be sought. These will then be compared with compositional measurements made on the Apollo 16 cosmic ray experiment, during which a solar flare occurred.

DESCRIPTION OF DETECTORS

The detectors consisted of nine different pieces of glass of types and total areas listed in table 19-III. The fused quartz (silicon dioxide (SiO_2)) and phosphate glass (GE-1457) detectors were pre-etched and examined before the experiment to ensure a good surface. Small corner portions of each type of glass were preirradiated (with californium-252 (^{252}Cf) fission fragments for SiO_2 and GE-1457 glass and with

TABLE 19-III.—*Apollo 17 Glass Detectors*

Type	Designation	Exposed area, cm^2	
		Sun	Shade
Fused quartz (FQ)	FQ-SiO_2 (Suprasil 2)	5.4	0
Phosphate[a]	GE-1457	0	1.62
Lead phosphate[b]	Lal	1.85	1.76

[a]6.30 weight percent phosphate, 11.03 percent barium oxide, 9.30 percent silver oxide, 8.47 percent potassium oxide, and 8.20 percent aluminum oxide.

[b]77.4 percent lead phosphate, 10 percent manganese phosphate, and 12.6 percent iron phosphate, melted in a mullite crucible (D. Lal, personal communication, 1972).

oxygen 16 (^{16}O) ions for the lead phosphate glass) to determine whether any thermal alteration of tracks occurred during the flight.

PROCEDURE AND RESULTS

Particle tracks, such as are illustrated in figure 19-12, were revealed under carefully controlled etching conditions with a fixed temperature bath, a fixed etchant stirring rate, and fresh etchant at each separate stage of etching. The general chemical attack
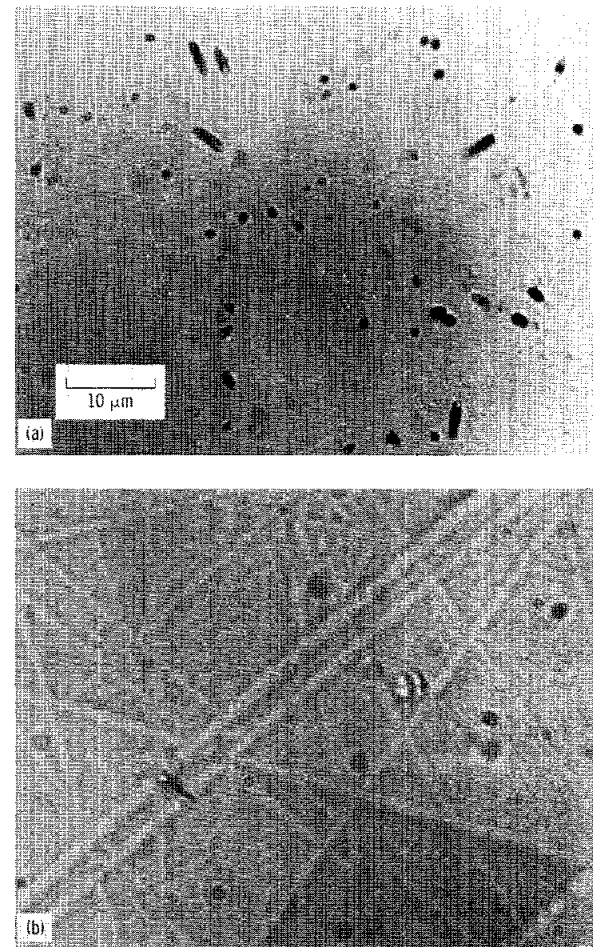
FIGURE 19-12.—Etched tracks in phosphate glass (GE-1457). (a) A typical view in the Apollo 16 detector, which was exposed during a solar flare known to have ejected particles into the interplanetary medium. (b) An atypical view in the Apollo 17 detector. The view is unusual in that it contains a track. Each detector was etched in 48 percent hydrofluoric acid to remove 0.5×10^{-4} cm of glass.

rate V_g was measured first, using control samples, by three methods: from the rate of motion of a right-angled edge relative to fixed markers in the glass, from the attack rate inferred from cone angle and track diameter measurements on individual tracks, and from the thickness change of glass plates with parallel faces. When a flight sample was etched, simultaneous and independent measurement of the general attack rate was made and checked with a predicted etch rate for consistency.

The GE-1457 glass was etched in 48 percent hydrofluoric acid (HF) for 5.0 min at 302.45 K to remove 0.5×10^{-4} cm of glass. Track measurements on each track were made more than once using a Leitz Ortholux microscope at a nominal magnification of 1000X and a filar eyepiece, which has a movable hairline. The threshold capability of the eyepiece was checked by an independent experiment. A group of identical glass samples of glass microscope slides was irradiated with ^{252}Cf fission fragments at normal incidence. Samples were then etched under identical etch conditions but in successive increments of 15-sec intervals in 5.7 percent HF at 295.45 K. Track diameter measurements allowed plotting of the track diameter as a function of etch time. For the range of track lengths examined, linearity is expected in track diameters because there is very little change in the cone angle. A straight line was obtained; this result implied that reliable dimension measurements are possible to a lower optical limit of 0.35×10^{-4} cm. Individual tracks were cataloged by constructing a grid-work matrix with each matrix element corresponding in row and column to that of each field of view seen through the optical microscope. This procedure makes possible the relocation of an individual track for remeasurement after successive etches. Individual particle range calculations were then made.

The differential energy spectrum in figure 19-13 was obtained starting with the measured track length distribution given in table 19-IV, in which the results are summarized. Tracks were grouped in length bins, and equivalent energies corresponding to the lower and upper limits were obtained using range-energy tables (ref. 19-12) for iron ions in aluminum, because the GE-1457 glass is closely similar to aluminum in its stopping power. This approximation introduces negligible additional errors. The energy between these two limits was evaluated so that the same number of particles within that bin fall on either side of the

energy representing the bin. It was assumed for the purposes of calculation that all particles were from the iron group with a cone angle of $\approx 7°$. This glass is sensitive to ions as light as neon, and it may contain tracks from ions lighter than those in the iron peak. Cone angle measurements are in progress and will be compared with existing calibration data that give cone angles of 30° to 35°, 10°, and 5° to 10° for neon, argon, and iron, respectively (ref. 19-4). It is hoped that the different chemical constituents that are present can be separated in this manner.

The resulting energy spectrum extends from a kinetic energy E of ≈ 0.02 to ≈ 0.4 MeV/amu. If the three highest energy data points ($0.08 \leqslant E \leqslant 0.4$) are fitted with a power law in kinetic energy, the flux is given by $3.52 \times 10^{-4}\ E^{-\left(1.7 ^{+\ 1.5}_{-\ 0.6}\right)}$ particles/cm^2-sec-sr-MeV/amu with E in MeV/amu.

Another interesting result is obtained from the analysis of the lead phosphate (LaI) glass detectors. One detector was exposed directly to the Sun while the other was in the down-Sun direction. The track density in the Sun-exposed portion was 872 ± 134 tracks/cm^2, whereas the track density in the down-Sun or shaded portion was 430 ± 67 tracks/cm^2.
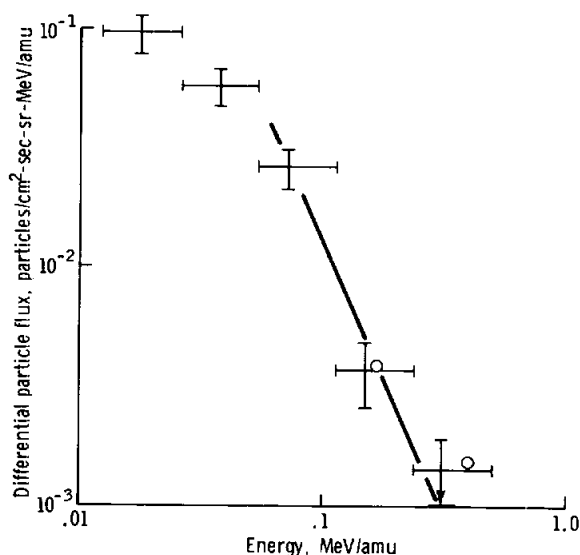
FIGURE 19-13.—Differential energy spectrum of heavy cosmic ray nuclei at the Moon from December 11 to 13, 1972, inferred from the distribution of stopping depths in phosphate glass (GE-1457). The two points marked by circles are the lowest energy data taken from the work of Price and Chan (part C, fig. 19-14).

TABLE 19-IV.—*Track Data in the Apollo 17 GE-1457 Phosphate Glass*

Particle range interval, cm	Number stopping	Energy interval, MeV/amu (a)	Differential flux J, particles/cm^2-sec-sr-MeV/amu (b)
0.5 to 0.85 × 10^{-4}	31	0.0121 to 0.0255	9.56 ± 0.17 × 10^{-2}
.85 to 1.43	38	0.0255 to 0.0537	5.66 ± 0.92 × 10^{-2}
1.43 to 2.41	37	0.0537 to 0.1130	2.66 ± 0.43 × 10^{-2}
2.41 to 4.05	11	0.1130 to 0.2370	3.73 ± 1.12 × 10^{-3}
4.05 to 6.85	9 (6)^c	0.2370 to 0.5000	1.44 ± 0.48 × 10^{-3}

[a]Determined from range-energy tables (ref. 19-12).

[b]For this detector: exposure time = 45.5 hr; effective solid angle = 1.55 sr; area scanned = 9.38 × 10^{-2} cm^2; index of refraction = 1.52; $J = (N/\Delta E)$ 4.2 × 10^{-5} particles/cm^2-sec-sr-MeV/amu, where N is track density and ΔE is difference in energy.

[c]The number in parentheses is the number of tracks that have not rounded. This means the particle stopped at a depth in the glass greater than the measured length of the track. It was assumed that some of the six sharp tracks in the length interval 4.05 to 6.85 × 10^{-4} cm could round out in the next larger length interval, hence the arrow on the highest energy data point in figure 19-13.

DISCUSSION

The glass-detector results show, at the higher energies (0.05 ≤ E (MeV/amu) ≤ 0.5), a steep spectral shape that can be fitted by a power law in kinetic energy: 6.33 × 10^{-5} $E^{-(2.3 {+1.2 \atop -0.9})}$. At lower energies, the spectrum flattens. Qualitatively, the shape of the spectrum at higher energies is similar to that measured for single solar flare events (refs. 19-2 to 19-5 and 19-13, the first four references referring to analysis of the April 17, 1972, solar flare observed by the Apollo 16 cosmic ray experiment). The spectral shape at higher energies is also qualitatively similar to that observed for the cumulative effect of many flares over 2.5 yr at a time of maximum solar activity (refs. 19-14 to 19-16). This aspect alone suggests a solar origin for these low-energy, heavy cosmic rays. The absolute flux level at any given energy is much lower in the Apollo 17 spectrum than in the Apollo 16 spectrum. This is consistent with the satellite monitors, which showed orders of magnitude more protons during the Apollo 16 experiment than during the Apollo 17 experiment. A significant fact is that steep spectra are observed in both experiments even though solar modulation has presumably changed between these events.

The spectral character of the heavy particles seen (fig. 19-13) implies that they are solar in origin. It must now be determined whether our knowledge of the actual solar activity allows an understanding of the presence of heavy solar particles.

To begin, one must determine what solar activity is and how it is assessed. In December 1972, the overall solar activity based on the plot of smoothed sunspot number as a function of time[1] (ref. 19-17) was ≈40 percent of that at solar maximum as compared with 5 to 10 percent at full solar minimum. Consequently, the Sun was not totally quiet on the basis of this definition. On a shorter time scale, flares that do eject particles are closely correlated spatially with sunspot groups (ref. 19-18). The relation of satellite monitor data to the actual presence of particles depends on the sensitivity of the detectors. As satellite particle detectors become more sensitive, the percentage of flares that are observed to generate energetic particles increases. This suggests the following working hypothesis: the generation of energetic particles is a normal feature of all solar flares. Some flares may be more prolific generators than others, however (ref. 19-19). Also, satellite data indicate that X-rays and protons are generated almost continuously from active regions on the Sun. These observations imply that a highly efficient, nonthermal mechanism must be operative nearly all the time. Flares may be the obvious, large-scale phenomena, whereas the slowly varying emission may be the result

---

[1]H. I. Leighton and J. V. Lincoln, personal communication, 1973.

of the superposition of large numbers of microflares (ref. 19-20). In support of this idea, a plot of the number of flares as a function of their areas shows an increasingly greater number of small flares (ref. 19-18).

As an example of the abundance of small flares, during the period December 10 to 13, 1972 (the actual Apollo 17 experiment occurred in the period December 11 to 13), the following were observed: 11 sunspot groups; 52 flares of subflare category (on an S, 1, 2, 3, 4 level of classification of the Sun area involved, with faint (F), normal (N), and brilliant (B) associated with each level); one flare of importance 1F; and three radio bursts (ref. 19-17).

Because the GE-1457 glass detector was exposed facing away from the Sun, the inferred solar origin of the particles implies that, farther out in the solar system than the Earth-Moon distance, magnetic irregularities exist that effectively enable the detector to record heavy ions even though it faces away from the Sun. It is important to note that the two lead phosphate (Lal) glass detectors showed a difference in track densities, namely a larger track density in the Sun-exposed portion by a factor of 2. This difference makes clear the solar origin for the particles.

It is also of interest to consider the relative abundance of heavy elements during the period of this experiment. From the satellite proton flux and the heavy-element flux observed by the investigators,

a value of the ratio of protons to heavy nuclei of $\approx 10\,000$ at 0.3 MeV/amu and a limit of $< 10\,000$ at 1 MeV/amu can be derived. By comparison, values of 1200 and 12 000, respectively, were observed during the April 17, 1972, flare (ref. 19-4). In short, the heavy-element enrichment relative to protons observed in a flare is seen here also.

SUMMARY

Glass track detectors were exposed to cosmic rays on the Moon from December 11 to 13, 1972, during a period of relatively quiet Sun activity as inferred from satellite proton counters. From 80 to 400 keV/amu, the differential flux of heavy cosmic ray nuclei decreases roughly as E^{-2}; this result together with the greater flux from the solar than the antisolar direction identify these nuclei as solar in origin.

ACKNOWLEDGMENTS

PART C

THE NATURE OF INTERPLANETARY HEAVY IONS WITH $0.1 < E < 40$ MeV/NUCLEON

P. B. Price[a] and J. H. Chan[a]

The University of California cosmic ray detector was a stack of seven sheets of Lexan, each 125 μm thick and 3.5 by 4.5 cm in size, that was placed in the shade facing away from the Sun. The top sheet was coated with an $\approx$ 100-nm-thick layer of aluminum to screen out ultraviolet light, which would increase the sensitivity to particle tracks in an undesirable way.

[a]University of California at Berkeley.

In a preliminary examination of 1-cm² portions from the top, middle, and bottom of the stack, two distinct populations of particles that entered the stack from the antisolar direction were discovered: (1) particles with a steeply falling energy spectrum, the overwhelming majority of which penetrated less than $\approx$ 40 μm into the top sheet, and (2) a very low flux of particles with ranges distributed apparently uniformly throughout all seven sheets. Evidence is

presented that the first group was of solar origin, even though the Sun was relatively quiet during the 45.5-hr exposure of the cosmic ray detectors, and that the second group consisted of galactic cosmic rays with a fairly flat energy spectrum.

SUPRATHERMAL IONS OF SOLAR ORIGIN

To study the population of interplanetary particles with a steeply falling energy spectrum, small portions of the top sheet are etched for short times, tracks on the top surface are located and measured, the surface is irradiated with ultraviolet light to increase the etching rate greatly, and, finally, the surface is re-etched to determine the total ranges of the particles. The initial and final lengths of each track are two parameters that allow charge Z and energy E to be determined. The minimum energy for which charge determination is possible is determined by the track length after the first etch.

The data obtained thus far are shown in figure 19-14. The energy spectra of the various species appear to have rather similar shapes, within the limited statistics. To facilitate a comparison, the spectrum of the carbon-nitrogen-oxygen (CNO) group

FIGURE 19-14.—Energy-dependent composition of low-energy interplanetary ions during solar quiet time. To display the enhancement of heavy elements at low energies, the fluxes of CNO and He have been scaled down by their abundances relative to Fe in the Sun. The enhancement appears to disappear at energies greater than $\approx$ 1 MeV/nucleon.

has been scaled downward by a factor of 25 and the helium (He) spectrum has been scaled downward by a factor of 500. The data then fall reasonably close to a single power law showing no strong dependence of composition on energy. The magnitudes of the ratios $Z \geqslant 20$:CNO:He $\approx 1:25:500$ are quite different from the solar photospheric ratios, which are approximately 1:50:3000. The heavy elements are thus more abundant in the energetic particles than in the Sun. The flux of He ions measured in the Lexan stack agrees reasonably well with the flux determined by electronic detectors on IMP-7, shown as a dashed line. During the time of exposure of the plastics, the He flux was about five times higher than its minimum value, shown as a dotted line, corresponding to a solar "quiet time." The shapes of the energy spectra are not a convincing proof that the particles observed during the Apollo 17 mission were of solar origin. To provide additional evidence, we measured the relative abundance of C, N, and O at an energy of ≈ 3.9 MeV/nucleon. The result is that O:C+N ≈ 1.65, which is indistinguishable from the solar abundance ratio (≈ 1.67) and much higher than that for galactic cosmic rays (≈ 0.74) and strongly suggests that the majority of the particles are solar in origin. Presumably they were scattered from magnetic field irregularities in interplanetary space until their directions of motion were isotropic and entered the detector from all directions.

In the upper part of figure 19-15, measurements of solar Fe fluxes during the Apollo 17, Apollo 12 (ref. 19-22), and Apollo 16 (ref. 19-5) missions are compared with the long-term average interplanetary Fe flux based on measurements of tracks accumulated in the Surveyor III camera glass during 1967 to 1970 by the investigators (ref. 19-16), by Fleischer et al. (ref. 19-14), and by Crozaz and Walker (ref. 19-15). It is seen that, even during a solar quiet time, objects on planetary surfaces and in interplanetary space are being irradiated with ions as heavy as Fe ($Z = 26$) and of mean energy on the order of 0.1 MeV/nucleon. The long-term contribution during solar quiet times is, however, inconsequential in comparison with the contribution from occasional intense solar flares. Most of the tracks that accumulated in the Surveyor III glass during a 2.6-yr period probably came during seven major flares, each lasting 1 to 2 days.

The discovery of heavy-particle enhancements in solar flares (ref. 19-16) was an unexpected dividend of the Apollo Program. Results of the present

FIGURE 19-15.–Flux of Fe ions in space. The points labeled 16 and 17 are measurements of the galactic cosmic rays in the plastic-detector experiments on the Apollo 16 and 17 missions. For ≈ 24 hr during the Apollo 16 mission, a weak flare produced an Fe ion flux ≈ 10 percent of the long-term average observed in the Surveyor III glass. During the Apollo 12 and 17 missions, the Fe ion flux was negligible by comparison. Clearly, the major contribution to the long-term average would be from occasional very intense solar flares.

experiment, together with those of studies of solar particle composition using plastic detectors on the Apollo 16 mission and in rocket flights (summarized in ref. 19-23), provide important clues to the mechanisms of solar particle emission. In this preliminary report, the emission mechanisms are not discussed, but the clues are summarized as follows.

1. At sufficiently low energies, heavy elements in solar flare particles are always enriched relative to their photospheric abundances.

2. The enrichment factor $Q \equiv (Z/\text{He})_{SP}/(Z/\text{He})_\theta$ is an increasing function of Z from He at least up to $Z \approx 40$ (ref. 19-24). The subscripts SP and θ refer to abundance ratios in solar particles and in the Sun, respectively. Because only the elements He, O, silicon (Si), Fe, $32 \leqslant Z \leqslant 38$, and $Z > 40$ have thus far been studied, a possible fine structure in the enrichments such as a correlation with ionization potential cannot be ruled out yet.

3. The enrichment factor decreases with energy and approaches a constant value at some characteristic energy on the order of the mean energy of the flare particles.

4. The mean energy, defined as $\int \phi(E)E\,dE/\int \phi(E)\,dE$, with $\phi(E)$ denoting the energy spectrum, appears to be an increasing function of the intensity of the flare, ranging from $\lesssim 1$ MeV/nucleon for the quiet Sun to ≈ 8 MeV/nucleon for the very intense flare on August 4, 1972 (ref. 19-21).

5. The maximum value of the enrichment factor (observed at the lowest energy accessible with the Lexan detector, ≈ 0.1 MeV/nucleon) is similar for all solar conditions, ranging from quiet Sun to the most intense flare.

6. Even at energies as low as ≈ 2 MeV/nucleon, solar flare Fe particles seem to be nearly completely ionized. The evidence is based on the shapes of differential rigidity spectra of He, O, and Fe (ref. 19-5) and on the minimum particle energies observed with rockets launched at Fort Churchill in Canada (ref. 19-25). Conditions at the accelerating region must be such as to remove even the inner electrons with ionization potentials of several keV. Once the particles are ionized, the amount of matter traversed between the solar atmosphere and the Moon is too little for the stripped heavy ion to reach charge equilibrium by electron capture.

LOW-ENERGY GALACTIC COSMIC RAYS

Half of each sheet in the Lexan stack has been etched 72 hr in a 6.25N sodium hydroxide solution saturated in Lexan etch products. Each sheet has been scanned in a stereomicroscope for tracks of cosmic rays with $Z \geqslant 14$. Cone length and residual range of particle tracks that are estimated on the basis of previous experience (ref. 19-26) to have $Z \gtrsim 20$ have been measured.

Tracks of particles with $Z \gtrsim 14$ observed in one-half the stack are listed in table 19-V. A sizable background of unwanted particles is immediately apparent. Seven of the 24 particles entered the sheets through the back of the detector. Although some may have reached the detector in a direct path between the legs and under the body of the lunar module, the solid angle for such paths is small. It is possible that such events occurred during the approximately 10 days when the detector was inside the spacecraft in transit to and from the Moon. Of the 17 particles that entered the detector from the front, six

TABLE 19-V.—*Cosmic Ray Tracks of Particles with Z ⩾ 14 in One-Half the Stack*

Sheet in which particle stopped	Direction from which particle entered	Z
7	Front; sky	14
5	Back; sky	14
7	Front; Moon	20
6	Back; sky	18
7	Front; sky	14
< 1	Back; Moon	26
1	Back; Moon	26
> 7	Front; sky	26
6	Back; sky	20
> 7	Front; Moon	26
6	Front; sky	20
> 7	Front; sky	26
> 7	Front; sky	26
5	Front; Moon	18
4	Front; sky	20
5	Front; Moon	20
2	Back; sky	16
4	Front; sky	14
4	Front; sky	18
4	Front; Moon	18
3	Front; sky	22
2	Front; Moon	24
1	Back; Moon	14
2	Front; sky	14

apparently entered from below the horizon. It is difficult to see how this large fraction of the total could be attributed to cosmic ray albedo from the lunar surface. It is more likely that these particles, and a comparable number with acceptable directions (front; sky), actually entered the detector while it was inside the spacecraft. With no shifting mechanism such as was used on the Apollo 16 experiment, it is necessary to make approximate corrections for the fraction of unwanted particles with acceptable directions, based on the fraction with unacceptable directions.

In figures 19-14 and 19-15, a corrected flux of nuclei with $Z \gtrsim 23$ that stopped in the stack has been plotted. It was assumed that $17 - (2 \times 6) = 5$ particles entered the front of the detector during its approximately 45-hr lunar exposure. The energy interval is ≈ 11 to 39 MeV/nucleon. Two points at ≈ 70 and 120 MeV/nucleon from the Apollo 16 University of California detector (ref. 19-27) are included in figure 19-15. The statistics are such that

we cannot be confident that the energy spectrum continues to drop with decreasing energy, but the trend is suggestive. When the other half of the stack is processed and analyzed, the statistical errors will decrease by $\approx \sqrt{2}$.

From the Z values in table 19-V, it is possible to assert with some confidence that the heavy nuclei in the energy interval 11 to 39 MeV/nucleon are of galactic rather than solar origin. The proportion of secondary nuclei with $17 \leqslant Z \leqslant 25$ relative to Fe is 11 to 6, which is too high for them to have come from the Sun.

From recent satellite measurements of the He flux in the same energy interval (ref. 19-28) and from abundance data at higher energy (summarized in ref. 19-29), we conclude that the abundance ratio He/Fe-group is independent of energy from ≈ 10 to ≈ 2000 MeV/nucleon. By using the previously described ultraviolet-sensitization and re-etch scheme, we shall be able to determine the fluxes of galactic CNO and He nuclei at energies of a few to ≈ 20 MeV/nucleon, an interval that has been largely unexplored until now.

CONCLUSIONS

Suprathermal ions with an energy spectrum that decreases by a factor of $\approx 1 \times 10^5$ in the interval 0.1 to ≈ 7 MeV/nucleon are believed to have been emitted by the Sun when it was relatively quiet. At very low energies, the Fe/CNO ratio and the CNO/He ratio are enhanced relative to their photospheric ratios at all energies studied (≈ 0.2 to ≈ 10 MeV/nucleon).

Particles with $14 \leqslant Z \leqslant 26$ were detected at energies between ≈ 10 and ≈ 40 MeV/nucleon. Their flux is slightly lower than the flux of such particles observed at energies of ≈ 60 to 150 MeV/nucleon on the Apollo 16 experiment. From their high abundance ratio of $17 \leqslant Z \leqslant 25$/Fe as well as their flux level, these particles are attributed to galactic cosmic rays. The abundance ratio of He/Fe appears to be independent of energy from ≈ 10 to ≈ 2000 MeV/nucleon.

ACKNOWLEDGMENTS

REFERENCES

19-1. Fleischer, R. L.; and Hart, H. R., Jr.: Composition and Energy Spectra of Solar Cosmic Ray Nuclei. Sec. 15, Part A, of the Apollo 16 Preliminary Science Report. NASA SP-315, 1972.

19-2. Price, P. B.; Braddy, D.; O'Sullivan, D.; and Sullivan, J. D.: Composition of Interplanetary Particles at Energies From 0.1 to 150 MeV/Nucleon. Sec. 15, Part B, of the Apollo 16 Preliminary Science Report. NASA SP-315, 1972.

19-3. Burnett, D.; Hohenberg, C.; Maurette, M.; Monnin, M.; et al.: Solar Cosmic Ray, Solar Wind, Solar Flare, and Neutron Albedo Measurements. Sec. 15, Part C, of the Apollo 16 Preliminary Science Report. NASA SP-315, 1972.

19-4. Fleischer, R. L.; and Hart, H. R., Jr.: Enrichment of Heavy Nuclei in the 17 April 1972 Solar Flare. Phys. Rev. Letters, vol. 30, no. 1, Jan. 1, 1973, pp. 31-34.

19-5. Braddy, D.; Chan, J. H.; and Price, P. B.: Charge States and Energy-Dependent Composition of Solar-Flare Particles. Phys. Rev. Letters, vol. 30, no. 14, Apr. 2, 1973, pp. 669-671.

19-6. Natowitz, Joseph B.; Khodai-Joopari, Arastoo; Alexander, John M.; and Thomas, T. Darrah: Detection of Long-Range Fragments from Decay of Cf^{252}. Phys. Rev., vol. 169, no. 4, May 20, 1968, pp. 993-999.

19-7. Blok, H.; Kiely, F. M.; and Pate, B. D.: The Track Lengths of Heavy Ions in Mica. Nucl. Inst. Meth., vol. 100, no. 3, May 1, 1972, pp. 403-411.

19-8. Huang, W. H.; and Walker, R. M.: Fossil Alpha-Particle Recoil Tracks: A New Method of Age Determination. Science, vol. 155, no. 3715, Mar. 3, 1967, pp. 1103-1106.

19-9. Gorenstein, Paul; and Bjorkholm, Paul: Detection of Radon Emanation from the Crater Aristarchus by the Apollo 15 Alpha Particle Spectrometer. Science, vol. 179, no. 4075, Feb. 23, 1973, pp. 792-794.

19-10. Turkevich, Anthony L.; Patterson, James H.; Franzgrote, Ernest J.; Sowinski, Kenneth P.; et al.: Alpha Radioactivity of the Lunar Surface at the Landing Sites of Surveyors 5, 6, and 7. Science, vol. 167, no. 3926, Mar. 27, 1970, pp. 1722-1724.

19-11. Biswas, S.; and Fichtel, C. E.: Composition of Solar Cosmic Rays. Space Sci. Rev., vol. 4, no. 1, 1965, pp. 709-736.

19-12. Northcliffe, L. C.; and Schilling, R. F.: Range and Stopping Power Tables for Heavy Ions, Texas A&M (College Station), 1970; Nuclear Data Tables, vol. 7, 1970, p. 233ff.

19-13. Lin, R. P.; Kahler, S. W.; and Roelof, E. C.: Solar Flare Injection and Propagation of Low-Energy Protons and Electrons in the Event of 7-9 July, 1966. Solar Phys., vol. 4, no. 1, 1968, pp. 338-360.

19-14. Fleischer, R. L.; Hart, H. R., Jr.; and Comstock, G. M.: Very Heavy Solar Cosmic Rays: Energy Spectrum and Implications for Lunar Erosion. Science, vol. 171, no. 3977, Mar. 26, 1971, pp. 1240-1242.

19-15. Crozaz, G.; and Walker, R. M.: Solar Particle Tracks in Glass from the Surveyor 3 Spacecraft. Science, vol. 171, no. 3977, Mar. 26, 1971, pp. 1237-1239.

19-16. Price, P. B.; Hutcheon, I.; Cowsik, R.; and Barber, D. J.: Enhanced Emission of Iron Nuclei in Solar Flares. Phys. Rev. Letters, vol. 26, no. 15, Apr. 12, 1971, pp. 916-919.

19-17. Leighton, H. I.; and Lincoln, J. V., eds.: Solar Geophysical Data. World Data Center A for Solar-Terrestrial Physics, National Oceanic and Atmospheric Administration (Boulder, Colorado), no. 341, part 1, Jan. 1973.

19-18. Smith, Henry J.: Solar Flares: Their Structure, Development, and Motion. AAS-NASA Symposium on the Physics of Solar Flares. NASA SP-50, 1964, pp. 1-14.

19-19. McCracken, K. G.: High Energy Particle Events Associated with Solar Flares. Solar Flares and Space Research, North Holland Publishing Company (Amsterdam), 1969, pp. 202-214.

19-20. Friedman, H.: X-Ray Observations of Solar Flares. Solar Flares and Space Research, North Holland Publishing Company (Amsterdam), 1969, pp. 87-94.

19-21. Price, P. B.; Chan, J. H.; Crawford, H. J.; and Sullivan, J. D.: Systematics of Heavy Ion Enhancements in Solar Flares. Proceedings of the 13th International Cosmic Ray Conference (University of Denver), 1973.

19-22. Chan, J. H.; Price, P. B.; and Shirk, E. K.: Charge Composition and Energy Spectrum of Suprathermal Solar Particles. Proceedings of the 13th International Cosmic Ray Conference (University of Denver), 1973.

19-23. Price, P. B.; Chan, J. H.; Hutcheon, I. D.; Macdougall, D.; et al.: Low-Energy Heavy Ions in the Solar System. Proceedings of the Fourth Lunar Science Conference, Pergamon Press (New York), Dec. 1973.

19-24. Shirk, E. K.; and Price, P. B.: Observation of Trans-Iron Solar Flare Nuclei in an Apollo 16 Command Module Window. Proceedings of the 13th International Cosmic Ray Conference (University of Denver), 1973.

19-25. Sullivan, J. D.; and Price, P. B.: On the Charge State of Low-Energy Fe Nuclei Accelerated by Solar Flares. Proceedings of the 13th International Cosmic Ray Conference (University of Denver), 1973.

19-26. Price, P. B.; Fleischer, R. L.; Peterson, D. D.; O'Ceallaigh, C.; et al.: High-Resolution Study of Low-Energy Heavy Cosmic Rays with Lexan Track Detectors. Phys. Rev. Letters, vol. 21, no. 9, Aug. 26, 1968, pp. 630-633.

19-27. O'Sullivan, D.; Thompson, A.; and Price, P. B.: Composition of Galactic Cosmic Rays with $30 < E < 130$ MeV/N. Nature Physical Science, vol. 243, May 7, 1973, pp. 8-9.

19-28. Garcia-Munoz, M.; Mason, G. M.; and Simpson, J. A.: A New Test for Solar Modulation Theory: The May-July 1972 Low Energy Galactic Cosmic Ray Proton and Helium Spectra. Astrophys. J. Letters, vol. 182, 1973, pp. L81-L84.

19-29. Webber, W. R.; Lezniak, J. A.; Kish, J. C.; and Damle, S. V.: Evidence for Differences in the Energy Spectra of Cosmic Ray Nuclei. Nature Physical Science, vol. 241, no. 109, Jan. 29, 1973, pp. 96-98.

20. Gamma Ray Spectrometer Experiment, NaI(Tl) Detector Crystal Activation

J. I. Trombka,[a] R. L. Schmadebeck,[a] M. Bielefeld,[b] G. D. O'Kelley,[c] J. S. Eldridge,[c] K. J. Northcutt,[c] A. E. Metzger,[d] E. Schonfeld,[e] L. E. Peterson,[f] J. R. Arnold,[ff] and R. C. Reedy[g]

Gamma ray spectra have been used recently to obtain geochemical analyses of the lunar surface and differential energy spectra of the diffuse gamma ray background (refs. 20-1 and 20-2). A major source of interference in the gamma ray spectral measurements may be attributable to the proton-induced activity in the scintillation detectors. The sources of this activity during space flight are the primary and secondary cosmic rays and, in addition, the trapped-proton flux when in near-Earth orbit. A number of individuals have noticed and discussed this problem (refs. 20-3 to 20-5). The detectors mounted in the Apollo 15 and 16 service modules could have been used for a study of the induced activity but they were unfortunately destroyed during reentry and therefore are not available for study.

In an attempt to obtain experimental data on the extent of the cosmic-ray-induced activity, a sodium iodide (thallium-activated) (NaI(Tl)) crystal was flown on board the Apollo 17 command module. No measurements were made during flight. After splashdown, the crystal was returned to the aircraft carrier U.S.S. *Ticonderoga*, where measurements of the induced activity were conducted for a 30-hr period. The crystal was then returned to the Oak Ridge National Laboratory (ORNL), where the measurements were continued in a low-level counting facility.

---

[a]NASA Goddard Space Flight Center.
[b]Computer Sciences Corporation.
[c]Oak Ridge National Laboratory.
[d]Jet Propulsion Laboratory.
[e]NASA Lyndon B. Johnson Space Center.
[f]University of California, San Diego.
[g]Los Alamos Scientific Laboratory, University of California.
[ff]Principal Investigator.

EXPERIMENT PROCEDURE

An NaI(Tl) crystal assembly physically identical to that flown on the Apollo 15 and 16 missions was used in this experiment (ref. 20-6). The Apollo 17 assembly did not include the photomultiplier, the proton anticoincidence mantle, and the thermal shield. The detector was a 7- by 7-cm right-cylindrical crystal. A glass plate was optically sealed to the crystal. Magnesium oxide was used as the optical reflector inside the crystal assembly. This type of assembly permitted hermetic sealing of the crystal and made possible a simple procedure for optically coupling the crystal assembly to a photomultiplier tube after flight. The crystal and reflector were enclosed in a steel jacket. An identical second crystal assembly that was not flown was used as a control throughout the measurement program. After splashdown, the flight (i.e., activated) crystal was returned to the recovery ship and optically mounted on a photomultiplier tube, and pulse-height spectra were obtained. The activated crystal was counted in a large, steel, low-level shield. The crystal counting was started approximately 1.5 hr after atmospheric reentry of the command module. Before splashdown, the control (unactivated) crystal was optically sealed to a photomultiplier tube and the background was determined in the steel shield. The same photomultiplier tube was used to count the flight and control crystal assemblies. After 30 hr of counting on board the recovery ship, the detector was flown back to the ORNL where measurements were continued. This procedure permitted the observation of the decay of the longer lived cosmic-ray-induced activities. Direct measurements of the induced activities were made by, again, optically sealing a photomultiplier tube to the activated crystal. Indirect measurements, using both

germanium (lithium-activated) (Ge(Li)) detectors and a large (4π) scintillation detector in a low-level counting system at the ORNL (ref. 20-7), were performed to determine the spectral distribution and the intensity of the emitted radiations. The 4π scintillation counter is divided in half. Both halves can be operated so as to require the occurrence of coincident events in both halves before an event is analyzed and recorded (coincidence spectra), or both halves can be operated without the coincidence requirement so that events can be analyzed and recorded independently (singles spectra).

PRELIMINARY RESULTS

To date, it has been possible to obtain qualitative identification of the following nuclear species: sodium-24 (^{24}Na), $\approx$ 15 hr; iodine-123 (^{123}I), $\approx$ 13.2 hr; iodine-124 (^{124}I), $\approx$ 4.8 days; iodine-125 (^{125}I), $\approx$ 60.1 days; iodine-126 (^{126}I), $\approx$ 13 days; xenon-127 (^{127}Xe), $\approx$ 36.4 days; sodium-22 (^{22}Na), $\approx$ 2.6 yr; and iodine-128 (^{128}I), $\approx$ 25 min. After suitable calibrations, quantitative concentrations of these radionuclides will be obtained. The present results indicate that the induced activity observed after recovery can be attributed mainly to species with half lives of approximately 12 hr and longer. Decay products with shorter half lives do not make a large contribution to the postrecovery integral count rate. This is not to imply that there are no short half-life components. In fact, an apparent line at approximately 0.44 MeV may be characteristic of ^{128}I. There are a few more regions with relatively short half lives (on the order of tens of minutes) that have not yet been identified.

The pulse-height spectrum obtained during the first 1.5 hr of counting after recovery is shown in figure 20-1. The spectrum has been corrected for background by subtracting the measurements obtained with the control crystal. Peak energies for the nuclides presently identified are indicated in figure 20-1. The peak positions for ^{123}I, ^{124}I, ^{126}I, and ^{128}I are displaced by $\approx$ 27 keV due to X-ray emission and absorption after electron capture.

Measurements of the flight and control crystals performed at the low-level counting laboratory at the ORNL before flight indicated that the potassium (K) and thorium (Th) content of the flight crystal was slightly higher than that for the control crystal. Thus, some indication of these elements would be expected

after background subtraction. This indication can be seen in the potassium-40 (^{40}K) and Th identification in figure 20-1. The energy identifications for ^{124}I, ^{126}I, and ^{24}Na indicated in figure 20-1 have been verified by measurements made with the Ge(Li) detector and in the low-level counting system. Both energy and half-life information has been used to determine the presence of these nuclear species. The ^{123}I and ^{128}I species were identified by use of the spectra obtained on board the recovery ship from both energy and half-life determinations. The ^{22}Na species has been tentatively identified on the basis of a preliminary analysis of the data obtained by the coincidence measurements in the low-level counting facility. The presence of ^{127}Xe has been determined by the identification of energy lines at 0.172, 0.203, and 0.375 MeV using the Ge(Li) detector. The work will be continued to obtain quantitative results and possibly to identify more nuclear species that have not been obvious from these early analyses.

Figure 20-2 is a pulse-height spectrum obtained by using the activated crystal mounted on a photomultiplier and counted in a lead shield at the ORNL. The counting took place 1.5 months after splashdown, and the counting time was 60 000 sec. The background count is also shown. The gain of the spectrometer was adjusted to observe the very-low-energy portion of the gamma ray pulse-height spectrum. The characteristic decay spectrum of the ^{125}I species can be easily seen.

DISCUSSION

The cosmic-ray-induced crystal activation is of considerable consequence in the analysis of the Apollo 15 and 16 gamma ray spectra obtained during transearth coast. In determining the magnitude and differential energy spectrum of the so-called diffuse gamma ray spectrum in the 0.3 to 30-MeV region, one of the major sources of interference can be attributed to the crystal activation. Thus, to make proper background corrections, both the magnitude and the spectral distribution of the cosmic-ray-induced activity had to be determined. Some theoretical and experimental work had been done to predict the magnitude of this effect (refs. 20-4 and 20-5), but the work on the Apollo 15 diffuse gamma ray measurements (ref. 20-2) indicated that these predictions were too high. To better determine the extent of this effect, the Apollo 17 experiment was performed.

0.159 MeV, ^{123}I

0.389 MeV, ^{124}I

0.44 MeV, ^{128}I
0.51 MeV (many sources)
0.603 MeV, ^{124}I
0.666 MeV, ^{126}I
0.723 MeV, ^{123}I
0.754 MeV, ^{126}I

1.27 MeV, ^{22}Na (possibly)
1.36 MeV, ^{24}Na (possibly)
1.46 MeV, ^{40}K, possible excess potassium (K) in activated crystal
1.69 MeV, ^{124}I

2.62 MeV (possibly), thorium line possibly excess in activated crystal

2.75 MeV, ^{24}Na

Calculated spallation continuum (ref. 20-5)

O   Apollo 17 data

—   Spallation continuum estimated from Apollo 15 results

Activity, count/sec/MeV

Energy, MeV

FIGURE 20-1.—Cosmic-ray-induced activity in the activated (flight) 7- by 7-cm NaI(Tl) crystal 1.5 hr after atmospheric reentry. The background obtained with the unactivated (control) crystal has been subtracted. Measurement of the spectrum, which was obtained by direct internal counting of the activated crystal, was started 1.5 hr after reentry of the Apollo 17 spacecraft; the counting time was 1800 sec.

One factor requiring consideration was the difference in the environment during the Apollo 15 and 16 missions compared with that during the Apollo 17 mission. First, the Apollo 15 and 16 crystals were stowed in the service module and were extended 7.6 m from the vehicle for approximately half of the flight time, whereas the Apollo 17 crystal was stowed in the command module for the total flight time. Thus, there was a difference in mass around the crystal that might cause a difference in the secondary proton and neutron flux in the region of the stowed crystals. Second, the exposure profiles of the primary flux, both in time and in spectral distribution, were different. The Apollo 17 crystal passed through the near-Earth trapped-proton flux twice, during launch and reentry, whereas the Apollo 15 and 16 detectors had passed through the trapped-proton belts only once (during launch) before measurement. The Apollo 15 measurement of the diffuse gamma ray

spectrum was made approximately 250 hr after lift-off, whereas the Apollo 17 measurements were made some 305 hr after lift-off. The significance of these differences in terms of trying to infer the magnitude of the cosmic-ray-induced activity in the Apollo 15 and 16 detectors from the Apollo 17 measurements has not yet been determined.

The shape of the proton-induced (spallation) gamma ray pulse-height spectrum can be divided into two parts, the discrete-line spectrum and the continuous spectrum. The discrete-line pulse-height spectrum for activated nuclear species in the crystal is produced by monoenergetic gamma rays emitted after electron capture. The continuum for such nuclear species is produced by the interaction within the crystal of electrons, positrons, radiation from positron annihilation, and gamma rays (other than those emitted after electron capture). If the material surrounding the crystal is radioactive (e.g., some
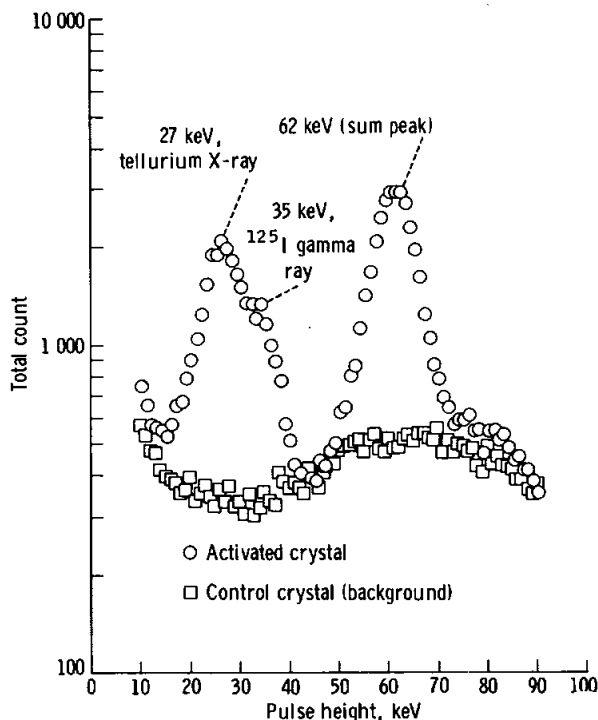
FIGURE 20-2.—Low-energy spectrum of the cosmic-ray-induced activity in the flight 7- by 7-cm NaI(Tl) crystal. The background obtained with the control crystal is also shown. The spectrum, which was obtained by direct internal counting of the activated crystal, was measured 1.5 months after splashdown of the Apollo 17 spacecraft; the counting time was 60 000 sec.

continuum inferred from the Apollo 15 data (ref. 20-2) is also shown. The latter magnitude is consistent with Apollo 17 results if it is considered that the discrete-line magnitude for ^{124}I and ^{126}I observed on Apollo 15 is reduced by a factor of 2 below that of Apollo 17. This comparison also assumes that the quantity of shorter half-life nuclides and the prompt gamma ray emission are small compared to those of the longer half-life emitters.

From the preliminary results, it seems that the dominant reactions are of the (p; p, xn) type. Neutron interactions do not seem to have an important part in producing the induced radiation seen during the postflight recovery measurements.

ACKNOWLEDGMENTS

^{24}Na, Th, and ^{40}K), then monoenergetic gamma rays independent of the mode of decay can be seen in the crystal as a discrete-line pulse-height spectrum. In figure 20-1, the discrete lines are indicated and the continuous distribution can be seen underneath.

In the Apollo 15 transearth spectrum (ref. 20-2), the ^{124}I 0.606-MeV and the ^{126}I 0.66-Mev lines can be identified. It has been calculated that the integrated count rate in this region above the continuum for Apollo 15 is one-half that observed in the same region above the continuum for the Apollo 17 mission. This difference cannot be attributed to the difference in exposure time alone. Thus, the difference in local mass and the passage through the near-Earth trapped-radiation belts a second time may be the causes of this increase.

In figure 20-1, the magnitude of the continuum and associated error as predicted in reference 20-5 is compared with the Apollo 17 measurement taken on board the recovery ship. The magnitude of the

REFERENCES

20-1. Metzger, A. E.; Trombka, J. I.; Peterson, L. E.; Reedy, R. C.; and Arnold, J. R.: Lunar Surface Radioactivity: Preliminary Results of the Apollo 15 and Apollo 16 Gamma-Ray Spectrometer Experiments. Science, vol. 179, no. 4075, Feb. 23, 1973, pp. 800-803.

20-2. Trombka, J. I.; Metzger, A. E.; Arnold, J. R.; Matteson, J. L.; et al.: The Cosmic Gamma-Ray Spectrum Between 0.3 and 27 MeV Measured on Apollo 15. Astrophys. J., vol. 181, 1973, pp. 737-746.

20-3. Peterson, Laurence E.: Radioactivity Induced in Sodium Iodide by Trapped Protons. J. Geophys. Res., vol. 70, no. 7, Apr. 1, 1965, pp. 1762-1765.

20-4. Dyer, C. S.; and Morfill, G. E.: Contribution to the Background Rate of a Satellite X-Ray Detector by Spallation Products in a Cesium Iodide Crystal. Astrophys. Space Sci., vol. 14, no. 1, 1971, pp. 243-258.

20-5. Fishman, G. J.: Proton-Induced Radioactivity in NaI(Tl) Scintillation Detectors. Summary Report SE-SSL-1497, Teledyne Brown Engineering (Huntsville, Ala.), Apr. 1972.

20-6. Arnold, J. R.; Peterson, L. E.; Metzger, A. E.; and Trombka, J. I.: Gamma Ray Spectrometer Experiment. Sec. 16 of the Apollo 15 Preliminary Science Report. NASA SP-289, 1972.

20-7. Eldridge, J. S.; O'Kelley, G. D.; Northcutt, K. J.; and Schonfeld, E.: Nondestructive Determination of Radionuclides in Lunar Samples Using a Large Low-Background Gamma-Ray Spectrometer and a Novel Application of Least Square Fitting. Proceedings of First International Conference on Radionuclide Metrology, J. Nuc. Instr. Meth. (Amsterdam, Holland), 1973.

21. Apollo Window Meteoroid Experiment

Burton G. Cour-Palais[a]

The purposes of the Apollo window meteoroid experiment were to use the Apollo command module (CM) heat shield window surfaces to obtain additional information about the flux of meteoroids with masses of 10^{-7} g and less, to examine the residue and the morphology of the craters produced by these meteoroids to obtain information regarding the dynamic and physical properties of the meteoroids, and to discover possible correlations with the lunar-rock-crater studies.

In addition to information regarding meteoroid flux, this experiment could yield information on the mass density and, possibly, on the composition of meteoroids. To determine the mass density would require the assumption that the velocity distribution as determined from optical and radar observations of much larger meteoroids is applicable to the smaller meteoroids.

Laboratory calibration data have been generated and are currently being analyzed. Glass targets identical to the CM heat shield windows were impacted by particles of different sizes, mass densities, and velocities using electrostatic accelerators for correlation with the observed crater characteristics.

When the effects of entry heating, subsequent immersion in salt water, and all the other contaminating sources are accounted for, the composition of the meteoroid residue in the crater or in the shock-fused glass will be determined by the use of a scanning electron microscope (SEM) nondispersive X-ray detector. The significance of the use of this detector is that compositions and mass densities obtained in space can be compared with those obtained from the lunar rock samples without the long-term exposure to the environmental effects of space. Knowledge of the mass density is also important for designing meteoroid shielding. Thus far, mass density can only be inferred from observations of meteoroid breakup in the atmosphere.

With the exception of the Apollo 11 spacecraft, all the CM heat shield windows have been examined for meteoroid impacts; thus far, 10 impacts have been observed. The flux represented by the number of impacts and the area-time of exposure by the Apollo windows is compatible with the flux estimates obtained from the results of penetration sensors mounted on the Pegasus 1, 2, and 3 satellites, by the Explorer 16 and 23 satellites, and by the Surveyor III shroud.

BASIC THEORY

Meteoroids are solid particles moving in interplanetary space that originate from both cometary and asteroidal sources. They are classified as sporadics when the orbits are random and as streams when many have nearly identical orbits. A meteor is the light phenomenon associated with the interaction of a meteoroid with the atmosphere of the Earth. The portion that survives interaction with the atmosphere and is found on the surface of the Earth is a meteorite. It is generally accepted that most meteorites are of asteroidal origin (ref. 21-1) and that the typical meteoroid originates from a cometary nucleus, is frangible, and does not reach the surface of the Earth. Thus, very little is known about the composition and the mass density of meteoroids, whereas meteorites have been collected and examined very thoroughly (ref. 21-2). Controversy exists as to whether the typical meteoroid is a low-density (1.0 g/cm³ or less) dust or ice ball or a stony object that froths during atmospheric entry and breaks off in chunks. If it is the latter, the mass density could be 2.5 to 3.0 g/cm³. The typical meteoroid has been described (ref. 21-3) as a conglomerate of dust particles bound together by frozen gases or "ices"; another author (ref. 21-4) postulates that meteoroids are "dust balls." The mass density of these conglom-

[a]NASA Lyndon B. Johnson Space Center.

erates is assumed to be no greater than 1 g/cm^3 because of the evidence of breakup high in the atmosphere. Recent experiments with carbonaceous chondrites in arc jets (ref. 21-5) have shown that a sufficient amount of water is present to cause frothing during the entry heating and that this frothy material breaks off along the path because of aerodynamic pressure. Thus, laboratory evidence has shown that the breakup of meteoroids in the atmosphere of the Earth is not necessarily indicative of a low-density conglomerate.

The near-Earth flux of meteoroids entering the atmosphere has been determined from photographic observation of meteors, radar echoes from the ionized column produced by meteoroids, and direct measurements by satellite detectors. The results of these observations have been combined in the plot of cumulative number of particles/m^2-sec for each size (fig. 21-1). Details of the observation techniques, direct measurements, and conversion of the observed data to mass can be found in references 21-6 to 21-8. Detectors flown on spacecraft have furnished information on the meteoroid flux in the mass range of 10^{-13} to 10^{-6} g (refs. 21-8 to 21-11). Fluxes for masses 10^{-7} g and less have been detected primarily by acoustic impact (microphone) sensors; fluxes of 10^{-9} to 10^{-6} g have been determined by the detection of perforations in thin metallic sheet sensors. The acoustic impact sensor measurements (ref. 21-8) indicate a much higher particle flux than do the penetration sensors for the same mass range (refs. 21-9 to 21-11). The examination of the Gemini spacecraft windows for meteoroid impacts confirmed the lower flux estimates obtained by the penetration sensors (ref. 21-12) for masses of 10^{-7} g and less. The cumulative flux plot of figure 21-1 reflects the low flux estimate of the penetration sensors and the Gemini window examination.

DESCRIPTION OF THE INSTRUMENT

The Apollo window meteoroid experiment is passive in that it uses approximately 0.4 m^2 of the external surfaces of the Apollo CM windows as meteoroid-impact detectors. The windows are made of 99-percent-pure-silica glass and are mounted almost flush with the external surface of the heat shield contour. The rendezvous windows were originally included in the total area of glass to be scanned but
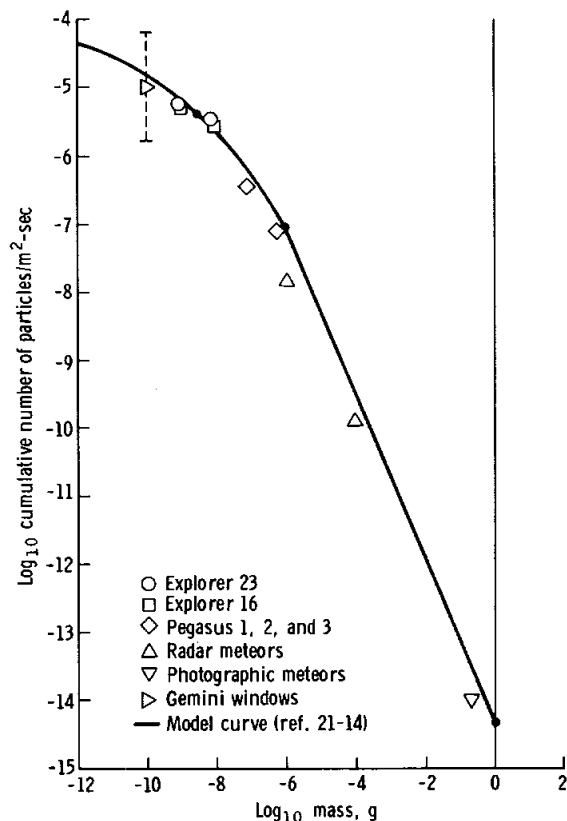
FIGURE 21-1.—A comparison of cumulative meteoroid flux-mass data with the adopted model.

have not been used since the Apollo 10 mission for the following reasons.

1. The rendezvous windows are inset into the heat shield and are fairly well shielded from the environment.

2. In all missions involving lunar module (LM) rendezvous, the surfaces of the rendezvous windows are subject to impacts by particles emanating from the thrusters of the LM reaction control system (RCS). During the postflight examination of the Apollo 9 spacecraft, the rendezvous windows showed a significant increase in pitting over that of previous missions with no LM rendezvous.

The window is an ideal detector because the surface is smooth and the spallation diameter can be many times the diameter of the impacting meteoroid. This ratio allows a 20X optical scan to detect the 40-μm-diameter crater that could be caused by a 4-μm-diameter meteoroid. Hence, the time necessary to scan the large areas involved is considerably

reduced, and the detection threshold is small enough to include cosmic dust particles.

During entry, the heat shield windows are subjected to a surface temperature of almost 1175 K for the side windows; the hatch window is subjected to a somewhat lower temperature. These temperatures are well below the annealing and softening temperatures of the glass; thus, the crater morphology is not affected. Both the temperature effect and the contamination caused by ablative products from the heat shield and the subsequent immersion in sea water can be accounted for in the chemical analyses.

EXAMINATION PROCEDURE

The heat shield and hatch windows from the Apollo 7 to 14 command modules were scanned at 20X magnification before flight to determine the general condition of the external surfaces. All chips, scratches, and other features that could be confused with meteoroid-impact craters were noted on a surface map. As a result of the stringent quality control and optical requirements, the windows have been generally free of such defects, and this mapping practice has been discontinued. The windows were received with a fairly thick coating of surface contamination that was removed before the optical scan by washing with water and isopropyl alcohol.

The windows were next scanned at 20X magnification by two different observers, and suspected impact craters were marked on a map. From experience with hypervelocity impacts in fused silica, it was possible to separate the meteoroid impacts from other surface effects.

Every suspected meteoroid crater was subjected to the following procedure.

1. The crater was photographed in detail with top and bottom lighting.

2. The crater depth and diameter were measured.

3. The section of the window containing the crater was removed by coring or sectioning as close as possible to the crater.

4. The window section was prepared for residue analysis with the SEM nondispersive X-ray detector by applying a thin carbon coating.

5. Residue analysis was performed, and all constituents were recorded.

6. The same window section was cleaned, and a thin gold coating was applied for normal, tilt, and stereoscopic crater photography at high magnifications.

The data from these examinations were compared with the laboratory test data mentioned previously, and the following meteoroid characteristics were determined.

1. The impact energy

2. The meteoroid mass, based on an average velocity and impact angle

3. The flux of particles of this mass and larger, using the exposure time and area.

RESULTS

The Apollo 17 windows were received with the outer surfaces contaminated with the hard deposit that has been present on all the Apollo windows examined. The results of a chemical analysis of samples taken from the Apollo 9 windows and the possible sources of the contaminants have been previously discussed (ref. 21-13) and are assumed to be typical of all the other spacecraft.

A preliminary scan of the Apollo 17 hatch and side window outer surfaces at 2X, sufficient to detect a crater 80 to 100 μm in diameter, revealed no meteoroid impacts. The crater reportedly seen by the crew during the mission on hatch window number 3 was actually a 450-μm-diameter bubble in the glass just beneath the surface. As a result of the scan, an even larger bubble (approximately 750 μm) was observed in window number 1. The Apollo 17 windows examined had numerous bubbles ranging from the large ones previously mentioned to those 50 μm in diameter but typically 100 to 200 μm in diameter.

Approximately 3.5 m^2 of Apollo heat shield windows have been optically scanned, and 10 meteoroid impacts have been identified, with spall diameters ranging from 25 to 445 μm (ref. 21-13). Three 1.7-cm-diameter cores were removed from Apollo 14 window number 1 for an SEM scan at magnification levels of 1000X and 10 000X. Approximately 1 cm^2 has been scanned at 1000X with a resolution of 20 nm and with an additional 693 fields of view examined. These fields of view consisted of 429 fields, each 10^2 μm^2 at 10 000X for a minimum-detectable crater diameter of 0.2 μm, and of 264 fields, each 10^4 μm^2 at 1000X for a minimum-detectable crater diameter of 2 μm. No hypervelocity impact craters (remelted lipped pits with or without a

concentric spall zone) were seen in either the scan or the field-of-view examinations. However, five pits that were between 5 and 20 μm in diameter and that had fractured central pits and a spall zone were observed. Many pits averaging 5 μm in diameter were seen in the coating layer in both examinations, 90 percent of which did not penetrate into the glass surface. These craters were cylindrical in section and were assumed to have been caused by debris from the RCS or explosive devices.

A list of the craters larger than 25 μm in diameter is given in table 21-I, which includes an estimate of the window exposure (product of area and time) to the meteoroid environment for each mission, the number of impacts observed, the minimum crater size, the resulting flux with 95-percent upper and lower confidence limits, and the minimum energy and mass of the impacting meteoroid. The flux estimate includes the window area, mission time, planetary shielding during the Earth- and lunar-orbital periods, allowance for the additional shielding provided by the LM during Earth/Moon transit, and a factor to account for the focusing effect of the gravitational field of the Earth (ref. 21-14) on the meteoroid population. The window areas quoted are lower than those given in reference 21-13, which were preliminary and did not include all the possible available shielding.

The mass determination is derived from the results obtained from an experimental hypervelocity impact calibration program performed on a linear accelerator with targets consisting of the same material and thickness as the Apollo windows. The thickness is important to preserve the correct impact shock characteristics that govern the resulting crater morphology. The projectiles used were spheres and irregular powders of iron (ρ = 7.8 g/cm^3), silicon (ρ = 2.3 g/cm^3), and lanthanum hexaboride (ρ = 2.6 g/cm^3) that ranged from 0.3 to 5 μm in diameter. Impact velocities ranged from 1 to 27 km/sec, depending on the projectile masses. The data have been analyzed, and a separate report is being prepared. However, data pertinent to the analysis of the window impact craters are shown in table 21-II, and the pertinent crater diameters are depicted in figure 21-2.

In summarizing the results obtained in the tests, three cratering regimes were evident (fig. 21-2). When the first concentric spallation was present, the pit lips were most often broken off and ejected. In extreme

TABLE 21-I.—*Meteoroid Craters and Related Information*

Mission	Window exposure, m²-sec	Number of impacts	Limiting crater diameter, μm	Meteoroid flux, number/m²-sec	95-percent confidence limits, number/m²-sec	Minimum meteoroid energy, ergs	Minimum meteoroid mass, g
Apollo 7 (Earth orbital without LM)	1.39 × 10⁵	5	125	3.59 × 10⁻⁵	8.38 × 10⁻⁵ 1.15 × 10⁻⁵	362	1.8 × 10⁻¹⁰
Apollo 8 (lunar orbital without LM)	1.13	1	65	1.70 × 10⁻⁵	9.48 × 10⁻⁵ 1.70 × 10⁻⁶	113	5.7 × 10⁻¹¹
Apollo 9 (Earth orbital with LM)	1.18	1	200	8.51 × 10⁻⁶	4.76 × 10⁻⁵ 8.51 × 10⁻⁷	650	3.3 × 10⁻¹⁰
Apollo 10 (lunar orbital with LM)	1.25	0	40	—	2.95 × 10⁻⁵ —	53	2.7 × 10⁻¹¹
Apollo 12 (lunar landing)	1.53	0	40	—	2.41 × 10⁻⁵	53	2.7 × 10⁻¹¹
Apollo 13 (circumlunar abort with LM)	1.01	1	445	1.89 × 10⁻⁵	1.06 × 10⁻⁴ 1.89 × 10⁻⁶	2260	1.1 × 10⁻⁹
Apollo 14 (lunar landing)	1.48	2	25	2.60 × 10⁻⁵	9.37 × 10⁻⁵ 2.60 × 10⁻⁶	26	1.3 × 10⁻¹¹
Apollo 15 (lunar landing)	1.81	0	100	—	2.03 × 10⁻⁵ —	222	1.1 × 10⁻¹⁰
Apollo 16 (lunar landing)	1.68	0	100	—	2.21 × 10⁻⁵ —	222	1.1 × 10⁻¹⁰
Apollo 17 (lunar landing)	1.86	0	100	—	1.98 × 10⁻⁵ —	222	1.1 × 10⁻¹⁰

TABLE 21-II.—*Data from Window Calibration Tests*

Test number	Projectile diameter, d_p, μm	Projectile velocity, V_p, km/sec	Projectile energy, E_p, ergs	Impact pressure, P_i, Mbar	E_p/P_i	Diameter of pit caused by projectile, D_p, μm	D_p/d_p	Inner spall diameter, D_i, μm	D_i/d_p	Outer spall diameter, D_o, μm	D_o/d_p	ρ, g/cm^3
T12-13A	0.40	22.9	0.21	5.1	0.04	0.87	2.18	–	–	–	–	2.33
T12-14A	.48	18.9	.25	3.5	.07	.93	2.02	–	–	–	–	2.33
T2-12-1 to 10	.78	5.0	.25	.6	.40	.80	1.00	4.30	5.5	–	–	7.8
T12-16A	1.04	11.9	1.00	1.4	.70	1.61	1.55	–	–	–	–	2.33
T6-14A	1.20	9.08	2.90	1.67	1.70	1.65	1.38	–	–	–	–	7.8
T11-3A	1.86	5.63	1.24	.37	3.40	2.56	1.38	–	–	8.46	4.55	2.33
T6-4A	1.80	7.20	6.20	1.12	5.60	2.30	1.28	–	–	–	–	7.8
T7-7C	2.24	5.27	6.30	.63	10.00	2.40	1.07	–	–	35.0	15.6	7.8
T11-4A	3.12	4.56	3.87	.27	14.30	4.95	1.59	–	–	20.44	6.55	2.33
T7-7B	2.88	5.09	12.50	.60	20.80	4.10	1.42	21.0	7.30	–	–	7.8
T11-6A	4.28	3.80	6.86	.21	32.70	4.27	1.00	15.20	3.55	31.87	7.45	2.33
Reference figure (fig. 68 of Ref. 21-15)	4.00	5.00	11.65	.28	42.00	4.60	1.15	17.30	4.33	38.20	9.55	2.78
T7-8B	3.92	4.07	20.40	.42	48.60	4.70	1.20	36.70	9.40	81.50	20.80	7.88
T7-6B	4.06	3.76	19.40	.38	51.70	4.10	1.01	32.50	8.00	75.00	18.50	7.88

D_p = diameter of the pit caused by a projectile

(a)

D_i = diameter of the inner spall zone

(b)

D_o = diameter of the outer spall zone

(c)
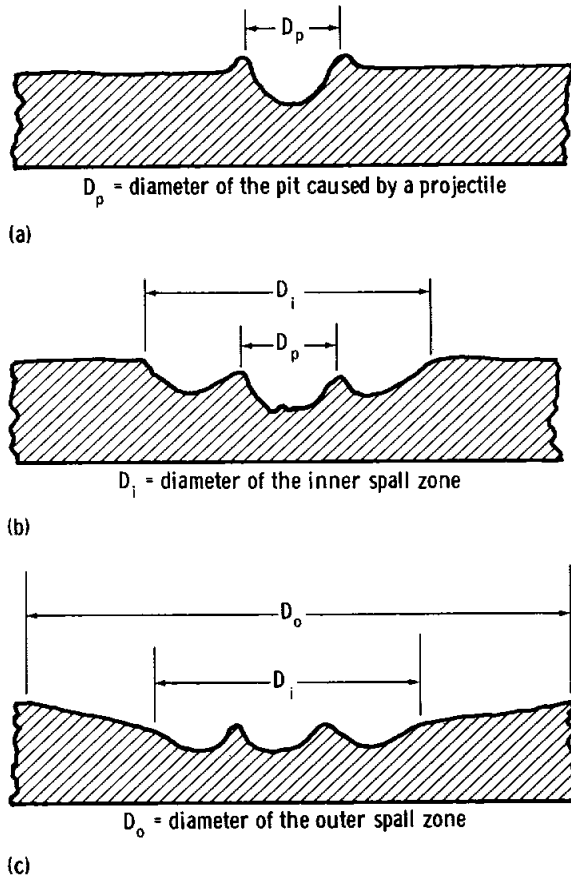
FIGURE 21-2.—Cratering regimes. (a) Pit only. (b) Pit and inner spall zone. (c) Pit and inner and outer spall zones.

cases, only the bottom of the pit remained. Melting of the glass began at an initial impact pressure of approximately 0.2 Mbar, and lips were well formed by 0.25 Mbar for all the test projectiles used. In some of the tests, a second spallation zone was observed approximately concentric with and at a shallower slope than the inner zone. Also present were intermediate regimes, such as pits with radial and concentric cracks and inner spalls with radial cracks extending beyond their peripheries.

The data from table 21-II are shown in figure 21-3(a) and 21-3(b), in which parametric functions involving the diameters of the pit and inner and outer spalls and the projectile density are plotted against the projectile energy. All three crater regimes can be represented within limits by the expression shown on each graph. If the two graphs are viewed together, it is apparent in nearly every case that the pit relationship does not hold when the spallation rela-

tionship does. This is due to the previously mentioned ejection of the pit lips during spallation and a resulting larger pit diameter as may be observed in figure 21-3(a). It is also apparent that spallation begins earlier for the silicon projectiles than for the iron projectiles, except in one case. This exception is for a very small iron projectile with a resulting low-impact energy. The aluminum projectile (ρ = 2.78 g/cm^3) shown in table 21-II and in figure 21-3(b) is from reference 21-15; it is included because the tests with the lanthanum hexaboride projectiles (ρ = 2.6 g/cm^3) were not very conclusive and a point for a projectile with a similar mass density was needed.

As the Apollo craters observed had remelted pits and well-defined outer spall zones, the equation used to obtain the impacting meteoroid mass was

$$D_O = 2.8 d_m \times \rho_m^{0.5} \times E_m^{0.31} \qquad (21\text{-}1)$$

where D_O is the crater outer spall diameter in centimeters; ρ_m is the meteoroid mass density, 2 g/cm^3; E_m is the meteoroid energy in ergs; and d_m is the meteoroid diameter in centimeters. An average meteoroid velocity of 20 km/sec is assumed to complete the determination of meteoroid masses.

The Apollo 14 core examinations were able to resolve down to 0.2-μm-diameter pits if there were any. Because the impact tests showed that pits approximately 2 μm in diameter and smaller in the Apollo window material did not have concentric spalls, it may be assumed that the pit equation from figure 21-3(a) is appropriate to determine the limiting meteoroid mass for the core. Thus

$$D_p = 1.8 \rho_m^{-0.18} \times E_m^{0.33} \qquad (21\text{-}2)$$

where D_p is the pit diameter in micrometers. The 5-μm pits observed in the cores were related to meteoroid mass by the equation

$$D_i = 1.22 d_m \times \rho_m^{0.5} \times E_m^{0.31} \qquad (21\text{-}3)$$

where D_i is the crater inner spall diameter in centimeters, because they represent an intermediate cratering regime.

DISCUSSION

The results of the mass and flux determinations are shown in figure 21-4 compared with the meteor-

oid flux model of reference 21-14 and the Pioneer 8 and 9 satellite data for the front film grid and time of flight detectors (ref. 21-16). In addition to the results of the optical scan given in table 21-I, figure 21-4 includes the data from the SEM scans of the 1.7-cm-diameter core taken from the Apollo 14 window. Thus, the flux relative to the five craters of 5 μm in diameter and larger is shown at a mass value of $10^{-11.42}$ g. In addition, the point at 10^{-12} g is the 95-percent upper-limit flux for the mass equivalent of the detection threshold at which no craters were observed.

This latest mass calibration of the craters found on the Apollo windows, based on the equations shown, differs from that reported in reference 21-13 by no more than a factor of 3, except for Apollo 15 for which the detectable crater threshold was also decreased. The previous masses were based on average spall-to-meteoroid-diameter ratios of 10, 15, and 25 for spall ranges of < 50 μm, 50 to 100 μm, and > 100 μm, respectively. Further analysis of the test data could result in changes; however, the mass levels shown are considered to be reasonably accurate.

Although statistically poor, the Apollo window data substantiate the curve of reference 21-14, which represents the mean near-Earth flux, except for Apollo 7 and 13. The Apollo 7 spacecraft was in Earth orbit and its windows obtained the most impacts (five); therefore, the result is more valid than the others. The Apollo 13 crater was the largest ever obtained on a window in the shortest exposure of any of the spacecraft. The Pioneer 8 and 9 results show an increase of 25 times the flux level predicted by the referenced model at 10^{-12} g, and the Apollo 14

2-μm-diameter upper limit at the same mass sets a possible limiting flux level for this size. The 5-μm-diameter craters found on the core do not appear to be meteoritic in origin and are discounted, although they are shown for completeness. It is possible that the Apollo 7 and 13 results, in conjunction with the Pioneer 8 results modified to a near-Earth environment, represent a better estimate of the small particle environment than that shown in reference 21-14. This fact would be consistent with the higher fluxes shown in reference 21-17 for the lunar-rock-crater distributions and with the revised estimate of the Explorer XXIII and Pegasus detectors shown in figure 6 of reference 21-18 in comparison with the same NASA design curve of reference 21-14. The dashed line in figure 21-4 represents such a possible cumulative flux distribution for particles smaller than 10^{-8} g.

Although these results are somewhat different from those reported in reference 21-13, it should be remembered that the Apollo window data, obtained for the most part outside the gravitational influence of the Earth, were correlated by a factor of 1.93 for comparison with the near-Earth reference model mentioned previously. Thus, the gravitational decrease in flux mentioned in reference 21-14 and confirmed in reference 21-19 is still present in the data, but the additional factor due to the different cratering characteristics of glass and the Explorer and Pegasus metallic detectors is not present. Analysis of the results is continuing.

(a) Pit diameter relationship to meteoroid energy and mass density.

(b) Inner and outer spallation diameter relationships to meteoroid energy and mass density.
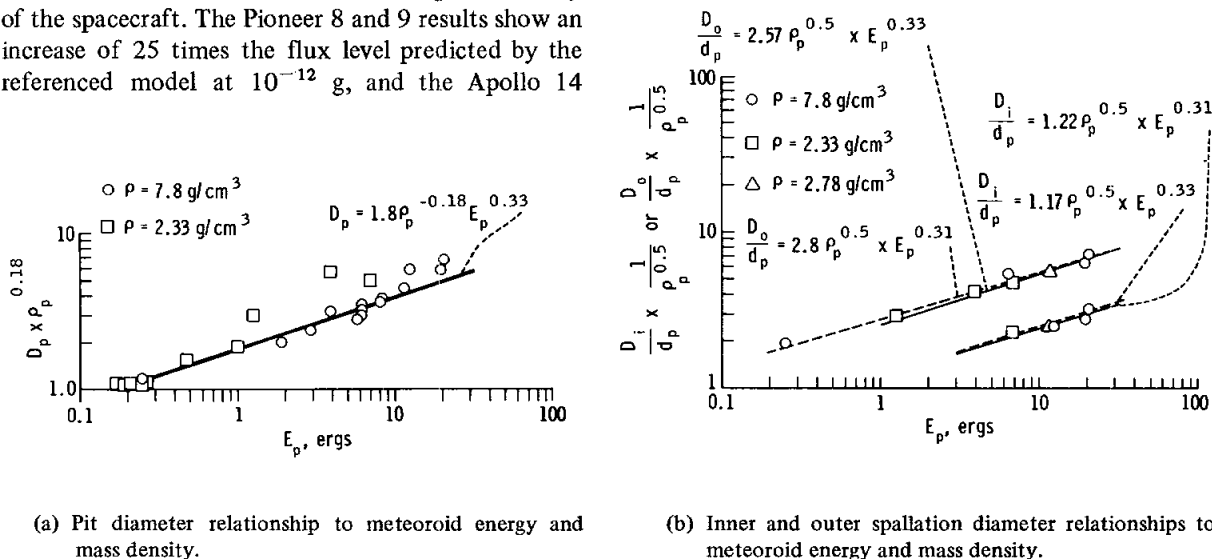
FIGURE 21-3.—Data from window calibration tests.
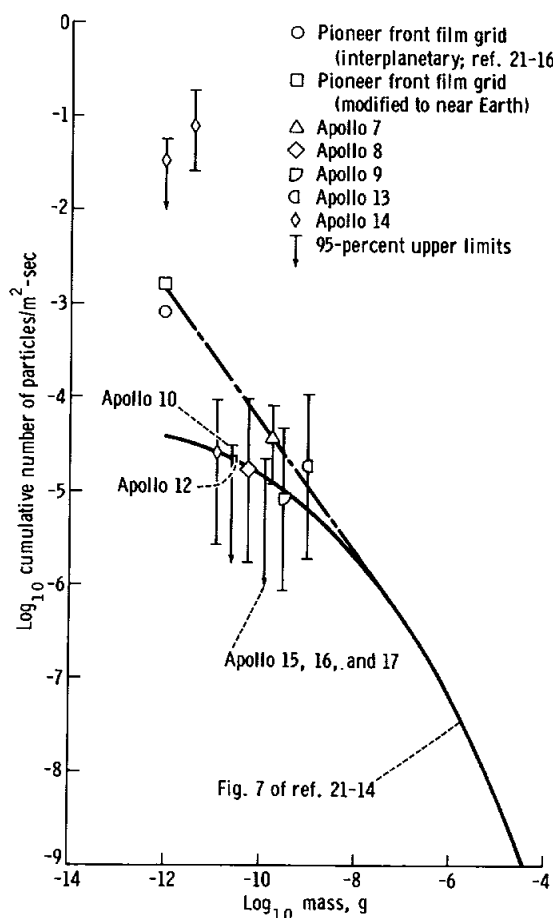
FIGURE 21-4.—Apollo results compared with other satellite data.

No further search for meteoritic residue in the craters has been made since the report given in reference 21-13; however, the possibility of identifying elements within the remelted zone in the pits still exists.

CONCLUSIONS

The estimate of the mass flux resulting from examination of the Apollo 17 and nine prior spacecraft window surfaces, a calibration based on experimental hypervelocity tests, and an accurate determination of the area-time product have shown a tendency for a higher flux than the near-Earth model environment of reference 21-14 for particles smaller than 10^{-8} g. The trend is in keeping with lunar-rock studies, the Pioneer 8 and 9 results, and other reports of increased small-particle activity for long-duration missions. Although a nondispersive X-ray analysis of

residue in and around meteoroid-impact sites on the Apollo 13 and 14 window surfaces revealed only spacecraft contaminants, as reported in reference 21-13, the possibility still exists that meteoritic residue may be detected by this experiment.

REFERENCES

21-1. Whipple, Fred L.: On Maintaining the Meteoritic Complex. Studies in Interplanetary Particles, Special Rept. 239, Smithsonian Astrophysical Observatory (Cambridge, Mass.), 1967, pp. 1-46.

21-2. Wood, J. A.: Physics and Chemistry of Meteorites. The Moon, Meteorites, and Comets. The Solar System, Vol. IV, University of Chicago Press, pp. 337-401.

21-3. Whipple, Fred L.: The Meteoritic Risk to Space Vehicles. Vistas in Astronautics, Pergamon Press (Los Angeles), 1958.

21-4. Opik, Ernst Julius: Physics of Meteor Flight in the Atmosphere. Interscience Pub., Inc. (New York), 1958.

21-5. Allen, H. Julian; and Baldwin, S., Jr.: Frothing as an Explanation of the Acceleration Anomalies of Cometary Meteors. J. Geophys. Res., vol. 72, no. 13, July 1, 1967, pp. 3483-3496.

21-6. Lovell, Alfred Charles Bernard: Meteor Astronomy. Clarendon Press (Oxford), 1954.

21-7. McKinley, Donald William Robert: Meteor Science and Engineering. McGraw-Hill Book Co., Inc. (New York), 1961.

21-8. Alexander, W. M.; McCracken, C. W.; Secretan, L.; and Berg, O.: Review of Direct Measurements of Interplanetary Dust from Satellites and Probes. Proceedings of the Third International Space Science Symposium, Interscience Pub., Inc. (New York), 1963, pp. 891-917.

21-9. Hastings, Earl C., Jr.: The Explorer 16 Micrometeoroid Satellite. Supplement III, Preliminary Results for the Period May 27, 1963, Through July 22, 1963. NASA TM X-949, 1964.

21-10. O'Neal, R. L.: The Explorer 23 Micrometeoroid Satellite. Description and Results for the Period Nov. 6, 1964, Through Nov. 5, 1965. NASA TN D-4284, 1968.

21-11. Clifton, Stuart; and Naumann, Robert: Pegasus Satellite Measurements of Meteoroid Penetration (Feb. 16, 1965, Through Dec. 31, 1965). NASA TM X-1316, 1966.

21-12. Zook, Herbert A.; Flaherty, Robert E.; and Kessler, Donald J.: Meteoroid Impacts on the Gemini Windows. Planet. Space Sci., vol. 18, no. 7, July 1970, pp. 953-964.

21-13. Cour-Palais, Burton G.; Brown, Milton L.; and McKay, David S.: Apollo Window Meteoroid Experiment. Sec. 26 of the Apollo 16 Preliminary Science Report. NASA SP-315, 1972.

21-14. Cour-Palais, B. G.; Whipple, Fred L.; D'Aiutolo, C. T.; Dalton, C. C.; et al.: Meteoroid Environment Model— 1969 (Near Earth to Lunar Surface). NASA SP-8013, 1969.

21-15. Block, R.; Fechtig, H.; Gertuer, W.; et al.: Natural and Simulated Impact Phenomena. Max Planck Institut fur Kernphysik (Heidelberg, Germany), 1971.

21-16. Berg, Otto E.; and Grun, Eberhard: Evidence of Hyperbolic Cosmic Dust Particles. Paper presented at XVth COSPAR Meeting (Madrid, Spain), May 1972.

21-17. Brownlee, D. E.; Hörz, F.; Hartung, J. B.; and Gault, D. E.: Micrometeoroid Craters Smaller Than 100 Microns. The Apollo 15 Lunar Samples, The Lunar Science Institute (Houston, Tex.), 1972, pp. 407-411.

21-18. Naumann, Robert J.; and Clifton, K. Stuart: Mass Influx Obtained from LLLTV Observations of Faint Meteors. NASA TN D-6868, 1972.

21-19. Cour-Palais, B. G.; Zook, H. A.; and Flaherty, R. E.: Meteoroid Activity on the Lunar Surface from the Surveyor 3 Sample Examination. Space Research XII. Akademie-Verlag (Berlin), 1972, pp. 319-331.

22. Apollo Lunar Sounder Experiment

R. J. Phillips,[a][‡][*] G. F. Adams,[b] W. E. Brown, Jr.,[a][†] R. E. Eggleton,[c][‡] P. Jackson,[b] R. Jordan,[a]
W. I. Linlor,[d][‡] W. J. Peeples,[e] L. J. Porcello,[b][‡] J. Ryu,[e] G. Schaber,[c] W. R. Sill,[e]
T. W. Thompson,[a] S. H. Ward,[e][†] and J. S. Zelenka[b]

The scientific objectives of the Apollo lunar sounder experiment (ALSE) are (1) mapping of subsurface electrical conductivity structure to infer geological structure, (2) surface profiling to determine lunar topographic variations, (3) surface imaging, and (4) measuring galactic electromagnetic radiation in the lunar environment. The ALSE was a three-frequency, wide-band, coherent radar system operated from lunar orbit during the Apollo 17 mission.

The concept of radar sounding is quite analogous to active seismic profiling; that is, a continuous series of short pulses of (electromagnetic) energy are propagated toward the Moon and are reflected from the lunar surface and from subsurface geologic interfaces. The energy reflected from the Moon is continuously recorded as the command and service module (CSM) moves in lunar orbit, and thus a profile of surface and subsurface structure is assembled. The capability to map the lunar interior is dependent on a low-electrical-loss subsurface; that is, the attenuation of the signal must not preclude a significant depth of exploration. Premission estimates of path loss, based on measurements from returned lunar samples, indicated a maximum depth of exploration of approximately 1 km. Further, for the reflection of energy at a geologic boundary, an electrical-property contrast must exist across an interface. The electrical property controlling the

amount of reflected energy is the dielectric constant ϵ. The premission estimate of the typical dielectric-constant ratio across an interface was 1.25.

Profiling is accomplished by maintaining an absolute timing reference between the firing of the radar transmitter and the reception of the energy returned from the lunar surface. The rate of transmitter firing is sufficiently high to make the profiling essentially continuous. In addition to acquiring the global profile for selenodesy studies, detailed profiles were acquired that may be used to address local selenomorphological problems.

In the active sounding mode, the quality of imagery is dependent, for a given frequency, on the diffuse backscattering properties of the lunar surface. One record of the surface backscattered energy is compiled from each transmitted pulse reflected from the Moon. A sequence of records then comprises a two-dimensional data array necessary to create an image. The image is typically bounded on one side by the spacecraft-nadir topographic profile, and the combination of profile and image is very useful for surface geologic interpretation.

The ALSE system was operated in three frequency ranges: 5 MHz (HF-1), 15 MHz (H-2), and 150 MHz (VHF). The HF-1 system is capable of the deepest exploration. The HF-2 system was operated simultaneously with the HF-1 system to provide partial overlap in depth of exploration, trading off depth of exploration for improved resolution. The VHF system was designed for shallow sounding and for surface imaging. All three frequencies are capable of surface profiling.

The ALSE had four major hardware components (fig. 22-1). At the heart of the system is the coherent synthetic aperture radar (CSAR) containing the transmitting and receiving elements. Separate transmit/receive antenna systems were provided for the

---

[a]Jet Propulsion Laboratory.
[b]Environmental Research Institute of Michigan.
[c]U.S. Geological Survey.
[d]NASA Ames Research Center.
[e]University of Utah.
[†]Principal Investigator.
[‡]Co-Investigator.
[*]Team Leader.

HF and VHF ranges. The received signal is fed to an optical recorder. The voltage into the recorder modulates the light-intensity output of a cathode ray tube (CRT). The CRT output was recorded on a contin-

uously moving strip of photographic film. The film, representing the prime data storage medium, was recovered during the transearth-coast extravehicular activity.

The CSAR receiver also monitored the average reflected electromagnetic power and transmitted these data, together with other engineering data, by way of the CSM 51.2-kbps telemetry channel. The average reflected power data are used for calibration purposes as well as for aid in data interpretation. A representative example of these data is shown in figure 22-2.

The CSAR also had a receive-only (nonsounding) capability to measure the noise background in the HF ranges. These data were also transmitted by way of the 51.2-kbps telemetry channel.
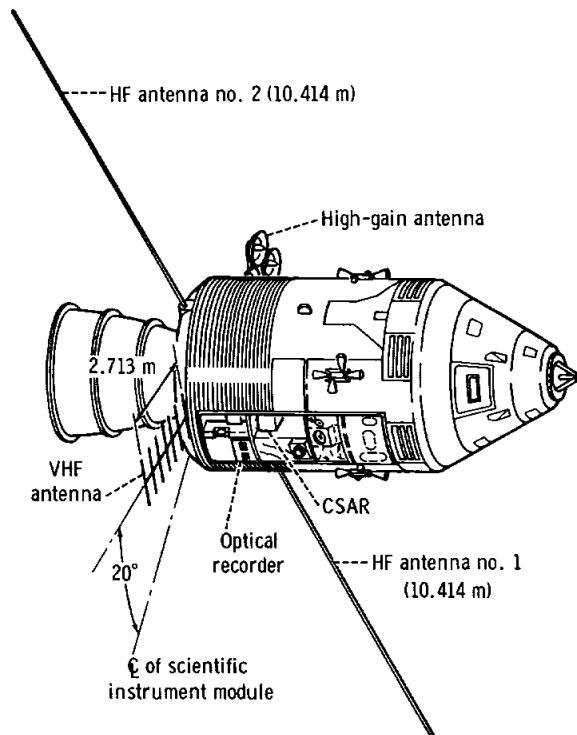
FIGURE 22-1.—The CSM, showing the ALSE configuration.

BASIC THEORY

Sounding

Power Returned

The electromagnetic energy transmitted by an ALSE antenna can be represented (approximately) by an envelope of spherically spreading rays. If an antenna-centered spherical coordinate system is defined as (r,θ,ϕ), then the ray distance from the antenna to the lunar surface is defined as $R(\theta,\phi)$. The power per unit area at the lunar surface is
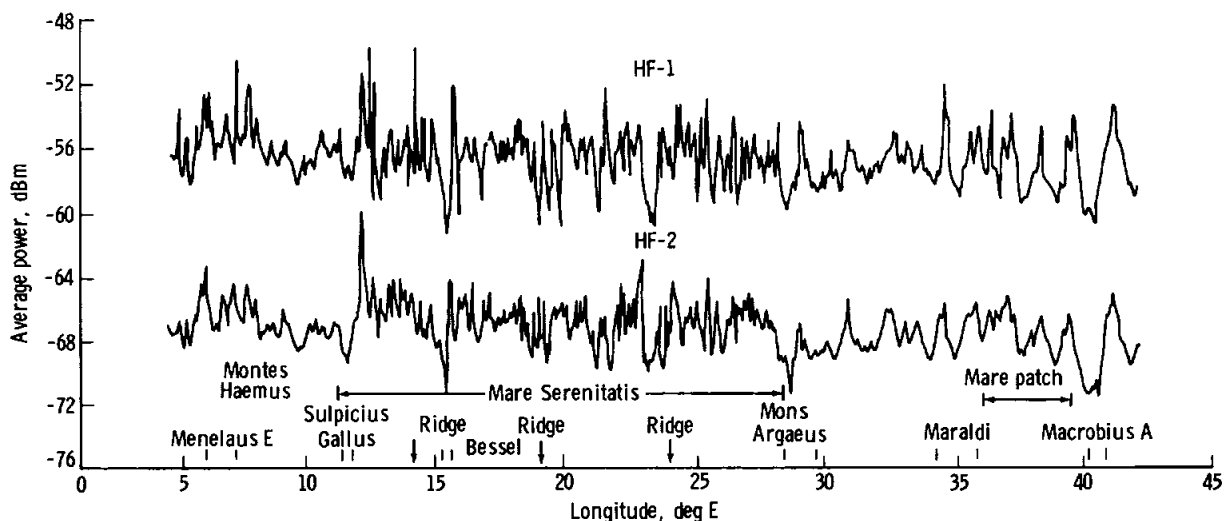
FIGURE 22-2.—Typical output of the specular power monitor on lunar revolution 17.

$$\frac{P_t G(\theta, \phi)}{4\pi R^2(\theta, \phi)} \qquad (22\text{-}1)$$

where $G(\theta, \phi)$ is the antenna gain and P_t is the peak power transmitted. For the remainder of this discussion, it is assumed that all reflections are specular in nature and are caused by dielectric-property contrasts only. The magnetic permeabilities of the lunar media are taken as that of free space. Assume that the incident ray has a direction u_i, where u indicates a unit vector. Then it is important to define three other vectors: the direction of reflection u_r, the direction of transmission into the subsurface u_t, and the outward-pointing normal to the local surface u_n. The vector u_r satisfies

$$u_r \cdot u_n = -u_i \cdot u_n \qquad (22\text{-}2)$$

and if $u_i \cdot u_n = -1$, then the reflected ray is scattered in the direction of the CSM. The received power is given by

$$P_r = \frac{P_t G^2(\theta, \phi) \lambda^2}{4[4\pi R(\theta, \phi)]^2} r_{0,1}(0) \qquad (22\text{-}3)$$

where λ is the free-space wavelength of the signal and $r_{0,1}(0)$ is the Fresnel reflection coefficient for normal incidence

$$r_{0,1}(0) = \left(\frac{\sqrt{\epsilon_0} - \sqrt{\epsilon_1}}{\sqrt{\epsilon_0} + \sqrt{\epsilon_1}} \right)^2 \qquad (22\text{-}4)$$

where ϵ_0 and ϵ_1 are the dielectric constants of free space and of the lunar surface material, respectively. A certain amount of energy is transmitted into the subsurface in a direction given by u_t where u_t satisfies

$$u_t \times u_n = \sqrt{\frac{\epsilon_0}{\epsilon_1}} \; u_i \times u_n \qquad (22\text{-}5)$$

The angles of incidence and refraction, γ_i and γ_t, are defined respectively by

$$\begin{aligned} \sin \gamma_i &= |u_i \times u_n| \\ \sin \gamma_t &= |u_t \times u_n| \end{aligned} \qquad (22\text{-}6)$$

The energy transmitted into the subsurface is a function of γ_i, γ_t, and the ray coordinates θ and ϕ. The energy transmission coefficient is designated as

$t_{0,1}(\gamma_i, \gamma_t, \theta, \phi)$, and the strength of a wave transmitted into the subsurface a ray distance R_d is approximately

$$\frac{P_t G(\theta, \phi)}{4\pi [R(\theta, \phi) + R_d]^2} t_{0,1}(\gamma_i, \gamma_t, \theta, \phi) \exp\left(-\omega \tan \delta_1 \frac{R_d}{C_1} \right) \qquad (22\text{-}7)$$

where ω is the radial frequency of the wave ($\omega = 2\pi f$, where f is the frequency in hertz) and $\tan \delta_1$ is the loss tangent of medium 1

$$\tan \delta_1 = \frac{\sigma_1}{\omega \epsilon_1} \qquad (22\text{-}8)$$

where σ_1 is the conductivity of medium 1. In equation (22-7), C_1 is the velocity of light in medium 1

$$C_1 = (\mu_0 \epsilon_1)^{-1/2} \qquad (22\text{-}9)$$

where μ_0 is the magnetic permeability of free space. If a discontinuity in dielectric constant occurs in the subsurface, say ϵ_1 to ϵ_2, then a fraction of the subsurface energy is reflected. If the local outward normal to the discontinuity is given by u_{ns}, then the condition $u_t \cdot u_{ns} = -1$ guarantees that subsurface reflected energy is scattered in the direction of the CSM. In this case

$$r_{1,2}(0) = \left(\frac{\sqrt{\epsilon_1} - \sqrt{\epsilon_2}}{\sqrt{\epsilon_1} + \sqrt{\epsilon_2}} \right)^2 \qquad (22\text{-}10)$$

and the power received is

$$\begin{aligned} P_{rs} \approx \; & \frac{P_t G^2(\theta, \phi) \lambda^2}{4\{4\pi [R(\theta, \phi) + R_d]\}^2} \\ & \times t_{0,1}{}^2(\gamma_i, \gamma_t, \theta, \phi) \exp\left(-2\omega \tan \delta_1 \frac{R_d}{C_1} \right) r_{1,2}(0) \end{aligned} \qquad (22\text{-}11)$$

This discussion can be extended to any number of interfaces, but the simple media described previously suffice to point out the energy considerations involved. It is desirable to have the ratio P_{rs}/P_r as large as possible so that both the surface and subsurface returns are within the linear dynamic range of the ALSE receiving system.

Time History

The ALSE transmitter generates a chirped (linear FM) pulse $g(t)$ of length τ

$$g(t) = P_\tau(t) \sin\left[2\pi(f_0 + \tfrac{1}{2}kt)t\right] \qquad (22\text{-}12)$$

where $p_\tau(t)$ is an approximately rectangular envelope of length τ, f_0 is the starting frequency of the sweep, and k is the sweep rate (one-half of the dispersion constant) for the chirp. For the ray distance $R(\theta,\phi)$ to the lunar surface, the surface reflection returns to the spacecraft in a time

$$t_0 = \frac{2R(\theta,\phi)}{C_0} \qquad (22\text{-}13)$$

where C_0 is the velocity of light in free space, given by $(\mu_0\epsilon_0)^{-\frac{1}{2}}$. The subsurface reflection, as discussed previously, arrives in a time

$$t_1 = \frac{2R(\theta,\phi)}{C_0} + \frac{2R_d}{C_1} \qquad (22\text{-}14)$$

In the simplest example, one would generate a transmitter pulse τ_0 as narrow as possible (i.e., design a system bandwidth as wide as possible) so as to achieve the best resolution. That is, two pulses can be resolved if separated by approximately τ_0, so that the minimum depth that can be resolved is

$$R_{d_{\min}} = \frac{\tau_0 C_1}{2} \qquad (22\text{-}15)$$

However, for the ALSE pulse

$$\tau \gg \Delta t = t_1 - t_0 = \frac{2R_d}{C_1} \qquad (22\text{-}16)$$

while the FM pulse sweeps over a maximum designable bandwidth. In the data processing stage, the pulse is collapsed (or compressed) to achieve the full bandwidth resolution consistent with low side lobes (fig. 22-3), the compression factor being equal to the time-bandwidth product of the signal. A dispersed pulse is used for two basic reasons: (1) the recording medium (film) has a relatively low dynamic range and the dispersion of energy is necessary to preserve the rather large dynamic range inherent in the data and required in the experiment; and (2) pulse compression increases the effective peak power of the pulse and hence the dynamic range of the data by the
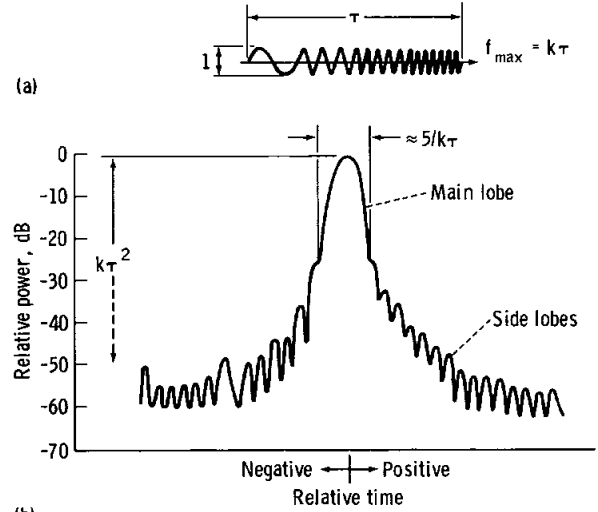
FIGURE 22-3.—Schematic illustration of chirp (linear FM) pulse with sweep rate k and the same pulse upon compression. (a) Pulse. (b) Compressed pulse.

time-bandwidth factor, thus negating a need for large-peak-power transmitters.

Figure 22-3 shows an idealized version of a linear FM sweep pulse (fig. 22-3(a)) and the same pulse upon compression (fig. 22-3(b)). One reason for choosing the linear FM sweep pulse is that during optical processing of the data, only simple optics are required for the compression step. One disadvantage of the dispersed energy scheme is the generation of side lobes upon compression as shown in figure 22-3(b). The side lobes tend to mask weak subsurface events. In practice, the frequency spectrum of the chirp signal is weighted to produce a decrease in the side lobes, at the expense of resolution. Additionally, any phase errors in the ALSE system tend to raise side-lobe levels. However, it is possible to compensate for systematic phase errors during digital processing and, hence, to preserve the low side lobes of the waveform.

Doppler History

To this point, the discussion has centered on a single pulse of electromagnetic energy. To complete the picture, the repetitive nature of the pulses must be considered. For the two HF systems, chirped pulses were transmitted at a rate of 400 pulses/sec; the VHF rate was 2000 pulses/sec. The received pulses are recorded side by side on the continuously moving optical recorder film. Across the film, in the

range direction, the time history of a single pulse is recorded. The along-track or azimuth history is recorded along the film. Consider a geologic feature or target on the surface in a ray direction u_r. If the spacecraft has a velocity V in the direction X, then each frequency of the return echo will have undergone a phase shift

$$\Delta\theta = \frac{2\pi|V|t^2}{\lambda} \, X \cdot u_i \qquad (22\text{-}17)$$

corresponding to the instantaneous Doppler-frequency shift

$$\Delta f_d = \frac{1}{2\pi}\frac{\partial\theta}{\partial t} = \frac{2|V|}{\lambda} \, X \cdot u_i \qquad (22\text{-}18)$$

Any return from the subsurface will have a Doppler-frequency shift determined by the angle between the direction of the spacecraft flight and the point on the surface where the subsurface ray emerges.

Because of the high pulse-repetition rate, a given target will be illuminated by many pulses. Because the spacecraft is in a different position for each transmitter firing, each pulse will arrive in general

from a different ray direction and hence will have a different Doppler-frequency shift. As the spacecraft traverses a target, the Doppler history of the target is recorded in the azimuth direction. Thus, the concept of the two-dimensional frequency spectrum of a target is realized (fig. 22-4). The range-frequency axis of this spectrum corresponds to the ordinary Fourier transform of the time history of the received energy, whereas the orthogonal frequency coordinate (azimuth) corresponds to the Doppler-frequency spectrum of the target. Models for two idealized lunar targets are compared in figures 22-4(a) and 22-4(b); the comparison includes the range-frequency spectra and the range-frequency/Doppler-frequency plane for each target. In practice, the signal is narrow-band-Doppler filtered, realizing a dynamic range improvement equivalent to the ratio of the total spectrum width to the filter bandwidth.

Profiling

As a result of the high pulse-repetition rate of the CSAR, a quasi-continuous surface profile is available. Elements of recovering the surface profile include, for
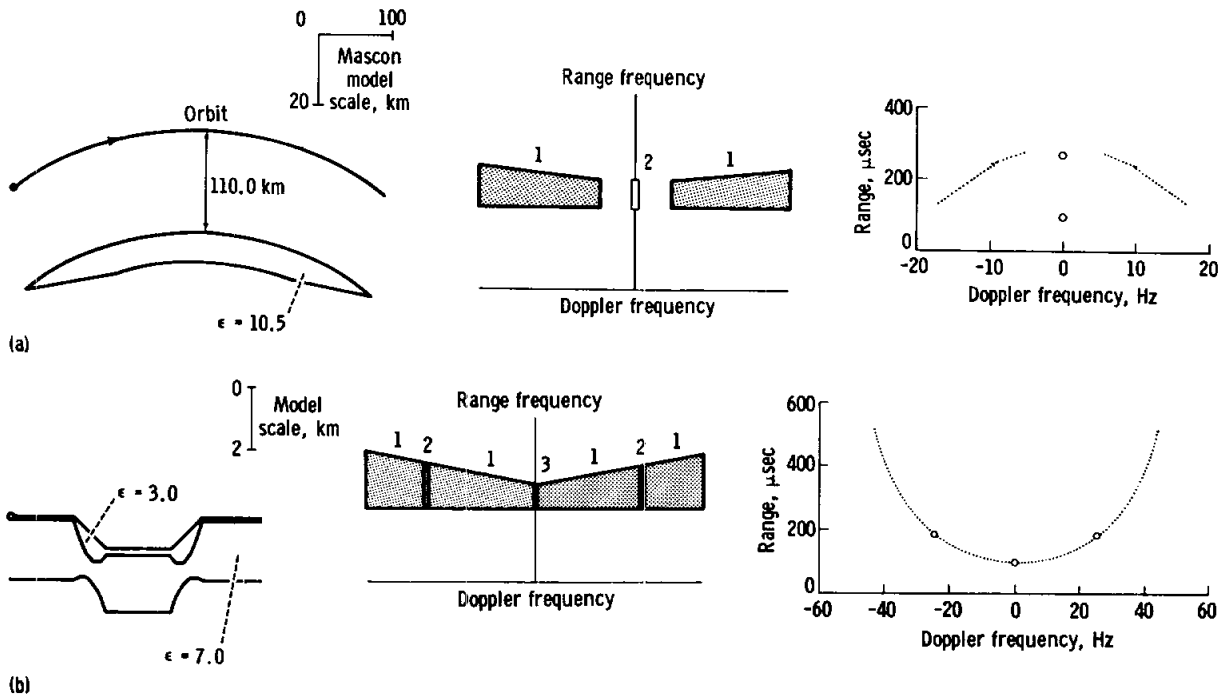
FIGURE 22-4.—A comparison of two schematic lunar models (left), showing their two-dimensional frequency response (center) and the range/Doppler-frequency plane (right). Numbers (1, 2, 3) in center diagrams indicate superposition of one, two, or three returns. No attempt is made to show relative strengths of returns. (a) Model of Serenitatis mascon. (b) Model of highland graben rille.

a given pulse, absolute location of the spacecraft in selenographic coordinates, absolute delay times through the ALSE system, and the estimated arrival time of a reflected surface pulse. Theoretically, the standard deviation of the range estimate for a perfectly flat surface is given by

$$\sigma_R \approx \lambda \, \frac{5}{\sqrt{2 \, \text{SNR}}} \approx \frac{\lambda}{10} \qquad (22\text{-}19)$$

where SNR is the signal-to-noise ratio for the compressed pulse. In practice, the range accuracy is limited by the topographic variation within a surface resolution element of the radar. The basic resolution element is given by the Fresnel zone radius

$$r_f = \sqrt{h\lambda} \qquad (22\text{-}20)$$

where h is the altitude of the spacecraft, or by the pulse illumination radius

$$r_\tau = \sqrt{\tau C_0 h} \qquad (22\text{-}21)$$

whichever is smaller. Additionally, if the radius of the typical specular facet r_s on the lunar surface is less than minimum (r_f, r_τ), then r_s controls the resolution.

In regions of complex topography, the ray returning to the spacecraft may not represent the spacecraft-nadir topography, and ray-tracing algorithms must be used to recover the true profile. Alternatively, the various rays can be sorted by their Doppler history, and Doppler filtering can be used to reduce the size of the resolution element.

Imaging

The imaging capability of the ALSE depends on the capability of the lunar surface to backscatter an incident ALSE pulse in the direction of the spacecraft. Assume as a model for the lunar surface a random distribution of point scatterers. Each scatterer has an isotropic scattering function, and the received signal is the sum of energy from all point scatterers. Consider a single frequency component of the chirp pulse f_0. For a single point scatterer, the amplitude of the received signal A_r is

$$A_r = \left[\frac{P_t G^2(\theta,\phi) \lambda^2 \sigma}{(4\pi)^3 R^4(\theta,\phi)} \right]^{1/2} \exp \left\{ i \left[2\pi f_0 \left(t - \frac{2R(\theta,\phi)}{C_0} \right) \right] \right\}$$

$$(22\text{-}22)$$

where σ is the scattering function of the point scatterer, and the complex representation of the sinusoid is used. The ray distance $R(\theta,\phi)$ may be decomposed into a slant range component R_0 orthogonal to the flightpath and a component along the flightpath X_0

$$R(\theta,\phi) = \sqrt{R_0^2 + X_0^2} \approx R_0 + \frac{X_0^2}{2R_0} \qquad (22\text{-}23)$$

if $X_0 \ll R_0$. The argument of the exponential term in equation (22-22) then becomes

$$i\phi = i \left[2\pi f_0 \left(t - \frac{2R_0}{C_0} - \frac{X_0^2}{C_0 R_0} \right) \right] \qquad (22\text{-}24)$$

where $2R_0/C_0$ is a constant-phase term and may be ignored for this discussion. Substituting $|V| t = X_0$, the last term of equation (22-24) is $2\pi f_0 |V|^2 t^2 / C_0 R_0$ with instantaneous frequency

$$f_i = \frac{2f_0 |V|^2 t}{C_0 R_0} = \frac{2|V|X_0}{\lambda R_0} \qquad (22\text{-}25)$$

As the spacecraft traverses in the X direction, then equation (22-25) reveals that a linear FM or chirp component is added to f_0. Further

$$\frac{X_0}{R_0} \approx \mathbf{X} \cdot \mathbf{u}_i \qquad (22\text{-}26)$$

and comparison to equation (22-18) shows that f_i is in fact the Doppler-frequency shift Δf_d.

In reality, σ is not an isotropic scattering function and this fact, together with phase instabilities in the ALSE hardware and finite antenna beamwidth, leads to some maximum $X_0 = \pm X_{max}$ through which a point scatterer may be coherently recorded. The range of Doppler frequencies then extends over

$$\pm \frac{2|V|X_{max}}{\lambda R_0} \qquad (22\text{-}27)$$

implying a Doppler bandwidth of

$$\Delta f_d = \frac{4|V|X_{max}}{\lambda R_0} \qquad (22\text{-}28)$$

The azimuth resolution implied is thus

$$t_{res} = \frac{\lambda R_0}{4|V| X_{max}} \qquad (22\text{-}29)$$

with a corresponding spatial resolution

$$\rho_a = \frac{\lambda R_0}{4 X_{max}} \qquad (22\text{-}30)$$

The total distance traversed by the spacecraft is $L = 2X_{max}$ so that $\rho_a = 0.5(\lambda R_0 / L)$. The factor in parentheses is the resolution obtained by a physical aperture of length L; the 0.5 is due to two-way propagation. Thus, the spacecraft sequentially records the scattered return along a flightpath of length L and synthesizes an antenna of this length. The chirped signal in the azimuth direction is compressed in the data processing stage, analogous to range compression, to achieve the desired resolution. Each individual point scatterer gives an unambiguous response to this step. The film is integrated in the azimuth direction for a time period that is typically chosen to give 5λ resolution; that is

$$\frac{R_0}{2L} = \frac{R_0}{4 X_{max}} = 5 \qquad (22\text{-}31)$$

or

$$t_{res(5\lambda)} = 5\lambda |V| \qquad (22\text{-}32)$$

The time resolution in the range direction is given by approximately

$$\rho_s = \frac{C_0}{2\beta} \qquad (22\text{-}33)$$

where β is the system bandwidth. If ψ is the angle between R_0 and the ground plane, then the ground range resolution is $\rho_r = \rho_s \sec \psi$.

THE ALSE SYSTEM

The HF Antennas

The HF-1 and HF-2 systems used a dipole antenna of 0.4 and 1.2 wavelengths, respectively. To achieve an antenna tip-to-tip length of 24 m, two extendable/retractable elements were required. A retracted element was spooled as two flat metallic ribbons, which, upon extension, curled together into a circular

rod (fig. 22-1). To match the complex antenna impedance to the radar, an electrical network was constructed and mounted in the antenna housing. A hybrid unit mounted in the scientific instrument module provided the power division and the appropriate electrical phase to feed the antenna elements as a dipole. To maintain low side lobes, the antennas were designed with extreme amplitude and phase linearity across the bandwidth. This was done at the expense of antenna efficiency; the minimum efficiency across the band was 65 percent for the HF-1 system and 43 percent for the HF-2 system.

The VHF Antenna

The VHF antenna was designed to satisfy a linear amplitude and phase response as well as a directionality requirement. The antenna was a yagi of five directors and one reflector (fig. 22-1). The yagi, mounted at the rear of the service module, was erected by a spring mechanism when the CSM separated from the Saturn launch adapter. The antenna had a beamwidth of 70° in the plane containing the antenna elements and a beamwidth of 50° in the orthogonal plane. To suppress ambiguity between terrain returns on the left and right sides of the spacecraft in the imaging mode, the antenna axis was pointed 20° off nadir.

The Radar (CSAR) System

The central element of the radar system (figs. 22-5 and 22-6) was the frequency reference, which provided a stable reference for all system timing and sweep generation. The FM sweep was obtained by driving a voltage-controlled oscillator (VCO) with a ramp voltage. Each frequency was swept approximately 10 percent as follows: HF-1, 5 to 5.53 MHz; HF-2, 15 to 16.6 MHz; and VHF, 150 to 166 MHz. The VCO was phase locked to a stable local oscillator to retain pulse-to-pulse coherency. The signal was transmitted after a slight shaping of the risetime and falltime of the pulses; the reflected signal was received in a broadband phase-locked receiver to preserve phase and amplitude response and then converted to a video signal for storage in the optical recorder. The receiver used stepwise automatic gain control to stay within the dynamic range constraints of the film. Additionally, the VHF receiver had a sensitivity time control wherein a gain of 20 dB was
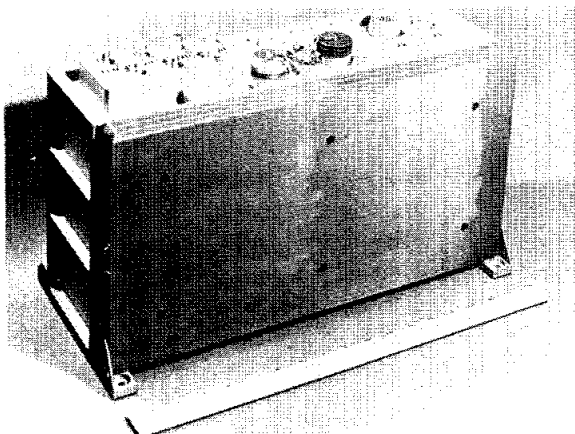
FIGURE 22-5.—Photograph of the CSAR.

added 13 μsec after detection of the specular return to enhance the imaging capability. The CSAR parameters are summarized in table 22-I.

The Optical Recorder

The primary function of the optical recorder (figs. 22-7 and 22-8) was to process the CSAR output, record the output of the CSAR on film, and time reference the received signals for later data reduction and analysis studies. The video signal from the CSAR was used to modulate the intensity of the CRT beam while the beam was deflected rapidly across the range direction of the film. Simultaneously, the film was slowly moved across the face of the CRT in the azimuth direction.

The CRT was swept at one of two basic rates depending on the operation mode of the CSAR. The sweep frequencies for the HF and VHF modes were approximately 396.8 and 1984.1 sweeps/sec, respectively. The VHF mode used an echo tracker function that enhanced the resolution of the recorded data. Instead of monitoring the entire 275 μsec that the receiver gate was open, a 70-μsec section, or "win-
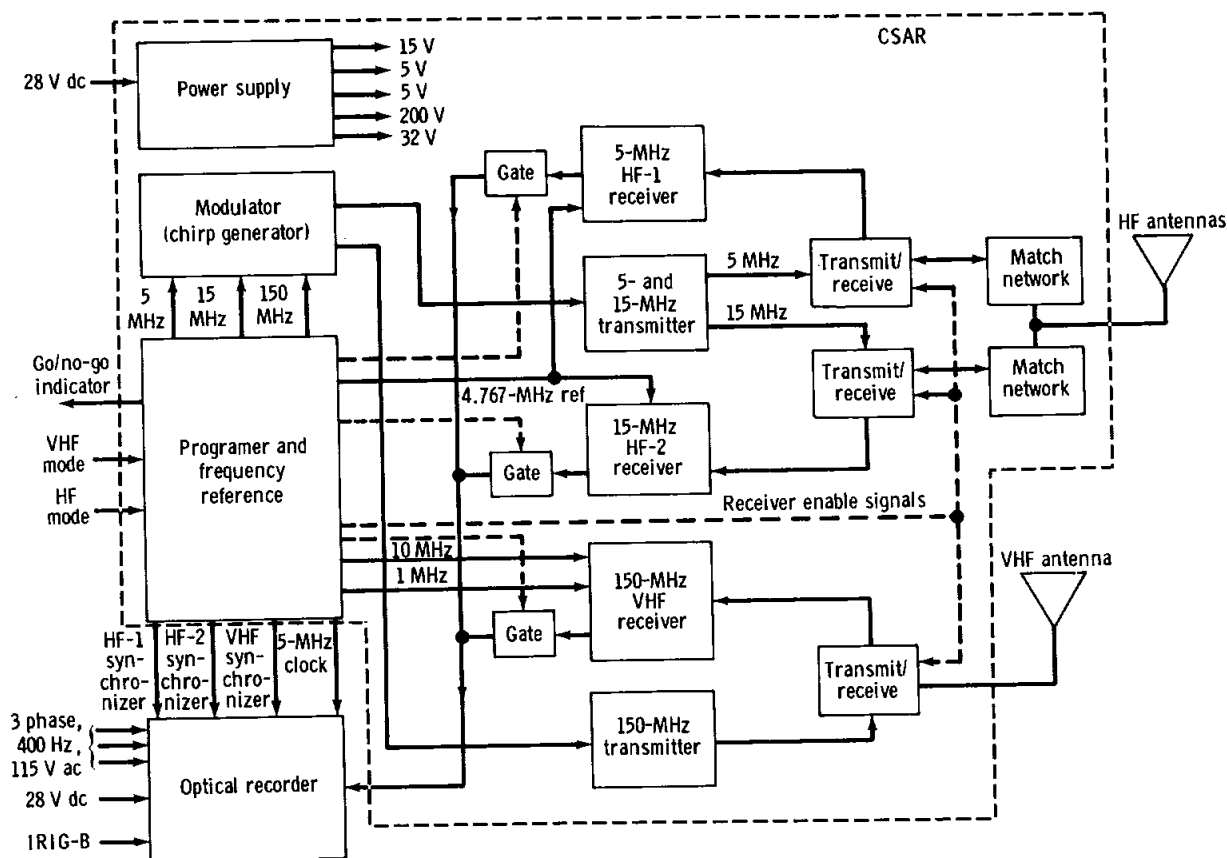
FIGURE 22-6.—Block diagram of the CSAR.

TABLE 22-I.—*ALSE Radar System Parameters*

Parameter	Operating mode		
	HF-1	HF-2	VHF
Nominal wavelength, m	60	20	2
Initial frequency, MHz	5	15	150
Frequency rate, kHz/μsec	2.222	20.0	2000
Frequency sweep, MHz	.533	1.6	16
Pulse duration, μsec	240	80	8
Pulse risetime, percent	3.6 ± 0.4	3.6 ± 0.4	10 ± 0.5
Pulse-repetition period, μsec	2520	2520	504
Pulse energy, J	.02 to .026	.007 to .009	.0007 to .0009
Time-bandwidth product	128	128	128
Receiver output frequency range, MHz	.233 to .766	.9 to 2.5	3.0 to 19.0
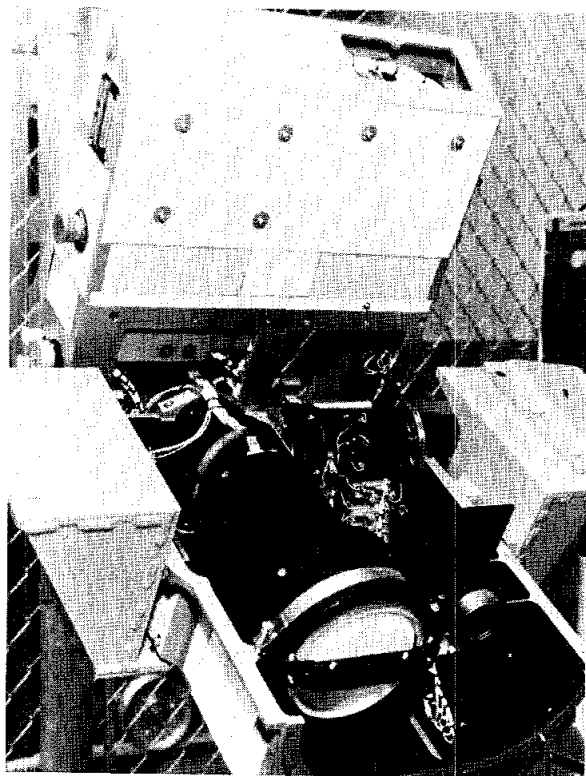
FIGURE 22-7.—Photograph of the optical recorder.

dow," of the data was recorded. The tracker circuit had the capability to shift the 70-μsec window in 25-μsec increments until the window contained the return signal. The 275-μsec gate is required to take into account variations in spacecraft orbit and lunar topography. For short periods of time, however, 70 μsec were sufficient to record the returned signal.

Because the time-bandwidth product of the CRT could not exceed 1300, echo tracking allowed a larger bandwidth and, hence, finer resolution.

Five auxiliary data tracks were included on the film exposed by the optical recorder, recording an IRIG-B time code as well as engineering information. Additionally, an optical recorder frequency response calibration signal was recorded at the start of every CRT sweep to maintain recorder calibration.

DATA PRODUCTS

Before considering the preliminary results, it is worthwhile to discuss the data products of the ALSE. The prime data storage medium is the signal film recovered from the optical recorder during the transearth-coast extravehicular activity. The signal film may be processed by optical techniques, by digital techniques, or by an optical-digital combination.

Optical processing techniques allow the use of optical setups for batch processing of the data. The linear FM property of both the signal and the Doppler signature of point targets may be viewed as a linearly varying diffraction grating. Such a grating will collapse or focus incident coherent collimated light, accomplishing the desired compression step (fig. 22-9). Additionally, spherical lenses are used for a Fourier transform of the data and to place the signal frequency plane in the optical path. Here, the range spectrum is shaped to reduce side-lobe levels, and, in general, two-dimensional range-Doppler filtering is performed. The focused output appears in the image plane; additional lenses (cylindrical telescopes, not
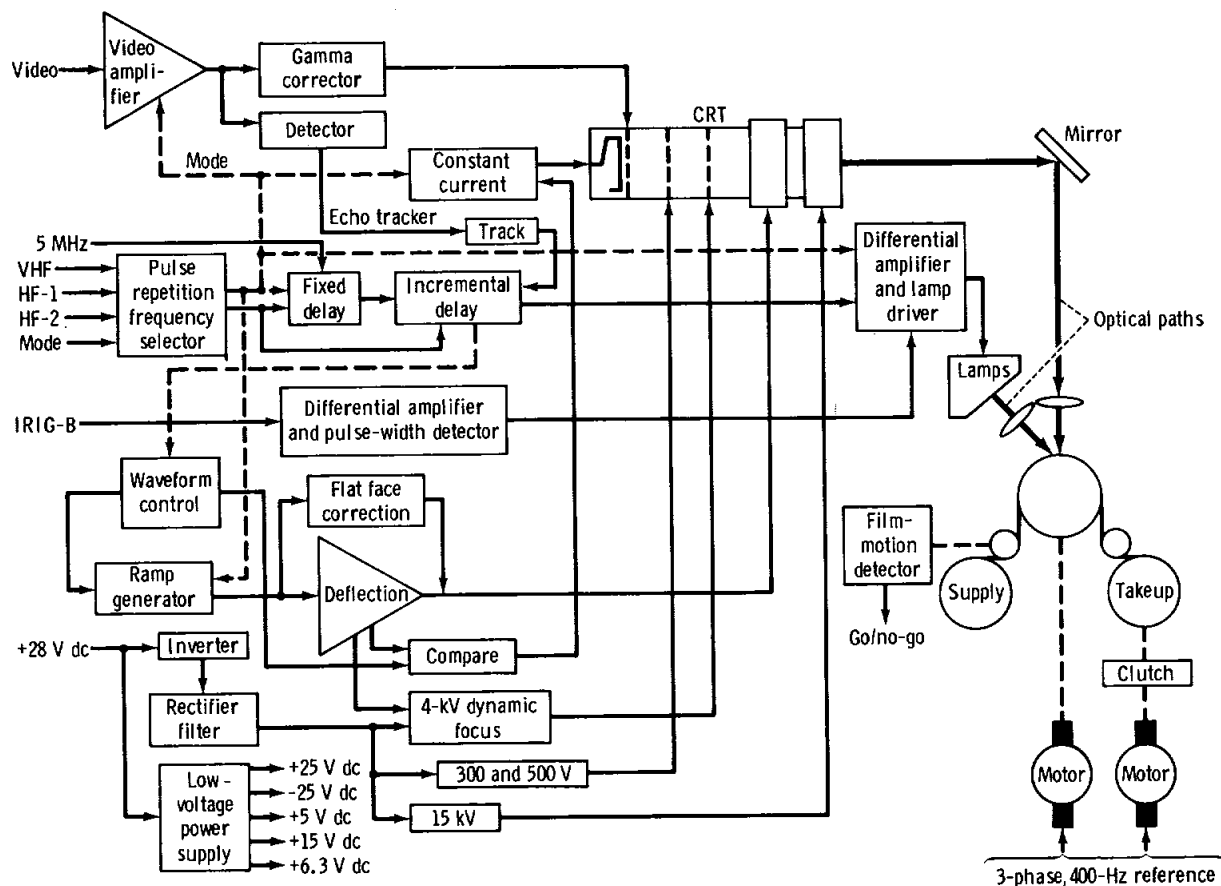
FIGURE 22-8.—Block diagram of the optical recorder.
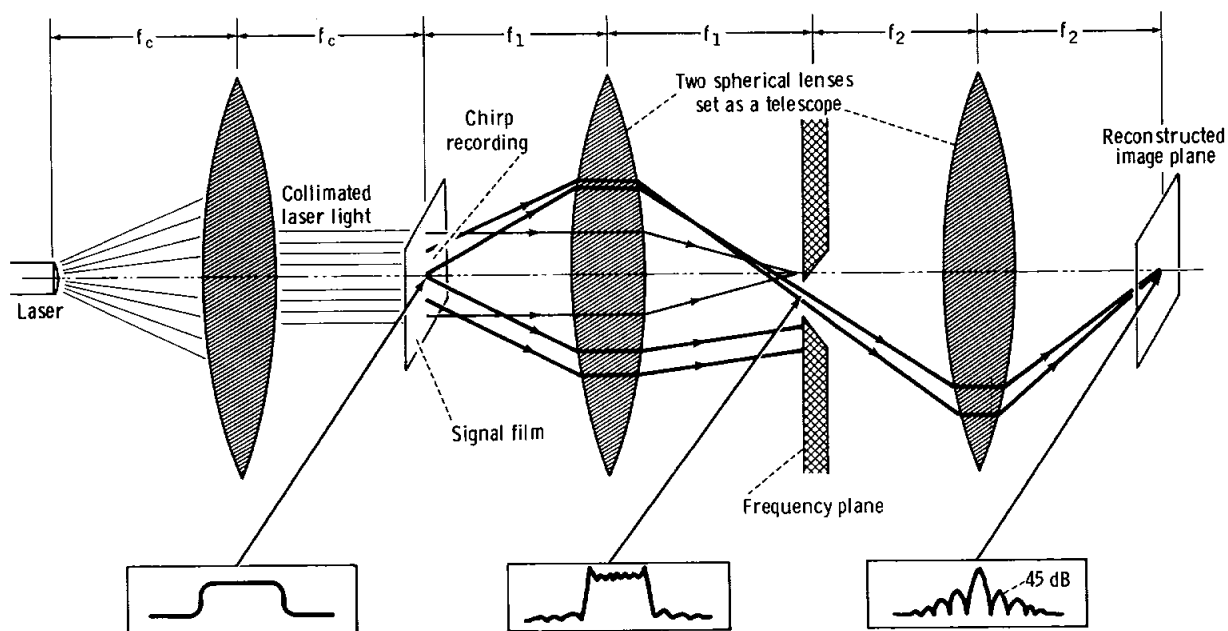
FIGURE 22-9.—Schematic illustration of optical setup. Focal distances are designated f_1, f_2, and f_c.

parison with figure 22-13 shows that the events are probably not side lobes but are likely subsurface or surface returns that are coherent for at least 15 km. It is possible that a time-varying systematic phase error could cause a similar response, but, to date, results obtained primarily from prelaunch testing have indicated that this is probably not the case. This possibility will be further investigated by comparing results from multiple orbits over similar lunar regions.

The general approach was to take nonoverlapping sets of records and to process 5-, 10-, and 15-km stacks. Events were plotted in cross sections, and those events that appeared to be alined for at least three separate stacks were connected by straight lines (fig. 22-16). In addition, single events are shown for the 15-km stacks.

It is important to note that the coherence length of a geologic structure may be much less than the actual physical length of the structure. It may be possible to map out the structure by a series of short stacks, but the structure may be noncoherent for a length equivalent to the physical length. An example of this is the second event shown on the right side of the cross sections in figure 22-16. The event persists in five 5-km stacks and three 10-km stacks, indicating a geologic length of 25 to 30 km. The event appears only in the most easterly 15-km stack and is noncoherent for the 15-km stack to the west. The most likely cause of the noncoherence is the (apparent or real) dip of the feature. The stacking process, as described previously, is only coherent for events approximately parallel to the actual lunar surface. (The topographic profile has been mapped into the horizontal line indicating zero apparent depth in fig.
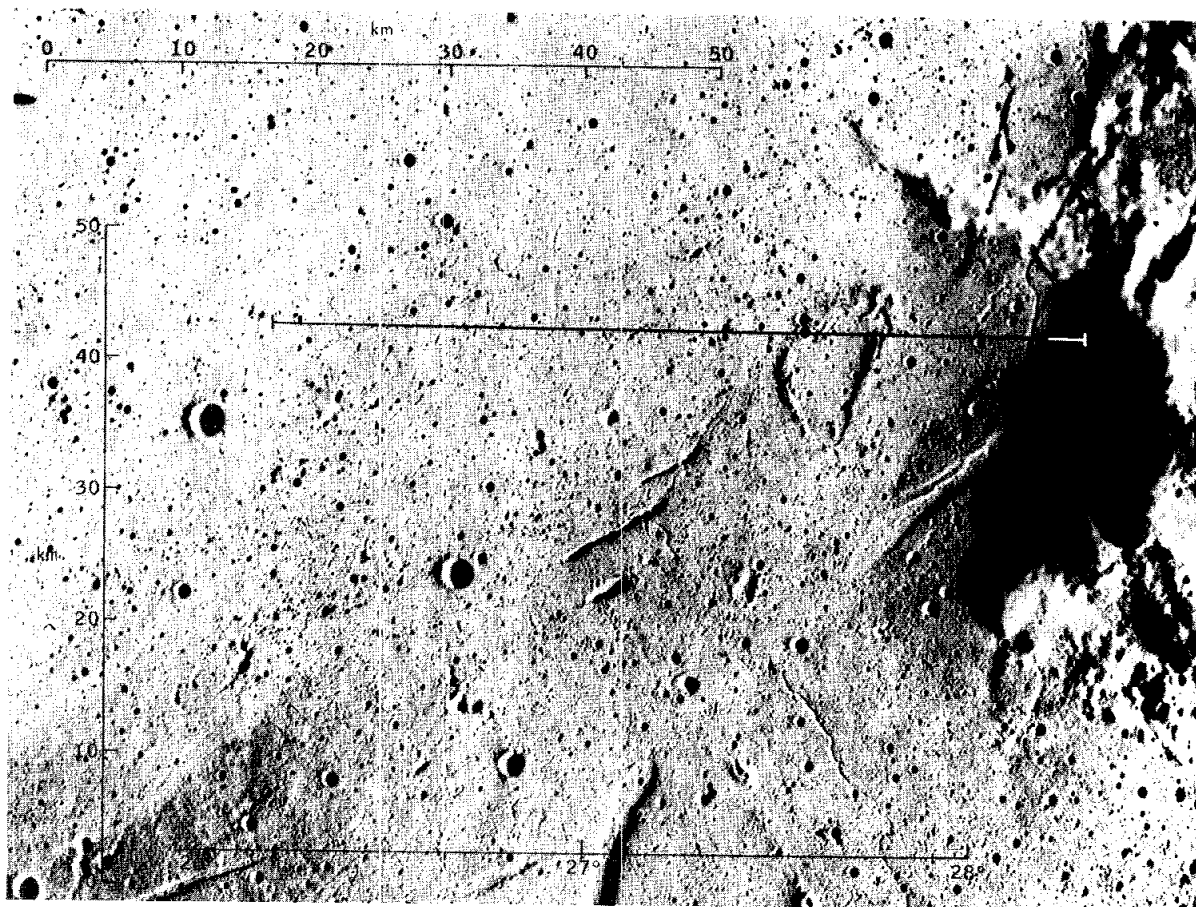
FIGURE 22-12.—Groundtrack for digital data reduction test area shown on Apollo 17 metric camera frame AS17-0598. Area is located at eastern boundary of Mare Serenitatis. Scale at bottom is longitude, degrees east.
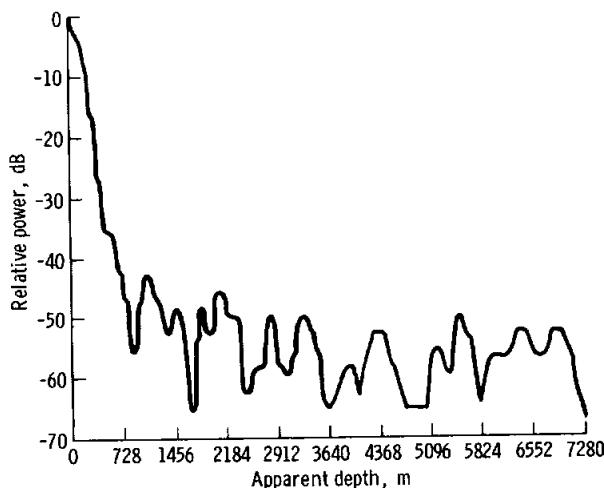
FIGURE 22-13.—Side-lobe response of the ALSE determined from 1200-record stack. Depth is derived by converting time to distance, using a relative dielectric constant of 4 to obtain velocity.
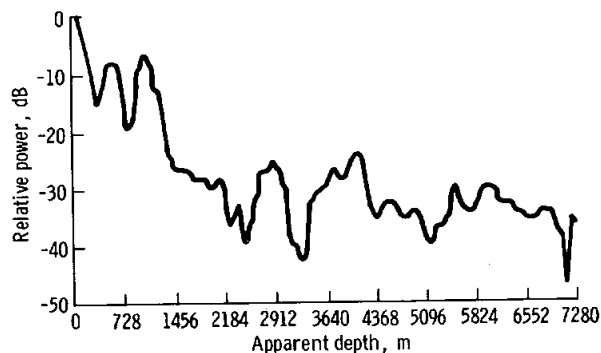
FIGURE 22-14.—Lunar return for one record, showing high clutter level. Depth is derived by converting time to distance, using a relative dielectric constant of 4 to obtain velocity.

22-16(c).) Later digital processing capabilities will include directional stacking. Events with a low signal-to-clutter-noise ratio may only show up for longer stacking lengths. An example of this case is the event that occurs on each of the 15-km stacks with an apparent depth of approximately 700 m.

As discussed previously, a surface location for these events requires the fortuitous occurrence of linear features that are parallel to the flightpath and that also present surface normals pointing to the spacecraft. Preliminary photogeologic examination of Apollo 15 and Apollo 17 photographs reveals no such features.
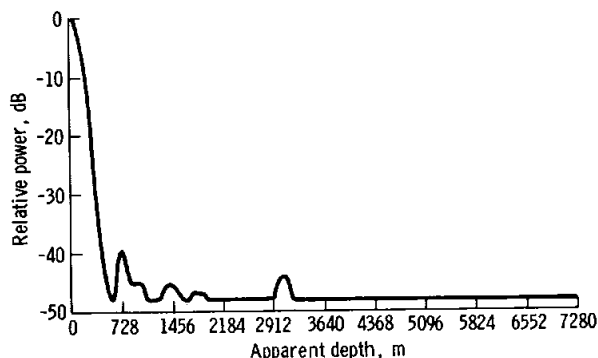
FIGURE 22-15.—Lunar return for 300-record (15 km) stack. Depth is derived by converting time to distance, using a relative dielectric constant of 4 to obtain velocity.
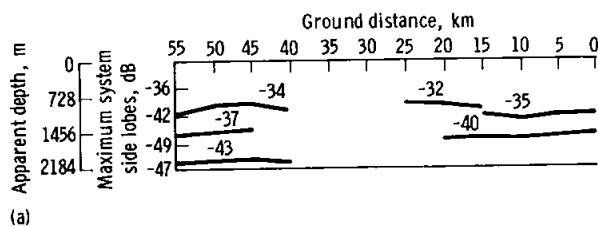
(a)
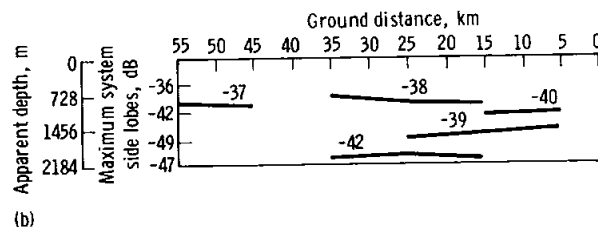
(b)
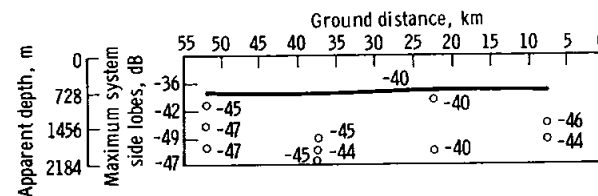
(c)

FIGURE 22-16.—Apparent cross section for eastern Mare Serenitatis region for 5-, 10-, and 15-km stacks. Depth is derived by converting time to distance, using a relative dielectric constant of 4 to obtain velocity. The data begin at approximately latitude 20° N, longitude 28.5° E, on lunar revolution 16. The inner ordinate scale indicates the position and maximum strength (relative to the specular surface return main lobe) of the surface return side lobes. Events are labeled with their relative energies. East is to the right; west, to the left. (a) 100 stacked spectra (5 km). (b) 200 stacked spectra (10 km). (c) 300 stacked spectra (15 km).

The event strengths relative to the surface specular strength are also shown in figure 22-16. If these are subsurface features, then they indicate a lunar loss tangent and a relative dielectric constant slightly lower than had been anticipated. Furthermore, a complex stratigraphy is indicated for the eastern margin of Mare Serenitatis.

Profiling and Imaging

Characteristics of Imagery

Data processing techniques to produce surface profile imagery and side-looking surface imagery in spacecraft flight-time/echo-delay-time coordinates are well developed and were available for quick-look images to yield preliminary results from the ALSE. The ALSE radar image is a composite of a surface

(a)

(b)
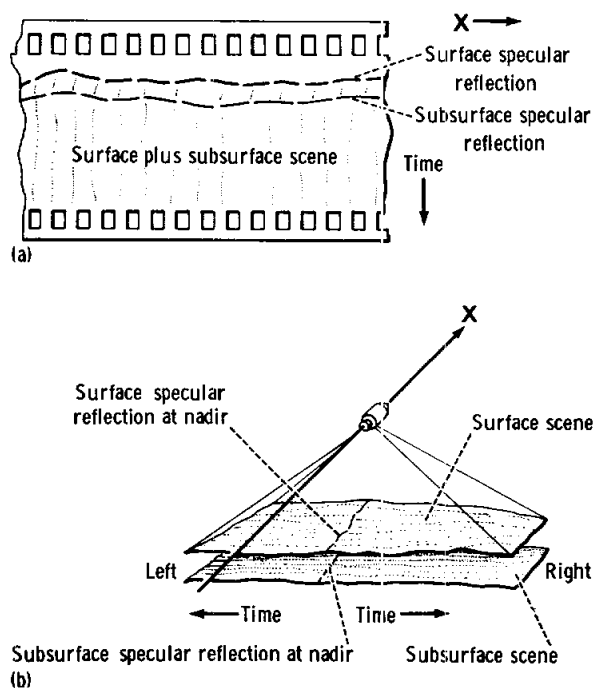
FIGURE 22-17.—Relationship between actual scene and radar image of scene. The earliest return is the surface specular reflection followed by backscatter creating the surface scene. At some later time, the much weaker subsurface specular reflection and scene, both generally not seen in imagery, superimpose upon the surface scene. Additionally, "left" and "right" scenes are superimposed. However, the VHF antenna was oriented 20° off nadir to suppress the left scene. (a) Radar image of scene. (b) Actual scene.

profile along the groundtrack of the spacecraft and two side-looking images (fig. 22-17). The profile appears at the top of the image, and the two side-looking surface images stretch below the profile and are superposed on each other. The side-looking imagery to the right and left of the spacecraft groundtrack for HF imaging have equal intensity. For VHF imaging, the 20° off-vertical positioning of the antenna beam greatly reduced the superposition, or left-right ambiguity problem. However, stereoscopic viewing of overlapping images from adjacent revolutions permits separation of the two images. (See the discussion under "Stereoscopic ALSE Imagery.")

The side-looking HF imagery (figs. 22-18(a) and 22-18(b)) is dominated by the discontinuous scattering of near-specular reflections from surface elements. There is little continuous imaging in the scene because, in preliminary processing, only a small part of the Doppler history of a feature, centered around zero Doppler shift, was retained. Thus, the near-specular returns from slopes with contours oblique to the spacecraft groundtrack, seen only with positive or negative Doppler shifts while approaching or departing from oblique slopes, are filtered out during conversion from signal film to image film. Only very weak signal returns near zero Doppler are passed to the image film for the oblique slopes.

The VHF imagery (fig. 22-18(c)) has much more pictorial content than the longer wavelength imagery. This detail results primarily from the finer ground resolution of the 2-m-wavelength radar and the greater abundance of small-scale features discernible at the 2-m wavelength. The slopes of these features with contours parallel to the spacecraft groundtrack densely populate the radar image with near-zero Doppler, near-specular, small images. This effect is conspicuous in part of figure 22-18(c), to the left of center.

Utility of Images

The profiles, when closely correlated with orbital camera photographs, yield abundant quantities of important metric data on the vertical relief and slopes of a host of lunar geologic features. Preliminary imagery, the first data produced, also contains "qualitative" profile information. Although the ellipticity of the CSM orbit has not yet been removed from the data, the profiles are immediately useful for addressing local selenomorphological problems. A later step

(a)

(b)

(c)
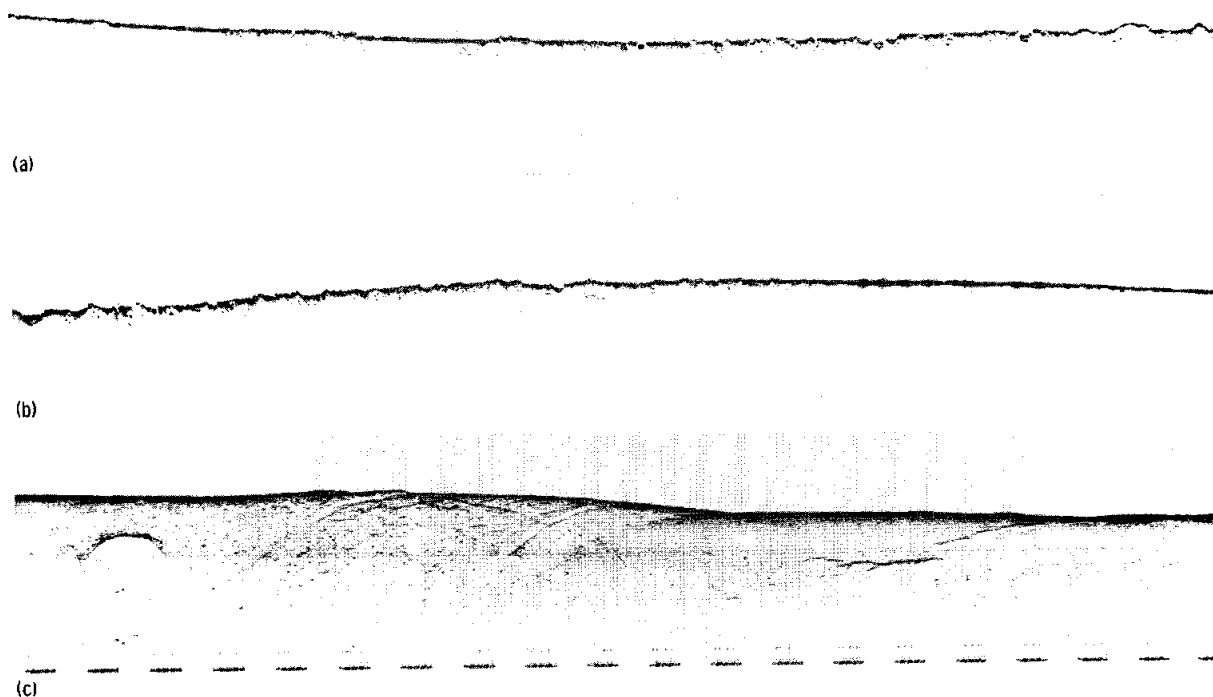
FIGURE 22-18.—Typical ALSE imagery. (a) HF-1 profile of one-half lunar revolution including (right to left) far-side highlands, Mare Crisium, and Mare Serenitatis. (b) HF-1 profile of one-half lunar revolution including (right to left) Mare Imbrium, Oceanus Procellarum, and far-side highlands. (c) VHF image of the Tranquillitatis-Serenitatis boundary region. Time marks (bottom) represent ground spacing of approximately 15 km.

in the ALSE data processing will include digitizing of the signal film and recovery of the "quantitative" profile, as discussed previously.

The global profiling capability of the ALSE is suggested by figures 22-18(a) and 22-18(b) showing an HF-1 image for one revolution of the Moon. The profile is superimposed on the sinusoid resulting from the elliptical orbit. As a point of reference, the crater Aitken, approximately 80 km wide under the orbital track and approximately 5 to 6 km deep from rim to floor, appears at the extreme left of figure 22-18(b). The spacecraft track may be followed, right to left and top to bottom, progressing from far-side highlands across Mare Crisium and Mare Serenitatis (all in fig. 22-18(a)) on to Mare Imbrium, Oceanus Procellarum, and far-side highlands (all in fig. 22-18(b)).

The local profiling-imaging capability of the ALSE is illustrated in figure 22-18(c), a north-looking VHF image recorded during revolution 73.

An important aspect of the ALSE imagery is that it provides a source of improved positional information across a substantial area of the eastern lunar far side. Unlike all Apollo orbital camera imagery, ALSE imagery does not depend on solar illumination. As a result, the ALSE side-looking surface imagery is the only Apollo imagery obtained between longitudes 68° and 152° W (other than very limited, 1-km-resolution earthshine photography, ref. 22-1). For determination of lunar positions in terms of a coordinate measured along the length of the orbit, this ALSE imagery is free from the troublesome mosaicking and rectification problems that beset the determination of lunar positions in this region from the melange of variously scaled and tilted Lunar Orbiter images covering the area.

One other significant aspect of the side-looking surface imagery is that, in some places, where slope effects are negligible or predictable, local differences in relative radar albedo can be read directly from the side-looking imagery.

Stereoscopic ALSE Imagery

A major aid to the use of the geometrically complex ALSE imagery derives from the observation format in which much of the data was obtained. Of the approximately six revolutions of data that were collected, a little more than two revolutions each were gathered during adjoining revolutions by using the HF systems (20-m- and 60-m-wavelength imagery) on the one hand and by using the VHF system (2-m-wavelength imagery) on the other. Essentially all the 60-m-wavelength imagery from adjacent revolutions and much of the 2-m-wavelength imagery from adjoining revolutions can be viewed stereoscopically with the result that the side-looking images from the two sides of the pair of adjoining orbital tracks become segregated in space in the stereoscopic image. Otherwise, the two side-looking images to the north and south of the track in a single composite radar image are superposed on each other in some monoscopic image space. The effect of stereoscopic viewing is as though a radar range of a strip of the lunar surface were wrapped around a hyperbolic cylindrical surface tangent to the radar profile (fig. 22-19). Stereoscopically, the lunar relief is seen superposed on the general cylindrical form of the image. The format of the radar data permits close correlation of the side-looking radar imagery with the orbital camera imagery. Thus, very exact location of the radar profile among and within lunar features, as recognized in the camera imagery, is possible.

Stereoscopic HF Imagery

A sample of stereoscopic HF imagery was studied and measured to evaluate the feasibility and the achievable precision of measuring the relative positions of individual features in the stereoscopic images. The locations numbered in figure 22-20 were identified in the three-dimensional image formed by viewing stereoscopically the radar images obtained on revolution 16-17 and revolution 17-18. For the time
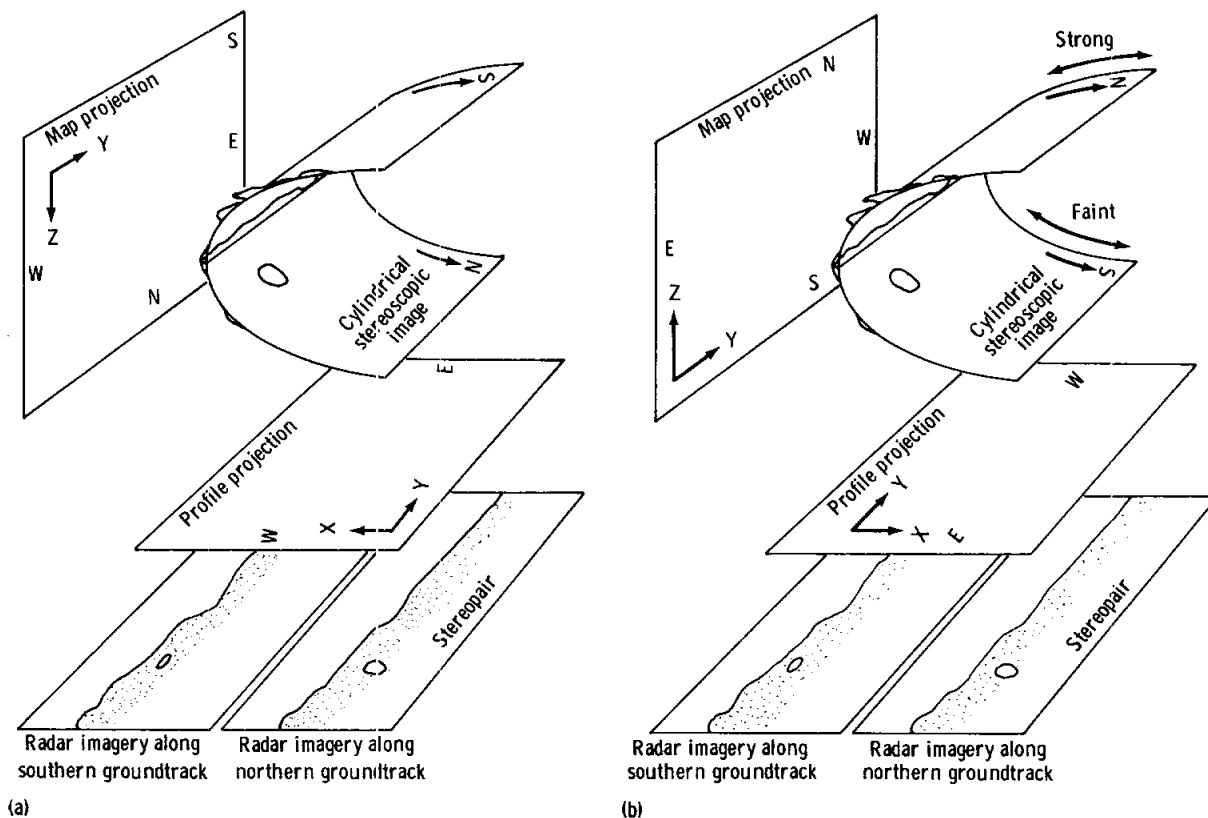
FIGURE 22-19.—Stereoscopic viewing geometry showing "map" and "profile" projections, as well as cylindrical cross-section profile. (a) HF. (b) VHF.
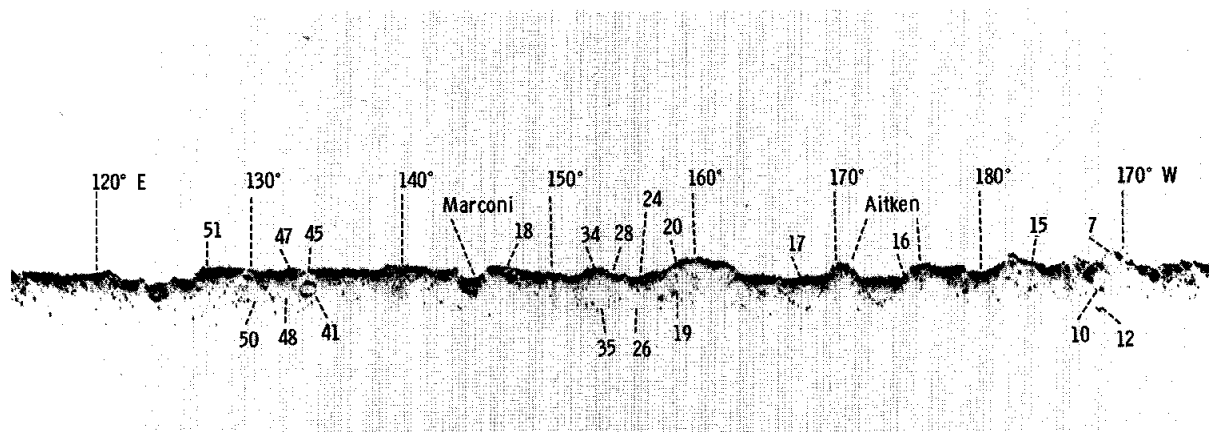
FIGURE 22-20.—A segment of 60-m-wavelength ALSE imagery in the western half and central part of
the lunar far side obtained on revolution 16-17. The numbered points correspond to those in figure
22-21 and are explained in the text. The longitudes in this figure and in figure 22-22 are
preliminary and are probably correct within approximately $0.5°$.
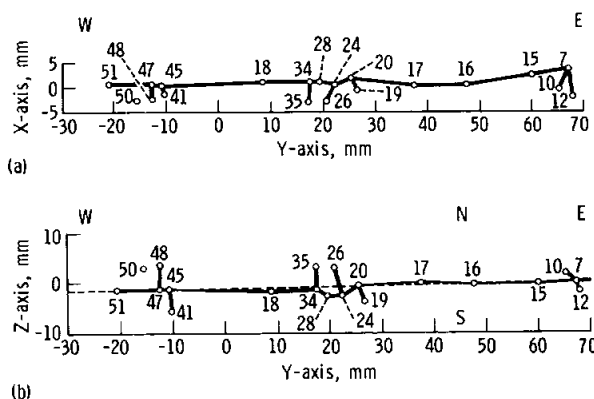
FIGURE 22-21.—Plots of the stereoscopic image coordinates
of points numbered in figure 22-20 as seen by stereo-
scopic viewing of the 60-m-wavelength ALSE images
along revolutions 16-17 and 17-18. Coordinates are
measured at the scale of the original 70-mm image film.
(a) Profile. (b) Map.

being, the map projection of the cylindrically dis-
torted image has been measured. Ultimately, measure-
ments rectified to conventional lunar coordinates will
be sought. The coordinates of the points in the
stereoscopic model were measured by using a com-
puterized analytical stereoplotter and are plotted in
figure 22-21. An interim arbitrary orthogonal coordi-
nate system was used (fig. 22-19(a)). The system was
oriented with the Y-axis approximately along the
profile (plus-Y eastward) and the X-axis in the plane
of the monoscopic images (plus-X upward in the
profile). The Z-axis was oriented perpendicular to the

plane of the monoscopic images in the direction of
stereoscopic depth (plus-Z northward). The coordi-
nates were read in millimeters at the scale of the
original 70-mm image film. In a set of 51 measured
points, readings of the coordinates in the plane of the
film were repeatable to within 5 or 10 μm and depth
measurements of the stereoscopic image perpendicu-
lar to the plane of the film were repeatable to within
approximately 50 μm in a range that varies from
more than 3.5 mm near longitude $170°$ W to more
than 9.5 mm near longitude $130°$ E. The range is
attributable in part to the variation in the spacing of
the spacecraft groundtracks. The stereoscopic image
in figure 22-22 shows the details of the area at the
eastern end of figures 22-20 and 22-21 and includes
all the points in that area the positions of which were
measured. The measured coordinates of this subset of
points are plotted in figure 22-23.

VHF Imagery

The VHF imagery from the area around the
Apollo 17 landing site, shown in figure 22-24, was
used to investigate the feasibility of using an analyti-
cal stereoplotter to measure and plot profiles from
the generally continuous scene in the stereoscopic
2-m-wavelength imagery. An interim orthogonal coor-
dinate system in the stereoscopic image was again
used, but the Y-axis was made approximately coinci-
dent with the foreground (northern) edge of the
image. Otherwise, the coordinate system is oriented
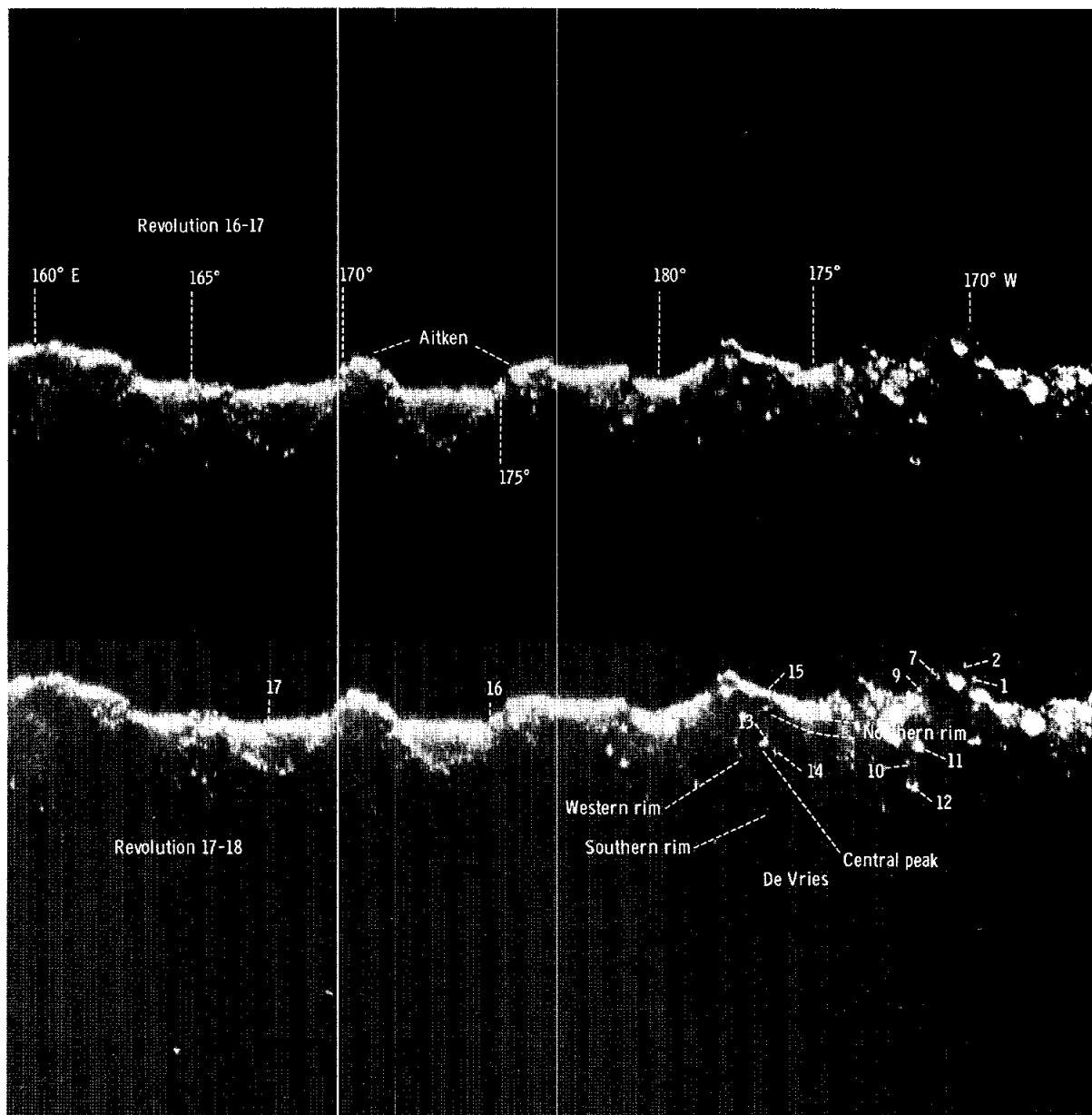
FIGURE 22-22.—Stereoscopic radar image in the central region of the lunar far side composed of 60-m-wavelength ALSE imagery obtained on revolutions 16-17 and 17-18. The numbered points correspond to those in figure 22-23 and are explained in the text.

as in the stereoscopic model for the 60-m-wavelength images. A profile trending perpendicular to the spacecraft groundtracks in the stereoscopic radar image then lies in an X-Z plane (fig. 22-19(b)). Coordinates in the stereoscopic image were again measured in millimeters at the scale of the original 70-mm image film.

An example of such a profile runs through the numbered points in figure 22-25 and is plotted in figure 22-26. The features in the radar image have been correlated with geologic units and terrain features using the nomenclature of Scott and Carr (ref. 22-2) and of the Apollo Lunar Geology Investigation Team (ref. 22-3). The profile in figure 22-26
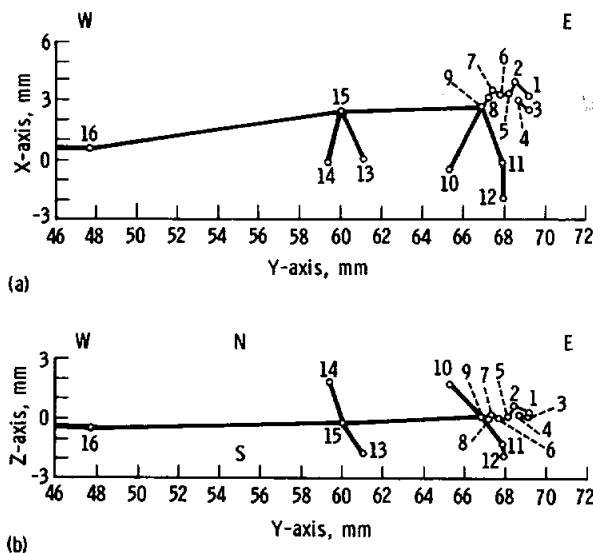
FIGURE 22-23.—Plots of the stereoscopic image coordinates of points numbered in figure 22-22 as seen by stereoscopic viewing of the 60-m-wavelength ALSE images along revolutions 16-17 and 17-18. Coordinates are measured at the scale of the original 70-mm image film. (a) Profile. (b) Map.

illustrates the general distribution of scenery in the stereoscopic image with the scene south of the spacecraft groundtracks lying behind or below (more negative values on the X-axis) the scene north of the groundtracks. The effect of high relief near the spacecraft groundtrack is also illustrated; for example, by the profile of the North Massif, which lies north of the groundtracks. The image of the crest of its south-facing slope (point 6) is recorded at earlier echo delay time (more negative values on the X-axis) than the radar image (point 104) of the edge of the plain to the south, which is, of course, closer to the groundtrack in map view.

Results From Surface Profile and Side-Looking Surface Imagery

The unadjusted HF-1 surface profile in figure 22-20 includes several features that are noteworthy. The profile from longitude 114° to 147° E is relatively flat compared to the remainder of the profile farther east. The relatively flat part of the profile is deeply notched by two large depressions. One is the 75-km-diameter crater Marconi, which was profiled off center toward the southern rim. Part of the crater floor shows in the profile, and the southern

rim appears in the side-looking imagery. The other depression has been recognized by El-Baz (ref. 22-4) in Apollo 16 orbital photographs. This depression is approximately 180 km in diameter, and the profile in figure 22-20 is a nearly central section of it. The crater is very old; approximately 50 percent of its interior is overlapped by superposed craters larger than 20 km in diameter. The crater was in an overexposed part of Lunar Orbiter I frame M-136 and is difficult to recognize there but is decipherable in enhanced copies. Apparently, the feature was overlooked in the preparation of Aeronautical Chart and Information Center lunar charts at scales of 1:5 000 000 and 1:2 750 000, as it is essentially unrecognizable in printed copy, although traces of the appropriate shading are present. In addition to the Apollo 16 coverage, Apollo 14 Hasselblad frames AS14-75-10298 to 10300 show much of the crater near the terminator at approximately 1-km resolution; subsequent frames 10303, 10308, 10313, 10315, 10317, and 10318 show the entire crater at lower resolutions. Several useful stereoscopic images can be formed from this set of photographs. The moderately rough plain between Marconi Crater and the depression appears to be very primitive in the sense of being a little-dissected remnant of an old plain situated between many large 25- to 100-km-diameter craters.

High points along the profile in figure 22-20 near longitudes 160° E, 177.5° W, and 170° W may represent the high parts of very ancient multi-ringed basins tentatively recognized during the preparation of geologic maps for planning ALSE observations.[1] In this preliminary mapping, the two basins in question can best be fitted by a 630-km-diameter circle centered north of the groundtrack of revolution 16-17 near latitude 9° S, longitude 164° E, and circles of 690, 930, and 1140 km centered south of the groundtrack near latitude 32° S, longitude 159° E.

Other noteworthy aspects of the present quick-look 60-m side-looking imagery of craters are illustrated by the images of two craters with central peaks that lie south of the groundtrack in figure 22-20. One crater, De Vries (fig. 22-22), is 60 km in diameter, and the other, lying near longitude 134° E between points 45 and 41 (fig. 22-20), measures
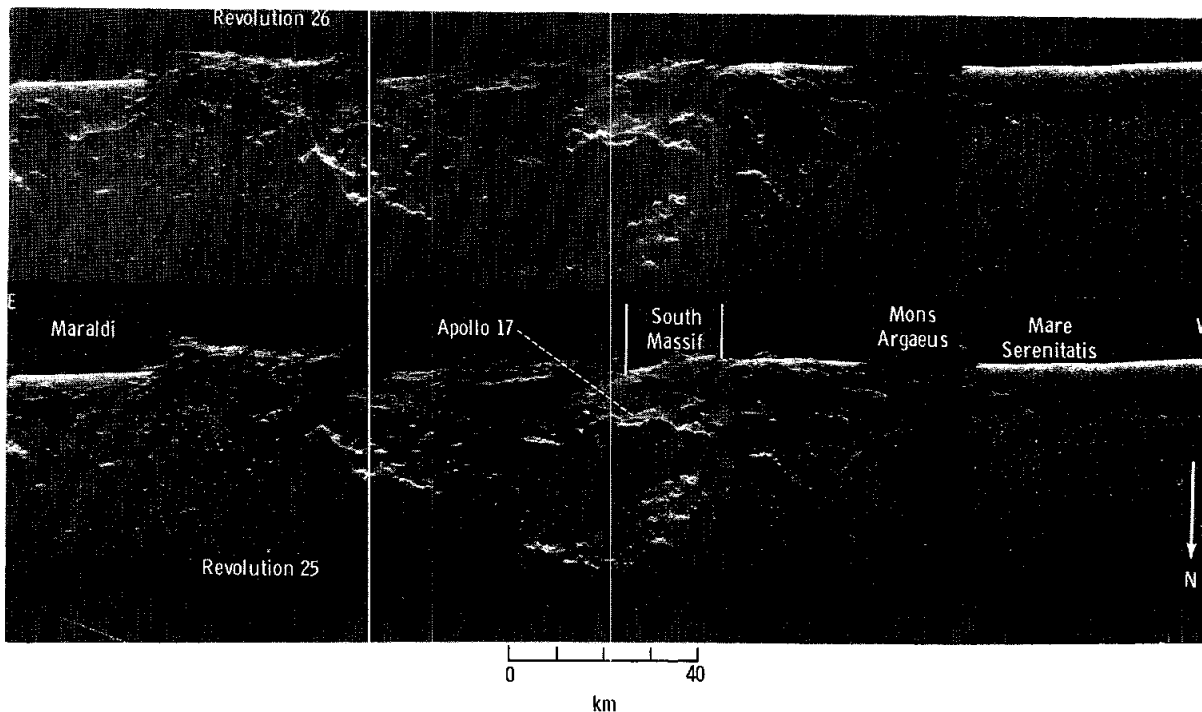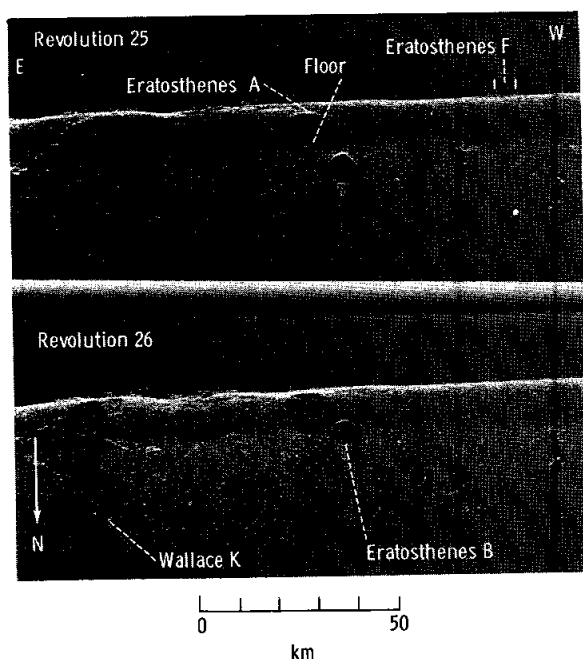
FIGURE 22-24.—Stereoscopic 2-m-wavelength ALSE radar image composed of imagery obtained on revolutions 25 and 26. The image covers a large region extending from southeastern Mare Serenitatis eastward across the mountains forming the southeastern border of the Serenitatis basin. The Apollo 17 landing site is near the center of the figure. The brightness change located approximately one-fourth of the distance from the profile to the opposite edge of the image is introduced by the sensitivity time control. The dark vertical band, approximately 30 km wide, through Mons Argaeus is due to the automatic gain control. The imagery north of the groundtracks is systematically brighter than that south of the groundtracks because of the nature of the radar antenna pattern. Thus, most of the scenery lies north of the groundtracks. Hence, in order to orient the profiles right side up, north is downward in the side-looking imagery, and, in order to place the features in the northward side-looking imagery in a distribution like that on a map, these images are printed with east on the left.

58 km in diameter. The central peak of De Vries Crater is close enough to the spacecraft ground-track, like the southern walls of Aitken Crater and its western neighbor, to reflect a fairly strong signal. The return from the more distant southern wall of De Vries Crater is barely discernible, and the still more distant northern walls of Aitken Crater and its neighbor are not detected. Further data reduction will be performed to minimize this systematic variation in image brightness. The near-circular image at longitude 134° E actually consists of the images of the central peak and part of the southern wall of the 58-km-diameter crater, the northern rim of which is essentially at the profile. This example illustrates that a geometric rectification of the imagery to eliminate the cross-track scale variation will substantially aid interpretation of the side-looking surface imagery.

The utility of the ALSE data for studying the tectonics of lunar basins may be seen in samples of VHF imagery in figures 22-18(c) and 22-27. In figure 22-18(c), the crater Dawes and the flat floor of Mare Tranquillitatis are on the left. An arched and frac-tured (rilles) boundary separates Mare Serenitatis and Mare Tranquillitatis, the outer basin of the former lying approximately 900 m lower than the latter. The wrinkle ridge (right) separates the outer and inner basins; the inner basin is 200 m lower. Phillips et al. (ref. 22-5) showed that the wrinkle ridge bounds the Serenitatis mascon. The same wrinkle ridge system may also be seen in figure 22-27. Here, in western Mare Serenitatis, the inner basin is also downdropped approximately 200 m. The profile in figure 22-27 suggests that the ridge represented a zone of elastic bending followed by mechanical failure.
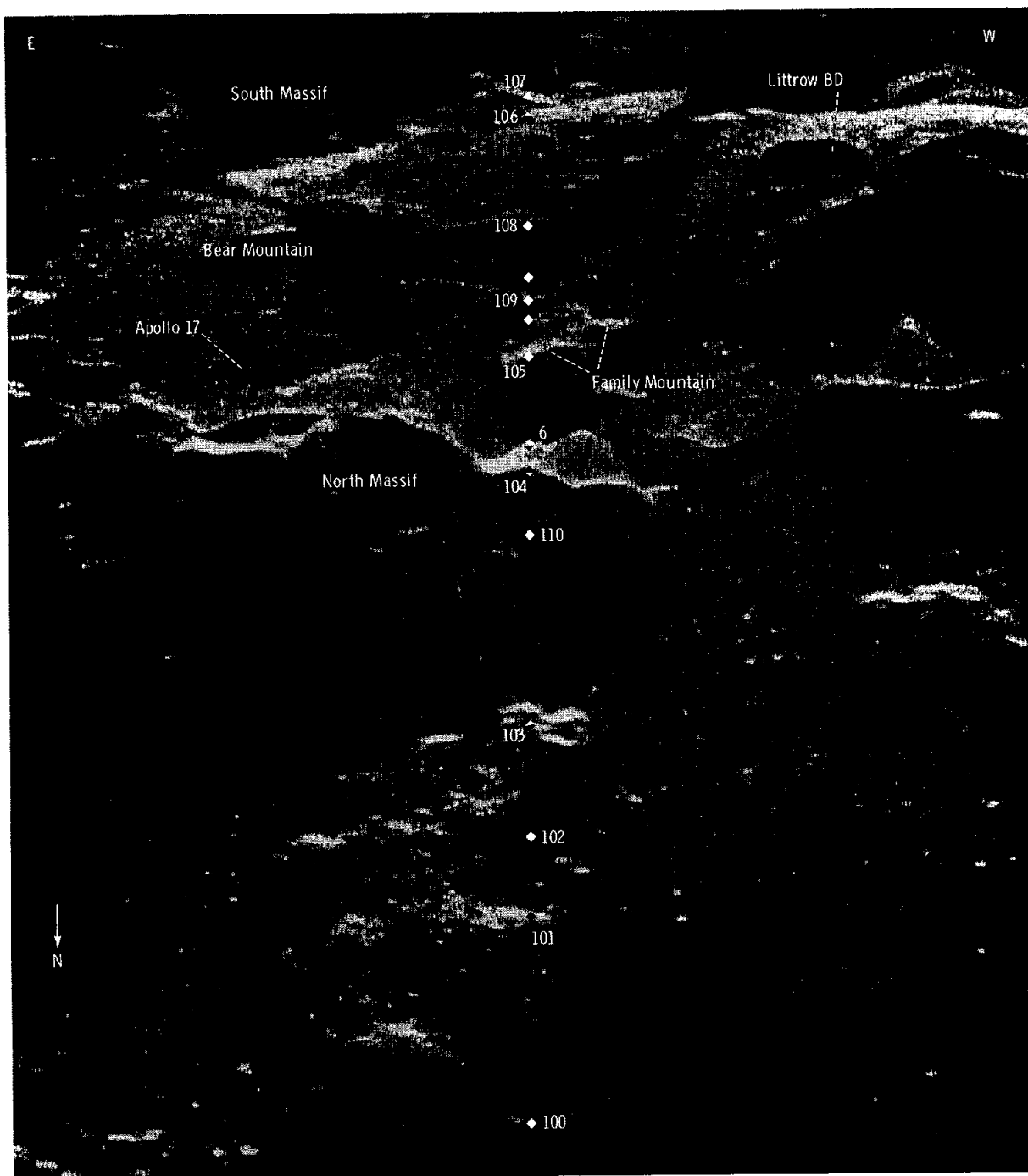
FIGURE 22-25.—ALSE 2-m-wavelength image of the area round the Apollo 17 landing site obtained during revolution 25. See figure 22-24 for the appearance of the scene in a stereoscopic view. The numbered points correspond to those in figure 22-26. The crater Littrow BD is 4 km in diameter.

The ALSE data shown here support the idea that the Serenitatis basin structure is consistent with a model of progressive tectonic failure as a consequence of a superisostatic load placed by the mascon. Such sagging at the lunar surface, with local faulting, could also be caused by a withdrawal of mare magmas from depth.
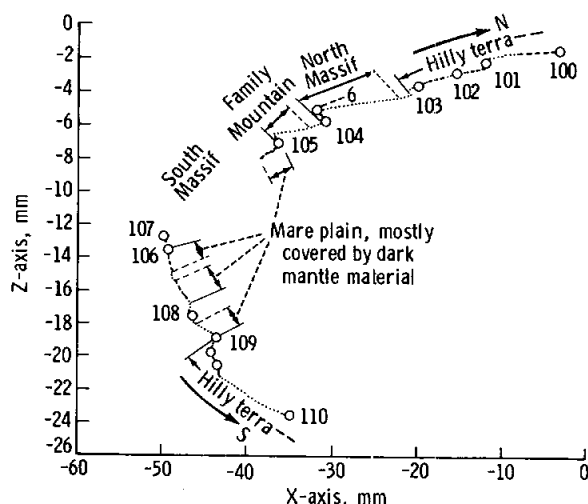
FIGURE 22-26.—Profile through the stereoscopic image in figure 22-24. The profile is in a plane oriented perpendicular to both the surface profile and the plane of the page in figure 22-24. The profile runs through the numbered points in figure 22-25.

Differences in Radar Albedo

Two types of variations in radar albedo have been noted in the 2-m-wavelength imagery. One is a bright horizontal band around a crater wall, and the other consists of highly reflective halos around certain small craters. Recognition of the quantitative albedo differences depends on the removal of variations in scene brightness due to topographic effects. In the following examples, topographic effects are assumed to be of second order.

The 2-m-wavelength imagery of the 6-km-diameter crater Eratosthenes B in southern Mare Imbrium shows a bright horizontal ring from approximately one-fourth to one-half of the distance from the rim crest to the floor (figs. 22-28 and 22-29). It can be seen in the stereoscopic image that the crater shape is that of a truncated cone. Thus, the bright ring is not due to a difference in slope. It is probably due to layering in the materials intersected by the crater, to the character of erosional debris covering part or all of the wall, or to a combination of these.

Two examples of small craters with surrounding radar-bright halos, Bessel G and Bessel F, 1.2 and 0.7 km in diameter, respectively, lie in southwestern Mare Serenitatis (fig. 22-27). The similarity of the images in both revolutions 25 and 26 is noteworthy. The bright halos extend from the crater rim crest outward
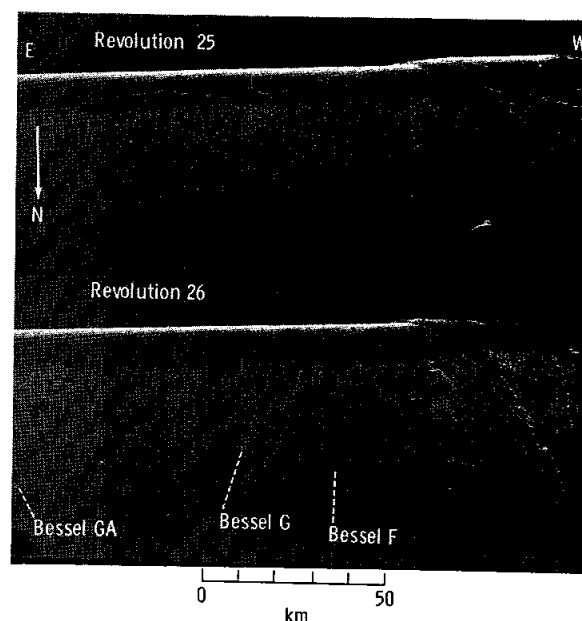
FIGURE 22-27.—Stereoscopic 2-m-wavelength ALSE radar image in southwestern Mare Serenitatis obtained on revolutions 25 and 26. The image shows two kilometer-size craters with radar-bright halos, Bessel G and Bessel F. A mare ridge trends from the lower right corner of the figure up across the surface profile image and thence eastward along the southern limb of the stereoscopic image. Where the ridge crosses the profile, it may be seen to mark a substantial step in the mare surface with the peripheral part of the mare standing higher.

approximately one crater diameter (fig. 22-30). The dark interior of the image of a crater slightly smaller than Bessel G interrupts the bright halo of Bessel G on the eastern side. Bessel G and Bessel F are very young craters with well-preserved rim and ray deposits. (See, for example, Apollo 17 metric camera frame AS17-1512 and Apollo 16 panoramic camera frames AS16-9910, 9912, 9915, and 9917.) The bright, blocky rim deposits form a continuous blanket from the rim crest outward for approximately one crater diameter. Bright filamentous rays extend at least seven crater diameters beyond the continuous rim deposits of Bessel G and 12 crater diameters in the case of Bessel F. The radar brightness of the rim deposit is probably a result of rock fragments in the continuous rim deposit. In fact, it appears that it may be possible to correlate individual bright reflections in the radar image with the larger fragments in the field of blocks surrounding the crater. The radar brightness of young lunar crater rim

FIGURE 22-28.—Stereoscopic 2-m-wavelength ALSE radar image of southeastern Mare Imbrium composed of imagery obtained on revolutions 25 and 26. The stereoscopic image includes a variety of typical craters a few kilometers in diameter.

deposits is known from Earth-based radar mapping (ref. 22-6). Apollo lunar sounder images like those of Bessel G Crater may explain the low-resolution brightness in terms of the energy component reflected from the individual blocks in the deposits. In this way, the ALSE imagery can substantially aid in geologically calibrating detailed Earth-based lunar radar images, which have been obtained for the whole Earth-side hemisphere of the Moon at 70- and 3.8-cm wavelengths (ref. 22-6). The ejecta deposits and the ray materials of Bessel G and Bessel F Craters make bright radar anomalies extending approximately five and six crater diameters, respectively, beyond their rim crests in the depolarized return (effectively the relative radar albedo) of the Earth-based 3.8-cm radar imagery.[2] At least the ejecta deposit of Bessel G Crater is a bright anomaly in the depolarized return in 70-cm Earth-based radar imagery.[3]

---

[2] S. H. Zisk, unpublished data.
[3] T. W. Thompson, unpublished data.
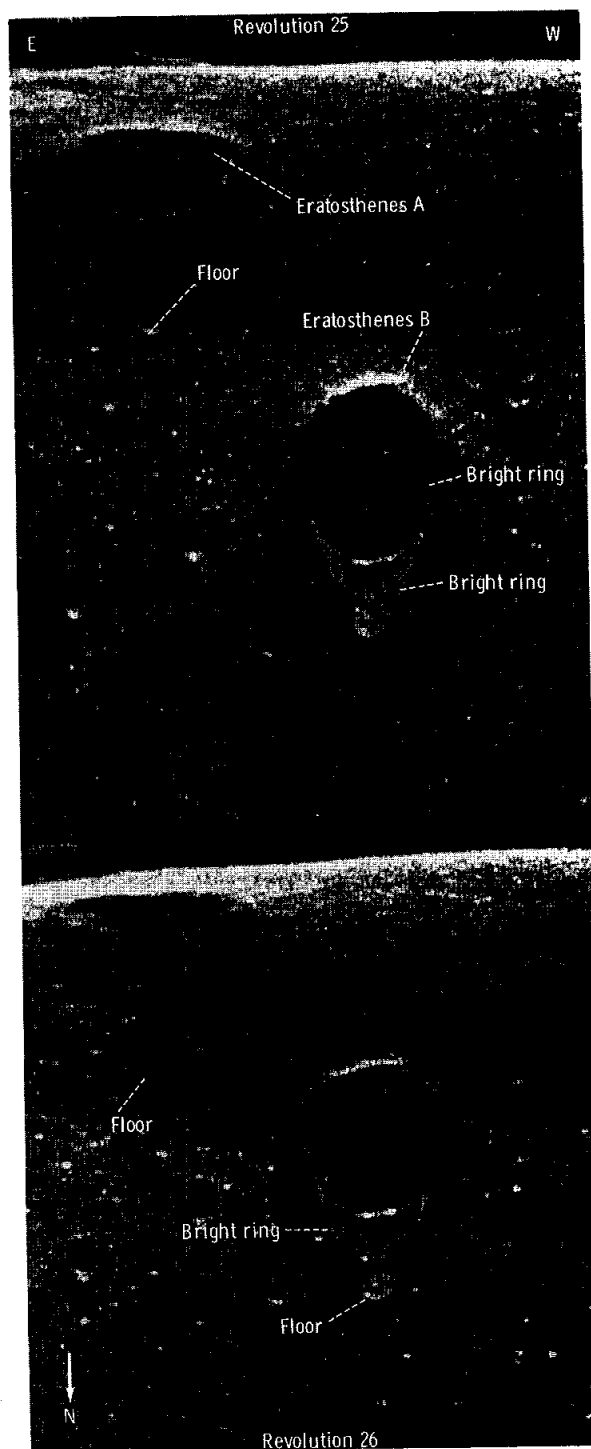
FIGURE 22-29.—Stereoscopic radar image of the 6-km-diameter crater Eratosthenes B with Eratosthenes A and other smaller nearby craters. Enlarged from figure 22-28.
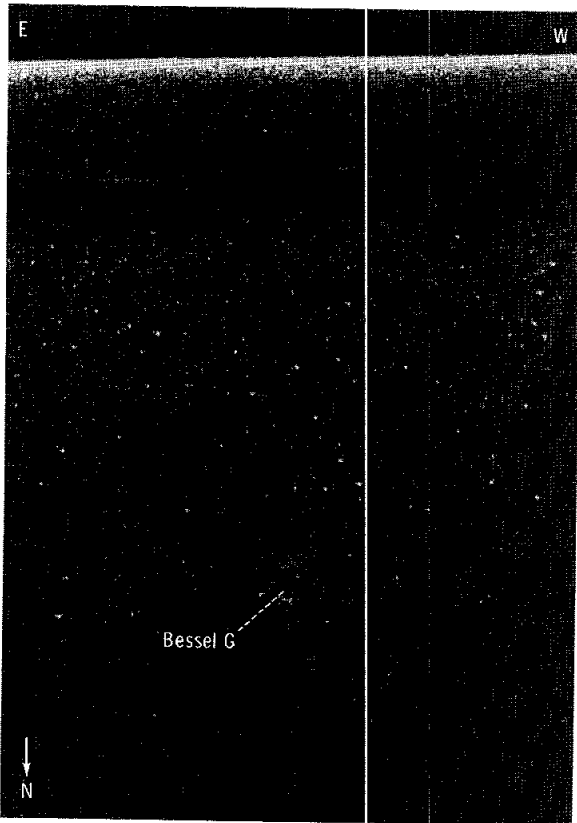
FIGURE 22-30.—Enlarged 2-m-wavelength ALSE image of the 1.2-km-diameter crater Bessel G and its surrounding radar-bright halo, obtained during revolution 26.

FIGURE 22-31.—Telemetry recordings of the receive-only noise levels observed on the lunar near side and far side. (a) Near side. (b) Far side.

GALACTIC NOISE DATA

The receive-only data showed a very high terrestrial component in both channels on the lunar near side, as can be seen in the comparison of the near-side and far-side noise measurements in figure 22-31. This result was particularly surprising at the HF-1 range, in which it would be expected that the ionosphere of the Earth would block most signals of surface origin.

The nighttime portion of the lunar far side provided, however, an opportunity to measure the galactic noise. The power measured by the antenna-receiver system, subjected to an isotropic noise of temperature T, is

$$P_n = KT\beta\eta \, \frac{\Omega}{4\pi} \qquad (22\text{-}34)$$

where K is the Boltzmann constant, β is the band-

width of the system, η is the efficiency of the system, and Ω is the effective solid angle of the source observed. For the case of the CSM in a 110-km lunar orbit, the ratio $\Omega/4\pi$ is equal to 0.67. The average radio brightness B can then be determined from the temperature through

$$B = \frac{2KTf^2}{C^2} \qquad (22\text{-}35)$$

The results for the noise brightness intensity measured on the nighttime lunar far side are shown in figure 22-32 along with a summary of measurements by other workers (ref. 22-7). The ALSE results are in generally good agreement with these other measurements, but they must be taken as preliminary because the CSM guidance and navigation system is a source of interference in the HF range the contribution of which is being investigated.

The near-side brightness intensities corresponding
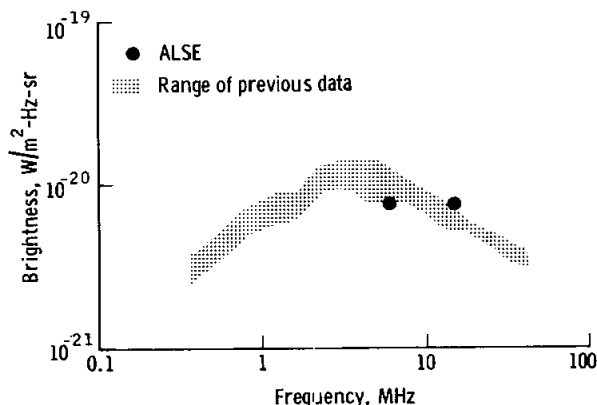
FIGURE 22-32.—Preliminary determination of noise brightness from the ALSE HF-1 and HF-2 channels. Range of results from other investigators (ref. 22-7) is also shown.

to the levels in figure 22-31 are, for both HF frequencies, approximately 2.3×10^{-19} W/m^2-Hz-sr.

SUMMARY

The four basic data products from the ALSE are sounding, profiling, imaging, and noise measurements. In this report, attention has been concentrated on the first three products, and both theory and preliminary results have been presented. This report provides background information on the experiment and on the data products. It presents preliminary examples of the types of analyses that can be performed and the conclusions to which they can lead.

Preliminary analysis of the data for subsurface features has been successful in indicating with a high probability the capability of the ALSE to achieve its fundamental goal of subsurface sounding. The imagery and profiling data are useful immediately for geologic interpretation, as demonstrated in the discussion.

Future reports and papers will use the ALSE data to help solve a systematic set of specific lunar problems.

ACKNOWLEDGMENTS

REFERENCES

22-1. Lloyd, D. D.; and Head, J. W.: Orientale Basin Deposits (Riccioli Area) in Apollo 16 Earthshine Photography. Sec. 29, Part E, of the Apollo 16 Preliminary Science Report. NASA SP-315, 1972.

22-2. Scott, D. H.; and Carr, M. H.: Geologic Map of the Taurus-Littrow Region of the Moon. Apollo 17 Pre-Mission Map. U.S. Geol. Survey Misc. Geol. Inv. Map I-800, sheet 1, 1972.

22-3. Apollo Lunar Geology Investigation Team: Preliminary Report on the Geology and Field Petrology at the Apollo 17 Landing Site. U.S. Geol. Survey Open-File Report, 1972. (Available from Center of Astrogeology, Flagstaff, Ariz.)

22-4. El-Baz, Farouk: Discovery of Two Lunar Features. Sec. 29, Part H, of the Apollo 16 Preliminary Science Report. NASA SP-315, 1972.

22-5. Phillips, R. J.; Conel, J. E.; Abbott, E. A.; Sjogren, W. L.; and Morton, J. B.: Mascons: Progress Toward a Unique Solution for Mass Distribution. J. Geophys. Res., vol. 77, no. 35, Dec. 10, 1972, pp. 7106-7114.

22-6. Thompson, Thomas W.; and Zisk, Sidney [Stanley] H.: Radar Mapping of Lunar Surface Roughness. Thermal Characteristics of the Moon, vol. 28 of Progress in Astronautics and Aeronautics, MIT Press (Cambridge, Mass.), 1972, pp. 83-117.

22-7. Alexander, J. K.; Brown, L. W.; Clark, T. A.; Stone, R. G.; and Weber, R. R.: The Spectrum of the Cosmic Radio Background Between 0.4 and 6.5 MHz. Astrophys. J., vol. 157, no. 3, Sept. 1969, pp. L163-L165.

23. Ultraviolet Spectrometer Experiment

William G. Fastie,[a†] *Paul D. Feldman,*[a] *Richard C. Henry,*[a] *H. Warren Moos,*[a] *Charles A. Barth,*[b]
Gary E. Thomas,[b] *Charles F. Lillie,*[b] *and Thomas M. Donahue*[c]

An ultraviolet spectrometer (UVS) on board the Apollo 17 orbiting spacecraft was used in an attempt to measure ultraviolet emissions from the lunar atmosphere. The only emissions observed in the lunar atmosphere were from a transient atmosphere introduced by the lunar module descent engine; 4 hr after the lunar module landed, these emissions were no longer detectable by the spectrometer. The absence of atomic hydrogen (H) expected to be present from the solar wind source leads to the conclusion that solar wind protons are neutralized and converted to molecular hydrogen (H_2) at the lunar surface.

During crossings of the solar-illuminated surface, the spectrometer measured significant variations in surface albedo. These variations are ascribed to variations in the refractive index of the lunar surface material.

The spectrometer made a number of nonlunar observations in lunar orbit and during transearth coast (TEC), including a search for the ultraviolet zodiacal light, solar atmosphere emissions, Earth emissions (including those from the geomagnetic tail), stellar emissions, and galactic emissions. Although significant data were obtained from all these observations, analysis of the data requires precise spacecraft attitude information in galactic coordinates; this information has not yet been received. During TEC, the fluorescence spectrum of H_2 was observed during a purge of the Apollo 17 fuel cells.

INSTRUMENT DESCRIPTION AND CALIBRATION

The Apollo 17 UVS has been described in great

detail elsewhere (ref. 23-1). In summary, it is of the Ebert type, which has been broadly used for space research, but employed new optical and electronic techniques that provided about an order of magnitude improvement in sensitivity. These improvements included exit slit mirrors that provided a 2.5 increase in the signal to the detector pulse-counting electronics (which permitted detection of single photoelectrons) and a precision wavelength scan system that permitted the summation of a large number of spectra without loss of spectral resolution.

The spectrometer is shown in figure 23-1. The triangular stand on which the instrument was mounted (fig. 23-1(a)) was attached to a spacecraft bulkhead that was perpendicular to the spacecraft longitudinal axis. The large baffle over the entrance slit excluded stray light and was designed with multiple angles in several sections to provide a very large capability for rejection of unwanted radiation. There were no external optical components.

As seen in figure 23-1(b), light rays passing through the spectrometer entrance slit are rendered parallel by an area on one side of the spherical Ebert mirror, which directs the rays to the grating. Diffracted rays from the grating go to the area on the other side of the Ebert mirror that focuses the rays through the entrance slit to the face of a solar-blind photomultiplier tube, which transforms each photoelectron produced by a photon into several million electrons. An accumulator circuit counts and stores these pulses for 0.1 sec, and the accumulated pulse count is transmitted to the spacecraft data system as a 16-bit word.

The wavelength scan system consisted of a synchronous, motor-driven, cyclical cam, which encapsulated the pin on a follower arm. The follower arm was attached to the grating shaft. The 3600-lines/mm grating was rotated approximately 5° by the cam drive system to scan the spectral region 118 to 168

---

[a]The Johns Hopkins University.
[b]University of Colorado.
[c]University of Pittsburgh.
[†]Principal Investigator.
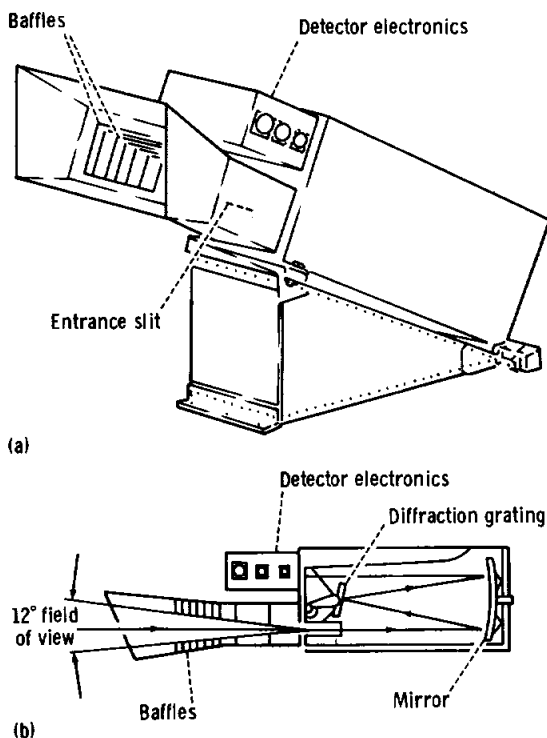
FIGURE 23-1.—Ultraviolet spectrometer. (a) Isometric view of the instrument mounted on a stand, which was attached to a bulkhead in the scientific instrument module bay of the Apollo 17 spacecraft. (b) Optical ray diagram.

nm once every 12 sec. The cam was programed to scan linearly in wavelength at the rate of approximately 7.5 nm/sec except for two 5-nm regions centered at 121.6 and 147.0 nm, where the scan rate was approximately 1.7 nm/sec to give temporal preference to Lyman-alpha radiation (121.6 nm) and to the resonance line of the heaviest atmospheric gas xenon (Xe) at 147.0 nm. The 144.5- to 149.5-nm region also included a fluorescent line of molecular hydrogen and one of carbon monoxide (CO).

The sensitivity S of the spectrometer to a gas column that is emitting 1×10^6 photons/sec-cm² (1 R) is given by

$$S \text{ (counts/sec)} = \frac{1 \times 10^6}{4\pi} \frac{A_s A_g}{F^2} QT \qquad (23\text{-}1)$$

where A_s = slit area ≈ cm² (1-nm resolution)
   A_g = grating area ≈1×10^2 cm²
   F = spectrometer focal length = 50 cm

Q = quantum efficiency of the detector ≈ 10 percent
T = transmission of the optical system ≈ 30 percent

or

S (counts/sec) ≈ 100 photoelectrons/sec/R

$$(23\text{-}2)$$

To provide precision measurements with the spectrometer, it is necessary to measure the value of Q over the exposed area of the photomultiplier tube and to measure the transmission of the optical system over the entire field of view of the spectrometer. No standard source exists for the far ultraviolet region, and a spatially uniform reference source to fill the wide aperture of the spectrometer is beyond the state of the art. A high-precision calibration was accomplished in a specially built vacuum facility, which provided an intense, high f-number, monochromatic beam that could be focused into a very small spot on any point of the entrance slit. The flight spectrometer was mounted in the vacuum chamber on a tilting platform so that the calibrating beam could be directed through the entrance slit to each area of the diffraction grating. A calibrated photomultiplier tube could be inserted in the monochromatic beam to measure the number of photons passing through the entrance slit. A National Bureau of Standards calibrated photodiode was used to calibrate the reference photomultiplier tube before and after each calibration of the spectrometer.

The calibration was performed at a total of 10 wavelengths in the spectral region that the instrument scanned. Successive calibrations provided very reproducible sensitivity values at all wavelengths. A cross-check of the system was provided by calibration of a spare instrument in the vacuum optical bench at the NASA Goddard Space Flight Center, which confirmed the absolute value of the calibration. We believe these careful techniques ensure that the signals observed in flight were measured to an accuracy of ± 10 percent.

LUNAR ATMOSPHERE OBSERVATIONS

The Apollo 17 UVS experiment has as its primary objective the measurement of the density and composition of the lunar atmosphere by observing resonance scattering and fluorescence of solar far ultra-

violet radiation. This technique can provide density measurements in the range 1×10^1 to 1×10^4 atoms/cm^3 for H, H$_2$, atomic oxygen (O), carbon (C), atomic nitrogen (N), CO, carbon dioxide, and Xe but, because of spectral range limitations, could not measure helium, neon, or argon-36, all of which may be present as major constituents of the lunar atmosphere, if the solar wind is the major source for the atmosphere. In addition, radiogenic argon-40 (^{40}Ar) from potassium-40 decay should be present. The present results indicate that the surface concentration of atomic hydrogen is less than 10 atoms/cm^3, almost three orders of magnitude less than predicted (ref. 23-2), whereas the concentration of H$_2$, if present, is less than 6.0×10^3 atoms/cm^3. This is consistent with the hypothesis that the solar wind protons are completely converted into hydrogen molecules at the lunar surface. None of the other observable constituents were detected. A transient atmosphere was observed shortly after lunar module touchdown but disappeared in a matter of hours. No evidence of outgassing was detected in the vicinity of the crater Aristarchus, where many transient optical phenomena have been reported.

Previous measurements of the lunar atmosphere based on an in situ pressure gage (ref. 23-3) indicated that the total surface density at the subsolar point may be as small as 1×10^7 atoms/cm^3. More recently, mass spectrometer measurements from lunar orbit (ref. 23-4) and from the lunar surface (ref. 23-5) have resulted in detection of neon, argon, and helium. Lunar outgassing, the only possible source of a substantial atmosphere, occurs at a rate several orders of magnitude less than the corresponding rate on Earth (ref. 23-6). Apart from ^{40}Ar and radiogenic helium (ref. 23-7), the lunar atmosphere may consist only of neutralized solar wind ions. Thus, the lunar atmosphere would be expected to be composed primarily of neon, argon, hydrogen, and helium, the subsolar surface concentrations of which would lie in the range 2×10^3 to 7×10^3 atoms/cm^3 (ref. 23-7).

The Apollo 17 UVS was mounted in the scientific instrument module (SIM) with the optic axis pointed 23° forward and 18° right of the SIM center line (when looking toward the spacecraft nose). The SIM center line nominally pointed through the center of the Moon when the spacecraft was constrained to local horizontal attitude. Atmospheric observations were made in various spacecraft attitudes as shown in figure 23-2. The principal mode of operation was the
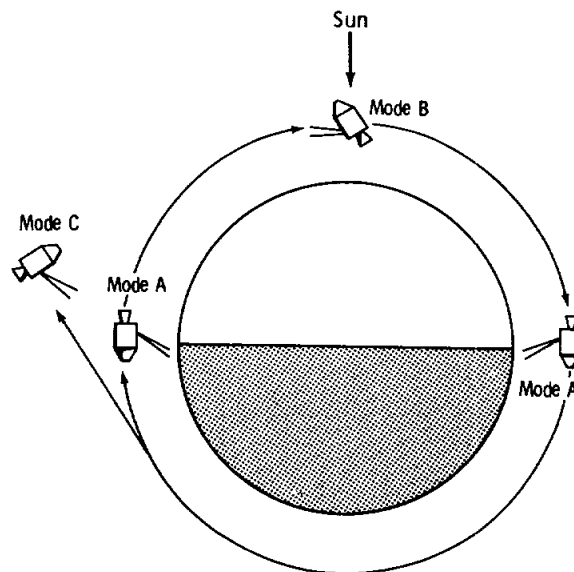
FIGURE 23-2.—Schematic representation of the modes of observation of the lunar atmosphere. Mode A, the principal orbital mode, consists of observation through the illuminated atmosphere above the terminator against the dark side of the Moon. In mode B, a contingency orbital mode, the spectrometer is pointed at a fixed point in space, and the line of sight extends through a tangential slice of illuminated atmosphere. Mode C was used immediately after transearth injection. The Apollo 17 UVS has a field of view of 12° by 12° and looks forward 23° relative to the normal to the spacecraft longitudinal axis.

observation through the illuminated atmosphere above the terminator against the dark side of the Moon (mode A in fig. 23-2). This was done automatically once per revolution if the spacecraft was maintained in the local horizontal attitude (twice if the spacecraft axis reversal was performed between terminator crossings). A total of 1200 of these terminator spectra was obtained.

To allow for the possibility that the atmospheric emissions might be too weak for detection in the principal mode, two special modes were provided to enhance the sensitivity. These modes resulted in most of the upper limits quoted herein. In the first mode, the spectrometer was pointed at a fixed point in space and, as the spacecraft moved in its orbit, the line of sight extended through a tangential slice of illuminated atmosphere (mode B in fig. 23-2). The enhancement provided by this mode is ≈ 20 for H and H$_2$ and ≈ 10 for O, based on Chamberlain's model of an evaporating corona with the lunar

surface as the critical level (ref. 23-8). The second mode (mode C in fig. 23-2) was used immediately after transearth injection (TEI) and is similar to mode A except for the much greater optical path length.

For all atmospheric constituents other than hydrogen (Lyman alpha, 121.6 nm), the sensitivity limit was set by the background count rate ($\approx$ 25 counts/sec), which was caused by solar cosmic ray protons. At 121.6 nm, solar radiation resonantly scattered from hydrogen atoms in the interplanetary medium produces a background of between 200 and 400 R (depending on the viewing direction), in good agreement with previous measurements (ref. 23-9). Emission rates of 6 to 12 R (450 to 900 counts/sec) are obtained when the scattered radiation is observed after reflection from the surface of the dark side of the Moon. Solar Lyman alpha scattered from the Earth hydrogen geocorona and then reflected from the Moon beyond the lunar terminator adds a 1-R contribution to the background for crossings of the terminator facing Earth. During TEC, the fixed areas of space observed in the tangential mode (mode B in fig. 23-2) were again observed to provide a sky background correction for the tangential mode.

We define

$$N_i(z_1, z_2) = \int_{z_1}^{z_2} n_i(z')dz' \qquad (23\text{-}3)$$

where z_1 and z_2 are two altitudes above the lunar

surface, and $n_i(z')$ is the density in atoms per cubic centimeter of atomic species i at altitude z', so that $N_i(0, z)$ is the vertical column density of that atomic species between the surface and altitude z. For observations at an angle θ to the local vertical, the emission rate $4\pi I_i$, in rayleighs, for resonance scattering of solar flux in the ith line is given by

$$4\pi I_i = 1 \times 10^{-6} g_i [N(0,z)][CH(\theta)] \qquad (23\text{-}4)$$

where g_i is the resonance g-factor and $CH(\theta)$ is the Chapman function (ref. 23-10). For molecular species, it is necessary to specify $g_{v',v''}$, where v' and v'' are vibrational quantum numbers of the excited and ground states, respectively. Table 23-I lists the transitions of interest, the resonance g-factors, the instrument sensitivity, and the minimum detectable concentration for the particular mode of observation.

Figure 23-3 shows the difference between the average of the sum of 70 spectra observed in mode B in lunar orbit and the average of 210 spectra obtained during TEC (mode C) when the spectrometer axis was pointed at the same point in space. The spacecraft altitude varied from 70 to 46 km, and the spacecraft was near the subsolar point throughout the observation. Wavelengths corresponding to the resonance transitions of O, C, Xe, and N, to the Lyman bands of H_2, and to the fourth-positive bands of CO are indicated. No emission features are apparent in the spectrum. Figure 23-4(a) shows a sum of 25 spectra

TABLE 23-I.—*Ultraviolet Spectrometer Observations*

Species	Energy-state transition	Wavelength, nm	Resonance g-factor, photon/sec/molecule	Mode of observation[a]	Sensitivity, photoelectrons/sec/R	Observed surface density,[b] atoms/cm^3
			Atomic			
H	$2_S - 2_P$	[c]121.6	2.2×10^{-3}	C	75	< 10
O	$3_P - 3_S$	130.4	2×10^{-5}	B	99	< 40
N	$4_S - 4_P$	120.0	3.6×10^{-6}	B	70	< 300
C	$3_P - 3_{P^0}$	165.7	2.1×10^{-4}	B	25	< 15
Kr	$1_S - 3_P$	123.6	1.6×10^{-7}	A	85	< 10 000
Xe	$1_S - 3_P$	147.0	1.5×10^{-6}	A	75	< 1 000
			Molecular			
H_2	$B^1\Sigma_u^+ - X^2\Sigma_g^+$ (6, 9)	146.2	4.0×10^{-8}	B	75	< 6 000
CO	$A^1\Pi - X^1\Sigma^+$ (1, 0)	151.0	7.5×10^{-8}	B	60	< 20 000

[a]See figure 23-2.

[b]At the subsolar point, except for H, krypton (Kr), and Xe, which are terminator values. The entries in this column are based on the spectral feature not exceeding 1 standard deviation in the counting rate.

[c]Lyman alpha.
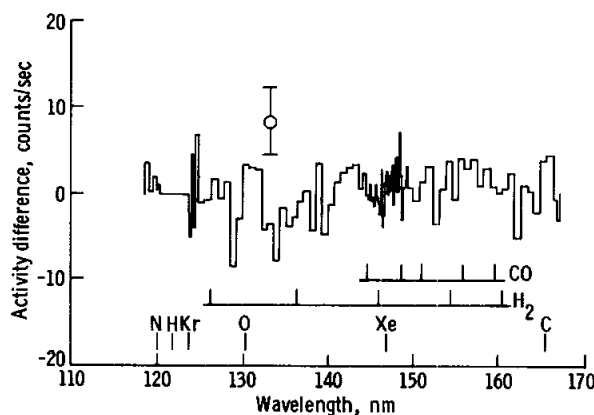
FIGURE 23-3.—The average of 70 spectra obtained during a tangential mode (mode B in fig. 23-2) observation with the sky background (observed during TEC) subtracted. The wavelengths of the principal emission features expected are indicated. The error bar represents 1 standard deviation in the observed counting rate.

obtained at the near-side terminator 2 hr after the lunar module had landed and indicates a slight enhancement at 130.4 nm (atomic oxygen) and at least one band of the CO fourth-positive system. None of these enhancements appear in figure 23-4(b), which shows the sum of 25 spectra obtained on the following orbit, 4 hr after landing.

In figure 23-5, the Lyman-alpha signal (121.6 nm) observed below the spacecraft between the terminator and a point 15° beyond the terminator (270° to 255°) (fig. 23-5(a)) is compared to the signal observed when the spacecraft was in full shadow (255° to 240°) (fig. 23-5(b)). The signal in figure 23-5(b) originated from solar radiation that was resonantly scattered from the solar system hydrogen atmosphere. The difference between the signals shown in figures 23-5(a) and 23-5(b) was initially misinterpreted as being of lunar atmospheric origin (ref. 23-1). More detailed data analysis, particularly of data from mode C (fig. 23-2), shows no signal that can be ascribed to an atomic hydrogen atmosphere to a limit of 10 atoms/cm^3 at the lunar surface. In mode C, the spacecraft altitude was increased by a factor of 5 with no increase in the Lyman-alpha (121.6 nm) signal. The signal difference (figs. 23-5(a) and 23-5(b)) is ascribed to an asymmetry in Lyman-alpha emission in the solar atmosphere. The existence of the asymmetry was confirmed by observations during TEC.

A number of conclusions emerge from the preceding results. The fact that xenon must be at best a minor component of the lunar atmosphere, despite its large mass (131.3), indicates that the mechanism of photoionization loss followed by acceleration in the solar wind electric field dominates over Jean's evaporative escape, at least for the heavy gases. The small concentrations of H, C, N, O, and CO, which are photodissociation products of many gases of volcanic origin, also place severe restrictions on present levels of lunar volcanism.[1] The most surprising result is the absence of atomic hydrogen to an upper limit almost three orders of magnitude below the predicted value (ref. 23-2). The effect of the terrestrial magnetic field in shielding the lunar surface from the incident solar wind proton flux would be important only late in the mission.[2] Other possible ways of accounting for the absence of hydrogen atoms are as follows.

1. Adsorption of solar wind protons in the lunar soil

2. Direct reflection of solar wind protons from the lunar surface

3. Neutralization and rapid escape from the lunar surface as suprathermal hydrogen atoms

4. Recombination to form molecular hydrogen

In current models of the interaction of the solar wind with the lunar soil (ref. 23-13), protons of $\approx$ 1-keV energy penetrate to a depth of $\approx$ 1 X 10^{-6} cm. They will neutralize to form hydrogen atoms and may combine with other H atoms to form hydrogen molecules. Diffusion to the surface or into the dust grains to a depth of $\approx$ 1 X 10^{-5} cm may occur. For adsorption within the soil to occur, the diffusion must be retarded, either by the formation of stable hydrides or by trapping in a lattice site. In either case, after sufficient exposure, the soil becomes saturated and diffusion from the surface will occur. Saturation occurs only for the outer surfaces of soil grains, which are exposed to the solar wind for periods ranging from 0.1 X 10^6 to 20 X 10^6 yr (ref. 23-14).

---

[1] The limits on the outgassing rates are being described in detail by G. E. Thomas et al.

[2] According to the empirical geomagnetic-tail model of Fairfield (ref. 23-11), the Moon should have entered the Earth bow shock 13 hr before the TEI maneuver. However, according to measurements of the solar wind at the surface of the Moon (ref. 23-12), the proton flux is not appreciably disturbed until the Moon enters the geomagnetic tail. The cut-off of solar wind flux should have occurred at approximately 18:00 G.m.t. on December 18, which was 44 hr after TEI.
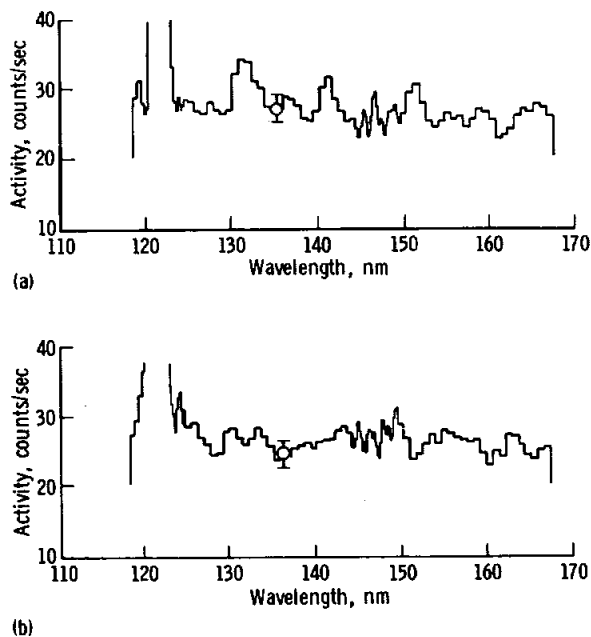
FIGURE 23-4.—Comparison of UVS spectra. The error bars represent 1 standard deviation in the observed counting rate. (a) Spectrum obtained 2 hr after lunar module landing, showing mild indication of emission features at 130.4 nm (O) and 151 nm (CO). (b) Spectrum obtained 4 hr after lunar module landing, showing no emission features.

Even for an exposure period of 1 million years (during which the solar wind is assumed constant), complete adsorption of the solar protons would give a density of 4 mg/cm^2 of hydrogen over the entire lunar surface. This value exceeds the measured composition of lunar soil by a factor of $\approx 1 \times 10^5$ (ref. 23-13).

The reflection of solar wind particles has been measured by several solar wind composition experiments on the lunar surface. The albedo for alpha particles is 10 percent (ref. 23-15), and the albedo for protons should not be significantly higher. In addition, significant reflection of solar wind ions would produce measurable perturbations of the solar wind magnetic field that have not been observed from lunar orbit (ref. 23-16).

A "sputtering" atmosphere of atomic hydrogen has been advocated (ref. 23-17), in which hydrogen atoms with average velocities of 15 km/sec are ejected from the lunar surface as a result of energetic ion impact. However, because hydrogen is a minor constituent of the lunar surface, the dominant com-
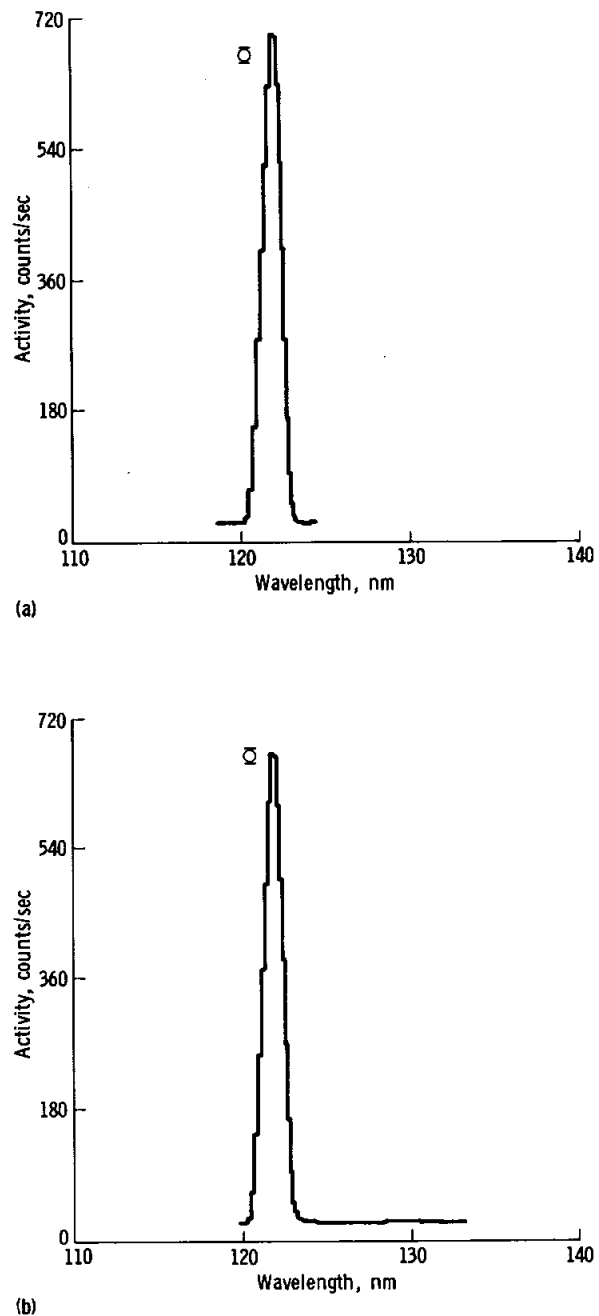
FIGURE 23-5.—Comparison of Lyman-alpha signals obtained on revolution 38. The signals are caused by reflected solar atmosphere radiation; the difference between the signals is due to asymmetry in the reflected solar radiation, not to a lunar H atmosphere. The error bars represent 1 standard deviation in the observed counting rate. (a) Signal observed just beyond the near-side terminator; coverage extends from 270° to 255°. (b) Signal observed when spacecraft was in full shadow; coverage extends from 255° to 240°

position of the sputtered material would probably be that of the lunar soil itself. Even if all the sputtered atoms were hydrogen with the previously mentioned average velocity, the maximum Doppler shift (0.006 nm) of the absorption line would not be sufficient to remove it from the wide solar Lyman-alpha line. The predicted value at the subsolar point of 340 atoms/ cm^3 for the previously mentioned sputtering model (ref. 23-17) is far above our detection limit shown in table 23-I.

Thus, efficient surface recombination of solar protons to molecular hydrogen appears to be the most probable explanation for the low atomic hydrogen density. It is reasonable to expect an efficient trapping of kilovolt protons on the lunar surface (ref. 23-18), followed by an upward diffusion of hydrogen atoms. This upward diffusion would promote recombination either within or at the surface of the soil grains. The molecular hydrogen would then be released by the surface at thermal energy. A theoretical model of Hodges (ref. 23-19) predicts H_2 concentrations of 3.6×10^3 atoms/cm³ at the subsolar point and 2.3×10^4 atoms/cm³ at the antisolar point.

As shown in table 23-I, the fluorescence in the H_2 Lyman bands from expected density would have escaped detection in the UVS experiment. The expected nighttime density, however, may ultimately be detected by the Apollo 17 neutral mass spectrometer surface experiment (ref. 23-20).

In conclusion, the Apollo 17 UVS experiment has revealed that atomic hydrogen is almost totally absent in the lunar atmosphere. To explain this observation, we believe that nearly 100-percent conversion of solar wind protons to molecular hydrogen probably occurs at the lunar surface. The expected H_2 density would have so far escaped detection. We would also expect that H_2 will predominate over H for the case of Mercury if its atmosphere is thin enough to allow direct solar wind impact on the surface. A related problem on which this result may bear is the formation of interstellar H_2 on dust particles (refs. 23-21 and 23-22).

LUNAR ALBEDO MEASUREMENTS

During the orbital mission, approximately 50 hr of data were obtained with the UVS observing the sunlit side of the Moon and approximately 50 hr of data were obtained on the dark side. Also during the mission, a rocket experiment conducted by the University of Colorado from the White Sands Missile Range measured the absolute spectral brightness of the Sun in the ultraviolet while the UVS was measuring the sunlit spectrum of the Moon. Thus, we were able to make an absolute measurement of the spectral albedo of the lunar surface.

Before the mission, laboratory measurements had been made of the spectral albedo of lunar dust samples obtained on the Apollo 11, 12, and 14 missions. The laboratory measurements showed that all three lunar samples had an ultraviolet albedo of approximately 2.2 ± 0.2 percent at all wavelengths in the range of 121.6 to 165.7 nm (ref. 23-23). Because almost all minerals are opaque in the spectral region to which the UVS is sensitive, body color plays a small role in the spectral properties of minerals, and refractive index effects probably dominate. Alternatively, metallic sputtering produced by solar wind impact (ref. 23-24) may coat the surface and create the observed grayness in the lunar samples. However, the laboratory-measured albedo is not inconsistent with the assumption that the refractive index, and therefore the mineralogical character of the lunar material, is the factor that controls the far ultraviolet albedo.

Figure 23-6 shows a spectrum obtained from the lunar surface near the subsolar point. The very substantial signals shown, combined with the rocket measurements described previously, permit an accurate measurement of the lunar albedo in the spectral range 118 to 168 nm. This in situ albedo measurement agrees very well with the 2.2-percent value observed in the laboratory.
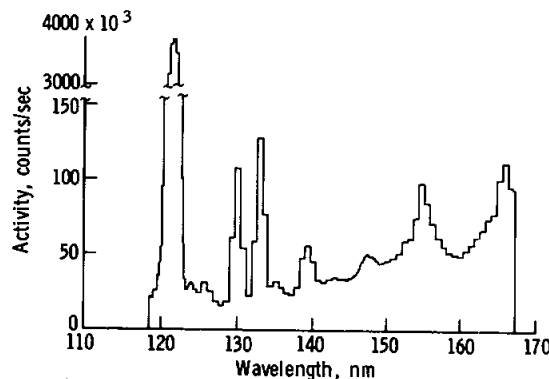
FIGURE 23-6.—Spectrum obtained from UVS observation of the lunar surface near the subsolar point.

Figure 23-7 shows the signal at 147 nm and its variation with lunar longitude during one albedo pass (revolution 28). This curve agrees closely with the behavior of the lunar albedo in the visible region as analyzed by Hapke (ref. 23-25). Figure 23-8 is a plot of the data shown in figure 23-7 divided by the Hapke function for the visible region. Large variations near the terminator are caused by shadowing effects. If the visible Hapke function were the same as the far ultraviolet function, the curve in figure 23-8 would be independent of lunar longitude. In figure 23-9, the residual longitude effect shown in figure 23-8 has been removed by an arbitrary modification of the part of the visible Hapke function that might reasonably be expected to change in the far ultraviolet. Also plotted on figure 23-9 are the normalized data from the next passage across the illuminated surface (revolution 29).

Figure 23-9 demonstrates that the small variations in albedo with longitude are reproducible from one orbit to the next. The most spectacular demonstration is in the crater Neper, which shows an albedo peak in the center of the crater and minimums at the crater edges. However, many other variations are clearly identifiable and are shown to be reproducible in figure 23-9. As might be expected, the variations from point to point on the maria are less pronounced than in other areas. This effect can most clearly be seen in figure 23-7.

Analysis of other bright-side passes demonstrates

that the maria show little albedo variation, but there are exceptions (e.g., the southern portion of Mare Crisium). Perhaps the most important observations at this stage of data reduction are that Neper Crater is an exception, that most craters are not distinguishable in the ultraviolet, and that most of the variations in the ultraviolet albedo seem to occur in regions that show little visible variations. Because we believe the albedo observations may have important geological or mineralogical significance, we are continuing data reduction and analysis and plan a program of intercomparison with other lunar observations.

During the passage of the unilluminated portion of the Moon, we observed a reflected Lyman-alpha signal from solar system hydrogen. We have also observed albedo variations in this signal that may be of particular importance because the signal includes
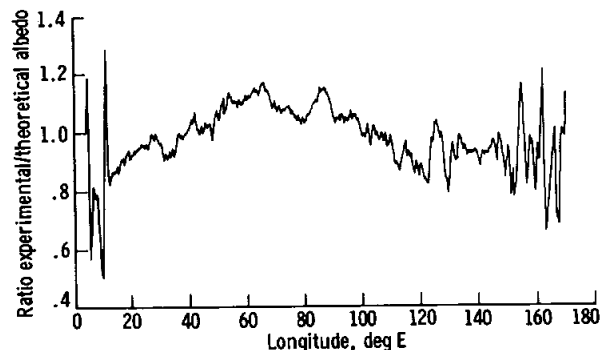
FIGURE 23-8.—Transit data of figure 23-7 divided by visible Hapke function.

FIGURE 23-7.—Variation of brightness with lunar longitude for the signal observed at 147 nm (fig. 23-6) as the spacecraft traversed the illuminated lunar surface on revolution 28.
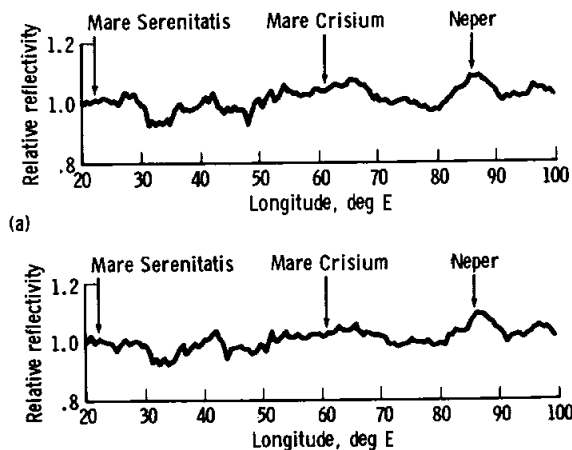
FIGURE 23-9.—Lunar transit data divided by far ultraviolet Hapke function. (a) Revolution 28. (b) Revolution 29.

areas that have not been studied in great detail. However, because the signal is so much weaker than the bright-side signal, little analysis of this data has been performed to date.

OTHER OBSERVATIONS

Twice during lunar orbit, when the spacecraft had just entered the shadow behind the terminator, the spacecraft was oriented so that ultraviolet zodiacal light emissions from the inner solar atmosphere could be observed. These data have only been preliminarily analyzed but generally support the ultraviolet zodiacal light observations by Orbiting Astronomical Observatory 2 (OAO-2) (ref. 23-26).

Several times during TEC, the UVS observed the Earth. Preliminary analysis (ref. 23-27) indicates that the data support the Orbiting Geophysical Observatory IV (OGO IV) orbital observations of the ultraviolet Earth airglow and provide an overall view of the Earth for comparison with other planets.

During TEC, the UVS was operated almost continuously to provide a detailed ultraviolet survey of our galaxy and to observe selected stellar spectra. A massive amount of data was obtained, but its analysis awaits viewing direction information in galactic coordinates. Preliminary analysis of the spectra of isolated bright stars demonstrates that significant data were obtained. The observed ultraviolet spectral distributions agree with previous observations and provide the most precise measurement of absolute ultraviolet brightness obtained to date (ref. 23-28).

The full sky survey described previously also provided a measure of the distribution of solar system Lyman-alpha (121.6 nm) emission that is produced by resonance re-radiation of solar radiation by atomic hydrogen in the solar system. The survey also provided an opportunity to search for a geomagnetic tail of atomic hydrogen downwind from the Sun. These data have not been analyzed.

Once during TEC, the UVS was operating during a molecular hydrogen purge of the fuel cells that produced the ultraviolet spectrum shown in figure 23-10. This spectrum arises from absorption by molecular hydrogen of Lyman-beta and Lyman-gamma solar radiation and fluorescent re-radiation of this energy at longer wavelengths. From knowledge of the brightness of these solar emission features and of the Franck-Condon factors for molecular hydrogen, we have calculated the expected fluorescence spec-
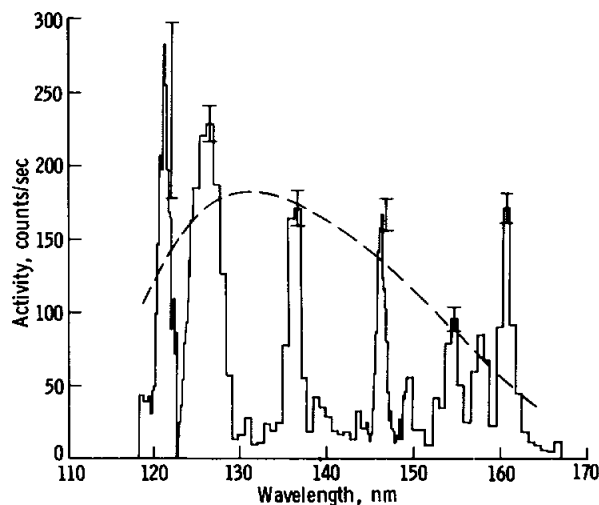
FIGURE 23-10.—Spectrum obtained in TEC during molecular hydrogen purge of fuel cells. The dashed curve represents a brightness of 2 R. The error bars represent 1 standard deviation in the observed counting rate.
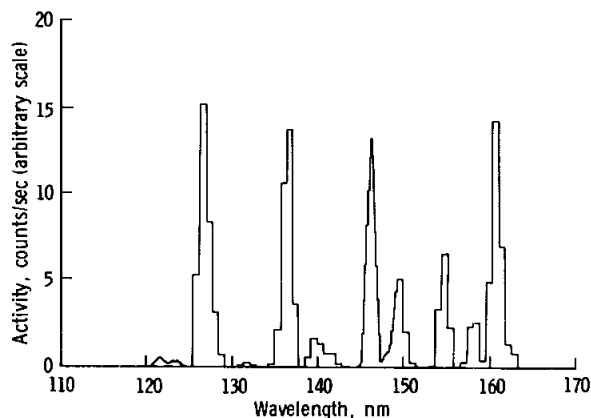
FIGURE 23-11.—Calculated fluorescence spectrum of molecular hydrogen excited by far ultraviolet solar radiation. (Intensity of one band normalized to experimental data (fig. 23-10).)

trum of molecular hydrogen. This theoretical spectrum is shown in figure 23-11 where the intensity of one of the bands has been normalized to the experimental data of figure 23-10. The observed and calculated distributions agree very well. We have also calculated that the observed spectral brightness gives a column density of approximately 1×10^{14} molecules/cm^2, in close agreement with the calculated column density based on a nominal H_2 purge rate and the spacecraft geometry.

The H_2 spectrum provides an internal calibration

of the UVS as a molecular hydrogen sensor and gives high reliability to the upper limit on H_2 at the subsolar point discussed in the section entitled "Lunar Atmosphere Observations" and shown in table 23-I. The H_2 observation is also important as an unambiguous means of identifying molecular hydrogen in the atmospheres of planets and comets (ref. 23-29).

REFERENCES

23-1. Fastie, William G.: The Apollo 17 Far Ultraviolet Spectrometer Experiment. The Moon, vol. 7, nos. 1/2, Mar./Apr. 1973, pp. 49-62.

23-2. Johnson, F. S.: Lunar Atmosphere. Rev. Geophys. Space Phys., vol. 9. no. 3, Aug. 1971, pp. 813-823.

23-3. Johnson, Francis S.; Carroll, James M.; and Evans, Dallas E.: Lunar Atmosphere Measurements. Proceedings of the Third Lunar Science Conference, vol. 3, MIT Press (Cambridge, Mass.), 1972, pp. 2231-2242.

23-4. Hodges, R. R.; Hoffman, J. H.; and Evans, D. E.: Lunar Orbital Mass Spectrometer Experiment. Sec. 21 of the Apollo 16 Preliminary Science Report. NASA SP-315, 1972.

23-5. Hoffman, J. H.; Hodges, R. R., Jr.; and Evans, D. E.: Lunar Atmospheric Composition Results From Apollo 17. Lunar Science IV (Abs. of papers presented at the Fourth Lunar Science Conference (Houston, Tex.), Mar. 5-8, 1973), pp. 376-377.

23-6. Hodges, R. R.; Hoffman, J. H.; Yeh, T. T. J.; and Chang, G. K.: Orbital Search for Lunar Volcanism. J. Geophys. Res., vol. 77, no. 22, Aug. 1, 1972, pp. 4079-4085.

23-7. Hodges, R. R.; Hoffman, J. H.; Johnson, F. S.; and Evans, D. E.: Composition and Dynamics of Lunar Atmosphere. Proceedings of the Fourth Lunar Science Conference, Pergamon Press (New York), Dec. 1973.

23-8. Chamberlain, J. W.: Planetary Coronae and Atmospheric Evaporation. Planet. Space Sci., vol. 11, no. 8, Aug. 1963, pp. 901-960.

23-9. Thomas, G. E.; and Krassa, R. F.: OGO 5 Measurements of the Lyman Alpha Sky Background. Astron. Astrophys., vol. 11, no. 2, Apr. 1971, pp. 218-233.

23-10. Barth, Charles A.: Planetary Ultraviolet Spectroscopy. Appl. Optics, vol. 8, no. 7, July 1969, pp. 1295-1304.

23-11. Fairfield, D. H.: Average and Unusual Locations of the Earth's Magnetopause and Bow Shock. J. Geophys. Res., vol. 76, no. 28, Oct 1, 1971, pp. 6700-6716.

23-12. Neugebauer, M.; Snyder, C. W.; Clay, D. R.; and Goldstein, B. E.: Solar Wind Observations on the Lunar Surface with the Apollo-12 ALSEP. Planet. Space Sci., vol. 20, no. 2, Oct. 1972, pp. 1577-1591.

23-13. Leich, D. A.; Tombrello, T. A.; and Burnett, D. S.: The Depth Distribution of Hydrogen in Lunar Materials. Lunar Science IV (Abs. of papers presented at the Fourth Lunar Science Conference (Houston, Tex.), Mar. 5-8, 1973), pp. 463-465.

23-14. Fleischer, Robert L.; and Hart, Howard R., Jr.: Surface History of Lunar Soil and Soil Columns. Lunar

Science IV (Abs. of papers presented at the Fourth Lunar Science Conference (Houston, Tex.), Mar. 5-8, 1973), pp. 251-253.

23-15. Geiss, J.; Buehler, F.; Cerutti, H.; Eberhardt, P.; and Filleux, Ch.: Solar Wind Composition Experiment. Sec. 14 of the Apollo 16 Preliminary Science Report. NASA SP-315, 1972.

23-16. Siscoe, G. L.; and Mukherjee, N. R.: Upper Limits on the Lunar Atmosphere Determined from Solar-Wind Measurements. J. Geophys. Res., vol. 77, no. 31, Nov. 1, 1972, pp. 6042-6051.

23-17. Gott, J. Richard, III; and Potter, A. E., Jr.: Lunar Atomic Hydrogen and Its Possible Detection by Scattered Lyman-α Radiation. Icarus, vol. 13, 1970, pp. 202-206.

23-18. Manka R. H.; and Michel, F. C.: Lunar Atmosphere as a Source of Lunar Surface Elements. Proceedings of the Second Lunar Science Conference, vol. 2, MIT Press (Cambridge, Mass.), 1971, pp. 1717-1728.

23-19. Hodges, R. R.: Helium and Hydrogen in the Lunar Atmosphere. J. Geophys. Res., vol. 78, 1973.

23-20. Hoffman, J. A.; Hodges, R. R., Jr.; and Evans, D. E.: Lunar Atmosphere Composition Results from Apollo 17. Proceedings of the Fourth Lunar Science Conference, Pergamon Press (New York), Dec. 1973.

23-21. Spitzer, L.; Drake, J. F.; Jenkins, E. B.; Morton, D. C.; et al.: Spectrophotometric Results from the Copernicus Satellite. IV, Molecular Hydrogen in Interstellar Space. Astrophys. J. Letters, vol. 181, May 1, 1973, pp. L116-L121.

23-22. Hollenbach, D.; and Salpeter, E. E.: Surface Recombination of Hydrogen Molecules. Astrophys. J., vol. 163, no. 1, Jan. 1971, pp. 155-164.

23-23. Lucke, R. L.; Henry, R. C.; and Fastie, W. G.: Far Ultraviolet Reflectivity of Lunar Dust Samples: Apollo 11, 12, and 14. Astron. J., vol. 78, no. 3, Apr. 1973, pp. 263-266.

23-24. Hapke, B. W.; Cohen, A. J.; Cassidy, W. A.; and Wells, E. N.: Solar Radiation Effects on the Optical Properties of Apollo 11 Samples. Proceedings of the Apollo 11 Lunar Science Conference, vol. 3, Pergamon Press (New York), 1970, pp. 2199-2212.

23-25. Hapke, Bruce W.: A Theoretical Photometric Function for the Lunar Surface. J. Geophys. Res., vol. 68, no. 15, Aug. 1, 1963, pp. 4571-4586.

23-26. Lillie, C. F.: OAO-2 Observations of the Zodiacal Light. The Scientific Results From the Orbiting Astronomical Observatory (OAO-2). NASA SP-310, 1972, pp. 95-108.

23-27. Feldman, P. D.; Fastie, W. G.; Henry, R. C.; Moos, H. W.; et al.: Far Ultraviolet Observations of the Earth's Airglow From Apollo 17. Paper presented at 54th Annual Meeting, Am. Geophys. Union (Washington, D.C.), Apr. 1972.

23-28. Henry, R. C.; Moos, H. W.; Fastie, W. G.; and Weinstein, A.: Low-Resolution Ultraviolet Spectroscopy of Several Stars. Paper presented at 16th Plenary Meeting, COSPAR (Konstanz, W. Germany), June 1973.

23-29. Feldman, P. D.; and Fastie, W. G.: Fluorescence of Molecular Hydrogen Excited by Solar Extreme Ultraviolet Radiation. Astrophys. J. Letters, Oct. 15, 1973.

24. Infrared Scanning Radiometer

F. J. Low[a][†] *and W. W. Mendell*[b]

The infrared scanning radiometer (ISR) is a thermal imaging device capable of mapping lunar surface thermal emission from lunar orbit. The principal experimental objective of the ISR is the measurement of lunar nighttime temperatures and cooling rates for that portion of the Moon overflown by the orbiting command and service module. Such data are related to the physical parameters (density and thermal conductivity) of the local surface layer.

The thermal emission at the surface of the Moon serves to balance the solar radiation absorbed at the surface and the heat flow into or out of the subsurface. Heat conduction through the surface is generally small because the lunar soil is an excellent thermal insulator. Therefore, the daytime temperature regime is dominated by such factors as albedo, Sun angle, and local slope. Conversely, the nighttime emission represents the reradiation of heat stored during the lunar day and is largely dependent on the physical properties of the surface layer.

A simple, one-dimensional model of the soil layer (ref. 24-1) can be used to demonstrate the general behavior of surface temperature. In such a model, families of temperature curves (faired curves in fig. 24-1) can be generated in terms of a single thermal parameter $\gamma = (k\rho c)^{-\frac{1}{2}}$, where k is the thermal conductivity, ρ is the bulk density, and c is the specific heat. This simplified model disregards radiative transfer in the surface layer, but it is still useful to characterize the thermal response in terms of γ. Earth-based measurements of the lunar midnight temperature (ref. 24-2) place $\gamma \approx 850$ cal^{-1} cm^2 K sec$^{\frac{1}{2}}$.

Shorthill and Saari's (ref. 24-3) thermal mapping of the eclipsed Moon from a telescope in Egypt demonstrated a wide variety of thermal behavior on the visible hemisphere. At a spatial resolution of approximately 20 km at the center of the disk, the Moon possessed hundreds of features that remained warm relative to their environs during the eclipse. Studies of these "thermal anomalies" indicated surface rock exposures associated with fresh impact features as an explanation. More recent correlations of the eclipse data with Earth-based radar measurements (ref. 24-4) show that a one-to-one correspondence does not exist between boulder fields and infrared anomalies.

In contrast to the eclipse cooling, which lasts for only a few hours, the lunar nighttime cooling regime lasts for 14 days. The nighttime thermal gradients extend deeper into the subsurface, and the surface temperature distributions are influenced by structure to a depth of a few tens of centimeters. Many observers (refs. 24-5 to 24-9) have attempted to map the nighttime Moon from Earth to take advantage of the improved subsurface resolution. However, the observational difficulties (ref. 24-8) associated with the low level of thermal emission and with the terrestrial atmosphere have precluded substantial success. The ISR provides a solution to the observational problem with an absolute radiometric measurement of lunar nighttime temperatures that represents an order-of-magnitude improvement in spatial and radiometric resolution over Earth-based work.

INSTRUMENT DESCRIPTION

The ISR is a thermal imaging line scanner (ref. 24-10). A schematic diagram of the optical system is shown in figure 24-2. The spherical-spherical Cassegrain optical system has a 17.78-cm (7 in.) aperture. The instantaneous field of view is 20 mrad, which translates to a circular lunar surface resolution element ranging from 2.0 to 2.6 km in diameter during accumulation of data from the spacecraft circularized orbit. This spatial resolution is an order-of-magnitude improvement over Earth-based observations.

[a]The University of Arizona.

[b]NASA Lyndon B. Johnson Space Center.

[†]Principal Investigator.

(a)

(b)

(c)
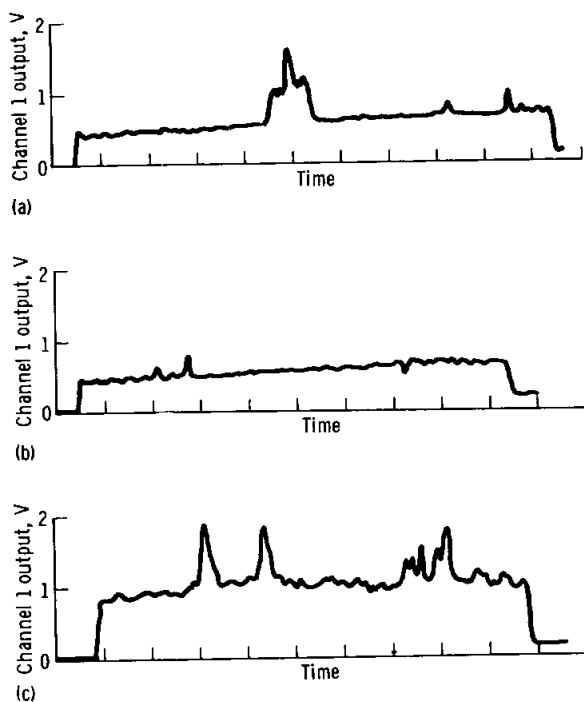
FIGURE 24-4.—Nighttime scans of the lunar surface. Each division on the ordinates represents 62.5 msec. (a) Scan at a scan center of latitude 7.0° N, longitude 35.9° W, a phase angle of 214.1°, and an altitude of 39.7 km. The crater Kepler A is thermally enhanced relative to the 92 K background in Oceanus Procellarum. The temperature in the crater ranges from 112 K on the wall to a maximum of 126 K in the center. (b) Scan at a scan center of latitude 18.9° N, longitude 2.0° E, a phase angle of 264.8°, and an altitude of 109.3 km. A predawn cold spot shows an 8 K contrast to the 90 K background in Montes Apenninus. (c) Scan at a scan center of latitude 22.5° S, longitude 178.4° E, a phase angle of 120.8°, and an altitude of 118.0 km. These large far-side anomalies are enhanced approximately 22 K relative to a 108 K background 2.5 days after lunar sunset.

spacecraft was 39.7 km at the time of the scan, making the ISR resolution element 0.8 km wide on the surface. The width of the broad base of the enhancement is 10 km, coinciding with the crater diameter. The thermal peak in the center is approximately 2 km across. The measured radiance in the central region increases linearly from both sides to the center, implying that the actual temperature at the center has not been fully resolved. The dramatic change of material properties within the crater probably reflects exposure of bedrock. The radial gradient may be caused by a corresponding radial distribution of slump material from the crater walls.

Unfortunately, no lunar photographs that contain a good view of the crater bottom have been found.

The scan shown in figure 24-4(b) contains predawn temperatures, the coldest for any given surface region. The scan center is located just north of Mare Vaporum and south of the Apollo 15 landing site. On the right portion of the scan is a negative anomaly, a region having depressed temperatures relative to its environs. In this case, the temperature difference is ≥8 K. A lower limit is given because the width of the deflection, only one resolution element, implies that the anomaly may not be fully resolved. The anomalous region lies south of the crater Conon in Montes Apenninus. The magnitude of the temperature contrasts implies that the thermal conductivity of the soil in that region is approximately one-half that of the surrounding material. These underdense regions cannot be impact features. The preservation of the density contrast also implies that the regions are relatively young on a geologic scale. Cold nighttime anomalies are particularly difficult to detect from Earth-based observations. Although such features have been reported previously (refs. 24-8 and 24-11), the ISR results provide the first opportunity to study them in detail.

The scan in figure 24-4(c) includes far-side anomalies. Our abbreviated data survey shows that such features are not common in the nighttime data on the lunar far side (fig. 24-5). A low frequency of occurrence was anticipated because near-side anomalies occur preferentially in the maria, regions which are generally absent in the other hemisphere. The two prominent anomalies on the left side of the

Dec. 11, 1972, 12:45:29.209 G.m.t.
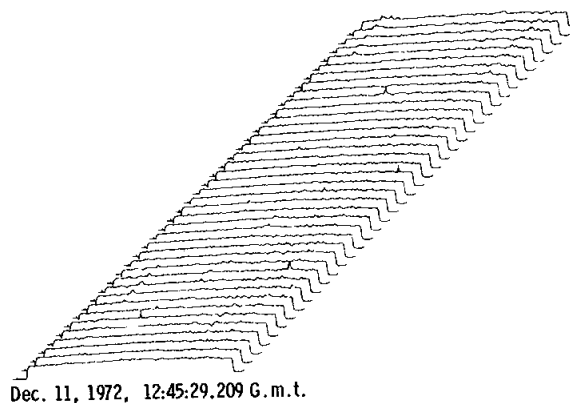
FIGURE 24-5.—Scan sequence of a featureless region northeast of Mare Orientale and South of the crater Hartwig. North is to the left; west is at the top.
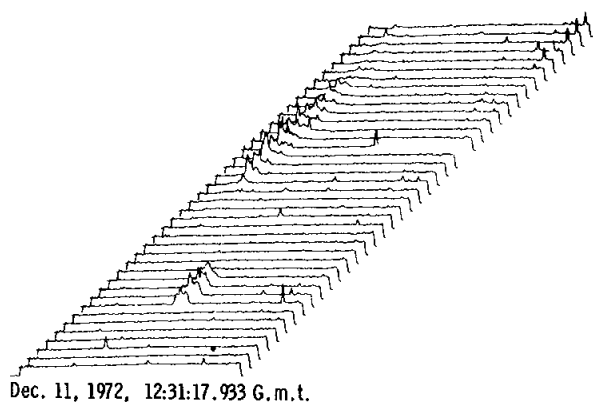
Dec. 11, 1972, 12:31:17.933 G.m.t.

FIGURE 24-6.—This sequence of nighttime scans runs westward approximately between 35° and 38° W longitude at latitude 7° N. The crater in the foreground is Kepler A, and the extended feature in the background is the crater Kepler. North is to the left; west is at the top.

Dec. 11, 1972, 12:36:59.643 G.m.t.

FIGURE 24-7.—This sequence of scans runs from 53° to 56° W longitude just north of the lunar equator. North is to the left; west is at the top.

scan (fig. 24-2(c)) are located between the large craters Aitken and Van de Graaff. The large peak at the right limb corresponds to the crater Birkeland; the smaller structure to its left is in the crater Van de Graaff.

In figure 24-6, the scan in figure 24-4(a) is shown in its full data context. In this sequence of scans, north is to the left and west is upward. The extended feature just past the middle of the sequence is the crater Kepler. An interesting aspect of this set is the general lack of features except for the two major craters. As part of the Kepler ejecta blanket, this region might have been expected to be littered with debris and, consequently, to show considerable thermal structure.

Farther to the west, near the equator south of the crater Reiner, an area in Oceanus Procellarum that is devoid of craters displays many thermal anomalies (fig. 24-7). This structure cannot be attributed to residual, postsunset, topographic cooling differences. Figure 24-5 shows that such structure is entirely absent in a highland region northeast of Mare Orientale and nearer the sunset terminator. It is probable that the amount of thermal structure is associated with the age of the region; older regions have a featureless, soil-like response.

In figure 24-1, lunar temperatures as measured by the ISR are plotted as a function of brightness longitude. The values were taken from scans made by the Apollo 17 spacecraft during revolution 20. An attempt was made to choose a point from each scan on the lunar equator. The spacecraft orbital motion

causes the actual sequence of the points to go from right to left on the figure. The first data point of the sequence lies 5.3 days after lunar sunset (abscissa of 0.43 in fig. 24-1) and was measured at 08:26 G.m.t. on December 12, 1972. The final point (at approximately the same lunation coordinate) was measured at 10:25 G.m.t. on the same day. A data gap exists near the subsolar point for this orbit.

The plotted temperatures will change as the ISR values are refined. The error estimate is 3 K for the nighttime measurements; the values probably are systematically low. No correction for albedo or topography has been made.

Theoretical curves for various values of γ are also plotted in figure 24-1. The theoretical calculations represent the cooling behavior at a single point, whereas the measured data are taken over many different types of material. The cooling curve apparently falls below $\gamma \approx 850 \ cal^{-1} \ cm^2 \ K \ sec^{\frac{1}{2}}$, even if the error estimate is taken into account. The elevated temperatures near lunar midnight fall in Oceanus Procellarum, where general thermal enhancement has been noted in eclipse measurements (ref. 24-12).

The data for lunar afternoon temperatures come from the highlands on the far side, and the morning points fall in Mare Fecunditatis and Mare Tranquillitatis. The combined effects of albedo and directionality of emissivity account for the apparent systematic deviations to either side of the theoretical curve.

CONCLUSIONS

This brief survey of the ISR data has confirmed that a variety of thermal behavior exists on the lunar surface. Further work on the measurements will establish the cooling behavior of the major types of lunar regions and the most significant exceptions within each category.

REFERENCES

24-1. Krotikov, V. D.; and Shchuko, O. B.: The Heat Balance of the Lunar Surface Layer During a Lunation. Soviet Astron.–AJ, vol. 7, no. 2, Sept.-Oct. 1963, pp. 228-232.

24-2. Mendell, W. W.; and Low, F. J.: Low-Resolution Differential Drift Scans of the Moon at 22 Microns. J. Geophys. Res., vol. 75, no. 17, June 10, 1970, pp. 3319-3324.

24-3. Shorthill, R. W.; and Saari, J. M.: Infrared Observation of the Eclipsed Moon. Boeing Sci. Res. Lab. Dcmt. AD-689076, D1-82-0778, Jan. 1969.

24-4. Thompson, T. W.; Masursky, H.; Shorthill, R. W.; Zisk, S. H.; and Tyler, G. L.: A Comparison of Infrared, Radar, and Geologic Mapping of Lunar Craters. Contribution 16, Lunar Sci. Inst., Symposium on the Geophysical Interpretation of the Moon (Houston, Tex.), June 1970.

24-5. Wildey, Robert L.; Murray, Bruce C.; and Westphal, James A.: Reconnaissance of Infrared Emission From the Lunar Nighttime Surface. J. Geophys. Res., vol. 72, no. 14, July 15, 1967, pp. 3743-3749.

24-6. Shorthill, Richard W.; and Saari, John M.: Radiometric and Photometric Mapping of the Moon Through a Lunation. Ann. N.Y. Acad. Sci., vol. 123, July 15, 1965, pp. 722-739.

24-7. Allen, David A.: Infrared Studies of the Lunar Terrain. I: The Background Moon. The Moon, vol. 2, no. 3, 1971, pp. 320-337.

24-8. Mendell, Wendell W.; and Low, Frank J.: Lunar Differential Flux Scans at 22 Microns, Final Report. NASA CR-121457, 1971.

24-9. Raine, W. L.: Thermal Mapping of the Lunar Surface. Final Rept. SE-SSL-1649, Contract NAS8-26343, Teledyne Brown Engineering (Huntsville, Ala.), Sept. 1972.

24-10. McIntosh, R. B., Jr.: and Mendell, W. W.: Infrared Scanning Radiometer for Temperature Mapping of the Lunar Surface on the Apollo 17 Flight. Proceedings of the Technical Program, Fourth Annual Electro-Optical Systems Design Conference, Industrial and Scientific Conference Management, Inc. (Chicago), 1972, pp. 356-361.

24-11. Low, Frank J.: Lunar Nighttime Temperatures Measured at 20 Microns. Astrophys. J., vol. 142, no. 2, Aug. 15, 1965, pp. 806-808.

24-12. Saari, J. M.; and Shorthill, R. W.: Thermal Anomalies on the Totally Eclipsed Moon of December 19, 1964. Nature, vol. 205, no. 4975, Mar. 6, 1965, pp. 964-965.

25. Biostack Experiment

H. Bücker,[a][†] G. Horneck,[a] E. Reinholz,[b] W. Rüther,[c]
E. H. Graul,[c] H. Planel,[d] J. P. Soleilhavoup,[d] P. Cüer,[e]
R. Kaiser,[e] J. P. Massué,[e] R. Pfohl,[e] W. Enge,[f]
K. P. Bartholomä,[f] R. Beaujean,[f] K. Fukui,[f] O. C. Allkofer,[f]
W. Heinrich,[f] E. V. Benton,[g] E. Schopper,[a] G. Henig,[a]
J. U. Schott,[a] H. François,[h] G. Portal,[h] H. Kühn,[i]
D. Harder,[j] H. Wollenhaupt,[a] and G. Bowman[k]

The objective of the Apollo 17 biostack experiment (biostack II) was to establish the biologic efficiency of individual particles of galactic cosmic radiation that penetrate biologic matter during space flight. Of special interest were the heavy (high atomic number) high-energy particles with high loss of energy on their path through material (HZE particles). For this purpose, layers of several biologic species were stacked alternately with various track detectors. The results will be very useful in estimating potential radiation hazards to astronauts during long-duration space missions. This work complements the results of the Apollo 16 biostack experiment (biostack I), in which a variety of radiobiologic end points have been found to differ in sensitivity to the penetration of HZE particles. *Artemia salina* eggs, for instance, hit by an HZE particle showed a high reduction in larval emergence and hatching as well as the induction of several developmental anomalies.

Preliminary analyses of the biostack II radiation detectors indicate a cosmic "background" radiation of 750×10^{-5} J/kg. A fluence of 30 to 90 particles/cm^2 of estimated charge $Z \geqslant 6$ was measured, depending on the detector threshold for the energy loss. These data are in agreement with the radiation results obtained in biostack I. Generally, the viability of the flown biologic objects did not appear to be affected by any additional random space flight factors. From these observations, a scientifically profitable evaluation of the biostack II experiment is anticipated.

EXPERIMENT THEORY

During space missions outside the Earth magnetosphere, a spacecraft encounters the full spectrum of galactic cosmic radiation. Outside the geomagnetic field, there is no cut-off effect. Therefore, the energy spectrum of cosmic ray nuclei includes particles of low energies. These heavy nuclei (HZE particles) of extremely high values of linear energy transfer (LET) in the Bragg peak may reach astronauts despite shielding by the spacecraft wall (ref. 25-1). Particles that penetrate the spacecraft may pass through or stop in biologic matter. Therefore, the radiation hazards to man during long-duration space missions, especially the HZE component of cosmic radiation which man does not encounter on Earth, must be precisely estimated. Thus, all biologic experiments in space should consider the possible influence of HZE particles in any observed biologic effects.

The biostack experiment provided a unique method to determine the biologic efficiency of HZE particles during space flight. The last two lunar missions provided the last opportunity for several years to study this phenomenon outside the Earth

[a]University of Frankfurt.

[b]Max Planck Institut für Biophysik, Frankfurt.

[c]University of Marburg.

[d]University of Toulouse.

[e]University of Strasbourg.

[f]University of Kiel.

[g]University of San Francisco.

[h]Atomic Energy Commission, Republic of France.

[i]Gesellschaft für Strahlen und Umweltforschung, Frankfurt.

[j]University of Würzburg.

[k]U.S. Representative for biostack, University of Frankfurt.

[†]Principal Investigator.

magnetosphere. The biostack II experiment on board the Apollo 17 spacecraft complemented biostack I on board Apollo 16 (ref. 25-2).

The biologic objects in biostack II were selected because of well-established scientific baseline information and technical points of view. These biologic objects were (1) spores of the bacterium *Bacillus subtilis*, (2) cysts of the protozoon *Colpoda cuculus*, (3) seeds of the crucifer *Arabidopsis thaliana*, (4) eggs of the shrimp *Artemia salina*, (5) eggs of the beetle *Tribolium confusum*, and (6) eggs of the grasshopper *Carausius morosus*. The biologic attributes studied in the six biologic species included inhibition of germination, inhibition of cell growth, inhibition of organ development, developmental anomalies in various stages of growth, and mutation induction.

The biologic area hit by an HZE particle was determined from adjacent physical track detectors including nuclear emulsions (Ilford K2 and K5), cellulose nitrate (CN) sheets, polycarbonate (Lexan) sheets, and silver chloride (AgCl) crystals. Thus, the biostack II experiment was well established to identify an individual HZE particle and to correlate possible biologic effects in its path or trajectory. The results will help to provide information on the mechanism of the biologic interaction of HZE particles, currently not available on Earth. Such information is necessary to predict possible radiation hazards to man in space.

In addition, the evaluation of the track detectors will yield the spectra of charge and energy as well as the energy loss of the particles studied. Establishing the modification of these spectra attributable to absorption by the biostack material will yield practical information for establishing radiation protection requirements for manned space flights.

INTERACTION OF HZE PARTICLES WITH BIOLOGIC MATTER

It has been established that HZE particles have high biologic efficiency. This statement is based on several balloon- and satellite-borne radiobiologic studies, because Earth-based equipment is currently incapable of producing accelerated heavy particles with exact properties of HZE particles. Many effects attributable to HZE particles were observed. These effects included mutation induction in *Escherichia coli* cells (ref. 25-3), in barley seeds (ref. 25-4), and in corn seeds (ref. 25-5); developmental disturbances in

Artemia salina eggs (refs. 25-4 and 25-6); damage to hair follicles of the black mice (refs. 25-7 and 25-8); and brain injuries in mice (ref. 25-9) and monkeys (ref. 25-10). The light flashes observed by the astronauts during the Apollo lunar missions stimulated systematic studies of this phenomenon on Earth (ref. 25-11) and in space (ref. 25-12). The results suggested that the light flashes might be caused by ionization of HZE particles in the tissue of the retina; however, there has been no confirmation of any hazards associated with this phenomenon.

The terms "dose" and "relative biologic efficiency" cannot be used to describe the biologic effects of the HZE particles encountered in space. More appropriately, the terms "ion kill" (ref. 25-13) and "microbeam" (ref. 25-14) are used to describe their radiobiologic characteristics. This choice of terms indicates that a single traversal by a heavy nucleus, with a sufficiently high LET, produces an energy dissipation in the biologic microstructure comparable to a beam of very narrow cross section. The LET distribution can properly be expressed in terms of integral track length; this gives a more complete
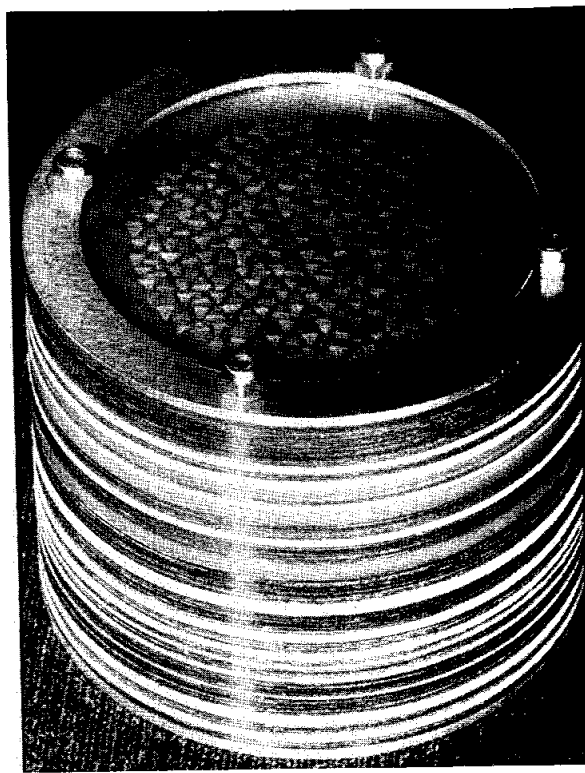
FIGURE 25-1.—Biostack software composed of biologic layers and sheets of radiation detectors.

picture of the energy dissipation pattern in tissue (ref. 25-1).

The understanding of these radiobiologic problems would be improved by space experiments investigating the critical LET values of HZE particles for different types of biologic damage. The biostack experiment met this requirement. Biostack I included a wide spectrum of biologic objects with established radiobiologic end points to which the degree of their response to HZE particles could be related (ref. 25-2). Some of the biologic processes studied were not influenced remarkably by a penetrating cosmic ion. Conversely, other biologic processes were almost totally disturbed or inhibited by the passage of a single ion; for example, the emergence and hatching of *Artemia salina* eggs and subsequent malformations in larvae. Correlation of these effects with the charge and energy loss of the effective HZE particle resulted in determination of the critical LET thresholds for several radiobiologic processes. Thus, the biostack I and biostack II experiments were well suited to help understanding of the complex phenomenon of biologic response to HZE particle penetration and interaction.

APOLLO 17 FLIGHT UNIT

The biostack II experiment had the same design concept as biostack I (ref. 25-2). A hermetically sealed, cylindrical aluminum container, 10 cm long and 12.5 cm in diameter, enclosed a stack of 257 sheets (fig. 25-1). Selected biologic objects in the resting state in monolayers (fig. 25-2) were sandwiched between several different visual particle detectors. This arrangement made it possible to trace the path of an HZE particle through the stack and to determine the trajectory of the heavy ion in the biologic layer (fig. 25-3). Individual evaluation of the biologic objects hit by an HZE particle, in parallel with characterization of the respective hitting HZE particle, permits estimation of the biologic efficiency of the HZE particle along its path into or through the biologic object.

The biostack II storage area in the Apollo 17 command module was the same as that used for biostack I on the Apollo 16 spacecraft. This area was chosen so that shielding to cosmic radiation would be minimal.

After their return to Frankfurt, an external inspection of the three biostack II units (flight unit,
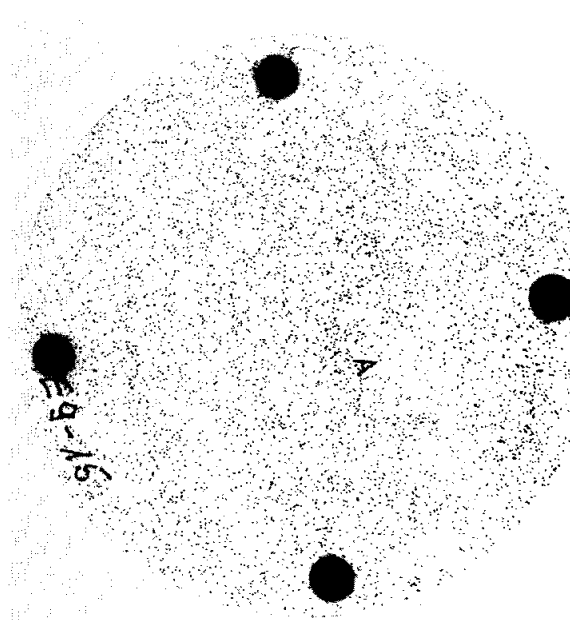
FIGURE 25-2.—A biologic layer of the biostack II flight unit consisting of *Artemia salina* eggs embedded in a foil of polyvinyl alcohol.

backup unit, and Earth control unit) revealed no damage. The biostack II flight unit (serial number (S/N 7)) and the backup unit (S/N 8), used as an Earth control at the NASA John F. Kennedy Space Center and the NASA Lyndon B. Johnson Space Center, were disassembled immediately after their arrival in Frankfurt. No alteration of or damage to the biologic objects and detectors could be noticed. Disassembly was accomplished without complication. During disassembly, the pattern of the biologic objects of each layer positioned directly over a K2 nuclear emulsion was transferred to the upper side of the corresponding emulsion by optical illumination (fig. 25-4), as established for biostack I (ref. 25-2). Further, a coordinate grid was placed on the bottom of each sheet of a nuclear emulsion by optical illumination. Following disassembly, the biologic and physical components of the biostack II flight unit and the Earth control unit were distributed to collaborating research laboratories for processing and evaluation.

PRELIMINARY OBSERVATIONS

Total Dose of Cosmic Ionizing Radiation

The total dose of cosmic ionizing radiation (background radiation) was measured by lithium fluoride

particles. Tracks of particles with charge $Z < 4$ are recorded only if not relativistic. The surviving tracks were divided into five groups (table 25-III). An example of a track from each group is shown in figure 25-8. The density of surviving nuclear stars was found to be 4500 ± 650 stars/cm^3 of AgCl.

BIOLOGIC FLIGHT OBJECTS

Viability studies of the flight controls were performed first. These controls are the biostack II biologic objects not hit by a heavy particle. Germination and outgrowth of *Bacillus subtilis* flight and Earth controls were studied in special incubation chambers on nutrient broth agar at 310 K (ref. 25-15). No significant differences were observed in germination and outgrowth (table 25-IV) or cell elongation rate (fig. 25-9) of the flight and Earth controls. The reduction in cell elongation rate after approximately 130 min of incubation is typical for these rather densely covered spore foils; however, this response gives no evidence of reduced viability of the

FIGURE 25-7.—Etch cone of a scattered HZE particle (approximately 750 μm long) in Daicel-71 CN.
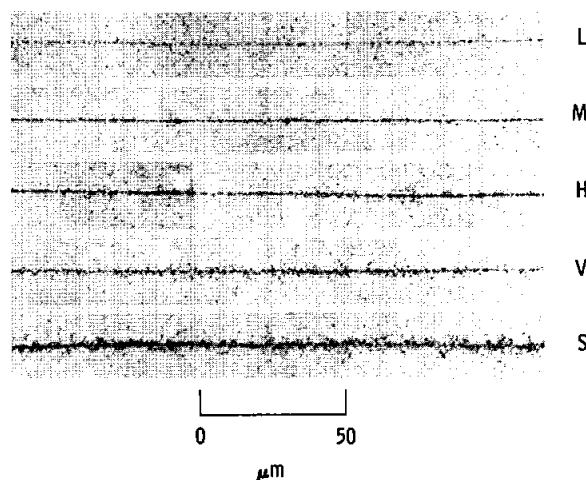
FIGURE 25-8.—Tracks recorded in AgCl crystals of biostack II. L = light ($Z \leqslant 6$), M = medium ($Z = 6$ to $Z = 9$), H = heavy ($Z = 9$ to $Z = 15$), V = very heavy ($Z = 14$ to $Z = 26$), S = super heavy ($Z > 20$).

TABLE 25-II.—*Particles Recorded in CN Sheets of Biostack II*

CN type	Sheet no.	Direction	Etch holes	Etch cones (1 or 2)	Stopping tracks from—		All tracks in—	
					Outside	Inside	20 cm^2	1 cm^2
[a]Daicel-71	E 2-5	Space	236	285	27	20	568	28.4
	E 13-27	Cabin	161	202	25	14	402	20.1
[b]USF 4b	E 2-1	Space	--	–	–	–	–	70 ± 8
	E 13-25	Cabin	–	–	–	–	–	40 ± 6

[a]Etched 4.0 hr at 313 K.
[b]Etched 8.0 hr at 313 K.

TABLE 25-III.—*Particles Recorded in AgCl Crystals of Biostack II*

Particle group	Geometric track width, μm	Estimated charge Z	Fluence, particles/cm²
Light	< 0.8	⩽ 6	254 ± 14
Medium	0.8 to 1.2	6 to 9	68.4 ± 6.5
Heavy	1.2 to 2.0	9 to 15	17.3 ± 1.9
Very heavy	2.0 to 3.0	14 to 26	4.4 ± 0.8
Super heavy	> 3.0	> 20	2.4 ± 0.7
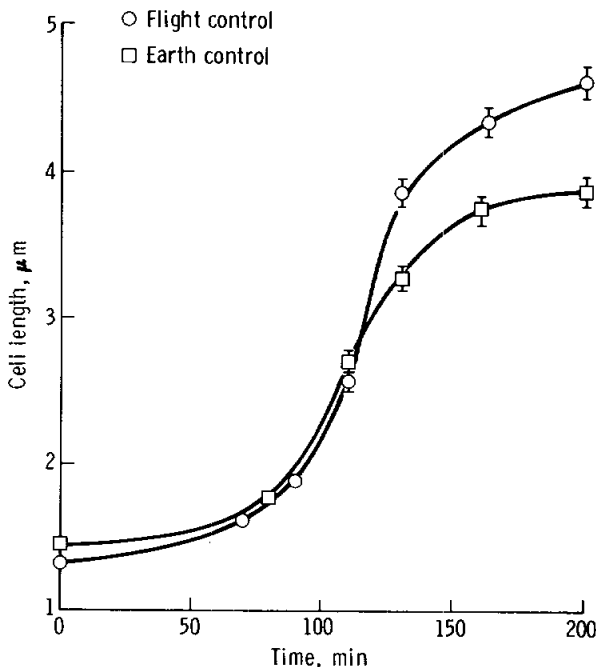
FIGURE 25-9.—Cell elongation rate after outgrowth of *Bacillus subtilis* spores of biostack II flight control and Earth control.

spores. Thus, space flight alone exerted no harmful influence on the viability of the spores.

Viability tests of the flight controls of *Artemia salina*, *Tribolium confusum*, and *Carausius morosus* were performed with small sections from the rim of the biologic foils. Breeding of *Artemia salina* in special salt water[1] containing living plankton, *Dunaliella viridis*, as the nutrient, resulted in a hatching of 84.2 percent for flight samples fixed to CN and of 90.8 percent for flight samples adjacent to nuclear emulsions. Thus, further investigation on the development of hit eggs will be possible. The eggs that have been hit by an HZE particle are identified from different track detectors positioned adjacent to the biologic layers. These detectors include K2 nuclear emulsions (fig. 25-10), CN sheets (fig. 25-11), and AgCl crystals. The last two detectors remained in fixed contact with the biologic layers during flight, disassembly, and physical evaluation. Investigation of developmental anomalies and histologic changes in the hit eggs is in progress.

DISCUSSION AND CONCLUSIONS

The first data read-out of the biostack II cosmic radiation detectors was in agreement with the results of the biostack I analysis. The total background dose and the particle flux recorded during the two flights are shown in table 25-V. The particle track detectors that were closest to space (i.e., near the command module wall) recorded fluences approximately 1.5 times greater than those directed toward the cabin. This decrease in fluence and a corresponding decrease in radiation dose through the stack are attributable to

TABLE 25-IV.—*Germination and Outgrowth of* B. Subtilis *Spores of Flight and Earth Controls*

Sheet no.	Control	Area covered by spores, percent	Germination, percent	Outgrowth, percent	Cell elongation onset time, min	Cell elongation rate, μm/min
E 3-35	Flight	23.2	97.7	80.7	80	4.8 × 10⁻²
F 3-41	Earth (Houston)	20.9	96.0	64.0	65	3.0
	Earth (Frankfurt)[a]	27.8	97.0	63.0	60	2.1

[a]Not etched.

FIGURE 25-10.—Shadows of two *Artemia salina* eggs on the K2 emulsion of the biostack II flight unit and the track of an HZE particle hitting an egg.

FIGURE 25-11.—Eggs of *Artemia salina* on a CN sheet of the biostack II flight unit and the track of a hitting HZE particle.

TABLE 25-V.—*Comparison of the First Data on Cosmic Radiation Obtained in Biostack I and II Flight Units*

| Flight unit | Background dose, J/kg hr | Flux, particles/cm² hr, recorded in— | | |
| | | K2 nuclear emulsion | CN directed toward— | |
			Space	Cabin
Biostack I	2.34 × 10⁻⁵	0.08	0.12	0.07
Biostack II	2.41	.13	.09	.07

the absorption by the stack material as the particles pass from the exterior (spacecraft wall) toward the interior.

From the studies of viability of the flight controls, the biostack II biologic objects, even *Artemia salina* flight control eggs, appeared to be unaffected by random space flight factors, whereas, in biostack I, there seemed to be an influence. Good agreement was observed on germination and outgrowth of *Bacillus subtilis* spores in both biostack experiments. However, after 130 min of incubation of biostack II sample spores, cellular elongation began to decline because of a rather high density of spores. This decline differs from the biostack results, where growth was followed up to the first and second cellular division (ref. 25-2). In the layers of biostack II, the spore was approximately 3 times higher than that of biostack I to increase the chance of spore hits

by HZE particles. The observed reduction in the cellular elongation rate did not influence the studied end points of germination and outgrowth.

From these initial observations, it can be seen that biostack II was a scientific success. The next postflight procedure will deal with the identification of the biologic area that has been penetrated by an HZE

TABLE 25-VI.—*Development of Two Strains of* Artemia salina *Eggs from Biostack I*

Sample	Radiation sensitive strain Hayward		Radiation resistant strain Utah	
	Emergence frequency, percent	Hatching frequency, percent	Emergence frequency, percent	Hatching frequency, percent
Flight eggs hit by an HZE ion . .	10	6	61	15
Flight controls	30	25	77	46
Ground controls	66	62	91	90

particle. Studies on the biologic effects attributable to HZE particles and the analysis of such biologically effective particles will follow. These studies will be based on the scientific results obtained from the evaluation of biostack I, which is still in progress.

Spores of *Bacillus subtilis* strain 168 in biostack I were found to be rather resistant to hits of HZE particles. Therefore, biostack II contained a second strain, pol⁻ (HA 101 (59) F, ref. 25-16), which is very sensitive to radiation, for comparison with the more radiation resistant strain 168.

Studies on strains of the same species of *Artemia salina* that differ in their radiation sensitivity have been performed on eggs from biostack I. The results were very informative. In the radiation sensitive strain (Hayward), only 10 percent of the hit eggs were able to pass the first stage of development; that is, the emergence from the egg. In contrast, the radiation resistant strain (Utah) showed an emergence frequency of 61 percent. After successful emergence, however, continued development stopped even in most hit objects of the radiation resistant strain, indicating a hatching decrease to 15 percent (table 25-VI). From these observations, it follows that the HZE-particle-induced damage in the encysted blastula of the eggs may influence gastrula formation and even the hatching process of the nauplius or larva of *Artemia salina*. Many nauplii that had succeeded in hatching from hit eggs did not survive the stage of first casting of the skin, which is accompanied by a high mitosis rate. Complex malformations observed in the nauplii from hit eggs are shortened extremities or abnormalities of the thorax and the abdomen (fig. 25-12). The biostack II studies may confirm these observations and extend them by systematic histologic investigations.

Three biostack units were available as Earth controls. Unit S/N 8 is already disassembled and serves as an untreated Earth control. Unit S/N 9 will be irradiated with accelerated oxygen and carbon

FIGURE 25-12.—Abnormal nauplius (with two abdomina) of *Artemia salina* hatched from an egg that has been hit by an HZE particle.

nuclei in the bevatron accelerator of the Lawrence Berkeley Laboratory, Berkeley, California. Unit S/N 10 will be submitted to vibration, acceleration, and shock at Centre National d'Etudes Spatiales, Toulouse, France, in order to study the influence of these launch parameters on the biologic objects.

REFERENCES

25-1. Schaefer, H. J.: Dosimetric Characteristics of HZE Particles in Space. NASA Joint Report NAMRL-1172, Nov. 1972.

25-2. Bücker, Horst; Horneck, G.; Reinholz, E.; Scheuermann, W.; et al.: Biostack Experiment. Sec. 27, Part A, of the Apollo 16 Preliminary Science Report. NASA SP-315, 1972.

25-3. Pfister, A.; Deltour, G.; Atlan, H.; Kaiser, R.; et al.: Etude De L'action Biologique Des Rayons Cosmiques—Au Moyen De Ballons Sondes. Behavioural Problems in

Aerospace Medicine, AGARD Conference Proceedings no. 25, Oct. 1967, pp. 16-1 to 16-8.

25-4. Eugster, J.: Mutationen Durch Kosmische Strahlung. Bild der Wissenschaft, vol. 2, 1964, pp. 26-34.

25-5. Curtis, Howard J.; and Smith, Harold H.: Corn Seeds Affected by Heavy Cosmic Ray Particles. Science, vol. 141, no. 3576, July 12, 1963, pp. 158-160.

25-6. Eugster, J.: Zur Biologischen Wirkung Der Kosmischen Strahlen Im Menschlichen Körper. Raketentechnik und Raumfahrt-forschung, vol. 7, Oct.-Dec. 1963, pp. 163-165.

25-7. Chase, H. B.: Cutaneous Effects of Primary Cosmic Radiation. J. Aviation Med., vol. 25, no. 4, Aug. 1954, pp. 388-391.

25-8. Chase, H. B.; and Post, J. S.: Damage and Repair in Mammalian Tissues Exposed to Cosmic Ray Heavy Nuclei. J. Aviation Med., vol. 27, no. 6, Dec. 1956, pp. 533-540.

25-9. Yagoda, H.; Behar, A.; Davis, R. L.; Kraner, K. L.; et al.: Brain Study of Mice Exposed to Cosmic Rays in the Stratosphere and Report of Nuclear Emulsion Monitoring. In Four Balloon Flights From Bemidji, Minnesota, July-August, 1960. Military Med., vol. 128, no. 7, July 1963, pp. 655-672.

25-10. Haymaker, W.; Bailey, O. T.; Benton, E. V.; Vogel, F. S.; et al.: Brain Study in Balloon-Borne Monkeys Exposed to Cosmic Rays. Aerospace Med., vol. 41, no. 9, Sept. 1970, pp. 989-1002.

25-11. Budinger, T. F.; Tobias, C. A.; Lyman, J. T.; Chapman, P. K.; et al.: Light Flash Phenomenon Seen by Astronauts. NASA CR-125453, 1971.

25-12. Benson, Richard E.; and Pinsky, Lawrence S.: Visual Light Flash Phenomenon. Sec. 27, Part C, of the Apollo 16 Preliminary Science Report. NASA SP-315, 1972.

25-13. Butts, J. J.; and Katz, R.: Theory of RBE for Heavy Ion Bombardment of Dry Enzymes and Viruses. Radiation Res., vol. 30, no. 4, Apr. 1967, pp. 855-871.

25-14. Schaefer, H. J.; and Sullivan, J. J.: Nuclear Emulsion Recordings of the Astronauts' Radiation Exposure on the First Lunar Landing Mission, Apollo 11. NASA CR-115804, 1970.

25-15. Bücker, H.; et al.: The Biostack Experiment on Apollo 16. Life Sciences and Space Research XI, Akademie Verlag (Berlin), 1973, pp. 295-305.

25-16. Taylor, G. R.; Chassay, C. E.; Ellis, W. L.; Foster, B. G.; et al.: Microbial Response to Space Environment. Sec. 27, Part B, of the Apollo 16 Preliminary Science Report. NASA SP-315, 1972.

26. Biocore Experiment

O. T. Bailey,[a] E. V. Benton,[b] M. R. Cruty,[b] G. A. Harrison,[c] W. Haymaker,[c†]
G. Humason,[d] H. A. Leon,[c] R. L. Lindberg,[e] B. C. Look,[c‡] C. C. Lushbaugh,[d]
D. E. Philpott,[c] T. Samorajski,[f] R. C. Simmonds,[g] K. P. Suri,[c]
J. W. Tremor,[c] C. E. Turnbill,[c] F. S. Vogel,[h] D. L. Winter,[c] and W. Zeman[i]

The biological cosmic ray experiment (BIOCORE) was conducted primarily to determine if heavy cosmic ray particles (stripped nuclei) injure the brain and eyes. Other tissues were also taken into consideration, particularly the skin, because the skin of balloon-borne black mice and black rabbits has been reported to have been severely damaged during exposure to cosmic ray particles (refs. 26-1 and 26-2). The idea of the pocket mouse experiment originated from reports by astronauts that they had periodically seen light flashes during Apollo missions (ref. 26-3). Such flashes are thought to represent an excitatory effect caused by cosmic ray particles as they traverse the retina (refs. 26-4 and 26-5). The questions arose whether, in addition to excitation, the retinal cells suffered damage and whether other cells, particularly those in the brain, may be damaged by cosmic radiation.

Lesions have been found in the brains of guinea pigs and monkeys flown at high altitudes in balloons (refs. 26-6 and 26-7). However, the lack of adequate monitoring by cosmic ray particle detectors precluded judgment as to the significance of the lesions. In the Apollo 17 experiment, great care was therefore taken to provide optimum monitoring for the brains

of the pocket mice and, to some extent, for the eyes and other head structures by implanting cosmic ray detectors under the scalp.

DESCRIPTION OF EXPERIMENT

Pocket Mouse

The pocket mouse (*Perognathus longimembris*) (fig. 26-1) was selected as the biological specimen for this experiment. This heteromyid rodent from the arid regions of the southwestern United States and northern Mexico does not require drinking water, subsists on seeds and plant material, and is a facultative homeotherm with an ability to drop its metabolic rate dramatically while at rest or in response to environmental stress (ambient temperature, lack of food, confinement) (refs. 26-8 to 26-10). In addition, the wastes are concentrated (less than 1×10^{-4} kg/day each of urine and feces) and food can be provided ad libitum because the mice are natural hoarders. The pocket mouse also was chosen for the experiment for the following reasons.

1. The availability of background information on the animal (ref. 26-11)

2. The small size of the animal (≈ 10 g) (2.2×10^{-2} lb) (range, 7 to 12 g), which permitted a reasonable number of mice in a small package

3. The ease of maintaining the animal in an isolated state

4. The ability of the animal to withstand environmental stresses

Radiation Monitors

The radiation monitors implanted under the scalp of the mice consisted of plastic nuclear track detec-

[a]Abraham Lincoln School of Medicine, University of Illinois.
[b]University of San Francisco.
[c]NASA Ames Research Center.
[d]Medical Division, Oak Ridge Associated Universities.
[e]Northrop Corporate Laboratories.
[f]Cleveland Psychiatric Institute.
[g]NASA Lyndon B. Johnson Space Center.
[h]Duke University.
[i]Indiana University School of Medicine.
[†]Principal Investigator.
[‡]Principal Engineer.
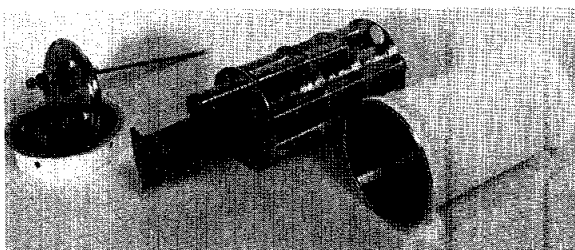
FIGURE 26-4.—Flight package (BIOCORE) partly dis-
assembled.

A layer of Teflon felt (0.0625 in.) thick and a fine
mesh stainless steel screen were wrapped around the
stainless steel tube to serve as a particle (dust) barrier
between the KO_2 and the mice. Two manually
controlled valves for flushing the package and two
pressure relief valves were located in the removable
end plate of the canister. The pressure relief valves
were set to maintain the package at 3.8×10^4 to
5.2×10^4 N/m^2 (5.5 to 7.5 psi) above the ambient
pressure. Between the relief valves and the atmo-
sphere within the package was a filter of Teflon felt
0.0016 m (0.0625 in.) thick and a fiber-glass high-
efficiency particulate air filter capable of filtering
0.3-μm particles. A shield was installed over the valves
to protect them and to support the package in the
CM locker. The overall package length was 0.35 m
(13.75 in.), and the total weight was 6.1 kg (13.5 lb).
Two maximum-minimum temperature recorders (de-
veloped for the microbial ecology evaluation device
(MEED) flown on Apollo 16 and 17) were located in
the end cap of two tubes containing mice.

Preparation of the hardware for flight was initiated
at the NASA John F. Kennedy Space Center (KSC)
on December 2, 1972, at 20:50 G.m.t. Five mice,
previously selected from a colony of 30 mice brought
to KSC from the NASA Ames Research Center
(ARC), were installed in five of the six mouse tubes,
each with 30 g of a special seed mixture (hulled
millet, oat groats, whole rye, and shelled sunflower
seeds). The sixth mouse tube was left empty. After
assembly, the package was flushed for 25 min with
oxygen. Pressure in the package then was reduced to
approximately 3.6×10^4 N/m^2 absolute (5.2 psia),
and a small amount of helium was added for leak
checking. After the leak check, the total package
pressure was further reduced and maintained at
2.3×10^4 to 3.1×10^4 N/m^2 absolute (3.3 to 4.5
psia) for 36 hr by adding oxygen on demand.
Supplying the mice with oxygen from an external

source during this initial period was necessary until
the KO_2 reaction with CO_2 and water vapor was
adequate to generate oxygen at the rate required to
satisfy the metabolic requirements of the mice. After
removal of the external oxygen supply, the total and
partial oxygen pressures were monitored until the
package was prepared for installation in the space-
craft at 19:00 G.m.t. on December 5, 1972. During
this period, the total pressure varied from a low of
2.2×10^4 N/m^2 absolute (3.2 psia) to a high of
3.4×10^4 N/m^2 absolute (4.9 psia), when monitoring
was discontinued.

Before the package was released for installation in
the spacecraft, the outside surface was cleaned with
Freon PCF. The package was installed in the A-6
locker before the locker was placed in the CM. Two
Beta webbing (Fluorel (RL-3603) coated) straps
retained the package in the locker. Micro-Syl cushion
material was cemented to the locker walls as required
to support the package, with one end of the canister
pressed against a locker end wall and the heat-sink
"feet" on the cylindrical portion against a side wall.
Thermal-conducting grease was applied to these con-
tacting surfaces to ensure a good thermal path from
the package to the locker walls. A radiation monitor
was taped to the inside surface of the bottom of the
A-6 locker to provide a measure of the local radiation
field near the BIOCORE. The monitor was obtained
from the backup units of the crew personal dosime-
ters.

Two identical BIOCORE packages were prepared;
the one with the most favorable startup characteris-
tics (serial number (S/N) 03) was selected for the
flight. The other (the backup package, S/N 05), on
return to ARC, was subjected to all the stresses
anticipated for the Apollo flight. The total pressure
within the backup control canister rose to a maxi-
mum of 8.3×10^4 N/m^2 absolute (12 psia) during
the test (fig. 26-5).

RECOVERY OF PACKAGE AND ANIMAL PROCESSING

The experiment package was removed from the
CM at 23:30 G.m.t. on December 19, 1972. The total
pressure in the package was 7×10^4 N/m^2 absolute
(10.1 psia) at that time. After removal from the CM,
the total pressure in the package was increased to
10×10^4 N/m^2 absolute (15 psia) and the package
was flushed with a 50:50 mixture of oxygen and

Cage	Mouse number	Mouse weight, g			Food weight, g		
		Start	End	Change	Start	End	Change
2	3486	11.0	11.0	0	30.0	9.7	-20.3
3	3550	10.8	9.2	-1.6	30.0	7.9	-22.1
4	3551	10.2	8.9	-1.3	30.0	17.7	-12.3
5	3329	9.8	8.2	-1.6	30.0	17.6	-12.4
6	3554	9.7	8.3	-1.4	30.0	2.0	-28.0
Average...		10.30	9.12	-1.18	30.0	10.98	-19.02
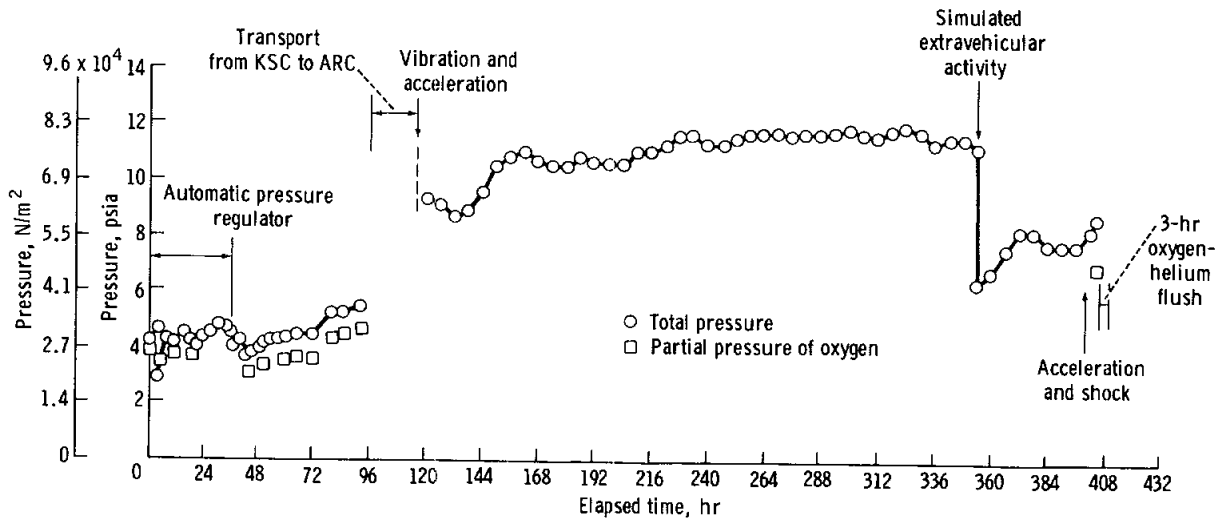
FIGURE 26-5.—Record of tests on backup canister. The test was started at KSC on December 2, 1972, and was completed at ARC on December 20, 1972. Mouse and food weights are indicated in the table.

helium. The package connected to the flushing system is shown in figure 26-6. This flushing was continued at a rate of $\approx 1.0 \times 10^{-4}$ standard m^3/min until the package arrived at the disassembly area in Pago Pago at 26:40 G.m.t.

The package was disassembled, and the mice and food were removed and weighed. The weights before and after the flight are listed in table 26-I. When placed in holding cages, all four living mice were spry. Two mice jumped repeatedly against the sides of their cages. Mouse A-3305 was the most lively. The fur of two of the mice (A-3326 and A-3400) was ruffled and matted as though moist. Initially, these two mice exhibited a reluctance toward spontaneous movement and sat in a hunched position. When prodded, they would run a short distance, then stop. For a time, one mouse (A-3326) was slightly uncoordinated and tended to lose its balance laterally. Activity in these two mice increased within 5 to 10 min. The appearance and degree of activity of the mice were comparable to that of mice after 16-day ground-based tests. None of the Apollo mice seemed interested in

eating. Autopsy performed shortly afterward revealed that three of the four mice had full stomachs; a record for the other one is not available.

The four living mice were anesthetized. Then, using a Harvard apparatus, the animals were perfused through the heart with a formaldehyde/acetic acid/ methyl alcohol mixture (FAM), which "fixed" the brain and other tissues in their natural state. The brain of the dead mouse was fixed by FAM introduced slowly into the intracranial cavity through the eye sockets using the Harvard apparatus. Autopsies were then performed. The heads were placed in bottles of FAM overnight, then transferred to 70 percent methyl alcohol, in which they were kept for a time. These fixatives were chosen because they would not cause significant brain shrinkage.

Head Processing

The initial procedure on return to ARC was to secure each Apollo mouse head in a specially designed aluminum box (fig. 26-7). The scalp over the monitor
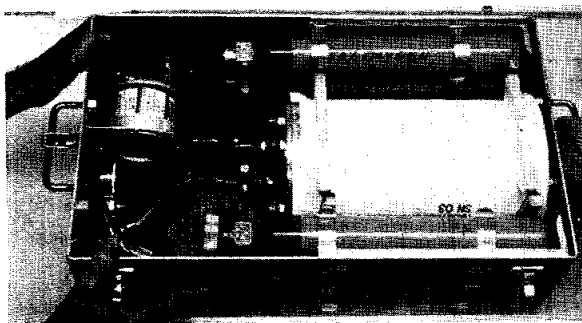
FIGURE 26-6.—Flight package connected to oxygen-helium flushing system as it appeared on opening in Samoa. A tube is attached to the outlet (upper) valve of the package, and another tube is attached to the inlet (lower) valve. On the recovery ship, the following procedure was followed. Total pressure within the package was first ascertained by the reading on the pressure gage (the large, cylindrical object in the upper left corner of the box). A needle valve (upper left, barely visible near the attendant's left thumb) was slowly opened to vent the pressure inside the canister to ambient pressure in the event the canister pressure was greater than ambient. The tube from the flow regulator (conical instrument to lower left near the attendant's right thumb) was then attached to the inlet valve of the package. The valves of the six oxygen-helium bottles and the inlet valve were then opened, and the flow regulator was slowly opened and set at the desired level. The gas then flowed through a manifold (U-shaped tube, of which the ends near the canister are visible) into the package to begin the flushing; the gas in the package escaped through the needle valve.

FIGURE 26-7.—Aluminum box used in securing each mouse head. The inside dimensions are 2.54 by 4.13 cm (1.0 by 1.625 in.). The ear bars are adjustable; the tips, 0.08 cm (0.03 in.) in diameter, are inserted into the external auditory canals. The upper jaw is held in place by a rod situated just behind the upper teeth and by a stiff wire pushed across the snout.

TABLE 26-I.—*Mouse and Food Weights*

Mouse number	Mouse weight, g		Food weight, g	
	Preflight	Postflight	Preflight	Postflight
A-3326	11.2	9.7	30.0	7.6
A-3400	10.7	8.6	30.0	16.2
A-3305	10.2	9.5	30.0	6.3
A-3356	10.1	8.9	30.0	17.4
[a]A-3352	10.0	7.2	30.0	20.1

[a]Dead when package was opened.

was removed, and photographs were taken of the position of the monitor in relation to the skull and the box. The box was then secured on the revolving stage of an assembly attached to a stereotaxic instrument (fig. 26-8). By means of a laser beam, the degree of tilt of the monitor off the horizontal was established by micrometers built into the assembly. From scales on the micrometers, a record of monitor

tilt was obtained. The edges of the monitor were coated with a radio-opaque silver paint, and X-rays were taken of each mouse head and box in three planes. After the position and tilt of the monitor on each Apollo mouse head were thus recorded, the monitors were removed for analysis. After removal from the box, the heads of the animals were decalcified, then returned to the box and dehydrated and infiltrated with paraffin. The boxes were then filled with paraffin and stored, awaiting the time that the heads could be serially sectioned. For each Apollo mouse head, two control mouse heads were processed in the same way and stored for use as histological controls for the Apollo mice.

As indicated previously, it was necessary to introduce needles through the heads of control animals in the trajectories at which cosmic ray particles had penetrated the subscalp monitors. To test this procedure, two "dummy" monitors were prepared and temporarily placed on the skull. These monitors consisted of stiff, thick paper on which the exit
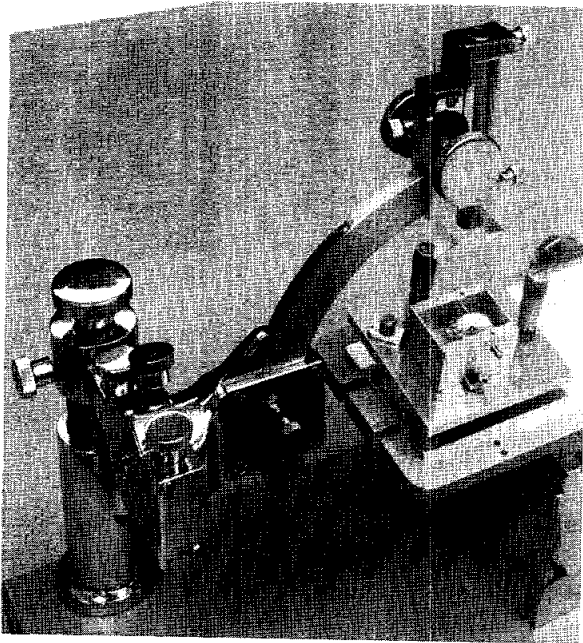
FIGURE 26-8.–Mouse head in aluminum box mounted on revolving stage. Turning of the micrometers will tilt the stage to the desired degree. A laser beam splitter is located at the end of the arm enclosure of the stereotaxic instrument. After removal of the beam splitter, an arm with a needle at its end is inserted through the holder for "tracking" a head.

and the tympanic bullae were the most dependable skull landmarks. Superimposition of transparencies revealed that every skull previously X-rayed had different dimensions. Hence, the position of the monitor assembly on the skull had first to be corrected in accordance with the distance between the ridges and the bullae.

Using a stereotaxic instrument, four needles were then run through the head in each of four control mice, two heads having dummy monitors and the other two heads having none. In the latter procedure, only the measurements taken from the X-rays were used to plot the needle trajectories. The same predetermined trajectories were used for all four heads. The needles were left in the heads for 24 hr, and, as the needles were withdrawn, gouaches of differing color were placed on the skull at the needle entrance and exit points for identification. The heads will be processed and sectioned horizontally to establish reproducibility of the tracking. Two other heads have been "tracked" with six and eight needles, respectively, to ascertain whether that many trajectories can be identified in brain sections. When the procedure is fully established and the subscalp monitors from the five Apollo mice have been completely analyzed, tracking of the control mouse heads will be performed.

Subscalp Monitor Data

The monitors from all five Apollo mice have been examined. For each of the monitors, the first step was to remove the heat-sealed edges with a punch. The paralene coating was peeled off the outer Lexan surfaces, except for two monitors (from mice A-3305 and A-3356) in which portions of the paralene adhered to the Lexan and could not be removed. The top (farthest from the mouse head) CN layer from mouse A-3352 was chemically etched at 313.16 K in 1×10^{-5} m^3 (10 ml) of 6.25N sodium hydroxide (NaOH) in successive stages to determine the optimum etch time for the remaining CN layers. Plastic track detectors etch preferentially along the cosmic ray trajectories, producing cones the size of which depends primarily on the particle linear energy transfer (LET), charge, and etch time. Consequently, an optimum etch time is one sufficiently long to develop visible cones for all high-LET particles, but not so long that many tracks etch completely through the CN or the Lexan layer. (Pragmatically, any particle that can register in CN or Lexan is defined as

points of four cosmic ray particles were arbitrarily indicated. To determine the relative position of the monitors and the skull landmark differences, 20.32- by 25.40-cm (8 by 10 in.) X-ray transparencies of the mouse heads and boxes were made (in the same planes as previously mentioned). The position of the Apollo mouse head with relation to its box had already been established. In addition, it was necessary to establish (1) the position of the control mouse head with relation to its box, (2) the relationship of the Apollo mouse head to the control mouse head, and (3) the position of the dummy monitor in relation to the control mouse box. All the measurements were accurate to 2.54×10^{-6} m.

The dummy monitor, ringed by radio-opaque paint, was then attached to the platform, and the platform was adhered to the skull. The dummy monitor was alined on the control head to within less than 100 μm of the position of the corresponding Apollo mouse monitor. Examination of the X-ray transparencies indicated that the sphenoidal ridges

high LET.) Such an etch time permits optimum differentiation of the particle tracks. A satisfactory etch time for the CN layers was 10 hr. The top CN layer from the remaining four monitors was etched subsequently, and all top CN layers were scanned under a light microscope. An average of 16 high-LET cosmic ray tracks per monitor was found in all but mouse A-3352. In this monitor, from the mouse that died in flight, only six high-LET tracks were present. Tracks observed in the monitors of mice A-3305 and A-3326 are shown in figure 26-9.

The surfaces of the Lexan layers were ultraviolet (UV) irradiated: the outside surfaces for 16 hr, then the inside surfaces for 32 hr, and again the outside surfaces for 16 hr. This process sensitizes the plastic and increases the preferential etch along high-LET particle trajectories. For preliminary analysis, the top Lexan layers from mice A-3305 and A-3352 were chemically etched at 343.46 K in 1×10^{-5} m^3 (10 ml) of 6.25N NaOH plus 5 percent Benax, in

successive stages, as long as 24 hr. The preliminary results indicate that some of the tracks that were etched through in the top CN layer stopped in the top Lexan layer. Successive etching of each Lexan layer will be performed individually. Because of the very limited size and very limited number of layers in each monitor, a slow, deliberate pace in processing is necessary. All layers of each monitor will be processed and scanned. and track parameter data will be taken. Then the LET, the charge group, the approximate stopping point, and the trajectory of each cosmic ray particle that has registered in a monitor will be computed.

Scalp

The scalps overlying the cosmic ray monitors in the four living mice were obtained for study at the time the subscalp monitors were removed. The position of the monitors was clearly visible as an indentation on the undersurface of the scalps. With
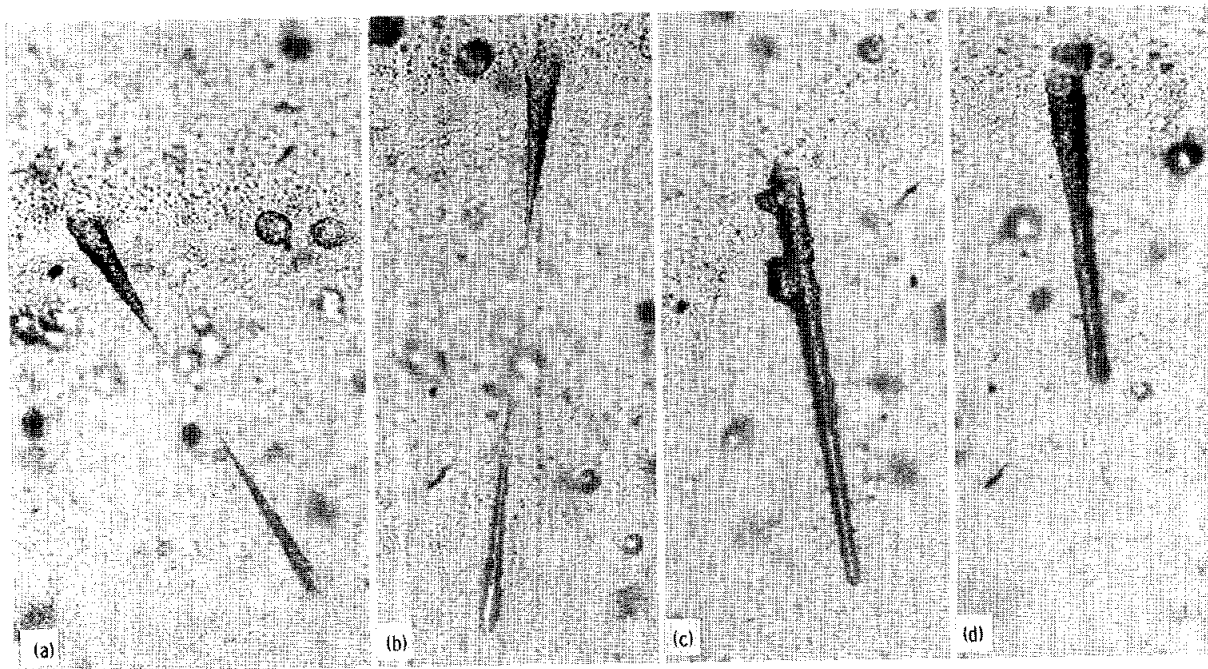
FIGURE 26-9.—Four tracks of highly ionizing cosmic ray particles as they pass through the CN detector. Tracks A, B, and D are from mouse A-3305, and track C is from mouse A-3326. These particles, possibly of the iron group, deposit substantial amounts of energy (>0.1 MeV/μm) in the vicinity of their trajectories. Particles C and D are more ionizing than particles A and B. The top surface of each monitor is at the top of each photograph. Because the tracks extended through the CN layer at a small angle (i.e., more or less vertically) and thus were difficult to photograph in their entirety, the microscope stage on which they were located was tilted before photography. Magnification, X200; scale, 1 cm = 32.5 μm. (From E. V. Benton and M. R. Cruty, University of San Francisco.)

an excess margin of approximately 2 mm, the scalps were cut to the shape of the monitors. The hair was trimmed to a length of several millimeters. The scalps were processed by a standard method and serially sectioned at 8 μm in the coronal plane, and the sections were stained by hematoxylin and eosin. Approximately 40 percent of the first scalp (A-3400) has been examined. The study was done without knowledge of the number or position of the tracks in the monitor. Four lesions have thus far been observed.

The first lesion involves a single hair follicle in its lower midportion bisecting the follicle horizontal to the skin surface (fig. 26-10(a)). In cross section, the follicle is rounded and is situated in a slightly eccentric position relative to the long axis of the hair shaft. The epithelium of one wall of the follicle is necrosed through its entire thickness, and there are several polymorphonuclear leukocytes in the adjacent dermis. The nuclei of the cells on the other side of the hair shaft show distortion in size, shape, and position. The lesion, which is approximately 75 μm wide, extends through six sections and thus measures
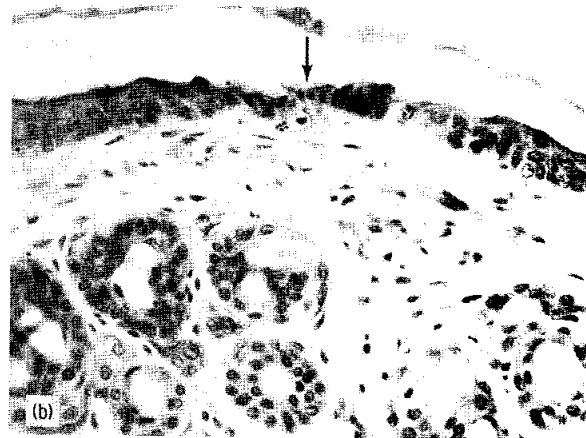
FIGURE 26-10.—Lesions in scalp of Apollo mouse A-3400 (from F. S. Vogel, Duke University). (a) Shown in the central part of the photograph is a hair within a hair follicle. The scalp surface lies at the top of the photograph. In the bottom of the hair follicle, the hair shaft is swollen to approximately twice its normal diameter, is globular, and has a fragmented appearance (arrow). The follicular epithelium to the right of the hair shaft is destroyed, as evidenced by extreme pyknosis of its nuclei. A few polymorphonuclear leukocytes lie in the dermis to the right of the damaged part of the hair follicle. (b) The epidermis (at the top of the photograph) is "dimpled" (thinned) in the region in which several epithelial cells are degenerated or dysplastic (arrow). A polymorphonuclear leukocyte lies in the immediately subjacent dermis. (c) The top of the scalp is at the top of the photograph. Some epidermal cells are damaged or have disappeared (arrow). Twenty-one polymorphonuclear leukocytes are recognizable in this photograph. At the bottom of the photograph is a vein. To the left, the vein is normal. In the portion of the vein in the leukocytic "corridor," some endothelial cells are swollen and polymorphonuclear leukocytes are adjacent to them. A small subepidermal vesicle is also visible (beneath the arrow).

48 μm in that dimension. The hair shaft is fragmented in the area of the lesion. The lesion is notably discrete; the epithelial cells of the hair follicle above and below are well preserved. This feature would suggest a very focal and intense injury, with a mild inflammatory cell response that signifies an antemortem reaction lasting several days.

The second lesion, principally in the epidermis (fig. 26-10(b)), extends through the depth of this epithelial layer (in this species of mouse, the epidermis is three to four cells thick) and has a cross width of approximately 80 μm. Thus, in the lateral dimension of the lesion, approximately eight epithelial cells show degenerative change and the contiguous epithelial cells appear dysplastic. Several polymorphonuclear leukocytes are present in the adjacent underlying dermis. There is no recognizable lesion in the hair follicle. The character of the tissue reaction dates this lesion as antemortem. The dysplastic epithelial cell reaction suggests a duration of at least several days.

The epithelial component of the third lesion is comparable to that of lesion 2. However, in addition, the third lesion is characterized by a broad column of polymorphonuclear leukocytes extending through the dermis to the interface between the dermis and the monitor (fig. 26-10(c)). The epidermal cells, through the width of the epidermis and for a breadth of five to six cells, are necrotic or pyknotic, with cytoplasm that stains intensely eosinophilic. Polymorphonuclear leukocytes (as many as 30 in a section) are columnated through the dermis in a corridor approximately 100 μm across. A collection of these inflammatory cells is present near the lower plane of the dermis. A large, thin-walled vein borders this collection. Within the region of the corridor, the endothelial cells of this vein appear swollen and have hyperchromatic nuclei. There are no visible extravasations of red blood cells. The presence of a small subepidermal vesicle in several sections is interpreted as evidence of edema and supports the possibility that the fragmented pattern of the collagen in the underlying dermis is also attributable, at least to some degree, to edema. A neighboring hair follicle shows no recognizable change.

The fourth lesion has the same histological features as the second and third lesions. Generally, the fourth lesion is intermediate in severity between these two. The epidermal changes are again characterized by necrosis of epithelial cells in a segment three to four cells wide and through the entire depth of the epidermis. There are some small subepidermal vesicles that presumably contain edema fluid. Polymorphonuclear leukocytes are scattered sparsely in the underlying dermis, but only through its outer half.

Retina

The left eyes of two Apollo mice (A-3400 and A-3356) were removed at autopsy and fixed by immersion in glutaraldehyde. Examination thus far has revealed no significant alterations in the retina. The remaining eyes were left in situ and will be available for examination when the entire head is serially sectioned.

Viscera

Lung Tissue.—Lung tissue was obtained from the four surviving Apollo mice, from four control mice that had been perfused with FAM in Samoa, from the five backup mice from KSC, and from several mice that had been subjected to high oxygen pressure (8.3×10^4 N/m^2 absolute (12 psia)) over a period of 7 days.

Immediately following perfusion of the mice on Samoa, the tissue was placed in 6 percent glutaraldehyde. On return to ARC, the specimens were postfixed 1 hr in 1 percent buffered osmium, dehydrated in acetone, and embedded in low-viscosity plastic. Thin sections were cut for examination under the electron microscope. The FAM perfusion had destroyed all ultrastructural detail except the outer cell membranes and the nuclear membrane. The finding of cytoplasmic rarefaction, blebbing, or blistering would be highly suspect under these conditions.

Because interpretation of sections by electron microscopy was impractical, the plastic embedded blocks were sectioned at 1 μm for light microscopy. A special silver method developed in the ARC laboratory for plastic-embedded specimens was used (ref. 26-12). In sections thus prepared, a minimal amount of perivascular edema was noted as well as some blistering and blebbing of the alveolar epithelial cells and the capillary endothelial cells. The latter type of change, especially, indicates excess fluid and is known to be widespread in oxygen-poisoned lungs. Preliminary investigation has not revealed any major damage to the alveolar walls or any significant amount of alveolar exudate. Some changes in the bronchiolar epithelium have been noted, but these

were not specific, and somewhat similar changes appeared on occasion in control pocket mice.

The five backup mice (from the S/N 05 canister) were perfused with FAM, stored in 10 percent neutral Formalin, and subsequently processed in paraffin for light microscopy. Moreover, a few small pieces of lung tissue were embedded in plastic so that sections could be cut at 1 μm in thickness and stained with silver for comparison. From what has been observed in these pocket mice and in the Apollo mice, there seems to be some indication of an increased fluid load in both series. Because all these animals (i.e., in both canisters) were living in an almost pure oxygen atmosphere, these indications of fluid buildup were not surprising. However, no major damage or any indication that these animals were suffering from "oxygen poisoning" were seen. In fact, the mice in oxygen test runs seemed rather resistant to oxygen effects. Electron microscopy of the lungs after 7 days of exposure to oxygen at a pressure of 8.3×10^4 N/m^2 absolute (12 psia) in a test run revealed remarkably little damage. There was some blebbing of the capillary endothelial cells and some fluid and debris in a few alveoli. Tissue for this study was clipped from ligated, nonperfused lungs and fixed by immersion in glutaraldehyde, then postfixed in osmium. Satisfactory ultrastructural detail was therefore possible. Light microscopy of these lungs is yet to be performed. More intensive study is planned to clarify some of the questionable areas. Some of the changes are minimal and some are found in both experimental and control animals. In these instances, quantitation is necessary to determine whether the changes are significant.

Liver.—The livers were examined without knowledge of which came from the Apollo mice and which came from the nine control mice perfused on Samoa. The livers of numerous oxygen-exposed and normal control mice also were studied. Serial sectioning of the livers was performed, and the sections were stained with periodic acid Schiff (PAS) hematoxylin and orange G. In one liver (which turned out to be that of Apollo mouse A-3305), an examination was made of 400 serial sections (5 μm thick) on 60 slides alternately stained by PAS and the Giemsa method. The liver of one Apollo mouse (A-3356) was regarded as normal and thus was classed as from a "control" mouse.

In some livers (mouse numbers not specified), mitotic figures were seen in scattered endothelial cells

or reticuloendothelial cells; they were seen in all sections of these livers in the absence of any other change. Mitotic figures were also found in and around large areas of focal necrosis and repair. Certain other changes were found in the livers of animals, some of which were classed as "controls." A field is shown in figure 26-11. The enlargement of the hepatic nuclei (nuclear "ballooning") and of the entire hepatic cell is considered a nonspecific degenerative change found in normal aged mice and, in an exaggerated form (accelerated aging perhaps), in animals exposed to photon radiation. Hepatic nuclear and cellular enlargement accompanied by mitosis, such as shown in figure 26-11, has previously been observed (by the investigators) only in animals exposed to large doses of gamma radiation. The presence of red blood cells within liver cells appears to be a new finding. It is postulated that the intracellular hemorrhage may be traumatic in origin and may be due to fluctuations in intra-abdominal pressure occurring in association with fluctuations in ambient pressure in test canisters. Of special interest were the alterations classed as "focal hepatic necrosis and repair." These alterations were found only in four (of a total of 40) mice: in three Apollo mice (A-3326, A-3400, and A-3305) and in one control mouse autopsied on Samoa (A-3494).

FIGURE 26-11.—Photomicrograph of liver from control mouse A-3282. Visible here are degenerated hepatic cells showing nuclear and cellular enlargement, a double mitosis (arrow), nucleolar prominence, cytoplasmic edema, and decrease in PAS-positive substance. A mitotic figure in an unidentifiable small cell is present (pointer). A hepatic cell with intracellular "hemorrhage" is adjacent to the hepatic cell in mitosis. (From C. C. Lushbaugh and G. Humason, Oak Ridge.)

In half the liver of Apollo mouse A-3305, 16 lesions were identified. (The other half of the liver went to another investigator.) The lesions were round or slightly oval. Fields are shown in figure 26-12. In evolution, the initial stage of the pathological process is regarded as a coagulative necrosis. The necrotic cells are chemotactic for polymorphonuclear leukocytes and become heavily infiltrated by them. The largest lesion in this necrotic state (approximately 600 μm in the greatest dimension) is shown in figure 26-12(a). In this instance, the lesion seems to surround a thrombosed vein. The central area of the lesion is partly liquefied and is hemorrhagic and infiltrated by inflammatory cells. The dead cells are finally completely lysed away. A central amorphous acidophilic mass of unknown nature surrounded by histiocytes, fibroblasts, and other cells is shown in figure 26-12(b). However, unlike most inflammatory granulomas, there is no circumferential fibrotic mass.

Mitotic figures are present in unidentifiable small connective tissue cells, but collagen is not produced (fig. 26-12(c)).

Other Tissues.—Many other tissues of the mice are being investigated; however, not enough observations have been made to warrant reports at this time.

Findings in Nonsurviving Mouse

Microscopic examination of the Apollo mouse that died (A-3352) revealed that the organs and viscera had undergone advanced autolysis. In the lungs, there appeared to be an abnormally large number of desquamated, hypertrophied alveolar macrophages, suggesting the possibility of antemortem pulmonary inflammation (pneumonitis). The cause of the inflammation was not evident, nor could the cause of death be established. From the amount of food consumed (9.9 g), it is estimated that death occurred 9 to 12
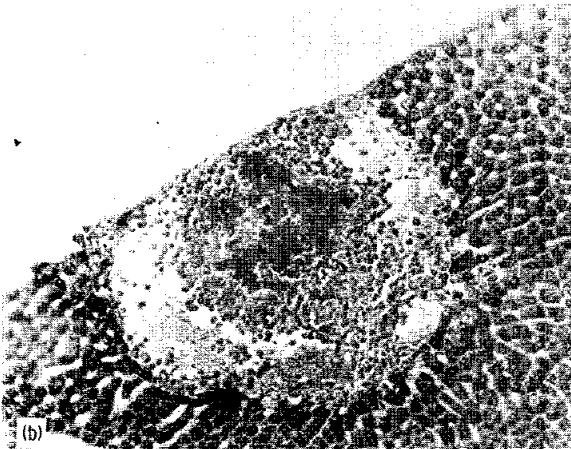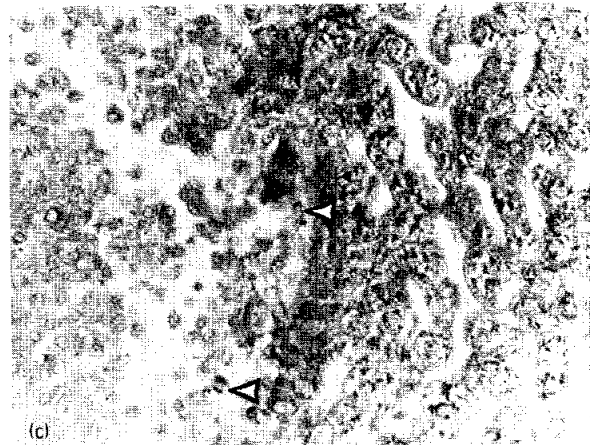
FIGURE 26-12.—Photomicrographs from liver of Apollo mouse A-3305 (from C. C. Lushbaugh and G. Humason, Oak Ridge). (a) Largest hepatic granulomatoid lesion found. Central liquefaction, adjacent to an apparently thrombosed vein, is surrounded by hepatic cells that have undergone coagulation necrosis and partial nuclear lysis. Magnification, ×350. (b) A lesion regarded as a later stage of the one in figure 26-12(a). Hepatic cells have been lost. An eosinophilic mass (Jenner-Giemsa stain) is surrounded by epithelioid histiocytes and poorly differentiated hematopoietic cells inside a space (possible vascular lake) containing red blood cells. Note the absence of a reactive connective tissue capsule. Magnification, ×350. (c) Higher magnification of same lesion shown in figure 26-12(b), showing the loose, structureless nature of the border area and two mitotic figures (pointers). The adjacent hepatic cells appear to be normal. Magnification, ×750.

days after the mouse was loaded into the flight canister.

COMMENT

An average of 16 high-LET tracks has been found in the subscalp monitor of each of the four surviving mice, and six high-LET tracks have been found in the monitor of the mouse that died. The reason for this difference has not yet been determined. When the monitors of all five Apollo mice have been fully analyzed, the heads of these mice as well as the heads of the respective control mice will be serially sectioned, stained, and examined.

Only a portion of the scalp overlying the monitor of one of the Apollo mice has thus far been examined. The lesions observed are unequivocally antemortem and are recent in origin (i.e., compatible with a duration of less than 13 days). Each lesion is characterized by epithelial cell necrosis, with the common feature of nuclear pyknosis and intense cytoplasmic eosinophilia. There is a slight leukocytic response in the dermis. Whether these leukocytes represent a response to local dermal necrosis or to local injury of the collagen in the dermis is unknown. The lesions are markedly discrete and notably similar in size, not only one to another but also in their various cross diameters.

These lesions cannot be attributed to cosmic ray particle "hits" unless precise topographic correspondence to tracks in the monitor is demonstrated and unless the scalps of the pocket mice on the ground-based backup "flight" (S/N 05) and the scalps of other control mice show no such changes. The precision with which serial sectioning of the scalps is done will allow a comparison.

The scalp lesions described in this report differ from those observed in the skin of black mice and of locally monitored black rabbits flown in balloons at high altitudes (refs. 26-1 and 26-2). The skin of these animals was studied 1 to 4 months after flight. In areas in which some white hairs appeared in the balloon-borne mice, all traces of melanin were absent, melanocytes had vanished, deep hair follicles had disappeared, and superficial hair roots giving rise to white hairs persisted. It was as though the affected areas had prematurely aged. A volume of skin between 0.5 and 1.0 mm³ was thus affected. In the rabbits, effects similar to those observed in the balloon-borne mice were seen. Even muscle fibers beneath the skin were degenerated. Damage to deep

hair follicles in a region of affected skin extended over an area 2 to 3 mm in diameter. The investigators (ref. 26-2) stated: "We cannot as yet draw definite conclusions concerning this pathology . . . ." In other studies of balloon-borne black mice, no skin lesions were observed (refs. 26-13 and 26-14).

The livers of the pocket mice have not been sufficiently studied to allow an appraisal of the nature of the alterations that were found. It is strange that the large lesions in the livers were found only in the mice flown on the Apollo 17 mission and in one mouse taken to Samoa as a control and autopsied there. When these lesions were found, a diligent search was made of the livers of numerous mice autopsied before the flight. No lesions were found that resembled the large lesions in question or that seemed to be a forerunner of them. The paucity of repair around the lesions in Apollo mouse A-3305 suggests that the lesions were generated during space flight. Not enough information is available yet to allow an estimate of the time of inception of the lesions in the liver of the control mouse taken to Samoa. The cause of these lesions has not been ascertained. At present, it seems unlikely that they were due to high-energy, heavy cosmic ray particles. Whether or not the scalp lesions are in any way related to the liver lesions needs to be considered.

ACKNOWLEDGMENTS

REFERENCES

26-1. Pfister, A.; Deltour, G.; Atlan, H.; Kaiser, R.; and Miro, L.: Etude de l'action biologique des rayons cosmiques—au moyen de ballons sondes. AGARD, EP-25, vol. 16, Oct. 1967, pp. 16-1 to 16-8.
26-2. Miro, L.; Deltour, G.; Pfister, A.; Kaiser, R.; and Grandpierre, R.: Current Status of French Research on

the Biological Effects of Heavy Ions in Cosmic Radiation as Observed in High-Altitude Balloons. Life Sciences and Space Research, vol. 8, North-Holland Pub. Co. (Amsterdam), 1970, pp. 39-44.

26-3. Chapman, P. K.; Pinsky, L. S.; Benson, R. E.; and Budinger, T. F.: Observations of Cosmic-Ray Induced Phosphenes on Apollo 14. NASA TM X-2440, 1971, pp. 1002-1006.

26-4. Tobias, C.; Budinger, T. F.; and Lyman, J. T.: Radiation-Induced Light Flashes Observed by Human Subjects in Fast Neutron, X-Ray and Positive Pion Beams. Nature, vol. 230, no. 5296, Apr. 1971, pp. 596-598.

26-5. Budinger, T. F.; Bichsel, H.; and Tobias, C. A.: Visual Phenomena Noted by Human Subjects on Exposure to Neutrons of Energies Less Than 25 Million Electron Volts. Science, vol. 172, no. 3985, May 1971, pp. 868-870.

26-6. Haymaker, W.: Studies of Brains Exposed to Cosmic Rays and to Accelerated Cosmic Particles. In Relations of Basic Research to Space Biology, Univ. California Press, 1963, pp. 347-378.

26-7. Haymaker, W.; Bailey, O. T.; Benton, E. V.; Vogel, F. S.; et al.: Brain Study in Balloon-Borne Monkeys Exposed to Cosmic Rays. Aerospace Med., vol. 41, no. 9, Sept. 1970, pp. 989-1002.

26-8. Bartholomew, G. A.; and Cade, T. J.: Temperature Regulation and Aestivation in the Little Pocket Mouse Perognathus longimembris. J. Mammal., vol. 38, no. 1, Feb. 1957, pp. 60-72.

26-9. Cade, T. J.: Evaluation of Torpidity in Rodents. Ann. Acad. Sci. Fenn., ser. A, IV, Biologica, vol. 71, no. 6, 1964, pp. 77-112.

26-10. Chew, Robert M.; Lindberg, Robert G.; and Hayden, Page: Temperature Regulation in the Little Pocket Mouse, Perognathus longimembris. Comp. Biochem. Physiol., vol. 21, no. 3, June 1967, pp. 487-505.

26-11. Lindberg, R. G.; Gambino, J. J.; and Hayden, P.: Circadian Periodicity of Resistance to Ionizing Radiation in the Pocket Mouse. Biochronometry, NAS Pub. (Washington, D.C.), 1971, pp. 169-185.

26-12. Corbett, R. L.: Modification for Electron Microscopy of the Corbett Ammoniacal Silver Stain. Proc. Electron Microscopy Soc. Amer., vol. 29, 1971, pp. 484-485.

26-13. Chase, Herman B.: Cutaneous Effects of Primary Cosmic Radiation. J. Aviat. Med., vol. 25, no. 4, Aug. 1954, pp. 388-391.

26-14. Chase, Herman B.; and Post, Janice S.: Damage and Repair in Mammalian Tissues Exposed to Cosmic Ray Heavy Nuclei. J. Aviat. Med., vol. 27, no. 6, Dec. 1956, pp. 533-540.

27. Visual Light Flash Phenomenon

L. S. Pinsky,[a] *W. Z. Osborne,*[a] *and J. V. Bailey*[b]

The Apollo 17 mission was the fourth mission during which an investigation of the so-called light flash phenomenon was conducted. During the Apollo 14 and 15 missions, 1-hr observing sessions were designated for the crewmen to darken the cabin (blindfolds used on Apollo 15) and to look for the phenomena. Their observations were reported in real time. The Apollo light flash moving emulsion detector (ALFMED) flown on Apollo 16 provided the first opportunity to record the passage of cosmic rays through the crewman's head and eyes and to correlate them with his observations (ref. 27-1).

APOLLO 17 PROTOCOL

The two 60-min observing sessions during the Apollo 17 mission were scheduled exactly as the sessions had been for Apollo 16. The first session was conducted during translunar coast (TLC) and the second during transearth coast (TEC). During the TLC session, the command module pilot (CMP) wore the ALFMED and the commander (CDR) wore a blindfold. The lunar module pilot (LMP) transcribed the comments of the other crewmen. During the TEC session, all three crewmen wore blindfolds. All comments from both sessions were recorded.

ANALYSIS OF EVENT RATES AND DESCRIPTIONS

Event descriptions from all the light flash observing sessions are listed in table 27-I. All the sessions lasted 60 min, and, in all cases where the observers began in a "light adapted" state, an average of 17.7 min was required to see the first event. When compared with the overall average (after the first

[a]University of Houston and NASA Lyndon B. Johnson Space Center.
[b]NASA Lyndon B. Johnson Space Center.

event) rate of one event per observer every 3.1 min, this 17-min "dead time" indicates that the crewman had to be very well dark adapted to observe the phenomenon.

All the crewmen have reported relative ease in distinguishing the eye in which the events occurred (table 27-I). The most common event type (63 percent) is the point or starlike flash that has also been described as a "nova." Next (25 percent) is the "streak." In almost all cases, the streaks have a sense of motion or direction; that is, a streak might appear to be "moving" from right to left rather than appearing as a motionless horizontal line. However, the motion is almost "instantaneous" and may originate from shape cues (ref. 27-2). The streaks, which have been described as "sharp and distinct" by some observers and "fuzzy and diffuse" by others, are virtually always straight. Some of the streaks have been described as having a gap in the middle. The final distinct event type (6 percent) was described as a "cloud." These events were seen as a "dull flash," were always in the periphery of the visual field, and had no distinguishable shape. They have been compared to the flash seen when lightning discharges inside a cloud. The remaining 6 percent of the events were composites of the other events, such as two stars simultaneously or a star and a cloud simultaneously. The LMP on the Apollo 14 mission added the following comments. "My experience is that even the so-called star, the supernova, is not as clear a phenomenon or clear a picture as I had in mind that they would appear. There still seemed to be at least two flashes, maybe a bright flash, followed an instant later by a more subdued flash, or perhaps a halo-like effect—there does not seem to be a set pattern in each case. Sometimes it's a very clear single flash; at times it seems followed by a halo. Sometimes it seems followed by an adjacent flash." The mean times between events per observer for those events occurring after the first event was seen (i.e., after the

TABLE 27-I.—Light Flash Event Description

Mission	Mission phase	Observer	Elapsed time from start of dark adaptation to first event, min	Total number of events reported	Eye in which event appeared					Event description					Comments
					Left	Right	Both	Unable to distinguish	Not reported	Streak	Star	Cloud	Double star	Star and cloud	
Apollo 14	TEC	CMP	29	12	2	6	–	–	4	2	8	1	1	–	Conducted in darkened cabin; crewmen's eyes closed. All crewmen reported that the event rate seemed subjectively lower and the events less brilliant than casually observed earlier in the mission.
		LMP	a17	22	6	12	1	–	3	5	13	3	1	–	
		CDR	18	14	4	10	–	–	–	3	8	1	2	–	
Apollo 15	TLC	CMP	10	22											All crewmen wearing blindfolds. Debriefing comments reflected no unusual observations. Most abundant events were stars. Streaks were present but less numerous, and there were no recollections of clouds.
		LMP	9	12	(Detailed descriptions recorded on tape on board and lost during playback dump to ground)										
		CDR	10	25											
	Lunar orbit	LMP	10	12	6	1	1	1	3	6	5	–	1	–	CMP and CDR were in command module but were occupied with other duties. LMP was facing lunar surface for first 50 min, away from surface for last 10 min.
	TEC	CMP	30	8	3	3	–	–	2	2	5	–	1	–	Debriefing comments indicated general alertness and lack of any overt fatigue. The event rate seemed markedly lower and the events seemed more subdued in brightness. All crewmen wearing blindfolds.
		LMP	26	9	1	2	–	–	6	3	5	–	1	–	
		CDR	17	6	2	3	–	–	1	–	6	–	–	–	
Apollo 16	TLC	LMP	(b)	47	21	26	–	–	–	7	36	2	2	–	LMP wearing ALFMED, CMP copying LMP comments, and CDR wearing blindfold.
		CDR	(b)	22	10	11	–	–	1	6	14	1	1	–	
	TEC	CMP	–	0	–	–	–	–	–	–	–	–	–	–	CMP said that he never observed the phenomenon at any time during the mission. All crewmen wearing blindfolds.
		LMP	(c)	d21	4	10	–	–	7	e1	e4	e2	–	e1	
		CDR	21	8	4	4	–	–	–	e1	–	–	–	–	
Apollo 17	TLC	CMP	15	17	6	7	2	2	–	5	10	1	–	1	CMP wearing ALFMED, LMP copying CMP comments, and CDR wearing blindfold.
		CDR	f39	11	8	2	–	–	1	6	4	1	–	–	
	TEC	CMP	–	0	–	–	–	–	–	–	–	–	–	–	All crewmen wearing blindfolds. Biomedical sensor indication of intermittent sleep by LMP; no data for other crewmen. Debriefing comments indicate that for majority of time, the other crewmen were in a state of "alert" observation.
		LMP	–	0	–	–	–	–	–	–	–	–	–	–	
		CDR	–	0	–	–	–	–	–	–	–	–	–	–	

a LMP attempted on two occasions after seeing the first flash to ruin his dark adaptation with a flashlight.
b Crewmen were already dark adapted and seeing flashes when 60-min timed session began.
c First seven flashes not reported real time; no time to first flash available (probably about 15 min).
d Including those not reported real time.
e Based only on last 14 events seen.
f High phosphene level reported during first half of session.

TABLE 27-II.—*Mean Times Between Events*

Mission phase	Mission	Mean time between events after dark adaptation, min	Average dark adaptation time, min
TLC	Apollo 15	$2.70 \begin{smallmatrix} +0.41 \\ -0.32 \end{smallmatrix}$	9.7
	Apollo 16	$1.74 \begin{smallmatrix} +0.24 \\ -0.17 \end{smallmatrix}$	—
	Apollo 17	$2.53 \begin{smallmatrix} +0.63 \\ -0.41 \end{smallmatrix}$	[a]15.0
	Average	$2.23 \begin{smallmatrix} +0.19 \\ -0.17 \end{smallmatrix}$	11.0
Lunar orbit	Apollo 15	$4.55 \begin{smallmatrix} +1.96 \\ -1.06 \end{smallmatrix}$	10.0
TEC	Apollo 14	$2.58 \begin{smallmatrix} +0.44 \\ -0.34 \end{smallmatrix}$	21.3
	Apollo 15	$5.35 \begin{smallmatrix} +1.54 \\ -0.98 \end{smallmatrix}$	24.3
	Apollo 16	$3.30 \begin{smallmatrix} +0.78 \\ -0.54 \end{smallmatrix}$	21.0
	Apollo 17	(No events seen)	—
	Average without Apollo 17	$3.39 \begin{smallmatrix} +0.39 \\ -0.32 \end{smallmatrix}$	—
	Average with Apollo 17	$4.37 \begin{smallmatrix} +0.50 \\ -0.41 \end{smallmatrix}$	22.6
TLC and TEC	Average without Apollo 17	2.67 ± 0.16	18.4
TLC and TEC	Average with Apollo 17	3.04 ± 0.15	—
TLC, lunar orbit, and TEC	Average with Apollo 17	3.10 ± 0.18	17.7

[a]CMP only.

observer was dark adapted) are listed in table 27-II. The mean dark adaptation time (i.e., time to first event) experienced for each session is also listed.

DISCUSSION

From the data presented in tables 27-I and 27-II, several observations can be made about the light flash phenomenon. The fact that dark adaptation is necessary indicates that the phenomenon is strongly connected with the retina rather than with a direct stimulation in the optic nerve or in any other part of the central nervous system. Therefore, the list of possibilities is narrowed to those capable of stimulating the retina when the observer's eyes are closed (ref. 27-3). Because the crewmen are exposed to cosmic rays and because ionizing radiation has been demonstrated to be capable of producing the same type of effect, the most probable explanation of the phenomenon is that it is caused by cosmic rays penetrating the eyes and retinas of the observers. Several mechanisms by which the charged particles stimulate the retina have been suggested. Among these mechanisms are direct ionization, Cerenkov radiation, and fluorescence (refs. 27-3 and 27-4).

Another interesting characteristic of the phe-

nomenon (table 27-II) is that the mean time between events and the dark adaptation times are uniformly longer for the TEC sessions than for the TLC sessions. Generally, fewer events are seen and a longer dark adaptation period is required during the TEC sessions than during the TLC sessions. Because the effect greatly exceeds any probable statistical errors, it is quite certain that a real effect has been observed. There are, as yet, no physical arguments that can explain this "transearth coast depression." In fact, most arguments tend to indicate a greater rate during TEC because the lunar module is no longer blocking a large part of the sky and the tank levels of the consumables are lower, thus providing less shielding. The only theory remaining is that the ability of the crewmen to dark adapt and the time required to do so has been impaired by some parameters of the mission (e.g., prolonged exposure to zero gravity, diet, fatigue, etc.). This theory is challenged by the crewmen, who claim general alertness and no other evidence of any loss of visual acuity. However, all the crewmen have indicated the subjective impression that the light flashes seemed less frequent and more subdued during the TEC sessions. Two extreme examples occurred. The more extreme example of the TEC depression occurred on Apollo 17 when none of the three crewmen were able to see even a single event during the 60-min TEC session, when two crewmen had seen a total of 27 events during the TLC session. (The LMP did not participate in the Apollo 17 TLC session.) The only other inability to observe the phenomenon occurred on the Apollo 16 mission when the CMP reported he was unable to observe even a single event at any time during the entire mission. The Apollo 16 CMP was the only Apollo crewmember who was briefed to look for the phenomenon but failed to see it. However, he has said that he does have relatively poor night vision, which may have a bearing on his inability to see the phenomena. Some of these questions may be answered more definitively when the final analysis of the ALFMED data is complete.

ALFMED DESCRIPTION

The ALFMED is an electromechanical device that is worn on the head somewhat like a helmet and supports cosmic-radiation-sensitive emulsions around the head of the test subject (figs. 27-1 to 27-4). A direct physical record is provided of cosmic ray
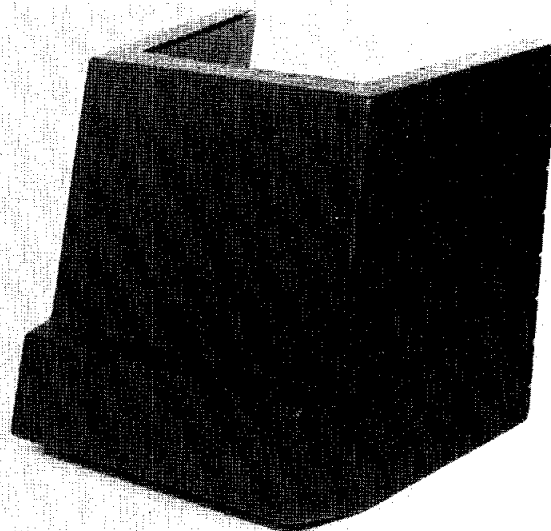
FIGURE 27-1.—Exterior view of ALFMED device.
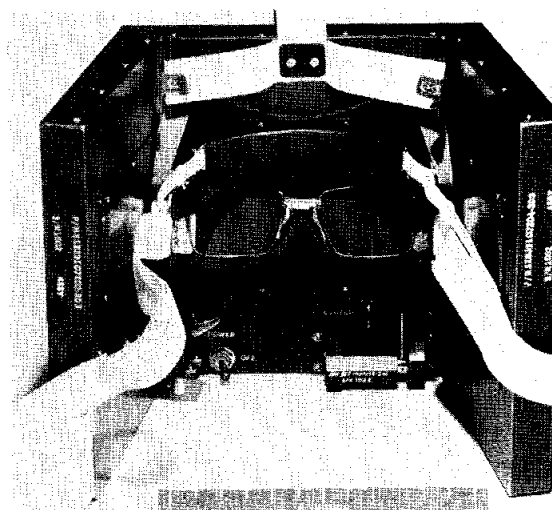
FIGURE 27-2.—Interior view of ALFMED device.

particles that pass through the emulsion plates and, in turn, through the head of the subject. The ALFMED contains two sets of glass plates coated on both sides with special nuclear emulsion and supported in a protective framework. One set of nuclear emulsion plates is fixed in position within the headset and surrounds the front and sides of the head. A second similar set of plates is located exterior and parallel to the inner fixed plates and may be translated at a constant rate (10 μm/sec) with respect to the fixed plates. This configuration provides a time resolution for events to within 1 sec. The total translation time
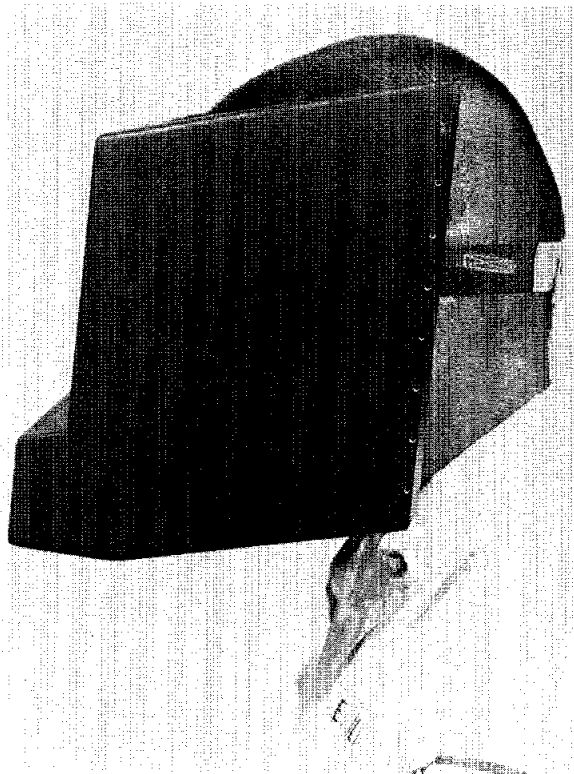
FIGURE 27-3.—The ALFMED device as worn by crewmen.

FIGURE 27-4.—View of ALFMED device emulsion plates.

available is 60 min, after which the moving plates may be returned to the original or "fiducial" position.

ALFMED DATA ANALYSIS PROCEDURE

The analysis of the ALFMED plates proceeds through the following steps.

1. Location scan—The moving plate is placed on a special microscope stage containing the fixed plate and is then oriented in the fiducial position (i.e., the relative orientation and translation of the plates during stowage) (fig. 27-4). The plates are then scanned for tracks that do not line up properly in that plate position (i.e., tracks that occurred while the plates were moving).

2. Translation scan—For all the candidate events located in the first step, a scan along the line of translation is made to locate the counterpart track. A measurement of the translation distance for each event is also made. This measurement yields the time of occurrence of the event.

3. Charge and energy measurement—The indi-

vidual tracks are subjected to a detailed analysis to determine the charge and energy of the particle (refs. 27-5 and 27-6).

4. Trajectory measurement—The direction of the track is measured, and the subsequent trajectory through the head is predicted.

5. Correlation with observations—The list of events is compared with the observations reported by the crewmen in an attempt to determine if cosmic rays do in fact cause the phenomenon; if there is an apparent charge, energy, or linear energy transfer (LET) threshold; or if some particular event types correlate with certain particle types (e.g., streaks caused by tracks tangent to the retina, etc.).

Scanning of both the Apollo 16 and 17 ALFMED plates has proceeded slowly and no preliminary data are yet available.

CONCLUSIONS

The ALFMED data should provide verification that cosmic rays are indeed the source of the phenomena and also information about apparent thresholds (in cosmic ray parameters). However, all the data that will be available from the Apollo light flash investigation can only yield likely clues as to the reason for the TEC light flash depression.

REFERENCES

27-1. Benson, Richard E.; and Pinsky, Lawrence S.: Visual Light Flash Phenomenon. Sec. 27, Part C, of the Apollo 16 Preliminary Science Report. NASA SP-315, 1972.

27-2. Tobias, C. A.; Budinger, T. F.; and Lyman, J. T.: Human Visual Response to Nuclear Particle Exposure. Proceedings of the National Symposium on Natural and Manmade Radiation in Space. NASA TM X-2440, Jan. 1972, pp. 416-422.

27-3. Chapman, P. K.; Pinsky, L. S.; Benson, R. E.; and Budinger, T. F.: Observations of Cosmic Ray Induced Phosphenes. Proceedings of the National Symposium on Natural and Manmade Radiation in Space. NASA TM X-2440, Jan. 1972, pp. 1002-1006.

27-4. Tobias, C. A.; Budinger, T. F.; and Lyman, J. T.: Radiation-Induced Light Flashes Observed by Human Subjects in Fast Neutron, X-ray and Positive Pion Beams. Nature, vol. 230, Apr. 30, 1971, pp. 596-597.

27-5. Powell, C. F.; Fowler, P. H.; and Perkins, B. H.: The Study of Elementary Particles by the Photographic Method. Pergamon Press (New York), 1959.

27-6. Schaefer, H. J.: The Dosimetric Characteristics of HZE Particles in Space. Naval Aerospace Med. Res. Lab. Rept. NAMRL-1172, Nov. 15, 1972.

28. Geological Observations From Lunar Orbit

R. E. Evans[a] and Farouk El-Baz[b]

Visual observations from orbit were first considered as a mission objective on Apollo 15. The concept and means of achieving the objective are described in reference 28-1, and summaries of the results have been published (refs. 28-2 to 28-4). Observations were also made from the command module (CM) during the Apollo 16 mission, and the results provided additional data which complemented the photographs and the geochemical remote sensing (refs. 28-5 and 28-6).

As on previous missions, the Apollo 17 crew (the command module pilot (CMP) in particular) was trained during a 2-yr period before the flight for the task of making the observations. During this training, the CMP conducted simulations of the task by studying aerial photographs of geologically complex regions in the United States and by flying over these regions to make on-the-scene interpretations.

Because the Apollo 17 groundtracks repeated approximately 80 percent of the lunar surface area previously overflown on Apollo 15, much was already known about the features in question. For this reason, emphasis was largely placed on color tones of geologic units and details of small-scale features.

Observations were made from the CM windows without disturbing the operations of the scientific instrument module. The tools available were limited to a booklet of graphics (some of which are shown here as examples), a pair of 10-power binoculars, a reference color wheel, two hand-held cameras (Hasselblad and Nikon), and voice-recording equipment.

The Apollo 17 crew made observations from orbit of 14 lunar surface areas (fig. 28-1). As shown in table 28-I, four of these targets were not formally scheduled in the flight plan. A brief summary of

visual observations during the Apollo 17 lunar orbit has been recently published (ref. 28-7).

The following paragraphs give detailed descriptions of the observation sites arranged from east to west as they are numbered in figure 28-1; some of the sites are grouped together for convenience. Excerpts from the Apollo 17 real-time air-to-ground transcript are given after editing for clarity. The edited quotations are followed by identification of the source of the statement (e.g., CMP, command module pilot; LMP, lunar module pilot; and CDR, commander) and the lunar revolution (rev) during which the observation was made. By consulting figure 28-1, the reader may check the Sun elevation angle at the time the observation was made. The terminators of revolution 1 (at long. 152° W and 29° E) shift westward one lunar degree for each additional revolution; the terminators of revolution 75 (at long. 134° E and 45° W) shift eastward for each preceding revolution.

KOROLEV, GAGARIN, AND PASTEUR

The largest light-plains-filled basin that was overflown on Apollo 17 is Korolev. This double-ring basin is approximately 450 km in diameter and a few kilometers deep (fig. 28-2). Its interior is filled with a generally smooth but intensely cratered light albedo unit that resembles the Cayley Formation mapped on the near side of the Moon and presumably sampled during the Apollo 16 mission to the Descartes highlands. The origin of the Cayley Formation remains enigmatic.

On Apollo 17, the sites Korolev, Gagarin, and Pasteur were studied from orbit to examine the detailed characteristics of the light plains fill. The smoothness of that fill was most striking:

We all had an opportunity to look at Korolev, at a very low grazing Sun. One of the striking things was the extreme absence of relief; the very smooth surface that existed in Korolev, independent, of course, of the craters that penetrate

---

1. Korolev
2. Aitken
3. Gagarin
4. Tsiolkovsky
5. Al-Khwarizmi
   (formerly Arabia)
6. Pasteur
7. Mare Smythii
8. Crisium-Serenitatis
9. Landing site
10. D-Caldera
11. Copernicus
12. Euler hills
13. Reiner γ
14. Post-TEI view
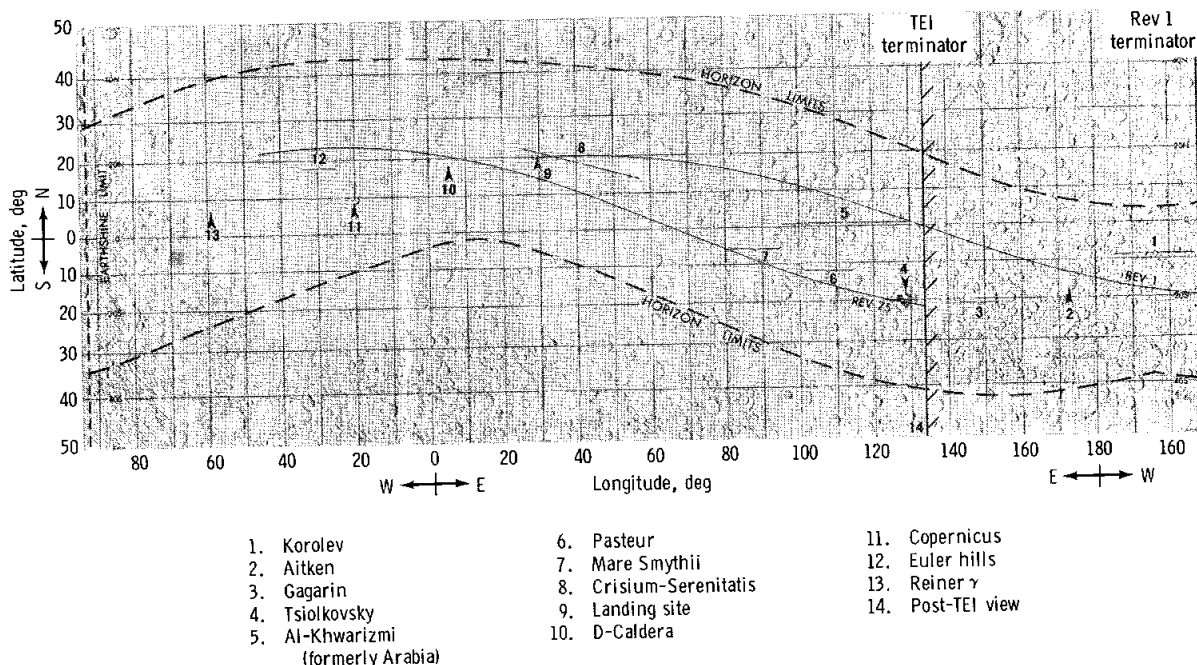
FIGURE 28-1.—Index map of Apollo 17 visual observation targets. The groundtracks for the first and last (75th) lunar revolutions are shown on the far side by vertical lines; the end points of the tracks on the near side delineate terminators of the respective revolutions. The dashed vertical line near longitude 95° W indicates the limit of earthshine illumination. The horizon limits enclose the maximum area of visibility from the CM windows throughout the mission.

its surface. And there was a ring in the floor next to the wall, about maybe one-sixth of a crater radius, that was somewhat brighter at the low grazing Sun, suggesting it may have had a different slope. And I believe I am correct in saying that the inner floor may be slightly raised. (LMP, rev 1)

Light plains materials were also observed and described in smaller craters west of Korolev:

There is a sequence of different kinds of crater filling on the far side, and I think that, as the orbital stay progresses, we may be able to pin down the relative age relationships and the characteristics of those crater-filling episodes. Whether they are single episodes that happen in a variety of craters or whether they are a function of the age and characteristics of the craters in which you find them is not clear right now. But they seem to form fairly distinct groupings of crater fill materials. (LMP, rev 5)

This indicates that there appears to be several generations of light plains fill rather than fill from a single event. This is confirmed by the orbital photographs of the area around Aitken Crater (part B of sec. 32). Some of the units observed and photographed on Apollo 17 appear to be even smoother than mare surfaces (fig. 28-3):

TABLE 28-I.—List of Apollo 17 Visual Observation Targets

Target	Coordinates	Revolution
Copernicus	10° N, 20° W	1, 28
Landing site	20° N, 30° E	15, 40, 62
Aitken	15° S, 173° E	27
Al-Khwarizmi (formerly Arabia)	1° N, 130° to 95° E	27
Crisium-Serenitatis	15° N, 55° E to 20° N, 25° E	27
Reiner γ	8° N, 58° W	28
D-Caldera	18° N, 5° E	40
Mare Smythii	4° S, 95° to 80° E	62
Tsiolkovsky	20° S, 132° to 125° E	64
Euler hills	18° N, 25° to 35° W	[a]73, 74
Korolev	5° S, 155° to 172° W	[a]2 to 5
Gagarin	20° S, 153° to 145° E	[a]55, 61 to 63
Pasteur	12° S, 115° to 100° E	[a]55, 61 to 63
Post-TEI areas	[b]N/A	[b]N/A

[a]Target not nominally scheduled in flight plan.
[b]N/A = not applicable.

One of those crater fill units that you also see in depressions other than craters is a very smooth, light, plains-forming material. And it is, although cratered, when you see it at the terminator, it is smoother than the mare; that is, it does not seem to have the swell, the sea swell characteristics or ridges or any other features other than the craters superimposed on it. (LMP, rev 5)

An observation that I think is significant is that most of the 30-km craters on the far side of the Moon seem to be fairly fresh. By fresh, I mean you do not have any real definite ray pattern to them, but streaked, 45° slope on the crater walls. On the bottom of the crater is a flat floor, or sometimes there is a domical type (domed up) floor. And the domical floor does not resemble anything like what slumped down the sides. (CMP, rev 27)

Few additional comments were made during the flight concerning the light plains materials. However, apart from the aforementioned characteristics, little could be added that would resolve the problem of their origin:

Pasteur and Hilbert make a pair of big craters that we spent some time studying ... Both appear to be very old, much older than Tsiolkovsky and they have a plains-forming fill, very flat looking at this distance, and very light colored. It is an event on the Moon of which we have relatively little understanding at this time, but possibly the Apollo 16 results, when they are fully known, through the analysis of the samples and other data, may shed some light on that event. (LMP, post-transearth-injection (TEI))
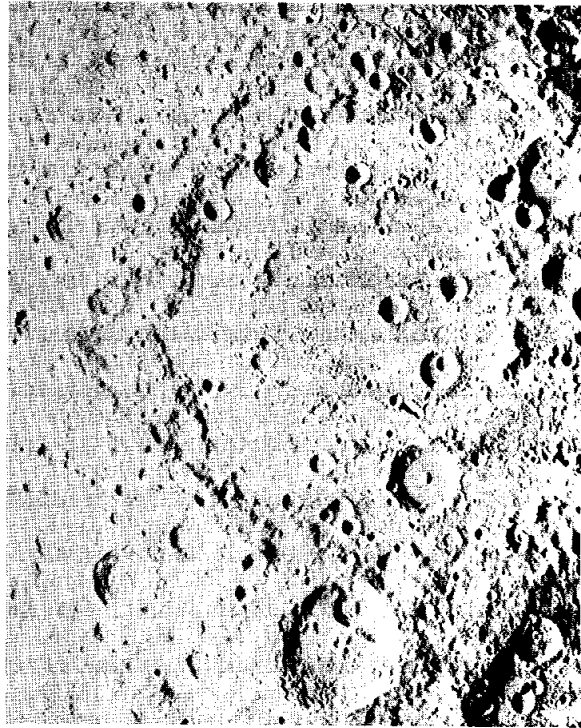
FIGURE 28-2.—Korolev basin: a double-ringed, light-plains-filled, 450-km-diameter crater. The right edge of the photograph coincides with the far-side terminator of the first lunar revolution of Apollo 17 (Lunar Orbiter I frame 35-M).
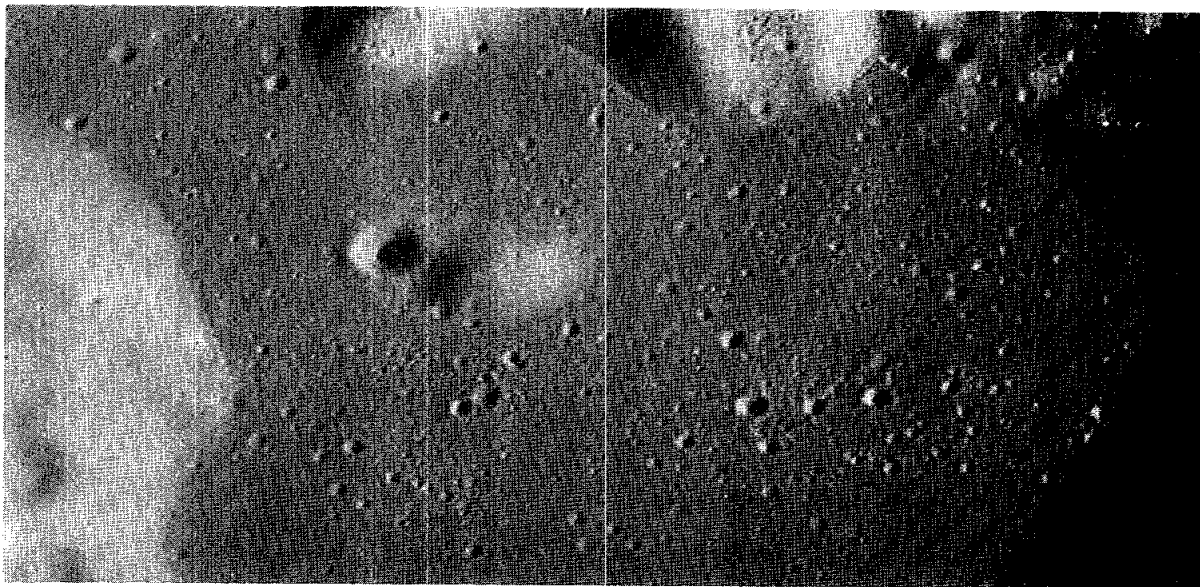
FIGURE 28-3.—Smooth light plains fill in an irregular structure near Sniadecki Crater on the lunar far side (AS17-151-23191).
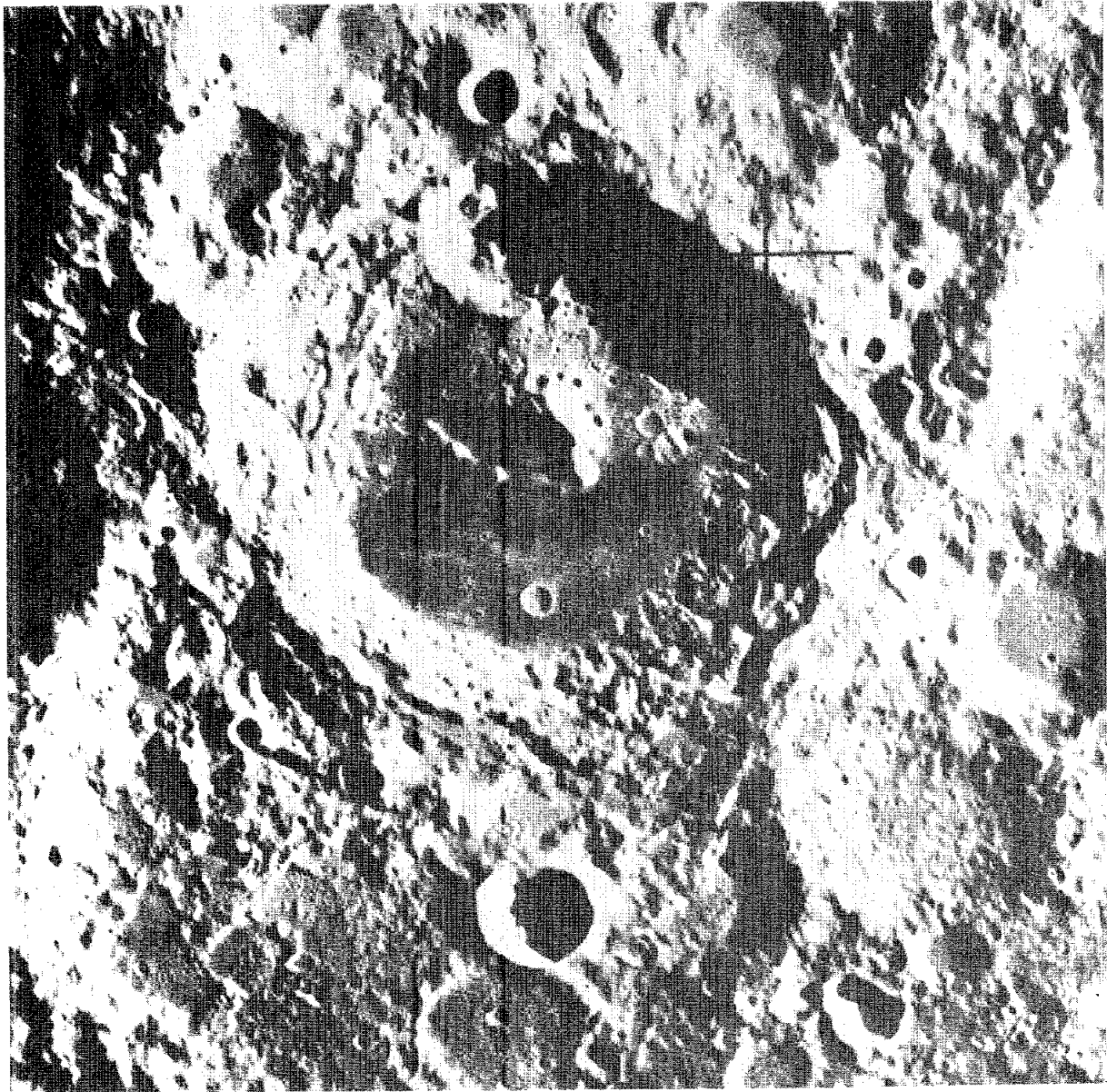
AITKEN (2 of 3)

Examine the interior of crater Aitken with emphasis on the following:
1. Albedo, textures, and structures of the dark floor fill; compare with floors of surrounding craters.
2. Nature of light swirls in the southwest quadrant of the floor.
3. Structures and rock exposures on the central peak, and possible "lava marks."

FIGURE 28-4.—Example of onboard graphics in support of visual observations from lunar orbit. This Zond 8 metric photograph of Aitken Crater (150 km in diameter) represents the same view of the crater as that seen by the Apollo 17 crew.

AITKEN

Aitken Crater, 150 km in diameter, is one of the few craters that display a dark mare-like floor. Observations were made to better understand the crater and its surroundings, the dark floor material, and the many interesting small-scale features in the floor (fig. 28-4).

The rim crest of Aitken Crater is very sharp and its secondary crater chains are distinct. However, it was not possible from the available photographs to establish without doubt whether or not the rim deposits are brighter than the surrounding highlands. When the CMP was queried about this particular aspect, he replied:

The rim deposits are a little bit brighter than the surrounding area. Where you would put it [place the crater in the lunar stratigraphic time scale] is probably early Eratosthenian. It is definitely not Copernican because I cannot see, at least at that low Sun, I cannot see any rays around it. But probably Eratosthenian—or somewhere in that area—because of the fresh slumping; it is not subdued at all. The walls of the crater themselves are not subdued. They are fairly fresh, but not as fresh as to be Copernican. And it seems to me like it was brighter at the higher Sun angles around there [on earlier revs], which indicates that there would still be some remnants of a bright rim around it.

On the side of crater Aitken, there are no visible rays that I can see at this low Sun angle. There is definitely a mare floor in there. It is a dark, low-albedo-type flat floor with swirls in it; no definite [topographic] expression to the swirls. One thing that is quite apparent is a flow scarp in the northeast corner, coming out of a little cloverleaf-like area. I am going to have to look the next pass over it to see if the south domical structure that is in there is breached. And I cannot tell whether the material is flowing to the east out of that domical structure or if it is flowing into the domical structure. (CMP, rev 27)

When the CMP was queried at that time whether or not he was able to distinguish high lava marks on the lower part of the crater wall, he replied:

The lava mark is what I would call a lava scarp in the northeast corner. There are some lava marks along the central peak. They are not nearly as apparent as the one up in the northeast corner. In the northeast corner is definitely a flow front, a lava flow front, that [laps up against] the older interior wall of the crater. (CMP, rev 27)

Some of the craters in the floor of Aitken, informally named on Apollo 17 the "cloverleaf cluster," display domical structures of unknown origin (fig. 28-5). An attempt was made to determine whether information could be gathered relative to the
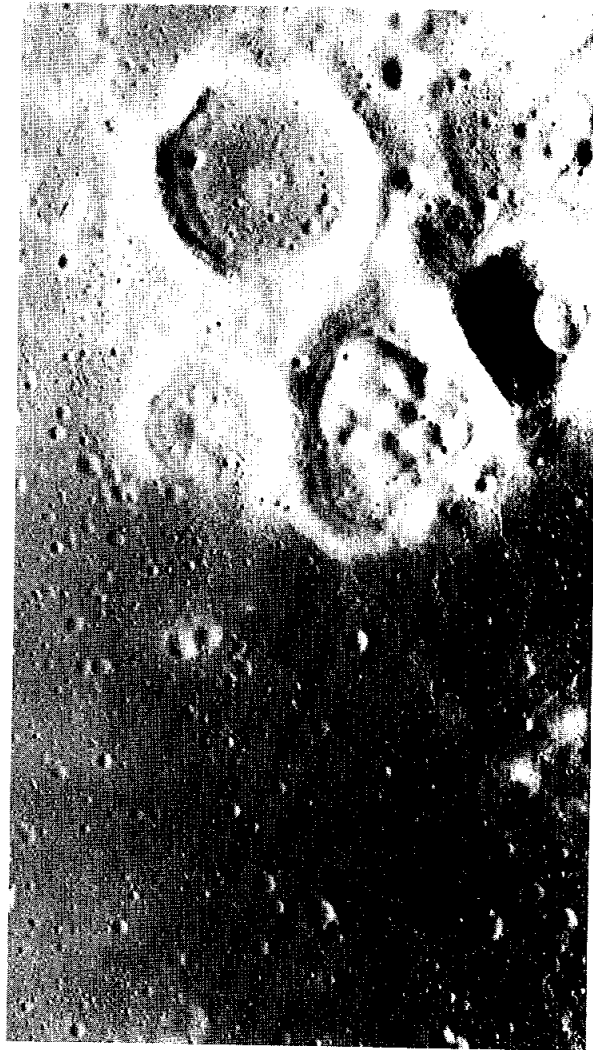
FIGURE 28-5.--Cluster of small craters (4 to 8 km in diameter) in the floor of Aitken Crater. Note the interior domical structures, the breaches in the walls, and the ridges and scarps in the dark floor material (lower right) (Apollo 17 panoramic camera frame AS17-1915).

color tone and the detailed characteristics of these domes:

The color of the domes in Aitken, although these colors are hard to visualize, is essentially the same as the surrounding material around [the crater]. Maybe a little bit lighter, a little bit lighter than the surrounding material. Of course, it is definitely lighter than the floor. The floor itself, is [somewhat] tan. (CMP, rev 27)

. . . at the cloverleaf cluster in Aitken [part B of sec. 32]. The southern domical crater of the cloverleaf has a breach on

the east side ... The domical structures themselves are younger than the floor ... Also, the texture is a coarser texture than the floor itself. In other words, the floor, to me, is kind of a standard flat mare floor. And I have to compare the texture of the domical hills to what I would imagine is some of the dacite flows that I have seen out in California, the heavy viscous-type flows ... Well, I am pretty sure they have got to be volcanic in origin. (CMP, rev 28)

TSIOLKOVSKY

The 200-km crater Tsiolkovsky was studied thoroughly on the Apollo 15 mission, and the results of these observations are available in references 28-1 and 28-4. On Apollo 17, further study was made of the crater and its many interesting features, especially the flow-like units on the northeast part of the crater rim (fig. 28-6 and 28-7).

The visual of Tsiolkovsky is hopefully pretty much recorded on the recorder. In summary, I concentrated primarily on the flow up in the northeast corner. To me, that particular piece in the crater on picture Tsiolkovsky, 4 of 5 [fig. 28-7(a)]. The piece that is down in the crater is on the right-hand side of the page, [must have been] in somewhat of a molten state. It looks like it is a landslide that has slid down the wall of the crater and was detached from the molten material, the rough-looking material that's on the rim of the crater Tsiolkovsky. (CMP, rev 64)

A similar flow unit occurs on the southern rim of the crater Tsiolkovsky. This unit apparently originated at a graben bounded by two parallel faults on the rim and flowed into the crater Waterman (ref. 28-1). The two units were thought to be similar in nature:

The flow that goes down into Waterman ... I did not get a chance to look at until I got to the west of it ... But the material that is in the floor of the crater Waterman is the same type of material as that in the little flow on the northeast corner. (CMP, rev 64)

The lineated unit on the northwest rim of Tsiolkovsky Crater was interpreted as a landslide on Apollo 15. One of the problems was the fact that there appeared to be a larger crater population on that unit than on the older floor materials of Fermi Crater (ref. 28-1). More information was required to fully understand this and the detailed characteristics of these small craters:

In the first observation of the mass of material that goes out into the crater Fermi, it looks like there is a whole bunch of craters in there that are essentially rimless. However, on close examination with the binoculars, I could not see any that did not have at least a slight indication of a rim. The rims were essentially very subdued. They extended out to about a half a crater diameter; and these are the craters in the
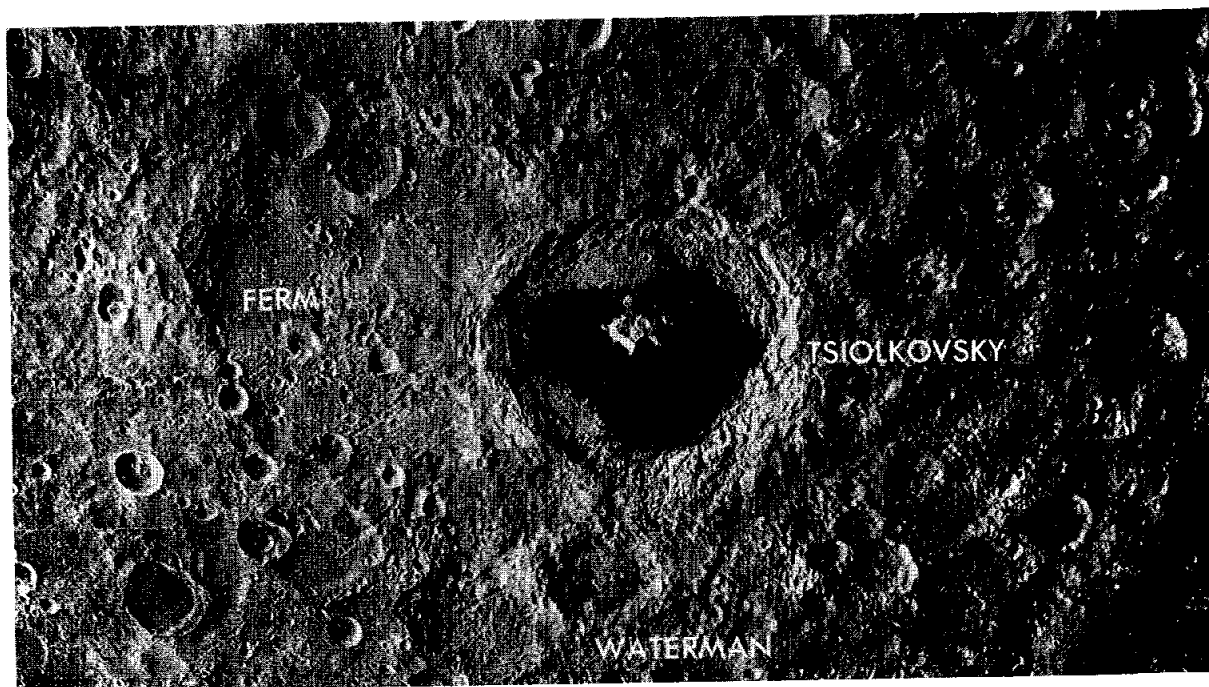
FIGURE 28-6.—Tsiolkovsky Crater (200 km in diameter) and its surroundings (Lunar Orbiter III frame 121-M).
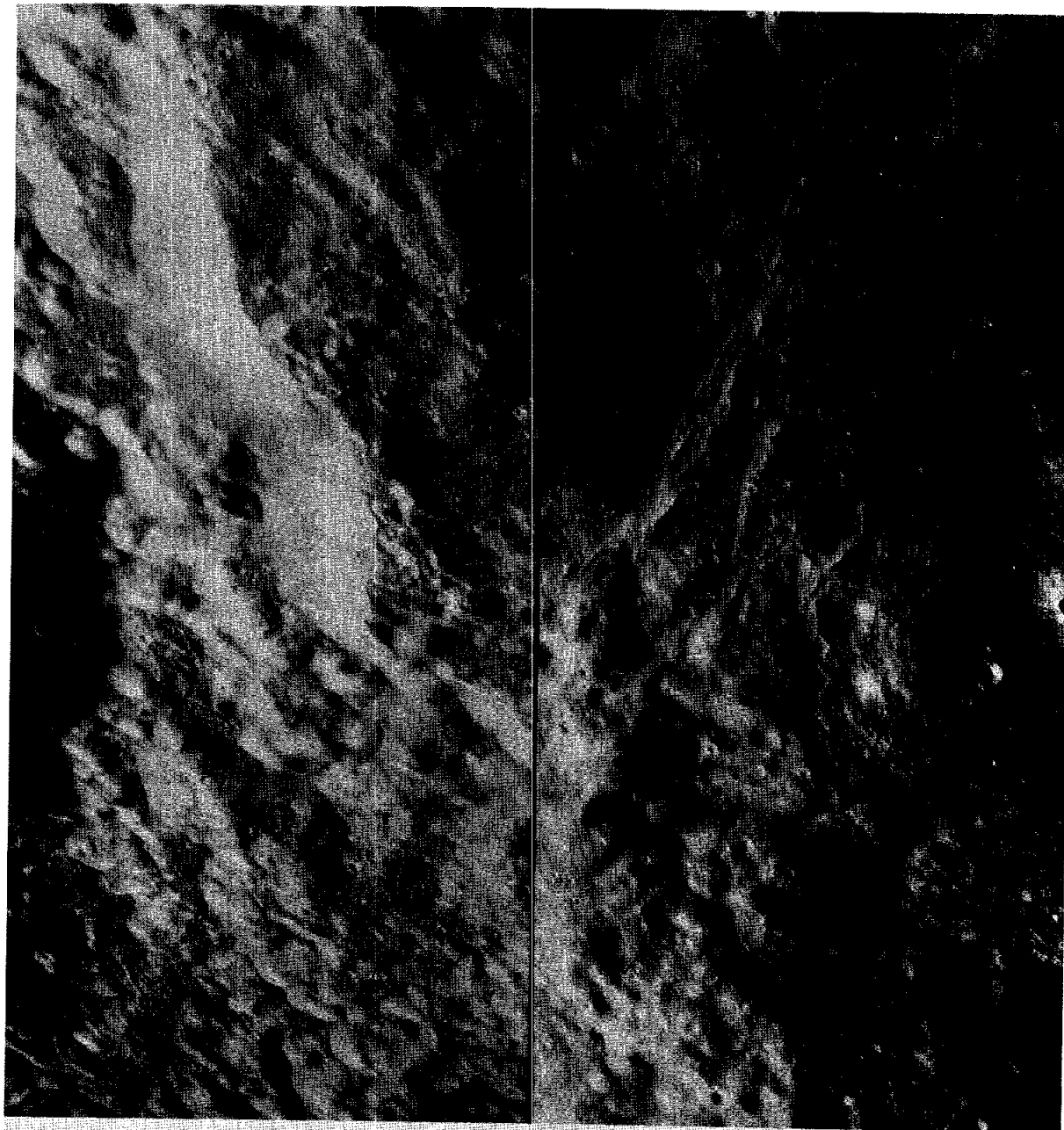
TSIOLKOVSKY (4 OF 5)

Examine the flow unit on the northeast rim of Tsiolkovsky:
1. Look for a source (fractures or vents).
2. Compare it with:
   a. the dark floor material.
   b. the light floor plains.
   c. the smooth patches on the wall terraces.

(a)

FIGURE 28-7.—Rim deposits of Tsiolkovsky Crater as seen on Apollo 17 onboard graphics compared to Apollo 17 photograph of a flow unit. (a) Hummocky rim deposits of Tsiolkovsky Crater as depicted on the onboard graphics in support of Apollo 17 visual observations.
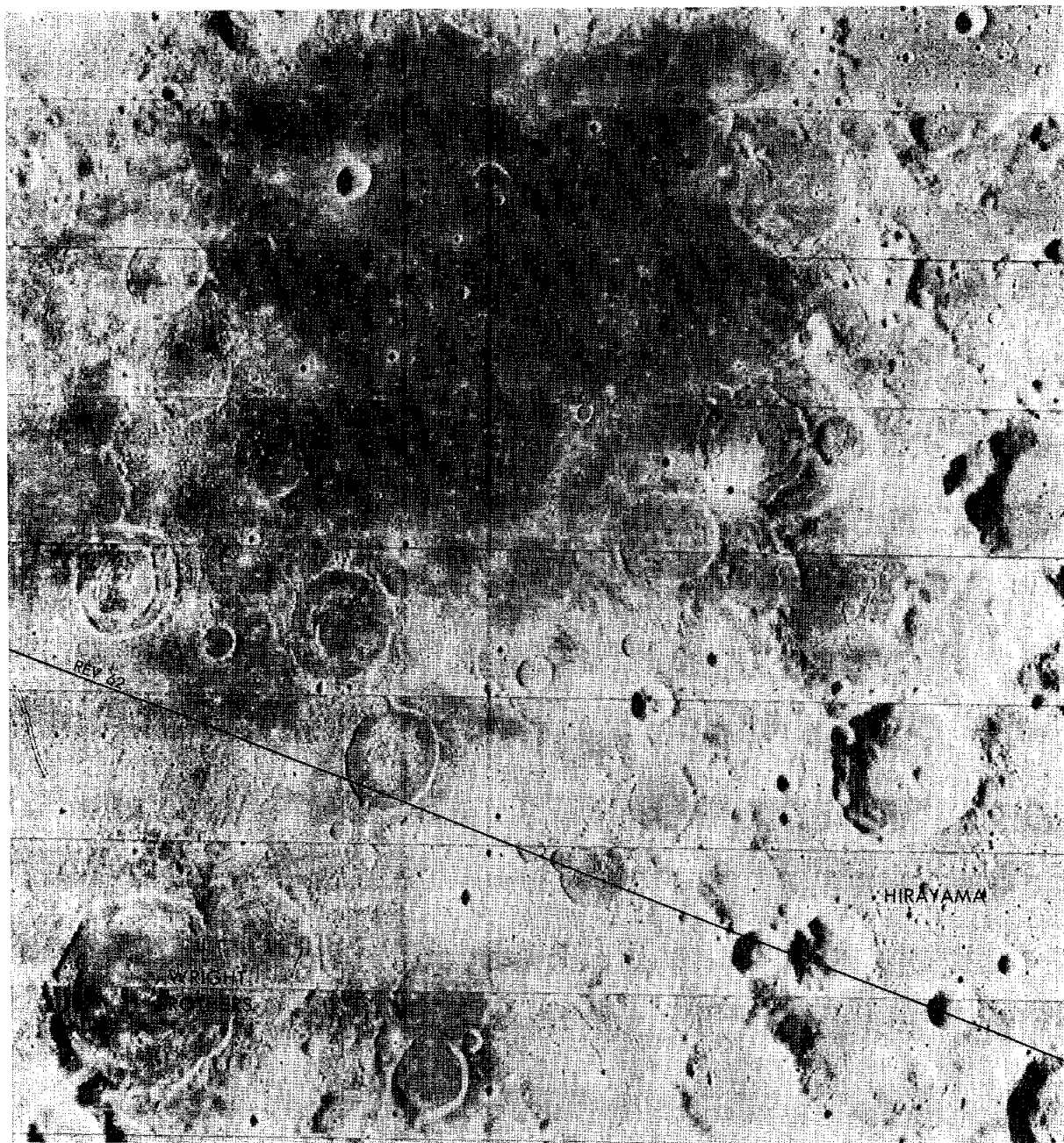
MARE SMYTHII (1 of 1)

Study the multi-ringed craters in Mare Smythii with particular attention to:
1. Symmetry of crater rim slopes.
2. Breaching of walls and resulting features (flow in or out?)
3. Inter-crater units and their relationships to the crater rims (impact ejecta, volcanic deposits, etc.)

FIGURE 28-9.—Numerous multi-ringed craters in Mare Smythii on the eastern limb of the Moon were the object of visual observation from orbit. Rim materials of these craters were compared to the hummocky units in the southern part of the basin.
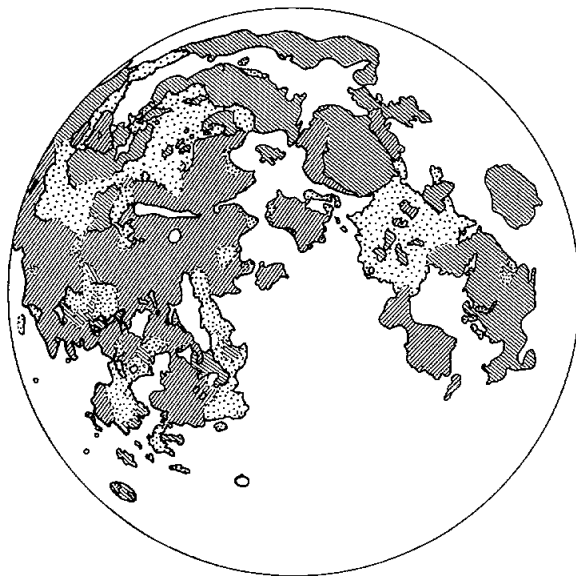
Color differences in the lunar maria

Blue Intermediate Red

FIGURE 28-10.—Generalized map of color differences in the lunar maria (ref. 28-12, p. 199).

extended, in real time, both to the east (to include eastern Mare Crisium, fig. 28-11) and to the west (to include the western rim of Mare Serenitatis, fig. 28-11). For clarity, the region will be divided into seven segments in the following discussion.

Mare Crisium

Some patches in Mare Crisium appear to have lower albedo than the rest of the mare. Boundaries between these units are difficult to draw, based on available photographs. Also, the relationship between the discontinuous circumbasin mare-ridge system and these units was not clear. The CMP was asked to study these relationships within the basin and report on the color tone of the mare materials:

I am looking at the eastern edge of Crisium now. As you come across there, it looks a little bit darker; I keep seeing browns all the time up here instead of gray tones. Maybe that is just the way I interpret them. They have kind of a brownish tint to them, and it is a darker brown than south of the ridge system there. (CMP, rev 27)

The CMP noted that the crater Condorcet H on the southeastern rim of Crisium displays an unusual diamond-shaped floor; he also noted a probable landslide in the adjacent Condorcet A Crater (fig. 28-12):

I am just now passing that crater I took a picture of on the last time [Condorcet H]. And instead of having a round bottom, it has a diamond-shaped fill in the bottom. And the diamond, itself, is about one-half of the crater diameter. (CMP, rev 27)

Condorcet A [appears to have] a landslide on it. And it does not look like a crater on the side of the wall, on the northwest wall of the crater . . . The area is oval or ellipse shaped. Of course, the top of the ellipse is toward the top of
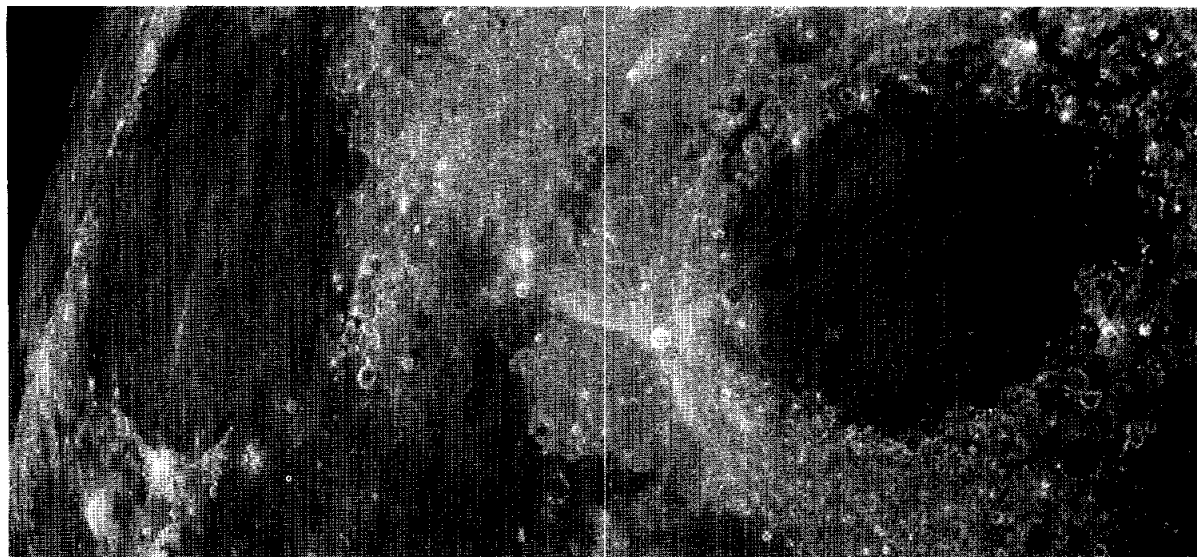
FIGURE 28-11.—Lunar near-side region encompassing Mare Crisium (right) and Mare Serenitatis (left). Note the albedo boundaries in both maria (AS13-60-8696).

FIGURE 28-12.—On the eastern rim of Mare Crisium, a landslide was described in Condorcet A Crater, and a diamond-shaped floor was found in a fairly fresh crater (arrow) near Condorcet H (AS17-149-22787).

the crater. And it looks like almost a flow out of the bottom of the ellipse, which is about a fourth of the way up from the bottom of the crater . . . The hole or the slope or the slide, or whatever you want to call it, down through there, is maybe one-eighth of the crater diameter. And the floor area is only just a real small portion of one-eighth size . . . There were some lineaments in the area; and, again, they are vertical-type lineaments downslope. (CMP, rev 28)

Picard Crater

Picard Crater, 30 km in diameter, is located in western Mare Crisium and displays a somewhat dark rim (fig. 28-13). Although the crater appears to be younger than the surrounding mare material, there are no rays and crater chains associated with its relatively smooth ejecta blanket. Detailed study of its characteristics from orbit was planned to aid in deciphering its origin. The similar, but smaller, Peirce Crater to the north was also studied for the same reason. The most obvious first question was related to the color of their rim deposits relative to the surrounding mare:

All those dark and light albedo changes around Picard and Peirce are not obvious at this particular angle yet. There is some hint of them . . . We are just about over the top of Picard; and the rim materials, which go out about a third of a crater diameter, as near as I can tell, are distinctly darker but not by much. They are more gray than the gray tan, or tannish gray of the rest of the mare. (LMP, rev 1)

Coming up at Picard now. Looking at it, a little bit from a distance, there is a darker albedo that goes about one-half a crater diameter. And then, on top of that darker albedo, it

FIGURE 28-13.—Picard Crater in western Mare Crisium (AS17-150-23038).

only goes out maybe a fourth of a crater diameter, there is a lighter-type material that seems to be covering it up. The lighter-type material though only goes in a generally westerly, from the south around to the west side and then from the northeast around to the northwest side, and it leaves the dark material draping down on the east side of Picard.

You can pretty well carry a light layer in the top portion of the wall all the way around to that part where the light part stops. And then you come to a dark layer again. And then, as you continue around from the west to go to the north side, it is a little bit in shadow on the east side, so I cannot tell for sure whether that light layer is in there or not. But starting on the south side, going around to the west again, you can see a layer of dark material, although there does not seem to be a change in the slope or the inner wall of the crater.

Just below the dark layer, there is a change in slope a little bit. It maintains that slope all the way down to the crater floor, where you get into the slump blocks. And then in the center of the crater, it looks like a mare-like fill with, I am about to lose sight of it again, something comparable to a central peak in it. (CMP, rev 24)

When queried as to whether or not the Crisium mare ridge system corresponds to the color boundary, and if not, does the ridge cross any color boundaries, the CMP stated:

This ridge system is running east and west down here. The color boundary is not nearly as apparent in Crisium as it is in Serenitatis, except that right under me right now, there is a

subdued crater with a southern part of a ridge. The ridge runs east-west, and it looks like we have got a flow coming out of it . . . The zero-phase point is following me right along here in Crisium, so I get a different color straight out from the window than I do out from the edge of it. So I think that is going to influence my thinking.

You can see some of the rays from the crater Proclus have spread out all the way across here. And they completely cover up the ridge system, so I cannot see any color distinction on the western edge of Crisium. (CMP, rev 27)

On the following revolution, the color tones around and within Picard Crater were again and more fully described:

Sure hope that color difference shows up in Picard . . . There is black material now you get on up here, the darker tannish-gray material covers essentially from the east all the way around to the south. It goes outside the rim as well as inside the rim. It drapes over the rim. That cannot be a shadow effect. (CMP, rev 28)

Additional details of the crater and its surroundings were also obtained on later revolutions:

You know you could, even as the zero phase went right across Picard, you could still see the darkness on the east from 9 o'clock around to 6 o'clock, if north is zero. And if north is zero as you look at the crater, then over about 1 o'clock there is some kind of a fault zone in the side of the rim, and that is another spot where the dark material drapes down into the rim and also outside of the rim. And then you have that same type of impression at about 11 o'clock. You have got a black streak going down inside the rim, and then it widens out going toward a little crater outside of the rim. (CMP, rev 36)

In the eastern wall of Picard—I am looking at it with the binoculars now—you can definitely see the first part of it up there has some vertical escarpments along the edge. And the vertical escarpments are in irregular layers, just like you would suspect if you eroded out a bunch of lava layers. In other words, they are discontinuous, but they are kind of intermingled along, and they go about a third of the way down from the top of the rim, down to where the talus starts sliding into the crater. (CMP, rev 40)

At a Sun angle of 50° to 55° (rev 50), the crater Picard still displays a dark halo. The dark halo appears slightly smaller, extending perhaps to one crater diameter, and is less distinct. (Paraphrased from CMP, rev 50)

Western Crisium

In the western part of the Crisium basin, observations were made of (1) the dark-halo craters in the mare fill and (2) the rim materials as displayed in massif units and in the ejecta blanket, including Proclus Crater and its bright rays.

Small, dark-halo craters in Mare Crisium.—The mare surface northwest of Yerkes Crater includes several dark-halo craters (fig. 28-14). Some of these display smooth rim deposits and are believed to be volcanic in origin (ref. 28-13), and others have hummocky ejecta blankets and are probably produced by impact. The following observations were made from orbit during the Apollo 17 mission.

West of Yerkes, there is a real small crater I am looking at with the binoculars. And the reason it stands out is because it is a fresh crater and yet there is a dark halo all the way around it. And it is also dark down on the inside of it. I still
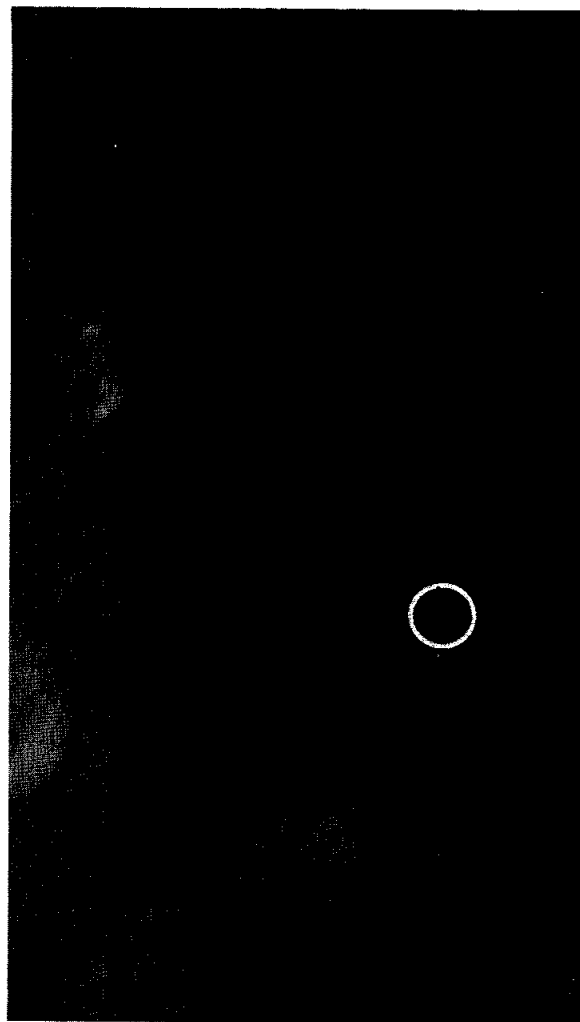
FIGURE 28-14.—Dark-halo craters in western Mare Crisium. The ejecta blanket of the circled crater was described as having an orange-tinted color (AS17-150-23044).

do not have a feeling for the relative size of things. I will try to get that one on the next pass. (CMP, rev 24)

All these dark-halo craters by Yerkes! The one that is farthest to the south looks like an impact-type crater. In other words, you have a definite ejecta blanket around it. The one that is hard to look at is in the middle of the field, but I think it is probably the second one down from the top. It has rounded ridges, and a rounded rim. The ejecta pattern or the dark halo is about twice the crater diameter. And it is either a highly eroded impact-type crater, or it is a volcanic-type structure. And, to me, it does not look like a highly eroded impact one. (CMP, rev 40)

The rays and ejecta blanket surrounding the bright-rayed crater in the area (fig. 28-14) were described as orange in color. The crater was compared to others in the Taurus-Littrow landing site and in the Sulpicius Gallus area (as discussed in the following paragraphs).

In the north, east, and west quadrants of that little crater, there is very clearly an orange pattern, an orange color to the ejecta. The other quadrant is a lighter color, a light gray. (LMP, rev 64)

In addition to the orange-tinted ejecta, blocks with a greenish hue were observed around impact craters in western Crisium. These observations may be important in establishing the importance and distribution of colored glasses collected on Apollo missions 11, 15, and 17.

I get the impression that these bright ones, see the bright one right down there in front of us [fig. 28-14], have a dark greenish-black or blackish-green [color], yes, a green cast to the rocks. The big blocks that are laying around in the crater and also the ones that are down in the bottom, a greenish cast to them. (CMP, rev 64)

Houston, we are just passing over a little polygonal crater that is maybe 15 km in diameter. It, again, has that dark greenish-black rock that is collected down at the bottom of it, and you also see it streaking down the side of it. But, I think one of the most significant features about the crater itself is that it has a swirl, and this looks like swirls rather than rays. It has a swirl pattern, radial from that most recent impact. (CMP, rev 66)

Rim materials of the Crisium Basin.—The sharpness of the massif units that ring the circular basins is one of the factors to be considered in deducing the relative age of the basin. The mountain rings of large circular basins and those of Imbrium were compared during the flight, based on what is known about their positions in the lunar stratigraphic sequence (ref. 24-14). The following are selected comments that compare Crisium with other overflown basins:

While we are in a relatively quiet period, we are going to make a few comments about some of the things that cross the two big basins that we are getting very familiar with, actually, three: Smythii, Crisium, and Serenitatis. [The obvious features are] the degradation of the walls of the major ring and the lack of any obvious blanket structures, in contrast to Imbrium and Orientale, which we have also had a pretty good look at. That contrast is quite striking.

The fronts of the major ring in Crisium are strikingly different from those of the Apennines in their general slopes; sharpness of topographical features; and in any appearance of having even a hint of boulder fields on their slopes like we observed, say, on the South Massif, anything like that. At least Serenitatis massifs seem to locally show fairly major boulder fields on their flanks. And I have not seen any around Crisium yet.

A crater, a fresh crater in the mare or a fresh crater in the rim area will have boulders, do not misunderstand me. But the front faces, the ring front faces, do not have boulders that I can see. And I think boulders are pretty obvious when they are there. We have seen them well defined on the central peaks of Tsiolkovsky, and I think any time you have a major boulder field, you can see it with the binoculars. (LMP, rev 62)

Proclus Crater, 35 km in diameter, was studied during Apollo 15, and its ray-excluded zone was attributed to shadowing at the time of impact (ref. 28-1). The rays of Proclus were studied during Apollo 17 to determine whether or not there is any similarity in appearance between those rays and the swirls of light-colored markings discussed in the section on Arabia:

I am looking north along Crisium, and there is Picard and Peirce. And you get the same pattern that looks like a swirl. The same type of albedo as a swirl with light places and dark places. The only difference being that you can definitely tell that these are ejecta from Proclus because the pattern is somewhat radial to Proclus itself. And then you have the same thing; there is a crater up on the north rim of Crisium, just outside of it is a 50-km crater. And it is a very bright one. And there the rays cross the Proclus swirls or rays. Here you have to definitely call them rays instead of swirls, and yet they look the same way. And the only distinction is that in Crisium they go essentially radial. They have a direction to them, whereas the ones over there in Marginis and next to Firsov do not have any particular direction to them. (CMP, rev 38)

On Apollo 17, an effort was made to study the unit in which Proclus Crater is located and to compare that unit to other hilly terra units in the vicinity of the Serenitatis and Imbrium basins.

There is a crater just on the west rim of Crisium, [with a] relatively fresh rim, fairly crisp rim, but no strong ray pattern. There is no ray pattern apparent at all. It looks like it predates the plains material around it, since they come

right up to the edge of the crater in one spot. That is [Proclus]! (LMP, rev 1)

The highlands look essentially the same as you pass from Crisium on across to Fertility. Again, they look so much like the Sculptured Hills . . . What I am referring to are the highlands bordering Crisium, in all of them you do see a definite radial pattern upslope and downslope, from the center of Crisium. But none of the lineaments look like Fra Mauro [the Fra Mauro Formation, bordering the Imbrium basin]. (CMP, rev 62)

Getting into areas that resemble, in their surface texture, the Sculptured Hills of the Taurus-Littrow landing area. Here we are just passing Proclus, so it is in the ray-excluded zone of Proclus where there is a mare surface projecting up into terrain that looks like Sculptured Hills. And that mare has a distinct bluish-gray color, in contrast to the regolith associated with the Sculptured Hills, between the Hills at least, which is a brown, let us call it a tannish gray. Quite a sharp color hue contrast to my eyes, at any rate. (LMP, rev 63)

Macrobius A Area

West of Macrobius Crater and especially in the vicinity of Macrobius A are several small cone-shaped craters that display dark halos (fig. 28-15). The Apollo 17 crew was asked to study these craters from orbit to determine whether they are volcanic cinder-cone-like features, or impact craters that excavated dark material from beneath a lighter mantle:

Next to Macrobius A, there is a dark halo crater, a very small one. And it does not have the appearance of a hummocky crater rim to it, at all. It looks like the material just kind of spreads out all over the area, but it does not have a hummocky appearance to it. I am going to take a look at that again when I come back around. On the other side, there is a small mound down in the bottom of the crater, also. It is a dome-shaped structure in the bottom of that small crater. It is right next to J-3, north of J-3 [fig. 28-15]. (CMP, rev 15)

I was looking at the dark rimmed craters, and some of them have what I would call an ejecta pattern around them; and the others just have kind of a raised rim with no apparent blocks. The one to the southwest of that hill by Yerkes looks like it has an ejecta pattern around it with blocks.

I was looking for any dark-halo craters in this area that might be sticking through the Proclus rays. You compare on either side of the Proclus ray, and the same size crater . . . You get the same albedo of ray material from the small craters in either case . . .

The two dark craters, the one just north of Macrobius A, and also north of J-3, that is the one that has the dark mound around it, it has got a small dome down in the center. It does not have any ejecta pattern around it; no rays, no nothing. To me, that sure looks like a cinder cone. The dark halo around it goes out for at least a crater and a half diameter. The raised dome down in the center of the crater is about a fourth of a crater diameter. And there are no rays. (CMP, rev 27)

The CMP at this point characterized the color of the dark-halo craters near Macrobius A as similar to that of Maraldi and the landing site; he characterized the color as "dark tannish gray." (Paraphrased from CMP, rev 27)

Maraldi Area

Before Apollo 17, the origin of the Sculptured Hills on the eastern rim of the Serenitatis basin was not fully understood. One of the possibilities was a volcanic, constructional origin (ref. 28-15), and the example usually given was the dome-shaped, isolated structure Maraldi γ (fig. 28-16). An objective of the Crisium-Serenitatis visual observations was to determine the nature of that structure.

From the pictures of Maraldi γ, it looked to me like it might have been a volcanic dome of some kind. Now when you look at it and compare it with the rest of the surrounding material, it looks just like any of the other Sculptured Hills. The domical structures on it are the same type of material that carries on through south of Maraldi. (CMP, rev 17)

The floor material of Maraldi Crater east of Mare Serenitatis was also studied from orbit, and some interesting color tones were discovered and later compared to materials in the Taurus-Littrow landing site and on the western rim of Mare Serenitatis.

It looks like maybe some kind of a mare fill has come in and filled up Maraldi itself. You can see flow lines, going down into Maraldi from Tranquillitatis. The impact craters inside Maraldi have a definite bluish tint to the halo that comes out as opposed to the bright or the white-type craters. Those have more of a darkish bluish tint to them. Oddly enough, that is the same type of bluish tinge that I see right in the landing site right now. In the Pentagon Complex, MOCR shows up that same type of a bluish tint. (CMP, rev 17)

Again, the fresh craters in Maraldi still look kind of bluish to me, not as much as they did yesterday, but they still have a bluish tint to them from the reflection of the Sun. In other words, they are fresh craters and one of them is about the size of MOCR, and the other one is about the size of Sherlock or Camelot. (CMP, rev 27)

Houston, even at the high Sun angle here, the ejecta of the four or five recent craters around Maraldi, still are bluish gray, light bluish gray. The floor of the crater Maraldi is essentially a darker gray today, I guess, than anything. And the ejecta patterns on that are the same albedo and color distinctions as the ones in the landing site. (CMP, rev 74)

When he was asked to compare the floor fill of Maraldi to that of the light plains materials in Maraldi E, the CMP replied:
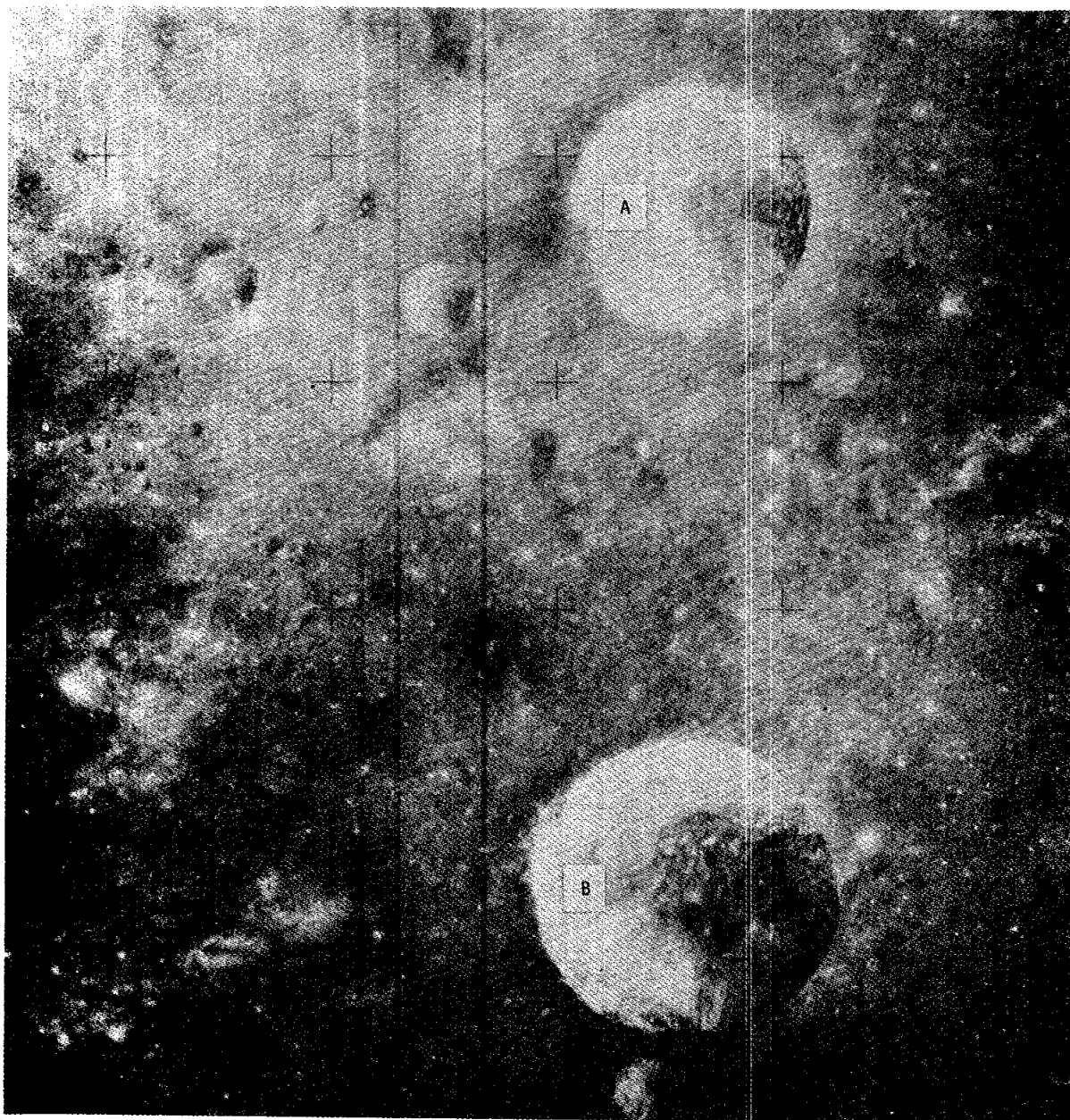
FIGURE 28-15.—Dark-halo craters near Macrobius A and B Craters (Apollo 15 metric camera frame AS15-557).

The floor fill in Maraldi is definitely a darker color. The light plains in Maraldi E are the light-tan material. And the floor of Maraldi looks just like the landing site. (CMP, rev 27)

Mare Serenitatis

As an additional tool for the extrapolation of ground-truth data, observations were made of the relationship of the dark material in the Taurus-Littrow landing site and the dark annulus of Mare Serenitatis (fig. 28-11). The following discussion will start with the eastern border of Mare Serenitatis, followed by observations of the color/stratigraphic units in the southern part of the mare. Detailed descriptions of the landing site area itself are given under a separate heading of this report.

Eastern Mare Serenitatis.—It was previously stated

CRISIUM-SERENITATIS (5 of 5)

1. Compare the floor fill of Maraldi to light p ains in Maraldi E.
2. Compare the albedo, texture and structure of Maraldi γ to those of the sculptured hills.
3. Examine the floor of Vitruvius A and compare the domical hills to those in the floor of the crater Aitken.

FIGURE 28-16.—Apollo 17 onboard graphic in support of visual observations of the Maraldi Crater area.

that the dark fill of Maraldi resembles that in the landing site area including a few craters with a bluish tint. The dark materials of the Taurus-Littrow area appear in photographs to continue into the Serenitatis basin and show intricate relationships with the mare ridges in the dark annulus. The following

observations are descriptions of these relationships as seen from orbit.

Right now, I am looking at the ridge system around the annulus of Serenitatis. And the dark material stops before you get to the crater that sticks into the eastern edge of Serenitatis. (CMP, rev 27)

The dark annulus around Serenitatis, as you look north, and I am kind of looking back, that dark has no continuity with the ridges at all. It [the color boundary] goes right down the middle of the ridges. As you look directly west of Littrow, the wrinkle ridge is there, and you have the dark tannish gray. And then you get out to the light tan of the Mare Serenitatis itself. (CMP, rev 35)

I am looking out of window 2 now, and you can definitely get three different color units: You have the light tan of Serenitatis; and then you have the darker annulus that stops somewhere in about the middle of the two ridge systems that go around; and then you come down south in the landing site area and the two dark units change. The landing site area is a darker gray. (CMP, rev 38)

The same color differences were amplified and more fully described at higher Sun angles (25° higher):

This is not a good viewing attitude at all, but we get a few isolated views that may be worth commenting on. The contrast, to my eye anyway, between the three color units around the landing site is a medium bluish gray to gray for the dark mantle; a light blue gray for the annulus around Serenitatis; and then, a tan gray for Mare Serenitatis proper.

The light-blue-gray annulus is also the locus of most of the circumferential grabens, that Serenitatis is noted for, in that area. And that is nothing new! But, in one place, there is a very subdued, flooded crater which seems to control a circular projection of the light blue gray out over the tan-gray mare. Most of the major wrinkle ridge system of Serenitatis, of course, is outside the annulus of blue gray, except locally, and one of those places was to the west of the Taurus-Littrow site. Although that wrinkle ridge system does, in the southern portions of Serenitatis, cross the contact between the light blue gray and the tan gray.

The impression I have had by looking at all the mare wrinkle ridge systems is that they are a late feature. They, at least at low Sun, and sometimes even at high Sun, they have very sharply defined ridges with steep slopes on either side that, in general, give me the impression that they are constructional, possibly associated with some thrusting movement. (LMP, rev 62)

Southern Mare Serenitatis.—An interesting observation was made of apparent layering in Dawes Crater (fig. 28-17) that is related to the units in southern Mare Serenitatis and their color boundaries:

The crater Dawes has, starting from the top going down the rim, a light-tan layer; it is a concentric layer all the way around. And then you come into a lighter one, almost like on the hills all around the landing site. The first layer goes down maybe about a third of the depth; and then the white
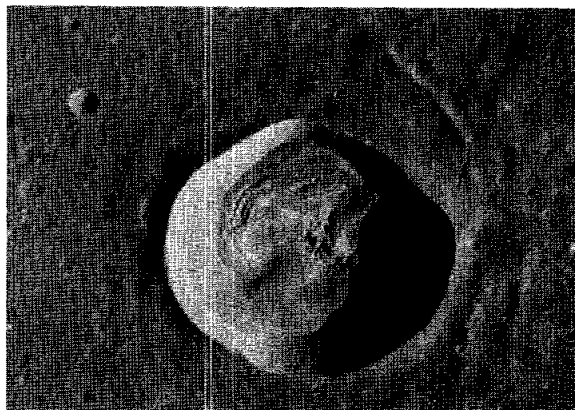
FIGURE 28-17.—Layering in Dawes Crater on the southeastern corner of Mare Serenitatis as seen from lunar orbit (AS17-150-23066).

concentric layer, in the western wall, goes down to not quite half of the distance from the top of the rim down to the bottom. The lower portion, a little better than a half, is kind of a tannish gray. It is all streaked. And the bottom of the crater itself is filled with, oddly enough, the same color of material as that lying around the edges of the crater. It has some radial rings, which give an indication of a subsidence of some kind, or of sliding downhill. That is really the first crater where I have been able to see any sort of layering in the walls. Now the first layer on the north side and also on the south side, in the dark-brownish layer of the thing, you can see parts are jagged. In other words, there is a slight change in slope. That looks like it is a very steep slope, which would indicate that it is a fairly compacted type of material in the first layer. And then the slope changes in the white layer on down a little bit more. And the white layer seems to sort of maintain the same slope as the dark-gray layer. (CMP, rev 39)

At higher Sun angles and to another observer, the sequence of layers in the walls of Dawes Crater suggested overturning of strata:

In Dawes, I think you can see the overturned [units]. The rim materials are made up of the brownish-gray material, and the walls underneath these are the bluish gray, which is the age relationship suggested by topography; that would be the lower unit is forming the rim, with inverted stratigraphy. (LMP, rev 62)

Layering was also noted in segments of the Rimae Menelaus that appear to have raised rims when observed at low Sun elevation angles:

Those rilles to the north of [Menelaus], there is a bunch of them crisscrossing. One is right on the edge of the Serenitatis basin. But they have got slightly raised rims around the edges. You can see some layering down inside the rille itself, in the one that runs in the east-west direction. (CMP, rev 15)

The color boundaries in southern Mare Serenitatis, particularly north of Menelaus Crater (fig. 28-18), received much discussion throughout the mission. The following observations were made of this area:

When I take a look at it from this angle, the ejecta from Plinius covers up the rilles and the annulus around Sereni- tatis . . . Now, we are getting into a relatively low Sun. And Serenitatis is a lot lighter colored than the light tan, to me. At this low Sun, you look out into Tranquillitatis, across Plinius, and that turns out to be the same kind of gray tan, it is darker . . . There is a definite color difference between them [Tranquillitatis and Serenitatis]. And it almost looks as if the color from Tranquillitatis extends on over, or kind of drapes over the edge, and covers up part of Serenitatis.

We are at the same Sun angle, and there is no doubt about it from Tacquet on up to Menelaus, there is a group of small rilles and those rilles have ejected material, around and over the rilles; not impact-type ejecta. It has got to be a volcanic ejecta of some kind. It is a darker brown than the tan of Serenitatis. (CMP, rev 28)

Going to come across the Tacquet area again, and there is a bright crater, a recent crater, in that dark annulus in the southern part of Serenitatis. It shows up again as that kind of a blue-gray brightness, as opposed to the tannish brightness of the bright craters in Serenitatis. There is still no apparent color tone or differentiation in the wrinkle ridge in this part of it. The only differentiation is that it looks like south of Tacquet you get the same color tone on over into Tranquilli- tatis as you get between Tacquet and Menelaus. (CMP, rev 35)

Looking at Menelaus, you can see where the dark edge of Serenitatis goes through the crater. And, the north wall is quite distinctly grayer, let us say bluish gray, than the south wall, which is very light gray in the talus. My guess is that it is a very nearly vertical contact at that point. (LMP, rev 66)

Sulpicius Gallus Area

The dark mantling materials on the western rim of the Serenitatis basin are more varied and perhaps more complex than on the southeastern rim. Mater- ials of the dark mare annulus in southern Serenitatis appear to be overlain by younger mare materials that also postdate the dark mantling units of the Sulpicius Gallus area on the western rim of Serenitatis. These rough and textured materials are to be contrasted with the patches of dark units between Montes Haemus and Montes Apenninus to the west (fig. 28-19). The objective of this observation was to compare these units to the Serenitatis mare materials, with emphasis on the color tones. (This task was added to planned observations in real time.)

When we are coming around the dark annulus, follow it around, by Menelaus and Tacquet, it seems to change colors a little bit when we get up to the Sulpicius Gallus. I guess the

FIGURE 28-18.—Contact between two mare units in south- ern Mare Serenitatis. The older and darker unit near the rim of Menelaus Crater (lower edge) displays rougher topography; the younger and lighter unit contains a broad wrinkle ridge (AS17-150-23069).

only thing you can say is that the southern part there, in the Tacquet region, has a more of a bluish tint. And, then to me, this has more of a brownish tint to it when you get to the Sulpicius Gallus region.

I am just passing Menelaus . . . and Sulpicius Gallus is just now coming up. I think the Sun angle has a lot to do with that, because this whole Sulpicius Gallus region looks kind of brownish to me. I will have to check that when the Sun gets a little bit higher. (CMP, rev 24)

I am just passing over Sulpicius Gallus, now. And just beyond Sulpicius Gallus, you got a gentle slope of the massif coming down and then it changes slope a little bit. And that might be what we have at one time or another called the high water mark, but I believe that is just a talus change in the slope. But as soon as you cross that area, we have a dark-tan material that essentially covers the highland. It is a hum- mocky material. There are a few rilles just north of Sulpicius Gallus; those rilles, again, have the dark-tan material on them. (CMP, rev 36)
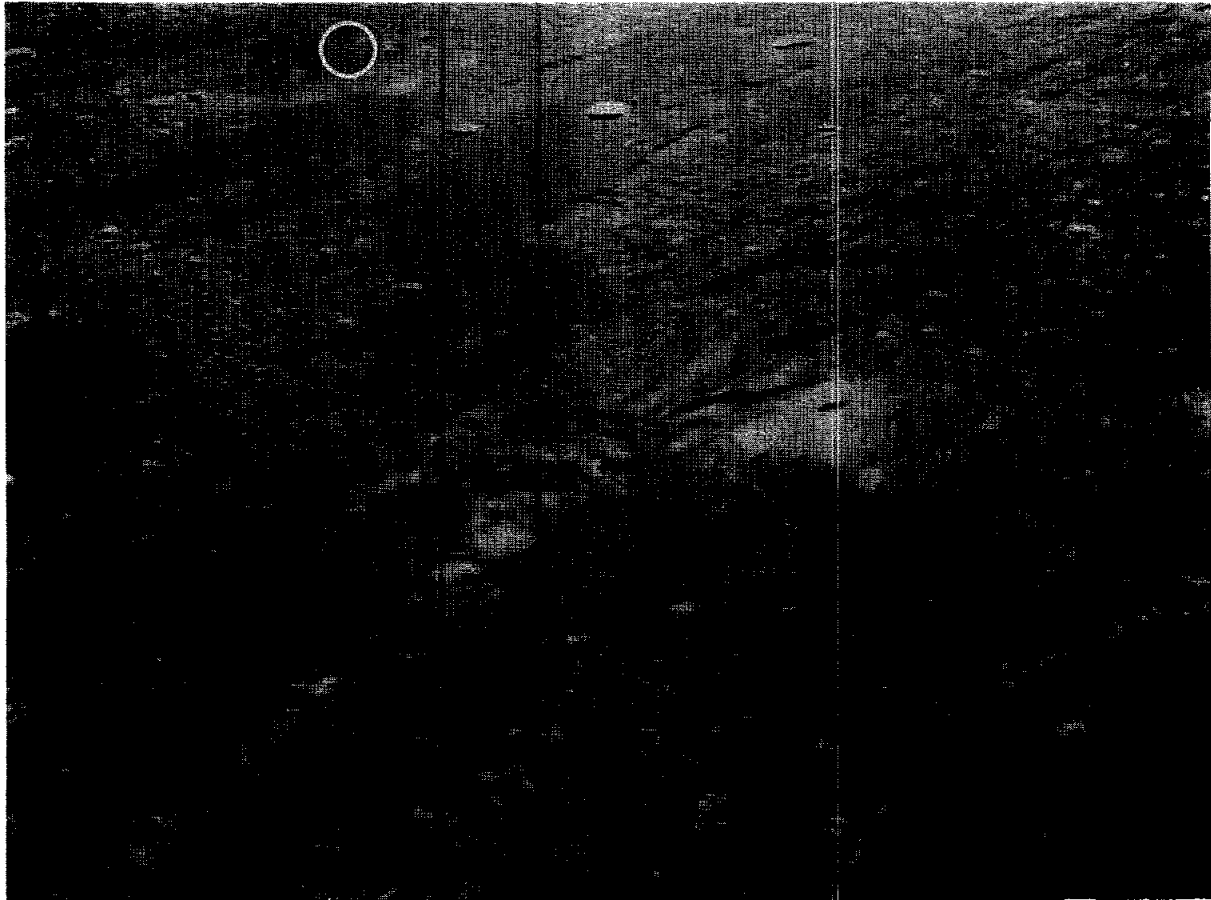
FIGURE 28-19.—Oblique view looking westward from the dark mantling deposits on the western rim
of Mare Serenitatis. Rimae Sulpicius Gallus are in the lower right corner; D-Caldera (circled) is near
the upper left edge of the photograph (AS17-153-23572).

As will be discussed later, the CMP noted an orange zone on the northeast rim of Shorty Crater. Ejecta blankets of several craters of comparable size and larger also displayed an orange color. Referring to these craters later in the mission, the LMP added:

Ron says that he already commented on those, and they look very obvious to me . . . [The color] is a light orange, in contrast to the brown gray of the dark mantle in the vicinity of Sulpicius Gallus. There is a good one right down there. Now, that one looks like a constructional cone that is orangish. And that is right out on a raised projection of the brown-gray dark mantle out onto the light-blue-gray annulus material. (LMP, rev 62)

In addition to the constructional-appearing, orange-tinted craters and the many orange-colored blankets around small impact craters in the Sulpicius Gallus region, an elongate depression with orange-related colors was also discovered (fig. 28-20).

There is a large gouge just south of the Sulpicius Gallus rille. The gouge is a rimless depression, and streaming down from the upper portion of that depression are not only our old friend the orange gray, but some would be a red brown gray, very clear coloration . . . There is another crater we will have to look at . . . There is a whole bunch of them down there . . . Yes, we are seeing an orange Moon now. In this whole dark mantle in here around Sulpicius Gallus there are scattered craters with a variety of orange to red-brown hues. And they all, except for that large rimless depression, which looked as if it was exposing some layers which were streaming those colors, all the other craters seem to be small impacts that apparently are penetrating just far enough into the dark mantle material to tap this zone of orange to red-brown material. (LMP, rev 64)

That rimless, V-shaped depression [fig. 28-20(b)] that had the streaked talus on it has a mottled rim area that has the orangish-tan or orangish-gray color as the spot. And it looked as if the more red-gray, red-brown-gray, if you will, material was lower in the section within the walls of the depression. This is a very steep-walled depression, by the way. It has talus
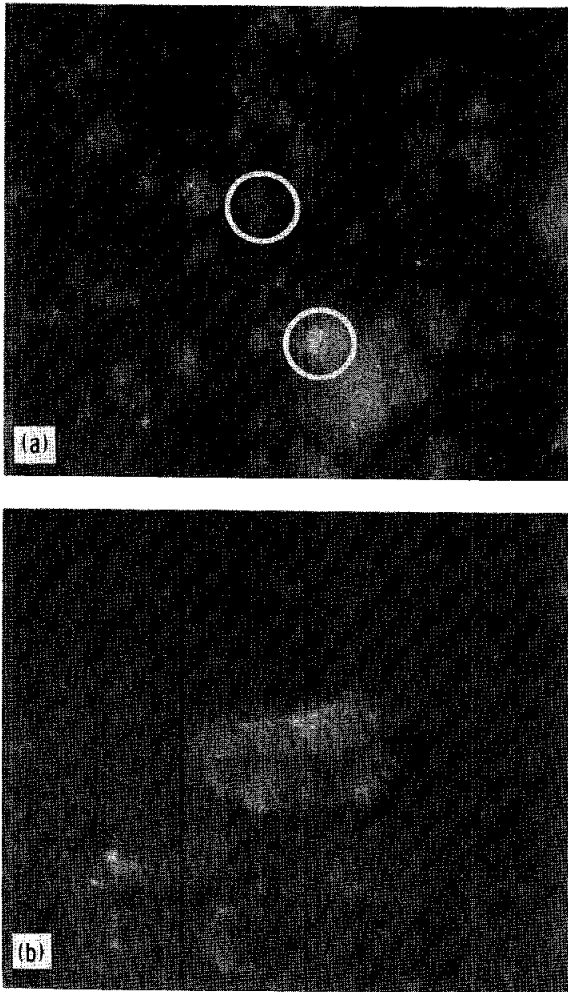
FIGURE 28-20.—Apollo 17 photographs of Sulpicius Gallus formation where orange-tinted material was observed during lunar orbit. (a) Two 0.5-km-diameter craters. The upper crater is an impact in the dark plain and exhibits orange-tinted ejecta (AS17-148-22771). (b) Elongate depression, approximately 6 km long, showing orange-tinted walls (AS17-149-22880). For general setting, see figure 28-19.

streaming down the sides of it, and the coloration streams in this same direction. It looks as if there may be layers or roughly horizontal zones that have the coloration that we are seeing, which are forming the talus slopes down below them. (LMP, rev 65)

These observations of the orange materials were also confirmed by the third crewmember:

Just so you are fully aware, we are not sort of just leaning and getting colorblind up here, I tell you, the last one Jack was talking about [the small impact crater, fig. 28-20(a)] was not even subtle. Its entire ray pattern was this color material,

with a definite contact between it and the dark material around it, and it had that orange-brown hue to it, without any question at all. (CDR, rev 64)

LANDING SITE AREA

The Taurus-Littrow landing site on the southeastern rim of Mare Serenitatis was studied from orbit for (1) regional characteristics that may reflect on the sampling area and (2) details of local structures that may help decipher the setting of explored sites.

General Setting

Observations from orbit began very early during the mission and continued throughout the orbital period. One of the more interesting problems was to see whether or not it is possible to define a source point for the landslide or white mantle on South Massif (figs. 28-21 and 28-22). The slide itself and the scarp that goes through it were obvious even at very low Sun elevation angles:

With respect to the landing site, when I first had it in view, there was a clear lightening in the area of the light mantle. It was not sharply defined; but around the crater Lara and Nansen and to the west of the scarp, there was very clearly, slightly brighter reflectivity. (LMP, rev 2)

I can now see down in through the shadow. I can see Bear Mountain. I cannot really make out the slide yet. Most of the North Massif is still in shadow due to the Sculptured Hills . . . But, I did see some sort of albedo change that went across the canyon about in the vicinity of the scarp. (CDR, rev 2)

You could really see a difference between South Massif and the mantle material through there. The mantle is not nearly as dark as it looks on the pictures, though. But South Massif, especially, looked whitish in color. I guess it is because the Sun was shining on it . . . You can see the slide and definitely see the scarp going across through there. (CMP, rev 3)

I got the landing site. We are right over the top of it, and the scarp is fantastically detailed at this [Sun angle] . . . The light unit is very obviously mantling the area. The scarp is very detailed, and, so far, [I] could not see any structure in the massifs at all . . . From this altitude and with that low Sun, there is no question of the sharpness of the topographic features in the landing area. The scarp, and even some of the apparent backflow features, that is, apparent flows to the west in the light mantle area, were extremely sharp, even those fronts going west were sharp. It looked even more like a mare ridge than it ever did before. (LMP, rev 5)

The scarp definitely cuts up through the North Massif. I cannot see a continuation into the South Massif at all. And it almost looks like a flow coming from the direction of Family Mountain, lapping up on the side of the North Massif. That is
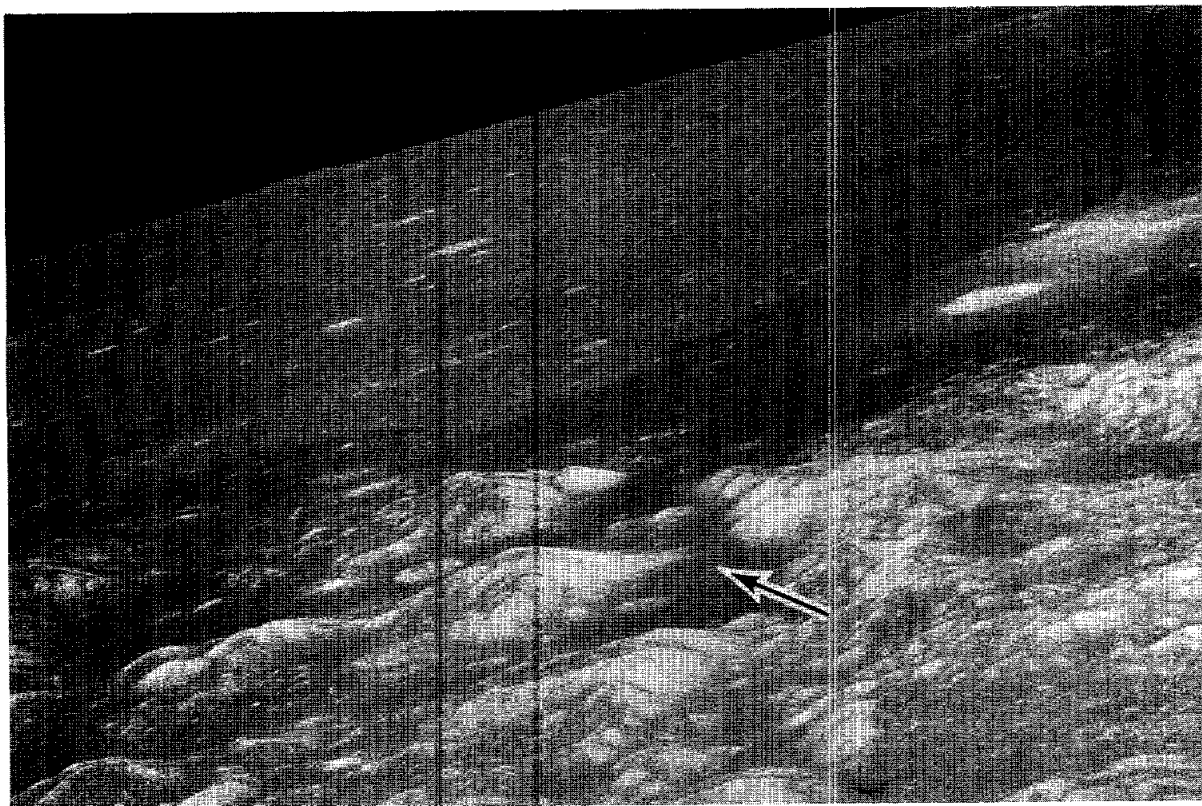
FIGURE 28-21.—Oblique view looking westward from the Taurus-Littrow landing site. Arrow, showing the direction of flight, indicates the landing point (AS17-148-22770).

the way it looks as you go on by it. I could not see anything that would lead you to believe that the slide area, so to speak, would come on across anything that would be the source of that slide area. (CMP, rev 15)

As discussed in earlier sections of this report, blue-gray rocks were sampled at several localities in the landing site. The same color tone was described from lunar orbit in the vicinity of larger craters in the subfloor materials as well as on the slide.

You still get that same bluish tint from the area in the landing site. At station number 2, on the landslide, it is going to be a pretty good little depression there. (CMP, rev 24)

Areas in the landing site where we now know there are extensive blocks of the subfloor material, particularly in the walls of the larger craters, I have the impression that those block fields, from this altitude, give a light bluish-gray appearance. (LMP, rev 66)

Just north of the bright-rayed craters in the Littrow area, there are five craters, probably in the range of 500 to 1000 m; and all five have the sequence of colors in the walls, from rim down, of a brown gray, blue gray, and then brown gray. They are all identical in that and quite clear. And that blue gray is comparable to the blue gray that is visible in the craters such as Sherlock in the landing area. (LMP, rev 72)

The differences in albedo, color tone, and texture between the massif units and the Sculptured Hills were obvious from orbital altitude both at low and high Sun elevation angles:

I can see the landing site now quite well. The slide area definitely shows up. The South Massif seems to have the Sun shining right on the walls. I am looking for any type of layering, or anything like that, and cannot see anything. The big difference between the massif structures and the Sculptured Hills is that the massifs look like they have a steeper slope. And they do not seem to have that type of covering over them, like the Sculptured Hills do. (CMP, rev 15)

The albedo differences are very definite: one is the dark mantle on the floor; one is the South and North Massifs; and the other is the Sculptured Hills. And the Sculptured Hills have a light-gray albedo between the Massifs and the dark mantle. This line is very evident and there is a definite break in slope that you can see between the South Massif and the white mantle out on the valley floor. (CDR, rev 62)

To me, the Sculptured Hills incorporate the albedo both of the North Massif, or South Massif, and the mantle area and combine them to give you a generally in-between gray albedo, but the sculpturing is produced by the darker albedo that looks like the mantle, and the lighter albedo that looks like the massifs. (CMP, rev 62)

FIGURE 28-22.—Taurus-Littrow landing site. Note that the scarp displays mare ridge characteristics between the North Massif (top) and the South Massif (lower half); it also appears as a flow that laps up against the North Massif (AS17-150-23006).

SHORTY CRATER

Much excitement was generated during the mission by the finding of orange soil on the rim of Shorty Crater (fig. 28-22). The CMP was asked, after the discovery, to determine whether the orange soil could be observed from orbit. An orange-tinted zone was described particularly on the north rim of Shorty. This finding also led to further concentration on craters of a similar size in western Mare Crisium, in the Littrow B area, and in the Sulpicius Gallus area.

The orange-tinted zone was obvious at intermediate Sun elevation angles (on rev 40) but harder to discern at high illumination (on rev 65):

I have got Shorty in the picture. It is a sharper crater than any of them . . . Did they find that orange stuff on the north side of it? . . . I would say they just barely got into the [orange] stuff, then, because the north rim has more of a tint of a different color to it . . . Would you believe an orangish tan through these binoculars? (CMP, rev 40)

Through these glasses, Shorty still looks light tannish orange. And it does not come all the way down to the center

of the crater. It is tangent to the north edge or perpendicular to the scarp. (CMP, rev 41)

On Shorty, I still have that light-orangish-tan material. It is essentially perpendicular to the line of the slide area there in the northern semicircle of the rim. (CMP, rev 62)

My impression of Shorty from the other day, and also from seeing these craters that seem to have orange around them, they look very much like impact craters from orbit. At any rate, if that is an alteration phenomenon, it is being localized around the structure created by the impact. But in this latter case, it looks as if the impact itself penetrated into a zone of that color. (LMP, rev 64)

The craters we are seeing around Sulpicius are very clearly orange gray and the whole, or at least most of the crater, is that way. We looked at Shorty today, and Ron said that even the little bit of orange that he saw the other day is not visible, and I agree with that. The amount of orange we saw on the surface certainly would not be comparable to what we are seeing around Sulpicius Gallus . . . And on a couple of quick scans, on previous revs, of the area, the dark mantle, near Littrow, I did not notice any obvious orange-gray craters. (LMP, rev 65)

I still get a feeling that there is just a tinge of the orange or tannish orange around Shorty, looking at it with the binoculars. (CMP, rev 74)

D-CALDERA

The low hills between the Montes Haemus to the east and Montes Apenninus to the west are interspersed with patches of superposed dark material (fig. 28-19). In one of these patches is a D-shaped depression (fig. 28-23) that was previously interpreted as a volcanic caldera (ref. 28-16). The structure is unique, with no equivalent formations on the Moon. It was studied from orbit to further characterize its nature:
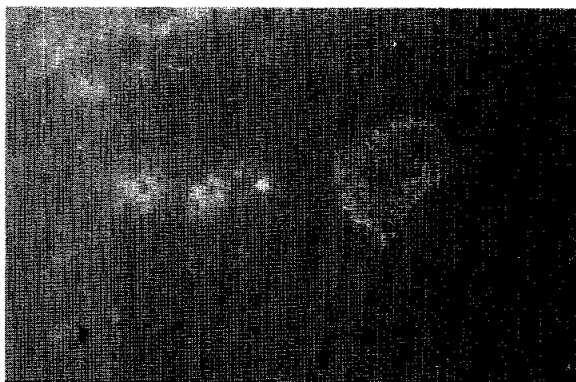
FIGURE 28-23.—The D-shaped depression in the dark mantling material west of the Montes Haemus exhibits a light-blue-gray tint. A darker bluish tone is also exhibited in the crater in the lower left corner (AS17-152-23286).

The D-Caldera is sure a depression. Like nothing I have ever seen before . . . At this point, you get a dark tan, a mare-type material. And then it is a light gray down in the D-Caldera itself. But it is a light gray down inside. It has got bumps that stick up, and the bumps themselves . . . are light tan. And down between the bumps in the caldera is a rough, blocky, gray material. (CMP, rev 28)

At higher Sun elevation angles, the floor of the depression was found to have a bluish tint to it that is also apparent in the Hasselblad color photographs.

D-Caldera is sure fascinating. I will try and take a quick look with the binoculars on that one . . . I hope the pictures will confirm a little bit of a topographic rise around the D-Caldera, just a slight one, and it is about half the width of the "D." And there seems to be a raised, flat rim around it. The color of the raised bumps down in the D-Caldera is the same as the surrounding material. The bumps that are raised up are smooth looking and the depression (floor material) is light bluish gray, very light bluish gray. (CMP, rev 36)

There is nothing surrounding D-Caldera that looks anything like the silver-gray material that was depressed with respect to the surrounding terrain. (CMP, rev 40)

Flow structures were also observed in the interior of the depression:

I was looking at D-Caldera and you got a lobate flow front sticking down in the crazy thing. (CMP, rev 42)

The light-blue-tinted materials observed in the D-Caldera were compared earlier to the somewhat darker tints of blue gray in the floor of Maraldi as well as in the Taurus-Littrow area. This comparison was also evident as the Sun elevation angle increased:

Ron's D-Caldera—I am just correlating apparent colors now, or hues—and the lighter-colored material there is comparable in hue to the subfloor color at the landing site. (LMP, rev 66)

COPERNICUS

Copernicus Crater was studied from orbit mainly in earthshine (fig. 28-24). In addition to details of the ejecta and interior, emphasis was placed on the central peaks and on a possible extension of the dark and blocky band that was observed in Lunar Orbiter II frame 162-H. Apparently, the viewing conditions were not adequate for this. Several other features of Copernicus were discussed throughout the orbital period of the flight:

I have got a visual on Eratosthenes and Copernicus. They are obviously different age craters in this light. You can see the ray patterns of Copernicus moderately well. You can even tell that they do cross Eratosthenes . . . On the upper portion of the rim and on the benches, there are the dark spots of lower albedo material. They form linear patterns

along the benches, although the topography is not too clear. But the dark spots are in arcuate linear arrangement parallel to the rim. And they appear to be elongate along the radius of the crater [Copernicus].

Copernicus H is also very obvious as a dark-rimmed crater, relative to the albedo of the ejecta blanket. And the northwest quadrant, which we mapped as a smooth floor material and somewhat darker albedo, is just as apparent here, although all the contrasts, of course, are less. The main thing that you can pick out in earthshine are albedo distinctions. (LMP, rev 1)

Additional details of the dark zone in the southern wall of Copernicus were provided under faint earthshine illumination conditions:

On the south side of Copernicus, you can see albedos real well, and there is a dark area that extends maybe half a crater diameter to three-quarters of a crater diameter to the south, and it carries down the crater wall to the crater floor. And this is in the south maybe from about 4:30 to 7:30. And in the rest of the crater, all the way you can see light albedo.

When asked if he was able to see any structure in the central peaks (both in earthshine and in sunlight), the LMP replied:

No, I cannot . . . The central peaks do stand out, though, as a much lighter albedo area within the crater. It looks to me like the best thing you can do in earthshine is work with albedos. Knowing the general topography from earlier photography. (LMP, rev 1)

And this is a good view of the central peaks, although from some distance; and, as Ron and I were discussing earlier, it is not at all clear that, in fact, that so-called dike does not come through as a unit that is clearly defined. (LMP, rev 65)

The CMP also confirmed that the structure in the central peak could not be studied:

I just got a real good view of Copernicus, but I am afraid I cannot help you out on that structure in the central peak. Just a little too dark. (CMP, rev 4)

I was looking at it through the binoculars last time, and I could not really see anything that was really defined as coming on through there. (CMP, rev 65)

Dark deposits both to the southeast (Copernicus CD area) and north (Montes Carpatus) were described from orbit. The relationships of these deposits to other units on the Moon have been previously discussed (ref. 28-13).

One of the things that we mapped on the southeast and south rim of Copernicus were dark-albedo areas within the ejecta. And those are apparent here very clearly. (LMP, rev 1)

And some of the dark-halo craters that we mapped originally on the north portion of the ejecta blanket, which were similar to Copernicus H, are very clearly darker halo, or have darker blankets around them than the ejecta blanket from Copernicus. (LMP, rev 65)
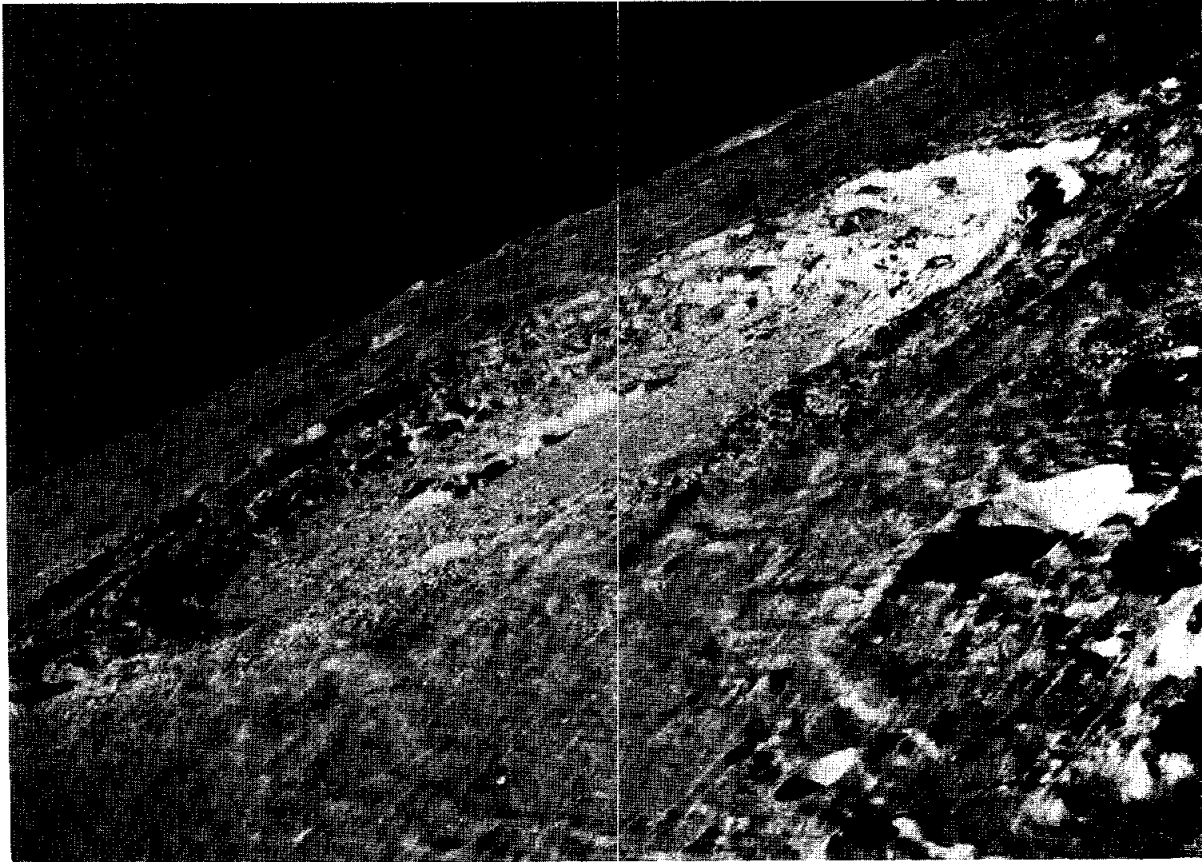
FIGURE 28-24.—Oblique view looking southward from Copernicus Crater (AS17-151-23265).

One of the questions we asked ourselves years ago, when we mapped the Copernicus area, was were we really seeing dark mantling deposits on some of the massifs of the Carpathians, and looking at it obliquely here, some of those areas that we have mapped as dark mantling are distinctly brownish gray versus the normal tan gray of most of the Carpathians. It looks like it is about the same color—extrapolating—as the dark mantle around Sulpicius and Taurus-Littrow. (LMP, rev 73)

EULER AREA

Near the end of the mission, very little time was available for observing some of the interesting features in the Euler area. Many structures believed to be volcanic occur to the south of Euler Crater (fig. 28-25), including what seems to be a main source of some of the Imbrium lava flows (ref. 28-17). There appears to be a color boundary within the walls of Euler itself as observed from orbit:

The lower part of Euler is blue gray, and the upper is a

very light gray, from the talus slope up to the rim. (LMP, rev 66)

Large boulders were observed on the central peaks of Euler. The observation was made possible by the low Sun illumination angle.

I can just start to see the peaks of Euler now. The tops of them are exposed in the sunlight, and it looks like there are massive quantities of large boulders on the peaks. (CDR, rev 66)

A chain of low-rimmed structures and collapse depressions forms a semicircle due west of Euler P (fig. 28-25). These landforms were interpreted as being extrusive, volcanic in origin:

That is my little [C] crater chain down there. Looks like a cinder cone chain. (CMP, rev 66)

As seen in figure 28-25, there are numerous sinuous rilles and arcuate depressions in the area. There appears to be intricate relationships between
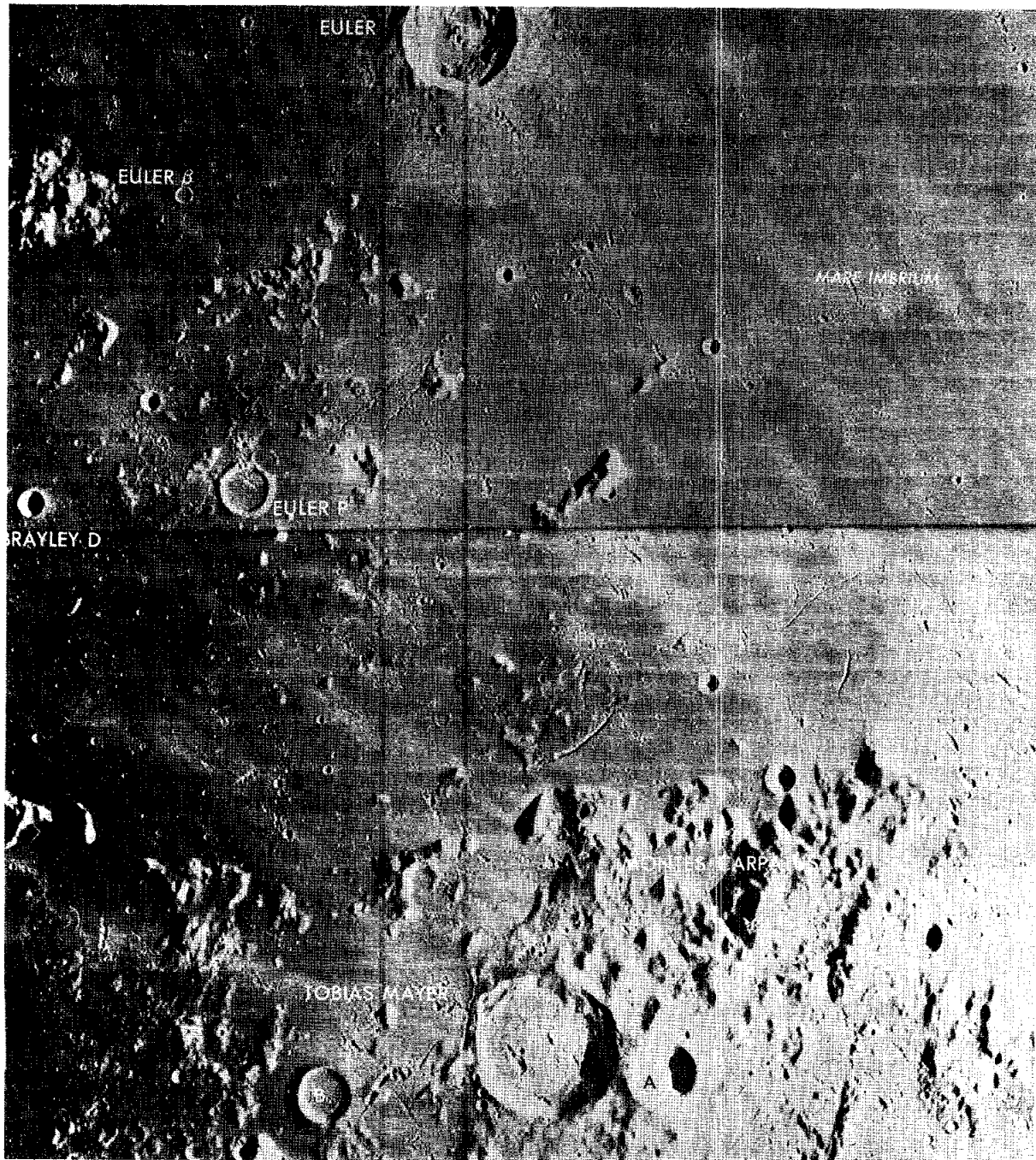
FIGURE 28-25.—Portion of Lunar Orbiter IV frame 133-H showing the southern part of Mare Imbrium, south of Euler Crater (30 km in diameter).

the rilles and the mare ridges and other scarps as described by the LMP:

I might summarize my impression of the rilles in the vicinity of Euler and their relationship to the mare ridges. I have been able, over the last day, to find rilles that clearly cross and separate portions of ridges. And ridges that clearly cross and partially bury rilles. And in another third case, a rille that appears to be leveed, that is, have flat banks on either side, but near the end of it, it transitions into a mare

ridge, very clearly. It looks as if, to me, that the rille and ridge problem in here is just one of repetitive compression and extension within the surficial flows of the Imbrium basin. And that, possibly during the compressive stages, there were extrusions locally along the ridge system; but in the main part, the ridge systems represent, I think, a doming. It looks like just a doming of the mare surface except for these local ridge-like extrusions.

I might also add that the rilles, to me, seem to be made up of zigzag straight-line segments rather than being truly sinuous. They appear sinuous because of the rounding of the corners, but my impression is that they are really made up of straight-line segments. (LMP, rev 73)

REINER γ

Reiner γ remains one of the most enigmatic structures on the Moon. It is similar in gross characteristics to the light-colored swirls discussed under the heading entitled "Al-Khwarizmi (Formerly Arabia)." However, it is only one feature with no obvious source. Even if the swirls near the eastern limb of the Moon are interpreted as unusual ray materials, the Reiner γ structure is harder to interpret because of its shape (fig. 28-26) and the complete lack of association with any impact structures. Observations from orbit during Apollo 17 added details that do not solve the problem but may add to the constraints on the theories of origin:

I am able to see some of the Reiner γ materials, and it is awful hard to say more than just the fact there is a very clear light-colored pattern off to the north of our position. (LMP, rev 1)

[The brightness of] Reiner γ from here almost looks like ejecta from a crater . . . The γ itself is dark . . . Zero phase is going right through it right now; it did not blot out the dark at all . . . The only light-colored stuff that you can see is right around Reiner γ itself. And intermixed within that is the dark. It is a dark annulus, except the annulus is on the inside of the white. And it looks like—I do not know if your eyes deceive you in this darkness or not—but the light-colored stuff is raised up with respect to the dark.

The light material around it . . . does not look like a ray. In other words, it does not thin out in different parts like a ray does. (CMP, rev 28)

I was trying to think if there was anything I could add to the Reiner γ observation. I am right over the light-albedo material that goes between Reiner and Reiner γ. It is kind of crooked; it goes for a little ways, and then it breaks off in another direction. So, it does not look like a straight ray at all.

Looking right down on Reiner now, and you sure have that dark annulus. The lighter-albedo stuff is essentially in the middle of it, is about half of the width, and it is lighter on the outside than it is on the inside.

It is very hard to see any great topographic expression to

it. The reason I say that is because it blends in with everything. (CMP, rev 36)

MISCELLANEOUS OBSERVATIONS

Flashes of Light

On the first lunar revolution, the LMP reported seeing a flash of light north of Grimaldi Crater (21:11:09 G.m.t. on Dec. 10). It is interesting to note that this is the same area where the CMP during Apollo 16 also reported seeing "a flash of bright light" (Riccioli). The following descriptions were made during Apollo 17 orbit:

Hey, I just saw a flash on the lunar surface! It was just out there north of Grimaldi. You might see if you got anything on your seismometers, although a small impact probably would give a fair amount of visible light. It was a bright little flash near the crater at the north edge of Grimaldi; the fairly sharp one to the north [small crater north of Grimaldi B] is where there was just a thin streak of light. (LMP, rev 1)

On the following day, the CMP also reported seeing a flash, this time near the rim of Mare Orientale (22:28:27 G.m.t. on Dec. 11):

Hey! You know, you will never believe it. I am right over the edge of Orientale. I just looked down and saw a light flash myself. Right at the end of the rille that is on the east of Orientale. (CMP, rev 14)

Visibility in Earthshine

The Earth disk was almost full at the beginning of the orbital period, and light reflected from the Sun by the Earth to the Moon was enough to study features on the surface but not in great detail. Following are some comments on the lighting conditions:

There is no question that right at the terminator you pick up relief that you normally would not believe is there in the mare. I remember Bill Anders talking about the appearance of a sea swell within the mare itself and that is certainly clearly shown right at the terminator. Unless you start to see the shadows from all the very small craters that otherwise do not show up as much more than just little depressions, if that. (LMP, rev 1)

Kepler ray pattern is very striking in this light; an anastomosing series or bands which only average being radial. In most cases, they are a little off radial, but by joining together, they give you a general radial pattern . . . Once again, albedo differences are very clear, such as the distinction between the wall or brighter wall materials and the rim which is brighter than the surrounding mare. (LMP, rev 1)
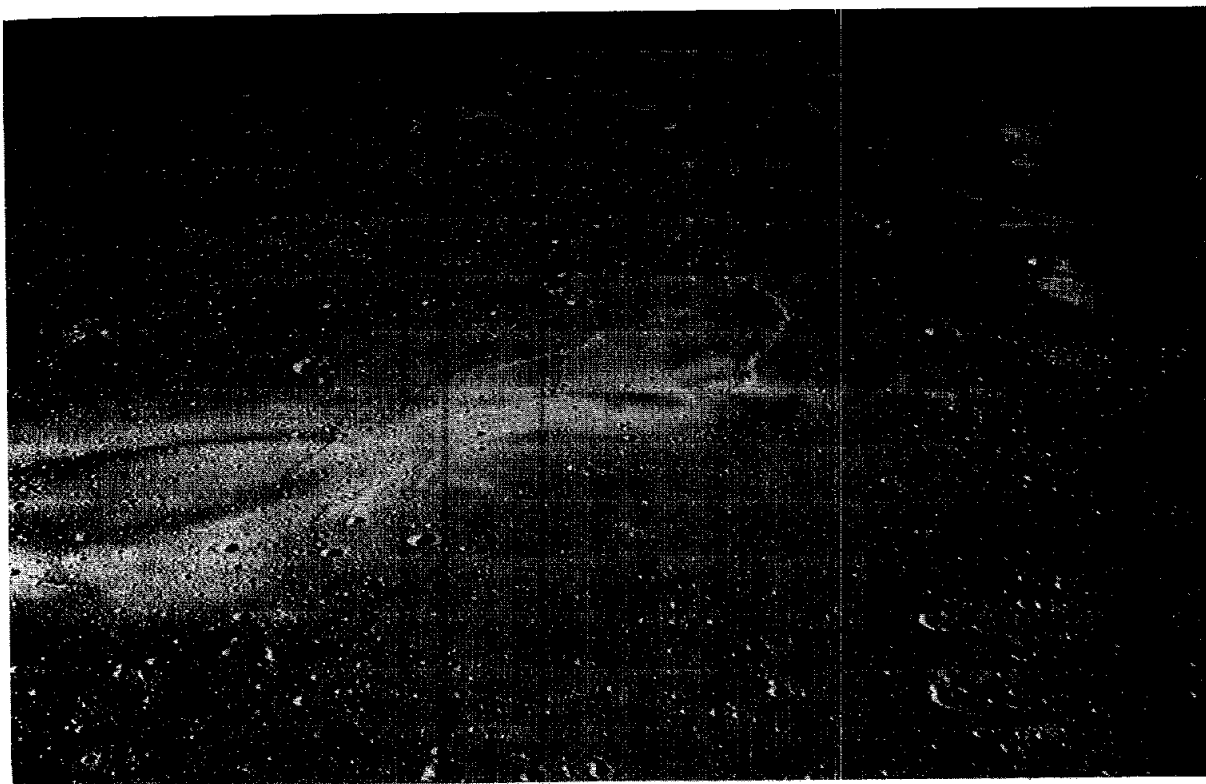
FIGURE 28-26.—North-looking Lunar Orbiter oblique view of the Reiner γ structure in western Oceanus Procellarum.

Looking at Oceanus Procellarum. And now, up to the northwest, Grimaldi is starting to show up. A very obvious dark area within the highlands of that part of the Moon, and one of the darkest mare regions that we have seen on the Moon. It is comparable, at least in the photographs, to that of Tsiolkovsky. (LMP, rev 1)

Amazing how much of the highlands to the west of Procellarum is still bright, and the contrast between fresh craters and the normal highland is very obvious still in earthlight, particularly along the zero-phase point with respect to the Earth. (LMP, rev 1)

This is a spectacular sight, you ought to take a look at Orientale. One of the largest fresh basins on the Moon. It still is probably 4 billion years old, or 3.8 at any rate, if our dating criteria are any good. It has the outer Cordillera ring and the inner ring called the Rook Mountains, very nicely shown . . . As we approach the terminator, the lighting is still excellent. Matter of fact, it appears brighter than what we were looking at over at Copernicus. Now, part of that may be we are seeing much sharper relief since the slopes, Earth-facing slopes, are nicely lit, and the backfacing slopes, of course, are in shadow. (LMP, rev 1)

You can even see a horizon in earthshine out there. (LMP, rev 1)

You sure can. You can see an earthlit horizon out there into the dark part of the Moon. (CDR, rev 1)

I noticed there is even a lot of difference in earthshine

and in the double umbra. You get in earthshine and it is hard to see the stars even if you do not have the Earth in there . . . The double umbra on the back side of the Moon is even better than the simulator! (CMP, rev 14)

Lineaments

Much discussion about small-scale lineaments on lunar slopes followed the description and photographs of the ones observed on Mons Hadley during the Apollo 15 mission. During Apollo 16, similar features were described in many regions of the Moon, on slopes as well as on flat surfaces (ref. 28-5). During Apollo 17, lineaments were observed and photographed during the surface stay time; some were also described from lunar orbit:

In a place where the Sun is just grazing the slope, it is a steep slope on the north rim of Crisium, I can see the horizontal lineaments that were such a controversy on [Apollo] 15 . . . There are some very steep slopes that just have grazing Sun on them now, and with the binoculars, you can see that horizontal lineation pattern.

Also, on that lineation question, not only where the Sun grazes a slope do you see the horizontal lineations, but they

are at the southern end of the shadowed area on a slope. You get a couple other lineations showing up at least in a couple of places I saw. One would be parallel to the slope, that is cross-contour, and the other was at an angle to that direction, say of about 30°. (LMP, rev 3)

Craters

Observations were made of various types of lunar craters. The first unplanned observation was that of Kopff Crater at latitude 17° S and longitude 90° W in Mare Orientale:

Delta-rim crater—just as has been, I think, discussed in the literature—has no obvious ejecta blanket around it, compared to other larger craters within the basin. We are directly over that crater right now. It is filled with mare, very smooth mare. Matter of fact, within that fill, I can see no craters. Getting very close to the Earth terminator, but you see good texture in the ejecta blanket of the large crater in the north part of the inner basin of Orientale. The radial ridge and valley patterns are very clear; the concentric coarse hummocks near the rim are apparent; and you can even see the patterns of secondaries. (LMP, rev 1)

Numerous craters on the far side display flat, somewhat dark floors; these floors are commonly domed in smaller craters. In larger and fresher craters (e.g., "The Bright One" in ref. 28-18), there are scarps and fronts indicative of fluid flow. During Apollo 17, the first impression of these features from orbit was that these floors were volcanic; however, the original melts were later (and after repeated observation) attributed to shock melting by impact.

Fresh, rayless craters on the far side, probably Eratosthenian in age, all appear to have a mare-type or volcanic-type floor, suggesting the possibility that a liquid mantle existed during the Eratosthenian era and was penetrated by these craters. (Paraphrased from CMP, rev 48)

I guess the feeling I was getting is that most of the [Eratosthenian] age craters all have some sort of a mound, a domical structure, down in the bottom of the crater. Even the smaller ones, some of the 30- to 50-km-size class. And the flat floors look volcanic. Some of the bigger ones, of course, are volcanic, the lava flows on the floor of these big craters. (CMP, rev 48)

While we are waiting for the site to come up again here, which seems to interest us every time we go over it, I think we sort of came to a general consensus on the problem of the smaller cone-shaped craters on the far side that have the little pool-like concentrations of material in the bottom. If you look at the freshest of those craters, there seems to be continuity between the streaks of very dark material that cover the walls and the rim of the fresh cone-shaped craters. As the crater gets older, that distinction becomes less

obvious; however, the pool remains, and all you lose is the dark streaks on the rim and on the walls of the crater. I think we sort of suspect that the pool in the bottom of the fresh craters is just the concentrated impact melt that some of which stayed there during the impact and others drained back after the impact from the walls. And then, with time, that pool may be subdued some. The structures in it, the swirls and little domes in that pool, are subdued possibly not only by the impact but by debris, slides, and avalanches off the walls of the crater. (LMP, rev 64)

Features of the large crater Archimedes (100-km diameter) were described in the context of lunar stratigraphy as seen within the Imbrium basin:

Archimedes is one of those craters that, in the early days of the lunar mapping program, helped establish some of the fundamental age relationships between the various units that were visible in the Earth-based photographs. In this particular case, it related to the sequence of events that created Imbrium and then flooded it with mare. And Archimedes is completely circular and it is filled with mare. And it, in itself, is superimposed on one of the main benches of the Imbrium basin. Now, to have mare filling of approximately the same level in the vicinity of a large mare region is one of the things that has suggested to many people that rather than single sources for mare lavas, you have a multitude of sources in a very fractured lunar crust. The ultimate source at depth, though, is still certainly a subject of controversy. (LMP, rev 62)

Unique features of the elongate Messier Crater, which is believed to be the result of an oblique impact (fig. 28-27), were described from orbit by the CDR:

It has got a very sharply raised lip, and it has got some very dark and rough rim deposits. It has also a very obvious
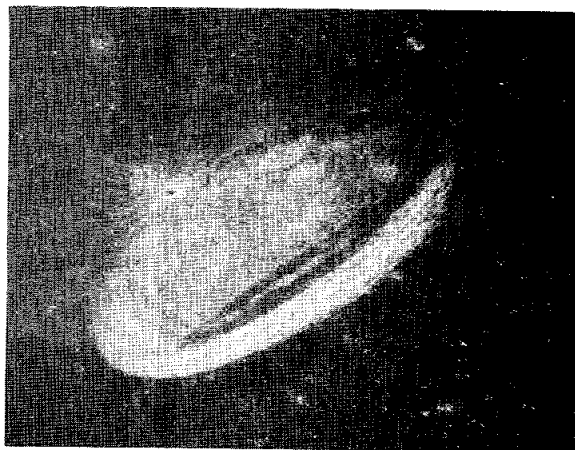
FIGURE 28-27.—Part of Apollo 15 panoramic camera frame AS15-127 showing the elongate Messier Crater in Mare Fecunditatis.

furrow, looks like it is elongated, generally to the east and west. I cannot tell, but because of the shape of it and because of those dark rim deposits, I am sure there must be a vent there somewhere, but it is too dark down in there. I cannot really see for sure whether there is one or not. But, if there is, I imagine it is pretty big. And I imagine the elongation was produced during the thrust of the initial dynamics, the formation by the impact. (CDR, rev 73)

Finally, during the post-TEI television transmission, the following statement was made by the LMP, summarizing the lunar surface history and pointing out the importance of that history to the study of the Earth:

. . . basalt flows, that some 3 to 4 billion years ago, in round numbers, were erupted on the Moon and filled many of the low areas that existed at that time. Not an awful lot has happened to the Moon since, except for the impact craters, some of the younger ones, since 3 billion years ago, which is one of the reasons it becomes so interesting to man. It is the Moon's frozen period of history that we cannot recognize very readily on Earth because of the dynamic processes of mountain building and oceans and weathering that are taking place even at the present time. Understanding that early history of the Moon may mean an understanding of the early history of the Earth. And, I think we are well on our way to a first-order understanding of that history as a result of the [Apollo] Program. (LMP, post-TEI)

REFERENCES

28-1. El-Baz, Farouk; and Worden, A. M.: Visual Observations From Lunar Orbit. Sec. 25, Part A, of the Apollo 15 Preliminary Science Report. NASA SP-289, 1972.

28-2. Worden, A. M.; and El-Baz, Farouk: Apollo 15 in Lunar Orbit: Significance of Visual Observations and Photography. The Moon, vol. 4, nos. 3/4, 1972, p. 535.

28-3. El-Baz, Farouk; Worden, A. M.; and Brand, V. D.: Apollo 15 Observations. Lunar Science—III (Rev. abs. of papers presented at the Third Lunar Science Conference (Houston, Tex.), Jan. 10-13, 1972), pp. 219-220.

28-4. El-Baz, Farouk; Worden, A. M.; and Brand, V. D.: Astronaut Observations From Lunar Orbit and Their Geologic Significance. Proceedings of the Third Lunar Science Conference, vol. 1, MIT Press (Cambridge, Mass.), 1972, pp. 85-104.

28-5. Mattingly, T. K.; El-Baz, Farouk; and Laidley, Richard A.: Observations and Impressions From Lunar Orbit. Sec.

28 of the Apollo 16 Preliminary Science Report. NASA SP-315, 1972.

28-6. Mattingly, T. K.; and El-Baz, Farouk: Impressions of the Lunar Highlands From the Apollo 16 Command Module. Lunar Science IV (Abs. of papers presented at the Fourth Lunar Science Conference (Houston, Tex.), Mar. 5-8, 1973), pp. 513-514.

28-7. Evans, R. E.; and El-Baz, Farouk: Visual Observations From Lunar Orbit on Apollo 17. Lunar Science IV (Abs. of papers presented at the Fourth Lunar Science Conference (Houston, Tex.), Mar. 5-8, 1973), pp. 231-232.

28-8. El-Baz, Farouk: Discovery of Two Lunar Features. Sec. 29, Part H, of the Apollo 16 Preliminary Science Report. NASA SP-315, 1972.

28-9. El-Baz, Farouk: Al-Khwarizmi: A New-Found Basin on the Lunar Farside. Science, vol. 180, no. 4091, June 15, 1973, pp. 1173-1176.

28-10. El-Baz, Farouk: The Alhazen to Abul Wáfa Swirl Belt: An Extensive Field of Light-Colored, Sinuous Markings. Sec. 29, Part T, of the Apollo 16 Preliminary Science Report. NASA SP-315, 1972.

28-11. El-Baz, Farouk: Light-Colored Swirls in the Lunar Maria. The Moon, vol. 4, nos. 3/4, 1972, p. 531.

28-12. Strom, R. G.: Lunar Mare Ridges, Rings and Volcanic Ring Complexes. The Moon: International Astronomical Union Symposium No. 47, 1972, pp. 187-215.

28-13. El-Baz, Farouk: The Lunar Dark Mantle: Its Distribution and Geologic Significance. Lunar Science IV (Abs. of papers presented at the Fourth Lunar Science Conference (Houston, Tex.), Mar. 5-8, 1973), pp. 217-218.

28-14. Wilhelms, D. E.; and McCauley, J. F.: Geologic Map of the Near Side of the Moon. U.S. Geol. Survey Misc. Geol. Inv. Map I-703, 1971.

28-15. Wolfe, E. W.; Freeman, V. L.; Muehlberger, W. R.; Head, J. W.; Schmitt, H. H.; and Sevier, J. R.: Apollo 17 Exploration at Taurus-Littrow. Geotimes, vol. 17, no. 11, 1972, pp. 14-18.

28-16. El-Baz, Farouk: Apollo 16 and 17 Lunar Orbital Photography. Lunar Science IV (Abs. of papers presented at the Fourth Lunar Science Conference (Houston, Tex.), Mar. 5-8, 1973), pp. 215-216.

28-17. Schaber, Gerald G.: Lava Flows in Mare Imbrium: Geologic Evaluation From Apollo Orbital Photography. Lunar Science IV (Abs. of papers presented at the Fourth Lunar Science Conference (Houston, Tex.), Mar. 5-8, 1973), pp. 653-654.

28-18. El-Baz, Farouk; and Roosa, S. A.: Significant Results From Apollo 14 Lunar Orbital Photography. Proceedings of the Third Lunar Science Conference, vol. 1, MIT Press (Cambridge, Mass.), 1972, pp. 63-83.

29. Stratigraphic Studies

Preliminary geologic interpretations have both added to and challenged previous concepts of lunar stratigraphy and processes. The Apollo 17 landing site focused interest on the mare units within and the highlands around the Serenitatis basin. The new photographs show that, contrary to premission expectations, the prominent dark annulus at the margin of the mare is older than the central lighter part (part C of sec. 30 and part A of this section). Several different mare units have been delineated on the basis of stratigraphic relations, color, albedo, and radar reflections (part A of sec. 33 and part A of this section). The dark mantle material in the vicinity of the landing site remains a complex problem; although the pyroclastic origin suggested before the mission has not been disproved, several alternative interpreta-

tions now seem plausible (part B of this section). Based on measurements of crater degradation, relative ages have been determined for several mare units in Serenitatis, Imbrium, and Vaporum. These ages are in good agreement with photogeologic interpretations and provide a reliable means of extending the delineation of individual mare units (part C of this section).

Photographs of the northeastern limb of the Moon filled a substantial gap in premission coverage, which allowed study of the previously ill-defined Crisium basin structure. As a result of this study, Crisium, formerly thought anomalous, can now be identified conclusively as a typical multi-ring impact basin; Mare Crisium is predominantly one unit of Imbrian age— older than previously thought (part D of this section).

PART A

BASALT STRATIGRAPHY OF SOUTHERN MARE SERENITATIS

K. A. Howard,[a] *M. H. Carr,*[a] *and W. R. Muehlberger*[b]

Mare Serenitatis has long been noted for its conspicuous dark border (fig. 29-1). The Apollo 17 metric photographs traverse this border in southern Mare Serenitatis and show clearly superposition relationships among the mare and mare-related stratigraphic units. These photographs, together with full-Moon photographs, albedo measurements, and color information (table 29-I), provide the basis for a revised stratigraphic framework for these presumedly basaltic rocks (figs. 29-2 and 29-3). In contrast to most previous studies, we conclude that the darker units are older than lighter ones. Similar conclusions

have been reached by Bryan and Adams (part C of sec. 30) and Boyce and Dial (part C of this section). The relatively light-colored central part of Mare Serenitatis is thought to represent the youngest basalt in the region; a very dark unit that includes the Apollo 17 landing site is one of the oldest.

HISTORY OF STRATIGRAPHIC CONCEPTS

Differences in the albedo, color, and structure of the surface of Mare Serenitatis are as pronounced as anywhere on the Moon. Mare Serenitatis has therefore been a test area for subdivision of the mare into different stratigraphic units. The dark outer ring has

[a]U.S. Geological Survey.
[b]University of Texas at Austin.

FIGURE 29-1.—Full-Moon photograph of Mare Serenitatis. Dark annulus borders mare. Exceptionally dark areas occur at southeastern (Littrow area) and southwestern (Sulpicius Gallus area) margins (U.S. Naval Observatory (Flagstaff, Ariz.) photograph 5818).

long been recognized, but numerous less conspicuous albedo boundaries also occur in the central mare and within the dark ring itself. Whitaker (refs. 29-3 and 29-4) amplified these albedo variations and probable color variations by a compositing technique; more recently, spectroscopic measurements (refs. 29-5 and 29-6) have demonstrated the reality of the color differences. Carr (ref. 29-1) divided the mare into

four albedo units and suggested that these represented different stratigraphic units—the lower the albedo, the younger the unit. This correspondence between age and albedo is now being challenged, so it is pertinent to examine briefly the rationale that lay behind that interpretation.

The inference that low albedo meant young age stemmed from two considerations: (1) from a specific

TABLE 29-I.—*Color and Albedo Data*

Stratigraphic unit	Albedo (Numbers refer to percent)			Color (Color differences are small)			
	Appearance on full-Moon photograph (fig. 29-1)	Geologic map (ref. 29-1)	Albedo map (ref. 29-2)	Orbital observations by Apollo 17 crew	Color-composite photographs (refs. 29-3 and 29-4)	Multispectral scans[a] (ref. 29-5)	Continuous-spectrum analysis (refs. 29-6 to 29-8)
Basalt near Plinius	Dark	5 to 6.1	8.5 to 9.0 minus	Bluish gray	Blue	Blue ± reddish blue	Very blue Similar to Apollo 11 site
Dark material of Littrow area	Very dark	5 to 6	7.9 to 8.5	Dark bluish gray	Blue to intermediate	Bluish red (p. 36) or blue (p. 67)	Very blue Similar to other areas of dark mantle
Sulpicius Gallus Formation	Very dark	6 to 7	7.9 to 8.5 plus	Tan-gray	Red	Red to bluish red (p. 36) or blue (p. 67)	
Basalt near Dawes	Dark	6.2 to 6.4	8.5 to 9.0		Blue	Blue	
Eastern ring basalt South and east	Dark	6.0 to 6.2	8.5 to 9.0 plus		Blue	Bluish red	Slightly blue
West central	Intermediate	6.1 to 6.2	8.5 to 9.0		Intermediate	Bluish red	Slightly bluer than south and east area
Le Monnier	Intermediate	6.0 to 6.1	9.0 to 9.6		Intermediate	Bluish red	Red
Basalt of southwest Mare Serenitatis Near Menelaus	Intermediate	6.1 to 6.2	9.0 to 9.6		Intermediate to blue	Bluish red	
Near Sulpicius Gallus Crater	Dark to intermediate	6.0 to 6.2	8.5 to 9.0		Blue	Bluish red	Blue
Near Aratus CA	Dark	6.1 to 6.2	8.5 to 9.0		Blue	Bluish red	
Basalt of Mare Serenitatis West of Bessel	Light	6.2 to 6.6	9.0 to 9.6		Blue	Very red	
Southeast Mare Serenitatis	Light	6.1 to 6.6	9.0 to 9.6	Tan-gray	Red	Red	Red

[a]Blue is T (Tranquillitatis) type; red is S (Serenitatis) type.
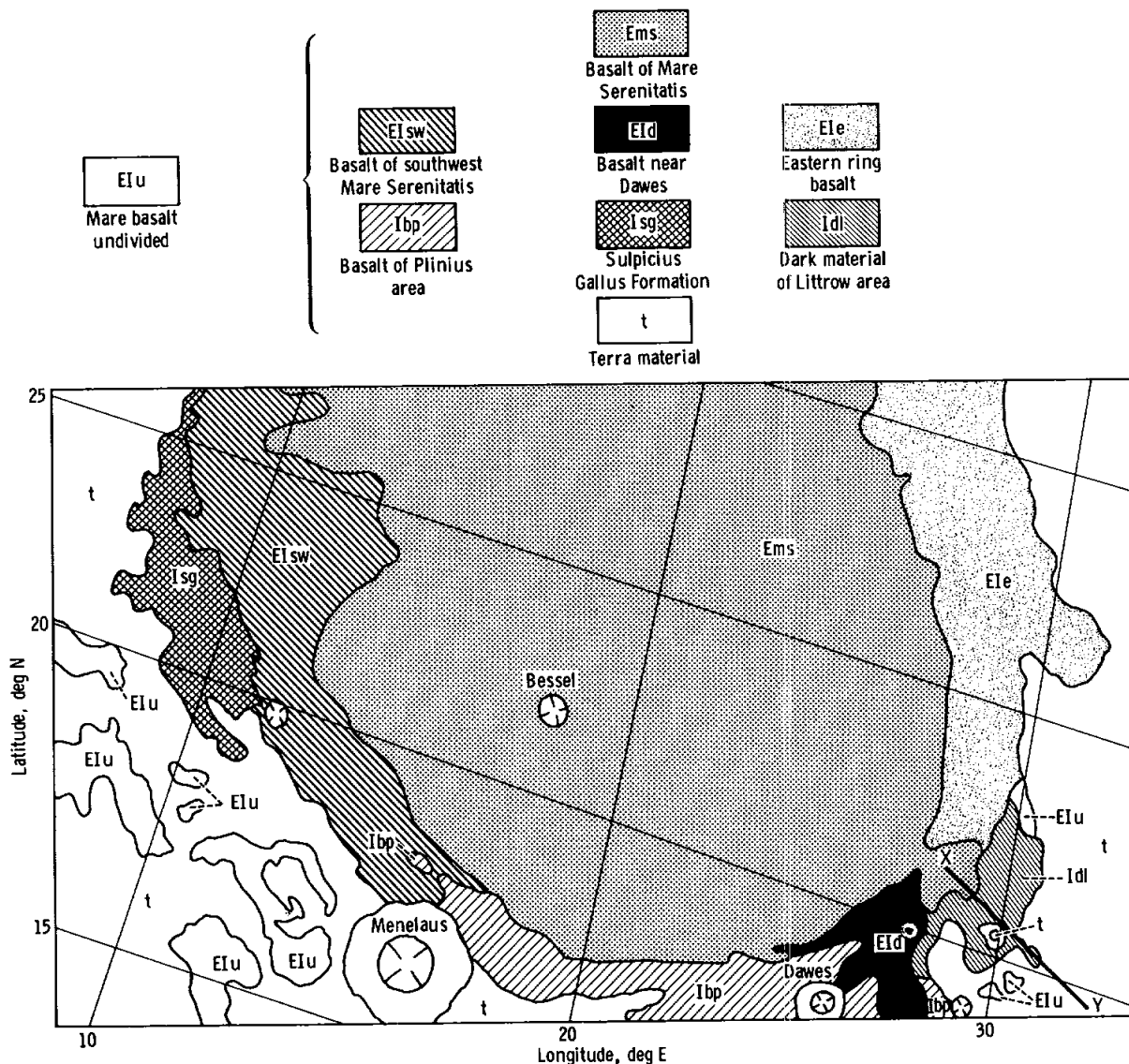
FIGURE 29-2.—Geologic sketch map of southern Mare Serenitatis at same scale as figure 29-1, showing distribution of major units discussed in this report. Line X-Y is cross section shown in figure 29-8.

model for the change in albedo with time (the "convergence model") and (2) from the number of superimposed bright-halo craters. The convergence model, never stated explicitly in print to our knowledge, assumed that there is a process of homogenization continuing on the lunar surface such that extremes of albedo converged with time upon a uniform albedo. There is considerable evidence for

this assumption on the local scale. Most young craters have bright halos, but the albedo around older is the same as that of the surroundings. Similarly, young dark craters, such as those to the southwest of Copernicus and those in Alphonsus, appear to blend more with their surroundings with increasing age; in Alphonsus, subdued elliptical craters on rilles have no dark halos whereas similarly situated fresh-appearing
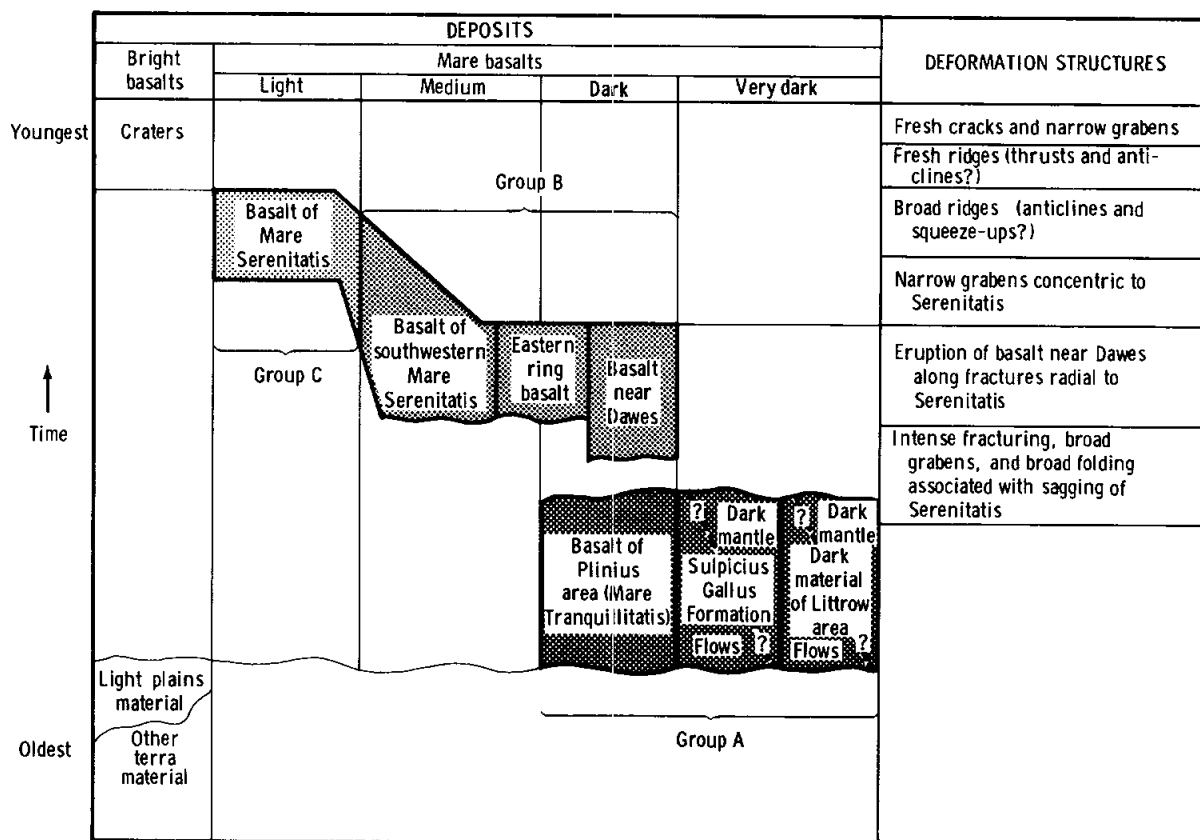
FIGURE 29-3.—Stratigraphic correlation chart of southern Mare Serenitatis.

craters have the dark halos. This observation of local convergence was thought possibly to be applicable to maria and similar-appearing but older light plains on a broader scale (refs. 29-9 to 29-11). Further, among mare units of differing albedos, there was some supporting evidence that this interpretation was correct. For example, any full-Moon photograph shows that more bright-halo craters occur within the center of Mare Serenitatis than within the outer ring, suggesting a younger age for the outer ring. However, crater counts on telescopic photographs (ref. 29-12) indicated slightly more large craters in the outer ring than in the mare center; on Lunar Orbiter IV photographs, no differences in the number of superposed craters on dark and light mare within Mare Serenitatis are apparent. Additional evidence that the low-albedo/young-age correlation was correct is the low albedo of the seemingly late Mare Imbrium flows (ref. 29-13) and mare that covers rays, as at Lichtenberg Crater (ref. 29-14), and the young age of the dark mare at the Apollo 15 landing site.

In southern Mare Serenitatis, there are a number of closely spaced grabens (the Menelaus rilles) within material having a lower albedo than the surrounding mare (figs. 29-4 and 29-5). At the western end of this dark area, one of the Menelaus rilles is in dark material for a length of approximately 40 km and terminates to the west in a low dome (Menelaus ſ) cut by the rille. These dark deposits were interpreted (refs. 29-1 and 29-15) as young volcanic flows originating from the rilles. They were thought to represent the last stage in the filling of the Mare Serenitatis basin. It will be argued in the following paragraphs, on the basis of recent Apollo photographs, that this interpretation was wrong and that the dark material north of Menelaus is the unburied portion of a faulted mare surface, older than most of the mare within Mare Serenitatis.

Also at the edge of Mare Serenitatis are two very-low-albedo nonmare areas. In the region of the Sulpicius Gallus rilles, much of the upland has an anomalous low albedo. Similar dark uplands adjacent

FIGURE 29-4.—Mosaic of Apollo 17 metric photographs across southern Mare Serenitatis. Photographs having suitably low Sun angles were selected from different orbits (Apollo 17 metric camera frames AS17-0448, 0449, 0452, 0604, 0805, and 0817).

FIGURE 29-5.—Geologic map across the mosaic strip shown in figure 29-4. Base map was compiled from Air Force Aeronautical Chart and Information Center lunar aeronautical charts. Map units are defined in figure 29-2; heavy lines indicate grabens.

to Sinus Aestuum were interpreted as a dark facies of the Imbrium ejecta by Shoemaker and Hackman (ref. 29-16). This interpretation was later rejected (refs. 29-1 and 29-15) because the dark material (1) appeared to subdue the underlying topography, (2) appeared partly to overlap the mare surface, and (3) appeared to be thin or absent locally on hills with bright summits. Furthermore, it was believed that the dark material was in some way related to the rilles (ref. 29-15), because its association with rilles is common (cf. Sulpicius Gallus, Littrow, Bode, Conon, Schröter, and Hadley rilles). Because the rilles clearly

postdated the Imbrium ejecta, it appeared likely that the dark material was also younger than the Imbrium basin. The dark unit at the Sulpicius Gallus rilles was named the Sulpicius Gallus Formation and was interpreted as a pyroclastic blanket (ref. 29-1). The upper age of the unit was uncertain because, although it appeared to overlap some mare, the unit appeared to be covered by other mare. The formation was accordingly given a broad age range (Imbrian to Eratosthenian).

Lunar Orbiter photographs showed that another dark unit in the Littrow rilles region also covers the

uplands and has similarly ambiguous relations with the adjacent mare (figs. 29-6 and 29-7). This unit is now commonly termed dark mantle. Here, as at the Sulpicius Gallus rilles, subjacent high-albedo material is exposed only on hilltops and steep slopes where creep of the near-surface materials apparently has removed the dark mantle. Around and to the north of Littrow B Crater is a plains unit that is more heavily cratered and presumably older than the mare; it also is covered with the dark mantle. The relations with the main mare to the west, however, are unclear on the Lunar Orbiter photographs. In a preliminary unpublished map of this area made using the Lunar Orbiter photographs, one of the authors (Carr) gave a very broad age range for the dark mantle (Copernican to Imbrian) because in places it appeared to cover the mare and in other places, as at the mare embayment west of Littrow BA Crater (fig. 29-4), it appeared to be covered by the mare. In the premission map of the Apollo 17 landing site (ref. 29-17), the unit was assigned a young age (Copernican), but the explanation on the map cautioned that the relations were ambiguous and that the unit might be time transgressive.
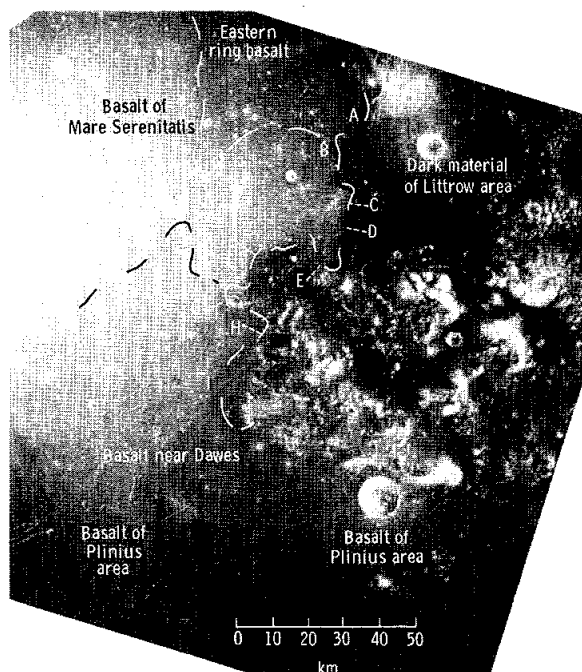
FIGURE 29-6.--High-Sun view of Littrow area taken on Apollo 15. Localities are discussed in text (Apollo 15 metric camera frame AS15-1115).

Based on Apollo 17 photographs, the mare material of southern Mare Serenitatis has been divided into several units, and the relative ages shown by superposition have been reevaluated. A brief description of the different unit follows, and the evidence on which ages have been assigned is presented.

STRATIGRAPHY

Stratigraphic Framework

In our revised stratigraphy, basalts of Mare Serenitatis fall into three broad age groups (fig. 29-3). The oldest group (A) includes three dark units that predate the inward tilting and graben faulting of the margin of Mare Serenitatis. (See section entitled "Structure.") These oldest units are the dark basalt of the Plinius area along the southern margin of the mare, the dark material of the Littrow area to the east, and the Sulpicius Gallus Formation in the west (fig. 29-2). The next youngest group (B) is dark lavas that embay the broad grabens but are somewhat faulted and tilted inward. Included in group B are a patch of basalt near Dawes, the dark basalt that forms most of the eastern sector of the dark ring, and the medium-dark basalt of southwestern Mare Serenitatis. The youngest group (C) is the light basalt that forms the central bulk of Mare Serenitatis. Albedo and color data on the various units are summarized in table 29-I. Other remote-sensing methods provide additional data on the units, as described by Thompson et al. (part A of sec. 33).

Basalt of Plinius Area

Old dark lava along the southern margin of Mare Serenitatis near Plinius appears continuous with the lavas of Mare Tranquillitatis to the south. This unit is cut by numerous broad rilles (grabens) concentric to Mare Serenitatis. Apollo 17 photographs (fig. 29-4) show that the unit forms a bench sloping inward toward Mare Serenitatis and that younger light-toned, flat-lying lava to the north laps against this slope and truncates the grabens. To the west, the old faulted lava can be traced along the Menelaus rilles (fig. 29-4), where the unit was designated the dark member of the Tacquet Formation (ref. 29-1). Here the unit is in a west-trending anticline embayed on both sides by the lighter less-faulted basalt of southwestern Mare Serenitatis (originally designated
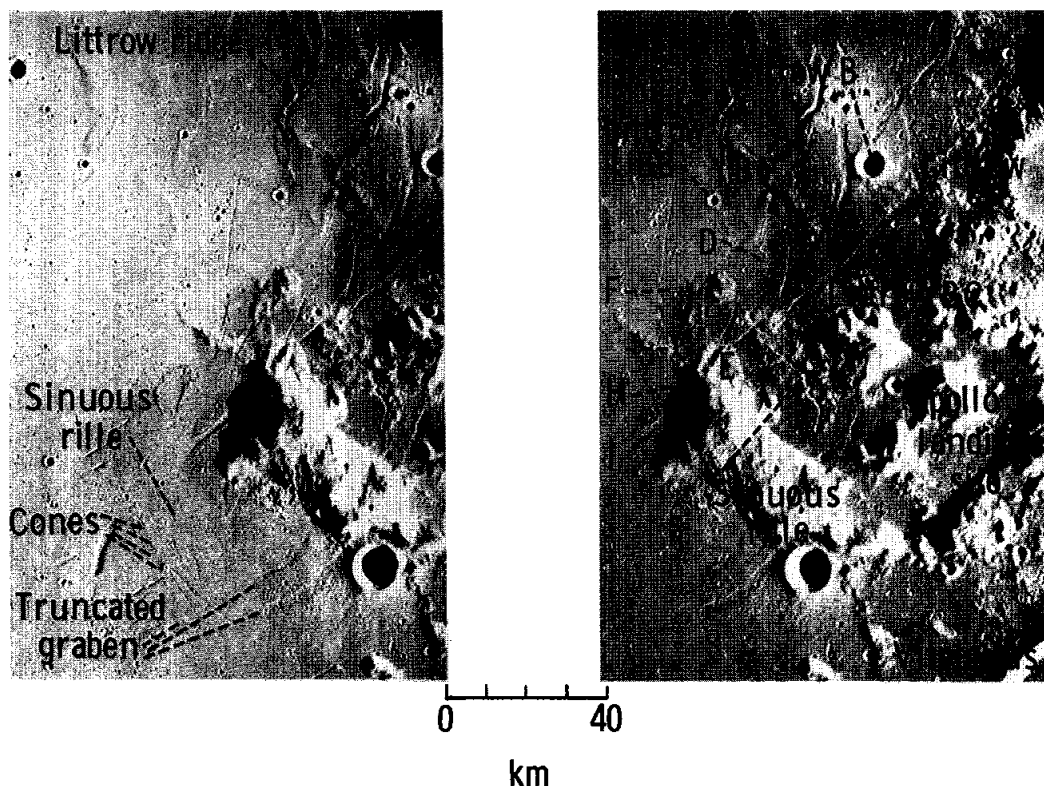
FIGURE 29-7.—Low-Sun stereoscopic view of same area shown in figure 29-6 (Apollo 17 metric camera frames AS17-0447 and 0449).

as the light member of the Tacquet Formation (ref. 29-1)). Perhaps the clearest example of superposition by younger units is at Menelaus ζ, where younger lava surrounds an inlier of the old faulted basalt and covers a broad rille that bisects the inlier. Like most of Mare Tranquillitatis, including the Apollo 11 landing site, the Plinius basalt is relatively blue in color, indicative of high titanium and iron (refs. 29-5 to 29-7 and part A of sec. 33). Its probable continuity with Apollo 11 basalt (ref. 29-18) suggests the Plinius basalt is Imbrian in age.

Dark Material of Littrow Area

Dark material of the Littrow area, including the Apollo 17 landing site, is here concluded to be old also. This very dark material includes both mare flows and a dark mantle, possibly of ash or cinders, that covers some adjacent hills. Most previous studies interpreted the dark mantle as younger than Mare Serenitatis (refs. 29-17 and 29-19 to 29-22), so the evidence for an old age for the unit will be examined here in some detail.

The premare age is based on physical superposition relations of younger mare against an irregular topographic surface of this dark material at numerous places. The western boundary of the dark material as seen at a high Sun angle (fig. 29-6) can be compared with topography viewed stereoscopically in figure 29-7. From points A to C in these photographs, the dark material is on hills and is terminated abruptly at the base of the hills by lighter mare rocks to the west (eastern ring basalt and basalt of Mare Serenitatis). From points C to D, stereoscopic viewing shows an inflection where light, relatively flat-lying mare material laps eastward against a gently west-sloping surface of the dark material of Littrow rilles. At point D, a southwest-trending rille is terminated abruptly by lighter mare at the albedo contact, then emerges again at point E. A short section of this rille exposed in the light mare between points D and E is subdued and may be slightly buried (ref. 29-17). At inflections at points G, H, and I, younger mare again laps eastward against sloping dark material, and, at point I, the mare truncates another rille in the dark material. Only at point F does the albedo boundary

of the dark material fail to coincide with an obvious topographic break; probably the dark material of the Littrow rilles was flat-lying here when the younger lavas were emplaced. Although some of our colleagues suggest alternative interpretations consistent with a young age of the dark mantle (sec. 6 of this report and part B of this section), the superposition relations strongly indicate to us that the dark material of Littrow predates younger mare materials to the west. Bright craters are conspicuously rare in the dark material compared to adjacent mare, which has been one reason for assigning a young age to the dark material (ref. 29-17). Some craters may, however, be dark when initially formed because the impact material is rich in opaque minerals; the apparent low frequency of craters (ref. 29-17) may result from their lower visibility in the dark material as compared with their appearance in typical mare. A high proportion of subdued craters relative to fresh ones in the dark material can be explained by rapid destruction of small craters where the surface is irregular or by poor cohesion of near-surface material.

The dark mantle part of the unit is most conspicuous in an area between Littrow B Crater and Littrow BC Crater to the southeast, where the low-albedo area includes hills higher than 500 m (fig. 29-7). Similarly, a heavily cratered plains unit to the north appears similar to Cayley Formation except for its low albedo, which suggests a dark mantle. The steepest slopes in the dark hills tend to be bright as if the mantle has sloughed off. The dark gentler slopes have no prominent albedo boundaries with dark mare-like plains to the south. These plains are warped and cut by broad grabens (Littrow rilles) concentric to Mare Serenitatis. Whether these plains, cut by the Littrow rilles, are all covered by dark mantle or whether they are formed by dark flows is uncertain. The dark mantle and the flows may have been deposited together in one series of eruptions, and they may be similar in albedo because of similar compositions. Alternatively, the dark mantle may cover most of the flows. This latter possibility is suggested by the apparently uniform albedo across flows and hills, a subdued appearance of craters and rilles in the area, an apparently low frequency of small craters (ref. 29-17), and a spectral response (ref. 29-8) that is like other areas of dark mantle but unlike most maria. The Apollo 17 landing site appears crisper and brighter on a full-Moon photograph than the rest of the dark unit at Littrow; possibly the lava

plains here are not covered by dark mantle. A likely source for the lava in this region is a rimless pit crater in a perched lava pool at point J (fig. 29-7). North of this pit crater, a sinuous rille leads northwestward down from the perched pool over partly darkened hills to a lower level of lava near point E. The rille is interpreted as a lava channel that formed where lava spilled northwestward; lava may also have flowed northeastward from the pool toward the Apollo 17 landing site.

The dark material of Littrow has a blue hue similar to the Plinius basalt and the rest of Mare Tranquillitatis (ref. 29-8). This material also has a high reflectance near 1 μm wavelength that is consistent with a glassy surface or ash (ref. 29-8). A preliminary age of 3.8 billion years on basalt from the Apollo 17 landing site was reported at the Fourth Lunar Science Conference (March 1973); this age suggests that the flows in this unit are even older than Apollo 11 basalt.

Sulpicious Gallus Formation

The Sulpicius Gallus Formation at its type locality is composed of very dark material around the Sulpicius Gallus rilles (ref. 29-1). It covers mountainous regions as a dark mantle and locally either covers or includes flat-surfaced mare flows (fig. 29-4). The flows form a dark bench that is faulted and against which abuts younger, less-dark basalt of southwestern Mare Serenitatis (fig. 29-4). As in the case of the dark material of Littrow, it is unclear whether the old faulted flows are covered by dark mantle or are themselves exposed but of the same low albedo. The color of the Sulpicius Gallus Formation is not well known but appears to be reddish compared to the rest of the dark annulus of Mare Serenitatis (table 29-I). If so, it is different from several other areas of dark mantle to the southwest that are similar spectrally to the Littrow rilles area (ref. 29-8).

Basalt Near Dawes

A patch of basalt northeast of Dawes, similar in albedo and color to the basalt of the Plinius area, embays several broad grabens in the Plinius basalts and in dark Littrow material (fig. 29-7). Its contacts with the more faulted Plinius basalts are commonly indistinct. The unit is itself cut by a deep depression shaped like a tongue depressor and by narrow rilles and crater chains concentric and radial to Mare

Serenitatis. The Dawes basalt is therefore older than the relatively unfractured light basalt of Mare Serenitatis. Narrow fissures formed radial to Mare Serenitatis while the basalt near Dawes erupted, as indicated by the alinements of four volcanic cones along these fissures (fig. 29-7 and parts B and C of sec. 30). The northern cone is breached northwestward, which together with a north-northwest-trending sinuous rille suggests the lava flowed downhill toward Mare Serenitatis.

Eastern Ring Basalt

Also younger than the dark Littrow materials is the mare that forms the dark border of Mare Serenitatis northward from the Littrow rilles area (fig. 29-6). This unit is referred to here as eastern ring basalt because it forms much of the eastern part of the dark ring of Mare Serenitatis. It appears to be redder than the dark basalt near Dawes or the basalt of the Plinius area, according to Soderblom's data (ref. 29-5), and includes at least three subunits as suggested by albedo and color (table 29-I). Contacts with lighter mare of Mare Serenitatis have no discernible topographic expression but are indicated by albedo only. An age older than the basalt of central Mare Serenitatis is suggested by (1) the presence of a few grabens and cracks and (2) the annular arrangement that is analogous to that of tilted old basalts along the southern border of Mare Serenitatis. Superposition relations are not clear cut, however. Based on their crater-degradation model, Soderblom and Lebofsky (ref. 29-23) obtained a relative age on this unit that is comparable to the Apollo 12 and 15 landing sites or near the Imbrian-Eratosthenian boundary (refs. 29-18 and 29-24).

Basalt of Southwestern Mare Serenitatis

Sparsely fractured medium-dark lavas in southwestern Mare Serenitatis embay the Sulpicius Gallus Formation and the basalts of the Plinius area. Locally, at very low Sun angles, a topographic inflection can be seen at the inner border of this unit against lighter basalt of Mare Serenitatis, but elsewhere this contact is indistinct. Besides being darker, the unit is slightly bluer than the basalt of Mare Serenitatis (ref. 29-5 and table 29-I). Several subunits appear to be present. Possibly the oldest one surrounds the basalt of Plinius in the Menelaus rille area

and was originally designated the light member of the Tacquet Formation (ref. 29-1). Another forms a slightly darker patch around the V-shaped crater Aratus CA, a probable vent at latitude 24° N (part A of sec. 30). Soderblom and Lebofsky (ref. 29-23) report a relative age on this unit near Sulpicius Gallus Crater close to the age of the eastern ring basalt.

Basalt of Mare Serenitatis

Light red basalt forms the central part of Mare Serenitatis. It appears to postdate all other units described and has slight areal variations in albedo (ref. 29-1) and spectral response (ref. 29-6). A large area west of Bessel appears to have anomalous color (table 29-I). In general, however, the unit appears nearly uniform in albedo and color over a large area, particularly in the southeastern part of the mare. The Mare Serenitatis basalt possibly may cover part of the secondary-crater field of the Eratosthenian (ref. 29-1) crater Plinius.[1] This coverage would indicate an Eratosthenian age for the basalt. To us, the photogeologic evidence for this relation is not completely convincing.

STRUCTURE

Structures in the basaltic rocks show that the Serenitatis basin sagged inward as the lavas were emplaced. The oldest basalts are tilted or stepped down toward Mare Serenitatis and cut by broad grabens concentric with the mare basin. Some of the grabens extend into highlands so the faults are not restricted to the basalt fill but are deep seated. The faults presumedly were caused by extension inward toward the sagging basin. The amount of extension can be estimated for the Littrow rilles using a topographic map. Average vertical displacements vary from approximately 5 to 40 m for seven grabens in a 37-km traverse across the Littrow rilles near latitude 21° N. Assuming normal faults with 60 degree dips, these grabens represent approximately 100-m horizontal extension or approximately 0.25 percent. How far this strain extends basinward under younger lavas is unknown.

Topographic maps in the Littrow area also show dip slopes of approximately 1 degree on many of the mare and plains patches (fig. 29-8). These dips suggest that a broad anticlinal crest concentric with Mare

---

[1] Personal communication, B. K. Lucchitta.
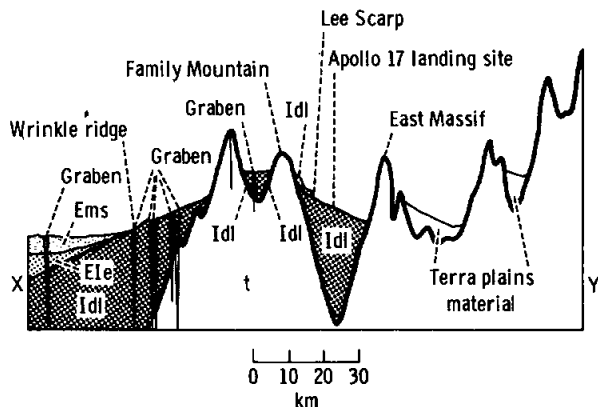
FIGURE 29-8.—Cross section from Mare Serenitatis through the Apollo 17 landing site; 25X vertical exaggeration. Line X to Y section shown in figure 29-2. Broad anticline in oldest basalts is concentric to Mare Serenitatis. Map units are defined in figure 29-2.

FIGURE 29-9.—Small fresh fissures or cracks in mare basalt just west of locality B in figure 29-7. Area shown is 3 by 3 km (Apollo 17 panoramic camera frame AS17-2313).

Serenitatis passes just west of the Apollo 17 landing site. A smaller concentric anticline in old basalts along the Menelaus rilles (fig. 29-4) has been mentioned previously.

The sagging was mostly, but not entirely, completed when the basalts of intermediate age were emplaced. Thus, the Dawes basalt appears to have run down the inclined surface toward Mare Serenitatis but was, in turn, faulted by continued extension. Some of the resulting new grabens northeast and north of Dawes (fig. 29-7) merge with chains of circular and elongate craters. These craters may be vents or may have formed by collapse into deep narrow fissures. The deep tongue-depressor trough (fig. 29-7) suggests lava withdrawal from beneath a solidified lava crust but appears even deeper than the thickness of the Dawes basalt, which it cuts. The Dawes basalt and adjacent older rocks are cut also by narrow fissures radial to Mare Serenitatis. The radially fissured area is in a local saddle in the sagged rim of Mare Serenitatis. Cone-shaped vents (fig. 29-7) suggest the Dawes basalt was erupted from these radial fissures.

Narrow cracks and grabens concentric with Mare Serenitatis formed in the eastern ring basalt and perhaps the basalt of southwestern Mare Serenitatis. These may also have been associated with the continued sagging of the mare. A single conspicuous rille in the young basalt of Mare Serenitatis southwest of Littrow BB Crater (fig. 29-7) probably formed after sagging had ended, for the basalt of Mare

Serenitatis does not appear to be sagged on photographs or laser altimetry (ref. 29-25). However, small cracks and grabens apparently continued to form locally in the basalts for a considerable time because the cracks are very fresh and sharp (fig. 29-9) and probably are younger than much of the regolith. Some tiny grabens cut the Apollo 17 bright mantle unit of upper Copernican age (sec. 6).

Mare ridges (or "wrinkle ridges") in Mare Serenitatis postdate the mare flooding. Evidence is presented by Howard and Muehlberger (part C of sec. 31) that some of these ridges are compressional anticlines and thrust faults. Other ridges may be squeeze-ups as suggested by Hodges (part B of sec. 31).

An inner system of ridges forms a nearly complete circle mainly within the basalt of Mare Serenitatis, and a few radial ridges extend outward into older basalts like spokes from this circle (ref. 29-26). Where these radial ridges cross into older basalt in the Plinius rilles (fig. 29-4), they become more subdued. There is apparent fault displacement along two parallel ridges 50 km north of Sulpicius Gallus Crater (fig. 29-4). Stereoscopic viewing shows that the area between these two ridges is depressed as a flat-bottomed graben. The ridge-bounded graben crosses the albedo contact between basalt of Mare Serenitatis and darker basalt of southwestern Mare Serenitatis, so the deformation
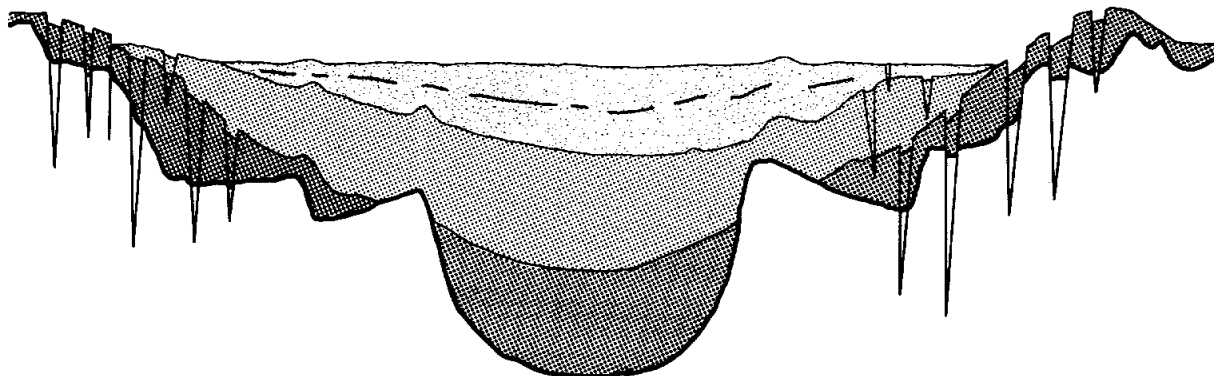
FIGURE 29-10.—Schematic cross section of Mare Serenitatis (greatly exaggerated vertical scale). Map units are defined in figure 29-2.

postdates both lavas. Elsewhere, too, the ridges postdate consolidation of the mare lavas (part C of sec. 31).

The early sagging of Mare Serenitatis was accompanied by extension faulting as the outer part of the basin sagged inward. Similar zones of extension faults rim natural and manmade sag structures on Earth and are accompanied by inward compression zones (refs. 29-27 to 29-30). Before lunar spacecraft missions, Baldwin (ref. 29-31) suggested that the mare ridges of Mare Serenitatis represent the corresponding compressional structures. Adding to the appeal of this possibility is a striking similarity of the mare ridges to sinuous thrusts in the compressional zone of a sagged Hawaiian lava lake that was described by Swanson and Peterson (ref. 29-30). The stratigraphic and structural sequence described in the present report, however, argues that the mare ridges are much younger than the graben rilles. Most ridges postdate solidification of the youngest basalt, which appears not to be appreciably sagged.

In its early history, Mare Serenitatis subsided as it filled with lava. This may have been the result of partial isostatic compensation due to the weight of the lava (ref. 29-31). Compensation was not complete, for Mare Serenitatis has a marked positive free-air gravity anomaly (ref. 29-32). Possibly the concentric rim anticlines reflect material that was

displaced outward isostatically. The Hawaiian volcanoes, which similarly are not completely compensated (e.g., ref. 29-33), cause a crustal sag by their weight that is also surrounded by an anticline resulting from subsurface outward displacement (ref. 29-34).

SUMMARY AND CONCLUSIONS

The major features of the stratigraphic and structural sequence can be summarized in a schematic cross section across Mare Serenitatis (fig. 29-10). The dark oldest basalts include flows coextensive with Mare Tranquillitatis and also flows and pyroclastic deposits (dark mantles) that erupted from the edge of the Serenitatis basin. The basin sagged, possibly isostatically, as basalts of intermediate age were emplaced. Sagging had nearly ceased by the time the youngest flows were deposited. Compressive movements including thrusting followed, and small extensional fissures formed in late Copernican time.

The revised stratigraphic sequence that we have elaborated has implications for lunar stratigraphy that transcend the boundaries of Mare Serenitatis. Dark mantle deposits and the darkest maria have commonly been assumed in geologic mapping to be relatively youthful (e.g., ref. 29-35). These assumptions must now be reevaluated and perhaps discarded.

PART B

GEOLOGIC SETTING OF THE DARK MANTLING MATERIAL IN THE TAURUS-LITTROW REGION OF THE MOON

B. K. Lucchitta[a]

A dark-colored surficial deposit covers lowlands and highlands along the southeastern margin of the Serenitatis basin. Sampling of this material was a major exploration objective of the Apollo 17 mission. Since completion of the mission, the dark mantle has

[a]U.S. Geological Survey.

been the subject of considerable controversy, inasmuch as no obvious stratified deposit was found in the landing area. Yet the material can clearly be seen in the vicinity on orbital photographs, and it is distinctly darker than all the dark mare surrounding the Serenitatis basin (fig. 29-11). Furthermore, the geologic setting as shown by Apollo 15 and 17
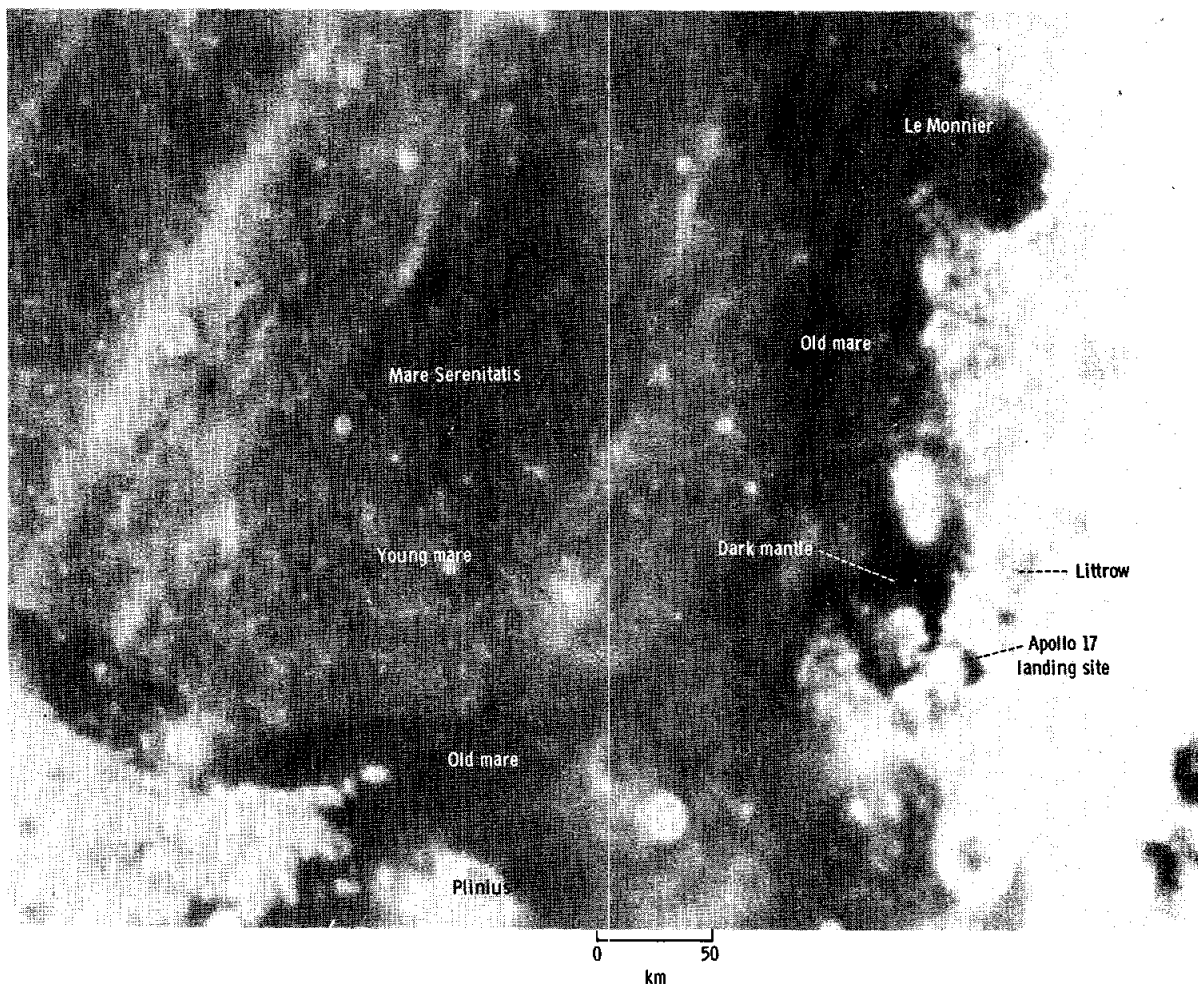
FIGURE 29-11.—Dark old mare surrounding light young mare in Serenitatis basin center, and dark mantle in vicinity of Apollo 17 landing site (U.S. Naval Observatory (Flagstaff, Ariz.) full-Moon photograph 5819).

panoramic photographs shows critical relations that must be accounted for in future interpretations.

GENERAL CHARACTERISTICS

The dark mantle covers older, dark mare material on a bench at the edge of the Serenitatis basin (fig. 29-12). Within the mountains rimming the basin, the dark deposit appears to be localized in depressions between massifs and hills and, in most places, wedges out against low hills and the base of steep slopes. However, dark mantling also occurs locally in patches or streaks on the slopes. In places, the material overlies pre-Imbrian massifs; Imbrian mare; Imbrian grabens; Imbrian, Eratosthenian, and early- and middle-Copernican craters; and fresh-looking scarps
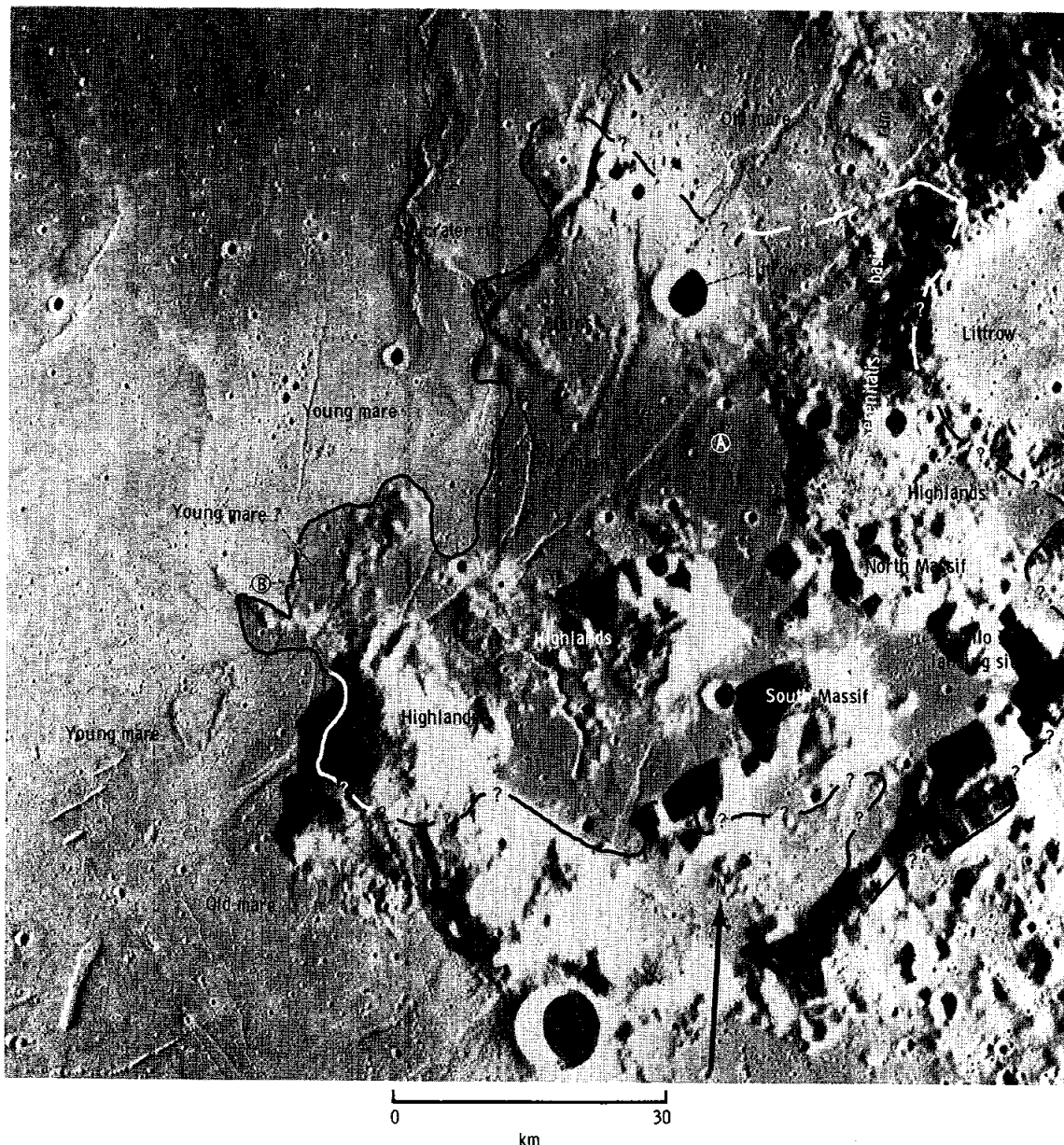
FIGURE 29-12.—Dark material mantles plains, mare, and highland material. Inside boundary of area A is the approximate area of dark mantle cover; in area B, dark mantle extends over apparently young mare (Apollo 17 metric camera frame AS17-0447).
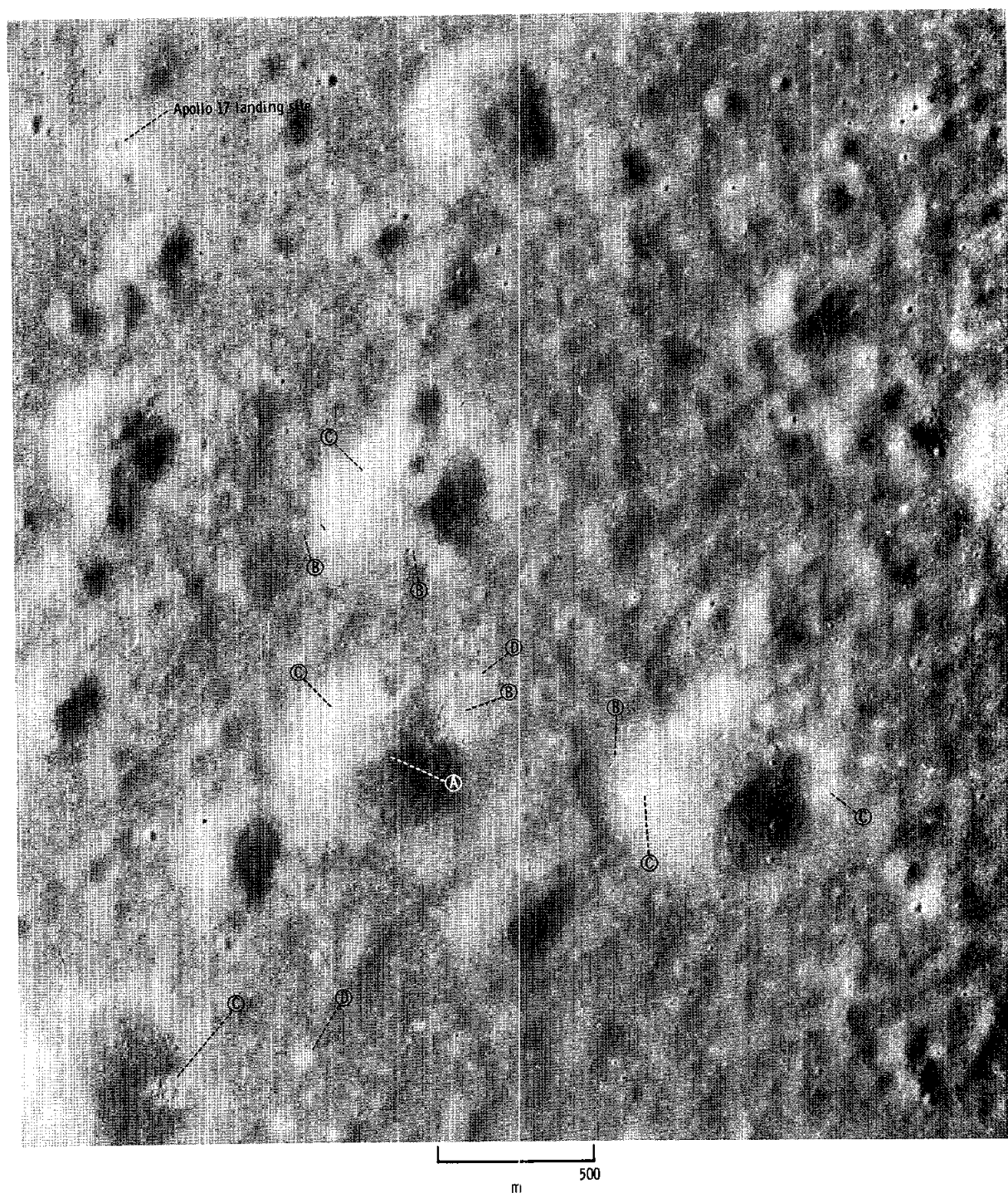
FIGURE 29-13.—Crater cluster of middle-Copernican age, covered by dark mantling material. Edge of dark patch on crater (area A) cuts sharply across irregular topography. Dark mantle is relatively thin, as indicated by protruding blocks (area B), exposures of valley floor material in crater walls (area C), and bright ejecta of very small craters (area D) (Apollo 17 panoramic camera frame AS17-2755).
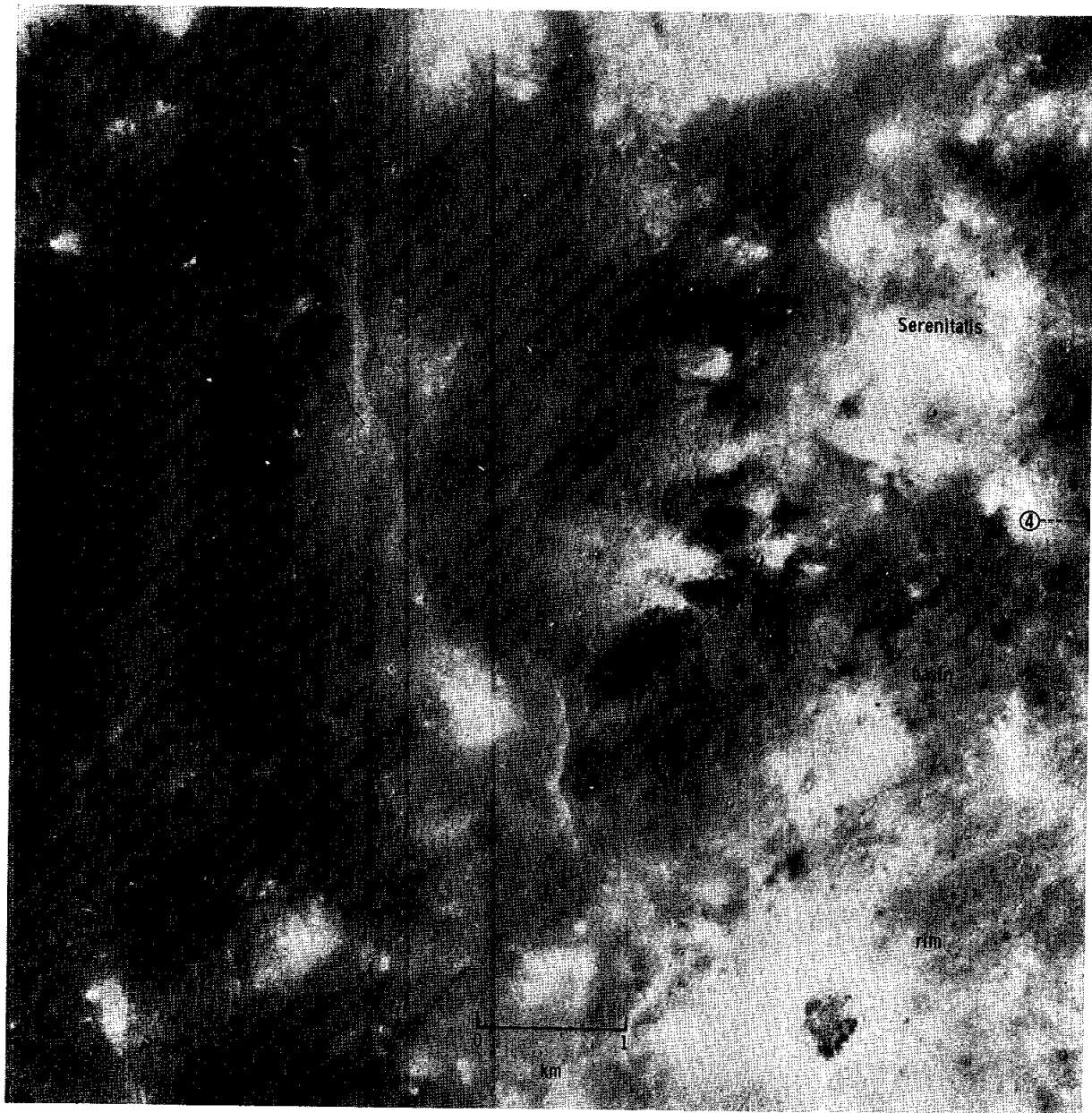
FIGURE 29-14.—Thick dark mantle at rim of Serenitatis basin. (1) Old graben covered by mantle; (2) apparently young scarp covered by mantle; (3) cluster of very small bright-haloed craters on scarp, indicating thin dark mantle; (4) dark-rayed crater in highland material; (5) very dark patches in highlands, locally on steep slopes. (a) Area under high-Sun illumination. Precipitous slope with mass-wasting lobes of light and dark material is indicated to the left of dashed line; to the right of dashed line, moderately dark mantle overlies undulating highland surface (Apollo 17 panoramic camera frame AS17-2757). (b) Same area as part (a) under low-Sun illumination. Note relief features evident in this illumination (Apollo 17 panoramic camera frame AS17-2314).

and mare ridges (refs. 29-17 and 29-21). The dark deposit is overlain only by ejecta from young craters (late Copernican) and bright avalanche material.

The dark mantle subdues the underlying topogra-

phy and, in places, occurs as irregular overlapping patches locally with straight margins (fig. 29-13); elsewhere, it occurs as halos around craters. Its appearance is smooth and velvety, and no blocks are
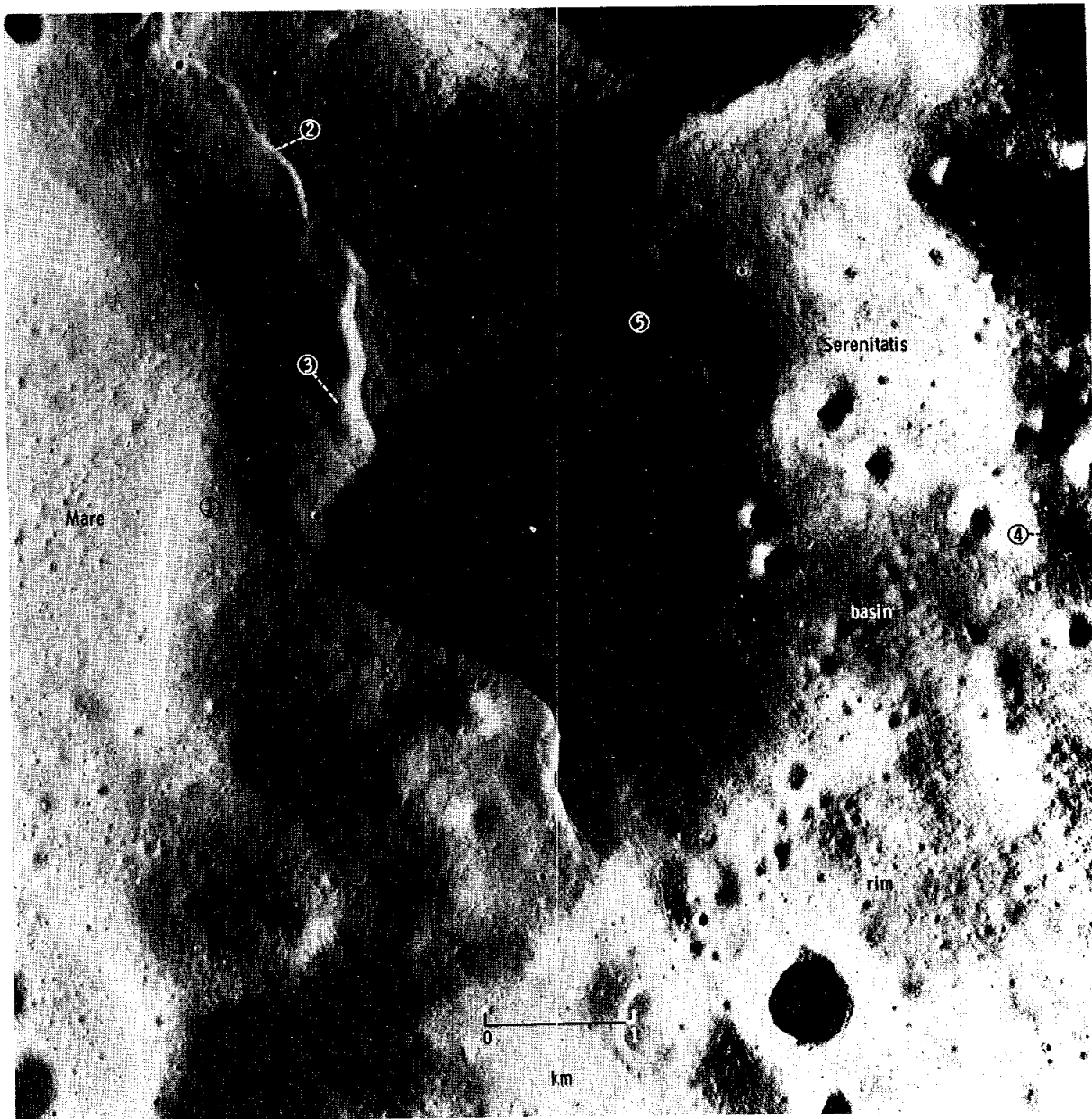
visible on photographs with 2-m resolution. Surface observations of the Apollo 17 crew substantiate a fine texture, similar to regolith, in the landing area (ref. 29-36). The albedo was determined by Pohn and Wildey (ref. 29-2) to be approximately 8 percent. In the lowlands, darker areas seem to be associated with a higher degree of smoothing of buried craters, suggesting that the mantle darkens with increasing thickness. Thickness probably varies from less than a meter to no more than a few tens of meters, as inferred from the size of craters covered but not totally obscured by the dark mantle and from the size and color of ejecta of superposed craters; craters penetrating the mantle have bright or light-colored ejecta aprons. Observations of the Apollo 17 crew indicate that in the landing area the dark mantle may measure only a few centimeters, but returned regolith samples so far have not substantiated a distinct dark surface layer. The presence of abundant dark glass spheres (sec. 7) is the only evidence so far that is possibly indicative of an unusual deposit in the traverse region.

SPECIAL RELATIONSHIPS

The dark mantle seems especially thick and dark at the rim of the Serenitatis basin, where it covers old grabens and fresh-looking scarps and extends continuously from mare onto highlands material (fig. 29-14). The western contact between dark mantle and mare material in one place (fig. 29-15) coincides with the contact between mare and an old crater that has the appearance of being excavated from plains material, covered by dark mantling material, and flooded by mare. This sequence would suggest that the dark mantle is older than mare material in this area. However, careful inspection of the contact shows that several small patches of dark material extend out over the mare material, suggesting that the dark mantle may be younger than the mare. This age relationship, however, is not demonstrated conclusively because the dark patches could be reworked material that has been mass wasted from adjacent slopes.
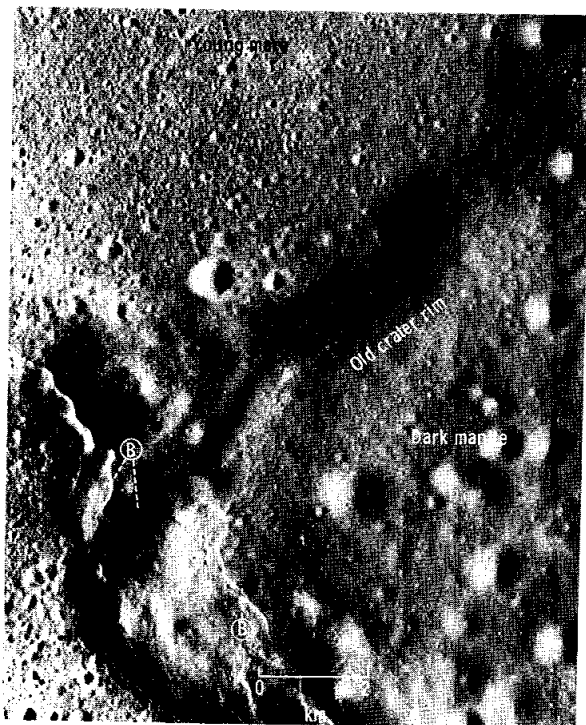
FIGURE 29-15.—Contact between old crater rim and mare; rim apparently was covered by dark mantling material and later flooded by mare. Note possible mantling on mare material below old crater rim in area A and lobate scarps that could be flow lobes in area B (Apollo 17 panoramic camera frame AS17-2313).

Farther south, the dark mantle extends out over mare terrain. The dark mantle is here underlain by older dark mare, and the boundary of the mantle seems to coincide with the boundary between older and younger mare (fig. 29-16). This relationship suggests that the dark mantle in this area is intermediate in age between the two mare materials. However, farther southwest, it seems to extend out over the young mare (figs. 29-12 and 29-17).

On the floor of the graben-like valley of the landing area, the dark mantle is lighter in color than at the margin of the Serenitatis basin. The lighter color indicates either that the mantle may be older and lightened by mixing with highland material or that the mantle is thinner (fig. 29-18). In turn, the dark mantle is partially overlain by a bright mantle extending northward across the floor of the landing site valley.

Southeast of the landing site, a crater cluster of probably middle-Copernican age is covered by dark mantle, the thinness of which is indicated by protruding blocks, exposures of valley subfloor material in crater walls, and bright ejecta of very small craters (fig. 29-13). The thinning may have been caused by mass wasting of the elevated crater rims or may indicate an originally thinner cover in this area. Farther east, toward the center of the valley, a darker tone and smoother topography suggest blanketing by thicker deposits (fig. 29-12).

In the highlands, there are two distinct types of dark mantling material:

1. Moderately dark material that has diffuse margins and generally is concentrated in depressions, in valleys, and locally at the base of massifs (fig. 29-18). This moderately dark material also occurs in gullies trending directly downhill and on subhorizontal benches and ledges that interrupt slopes (fig. 29-19).

2. Very dark-colored patches, lobes, and streaks on steep slopes, in places associated with craters; these are conspicuous on top of the North Massif northwest of the landing site (fig. 29-20). This material generally has a velvety surface appearance; however, in places it shows very sharp small pits, craters, and scarplets. Its fresh appearance and its position on steep slopes suggest that it is young material.

Two exposures in the highlands north of the Littrow valley show that locally the moderately dark mantle is underlain by very dark mantle. One exposure is in the walls of a young crater that

FIGURE 29-16.—Dashed line shows contact between young mare devoid of dark mantle and old mare covered by dark mantle. Mare ridge (1) locally coincides with contact for some distance (2) and appears to be covered where it extends into dark mantle area (3). Note lobate fresh structures that could be flows, covered by dark mantle (4) and fresh-looking structure possibly younger than the mantle (5) (Apollo 17 panoramic camera frame AS17-2313).
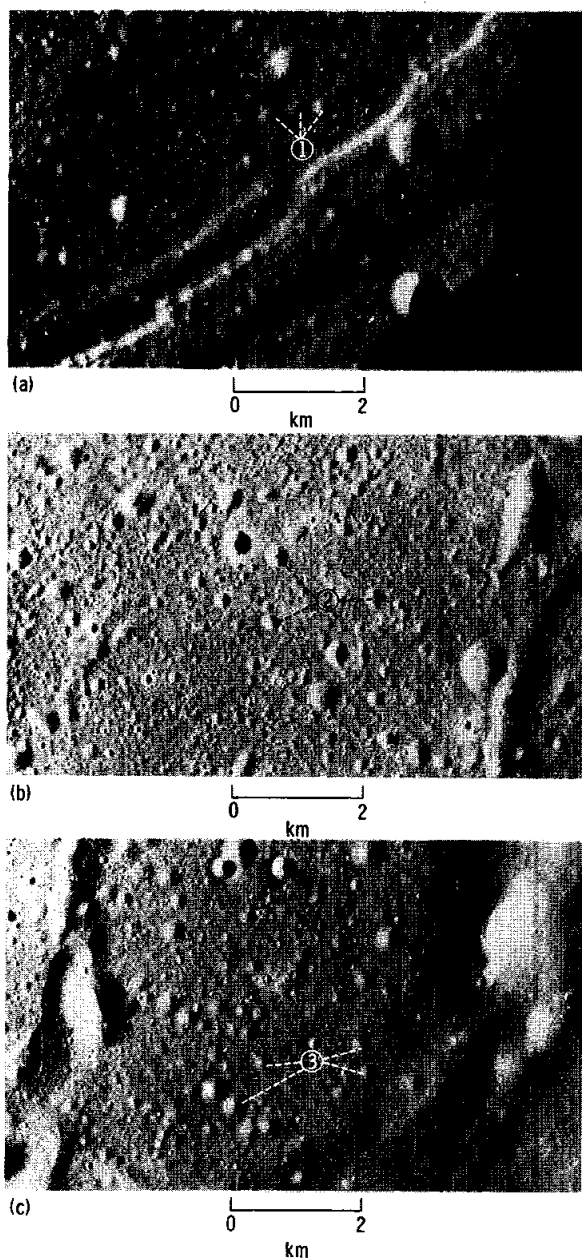
FIGURE 29-17.—Dark mantling produces varying effects on three types of terrain (Apollo 17 panoramic camera frame AS17-2320). (a) Old dark mare surface; most old craters are shallow bowl-shaped depressions (1). (b) Young light mare surface; most old craters are steep-sided, shallow, bowl-shaped irregular depressions (2). (c) Dark mantle on probable young mare; most craters are circular, shallow cone-shaped depressions (3).

penetrates the moderately dark mantle (fig. 29-21). A thin, very dark bed crops out in the upper wall of this crater and sheds lobes of debris into the crater. Higher up in the wall, a thin but distinct bed of similar appearance is present in what probably is the overturned flap of crater ejecta. The other exposure is on the precipitous slopes of the highland margin facing the Serenitatis basin (fig. 29-14). Here, the moderately dark mantle is underlain by a thin and very dark bed that produces several dark lobes on the slope. These relationships suggest that the moderately dark mantle in the highlands locally is a mixture of mass-wasted, bright highland material and older underlying dark mantling material.

The absence of thick dark mantling material on most of the highland slopes can be explained by active mass-wasting processes, which would remove unconsolidated material rapidly from steep slopes. However, a very thin dark layer may remain on steep slopes but be difficult to recognize. Alternatively, if the dark mantle was emplaced by flow (as opposed to some process of fallout), it may never have covered all the highlands.

CRATERS

Dark-halo craters in the Taurus-Littrow region have been described as possible vents for the dark mantle deposit (ref. 29-20). Most of these small dark-halo craters have shapes typical of impact craters of similar size (fig. 29-22(a)), and many are located where dark mantling material may have been excavated and ejected from beneath the surface. Therefore, many of these small dark-halo craters may be of impact origin. However, some small dark-halo craters in the Taurus-Littrow area have characteristics unlike small bright-halo impact craters elsewhere. Some, for example, are located on bright, steep slopes (fig. 29-22(b)) apparently without dark material in the subsurface. Yet dark material seems to have emanated from the craters and to have slumped back into them. There are also maar-like craters with dark halos, low degraded rims, steep walls, and flat or rocky floors (fig. 29-22(c)), and very subdued craters with dark rays (fig. 29-22(d)). Other craters with bright floors and broad very dark rims (fig. 29-22(e)) are also unlike impact craters elsewhere. Many dark patches and some dark streaks on crater rims (figs. 29-22(f) and (g)) have no obvious source but typically are associated with very small (< 10 m diameter) sharp pits.
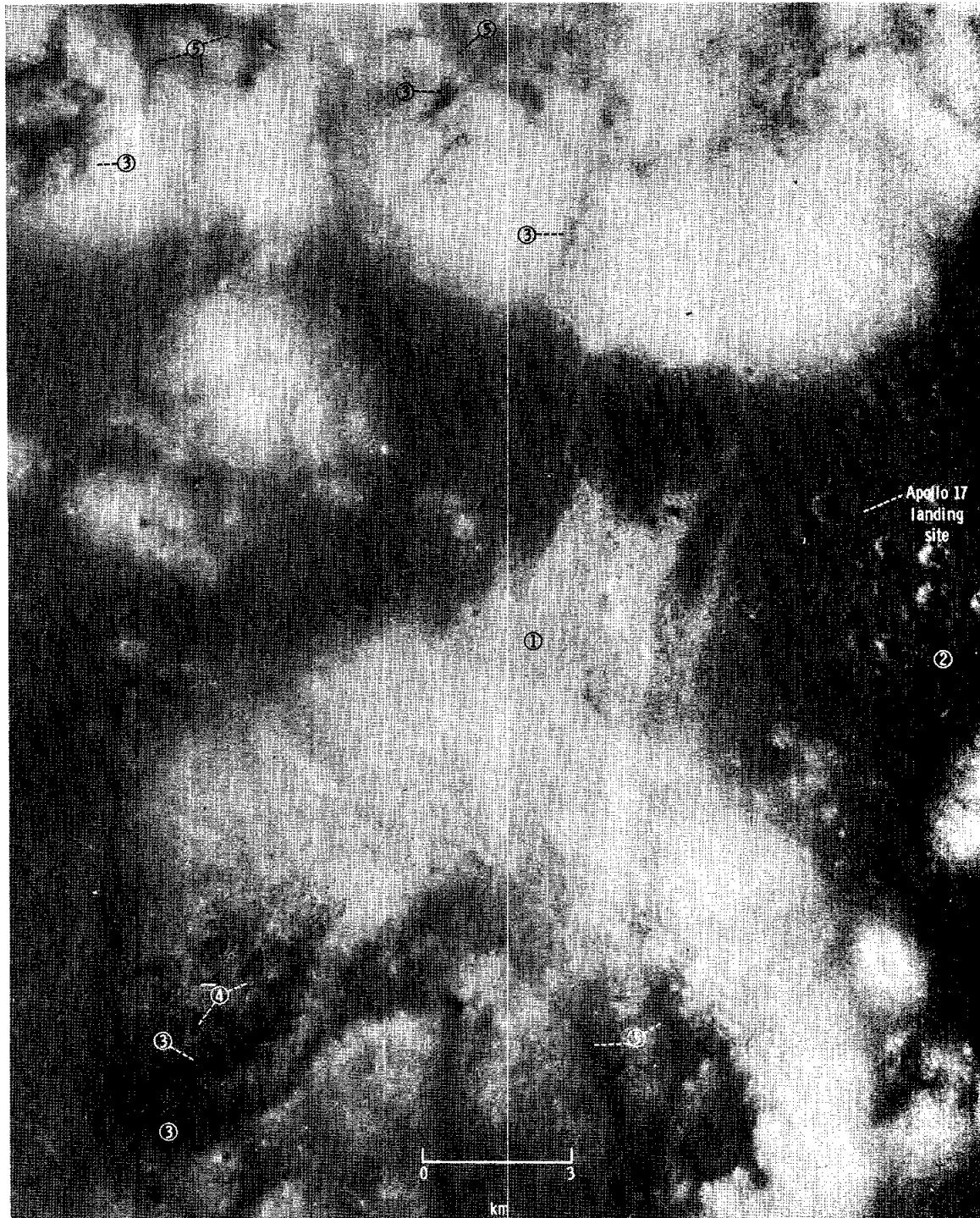
FIGURE 29-18.—Apollo 17 landing site area. (1) Bright mantle overlying dark mantle; (2) cluster of craters of middle-Copernican age; (3) dark patches and streaks on steep highland slopes; (4) dark mantle covering bouldery outcrop ledges; and (5) moderately dark mantle material concentrated in lows (Apollo 15 panoramic camera frame AS15-9557).
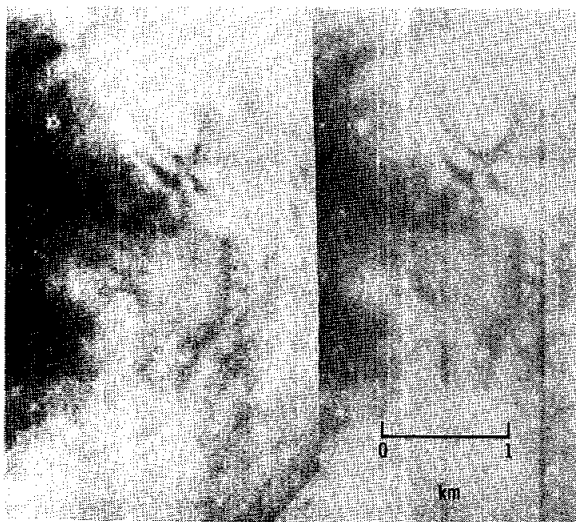
FIGURE 29-19.—Stereopair showing dark material on sub-horizontal ledges on steep slopes (Apollo 15 panoramic camera frames AS15-9550 and 9557).

DISCUSSION

In premission analysis, the dark mantle was interpreted as a very young pyroclastic blanket. Further study of orbital photographs and surface investigations of the Apollo 17 mission suggest the following possibilities.

1. The dark mantle is a thick, very dark regolith on old mare material. From this hypothesis, it follows that the dark mantle in the highlands is a regolith developed on lavas extruded in the highlands. The dark mantle burying low hills is a regolith on lavas that flooded these hills. Very dark patches on steep slopes are either from fresh outcrops or from patches of lava that developed regolith. Dark halos around craters would be composed of reworked regolith, and dark cover on young craters would be fallback regolith ejecta or deposits from adjacent young impact craters. Dark, streaked, young craters in the highlands would have penetrated into buried flows, sills, or dikes, and dark regolith would have developed on the ejecta. Multiple thin sheets of lava with well-developed regolith in the highlands may create the impression of "draping" over the topography.

The hypothesis does not explain why thick dark mantle deposits are maintained on steep slopes that are known to mass waste rapidly. Neither does it explain why the dark mantle is present on young
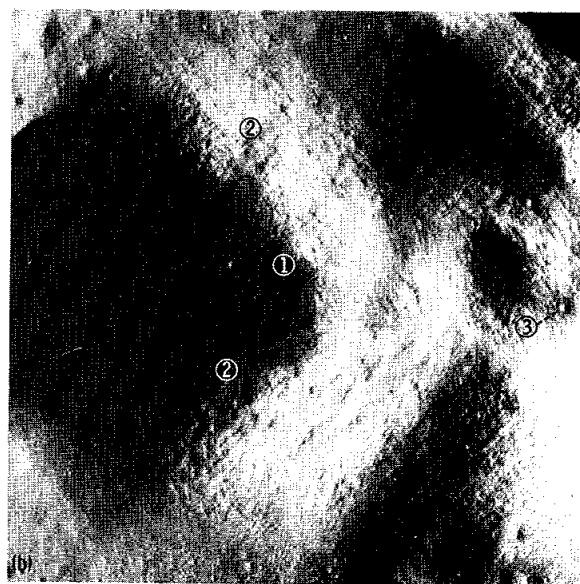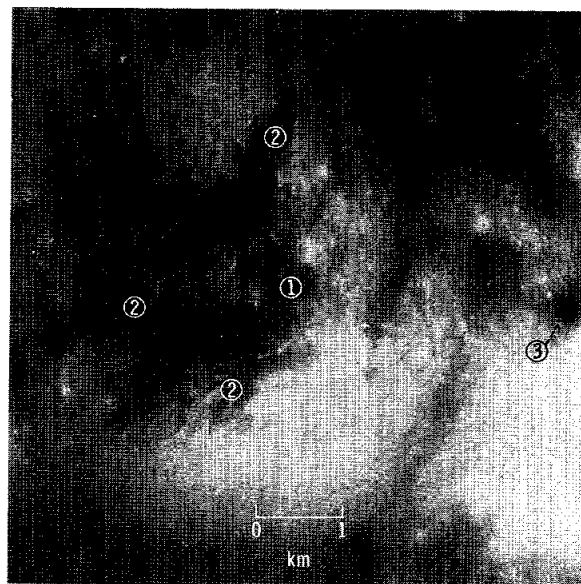
FIGURE 29-20.—Area on top of North Massif northwest of Apollo 17 landing site. Note (1) very fresh-looking dark mantling material on top of massif; (2) downslope streaks toward top, left, and bottom of photograph; and (3) the subdued crater with dark rays. (a) Area viewed in high-Sun illumination (Apollo 17 panoramic camera frame AS17-2757). (b) Area viewed in low-Sun illumination. Note relief features evident in this photograph (Apollo 17 panoramic camera frame AS17-2314).
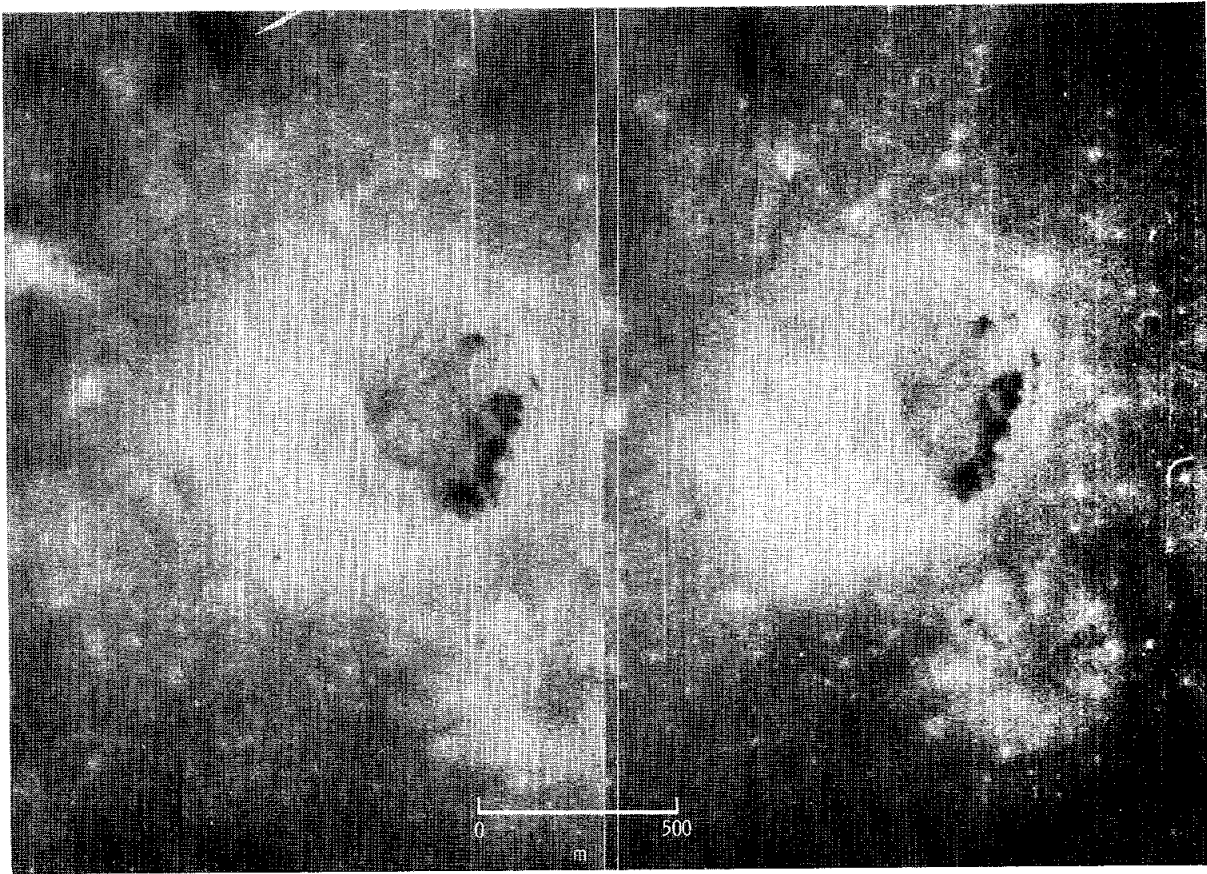
FIGURE 29-21.—Stereopair showing young crater penetrating moderately dark mantling material in
highlands north of landing area. Note lobes of very dark material apparently originating from dark
bed in upper crater wall and thin band of dark material above it in ejecta material of the rim
(Apollo 15 panoramic camera frames AS15-9554 and 9559).

fault scarps or on very fresh-looking lobate scarps
(probable flow fronts) that appear to be younger than
the young mare. The tentative evidence that the dark
mantle locally extends out over the young mare
further weakens the argument. If the dark mantle is a
regolith on young lavas, its substantial thickness in
places defies easy explanation. Furthermore, to ac-
count for the unusually dark color of the mantle, the
regolith must have developed under distinctly differ-
ent conditions than elsewhere on the Moon, or else
the composition of the original lava was unique to
this region.

2. The mantle is composed of dark ejecta mate-
rial. Objections to this hypothesis are that no crater
of suitable age is present within a reasonable distance,

and the patches of dark mantling material do not
have the configuration of typical rays. Impact into a
lava lake is an alternative hypothesis that accounts for
the lack of a visible source crater. The apparent
young age of the dark material in places, however,
weakens this interpretation.

3. The dark mantle is a pyroclastic deposit or
ash-flow tuff. It may be very thin and locally may be
mixed into thick regolith developed on old mare.
Dark-halo craters could be vents or impact craters
that have reworked pyroclastic deposits. The patchy
nature of the dark mantle suggests multiple sources.
This hypothesis fits most observations. A pre-
Serenitatis mare age is suggested in some places, but
evidence elsewhere suggests a locally younger age.

4. The dark mantle has a different origin in different places: a regolith with or without a pyroclastic component; a pyroclastic deposit or ash-flow tuff; or reworked material from dikes or sills. The argument that the dark mantle may have different origins is strengthened by its apparently different ages but weakened by its uniform color and surface texture as viewed on orbital photographs.

Neither the origin nor the age of the dark mantling material in the Taurus-Littrow region is yet established, and no firm hypothesis can be advanced until thorough studies are made of the new evidence from crew observations, orbital photographs, and returned samples.
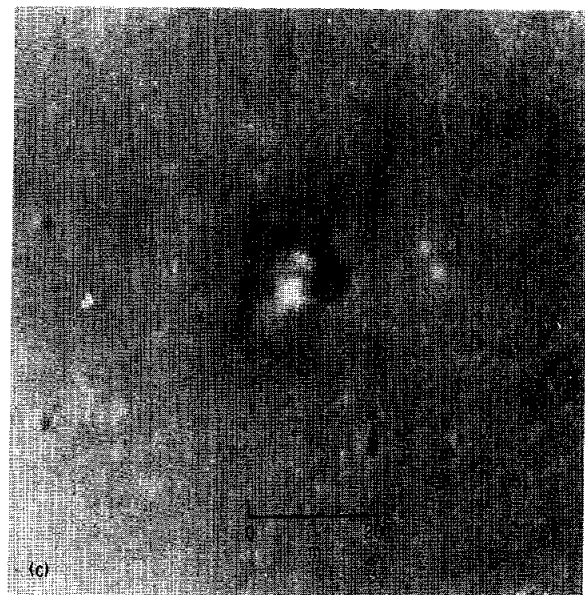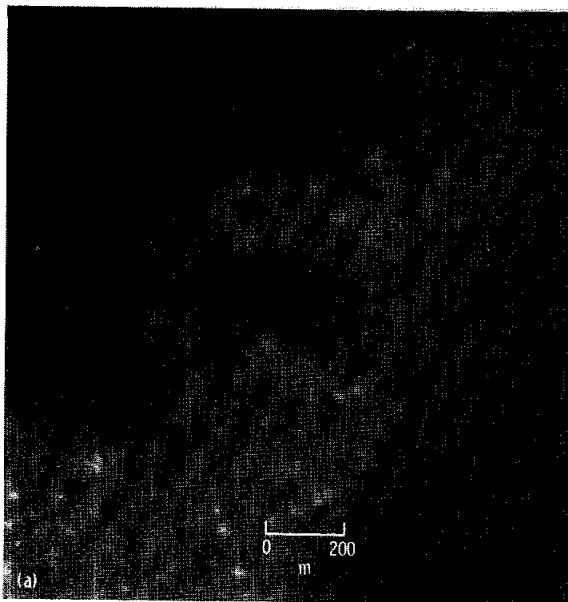
FIGURE 29-22.—Dark-halo craters in Taurus-Littrow region. (a) Dark-halo crater with shape typical of small impact craters (Apollo 15 panoramic camera frame (AS15-9559). (b) Dark-halo crater on hill (sloping steeply to upper left). Crater has bright walls and is half filled with dark material (Apollo 15 panoramic camera frame (AS15-9559). (c) Dark-halo crater with subdued rim, steep walls, and deep interior (Apollo 15 panoramic camera fram AS15-9559). (d) Very subdued crater with distinct ray-like halo (Apollo 15 panoramic camera frame AS15-9559). (e) Crater with subdued, mantled rim and fresh-looking rocky floor (Apollo 15 panoramic camera fram AS15-9557). (f) Dark patch across crater rim (Apollo 15 panoramic camera frame AS15-9559). (g) Dark patch on crater rim; dots outline rim crest (Apollo 15 panoramic camera frame AS15-9559).
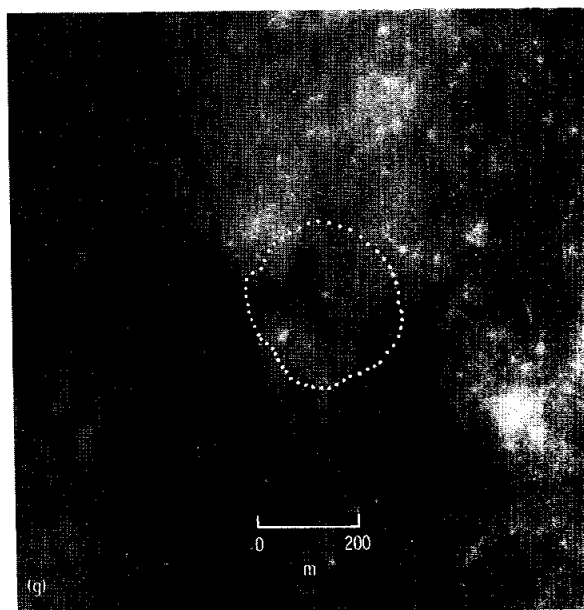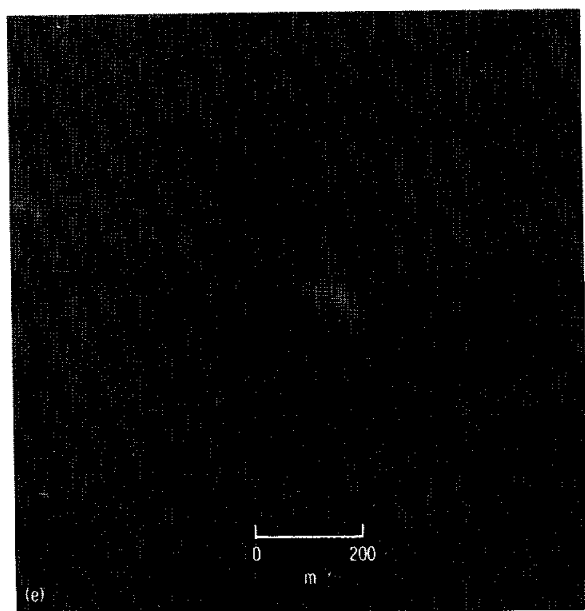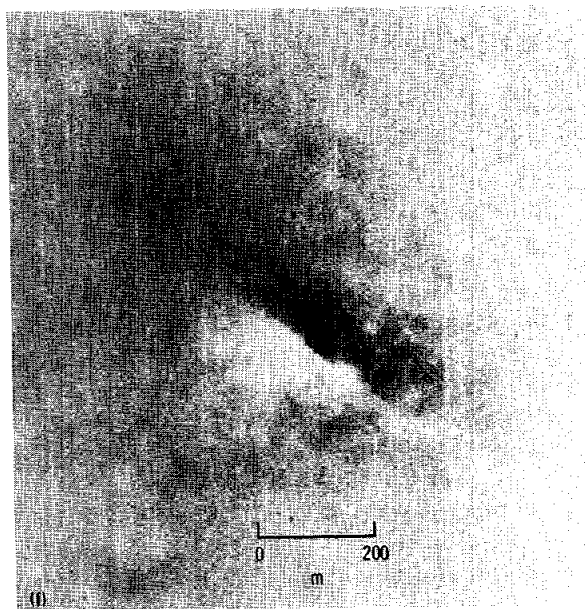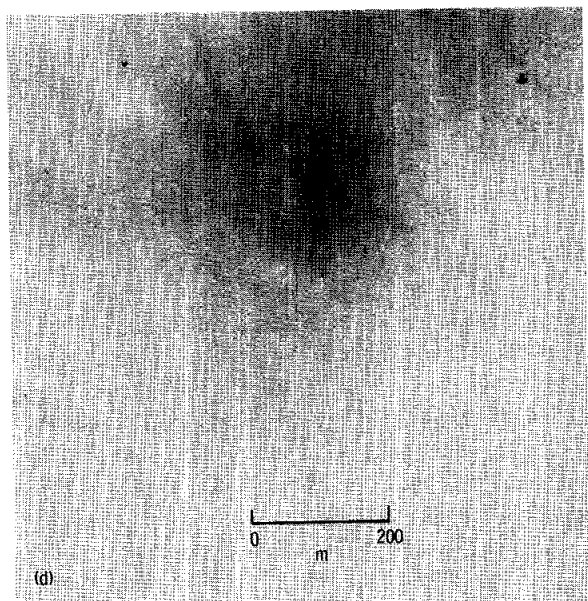
PART C

RELATIVE AGES OF SOME NEAR-SIDE MARE UNITS
BASED ON APOLLO 17 METRIC PHOTOGRAPHS

Joseph M. Boyce[a] *and Arthur L. Dial, Jr.*[a]

The lunar maria formed at different times and in multiple stages of extrusion. An understanding of their evolution is essential in placing the Apollo samples in a regional context and in interpreting the regional geology of a vast part of the lunar surface.

Relative ages of lunar maria were determined in this study by the crater-morphology technique described by Soderblom and Lebofsky (ref. 29-23). This method involves visual examination of orbital photographs to determine the maximum diameter of craters D_s the internal slopes of which have been eroded to slopes less than the Sun elevation angle S_s. Craters larger than this maximum diameter all have shadowed interiors because their walls are still steeper than the Sun elevation angle. Using a model of small-impact erosion (ref. 29-37), measurements of D_s are converted to an equivalent diameter D_L of a crater eroded to an interior slope of 1 degree under the same flux that has eroded a crater of diameter D_s to a slope S_s. Values of D_L can be considered synonymous with relative age; as shown by Soderblom and Lebofsky (ref. 29-23), D_L is directly proportional to the total number of craters that have accumulated on the surface. The limitations and errors in this technique are described in reference 29-23 and will not be reviewed here.

[a]U.S. Geological Survey.

The crater-morphology technique has been applied to the maria in a few scattered locations (refs. 29-23 and 29-38), but it has not yet been applied as a continuous mapping technique on mare flows. Apollo 17 metric photographs provide an excellent data base for the determination of these age relations in a belt that includes parts of Mare Serenitatis, Mare Vaporum, and Mare Imbrium.

The consistency of the technique was tested by comparing D_L values obtained from two sites at three different Sun angles (table 29-II). The results indicate that D_L is a constant for a particular site even though the measured values of D_s and S_s differ.

RESULTS

Relative flux ages were determined for 110 areas on parts of three maria (Serenitatis, Vaporum, and Imbrium), using 30X enlargements of Apollo 17 metric photographs. Figure 29-23 is a frequency plot of the age determinations that were used to define the age ranges of the mare units mapped from these data. Figure 29-24 shows the distribution of the six mare age units, and several relationships are apparent.

1. Three principal units were found in central and southern Mare Serenitatis. The major part of that mare is composed of an intermediate-age unit ($D_L \approx 250$ m). A slightly older unit ($D_L \approx 280$ m) occupies the

TABLE 29-II.—*Comparison of Relative Ages, as Indicated by Values of* D_L, *of Two Test Areas*[a]

Area	Apollo 17 metric camera frame number	D_s, m	S_s, deg	D_L, m
Southwestern Mare Serenitatis (area 1)	AS17-0801	360 to 510	11	245 + 45
	AS17-1512	350 to 540	12	240 + 50
	AS17-1816	550 to 800	20	245 + 45
Southwestern Mare Serenitatis (area 2)	AS17-0801	290 to 540	10	245 + 75
	AS17-1512	430 to 510	11	265 + 25
	AS17-1816	630 to 770	19	255 + 25

[a]Measurements of each area were made on three different photographs.

east central part. Units at the southeastern edge of Mare Serenitatis are significantly older ($D_L \approx 320$ to 360 m).

2. The northern embayments of Mare Vaporum contain deposits of approximately the same age as those in southeastern Mare Serenitatis.

3. Mare Imbrium is composed of several age units that include the following: (a) two young units in the vicinity of the crater Euler ($D_L \approx 160$ m and $D_L \approx 200$ m); (b) an intermediate-age unit ($D_L \approx 250$ m) in the southeastern part of the mare; and (c) several old units south and east of the crater Timocharis. Some

FIGURE 29-23.—Histogram of relative ages D_L determined for mare units. Frequencies of individual ages obtained in this study are shown. Units defined on the basis of age are indicated; each range is represented by a symbol used to map the units in figure 29-24.

of the very old ages in this area possibly may be caused by thin blankets that have partly obscured craters on an older surface.

4. A unit in Oceanus Procellarum near the crater Brayley is intermediate in age ($D_L \approx 250$ m).

It should be noted that our results have been grouped into rather broad and somewhat arbitrary units on the basis of figure 29-23. These units can be further subdivided for more detailed study at a later date. The complex region near Euler has several flow units with different relative ages (ref. 29-39) that could be mapped in much more detail with additional study.

Absolute ages for the units in figure 29-24 can be estimated by comparing relative ages (values of D_L) with crystallization ages determined for Apollo samples. Soderblom and Lebofsky (ref. 29-23) and Soderblom and Boyce (ref. 29-38) have shown theoretically and observationally that D_L is linearly proportional to the net accumulated flux. Figure 29-25 compares isotopic ages with D_L values (refs. 29-23 and 29-38) for Copernicus (ref. 29-40); for the Apollo 11, 12, and 15 maria (refs. 29-41 and 29-42); and for the minimum ages of the Fra Mauro Formation (Apollo 14 area) and the Cayley Formation (Apollo 16 area) (refs. 29-43 and 29-44). This plot allows the absolute age of surfaces dated in this study to be estimated. For example, the youngest deposits near Euler have an age near 2.2 billion years. A reliable value for the Apollo 17 site cannot be obtained because of the small sample of craters of the appropriate diameters. A D_L value of 470 ± 70 m for the dark, elevated rolling plains near Littrow B (ref. 29-5) yields an absolute age of 3.7 to 3.8 billion years.
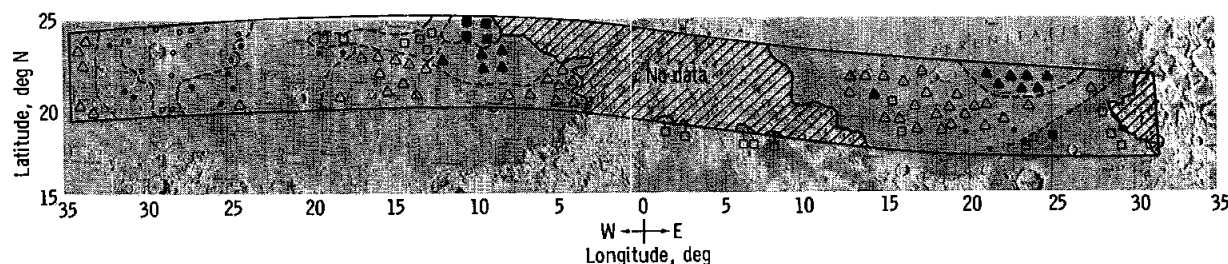
FIGURE 29-24.—Areal distribution of mare units as defined by relative ages. The symbols are the same as those shown in figure 29-23. No data are presented for the uplands (hachured areas). The dashed lines are intended to accentuate units of approximately uniform age.
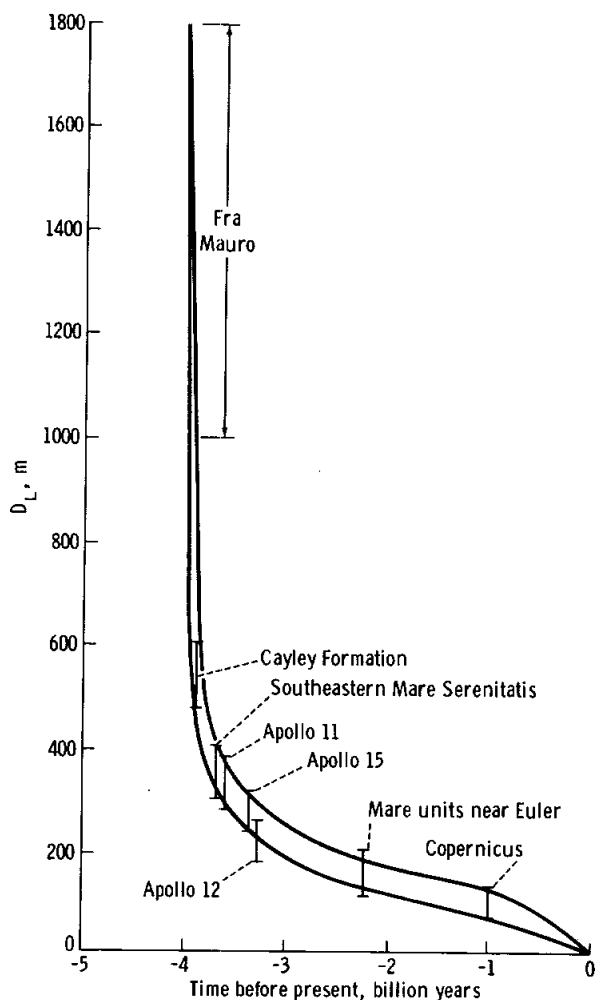
FIGURE 29-25.—Comparison of crystallization ages of Apollo samples and relative ages determined from orbital photographs by method described here. Values of D_L for the oldest and youngest units studied here are included.

COMPARISONS WITH OTHER INVESTIGATIONS

The sequence of evolution of the basalts in Mare Serenitatis inferred from this study is compatible with that based on superposition criteria deduced from Apollo 17 photographs (part A). Additionally, we find the mare materials near Euler are very young—a result consistent with the studies of Soderblom (ref. 29-5), Soderblom and Lebofsky (ref.

29-23), and Schaber (ref. 29-39 and part E of sec. 30). Except for a few questionably old units in southeastern Mare Imbrium, the old units at the northern border of Mare Vaporum, and the south-eastern margin of Mare Serenitatis, the remainder of the maria studied (southern Mare Imbrium and central Mare Serenitatis) are of intermediate age.

There is some agreement between the regional color variations (refs. 29-4 and 29-5 and part A of sec. 33) and the distribution of relative ages determined from this study. In the color studies, the mare materials bordering southeastern Mare Serenitatis and northern Mare Vaporum were found to have higher relative reflectance in the blue (0.4 to 0.5 μm) and are among the "bluest" materials on the Moon (refs. 29-5 and 29-6). The same areas were found to have D_L values of 300 to 400 m. Materials exposed in the center of Mare Serenitatis have low relative reflectance in blue and D_L values of 200 to 300 m. The youngest unit ($D_L \approx 160$ m), found in southern Mare Imbrium, also has a high blue reflectivity (refs. 29-4 and 29-23). These results are consistent with the mare-filling stages derived by Soderblom (ref. 29-5) that consist of (1) an early "blue" stage (Mare Tranquillitatis, Mare Fecunditatis, and Mare Vaporum), (2) an intermediate "red" stage (Mare Serenitatis, Mare Crisium, and parts of Mare Humorum and Mare Imbrium), and (3) a young "blue" stage (Oceanus Procellarum and parts of Mare Imbrium and Mare Humorum).

CONCLUSIONS

From this preliminary study, which broadly classifies the mare surfaces into relative age units, the following can be concluded.

1. The sequence of emplacement of the major mare units investigated is, from oldest to youngest: (a) the dark unit in southern Mare Serenitatis, northern Mare Vaporum, and possibly in Mare Imbrium east and southeast of Timocharis; (b) the lighter units in central Mare Serenitatis and south-central Mare Imbrium; and (c) a series of young flows found near Euler.

2. The emplacement of these mare units probably occurred over an interval of approximately 1.5 billion years, extending from 3.7 to 2.2 billion years ago.

PART D

GEOLOGIC MAP OF THE NORTHERN CRISIUM REGION

Don E. Wilhelms[a]

Apollo 17 metric photographs (fig. 29-26) provide the best available coverage for geologic interpretation of northern Mare Crisium and the northern Crisium basin. The area was covered previously by low-resolution telescopic and Lunar Orbiter IV photographs and by oblique, high-illumination, or low-resolution photographs from earlier Apollo missions. One region in particular, between Alhazen Crater and longitude 66° E, had previously been covered very poorly. The Apollo 17 photographs provide excellent monoscopic (fig. 29-26) as well as stereoscopic viewing because of the favorably low Sun illuminations (15° to 49°). These new photographic data allow the geology of the basin, the mare, and other nearby terrains to be reevaluated. This reexamination, together with data from continuing Moon-wide photogeologic studies and analyses of returned rocks from Apollo landing sites, has produced a simple evolutionary picture of the region, expressed by fewer map units and explained by fewer basic processes than previously thought necessary (refs. 29-35 and 29-45 to 29-48).

CRISIUM BASIN

The earliest discernible event was the large impact that created the Crisium basin and its concentric raised rings and intervening troughs. The raised rings are composed of prebasin rock and basin ejecta of pre-Imbrian age (three map units: rugged terra, rounded terra hills, and undivided terra, fig. 29-27). The troughs are filled by debris derived from these raised rings and by younger plains and mare materials. This alternation of older rings and younger trough material is basically the scheme of all lunar multi-ringed basins, and many investigators have considered Crisium a typical example (refs. 29-35, 29-45, 29-48, and 29-51). Others (e.g., ref. 29-11, p. 445) stressed anomalous aspects of Crisium such as atypical ring

morphology or spacing and an apparent east-west elongation of the basin.

To determine the degree of similarity with other basins, the rings were reexamined and the generalized positions of their crests plotted on the stereoscopic Apollo 17 photographs. Three rugged rings are delineated in the circummare terra (fig. 29-27), and another ring is believed to lie within the mare. The outermost ring, 970 km in diameter, is incomplete and topographically low. It bounds the basin-concentric mare northwest of the crater Macrobius and is expressed as a raised arc near the eastern map boundary. The next ring inside is 680 km in diameter and consists of medium-sized peaks. Northwest of Mare Crisium, in and near a depressed area partly flooded by mare, this ring is divided into several blocks and fractured along a northwest trend. The most conspicuous ring, 500 km in diameter, bounds Mare Crisium proper and consists mainly of high broad massifs. The innermost ring (not delineated in fig. 29-27) consists of a few small but steep terra peaks in the mare north of Yerkes Crater and in the inner part of the eastern embayment. The mare in which these peaks occur forms a shelf around the topographically lower, island-free central Mare Crisium. The boundary between shelf and central mare, particularly abrupt in the northwest, coincides with a concentric complex of mare ridges and scarps.

In this interpretation, the similarities with other basins considerably outweigh the dissimilarities. The spacing of the three rugged rings increases outward by the factor of approximately 1.4 (or the square root of 2, according to Hartmann and Wood (ref. 29-52)) that seems to be common to lunar basin rings. Critical to the comparison proposed here is identification of the 680-km ring as equivalent to the Montes Cordillera ring of the Orientale basin (950-km diameter; e.g., see fig. 29-33 of ref. 29-53) and to the Caucasus-Apenninus-Carpatus ring of the Imbrium basin (1480-km diameter). This Crisium ring, like its counterparts at Orientale and Imbrium, is the outermost conspicuous ring of the basin and is bounded

---

[a] U.S. Geological Survey.
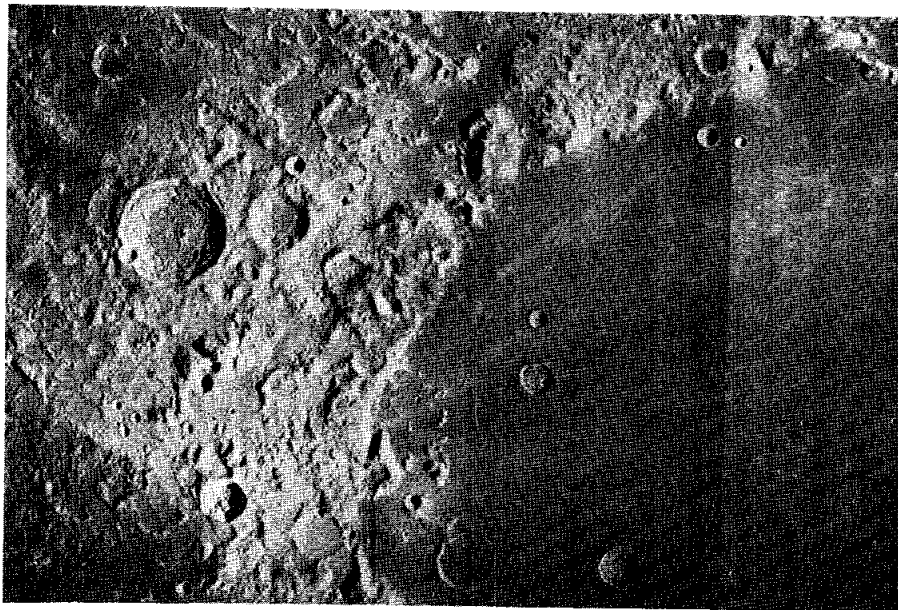
FIGURE 29-26.—Northern Mare Crisium and Crisium basin. Approximate scale and coordinates are given in figure 29-27 (Apollo 17 metric camera frames, right to left, AS17-0274, 0278, 0281, 0286, 0289, 0293, and 0294).
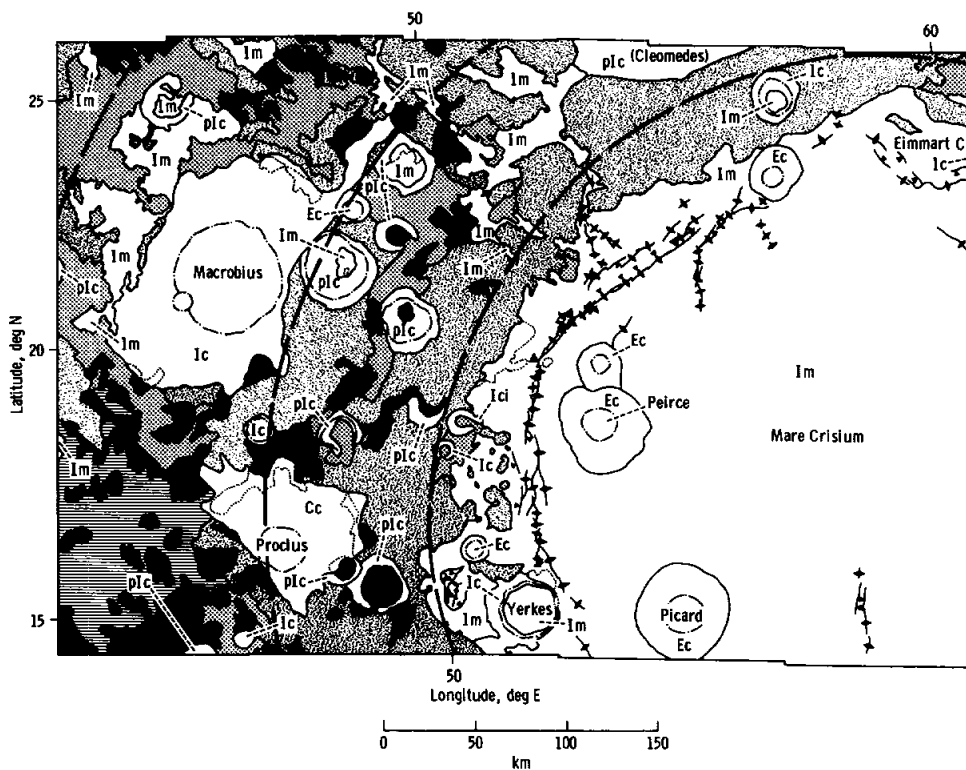
FIGURE 29-27.—Geologic map of northern Crisium region, based on photomosaic of figure 29-26. Detailed description of map units is listed separately.
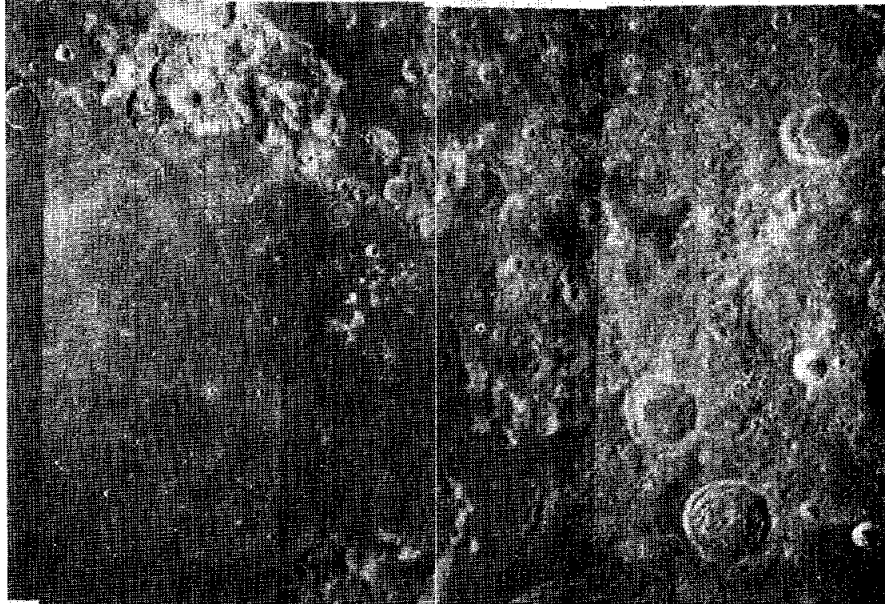
FIGURE 29-26.—Concluded.
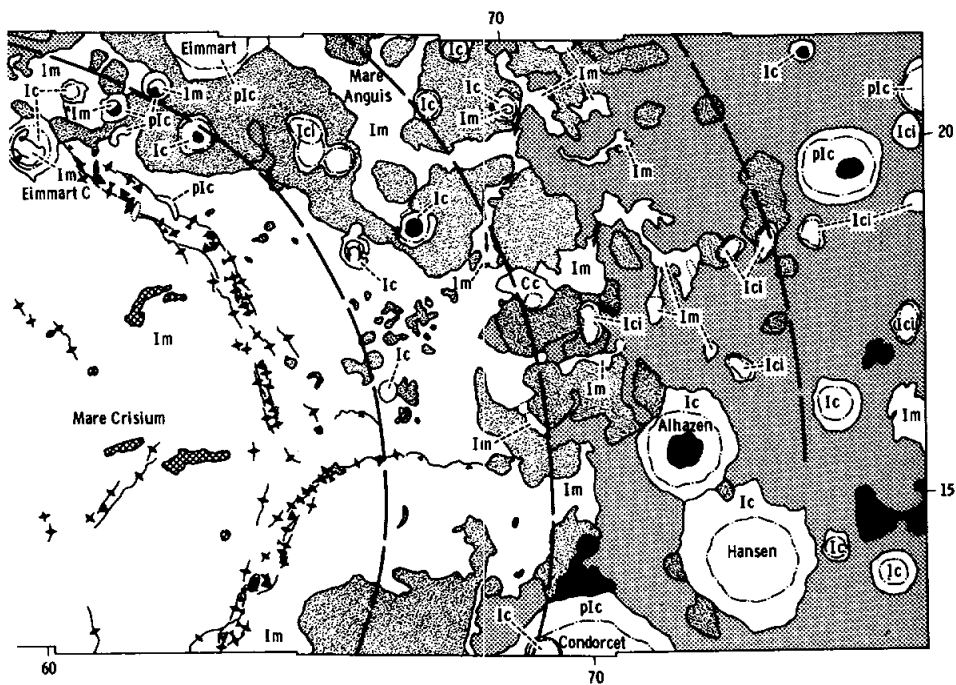
FIGURE 29-27.—Concluded.

Explanation

─────────── Contact

·························· Contact of terra or crater material buried by mare material or crater ejecta

───◆─────── Mare ridge: line marks crest; barbs point downslope

───◆─────── Asymmetric mare ridge: line marks crest; longer barb points down higher scarp

───■─────── Abrupt, low mare scarp: line marks base; barb points downslope

───▼─────── Gentle, high mare scarp: line marks approximate base; barb points downslope

───⊥─────── Mare ridge coincident with base of gentle, high mare scarp

| Slope in mare: inferred gentle slope or slope over buried terra

───•─────── Graben

─ · ─ · ─ · ─ Crater rim crest

━━━ ━━━ Crest of basin ring structure (generalized)

Description and interpretation of geologic units

Cc   Material of rayed craters (Copernican) - Bright wall material and fresh-looking striated ejecta and satellitic craters; relatively more extensive than similar material of older craters.
Interpretation: Primary impact origin.

Ec   Material of fresh unrayed craters (Eratosthenian) - Ejecta easily distinguished on mare but ill-defined in hilly terra.
Interpretation: Primary impact origin.

Im   Planar mare material (Imbrian) - Morphology and size-frequency distribution of superposed craters visible on panoramic photographs indicate only one major unit of Imbrian age (as opposed to Eratosthenian, ref. 29-35); second (younger?) unit (refs. 29-45 and 29-48) suggested by lower albedo in east (fig. 29-26) but not detected in crater studies.
Interpretation: Basaltic lava.

Positive-relief mare material (Imbrian?) - Confined to eastern Mare Crisium; characterized by ridges, irregular low hills, and low cones surmounted by incomplete rings 1.5 to 3.5 km in diameter; surrounded by dark mare (fig. 29-26).
Interpretation: Cinder cones and other features closely related to mare in origin; dark mantle may be finer pyroclastic material.

Material of planar and undulating terra (Imbrian) - Concentrated west of Crisium. Gradational contacts with adjacent hilly terra (ref. 29-49).
Interpretation: Small patches could be derived by mass wasting of local materials. Broad areas (e.g., south of Macrobius) probably composed of ejecta from distant sources; partial Imbrium basin source suggested by proximity to Imbrium; surface beds possibly composed of Orientale basin ejecta, as suggested by crater populations (ref. 29-50) and, in part, by Macrobius crater ejecta. Volcanic origin unlikely because of gradational contacts, as well as the demonstrated impact origin of similar plains material at the Apollo 16 landing site.

Ic   Material of moderately fresh premare craters (Imbrian) - Ejecta detectable only short distance from rim crest, except around Macrobius where superposed on low-relief terrain.
Interpretation: Macrobius of impact origin; other craters probably impact but diagnostic criteria not detected; four flooded craters in Mare Crisium (Yerkes, Eimmart C, and two small unnamed shallow-floored craters in eastern mare embayment) probably resembled the impact craters Picard or Peirce before flooding; alternatively, these may be calderas (smooth-rimmed crater class of Wilhelms and McCauley, ref. 29-35).

Ici   Material of irregular craters (Imbrian) - Noncircular rim crests; similar to numerous craters of south basin rim (ref. 29-48).
Interpretation: Secondary impact craters of basins or large craters or, alternatively, volcanic.

pIc   Material of subdued premare craters (pre-Imbrian) - Expressed mainly as raised rings, commonly broken.
Interpretation: Origin uncertain because of degradation. Cleomedes (centered north of area) probably of impact origin; irregular pits on north-facing slope of main Crisium rim possibly Cleomedes secondary craters.

Material of rugged terra (pre-Imbrian) - Large massifs and peaks with steep, smooth, bright slopes; similar to North and South Massifs at Apollo 17 site; also debris derived from slopes.
Interpretation: Bedrock uplifted by Crisium impact.

Material of rounded terra hills (pre-Imbrian) - Small, mostly equidimensional hills divided by regular, partly grid-like lineations with dominant northwest strike. Occurs only in area west of Crisium including Apollo 17 site. (Also termed "hilly terra material" (refs. 29-17, 29-21, and 29-46) and "Sculptured Hills" (informal Apollo 17 mission designation).)
Interpretation: Crisium basin ejecta fractured along trends of "lunar grid," possibly reinforced by Imbrium, Serenitatis, and Crisium basin structures, and rounded by erosion (refs. 29-17, 29-21, and 29-46).

Terra material, undivided (dominantly pre-Imbrian, but may include material of Imbrian age) - Hilly terra material not included in previous two units; also small undulatory or planar patches.
Interpretation: Pre-Crisium bedrock and Crisium ejecta degraded beyond recognition by erosion and mantles of younger impact ejecta.

outwardly by generally high terrain and inwardly by a deep trough. It contains fewer basin-concentric elements and is more degraded than the corresponding but younger rings of Imbrium and Orientale, but these departures are minor. The next inward rings in all three basins also are comparable. In general distribution of large massifs and smaller peaks, the conspicuous 500-km Crisium ring resembles the corresponding outer Rook ring of Orientale (680 km) and the Alpes-Archimedes ring of Imbrium (1040 km) despite its prominence, which superficially suggests analogy to the Cordillera and Caucasus-Apenninus-Carpatus rings. In addition, the outer incomplete 970-km Crisium ring is similar in position and morphology to an outer ring of Imbrium that bounds the southern edge of Sinus Medii (ref. 29-35).

Completing the comparison, the innermost ring (approximately 425 km) of small isolated peaks appears to correspond to the inner Rook ring of Orientale (480 km) and the inner ring of Imbrium (660 km). In the less deeply flooded Orientale basin, the relatively small peaks of the inner Rook ring rise above a scarp-bounded shelf, which, if flooded, would resemble the shelf in Crisium. This inner Crisium ring and the 500-km Crisium ring apparently are closer together, however, than are the two Rook rings and do not obey the 1.4 spacing ratio. The exact value of this anomalous Crisium spacing is uncertain because of burial of the inner ring by mare.

The appearance of asymmetry of the basin is due mainly to an east-west elongation of the mare and only partly to a minor ellipticity of the basin rings. The presence of numerous small but steep peaks in the large eastern embayment suggests that most of the asymmetry is due to foundering of the 500-km ring. The margins of the embayment trend northwest, east-west, and concentrically with the basin. The northwest trend is probably of internal origin and not related to the basin because it pervades much of the region, notably in the rounded terra hills. It coincides with a Crisium radial direction only in the depressed area northwest of the basin (ref. 29-54, pp. 180-181) and with the Crisium concentric directions only along the eastern embayment. The northwest and east subsidences therefore occurred where endogenous and basin structures coincided.

POSTBASIN MATERIALS

After the subsidence and before mare flooding, during a continued intense period of impact cratering on the entire Moon, light-colored plains materials were deposited in depressions in the basin structure. Earlier systematic mappers in the region (refs. 29-35, 29-45, 29-47, and 29-48) called on volcanism, to varying degrees, to explain the plains, rounded terra hills, and certain craters. Impact ejecta or mass-wasted debris (or both) now seem more probable components of the plains, in light of petrologic data from the Apollo landing sites and contact relations apparent on stereoscopic photographs (refs. 29-49, 29-50, and 29-55). The origin of some craters (Ici and Ic, fig. 29-27) is still in doubt, but the origin of dark-halo craters (unmapped, ref. 29-56) and the rounded hills seems to be adequately accounted for by nonvolcanic means (refs. 29-17, 29-21, 29-46, and 29-49).

After formation of the plains and most of the large craters in the region, the presumably basaltic mare materials were emplaced in the central Crisium basin and in numerous peripheral depressions bounded by structures approximately radial and concentric to the basin. Mare Crisium consists mainly of planar flows and partly of forms with positive relief. The innermost of the peripheral mare patches is at a higher level than Mare Crisium, and each of the succeeding patches is slightly higher than its inner neighbor. An exception is the mare patch at the eastern boundary of the mapped area, which is on the outer flanks of the Crisium basin. A single mapped patch may have two or three levels, the highest level outward. The levels of the circumferential mare patches thus imply a stepped basin structure. In places between two levels, the lava seems to have flowed over a buried terra scarp (shown by arrows superposed on dotted lines).

In the long postmare history of the region, the only deposits that seem to have formed are sheets of fine-textured impact ejecta and fields of secondary impact craters. These deposits appear to be extensive on high-resolution photographs taken at low Sun angle but are minor volumetrically. Their preservation attests to a sluggishness of the later degradational processes that contrasts with the intense activity in the much shorter period between formation of the Crisium basin and its filling by mare material. Materials of the Crisium basin and of the craters formed before mare flooding (later pre-Imbrian time and Imbrian period) are texturally distinguishable only on low slopes around the largest craters and are doubtless mixed chaotically in a surficial fragmental layer.

SUMMARY

The Crisium basin is a typical, large lunar impact basin, modified by smaller impacts, subsidence, infilling by plains and mantles of impact origin, mass wasting, and basaltic volcanism. Modification processes were much more intensive during the first third of lunar history than during the two-thirds following mare formation. No evidence for terra volcanism exists in the Crisium basin region.

REFERENCES

29-1. Carr, M. H.: Geologic Map of the Mare Serenitatis Region of the Moon. U.S. Geol. Survey Misc. Geol. Inv. Map I-489, 1966.

29-2. Pohn, Howard A.; and Wildey, Robert L.: A Photoelectric-Photographic Study of the Normal Albedo of the Moon. U.S. Geol. Survey Prof. Paper 599-E, 1970.

29-3. Whitaker, E. A.: The Surface of the Moon. Sec. 3 of The Nature of the Lunar Surface. Proceedings of the 1965 IAU-NASA Symposium, The Johns Hopkins Press (Baltimore), 1966, pp. 79-98.

29-4. Whitaker, Ewen A.: Lunar Color Boundaries and Their Relationship to Topographic Features: A Preliminary Survey. The Moon, vol. 4, nos. 3/4, June/July 1972, pp. 348-355.

29-5. Soderblom, L. A.: The Distribution and Ages of Regional Lithologies in the Lunar Maria. Ph. D. Thesis, Calif. Inst. of Tech., Pasadena, Calif., 1970.

29-6. McCord, Thomas B.: Color Differences on the Lunar Surface. J. Geophys. Res., vol. 74, no. 12, June 15, 1969, pp. 3131-3142.

29-7. McCord, Thomas B.; and Johnson, Torrence V.: Relative Spectral Reflectivity 0.4-1 μ of Selected Areas of the Lunar Surface. J. Geophys. Res., vol. 74, no. 17, Aug. 15, 1969, pp. 4395-4401.

29-8. Pieters, Carle; McCord, T. B.; Zisk, S. H.; and Adams, J. B.: Lunar Black Spots and the Nature of the Apollo 17 Landing Area. J. Geophys. Res., vol. 78, no. 26, Sept. 10, 1973.

29-9. Sukhanov, A. L.: Mechanism of Origin of the Formation of the Lunar Seas. Akad. Nauk SSSR, Doklady, vol. 181, July 11, 1968, pp. 309-312.

29-10. Wilhelms, D. E.: Summary of Lunar Stratigraphy—Telescopic Observations. U.S. Geol. Survey Prof. Paper 599-F, 1970.

29-11. Stuart-Alexander, Desiree E.; and Howard, Keith A.: Lunar Maria and Circular Basins—A Review. Icarus, vol. 12, no. 3, May 1970, pp. 440-456.

29-12. Dodd, Robert T., Jr.; Salisbury, John W.; and Smalley, Vern G.: Crater Frequency and the Interpretation of Lunar History. Icarus, vol. 2, nos. 5-6, Dec. 1963, pp. 466-480.

29-13. Schaber, G. G.: Geologic Map of the Sinus Iridum Quadrangle of the Moon. U.S. Geol. Survey Misc. Geol. Inv. Map I-602, 1969.

29-14. Moore, H. J.: Geologic Map of the Seleucus Quad-

rangle of the Moon. U.S. Geol. Survey Misc. Geol. Inv. Map I-527, 1967.

29-15. Carr, M. H.: Dark Volcanic Materials and Rille Complexes in the North-Central Region of the Moon. Part A of Astrogeological Studies, Annual Progress Report, July 1964—July 1965, U.S. Geol. Survey, Nov. 1965, pp. 35-43.

29-16. Shoemaker, Eugene M.; and Hackman, Robert J.: Stratigraphic Basis for a Lunar Time Scale. The Moon—Symposium No. 14 of the International Astronomical Union, Leningrad, Dec. 1960, Academic Press, Inc. (New York), 1962, pp. 289-300.

29-17. Scott, D. H.; and Carr, M. H.: Geologic Map of the Taurus-Littrow Region of the Moon. U.S. Geol. Survey Misc. Geol. Inv. Map I-800, sheet 1, 1972.

29-18. Trask, N. J.: Geologic Comparison of Mare Materials in the Lunar Equatorial Belt, Including Apollo 11 and Apollo 12 Landing Sites. U.S. Geol. Survey Prof. Paper 750-D, 1971, pp. 138-144.

29-19. Carr, M. H.: Sketch Map of the Region Around Candidate Littrow Apollo Landing Sites. Sec. 25, Part H, of the Apollo 15 Preliminary Science Report. NASA SP-289, 1972.

29-20. El-Baz, Farouk: The Cinder Field of the Taurus Mountains. Sec. 25, Part I, of the Apollo 15 Preliminary Science Report. NASA SP-289, 1972.

29-21. Lucchitta, B. K.: Geologic Map of Part of the Taurus-Littrow Region of the Moon. U.S. Geol. Survey Misc. Geol. Inv. Map I-800, sheet 2, 1972.

29-22. Wolfe, E. W.; Freeman, V. F.; Muehlberger, W. R.; Head, J. W.; Schmitt, H. H.; and Sevier, J. R.: Apollo 17 Exploration at Taurus-Littrow. Geotimes, vol. 17, no. 11, 1972, pp. 14-18.

29-23. Soderblom, Laurence A.; and Lebofsky, Larry A.: Technique for Rapid Determination of Relative Ages of Lunar Areas from Orbital Photography. J. Geophys. Res., vol. 77, no. 3, Jan. 10, 1972, pp. 279-296.

29-24. Carr, M. H.; Howard, K. A.; and El-Baz, Farouk: Geologic Maps of the Apennine-Hadley Region of the Moon: Apollo 15 Pre-Mission Maps. U.S. Geol. Survey Misc. Geol. Inv. Map I-723, 1971.

29-25. Sjogren, W. L.; and Wollenhaupt, W. R.: Lunar Shape via the Apollo Laser Altimeter. Science, vol. 179, no. 4070, Jan. 19, 1973, pp. 275-278.

29-26. Carr, M. H.: The Geology of the Mare Serenitatis Region of the Moon. Part A of Astrogeological Studies, Annual Progress Report, July 1965—July 1966, U.S. Geol. Survey, Dec. 1966, pp. 11-16.

29-27. Houser, F. N.: Subsidence Related to Underground Nuclear Explosions, Nevada Test Site. Bull. Seismol. Soc. Am., vol. 59, Dec. 1969, pp. 2231-2251.

29-28. Hamilton, D. H.; and Meehan, R. L.: Ground Rupture in the Baldwin Hills. Science, vol. 172, no. 3981, Apr. 23, 1971, pp. 333-344.

29-29. Howard, Keith A.: Volcanic Collapse Structures and Man-Made Analogs. Geol. Soc. Am. Abs., vol. 4, no. 3, 1972, p. 173.

29-30. Swanson, D. A.; and Peterson, D. W.: Partial Draining and Crustal Subsidence of Alae Lava Lake, Kilauea Volcano, Hawaii. U.S. Geol. Survey Prof. Paper 800-C, 1972, pp. 1-14.

29-31. Baldwin, Ralph B.: The Measure of the Moon. Univ. of Chicago Press, 1963.

29-32. Muller, P. M.; and Sjogren, W. L.: Mascons: Lunar Mass Concentrations. Science, vol. 161, no. 3843, Aug. 16, 1968, pp. 680-684.

29-33. Howard, Keith A.: Mascons, Mare Rock, and Isostasy. Nature, vol. 226, no. 5249, June 6, 1970, pp. 924-925.

29-34. Moore, J. G.: Relationship Between Subsidence and Volcanic Load, Hawaii. Bull. Volcanologique, vol. 34, no. 2, 1970, pp. 562-576.

29-35. Wilhelms, D. E.; and McCauley, J. F.: Geologic Map of the Near Side of the Moon. U.S. Geol. Survey Misc. Geol. Inv. Map I-703, 1971.

29-36. Apollo Lunar Geology Investigation Team: Preliminary Report on the Geology and Field Petrology at the Apollo 17 Landing Site. Interagency Rept.: Astrogeology 69, U.S. Geol. Survey, Dec. 17, 1972.

29-37. Soderblom, L. A.: A Model for Small Impact Erosion Applied to the Lunar Surface. J. Geophys. Res., vol. 75, no. 14, May 10, 1970, pp. 2655-2661.

29-38. Soderblom, Laurence A.; and Boyce, J. M.: Relative Ages of Some Near-Side and Far-Side Terra Plains Based on Apollo 16 Metric Photography. Sec. 29, Part A, of the Apollo 16 Preliminary Science Report. NASA SP-315, 1972.

29-39. Schaber, Gerald G.: Lava Flows in Mare Imbrium: Geologic Evaluation From Apollo Orbital Photography. Lunar Science IV (Abs. of papers presented at the Fourth Lunar Science Conference (Houston, Tex.), Mar. 5-8, 1973), pp. 653-654.

29-40. Silver, Leon T.: U-Th-Pb Isotopic System in Apollo 11 and Apollo 12 Regolithic Materials and a Possible Age for the Copernican Event [abs.]. Trans. Am. Geophys. Union, vol. 52, no. 7, July 1971, p. 534.

29-41. Papanastassiou, D. A.; and Wasserburg, G. J.: Lunar Chronology and Evolution From Rb-Sr Studies of Apollo 11 and 12 Samples. Earth Planet. Sci. Letters, vol. 11, Aug. 1971, pp. 37-62.

29-42. Wasserburg, G. J.; and Papanastassiou, D. A.: Age of an Apollo 15 Mare Basalt: Lunar Crust and Mantle Evolution. Earth Planet. Sci. Letters, vol. 13, no. 1, Dec. 11, 1971, pp. 97-104.

29-43. Papanastassiou, D. A.; and Wasserburg, G. J.: The Rb-Sr Ages of Igneous Rocks From the Apollo 14 Mission and the Age of the Fra Mauro Formation. Earth Planet. Sci. Letters, vol. 12, no. 1, Sept. 1971, pp. 36-48.

29-44. Papanastassiou, D. A.; and Wasserburg, G. J.: The Rb-Sr Age of a Crystalline Rock From Apollo 16. Earth Planet. Sci. Letters, vol. 16, no. 2, Oct. 1972, pp. 289-298.

29-45. Casella, C. J.; and Binder, A. B.: Geologic Map of the Cleomedes Quadrangle of the Moon. U.S. Geol. Survey Misc. Geol. Inv. Map I-707, 1972.

29-46. Scott, D. H.; and Pohn, H. A.: Geologic Map of the Macrobius Quadrangle of the Moon. U.S. Geol. Survey Misc. Geol. Inv. Map I-799, 1972.

29-47. Wilhelms, D. E.: Geologic Map of the Taruntius Quadrangle of the Moon. U.S. Geol. Survey Misc. Geol. Inv. Map I-722, 1972.

29-48. Olson, A. B.; and Wilhelms, D. E.: Geologic Map of the Mare Undarum Quadrangle of the Moon. U.S. Geol. Survey Misc. Geol. Inv. Map I-837, 1973.

29-49. Wilhelms, Don E.: Preliminary Geologic Map of the Region Around the Candidate Proclus Apollo Landing Site. Sec. 25, Part J, of the Apollo 15 Preliminary Science Report. NASA SP-289, 1972.

29-50. Chao, E. C. T.; Soderblom, L. A.; Boyce, J. M.; Wilhelms, D. E.; and Hodges, C. A.: Lunar Light Plains Deposits (Cayley Formation)—A Reinterpretation of Origin. Lunar Science IV (Abs. of papers presented at the Fourth Lunar Science Conference (Houston, Tex.), Mar. 5-8, 1973), pp. 127-128.

29-51. Hartmann, William K.; and Kuiper, G. P.: Concentric Structures Surrounding Lunar Basins. Commun. Lunar Planet. Lab., Univ. of Ariz., vol. 1, no. 12, June 20, 1962, pp. 51-66.

29-52. Hartmann, W. K.; and Wood, C. A.: Moon—Origin and Evolution of Multi-Ringed Basins. The Moon, vol. 3, no. 1, 1971, pp. 3-78.

29-53. Wilhelms, Don E.: Reinterpretations of the Northern Nectaris Basin. Sec. 29, Part F, of the Apollo 16 Preliminary Science Report. NASA SP-315, 1972.

29-54. Hartmann, William K.: Radial Structures Surrounding Lunar Basins. II: Orientale and Other Systems; Conclusions. Commun. Lunar Planet. Lab., Univ. of Ariz., vol. 2, no. 36, 1964, pp. 175-191.

29-55. Eggleton, R. E.; and Schaber, G. G.: Cayley Formation Interpreted as Basin Ejecta. Sec. 29, Part B, of the Apollo 16 Preliminary Science Report. NASA SP-315, 1972.

29-56. Lucchitta, Baerbel Koesters: Geologic Sketch Map of the Candidate Proclus Apollo Landing Site. Sec. 25, Part K, of the Apollo 15 Preliminary Science Report. NASA SP-289, 1972.

30. Volcanic Studies

The peculiar crater Aratus CA in Mare Serenitatis is comparable in shape, if not in scale, to a terrestrial volcanic vent and lava channel and may have been the source of some of the Serenitatis basalts (part A). Cinder cones have been identified within the dark annulus at the southern edge of Mare Serenitatis (parts B and C). Between Mare Serenitatis and Mare Vaporum, an unusual D-shaped depression, first recognized on Apollo 15 photographs, appears in low-Sun-angle Apollo 17 photographs to surmount a low dome in mare basalt; this feature is interpreted as a collapse caldera (part D). The prominent lava channels and distinct flows in southwestern Mare Imbrium have now been carefully mapped, and a relatively recent Eratosthenian age for these lavas is indicated (part E).

PART A

COMPARATIVE GEOLOGY OF CRATER ARATUS CA (MARE SERENITATIS) AND BEAR CRATER (IDAHO)

Ronald Greeley[a]

Aratus CA (lat. 24.5° N, long. 11.3° E; fig. 30-1) is an irregular-shaped crater 8.6 km long by 3 km wide in western Mare Serenitatis, which was photographed during the Apollo 15 and 17 missions. It is similar in form to Bear Crater (fig. 30-2), a small volcanic vent formed in Holocene basalt flows of the Snake River Plains, Idaho. In this report, the two features are compared and it is concluded that Aratus CA may have a geologic structure and history similar to that of Bear Crater.

BEAR CRATER

Bear Crater is the summit vent of a basalt shield volcano 45 km south-southeast of Craters of the Moon National Monument, Idaho. Although the outer flanks of the shield have been flooded by younger basalt flows (fig. 30-3), the summit region is exposed and only moderately weathered, and its primary surface features (channels, collapse depressions) are well preserved. The general structure and eruptive history for Bear Crater have been deduced from photogeology and ground reconnaissance for comparisons with Aratus CA and similar lunar surface features.

Bear Crater is approximately 780 m long, 254 m wide, and 80 m deep and appears to have formed three merged eruptive centers. Spatter ramparts of agglutinate occur as knobs at the southern end of the crater, and to a less pronounced degree at the northern end. The floor of Bear Crater is covered with talus, alluvium, and eolian deposits of unknown thickness. The smooth rounded floor of the crater grades upward to the talus slopes of the crater wall. Outcrops are restricted to sections of the crater wall and channel sides. Composite measured sections indicate that the shield was built of layers of basalt from multiple eruptions. The dip of the layers near the vent (fig. 30-4) averages approximately 15°, somewhat greater than the present slope on the flank of the shield. Entrances to large lava tubes were not

[a]University of Santa Clara.

FIGURE 30-1.—Aratus CA Crater in western Mare Serenitatis. Area of photograph is 17.4 by 25 km; north is to the right.

FIGURE 30-2.—Bear Crater at Snake River Plains, Idaho. Area of photograph is 3.3 by 2.5 km; north is at the top.

found within the crater. Small (1- to 2-m wide) tubes exist in the pahoehoe basalt of the upper rim at the northern end of Bear Crater but were not found elsewhere. The tubes trend generally downdip; some apparently connect with "North Hole," a 66-m-diameter, flat-floored collapse depression (fig. 30-4).

Surface features on the shield (figs. 30-3 and 30-4) include lava channels, collapsed lava tubes, collapse depressions, and primary flow structures (e.g., pahoehoe ropes). Bear Channel I (fig. 30-4) is a prominent structure originating on the eastern side of the crater. Although it is initially rather wide (222 m) and deep (49 m), it tapers to a narrow (approximately 21 m), shallow (approximately 2.5 m) structure. The channel meanders 2.8 km to the south, where it is buried by younger pahoehoe flows erupted from rifts of Craters of the Moon. The degree of channel meandering increases in its lower portion, where the general gradient is less (fig. 30-5(a)). It is unlikely that most of the channel was a lava tube with a freestanding

roof. Overflow from the channel has created broad, slightly raised levees along some parts of the channel, as indicated in the topographic profiles (figs. 30-5(d) and 30-5(e)). Flow directions obtained from pahoehoe festoons along the channel rim show that surface drainage back into the open channel occurred during the final stages of flow.

Bear Channels II and III may represent a single flow structure originating at the northern part of the vent. The structure apparently was intersected and partly eroded by the younger Bear Channel I. Bear Channels II and III, unlike Channel I, are collapsed lava tubes/lava channels. (In active flows, parts of a lava river may remain open as a channel, whereas other parts of the river may become roofed to form tubes (refs. 30-1 and 30-2).)

The northern end of the Bear Crater complex developed during initial eruptions. Lavas were fluid enough to permit the formation of lava tubes, which carried lava away from the vent to build the early shield structure. Bear Channels I and II were the dominant conduits carrying lava to the southeastern

FIGURE 30-3.—Photogeologic sketch map of Bear Butte Shield volcano, showing the relationship of Bear Crater to the shield and the surrounding lava flows.

part of the shield. The eruptive center shifted south and eventually formed the main part of Bear Crater. Lack of lava tubes associated with this phase indicates that viscosities of the lava increased slightly, although not to such a degree that aa lavas were erupted. The southern end of the shield continued to build by accretion of lavas carried through Bear Channel I and as sheet flows that spilled over the rims of the crater and channel. Crustal foundering of these sheet flows resulted in the formation of at least one collapse depression. Bear Channel I widened during and after active lava flow through slumping and subsidence of its rims. In the final eruptive stage, fountaining produced spatter ramparts of agglutinate along parts

of the crater rim. Withdrawal of lava down the vent produced a crater floor lower than the level of the last formed channel. Gradation subsequently has smoothed and rounded parts of the shield, the crater, and the channels.

ARATUS CA CRATER

Aratus CA is associated with a set of mare ridges approximately 90 km east of the contact between Mare Serenitatis and the highlands. Some mare ridges are interpreted as extrusive, intrusive, or combination extrusive-intrusive features (ref. 30-3). Parts of the crater show different stages of degradation, and, although all of the floor and most of the crater walls are covered with talus, outcrops are exposed discontinuously in at least three horizons in the southern crater rim, indicating that Aratus CA was the site of multiple eruptions. Initial eruptions are interpreted as having formed the older, fusiform part of the crater, at which time the northeast-trending trench was formed. The trench is 3.9 km long and averages 640 m in width. The trench may be interpreted as a flow channel, in which the northern end is roofed as a lava tube (as yet uncollapsed), or the trench may be a structurally controlled collapse depression. The latter interpretation tentatively is favored in this report. In either case, the trench has widened as a result of subsidence along its rims, especially near the juncture with the main crater. Other parts of Aratus CA display fractures that are subparallel to the crater rims, and the fractures probably represent incipient subsidence.

Spillover of lava from the crater rims during an early or intermediate eruptive phase resulted in a lava flow channel (or lava tube, now collapsed) on the southern rim of the crater. The channel is small, averaging approximately 240 m in width, and trends almost due south for a distance of approximately 11 km from the main crater. By comparison, a length of 11 km is common in terrestrial lava flow channels and lava tube systems.

The subcircular crater in the west-central part of Aratus CA is superimposed on other parts of the structure and apparently was formed during the last eruptive stages. The rims and slopes of the feature are softened, and there are fewer large talus blocks than in the other parts of Aratus CA. This crater may represent a pyroclastic eruptive phase, but evidence to support this hypothesis is tenuous. In terrestrial
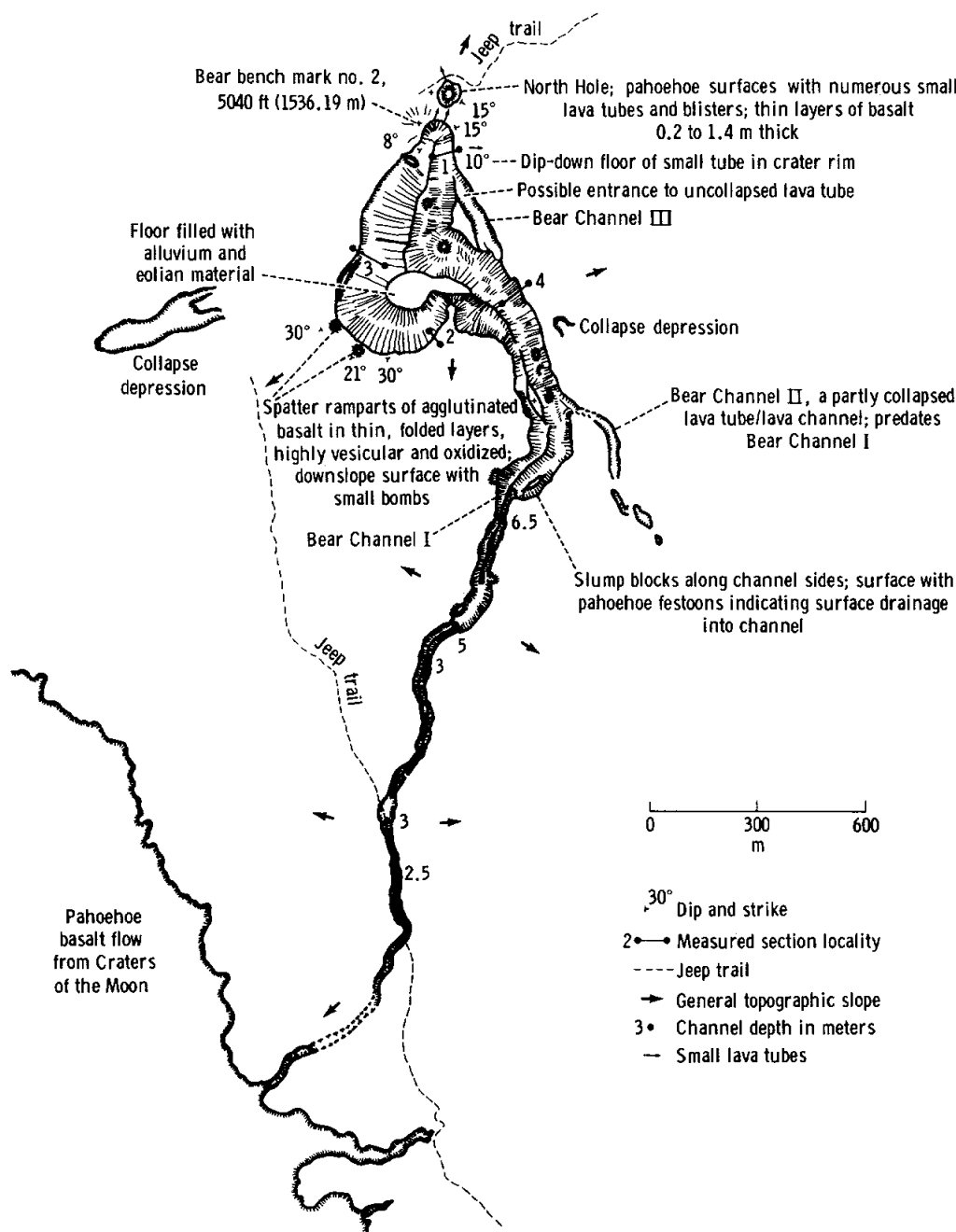
FIGURE 30-4.—Geologic sketch map of Bear Crater.

basaltic eruptions, including Bear Crater, the final eruptive stages are occasionally marked by pyroclastic activity.

The interpretation of the origin and eruptive history for Aratus CA is tentative and subject to revision after more detailed analysis of the Apollo photographs. To make comparisons with terrestrial features and to evaluate the relationships of topography to surface feature morphology, topographic data with an effective contour interval on the order of 5 m are required for selected parts of the lunar surface. Individual flow contacts were not detected during
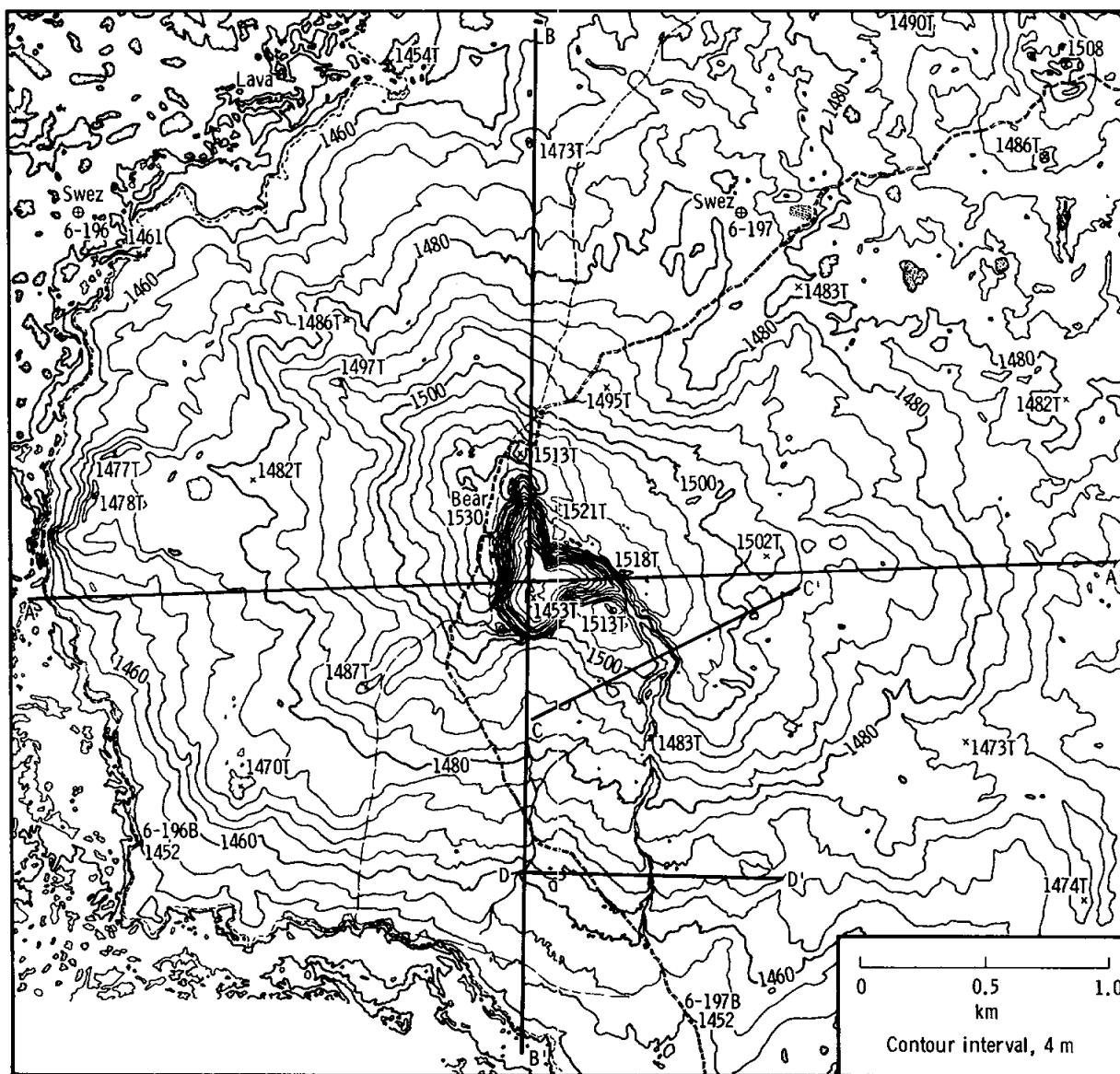
(a)

FIGURE 30-5.—Preliminary topographic map and profiles of Bear Crater and vicinity. Topography by
U.S. Geological Survey. (a) Topographic map.

initial examination of the photographs. However, differences in crater frequencies are apparent on several surfaces in the vicinity of Aratus CA. The unit immediately surrounding the crater (to a radius of approximately 9 km) appears to have fewer craters than do the adjacent surfaces; this lower crater frequency may be an indication of different flow units or of blanketing by pyroclastics.

A direct 1:1-scale comparison between Aratus CA

Crater and Bear Crater is not possible because the lunar feature is approximately 11 times larger; however, other terrestrial basaltic vents are often equivalent in size to Aratus CA. The flow channel extending southward from Aratus CA is comparable in size to many basalt flow channels. In addition, lunar basalt flows that are distinguished clearly by low illumination (e.g., Mare Imbrium flows) are longer than terrestrial basalt flows. This length may be explained,
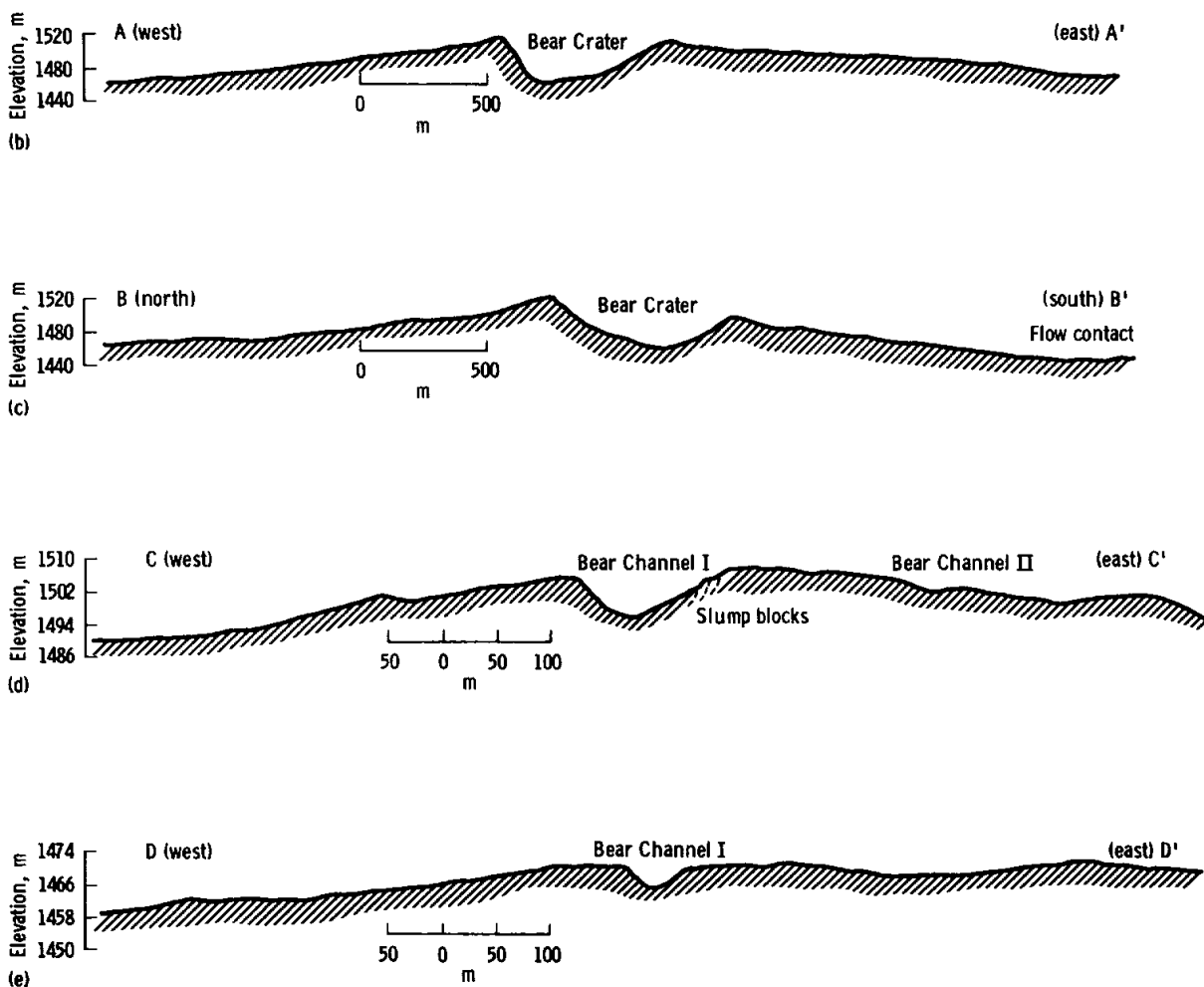
FIGURE 30-5.—Concluded.—(b) Profile A. Vertical exaggeration, 3.25X. (c) Profile B. Vertical exaggeration, 3.25X. (d) Profile C. Based on 1:3000-scale topographic map with 2-m contour interval. Vertical exaggeration, 3.75X. (e) Profile D. Based on 1:3000-scale topographic map with 2-m contour interval. Vertical exaggeration, 3.75X.

at least partly, by the lower viscosity and thermal conductivity of some mare basalts (ref. 30-4). Thus, surface flow features on the Moon are expected to be larger than their terrestrial counterparts.

CONCLUSIONS

In form, structure, and eruptive history, Aratus CA Crater appears to be similar to Bear Crater. The lunar feature is interpreted as a basaltic vent in Mare Serenitatis that resulted from multiple eruptions, including the eruption of basalts with properties allowing the formation of flow channels and lava tubes. The feature has been degraded subsequently to the stage in which most of the outcrops in the crater walls are covered by talus.

PART B

MARE SERENITATIS CINDER CONES AND TERRESTRIAL ANALOGS

David H. Scott[a]

Small volcanic cones with summit craters or breached walls occur in several areas on the Moon. Most of these features have basal diameters of approximately 1 to 2 km and probably are not more than a few hundred meters in height. None have been so clearly photographed, however, as those shown in Apollo 17 metric and panoramic camera coverage of the southeastern margin of the Serenitatis basin. Two cones (A and B in fig. 30-6) approximately 10 km apart project above mare material of Eratosthenian to Imbrian age (sec. 29, part A). Between the cones, small mounds (C, D, and E in fig. 30-6) appear to be alined along the buried extension of a rille (F in fig. 30-6, mostly outside photograph) and are probably volcanic extrusions or domes. In both scale and morphology, these and other lunar cones are remarkably similar to terrestrial cinder cones (figs. 30-7 and 30-8), and their interpreted volcanic origin is not dependent on controversial criteria such as dark halos, smooth rims, or their association with materials assumed to be volcanically derived. Summit craters may be coincidental and the result of impacts on the crests of hills, but their occurrence with cones having breached surfaces or along structural lineaments (or both) strongly favors a volcanic or volcano-tectonic origin. Like their terrestrial counterparts, these cones probably are composite structures made up of interlayered pyroclastic material and lava flows.

Figure 30-7 is a radar image of a part of the San Francisco volcanic field in northern Arizona. Fine details in topography are enhanced by this imagery, which shows the partial burial of a lunar-like rille by a lava flow (A in fig. 30-7), an association more common on the Moon than on Earth. This basalt flow and rille should be compared with those in part D of section 31, figures 31-43 and 31-44. The flow was extruded from the base of a young cinder cone (B in fig. 30-7), and several older flows are faintly visible in

the area, one from a breached crater (C in fig. 30-7) in the eastern part of the photograph.

Figure 30-8 shows cinder cones and basalt flows in the Lunar Crater volcanic field, Nevada. These cones also are alined along structural breaks (A, B, and C in fig. 30-8) and are associated with small, scattered mounds (D and E in fig. 30-8) similar to those of figure 30-6; there are some slight differences, however. No obvious flows issue from the lunar cones, and they appear to be more subdued than some of the terrestrial forms and have no sharp breaks between
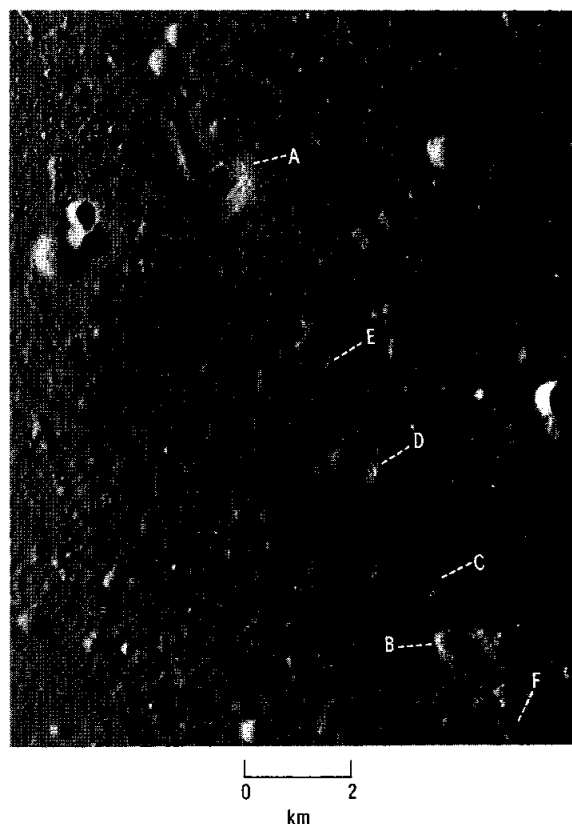
FIGURE 30-6.--Lunar volcanic features in Mare Serenitatis. Cinder cones (A and B), volcanic mounds (C, D, and E), and a rille (F) (Apollo 17 panoramic camera frame AS17-2317).

[a]U.S. Geological Survey.

FIGURE 30-7.—Terrestrial cinder cones in Arizona. Lava flow in a rille (A), basalt extruded from the base of a cone (B), and flow from a breached crater (C) (U.S. Geol. Survey radar image).

FIGURE 30-8.—Terrestrial cinder cones in Nevada. Breached cones along a fracture (A, B, and C) and small cinder mounds (D and E) (U.S. Geol. Survey photograph).

their bases and the surrounding terrain. It is possible that the Serenitatis lavas were more fluid and that flow-front scarps did not form. The cinder cones of figure 30-8 are approximately 10 000 yr old or less, whereas the ages of those in figure 30-6 are probably on the order of several billion years. That they are somewhat more degraded is understandable even though the erosion of these particular lunar features may be mainly attributable to the relatively slow process of mass wasting and meteoroid bombardment.

Many analogs exist between lunar and terrestrial features but generally at grossly different scales. The cinder cones and associated features illustrated in this paper are similar in size; thus, morphologic comparisons are more readily made. Such factors as the lunar gravity, probably lower volatile content of the magma, and lack of an atmosphere on the Moon must

be considered, however, as these affect the interior flow properties and the exterior ballistics of the erupting lava. McGetchin and Head (ref. 30-5) concluded that the net effect of these variations is a much wider distribution of ejecta around a volcanic source on the Moon than on Earth. The terrestrial-like cinder cones in southeastern Mare Serenitatis thus show that for the formation of the cones and mounds, the dynamic pressure or volatility (or both) of these eruptions must have been lower than for comparable terrestrial features.

PART C

SOME VOLCANIC AND STRUCTURAL FEATURES OF MARE SERENITATIS

W. B. Bryan[a] *and Mary-Linda Adams*[a]

Relationships between volcanic and structural features along the southern edge of Mare Serenitatis can be examined in detail because of the favorable low-angle lighting in the Apollo 17 photography. Metric camera photographs enlarged 2X were observed at 1X or 6X magnification. Relief was estimated from parallax differences, assuming a nominal spacecraft elevation of 110 km and a mean photographic scale of 0.7 km/mm.

This section includes a summary of observations of (1) contact relations between the dark border material and the central mare fill, (2) a late-stage lava flow with associated cinder cones, and (3) certain structural features related to the development of the mare basin and its associated volcanic landforms. The section is concluded with a chronologic summary of volcanic and structural events that we believe are critical to understanding the development of Mare Serenitatis.

DARK MARGIN AND CENTRAL MARE FILL

In figure 30-9, the contact relation between the light central fill and the marginal dark border fill is clearly shown. In addition to the obvious albedo difference, a contrast in surface texture is evident. Impact cratering and ridges on the light central fill appear crisp, whereas many craters, ridges, and rilles in the dark border appear softer and more subdued. The boundary between the light and dark fill corresponds to a distinct break in slope and has the general character of a shoreline. The relatively flat, smooth surface of the light-colored material enters small embayments in the inclined, undulating surface of the dark border material. A crater, approximately 10 km in diameter (lower center, fig. 30-9), is partly inundated by the light central fill, which has left a

"high lava mark" on the inner wall of the crater. No evidence of fracturing or buckling of mare material is apparent along the albedo boundary, as would be expected if it were a structurally produced hinge line.

The dark fill in and near the Apollo 17 landing site is topographically lower than the dark border fill on the southern side of Mare Serenitatis. We have been unable to identify faults of sufficient magnitude to account for this elevation difference. The dark mantle on highland material in this area is not as conspicuous in these low-Sun-angle photographs as it is in the

0   20
km
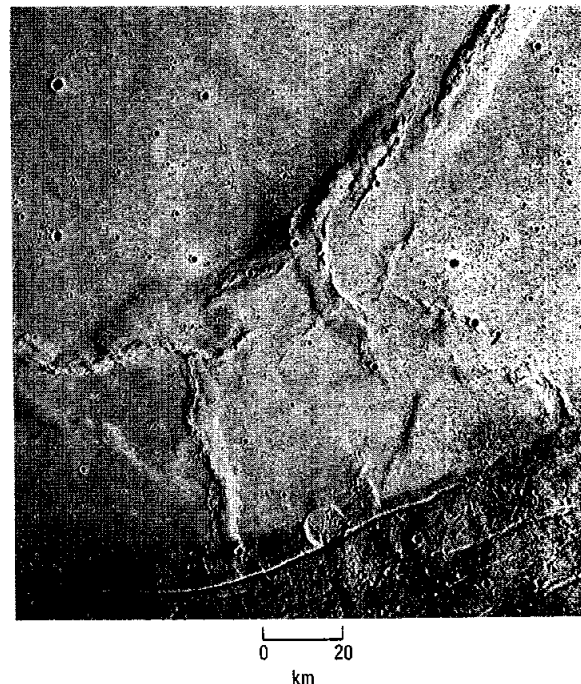
FIGURE 30-9.—Southern margin of central light fill in Mare Serenitatis. Note sharp to degraded tensional faults in dark border material, concentric and radial wrinkle ridges in light mare material, and subdued extension of radial wrinkle ridges into dark border material (Apollo 17 metric camera frame AS17-0451).

---

[a]Woods Hole Oceanographic Institution.

Apollo 15 photographs, which were made at a higher Sun angle.

LAVA AND EXTRUSIVE VENTS
EAST OF DAWES CENTER

On the southeastern side of Mare Serenitatis (fig. 30-10), graben fractures in the dark border are buried beneath lighter colored mare material, evidently a late-stage flow, which appears to have originated outside the mare and flowed down the sloping dark border surface, following a shallow depression in this surface. This flow appears on the lower left side of figure 30-10. Howard et al. (part A of sec. 29) have called it the Dawes basalt. Two rille-like features on its surface converge on a line of four vents 1 to 2 km in diameter.

Two of these vents (B in fig. 30-10) are cones distinct in their morphology from the many small impact craters of similar diameter adjacent to them on the Dawes basalt surface. The northern cone is breached on its downslope side, as would be expected of a cone serving as a vent for lava flow. A very faint, rille-like channel can be traced for approximately 10 km downslope from this cone. Both this cone and the larger southern cone are distinct, raised mounds with rounded rims and crater floors that are above the general surface of the surrounding basalt. Internal and external slopes are approximately equal. These features are typical of terrestrial volcanic cinder cones, in which the cone is a positive addition of material composed of ejected debris around a relatively small central vent. In contrast, the nearby small impact craters are steep-walled, conical pits with sharp rims and outer walls sloping much more gently than the inner walls; they are predominantly negative relief features representing excavation and dispersion of surface material. Applying these criteria, we feel confident that these two cones are extrusive volcanic features. The larger southern cone, approximately 1.5 km wide at its base and approximately 300 m high, is almost identical in size and shape to Sunset Crater in Arizona (ref. 30-6). The northern cone is slightly smaller, measuring approximately 1 km across its base and approximately 200 m high. A smaller cone approximately 5 km to the northwest may be a small satellite to this larger cone. Two irregular, pitted mounds between the northern and southern cinder cones may also be vents but do not show well-defined conical morphology.


```
L_____J
0                20
        km
```

FIGURE 30-10.—Southeastern margin of Mare Serenitatis, showing margin of lava flow mantling dark borders (A), possible breached cinder cones (B), and collapsed and partly buried lava tube (C) (Apollo 17 metric camera frame AS17-0447).

The Dawes basalt can be distinguished from the adjacent dark mantle by its smoother surface, in which it resembles the central fill of Mare Serenitatis. The surface of the flow is slightly convex, with a subtle break in slope coinciding with the change from the smoother Dawes basalt surface to the more hummocky surface of the dark mantle. Albedo differences are slight, but the Dawes basalt appears to be slightly lighter in color. The boundaries of the Dawes basalt shown by Howard et al. (part A of sec.

29, fig. 29-5) are in reasonable agreement with the boundary indicated as "A" in figure 30-10. Dawes impact debris tends to obscure contact relations along the western side of the Dawes basalt, and contact relations between the Dawes and the light central Serenitatis fill are also extremely subtle.

The Dawes basalt is cut by several sharp rifts or lines of small pit craters that follow the general trend of the buried graben fractures. A larger, elongated pit on the left side of the lava flow is partly filled by ponded lava. It is alined with a small depression upslope and with irregular, rough features downslope that resemble partly collapsed domes or vent structures (C in fig. 30-10). These features may represent a large, partly collapsed lava tube that could be a source of some of the central mare fill.

STRUCTURAL FEATURES

Graben-like rilles are conspicuous in the dark border material (fig. 30-9). One of the sharpest and freshest of these grabens can be traced across the southern wall and floor of the large, partly drowned impact crater on the light-dark "shoreline," and thus is younger than the crater. In contrast, the blurred and degraded appearance of other grabens suggests that they are older features. These grabens crosscut highland material but are truncated or buried by the light central fill of Mare Serenitatis, as discussed in part A of section 29.

Wrinkle ridges are prominent in the light central fill of Mare Serenitatis (fig. 30-9). These have been discussed by Bryan (ref. 30-7) and by Howard and Muehlberger (part C of sec. 31), who attribute them to compressional deformation. There is a distinct change in the character of wrinkle ridge deformation between the light fill and dark border material where the radial ridges cross the light-dark boundary. Within the light fill, the ridges are broad, convex swells, commonly topped by intensely crumpled, sharp ridges. Some sharp ridges also appear to develop independently of preexisting swells. However, the sharp crumbling terminates abruptly at the albedo boundary, and the ridges continue into the dark border as low, undulating swells. Within the light central fill, many of the sharp ridges have a saw-toothed or zigzag pattern resulting from tilting and rotation of distinct blocky crustal units measuring 1 to 4 km on a side.

Laboratory experiments on fracturing of basalt (ref. 30-8) have shown that induced fractures tend to follow preexisting zones of weakness in the rock. This principle may explain both the large-scale and fine-scale patterns of fracturing, as well as the difference in response of the light and dark fill. Broad welts probably develop above preexisting zones of deformation in older buried mare fill, because less energy is expended in this way than in deforming previously undisturbed crust, especially if the same stress pattern continues to operate. For the same reason, the more intense crumpling produced by continued deformation is mainly localized along the crests of the broad welts. In detail, the intense crumpling developed by displacement around crustal blocks bounded by fractures or joints spaced at 1 to 4 km. The existence of these coherent blocks suggests that wrinkle ridge deformation took place before impact events had brecciated the surface and created a deep regolith. The absence of sharp, angular ridges in the dark border material may indicate that it consists of a relatively deep friable or highly brecciated regolith, which would tend to dissipate deforming stresses over many small-scale intergranular fractures.

VOLCANIC AND STRUCTURAL CHRONOLOGY

The sharp and relatively straight light-dark boundary relationship along the southern edge of Mare Serenitatis is difficult to explain if the dark material is assumed to be a younger deposit that covers the lighter fill. If the dark material consisted of young lava flows, these should produce a much more irregular, scalloped boundary, which is not observed. If the dark material were a young ash deposit, the boundary should be much less distinct. The shoreline relation, in which light material embays the dark material, indicates that it onlaps a preexisting sloping surface on the dark border material. The most reasonable interpretation is that the central, light-colored material is a younger mare fill that accumulated in a depression formed by isostatic subsidence of the older, dark fill. Although many workers have stated that the dark margin is relatively young, Howard et al. (part A of sec. 29) have reviewed the assumptions leading to this interpretation and also conclude that the dark margin represents the earliest filling of Mare Serenitatis. They note the similarity in color and albedo of the dark surfaces at the Apollo 11 and 17 landing sites and along the southern margin of Mare Serenitatis; this similarity in appearance also

suggests similar composition and age of surface material at all of these locations.

The distinctly lower elevation of the dark border material at the Apollo 17 landing site compared to that of the southern side of Mare Serenitatis suggests that the dark material did not well up within the mare basin and overflow into adjacent valleys and into Mare Tranquillitatis. It seems more likely that the dark material originated in the highland valleys and flowed into the mare, much like the more recent Dawes basalt. These many independent flows would then have established their own local base levels where they are ponded or deflected by intervening highland barriers.

During and following this initial basin filling, collapse of the central part of the mare caused local marginal tension, producing a series of arcuate graben faults. Low swells and crenulations radial to the mare center may have also formed at this time. Impact events created a deep regolith on the dark border material. Filling of the mare basin continued, but the source and mechanism remain obscure. The Dawes basalt may represent a late-stage contribution to this fill. This light fill onlapped the sloping dark border, drowning preexisting grabens and impact craters. A "high lava mark" present locally suggests the occurrence of some drainback from the margins, implying vents within the mare, thermal shrinkage, or an early subsidence event shortly after ponding of the lava. Continued collapse of the central part of Mare Serenitatis caused compressional deformation of the crust, first forming low linear swells and welts, then more intense crumpling of the crust along crests of the welts. Some of this deformation extended into the dark margin, possibly localized by preexisting zones of weakness in the old fill. Differences in the response of the light and dark material to deforma-

tional stresses indicate that the dark margin is much more incoherent than the light fill, which tends to fracture around distinct blocky units. This difference suggests that the light fill was relatively fresh, brittle rock at the time of deformation, whereas the dark border may have been much more brecciated by impact events over an extended period.

Late-stage gas eruptions in the Taurus-Littrow area may have redistributed brecciated dark mantle as ash, as suggested by El-Baz (ref. 30-9). Some such mechanism seems necessary to explain the distribution of dark mantle over highland areas, but we have not identified cinder cones like those on the Dawes basalt. Possibly, much of this material was distributed by impact events. Although we do not exclude the possibility of volcanic activity associated with wrinkle ridges, the morphology of the ridges in the southern part of Mare Serenitatis is indicative of warped, crumpled, and broken surface crust rather than of freshly extruded volcanic material.

CONCLUSIONS

The Apollo 17 metric camera photographs provide definitive evidence for a sequence of volcanic and structural events associated with the development of Mare Serenitatis. These events are relevant to the interpretation of other orbital science experiments and to samples of dark border material collected at Apollo landing sites. Cinder cones associated with volcanic vents on the Dawes basalt are similar in size and shape to typical terrestrial cinder cones. Detailed morphology of deformational features produced by both tensional and compressional stresses suggests distinct differences in physical properties of the central light fill and dark border material.

PART D

"D-CALDERA": NEW PHOTOGRAPHS OF A UNIQUE FEATURE

Farouk El-Baz[a]

A unique D-shaped structure at latitude 18°40' N, longitude 05°20' E was discovered during the Apollo 15 mission within one of several smooth, dark patches in the hilly region between Montes Haemus and Montes Apenninus. Its unusual shape and interior morphology have generated much interest among selenologists (refs. 30-10 and 30-11). Orbital photographs and visual observations (sec. 28) were planned for the Apollo 17 mission to acquire additional information pertaining to the setting and detailed characteristics of this structure. Photographs of the area were obtained by using the metric and Hasselblad cameras (with both color and high-speed black-and-white film); no panoramic camera photography of the region was planned because the area had been adequately covered with the same camera during the Apollo 15 mission. The purpose of this report is to give a brief description of the Apollo 17 photographs of the D-shaped structure and its surroundings.

The patches of dark material between Montes Haemus and Montes Apenninus are separated by hilly and rugged units that are segmented by fractures radial to Mare Imbrium. Two of these fractures bound the area of the D-shaped structure. The Apollo 17 low-Sun photographs of the area indicate that a horst, at least 150 km long and 30 km wide (fig. 30-11), has been uplifted relative to the surroundings. The fault on the western side of the horst continues southward into eastern Mare Vaporum, as suggested by a prominent mare ridge system (fig. 30-11).

The dark patches filling the valleys between the foothills of the mountains have been previously mapped as Imbrian mare material (ref. 30-12). Flow structures and collapse depressions evident in the Apollo 17 low-Sun photographs further suggest that they may be basalt flows (fig. 30-12(a)). Thus, the units are most probably volcanic in origin and younger than the surrounding and underlying highlands (ref. 30-13).

The D-shaped structure is a depression, 2 km wide and 3 km long. The feature is approximately 300 m deep and displays a raised rim that is 1.5 km wide. The floor is occupied by two different morphological units:

1. A flat unit that is subdivided into two albedo units, gray and white; the latter forms an annulus around the gray unit (ref. 30-11). Apollo 17 visual observations (sec. 28) and color photographs indicate that the whole floor has a bluish tone.

2. Approximately 50 disconnected, smooth, bulbous structures of various sizes; these structures produce a blister-like appearance.

There is a 1-km-diameter crater west of the D-shaped structure that, before the Apollo 17 mission, was believed to have a dark halo. The Apollo 17 low-Sun photographs indicate that the darkening is probably due to slope effects; the crater is near the border of an 18-km-wide dome that encircles the D-shaped structure (fig. 30-12(b)) and that appears to have fewer craters on it than on the surrounding mare (fig. 30-12(c)). It is proposed that the D-shaped structure is a collapse caldera atop an extrusive volcanic dome. It is further proposed to adopt the informal name "D-Caldera" to designate the feature.

From the preceding description, the following sequence of events may be reconstructed to explain the formation of observed features (fig. 30-13).

1. The Imbrium event clearly affected the triangular-shaped region between Montes Haemus to the east and Montes Apenninus to the west. Pre-Imbrian terrain was faulted, most of the major faults being radial to the Imbrium basin. Deposition of Imbrium ejecta is evidenced by the linear ridge units, also radial to the basin. The ejecta is probably kilometers thick because it masks preexisting structures (fig. 30-13(a)).

2. Faulting must have continued as a result of adjustment of the crust after formation of the Imbrium basin. At some later date, basaltic lavas migrated to the surface along the fractures and formed relatively thin mare patches; older highland

---

[a]National Air and Space Museum, Smithsonian Institution.
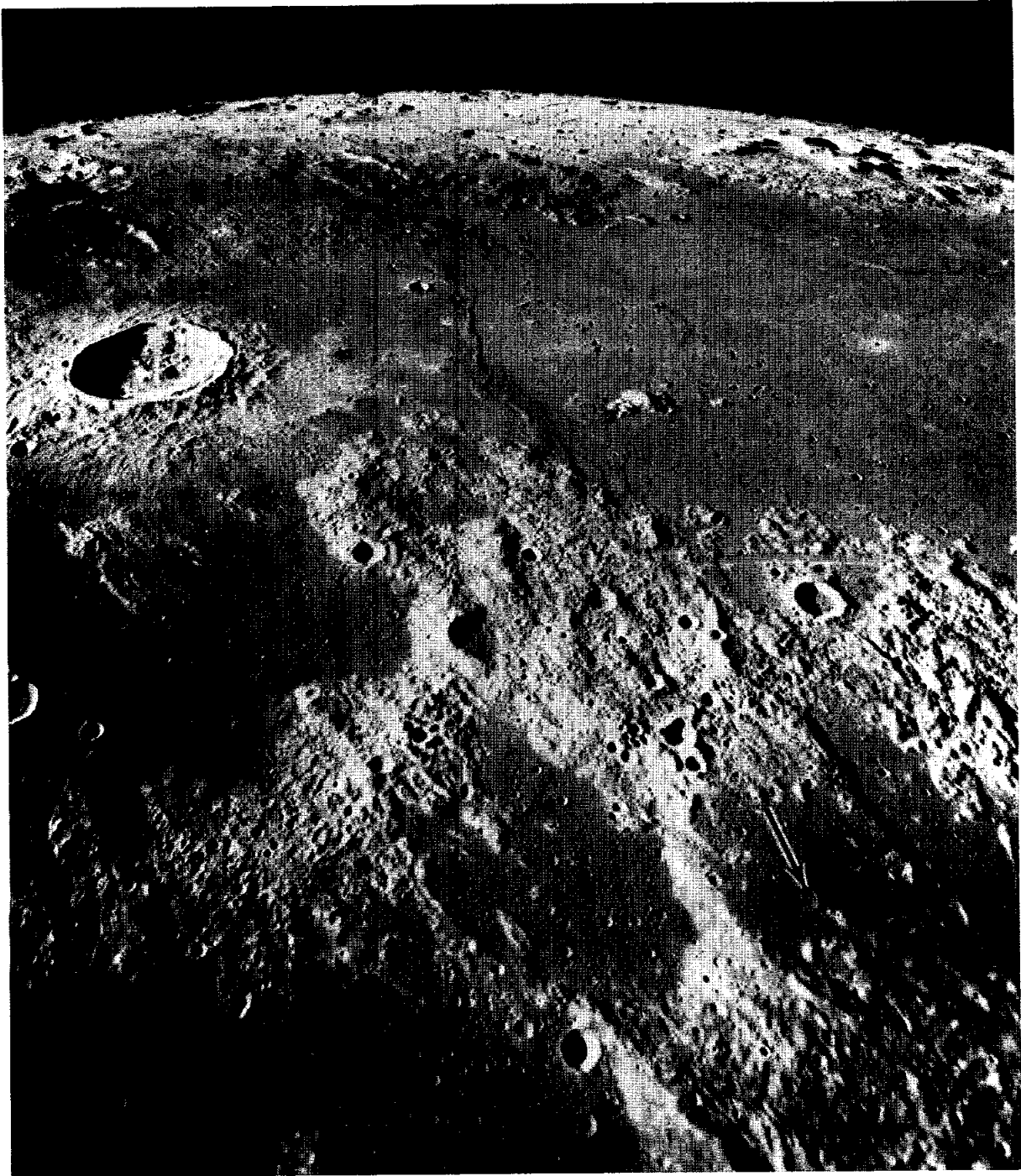
FIGURE 30-11.—Oblique view (looking southward) showing most of Mare Vaporum (upper right) and the 40-km-diameter crater Manilius (upper left). Four of the dark patches of mare material between Montes Haemus and Montes Apenninus are in the lower half of the photograph. The D-shaped structure is indicated by an arrow. The fault that separates the two patches in the lower right continues into Mare Vaporum, as indicated by the mare ridge in the upper middle portion of the photograph (Apollo 17 metric camera frame AS17-1671).
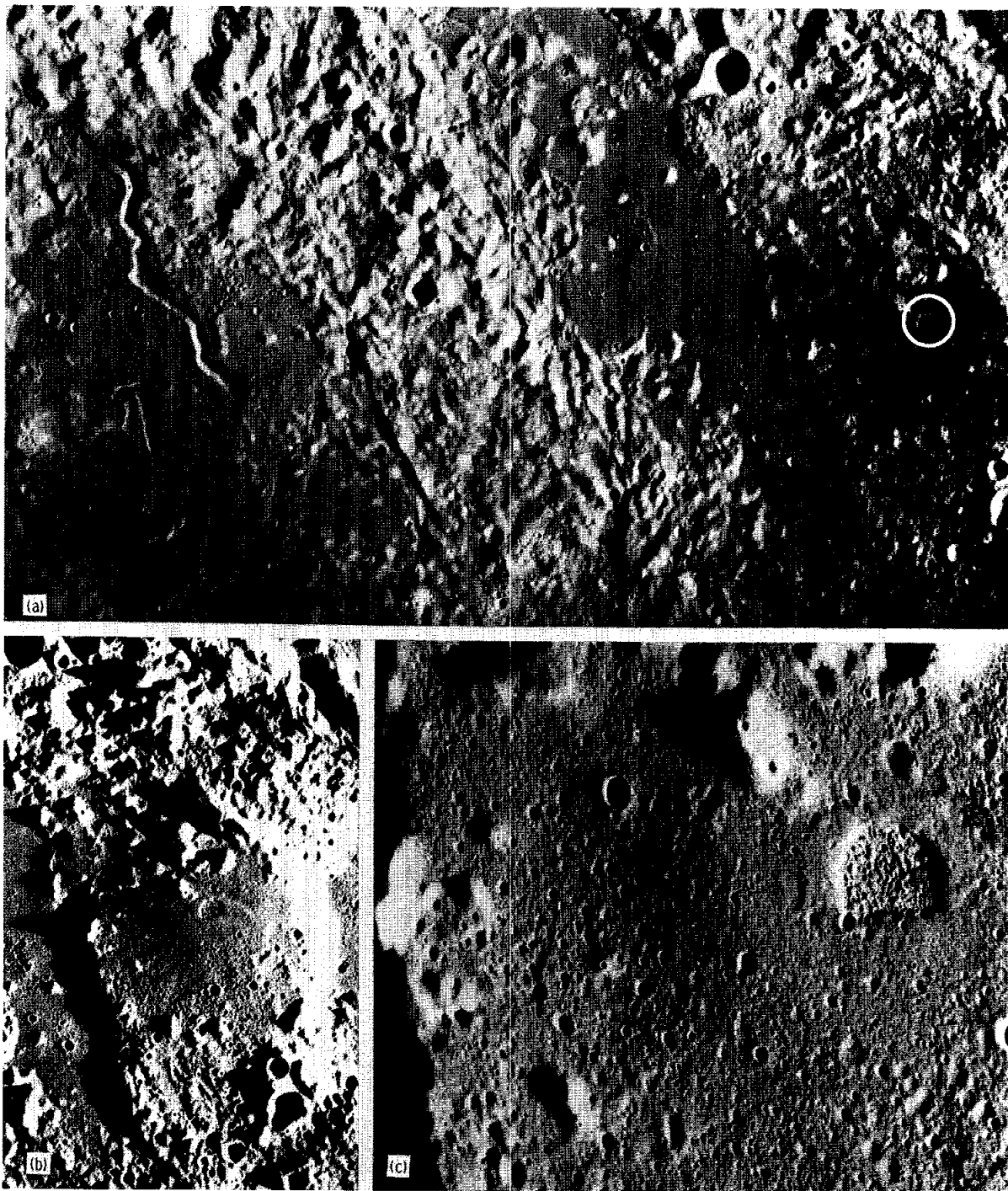
FIGURE 30-12.—Three views of the D-shaped feature. (a) Dark patches atop highland units have flow scarps and mare ridge structures (right of center) and collapse depressions and flow channels (left edge) similar to basaltic lava flow. The straight part of the D-shaped structure (circled) is 3 km long (Apollo 17 metric camera frame AS17-1822). (b) Low-Sun-angle view of the area surrounding the D-shaped structure, showing the dome that encircles it (Apollo 17 metric camera frame AS17-1237). (c) The small, bulbous domes in the floor of the D-shaped depression are shown in this view taken during the Apollo 17 mission using the Hasselblad camera with very-high-speed black-and-white film. The dome that encircles the structure displays fewer craters than does the surrounding mare surface (AS17-154-23672).
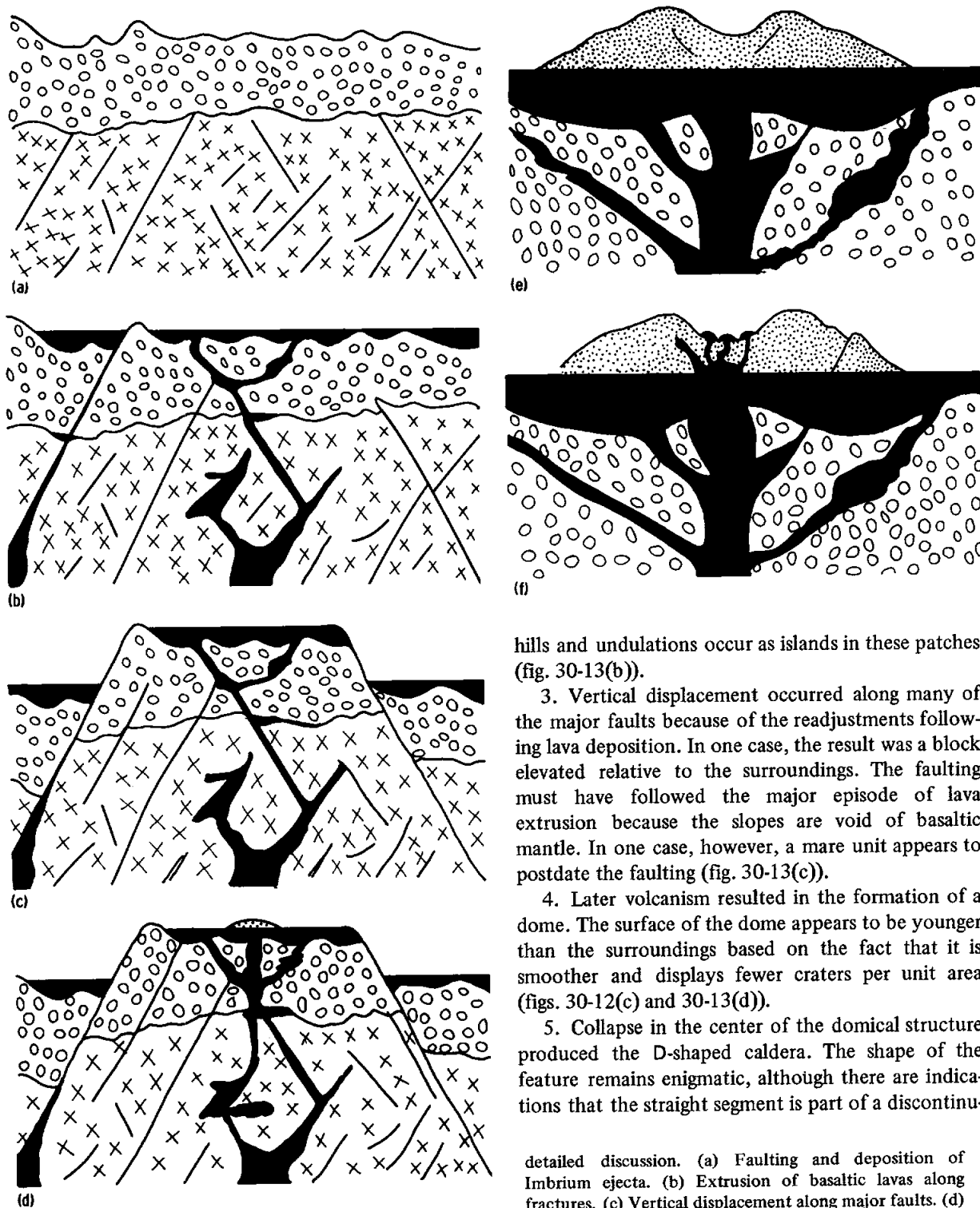
FIGURE 30-13.—Schematic illustration of the stages of faulting and subsequent volcanism that led to the formation of the D-shaped collapse caldera. See text for

hills and undulations occur as islands in these patches (fig. 30-13(b)).

3. Vertical displacement occurred along many of the major faults because of the readjustments following lava deposition. In one case, the result was a block elevated relative to the surroundings. The faulting must have followed the major episode of lava extrusion because the slopes are void of basaltic mantle. In one case, however, a mare unit appears to postdate the faulting (fig. 30-13(c)).

4. Later volcanism resulted in the formation of a dome. The surface of the dome appears to be younger than the surroundings based on the fact that it is smoother and displays fewer craters per unit area (figs. 30-12(c) and 30-13(d)).

5. Collapse in the center of the domical structure produced the D-shaped caldera. The shape of the feature remains enigmatic, although there are indications that the straight segment is part of a discontinu-

detailed discussion. (a) Faulting and deposition of Imbrium ejecta. (b) Extrusion of basaltic lavas along fractures. (c) Vertical displacement along major faults. (d) Formation of dome by late-stage extrusion. (e) Formation of D-shaped caldera by collapse. (f) Formation of bulbous floor structures by minor extrusions.

ous fault in the mare unit (fig. 30-12(b)). It is probable that the depression would have been circular had that fault not existed (fig. 30-13(e)).

6. The collapse appears to have been followed by numerous small extrusions that formed the bulbous structures in the caldera floor (fig. 30-13(f)). These positive features appear to be small domes, and several seem to have repeated the collapse sequence as they display apex craters (ref. 30-11).

The preceding sequence, which is deduced from the characteristics of the region studied, may be pertinent to lunar volcanic processes that result in the formation of small-scale domes and collapse depressions.

PART E

ERATOSTHENIAN VOLCANISM IN MARE IMBRIUM: SOURCE OF YOUNGEST LAVA FLOWS

Gerald G. Schaber[a]

Orbital photographs taken at low-Sun illumination during both the Apollo 15 (ref. 30-14) and Apollo 17 missions have provided excellent data on the lava flows in southwestern Mare Imbrium. These photographs have been used recently to present a detailed photogeologic evaluation of these flows and their role in mare volcanism of Eratosthenian age in the basin (ref. 30-15). Eruption of these flood basalts apparently took place in at least three major episodes with suggested dates of 3.0 ± 0.4 billion years (phase I), 2.7 ± 0.3 billion years (phase II), and 2.5 ± 0.3 billion years (phase III) using the mare age-dating method described by Soderblom and Lebofsky (ref. 30-16) and recent data by Soderblom and Boyce (ref. 30-17).[1]

_____

[a]U.S. Geological Survey.

[1]The method involves visual examination of an orbital photograph to determine the maximum diameter D_s of craters the internal slopes of which have been reduced to slopes less than the Sun elevation angle S_s. Using the Soderblom (ref. 30-18) model of small crater impact erosion, measurements of D_s are converted to an equivalent diameter D_L of a crater eroded to an interior slope of 1° under the same flux that has eroded a crater of diameter D_s to a slope of S_s. Values of D_L are considered synonymous with relative age, which is directly proportional to the total number of craters that have accumulated on the surface. The D_L values measured for the three phases of Eratosthenian basalts in Mare Imbrium are 235 ± 20, 175 ± 5, and 160 ± 5 m, respectively. The D_L value for the youngest flows is in agreement with that of Boyce and Dial (part C of sec. 29).

The lavas of the Eratosthenian eruptive phases flowed directly toward the center of the Imbrium basin with the earliest (phase I) materials pooling, in what must have been the lowest portion, near the breached southeastern rim of the Sinus Iridum Crater (fig. 30-14). Present topography of the basin shows that this region is still the lowest point (ref. 30-20). The average surface slopes from the volcanic source region southwest of Euler Crater to the basin center are estimated to be between 1:100 and 1:1000. Lavas assigned to the three eruptive phases extended for 1200, 600, and 400 km, respectively, indicating a marked decrease in lava volume available for extrusion between 3.0 and 2.5 billion years. Flow thicknesses and areal extent indicate that a minimum of 4.0×10^4 km^3 of mare material covering an area of 2.0×10^5 km^2 was probably deposited in the Imbrium basin during this 0.5-billion-year interval.

The youngest lavas (phase III) have been traced to a possible source fissure at latitude 22°50' N, longitude 31°20' W (fig. 30-15, lower left). A very-low-albedo, linear cinder cone complex on the southeastern end of the island Euler β trends northeast-southwest and may be structurally related to the inferred eruptive vent (fig. 30-16). The presence of a distinct linear fissure cannot be visually documented on the Apollo photographs, but its approximate location and northeast-southwest trend were suspected after photogeologic mapping showed that the phase III flow lobes narrow sharply southwestward
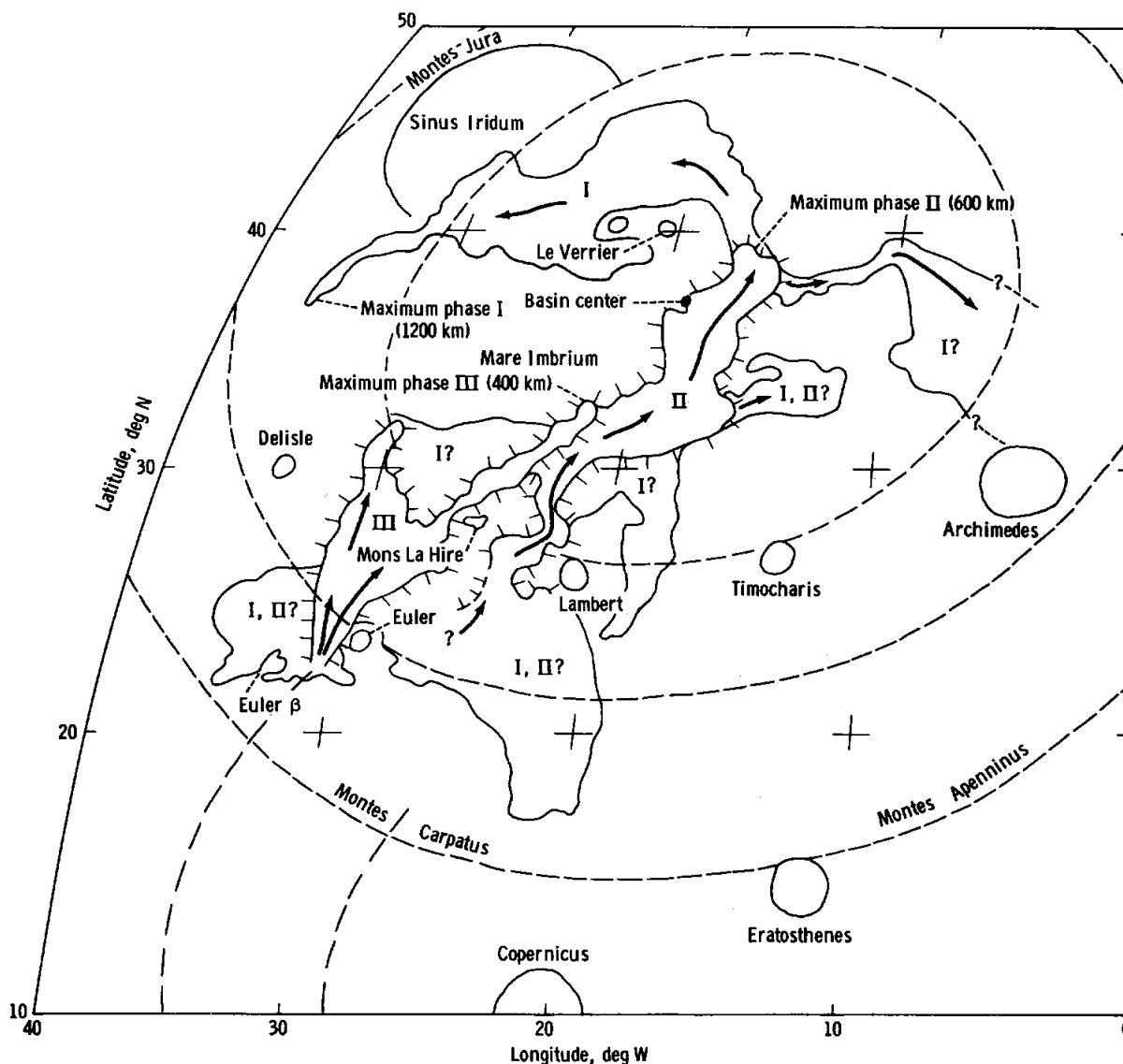
FIGURE 30-14.—Areal distribution of earliest (phase I) to most recent (phase III) Eratosthenian-age
mare material in the Imbrium basin. Arrows indicate direction of flow; hachures point downslope
and indicate flow-scarp limits of each phase. Dashed lines represent basin ring structures. (Base
after ref. 30-19).

and terminate between the crater Euler and the
dark-mantled terra island Euler β (fig. 30-15). The
absence of such distinct flow scarps south of this
region suggests that the fissure source is nearby but
possibly obscured by the lava flows. The pattern of
flows at their narrowest point suggests that the fissure
vent may have been on the order of 20 km in length.

Islands south of the crater Euler are, for the most

part, dark-mantled premare terra, and their distribu-
tion appears to be controlled by normal faults (fig.
30-17). Several low-albedo, probably volcanic com-
plexes were photographed by the Apollo 17 crewmen
in this region (figs. 30-18 and 30-19). It has been
suggested (ref. 30-15) that virtually all the Eratos-
thenian-age mare mapped in the Imbrium basin may
have had a single eruptive source region bounded by
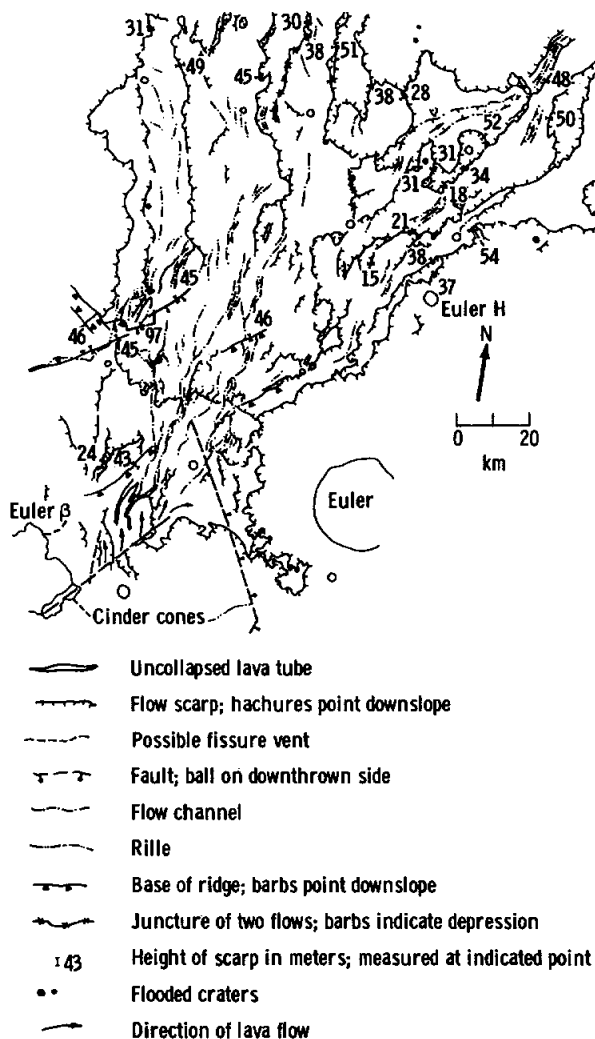
FIGURE 30-15.—Photogeologic map of the lava flows and probable source vent of the phase III eruptives in southwestern Mare Imbrium, west of the crater Euler. Mapped on photomosaic composed of Apollo 15 metric camera photograph AS15-1701 and Apollo 17 metric camera photograph AS17-2295. (See fig. 30-21(a).)

Legend:

- Uncollapsed lava tube
- Flow scarp; hachures point downslope
- Possible fissure vent
- Fault; ball on downthrown side
- Flow channel
- Rille
- Base of ridge; barbs point downslope
- Juncture of two flows; barbs indicate depression
- ₁43 Height of scarp in meters; measured at indicated point
- •• Flooded craters
- Direction of lava flow

FIGURE 30-16.—A mosaic of Apollo 15 Hasselblad photographs AS15-95-12931 and 12932 showing Euler β, a dark-mantled island 75 km west-southwest of the crater Euler. The "X" indicates a low-albedo, linear cinder cone complex. (See figs. 30-14 and 30-15 for more detailed location.)

latitudes 18° to 23° N and longitudes 28° to 32° W (fig. 30-17). The locus of this volcanic province may have been determined by the intersection of major ring faults (fig. 30-14) concentric to the Imbrium basin and to the poorly defined basin centered about the crater Copernicus (ref. 30-19). Latham et al. (ref. 30-21) have recently identified nine currently active lunar seismic areas with focuses at 600- to 1000-km depths. The epicenter of one of these regions coincides with the proposed fissure vent described here.

This location is probably not fortuitous; at the time of Eratosthenian volcanism in the Imbrium basin, basin ring fractures perhaps acted as conduits for the magmas generated at depth. Partial melting may still be taking place on a small scale at depths of 1000 km. Stresses resulting from this process may accumulate in the basin ring fractures and may be released by cyclic tidal forces, which Latham et al. (ref. 30-21) suggest as a triggering mechanism of internal lunar seismicity.

Seven of the nine active lunar seismic regions suggested by Latham and his colleagues are associated with basin rings or regions of intersection of two or more basins. This association appears to fit a relationship between concentric basin structures and major dark mantle/mare plateau volcanic provinces (ref. 30-22).

Photogrammetric measurements of the phase III flow scarps indicate common average heights of 30 to 35 m with a range over a variety of flows from 10 to 63 m (fig. 30-15). Detailed study of the relationships between flow lobes and associated mare ridges indicates that not all ridges completely postdate the eruptive events. Several of the ridges existed on the preflow surface, although with less complexity and lower topographic profile. The presence of leveed flow channels at mare ridge crests and ponding of lava against preflow mare ridge slopes are direct evidence of this relationship (fig. 30-20). The leveed channels were probably created by rapid, constricted flow during overflow of a lava lake ponded behind the

0   10   20
km
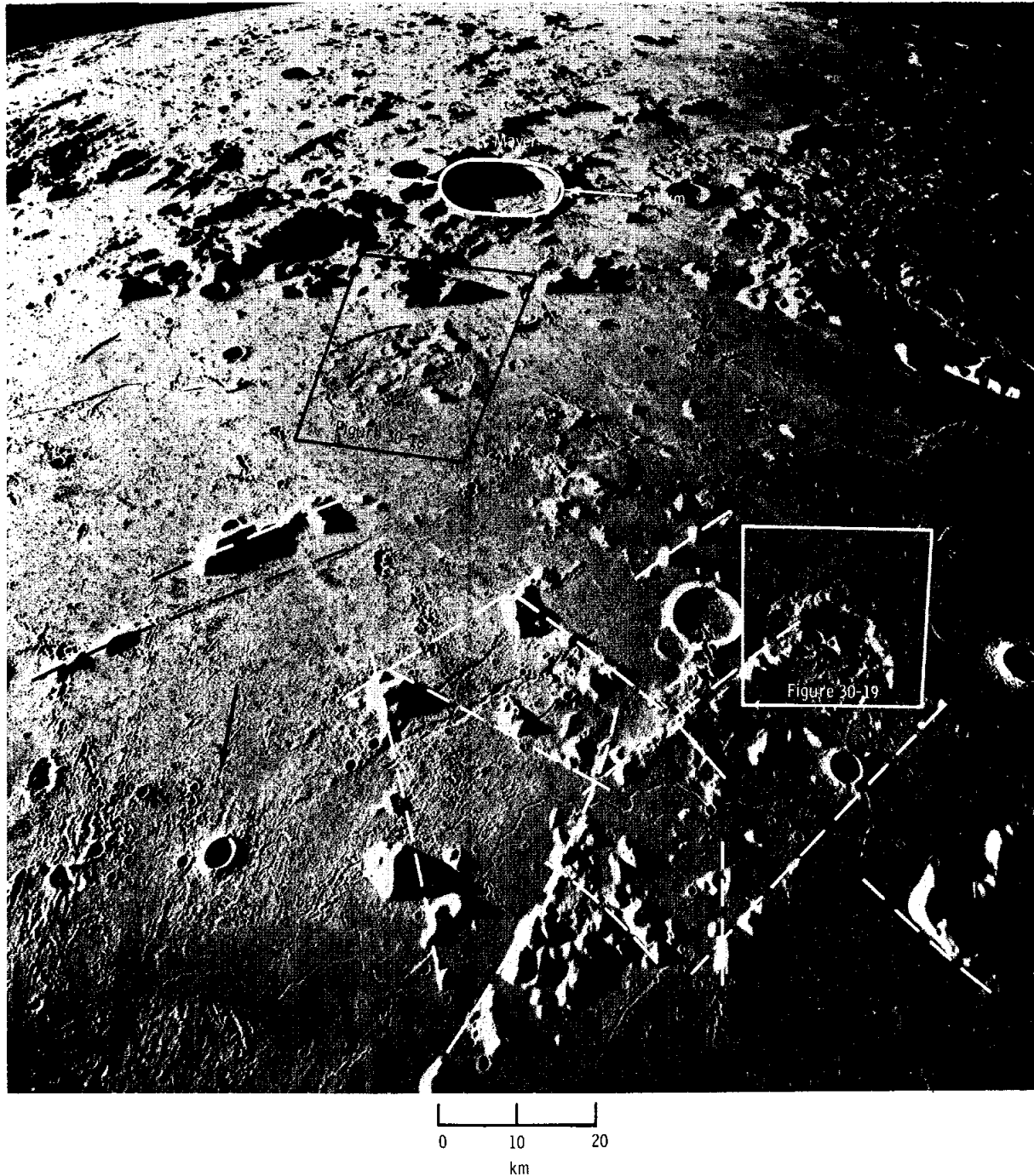
FIGURE 30-17.—South-looking oblique photograph showing the suggested regional volcanic source area for all Eratosthenian-age mare lavas in the Imbrium basin. Structural control of mare islands is indicated by dashed lines; areas of figures 30-18 and 30-19 are indicated (Apollo 17 metric camera frame AS17-2450).
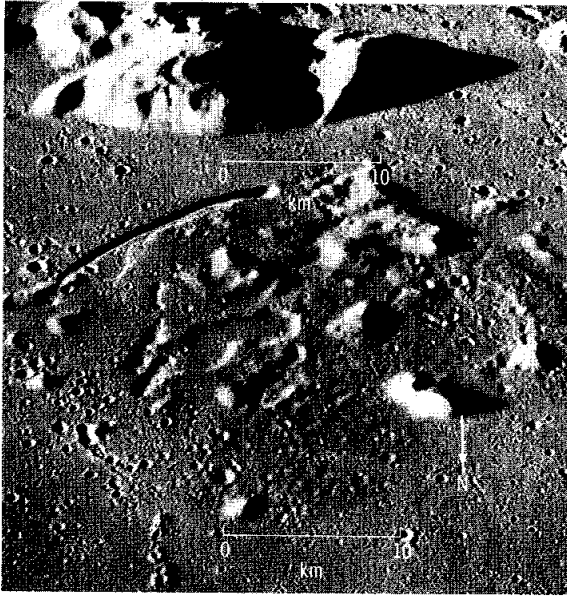
FIGURE 30-18.—Nikon 35-mm photograph showing a low-albedo volcanic plateau within the regional volcanic source province of the Eratosthenian lavas in the Imbrium basin (AS17-155-23736). See figure 30-17 for location of this area in the regional volcanic province.

FIGURE 30-19.—Nikon 35-mm photograph showing arcuate volcanic cinder cone complex with associated lava flows (AS17-155-23738). See figure 30-17 for location of this area in the regional volcanic province.

ridge. The largest ridge northeast of Mons La Hire best illustrates the evidence for pre-phase II ridge topography with the dike-like, sinuous features on the ridge crest probably formed in the post-phase III period (figs. 30-20, 30-21(a), and 30-21(b)). Growth of this particular ridge may have begun in Imbrian time. Present photogeologic evidence indicates that the flows surmounted slopes of at least 0.5°. Postflow normal faulting with displacements of at least 145 m is present in the ridge system approximately 60 km north of Euler β (fig. 30-15).

Subdued, 1- to 2-km-wide and 40- to 50-m-deep, leveed channels are present lengthwise along the center of the most extensive phase III flows (fig. 30-15). This type of lava channel is common in terrestrial basalt flows, but the lunar channels are several orders of magnitude larger. The braided lava channels in a complex series just north of the suggested phase III source vent are on the order of 400 to 800 m wide and 40 to 70 m deep (fig. 30-22). Lunar application of the equations of Shaw and Swanson (ref. 30-23) and Daneš (ref. 30-24) has shown that, even on nearly horizontal slopes, the

lunar flow heights and extreme lengths are in accord with calculated values when the reduced-gravity environment and the higher density of the basalt melt are considered (ref. 30-15). In addition, the high rates of lava extrusion appear to be the primary cause of extreme flow lengths; the reduced viscosity of lunar basalts (ref. 30-4) probably plays a secondary role.

The orbital photographic documentation of southern Mare Imbrium begun by the Apollo 15 crewmen and completed by the Apollo 17 crewmen has enabled photogeologists to understand more clearly at least those volcanic processes that resulted in late-stage mare flooding. The distinct lava flows in the Imbrium basin were recognized as perhaps the best preserved result of such processes (ref. 30-25); until the Apollo missions, however, photographic resolution and quantitative topographic data were insufficient for a thorough evaluation.

REFERENCES

30-1. Greeley, Ronald: Observations of Actively Forming Lava Tubes and Associated Structures, Hawaii. Mod. Geol., vol. 2, no. 3, 1971, pp. 207-223.

30-2. Greeley, Ronald: Additional Observations of Actively

0   10

km
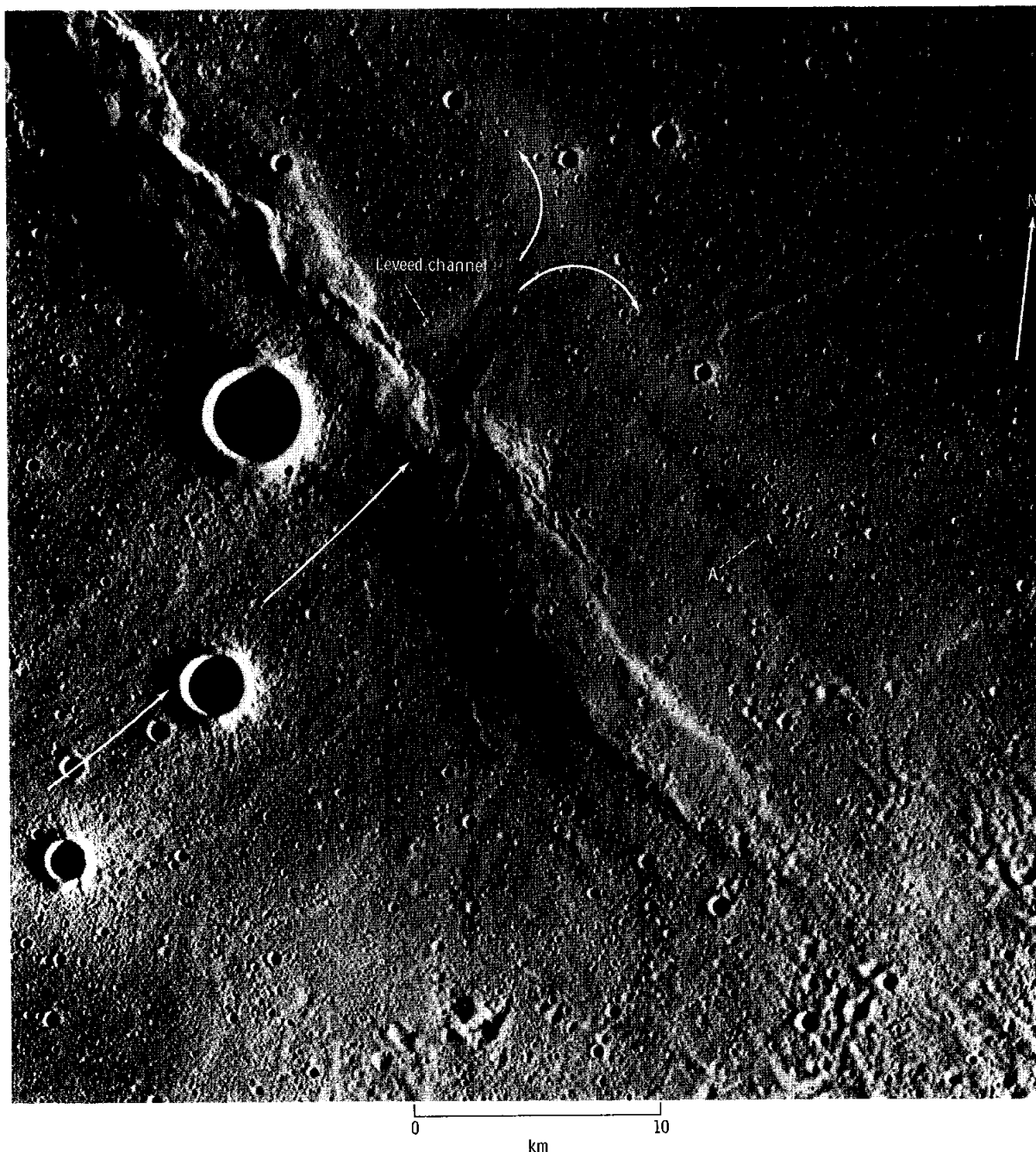
FIGURE 30-20.—Enlargement of part of Apollo 15 metric camera photograph AS15-1155 showing
ponding (A) of a phase II lava flow against the 0.5° to 0.7° slope of a preflow mare ridge. The
higher part of the ridge is probably the result of postflow movement. Note the leveed channel on
the ridge at the point negotiated by the flow. Sun elevation angle is approximately 5°.

FIGURE 30-21.—Composite photogeologic map of lava flow scarps in southwestern Mare Imbrium.
Outlined area "A" indicates coverage of figure 30-15. Arrows indicate position of flow channels
and flow direction. Other symbols are the same as those used in figure 30-15. (a) Annotated
photobase mosaic composed of three rectified Apollo 15 metric camera oblique photographs
(frames AS15-1553, 1556, and 1557). (Rectification by U.S. Army Map and Topographic
Command.) (b) Photogeologic map. Stippled pattern represents phase III materials, and horizontal
line pattern represents earlier phase II deposits. Some phase I materials may be included in the
latter. Heavy lines with double barbs indicate mare ridge trends.

Carlini

Maximum extent phase III

Heis

Heis D

Carlini B

"A"

Mons La Hire

Lambert

(a)

0   20   40
km

N

Carlini

Maximum extent phase III

Heis

Heis D

Carlini B

"A"

Mons La Hire

Lambert

(b)

0   20   40
km

N
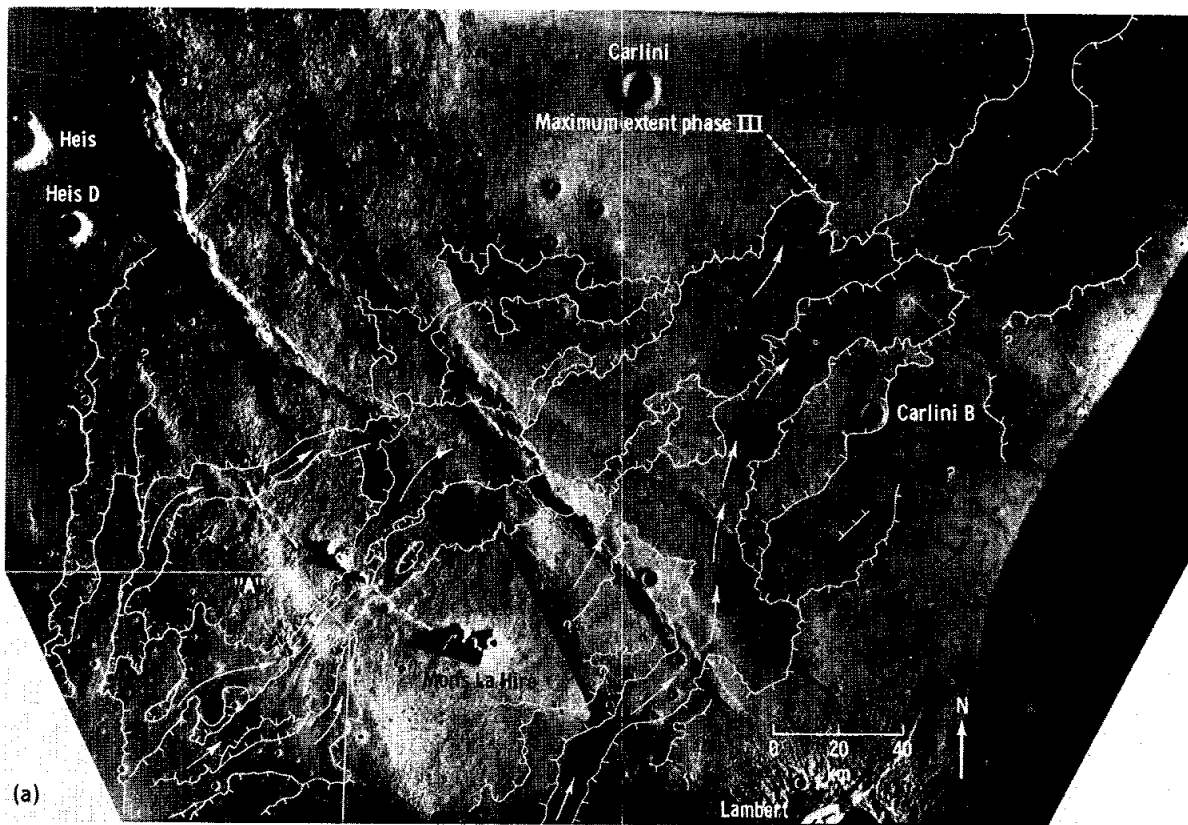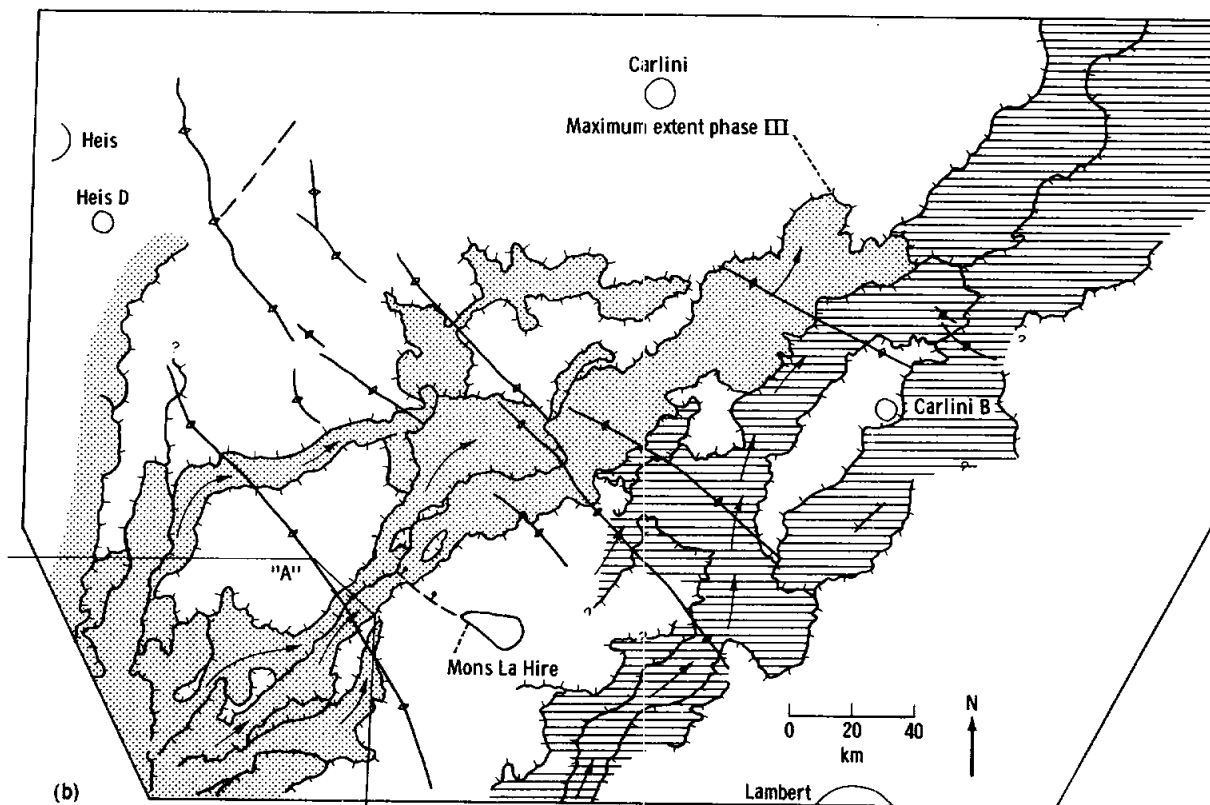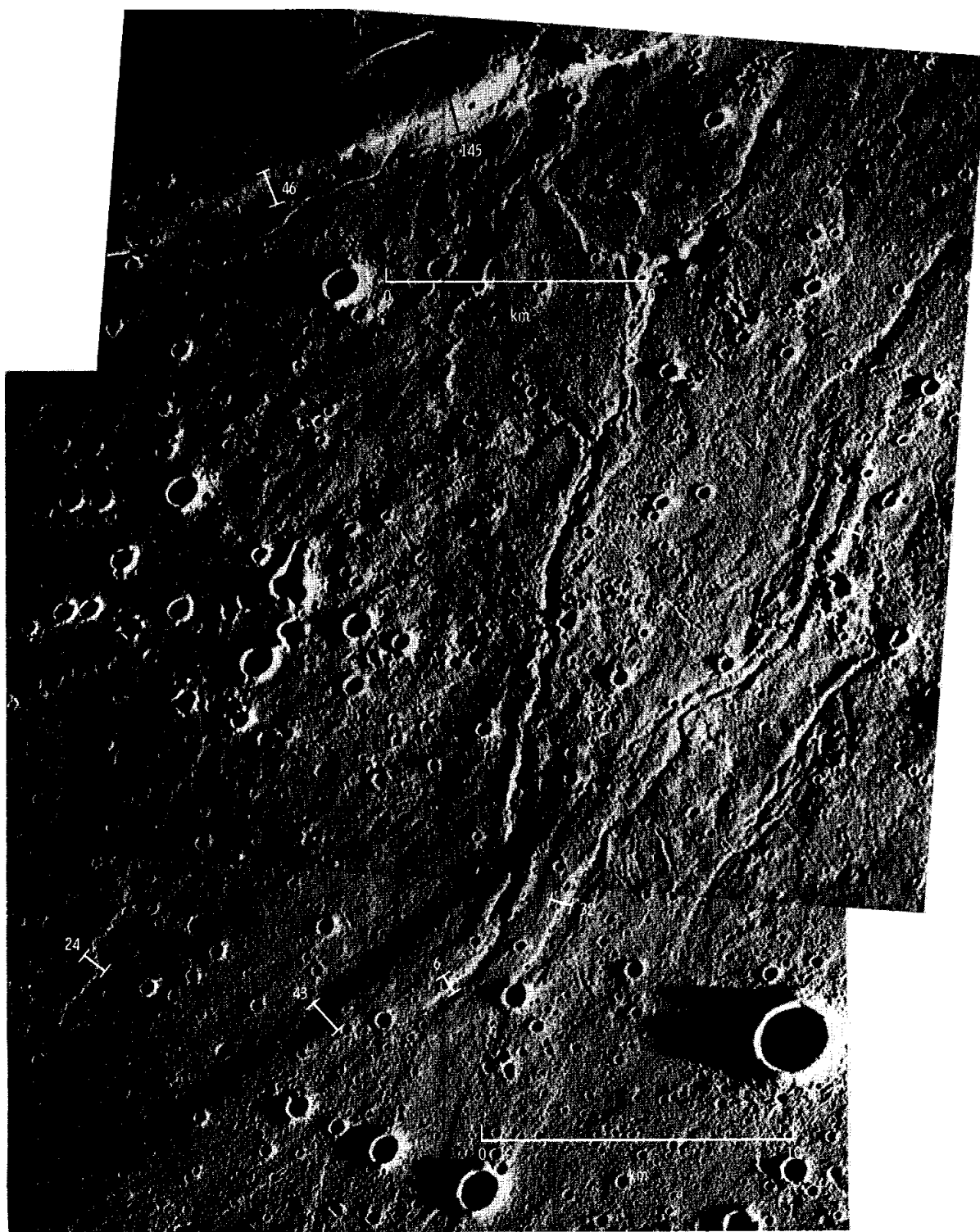
FIGURE 30-22.—Apollo 17 Hasselblad photographs AS17-155-23717 and 23718 showing the braided lava channels near the source vents of the phase III eruptives. Numbers (e.g., 24) are heights in meters measured at indicated points. The Sun elevation angle is approximately 1°.

Forming Lava Tubes and Associated Structures, Hawaii. Mod. Geol., vol. 3, no. 3, 1972, pp. 157-160.

30-3. Strom, R. G.: Lunar Mare Ridges, Rings and Volcanic Ring Complexes. Mod. Geol., vol. 2, 1971, pp. 133-157.

30-4. Murase, Tsutomu; and McBirney, Alexander R.: Viscosity of Lunar Lavas. Science, vol. 167, no. 3924, Mar. 13, 1970, pp. 1491-1493.

30-5. McGetchin, Thomas R.; and Head, James W.: Lunar Cinder Cones. Science, vol. 180, no. 4081, Apr. 6, 1973, pp. 68-71.

30-6. Green, Jack; and Short, Nicholas M., eds.: Volcanic Landforms and Surface Features, A Photographic Atlas and Glossary. Springer-Verlag (New York), 1971.

30-7. Bryan, W. B.: Wrinkle-Ridges as Deformed Surface Crust on Ponded Mare Lava. Lunar Science IV (Abs. of papers presented at the Fourth Lunar Science Conference (Houston, Tex.), Mar. 5-8, 1973), pp. 103-105.

30-8. Koons, Mary-Linda: Brittle Fracture in Oceanic Basalts. M.A. Thesis, Temple Univ., 1972.

30-9. El-Baz, Farouk: The Cinder Field of the Taurus Mountains. Sec. 25, Part I, of the Apollo 15 Preliminary Science Report. NASA SP-289, 1972.

30-10. Whitaker, Ewen A.: An Unusual Mare Feature. Sec. 25, Part N, of the Apollo 15 Preliminary Science Report. NASA SP-289, 1972.

30-11. El-Baz, Farouk: New Geological Findings in Apollo 15 Lunar Orbital Photography. Proceedings of the Third Lunar Science Conference, vol. 1, MIT Press (Cambridge, Mass.), 1972, pp. 39-61.

30-12. Hackman, R. J.: Geologic Map of the Montes Apenninus Region of the Moon. U.S. Geol. Survey Misc. Geol. Inv. Map I-463, 1966.

30-13. El-Baz, Farouk: The Lunar Dark Mantle: Its Distribution and Geologic Significance. Lunar Science IV (Abs. of papers presented at the Fourth Lunar Science Conference (Houston, Tex.), Mar. 5-8, 1973), pp. 217-218.

30-14. Whitaker, Ewen A.: Mare Imbrium Lava Flows and Their Relationship to Color Boundaries. Sec. 25, Part M, of the Apollo 15 Preliminary Science Report. NASA SP-289, 1972.

30-15. Schaber, Gerald G.: Lava Flows in Mare Imbrium:

Geologic Evaluation From Apollo Orbital Photography. Lunar Science IV (Abs. of papers presented at the Fourth Lunar Science Conference (Houston, Tex.), Mar. 5-8, 1973), pp. 653-654.

30-16. Soderblom, Laurence A.; and Lebofsky, Larry A.: Technique for Rapid Determination of Relative Ages of Lunar Areas From Orbital Photography. J. Geophys. Res., vol. 77, no. 2, Jan. 10, 1972, pp. 279-296.

30-17. Soderblom, Laurence A.; and Boyce, Joseph M.: Relative Ages of Some Near-Side and Far-Side Terra Plains Based on Apollo 16 Metric Photography. Sec. 29, Part A, of the Apollo 16 Preliminary Science Report. NASA SP-315, 1972.

30-18. Soderblom, Laurence A.: A Model for Small-Impact Erosion Applied to the Lunar Surface. J. Geophys. Res., vol. 75, no. 14, May 10, 1970, pp. 2655-2661.

30-19. Wilhelms, D. E.; and McCauley, J. F.: Geologic Map of the Near Side of the Moon. U.S. Geol. Survey Misc. Geol. Inv. Map I-703, 1971.

30-20. Anon.: Topographic Lunar Map—Sheet 2 (1:5 000 000); Edition 1-AMS. U.S. Army Corps of Engineers, Army Map Service, 1960.

30-21. Latham, G.; Dorman, J.; Duennebier, F.; Ewing, M.; et al.: Moonquakes, Meteoroids, and the State of the Lunar Interior. Lunar Science IV (Abs. of papers presented at the Fourth Lunar Science Conference (Houston, Tex.), Mar. 5-8, 1973), pp. 457-459.

30-22. Carr, M. H.: The Geology of the Mare Serenitatis Region of the Moon. In Part A of Astrogeologic Studies Annual Progress Report, July 1, 1965 to July 1, 1966, U.S. Geol. Survey, Dec. 1966, pp. 11-16.

30-23. Shaw, H. R.; and Swanson, D. A.: Eruption and Flow Rates of Flood Basalts. Proceedings of the Second Columbia River Basalt Symposium, Eastern Washington State College Press (Cheney, Wash.), 1970, pp. 271-299.

30-24. Daneš, Z. F.: Dynamics of Lava Flows. J. Geophys. Res., vol. 77, no. 8, Mar. 10, 1972, pp. 1430-1432.

30-25. Kuiper, Gerard P.: Interpretation of Ranger VII Records. Ranger VII, Part II. Experimenters' Analyses and Interpretations. JPL Tech. Rept. 32-700, 1965, pp. 9-73.

31. Mare Ridges and Related Studies

The high-resolution metric and panoramic cameras flown on the last three Apollo missions have added considerable detail to the photographic record of the Moon. Mare ridges and rilles on the lunar surface are now visible in greater detail, but their genesis remains perplexing. Some rilles may have formed as lava channels or tubes; ridges may be products of intru-

sion, extrusion, or tectonism—or some combination of these processes (part A). Some ridges may have formed by autointrusion of the molten lower part of lava lakes into the surficial crust (part B). Ridges in the Taurus-Littrow area may have been caused by low-angle thrust faulting (part C), but small-scale features also suggest volcanic extrusion (part D).

PART A

VOLCANISM IN THE LUNAR MARIA

Richard A. Young,[a] *William J. Brennan,*[a]
Robert W. Wolfe,[a] *and Douglas J. Nichols*[a]

The lunar maria were formed and have been modified during an extended period by volcanic and tectonic processes. Lava flows, sinuous rilles, mare ridges, faults, and fracture systems constitute a closely interrelated assemblage of mare surface features that overlap temporally and spatially. Some prominent ring structures have evolved from flooded premare impact craters by volcanic and tectonic modification.

SINUOUS RILLES

In this discussion, sinuous rilles are considered to be different in origin from graben-type fractures. Pertinent discussions of the planimetric shapes of rilles appear in reference 31-1. Sinuous rilles have most likely developed as lava tubes or channels in the thicker portions of flows, in areas of converging flow lines, or by channelization between or around obstructions (refs. 31-2 and 31-3). In the Herigonius rille system, where two rilles emerge from mare ridge

summits, a possible roof remnant has been identified along one of the major rille segments (area A in fig. 31-1). This feature suggests a lava tube origin as opposed to open channel flow. If closed lava tubes did form on the Moon, collapse of the roofs would occur either simultaneously with drainage of the tubes or as a result of the postmare impact flux documented in reference 31-4. Other sinuous rilles could have formed as open channels with levees (ref. 31-1) or as channels merging with tubes as in terrestrial analogs (refs. 31-5 and 31-6).

Whether a particular sinuous rille developed as a closed lava tube or as an open channel, it must be the same age as the surface flow within which it has developed. This relationship suggests that the relative length of prominent rilles within different mare regions indicates the dimensions of the mare regions covered during specific flooding episodes. It is assumed that a particular "flow" might be fed by several widely spaced vents. One of the longest sinuous lunar rilles north of the crater Brayley (fig. 31-2) is at least 340 km in length. Such long rilles could be composed of two or more sections, similar

[a]State University of New York at Geneseo.

Enlarged area A

```
0                    15
         km
```
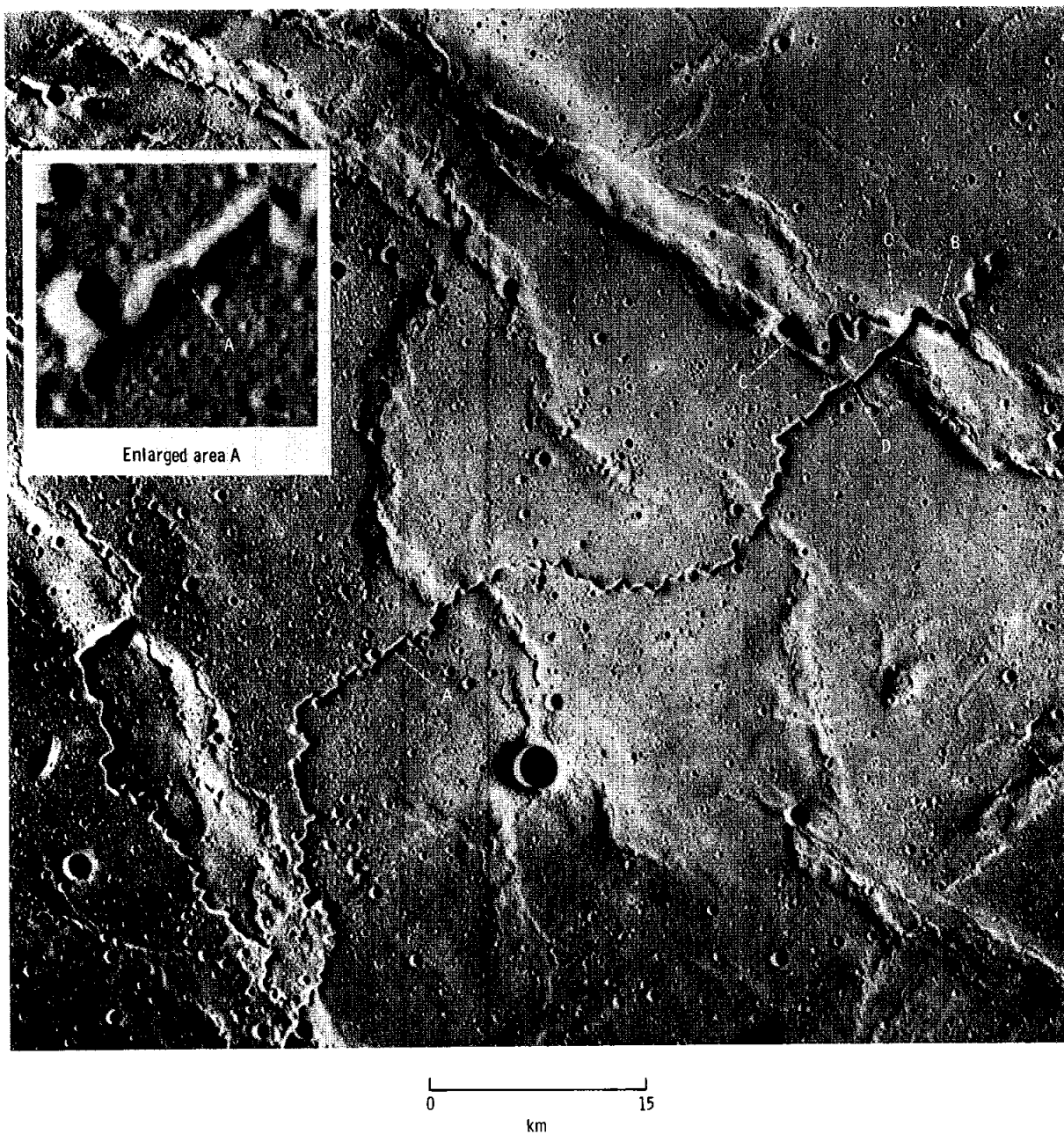
FIGURE 31-1.—Herigonius rille complex: (A) collapsed roof(?) remnant; (B) secondary(?) vent; (C)
blocked primary(?) vent; (D) and (E) intrusive or extrusive(?) postrille features (Apollo 16 metric
camera frame AS16-2837).

to the Herigonius rilles, issuing from more than one
vent, some of which may no longer be visible.

MARE RIDGES

Mare ridges have apparently formed by intrusion,
extrusion, and tectonic activity or by combinations
of these processes along different segments of the
same ridge (ref. 31-7). Partial filling of adjacent
craters, conspicuous elevation differences of mare
surfaces across the ridges, and "squeeze-up" type
structures can all be recognized along some ridge
elements.

The age relationships of ridges relative to associ-
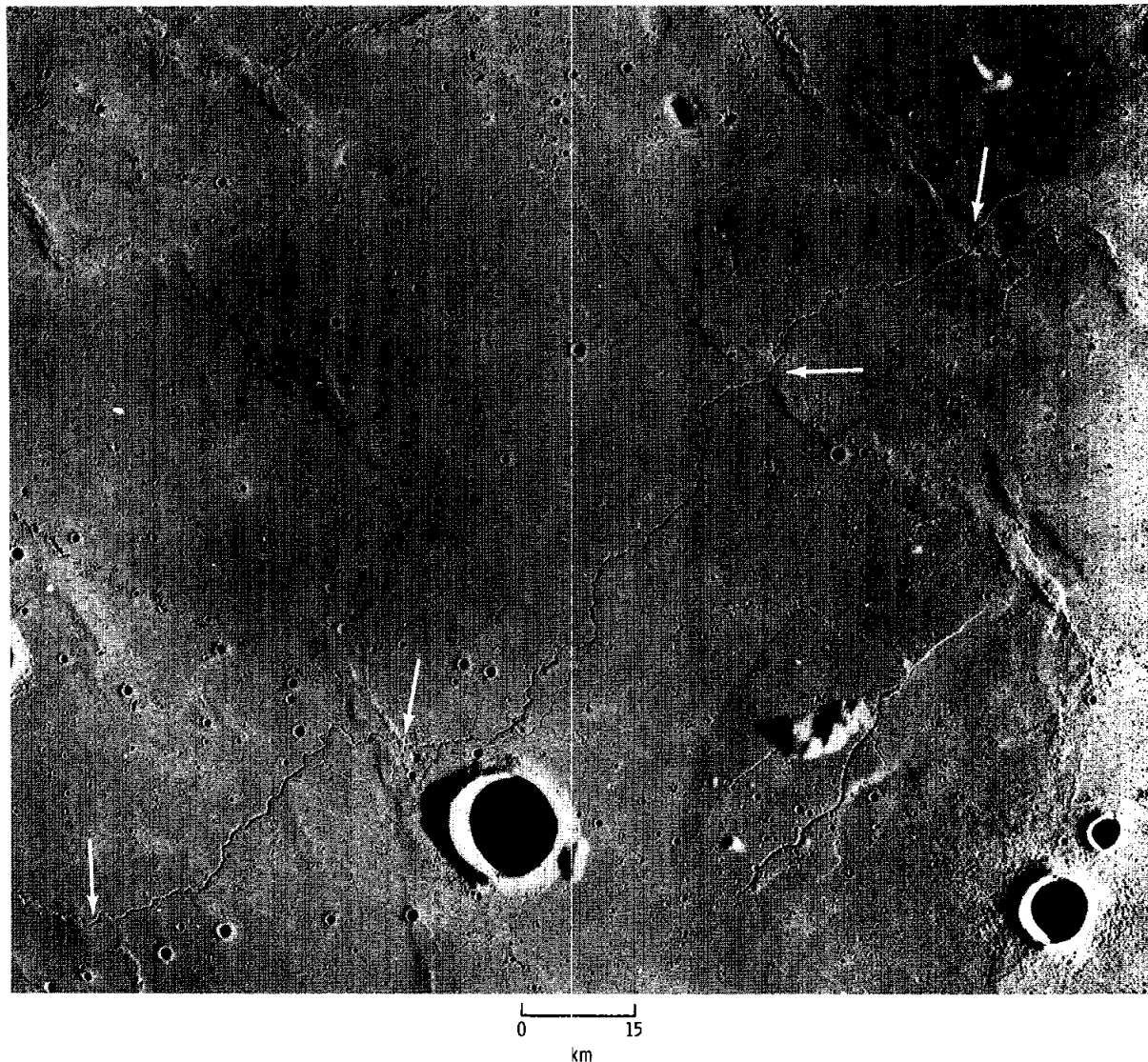
FIGURE 31-2.—Rille north of crater Brayley in southwestern Mare Imbrium. Note rille/ridge relationships (Apollo 17 metric camera frame AS17-2928).

ated features imply a complex origin for most ridges. Where prominent sinuous rilles intersect mare ridges, the rilles often appear to have been distorted, filled, or displaced by growth or deformation of the ridge (fig. 31-2). These relationships indicate that ridge volcanism or deformation followed rille formation.

Mare ridges exhibit a variety of temporal relationships with mare surface flows, rilles, and fractures. Near the Herigonius rille complex, the two larger northwest-southeast trending ridges that have sinuous rille vents located along their summits appear to have deflected or otherwise influenced the development of

the sinuous rilles and, by inference, the flows in which they formed (fig. 31-3). The rilles closely follow the prominent ridge in area A (fig. 31-3), and they also show deformation along the ridge flank near the rille junction. The rille that issues near area B (fig. 31-1) and crosses the most prominent ridge without conspicuous deformation suggests that flow may have persisted across a low section of the initial ridge while ridge formation continued, eventually producing a complex vent that fed rilles extending both north and south. Deformation of the ridge appears to have closed off a portion of the vent system in area C (fig.
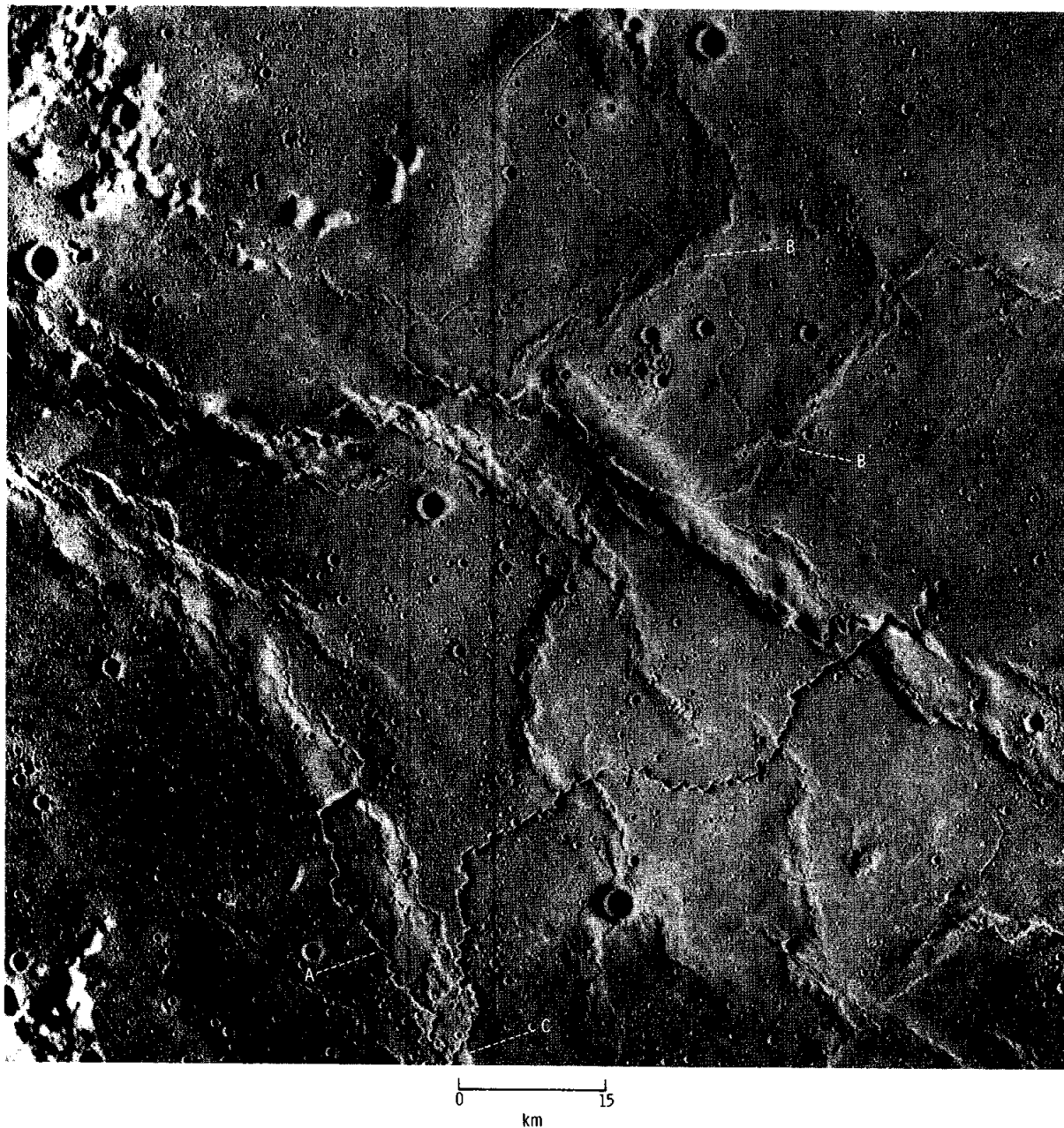
FIGURE 31-3.—Herigonius rille complex: (A) rille trend influenced by preexisting ridge; (B) areas
where ridge growth has deformed rilles; and (C) rille sections showing deformation or filling across
ridge (Apollo 16 metric camera frame AS16-2837).

31-1) with a resulting shift of activity to the
northeast edge of the ridge at area B. Alternatively,
lava could have poured out along the entire straight
section of the rille at area E. A minor obstruction
(intrusion?) in the rille where it crosses the large ridge
can be seen in area E (fig. 31-1). Northwest of this

complex vent (fig. 31-1, B), portions of the rilles that
cross smaller ridge segments near area B (fig. 31-3)
clearly show ridge deformation postdating the devel-
opment of the rilles.

The long prominent rille near the crater Brayley
exhibits a "braided" or bifurcating character near

several ridge-crossing segments (fig. 31-2). These multiple channels could possibly have formed when ridge tectonism or volcanism caused subtle surface deformation, or they might be the result of multiple feeder vents near the ridge systems (fig. 31-2).

Along the mare ridge system in Mare Serenitatis near the crater Littrow, there is evidence of local flows from several parts of the ridge partly filling adjacent craters of various sizes (fig. 31-4). The same relationship between ridges and adjacent craters is evident along the ridge system in eastern Mare Cognitum in the general vicinity of the crater Bonpland D. These ridge/crater relationships in both cases imply a significant interval for cratering of the adjacent surfaces before renewed (secondary) volcanism along the ridges. This conclusion is based on the assumption that the main portion of the ridge

FIGURE 31-4.—Mare ridges west of crater Littrow in Mare Serenitatis. Flow of ridge material into craters has occurred at all points indicated. Details can be seen better on Apollo 15 panoramic camera frame AS15-9303. Note apparent continuation of ridge elements into flow-like features within dark mare material to the east (Apollo 17 metric camera frame AS17-0597).

developed contemporaneously with the surface flows in these areas; however, the entire ridge might, in fact, be considerably younger than the surrounding flows.

All these relationships demonstrate that mare ridges have complex origins in time. Some retain topographic expression during two or more episodes of adjacent mare flooding and serve to channel or direct flows. Others are submerged temporarily by younger flows and later deform the surface by extrusive, intrusive, and tectonic activity. Still other ridges might have developed their present topographic expression entirely during one limited episode of mare flooding. The evidence suggests most strongly that repetitive deformation and volcanism along premare basement fractures have formed the mare ridges.

Although mare ridge development can occur before, during, and after the extrusion of the adjacent mare surface flows, the latest surficial activity observable along many ridges appears to have accompanied or followed local mare flow extrusion and rille development.

The interrelated nature of sinuous mare rilles, ridges, and flows is clearly illustrated northwest of the crater Euler (fig. 31-5) where both well-defined surface flows and associated rilles have been deformed by ridge development before all the features were in turn offset by prominent northeast-southwest trending faults or flexures. (Similar relationships are shown in fig. 31-11.) All these relationships are best demonstrated on stereographic photographs.

AGES OF MARE FAULTS AND FRACTURE SYSTEMS

Graben-type faulting is prominent in many mare regions, including the southeastern edge of the Serenitatis basin (fig. 31-6). In this region, faulted dark mantle material or flows appear to cover the mare ridges (area A), and all surface features appear to be displaced to some extent by faults. Some grabens are embayed by dark mare flows (fig. 31-7, E) that are nearly indistinguishable from the older adjacent dark mare material. The flows filling the grabens have small subsidence structures superimposed on them (fig. 31-7, D). In contrast to the preceding interpretation, the southwestern corner of figure 31-6 contains secondary craters that are interpreted as ejecta from the crater Plinius (out of view
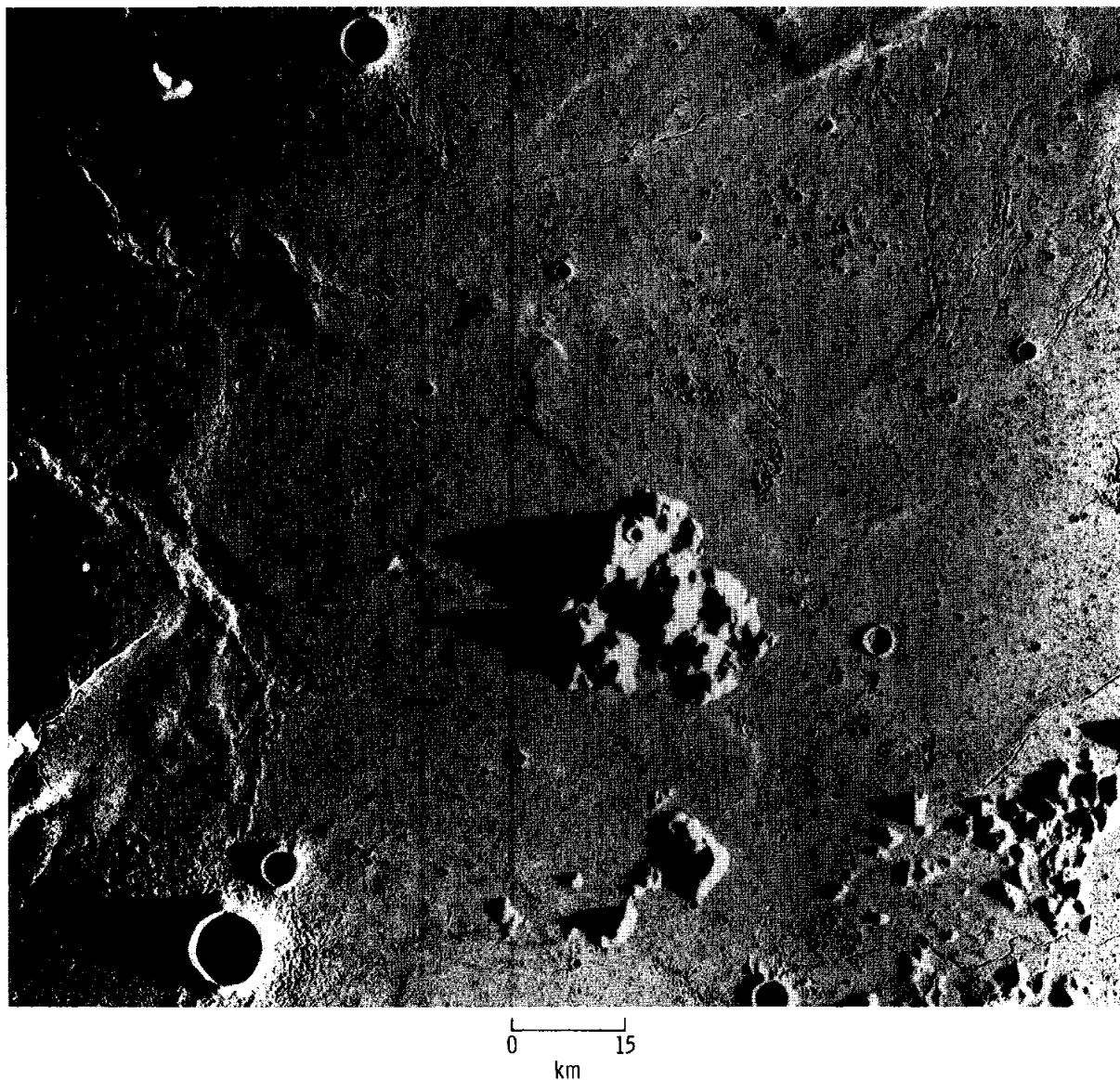
FIGURE 31-5.—Mare surface northwest of crater Euler: (A) rille deformed by flexure; (B) lava channel with levees; (C) rilles deformed by mare ridge; (D) collapsed lava tube(?); (E) rille passing into normal fault; and (F) collapsed lava tube(?). Note evidence of deformation of surfaces, rilles, and flows by volcanism and tectonism (Apollo 17 metric camera frame AS17-2732).

to the southwest) and that are superimposed on the dark mare material but not on the lighter (younger?) mare surface immediately north of the grabens.[1] This contradictory evidence for the relative ages of the dark and light surfaces permits the interpretation that

---

[1] B. K. Lucchitta, personal communication, 1973.

the grabens, instead of being younger than the ridge at area A (fig. 31-6), might have been partially filled by volcanism occurring along the mare ridge.

Approximately two crater diameters northeast of the crater Dawes (fig. 31-7) where the grabens are partially flooded by younger flows containing a sinuous rille (fig. 31-7, C), two cones (A and B) are alined along a conspicuous fracture. These cones are

FIGURE 31-6.—Southeastern edge of Mare Serenitatis: (A) ridge covered by later volcanism; (B) grabens; and (C) crater Dawes (Apollo 17 metric camera frame AS17-0599).

two of the most volcano-like features yet recorded on Apollo photographs. Another prominent volcanic cone or dome is shown in area A of figure 31-8 along a small ridge. Near the crater Dawes, the younger flows appear to have flowed from the southeast, as indicated by the rille trend, and were affected by small collapse depressions that also intersect the rille (areas C and D in fig. 31-7).

The preceding relationships make it appear likely that faulting of the mare surfaces is closely interrelated with the volcanic flooding; further, it appears that dark mare materials or flows should not always be interpreted as the youngest deposits in any given area of the Moon.

TECTONO-VOLCANICALLY MODIFIED PREMARE IMPACT CRATERS

The following examples illustrate several stages in the modification of impact craters by tectonism, volcanism, younger impacts, and mass wasting.

Krieger Crater

Krieger is an impact crater (fig. 31-9) with a rim, floor, and ejecta blanket that have been affected by several processes. The southern rim was partly obliterated by the impact that formed the crater Krieger B, and ejecta from this impact partly fills the floor of

FIGURE 31-7.—Area northeast of crater Dawes: (A) volcanic cones(?); (B) sinuous rille; (C) graben embayed by younger flows; and (D) subsidence lineaments (Apollo 17 metric camera frame AS17-0599).

FIGURE 31-9.—Crater Krieger, Aristarchus plateau (Apollo 15 metric camera frame AS15-2340).

FIGURE 31-8.—Domes or cones southeast of Maraldi D in northern Mare Tranquillitatis (Apollo 17 metric camera frame AS17-0303).

Krieger. A portion of the northern rim slumped or slid into the interior, forming an irregular deposit of debris at the base of the inner wall. The western rim has been partly destroyed and subsequently breached by mare material that partly fills the crater floor. The level of the mare surface to the west is higher than the floor of Krieger, which suggests that mare material has flooded the crater through a low point in the western rim, with the source of the mare material being exterior to the crater. However, the rille that extends from the gap in the western rim out onto the mare surface is widest at the gap and narrows progressively away from the gap into the mare. In many terrestrial lava channels, the width decreases away from the source. Similar relationships can be observed in several sinuous rilles along the southern portion of figure 31-9. Therefore, it is also possible that the source of mare flow material on the floor of the crater lies within Krieger and that the difference in elevation between the crater floor and mare surfaces is the result of postvolcanic subsidence of the crater floor.

The overall result of these processes is the rapid destruction of the crater ejecta rim, especially its circular form.

Herigonius ν Crater

The northwestern half of Herigonius ν (fig. 31-10) is bounded by a rim that varies in both width and height and that grades into an isolated highland area. The northeastern tip of this rim segment has been cut by a short high-angle fault. The eastern side of this faulted tip has moved relatively upward with respect to the western side. The entire northwestern half of the crater rim appears to be of impact origin. The southeastern half of the crater rim is low and narrow and barely protrudes above the surface of the mare material that both fills and surrounds the crater. The eastern side of this low, narrow rim segment has been partly destroyed by a cluster of secondary impact craters.

It seems improbable that impact, mass-wasting, and tectonic processes would have reduced only the southeastern portion of the rim to such a uniform configuration. A more likely possibility is that, after this portion of the original ejecta rim was partially destroyed by the aforementioned processes and then inundated by mare lavas, subsequent fissure volcanism—along a nearly circular fracture produced by the initial impact—formed the present low, narrow rim. This lower segment of the rim resembles the nearly linear low ridge that lies approximately one crater diameter to the west. This ridge is also narrow and appears to fill a portion of a fracture. An intrusive origin for this ridge seems likely. The smoothly
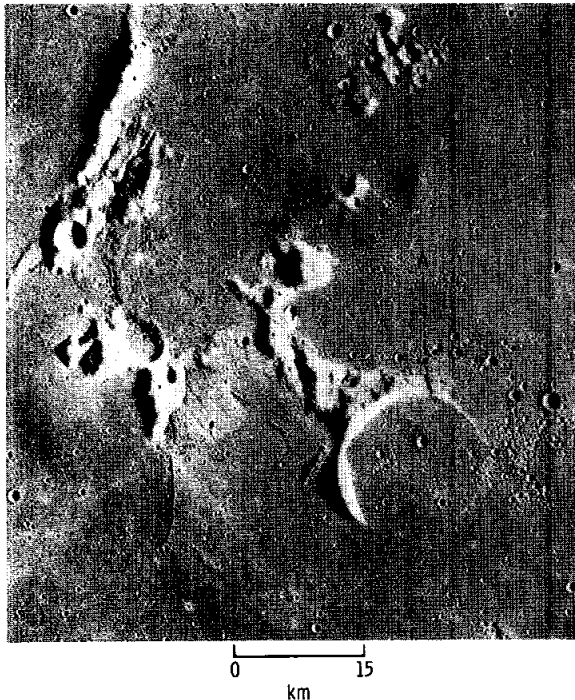
FIGURE 31-10.—Crater Herigonius ν northeast of Herigonius rille complex: (A) fault (Apollo 16 metric camera frame AS16-2834).

curved form of the southeastern rim segment of Herigonius ν in contrast to the more irregular northwestern portion can easily be accounted for if they are volcanic and impact features, respectively. Ejecta rims are prominent topographic features and as such are subject to erosion by mass wasting and younger impacts. However, impact fractures would be affected only by much larger impacts and not at all by most minor surface processes, and subsequent volcanism along the impact fractures could reconstruct a secondary volcanic rim almost circular in shape.

The low topographic expression of the southeastern portion of the crater rim and the absence of obvious flow features suggest that the main sources of magma lay outside the crater. Isostatic uplift of the crater floor may in part account for the difference in elevation between it and the mare surface immediately to the southeast.

Lambert R Crater

The ring complex of Lambert R (fig. 31-11) exhibits many of the characteristics also seen in other lunar ring structures, particularly the circular form. Evidence of volcanic activity exists in the form of sinuous rilles (northwestern portion) and flow features, including flow fronts (southern portion). A small, narrow, arcuate ridge segment similar in morphology to that previously described in figure 13-10 is located just outside the southeastern portion of Lambert R (fig. 31-11, C). It exhibits a concentric relationship with the ring complex. Tectonism as well as volcanism along the structure may be partly responsible for differences in elevation between the interior and the surrounding mare. Some flexuring is apparent on the eastern side.

The existence of the sinuous rille that crosses the northwestern rim in area A of figure 31-11 suggests that the last major episode of volcanism may have inundated that portion of the ring. Later, smaller-scale eruptions could have reestablished the ring. The presence of material filling the portion of the rille that crosses the ring supports this interpretation.

Only along the southwestern side is there any suggestion of a possible relict ejecta rim. The hills with high albedo in that region resemble terra material and are similar to those around the Flamsteed P ring described in references 31-8 and 31-9. They appear to be more densely cratered than the adjacent mare; the abundant clusters of secondary craters make this comparison somewhat uncertain, however. Carr (ref. 31-10) mapped these hills as rim ejecta.

CONCLUSIONS

The filling of the lunar maria and the contemporaneous development of distinctive surface features have involved volcanism and tectonism along premare basement fractures to form mare ridges and fault systems as well as primary surface features such as sinuous rilles (collapsed lava tubes) and volcanic flows. In general, mare ridges appear to have undergone continued deformation or growth by tectonic and volcanic processes (extrusive and intrusive) after the surrounding mare surface flows were extruded. However, in some cases, portions of mare ridges were obviously present as topographic prominences when the surrounding flows were extruded.

The modification of impact craters by other impacts, mass wasting, tectonism, and volcanism has, in certain cases, been followed by reestablishment of circular ridge systems above flooded premare craters of impact origin.

FIGURE 31-11.—Crater Lambert R in Mare Imbrium: (A) sinuous rille showing alteration along crater edge; (B) arcuate rille deformed by ridge; and (C) intrusive(?) ridge element (Apollo 17 metric camera frame AS17-2286).

All these features developed over an extended period and show complex interrelations in time and space. No consistent, uniform sequence of events in the development of these complex surfaces is apparent. On the contrary, it appears that all types of surface features may have undergone a more or less continuous process of formation and modification during the evolution of the lunar maria.

ACKNOWLEDGMENTS

FIGURE 31-16.—Mauna Ulu lava lake, Hawaii. Ridge developed at juncture of circulating crustal plates; left plate is plunging beneath folded upper plate on right (ref. 31-18). (The top of the ridge between the arrows is approximately 4 m wide.)

0   2
km

FIGURE 31-15.—Ridge outlining buried crater rim in western Oceanus Procellarum, north of crater Schiaparelli (Apollo 15 metric camera frame AS15-2489).

ridges atop arches, the sense of offset is seldom consistent along a single ridge or arch.

STRUCTURAL FEATURES OF HAWAIIAN LAVA LAKES AND COMPARISONS WITH MARE RIDGES

The formation of structural features observed in two recent terrestrial lava lakes suggests possible origins for some mare ridges. Structures forming on a circulating lava lake in Mauna Ulu were documented by Duffield (ref. 31-18). Active circulation of the melt prevented formation of a stable crust, and the thin (< 2 cm, ref. 31-18) chilled surface was continuously broken, rafted, and eventually resorbed in the molten lava. Crustal plates migrated away from zones of magmatic upwelling and overrode one another at zones of crustal convergence, with concomitant formation of ridges in upper plates and "squeeze-outs" of lava at the junctures (figs. 31-16 and 31-17). The morphologies of these ephemeral features resemble in

FIGURE 31-17.—Mauna Ulu lava lake, Hawaii. Squeeze-outs (splash) and overthrusting at junction of crustal plates in circulating lava lake. Plates on each side of junction are flat; appearance of curvature is optical illusion caused by striated texture of crust. Squeeze-out ridge at upper left is about 1 m wide (photograph by W. A. Duffield).

miniature those of some mare ridges (e.g., see fig. 31-25). If lava lakes existed in some parts of the maria and if circulation of lava continued after the lakes crusted over, ridges might have formed where crustal fragments were rafted against or over one another. The preservation of such structures analogous to the ephemeral ridges at Mauna Ulu (figs. 31-16 and 31-17) seems problematic, but if circulation were sluggish enough and the crust thick enough, the process might be applicable to the formation of
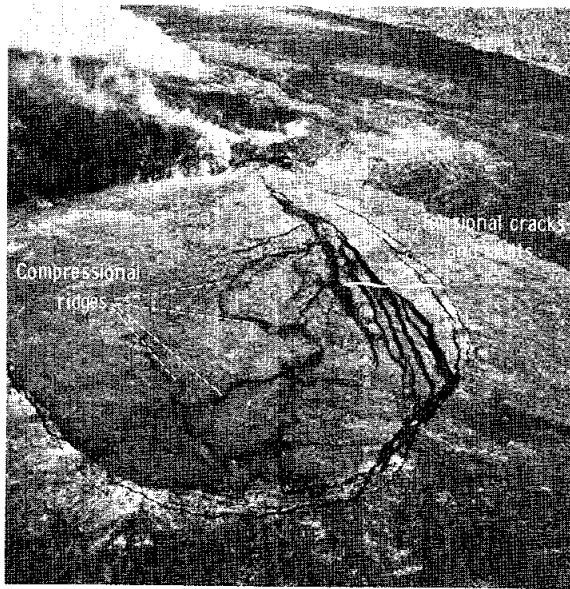
FIGURE 31-18.—Aerial view of Alae lava lake, Hawaii, March 1, 1971. Tensional faults over buried rim of Alae crater; sinuous compressional ridges near axis of subsidence (ref. 31-19).
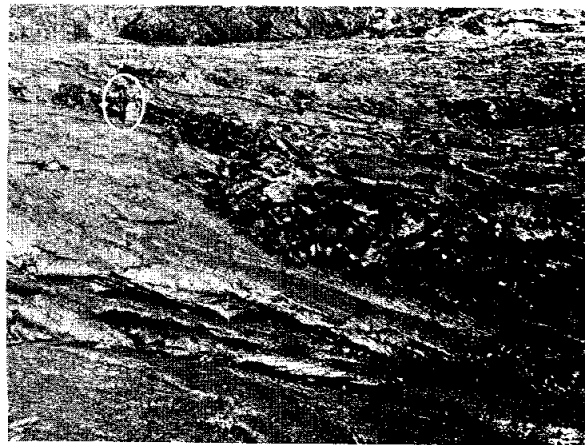

FIGURE 31-19.—Alae lava lake, Hawaii. Compressional ridge at buckled toe of thrust fault in subsiding crust of lava lake; man circled for scale (ref. 31-19).

FIGURE 31-20.—Alae lava lake, Hawaii. Autointrusive dike filling tension crack over buried crater rim; dike ubsequently fractured during additional subsidence of lake crust. The rod across the crack is 1.5 m long (ref. 31-19).

some lunar ridges where no relation to buried topography is apparent.

The complex history of Alae lava lake, on the eastern rift of Kilauea Volcano, Hawaii, has been described in detail in reference 31-19. Originally a 165-m-deep pit crater, Alae was filled to overflowing by lava from the Mauna Ulu eruptions of 1969-71; partial drainage occurred by way of a lava tube, causing the chilled crust on the lake to subside. Extension structures—such as concentric cracks, graben, and normal faults—formed over the preexisting crater rim and over an older, more deeply buried inner rim as well (fig. 31-18). The central subsidence bowl became a zone of compression, but, instead of simply buckling, the crust broke into thrust plates (fig. 31-19), and prominent ridges formed lobate and boxwork patterns at the margins of the overriding plates (ref. 31-19, figs. 31-19 and 31-20).

The geographical relationship of tensional and compressional zones at Alae contrasts with the proposal that buried topography localized compressional structures on the Moon as mare lavas subsided (ref. 31-13). Furthermore, the compressional ridges at Alae did not form the en echelon patterns typical of many lunar ridges, whereas the extensional fractures and faults over the buried crater rims did develop en echelon, interconnected networks (fig. 31-18) resembling the mare ridge patterns—suggesting perhaps a more promising analogy, to which the remainder of this paper will be devoted.

The circumferential tension cracks at Alae commonly were intruded by molten lava from below the crust (autointrusion), possibly as a result of density differences between melt and crust as well as lithostatic pressure imposed by the sinking central crust; some of these dikes were themselves subsequently fractured (fig. 31-20). In lunar lava lakes, crustal subsidence may have caused intrusion and extrusion of underlying molten lava into and onto the solidi-

fied, sagging crust through tensional fracture systems; resulting landforms might be analogous to terrestrial laccoliths and squeeze-ups (refs. 31-7 and 31-20).

According to Duffield and Nakamura (ref. 31-21), en echelon faults and fractures may be caused by dilation in a direction oblique to the trend of the fault zone and approximately normal to lines of rupture. Unlike such fractures related to transcurrent faulting, those caused by tension are characterized by the contemporaneous development of right-lateral (dextral) and left-lateral (sinistral) patterns[2] (fig. 31-21). Such an extensional en echelon pattern is exemplified by the Koae fault system at Kilauea (ref. 31-21). If, on the Moon, such fractures localized extrusions, then tension rather than transcurrent faulting at depth (ref. 31-16) might explain ridges where both sinistral and dextral patterns occur along the same structural trend (fig. 31-22).

Possible evidence for an autointrusive or squeeze-up origin may be the circular ridges over buried crater rims (figs. 31-14 and 31-15), which are similar in shape to larger linear ridges; these are not readily explained by either transcurrent faulting or lateral compression. Commonly, as at Lambert R (figs. 31-14(a) and 31-14(b)), such ridges are narrow and discontinuous, suggesting extrusive squeeze-ups along en echelon cracks. Very small flooded craters seem to show a gradational sequence from rimmed depressions, which appear only as mantled topography (fig. 31-23), to those where marginal fracturing occurs at the rim (fig. 31-24), and others in which ridges have formed at the rim (fig. 31-15). This apparent sequence, as well as the high degree of circularity and common preservation of rim remnants (fig. 31-14(a)), seems to preclude formation of many circular ridges as deeply rooted volcanic "ring dikes."

A squeeze-up model might also explain the broad arches topped by wrinkle ridges. If the crust above laccolithic autointrusives were broken by axial tension cracks, squeeze-ups along these cracks might form the narrow crenulate, braided, and en echelon ridges. That extrusion does occur is exemplified where ridge material overlaps small craters (ref. 31-8), as shown in figure 31-25. Although Strom (ref. 31-8) interpreted such extrusives as postmare dikes tectoni-

---

[2] As used here, "dextral arrays" are fracture patterns identical to those normally formed by right-lateral transcurrent faulting; "sinistral arrays" are fracture patterns like those commonly associated with left-lateral faulting.
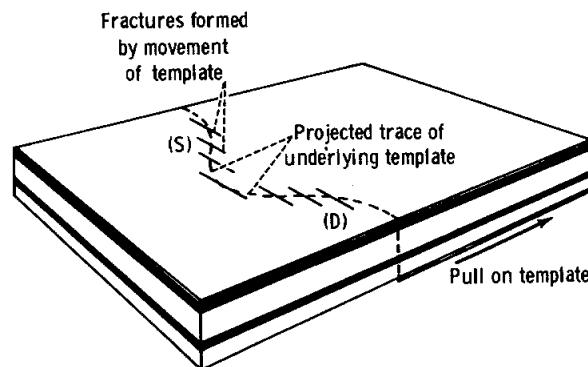

FIGURE 31-21.—Sketch showing fracture pattern that results from unidirectional horizontal dilation of tabular clay model, produced by movement of underlying template; dextral ((D) right lateral) and sinistral ((S) left lateral) arrays formed contemporaneously (after ref. 31-21).
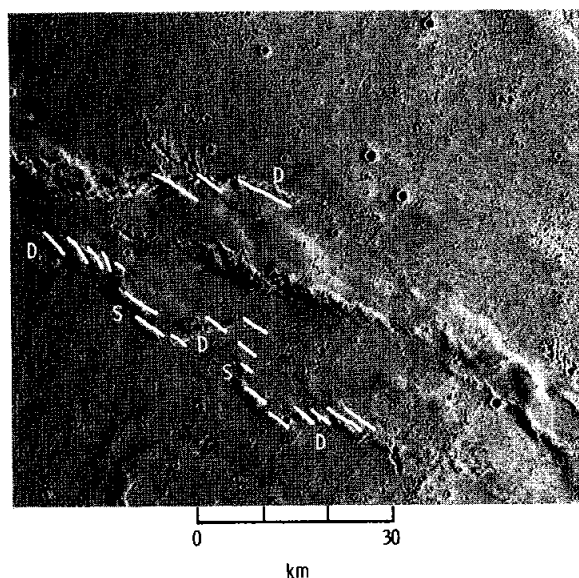

FIGURE 31-22.—Ridges in southwest Mare Serenitatis, showing both dextral (D) and sinistral (S) en echelon patterns; compare with figure 31-21 (Apollo 17 metric camera frame AS17-0605).

cally controlled, some of these may be derived from the lower molten part of ponded lava, forced upward through fissures in the lava crust (figs. 31-26 and 31-27).

Mare ridges are laterally continuous with tension cracks in several places; notably in Mare Imbrium (at its closest point to Mare Serenitatis) where a graben is continuous with a ridge (Lunar Orbiter IV photo-
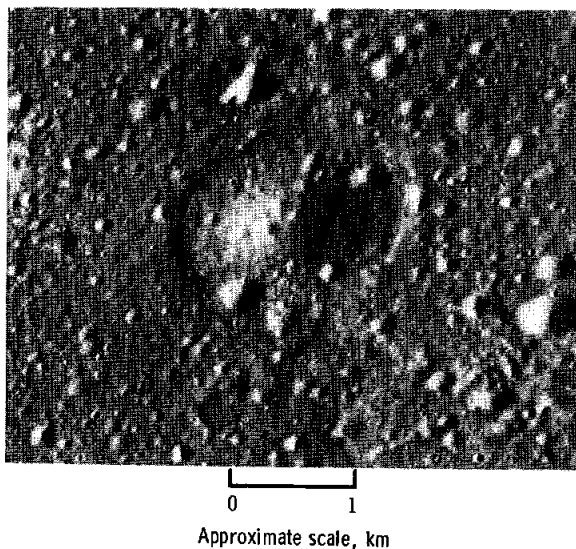
0   1

Approximate scale, km

FIGURE 31-23.—Small crater draped by mare lava in western
Oceanus Procellarum (Apollo 15 panoramic camera frame
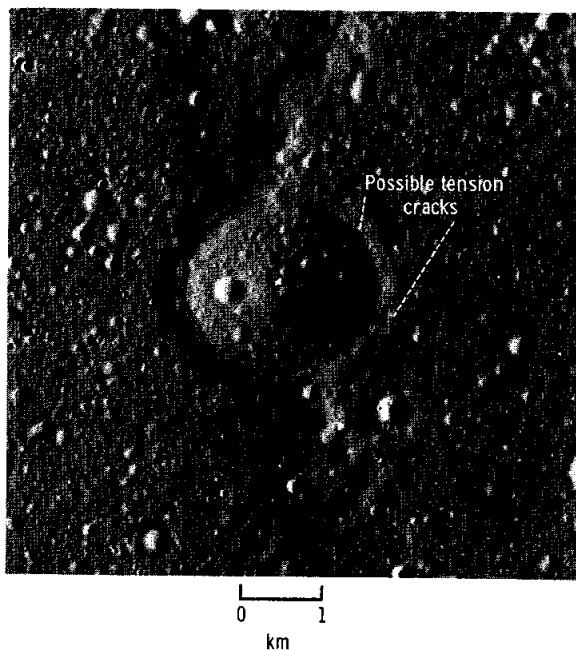AS15-10352).

0   1

km

FIGURE 31-24.—Small crater draped by mare lava, with
possible tension cracks over buried rim (Apollo 15
panoramic camera frame AS15-10361).

0   1

km

FIGURE 31-25.—Apparent extrusion of lava from mare ridge
superposed on crater wall (arrow) in eastern Mare
Serenitatis (Apollo 15 panoramic camera frame AS15-
9303).

graph 103 H_1); thus, a tensional stress environment is
evidently compatible to both. A similar example (fig.
31-28) is at the eastern margin of Mare Serenitatis.

The ridges, at least in some cases, are compara-
tively young (relative to mare surfaces), as indicated
by their relationship to the well-known lava flows in
southwestern Mare Imbrium near the crater Euler
(fig. 31-29). Major deformation occurred after em-
placement of the flows (refs. 31-14, 31-22, and
31-23), possibly by laccolithic doming, with extru-
sion of lava along axial tension cracks. If the intrusive
and extrusive material of the arches and ridges were
derived from ponded lava, a crust thick enough to

FIGURE 31-26.—Apparent flow lobes (arrows) probably
extruded from fissure; mare-flooded highland southwest
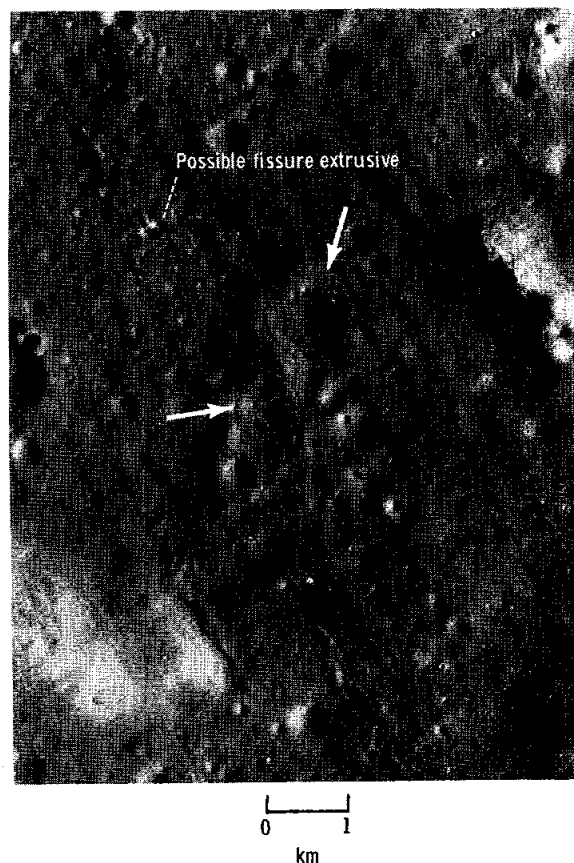of Apollo 17 landing site (Apollo 17 panoramic camera
frame AS17-2316).

FIGURE 31-27.—Thin lava flow, possibly extruded from
fissure, "coating" craters; south of Apollo 17 landing site
(Apollo 17 panoramic camera frame AS17-2309).

support the superposed flows must have formed
before their emplacement. The northeastern trend of
the flows indicates a topographic slope down toward
the central part of the Imbrium basin at the time this
extrusive activity occurred, suggesting some subsi-
dence of the preexisting lava surface.

In a few places, ridges are narrow, linear, smooth,
and continuous; a prominent example (fig. 31-30)
occurs near Montes Harbinger, east of the Aristarchus
plateau. Neither folding nor faulting seems applicable
in this case, and the ridge may be a good candidate
for a squeeze-up origin; it merges with a more typical
crenulate mare ridge to the southwest.

PROBLEMS OF SCALE AND MECHANISM

The preceding examples suggest that lava lakes
may have existed in the lunar maria at some time, and

that some mare ridges have formed as autointrusives
and extrusives, following the development of a chilled
crust, sagging of the central parts of basins and
flooded craters, and consequent extension fracturing
over buried topographic highs. On the Moon, subsi-
dence of mare crust may have resulted from (1)
withdrawal of magma, (2) a greater density of the
surficial crystallized rock compared to that of the
underlying molten lava, (3) loading caused by super-
position of additional lavas, or (4) degassing.

Terrestrial squeeze-ups in lava flows (fig. 31-31)
commonly protrude above the surface of the lava
(refs. 31-24 and 31-25). In Hawaiian lava lakes,
however, solidified autointrusive dikes seldom pro-
trude above the crust, and some factor in addition to
subsidence thus seems required to account for the
massive ridges on the Moon. As crystallization and
subsidence progressed, accumulation of volatiles

FIGURE 31-29.—Lava flows predating formation of arches and superposed wrinkle ridges, view north (Apollo 15 metric camera frame AS15-1555).
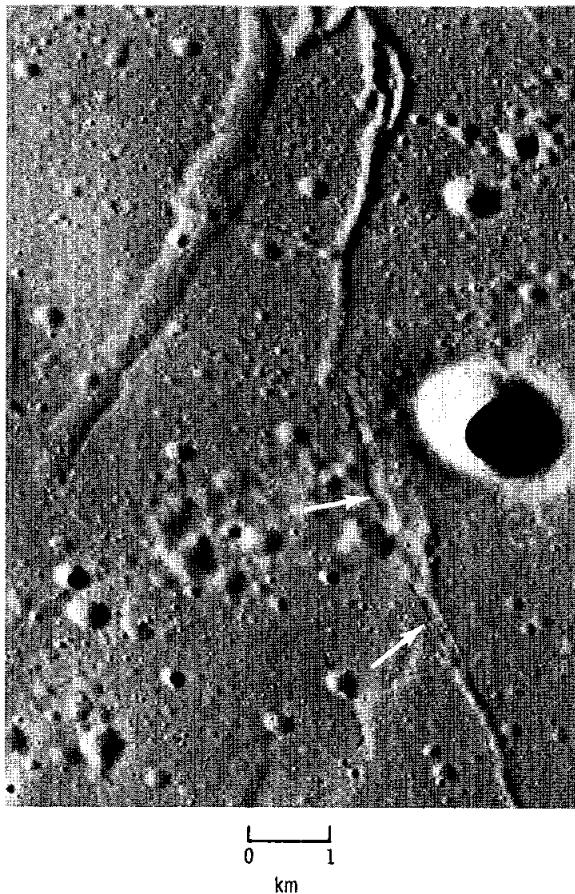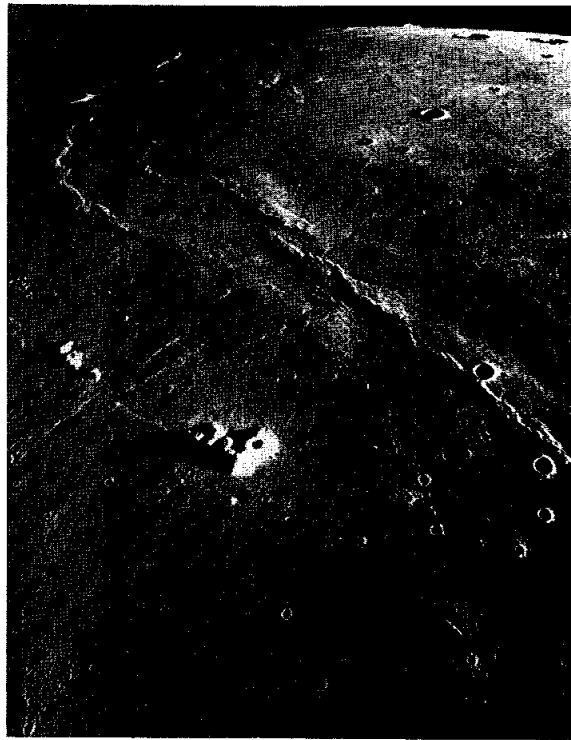
```
|_____|
0            1
     km
```

FIGURE 31-28.—Ridge continuous with rille (tension crack) in eastern Mare Serenitatis, north of Apollo 17 landing site (Apollo 17 panoramic camera frame AS17-2318).

along buried topographic highs may have augmented the driving force, as suggested in figure 31-32.

Core drilling of the crust of Kilauea Iki lava lake revealed a zone of alkaline-rich melt at the base of the crust; upon crystallization of the zone, the alkalis and other volatiles migrated upward through cracks in the crust (ref. 31-26). According to Duffield (ref. 31-18), gases that collect beneath the crusts of Hawaiian lava pools tend to be relatively concentrated at the crests of crustal flexures. If lava lake conditions could have existed on the Moon and if the crust had sagged, volatile pressure might have sufficiently augmented the lithostatic pressure and density differential to force protrusion of dikes above the surface. Possible lunar evidence for the localization of volatiles as shown in figure 31-32 are the deep craters or irregularly shaped pits at mare/terra contacts at the heads of some rilles, (e.g., Hadley); volatiles may have

migrated to the upper margins of a sagging mare along the lava/terra interface. Craters on mare ridges (as in Oceanus Procellarum, northwest of Gruithuisen Crater) suggest explosive activity accompanying ridge development (ref. 31-27).

According to Williams (ref. 31-28), the propelling force of domical protrusions on Earth seems to be volatile pressure, accounting for the periodic explosions that accompany extrusion of terrestrial domes and spines. As crystallization in a magma chamber proceeds, gas pressure increases rapidly, and extrusion of viscous domes and plugs commonly marks the close of volcanic activity. Hollow spines and irregular protrusions also occur on basalt flows, presumably as a result of volatile pressure (ref. 31-29). Lunar lavas apparently are depleted in volatiles, but enrichment of those present may be sufficient to cause the viscous upwelling resulting from "a delicate balance between temperature, rate of cooling, uplift, viscosity, and pressure" (ref. 31-28).

If mare ridges are in part extrusive, the lava appears to have had a higher viscosity than that of the earlier crustal lavas. Cooling and crystallization of

FIGURE 31-30.—Linear mare ridge, apparently continuous with more typical wrinkle ridge; western Mare Imbrium, near Montes Harbinger (Apollo 15 panoramic camera frame AS15-10306).

FIGURE 31-31.—Bulbous squeeze-up on 1919 lava flow in Kilauea caldera (ref. 31-25, photograph by G. A. Macdonald).
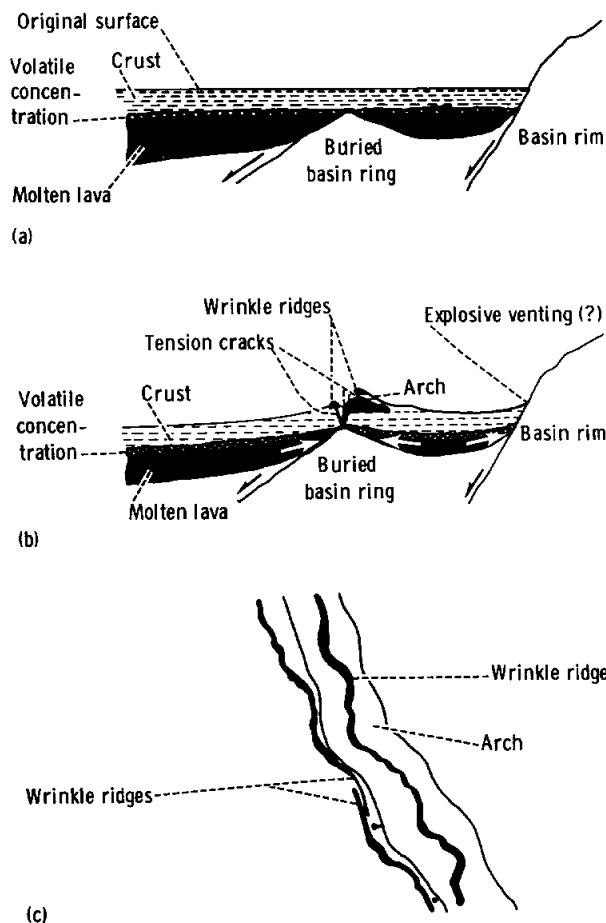

FIGURE 31-32.—Diagrams illustrating hypothetical roles of subsidence, volatile activity, and buried topography in formation of wrinkle ridges and arches. (a) Cross-sectional view of ponded lava in mare basin (only one phase of flooding shown). (b) Formation of autointrusive laccoliths, dikes, and squeeze-ups after subsidence and fracturing of mare crust. (c) Plane view of ridges and arch shown in part (b).

autointrusive material as it migrates upward might cause an increase in viscosity; this apparently was the case at Alae where pahoehoe crust was intruded by the more viscous aa lava of the dikes (ref. 31-19). Additionally, crystal-liquid fractionation may ultimately produce a high-viscosity melt; calculations by Weill et al. (ref. 31-30), based on compositions of Apollo 11 and 12 basalts, indicate that the intergranular material is a silica-rich residual liquid with viscosity approximately 10^4 greater than that of the initial molten lava—a result possibly applicable to the wrinkle ridge problem.

CONCLUSIONS

The autointrusive hypothesis suggested here for the origin of some of the mare ridges has the following advantages.

1. The inconsistent en echelon patterns of ridges (with both dextral and sinistral arrays along the same structural trend) can be attributed to extrusion along tension fractures rather than to large-scale transcurrent faulting.

2. Circular ridges over buried crater rims can be explained in this context without requiring a post-mare period of lava extrusion along crater fractures; the latter mechanism seems particularly unlikely at small craters, such as the one in figure 31-15.

3. The highly contorted, braided, and discontinuous patterns of many ridges seem more likely related to shallow structures than to major tectonic control.

4. The combination of broad arches and superposed narrow crenulate ridges seems better explained as a result of autointrusion and extrusion—with contemporaneous normal faulting in some cases—than by compressional buckling or thrust faulting, although both of the latter processes may also occur.

5. Some of the textures of the Apollo 11 ilmenite basalts were interpreted by James and Jackson (ref. 31-31) as indicative of lava lake conditions, including hornfels textures, caused by metamorphism of crustal fragments depressed into molten lava. Although they proposed only local ponding in flooded craters, the hypothesis suggested herein may be compatible with their interpretations.

That a lava lake hypothesis does not explain all mare ridges is convincingly demonstrated by the following examples.

1. Some ridges are continuous across lavas of different ages, as at the margin of Mare Serenitatis (part A of sec. 29).

2. Several ridges extend into terra, as near the Apollo 17 landing site (ref. 31-32) and near Fra Mauro (ref. 31-33).

Additional problems include the manner in which mare flooding occurred. The prominent flow scarps in Mare Imbrium and the layering in the walls of Rima Hadley (ref. 31-34) suggest that mare accumulation may have been by superposition of many relatively thin flows—rather than by massive flooding. However, the Imbrium flows exhibit the only prominent flow fronts yet found on the Moon, suggesting that they may be anomalous—a late-stage extrusion of a relatively small volume of lava (ref. 31-23), probably somewhat more viscous than that initially predominant in the maria. The apparent layering at Rima Hadley might have occurred within a single flow unit, or alternatively, early flood lavas may have remained molten at depth, despite superposition of thin flows at the surface.

The superposition of ridge material on a few adjacent impact craters indicates a hiatus between crust formation and ridge extrusion. However, such craters are consistently small—on the order of a kilometer—and thus require a solid crust of only a few hundred meters for their formation. Total thickness of the maria may be as great as several kilometers (refs. 31-35 and 31-36) so that the time of complete crystallization of successive ponded lavas may have been very long. Numerous small flooded craters (on the order of a few kilometers) suggest a depth of surficial lava of only a few hundred meters; alternatively, these craters could perhaps have formed by impact in a lake crust of appropriate thickness for flooding without destruction.

In conclusion, the suggestion that some mare ridges formed as squeeze-ups and autointrusions in tension fractures over buried topography in the crusts of lava lakes merits addition to the list of genetic hypotheses pertaining to these most prominent and perplexing structures of the lunar maria.

ACKNOWLEDGMENTS

PART C

LUNAR THRUST FAULTS IN THE TAURUS-LITTROW REGION

K. A. Howard[a] *and W. R. Muehlberger*[b]

"Wrinkle ridges" in the Taurus-Littrow region along the eastern margin of Mare Serenitatis appear very fresh and are probably among the youngest on the Moon. They include both mare ridges and similar-looking one-sided scarps. Evidence will be presented here to suggest that these ridges and scarps may be anticlines and thrust faults that resulted from sliding on a décollement surface. Alternative interpretations are presented by Scott (part D) and Hodges (part B).

The largest of these fresh mare ridges is referred to here as "Littrow ridge." It extends 130 km south from Le Monnier Crater to near Littrow B Crater. Figure 31-33 shows that the north end of Littrow ridge banks up against the highlands as a sinuous scarp resembling a flow front. We suggest that this is a consequence of thrusting the edge of a flat plate of relatively hard basalt against a homogeneous mountain, as indicated in figure 31-34(a). In the mountain, the fault cuts up to the surface through regolith rather than continuing as a horizontal plane into the mountain block. Littrow ridge is not likely to be a flow front, because at its south end it crosses two stratigraphic units (fig. 31-35). Evidence is presented elsewhere (part A of sec. 29) that the eastern ring basalt, on the left side of figure 31-35, overlaps the dark Littrow material on the right. The Littrow ridge has numerous bright blocky areas in the younger basalt, but, southeast of the geologic contact, the ridge-scarp assumes the very dark, unblocky character of the older material. The ridge thus appears to be a fault-bounded flexure that deforms both units. The ground to the left of the ridge appears to be overriding eastward along a thrust with small displacement.

Another branch of Littrow ridge lies a few kilometers to the west of the area in figure 31-35. As shown in figure 31-36, an elongate crater on this
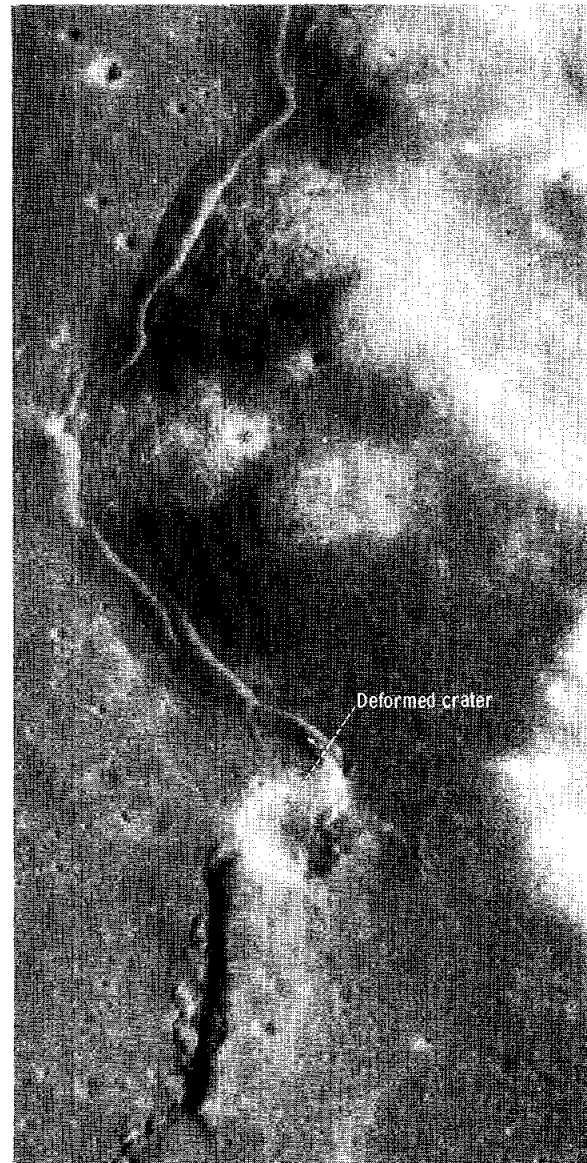

FIGURE 31-33.—North end of Littrow ridge near Le Monnier Crater. The ridge is banked against the highlands, suggesting thrusting as shown in figure 31-34(a). Area shown is 7 km across. Note the 1300-m wide crater deformed by the ridge (Apollo 15 panoramic camera frame AS15-9303).

---

[a]U.S. Geological Survey.
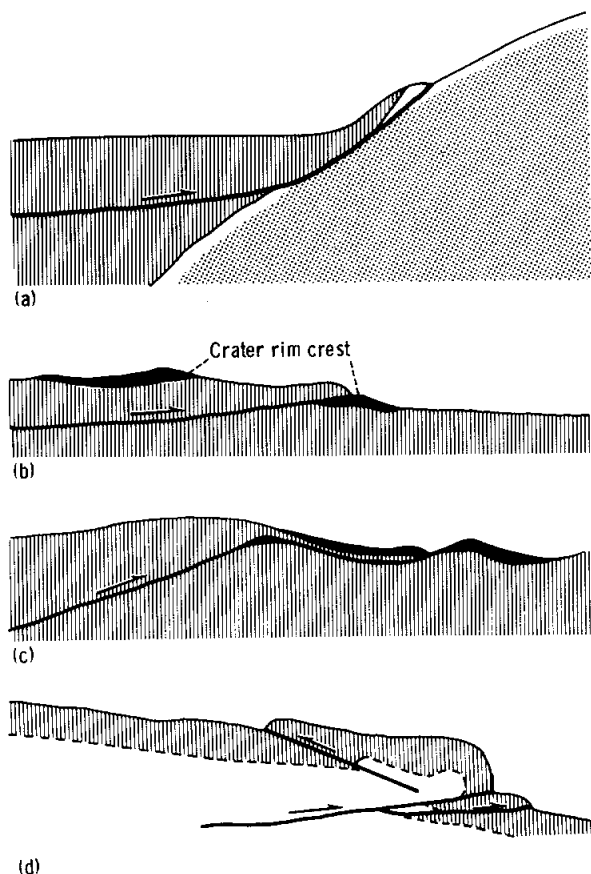[b]The University of Texas at Austin.

FIGURE 31-34.—Schematic cross sections of wrinkle ridges showing thrust-fault interpretation. (a) Ridge banked against highlands shown in figure 31-33, interpreted as a basalt slab riding up against the highlands. The Lee-Lincoln Scarp at the Apollo 17 site similarly banks up against North Massif to a height of 350 m (see fig. 31-38). (b) Truncated crater shown in figure 31-36. Ejecta blanket of the crater is indicated as a stratigraphic marker (black). (c) Flow lobe into crater, as shown in figure 31-36. Ejecta blanket (black) is suggested to be stretched out in lobe that rides into the crater. (d) "Backflow" features on the Lee-Lincoln Scarp at the Apollo 17 site. A photograph is shown in figure 31-38. Arbitrary stratum shown in cross section; height of main scarp is 80 m.

branch of the ridge is sharply truncated by an east-facing scarp at the margin of the ridge, and our impression is that part of the crater is missing. This can be explained if the ridge is a buckled thrust plate that has overridden the missing part of the crater, as suggested in figure 31-34(b). The offset is small. A similar situation is at the Apollo 17 landing site where Lee Scarp truncates Lara Crater (sec. 6 of this report).
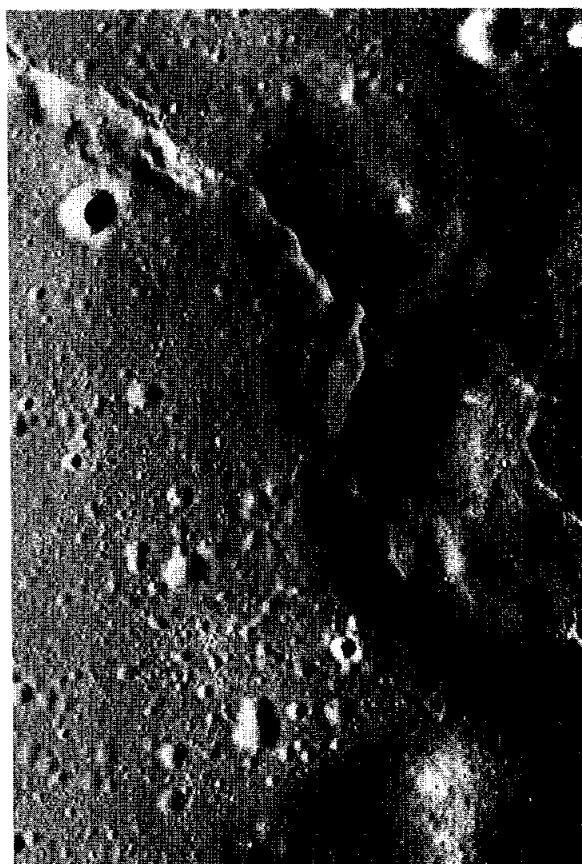
In other places, Littrow ridge has flowed into

FIGURE 31-35.—South end of Littrow ridge, 20 km west of Littrow B Crater. Area shown is 7 km across. Dark material of Littrow area occupies the hilly area on the east; younger eastern ring basalt laps against it from the west. The wrinkle ridge deforms both units. It is bright and blocky where it deforms the eastern ring basalt but becomes dark and is not blocky where it crosses into the Littrow material (Apollo 17 panoramic camera frame AS17-2313). (Locality "B" in fig. 29-7 of part A of sec. 29).

several craters, as shown in figure 31-36. These flows may be the manifestation of a flexible thrust plate overriding the ground surface (fig. 31-34(c)). The slabs of rock that flow into such craters are on the order of half a kilometer across and many meters thick. They are probably large and heavy enough to have flowed or slid under their own weight.

The Lee-Lincoln Scarp at the Apollo 17 landing site (shown in fig. 31-38 of part D) banks up against hills in a manner very similar to Littrow ridge in figure 31-33. The Lee-Lincoln Scarp has a sinuous trace like a flow front. It cannot be the front of a lava

FIGURE 31-36.—West branch of Littrow ridge, 10 km west of the area shown in figure 31-35. Area shown is 4 km across. A crater on top of the ridge is truncated by the edge of the ridge, and part of the crater appears to be missing; this suggests thrust faulting. Other craters are overridden by flow lobes from the ridge, possibly by thrusting over the ground surface as indicated in figure 31-34(b) (Apollo 17 panoramic camera frame AS17-2313).
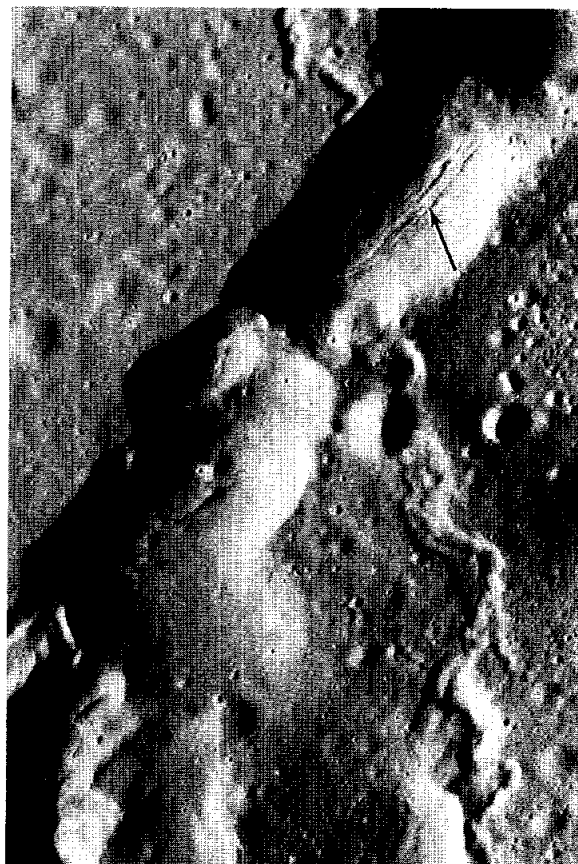

FIGURE 31-37.—Symmetrical portion of Littrow ridge, with fissures along the crest (15 km northwest of area shown in fig. 31-35). Area shown is 5 km across. The fissures are believed to be a consequence of stretching over the anticline, as in pressure ridges of terrestrial lavas.

flow, however, because it climbs over mountains. In the Apollo 17 valley, the scarp offsets the basalt surface down 80 m to the east and so must be a fault. Locally, there are "backflow" features or scarps that face the opposite way from the main scarp. These may be antithetic thrusts caused by buckling, as suggested in figure 31-34(d). Probably as a result of similar antithetic thrusts, parts of the Littrow ridge have both symmetric and asymmetric scarps (fig. 31-37), and the direction of asymmetry changes along strike. This deformation is possibly analogous to obduction and subduction in terrestrial plate tec-

tonics, where one plate rides over in some areas and the other plate rides over in other areas. This relationship suggests a mobile substratum or décollement.

The supposed upper thrust plates described here are generally buckled into anticlinal ridges. Similar buckle folds occupy the upper plates of some uneroded thrust faults that reach the ground surface on Earth (refs. 31-19 and 31-37; figs. 31-18 and 31-19). Rarely, the lunar anticlines are fissured along their crests by stretching (fig. 31-37).

Littrow ridge appears to be much younger than the lavas that it deforms. This conclusion is based on the observation that craters of presumed impact origin are deformed by the ridge (figs. 31-33 and 31-36), and the same relationship applies at Lara

Crater on the Lee-Lincoln Scarp (sec. 6 of this report). The deformed craters in figures 31-33 and 31-36 are 1300 and 650 m across, respectively. The cratering flux in mare-age time (refs. 31-38 and 31-39) would require several tens of millions of years for random impacts to make these craters in an area the size of Littrow ridge. A similar ridge deforms the even larger (3 km) crater Littrow BB. Apparently,

then, the basalts solidified many millions of years before the fresh ridges formed.

If the thrust explanation is correct, then, in postmare time, eastern Mare Serenitatis and the adjacent highlands were subjected to east-west compression. This compression caused sliding on a décollement surface. This surface could be in part an old regolith at an unconformity in the basalt sequence.

PART D

SMALL STRUCTURES OF THE TAURUS-LITTROW REGION

David H. Scott[a]

Apollo 17 premission geologic studies of the Taurus-Littrow region of the Moon revealed numerous small structures, in both mare and terra, having somewhat similar morphologies and variously resembling fault scarps, flow fronts, and mare ridges. Many of these features are too small to be identified on Lunar Orbiter IV photographs, which provided the most comprehensive, high-resolution coverage of this area before the later Apollo missions. The panoramic- and metric-camera photographs of Apollo 17 were taken at lower Sun angles than those of Apollo 15, which were used for the geologic mapping (refs. 31-40 and 31-41), and thus more clearly reveal fine details of texture and relief. In the illustrations of this part, several of these small structures are compared. It is concluded that they probably developed as lava extrusions from fractures and fissures; they cannot be easily explained by faulting.

Figure 31-38 shows the prominent ridge and scarp (generally referred to as the Lee-Lincoln Scarp) that extends across the Littrow valley between the North and South Massifs. This is the largest example of a composite structure that is morphologically variable along its length and may reflect various modes of origin from place to place. It was traversed by the Apollo 17 crew near its southern extremity (outside the photograph) where the scarp is less continuous and several breaks occur in the wall. Along the

southern and central parts of the structure (areas A and B), mare-type ridges and overlapping lobes suggest emplacement as lava flows from the west. To the north, where it crosses the steep face of North Massif (area C), it has the form of a ledge-like scarp or terrace, believed by some geologists to be indicative of normal- or high-angle reverse faulting (ref. 31-41 and part C of this section). The material forming the ledge, however, appears smoother and more youthful than that of the massif (ref. 31-42) and may consist of lava extruded along a fissure. In many respects, this structure resembles the mare ridge/highland ledge (which is not readily interpreted as a faulted structure) along the southwestern rim of the crater Le Monnier shown in Apollo 15 panoramic camera frame AS15-9303 (fig. 31-33).

The northern en echelon extension of the Lee-Lincoln Scarp is shown in figure 31-39 with probable flow fronts visible in places (areas A and B) but having a sinuous to somewhat cuspate appearance (area C) more like the structures in the hilly material of figure 31-40, located about 50 km to the south. In figure 31-40, two opposing scarplets (areas A and B) resemble slabs of rock separated along sheet-joints parallel or subparallel to the surface. These are formed on Earth by a complex of processes including pressure release and strong diurnal thermal variations. There are no obvious remnants of the intervening portions of the slab, however, and one of the structures appears to be intergradational (at area C) with a mare ridge.
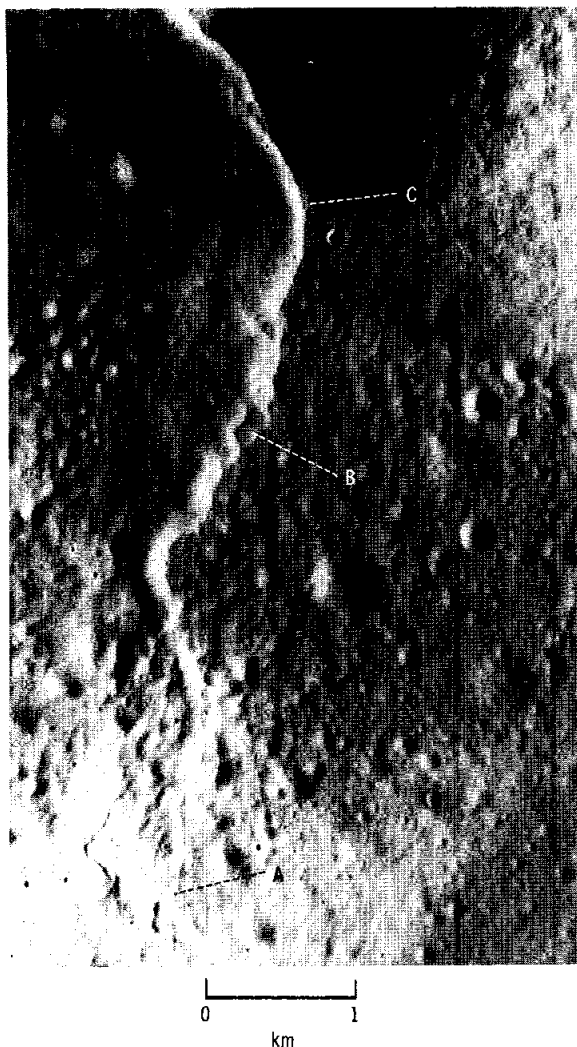
[a]U.S. Geological Survey.

FIGURE 31-38.—Composite structure (Lee-Lincoln Scarp) extending across the valley floor and North Massif near Apollo 17 landing site: (A) and (B) mare-type ridges and lobate, overlapping flow fronts; (C) ledge along North Massif (Apollo 17 panoramic camera frame AS17-2314).

FIGURE 31-39.—En echelon extension of the structure in figure 31-38: (A) and (B) flow fronts; (C) curved flow front similar to those in figure 31-40 (Apollo 17 panoramic camera frame AS17-2314).

Figures 31-41 and 31-42 show two ledges along the face of a massif just north of the crater Vitruvius. In places, they have the appearance of "strand lines" (refs. 31-43 and 31-44) that are common around mare embayments in this area (Apollo 17 panoramic camera frame AS17-2297) and presumably mark the highest occurrence of basalt fill. Unlike most strand lines, however, the ledges are discontinuous and do not maintain positions of equal elevation along their extent. The ledge (A) shown in figure 31-41 may abruptly change strike and continue normal to the

massif as a small scarp (B) within mare material. The scarp, in turn, seems to merge with a mare ridge (C). In figure 31-42, the ledge (A) remains within the massif but becomes discontinuous and breaks up into lobate scarps and ridges (B) that seem partly to bury a linear trough or fissure (areas C and D). The texture of the material forming the ledge and ridges appears to be smoother than that of the massif but rougher than the adjacent mare that embays it.

A transition from mare ridge to flow front morphology is illustrated in figure 31-43. The large rille (A), Rima Littrow III, is nearly buried by overlapping apparent lava flows (areas B and C) that become younger and more ridge-like (D) to the south. Relationships are not simple, however, as the direction of flow seems to be upslope toward the northeast. This may be due to subsequent downwarping of the Serenitatis basin to the west, but the position of the flow with respect to the highland barrier (E) in the northwest part of the photograph is difficult to reconcile in this case. Lava may have been extruded from fissures near the present front and
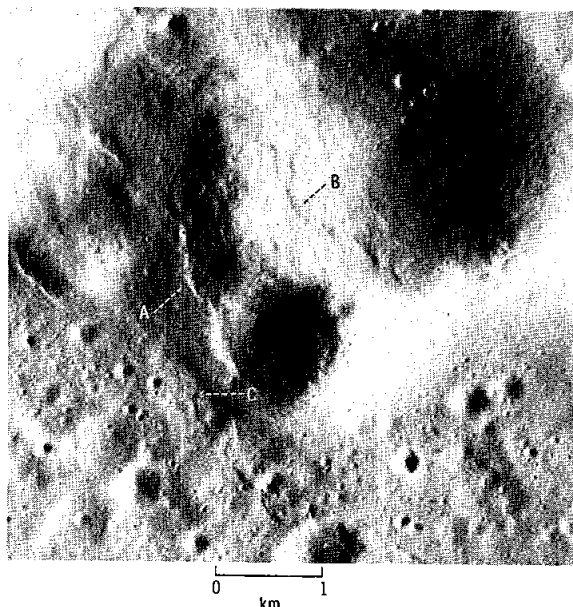
FIGURE 31-40.—Areas A and B are opposing flow fronts resembling slabs separated by sheet-jointing; (C) transition to mare ridge (Apollo 17 panoramic camera frame AS17-2314).
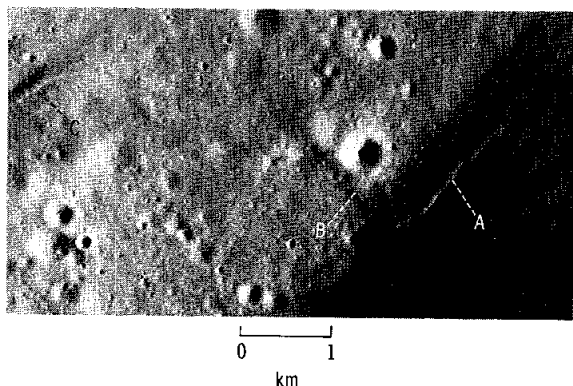

FIGURE 31-41.—Area A is ledge on massif; (B) small scarp in mare material; (C) mare ridge (Apollo 17 panoramic camera frame AS17-2314).

FIGURE 31-42.—Area A is ledge on massif similar to the one in area A of figure 31-41; (B) lobate flows covering central part of linear trough shown at areas (C) and (D) (Apollo 17 panoramic camera frame AS17-2318).

flowed downslope to the southwest. The older flows appear to have been more fluid than those that form the fresh-appearing ridges south of the rille.

A photographic summary of structures similar to those discussed and illustrated in the preceding photographs is contained in figure 31-44 near Mons Argaeus. A large flow with a very prominent front buries one rille (A) and partly buries another (B) but has no discernible source. It probably originated from

numerous local fissures which have locations that may be coincident in places with sharp, irregular ridges on its flanks and surface (C). A small ledge (D) is faintly visible descending the southwestern face of the massif to the valley floor where it merges with a

FIGURE 31-43.—Area A is Rima Littrow III; (B) and (C) overlapping lava flows; (D) mare ridge; (E) prominent hill. Arrow points down regional slope (Apollo 17 panoramic camera frame AS17-2316).

FIGURE 31-44.—In area A, lava flow completely buries rille and partly buries another in area B; (C) one of several ridges on surface and flanks of lava flow; (D) small ledge on massif; (E) ledge transition to mare ridge; (F) young crater partly buried by flow; (G) and (H) flow front merges with mare ridges (Apollo 17 panoramic camera frame AS17-2316).

mare-type ridge (E). In the southeast, a lava flow buries one side of a small (1 km) young (Eratosthenian) crater (F) and develops into ridge structures to the east (G) and west (H).

In conclusion, the small structures expressed as scarps, ledges, flow fronts, and mare-type ridges seem closely interrelated and probably have common origins. The general appearance and geometry of these structures have never been convincingly explained by faulting—either normal, thrust, or high-angle reverse. The abundant photographic evidence provided by the Apollo 17 panoramic camera indicates that they probably have developed as extrusions from fractures and fissures with little associated faulting or folding.

REFERENCES

31-1. Oberbeck, Verne R.; Aoyagi, Michio; Greeley, Ronald; and Lovas, Michael: Planimetric Shapes of Lunar Rilles. Sec. 29, Part Q, of the Apollo 16 Preliminary Science Report. NASA SP-315, 1972.

31-2. Greeley, Ronald: Lava Tubes and Channels in the Lunar Marius Hills. The Moon, vol. 3, no. 3, Dec. 1971, pp. 289-314.

31-3. Oberbeck, Verne R.; Quaide, William L.; and Greeley, Ronald: On the Origin of Lunar Sinuous Rilles. Mod. Geol., vol. 1, 1969, pp. 75-80.

31-4. Soderblom, L. A.: The Process of Crater Removal in the Lunar Maria. Sec. 25, Part P, of the Apollo 15 Preliminary Science Report. NASA SP-289, 1972.

31-5. Greeley, Ronald; and Hyde, Jack H.: Lava Tubes of the Cave Basalt, Mount St. Helens, Washington. Bull. Geol. Soc. Am., vol. 83, no. 8, Aug. 1972, pp. 2397-2418.

31-6. Cruikshank, D. P.; and Wood, C. A.: Lunar Rilles and Hawaiian Volcanic Features: Possible Analogues. The Moon, vol. 3, no. 4, Mar. 1972, pp. 412-447.

31-7. Colton, George W.; Howard, Keith A.; and Moore, Henry J.: Mare Ridges and Arches in Southern Oceanus Procellarum. Sec. 29, Part S, of the Apollo 16 Preliminary Science Report. NASA SP-315, 1972.

31-8. Strom, R. G.: Lunar Mare Ridges, Rings and Volcanic Ring Complexes. Mod. Geol., vol. 2, 1971, pp. 133-157.

31-9. Fielder, G.: Volcanic Rings on the Moon. Nature, vol. 213, Jan. 28, 1967, pp. 333-336.

31-10. Carr, M. H.: Geologic Map and Section of the Timocharis Region of the Moon. U.S. Geol. Survey Misc. Geol. Inv. Map I-462, 1965.

31-11. Green, Jack: Comparison of Lunar and Terrestrial Surface Features. Proceedings of Lunar and Planetary Exploration Colloquium, vol. 1, North American Aviation, Inc. (Downey, Calif.), 1959, pp. 2-3.

31-12. Green, Jack: Tidal and Gravity Effects Intensifying Lunar Defluidization and Volcanism. New York Acad. Sci. Annals, vol. 123, July 15, 1965, pp. 403-469.

31-13. Baldwin, Ralph B.: The Measure of the Moon. Univ. of Chicago Press, 1963.

31-14. Bryan, W. B.: Wrinkle-Ridges as Deformed Surface Crust on Ponded Mare Lava. Lunar Science IV (Abs. of papers presented at the Fourth Lunar Science Conference (Houston, Tex.), Mar. 5-8, 1973), pp. 103-105.

31-15. Quaide, William: Rilles, Ridges and Domes—Clues to Maria History. Icarus, vol. 4, no. 4, Sept. 1965, pp. 374-389.

31-16. Tjia, H. D.: Lunar Wrinkle Ridges Indicative of Strike-Slip Faulting. Bull. Geol. Soc. Am., vol. 81, Oct. 1970, pp. 3095-3100.

31-17. Wilhelms, D. E.; and McCauley, J. F.: Geologic Map of the Near Side of the Moon. U.S. Geol. Survey Misc. Geol. Inv. Map I-703, 1971.

31-18. Duffield, W. A.: A Naturally Occurring Model of Global Plate Tectonics. J. Geophys. Res., vol. 77, 1972, pp. 2543-2555.

31-19. Swanson, Donald A.; and Peterson, Donald W.: Partial Draining and Crustal Subsidence of Alae Lava Lake, Kilauea Volcano, Hawaii. U.S. Geol. Survey Prof. Paper 800-C, 1972, pp. C1-C14.

31-20. Hodges, C. A.: Geologic Map of the Langrenus Quadrangle of the Moon. U.S. Geol. Survey Misc. Geol. Inv. Map I-739, 1973.

31-21. Duffield, Wendell; and Nakamura, Kazuaki: A Photogeologic Method for Determining the Direction of Horizontal Dilation From Patterns of En Echelon Fracturing. U.S. Geol. Survey Jour. Res., vol. 1, no. 3, 1973, pp. 283-287.

31-22., Whitaker, Ewen A.: Mare Imbrium Lava Flows and Their Relationship to Color Boundaries. Sec. 25, Part M, of the Apollo 15 Preliminary Science Report. NASA SP-289, 1972.

31-23. Schaber, Gerald G.: Lava Flows in Mare Imbrium: Geologic Evaluation From Apollo Orbital Photography. Lunar Science IV (Abs. of papers presented at the Fourth Lunar Science Conference (Houston, Tex.), Mar. 5-8, 1973), pp. 653-654.

31-24. Colton, H. S.; and Park, C. F., Jr.: Anosma or "Squeeze-Ups." Science, vol. 72, 1930, p. 579.

31-25. Wentworth, C. K.; and Macdonald, G. A.: Structures and Forms of Basaltic Rocks in Hawaii. U.S. Geol. Survey Bull. 994, 1953.

31-26. Richter, D. H.; and Moore, J. G.: Petrology of the Kilauea Iki Lava Lake, Hawaii. U.S. Geol. Survey Prof. Paper 537-B, 1966.

31-27. Scott, D. H.; and Eggleton, R. E.: Geologic Map of the Rümker Quadrangle of the Moon. U.S. Geol. Survey Misc. Geol. Inv. Map I-805, 1973.

31-28. Williams, Howell: History and Character of Volcanic Domes. Calif. Univ. Pub. Geol. Sci., vol. 21, 1932, pp. 51-146.

31-29. Hodges, C. A.: Comparative Study of S.P. and Sunset Craters and Associated Lava Flows. Plateau, vol. 35, no. 2, 1962, pp. 15-35.

31-30. Weill, D. F.; Grieve, R. A.; McCallum, I. S.; and Bottinga, Y.: Mineralogy-Petrology of Lunar Samples. Microprobe Studies of Samples 12021 and 12022; Viscosity of Melts of Selected Lunar Compositions. Proceedings of the Second Lunar Science Conference, vol. 1, MIT Press (Cambridge, Mass.), 1971, pp. 413-430.

31-31. James, Odette B.; and Jackson, Everett D.: Petrology of the Apollo 11 Ilmenite Basalts. J. Geophys. Res., vol. 75, no. 29, Oct. 10, 1970, pp. 5793-5824.

31-32. Wolfe, Edward W.; Freeman, Val L.; Muehlberger, William R.; Head, James W.; Schmitt, Harrison H.; and Sevier, John R.: Apollo 17 Exploration of Taurus-Littrow. Geotimes, vol. 17, no. 11, Nov. 1972, pp. 14-18.

31-33. Eggleton, R. E.: Geologic Map of the Fra Mauro Region of the Moon. U.S. Geol. Survey Misc. Geol. Inv. Map I-708, 1970.

31-34. Swann, G. A.; Bailey, N. G.; Batson, R. M.; Freeman, V. L.; et al.: Preliminary Geologic Investigation of the Apollo 15 Landing Site. Sec. 5 of the Apollo 15 Preliminary Science Report. NASA SP-289, 1972.

31-35. Marshall, C. H.: Thickness of the Procellarian System, Letronne Region of the Moon. U.S. Geol. Survey Prof. Paper 424-D, 1961.

31-36. Latham, G.; Ewing, M.; Dorman, J.; Press, F.; et al.: Seismic Data From Man-Made Impacts on the Moon. Science, vol. 170, no. 3958, Nov. 6, 1970, pp. 620-626.

31-37. Koch, Thomas W.: Analysis and Effects of Current Movement on an Active Fault in Buena Vista Hills Oil Field, Kern County, California. Amer. Assoc. Petroleum Geol. Bull., vol. 17, no. 6, June 1933, pp. 694-712.

31-38. Hartmann, William K.: Lunar Cratering Chronology. Icarus, vol. 13, no. 2, Sept. 1970, pp. 299-301.

31-39. Cruikshank, D. P.; Hartmann, W. K.; and Wood, C. A.: Moon: Ghost Craters Formed During Mare Filling. The Moon, 1973.

31-40. Scott, D. H.; and Carr, M. H.: Geologic Map of the Taurus-Littrow Region of the Moon. U.S. Geol. Survey Misc. Geol. Inv. Map I-800, sheet 1 of 2, 1972.

31-41. Lucchitta, B. K.: Geologic Map of the Taurus-Littrow Region of the Moon. U.S. Geol. Survey Misc. Geol. Inv. Map I-800, sheet 2 of 2, 1972.

31-42. Apollo Lunar Geology Investigation Team: Preliminary Report on the Geology and Field Petrology at the Apollo 17 Landing Site. U.S. Geol. Survey Interagency Rept., Astrogeol. 69, Dec. 17, 1972.

31-43. Carr, M. H.; Howard, K. A.; and El-Baz, Farouk: Geologic Maps of the Apennine-Hadley Region of the Moon. U.S. Geol. Survey Misc. Geol. Inv. Map I-723, sheet 2 of 2, 1971.

31-44. West, Mareta N.: Selected Volcanic Features. Sec. 25, Part L, of the Apollo 15 Preliminary Science Report. NASA SP-289, 1972.

32. Crater Studies

Morphometric analysis of 25 far-side craters confirms their similarity to near-side craters, implies an impact genesis, and reveals a new shape discontinuity at a diameter of 17 km (part A). The large prominent crater Aitken, on the far side, exhibits a number of unusual volcanic features in its floor, notably the clustered domes in small craters (parts B and C).

Experimental impacts have produced craters with associated ridges resembling the lunar "herringbone pattern" common along chains of secondary craters; similar ridges have been discovered at the Davy Crater chain, suggesting that the widely held interpretation of that chain as volcanic may be incorrect (part D).

PART A

LUNAR CRATER MORPHOMETRY

Richard J. Pike[a]

Morphometry, the quantitative study of shape, complements visual observation and photointerpretation in analyzing the most outstanding landforms of the Moon, its craters (refs. 32-1 and 32-2). All three of these interpretative tools, which were developed throughout the long history of telescopic lunar study preceding the Apollo Program, will continue to be applicable to crater analysis until detailed field work becomes possible. Although no large (> 17.5 km diameter) craters were examined in situ on any of the Apollo landings, the photographs acquired from the command modules will markedly strengthen results of less direct investigations of the craters. For morphometry, the most useful materials are the orbital metric and panoramic photographs from the final three Apollo missions. These photographs permit preparation of contour maps, topographic profiles, and other numerical data that accurately portray for the first time the surface geometry of lunar craters of all sizes. Interpretations of craters no longer need be compromised by inadequate topographic data. In the pre-Apollo era, hypotheses for the genesis of lunar craters usually were constructed without any numerical descriptive data. Such speculations will have little credibility unless supported by accurate, quantitative data, especially those generated from Apollo orbital photographs. This paper presents a general study of the surface geometry of 25 far-side craters and a more detailed study of rim-crest evenness for 15 near-side and far-side craters. Analysis of this preliminary sample of Apollo 15 and 17 data, which includes craters between 1.5 and 275 km in diameter, suggests that most genetic interpretations of craters made from pre-Apollo topographic measurements may require no drastic revision. All measurements were made from topographic profiles generated on a stereoplotter at the Photogrammetric Unit of the U.S. Geological Survey, Center of Astrogeology, Flagstaff, Arizona.

[a]U.S. Geological Survey.

FAR-SIDE CRATERS

Through photometric processing of Zond 3 imagery, Mironova (refs. 32-3 and 32-4) generated the first morphometric measurements ever made on lunar far-side craters. The 29 craters profiled and measured in that study range in diameter from 16 to 100 km and vary in relative age. From a brief analysis of surface geometry, Mironova concluded that the far-side craters were similar in shape to near-side craters and were volcanic. Both interpretations are examined with reference to new data on far-side craters as well as to prior results in near-side crater morphometry.

According to previous work (ref. 32-2), most lunar near-side craters are geometrically similar to terrestrial meteorite-impact craters and do not resemble volcanic craters except for some maars and tuff rings. The morphometric criteria that reveal this distinction best are three ratios of crater dimensions (fig. 32-1): rim height/diameter, rim height/crater depth, and outer-rim width/diameter. Although, statistically, rim-crest circularity also is a good genetic discriminant, it can break down when applied to anomalous individual craters, which include highly circular maars and calderas as well as polygonal and asymmetric impact craters. Additional criteria, for making shape comparisons among lunar craters alone, are the depth/diameter ratio and the slope of crater rims.

The dimensions of 25 different far-side craters were obtained from topographic profiles and rim-crest outlines reduced photogrammetrically from Apollo 15 metric camera photographs (table 32-I and fig. 32-2). Two profiles, intersecting at 90° at the crater center, were made across the 15 largest craters from stereographic models leveled primarily on the flat inner floors. Thus, the smaller craters that are situated along these profiles probably are leveled with the same degree of accuracy. The sample craters vary in appearance from fresh to subdued; despite efforts to represent correctly all degrees of relative age, the resulting sample is weighted toward fresher craters. The six dimensions recorded for each crater (fig. 32-1) are averaged values of rim diameter, width of the inner- and outer-rim flanks, diameter of the inner flat floor, depth, and height of the rim crest above the exterior datum. Other values in table 32-I were calculated from these data. A simple index of rim-crest circularity was also computed.

Apollo depth/diameter results from far-side craters fit near-side depth/diameter relations, obtained from
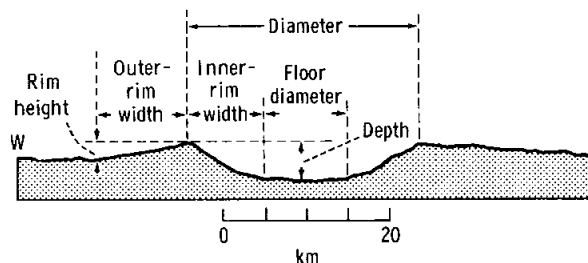

FIGURE 32-1.—Six crater dimensions. Topographic profile across the near-side crater Proclus from photogrammetry of Apollo 17 metric camera photographs. Corrected for planetary curvature. No vertical exaggeration. Directions are approximate only.

800 craters (ref. 32-2), more accurately than do the Zond 3 data, which generally represent craters as being excessively shallow (fig. 32-3). Despite the scarcity of fresh craters in the 10- to 20-km-diameter range spanning the inflection in the depth/diameter plot, the Apollo results agree well with the near-side measurements. There is some suggestion that the Apollo data show craters as slightly deeper than do older shadow-length measurements. Additional photogrammetric data (near-side measurements, not shown here) support both findings for far-side craters.

Using the depth/diameter proportion, Mironova (ref. 32-3) deduced a volcanic genesis for both near-side and far-side craters from the same type of analog argument by which Baldwin (ref. 32-5) inferred the impact origin of near-side craters. Although the depth/diameter relation has become the most often used morphometric criterion of crater genesis, the generous overlap among depth/diameter fields describing all types of lunar and terrestrial craters demonstrates that it is also the least reliable of all available geometric discriminants (ref. 32-2). Accordingly, neither set of far-side depth/diameter data can support any specific genetic hypothesis. Crater depth measurements are better applied to the analysis of relative age (ref. 32-5).[1]

Both Apollo and Zond 3 rim height measurements are consistent with an impact origin for large far-side craters (fig. 32-4). Despite errors and the paucity of points, both sets of results are at least roughly similar

---

[1] Pike, R. J.: Meteoritic Origin and Consequent Endogenic Modification of Large Lunar Craters—A Study in Analytical Geomorphology. Unpublished Thesis, Univ. of Michigan, 1968.

TABLE 32-I.—*Morphometric Properties of Far-side Craters*

| Name or location	Rim diameter, km	Outer-rim width, km	Floor diameter, km	Inner-rim width, km	Depth, m	Outer-rim height, m	Inner-rim slope, deg	Outer-rim slope, deg	Circularity[a]
In Sklodowska	1.6	0.4	—	0.8	300	95	20.6	13.4	0.90
In Sklodowska	2.8	.5	—	1.4	550	125	21.5	14.0	.88
In Hirayama	3.5	1.0	—	1.7	500	175	16.2	9.9	.84
In Curie	4.3	.9	—	2.1	600	175	15.8	11.0	.64
In Tsiolkovsky	4.9	1.0	—	2.4	950	100	21.3	5.7	.73
In Hilbert	6.0	1.0	—	3.0	950	150	17.6	8.5	.79
In Pasteur[b]	9.9	1.8	2.8	3.6	1100	105	17.2	3.3	.79
In Saha[b]	15.7	3.6	9.0	3.4	880	280	14.7	4.4	.80
In Gagarin	16.0	3.5	10.0	3.0	1350	650	24.2	10.5	.90
In Gagarin	17.0	4.5	6.0	5.5	1700	450	17.2	5.7	.89
In Hilbert	17.0	3.0	5.0	6.0	1800	400	16.7	7.6	.79
On western rim of Gagarin	26.0	6.0	13.0	6.5	2600	725	21.8	6.9	.86
Izsak	33.2	7.7	13.0	10.1	3400	1025	18.6	7.6	.86
Gilbert M	34.0	5.5	18.0	8.0	3100	850	21.2	8.8	.84
Gansky	44.0	12.0	22.0	11.0	3550	950	17.9	4.5	.78
South of Saha	50.5	13.3	24.0	13.3	3640	1380	15.4	5.9	.83
Schorr	53.5	13.0	26.0	13.8	3700	730	15.1	3.2	.77
Ritz	59.0	15.5	24.0	17.5	3750	1800	12.1	6.6	.71
King	71.0	17.0	40.0	15.5	3830	1690	13.9	5.7	.80
Langemak[b]	110.0	17.0	60.0	25.0	4370	880	9.9	3.0	.68
Sklodowska	128.0	18.0	83.0	22.5	4500	1850	11.3	5.9	.78
Curie[b]	158.0	29.0	100.0	29.0	3850	1500	7.5	2.9	.73
Hilbert	178.0	35.0	125.0	26.5	4100	1500	8.8	2.5	.80
Tsiolkovsky	190.0	40.0	140.0	25.0	4700	1750	10.7	2.5	.83
Gagarin[b]	275.0	43.0	200.0	37.5	5375	(3350?)	8.2	(4.5?)	.79

[a]Ratio of areas of circles inscribed and circumscribed on rim-crest outline.
[b]Older appearing craters.
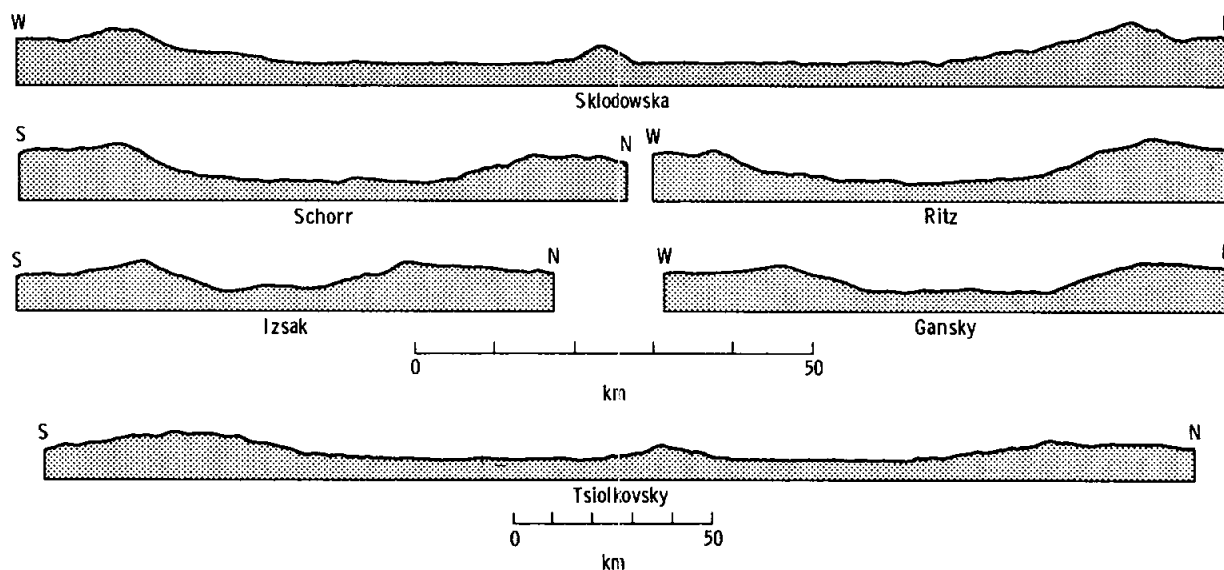
FIGURE 32-2.—Topographic profiles across six lunar far-side craters from photogrammetry of Apollo 15 metric camera photographs. No vertical exaggeration. Corrected for planetary curvature. Directions are approximate only.
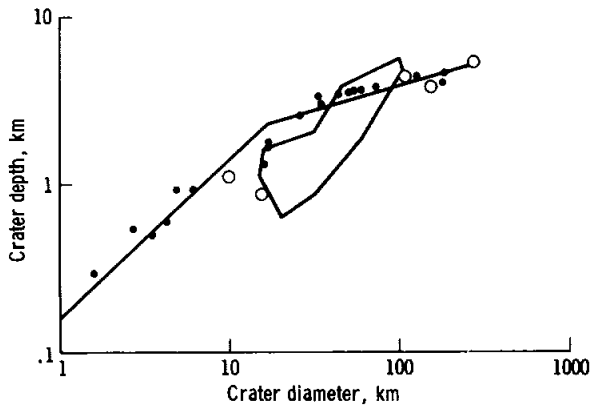
FIGURE 32-3.—Logarithmic depth/diameter plot for 25 lunar far-side craters (dots and circles). Circles are markedly older appearing craters. Polygon contains Zond 3 data for 29 far-side craters. Inflected curve is best fit to 800 lunar near-side craters.
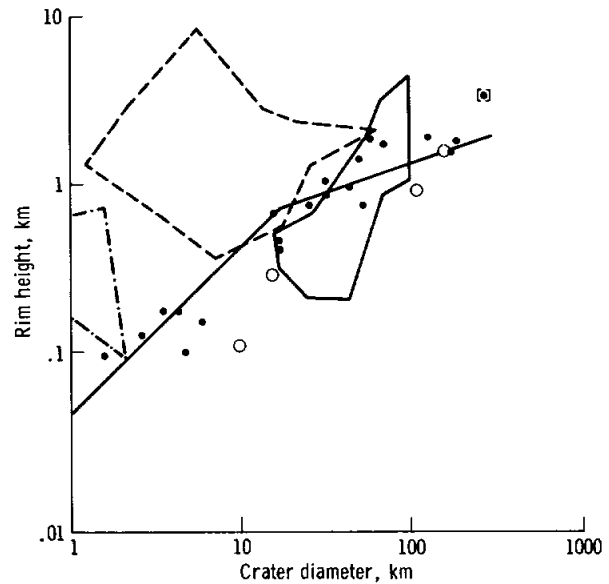

FIGURE 32-4.—Logarithmic rim height/diameter plot for 25 lunar far-side craters (dots and circles). Circles are markedly older appearing craters. Bracketed data point (crater Gagarin) is from inadequate data. Solid polygon contains Zond 3 data for 29 far-side craters. Inflected curve is best fit to 325 lunar near-side craters; terrestrial meteorite craters (not shown) also follow this trend. Dashed polygon contains data for 44 terrestrial calderas. Dashed-dotted polygon contains data for seven craters atop lunar mare domes.

to rim heights of terrestrial meteorite and experimental explosion craters, whereas they are much lower than the heights of terrestrial volcanic calderas and lunar dome-summit craters. The most recently published rim height/diameter relation for near-side craters (ref. 32-2) inflects at the same crater diameter (approximately 17 km) as the depth/diameter relation. Although the Apollo far-side measurements do not agree closely with prior height/diameter data, in this respect they still are superior to the Zond 3 rim heights, which are too low for smaller craters and excessive for larger craters. Additional photogrammetric information (near-side measurements, not shown here) suggests that the 17-km-diameter elbow in the height/diameter relation may not be as abrupt as the depth/diameter inflection.

The ratio of rim height to crater depth, which may be an effective quantitative criterion of origin for most types of rimmed lunar and terrestrial craters (ref. 32-6), is constant for normal, rimmed lunar craters of all sizes. The height/depth relation for the 25 far-side craters measured from Apollo data (not shown here graphically) is similar to that established previously for near-side craters (ref. 32-2). The Zond 3 height/depth ratios also are generally similar; the agreement implies that, despite absolute error, photometric analysis of the Zond far-side imagery at least preserved the relative proportions between crater depth and rim height. Both sets of far-side height/depth measurements agree with similar measurements of terrestrial meteorite craters and experimental

explosion craters. Both Zond and Apollo rim height/crater depth values are much lower than similar measurements describing terrestrial calderas and cinder cones or summit craters atop lunar domes (ref. 32-2).

The ratio of exterior rim width to crater diameter also may be a genetic criterion for most types of lunar and terrestrial craters (ref. 32-7). This parameter, like the height/depth ratio, has a fairly constant range of values over the entire diameter span of normal, rimmed lunar craters. Rim widths measured on profiles made from Apollo metric camera photographs are systematically, if only slightly, larger than values estimated visually from lunar photographs (ref. 32-2). Although the slope of the rim width/crater diameter relation remains approximately 1.00, the Y-intercept for the Apollo far-side values is 0.210 as compared with 0.170 for visual data. This change does not affect genetic implications made from prior rim width measurements. As a function of crater diameter, the rims of far-side craters measured from

Apollo data are significantly narrower than rims of nearly all types of terrestrial volcanic craters, but are similar in width to rims of terrestrial meteorite craters (ref. 32-7). Rim width measurements of far-side craters, which were not included in the analysis of thd Zond 3 data, also are consistent with an impact genesis of the lunar craters.

Although in part dependent on geologic structure, the planimetric radial symmetry of the rim crest of a crater can have considerable genetic significance (ref. 32-8). The index of circularity used here is the ratio of the area of the largest circle inscribed within the rim-crest outline to the area of the smallest circle circumscribed around the outline. It is selected over more comprehensive parameters of circularity because it can be accurately determined for craters shown only as small photographic images and thus is more widely applicable. The average circularity of all 25 far-side craters, 0.80, is high; the range of values is 0.64 to 0.90. The difference in circularity for craters above and below the 17-km-diameter location of the inflection in the depth/diameter curve, only 0.02, is not significant. These values are more consistent with an impact genesis of the 25 sample craters than with a volcanic origin, which typically results in a much lower degree of planimetric radial symmetry (ref. 32-9).

The relative steepness of crater rims, a dimension which can be measured reliably from the Apollo photographs, varies fairly systematically with crater diameter and relative age. The angles of inner- and outer-rim slope used here are highly generalized values. Respectively, they are average slope between the rim crest and the juncture of the inner-rim slope and the flat floor, and average slope between the rim crest and the break in slope at the base of the outer-rim flank. The average rim slopes differ substantially from the maximum rim slopes, which were calculated over much shorter distances and used in the analysis of Zond 3 imagery; a direct comparison is not meaningful. The slope values used here are preferable because they are more representative and less subject to chance errors in raw data.

A graph of inner-rim slope angle as a function of crater diameter reveals a new size-dependent morphometric discontinuity at the 10- tc 20-km-diameter range (fig. 32-5). The break in the distribution, which is duplicated in a comparable graph for 14 near-side craters (not shown), probably is real. The discontinuity in the outer-rim slope data may be accidental
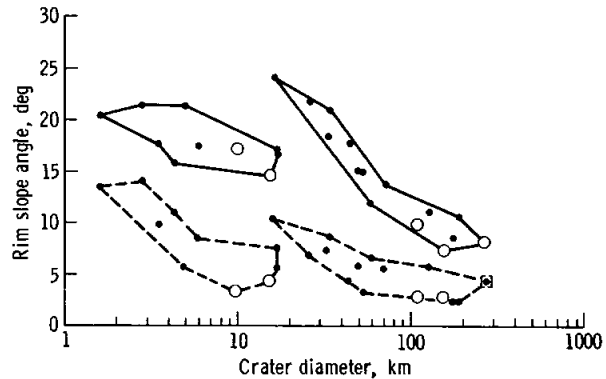

FIGURE 32-5.—Semilogarithmic rim slope angle/diameter plot for 25 lunar far-side craters (dots and circles). Circles are markedly older appearing craters. Bracketed data point (crater Gagarin) is from inadequate data. Solid lines enclose inner-rim slope data; dashed lines enclose outer-rim slope data.

and characteristic only of this sample of far-side craters, because the near-side data show no such break. The inflection almost certainly results from the appearance of a well-defined, flat interior floor in young craters approximately 10 to 20 km in diameter (table 32-I). The increasing steepness within craters just above the critical size threshold arises from differences in interior profile geometry between floorless and flat-floored craters. In a floorless crater, the interior rim slope is measured between the center of the crater bottom and the rim crest; the slope length includes a considerable proportion of gentle terrain near the lowest part of the crater. In a crater with a flat floor, inner-rim slope is measured only between the rim crest and the edge of the floor; the gentler terrain between the floor edge and the crater center is omitted, and the resulting slope value is higher. Formation of flat floors within lunar craters is a difficult problem with no unique solution. The floor phenomenon appears to be both size and age related, as is the appearance of terraced rims and central peaks. The various hypotheses offered to explain the 10- to 20-km-diameter discontinuity have been discussed at length elsewhere (refs. 32-10 and 32-11).

Aside from the discontinuity at 10 to 20 km diameter and in view of the vagaries of lunar surface events affecting rim shape, the negative relation between rim slope and crater size is remarkably systematic. This relation, together with other geometric relations discussed in this subsection, suggests

that lunar craters inherently have highly predictable shapes. Such regularity of form is consistent with genesis by a single major process operating over an uncommonly broad size range. Whereas impact is such a process, volcanic eruption produces landforms that vary much more in shape than do the far-side craters described here and the near-side craters with which they compare so closely.

Detailed morphometric examination of 25 lunar far-side craters from exceptionally high-quality data suggests that (1) differences between near-side and far-side craters are negligible and that (2) the far-side craters more probably formed by the impact of large cosmic bodies rather than by volcanism. Mironova (ref. 32-3) also reached the first conclusion but, as revealed by the results presented here, not for the same reasons. Evidently, the photoclinometric method, the only way to obtain quantitative data from the Zond 3 imagery, did not yield morphometric information as accurate as that of even the older shadow-length crater measurements. Mironova's conclusion that lunar far-side craters formed from volcanic eruptions is not supported by this study. Rather, the results obtained from Apollo metric cameras, and indeed most of the Zond 3 measurements, are more consistent with an impact genesis for the lunar far-side and near-side craters.

RIM-CREST EVENNESS

High-quality topographic data from Apollo 15 to 17 photographs make it possible to examine quantitatively a hitherto unstudied aspect of lunar crater shape: configuration of the rim-crest profile. Millman (ref. 32-12) made a detailed numerical analysis of the rim of the New Quebec Crater, a terrestrial meteorite crater, but all prior evaluations of crater rim-crest shape on the Moon have been qualitative. Although data are not yet available for a thorough investigation of rim-crest shape with respect to every aspect, such as relative crater age or location (mare versus terra, far side versus near side), two variations can be treated in this initial study: (1) that of rim-crest height with azimuth of rim-crest segments and (2) that of rim-crest relief with crater size.

The first problem arose from certain pre-Apollo lunar contour maps that portray many craters with a systematic symmetry in the altitude of their rim crests. On both the 1:5 000 000 U.S. Army Map Service Topographic Lunar Map and the various 1:1 000 000 U.S. Air Force Lunar Aeronautical

Charts, the rim crests of larger craters generally are much higher along the eastern and western parts of the walls than along the northern and southern rim segments. Such a systematic rim height relation, which is not evident upon photointerpretation or visual observation of the lunar surface, would have structural implications and would complicate measurement of crater average depths and rim heights.

The second problem stems from the common telescopic observation that rim crests of lunar craters below a certain diameter appear relatively even, whereas rim crests of larger craters are significantly less even. The critical diameter has been suggested as 16 km (ref. 32-13) and as 50 to 60 km (ref. 32-14). This observation, which corresponds to previously discussed size-dependent differences among lunar craters, may to some extent have arisen because of the reduced detail visible in small craters at the limit of Earth-based telescopic resolution.

To examine both variations, circular topographic profiles of crater rim crests were obtained from photogrammetry of Apollo 15 and 17 metric camera photographs. The 15 sample craters selected for this study range in diameter from 2.5 to 190 km and include far-side and near-side craters, upland and postmare craters, and both old and young craters. Between 20 and 36 elevations (average, 28) located along the crater rim crests were determined in each stereographic model. After the north direction (0°) had been ascertained for all craters, the location of each sample elevation on the rim crest was read to the nearest 10° azimuth. Seven quantities were calculated for each crater from the resulting elevations (table 32-II): (1) total relief (maximum difference in elevation) along the rim crest, (2) the ratio of rim-crest relief to crater diameter, (3) mean elevation of the rim crest (arbitrary datum), and (4) to (7) deviation from mean elevation of the heights of the northern, southern, eastern, and western walls, expressed as a plus or minus percentage of total rim-crest relief. The deviations were averaged from the three (occasionally fewer) elevations closest to the four cardinal directions.

The solution to the first problem appears unambiguous; no systematic relation exists among the sample rim-crest data. When averaged for all 15 craters in table 32-II, the four deviations from mean rim-crest elevation are −0.02 (north), 0.08 (east), 0.00 (south), and −0.07 (west), respectively. The tendency toward slightly higher eastern walls and lower western walls may reflect difficulties in obtaining precise photo-

TABLE 32-II.—*Morphometric Properties of Crater Rim Crests*

Crater name or location	Diameter, km	Rim-crest relief, m	Relief/diameter ratio	Deviation of elevation from mean, percent, at—				Mean (absolute) deviation, percent
				90°	270°	0°	180°	
Linné	2.5	93	0.037	0.40	0.08	− 0.24	− 0.14	0.22
In Pasteur	10	593	.059	−.05	.28	−.02	.08	.11
Peirce B	11	250	.023	−.14	−.14	−.44	−.14	.22
Peirce	20	440	.022	−.16	.19	−.08	.17	.15
Proclus	28	1060	.038	−.09	.18	.19	−.19	.16
Izsak	32	810	.025	−.44	.13	−.02	−.21	.20
Timocharis	38	530	.014	.33	.30	.11	−.21	.24
Gansky	44	2920	.066	.14	−.22	−.26	.47	.27
South of Saha	51	1119	.022	−.21	−.24	.22	.06	.18
Schorr	54	3140	.058	.45	−.15	.42	.07	.27
Ritz	59	3720	.063	.04	−.11	−.28	.23	.17
Sklodowska	128	2410	.019	.00	−.21	.35	−.13	.17
Langrenus	135	1450	.011	.36	−.17	−.37	.15	.26
Hilbert	178	3640	.020	.33	−.41	.20	−.21	.29
Tsiolkovsky	190	3966	.021	.28	−.67	.09	.08	.28

grammetric control in several of the models. The resulting tilt is most evident for craters in the uneven upland terrain; very good leveling was achieved for models of craters on the relatively flat mare surfaces. Fortunately, elevation errors arising from model tilt do not seriously affect analysis of opposite rim-crest segments. Results from the preliminary sample imply that most variation in height along the rim crest of a lunar crater occurs randomly with respect to azimuth. The systematic azimuth variations observed by compilers of the earlier contour maps and charts probably resulted from the high-contrast, east-west illumination of the lunar surface and the inadequate photogrammetric separation in the available Earth-based photographs.

The answer to the second problem is less certain. The sample results show that relief of most crater rim crests is commensurate with crater size and does not increase significantly at any well-marked diameter threshold. The relation between rim-crest relief and crater diameter, expressed as the ratio of the two values, is highly systematic for eight of the 15 craters in table 32-II; the mean value of the ratio is 0.022, and the range is only 0.006. Ratio values for the remaining seven craters generally are higher and are considerably more scattered; the mean value of the ratio is 0.043, and the range is 0.055. However, the rims of some larger craters appear to be disproportionately more uneven than are the rims of smaller craters. Mean absolute values of the four elevation deviations calculated for the first problem (table

32-II) tend to be slightly higher for the larger craters. Deviation from mean rim-crest elevation averages 0.19 for the seven smallest craters and 0.23 for the seven largest craters. Because elevation errors arising from tilt in the stereographic models directly affect the value of rim-crest relief, this difference may not be significant. Additional data, especially for craters of less than 17.5 km diameter, will be required to clarify the relation between rim-crest evenness and crater diameter.

SUMMARY

The research described here exemplifies only two of the various ways in which morphometry can furnish insight into processes that have shaped the craters of the Moon. Both studies correct prior erroneous conclusions reached on the basis of data obtained from inferior sources. Results of the first study principally show that (1) craters on the lunar far side do not differ in shape from near-side craters, (2) the shapes of far-side craters are more consistent with an impact origin than with a volcanic origin, and (3) the inner slopes of crater rims are much gentler in craters larger than 17.5 km in diameter than they are in smaller craters. Findings from the second study reveal that (1) the height of crater rim crests does not vary preferentially with azimuth of rim-crest segments and (2) relief along most crater rim crests probably does not increase significantly at any well-defined diameter threshold.

PART B

AITKEN CRATER AND ITS ENVIRONS

Farouk El-Baz[a]

The crater Aitken is among the most significant features photographed during the Apollo 17 mission. This was the first Apollo mission to fly over Aitken, located at latitude 17° S, longitude 173° E, in as yet undivided highlands. The crater is approximately 150 km in diameter and, based on shadow measurements, approximately 5 km deep.

Aitken is one of few fresh-looking and therefore relatively young craters on the lunar far side; its rim deposits are clearly superposed on older, unnamed features. The crater is characterized by (1) a slightly high albedo, continuous ejecta blanket that extends outward to approximately one crater diameter; (2) flow patterns and dunes extending beyond the continuous ejecta blanket to approximately two crater diameters; (3) sharp secondary-crater chains that also extend outward to two crater diameters; (4) irregularly terraced crater walls having very few flat surfaces; (5) dark mare-like fill with some light-colored swirls; and (6) a cluster of craters 6 km in diameter with interior domical structures and "high lava marks" on their walls.

Before the Apollo 17 mission, Aitken Crater was photographed by the Lunar Orbiter II and Zond 8 spacecraft. However, the Apollo 17 coverage added numerous details, as summarized in the following description of the general setting of the crater and its features.

CRATER SURROUNDINGS

Aitken Crater is in a rugged and densely pitted area of the lunar far-side highlands. As shown in figure 32-6, the continuous ejecta blanket that extends 100 to 150 km from the rim crest is somewhat brighter than the surroundings. In this zone, thick debris mantles and subdues preexisting topography.

Chains and clusters of craters that are most probably secondary to Aitken Crater are best portrayed in the low-Sun-angle photography of Zond 8; one crater chain measures approximately 300 km in length (fig. 32-7). Numerous craters in the vicinity of Aitken are filled with light plains materials. Some of these craters are younger than Aitken, indicating that the plains materials are not Aitken ejecta but may be locally derived. Intercrater light plains in the same region, however, are more densely pitted and are overlain by craters secondary to Aitken and by fine ejecta. These observations suggest multiple sources for the light plains units in the lunar highlands.

Flow scarps probably related to the deposition of the ejecta blanket of Aitken Crater occur beyond the continuous rim deposits. These small-scale structures are best studied in high-resolution Apollo 17 panoramic camera photographs. Two examples in the region north-northeast of the crater are shown in figure 32-8.

Scarps in both areas display lobate fronts and appear to cross the terrain with complete disregard of preexisting topography. The scarps are reminiscent of the flow scarps in the area of the crater Mandel'shtam (ref. 32-15). Similar but not identical scarps were also observed around King Crater (refs. 32-16 and 32-17), where they show definite relationships to the preexisting terrain—accelerating downslope and decelerating upslope (ref. 32-16). No such relationship is clear in the case of the flow scarps near Aitken Crater.

CRATER INTERIOR

Although generally circular, the rim crest of Aitken Crater is crenulate and marked by a few straight segments. There is an affinity toward northeast-southwest and northwest-southeast linear trends.

The wall of Aitken Crater is irregular. There is one steep scarp in the northeastern part and only one discontinuous terrace that extends to approximately one-fifth of the crater depth, and the rest of the wall is made up of domical and irregular blocks (fig. 32-9).

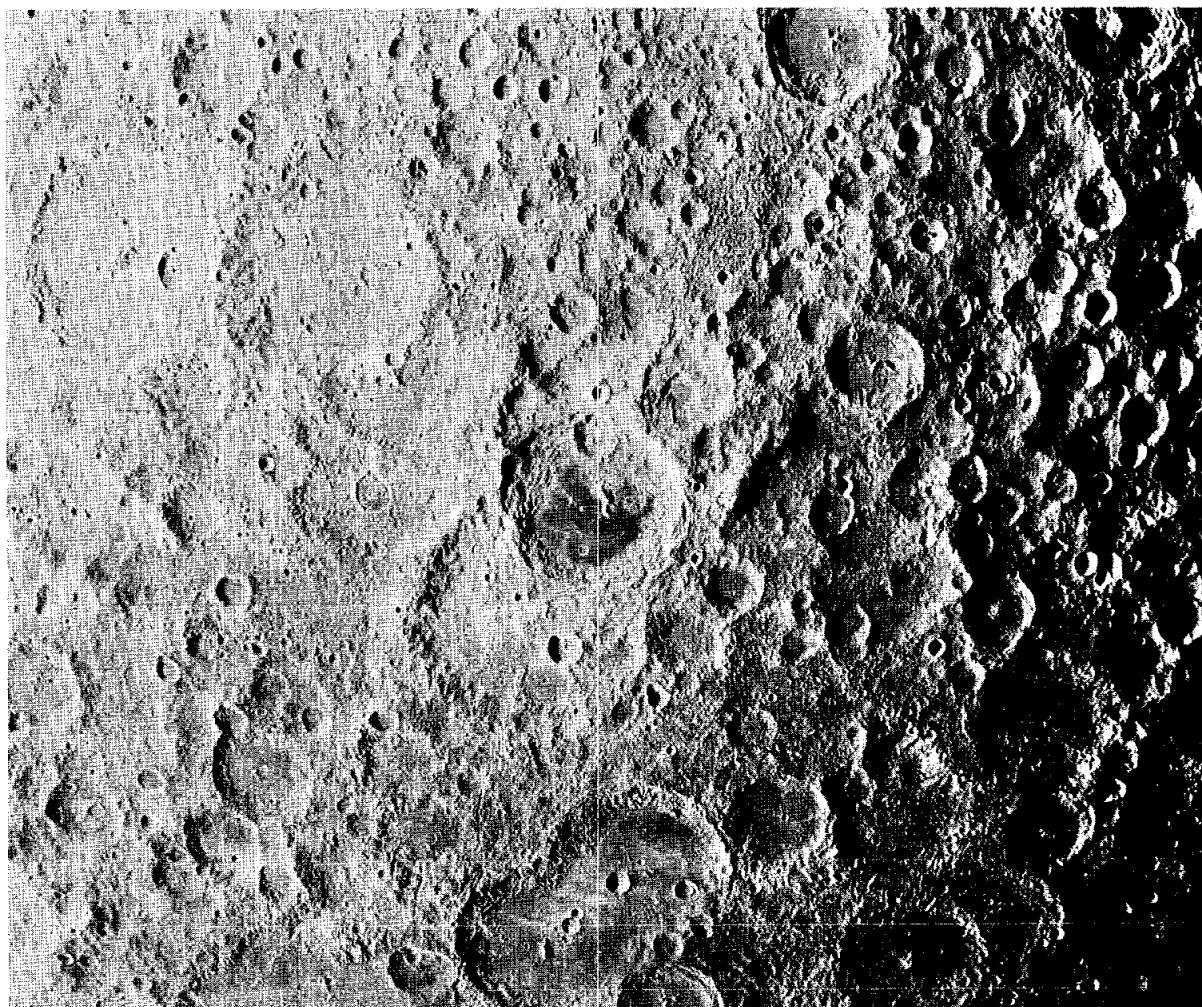[a]National Air and Space Museum, Smithsonian Institution.

FIGURE 32-6.—Part of Lunar Orbiter II frame 33-M centered on the crater Aitken (lat. 17° S, long. 173° E). Relative high albedo rim deposits of Aitken extend outward to one crater diameter. Icarus Crater with its large central peak is in the upper right corner; west of it is Daedalus Crater. Northwest of Aitken is the pair of old subdued craters, Heaviside (right) and Keeler (left). Due south of Aitken Crater is the crater Van de Graaff, on the northeastern rim of Mare Ingenii.

By comparison with other large craters (e.g., Copernicus), only very few flat areas (the so-called "pools") are observed on the wall terraces.

The jumbled appearance of the crater wall may be ascribed to post-Aitken events, particularly those events that formed the 30-km-diameter crater on the northern wall and the 12-km-diameter crater on the northern rim of Aitken Crater (fig. 32-9). These probable impact craters may have caused massive slumping and downslope movement along the wall of Aitken. The effects of this slumping are obvious in (1) widening of the crater in places and the crenula-tions along the eastern and western parts of the wall; (2) the presence of a large and relatively flat unit that is interpreted as a landslide next to the steep scarp on the northeastern part of the wall; (3) the apparent lack of flat pools and sharp terraces, in spite of the relative freshness of other features of the crater; and (4) complete destruction of the northern part of the wall by the superposition of the unnamed 30-km-diameter crater.

The floor of Aitken Crater displays several unique features. It is filled with dark mare-like material, which, in the southwestern quadrant, is marked by
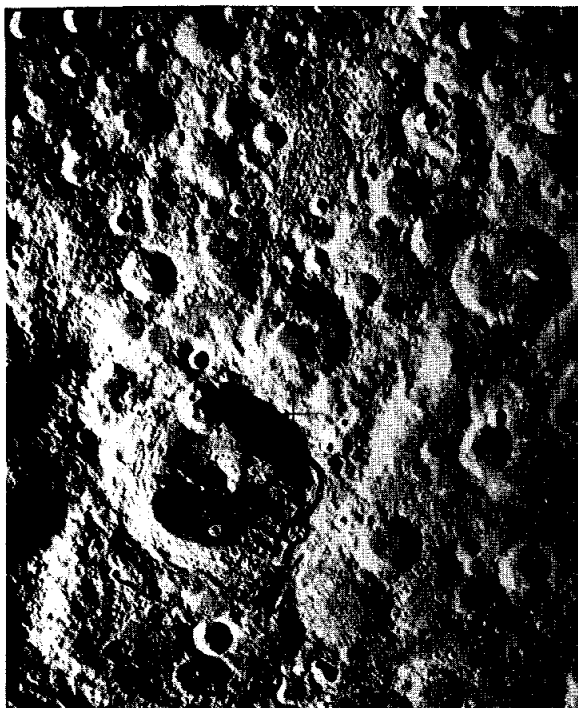
FIGURE 32-7.—Zond 8 photograph of Aitken Crater (150 km in diameter) and its surroundings. A major chain of secondary craters extends toward the north. Smaller chains are in the north-northwest sector. Secondary-crater clusters randomly surround the crater. Light plains material fills the floors of smaller surrounding craters in contrast to the darker mare-like fill in the floor of Aitken. Note the sharpness of the crater rim crest. Area of figure 32-8(a) is indicated by "1"; area of figure 32-8(b) is indicated by "2".
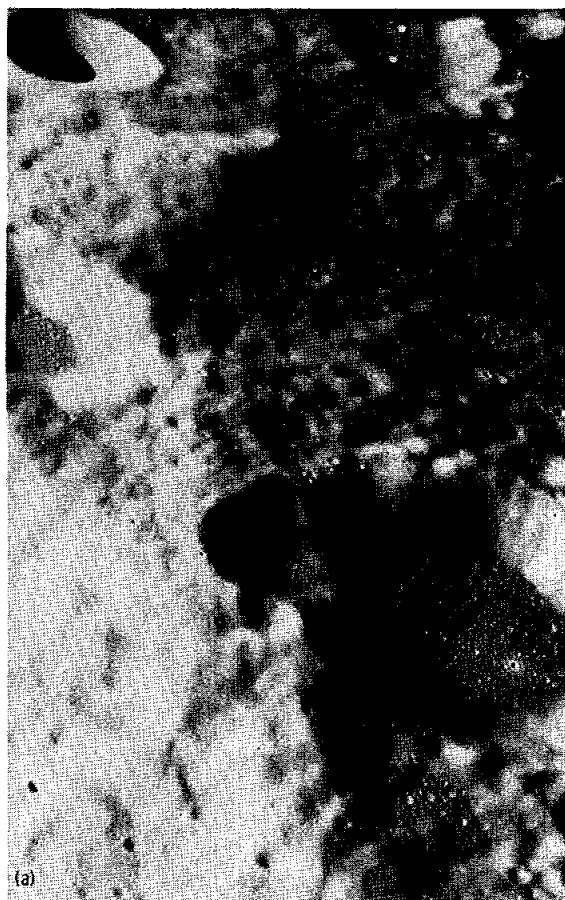

FIGURE 32-8.—Flow scarps and other flow structures north-northeast of the crater Aitken as seen in Apollo 17 panoramic camera photographs. The flow direction is from west (left) to east (right). Both areas appear to be part of a discontinuous system. (a) Part of Apollo 17 panoramic camera frame AS17-1914

light-colored swirls (fig. 32-10). These swirls are at the northern edge of the Ingenii belt of light-colored markings (ref. 32-18).

The central peak of the crater consists of two segments. The larger and topographically higher segment to the east trends generally north-south, and the smaller and topographically lower portion is represented by a row of discontinuous hills (fig. 32-9). This arrangement of the central peak complex suggests an incipient ring. Smaller probable impact craters such as Tycho and Aristarchus display a clustered central feature; larger craters such as Schrödinger display a complete ring structure. Aitken Crater appears to display characteristics that lie between these two types.

Numerous flow scarps are clearly visible in the dark mare floor, particularly in the eastern and southwestern parts (fig. 32-10). In two places, the flow scarps are related to smaller craters in the floor (figs. 32-10 and 32-11). These craters range in size from 4 to 7 km. The interiors of three in one cluster are occupied by equal-size, perfectly domical structures (fig. 32-12). The domical structures are very unusual in appearance and somewhat resemble those reported in the Mons Rümker area (ref. 32-19). The three craters in the eastern part of the floor, as well as an isolated one in the southwestern floor of Aitken, are breached; the breaches lead to flow scarps in the floor fill, suggesting that the craters are related to the fill. They may have been the source of the mare
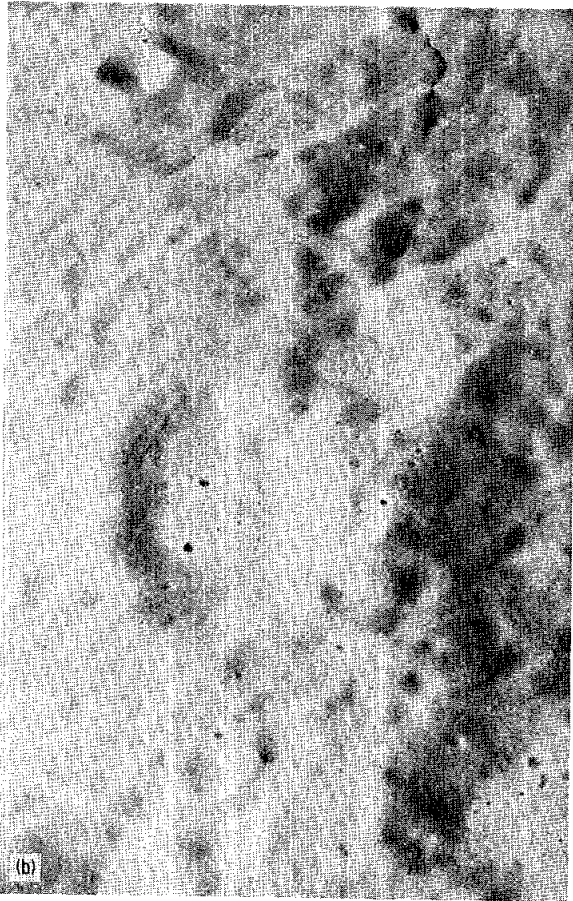
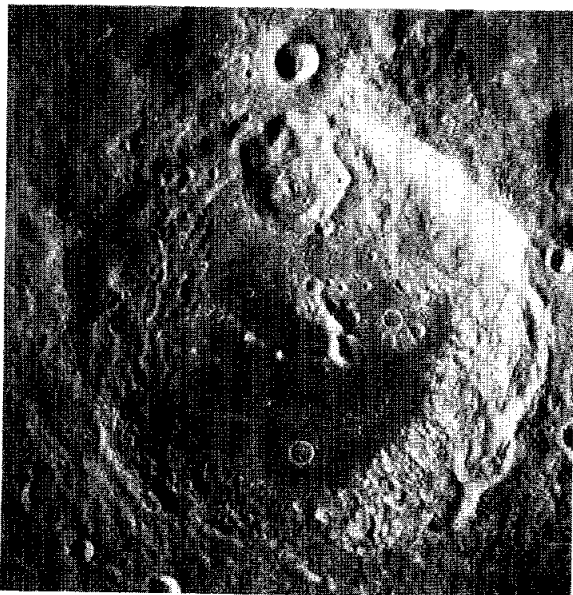FIGURE 32-8.—Concluded. (b) Part of Apollo 17 panoramic camera frame AS17-1676.

material, or at least part of it. The domical structures in their interiors may represent the last stages of volcanic eruption. These structures were described by the Apollo 17 command module pilot as resembling the dacite domes in northern California and Oregon (sec. 28). Late stages of eruption commonly produce more viscous materials represented by domical structures (ref. 32-20).

Some of the craters described previously as well as a crater in the southern part of the floor (fig. 32-13) show a ringed interior that is interpreted as a high lava mark (i.e., a preserved strand line of an earlier higher level of lava within the craters than exists today). The lava level may have receded because of drainage back into the source chamber or because of loss of volatiles or loss in volume as a result of crystallization (or both). Similar lava marks were observed in Palus Putredinis during the Apollo 15 mission (ref. 32-21) and in Mare Nubium during the Apollo 16 mission (ref. 32-15).
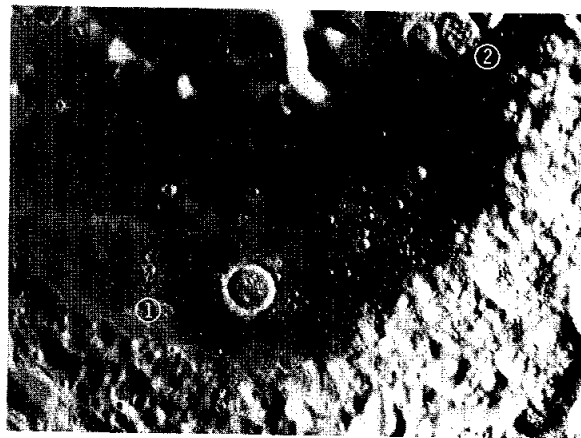

FIGURE 32-10.—Apollo 17 Hasselblad frame AS17-150-22962 showing the southern part of the floor of Aitken Crater. Note the light-colored markings in the dark mare floor, also the flow scarps in the southwestern and eastern portions. The scarp and/or ridge in the southwestern corner leads to a partially flooded crater (1), and one ridge or flow structure in the eastern part of the wall leads to a breach in an unusual crater (2). See also figure 32-11.

FIGURE 32-9.—Vertical view of Aitken Crater obtained by Apollo 17 mapping camera. Note the sharp crenulations of the rim crest and the irregular nature of the crater wall. The crater in the northern part of the wall is 30 km in diameter (Apollo 17 mapping camera frame AS17-0341).

FIGURE 32-13.—Apollo 17 Hasselblad frame showing an 8-km-diameter crater in the floor of Aitken Crater that displays a high lava mark on the inner wall (AS17-149-22797).
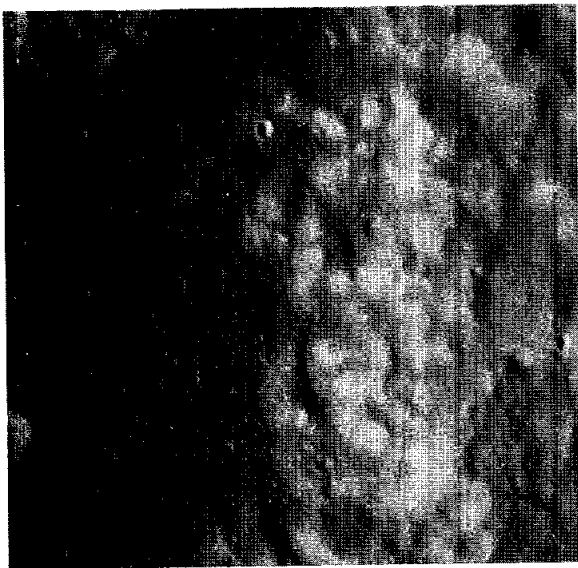
FIGURE 32-11.—Detail of the eastern part of the floor of Aitken Crater. Numerous flow scarps and ridges are displayed in the dark mare-like unit. One is clearly related to a breach in the crater in the upper left corner of the photograph. A few of the scarps appear to lap up against the lower part of the crater wall. A large and discontinuous scarp is present at a higher level on the southeastern wall of the same crater. This large scarp is probably unrelated to those in the floor (AS17-149-22796).
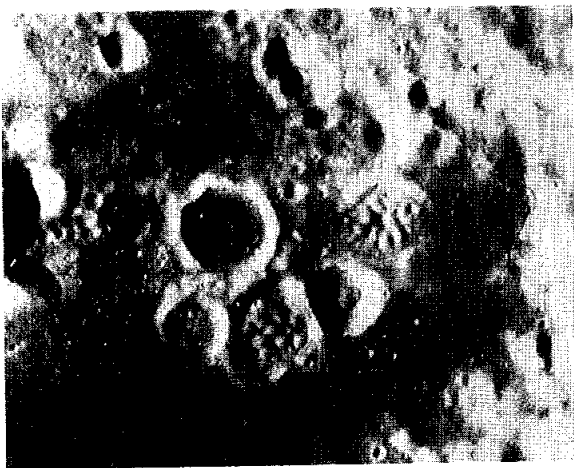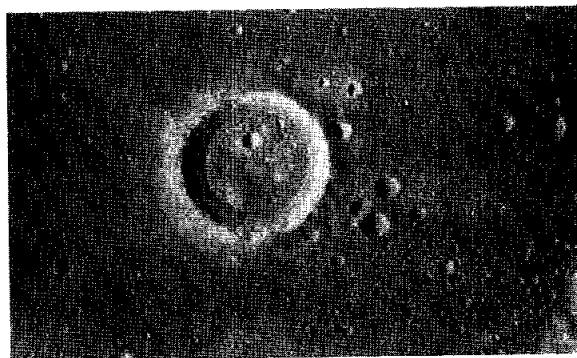

FIGURE 32-12.—A cluster of craters in the eastern part of the floor of Aitken Crater. Framelet width is 6.3 km (Lunar Orbiter II frame 33-H).

CONCLUSIONS

Characteristics of the rim deposits and ejecta blanket of Aitken Crater indicate a probable impact origin. The freshness and lesser degradation of the rim crest may have been caused by post-Aitken events.

The dark floor fill, its flow scarps, and smaller craters with domical structures are probably volcanic in origin. The variety of landforms suggests episodic eruptions represented by the dark basalt-like floor material and finally the more viscous domical materials in the smaller craters.

This combination of impact and volcanic structures makes Aitken Crater particularly attractive for future study and analysis. In addition to the fact that it is one of very few craters on the lunar far side with a dark mare floor, the crater is young enough for its features to be well preserved. Extensive photographic coverage of Aitken Crater by the Apollo 17 crewmen will permit detailed investigation of its many interesting features.

PART C

VOLCANIC FEATURES OF FAR-SIDE CRATER AITKEN

W. B. Bryan[a] *and Mary-Linda Adams*[a]

The crater Aitken is on the lunar far side, centered at approximately latitude 17° S, longitude 173° E. Aitken Crater, which measures approximately 130 km from rim to rim, shows many of the features usually attributed to impact, the most important being the terraced, hummocky inner crater walls and a raised central peak. In many respects, it resembles the well-known crater Tsiolkovsky, which is at the same latitude but approximately 40° to the west. However, the outer walls and surrounding slopes of Aitken Crater do not show the extensive ejecta blanket or the prominent landslide deposits so evident at Tsiolkovsky Crater.

Post-impact volcanism at Aitken Crater is suggested by several features (fig. 32-14), the most obvious being the mare-type filling that floors the crater and virtually makes an island of the central peak. Light-colored swirls on the surface of this filling resemble those in Mare Marginis: they do not appear to have any appreciable relief. The swirls may represent fumarolic alteration of the lava, or dust deposits from postfill landslides on the crater walls. The dark floor filling also shows several elongated pits and irregular rille-like features that also are characteristic of mare fill and that may represent vents or collapsed lava tubes.

Aitken Crater shows several unusual features that may represent volcanic events extending beyond the period of mare-type crater flooding. Among these are the circular, maar-like depressions that appear in the southern and northwestern parts of the crater. These might represent volcanic craters flooded by lava following a period of explosive eruptions; or, alternatively, they may be impact craters produced in thin crust of the ponded mare-type fill before this fill was completely crystallized. On the eastern side of the main crater floor, several more circular craters enclose peculiar clusters of dome-like features that might be extrusions of more viscous lava.

A small crater approximately 100 km west of Aitken Crater also shows what may be a filling of relatively viscous lava (fig. 32-15). It is difficult to interpret this crater filling as slump from walls of a crater produced by impact because the walls are only a little higher in elevation than the surface of the filling and because the central filling does not slope from the walls toward the center of the crater. Rather, the central filling has an almost horizontal (although rough) surface, and its contact with the crater walls closely follows a low, moat-like depression. The alinement of two large pits or craters ("B" in fig. 32-15) along the peripheral depression suggests that they originated internally; they may be explosion craters. The conspicuous fractures on the upper surface of the dome may have been produced by endogenous growth. By analogy with terrestrial volcanic domes, cooling might be expected to produce the hexagonal shrinkage cracks typical of columnar jointing. However, this fracturing probably would be much smaller in scale than that observed in this crater.

The volcanic fillings in Aitken Crater and in the smaller crater to the west are relatively youthful in appearance compared to the generally old highland-type topography surrounding them. Our initial impression, which should be checked by more detailed work, is that the volcanic activity is considerably younger than the impact events that produced the host craters and is probably contemporary with mare volcanism on the lunar near side.

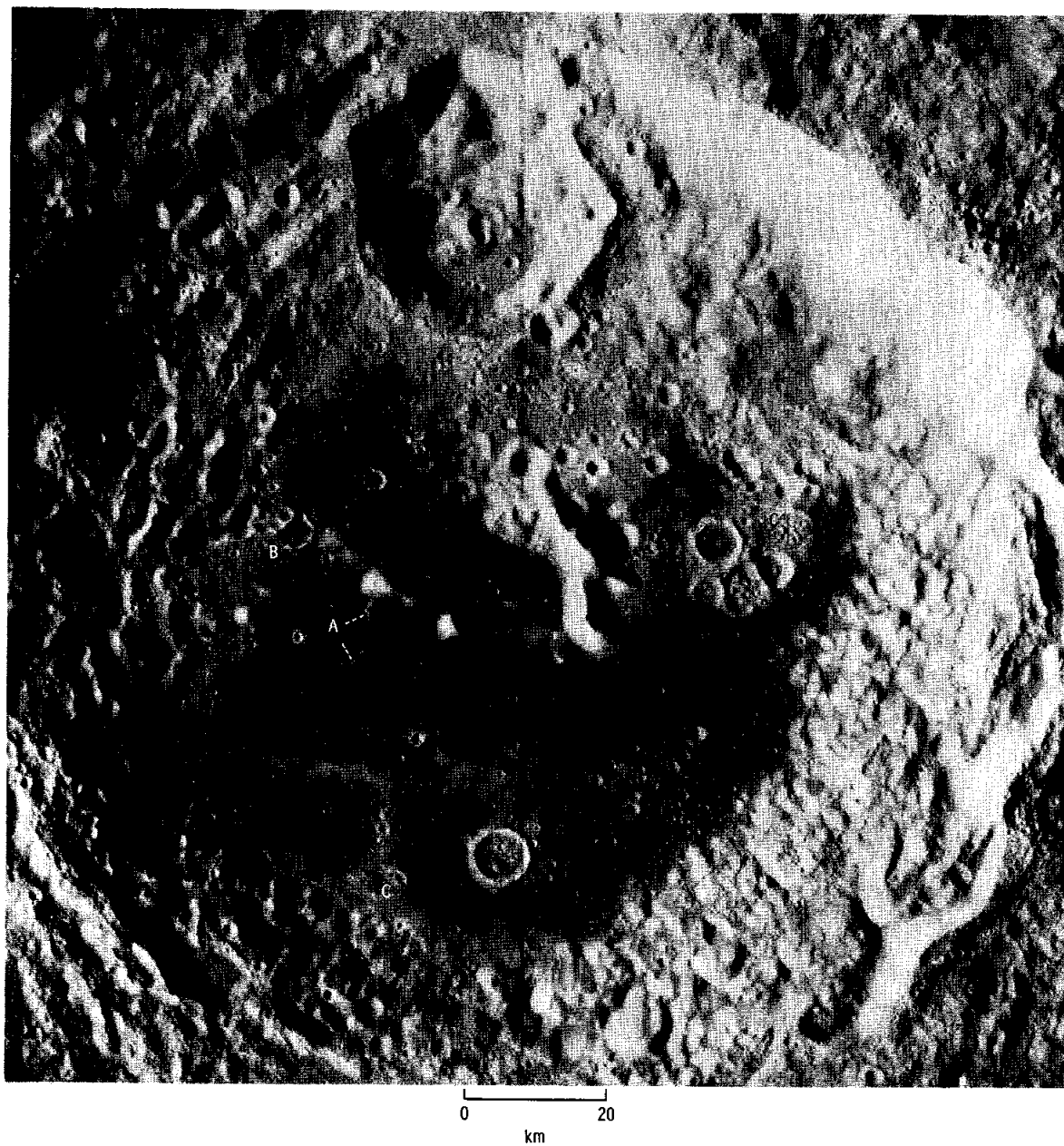[a]Woods Hole Oceanographic Institution.

FIGURE 32-14.—The crater Aitken, showing elongated pits and rille-like features in mare-type filling (A), maar-like depressions (B), and depressions with clusters of possible lava domes (C) (Apollo 17 metric camera frame AS17-0481).
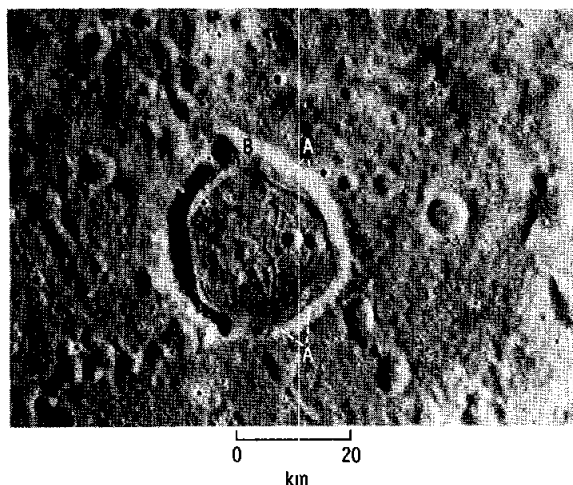
FIGURE 32-15.—Possible volcanic extrusion in small crater west of Aitken Crater. Note the irregular fractured surface; peripheral depression (A); and possible marginal explosion pits (B) (Apollo 17 metric camera frame AS17-0484).

PART D

THE LUNAR HERRINGBONE PATTERN

Verne R. Oberbeck[a] *and Robert H. Morrison*[a]

The lunar herringbone pattern was first noted on Lunar Orbiter and Apollo 8 photographs of Copernicus secondary craters as a series of lineations forming V-shaped patterns that, when combined, give the appearance of a herringbone pattern (ref. 32-22). Later, a study of this pattern showed conclusively that its components are V-shaped ridges that typically are associated with secondary craters (ref. 32-23). Figure 32-16 shows the location of four secondary-crater chains, each of which is shown in greater detail in figure 32-17.

Arrows superimposed on each photograph (fig. 32-17) point toward Copernicus Crater. Figure 32-17(a) includes part of the crater chain originally used in reference 32-22 to illustrate the herringbone

pattern. The overall appearance is that of intersecting lineations projecting from either side of the crater-chain axis of symmetry to form nested V's. At least two well-developed series of V-shaped ridges are visible on this crater chain. Figures 32-17(b) and 32-17(c) show two crater pairs with subdued ridges, whereas figure 32-17(d) shows groups of secondary craters exhibiting well-defined V-shaped ridges. Each V-shaped ridge opens in a direction away from Copernicus Crater, and each gives the appearance of the head of an arrow pointing in the general direction of Copernicus, especially when the crater-chain axis of symmetry is along a line radial to Copernicus.

Recently, a subdued herringbone pattern near the crater Theophilus was observed on Apollo 16 photographs, and its components were simulated experimentally by simultaneous impact of two projectiles near one another on a sand target (ref. 32-24). A
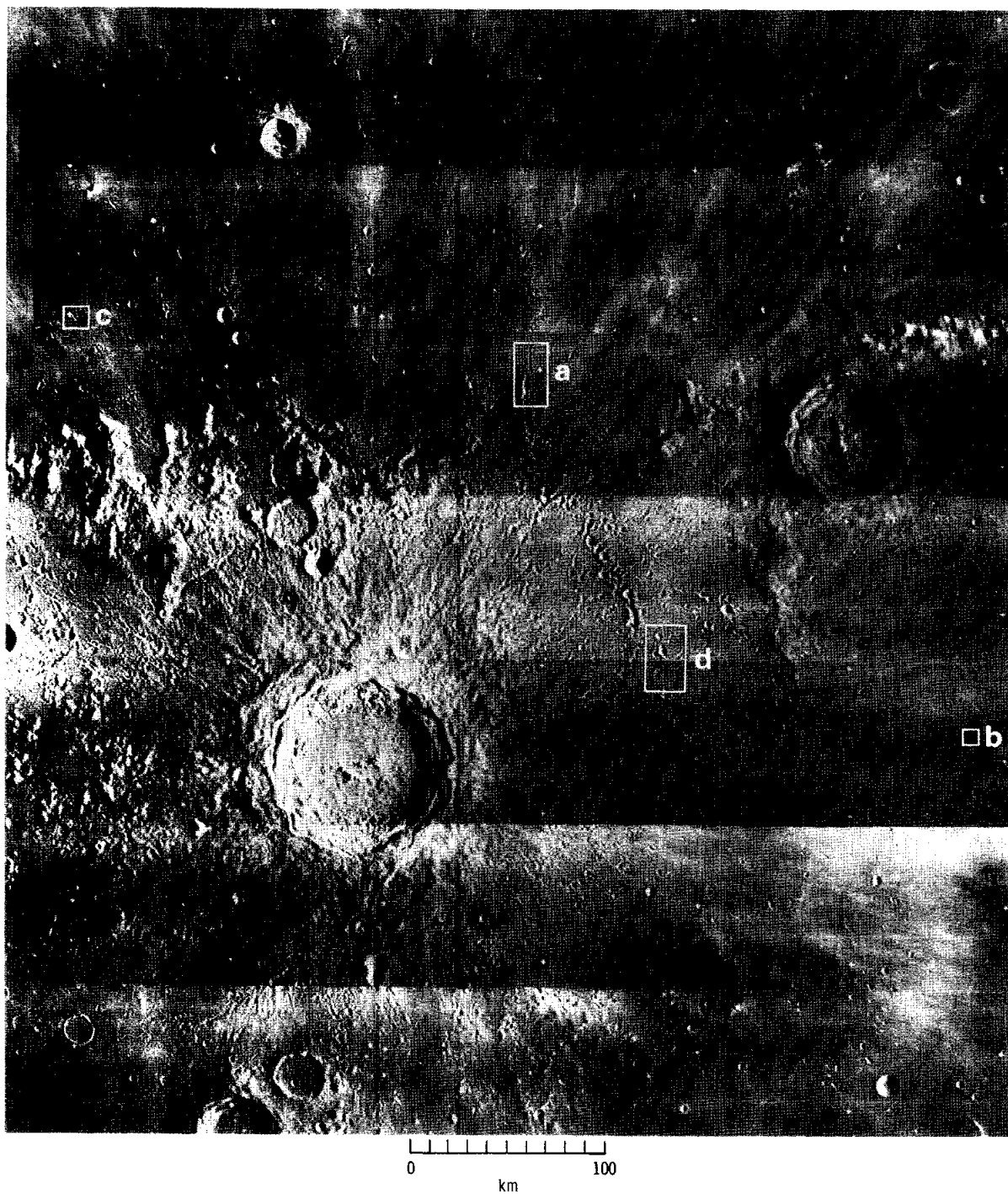
_____

[a]NASA Ames Research Center.

FIGURE 32-16.—Photomosaic of Copernicus Crater and environs composed of Lunar Orbiter IV moderate-resolution frames M-121 and M-138. Outlined areas correspond to parts of figure 32-17.
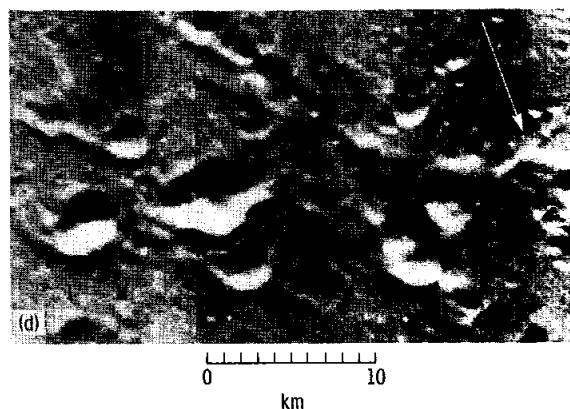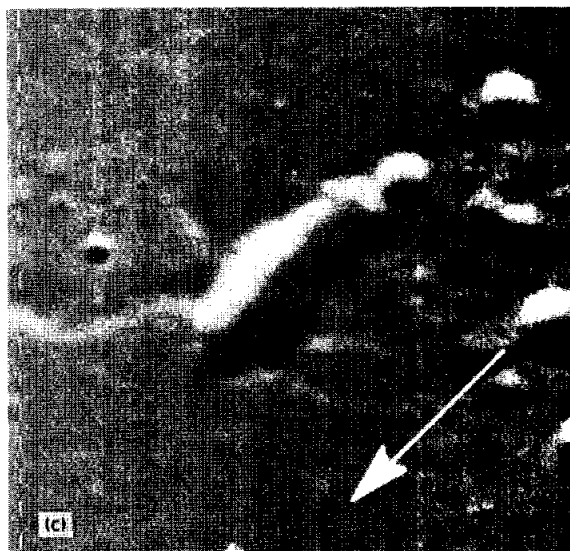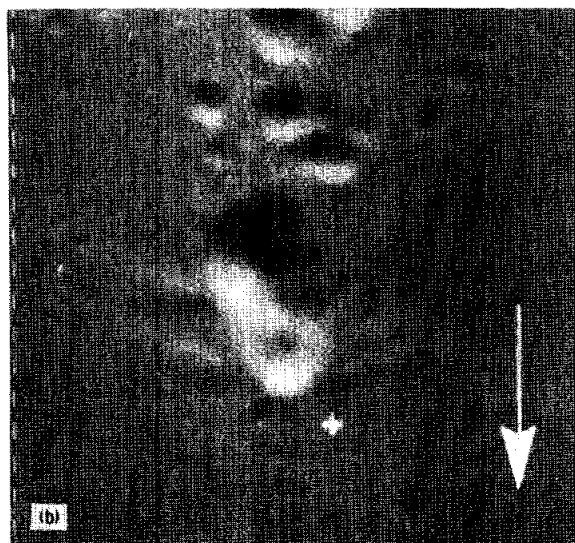
FIGURE 32-17.—Groups of secondary craters near Copernicus Crater. Locations of parts are shown in figure 32-16. Arrows point toward Copernicus Crater. (a) Crater chain showing V-shaped ridges (Lunar Orbiter IV frame H-121). (b) Crater pair with subdued ridges (Lunar Orbiter IV frame H-114). (c) Crater pair with subdued ridges (Lunar Orbiter IV frame H-121). (d) Six crater pairs with prominent ridges (Lunar Orbiter IV frame H-121).

result of this last study was the hypothesis that the herringbone pattern is produced by collision of material ejected from two adjacent secondary-impact craters formed nearly simultaneously by impact of material ejected from a primary crater.

This paper presents several better defined examples of the V-shaped components of the herringbone pattern observed on the Apollo 17 and 15 metric and panoramic photographs and explains the impact mechanism for the formation of the V-shaped ridge components of the pattern. Also presented are

observations of isolated crater chains having herring-bone patterns, but not obviously associated with any primary craters. These patterns suggest that some crater chains of presumed volcanic origin may, in fact, have been produced by the impact process.

Figure 32-18 is a metric camera photograph of the area north-northwest of Copernicus Crater. Also shown, in the insets, are magnifications of three groups of secondary craters, located approximately 350 km from Copernicus. Inset (a) shows a well-developed crater chain with long ridges radiating from the points of crater overlap. The ridges meet the crater chain at acute angles on each side of the crater chain and give the general appearance of V-shaped ridges. Inset (b) shows a crater chain and V-shaped ridges that are more subdued because of the shallower

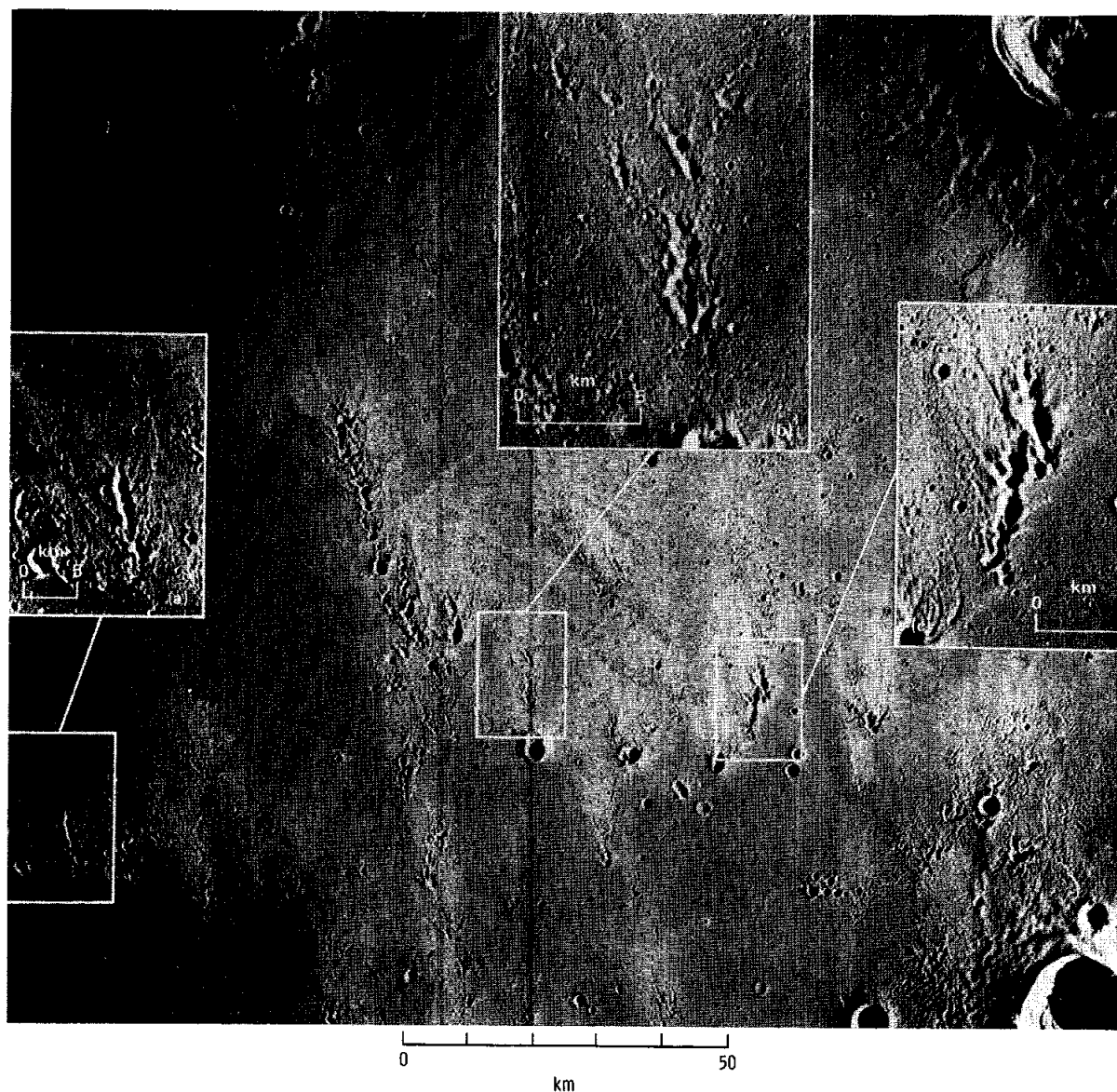FIGURE 32-18.—Area north-northwest of Copernicus Crater showing three groups of secondary craters: inset (a), a well-developed crater chain with long ridges radiating from the points of crater overlap; inset (b), a crater chain with ridges subdued because of shallowness of craters; and inset (c), a crater chain with long, well-defined V-shaped lineations (Apollo 17 metric camera frame AS17-2289).

craters. Inset (c), however, shows long well-defined V-shaped lineations. In each case, the V's point toward Copernicus Crater. The group of craters in inset (b) is near a prominent chain of Copernicus secondaries that points to a group of large secondary craters in the upper left corner of figure 32-18. Three of these craters are magnified in inset (c) of figure 32-19, which is an Apollo 15 metric camera photo-
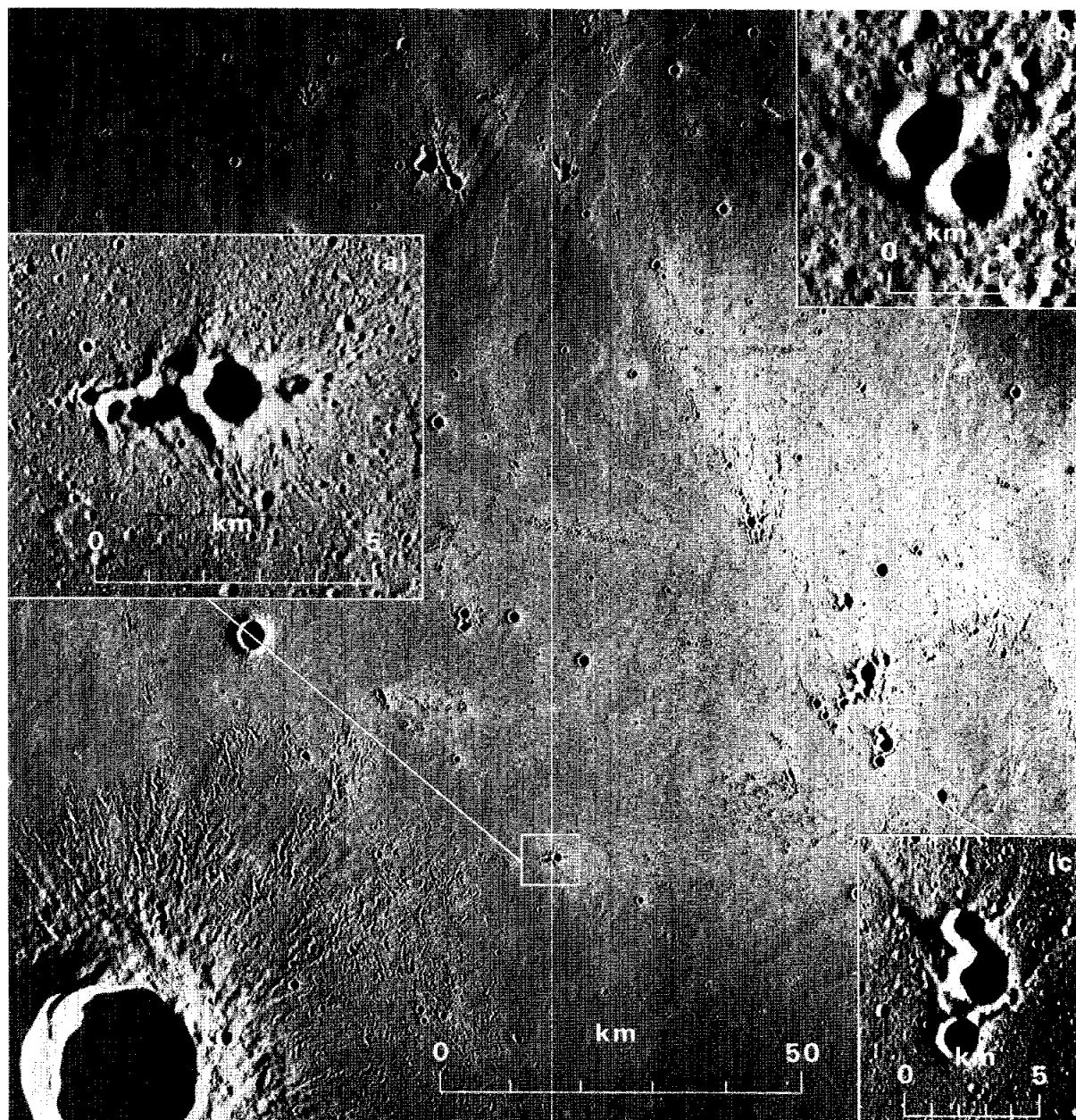
FIGURE 32-19.—Area northeast of Euler Crater showing three groups of secondary craters: inset (a), crater chain with very-well-developed V-shaped ridge radiating from a point between the largest crater and the smaller craters; inset (b), crater doublet with V-shaped ridges radiating from points between and in front of the craters; and inset (c), crater triplet (upper left in fig. 32-18) with well-developed ridges emanating from points between the craters (Apollo 15 metric camera frame AS15-1699).

graph of the area northwest of that shown in figure 32-18. The three craters are seen to be part of the prominent chain of craters of figure 32-18 that continues in a northwest direction across the lunar surface area shown in figure 32-19. The three craters are shown once again in much greater detail in an Apollo 17 panoramic camera photograph (fig. 32-20). The V-shaped ridges associated with these three craters are even more well defined than those associated with the secondaries south of this area. The well-developed ridges emanate from points between the craters.

Two other insets of figure 32-19 are magnified views of a crater doublet and a crater chain. The crater doublet of inset (b) also probably is made up of secondary craters of Copernicus because of its proximity to the major secondary-crater string pointing to Copernicus. The V-shaped ridges radiate from points between the craters and in front of them. The
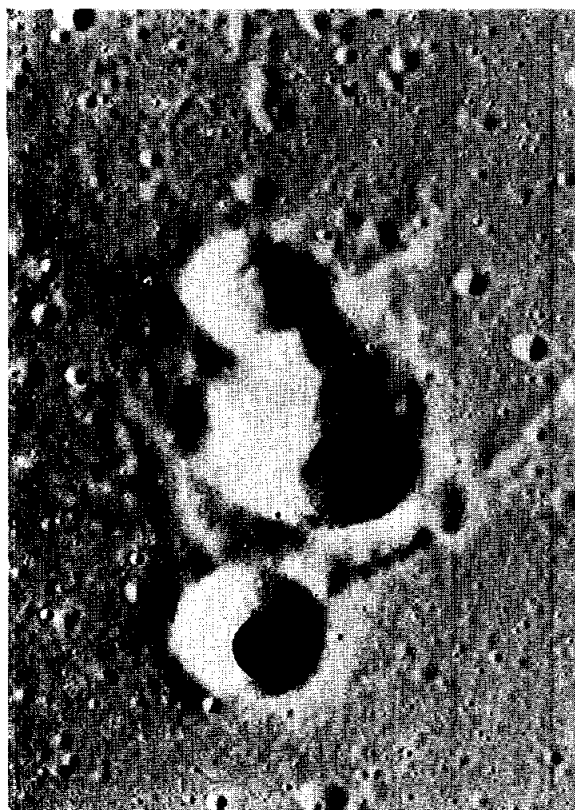
crater chain shown in inset (a) has a very-well-developed V-shaped ridge radiating from a point between the largest crater and the other smaller craters, and there are also several other more subdued V's. All point to the west, however. These craters may be secondaries of Euler, because they point in its general direction; but they are most probably derived from a larger crater to the west, because they are very much larger than other secondary craters seen in the Euler ejecta blanket. A possible candidate source crater for this crater chain is Aristarchus because the axis of symmetry of the crater chain is on a line radial to Aristarchus; in addition, secondaries near Aristarchus have well-developed V-shaped ridges. For example, figure 32-21 is an Apollo 17 metric camera photograph of a very long southeast-striking chain of secondary craters in the area southeast of Aristarchus. The chain can be traced to a point near Aristarchus and is on a radial line from Aristarchus. The inset at the bottom of figure 32-21 is a magnification of a small part of this chain. Most herringbone pattern components in this section of the chain are found to be associated with singular, nearly circular craters. However, there are at least two examples of V-shaped ridges radiating from points between adjacent secondary craters. In all cases, the V's point toward Aristarchus Crater.

SIMULATION OF HERRINGBONE PATTERN COMPONENTS

The preceding association of the herringbone pattern with lunar secondary craters is characteristic of the pattern. This association suggests that the origin of the herringbone pattern is related to the origin of the secondary craters and that the exact mechanism of formation of the herringbone pattern may be revealed by a study of the formation of secondary craters. The most common hypothesis for formation of secondary craters is production by impact of material ejected from a primary crater. If these craters were produced in this way, it is reasonable to assume that adjacent craters would have been formed at the same time or nearly the same time. Herringbone pattern components might then be formed as a result of simultaneous formation of craters near one another. Preliminary results of simultaneous impact were presented in reference 32-24. More definitive results now are available and are presented along with the description of the

FIGURE 32-20.—Portion of Apollo 17 panoramic camera frame AS17-3094 showing chain of three secondary craters (inset (c), fig. 32-19).
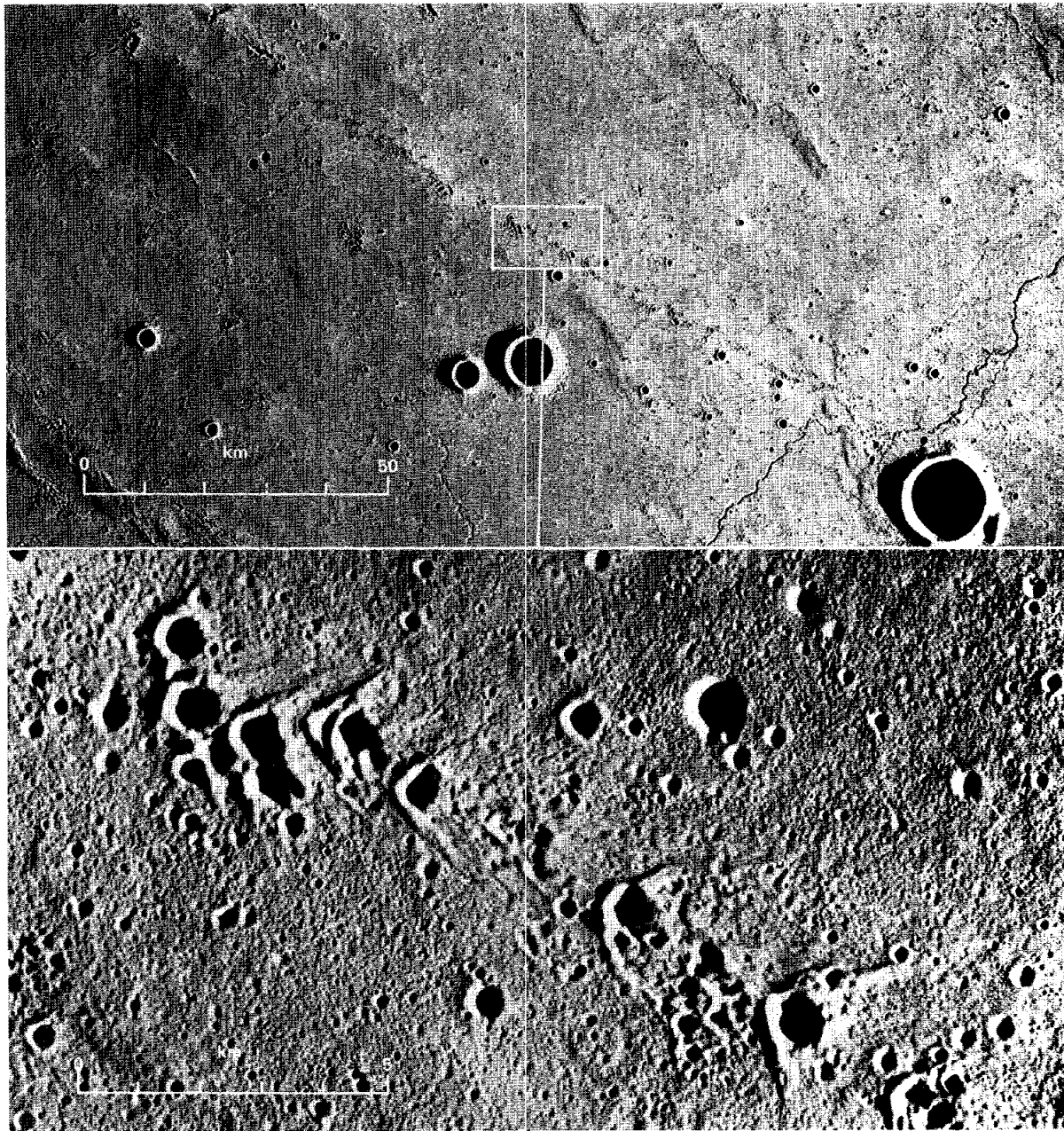
FIGURE 32-21.—Area southeast of Aristarchus Crater showing a crater chain and detail (inset) (Apollo 17 metric camera frame AS17-2930).

mechanism involved in the production of the herringbone pattern.

Most lunar secondary craters with an associated herringbone pattern that can be related to a large primary crater occur within annular areas around the crater from 100 to 400 km wide. Thus, to simulate the typical pair of adjacent lunar secondary craters, the conditions of ejection velocity and angle required to project fragments to distances in the previously mentioned range are determined, and two projectiles are launched simultaneously at these conditions into a sand target. The resulting crater pairs then are compared to lunar craters.

The following equation was used to calculate the

angular range η of fragments ejected from the lunar surface.

$$\eta = 2 \arctan\left[\frac{V^2\sin\theta\cos\theta}{R_m g_m - V^2\sin^2\theta}\right] \qquad (32\text{-}1)$$

where θ is the ejection angle measured from the normal to the surface, g_m is the lunar acceleration of gravity, R_m is the radius of the Moon, and V is the ejection velocity. This equation was obtained by modifying equation (1) given in reference 32-25 to account for the fact that θ is measured from the surface normal instead of the horizontal. When the angular range η is converted to kilometers on the lunar surface and set equal to constant values ranging from 100 to 400 km and V is solved as a function of θ, the curves of figure 32-22 result.

Any pair of V,θ values within the boundaries of the 100- and 400-km V,θ curves delimits possible conditions for the formation of secondary craters found at distances in this range. However, the lunar secondary craters may be simulated adequately by launching projectiles at each impact angle (equal to the ejection angle) and impact velocity equal to the midpoint of the envelope defined by the 100- and 400-km curves at that angle.

A series of experiments was performed by impacting two Lexan plastic projectiles simultaneously at angles and average velocities near the midpoints of the ballistic curves of figure 32-22. A separate series of experiments also was performed to verify that the results were representative of those that would have been obtained over the entire envelope width. Photographs of representative craters obtained in the first test series are shown in figure 32-23, and their conditions of impact angle and velocity are designated by circles in figure 32-22. In each case, the projectiles impacted from the direction at the bottom of the figure. Well-developed ridges radiate from between the craters of all crater pairs. However, the ridge is V-shaped only for those craters produced by projectiles impacting the target at high angles from the normal to the target surface. Additional experiments performed at the same angles and velocities but by projectiles that impact at different times show that the angle of the V-shaped ridges is smaller when the up-range crater is formed first than it is when both craters form simultaneously. However, study of all cratering parameters showed that V-shaped ridges resembling most lunar herringbone components re-
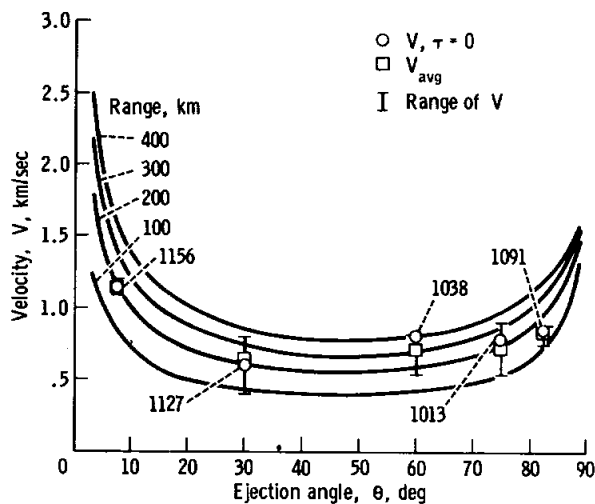

FIGURE 32-22.—Theoretical ballistic curves, where τ is the time between impact of first and second projectiles and V_{avg} is the average velocity. The four-digit numbers designating the V, $\tau = 0$ data points are experiment numbers that correspond to photographs of representative craters shown as parts of figure 32-23.

sulted only when the impact angle measured from the normal was greater than 60°.

The ridges between the laboratory craters and between the lunar secondary craters formed as a result of collision of material ejected from adjacent craters. This conclusion is confirmed from observation of high-speed motion picture records of the growth of two craters formed by the simultaneous impact of two projectiles at a 60° impact angle and a velocity of 0.82 km/sec. Selected frames (fig. 32-24) show that the ejecta plumes of the two craters begin to interact at 5 msec after impact of the projectiles. At 10 msec after impact, some modification of the ejecta plumes has occurred, as shown by a bifurcation of the leading edge of the up-range ejecta plume. The short up-range arm of this bifurcating ejecta plume represents material that has collided with that ejected from the down-range crater. Material missing the ejecta plume of the down-range crater is represented at 10 msec by the longer arm of the bifurcated ejecta plume. As crater growth continues from 20 to 100 msec, the collision zone grows in length. At 40 msec after impact, the nearly vertical collision zone is the prominent feature of the combined ejecta plumes. For purposes of illustrating the mechanism for the ridge formation, one may imagine the ejecta plumes as being frustums of inverted right-circular cones, the

from which the impacting fragments arrived. This hypothesized mode of formation has been confirmed by detailed calculations of a more rigorously developed model, even where the collision is assumed not to be perfectly inelastic and where equations of motion of particles before collision are related to equations of motion of collision products through conservation of momentum equations. The results show a concentration of ejected particles in a zone perpendicular to the crater pair. Based on these modeling observations, it is concluded tentatively that lunar herringbone components result from collision of material ejected from the adjacent craters.

Although most lunar herringbone patterns occur in association with long secondary-crater chains, laboratory simulations of the herringbone pattern components presented thus far were accomplished by impacting only two projectiles to form only two adjacent craters. Two projectiles were used to provide good control of the experimental conditions. However, one additional experiment was performed whereby three projectiles impacted simultaneously to form a chain of three craters. Figure 32-25(a) shows this crater chain and two well-developed ridges radiating from between adjacent craters, and it is apparent that formation of an additional crater does not impair formation of the ridges. The chain of three secondary craters from Copernicus (figs. 32-19 (inset (c)) and 32-20) also is included (fig. 32-25(b)) for comparison with the experimental craters.

In all of the experimental results thus far presented, the axis of symmetry of each crater pair was parallel with the flight line of the projectiles, and the projectiles impacted with sufficient separation on the target surface to produce nearby tangential craters. These conditions model the typical secondary craters, for which the axis of symmetry of adjacent circular craters is on a radial line from the center of the primary crater. Although most secondary craters of Copernicus and Aristarchus illustrated in the preceding figures were of this type, there are also many examples of lunar crater chains for which the axis of symmetry is at an angle to the radial line from the primary crater. Figure 32-26 shows some examples of these Copernicus secondary craters and their laboratory analogs. Each photograph is oriented such that the direction of the flight line of the projectiles or the radial line from the primary crater is from bottom to top. The axis of symmetry of the Copernicus secondaries shown in set A is coincident with the radial line
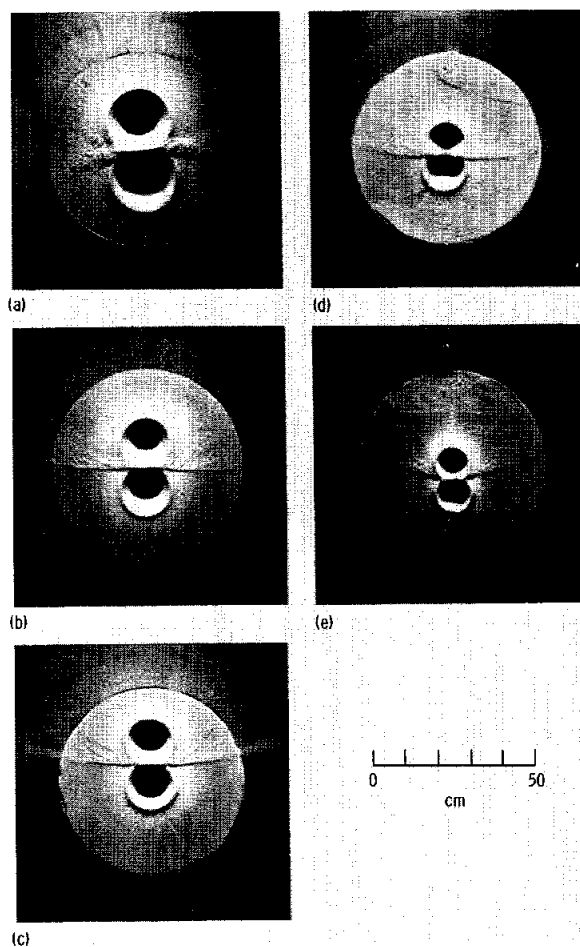

FIGURE 32-23.—Photographs of experimental crater doublets resulting from simultaneous impact at various angles. Projectiles impacted from the direction at bottom of photographs (experiment numbers in parentheses). (a) θ = 7.5° (1156). (b) θ = 30° (1127). (c) θ = 60° (1038). (d) θ = 75° (1013). (e) θ = 82.5° (1091).

axes of symmetry of which are at some small angle with respect to the surface normal. If one were to assume that the collision was inelastic, then the collision zone would be approximated as a conic section. In this case, intersection of the two conical ejecta plumes results in a section approximated by a hyperbola. Net horizontal components of velocity of all collision products along this hyperbola are directed down range because of the higher horizontal components of velocity for material ejected from the up-range crater toward the down-range crater. Therefore, the collision hyperbola moves down range and gradually deposits as a V-shaped ridge on the target surface with the V pointing toward the direction

$\theta = 60°$

V = 0.82 km/sec
τ = 0.3 msec

0 ⊢———⊣———⊣———⊣———⊣———⊣ 50
cm

t = 0.1 msec

t = 5 msec

t = 10 msec

t = 20 msec

t = 30 msec

t = 40 msec

t = 60 msec
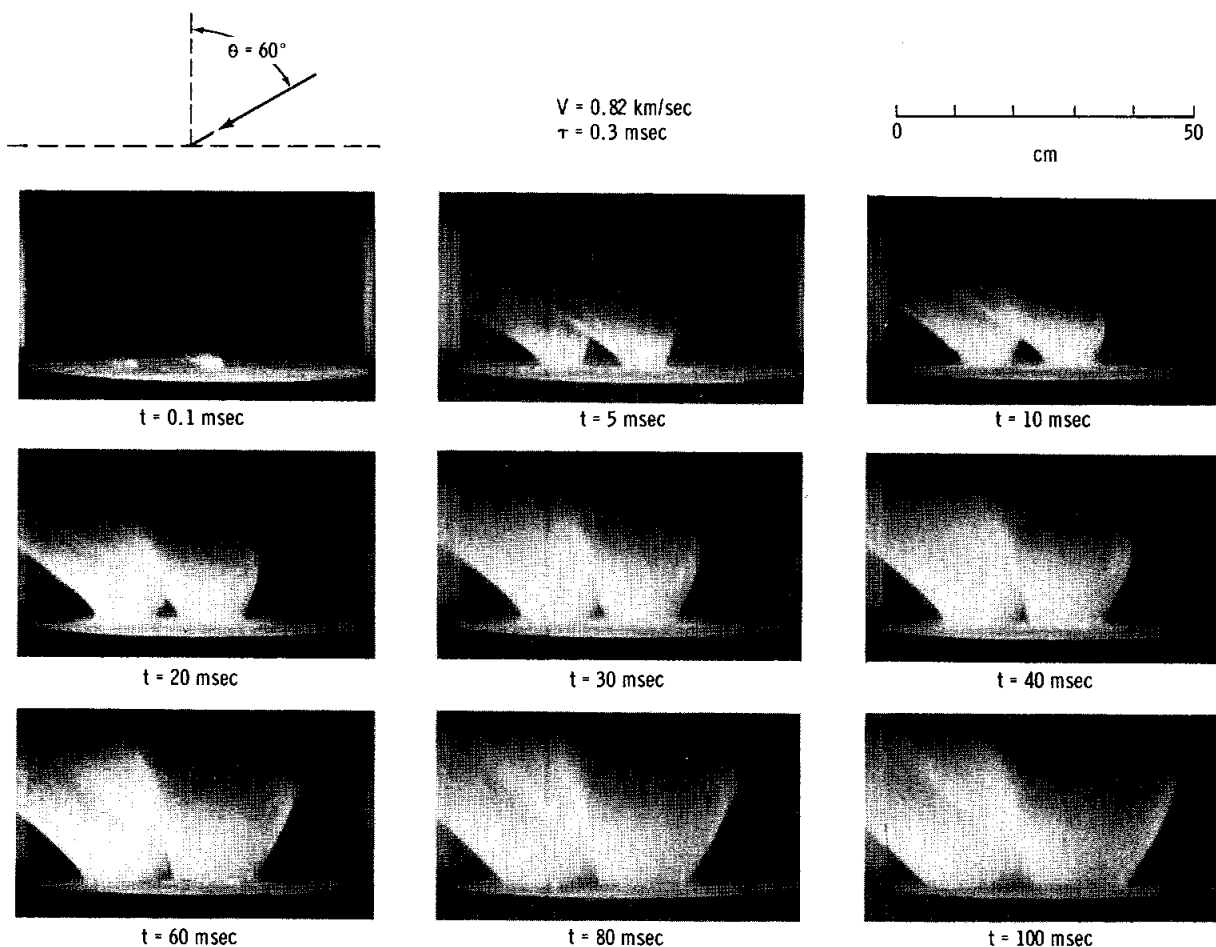
t = 80 msec

t = 100 msec

FIGURE 32-24.—Selected frames from high-speed motion picture record showing interaction of ejecta plumes; t is time after impact.

from Copernicus and is the typical case (ref. 32-23). When this occurs, the V-shaped ridge is positioned symmetrically about the crater-pair axis of symmetry. Experimental craters of set A that simulate this case have a similarly positioned axis of symmetry for the V-shaped ridge. However, when the axes of symmetry of the lunar and laboratory crater chains are at an angle α to the radial line from the primary crater or to the flight line, respectively, the ridge axis of symmetry is rotated with respect to the crater-pair axis of symmetry. For each crater pair shown in set C, the crater-pair axis of symmetry is rotated counterclockwise, but the ridge axis of symmetry is rotated clockwise with respect to the crater-pair axis. Set D shows the opposite case, in which the crater-pair axis of symmetry is rotated clockwise but the ridge axis of symmetry is rotated counterclockwise with respect to the crater-pair axis.

Other changes in laboratory craters, due to changes in azimuth of the crater pairs, also resemble the effects observed for lunar craters. Note that for the lunar and laboratory craters shown in sets C and D of figure 32-26, the arm of the V-shaped ridge down range or farthest from the primary crater is longer and wider than that up range or closest to the primary crater.

One other detailed comparison can be made between laboratory and lunar craters. Some examples of apparently single-particle, circular secondary craters derived from Aristarchus, with V-shaped ridges, have been illustrated in figure 32-21. At first, it seemed difficult to account for such features by the proposed mechanism of collision of particles ejected from separate impact points. However, when two projectiles were impacted very near one another, a nearly circular crater resulted with a V-shaped ridge
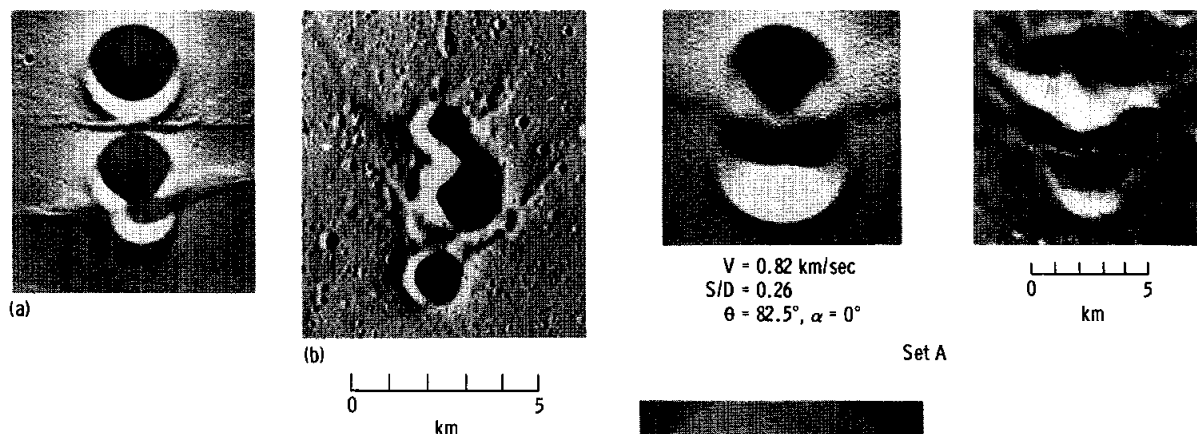
(a)

(b)

L_I_I_I_I_I_I
0   5
    km

FIGURE 32-25.—Comparison of three simultaneously pro-
duced laboratory craters with lunar crater triplet. (a)
Experimental craters. (b) Lunar craters (figs. 32-19 (inset
(c)) and 32-20) (part of Apollo 15 metric camera frame
AS15-1699).

radiating from the up-range side of the crater. In set
B, figure 32-26, a laboratory crater produced in this
way is compared with a lunar crater. In the labora-
tory example, ridge development is subdued because
the projectiles impacted at almost the same place.
Slightly greater separation, however, yields circular
craters with better developed ridges.

ISOLATED CRATER CHAINS

Study of lunar crater chains having herringbone
patterns has shown that some cannot be traced easily
to their source craters. There are good examples of
these west of Aristarchus. Figure 32-27 shows the
area covered by Apollo 15 metric camera frame
AS15-2490. Locations of several chains are plotted
and indicated by letter on this chart. Each arrow
indicates the inferred direction to the primary crater,
based on the crater-chain axis of symmetry and the
direction in which the V-shaped ridges point. Magni-
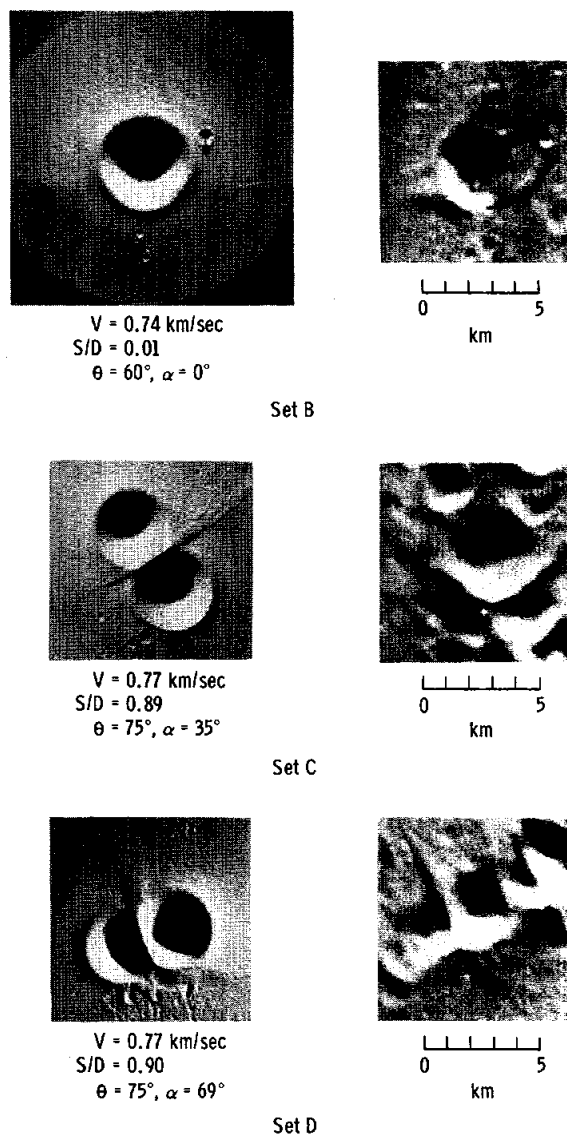
FIGURE 32-26.—Comparison of laboratory craters with
lunar secondary craters near Copernicus Crater (experi-
mental craters, left; lunar craters, right), where S/D is the
ratio of the separation between impact points to the
average crater diameter and α is the angle between the
crater axis of symmetry and the flight line or radial line
from the primary crater. Projectiles impacted from the
direction at bottom of photographs. (Lunar crater photo-
graphs are from Lunar Orbiter IV frame H-121.)

V = 0.82 km/sec
S/D = 0.26
θ = 82.5°, α = 0°

Set A

V = 0.74 km/sec
S/D = 0.01
θ = 60°, α = 0°

Set B

V = 0.77 km/sec
S/D = 0.89
θ = 75°, α = 35°

Set C

V = 0.77 km/sec
S/D = 0.90
θ = 75°, α = 69°

Set D

FIGURE 32-27.—Western Oceanus Procellarum. Outlined area is included in Apollo 15 metric camera
frame AS15-2490 (fig. 32-28). Points designated "a" to "f" indicate secondary-crater chains that
are shown as insets (with corresponding letters) in figure 32-28. The arrows indicate the inferred
direction to the primary crater (part of Lunar Earthside Chart LMP-1).

fied photographs of these crater groups are shown as
insets on the metric camera photograph of figure
32-28. The apparent source craters of only two crater
chains can be found. Aristarchus and Kepler appear
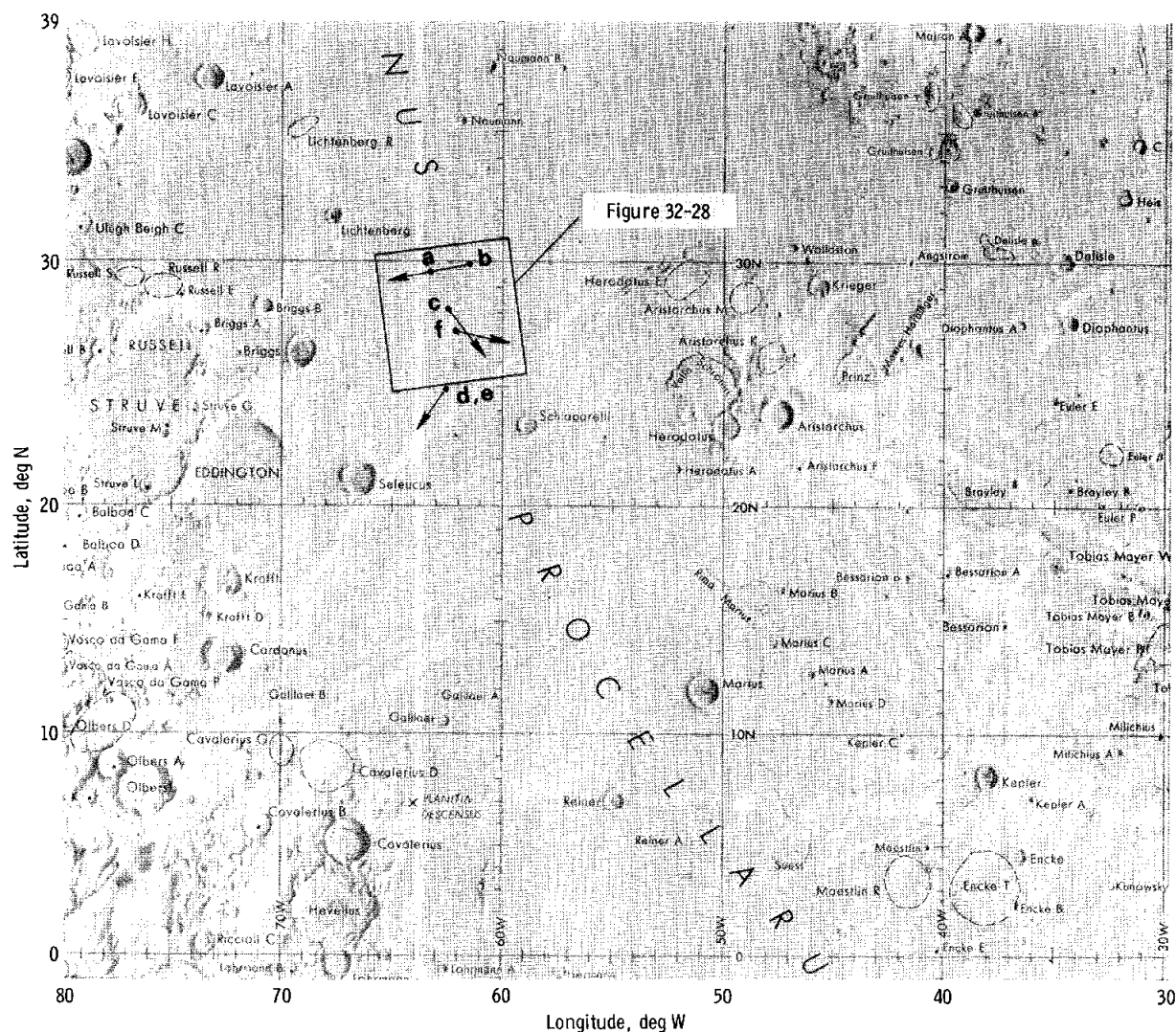to be the source craters for the crater chains shown in
insets (f) and (c), respectively. However, the sources
of the other crater chains are not obvious. The chains
in insets (a) and (b) are apparently due to a source to
the west of the area, and the doublets in insets (d)
and (e) are apparently due to a source to the south. It
is probable that the sources of some isolated crater

chains may never be located and that they can be
identified as secondary-impact craters only through
the presence of a herringbone pattern or ridges
radiating from the crater chain. However, it is of
considerable interest that this area of the lunar
surface (fig. 32-28) contains secondary-impact crater
groups derived from at least four different primary
craters. Therefore, this serves as direct evidence for
long-range transport of foreign constituents to one
common lunar surface area.

One unexpected result of these observations is the
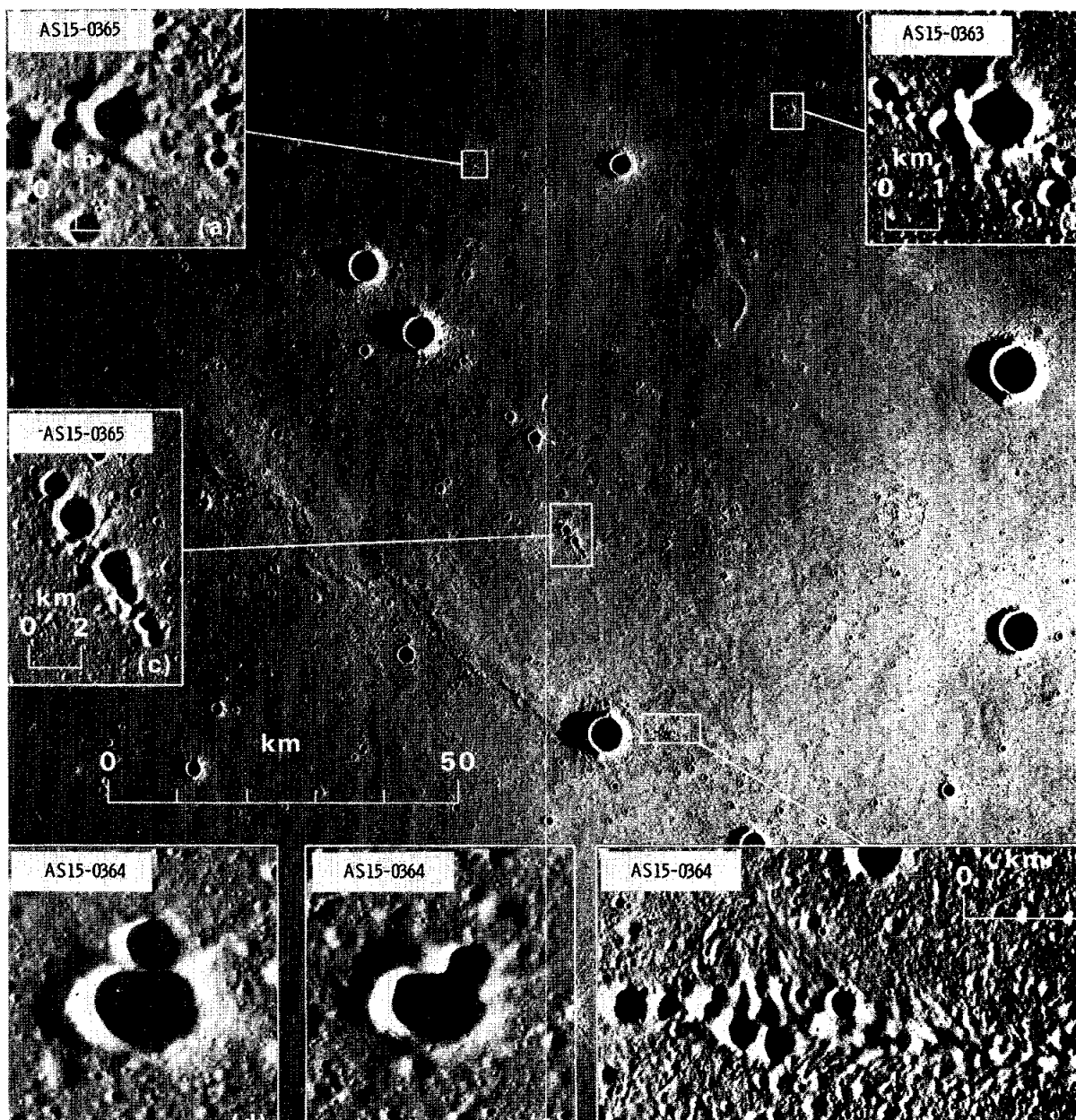
FIGURE 32-28.—Area northwest of Aristarchus Crater (Apollo 15 metric camera frame AS15-2490).
Insets (Apollo 15 panoramic camera frames) correspond to locations designated in figure 32-27.

suggestion, based on the presence of such ridges, that the Davy Crater chain may be a secondary-impact crater chain. Figure 32-29 includes portions of Apollo 16 metric and panoramic photographs of the Davy Crater chain that were exposed under several different lighting conditions. The arrow superimposed on each photograph points to a part of the crater chain that has well-developed ridges radiating from the point of crater overlap. These ridges are especially evident on the panoramic camera frame AS16-4668.

Although ridges might also result from simultaneous pyroclastic eruptions, a preliminary search for

FIGURE 32-29.—Davy Crater chain at various Sun elevation angles. Pointers indicate well-developed ridges radiating from points of crater overlap. (a) Sun elevation angle = 38° (Apollo 16 metric camera frame AS16-2970). (b) Sun elevation angle = 16° (Apollo 16 metric camera frame AS16-1677). (c) Sun elevation angle = 7° (Apollo 16 metric camera frame AS16-1283). (d) Sun elevation angle = 15° (Apollo 16 paroramic camera frame AS16-4668).

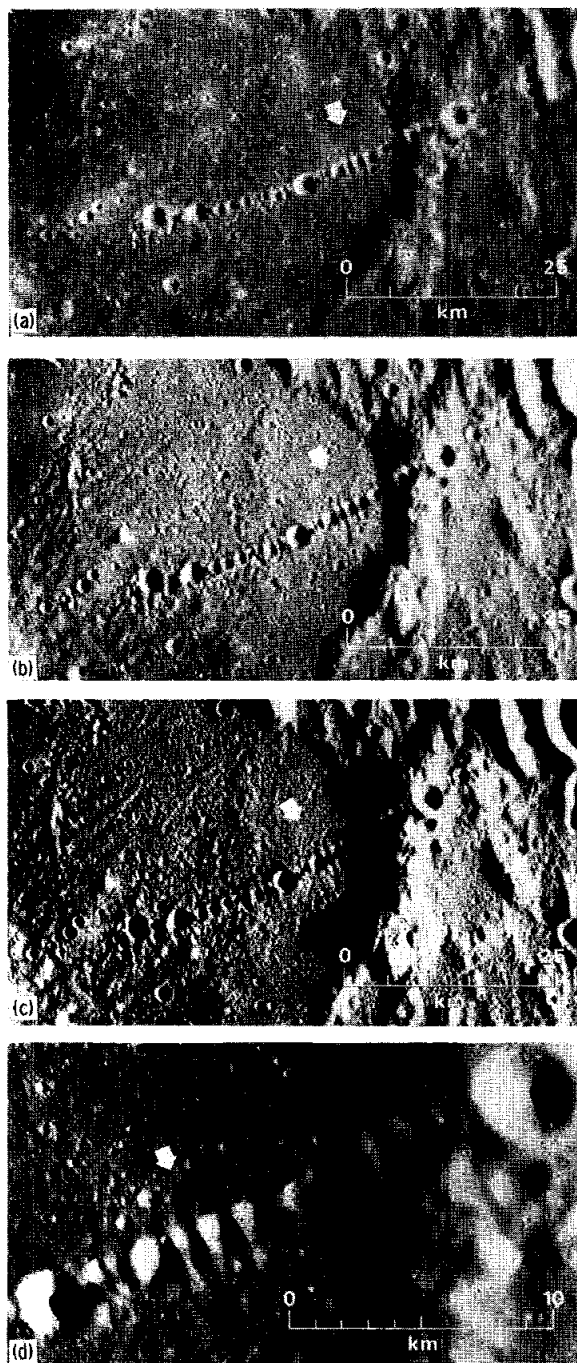ridges associated with such eruptions in Hawaii has not revealed them.[2] In addition, it seems unlikely that many adjacent eruptions would occur at exactly the same time, whereas simultaneous impact formation of adjacent secondary craters should be expected. If the Davy Crater chain is due to secondary impact, it would be of interest to locate the primary crater. In principle, it may be possible to determine the direction and angle of impact of the secondary fragments from study of crater-chain ridge structure. It may not be possible, however, to determine the impact velocity; therefore, it may be difficult to compute the range to the primary crater.

CONCLUDING REMARKS

In summary, these preliminary results indicate that the lunar herringbone pattern is a common characteristic of secondary-impact cratering. The pattern results from collision of material ejected from separated impact points. Moreover, these results suggest that many lunar secondary craters were produced by fragments impacting the lunar surface at high angles from the surface normal. Finally, many isolated crater chains, such as the Davy Crater chain, that previously were thought to be volcanic forms may in fact have been produced by secondary impacts.

REFERENCES

32-1. Baldwin, Ralph B.: The Measure of the Moon. Univ. of Chicago Press, 1963.
32-2. Pike, R. J.: Geometric Similitude of Lunar and Terrestrial Craters. Sec. 15 of Proceedings of the 24th International Geological Congress (Montreal), Aug. 21-30, 1972, pp. 41-47.
32-3. Mironova, M. N.: Structural Characteristics of Some Craters on the Far Side of the Moon. In Astrometry and Astrophysics, No. 1: Physics of the Moon and Planets. NASA TT F-566, 1970, pp. 33-45.
32-4. Mironova, M. N.: Height Profiles of Twenty-Nine Craters on the Far Side of the Moon. In Astrometry and Astrophysics, No. 1: Physics of the Moon and Planets. NASA TT F-566, 1970, pp. 46-57.
32-5. Baldwin, Ralph B.: The Face of the Moon. Univ. of Chicago Press, 1949.
32-6. Pike, R. J.: Height-Depth Ratios of Lunar and Terrestrial Craters. Nature Phys. Sci., vol. 234, Nov. 15, 1971, pp. 56-57.
32-7. Guest, J. E.; and Murray, J. B.: Nature and Origin of

[2] Ronald Greeley, personal communication, 1973.

Tsiolkovsky Crater, Lunar Farside. Planet. Space Sci., vol. 17, no. 1, Jan. 1969, pp. 121-141.

32-8. Murray, J. B.; and Guest, J. E.: Circularities of Craters and Related Structures on Earth and Moon. Mod. Geol., vol. 1, no. 2, 1970, pp. 149-159.

32-9. Pike, Richard J.: Crater Morphometry. Sec. 29, Part L, of the Apollo 16 Preliminary Science Report. NASA SP-315, 1972.

32-10. Quaide, William L.; Gault, Donald E.; and Schmidt, Richard A.: Gravitative Effects on Lunar Impact Structures. Ann. N.Y. Acad. Sci., vol. 123, July 15, 1965, pp. 563-572.

32-11. Pike, Richard J.: Genetic Implications of the Shapes of Martian and Lunar Craters. Icarus, vol. 15, no. 3, Dec. 1971, pp. 384-395.

32-12. Millman, Peter Mackenzie: A Profile Study of the New Quebec Crater. Canada Dominion Observatory Publ., vol. 18, no. 4, 1956, pp. 61-82.

32-13. Firsoff, V. A.: Strange World of the Moon, An Inquiry Into Its Physical Features and the Possibility of Life. Basic Books Inc. (New York), 1959.

32-14. Shoemaker, Eugene M.: Preliminary Analysis of the Fine Structure of the Lunar Surface in Mare Cognitum. Ranger VII, Part II, Experimenters' Analyses and Interpretations. JPL Tech. Rept. no. 32-700, 1965, pp. 75-134.

32-15. Mattingly, T. K.; El-Baz, Farouk; and Laidley, Richard A.: Observations and Impressions From Lunar Orbit. Sec. 28 of the Apollo 16 Preliminary Science Report. NASA SP-315, 1972.

32-16. El-Baz, Farouk: King Crater and Its Environs. Sec. 29, Part M, of the Apollo 16 Preliminary Science Report. NASA SP-315, 1972.

32-17. Howard, Keith A.: Ejecta Blankets of Large Craters Exemplified by King Crater. Sec. 29, Part N, of the Apollo 16 Preliminary Science Report. NASA SP-315, 1972.

32-18. El-Baz, Farouk: New Geological Findings in Apollo 15 Lunar Orbital Photography. Proceedings of the Third Lunar Science Conference, vol. 1, MIT Press (Cambridge, Mass.), 1972, pp. 39-61.

32-19. Scott, D. H.; and Eggleton, R. E.: Geologic Map of the Rümker Quadrangle of the Moon. U.S. Geol. Survey Misc. Geol. Inv. Map I-805, 1973.

32-20. Williams, Howel: The History and Character of Volcanic Domes. Calif. Univ. Publ., Dept. Geol. Sci. Bull., vol. 21, no. 5, 1932, pp. 51-146.

32-21. Scott, David R.; Worden, Alfred M.; and Irwin, James B.: Crew Observations. Sec. 4 of the Apollo 15 Preliminary Science Report. NASA SP-289, 1972.

32-22. O'Keefe, J. A.; Cameron, W. S.; and Masursky, Harold: Hypersonic Gas Flow. Ch. 2 of Analysis of Apollo 8 Photographs and Visual Observations. NASA SP-201, 1969, p. 30.

32-23. Guest, J. E.; and Murray, J. B.: A Large Scale Surface Pattern Associated with the Ejecta Blanket and Rays of Copernicus. The Moon, vol. 3, no. 3, Dec. 1971, pp. 326-336.

32-24. Oberbeck, Verne R.; Morrison, Robert H.; and Wedekind, John: Lunar Secondary Craters. Sec. 29, Part K, of the Apollo 16 Preliminary Science Report. NASA SP-315, 1972.

32-25. Giamboni, Louis A.: Lunar Rays: Their Formation and Age. Astrophys. J., vol. 130, no. 1, July 1959, pp. 324-335.

33. Remote Sensing and Photogrammetric Studies

Remote sensing data, including Earth-based measurements of color differences, eclipse temperatures, and radar backscatter as well as results of orbital bistatic-radar and X-ray fluorescence experiments, delineate surface types in Mare Serenitatis that correlate well with photogeologic map units. Differences in the remote sensing data apparently reflect differences in chemical composition, blockiness, and thickness of the regolith formed on individual rock units (part A). Studies of depolarized Earth-based radar echoes (3.8-cm wavelength) at the Apollo 17 landing site suggest that the amplitude of the echoes may be strongly modified by topography. Specifically, slopes tilted toward the radar source enhance the echoes; thus their effect must be considered before inferences can be drawn as to surface blockiness, dielectric constants, or electromagnetic absorption by the regolith (part B).

Comparisons of slope-frequency distributions obtained independently from bistatic-radar and photo-grammetric methods show good correspondence; a common result is that the distribution functions are highly dependent on slope length in the maria, but less so in the highlands (part C). Investigation of the effect of photogrammetric reading error on slope-frequency distributions suggests that the errors are insignificant, provided that slope lengths are large, errors of elevation measurement are small, and the quality of the photographs is comparable to that of the Apollo metric and panoramic cameras (appendix to part C). Repeatability of elevation measurements, critical to optimum use of photogrammetric products, is to some extent dependent on Sun elevation angle (part D). Data from the laser altimeter combined with spacecraft attitudes provide the required constraints for preparation of cartographic products by photogrammetric reduction of lunar surface photographs; altimeter measurements also indicate broad-scale topographic relief around the entire circumference of the Moon (part E).

PART A

REMOTE SENSING OF MARE SERENITATIS

T. W. Thompson,[a] *K. A. Howard,*[b] *R. W. Shorthill,*[c] *G. L. Tyler,*[d] *S. H. Zisk,*[e]
E. A. Whitaker,[f] *G. G. Schaber,*[b] *and H. J. Moore*[b]

Mare Serenitatis is a circular mare approximately 600 km in diameter in the northeast quadrant of the lunar near side. It occupies an old multi-ringed basin (refs. 33-1 and 33-2) and is the site of a prominent mascon (ref. 33-3). A conspicuous dark annulus in this mare prompted subdivision of the mare materials into different stratigraphic units (refs. 33-2 and 33-4). A revised stratigraphic sequence for the southern part of Mare Serenitatis, based on photogeologic interpretation of Apollo 15 and 17 photographs, is summarized as follows after Howard et al. (part A of sec. 29). The oldest three units are:

1. The dark material of the Littrow (Apollo 17 landing site) area at the southeast margin
2. The dark basalt of the crater Plinius area along the south border of Mare Serenitatis
3. The Sulpicius Gallus Formation at the southwest margin

Younger than these three are units that are slightly lighter parts of the dark annulus: (1) basalt near the crater Dawes, (2) eastern ring basalt, and (3) basalt of southwestern Mare Serenitatis. Youngest of all is the light mare basalt that forms the central part of Mare Serenitatis.

In this report, the authors examine the Earth-based observations of optical color differences, infrared eclipse temperatures, and radar backscatter for Mare Serenitatis. Different surface types can be defined by correlating differences in these Earth-based observations. These surface types correlate with

Apollo orbital data collected by the bistatic radar and X-ray fluorescence experiments of the Apollo 15 mission and with geologic units defined from Apollo observations by Howard et al. (part A of sec. 29). These data suggest that variation in chemical and mineralogical composition is a factor causing the differences in these remote observations of Mare Serenitatis.

This report is divided into four sections as follows:

1. "Earth-Based Observations," which reviews the Earth-based data sets of optical color differences, 11-μm eclipse temperatures, and 3.8- and 70-cm radar backscatter. Correlated differences in these data define five surface types.

2. "Orbital Observations," which shows that these five surface types are also seen on Apollo photographs and in the Apollo 15 bistatic-radar and X-ray fluorescence results.

3. "Physical Properties of Surface Types," which shows that different surface chemical compositions could cause the observed differences that define the surface types.

4. "Correlation of Surface Types With Geologic Units," which shows that there is excellent agreement between the surface types defined by these remote observations and the geologic units and stratigraphy defined by Howard et al. (part A of sec. 29).

EARTH-BASED OBSERVATIONS

Earth-based observations of Mare Serenitatis at visible, infrared, and radar wavelengths are shown in figure 33-1. The full Moon photograph (ref. 33-5 and fig. 33-1(a)) shows the albedo differences over the mare floor. Other than the obvious brightness differences between maria and terrae, the most striking albedo difference is that between the dark ring on the
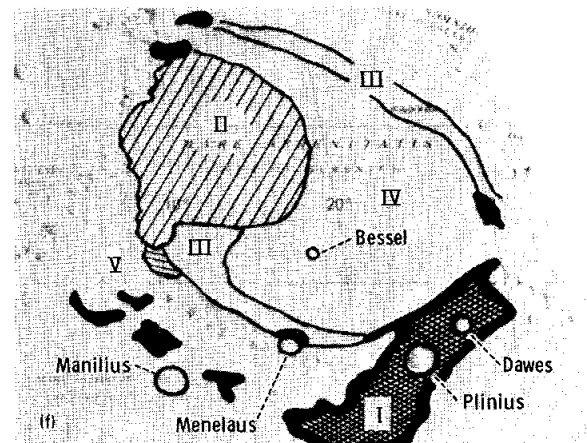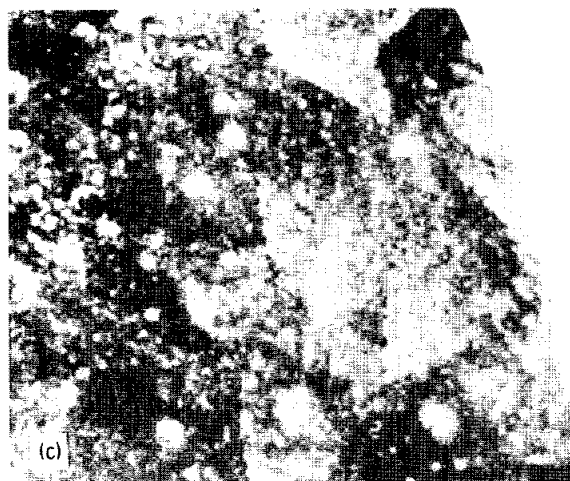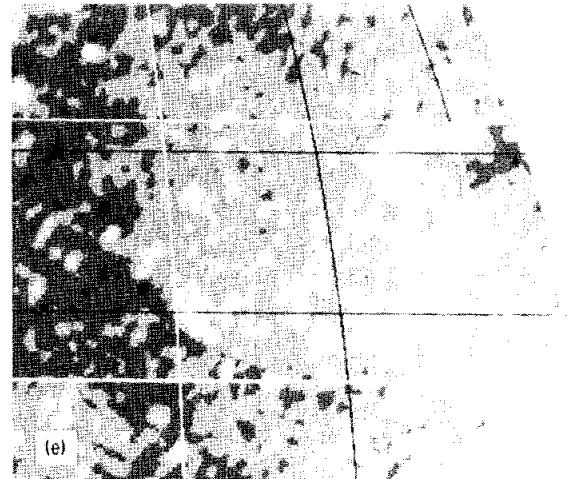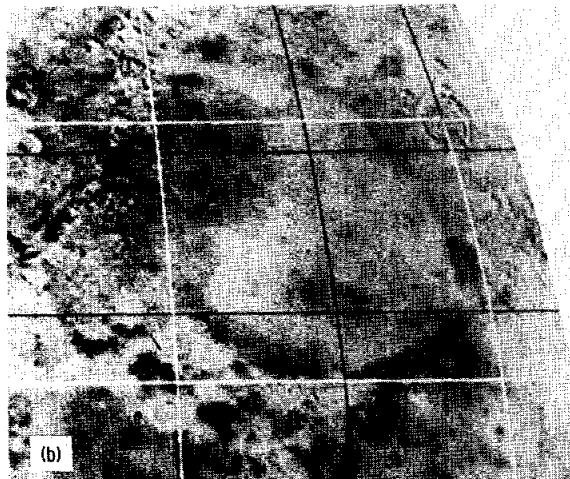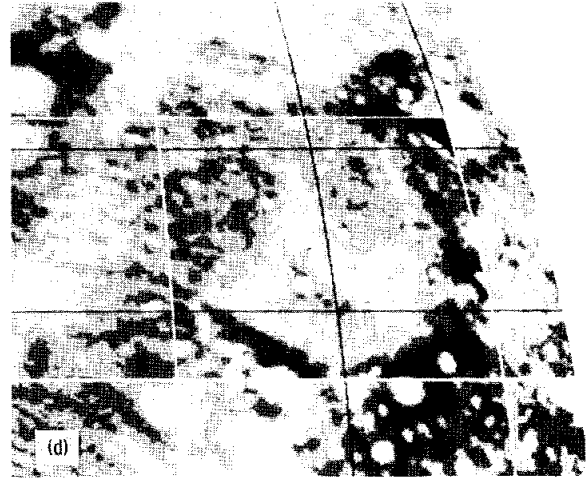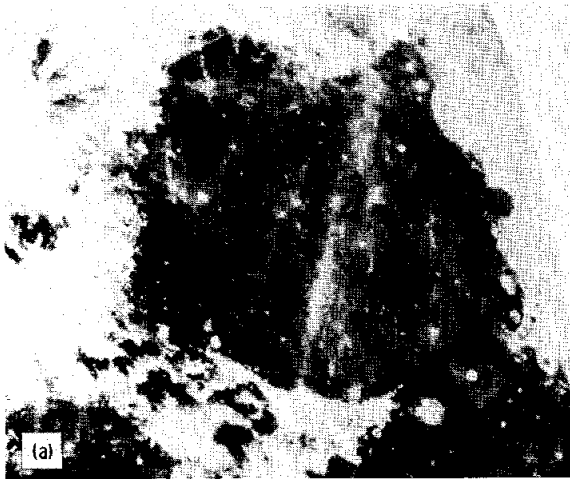
[a]Jet Propulsion Laboratory.
[b]U.S. Geological Survey.
[c]Boeing Aerospace Company.
[d]Stanford University.
[e]MIT Haystack Observatory.
[f]Lunar and Planetary Laboratory, University of Arizona.

(a)

(d)

(b)

(e)

(c)

(f)

mare perimeter and the central mare. This difference is also shown in figure 29-1 of section 29, part A.

Color-Difference Photography

Complex surfaces can be investigated by color-composite photography (ref. 33-6) as shown by the color-difference photograph in figure 33-1(b). The Moon was photographed at two wavelengths, 0.82 μm (photographic infrared) and 0.36 μm (photographic ultraviolet). A positive of the infrared and a negative of the ultraviolet were matched and overprinted. This process minimizes albedo differences and enhances any color differences. The dark shades of figure 33-1(b) are bluer than average, and the light shades of the figure are redder than average. The color-difference photograph shown here was digitally enhanced to increase the color contrast. It reveals mare regions with striking color differences, which are not always correlative with albedo. These color differences are generally attributed to different chemical and mineralogical compositions (refs. 33-6 to 33-9).

Radar Backscatter

The 3.8- and 70-cm radar maps in figures 33-1(c) and 33-1(d), respectively, were obtained by delay-Doppler mapping of backscattered radar echoes (ref. 33-10). These two images show departures of the depolarized echoes from the expected echo strengths; brighter areas have higher echo strengths. These stronger echoes are generally attributed to wavelength-size rocks, which are on the surface or buried no deeper than 10 wavelengths (refs. 33-10 and 33-11). The composition of the regolith can also affect the echo strength (ref. 33-12).

FIGURE 33-1.—Remote observations of Mare Serenitatis. (a) Full Moon photograph. White light; resolution approximately 1 km. (b) Color-difference photograph. Dark tones are bluer; lighter tones are redder than the average color; resolution approximately 1 km. (c) 3.8-cm radar map. Radar backscatter enhancements are bright; resolution approximately 2 km. (d) 70-cm radar map. Radar backscatter enhancements are bright; resolution approximately 10 km; each tone is 2X in power. (e) 11-μm eclipse temperature. Thermal enhancements are bright; resolution approximately 15 km. Each tone is 4 K. (f) Surface types. Indicated surface types are traced over a section of the LEM-1 photomosaic and described in the text.

Infrared Eclipse Temperatures

The 11-μm eclipse temperature image in figure 33-1(e) was obtained during a total eclipse of the Moon (ref. 33-13). These data show the departures in temperature from an average temperature for the area shown, and each tone represents a 4 K increment (ref. 33-14). The differences in eclipse temperatures are controlled by the abundances of surface rocks greater than 10 cm in diameter (ref. 33-11).

Definition of Surface Types

The radar and infrared data sets have been compared on a global basis (ref. 33-11) as well as on a regional basis (ref. 33-15). In this report, a more comprehensive synthesis is undertaken for Mare Serenitatis.

Five distinct surface types are defined by their color, albedo, radar scatter, and infrared characteristics (table 33-I) and are shown in figure 33-1(f). The term "type" will be used for surfaces defined by the remote observations and the term "unit" for the geologic units defined by photogeology. Surface types I, II, and III were defined previously (ref. 33-12). We have added a type IV surface, the central area of Mare Serenitatis, and a type V surface, the Sulpicius Gallus Formation (ref. 33-4).

The important difference between the color and the radar scattering is the penetration depth. Whereas only the uppermost 100 μm provide the color, the radar echoes are influenced significantly by a few meters of depth (5 wavelengths) (ref. 33-12). Thus, positive correlation between color and radar data suggests that if chemical differences are responsible for the color variations, then these chemical differences may persist to a depth of at least 5 m. The eclipse temperatures, which respond only to surface rock, provide an important clue to surface and subsurface structure when combined with the color and radar data. If surface rock populations are nearly uniform as suggested by the nearly constant eclipse temperatures, then the changes in radar backscatter in Mare Serenitatis must arise from some variation in the scatter from subsurface rocks.

ORBITAL OBSERVATIONS

Differences between the surface types are also shown in the Apollo orbital bistatic-radar, photography, and X-ray fluorescence experiments.

TABLE 33-I.—*Characteristics of Surface Types Defined by Remote Observations of Mare Serenitatis*

[Numbers give relative rank of the indicated quantity]

Surface type	Color (a)	Albedo (b)	Radar scatter (c)	Infrared characteristic (d)	Inferred chemistry (e)
I	1	2	3	2	1
II	2	4	2	2	2
III	3	3	3	2	3
IV	4	4	1	2	4
V	4	1	3	1	4

[a]Bluest, 1; reddest, 4.
[b]Darkest, 1; lightest, 4.
[c]Strongest, 1; weakest, 3.
[d]Coolest, 1; warmest, 2.
[e]Highest in titanium (Ti) and iron (Fe), 1; lowest in Ti and Fe, 4.

TABLE 33-II.—*Bistatic Radar rms Slopes for Remote Sensing Surface Types*

Surface type	Approximate track coordinates	Range of rms slopes, S-band, deg	Range of rms slopes, VHF, deg	Description
I	19.8° N, 28.0° E to 20.5° N, 26.5° E	3.3 to 4.0 (avg. ≈ 3.6)	2.2 to 2.8 (avg. ≈ 2.5)	Dark surface transected by linear riles
II	23.5° N, 10° E to 24.2° N, 8° E	4.0 to 5.0 (avg. ≈ 4.5)	2.0 to 3.5 (avg. ≈ 3.1)	Cratered mare surface
III	23.0° N, 13.6° E to 23.5° N, 10° E	3.7 to 4.5 (avg. ≈ 4.0)	2.2 to 3.1 (avg. ≈ 2.5)	Cratered mare surface
IV-A	20.5° N, 26.5° E to 23.6° N, 21.2° E	3.2 to 4.1 (avg. ≈ 3.6)	1.4 to 3.0 (avg. ≈ 2.2)	Cratered mare surface, locally very smooth appearance
IV-B	23.6° N, 21.2° E to 22.5° N, 16.6° E	3.5 to 4.5 (avg. ≈ 3.7)	2.3 to 3.0 (avg. ≈ 2.5)	Ejecta of Bessel, crater clusters, and local smooth areas
IV-C	22.5° N, 16.6° E to 23.0° N, 13.6° E	3.3 to 4.0 (avg. ≈ 3.5)	1.9 to 2.2 (avg. ≈ 2.1)	Cratered mare surface, locally very smooth appearance
V	Not sampled	–	–	Dark surface with craters and linear rilles
Uplands near Mons Argaeus	19.7° N, 28.5° W	4 to 4.3 (avg. ≈ 4.1)	4 to 4.5 (avg. ≈ 4.2)	Mountains of Mons Argaeus

Bistatic-Radar Observations

The bistatic-radar investigations (ref. 33-16) provide information on the roughness of surface types II, III, and IV. In this experiment, S-band (13 cm) and VHF (110 cm) continuous-wave transmissions from the command and service module were reflected from the lunar surface toward the Earth where the reflected echo was received and processed. Analysis of the echo yielded an estimate of surface roughness in terms of rms slopes.

The trace of the points of the Apollo 15 bistatic-radar experiment crosses Mare Serenitatis from the region of Mons Argaeus to a point approximately 8 km north of Bessel Crater and then to longitude 10° E and latitude 23.6° N. Roughness (rms slope) estimates are representative of areas 5 to 10 km in radius for each specular point; the results are shown in table 33-II. The rms slopes are large where the surfaces visually appear rough and are small where they appear smooth. Type II, III, and IV surfaces differ in surface roughness. Type II has larger rms slopes than type III (ref. 33-17). Type IV has the lowest rms slope, except in the vicinity of the crater Bessel where an increase in roughness can be attributed to ejecta from Bessel and crater clusters. Type I cannot be distinguished from type IV by the bistatic radar; type V was not sampled.

Photography

Apollo orbital photographs show a noticeable difference in the crater populations of the type I and IV surfaces. Figure 33-2, an enlarged metric camera photograph, shows the contact of these two surfaces. The type I surface has more kilometer-size craters and is older (part C of sec. 29) than the type IV surface. A detailed study of the Apollo 17 metric photographs across this contact showed significantly fewer craters with diameters of 60 m and less in the older type I material, suggesting a deep regolith and possible mantle. Presumably, these smaller craters were formed entirely in a fine-grained material and did not exhume bedrock. Thus, these craters were probably destroyed by erosion faster than similar-size craters that penetrated into bedrock of the younger type IV material. Assuming a crater depth-to-diameter ratio of 1 to 5, the depth of this fine-grained material in the type I material is 12 m or more.

Apollo photographs also indicate more surface
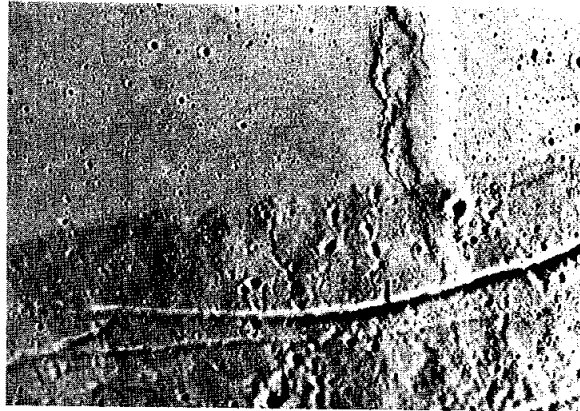
FIGURE 33-2.—A small region from Apollo 17 metric photograph AS17-0451 located at 23° E, 18° N, showing a belt 50 km in length along the contact between the type I material (the darker material to the south) and the younger type IV material.

rocks on the type IV surface than on the type I surface. Panoramic photographs across the type I to type IV boundary were enlarged, and rocks 2 m and larger were counted for five areas of 25 km². Rock populations were 12 to 16 rocks/km² for the type IV material and 0.2 to 2.5 rocks/km² for the type I material. This large contrast in rock population would be expected to give different eclipse temperatures; these different temperatures were not observed. Refined estimates of surface rock abundances may be given by the infrared scanning radiometer (sec. 24) that was flown on Apollo 17.

X-Ray Fluorescence Observations

The X-ray fluorescence experiment flown on the Apollo 15 mission indicated a chemical composition difference between the type I and type IV surfaces. Aluminum-to-silicon intensity ratios for Mare Serenitatis and Mare Tranquillitatis prepared by Adler et al. (ref. 33-18) are listed in table 33-III. For Mare Serenitatis, five of seven observed ratios range from 0.55 to 0.62; for Mare Tranquillitatis, 11 of the 12 points range from 0.67 to 0.89. The measurement points for Mare Tranquillitatis are in lunar areas observed to have the same blue color, low radar backscatter, thermal enhancement, and dark albedo that characterize the type I surface. Five measurement points for Mare Serenitatis are in the central area, the type IV surface, and two points share the type II and IV units. Thus, the type I surface has a

TABLE 33-III.—*Aluminum-to-Silicon Intensity Ratio for Mare Serenitatis and Mare Tranquillitatis*[a]

Intensity ratio	Surface type	Longitude, deg E	Latitude, deg N
Mare Serenitatis			
0.62	II, IV	13	23
.57	II, IV	14	24
.61	IV	16	22
.55	IV	16	24
.59	IV	20	23
.80	IV	23	23
.77	IV	26	22
Mare Tranquillitatis			
0.76	I	20	9
.80	I	22	13
.74	I	23	8
.75	I	26	7
.70	I	26	12
.72	I	28	10
.67	I	29	5
.38	I	31	3
.72	I	31	8
.71	I	34	8
.67	I	36	6
.89	I	39	4

[a]Reference 33-18.

high aluminum-to-silicon ratio and the type IV surface has a low ratio.

PHYSICAL PROPERTIES OF SURFACE TYPES

The variations in the remote sensing data are explicable as results of variations in regolith composition, blockiness, and thickness.

Chemical variations in the surface material are reflected primarily in the color and by X-ray fluorescence. The remote sensing responses of the bluest surface, type I, are identical to those of the Apollo 11 site in Mare Tranquillitatis, where rocks are high in titanium (Ti) and iron (Fe). Thus, the responses that characterize type I may result, in part, from high Ti and Fe contents. Darker and bluer maria are expected to have high Ti and Fe contents relative to lighter and redder maria, according to Pieters et al. (ref. 33-19). Types I and IV have the extreme colors, from which a

relation to Ti content is inferred, as shown in table 33-I. This relation, however, is not entirely certain, as shown by the high-titanium orange glass returned by the Apollo 17 crew. The X-ray fluorescence results confirm that type I and IV materials differ chemically.

The composition of type I may contribute also to its lower radar backscatter compared to type IV. Different chemical compositions of regolith can cause the radar backscatter to vary by a factor of 2, according to calculations by Thompson et al. (ref. 33-12). Our data then are consistent with a model in which the bluer materials have a higher electrical loss, which attenuates the component of backscatter from buried rocks. Measurements of terrestrial rocks and their dusts by Campbell and Ulrichs (ref. 33-20) and of returned lunar rocks and dust by Gold et al. (ref. 33-21) indicate that the electrical loss can vary by almost an order of magnitude between different rock compositions. However, Gold et al. (ref. 33-21) suspect sample contamination of earlier Apollo samples by water, which would increase the electrical loss. Thus, the relation between chemistry and electrical loss may require further investigation.

Block variations in the regolith can also explain the radar data. If rocks are everywhere more abundant on the younger type IV (red) surfaces than on bluer surfaces, this condition will explain the higher radar return from the type IV surfaces. The conclusion that rocks are more abundant on type IV surfaces is tentative, however, because the eclipse temperatures (which depend upon surface rocks) are nearly constant across Mare Serenitatis. (A slight thermal enhancement in eastern Mare Serenitatis seems to be correlated with wrinkle ridges and will be the subject of a future study.) The small changes in bistatic-radar rms slopes indicate that slopes can be ruled out as major factors in altering radar backscatter for the areas considered here (part B).

The thicker regolith of the type I material, deduced in our detailed investigation of the type I to type IV contact shown in figure 33-2, could also account for the reduced radar echoes as compared to echoes from type IV material. One might expect high backscatter from a thin regolith, in which the bedrock interface and numerous blocks are near the surface. The opposite result, however, is suggested by the generally lower radar echo from mare areas than from highland areas, where the regolith is generally thicker. Inasmuch as highland areas contrast chemi-

cally with mare areas, we are uncertain which way regolith thickness alone influences the radar return.

Because variations in chemical composition, blockiness, and possibly thickness of the regolith can individually explain the radar data, the extent of influence of each factor on the radar return is uncertain at present.

CORRELATION OF SURFACE TYPES WITH GEOLOGIC UNITS

The surface types defined by the remote observation agree well with geologic units defined by photogeology. The geologic units and stratigraphy of Mare Serenitatis have been defined by Howard et al. (part A of sec. 29). The oldest basalt units are the dark Littrow material, the basalt near Plinius, and the Sulpicius Gallus Formation; intermediate age units are the basalt near Dawes, the basalt of southwestern Mare Serenitatis, and the eastern ring basalt; the youngest basalt is in central Mare Serenitatis.

Oldest Basalt Units

The basalt near Plinius is the surface type I. As previously noted, the Earth-based observations show this type I material is similar to and probably continuous with the Apollo 11 landing site in Mare Tranquillitatis. The Plinius basalt, therefore, should have the high Ti and Fe contents that characterize the returned Apollo 11 samples.

The Sulpicius Gallus Formation has unusual properties at visual and nonvisual wavelengths. This formation mantles the terra, yet it has a lower albedo than average mare, and it has a low radar echo and low infrared return, indicating few blocks in the formation. Most significantly, this area is as red as the central mare surface of Serenitatis, suggesting it is chemically different from other "black spots" (ref. 33-19), including the dark Littrow material, and is different from Plinius basalt. The Sulpicius Gallus Formation, which was earlier defined as surface type V from the Earth-based observation, is a very distinct geologic unit.

The unit most significant to the latest Apollo mission is the dark Littrow material in the vicinity of the Apollo 17 landing site. This unit also mantles terra. It has very low albedo and a very low 3.8-cm radar echo (ref. 33-19). Although Pieters et al. (ref. 33-19) report a strong blue color, the color-difference

photograph in figure 33-1(b) and measurements by Riley and Hall (ref. 33-22) suggest this area is little different in color from the red central area of Mare Serenitatis. This small area is not well resolved by the 70-cm and infrared images. The unit has some of the properties of the surface type V and some of the surface type I.

Intermediate Age Basalt Units

The Dawes basalt is next younger in age and forms a small area in southeastern Mare Serenitatis. This unit is surface type I because of its blue color. The unit has slightly lower 3.8-cm radar backscatter (one-half to three-fourths times) than the adjacent older Plinius basalt.

The eastern ring basalt, also of intermediate age, includes both surface types I and III. The type I (bluer) material occupies a patch 70 km across located between the Apollo 17 site and the crater Le Monnier to the north. Le Monnier Crater is flooded with type III mare, and further data on this unit may come from Lunokhod 2, which landed there. The Earth-based data indicate that type III eastern ring basalt continues along the entire northern dark ring of Mare Serenitatis and terminates in a small patch of type I material. The basalt of southwestern Mare Serenitatis, of equivalent age, is also type III.

Youngest Basalt Units

The youngest mare material in central Mare Serenitatis has a relatively high albedo. The color-difference photograph in figure 33-1(b) shows that this material may be subdivided into a central unit and a unit northwest of Bessel. The former is defined as surface type IV (table 33-I) and has the reddest color and the highest radar backscatter of all Mare Serenitatis units. The unit northwest of Bessel is bluer and has been classified as surface type II. Surprisingly, the type II and IV materials have the same albedo but different colors.

CONCLUSIONS

The geologic units of Mare Serenitatis have been defined by Howard et al. (part A of sec. 29) mainly from the interpretation of orbital and telescopic photographs. These geologic units agree well with surface types that can be defined from other Earth-based observations and correlated with Apollo orbital

data. Both Earth-based and orbital measurements are consistent with the hypothesis that chemical differences of surface materials cause the observed color, and they may also modify the radar backscatter by attenuating echoes from buried rocks. Earth-based and X-ray fluorescence data for type I are identical to those at the Apollo 11 landing site. The data suggest that there are chemical differences between the various units defined by geological interpretation of Apollo photographs.

This study of Mare Serenitatis indicates that Earth-based observations delineate units consistent with photogeologic interpretation and can extend geologic mapping to lunar areas not covered by Apollo photographs and orbital experiments. Also, photogeologic interpretation has permitted subdivision of surface types defined by remote observation. Thus, these two aspects of surface definition should be considered concurrently in describing the physical properties of the lunar surface.

ACKNOWLEDGMENT

PART B

CALIBRATION OF RADAR DATA FROM APOLLO 17 AND OTHER MISSION RESULTS

H. J. Moore[a] *and S. H. Zisk*[b]

A large quantity of data on backscattered polarized and depolarized radar echoes from the Moon has been collected from Earth at 3.8-cm wavelength (ref. 33-23). Depolarized echoes are particularly interesting because theory indicates that relatively strong depolarized echoes can be caused by the following factors.

1. An increase in the number of blocks 0.5 to 50 cm across in the upper one-half meter of the lunar regolith

2. An increase in the dielectric constant of a normally rough or blocky surface

3. A decrease in the electromagnetic absorption in the upper meter or so of the regolith

4. To a variable extent, a slope that tilts the surface toward the Earth-based radar

However, the quantitative aspects of the depolarized echoes are poorly understood, and attempts to use the data to predict surface roughness due to blocks and fragments have been only partly successful (ref. 33-24). Data from the Apollo 17 landing site suggest that topography and slopes play an important role in controlling the amplitude of the depolarized radar echoes. This variable must be assessed before the effects of blocks, dielectric constant, and electromagnetic absorption can be determined.

We have examined the radar data on depolarized radar echoes for the general areas of (1) the Apollo 11, 12, 14, 15, 16, and 17 landing sites, (2) the Ranger VII, VIII, and IX impact sites, and (3) the Surveyor I, III, V, and VII landing sites. These data were then compared with photographic data. Surveyor VI was excluded because it landed near the center of the lunar disk where echo data are poor.

Three problems concerning the echo data are briefly discussed: (1) the frequency distributions of echo strengths from site to site, (2) the areal distribution of echoes, and (3) detailed correlation of echoes with the photographs of the Apollo 17 landing area.

FREQUENCY DISTRIBUTIONS OF ECHOES

Frequency distributions of depolarized radar echo strengths[1] (obtained manually from computer print-

[1] Echo strengths are in units of relative power: watts/(watts m^2) or m^{-2}.

outs for the sites previously mentioned, table 33-IV) of a small area within the Surveyor I area (Flamsteed in table 33-IV) and of the Diophantus area suggest a mixture of two populations of echo strengths for most of the areas. Significant parts of the distributions are approximately Gaussian as is shown by the nearly straight lines of figure 33-3 where cumulative frequency of echo strengths have been plotted against $\log_2$ echo strength on probability paper. Most of the distributions are nearly linear for at least 90 percent of the sample. Particularly good examples of Gaussian distributions are the Apollo 14 and Ranger IX areas (fig. 33-3(b)). Other site areas tend to be linear from the smallest values to higher values (near $1250\ m^{-2}$), above which positive departures from linearity occur (e.g., figs. 33-3(a) and 33-3(c)). Some of the distributions depart from linearity at both high and low
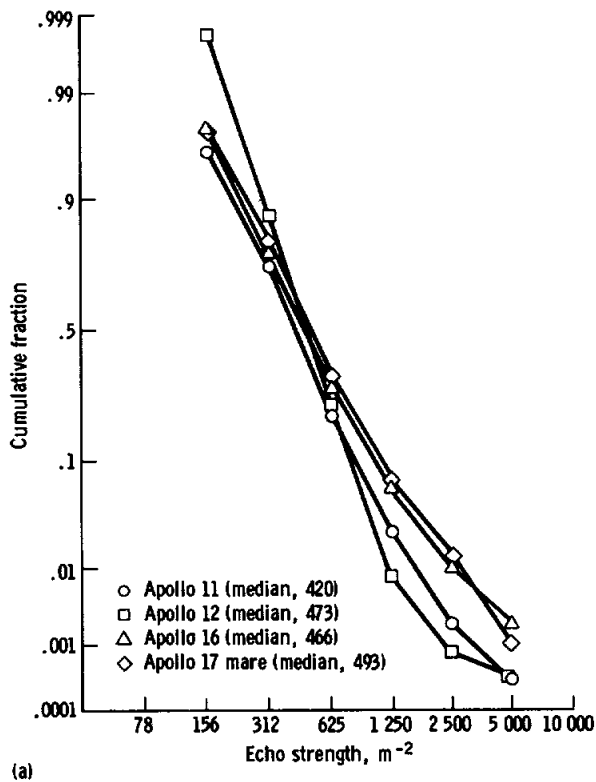
FIGURE 33-3.—Cumulative frequency distributions of depolarized radar echo strengths plotted on probability-log graphs. (See table 33-IV.) (a) Apollo 11, 12, and 16 areas and mare-dominated area west of Apollo 17 landing site. (b) Apollo 14 and 15, Surveyor I, and Ranger VII and IX areas. (c) Apollo 17 upland, Diophantus, Surveyor VII, and Flamsteed areas.
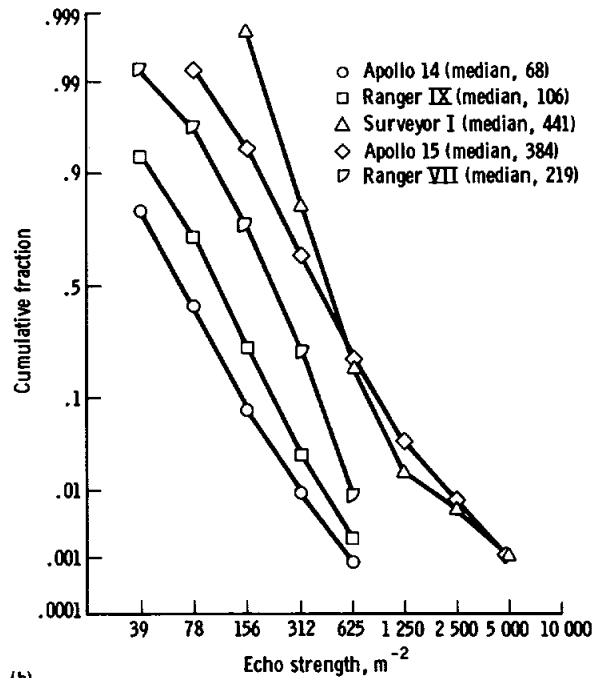
TABLE 33-IV.—*Cumulative Frequency Distributions of Depolarized Radar Echoes and Median Echoes of Apollo, Surveyor, and Ranger Sites*

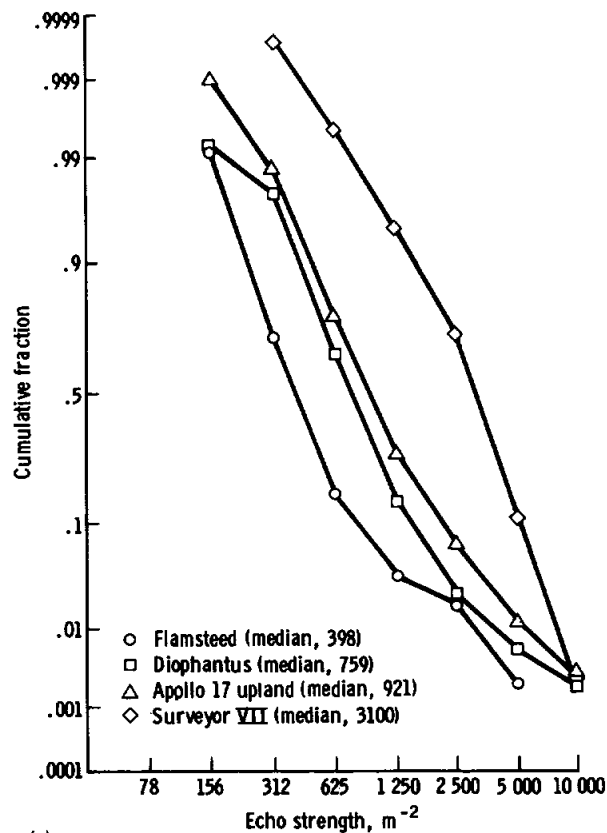| Parameter	Apollo 11, Ranger VIII, Surveyor V	Apollo 12, Surveyor III	Apollo 14	Apollo 15	Apollo 16	Apollo 17 mare	Apollo 17 upland	Surveyor I	Surveyor VII	Ranger VII	Ranger IX	Flamsteed Crater	Diophantus Crater
Echo strength, m^{-2} :													
0	—	—	1.0	—	—	—	—	—	—	1.0	1.0	—	—
39	—	—	.803	1.0	—	—	—	—	—	.993	.931	—	—
78	1.0	1.0	.413	.993	1.0	1.0	1.0	1.0	—	.965	.708	1.0	1.0
156	.958	.998	.079	.940	.974	.976	.999	.998	1.0	.761	.241	.999	.992
312	.730	.868	.009	.636	.768	.812	.987	.815	.9997	.223	.027	.710	.975
625	.197	.221	.0008	.197	.280	.323	.775	.169	.995	.008	.002	.158	.654
1 250	.023	.008	—	.038	.061	.065	.277	.016	.946	—	—	.031	.146
2 500	.001	.0008	—	.007	.010	.013	.054	.005	.719	—	—	.018	.023
5 000	.0003	.0003	—	.001	.002	.001	.012	.001	.112	—	—	.002	.006
10 000	—	—	—	.0002	—	—	.003	—	.002	—	—	—	.002
Number of values in sample	5840	3538	2440	4209	492	3512	4486	2756	3024	2251	—	456	5506
Median, exponential	380	410	65	360	420	440	850	380	2900	200	99	310	700
Median, Gaussian	420	473	68	384	466	493	921	441	3100	219	106	398	759
Approximate cent angle, deg	23	23	18	26	18	36	36	44	43	23	14	44	42
$+1\sigma$	684	684	124	718	863	915	1707	683	4540	346	179	625	1207
-1σ	251	332	35	213	272	291	562	303	1842	131	57	262	483
$(\log + \sigma) - (\log - \sigma)$	1.002	.723	1.265	1.215	1.155	1.146	1.111	.813	.902	.971	1.144	.869	.916

values of echo strength. For example, the Diophantus area departs positively above 1250 m^{-2} and negatively below 312 m^{-2} (fig. 33-3(c)). Both the Ranger VII and Surveyor VII areas depart negatively from linearity at high and low values (figs. 33-3(b) and 33-3(c)). Thus, one should consider the possibility that two or more populations of echo strength are present in the distributions.

Cumulative frequencies of echo strength plotted on log-log paper reveal the character of the distribution for large values of echo strength (fig. 33-4). In many cases, distributions of the largest echo strengths are nearly linear on log-log plots. The upland part of the Apollo 17 area is a good example (fig. 33-4(c)). Notable exceptions include the Surveyor I (fig. 33-4(b)) and Surveyor VII (fig. 33-4(c)) sites. Features responsible for the frequency distributions of large values of echo strength are discussed in the following paragraphs.
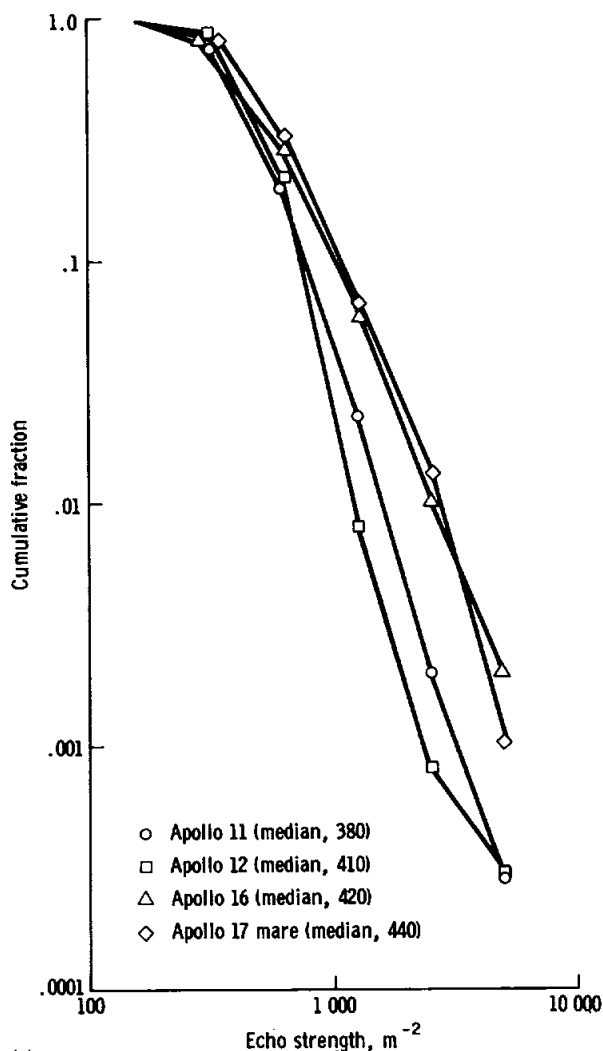
AREAL DISTRIBUTION OF ECHOES

Stronger echoes (> 1250 m^{-2}) can often be correlated with Earth-facing slopes larger than the resolution cell of the radar (≈ 2.0 km). Comparison of approximately 1:1 000 000 scale maps of depolarized radar echoes with photographs and lunar charts show that large values of echo strength are usually associated with. craters in mare areas and mountains, craters, and massifs in upland terrain. Some features, especially fresh craters, smaller than a resolution cell (≈ 2.0 km) also gave large echoes. Echo strengths larger than 625 m^{-2} are associated with the crater Moltke and its flanks, Moltke B, and Sabine E in the Apollo 11 (and Surveyor V, Ranger VIII) area. Values larger than 1250 m^{-2} are associated with the east or Earth-facing wall of Moltke. Depolarized echo maps of the Diophantus-Delisle area clearly show that slopes of crater walls facing the Earth (northwestern walls) have the largest echo strengths; those facing away have smaller echoes. Echoes from the northwestern wall of Diophantus exceed 10 000 m^{-2}, whereas the opposite wall has values less than 2500 m^{-2}. At sites near uplands, such as Apollo 15, echo strengths larger than 1250 m^{-2} are associated with Earth-facing slopes in the Montes Apenninus, while slopes facing the opposite directions have values of 625 m^{-2} and less. Thus, large-scale topography affects the magnitude of echo strength.

Comparison of the photographs and depolarized echo maps also indicates that these features produce the positive departures from linearity seen in figure 33-3. For Flamsteed, a small sample within the Surveyor I sample, all values in excess of 1250 m^{-2} are due to the west walls of Flamsteed, Flamsteed E, and a small crater 35 km north of Flamsteed E. Some, but not all, echoes above 625 m^{-2} are also associated with these craters. Similar correlations occur at other sites, so we conclude that the positive departures from linearity in the frequency distribution are caused by steep Earth-facing slopes.

Topographic features smaller than the resolution cell of the radar also affect echo strengths. This can be illustrated by South Ray Crater at the Apollo 16 landing site. Echo strengths near South Ray, which is approximately 680 m across, are large. Values of echo strength overlying South Ray are approximately 2060 m^{-2}; those approximately 2 km away from it are 1550 to 2690 m^{-2}. (The values used here are 10 times larger than those used in reference 33-24, which were purposely divided by 10 as a matter of convenience.) Because the resolution cells are near 2 km, roughness due to the crater, ejected blocks, and the hummocky flanks may contribute to the echo strength. Echo strengths between 990 and 1570 m^{-2} are associated with North Ray, a 1-km crater at the Apollo 16 site. For North Ray, it is likely that some of the echoes arise from the slopes of crater walls and west flanks of the craters that face the Earth, and some of the echoes arise from buried fragments. Similar results are found in the Diophantus area where craters smaller than 500 m with bright halos produce relatively large echoes. Thus, it seems likely that Earth-facing slopes at all scale lengths down to 0.5 cm substantially affect the radar echoes.

DETAILED CORRELATION OF ECHOES AT THE APOLLO 17 LANDING SITE

Correlations of depolarized radar echoes for the Apollo 17 landing site were made at scales near 1:1 000 000 and 1:250 000. Correlations at the smaller scale (fig. 33-5) yield the results described in the previous section. Large craters have strong echoes, especially on their Earth-facing (northeastern) walls. Examples include Vitrivius E, Littrow B, and the crater complex north of Littrow B. Earth-facing slopes in the highland region have large echo strengths, whereas those facing away are substantially

(a)

o Apollo 11 (median, 380)
□ Apollo 12 (median, 410)
△ Apollo 16 (median, 420)
◇ Apollo 17 mare (median, 440)

(b)

o Apollo 14 (median, 65)
□ Ranger IX (median, 99)
△ Surveyor I (median, 380)
◇ Apollo 15 (median, 360)
▽ Ranger VII (median, 200)

(c)

o Flamsteed (median, 310)
□ Diophantus (median, 700)
△ Apollo 17 upland (median, 850)
◇ Surveyor VII (median, 2900)

FIGURE 33-4.—Cumulative frequency distributions of de-polarized radar echo strengths plotted on log-log graphs. (See table 33-IV.) (a) Apollo 11, 12, and 16 areas and mare-dominated area west of Apollo 17 landing site. (b) Apollo 14 and 15, Surveyor I, and Ranger VII and IX areas. (c) Apollo 17 upland, Diophantus, Surveyor VII, and Flamsteed areas.
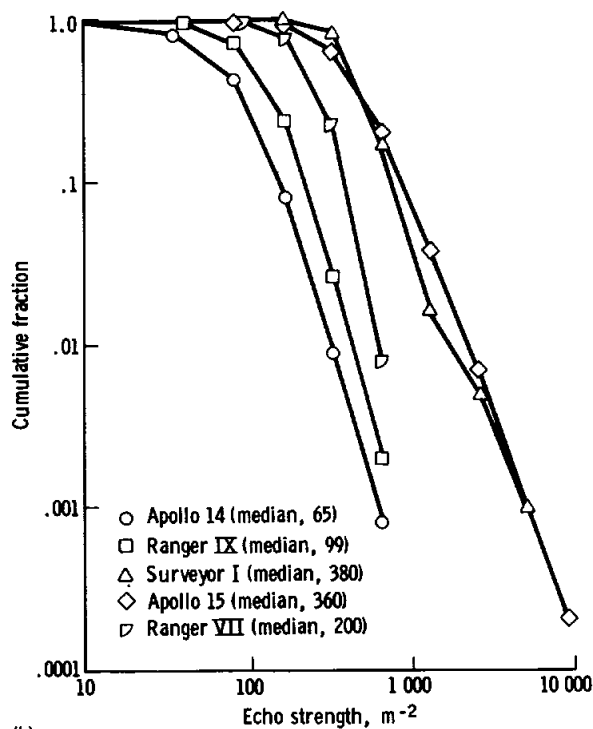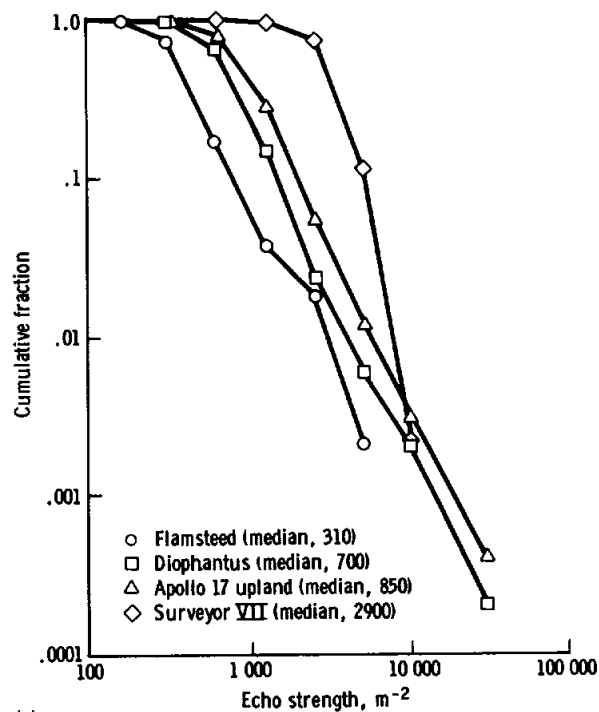
less. Figure 33-5(a) shows that echo strengths in the eastern part of the map area are generally larger than those in the western part. The magnitude of the difference is seen in the frequency distributions of echo strength for Apollo 17 upland (fig. 33-3(c)) that includes the uplands of figure 33-6(a) and additional uplands to the east and the frequency distributions of echo strengths for Apollo 17 mare (fig. 33-3(a)),
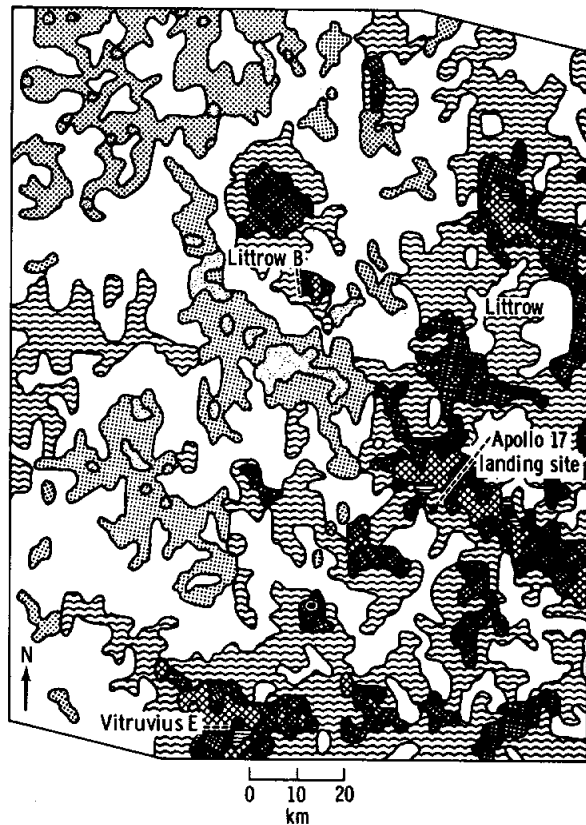
Values of echo strength, m^{-2}

● >10 000		625 to 1 250
5 000 to 10 000		312 to 625
2 500 to 5 000		156 to 312
1 250 to 2 500		<156

(a)

FIGURE 33-5.—Correlation of echoes to topography in the Taurus-Littrow area. (a) Generalized contour map of depolarized radar echoes in the Taurus-Littrow area near Apollo 17 landing site. (b) Topography of Taurus-Littrow area near Apollo 17 landing site (Apollo 15 metric camera frame AS15-0972). Area of photograph is same as that of part (a).

which includes the mare-dominated area of figure 33-5(a) and additional mare surfaces to the west and northwest. Here, roughness (fig. 33-5(b)) correlates with specific radar echoes as well as the frequency distributions.

Not all the echo strengths can be accounted for by large-scale slopes or surface roughness. The low values of echo strength just south of Littrow B (fig. 33-5) contrast with the higher ones to the west, but no similar contrast in surface roughness is evident. Additionally, echoes from some low hills in the southwestern corner of the area of figure 33-6 are not particularly large. Here, small-scale roughness or blocks smaller than photographic resolution may be responsible for the differences in echo strength for the surfaces.

Details of the Apollo 17 landing site further illustrate the influence of surface topography on

depolarized radar echoes. The Apollo 17 lunar module (LM) landed on a mare regolith in a valley surrounded by hills rising some 2450 m above the valley floor. North of the LM (fig. 33-6), the North Massif rises some 2000 m above the valley floor and slopes are as large as 25°. Here, and for similarly oriented Earth-facing steep slopes, values of echo strengths exceed 4000 m^{-2} and are as large as 9670 m^{-2} (fig. 33-6(a)). In contrast, the steep slopes (> 25°) of the South Massif to the southwest of the LM face away from the Earth, and depolarized echo strengths range between 314 and 900 m^{-2}. In this case, it is difficult to attribute the differences in the echoes to anything but slopes because the crewmen reported that rock outcrops were present high on both slopes and, in both cases, boulders from the outcrops were present on and at the bases of the slopes.
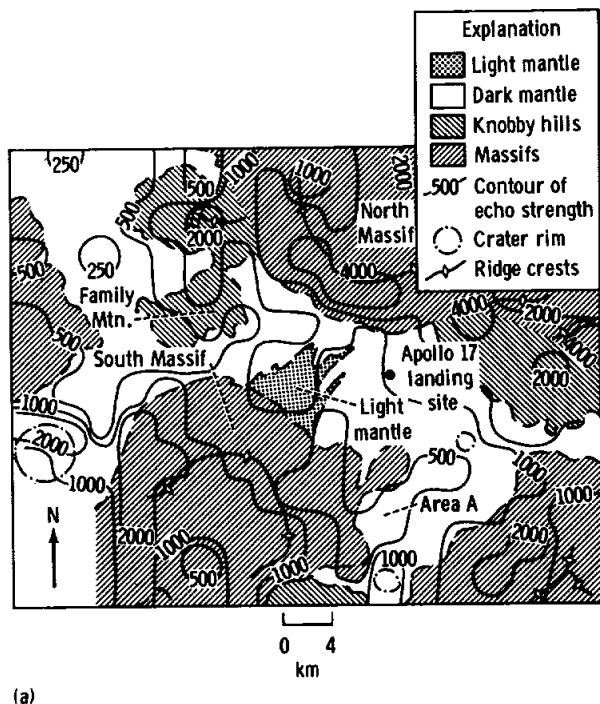
FIGURE 33-6.—Correlation of echoes to topography of the Apollo 17 landing site. (a) Contour map of depolarized radar echoes at the Apollo 17 landing site. (b) Photographic mosaic of Apollo 17 landing site (Apollo 17 panoramic camera frames AS17-2309, 2311, 2312, and 2314).

The regolith of the valley floor near the LM had echo strengths from 564 to 1103 m^{-2}, which are somewhat larger than the median values for mare areas (table 33-IV). Echo strengths decrease from the LM area toward the southwest where there are few large craters. Some of the lower echo values (505 to 589 m^{-2}) were from the eastern part of the light mantle. The difference correlates well with the observations of the LM pilot who reported that 3 to 5 percent of the surface was covered by 1-cm and larger-size fragments near the LM area and 1 percent of the surface was covered by 1-cm and larger-size fragments near and on the light mantle. The panoramic camera photographs also show (fig. 33-6(b)) that there are more large steep-walled craters near the LM than on the eastern edge of the light mantle. The lowest echo strengths are found where large craters are absent, rare, or subdued by mantling; as near the southeastern edge of the light mantle, just south of Family Mountain, northwest of Family Mountain, and area A (fig. 33-6(a)).
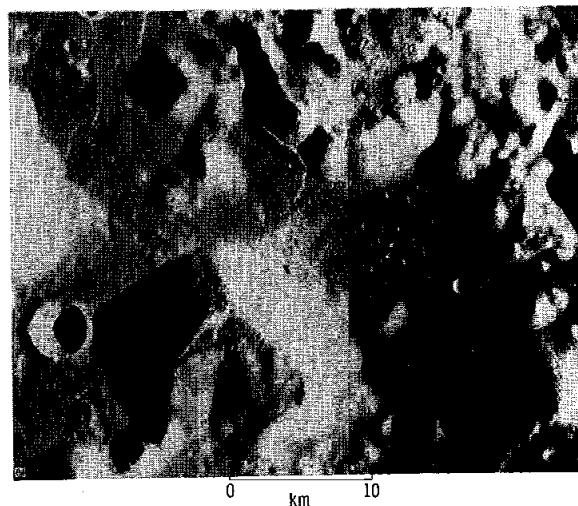
In contrast to some premission inferences, the large depolarized echoes near the light mantle do not correlate with the light mantle. There are two lines of evidence for this: (1) the large echoes are displaced westward of the light mantle and include mare surfaces west of it, and (2) the large echoes span the valley from the base of the South Massif to the base of the North Massif whereas the light mantle does not (fig. 33-6(a)). The orbital photographs suggest that the large echo values are caused by a concentration of craters up to several hundred meters across that form a band along the western part of the light mantle and adjacent mare and extend beyond the mantle to the base of the North Massif.

Comparison between echoes at the Apollo 16 landing site and Apollo 17 landing site supports the postulate that factors other than small fragments and blocks produce differences in depolarized radar echoes. For the Apollo 16 landing site, the echo was 530 m^{-2} or approximately one-half the value of 1103 m^{-2} at the Apollo 17 landing site. Although precise data are not at hand, it is our impression that the number of blocks and fragments in the immediate vicinity of the Apollo 17 landing site was no larger than the number in the immediate vicinity of the Apollo 16 landing site.

CONCLUSIONS

Topography appears to be an important factor in controlling the amplitude of depolarized echoes. This is particularly evident at the Apollo 17 landing site

where echoes from the Earth-facing slopes of the North Massif are substantially larger than those from opposing slopes on the South Massif; also, in the region of the light mantle, the relatively large values of echo strength correlate with craters up to several hundred meters across—rather than with the mantle itself.

The cumulative frequency distributions of the depolarized echoes are, in some respects, similar to slope-frequency distributions obtained for mare and upland surfaces. Thus, the contribution of topography must be examined in more detail.

The extent to which contributions of the four variables (mentioned in the introduction) to the radar echo can be distinguished remains to be seen. Perhaps a suitable test to assess the role of topography on depolarized radar echoes will be to compare the echoes with the rms slopes obtained by the bistatic-radar experiment on the Apollo 14, 15, and 16 missions.

PART C

COMPARISON BETWEEN PHOTOGRAMMETRIC AND BISTATIC-RADAR SLOPE-FREQUENCY DISTRIBUTIONS

H. J. Moore[a] *and G. L. Tyler*[b]

Stereoscopic photographs taken by the metric and panoramic cameras can be used to obtain information on the roughness and slope-frequency distributions of lunar surfaces (see appendix to this part). Bistatic radar on board Apollo 14, 15, and 16 spacecraft may also be used to obtain information on lunar surface roughness at two wavelengths—13 cm (S-band) and 116 cm (VHF).

This section will briefly compare the results for lunar surface roughness estimates and slope-frequency distributions obtained by using photogrammetric techniques with those obtained by using bistatic radar. Three topics will be discussed: (1) the form of the slope-frequency distributions, (2) the change of roughness estimates of the lunar surface with scale, and (3) the magnitude of surface roughness.

PHOTOGRAMMETRIC RESULTS

Method

The following results were obtained by using stereoscopic pairs of metric and panoramic positive transparencies (table 33-V) in an analytical stereo-plotter. Stereomodels were leveled and scaled from ancillary data derived from orbital support data.[2] To calculate slopes, three elevation measurements were averaged for points separated by a horizontal fixed interval. This fixed horizontal interval will be referred to as slope length ΔL in the following discussion. Approximately 500 to 600 slopes were determined for each slope-frequency distribution. Slope-frequency distributions with 25-m slope length are corrected for reading errors as outlined in the appendix. Slope-frequency distributions for larger slope lengths do not require this correction. Two statistical descriptors are used, mean absolute slope and algebraic standard deviation. Mean absolute slope is the average of the absolute slope angle values. Algebraic standard deviation is estimated from the cumulative absolute slope-frequency distribution and taken as the slope corresponding to a cumulative fraction of 0.32 ($\approx$ 31.74 percent) for slope lengths of 25 m. For larger slope lengths, mean absolute slopes and algebraic standard deviations are calculated by use of the U.S. Geological Survey terrain-analysis computer program.

---

[a]U.S. Geological Survey.
[b]Stanford University.

---

[2] Apollo photographic evaluation is on microfilm at the Mapping Sciences Branch, NASA Lyndon B. Johnson Space Center.

TABLE 33-V.—*Algebraic Standard Deviations and Mean Absolute Slopes from Photogrammetric Techniques for Various Lunar Terrains*

Terrain type	Algebraic standard deviation, deg						Mean absolute slope, deg						Frame no.
	ΔL 25 m	ΔL 50 m	ΔL 100 m	ΔL 200 m	ΔL 500 m	ΔL 1000 m	ΔL 25 m	ΔL 50 m	ΔL 100 m	ΔL 200 m	ΔL 500 m	ΔL 1000 m	
Mare Serenitatis	5.8	4.8	3.4	2.3	1.4	1.2	4.7	3.7	2.5	1.7	1.3	1.2	[a] AS15-9560 and 9565
Mare Serenitatis	6.1	4.9	3.6	2.5	1.3	.8	4.8	3.8	2.8	1.8	1.0	.7	[a] AS15-9562 and 9567
Cayley Plain	6.2	6.3	5.6	4.9	3.4	1.5	5.4	4.5	3.8	3.2	2.3	2.0	[a] AS16-4558 and 4563
Uplands, near Proclus	6.4	6.0	5.0	4.3	3.2	2.2	5.4	4.6	3.9	3.3	2.6	2.1	[a] AS15-9508 and 9513
Uplands, north of Vitruvius	7.8	6.6	5.9	5.5	5.2	4.7	6.2	5.5	5.1	4.9	4.7	4.3	[a] AS15-9550 and 9555
Uplands, near Glaisher	9.9	8.8	8.2	7.8	7.3	6.7	8.4	7.9	7.5	7.3	6.9	6.4	[a] AS15-9484 and 9489
Mare Fecunditatis	–	–	–	–	3.6	2.6	–	–	–	–	3.1	2.0	[b] AS16-2931 and 2932
Uplands, near Censorinus	–	–	–	–	10.5	9.2	–	–	–	–	7.8	6.3	[b] AS16-2167 and 2168
Littrow, landing site	4.5	–	–	–	–	–	3.8	–	–	–	–	–	[a] AS17-2750 and 2755
Littrow, west of landing site	4.6	–	–	–	–	–	3.9	–	–	–	–	–	[a] AS17-2750 and 2755
Hadley, landing site	6.8	–	–	–	–	–	5.7	–	–	–	–	–	[a] AS15-9509 and 9514

[a] Apollo panoramic camera photograph.
[b] Apollo metric camera photograph.

Slope-Frequency Distributions

Slope-frequency distributions of lunar surfaces are a function of terrain type and slope length. For mare surfaces, the absolute slope-frequency distributions (cumulative and incremental) are neither exponential nor Gaussian. However, a large part of the distributions approach an exponential form (fig. 33-7). The logarithm of cumulative frequencies plotted against absolute slopes tends to be linear for the first 90 percent or more of the sample. This approximation holds for distributions with slope lengths ΔL of 25 to 500 m. Cumulative frequency distributions for the Cayley Plains at the Apollo 16 landing site (ref. 33-25) are similar to maria distributions and show a tendency for linearity (fig. 33-8). Inspection of the incremental form of the distribution for 25.1-m slope length (fig. 33-8(a)) shows the steps between 4° and 10° are parallel to the cumulative curve, while a small mode occurs at 13.5°. The frequency of slope angles between 0° and 1° is larger than expected on the basis of the adjacent steps but consistent with overall trends. For the incremental form of the Apollo 16 distribution at 201-m slope length (fig. 33-8(b)), the steps decrease uniformly from 0° to 6° and the tail of the cumulative curve above 7° is the result of large craters at the site.

Knobby and cratered upland terrain slope-frequency distributions depart markedly from those of the maria and Cayley Plains. For the uplands north of Vitruvius, the logarithm of cumulative frequencies plotted against slope forms convex upward curves (fig. 33-9). On the basis of other observations, it is believed that this area is typical of upland terrain. The incremental forms of the distributions have two or more modes. At 25.2-m slope length, a mode occurs at 6.5°. This mode is almost as large as the mode near 0.5°. At the larger slope length (fig. 33-9(b)), frequencies of a mode near 4.5° exceed the frequencies near 0.5° and 1.5°. These modes can be related to topography seen in Apollo metric and panoramic camera photographs, which show large hills and undulations. In other areas, crater clusters can cause similar slope-frequency distributions.

Few, if any, of the slope-frequency distributions are normal (Gaussian). The curvature of a normal distribution is larger than the distributions here—particularly those of the maria. Thus, many lunar slope-frequency distributions have tails at large slope angles.
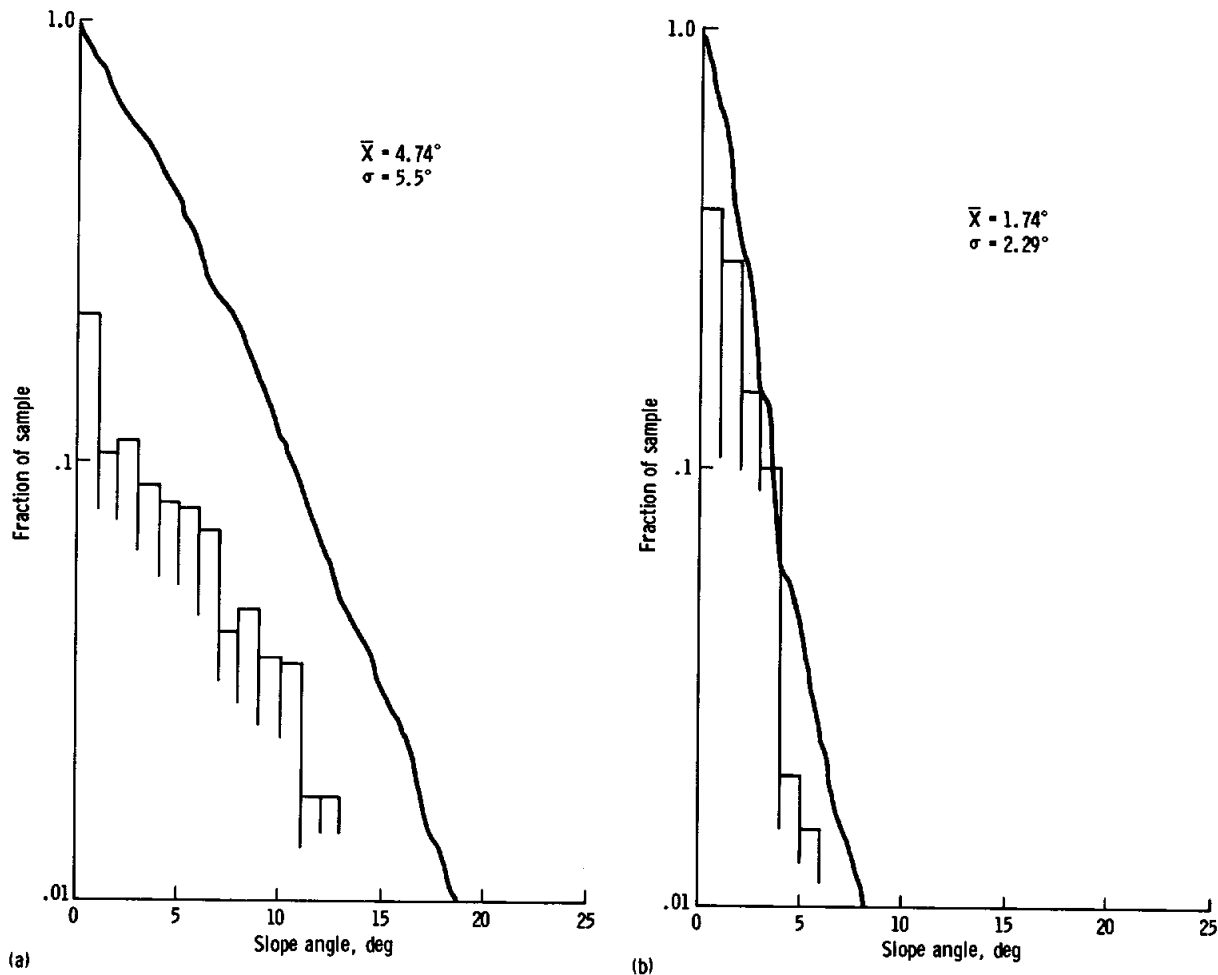
FIGURE 33-7.—Frequency distribution of absolute slope values for surface in Mare Serenitatis. Bars represent fraction of sample contained in 1° increments of slope angle. Solid lines indicate cumulative fraction of sample with absolute slopes larger than angle indicated. The quantity $\bar{X}$ is mean absolute slope and σ is algebraic standard deviation of distribution. (a) Slope length ΔL 25 m. (b) Slope length ΔL 200 m.

Slope Length

Mean absolute slopes and algebraic standard deviations depend on slope length and lunar terrain type. For mare areas, both mean absolute slopes and algebraic standard deviations vary rapidly with slope length over the interval of 25 to 500 m (fig. 33-10) and, for the Cayley area, the change is less. Upland surfaces show the least dependence between slope length and mean absolute slopes and algebraic standard deviations.

Reasons for this variation are evident in both the Apollo 17 photographs and the slope-frequency distributions. The uplands are characterized by large undulations, hills, and craters so that the surfaces are initially rough; and, because of the mechanical behavior of the nearly cohesionless regolith, it is difficult to increase surface roughness at smaller slope lengths. Thus, there is probably a limiting roughness for lunar surfaces until a size range is reached where blocks, fragments, clods, and grains dominate the topography.

Magnitude

Algebraic standard deviations and mean absolute slopes for the slope-frequency distributions are a
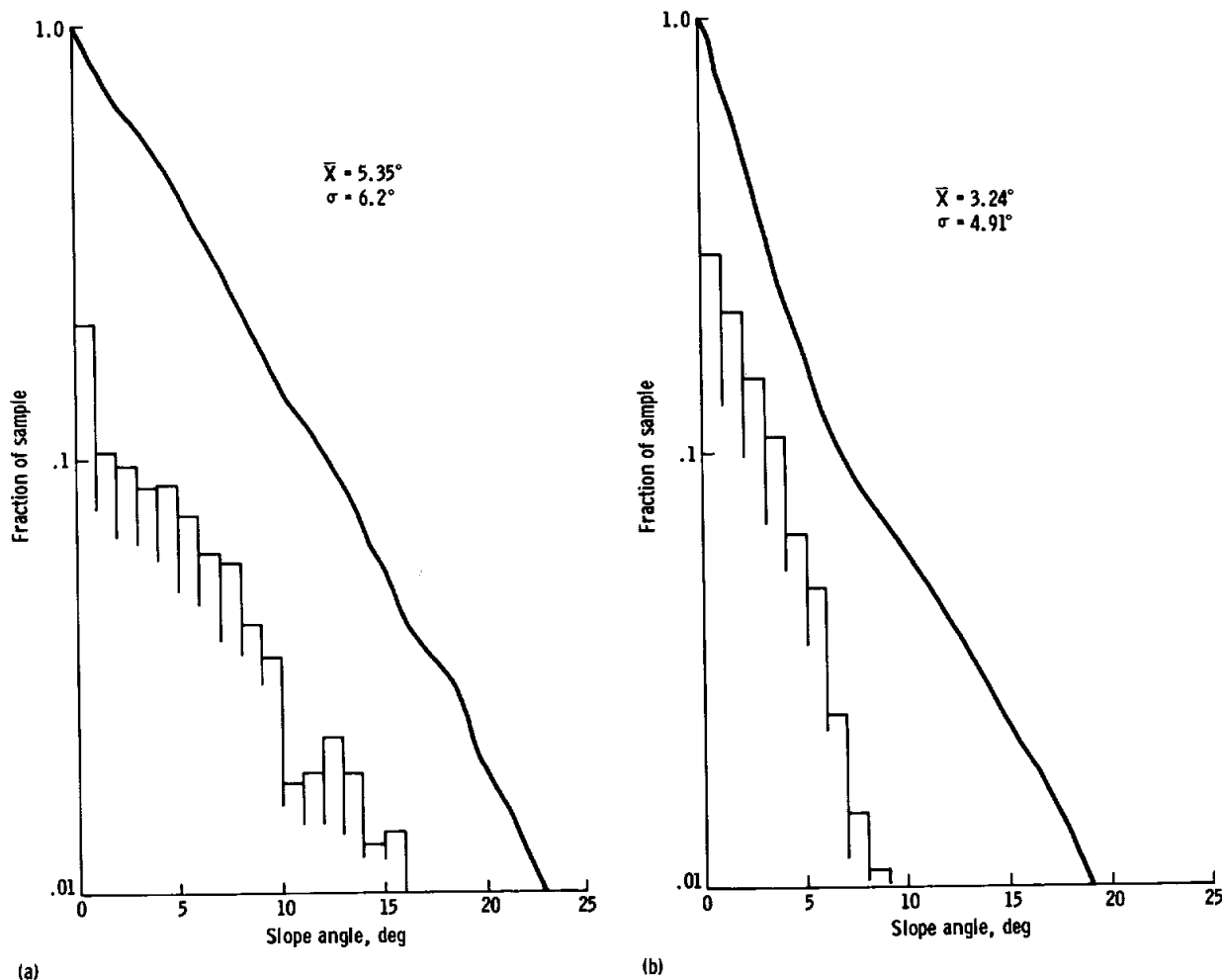
FIGURE 33-8.—Frequency distributions of absolute slope values for Cayley Plain at the Apollo 16 landing site. Bars represent fraction of sample for 1° increments of slope angle. Solid lines indicate cumulative fraction of sample with absolute slopes larger than angle indicated. The quantity $\bar{X}$ is mean absolute slope and σ is algebraic standard deviation. (a) Slope length ΔL 25.1 m. (b) Slope length ΔL 201 m.

function of terrain type and slope length. These are summarized for 10 sites in table 33-V, which shows algebraic standard deviations and mean absolute slopes for slope lengths of 25 to 1000 m.

From current data at a slope length of 25 m, algebraic standard deviations—which are equivalent to rms slopes of the bistatic radar—are near 4.5° to 6.0° for the mare areas. The Apollo 15 site (Hadley region) is an exception to this, and the algebraic standard deviation is 6.8° at a 25-m slope length. Slope-frequency distributions suggest this anomaly is due to undulations in the topography. The Cayley Plains at 25-m slope length are similar to the mare surfaces in magnitude (table 33-V). Uplands are

typically rougher than the maria and Cayley, and algebraic standard deviations are 6.4° to 9.9° for slope lengths near 25 m.

Larger differences are found between the maria, Cayley Plains, and uplands at larger slope lengths. At 200-m slope lengths, algebraic standard deviations for the mare areas are 2.5° and less, that for the Cayley Plains is 4.9°, and those for the uplands are 4.3° and larger.

Data based on metric photography (table 33-V) suggest a possible problem. The algebraic standard deviation for Mare Fecunditatis at 500-m slope length is 3.6° and that for the Censorinus upland is near 10.5°. These values are plotted in figure 33-10. Mare
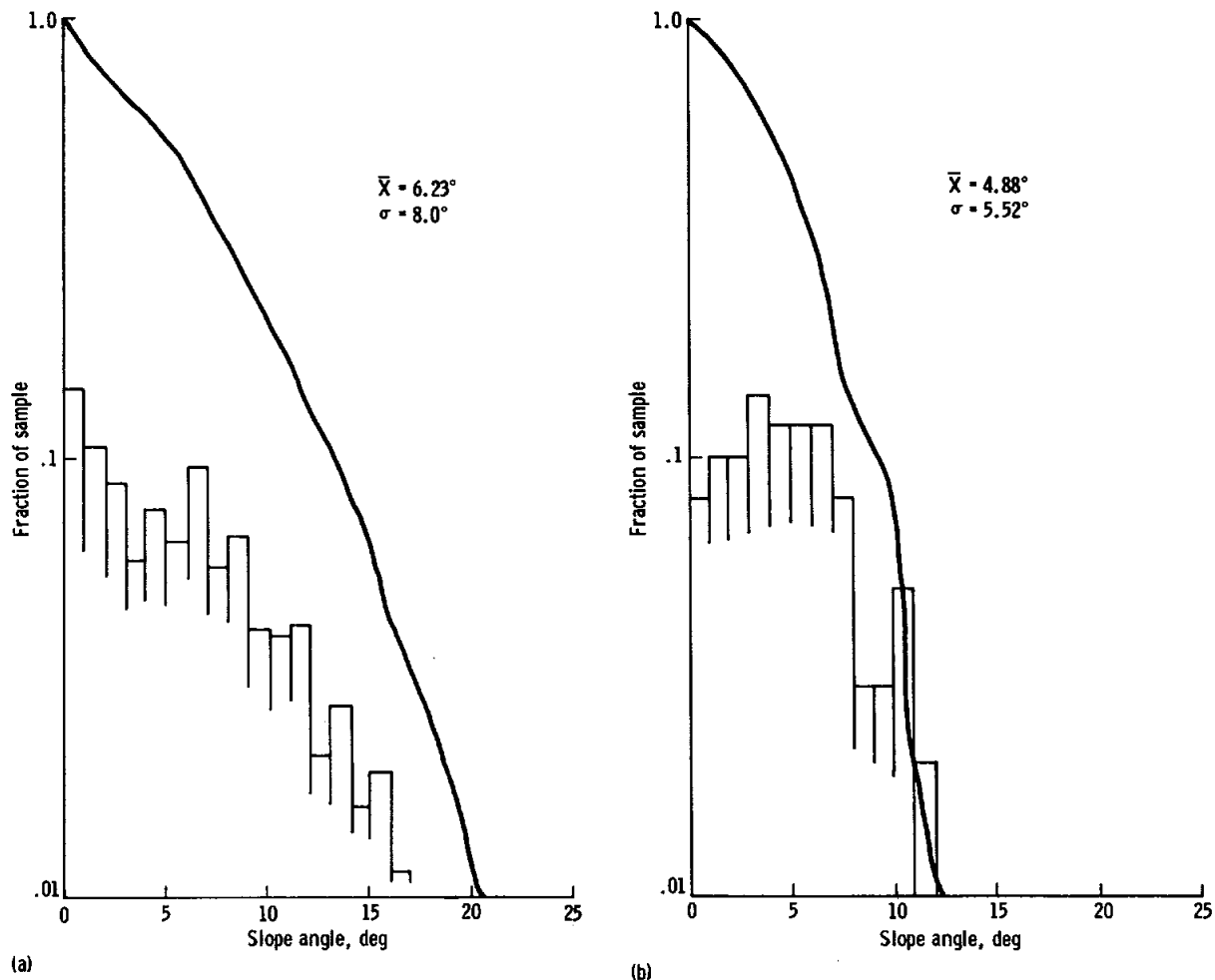
FIGURE 33-9.—Frequency distribution of absolute slope values for upland surface north of Vitruvius. Bars represent fraction of sample for 1° increments of slope angles. Solid lines indicate cumulative fraction of sample with absolute slopes larger than angle indicated. The quantity X is the mean absolute slope and σ is algebraic standard deviation of distribution. (a) Slope length ΔL 25.2 m. (b) Slope length ΔL 201 m.

Fecunditatis is either rougher than the Mare Serenitatis areas sampled or, alternatively, the differences are related to the local areas sampled. A similar conclusion is reached when comparing Censorinus values and other uplands. This problem is not resolved at this time.

RADAR RESULTS

Method

The radar data discussed here were obtained from the bistatic-radar experiments on Apollo 15 and 16 (refs. 33-16 and 33-26). Radio-frequency transmissions from the orbiting command and service module were received on Earth after reflection from the lunar surface. Two wavelengths were used simultaneously, 13 cm and 116 cm (2287.5 MHz and 259.7 MHz). Because scattering from the lunar surface is wavelength dependent, the data provide a sampling of lunar surface properties on two different scales. At the present time, this wavelength dependence is understood only in a general way. One considers the radar data as reflecting a fictitious surface that is a smoothed version of the actual lunar surface. In the case of the 13-cm data, the smoothing function eliminates components of the lunar surface with a frequency greater than approximately 0.5 cycles/m; for the 116-cm data, the corresponding frequency is
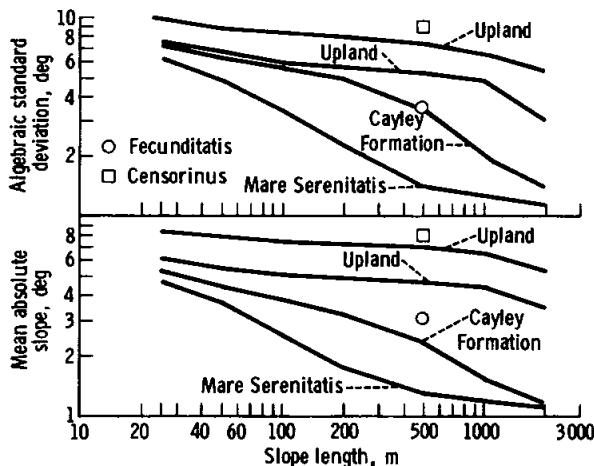
FIGURE 33-10.—Comparison between algebraic standard
deviation and mean absolute slopes for lunar slope-fre-
quency distributions.

approximately 5.0 cycles/m. The precise form of the
smoothing function is unknown and probably surface
dependent. A much more thorough discussion of this
point may be found elsewhere (ref. 33-17). Simulta-
neous 13- and 116-cm data are given for the Apollo
15 experiment only. Simultaneous data were ob-
tained with the Apollo 16 experiment, but, in that
case, the 116-cm data lacked sufficient signal-to-noise
ratio for the processing required to determine slope-
distribution functions.

Lunar slope-frequency distributions may be in-
ferred directly from the bistatic-radar data. The
method is based upon a geometric optics model of
the scattering and a previously developed inversion
technique (refs. 33-27 to 33-29). Earlier comparisons
of lunar rms slopes obtained using photographic
techniques with those obtained from the radar have
given good results (ref. 33-30).

For a particular location, the data are averaged
along the bistatic-radar track on the lunar surface. In
all cases, this track trends along a nearly east-west
direction for a distance of up to 2° lunar longitude.
In latitude, the extent of the averaging area is
determined by lunar surface roughness. For the
present data, this extent varies between approxi-
mately 0.5° and 1.0°. The data are uncorrected for
the spacecraft antenna pattern. In general, as a result
of this effect, one may anticipate a slight suppression
of the slope distribution for slopes greater than
approximately 15°. To facilitate comparisons, all data

have been normalized by the maximum of their
distribution functions.

Slope Distributions

The frequency distributions given here are pre-
sented in their incremental form; that is, each figure
presents the frequency with which a slope in a
particular range occurs with respect to all the slopes
in a total sample area. Slope increments are given in
1° steps. These curves differ from those obtained
photogrammetrically in that the radar method counts
slopes at a given point according to the steepest slope
at that point, whereas the photogrammetric tech-
nique yields unidirectional slopes. The photogram-
metric slopes correspond to the slopes that would be
encountered while walking in a straight line across the
same surface.

Figure 33-11 presents a slope-frequency distri-
bution derived from 13-cm data in a region mapped
geologically as predominantly Cayley Formation. The
distribution has an apparent exponential form and
shows the existence of significant slopes at slope
angles greater than 15°. As mentioned previously,
these data apply to a smoothed version of the lunar
surface from which surface frequency components
with periods shorter than approximately 0.5 m have
been removed. The apparent slight modality in the
data may not be real. These data are quite similar to
distributions obtained from the floor of Ptolemaeus.
The Ptolemaeus floor apparently has fewer slopes
greater than approximately 8°.

Figure 33-12 gives distributions inferred from 13-
and 116-cm data for a region near Vitruvius. The two
distributions are quite distinct; this region appears
much smoother on the set of scales associated with
the 116-cm wavelength than on the set of scales
associated with the 13-cm wavelength. In our data
thus far, this is an anomalous highland result. It has
been a general observation that 13- and 116-cm slopes
in highland areas show much less marked wavelength
dependence (refs. 33-17 and 33-29).

Figure 33-13 gives bistatic-radar results for a
region in central Mare Serenitatis. Both distributions
closely resemble Gaussians for low values of slope
length but depart from the normal distribution for
values of slope greater than approximately 1½ to 2
standard deviations. The elevated tails of this distribu-
tion with respect to the Gaussian are a general feature
of maria distributions observed thus far.

Slope Length

No single surface scale may be assigned to the radar data, nor is there a quantitatively well-known relationship between surface slope and radar wavelength. Slope data inferred from bistatic-radar observations correspond to a weighted average over all slopes with lengths greater than some minimum value. This weighting is also thought to vary weakly with slope. For the data here, the minimum slope lengths that will affect the data are estimated to be approximately 0.2 and 2.0 m for the 13- and 116-cm data, respectively. The scale length of slopes of maximum importance in the weighting is estimated to be greater than 10 to 100 wavelengths. For both wavelengths, slopes longer than about 500 m are unimportant. Within a slope distribution, higher slopes are expected to correspond to slightly shorter scales.

Previous comparisons of bistatic-radar data with slopes obtained from photogrammetry and photoclinometry (ref. 33-30) indicate that the bistatic-radar data correspond to a surface sampling scale of approximately 230 wavelengths. This result is based upon observations at 220-cm wavelength made with the lunar Explorer 35 spacecraft. If this result scales with wavelength, then the corresponding values of surface sample length for the 13- and 116-cm data are 30 and 270 m, respectively. These values must be interpreted as an approximate mean for the bistatic-radar slope length weighting function.

A striking feature of the bistatic-radar data is the similarity of the 13- and 116-cm results for slope distributions and rms slopes in the lunar highlands. This result can be understood in terms of surfaces that contain no significant roughness component on scales less than a few times the longer wavelength. In maria, a strong wavelength dependency is observed. Thus, the radar results are generally consistent with the photogrammetric results in which only a weak dependence on slope length is observed in highlands areas, but for which much stronger dependencies exist in maria areas (cf. fig. 33-10).

Magnitude

The magnitude of lunar rms algebraic slopes inferred from bistatic radar is also a strong function of lunar terrain type and slope lengths. Lunar rms slopes are obtained directly from normalized measures of the bistatic-radar echo bandwidth. The rms
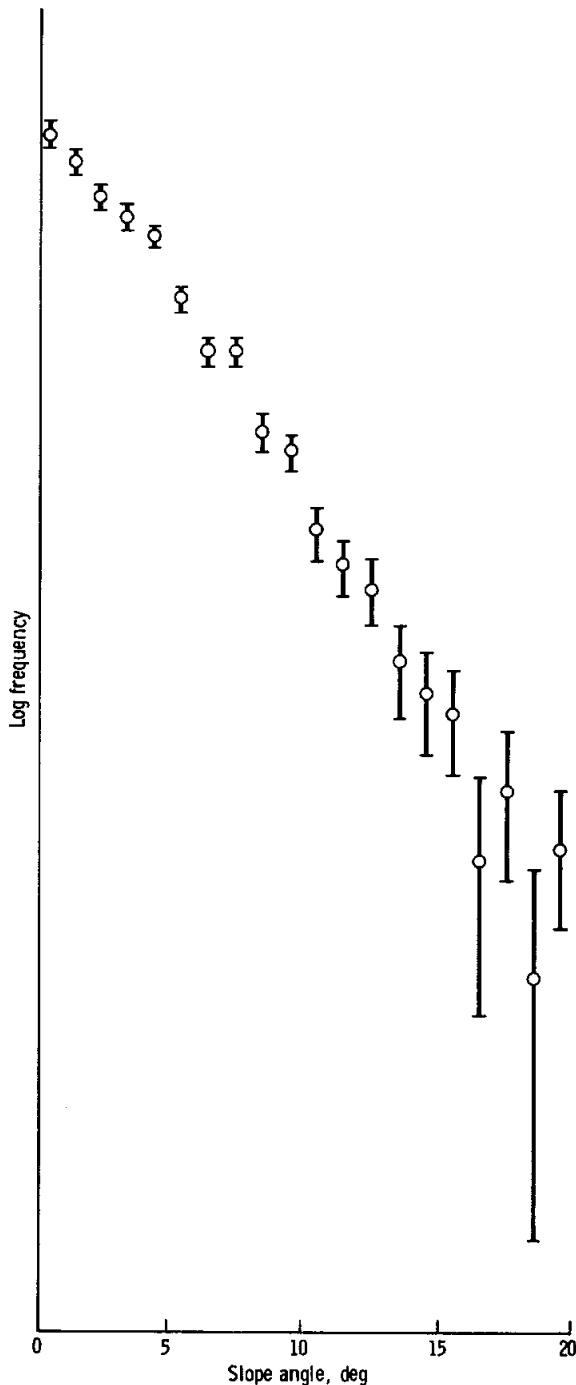

FIGURE 33-11.—Incremental slope-frequency distribution derived from 13-cm bistatic-radar data in a region mapped as predominantly Cayley Formation (lat. 8.1° S, long 10° E).

FIGURE 33-12.—Incremental slope-frequency distributions inferred from 13- and 116-cm bistatic-radar data for a region near Vitruvius. (a) 13-cm data (lat. 18.9° N, long. 31.5° E). (b) 116-cm data (lat. 19° N, long. 31.5° E).
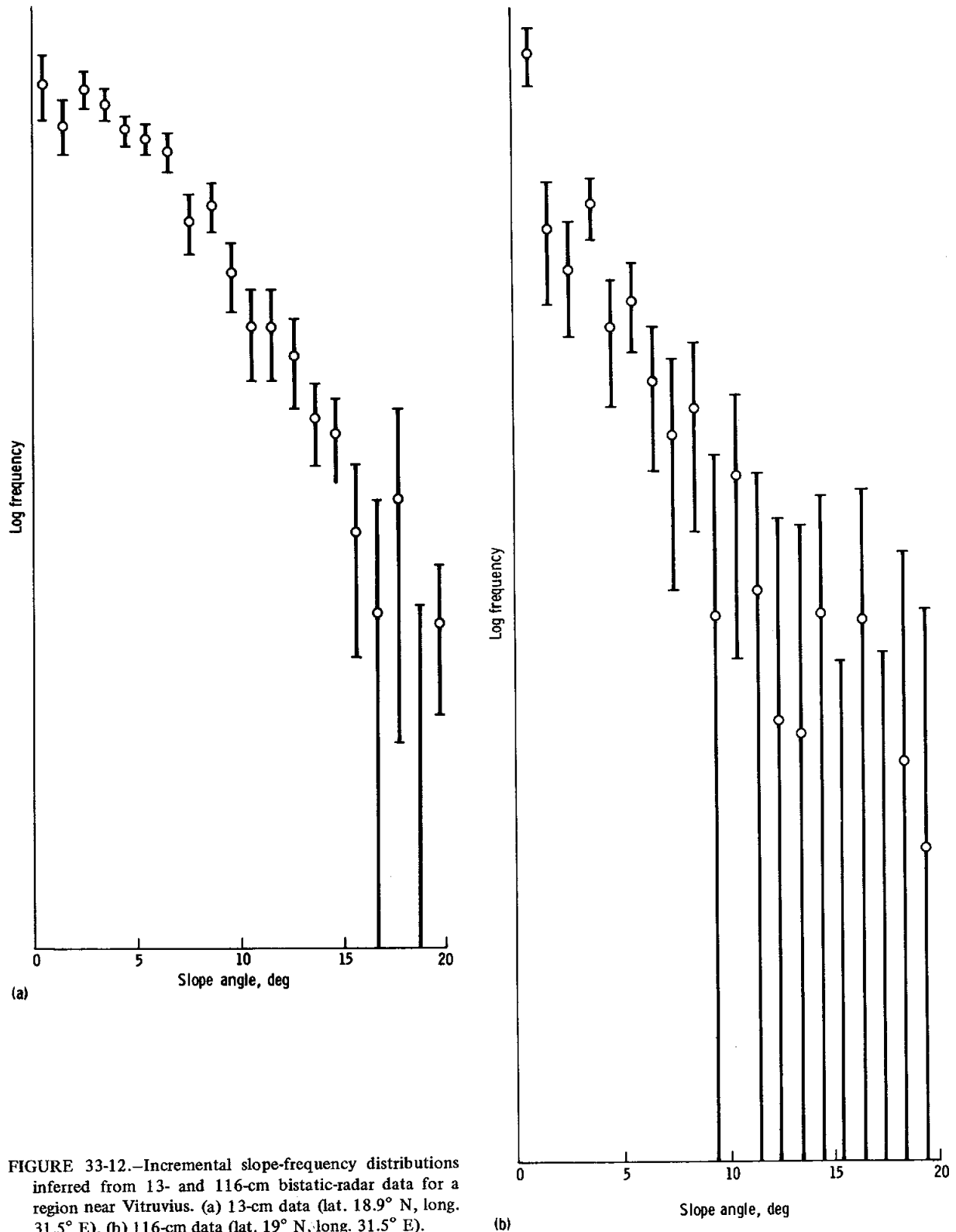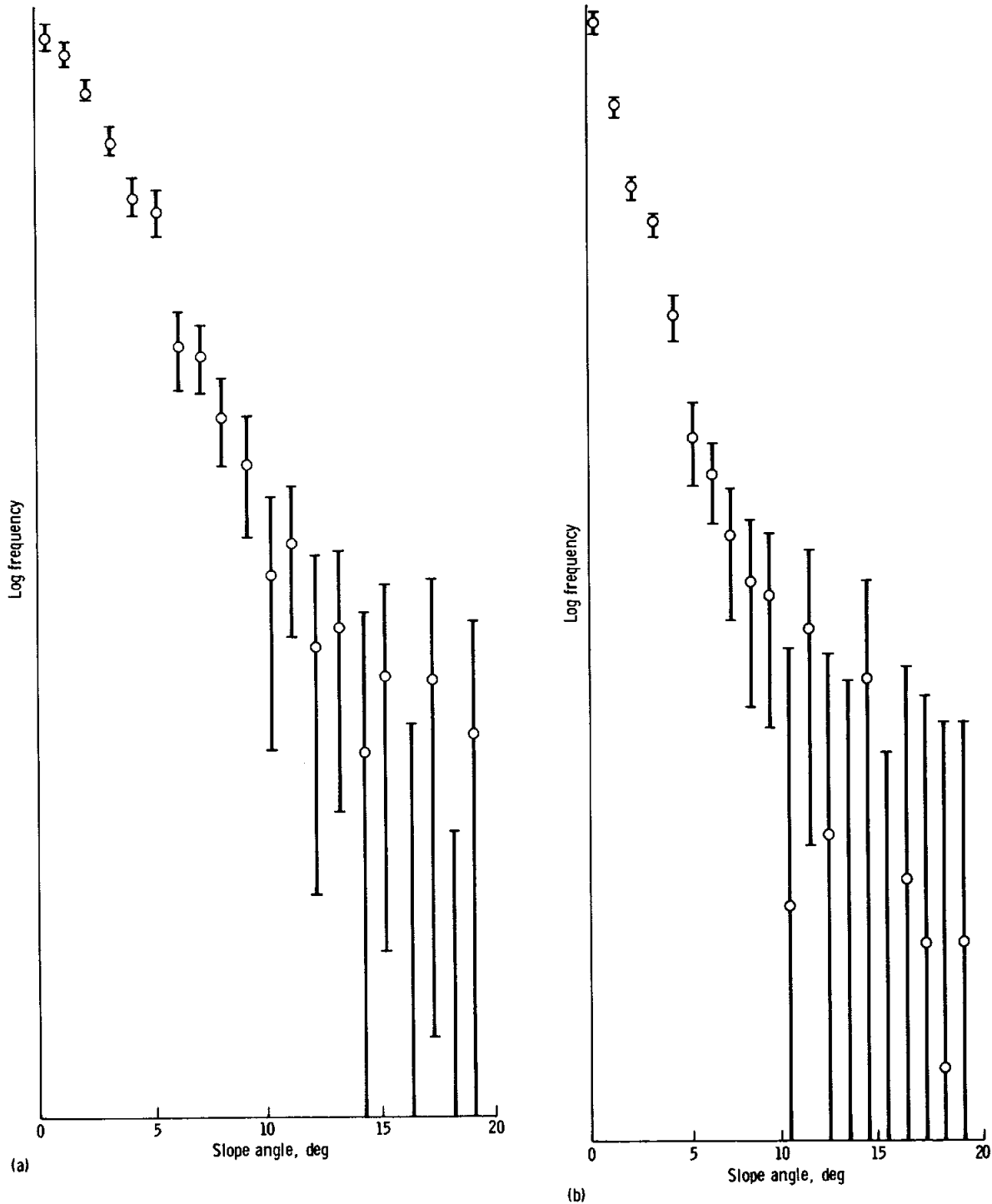
(a)

(b)

FIGURE 33-13.—Incremental slope-frequency distributions
inferred from 13- and 116-cm bistatic-radar data for a
region in central Mare Serenitatis. (a) 13-cm data (lat.
20.1° N, long. 27.2° E). (b) 116-cm data (lat. 20.2° N,
long. 26.9° E).

slopes have been obtained at both 13 and 116 cm for a wide variety of lunar terrain. Within the highlands, the rms slopes obtained at the two wavelengths are nearly equal and vary between tan 6° and tan 8°. Within maria units, rms slopes inferred from the 116-cm data vary between tan 1° and tan 2°; maria rms slopes at 13 cm are in the range tan 2° to tan 4°. At the same location, the slopes obtained within maria at 116-cm wavelength are typically one-half as large as those obtained at 13 cm. On the basis of the smoothed surface model for the bistatic-radar echo (ref. 33-31), we conclude that on a 0.2- to 2-m surface scale, within maria, the maria are rougher than the highlands, although overall on larger scales the opposite is the case. A more complete discussion of this point may be found in references 33-16 and 33-17.

CONCLUSIONS

The data presented here provide examples of lunar slope-frequency distributions obtained by two completely independent methods. The results are similar in that certain features are observed with both techniques.

1. Lunar slope distributions may be either modal or well behaved; for example, approximately exponential or Gaussian.

2. The slope-frequency distributions are more peaked than the Gaussian distribution with the same rms slope. Stated another way, the distributions have elevated tails with respect to best-fit Gaussians where the fit is restricted to the low slope values.

3. The distribution functions are highly dependent upon slope length. In the maria, this dependency can be quite strong; in highland regions, this dependency is somewhat weaker.

Interpretations of slope-frequency distributions may provide strong constraints upon models of lunar surface evolution.

ACKNOWLEDGMENTS

APPENDIX TO PART C

EFFECT OF PHOTOGRAMMETRIC READING ERROR ON SLOPE-FREQUENCY DISTRIBUTIONS

H. J. Moore[a] *and Sherman S. C. Wu*[a]

Lunar slope-frequency distributions obtained by photogrammetric techniques are compared with results from the bistatic-radar investigations of the Apollo 14, 15, and 16 missions (refs. 33-16, 33-17, and 33-32) and of Explorer 35 (ref. 33-27). Algebraic standard deviations of slope-frequency distributions from photogrammetric data are equivalent to rms

slopes of slope-frequency distributions from bistatic-radar data. Photogrammetrically derived algebraic standard deviations of the distributions are often larger than those obtained by the radar (ref. 33-25) when photogrammetric results at 25-, 200-, and 500-m slope lengths are compared with rms slope estimates from Apollo S-band (13-cm wavelength), Apollo VHF (1.16-m wavelength), and Explorer 35 (2.2-m wavelength) radar. One factor that may

[a]U.S. Geological Survey.

contribute to overestimates in the photogrammetric method arises from elevation errors (ref. 33-25). Repeated elevation measurements obtained photogrammetrically are normally distributed about the true value under ideal conditions that include large sample size. These normally distributed elevation errors introduce "noise" in the resulting slope-frequency distribution that can affect the results.

This appendix discussed the effect of reading error on two hypothetical slope-frequency distributions and two slope-frequency distributions from actual lunar data in order to ensure that these errors do not cause excessive overestimates of algebraic standard deviations for the slope-frequency distributions. The errors introduced are insignificant when the reading error is small and the slope length is large. A method of correcting for the errors in slope-frequency distributions is presented and applied to 11 distributions obtained from Apollo 15, 16, and 17 panoramic camera photographs and Apollo 16 metric camera photographs.

EFFECT OF READING ERROR ON HYPOTHETICAL DISTRIBUTIONS

In the method for obtaining slope-frequency distributions, three or more elevations are read by the photogrammetrist at points separated by fixed horizontal intervals ΔL along a preplanned traverse. From the three or more elevations read for a given point, a standard error of elevation is obtained for each point.

$$S_E = \sqrt{\frac{\sum_{i=1}^{n} \left(E_i - \bar{E}\right)^2}{(n - 1)}} \qquad (33\text{-}1)$$

where S_E = standard error of elevation measurements
E_i = individual elevation measurement
$\bar{E}$ = mean of n elevation measurements
n = number of elevation measurements

For the average of the three or more elevations, the standard error of the estimate of the mean is calculated as

$$S_{\bar{E}} = \frac{S_E}{\sqrt{n}} \qquad (33\text{-}2)$$

where $S_{\bar{E}}$ is the standard error of the estimate of the mean elevation. The standard error of the estimate of the mean represents a normal frequency distribution

of errors about the mean elevation. Normal frequency distributions of errors of estimates of the mean for two adjacent points are then combined to yield a normal frequency distribution of errors of differences of elevations between the two adjacent points. This yields the standard error of elevation differences.

$$S_{\Delta \bar{E}} = \sqrt{\left(S_{\bar{E}}\right)_A^2 + \left(S_{\bar{E}}\right)_B^2} \qquad (33\text{-}3)$$

When the error frequency distribution between differences in elevation of adjacent points $S_{\Delta \bar{E}}$ is divided by a fixed interval between the points (slope length or ΔL), a frequency distribution of errors results. This error distribution is in terms of slope or tangent slope angle.

Two types of hypothetical slope-frequency distributions were used to calculate the effects of the reading error on algebraic standard deviations and absolute mean slopes. The first type was a normal or Gaussian distribution.

$$\eta_p = \frac{1}{\sigma_p \sqrt{2\pi}} \exp\left[-\frac{1}{2} \left(\frac{P}{\sigma_p}\right)^2\right] \qquad (33\text{-}4)$$

where η_p = probability density function of slopes of P magnitude
σ_p = algebraic standard deviation
P = slope or tangent of the slope angle

The second distribution was

$$N_p = \exp\left(\frac{-P}{\bar{p}}\right) \qquad (33\text{-}5)$$

where N_p = cumulative fraction of slopes equal to P and larger
P = absolute value of slope or tangent of slope angle
$\bar{p}$ = absolute mean slope

Symmetry of slopes about zero slope was assumed for the second distribution so that, for the positive set of slopes

$$\Delta N_p = \frac{\exp\left(\frac{-P_A}{\bar{p}}\right) - \exp\left(\frac{-P_B}{\bar{p}}\right)}{2} \qquad (33\text{-}6)$$

where P_A and P_B are two positive values of slope equal to zero or larger; and

$$\Delta N_p = \frac{\exp\left(\frac{P_C}{\bar{P}}\right) - \exp\left(\frac{P_D}{\bar{P}}\right)}{2} \qquad (33\text{-}7)$$

where P_C and P_D are two negative values of slope equal to zero or more negative. Frequency distributions of errors of slope were then computed in incremental values of P, introduced into the equations for the hypothetical slope-frequency distributions in compatible incremental form, and then summed up to give an apparent slope-frequency distribution. This was done for values of $\Delta L/\sigma_{\Delta E}$ of 10, 20, 40, 80, and 160, where $\sigma_{\Delta E}$ is the standard deviation of elevation differences for a large sample and is analogous to $S_{\Delta E}$ (eq. (33-3)).

Algebraic standard deviations of the hypothetical normal frequency distributions of slopes are larger than the algebraic standard deviation of the hypothetical distribution and the ratio of slope length ΔL and the standard deviation of elevation differences $\sigma_{\Delta E}$. In certain cases, the differences in the algebraic standard deviations can be substantial, especially when $\Delta L/\sigma_{\Delta E}$ is small and the algebraic standard deviation of the hypothetical distribution is small. In figure 33-14, algebraic standard deviations of the hypothetical distribution are on the right, and the solid lines represent the algebraic standard deviations for the apparent distributions. For example, if the standard error of elevation reading S_E is ± 1 m, if the slope length ΔL is 8.16 m, and if the algebraic standard deviation of the hypothetical distribution is 0.01746 (tan 1°); then the standard error of the mean is $1/\sqrt{3}$ for three elevation readings for each point, the standard deviation of elevation differences is $\sqrt{2/3}$, and the ratio $\Delta L/\sigma_{\Delta E}$ is 10. Then, from figure 33-14, the algebraic standard deviation of the apparent distribution resulting from reading error is near 0.1405 (tan 8°). This is substantially larger than 0.01746 (tan 1°), and a nearly level undulating surface appears rough. This example is extreme and unlikely, but it illustrates the point. As will be shown, most of our data are affected by one-third of a degree and less.

Figure 33-15 shows a similar relationship for absolute mean values of slope using the second, or exponential, hypothetical slope-frequency distribution. Here again, apparent absolute mean slopes are substantially larger than the mean slopes of the hypothetical distribution. Thus, reading errors introduce fictitious estimates of surface roughness, which

(Standard error of slope)$^{-1}$

FIGURE 33-14.—Algebraic standard deviations of apparent slope-frequency distributions as a function of standard error of slopes resulting from elevation reading errors for normal or Gaussian hypothetical slope-frequency distributions. Algebraic standard deviations for the hypothetical slope-frequency distributions are indicated on the right as slope angles. Solid lines indicate apparent algebraic standard deviations for various values of the ratio of slope length and standard deviations for various values of the ratio of slope length and standard deviation of elevation differences for adjacent points $\Delta L/\sigma_{\Delta E}$.

may be significantly larger than the actual surface roughness when the actual surface is relatively smooth and the ratio $\Delta L/\sigma_{\Delta E}$ is small.

The form of the slope-frequency distribution is also affected by the reading error. One example is shown in figure 33-16. The starting hypothetical distribution, which is shown in algebraic and incremental form (fig. 33-16(a)), is the exponential type for a mean absolute slope of 0.0699 (tan 4°). Figure 33-16(b) shows the apparent distribution in algebraic form with $\Delta L/\sigma_{\Delta E} = 40$. The absolute mean of the apparent distribution has increased to 4.4° and the form of the apparent distribution has changed. The fraction of slopes near zero has been reduced,
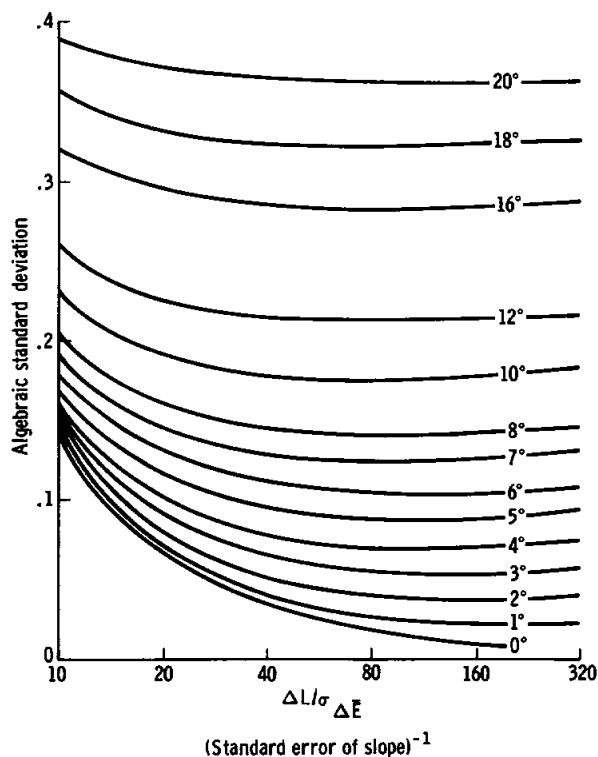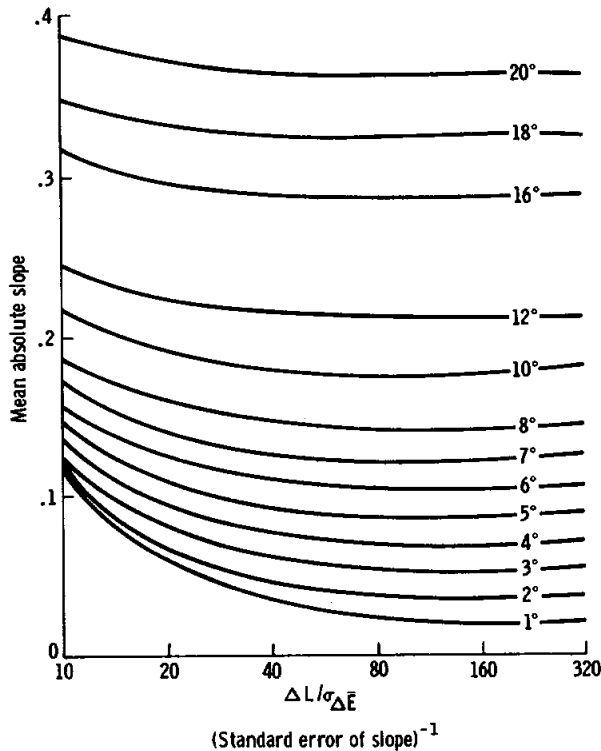
FIGURE 33-15.—Mean absolute slopes of apparent slope-frequency distributions as a function of standard error of slopes resulting from elevation reading errors for exponential hypothetical slope-frequency distributions. Mean absolute slopes for the hypothetical slope-frequency distributions are indicated on the right as slope angles. Solid lines indicate apparent mean absolute slopes for various ratios of slope length and standard deviation of elevation differences for adjacent points $\Delta L / \sigma_{\Delta \overline{E}}$.

whereas those above $+1/8$ and below $-1/8$ have increased. Thus, it is clear that reading errors must be taken into account.

METHOD OF CORRECTION FOR ACTUAL DISTRIBUTION

As discussed previously, lunar slope distributions derived by the photogrammetric methods are always rougher than the actual surface because of the measurement errors. This is obvious for perfectly flat, level surfaces for which pseudoslopes result from reading errors. The magnitude of the corrections depends on the magnitude of the slopes and the slope base length ΔL. The following paragraphs describe an approach to corrections to slope-frequency distributions obtained by photogrammetric techniques.
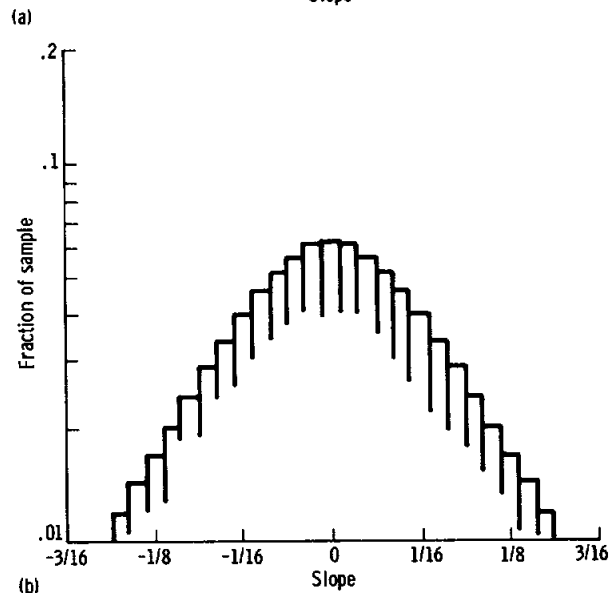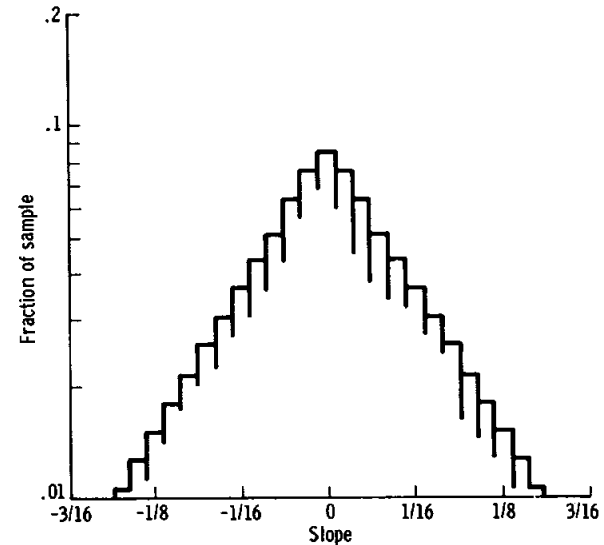
FIGURE 33-16.—Histograms illustrating effect of reading error on hypothetical exponential slope-frequency distribution. Note difference in peakedness of the two distributions. (a) Starting hypothetical distributions. (b) Apparent distribution produced by reading error.

Theoretical Approach

Because slopes are expressed as the ratio of the elevation difference and the horizontal distance between a pair of adjacent points (i.e., $P = \Delta E / \Delta L$), the standard error of the slope S_p is also a function of the standard errors of the elevation difference and the horizontal distance. When slopes are measured at

equally spaced intervals (constant), S_p can be simply determined as

$$S_p = \pm \frac{1}{\Delta L} S_{\Delta E} = \pm \frac{1}{\Delta L} \sqrt{S_{\overline{E}_i}^2 + S_{\overline{E}_{i+1}}^2} = \frac{\sqrt{2}}{\Delta L} S_{\overline{E}}$$

(33-8)

where $S_{\overline{E}}$ is the averaged standard error of the elevation means. For small slope angles θ, $S_{\overline{E}}/\Delta L \approx \theta$ so that

$$S_p = \pm \sqrt{2}\ \theta$$

(33-9)

If one assumes a level terrain with a perfectly smooth surface $P_t = 0$, $P_m = P_t \pm S_p = 0 \pm \sqrt{2}\ \theta = \pm \sqrt{2}\ \theta$, where P_m are measured slopes. Because the chances of a positive error and a negative error are 50 percent, a pseudoslope frequency distribution with an algebraic standard deviation of $\sqrt{2}\ \theta$ will result from the reading error. When slopes become larger, the chances of significant increases in pseudoslopes decrease until a slope is reached where no correction should be applied. This will be clear from the detailed development in the following discussion.

PRACTICAL APPROACH

Based on the general discussion earlier, the corrections to the slope-frequency distributions are developed according to each value of slope. Let the two end points of a slope be i and $i + 1$ as indicated in figure 33-17(a). If points i and $i + 1$ have standard errors of mean elevations of $\pm S_i$ and $\pm S_{i+1}$, respectively, then the chance of a positive S_i (or a positive S_{i+1}) is equally as likely as a negative S_i (or a negative S_{i+1}). This can be expressed in terms of probability Pr as

$$\mathrm{Pr}\left(+S_i\right) = \mathrm{Pr}\left(-S_i\right) = \mathrm{Pr}\left(+S_{i+1}\right) = \mathrm{Pr}\left(-S_{i+1}\right) = \frac{1}{2}$$

(33-10)

Let $\epsilon = S_{i+1}/\Delta L$, $\epsilon_1 = S_i/\Delta L$, and $\Delta \epsilon = (S_{i+1} - S_i)/\Delta L = \epsilon - \epsilon_1$; and let P_t be the true slope and P_m be the measured slope.[3] Then, we have the following three cases for the condition that absolute values are used for slopes.

---

[3]Quantities θ in equation (33-9) and ϵ in equations (33-11) to (33-14) are not the same.
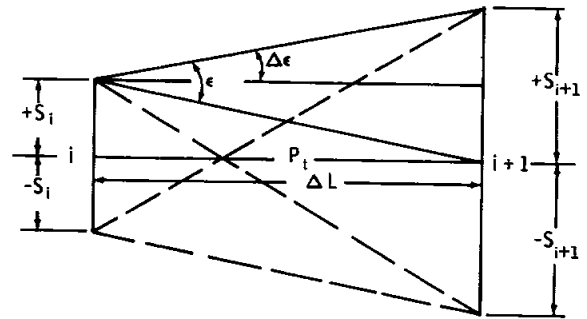
(a)
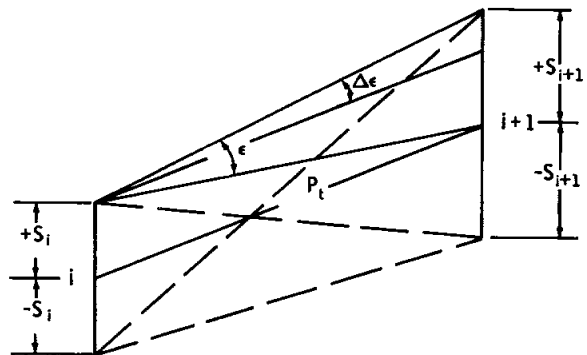
(b)
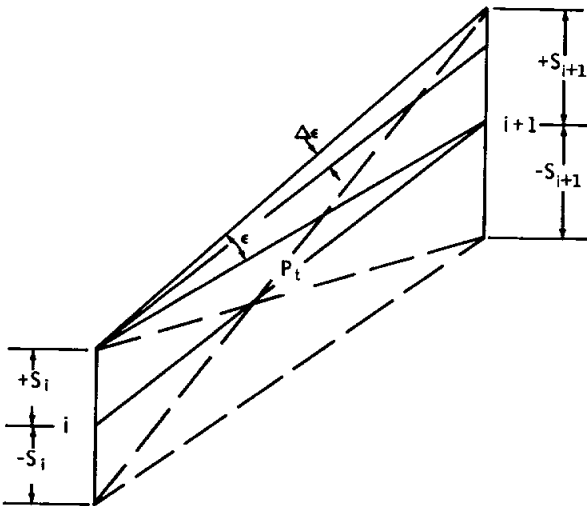
(c)

FIGURE 33-17.—Corrections to slope-frequency distributions. (a) True slopes equal to zero, case 1 (eq. (33-11)). (b) True slopes smaller than 2ϵ but larger than zero, case 2 (eq. (33-12)). (c) True slopes larger than or equal to 2ϵ, case 3 (eq. (33-13)).

Case 1: $P_t = 0$

$$\text{Pr}\left(+S_i \text{ and } +S_{i+1}\right) = \text{Pr}\left(P_m = P_t + \Delta\varepsilon\right) = 1/4 \rightarrow 1/4\left(P_t + \Delta\varepsilon\right) \tag{i}$$

$$\text{Pr}\left(-S_i \text{ and } -S_{i+1}\right) = \text{Pr}\left(P_m = P_t + \Delta\varepsilon\right) = 1/4 \rightarrow 1/4\left(P_t + \Delta\varepsilon\right) \tag{ii}$$

$$\text{Pr}\left(+S_i \text{ and } -S_{i+1}\right) = \text{Pr}\left(P_m = P_t + 2\varepsilon - \Delta\varepsilon\right) = 1/4 \rightarrow 1/4\left(P_t + 2\varepsilon - \Delta\varepsilon\right) \tag{iii}$$

$$\text{Pr}\left(-S_i \text{ and } +S_{i+1}\right) = \text{Pr}\left(P_m = P_t + 2\varepsilon - \Delta\varepsilon\right) = 1/4 \rightarrow 1/4\left(P_t + 2\varepsilon - \Delta\varepsilon\right) \tag{iv}$$

$$\therefore \ P_m = (\text{i} + \text{ii} + \text{iii} + \text{iv}) = 1/4\left(4P_t + 4\varepsilon\right) = P_t + \varepsilon = \varepsilon \tag{33-11}$$

Case 2: $0 < P_t < 2\varepsilon$

$$\text{Pr}\left(+S_i \text{ and } +S_{i+1}\right) = \text{Pr}\left(P_m = P_t + \Delta\varepsilon\right) = 1/4 \rightarrow 1/4\left(P_t + \Delta\varepsilon\right) \tag{i}$$

$$\text{Pr}\left(-S_i \text{ and } -S_{i+1}\right) = \text{Pr}\left(P_m = P_t - \Delta\varepsilon\right) = 1/4 \rightarrow 1/4\left(P_t - \Delta\varepsilon\right) \tag{ii}$$

$$\text{Pr}\left(+S_i \text{ and } -S_{i+1}\right) = \text{Pr}\left(P_m = 2\varepsilon - P_t - \Delta\varepsilon\right) = 1/4 \rightarrow 1/4\left(2\varepsilon - P_t - \Delta\varepsilon\right) \tag{iii}$$

$$\text{Pr}\left(-S_i \text{ and } +S_{i+1}\right) = \text{Pr}\left(P_m = 2\varepsilon + P_t - \Delta\varepsilon\right) = 1/4 \rightarrow 1/4\left(2\varepsilon + P_t - \Delta\varepsilon\right) \tag{iv}$$

$$\therefore \ P_m = (\text{i} + \text{ii} + \text{iii} + \text{iv}) = 1/4\left[2P_t + 2\varepsilon + 2(\varepsilon - \Delta\varepsilon)\right] = 1/2\left(P_t + \varepsilon + \varepsilon_1\right) \tag{33-12}$$

Case 3: $2\varepsilon \leq P_t$

$$\text{Pr}\left(+S_i \text{ and } +S_{i+1}\right) = \text{Pr}\left(P_m = P_t + \Delta\varepsilon\right) = 1/4 \rightarrow 1/4\left(P_t + \Delta\varepsilon\right) \tag{i}$$

$$\text{Pr}\left(-S_i \text{ and } -S_{i+1}\right) = \text{Pr}\left(P_m = P_t - \Delta\varepsilon\right) = 1/4 \rightarrow 1/4\left(P_t - \Delta\varepsilon\right) \tag{ii}$$

$$\text{Pr}\left(+S_i \text{ and } -S_{i+1}\right) = \text{Pr}\left(P_m = P_t - 2\varepsilon + \Delta\varepsilon\right) = 1/4 \rightarrow 1/4\left(P_t - 2\varepsilon + \Delta\varepsilon\right) \tag{iii}$$

$$\text{Pr}\left(-S_i \text{ and } +S_{i+1}\right) = \text{Pr}\left(P_m = P_t + 2\varepsilon - \Delta\varepsilon\right) = 1/4 \rightarrow 1/4\left(P_t + 2\varepsilon - \Delta\varepsilon\right) \tag{iv}$$

$$\therefore \ P_m = (\text{i} + \text{ii} + \text{iii} + \text{iv}) = 1/4\left(4P_t\right) = P_t \tag{33-13}$$

Corrections

From equation (33-11), one finds that when the true slope equals zero, the measured slope is always larger by an amount of ε, when standard errors of measurement exist. From equation (33-12), one can find the true slope by using the equation

$$P_t = 2P_m - \varepsilon - \varepsilon_1 \tag{33-14}$$

For case 3, equation (33-13) indicates that corrections should not be applied. Therefore, we can conclude that the slope correction should be applied as indicated in table 33-VI.

ACTUAL SLOPE-FREQUENCY DISTRIBUTIONS

Eleven slope-frequency distributions were corrected by using the method outlined in the previous section; two of them were at the Apollo 17 landing site. Panoramic camera positives were used for nine of the distributions, and metric camera positives were

TABLE 33-VI.—*Slope Corrections*

Range of true slope	Measured slope	Corrected slope
$P_t = 0$	ϵ	0
$0 < P_t < 2\epsilon$	$1/2(P_t + \epsilon + \epsilon_1)$	$2P_m - \epsilon - \epsilon_1$
$2\epsilon \leqslant P_t$	P_m	$P_t = P_m$

TABLE 33-VII.—*Effect of Standard Error of Measurement on Actual Lunar Slope-Frequency Distribution Obtained by Using Apollo Photography and Photogrammetry*

Location	Frame no.	Absolute mean corrected, deg	Absolute mean uncorrected, deg	Estimated algebraic standard deviation corrected, deg (a)	Slope length, m	$\Delta L/\sigma_{\Delta\bar{E}}$	Approximate corrections, deg (b)
Mare Serenitatis	[c]AS15-9560 and 9565	4.74	4.94	5.8	25	48	0.25
Mare Serenitatis	[c]AS15-9562 and 9567	4.82	5.00	6.1	25	54	.22
Descartes	[c]AS16-4558 and 4563	5.35	5.54	6.2	25	46	.25
Hadley	[c]AS15-9509 and 9514	5.69	5.81	6.8	25	56	.18
Uplands near Proclus	[c]AS15-9508 and 9513	5.37	5.57	6.4	25	46	.25
Uplands north of Vitruvius	[c]AS15-9550 and 9555	6.23	6.39	7.8	25	48	.20
Uplands near Glaisher	[c]AS15-9484 and 9489	8.35	8.47	10.5	25	40	.22
Mare Fecunditatis	[d]AS16-2931 and 2932	3.12	3.21	3.6	500	96	.10
Censorinus uplands	[d]AS16-2167 and 2168	7.76	7.82	9.0	505	74	.07
Littrow, near landing site	[c]AS17-2750 and 2755	3.79	4.08	4.5	25	47	.32
Littrow, west of landing site	[c]AS17-2750 and 2755	3.91	4.27	4.6	25	45	.33

[a]Estimated graphically as the value of slope angle corresponding to the cumulative fraction of 0.32.
[b]Estimated graphically from results of studies of hypothetical distributions.
[c]Apollo panoramic camera photographs.
[d]Apollo metric camera photographs.

used for the other two distributions (table 33-VII). Absolute mean slopes of the apparent frequency distribution (before corrections are made) are approximately 0.2 larger than those corrected for reading error effects when $\Delta L/\sigma_{\Delta\bar{E}}$ is near 50 and the mean is near 5° (table 33-VII). For larger mean slopes near 8.0° and $\Delta L/\sigma_{\Delta\bar{E}} = 40$ (table 33-VII, see uplands near Glaisher), the correction of mean slope is 0.12° and less than the correction of the smoother surfaces. When $\Delta L/\sigma_{\Delta\bar{E}}$ is large, the corrections for mean slope are smaller. Samples from Fecunditatis and the Censorinus uplands illustrate the smaller corrections, which are 0.09 and 0.06 for values of $\Delta L/\sigma_{\Delta\bar{E}}$ of 96 and 74, respectively. Although, $\Delta L/\sigma_{\Delta\bar{E}}$ for Fecunditatis is larger than that for Censorinus, the corrections

are larger because the surface of Mare Fecunditatis is significantly smoother than that of the Censorinus uplands. These results are in keeping with the results from the analyses of the hypothetical distributions. Approximate corrections, estimated graphically from the results of studies of the hypothetical distributions, are in good agreement with the corrections for the photogrammetrically derived distributions (table 33-VII).

Although the corrections for absolute mean slope seem rather small, their effect on the frequency distributions is clearly evident. An example is shown in figure 33-18 for the data from the Apollo 17 landing site. The traverse paths are shown in figure 33-19. For the corrected distribution, approximately
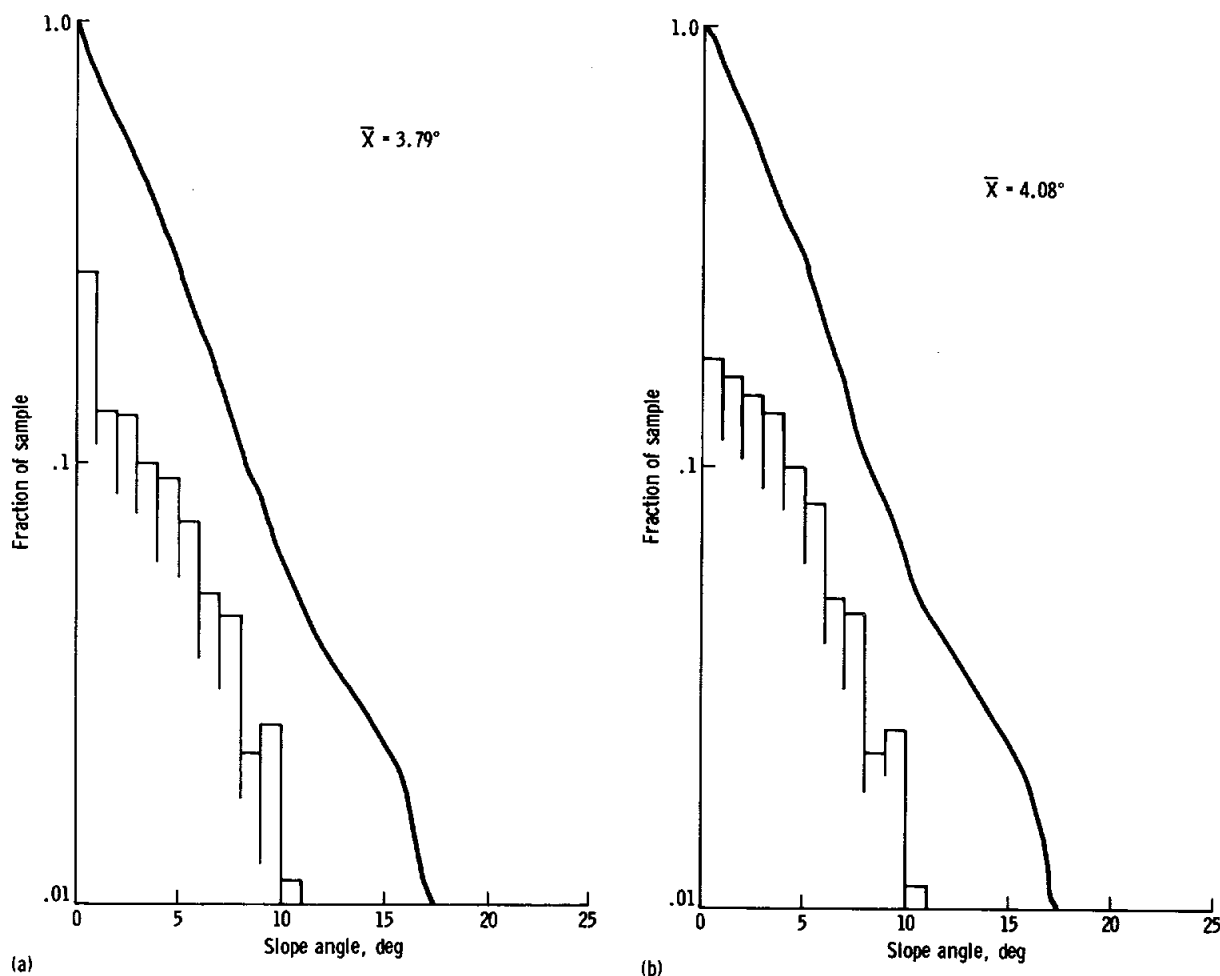
FIGURE 33-18.—Slope-frequency distribution of Apollo 17 landing site. (a) Corrected for reading error. (b) Uncorrected for reading error.

27 percent of the slopes are between $0°$ and $1°$, whereas only 17.5 percent of the slopes in the uncorrected distribution are between $0°$ and $1°$. This is in keeping with the results from the analyses of the hypothetical distributions.

CONCLUSIONS

Photogrammetric reading error introduces small errors into slope-frequency distributions, calculated mean absolute slopes, and algebraic standard deviations. These errors are insignificant provided the slope length for the data is large and the error of elevation measurement is small.

Although reading error is insignificant for the slope distributions described here, other spacecraft imagery do not have the excellent quality of the Apollo metric and panoramic photographs, and the effect of reading error must be considered.

ACKNOWLEDGMENTS
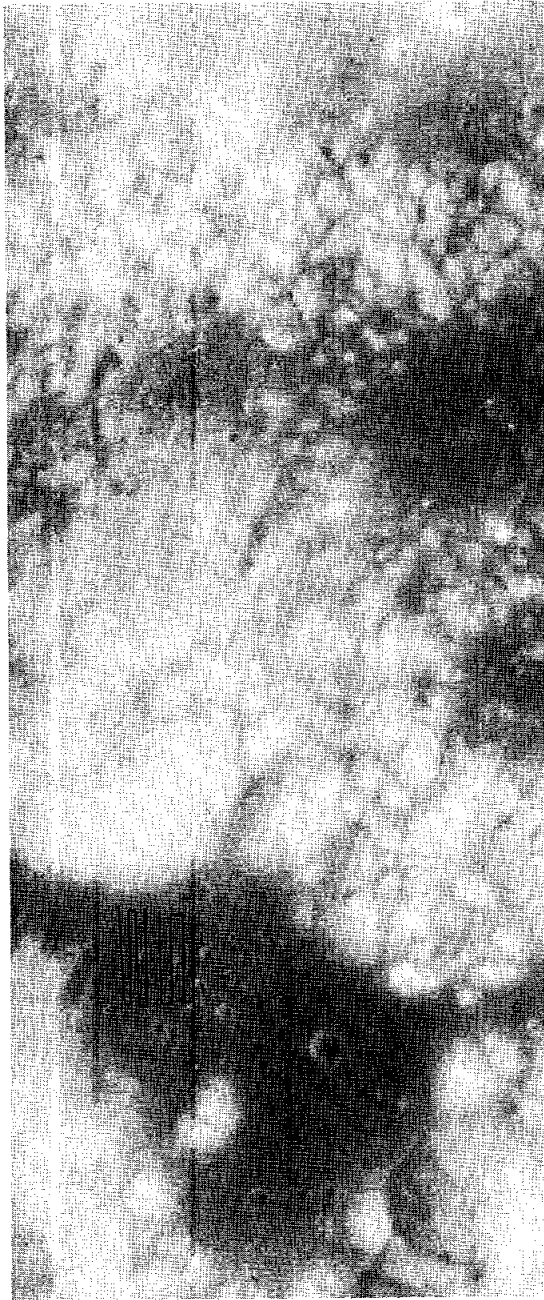
FIGURE 33-19.—Apollo 17 panoramic photograph showing
    traverse lines for slope-frequency distributions. Traverse
    to right is for the landing site; traverse to left is westward
    of landing site.

PART D

REPEATABILITY OF ELEVATION MEASUREMENTS—APOLLO PHOTOGRAPHY

Sherman S. C. Wu,[a] *Francis J. Schafer,*[a] *Gary M. Nakata,*[a] *and Raymond Jordan*[a]

Stereoscopic photographs of the Moon taken by the metric and panoramic cameras on board the service module of Apollo spacecraft provide a source for quantitative data on lunar topography. The accuracy of the topographic data depends, in part, on the repeatability of elevation measurements. The repeatability depends on contrast in the stereoscopic image and is affected by many factors, such as photographic quality, the photogrammetric instrument used, and illumination conditions. For the Moon, illumination conditions are important so that repeatability of elevation measurements may be statistically related to Sun elevation angles, local slopes, and albedos of surfaces. We have examined the effect of Sun elevation angle on repeatability, using Apollo 15 photographs (Wu, unpublished data), and extended the results to slope-related effects.

DISCUSSION OF RESULTS

From this preliminary evaluation, repeatability of elevation measurement can be related to contrast in the immediate scene of the stereoscopic image. The contrast is, in part, dependent on Sun elevation angle, and high-contrast low-Sun photographs allow the observer to perceive a well-defined surface. At high Sun elevation angles, low contrast results in loss of detail and the surface may be poorly defined. The results comparing repeatability and slope angle are not as clear, but a correlation of slope angle and standard error was found for the metric camera data in the Taurus-Littrow area. This correlation could arise from contrast differences resulting from the angle between the Sun and local slopes partly tilted toward the Sun. Alternatively, the correlation could be related to albedo because the area traversed also includes units with a wide range of albedos—higher albedos occurring in the rougher terrain and lower albedos occurring in the smoother terrain. Thus, we cannot distinguish between the effect of slope and

---

[a]U.S. Geological Survey.

albedo because the data were collected in an area where albedo and topography correlate with one another. Additionally, the lengths and slopes for one of the traverses on metric photography occur at an angle near 90° to the Sun direction. Nevertheless, the results from the low Sun elevation angles (16.5° and 30.5°) suggest a correlation of some kind that may be related to slope tilted away from or toward the Sun, or related to albedo, both albedo and slope, or some other factor unknown at this time.

EVALUATION OF SUN ELEVATION ANGLE

Elevation measurements from Apollo 15 metric camera stereomodels of 11 different sites, each having different Sun elevation angles that vary in approximately 10° intervals from 1° to 80°, reveal a clear relation between repeatability of elevation measurements and Sun elevation angle. By using an analytical stereoplotter, three elevations were measured for each of 35 points in each stereomodel. Standard errors of measurements (a measurement of repeatability) were calculated for each of the points.

$$S_E = \sqrt{\frac{\sum_{i=1}^{n}\left(E_i - \overline{E}\right)^2}{(n-1)}} \qquad (33\text{-}15)$$

where S_E = standard error of elevation measurement
E_i = individual elevation measurement
$\overline{E}$ = mean of n elevation measurements
n = number of elevation measurements

Then, the 35 values of S_E for each stereomodel were averaged and a regression curve was fitted to the averaged values for the 11 Apollo 15 models. Results are shown in figure 33-20 where it may be seen that the standard error curve has a minimum of approximately ± 7.4 m at a Sun elevation angle near 20°. Average standard errors become large for large Sun
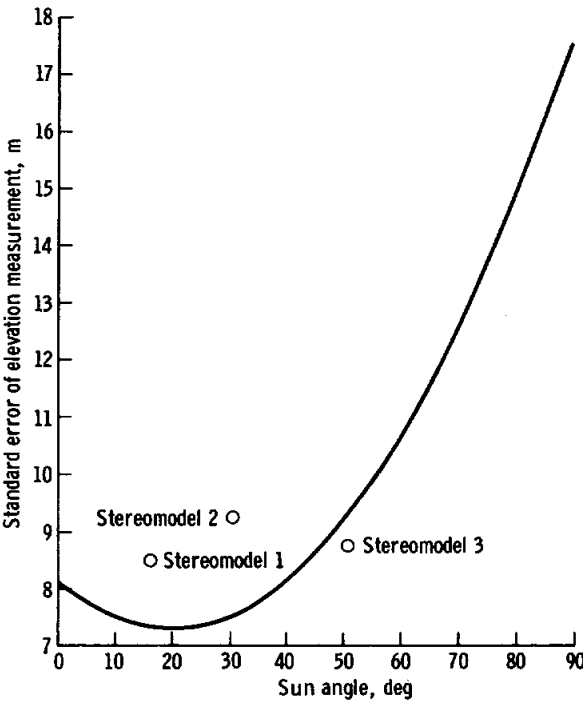
FIGURE 33-20.—Repeatability of elevation measurements and Sun elevation angle for Apollo 15 and 17 stereomodels.

elevation angles and reach values of ± 15 m at 80° Sun angle. Thus, topographic data collected using photographs with relatively low Sun elevation angles should be more precise.

Also shown in figure 33-20 and listed in table 33-VIII are the results from three Apollo 17 metric camera stereomodels for which standard errors of ± 8.5, ± 9.2, and ± 8.9 m are obtained (stereomodels 1, 2, and 3). Results for Apollo 17 photography are consistent with the Apollo 15 results, but more data are needed to demonstrate a relationship between Sun elevation angle and standard error for Apollo 17 metric camera stereomodels. From these stereomodels, a large number of elevations were measured along traverses shown in figure 33-21.

EFFECT OF SLOPES

Factors other than Sun elevation angle affect contrast and hence the repeatability of measurements. Such factors include topography and albedo of the surface. Slopes facing the Sun have less contrast than those facing away from the Sun (but not in shadow). Areas with high albedos have less

TABLE 33-VIII.—*Apollo 17 Photography and Summary of Results*

Parameter	Stereomodel 1 Sun angle = 16.5°	Stereomodel 2 Sun angle = 30.5°	Stereomodel 3 Sun angle = 50.5°	Apollo 17 landing site 4	West of landing site 4
Frame nos.	[a]AS17-0446 and 0447	[a]AS17-1499 and 1500	[a]AS17-2086 and 2087	[b]AS17-2750 and 2755	[b]AS17-2750 and 2755
Model scale	1:1 450 000	1:1 450 000	1:1 450 000	1:180 000	1:180 000
Number of slopes	573	584	724	624	639
Averaged standard error of elevation reading, m	8.51	9.23	8.87	.98	1.03
Mean slope, deg	5.76	5.71	4.97	3.79	3.91

[a]Metric camera photographs.
[b]Panoramic camera photographs.

FIGURE 33-21.—Profile traverses used for standard error of measurements and analysis of slope effects. (a) Sun elevation angle of 16.5° (Apollo 17 metric camera frame AS17-0446). (b) Sun elevation angle of 30.5° (Apollo metric camera frame AS17-1500). (c) Sun elevation angle of 50.5° (Apollo 17 metric camera frame AS17-2087).
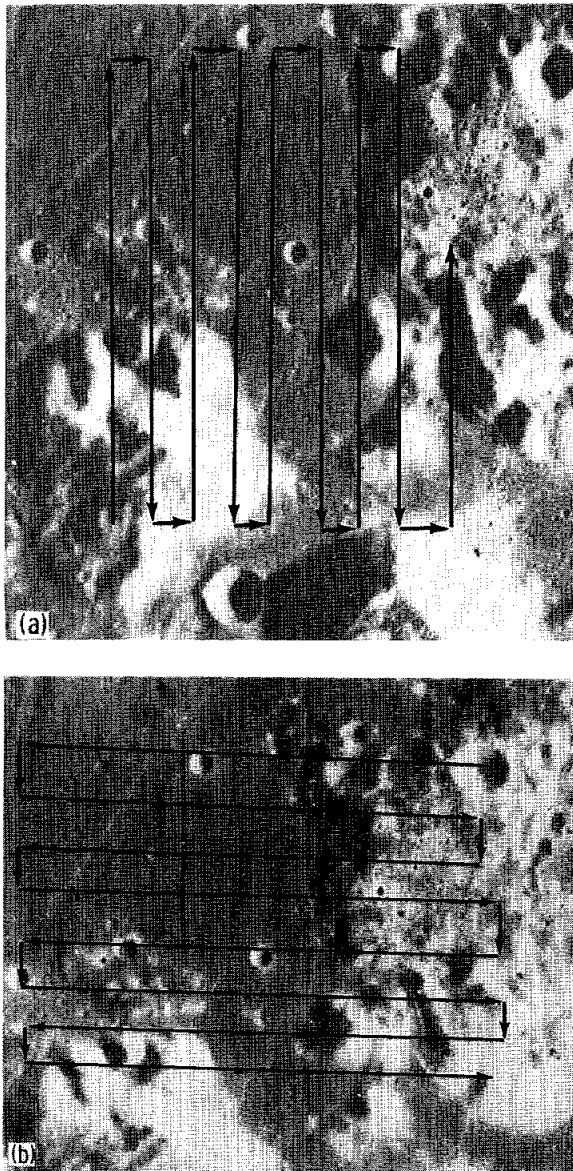
contrast than those with lower albedos. We have obtained data correlating standard errors of measurement and local slope angle.

In this study, three elevations were measured on second-generation metric camera master-positive transparencies at points separated by fixed horizontal intervals of approximately 500 m along traverses
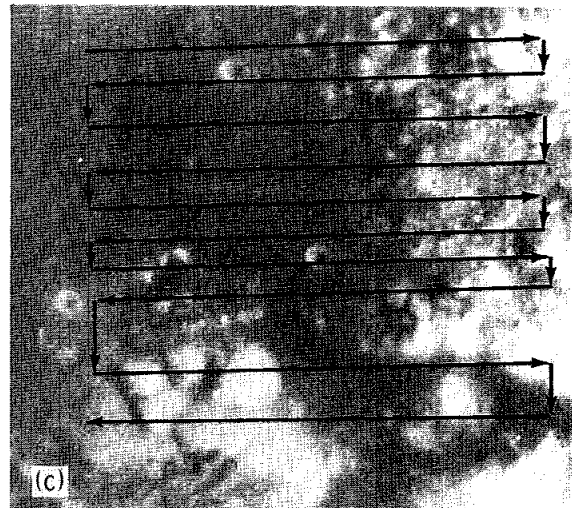
shown in figure 33-21. Standard errors of measurement were then correlated with 570 or more values of absolute slope (tables 33-VIII and 33-IX). The results of these correlations are shown in figure 33-22. A good correlation between standard error and slope angle is found for the case (fig. 33-22(a)) where the area Sun elevation angle is 16.5°; but where Sun elevation angles are 30.5° and 50.5°, little or no correlation is found between standard error and slope angle.

A similar study conducted with panoramic photographs for two areas confined to the area of the Apollo 17 landing site, where albedo is more or less uniform, suggests a variation of standard error with slope angle. The methods used here are the same as those used for the metric camera data, and approximately 620 points were measured three times each (tables 33-VIII and 33-IX). Spacing between the fixed intervals was approximately 25 m along traverses shown in figure 33-19. Here, a positive correlation between standard errors of elevation measurements and slope is found (fig. 3-23) and standard errors for small slopes tend to be smaller than those for large slopes.

In the panoramic photographs, the dependence between standard error and slope could arise solely from low-contrast areas where local bright slopes are generally inclined toward the Sun and local high-contrast areas where slopes are inclined away from the Sun. Because the traverses were confined to the dark floor of the Taurus-Littrow valley, we postulate that slopes measured perpendicular to the Sun direction have components generally tilted toward the Sun.

TABLE 33-IX.—Correlation of Average Standard Error with Absolute Slope of Terrain

Stereomodel 1 [a]AS17-0446 and 0447 Sun angle = 16.5°			Stereomodel 2 [a]AS17-1499 and 1500 Sun angle = 30.5°			Stereomodel 3 [a]AS17-2086 and 2087 Sun angle = 50.5°			Stereomodel 4 [b]AS17-2750 and 2755 Sun angle = 50.5° Landing site			Stereomodel 4 [b]AS17-2750 and 2755 Sun angle = 50.5° West of landing site		
Slope, deg	Average standard error, m	Frequency	Slope, deg	Average standard error, m	Frequency	Slope, deg	Average standard error, m	Frequency	Slope, deg	Average standard error, m	Frequency	Slope, deg	Average standard error, m	Frequency
0.3	8.2	105	0.3	9.0	98	0.4	7.4	160	0.3	1.1	170	0.3	1.1	164
1.5	7.7	73	1.5	7.6	73	1.5	8.1	100	1.5	.9	81	1.5	1.1	89
2.5	7.6	88	2.4	8.9	76	2.4	8.0	102	2.5	1.0	80	2.5	.9	84
3.4	7.5	57	3.4	8.8	56	3.5	8.6	71	3.5	.9	62	3.4	1.0	59
4.5	8.7	32	4.5	10.0	37	4.5	8.8	43	4.4	.8	58	4.5	1.0	60
5.5	8.0	28	5.4	8.6	49	5.5	10.6	31	5.5	.9	46	5.5	.9	51
6.5	7.8	19	6.4	9.3	25	6.6	10.8	32	6.6	1.0	31	6.4	1.1	39
7.4	7.2	20	7.5	10.0	18	7.4	9.4	23	7.5	1.0	28	7.5	.9	20
8.5	9.7	27	8.3	8.0	17	8.6	12.3	22	8.5	1.1	14	8.7	1.0	11
9.4	8.4	18	9.5	11.5	16	9.6	8.8	26	9.4	.9	16	9.5	.8	10
10.5	8.7	14	10.6	10.8	18	10.4	10.1	21	10.4	1.0	7	10.4	1.0	12
11.5	8.2	7	11.4	11.7	15	11.5	13.2	15	11.5	.9	6	11.2	1.7	8
12.4	13.0	11	12.5	8.4	16	12.4	11.4	21	12.3	1.3	4	12.8	1.9	4
13.5	10.3	8	13.5	11.1	11	13.5	9.9	5	13.7	1.0	3	13.6	1.1	4
14.4	12.8	7	14.4	7.8	8	14.7	10.2	7	14.3	1.1	3	14.3	.8	4
15.5	8.7	5	15.3	12.3	11	15.5	9.5	8	15.8	1.2	3	15.6	1.4	4
16.4	9.4	14	16.5	11.2	7	16.4	12.2	9	16.5	1.2	5	16.2	1.0	5
17.4	12.1	8	17.3	14.5	6	17.6	7.4	4	24.0	1.5	2	17.5	1.4	3
18.5	11.5	5	18.7	6.9	8	18.3	11.1	7				18.5	1.3	2
19.6	10.8	7	19.2	12.5	3	19.7	6.9	3						
20.5	11.0	5	20.5	10.9	7	20.4	13.7	6						
21.7	10.4	3	21.3	11.8	3	22.6	8.7	2						
22.7	12.0	2	23.5	7.4	2	24.4	7.0	2						
23.4	19.5	3												
24.5	7.5	4												
27.6	12.8	2												

[a]Apollo 17 metric camera photographs.
[b]Apollo 17 panoramic camera photographs.
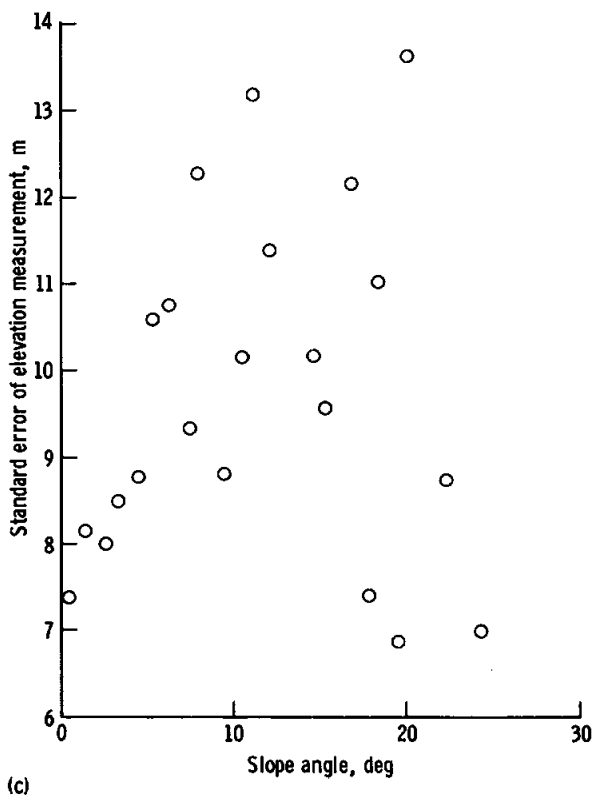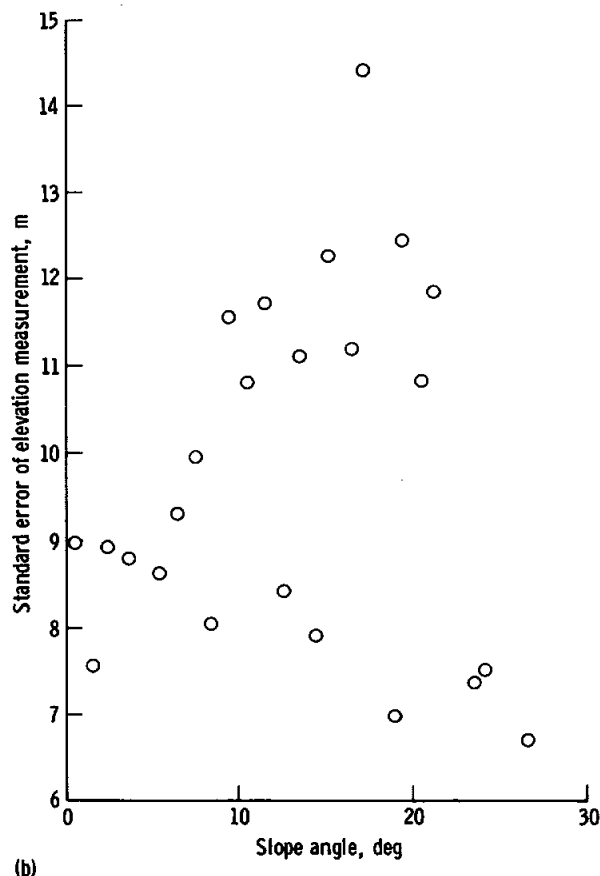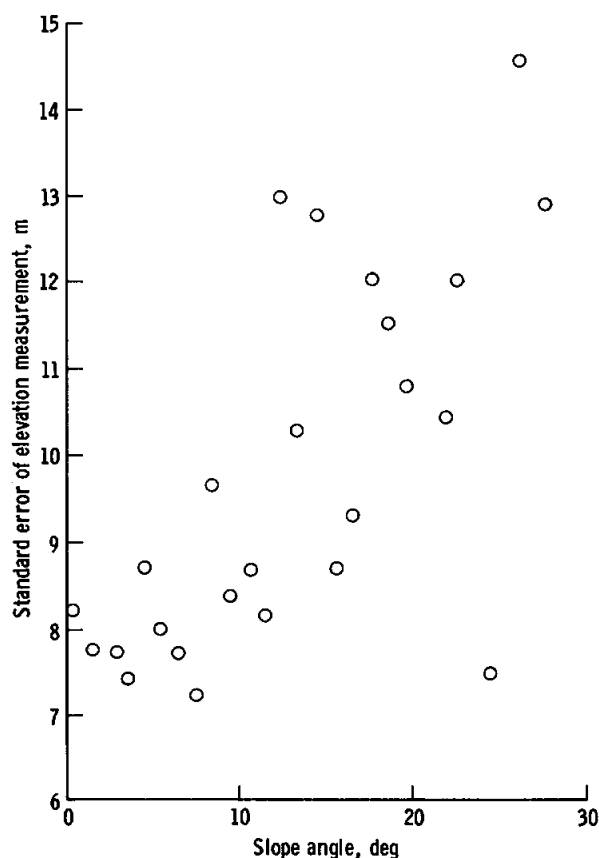
FIGURE 33-22.—Standard errors for elevation measurements and absolute slope angle. (a) Stereomodel 1 with Sun elevation angle of 16.5° (from Apollo 17 metric camera frames AS17-0446 and 0447). (b) Stereomodel 2 with Sun elevation angle of 30.5° (from Apollo 17 metric camera frames AS17-1499 and 1500). (c) Stereomodel 3 with Sun elevation angle of 50.5° (from Apollo 17 metric camera frames AS17-2086 and 2087).

Further studies should concern algebraic values of slope angle measured in a plane parallel to the Sun angle in areas of uniform albedo. These values should be related to similar values in areas with different albedos.
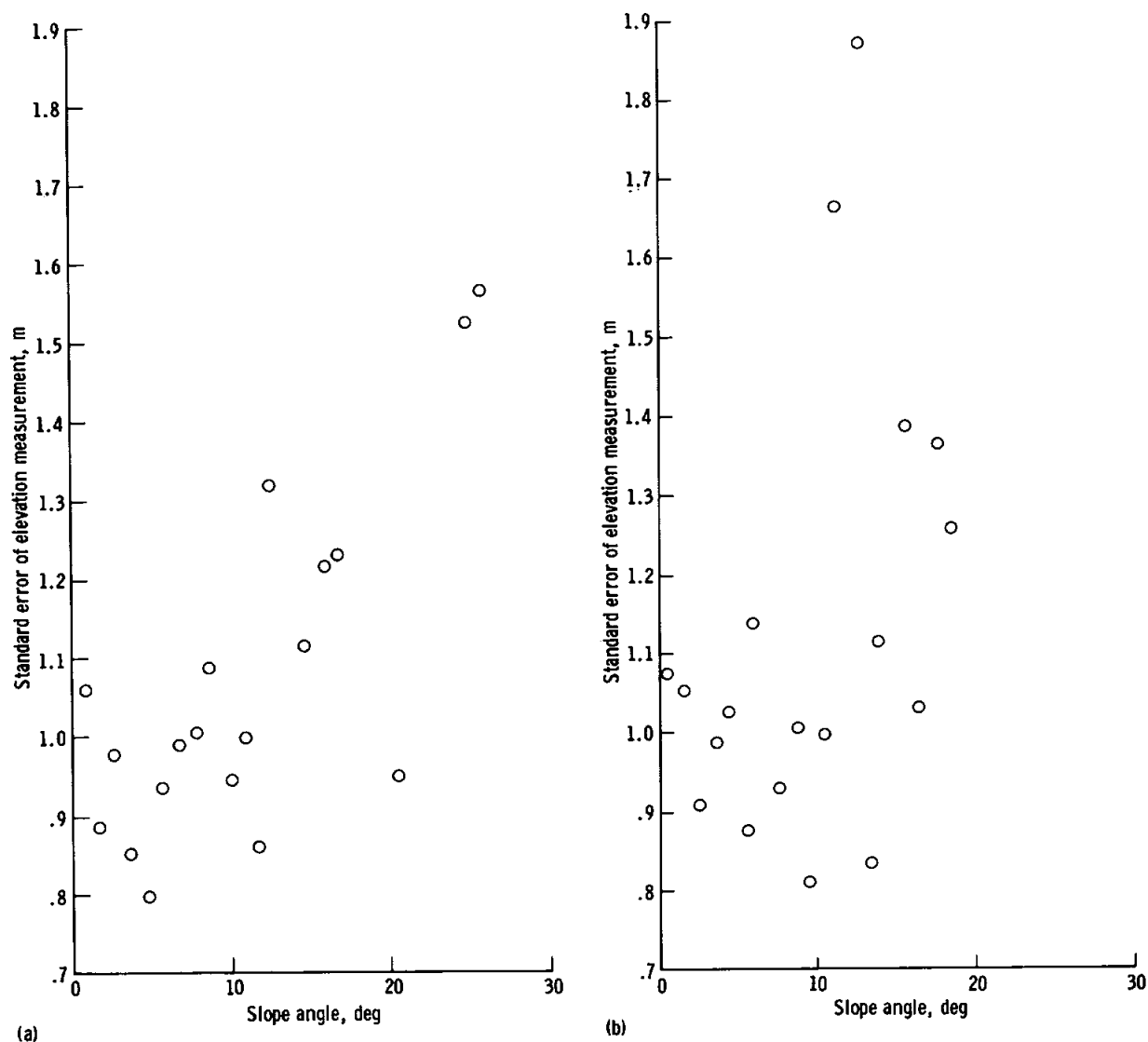
ACKNOWLEDGEMENTS

FIGURE 33-23.—Standard errors of elevation measurements and absolute slope angles for panoramic camera stereomodel of the Apollo 17 landing site (from Apollo 17 panoramic camera frames AS17-2750 and 2755). (a) Area near the lunar module. (b) Area west of lunar module.

PART E

APOLLO 17 LASER ALTIMETER

W. R. Wollenhaupt,[a] W. L. Sjogren,[b] R. E. Lingenfelter,[c] G. Schubert,[c] and W. M. Kaula[c]

The laser altimeter measures precise altitudes of the command service module (CSM) above the lunar surface and can function either with the metric (mapping) camera or independently. In the camera mode, the laser altimeter ranges at the time of each exposure, which varies between 20 and 28 sec (i.e., 30 to 43 km along the lunar surface). In the independent mode, the laser altimeter ranges every 20 sec.

These altitude data and the spacecraft attitudes that are derived from simultaneous stellar photography are used to constrain the photogrammetric reduction of the lunar surface photographs when cartographic products are generated. In addition, the altimeter measurements alone provide broad-scale topographic relief around the entire circumference of the Moon (i.e., they provide direct information on the figure of the Moon).

THE INSTRUMENT

The laser altimeter weighs approximately 22.5 kg (50 lb) and consists of a ruby laser, transmitting and receiving optics and telescopes, and a range counter. When a signal is received from the control circuit (ref. 33-33), the pulse-forming network discharges through flashlamps, producing a light pulse that primes the ruby rod such that light amplification occurs. A Q-switch is used to transfer the light pulse to the output resonant reflector. The Q-switch is a rapidly rotating mirror that moves into angular alinement with the output resonant reflector at the point of maximum gain in the ruby rod. This alinement creates a very high feedback situation, which sweeps out the energy stored in the ruby rod in the form of a laser pulse of approximately 15 nsec duration (ref. 33-33). The output of the laser at this point has a diameter of 0.635 cm (0.25 in.) and a beam width of

4.8 mrad. A 16-power telescope then transforms the beam to a 10.16-cm (4 in.) diameter with a beam width of 0.3 mrad. This range corresponds to 30 m on the lunar surface for a spacecraft altitude of 100 km. A portion of the output is applied to a photodiode to generate a start pulse, which is sent to the range counter through a delay line. The delay line is calibrated to compensate for the delay through the receiver photomultiplier and the video amplifier. The range counter counts increments of 6.67 nsec (providing a 1-m resolution) supplied by a 149.8962-MHz crystal oscillator. The return pulse, which is reflected from the lunar surface, is applied to the photomultiplier tube through the receiver telescope. The electrical output of the photomultiplier, amplified by the video amplifier, stops the range counter. Finally, the count is converted to range and telemetered.

MISSION OPERATORS

Several changes were made to the Apollo 17 laser altimeter in an attempt to avoid the degraded performance experienced during the Apollo 15 and 16 missions. The major modifications were (1) changed to an oil-impregnated type bearing in the Q-switch rotor to eliminate contamination of the optical surfaces and (2) changed envelopes on flashlamps to a high-quality quartz (Suprasil) to maintain a higher flashlamp light output level. The laser altimeter operated excellently throughout the mission, so well that it was turned on for six consecutive revolutions toward the end of the mission. Laser firings totaling 4026 were made on lunar revolutions 1 and 2, 13 and 14, 15, 23 and 24, 27 to 29, 38 and 39, 49, 62 and 63, 65 and 66, 67 to 72, and 73 and 74. There will be 11 to 12 almost complete sets of data containing measurements around the entire circumference of the Moon in the orbital plane.

ANALYTICAL TECHNIQUES

An accurate estimate of spacecraft position with

[a]NASA Lyndon B. Johnson Space Center.
[b]Jet Propulsion Laboratory.
[c]University of California at Los Angeles.

respect to the Moon is required to interpret the altimeter measurements for the purpose of seleno-detic figure investigation. This estimate was made by reducing the Earth-based Doppler radio tracking data of the orbiting CSM. These are essentially line-of-sight velocity measurements taken every 10 sec by at least two tracking stations of the Space Tracking and Data Acquisition Network. The Doppler data are processed using a weighted least-squares technique to determine a unique orbit for the CSM. A theoretical model of the Earth-Moon system is included in the computa-tions. The accuracy of the determined orbit limits the accuracy of the laser altimeter results. The dominant error source in the orbit determination and trajectory prediction process is the mathematical model used to describe the lunar gravitational effects. No known mathematical model accurately describes the ob-served gravitational effects, at least in a global sense. (The far side has never been measured.) The absolute radial position uncertainty is approximately 400 m. However, the relative radial position uncertainty of successive altimetry points along an orbital track is less than 10 m. Furthermore, the relative position un-certainty between two nearly parallel tracks will be appreciably less than 400 m, since the two orbits will be affected similarly by the principal error source, the inadequacy of the gravitational model.

After the spacecraft orbit has been determined, the laser altimeter measurements are subtracted from the corresponding selenocentric radius vectors of the CSM orbit to obtain complete lunar topographic profiles. Because the CSM orbit is a dynamic solution about the center of gravity (c.g.) of the Moon, the profile is referenced to the c.g. rather than the center of the optical figure. (The c.g. is also the more important center, of course, in analyzing the struc-tural significance of the topographic elevations. There are also corrections that can be applied to the laser measurements to correct for timing and laser pointing to adjust the slant range measurements to altitudes above the local vertical. The data required to make these corrections are usually not available until several months after the mission. However, these corrections should not significantly change the fol-lowing results.

PRELIMINARY RESULTS

The topographic profile resulting from the analysis of altimetry measured on revolutions 27 to 29 of the Apollo 17 spacecraft is given in figure 33-24. For most of the larger near-side features, the altitudes are remarkably close to those measured by the Apollo 15 experiment, the groundtrack of which is usually within approximately 200 km of that of the Apollo 17 experiment and intersects it over Mare Serenitatis. The elevations of Mare Serenitatis and the two adjacent maria, Imbrium and Crisium, are virtually the same in both the Apollo 15 and 17 data. The Montes Apenninus and Montes Taurus are also approximately the same in the two orbits. However, farther west there is some difference (due to diverging groundtracks); the Montes Carpatus show up in the Apollo 17 data, and Oceanus Procellarum is perhaps 0.5 km lower under Apollo 17 than under Apollo 15. Two pronounced features unique to the Apollo 17 data are the deep craters Reiner and Neper, with depths of 5 and 6 km, respectively, below the 1738-km sphere. For a crater as small as Reiner (25-km diameter), this depth is quite remarkable.

On the far side, the appearance of the Apollo 17 profile is also similar to the Apollo 15 profile but, because the terrain is so much rougher, only a qualitative comparison can be made. The Apollo 17 data also show a depression near 180° longitude, but not quite as broad or as deep as shown by Apollo 15 data; the greatest depth is not quite 4 km below the 1738-km sphere.

From the limited data available at this time, it appears that Apollo 17 altimetry gives approximately the same mean radius of 1737.3 km, and an offset of center-of-figure from center-of-mass along the Earth-Moon line slightly larger than 2 km.

The Apollo 17 groundtrack intersects the Apollo 16 groundtrack at a greater angle near longitudes 100° E and 80° W, both in terrae terrain. Nonethe-less, the two profiles appear to agree within 0.50 km in these regions.

REFERENCES

33-1. Stuart-Alexander, Desiree E.; and Howard, Keith A.: Lunar Maria and Circular Basins—A Review. Icarus, vol. 12, no. 3, May 1970, pp. 440-456.

33-2. Wilhelms, D. E.; and McCauley, J. F.: Geologic Map of the Near Side of the Moon. U.S. Geol. Survey Misc. Geol. Inv. Map I-703, 1971.

33-3. Muller, P. M.; and Sjogren, W. L.: Mascons: Lunar Mass Concentrations. Science, vol. 161, no. 3843, Aug. 16, 1968, pp. 680-684.

33-4. Carr, M. H.: Geologic Map of the Mare Serenitatis Region of the Moon. U.S. Geol. Survey Misc. Geol. Inv. Map I-489, 1966.
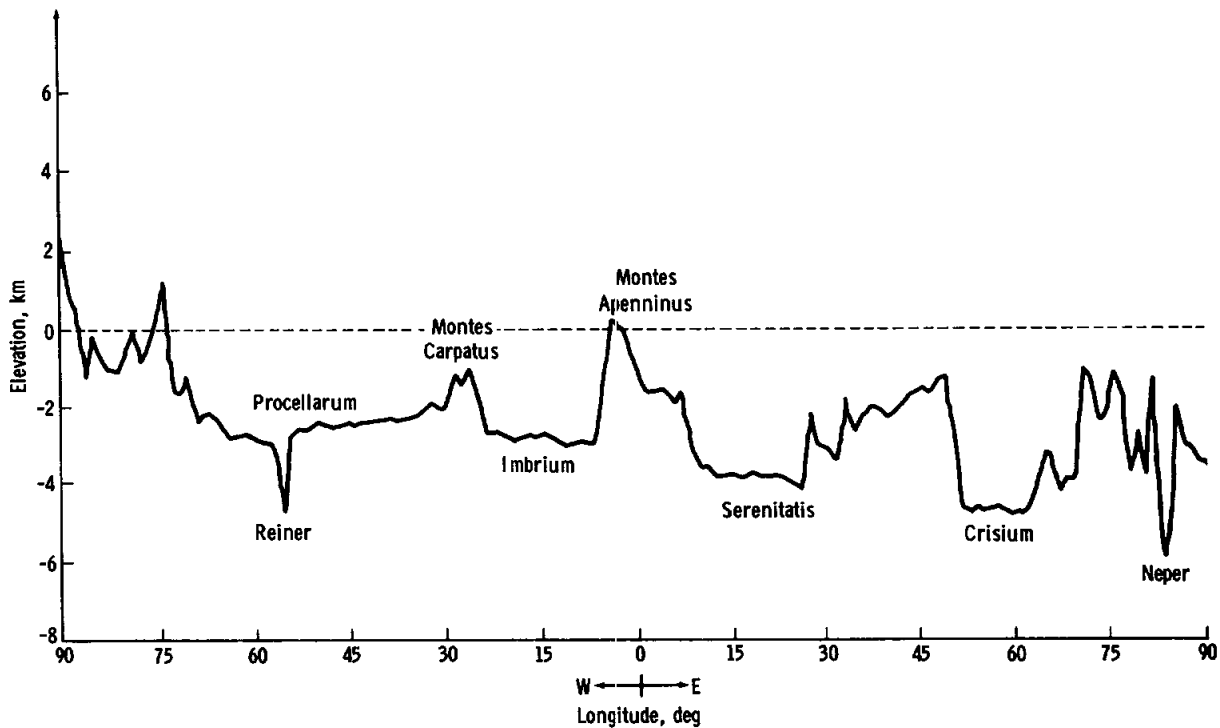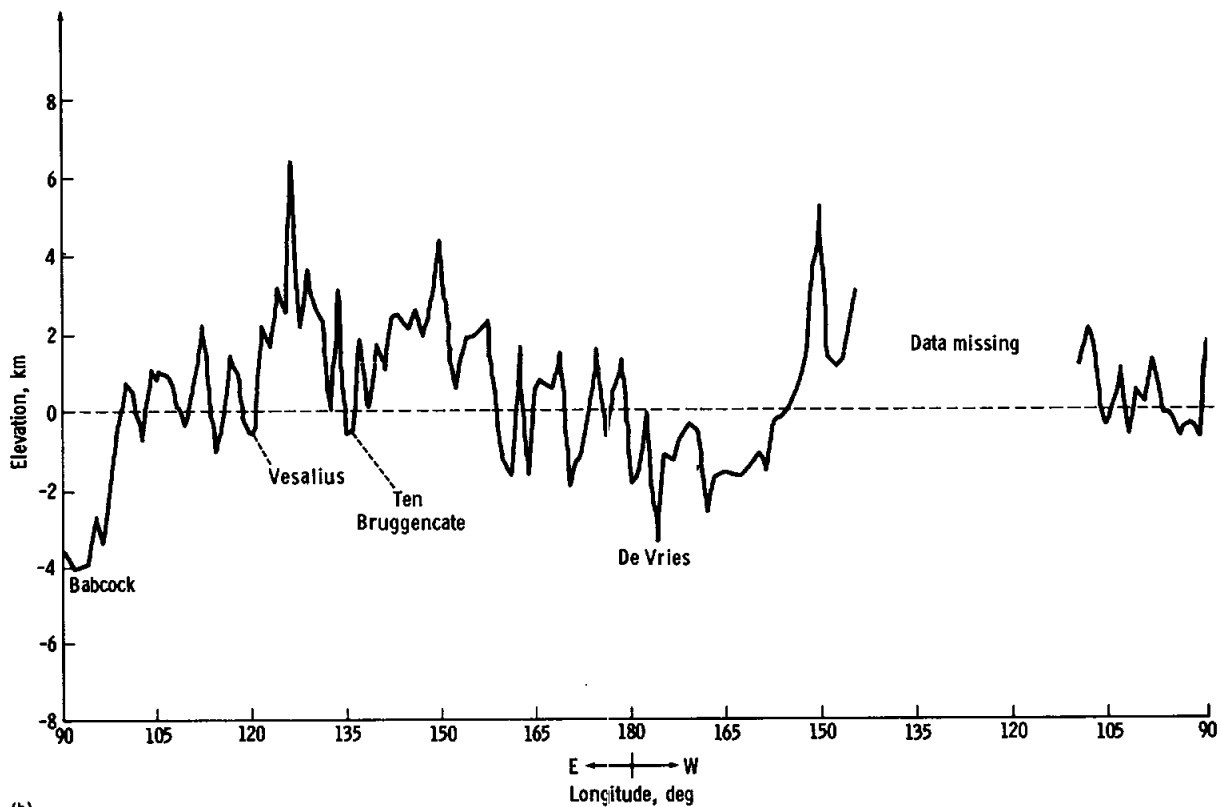
FIGURE 33-24.—Profile of Apollo 17 elevations with respect to a 1738-km sphere about the center of mass. (a) Lunar near side. (b) Lunar far side.

33-5. Kuiper, Gerard P.; Whitaker, E. A.; Strom, R. G.; Fountain, J. W.; and Larson, S. M.: Consolidated Lunar Atlas. U.S.A.F. Photographic Lunar Atlas, Supp. nos. 3 and 4, Lunar and Planetary Lab., Univ. of Arizona, 1967.

33-6. Whitaker, Ewen A.: Lunar Color Boundaries and Their Relationship to Topographic Features: A Preliminary Survey. The Moon, vol. 4, nos. 3/4, June/July 1972, pp. 348-355.

33-7. McCord, Thomas B.: Color Differences on the Lunar Surface. J. Geophys. Res., vol. 74, no. 12, June 15, 1969, pp. 3131-3142.

33-8. McCord, Thomas B.; and Johnson, Torrence V.: Relative Spectral Reflectivity (0.4-1μ) of Selected Areas of the Lunar Surface. J. Geophys. Res., vol. 74, no. 17, Aug. 15, 1969, pp. 4395-4401.

33-9. McCord, T. B.; Charette, M. P.; Johnson, T. V.; Lebofsky, L. A.; and Pieters, C.: Spectrophotometry (0.3 to 1.1 micron) of Visited and Proposed Apollo Lunar Landing Sites. The Moon, vol. 5, Sept. 1972, pp. 52-89.

33-10. Thompson, Thomas W.; and Zisk, Sidney [Stanley] H.: Radar Mapping of Lunar Surface Roughness. In Thermal Characteristics of the Moon, MIT Press (Cambridge, Mass.), 1972, pp. 83-117.

33-11. Thompson, T. W.; Masursky, H.; Shorthill, R. W.; Zisk, S. H.; and Tyler, G. L.: A Comparison of Infrared Radar and Geologic Mapping of Lunar Craters. Lunar Science Institute, Symposium on the Geophysical Interpretation of the Moon (Houston, Tex.), June 1970.

33-12. Thompson, T. W.; Shorthill, R. W.; Whitaker, E. A.; and Zisk, S. H.: Mare Serenitatis: A Preliminary Definition of Surface Units by Remote Observations. Lunar Science Institute, Symposium on the Geophysical and Geochemical Exploration of the Moon and Planets (Houston, Tex.), Jan. 1973.

33-13. Shorthill, R. W.; and Saari, J. M.: Nonuniform Cooling of the Eclipsed Moon: A Listing of Thirty Prominent Anomalies. Science, vol. 150, no. 3693, Oct. 8, 1965, pp. 210-212.

33-14. Shorthill, Richard W.: Infrared Atlas Charts of the Eclipsed Moon. The Moon, vol. 7, nos. 1/2, Mar./Apr. 1973, pp. 22-45.

33-15. Zisk, S. H.; Carr, M. H.; Masursky, H.; Shorthill, R. W.; and Thompson, T. W.: Lunar Apennine-Hadley Region: Geological Implications of Earth-Based Radar and Infrared Measurements. Science, vol. 173, no. 3999, Aug. 21, 1971, pp. 808-811.

33-16. Howard, H. T.; and Tyler, G. L.: Bistatic-Radar Investigation. Sec. 23 of the Apollo 15 Preliminary Science Report. NASA SP-289, 1972.

33-17. Tyler, G. L.; and Howard, H. T.: Dual-Frequency Bistatic-Radar Investigations of the Moon with Apollos 14 and 15. J. Geophys. Res., vol. 78, no. 23, Aug. 10, 1973, pp. 4852-4874.

33-18. Adler, I.; Trombka, J.; Gerard, J.; Lowman, P.; et al.: Apollo 15 Geochemical X-Ray Fluorescence Experiment: Preliminary Report. Science, vol. 175, no. 4020, Jan. 28, 1972, pp. 436-440.

33-19. Pieters, C.; McCord, T. B.; Zisk, S. H.; and Adams, J. B.: Lunar Black Spots and the Nature of the Apollo 17 Landing Area. J. Geophys. Res., vol. 78, no. 26, Sept. 10, 1973.

33-20. Campbell, Malcolm J.; and Ulrichs, Juris: Electrical Properties of Rocks and Their Significance for Lunar Radar Observations. J. Geophys. Res., vol. 74, no. 25, Nov. 15, 1969, pp. 5867-5881.

33-21. Gold, T.; Bilson, E.; and Yerbury, M.: Grain Size Analysis and High Frequency Electrical Properties of Apollo 15 and 16 Samples. Lunar Science IV (Abs. of papers presented at the Fourth Lunar Science Conference (Houston, Tex.), Mar. 5-8, 1973), pp. 293-294.

33-22. Riley, L. A.; and Hall, J. S.: High Resolution Measures of Polarization and Color of Selected Lunar Areas. Lowell Observatory Bull. No. 159, vol. VII, no. 22.

33-23. Zisk, S. H.; and Hagfors, T.: Radar Atlas of the Moon, Final Report: Vols. 2 and 3. MIT Lincoln Lab. (Cambridge, Mass.), 1970.

33-24. Zisk, S. H.; and Moore, H. J.: Calibration of Radar Data From Apollo 16 Results. Sec. 29, Part X, of the Apollo 16 Preliminary Science Report. NASA SP-315, 1972.

33-25. Wu, Sherman S. C.; and Moore, H. J.: Frequency Distributions of Lunar Slopes. Sec. 30, Part C, of the Apollo 16 Preliminary Science Report. NASA SP-315, 1972.

33-26. Howard, H. T.; and Tyler, G. L.: Bistatic-Radar Investigation. Sec. 25 of the Apollo 16 Preliminary Science Report. NASA SP-315, 1972.

33-27. Tyler, G. L.; and Simpson, R. A.: Bistatic Radar Measurements of Topographic Variations in Lunar Surface Slopes with Explorer 35. Radio Science, vol. 5, no. 2, Feb. 1970, pp. 263-271.

33-28. Tyler, G. L.; and Ingalls, D. H. H.: Functional Dependence of Bistatic-Radar Frequency Spectra on Lunar Scattering Laws. J. Geophys. Res., vol. 76, no. 20, July 1971, pp. 4775-4785.

33-29. Parker, M. N.; and Tyler, G. L.: Bistatic-Radar Estimation of Surface-Slope Probability Distributions with Applications to the Moon. Radio Science, vol. 8, no. 3, Mar. 1973, pp. 177-184.

33-30. Tyler, G. L.; Simpson, R. A.; and Moore, H. J.: Lunar Slope Distributions: A Comparison of Bistatic Radar and Photographic Results. J. Geophys. Res., vol. 76, no. 11, Apr. 1971, pp. 2790-2795.

33-31. Hagfors, T.: Relationship of Geometric Optics and Autocorrelation Approaches to the Analysis of Lunar and Planetary Radar. J. Geophys. Res., vol. 71, no. 2, Jan. 15, 1966, pp. 379-383.

33-32. Howard, H. T.; and Tyler, G. L.: Bistatic-Radar Investigation. Sec. 17 of the Apollo 14 Preliminary Science Report. NASA SP-272, 1971.

33-33. Anon.: Operating and Instruction Manual for Laser Altimeter. RCA (Burlington, Mass.), CR70-588-14J1, 1970.

34. Astronomical Photography

Polarized and red- and blue-filter photographs of the zodiacal light were obtained for the first time on the Apollo 17 mission, allowing interpretations of zodiacal dust compositions (part A). Solar corona photographs obtained on the Apollo 17 mission show coronal streamers that apparently corroborate Earth-based observations; moreover, visual observations by the crew indicate clearly identifiable streamers which extend to approximately 100 solar radii (part B).

PART A

ZODIACAL LIGHT PHOTOGRAPHY

R. D. Mercer,[a] *L. Dunkelman,*[b] *and R. E. Evans*[c]

The Apollo 17 mission provided the fourth and final opportunity to photograph astronomical phenomena from the double umbra, the darkest region of the universe yet reached by man. In this region, no sunlight or earthshine illuminated the spacecraft during a portion of each lunar orbit. Moreover, the dark lunar disk provides such excellent occultation of the Sun that regions of the solar corona and the close-in zodiacal light have only become accessible for natural study from lunar-orbiting Apollo spacecraft. In this situation, crewmen using high-quality, but unsophisticated, hand-operated camera systems have been able to obtain data quickly that cannot be gathered from the ground or from Earth-orbiting satellites by any techniques yet devised. The zodiacal light extending eastward from the Sun was recorded in three separate series of photographs. Each of these presunrise series includes overlapping frames covering elongation angles from 80° to 0.5° eastward along the ecliptic plane. Before this mission, no data in color or polarized light had ever been obtained in the ecliptic plane from approximately 3° to 18° from the Sun.

This zodiacal light photography continues the work begun on Apollo 14 and continued through subsequent lunar missions. The Apollo 15 mission provided excellent photographs in unpolarized white light (ref. 34-1). On the Apollo 16 mission, there was an unsuccessful attempt to obtain plane-polarized white-light measurements of zodiacal light (ref. 34-2).

THEORY

Sunlight scattered from the countless small particles of interplanetary dust in heliocentric orbits gives rise to the zodiacal light. It appears as a wedge-shaped band of light superimposed on the constellations of the zodiac, from which it derives its name. The reflecting and refracting properties of the particles can cause subtle changes in the observed light, changes that can be analyzed to determine the nature of the particles. Desired information includes the

---

[a]Dudley Observatory.
[b]NASA Goddard Space Flight Center.
[c]NASA Lyndon B. Johnson Space Center.

number of particles along any given line of sight, the range and distribution of particle sizes, their surface characteristics including dielectric compared to metallic properties, and the variations in these parameters as a function of distance from the Sun. The brightness, polarization, and color of the scattered light as compared to direct sunlight are the optical means available to astronomers for assessing particle characteristics (ref. 34-3).

Differences in color brightnesses may indicate the local distributions of particle sizes within a given region; that is, the ratio of these brightnesses may provide information on the ratio of micrometer-size and larger particles to the submicrometer-size particles. It may also produce some evidence on the types of constituent materials from which these particles are composed (ref. 34-4).

EQUIPMENT

The Nikon 35-mm camera was used with the 55-mm lens set at $f/1.2$ and the polaroid or color filters just ahead of the objective lens. Emulsion was Kodak type 2485, high-speed, black-and-white recording film. The camera was bracket mounted behind the right rendezvous window and pointed almost parallel to the plus-X axis of the spacecraft when color filters were used; it was pointed 30° away from the plus-X axis towards the minus-Z axis when the larger polaroid filter was used to gain the necessary extra window clearance. When the color filters were used, a light-tight window shade with an opening for the camera lens was used to exclude from the camera optics the stray cabin light that might otherwise be reflected from the window. During polaroid photography, cabin lighting was reduced to a minimum. Because filter orientation had to be manually changed by the 90° rotation between frames, the window shade could not be used.

Preflight calibration exposures were added to the flight film. These calibrations were performed by using an illuminated step-wedge from the High Altitude Observatory to provide brightness values in terms of the surface brightness of the Sun (ref. 34-5). The preflight calibration exposure underwent the same radiation, temperature, pressure, and humidity conditions as the data frames. Every shutter speed planned for use in the data frames was used in the calibration frames so that emulsion reciprocity characteristics could be completely taken into account.

PROCEDURES

To collect polarization data on the Apollo 17 mission, a series of photographic sets was taken eastward along the ecliptic plane while the spacecraft was in the double umbra on revolution 49. Each set was composed of two photographs through a polaroid filter that was rotated 90° in orientation between the two photographs. The maximum change in polarized brightness occurs between two perpendicular planes: the first plane contains the Sun, the spacecraft, and whatever point in the zodiacal light is being observed; the second plane is perpendicular to the first plane along the line of sight. Ground-based polarization measurements have been made over a number of years of the outer zodiacal light, but airglow and atmospheric effects made data reduction difficult (ref. 34-6).

For the zodiacal light tasks, the optical axis of the camera was initially pointed in the direction of the motion of the spacecraft with respect to the Moon. The optical axis was maintained in this attitude by pitching the spacecraft at lunar-orbital rate. This allowed the 36° by 24° field of view to be aimed close to the ecliptic plane, with one corner of the frame viewing that portion of the lunar limb cutting across the ecliptic. Stellar images on the data frames provide excellent postflight references on pointing accuracies; they also indicate image motion on the longer exposures caused by the pitching rate of the spacecraft and other small attitude corrections.

A series of zodiacal light photographs in red-filtered light was obtained on revolution 23. The bandpass was approximately 620 to 700 nm. Exposure times of 90-sec duration were used initially for positions farthest from the Sun. These exposure times were correspondingly decreased as the brightness of the zodiacal light increased; the final exposure duration was one-thirtieth of a second within 0.5° of the Sun. The red series of exposures provided 10 frames of data; all were conducted at the times and exposure durations specified in the checklists except that the third exposure, scheduled for a 60-sec duration, was underexposed because of an early shutter closure. However, the overlap between frames was such that this region was recorded by exposures both before and after the lost data frame. A second identical series of photographs was made on revolution 28 in blue-filtered light with an approximate bandpass of 420 to 510 nm. The blue series of 11 exposures was
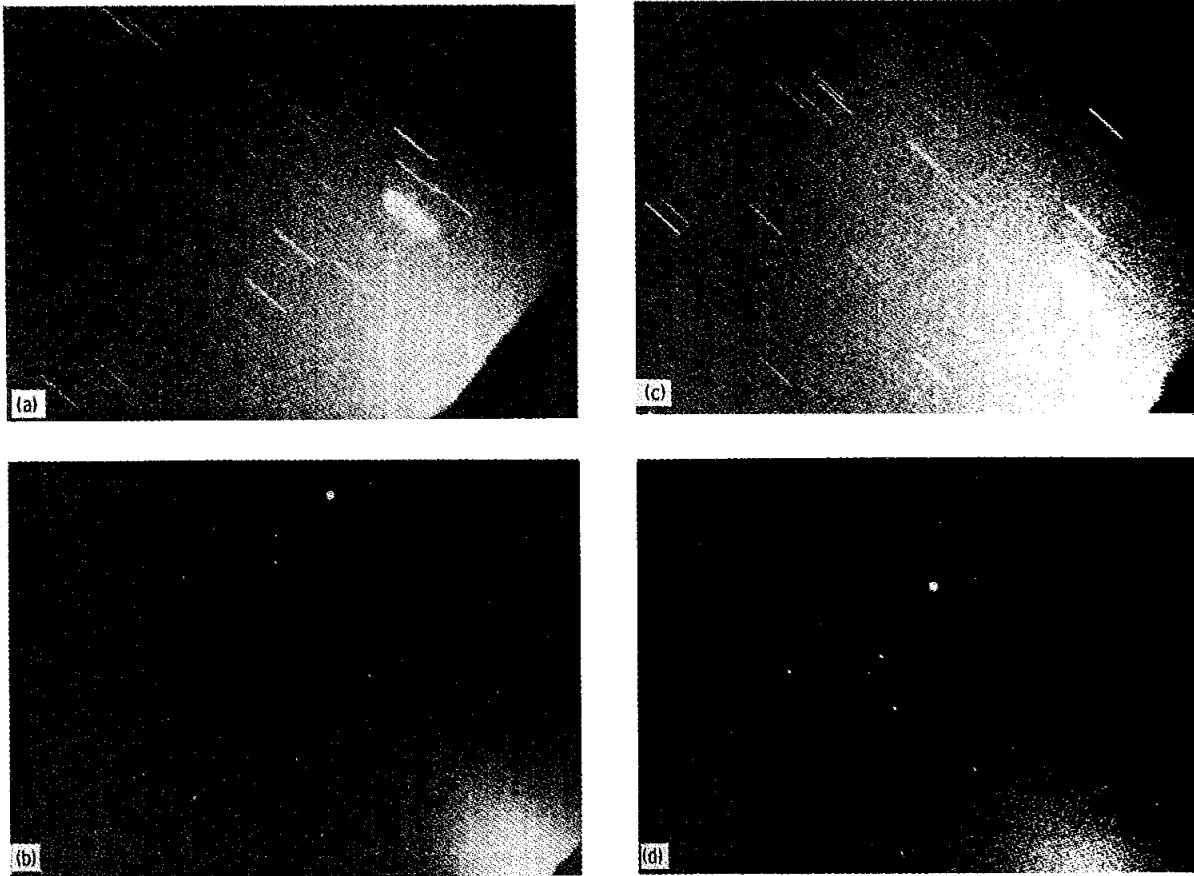
FIGURE 34-1.—The zodiacal light photographed on December 12, 1972, using a Nikon 35-mm camera with the 55-mm lens set at $f/1.2$, color filters, and Kodak type 2485 film. The red ($\approx$ 620 to 700 nm) zodiacal light scenes, located eastward on the ecliptic plane, are shown in (a) and (b). The blue ($\approx$ 420 to 510 nm) zodiacal light scenes, located eastward on the ecliptic plane, are shown in (c) and (d). (a) A 40-sec exposure centered at $35°$ elongation, with the Sun $15°$ below the lunar limb at the lower right corner (AS17-159-23908). (b) A 2-sec exposure centered at $25°$ elongation, with the Sun $3.5°$ below the lunar limb (AS17-159-23912). (c) A 40-sec exposure centered at $35°$ elongation, with the Sun $15°$ below the lunar limb at the lower right corner (AS17-159-23937). (d) A 2-sec exposure centered at $25°$ elongation, with the Sun $3.5°$ below the lunar limb (AS17-159-23941).

performed exactly as planned. Because the blue series used the same timing and duration of exposures as the red series, a direct frame-for-frame comparison can be made to study spectral content differences, once account is taken of film-sensitivity variation with wavelength.

RESULTS

The most striking quick-look results came from the comparison of corresponding red and blue images (fig. 34-1). As expected, the calibration data showed the film to be more sensitive to blue light than to red light. However, the inner zodiacal light within approximately $15°$ of the Sun showed a stronger red component in and close to the ecliptic plane. Yet, the inner zodiacal light well out of the ecliptic plane and almost all the outer zodiacal light produced a stronger blue component.

The entire 22-frame sequence in polarized light was performed exactly as desired, and useful data were recorded on every frame. Although visual comparisons of equivalent polaroid frames do not

show any obvious variation in features, very good isophote maps can be made from these data frames for more sensitive comparisons that will be made in the future.

All three crewmen made excellent sketches of the zodiacal light and the solar corona (part B). These sketches will be very useful in determining when visual observations may be able to extract details not apparent on the photographs.

PART B

SOLAR CORONA PHOTOGRAPHY

R. M. MacQueen,[a] *C. L. Ross,*[a] *and R. E. Evans*[b]

The outer atmosphere of the Sun (the solar corona) extends from near the visible solar limbs throughout the interplanetary medium. Thus, the Earth is actually embedded in the coronal flow (solar wind) that moves outward from the solar surface. This flow of material from the Sun has been observed in situ in the vicinity of the Earth orbit by interplanetary satellite probes during the past decade. However, the nature of the solar wind flow near the Sun where the outflowing gas is accelerated is poorly understood and has yet to be observed. The structure of the corona near the Sun, where the material can be contained by the coronal magnetic field, is also complex and poorly understood. The evolution of coronal structures is particularly obscure. Other fundamental questions include the origin and growth of major coronal structures and their relationship to solar activity.

Because the brightness of the solar corona is less than one one-hundredth million of that of the direct solar disk, observations of the corona can only be made when the solar disk is blocked, However, because of the large dynamic range of the radiance of the solar corona ($\approx 10^4$), the sensors of such instruments must be selected for a given portion of the corona. Atmospheric scattering of sunlight prohibits observations of the outer corona (greater than 1 solar radius above the solar limb) with coronagraphs from Earth observatories and, because of sensor constraints, Earth-orbiting instruments are generally designed to observe the inner corona (less than 10 solar radii above the solar limb).

The geometry of the lunar orbit of the Apollo command and service module (CSM) provided a unique opportunity for observations of the outer solar corona by occulting the CSM from both sunlight and earthshine (sunlight reflected from the Earth). Solar coronal observations from the Apollo 15 mission provided photographs of streamers extending to 40 solar radii from the solar limb, and the Apollo 16 observations provided excellent data on the radiance of the corona as a function of distance from Sun center. Because the solar corona is constantly changing as a function of solar activity, the Apollo 17 observations were designed to corroborate the Apollo 16 data on radiance as a function of distance and to provide data on any new coronal streamers present during the Apollo 17 mission.

Solar corona photography was scheduled on revolution 25 to observe the eastern half of the corona and on revolution 61 to observe the western half. The sequence scheduled on revolution 61 was not accom-

---

[a]High Altitude Observatory.
[b]NASA Lyndon B. Johnson Space Center.

plished. The revolution-25 sequence consisted of seven photographs with exposures of 10, 4, 1, 1/2, 1/8, 1/30, and 1/60 sec, starting 75 sec before sunrise and ending 10 sec before sunrise. The sequence was made using the Hasselblad electric camera with 80-mm lens set at $f/2.8$ and with high-speed, black-and-white, Kodak type 2485 recording emulsion. The spectral region photographed with the spacecraft-window/2485-film combination is approximately 425 to 700 nm. This spectral region was not chosen to provide spectral information on the solar corona but rather to utilize the maximum bandwidth and shorten the exposures as far as possible.

RESULTS

Two coronal streamers are evident in the photograph taken 10 sec before sunrise. Although these streamers seem to appear in the photograph taken 30 sec before sunrise, photographic techniques and microdensitometry will be required to determine their full extent. One streamer lies almost along the ecliptic plane; the other is south of the ecliptic plane and apparently corresponds to a feature that has been

FIGURE 34-2.—The solar corona photographed approximately 75 sec before sunrise on December 12, 1972 (AS17-154-23647).

observed by both the Orbiting Solar Observatory 7 (OSO-7) and the Mauna Loa Observatory for two solar rotations (mid-October to mid-December) before the Apollo 17 observations. The OSO-7 and the Mauna Loa Observatory observations are being analyzed to determine the evolutional characteristics of the streamer, and the Apollo 17 data could provide information on the full extent of the streamer from Sun center at the time of the Apollo 17 observations. In addition, the crew made real-time sketches that show the same two streamers; both the sketches and debriefing comments of the crew indicate clearly identifiable streamers extending to Jupiter, which is $24.4°$ (≈ 100 solar radii) from Sun center. This identification is a tribute to the wide dynamic range or adaptability of the human eye.

Microdensitometer tracing of the 10-, 4-, 1-, 1/2- and 1/8-sec exposures has been accomplished, and preliminary analysis shows good correlation between the Apollo 16 and the Apollo 17 data on radiance as a function of distance from Sun center. Radiance information from the Apollo 17 data will extend to approximately $25°$ from Sun center. In addition, attempts to enhance the contrast between the coronal streamers and the background are in progress to extend the available data on the streamers that were observed for several months. Digital techniques of picture averaging and enhancement, currently under development as part of the High Altitude Observatory Apollo Telescope Mount Program for the Skylab missions, will be applied to these photographs. All data reduction thus far has been accomplished on the High Altitude Observatory Boller and Chivens model 14213 microdensitometer. The flight film was calibrated photometrically both preflight and postflight with a sensitometer developed by the High Altitude Observatory.

Figure 34-2 is frame AS17-154-23647, which was taken on December 12, 1972, at 20:32:36 G.m.t., 75 sec before lunar sunrise. The Sun is approximately $3°$ below the lunar limb, and the overexposed image of Jupiter is $24.4°$ from Sun center. Figure 34-3 is a sketch made in orbit by the lunar module pilot showing Jupiter on the ecliptic plane with the coronal streamers on each side of the ecliptic. The sketch complements the OSO-7 data, which ends at 10 solar radii, and the Apollo 17 photographs by extending the observations to approximately $25°$ from Sun center.
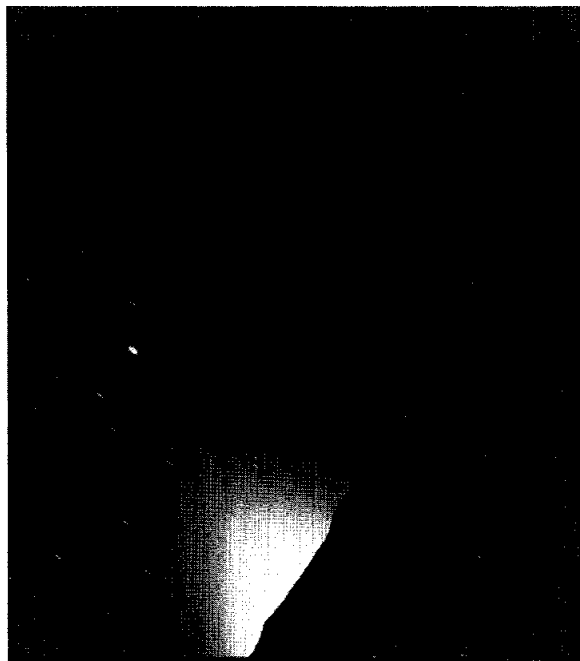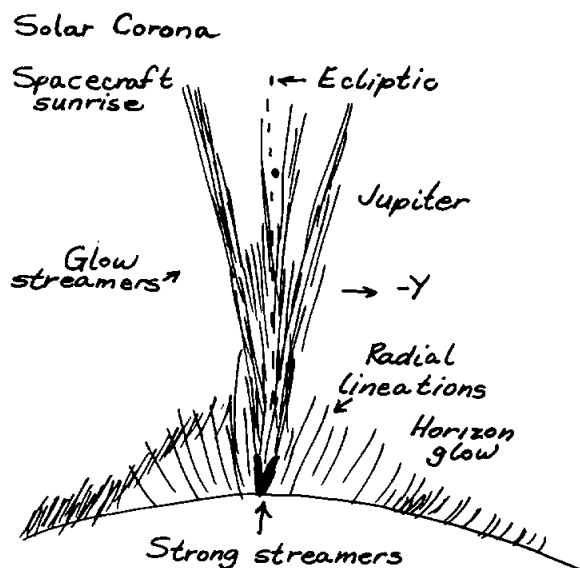
FIGURE 34-3.—A solar corona sketch made by the lunar module pilot in lunar orbit that shows the eastern half of the corona with Jupiter 24.4° from Sun center.

ACKNOWLEDGMENTS

REFERENCES

34-1. Mercer, R. D.; Dunkelman, L.; Ross, C. L.; and Worden, A.: Lunar Orbital Photography of Astronomical Phenomena. Space Research XIII, Akademie-Verlag (Berlin), 1973.

34-2. Mercer, R. D.; Dunkelman, L.; and Mattingly, Thomas K.: Gum Nebula, Galactic Cluster, and Zodiacal Light Photography. Sec. 31, Part A, of the Apollo 16 Preliminary Science Report. NASA SP-315, 1972.

34-3. Van de Hulst, H. C.: Light Scattering by Small Particles. John Wiley & Sons (New York), 1957.

34-4. Giese, R. H.; Hanner, M.; and Leinert, C.: Color Dependence of Zodiacal Light Models. Planet. Space Sci., 1973.

34-5. Pizzo, V.; and Gosling, J. T.: A Sensitometer Box for Solar Corona Photometry. Am. Astronaut. Soc. Phot. Bull., no. 1, 1972, p. 19.

34-6. Weinberg, J. L., ed.: The Zodiacal Light and the Interplanetary Medium. NASA SP-150, 1967.

APPENDIX A

Glossary

agglutinate—a deposit of originally molten ejecta

albedo—the percentage of the incoming radiation that is reflected by a natural surface

anomaly—an area of a geophysical survey (e.g., a magnetic or gravitational survey) that is different in appearance from the survey in general

anorthite—a calcium-rich variety of plagioclase feldspar

anorthosite—a granular, plutonic, igneous rock composed almost exclusively of a soda-lime feldspar

apatite—any of a group of calcium-phosphate minerals that occur variously as hexagonal crystals, as granular masses, or in fine-grained mass as the chief constituent of phosphate rock

aphanite—a dark rock of such close texture that the individual grains are invisible to the unaided eye

aphyric—not having distinct crystals

augite—one of a variety of pyroxene minerals that contain calcium, magnesium, and aluminum; usually black or dark green in color

bit—abbreviation of binary digit; a quantum of information

bleb—a small particle of distinctive material

bow shock—a shock wave in front of a body, such as an airfoil

breccia—rock consisting of sharp fragments embedded in a fine-grained matrix

cataclasis—rock deformation accomplished by fracture and rotation of mineral grains or aggregates; granulation

chadacryst—a term applied to crystals in igneous rocks that are allothigenous, or foreign to the body of rock in which they occur

chrondrite—a meteoritic stone characterized by the presence of rounded granules

clast—a discrete particle or fragment of rock or mineral; commonly included in a larger rock

clinopyroxene—a mineral that occurs in monoclinic, short, thick, prismatic crystals and that varies in color from white to dark green or black (rarely blue)

coherent—moving in unison or having some other fixed relationship, usually in phase

collimator—an optical device that renders rays of light parallel

comminution—the reduction of a substance to a fine powder

conchoidal—a term used to describe a shell-like surface shape that has been produced by the fracturing of a brittle material

cristobalite—an isometric variety of quartz that forms at high temperatures (SiO_2)

Curie temperature—the temperature in a ferromagnetic material above which the material becomes substantially nonmagnetic

dacite—the extrusive equivalent of quartz diorite (tonalite)

décollement—the independent disruption by folding or faulting of sedimentary beds by sliding over the underlying beds

dendrite—a crystallized arborescent form

devitrification—the change of a glassy rock from the glassy state to a crystalline state after solidification

dielectric constant—a measure of the amount of electrical charge a given substance can withstand at a given electric field strength

druse—a crust of small crystals lining the sides of a cavity, usually the same minerals that constitute the enclosing rock

dunite—a peridotite that consists almost entirely of olivine and that contains accessory chromite and pyroxene

epicenter—the point on a planetary surface directly above the focus of an earthquake

equant—a term applied to crystals that have approximately the same diameter in every direction

eucrite—a meteorite composed essentially of feldspar and augite

euhedral—pertaining to minerals the crystals of which have had no interference in growth

exsolution—unmixing; the separation of some mineral-pair solutions during slow cooling

feldspar—a group of abundant rock-forming minerals

fiducial—taken as a symbol of reference

flux—the rate of flow of some quantity, as energy or gas molecules

fractional process—separation of a substance from a mixture (e.g., one isotope from another of the same element)

Fresnel zone—any one of the array of concentric surfaces in space between transmitter and receiver over which the increase in distance over the straight line path is equal to some multiple of one-half wavelength

gabbro—a granular igneous rock of basaltic composition with a coarse-grained texture

gardening—the overturning, reworking, and changing of the lunar surface due to such processes as meteoroid impact, volcanic action, aging, and such

Gaussian distribution—normal statistical distribution

graviton—the hypothetical elementary unit of gravitation that is equivalent to the electron in electromagnetic theory

holocrystalline—consisting wholly of crystals

ilmenite—a mineral rich in titanium and iron; usually black with a submetallic luster

indurated—a term used to describe masses that have been hardened by heat; baked

isophote—a line of equal or constant illuminance

isostatic—subjected to equal pressure from all sides

isotopic—relating to, or having the relationship of any of two or more species of atoms of a chemical element that possess the same atomic number and position in the periodic table and nearly identical chemical behavior but with differing atomic mass or mass number and different behavior in the mass spectrograph, in radioactive transformations, and in physical properties; formed in the same sedimentary basin or geologic province

isotropic—exhibiting properties (as velocity of light transmission) with the same values when measured along axes in all directions

lamella—a layer of a cell wall

lath—a long thin mineral crystal

limb—the edge of the apparent disk of a celestial body

lithic—of, relating to, or made of stone

lithology—the physical character of a rock, as determined with the unaided eye or with a low-power magnifier

lossy—descriptive of an insulating material that dissipates electrical energy, usually in excess of that normally expected

maar—a crater formed by violent explosion not accompanied by igneous extrusion

mafic—pertaining to or composed dominantly of the magnesian rock-forming silicates

magma—molten rock material that is liquid or pasty

magnetosphere—the region of the atmosphere where the geomagnetic field plays an important role; the magnetosphere extends to the boundary between the atmosphere and interplanetary plasma

mascon—a large mass concentration beneath the surface of the Moon

maskelynite—a feldspar found in meteorites

massif—a mountainous mass

metamorphic—a term used to describe rocks that have formed in a solid state as a result of drastic changes in temperature, pressure, and chemical environment

mica—any of various colored or transparent minerals crystallizing in monoclinic forms that readily separate into very thin leaves

morphology—the study of the shape or form of geologic features

multiplex—to transmit two or more signals simultaneously within a single channel

muscovite—a mineral that is a colorless to pale brown potassium mica

mylonite—a fine-grained laminated rock formed by extreme microbrecciation and milling of rocks during movement on fault surfaces; metamorphism is dominately cataclastic with little or no growth of new crystals

norite—a type of gabbro in which orthopyroxene is dominant over clinopyroxene

oikocryst—a matrix or host crystal through which smaller crystals (chadacrysts) of other minerals are distributed as poikilitic inclusions

olivine—an igneous mineral that consists of a silicate of magnesium and iron

ophitic—a rock texture characterized by lath-shaped plagioclase crystals enclosed in augite

peridotite—an essentially nonfeldspathic plutonic rock consisting of olivine, with or without other dark minerals

perilune—the orbital point nearest the Moon, when the Moon is the center of attraction

permeability—the ratio of the magnetic induction to the magnetic-field intensity in the same region

phenocryst—a large crystal of the earliest generation in a porphyritic igneous rock

photogrammetry—the science of obtaining reliable measurements by means of photography

photosphere—the intensely bright portion of the Sun visible to the unaided eye

pigeonite—a variety of pyroxene

plagioclase—a feldspar mineral composed of varying amounts of sodium and calcium with aluminum silicate

plasma—an electrically conductive gas; specifically, a mass of ionized gas flowing out of the Sun

plutonic—pertaining to igneous rock that crystallizes at depth

poikilitic—a term to describe the condition in which small granular crystals are irregularly scattered without common orientation in a larger crystal of another mineral

porphyritic—having larger crystals set in a finer groundmass

pyroxene—a mineral occurring in short, thick, prismatic crystals or in square cross section; often laminated; and varying in color from white to dark green or black (rarely blue)

rarefaction wave—a wave in a compressible fluid such that when a fluid particle crosses the wave in the direction of its motion, the density and pressure of the particle decrease

regolith—the layer of fragmental debris that overlies consolidated bedrock

slickenside—a polished and striated surface that results from friction along a fault plane

solar wind—streams of plasma flowing outward from the Sun

spall—a relatively thin, sharp-edged piece of rock that has been produced by exfoliation

specular reflection—reflection in which the reflected radiation is not diffused

spinel—a mineral that is noted for great hardness $(MgAl_2O_4)$

talus—a collection of fallen disintegrated material that has formed a slope at the foot of a steeper declivity

tectonism—crustal instability; the structural behavior of an element of the crust of the Earth during or between major cycles of sedimentation

tektite—a glassy body of probably meteoritic origin and of rounded but indefinite shape

terminator—the line separating illuminated and dark portions of a celestial body

terra—that portion of the lunar surface other than the maria;

the lighter area of the Moon that is visible to the unaided eye

translunar—outside the orbit of the Moon

transponder—a combined receiver and transmitter which transmits signals automatically when triggered by an interrogator

troilite—a mineral that is native ferrous sulfide

vesicle—a small cavity in a mineral or rock, ordinarily produced by expansion of vapor in a molten mass

vug—a small cavity in a rock

zodiacal light—a faint cone of light extending upward from the horizon in the direction of the ecliptic

APPENDIX B

Abbreviations and Acronyms

ALFMED	Apollo light flash moving emulsion detector	LMS	lunar mass spectrometer; also known as the LACE
ALSE	Apollo lunar sounder experiment	LNPE	lunar neutron probe experiment
ALSEP	Apollo lunar surface experiments package	LRC	NASA Langley Research Center
ARC	NASA Ames Research Center	LRL	Lunar Receiving Laboratory, NASA Lyndon B. Johnson Space Center
ASSB	Apollo Site Selection Board		
ATS	Applications Technology Satellite	LRV	lunar roving vehicle (Rover)
BIOCORE	biological cosmic ray experiment	LSCRE	lunar surface cosmic ray experiment
CDR	commander	LSG	lunar surface gravimeter
c.g.	center of gravity	LSPE	lunar seismic profiling experiment
CM	command module	LSPET	Lunar Sample Preliminary Examination Team
CMP	command module pilot	LSS	lunar soil simulant
CN	cellulose nitrate	MCC	midcourse correction
CS	ALSEP central station	MESA	modularized equipment stowage assembly
CSAR	coherent synthetic aperture radar	OAO	Orbiting Astronomical Observatory
CSM	command and service module	OGO	Orbiting Geophysical Observatory
DAC	data acquisition camera	ORNL	Oak Ridge National Laboratory
DC	data camera	OSO	Orbiting Solar Observatory
DSEA	data storage electronics assembly	PLSS	portable life-support system
DT	drive tube	RCS	reaction control system
DU	digital unit	rev	revolution
EL	Hasselblad electric camera	RF	radio frequency
EP	explosive package	rms	root mean square
EVA	extravehicular activity	RTG	radioisotope thermoelectric generator
GET	ground elapsed time	SEM	scanning electron microscope
G.m.t.	Greenwich mean time	SEP	surface electrical properties
GOA	geometrical optics approximation	SIM	scientific instrument module
HED	horizontal electric dipole	SIVB	third stage (IVB) of Saturn launch vehicle
HFE	heat flow experiment	SM	service module
HZE	high-charge energy	TD&E	transposition, docking, and extraction
IAU	International Astronomical Union	TEC	transearth coast
IR	infrared	TEI	transearth injection
ISR	infrared scanning radiometer	TGE	traverse gravimeter experiment
JSC	NASA Lyndon B. Johnson Space Center	TLC	translunar coast
KREEP	potassium, rare-Earth elements, and phosphorus	TLD	thermoluminescence dosimetry
		TLI	translunar injection
KSC	NASA John F. Kennedy Space Center	UV	ultraviolet
LACE	lunar atmospheric composition experiment; also known as the LMS	UVS	ultraviolet spectrometer
		VCO	voltage controlled oscillator
LEAM	lunar ejecta and meteorites experiment	VHBW	very-high-speed black-and-white (film)
LET	linear energy transfer	VHF	very high frequency
LM	lunar module	VMD	vertical magnetic dipole
LMP	lunar module pilot	VSA	vibrating string accelerometer

APPENDIX C

Units and Unit-Conversion Factors

In this appendix are the names, abbreviations, and definitions of International System (SI) units used in this report and the numerical factors for converting from SI units to more familiar units.

Names of International Units Used in This Report

Physical quantity	Name of unit	Abbreviation	Definition of abbreviation
Basic Units			
Length	meter	m	
Mass	kilogram	kg	
Time	second	sec	
Electric current	ampere	A	
Temperature	kelvin	K	
Luminous intensity	candela	cd	
Derived Units			
Area	square meter	m^2	
Volume	cubic meter	m^3	
Frequency	hertz	Hz	sec^{-1}
Density	kilogram per cubic meter	kg/m^3	
Velocity	meter per second	m/sec	
Angular velocity	radian per second	rad/sec	
Acceleration	meter per second squared	m/sec^2	
Angular acceleration	radian per second squared	rad/sec^2	
Force	newton	N	$kg \cdot m/sec^2$
Pressure	newton per square meter	N/m^2	
Work, energy, quantity of heat	joule	J	$N \cdot m$
Power	watt	W	J/sec
Voltage, potential difference, electromotive force	volt	V	W/A
Electric field strength	volt per meter	V/m	
Electric resistance	ohm	Ω	V/A
Electric capacitance	farad	F	$A \cdot sec/V$
Magnetic flux	weber	Wb	$V \cdot sec$
Inductance	henry	H	$V \cdot sec/A$
Magnetic flux density	tesla	T	Wb/m^2
Magnetic field strength	ampere per meter	A/m	
Luminous flux	lumen	lm	$cd \cdot sr$
Luminance	candela per square meter	cd/m^2	
Illumination	lux	lx	lm/m^2
Specific heat	joule per kilogram kelvin	$J/kg \cdot K$	
Thermal conductivity	watt per meter kelvin	$W/m \cdot K$	
Supplementary Units			
Plane angle	radian	rad	
Solid angle	steradian	sr	

Unit Prefixes

Prefix	Abbreviation	Factor by which unit is multiplied
giga...............................	G	10^9
mega..............................	M	10^6
kilo...............................	k	10^3
centi..............................	c	10^{-2}
milli	m	10^{-3}
micro	μ	10^{-6}
nano	n	10^{-9}

Unit-Conversion Factors

To convert from—	To—	Multiply by—
ampere/meter	oersted	1.257×10^{-2}
candela/meter^2	foot-lambert	2.919×10^{-1}
candela/meter^2	lambert	3.142×10^{-4}
joule	British thermal unit (International Steam Table)	9.479×10^{-4}
joule	Calorie (International Steam Table)	2.388×10^{-1}
joule	electron volt	6.242×10^{18}
joule	erg	1.000×10^7 a
joule	foot-pound force	7.376×10^{-1}
joule	kilowatt-hour	2.778×10^{-7}
joule	watt-hour	2.778×10^{-4}
kelvin	degrees Celsius (temperature)	$t_C = t_K - 273.15$
kelvin	degrees Fahrenheit (temperature)	$t_F = 9/5 \ t_K - 459.67$
kilogram	gram	1.000×10^3 a
kilogram	kilogram mass	1.000×10^3 a
kilogram	pound mass (pound mass avoirdupois)	2.205×10^0
kilogram	slug	6.852×10^{-2}
kilogram	ton (short, 2000 pound)	1.102×10^{-3}
lumen/meter^2	foot-candle	9.290×10^{-2}
lumen/meter^2	lux	1.000×10^0 a
meter	angstrom	1.000×10^{10} a
meter	foot	3.281×10^0
meter	inch	3.937×10^1
meter	micron	1.000×10^6 a
meter	mile (U.S. statute)	6.214×10^{-4}
meter	nautical mile (international)	5.400×10^{-4}
meter	nautical mile (U.S.)	5.400×10^{-4}
meter	yard	1.094×10^0
meter/second^2	foot/second^2	3.281×10^0
meter/second^2	inch/second^2	3.937×10^1
newton	dyne	1.000×10^5 a
newton	kilogram force (kgf)	1.020×10^{-1}
newton	pound force (avoirdupois)	2.248×10^{-1}
newton/meter^2	atmosphere	9.870×10^{-6}
newton/meter^2	centimeter of mercury (0° C)	7.501×10^{-4}
newton/meter^2	inch of mercury (32° F)	2.953×10^{-4}
newton/meter^2	inch of mercury (60° F)	2.961×10^{-4}
newton/meter^2	millimeter of mercury (0° C)	7.501×10^{-3}
newton/meter^2	torr (0° C)	7.501×10^{-3}
radian	degree (angle)	5.730×10^1
radian	minute (angle)	3.438×10^3
radian	second (angle)	2.063×10^5

Unit-Conversion Factors—Concluded

To convert from—	To—	Multiply by—
tesla	gamma	1.000×10^9 [a]
tesla	gauss	1.000×10^4 [a]
watt	British thermal unit (thermochemical)/ second	9.484×10^{-4}
watt	calorie (thermochemical)/second	2.390×10^{-1}
watt	foot-pound force/second	7.376×10^{-1}
watt	horsepower (550 foot-pound force/second)	1.341×10^{-3}
weber	maxwell	1.000×10^8 [a]

[a]An exact definition.

1. Report No. NASA SP-330	2. Government Accession No.	3. Recipient's Catalog No.
4. Title and Subtitle APOLLO 17 PRELIMINARY SCIENCE REPORT		5. Report Date December 1973
		6. Performing Organization Code
7. Author(s) NASA Editorial Review Board, Robert A. Parker (Chairman)		8. Performing Organization Report No. JSC S-381
9. Performing Organization Name and Address Lyndon B. Johnson Space Center (JSC) Houston, Texas 77058		10. Work Unit No. 914-40-52-01-73
		11. Contract or Grant No.
12. Sponsoring Agency Name and Address National Aeronautics and Space Administration Washington, D.C. 20546		13. Type of Report and Period Covered Special Publication
		14. Sponsoring Agency Code

15. Supplementary Notes
The JSC Director has waived the use of the International System of Units (SI) for this special publication, because, in his judgment, the use of SI units would impair the usefulness of the report or result in excessive cost.

16. Abstract

The Apollo 17 flight and lunar landing, the sixth and final lunar landing and third extended science capability mission in the Apollo Program, are discussed with emphasis on the scientific endeavors conducted on the lunar surface. The scientific investigation of the mission is presented in three interrelated types of activities: the lunar surface sampling and observation, the lunar surface experiments, and the inflight experiments. Collection, documentation, and description of the lunar samples are discussed with a preliminary evaluation and analysis. The lunar surface experiments are described, including the results and their relationship to the scientific objectives of each experiment. The geochemical, photographic, geophysical, topographic, and medical data resulting from experiments conducted in flight are presented.

17. Key Words (Suggested by Author(s)) ˙Experimentation ˙Lunar Geology ˙Observation ˙Apollo 17 Flight ˙Apollo Project (Program)		18. Distribution Statement		
19. Security Classif. (of this report) None	20. Security Classif. (of this page) None		21. No. of Pages	22. Price*

*"The aeronautical and space activities of the United States shall be
conducted so as to contribute . . . to the expansion of human knowl-
edge of phenomena in the atmosphere and space. The Administration
shall provide for the widest practicable and appropriate dissemination
of information concerning its activities and the results thereof."*
—NATIONAL AERONAUTICS AND SPACE ACT OF 1958

NASA SCIENTIFIC AND TECHNICAL PUBLICATIONS

TECHNICAL REPORTS: Scientific and
technical information considered important,
complete, and a lasting contribution to existing
knowledge.

TECHNICAL NOTES: Information less broad
in scope but nevertheless of importance as a
contribution to existing knowledge.

TECHNICAL MEMORANDUMS:
Information receiving limited distribution
because of preliminary data, security classifica-
tion, or other reasons. Also includes conference
proceedings with either limited or unlimited
distribution.

CONTRACTOR REPORTS: Scientific and
technical information generated under a NASA
contract or grant and considered an important
contribution to existing knowledge.

TECHNICAL TRANSLATIONS: Information
published in a foreign language considered
to merit NASA distribution in English.

SPECIAL PUBLICATIONS: Information
derived from or of value to NASA activities.
Publications include final reports of major
projects, monographs, data compilations,
handbooks, sourcebooks, and special
bibliographies.

TECHNOLOGY UTILIZATION
PUBLICATIONS: Information on technology
used by NASA that may be of particular
interest in commercial and other non-aerospace
applications. Publications include Tech Briefs,
Technology Utilization Reports and
Technology Surveys.

Details on the availability of these publications may be obtained from:

SCIENTIFIC AND TECHNICAL INFORMATION OFFICE

NATIONAL AERONAUTICS AND SPACE ADMINISTRATION
Washington, D.C. 20546